MECHANISM-BASED DESIGN OF COMPOSITE STRUCTURES

FINAL REPORT

Volume I:

- Executive Summary
- Overview Papers
- Research Papers on Micromechanics and Computer-Aided Design Tools

Volume II:

- **Research Papers on Micromechanics and Computer-Aided Design Tools**

Volume III:

- Research Papers on Processing and Performance

DISTRIBUTION STATEMENT A
Approved for public release;
Distribution Unlimited

Program Director:
George J. Dvorak
Rensselaer Polytechnic Institute
Troy, NY 12180-3590

University Research Initiative
Contract No.: N00014-92J-1779
May 1, 1992 - August 30, 1997

Sponsored by the Defense Advanced Research Projects Agency
Dr. William Coblenz

Monitored by the Office of Naval Research
Dr. Steven Fishman

19980209 075

MECHANISM-BASED DESIGN OF COMPOSITE STRUCTURES

FINAL REPORT

Volume I:

- Executive Summary
- Overview Papers
- Research Papers on Micromechanics and Computer-Aided Design Tools

Volume II:

- **Research Papers on Micromechanics and Computer-Aided Design Tools**

Volume III:

- Research Papers on Processing and Performance

Program Director:
George J. Dvorak
Rensselaer Polytechnic Institute
Troy, NY 12180-3590

University Research Initiative
Contract No.: N00014-92J-1779
May 1, 1992 - August 30, 1997

Sponsored by the Defense Advanced Research Projects Agency
Dr. William Coblenz

Monitored by the Office of Naval Research
Dr. Steven Fishman

MECHANISM-BASED DESIGN OF COMPOSITE STRUCTURES

Volume II:

- **Research Papers on Micromechanics and Computer-Aided Design Tools**

Dvorak, G.J., ASME 1992 Nadai Lecture - Micromechanics of Inelastic Composite Materials: Theory and Experiment.

Dvorak, G.J., Bahei-El-Din, Y.A., and Wafa, A.M., The Modeling of Inelastic Composite Materials with the Transformation Field Analysis.

Dvorak, G.J., and Zuiker, J.R., Effective Local Properties for Modelling of Functionally Graded Composite Materials.

Dvorak, G.J. and Sejnoha, M., Initial Failure Maps for Fibrous CMC Laminates.

Dvorak, G.J., and Sejnoha, M., Initial Failure Maps for Ceramic and Metal Matrix Composite Laminates.

Fish, J. and Belsky, V., Convergence of the Multi-Grid Method for a Periodic Heterogeneous Medium. Part 1:1-D Case.

Fish, J., and Belsky, V., Multi-Grid Method for a Periodic Heterogeneous Media. Part 2: Multiscale Modeling and Quality Control in Multidimensional Case.

Fish, J., and Belsky, V., The Multi-Grid Method for a Periodic Heterogeneous Medium. Part 3: Multiscale Modeling and Adaptivity.

Fish, J., and Guttal, R., The *p*-version of Finite Element Method for Shell Analysis.

Fish, J., and Guttal, R., Recent Advances in The *p*-version of the Finite Element Method for Shells.

Fish, J., Pan, L., Belsky, V., and Gomaa, S., An Accelerated Unstructured Multigrid Method for Shells.

Fish, J., and Belsky, V., Generalized Aggregation Multilevel Solver.

Fish, J., and Guttal, R., The *s*-Version of Finite Element Method for Laminated Composites.

Fish, J., and Shek, K.-L., Computational Plasticity for Composite Structures Based on Mathematical Homogenization: Theory and Practice.

Fish, J., Suvorov, A., and Belsky, V., Hierarchical Composite Grid Method for Global-local Analysis of Laminated Composite Shells.

Fish, J., and Shek, K.-L., Finite Deformation Plasticity for Composite Structures: Computational Models and Adaptive Strategies.

O'Bara, R.M., Beall, M.W., and Shephard, M.S., Analysis Model Visualization and Graphical Analysis Attribute Specification System.

Reiter, T., and Dvorak, G.J., Micromechanical Models for Graded Composite Materials.

Reiter, T., and Dvorak, G.J., Micromechanical Models for Graded Composite Materials: II. Thermomechanical Loading.

Shek, K.-L., Beall, M.W., Dvorak, G.J., and Shephard, M.S., Bimodal Plasticity Evaluation Tool.

Shephard, M.S., Wong, V.S., Collar, R.R., and Wentorf, R., Reliable Automated Engineering Analysis in an Integrated Design Environment.

Shephard, M.S., Beall, M.W., Garimella, R., and Wentorf, R., Automatic Construction of 3-D Models in Multiple Scale Analysis.

Shephard, M.S., and Schroeder, W.J., Analysis Data for Visualization.

Zuiker, J.R., and Dvorak, G.J., Coupling in the Mechanical Response of Functionally Graded Composite Materials.

ASME 1992 Nadai Lecture—Micromechanics of Inelastic Composite Materials: Theory and Experiment

George J. Dvorak
Department of Civil and Environmental Engineering, Rensselaer Polytechnic Institute, Troy, NY 12180
Fellow ASME

Some recent theoretical and experimental results on modeling of the inelastic behavior of composite materials are reviewed. The transformation field analysis method (G. J. Dvorak, Proc. R. Soc. London, *Series A437, 1992, pp. 311-327) is a general procedure for evaluation of local fields and overall response in representative volumes of multiphase materials subjected to external thermomechanical loads and transformations in the phases. Applications are presented for systems with elastic-plastic and viscoelastic constituents. The Kroner-Budiansky-Wu and the Hill self-consistent models are corrected to conform with the generalized Levin formula. Recent experimental measurements of yield surfaces and plastic strains on thin-walled boron-aluminum composite tubes are interpreted with several micromechanical models. The comparisons show that unit cell models can provide reasonably accurate predictions of the observed plastic strains, while models relying on normality of the plastic strain increment vector to a single overall yield surface may not capture the essential features of the inelastic deformation process.*



George J. Dvorak

Dr. Dvorak was born and educated in Prague, Czechoslovakia. In 1964 he joined the solid mechanics group at Brown University, where he studied with D. C. Drucker. His initial research interests were in modeling of mechanisms of fracture in metals. He started to work in mechanics of composite materials in the late 1960's. In this field, he developed several theoretical models of plasticity of composite materials, applied them to problems in fatigue and fracture of fibrous metal matrix laminates, and directed experimental studies to support predictions of the theoretical models. His other interests include damage development in brittle and ductile systems, thermal stresses and heat conduction in coated fiber composites, and modeling of fabrication processes in ductile intermetallic matrix composites. Among his significant recent achievements is the formulation of the uniform field technique for heterogeneous solids, the transformation field method described, in part, in the Nadai Award Paper. He is also credited with finding many exact results in micromechanics, and with correcting some errors in heuristic micromechanical models. After holding teaching positions at Duke University and The University of Utah, Dr. Dvorak is now Head of the Civil and Environmental Engineering Department at Rensselaer, where he also directs an ARPA/ONR sponsored URI project on mechanism-based design of high-temperature composite materials.

George J. Weng

1 Introduction

This paper provides a brief summary of some recent results in inelastic analysis of heterogeneous media and composite materials. Both theoretical and experimental aspects are explored. In the theoretical part, we discuss the transformation field analysis method for incremental solution of thermomechanical loading and eigenstrain problems, which was recently introduced by Dvorak (1991, 1992). When used with a selected

Contributed by the Materials Division for publication in the JOURNAL OF ENGINEERING MATERIALS AND TECHNOLOGY. Manuscript received by the Materials Division July 19, 1993.

micromechanical model, the analysis provides piecewise uniform approximations of the instantaneous local strain and stress fields in the phases, and estimates of the overall instantaneous thermomechanical properties of representative volumes of composite materials consisting of elastic-plastic, viscoelastic, or viscoplastic phases. The method incorporates many of the currently used approaches to problems of this kind as special cases, this is shown for unit cell models, the Mori-Tanaka and the self-consistent methods, as well as for other methods that utilize the Eshelby solution. The experimental part focuses on detection of yield surfaces and plastic strains in unidirectionally reinforced boron-aluminum tubes subjected to incremental loading in axial tension, torsion and internal pressure. Interpretation of the experimental results with several theoretical models shows that the observed shape and position of the yield surfaces is well predicted by the bimodal plasticity theory of Dvorak and Bahei-El-Din (1987), and the plastic strains are reasonably well approximated by the periodic hexagonal array unit cell model of Teply and Dvorak (1988). The experimentally found overall yield surface is shown to be a locus of yield vertices, where the plastic strain increments are confined within a cone of normals. Therefore, theories based on normality to a single yield surface are bound to be of little value in predicting the observed response.

Section 2 contains definitions of local and overall properties and of the eigenstress and eigenstrain influence functions and concentration factors that form a foundation for the transformation analysis of micromechanical models. Section 3 shows the formulation leading to the governing equations for local stress and strain fields in composites with elastic-plastic and viscoelastic phases. Section 4 discusses corrections of certain shortcomings in the Kroner-Budiansky-Wu (KBW), and Hill (1965) self-consistent models that are indicated by the formulation of the transformation method. Section 5 surveys the bimodal theory and the periodic hexagonal array model that are used in §6 to interpret the experimental results.

The notation used is fashioned after that introduced by Hill (1963); (6×1) vectors are denoted by boldface lower case Roman or Greek letters (6×6) matrices by boldface uppercase Roman letters, and $\mathbf{A}\mathbf{A}^{-1} = \mathbf{A}^{-1}\mathbf{A} = \mathbf{I}$, if the inverse exists. Scalars are denoted by lightface letters. Script characters are reserved for quantities that change during deformation. Volume averages of fields in V_r, such as $\mathbf{A}_r(\mathbf{x})$ or $\epsilon_r(\mathbf{x})$ or of $\sigma(\mathbf{x})$ in V are denoted by $\mathbf{A}_r$, ϵ_r or σ.

2 Overall and Local Fields

Consider a representative volume V of a heterogeneous medium of any microgeometry, e.g., that found in a polycrystal, fiber or particulate composite, or laminated plate or shell. The medium consists of two or more perfectly bonded homogeneous or homogenized elastic phases residing in several local volumes V_r $(r = 1, 2, \ldots N)$, none containing more than one phase. The geometry of the heterogeneous microstructure is given or assumed to be represented by a certain micromechanical model, such as a unit cell model of a periodic or random microstructure, or the self-consistent and Mori-Tanaka models. In the SCM or M-T models, V_r would refer to usually ellipsoidal inhomogeneities of one phase. In the unit cell models of composites or polycrystals, and in several models of laminated plates or shells which regard the composite structure as consisting of homogeneous layers with certain effective properties, the local fields are typically found with the finite element method. In such models, V_r would designate a single constant strain element, or a volume associated with an integration point in a higher order element.

At any given time t, the volume V is subjected to certain homogeneous boundary conditions on the surface S of V,

$$\mathbf{u}(S) = \epsilon^0(t)\mathbf{x} \quad \mathbf{t}(S) = \sigma^0(t)\mathbf{n}, \tag{1}$$

where σ^0 and ϵ^0 denote uniform overall stress and strain derived from prescribed tractions $\mathbf{t}(S)$ and displacements $\mathbf{u}(S)$, defined in cartesian coordinates $\mathbf{x}$.

In addition to (1), the representative volume may be subjected to certain local eigenstrain and eigenstress fields in $V_r \in V$,

$$\mu_r(\mathbf{x},t) = \epsilon_r^{in}(\mathbf{x},t) + \mathbf{m}_r\theta^0 + \ldots \quad \lambda_r(\mathbf{x},t) = \sigma_r^{re}(\mathbf{x},t) + \ell_r\theta^0 + \ldots \tag{2}$$

where ϵ_r^{in} is an inelastic strain caused in V_r during previous loading steps, and σ_r^{re} the corresponding relaxation stress that would be created by ϵ_r^{in} at a fully constrained material point $\mathbf{x}$; $\mathbf{m}_r$ is the thermal strain tensor containing the coefficients of thermal expansion of the phase residing in V_r, ℓ_r is the associated thermal stress tensor, and θ^0 a prescribed uniform change in temperature. Additional contributions in (2) may be provided by such sources as swelling associated with moisture adsorption or diffusion, and by shape and volume changes produced by a phase transformation. While the fields (2) are, in general, independent of the current applied loads or displacements (1), and of each other, they have to be compatible with (1) in the sense that each component of (2) must produce a uniform overall eigenstrain in V under $\mathbf{t}(S) = \mathbf{0}$, and a uniform overall eigenstress under $\mathbf{u}(S) = \mathbf{0}$. For example, the inelastic fields ϵ_r^{in} and σ_r^{re} would result from a certain history of uniform overall deformation of V, and the thermal fields from a uniform change of temperature in V.

In what follows, the local eigenstrains and eigenstresses will be referred to jointly as transformation fields, and regarded as deformations or loads imposed in addition to but independently of (1) on an otherwise elastic heterogeneous solid.

At small total strains, one may assume that the total local fields caused in the local volumes $r = 1, 2, \ldots N$, by the loads (1) and transformations (2) can be additively decomposed as

$$\epsilon_r(\mathbf{x},t) = \mathbf{M}_r\sigma_r(\mathbf{x},t) + \mu_r(\mathbf{x},t), \quad \sigma_r(\mathbf{x},t) = \mathbf{L}_r\epsilon_r(\mathbf{x},t) + \lambda_r(\mathbf{x},t), \tag{3}$$

where the $\mathbf{L}_r$ and $\mathbf{M}_r = \mathbf{L}_r^{-1}$ are the elastic stiffness and compliance tensors of the phase within V_r. The $\mu_r(\mathbf{x}, t)$ represent that part of the total local strain not caused by stress-induced elastic deformation, and $\lambda_r(\mathbf{x}, t)$ that part of the total stress not related to the total local strain. Since the eigenstrain leaves an unconstrained volume V_r free of stress, one finds that for $\epsilon_r = \mathbf{0}$, or for $\sigma_r = \mathbf{0}$,

$$\lambda_r(\mathbf{x},t) = -\mathbf{L}_r\mu_r(\mathbf{x},t) \quad \mu_r(\mathbf{x},t) = -\mathbf{M}_r\lambda_r(\mathbf{x},t). \tag{4}$$

The local fields caused in V by the purely mechanical, uniform overall strains and stresses (1) may be evaluated using certain mechanical influence functions suggested by Hill (1963),

$$\epsilon_r(\mathbf{x},t) = \mathbf{A}_r(\mathbf{x})\epsilon^0(t) \quad \sigma_r(\mathbf{x},t) = \mathbf{B}_r(\mathbf{x})\sigma^0(t). \tag{5}$$

These can be found from an elasticity solution of a selected micromechanical model of the heterogeneous material in V, and are thus assumed to be known.

The local fields caused by the transformation (2) are the residual fields that are present in V even if the overall applied strain or stress in (1) and (5) vanish; their evaluation has been discussed in some detail by Dvorak and Benveniste (1992). Of particular interest here is the response of the elastic heterogeneous medium both to piecewise uniform transformations $\mu_r(t)$, $\lambda_r(t)$ in the local volumes V_r, e.g., those induced by a uniform change in temperature or by a phase transformation, and to nonuniform transformation fields that may be induced in V_r, for example, by inelastic deformation. In the latter case, the subdivision of the individual phases into local volumes V_r must be sufficiently refined, so that the actual transformation fields (2) can be approximated by piecewise uniform distributions $\mu_r(t)$, $\lambda_r(t)$. In either case, the residual fields are considered as caused by a piecewise uniform distribution or approximation of (2), and are sought in the form

$$\epsilon_r(\mathbf{x},t)=\sum_{s=1}^{N}\mathbf{D}_{rs}(\mathbf{x})\mu_s(t)\quad \sigma_r(\mathbf{x},t)=\sum_{s=1}^{N}\mathbf{F}_{rs}(\mathbf{x})\lambda_r(t). \tag{6}$$

The $\mathbf{D}_{rs}(\mathbf{x})$ and $\mathbf{F}_{rs}(\mathbf{x})$ are the transformation influence functions (Dvorak, 1990), which may be derived either in terms of the Green's function of a certain comparison homogeneous medium, or from the same micromechanical models that one would use to find the mechanical influence functions in (5), under the homogeneous boundary conditions $\epsilon^0 = \mathbf{0}$ and $\sigma^0 = \mathbf{0}$, respectively; (Dvorak and Benveniste, 1992). For example, in two-phase media, with $r = \alpha, \beta$, there are exact connections involving phase properties and the mechanical influence functions (Dvorak 1990, Eqs. 123-126)

$$\begin{aligned}&\mathbf{D}_{r\alpha}=(\mathbf{I}-\mathbf{A}_r)(\mathbf{L}_\alpha-\mathbf{L}_\beta)^{-1}\mathbf{L}_\alpha \quad \mathbf{D}_{r\beta}=-(\mathbf{I}-\mathbf{A}_r)(\mathbf{L}_\alpha-\mathbf{L}_\beta)^{-1}\mathbf{L}_\beta\\ &\mathbf{F}_{r\alpha}=(\mathbf{I}-\mathbf{B}_r)(\mathbf{M}_\alpha-\mathbf{M}_\beta)^{-1}\mathbf{M}_\alpha \quad \mathbf{F}_{r\beta}=-(\mathbf{I}-\mathbf{B}_r)(\mathbf{M}_\alpha-\mathbf{M}_\beta)^{-1}\mathbf{M}_\beta.\end{aligned} \tag{7}$$

In multiphase solids, the mechanical influence functions in (5) are often replaced by their phase volume averages, the mechanical strain and stress concentration factors $\mathbf{A}_r$ and $\mathbf{B}_r$. Similarly, the transformation influence functions $\mathbf{D}_{rs}(\mathbf{x})$ and $\mathbf{F}_{rs}(\mathbf{x})$ in (6) are replaced by their volume averages $\mathbf{D}_{rs}$ and $\mathbf{F}_{rs}$, taken over V_r. If the $\mathbf{A}_r$ and $\mathbf{B}_r$ are estimated from either the self-consistent or Mori-Tanaka models, then Dvorak and Benveniste (1992 Eq. 59) show that the respective estimates of the $\mathbf{D}_{rs}$ and $\mathbf{F}_{rs}$ are given by the exact connections

$$\begin{aligned}&\mathbf{D}_{rs}=(\mathbf{I}-\mathbf{A}_r)(\mathbf{L}_r-\mathbf{L})^{-1}(\delta_{rs}\mathbf{I}-c_s\mathbf{A}_s^T)\mathbf{L}_s\\ &\mathbf{F}_{rs}=(\mathbf{I}-\mathbf{B}_r)(\mathbf{M}_r-\mathbf{M})^{-1}(\delta_{rs}\mathbf{I}-c_s\mathbf{B}_s^T)\mathbf{M}_s,\end{aligned}\qquad r,s=1,2\ldots N \tag{8}$$

here the $c_s = V_s/V$ are the phase volume fractions, and $\mathbf{L}$, $\mathbf{M}$ designate the respective estimates of the overall stiffness and compliance tensors; δ_{rs} is the Kronecker symbol, but no summation is implied by the repeated subscripts.

Evaluation of the mechanical and transformation concentration factor tensors in unit cell models has been discussed by Dvorak et al. (1993). In particular, the kth column of the $\mathbf{D}_{rs}$ matrix for any two elements V_r and V_s of a unit cell was found as

$$\mathbf{d}_{rs}^k=\hat{\mathbf{B}}_s\mathbf{P}_s\mathbf{K}^{-1}\mathbf{f}_r, \tag{9}$$

where the local strains ϵ_s are related to the overall displacements $\mathbf{u}$ by $\epsilon_s = \hat{\mathbf{B}}_s\mathbf{P}_s\mathbf{u}$, $\mathbf{K}$ is the overall stiffness matrix, and $\mathbf{f}_r$ is the overall load vector corresponding to the eigenstrain μ_r.

Dvorak and Benveniste (1992 Eqs. 47-50) show that regardless of the evaluation method, the transformation influence functions $\mathbf{F}_{rs}$ and $\mathbf{D}_{rs}$ must comply with the exact connections

$$\begin{aligned}&\sum_{r=1}^{N}\mathbf{D}_{sr}(\mathbf{x})=\mathbf{I}-\mathbf{A}_s(\mathbf{x}) \quad \sum_{r=1}^{N}\mathbf{F}_{sr}(\mathbf{x})=\mathbf{I}-\mathbf{B}_s(\mathbf{x})\\ &\sum_{r=1}^{N}\mathbf{D}_{sr}(\mathbf{x})\mathbf{M}_r=\mathbf{0} \quad \sum_{r=1}^{N}\mathbf{F}_{sr}(\mathbf{x})\mathbf{L}_r=\mathbf{0}\\ &c_s\mathbf{D}_{sr}\mathbf{M}_r=c_r\mathbf{M}_s\mathbf{D}_{rs}^T \quad c_s\mathbf{F}_{sr}\mathbf{L}_r=c_r\mathbf{L}_s\mathbf{F}_{rs}^T\\ &\sum_{r=1}^{N}c_r\mathbf{D}_{rs}=\mathbf{0} \quad \sum_{r=1}^{N}c_r\mathbf{F}_{rs}=\mathbf{0}.\end{aligned} \tag{10}$$

One can easily verify that (10) are satisfied when the transformation influence functions are evaluated from (7); this has to be carried out numerically if the functions are found from (9). The estimates (8) comply with (10) for two-phase systems and in multiphase systems that consist of or are reinforced by inhomogeneities of the same shape and alignment, and thus admit only a single constraint tensor $\mathbf{L}^*$ or $\mathbf{M}^*$ (see (41) below). Such compliance does not obtain in systems with multiple $\mathbf{L}^*$ or $\mathbf{M}^*$. Benveniste et al. (1991) show that the self-consistent and Mori-Tanaka methods do or do not yield diagonally symmetric estimates of $\mathbf{L}$ under similar circumstances.

Note that the concentration factor tensors $\mathbf{A}_r$, $\mathbf{B}_r$, $\mathbf{D}_{rs}$ and $\mathbf{F}_{rs}$ follow from solutions of certain elasticity problems, and thus depend only on the elastic moduli $\mathbf{L}_r$, and on the overall and local geometry. As long as those remain constant under the loading conditions (1) and (2), so do the concentration factor tensors. (Of course, if the $\mathbf{L}_r$ change, e.g., as functions of temperature, then the concentration factors may need to be reevaluated.) Under such circumstances, the fields (5) and (6) may be superimposed, and the volume averages of the fields generated in each local volume V_r within the representative volume V by the loadings (1) and (2) may be written as

$$\epsilon_r(t)=\mathbf{A}_r\epsilon^0(t)+\sum_{s=1}^{N}\mathbf{D}_{rs}\mu_s(t)\quad \sigma_r(t)=\mathbf{B}_r\sigma^0(t)+\sum_{s=1}^{N}\mathbf{F}_{rs}\lambda_r(t). \tag{11}$$

Since the coefficients are constant, one may readily write the corresponding relations for the local strain and stress rates as

$$\dot{\epsilon}_r(t)=\mathbf{A}_r\dot{\epsilon}^0(t)+\sum_{s=1}^{N}\mathbf{D}_{rs}\dot{\mu}_s(t)\quad \dot{\sigma}_r(t)=\mathbf{B}_r\dot{\sigma}^0(t)+\sum_{s=1}^{N}\mathbf{F}_{rs}\dot{\lambda}_r(t). \tag{12}$$

Note that (11) and (12) represent three distinct fields that coexist in the heterogeneous solid under the loading conditions (1_1) and (2_1) or (1_2) and (2_2): One in response to overall uniform strain or stress, the residual field caused by the transformations, and the transformation strain or stress field itself. The first and the sum of the last two must comply with compatibility and equilibrium requirements. However, the eigenstrain and eigenstress fields themselves are not expected to meet such requirements, particularly at interfaces between phases or the V_r subvolumes. It is also of interest to note that if (11_1) is applied to the fields caused by a transformed homogeneous inclusion of ellipsoidal shape in an infinite homogeneous solid, then the self-induced strain in V_r is $\epsilon_r = \mathbf{D}_{rr}\mu_r = \mathbf{S}\mu_r$, and $\mathbf{D}_{rr} = \mathbf{S}$, the Eshelby tensor.

Turning our attention to the overall fields, we record here the relations between the local and overall total stresses and strains (Hill, 1963)

$$\epsilon(t)=\int_V\epsilon_r(\mathbf{x},t)dV\quad \sigma(t)=\int_V\sigma_r(\mathbf{x},t)dV. \tag{13}$$

These are valid for any representative volume V subjected to the boundary conditions (1) and/or transformations (2).

However, if (2) are applied in addition to (1), the transformation fields cause independent contributions to the total overall strain or stress. If V is free of external tractions, then the local eigenstrains $\mu_r(\mathbf{x}, t)$ cause an overall eigenstrain $\mu(t)$, and, if V is fully constrained then the local eigenstresses $\lambda_r(\mathbf{x}, t)$ cause an overall eigenstress $\lambda(t)$. We recall that to be admissible in (2), each of the local transformation fields should produce a uniform contribution to the respective overall field. In such circumstances, the local and overall transformation fields are connected by the Levin (1967) formula, generalized by Rice (1970) and Hill (1971), and derived by Dvorak (1991), and Dvorak and Benveniste (1992) in the form

$$\mu(t)=\int_V\mathbf{B}_r^T(\mathbf{x})\mu_r(\mathbf{x},t)dV\quad \lambda(t)=\int_V\mathbf{A}_r^T(\mathbf{x})\lambda_r(\mathbf{x},t)dV. \tag{14}$$

The overall response of the material within V to (1) and (2) then follows from the constitutive relations

$$\epsilon(t)=\mathbf{M}\sigma(t)+\mu(t)\quad \sigma(t)=\mathbf{L}\epsilon(t)+\lambda(t), \tag{15}$$

where $\mathbf{L}$ and $\mathbf{M} = \mathbf{L}^{-1}$ are the overall elastic stiffness and compliance tensors.

Since the $\mathbf{L}$ and $\mathbf{M}$ are constant, (15) provide an analogous relation for the overall rates as

$$\dot{\boldsymbol{\epsilon}}(t) = \mathbf{M}\dot{\boldsymbol{\sigma}}(t) + \dot{\boldsymbol{\mu}}(t) \quad \dot{\boldsymbol{\sigma}}(t) = \mathbf{L}\dot{\boldsymbol{\epsilon}}(t) + \dot{\boldsymbol{\lambda}}(t). \tag{16}$$

This may be compared with the more frequently used rate relations

$$\dot{\boldsymbol{\epsilon}}(t) = \mathfrak{M}\dot{\boldsymbol{\sigma}}(t) + \boldsymbol{m}\dot{\theta}(t) \quad \dot{\boldsymbol{\sigma}}(t) = \mathfrak{L}\dot{\boldsymbol{\epsilon}}(t) + \boldsymbol{\ell}\dot{\theta}(t), \tag{17}$$

where $\mathfrak{L}$ and $\mathfrak{M} = \mathfrak{L}^{-1}$ are the instantaneous overall stiffness and compliance tensors of the heterogeneous material in V, and $\boldsymbol{\ell}$, $\boldsymbol{m}$, are the instantaneous thermal stress and strain tensors, represented typically by (6×6) and (6×1) arrays, respectively. Since the instantaneous tensors reflect the presence of inelastic straining, they change during deformation. Their evaluation involves a total of $21 + 6 = 27$ coefficients and is often quite difficult. In contrast, the $\mathbf{L}$ and $\mathbf{M}$ in (15), (16) can be found relatively easily by several homogenization methods, and remain constant. This reduces the evaluation of the instantaneous response to finding the (6×1) array of overall eigenstrains $\boldsymbol{\mu}(t)$, or eigenstresses $\boldsymbol{\lambda}(t) = -\mathbf{L}\boldsymbol{\mu}(t)$. Of course, if some of the local transformations (2) are known, e.g., under a thermal change, then (15) readily provide corresponding contributions to the desired $\boldsymbol{\mu}(t)$ and $\boldsymbol{\lambda}(t)$.

3 The Transformation Field Analysis Method

Here we consider any of the composite materials discussed in §1, but allow for inelastic deformation of one or more phases. The response of the constituents may be described, for example, by certain constitutive relations that reflect elastic-plastic, viscoelastic and viscoplastic behavior. In general, each phase may exhibit a different type of inelastic response, providing that all conform with the additive decomposition of the total local strains and stresses indicated by (3). The goal is to extend the Eqs. (11) and (12) for the local fields under known overall and transformation loads and their rates into systems for evaluation of such fields during local inelastic deformation. Once the local fields are known, one can find the local inelastic strains and relaxation stresses from (2) and (3), and then employ (13) or (14) and (15) to find the overall instantaneous response.

First, (2) are converted to volume averages over V_r and used in (11) and (12), to separate the parts of $\boldsymbol{\mu}_r(t)$ and $\boldsymbol{\lambda}_r(t)$ that depend on known quantities, such as $\mathbf{m}_r\theta^0$ and $\boldsymbol{\ell}_r\theta^0$, from the $\boldsymbol{\epsilon}_r^{in}(t)$ and $\boldsymbol{\sigma}_r^{re}(t)$ that depend on the as yet unknown local stress or strain history. The thermal contributions can be written as (Dvorak and Benveniste, 1992, Eq. 76)

$$\mathbf{a}_r = \sum_{s=1}^{N} \mathbf{D}_{rs}\mathbf{m}_s, \quad \mathbf{b}_r = \sum_{s=1}^{N} \mathbf{F}_{rs}\boldsymbol{\ell}_s. \tag{18}$$

After rearrangement, (11) and (12) become

$$\boldsymbol{\epsilon}_r(t) - \sum_{s=1}^{N} \mathbf{D}_{rs}\boldsymbol{\epsilon}_s^{in}(t) = \mathbf{A}_r\boldsymbol{\epsilon}^0(t) + \mathbf{a}_r\theta^0$$

$$\boldsymbol{\sigma}_r(t) - \sum_{s=1}^{N} \mathbf{F}_{rs}\boldsymbol{\sigma}_s^{re}(t) = \mathbf{B}_r\boldsymbol{\sigma}^0(t) + \mathbf{b}_r\theta^0, \tag{19}$$

and

$$\dot{\boldsymbol{\epsilon}}_r(t) - \sum_{s=1}^{N} \mathbf{D}_{rs}\dot{\boldsymbol{\epsilon}}_s^{in}(t) = \mathbf{A}\dot{\boldsymbol{\epsilon}}^0(t) + \mathbf{a}_r\dot{\theta}^0(t)$$

$$\dot{\boldsymbol{\sigma}}_r(t) - \sum_{s=1}^{N} \mathbf{F}_{rs}\dot{\boldsymbol{\sigma}}_s^{re}(t) = \mathbf{B}_r\dot{\boldsymbol{\sigma}}^0(t) + \mathbf{b}_r\dot{\theta}^0(t). \tag{20}$$

Next, the local constitutive relations are introduced to express the local inelastic strains and their rates in terms of local stresses or stress rates. Similarly, the local relaxation stresses are written as functions of the local strains or strain rates. This provides governing equations for evaluation of the total local fields. The procedure is best illustrated by examples involving different types of phase response.

3.1 Elastic-Plastic Phases. The phases are assumed to be inviscid, hence one can adopt an arbitrary time scale and write the local constitutive relations for the total rates as in (17)

$$\dot{\boldsymbol{\epsilon}}_r(t) = \mathfrak{M}_r\dot{\boldsymbol{\sigma}}_r(t) + \boldsymbol{m}_r\dot{\theta}^0(t) \quad \dot{\boldsymbol{\sigma}}_r(t) = \mathfrak{L}_r\dot{\boldsymbol{\epsilon}}_r(t) + \boldsymbol{\ell}_r\dot{\theta}^0(t), \tag{21}$$

where $\mathfrak{M}_r = \mathfrak{L}_r^{-1}$, and $\boldsymbol{m}_r = -\mathfrak{L}_r\boldsymbol{\ell}_r$, are the instantaneous mechanical and thermal compliance and stiffness tensors; they depend both on the current state at t, and on the past history.

The inelastic rates follow from

$$\dot{\boldsymbol{\epsilon}}_r^{in}(t) = \mathfrak{M}_r^p\dot{\boldsymbol{\sigma}}_r(t) + \boldsymbol{m}_r^p\dot{\theta}^0(t) \quad \dot{\boldsymbol{\sigma}}_r^{re}(t) = \mathfrak{L}_r^p\dot{\boldsymbol{\epsilon}}_r(t) + \boldsymbol{\ell}_r^p\dot{\theta}^0(t), \tag{22}$$

where

$$\mathfrak{M}_r^p = \mathfrak{M}_r - \mathbf{M}_r \quad \mathfrak{L}_r^p = \mathfrak{L}_r - \mathbf{L}_r$$

$$\boldsymbol{m}_r^p = \boldsymbol{m}_r - \mathbf{m}_r \quad \boldsymbol{\ell}_r^p = \boldsymbol{\ell}_r - \boldsymbol{\ell}_r.$$

Moreover, we recall from (4) and (2) that

$$\dot{\boldsymbol{\sigma}}_r^{re}(t) = -\mathbf{L}_r\dot{\boldsymbol{\epsilon}}_r^{in}(t) \quad \dot{\boldsymbol{\epsilon}}_r^{in}(t) = -\mathbf{M}_r\dot{\boldsymbol{\sigma}}_r^{re}(t). \tag{23}$$

Now, substitute (22_1) into (23_1) and use the result to replace the relaxation stress terms in (19_2) and (20_2). An analogous sequence provides an expression for the inelastic strains in (19_1) and (20_1). For the composite material with elastic-plastic phases, this leads to the following systems of governing equations that must be satisfied by the local increments at each point t of the thermomechanical loading path,

$$\delta_{rs}\mathbf{I} + \sum_{s=1}^{N} \mathbf{F}_{rs}\mathbf{L}_s\mathfrak{M}_s^p\dot{\boldsymbol{\sigma}}_s = \mathbf{B}_r\dot{\boldsymbol{\sigma}}^0 + \left(\mathbf{b}_r - \sum_{s=1}^{N} \mathbf{F}_{rs}\mathbf{L}_s\boldsymbol{m}_s^p\right)\dot{\theta}^0$$

$$\delta_{rs}\mathbf{I} + \sum_{s=1}^{N} \mathbf{D}_{rs}\mathbf{M}_s\mathfrak{L}_s^p\dot{\boldsymbol{\epsilon}}_s = \mathbf{A}_r\dot{\boldsymbol{\epsilon}}^0 + \left(\mathbf{a}_r - \sum_{s=1}^{N} \mathbf{D}_{rs}\mathbf{M}_s\boldsymbol{\ell}_s^p\right)\dot{\theta}^0. \tag{24}$$

where δ_{rs} is the Kronecker's symbol, but no summation is implied by repeated subscripts.

The solution of the governing equations is usually sought in the form

$$\dot{\boldsymbol{\sigma}}_r = \mathfrak{B}_r\dot{\boldsymbol{\sigma}}^0 + \boldsymbol{\mathfrak{b}}_r\dot{\theta}^0 \quad \dot{\boldsymbol{\epsilon}}_r = \mathfrak{A}_r\dot{\boldsymbol{\epsilon}}^0 + \boldsymbol{a}_r\dot{\theta}^0, \tag{25}$$

where $\mathfrak{B}_r$, $\boldsymbol{\mathfrak{b}}_r$ and $\mathfrak{A}_r$, $\boldsymbol{a}_r$ are the instantaneous mechanical and thermal concentration factor tensors.

For example, in a two-phase system, $r, s = \alpha, \beta$, under a history of uniform overall stress applied through certain tractions at the surface S of V, and uniform temperature change in V, one can solve (24_1) and find the instantaneous stress concentration factors as

$$\mathfrak{B}_\alpha = [\mathbf{I} + \mathbf{F}_{\alpha\alpha}\mathbf{L}_\alpha\mathfrak{M}_\alpha^p - (c_\alpha/c_\beta)\mathbf{F}_{\alpha\beta}\mathbf{L}_\beta\mathfrak{M}_\beta^p]^{-1} \times [\mathbf{B}_\alpha - (1/c_\beta)\mathbf{F}_{\alpha\beta}\mathbf{L}_\beta\mathfrak{M}_\beta^p]$$

$$\boldsymbol{\mathfrak{b}}_\alpha = [\mathbf{I} + \mathbf{F}_{\alpha\alpha}\mathbf{L}_\alpha\mathfrak{M}_\alpha^p - (c_\alpha/c_\beta)\mathbf{F}_{\alpha\beta}\mathbf{L}_\beta\mathfrak{M}_\beta^p]^{-1} \times [\mathbf{b}_\alpha - \mathbf{F}_{\alpha\alpha}\mathbf{L}_\alpha\boldsymbol{m}_\alpha^p - \mathbf{F}_{\alpha\beta}\mathbf{L}_\beta\boldsymbol{m}_\beta^p]. \tag{26}$$

Similar expressions follow for $\mathfrak{B}_\beta$ and $\boldsymbol{\mathfrak{b}}_\beta$ by exchange of subscripts.

In the general case of many phases or subvolumes $r, s = 1, 2, \ldots N$, the instantaneous concentration factors follow from (24) in matrix notation as

$$\mathfrak{B}_r = [\text{diag }(\mathbf{I}) + [\mathbf{F}_{rs}\mathbf{L}_s\mathfrak{M}_s^p]]^{-1}[\mathbf{B}_r],$$

$$\{\boldsymbol{\mathfrak{b}}_r = [\text{diag }(\mathbf{I}) + [\mathbf{F}_{rs}\mathbf{L}_s\mathfrak{M}_s^p]]^{-1}\{\{\mathbf{b}_r\} - \{\mathbf{F}_{rs}\mathbf{L}_s\boldsymbol{m}\}_s^p\} \tag{27}$$

$$\mathfrak{C}_r = [\text{diag } (\mathbf{I}) + [\mathbf{D}_{rs}\mathbf{L}_s\mathbf{M}_s\mathfrak{L}_s^p]]^{-1}[\mathbf{A}_r],$$

$$\{a_r = [\text{diag } (\mathbf{I}) + [\mathbf{D}_{rs}\mathbf{M}_s\mathfrak{L}_s^p]]^{-1}\{\{\mathbf{a}_r\} - \{\mathbf{D}_{rs}\mathbf{M}_s\ell\}_s^p\}. \quad (28)$$

The instantaneous overall response of the selected system may be then found in two different ways. One approach employs the connections (13) between local and overall total strains and stresses. In particular, we recall that for $\dot{\theta} = 0$, (14), (16) and (20) imply the following relations for the overall and local strain rates at any point of the overall loading path,

$$\dot{\epsilon}^e = \mathbf{M}\dot{\sigma} \quad \dot{\epsilon} = \mathfrak{M}\dot{\sigma} \quad (29)$$

$$\dot{\epsilon}_r^e = \mathbf{M}_r\dot{\sigma}_r \quad \dot{\epsilon}_r = \mathfrak{M}_r\dot{\sigma}_r, \quad (30)$$

where we assume that the local fields in V_r remain uniform during the entire deformation history. Now, write the local stresses as in (5) and (25), and use (3) and (21) to obtain

$$\dot{\epsilon}_r^e = \mathbf{M}_r\mathbf{B}_r\dot{\sigma} \quad \dot{\epsilon}_r = \mathfrak{M}_r\mathfrak{B}_r\dot{\sigma}, \quad (31)$$

where $\mathbf{M}_r$, $\mathbf{B}_r$ and $\mathfrak{M}_r$, $\mathfrak{B}_r$ are the instantaneous local compliances and stress concentration factors, respectively; $\dot{\sigma}$ denotes the overall stress rate. Next, employ the relation between the local and overall total strain averages that follow from (13) as

$$\dot{\epsilon} = \sum_{r=1}^{N} c_r\dot{\epsilon}_r, \quad (32)$$

where c_r denote the volume fractions V_r/V. Then substitute from (31) and (29) to find the overall instantaneous compliances as

$$\mathbf{M} = \sum_{r=1}^{N} c_r\mathbf{M}_r\mathbf{B}_r \quad \mathfrak{M} = \sum_{r=1}^{N} c_r\mathfrak{M}_r\mathfrak{B}_r. \quad (33)$$

Another approach to evaluation of the overall properties is indicated by the generalized Levin's (1967) formula (14) for the local and overall transformation fields, and by the overall constitutive relations (15). For the averages of the inelastic strains, (14) provides

$$\dot{\epsilon}^{in} = \sum_{r=1}^{N} c_r\mathbf{B}_r^T\dot{\epsilon}_r^{in}. \quad (34)$$

Recalling that $\dot{\epsilon}^{in} = \dot{\epsilon} - \dot{\epsilon}^e$, and $\dot{\epsilon}_r^{in} = \dot{\epsilon}_r - \dot{\epsilon}_r^e$, one can find from (29)–(31) and (34) that

$$\mathfrak{M} = \mathbf{M} + \sum_{r=1}^{N} c_r\mathbf{B}_r^T(\mathfrak{M}_r - \mathbf{M}_r)\mathfrak{B}_r. \quad (35)$$

Note that the elastic $\mathbf{M}$ follows only from (33_1), but the instantaneous $\mathfrak{M}$ is given by both (33_2) and (35). Since the c_r, $\mathbf{B}_r$ and $\mathbf{M}_r$ are constant, and $\mathfrak{M}_r$ depends on the local deformation history, *the evaluation of the instantaneous stress concentration factor $\mathfrak{B}_r$ must be subjected to certain conditions that guarantee that* (33_2) *and* (35) *provide a unique evaluation of the instantaneous overall compliance* $\mathfrak{M}$. It can be verified that the results (27) satisfy this requirement, providing of course that the transformation concentration factor tensors comply with (10). For example, in a two-phase system, one can solve (33_2) and (35) for one of the local $\mathfrak{B}_r$ and recover after some manipulation the expression given in (26_1), (Dvorak 1992, Appendix).

3.2 Viscoelastic Phases. Another example can be given for a composite consisting of viscoelastic phases, which exhibit time-dependent deformation. In this case, we assume that an overall history of uniform overall strain is applied by imposing certain surface displacements at S of V, together with a uniform temperature change history within V. The phase constitutive equations are written in the usual form (Christensen, 1971), but adjusted here to provide the expression for the relaxation stress

$$\sigma_r^{re}(t) = \int_0^t \mathbf{G}_r(t-\tau)\frac{d\epsilon_r(\tau)}{d\tau}d\tau - \mathbf{L}_r\epsilon_r(t). \quad (36)$$

The assumption is that the phases are thermorheologically simple, so that any effect of temperature on the relaxation functions $\mathbf{G}_r(t-\tau)$ could be accounted for by replacing the time variable by a new variable that depends both on time and a temperature dependent shift function.

For a local deformation history starting from $\epsilon = \mathbf{0}$ at $t = 0$, (36) can be differentiated with respect to time. The result is then used to find the rate of relaxation stress as

$$\dot{\sigma}_r^{re}(t) = \dot{\sigma}_r(t) - \mathbf{L}_r\dot{\epsilon}_r(t) = \dot{\mathbf{G}}_r(0)\epsilon_r(t) + \int_0^t \ddot{\mathbf{G}}_r(t-\tau)\epsilon_r(t)d\tau. \quad (37)$$

Then, (19_1) and (20_1) are rewritten using (23) as

$$\epsilon_r(t) + \sum_{s=1}^{N}\mathbf{D}_{rs}\mathbf{M}_s\sigma_s^{re}(t) = \mathbf{A}_r\epsilon^0(t) + \mathbf{a}_r\theta^0(t)$$

$$\dot{\epsilon}_r(t) + \sum_{s=1}^{N}\mathbf{D}_{rs}\mathbf{M}_s\dot{\sigma}_s^{re}(t) = \mathbf{A}_r\dot{\epsilon}^0(t) + \mathbf{a}_r\dot{\theta}^0(t). \quad (38)$$

After substitution from (36) and (37), one finds the systems of governing equations for both the total strain and strain rates. The outcome is self-evident.

As a specific application, we consider a two-phase system $r = \alpha, \beta$. Since (13) provides the connections $\epsilon = c_\alpha\epsilon_\alpha + c_\beta\epsilon_\beta$, it is sufficient to evaluate the local fields in only one phase. Note also that the last relation (10) indicates that $c_\alpha\mathbf{D}_{\alpha\alpha} + c_\beta\mathbf{D}_{\beta\alpha} = \mathbf{0}$. Then, for the phase $r = \beta$, one can find from (36)–(38) the following relations for the local strain and strain rate

$$\Omega_1\dot{\epsilon}_\beta(t) = \Omega_2\epsilon_\beta(t) + \Omega_3\int_0^t \ddot{\mathbf{G}}_\beta(t-\tau)\epsilon_\beta(\tau)d\tau - \Omega_4\dot{\epsilon}^0(t) - \Omega_5\dot{\theta}^0(t)$$

$$\Omega_1\epsilon_\beta(t) = \Omega_3\int_0^t \mathbf{G}_\beta(t-\tau)\dot{\epsilon}_\beta(\tau)d\tau - \Omega_4\epsilon^0(t) - \Omega_5\theta^0(t), \quad (39)$$

where

$$\Omega_1 = \mathbf{D}_{\alpha\alpha} + (c_\beta/c_\alpha)\mathbf{D}_{\beta\alpha}$$

$$\Omega_2 = \Omega_3\dot{\mathbf{G}}_\beta(0)$$

$$\Omega_3 = (\mathbf{D}_{\beta\alpha}\mathbf{D}_{\alpha\beta} - \mathbf{D}_{\alpha\alpha}\mathbf{D}_{\beta\beta})\mathbf{J}_\beta(0)$$

$$\Omega_4 = \mathbf{D}_{\beta\alpha}(\mathbf{A}_\alpha - 1/c_\alpha\mathbf{I}) - \mathbf{D}_{\alpha\alpha}\mathbf{A}_\beta$$

$$\Omega_5 = \mathbf{D}_{\beta\alpha}\mathbf{a}_\alpha - \mathbf{D}_{\alpha\alpha}\mathbf{a}_\beta.$$

For any number of phases, the governing equations are solved under the initial conditions $\epsilon_r = \mathbf{0}$, $\theta^0 = 0$ at $t = 0$, under the boundary condition $\epsilon = \epsilon^0(t)$ on S of V, and for $\theta = \theta^0(t)$ in V. $\mathbf{J}_\beta(0)$ is creep compliance.

The two examples illustrate the application of the method to composite materials consisting of inviscid and time-dependent phases. Similar applications are possible to viscoplastic phases. A more extensive treatment of these subjects and associated solution methods has been given by Dvorak (1992) and Dvorak et al. (1993). The latter work explores applications to unit cell models, which are typically analyzed by the finite element method. It shows that the TFA and finite element methods deliver the same numerical results for the local fields, but that the TFA method is more efficient with meshes up to about 100 elements, and of course, it does not require implementation of inelastic constitutive relations in a finite element program.

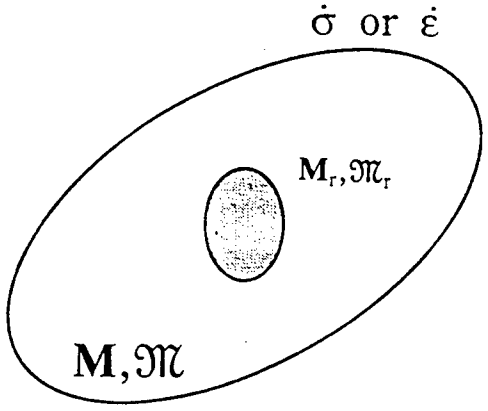


Fig. 1 Schematic of Hill's self-consistent model. In the Mori-Tanaka model, the overall compliances M and $\mathfrak{M}$ are replaced by the matrix compliances M_1 and $\mathfrak{M}_1$, and the overall stress rate $\dot{\sigma}$ by the volume average of the matrix stress rate $\dot{\sigma}_1$.

4 Correction of the K-B-W and Hill Models

Following the early work of Bruggeman (1935) and Hershey (1954), Kroner (1961), Budiansky and Wu (1962) and Hill (1965) presented self-consistent models for prediction of overall instantaneous properties of inelastic polycrystals that are easily extended to composites. The key assumption of such models is that interactions between the phases in the representative volume are approximated by embedding each phase or crystal grain of elastic compliance $\mathbf{M}_r$ into an effective homogeneous medium (of compliance **M** or $\mathfrak{M}$) which is then loaded as indicated by (1), Fig. 1. The goal is to estimate the local fields at each step of loading, or with reference to (5) and (25), to estimate the elastic and instantaneous stress or strain concentration factors. To simplify further, the embedded phases are assumed to be of a particular ellipsoidal shape, so that the Eshelby (1957) tensor **S** of the transformed homogeneous inclusion in the effective medium can be utilized in the solution.

The Kroner, Budiansky and Wu, or K-B-W model further assumed that $\mathbf{M}_r = \mathbf{M}$, and that an overall inelastic strain ϵ^{in} had accumulated in the effective medium. Since the entire aggregate was assumed to be homogeneous, the total strain in a phase strained inelastically by ϵ_r^{in} was found as

$$\dot{\epsilon}_r = \dot{\epsilon}^0 + \mathbf{S}(\dot{\epsilon}_r^{in} - \dot{\epsilon}^{in}). \tag{40}$$

Here, $\dot{\epsilon}^0$ is the overall applied strain rate, and **S** depends on **M** and the inclusion shape. In the case of a spherical inclusion in an isotropic medium, **S** reduces to a scalar with the evaluation $2(4 - 5\nu)/(15(1 - \nu))$. Then, the ϵ_r^{in} was expressed by (22), and both the total and inelastic overall strains were evaluated as a volume average of the local strains (32). For the homogeneous aggregate, where $\mathbf{B}_r = \mathbf{I}$, this is in agreement with (14_1).

Hill (1965) concluded that in the K-B-W model, the effective medium imposed a purely elastic constraint on the inelastically deforming phase, and thus "disregarded the pronounced directional weakness in the constraint of an already yielded aggregate". Taking into consideration the local heterogeneity and both local and overall elastic anisotropy, he proposed to embed each phase as an inhomogeneity in a large volume $V \gg V_r$ of an effective medium with elastic compliance **M** (taken from (33_1)) and as yet unknown instantaneous overall compliance $\mathfrak{M}$. The key assumption in this model is that at each point of the loading path, $\mathfrak{M}$ is constant in $V - V_r$, and $\mathfrak{M}_r$ in V_r, even though both actually depend on the local deformation history which is not necessarily uniform. However, if $\mathfrak{M}$ is taken as constant, the boundary conditions (1) are prescribed at the surface S of V, and the inhomogeneity is assumed to have an ellipsoidal shape, then at least the local fields σ_r and ϵ_r are uniform (Eshelby, 1957), and one finds the self-consistent estimates of the stress concentration factors in (5), and (33) as

$$\mathbf{B}_r = (\mathbf{M}^* + \mathbf{M}_r)^{-1}(\mathbf{M}^* + \mathbf{M}) \quad \mathfrak{B}_r = (\mathfrak{M}^* + \mathfrak{M}_r)^{-1}(\mathfrak{M}^* + \mathfrak{M}). \tag{41}$$

The $\mathfrak{M}^* = \mathbf{S}(\mathbf{I} - \mathbf{S})^{-1}\mathbf{M}$ and $\mathfrak{M}^* = \mathbf{S}(\mathbf{I} - \mathbf{S})^{-1}\mathbf{S}\mathfrak{M}$ (with **S** evaluated in **M** and $\mathfrak{M}$, respectively) are Hill's constraint tensors that can be interpreted as compliances of the cavity in the effective medium **M** or $\mathfrak{M}$ containing V_r, under boundary conditions analogous to (1) prescribed at S_r. After substitution from (41), (33) provides two systems of implicit algebraic equations for the coefficients of **M** and $\mathfrak{M}$.

Since the late 1960's, Hill's self-consistent model has been accepted in the micromechanics literature as the standard procedure in analysis of inelastic heterogeneous media. However, we recall that in addition to the relations (13) and (32) for the total strains, an admissible model must satisfy the generalized Levin's (1967) formula (14) or (34) for the local and overall transformation fields. Clearly, if the $\mathfrak{B}_r$ are taken from (41), then (33_2) and (35) yield entirely different estimates of $\mathfrak{M}$.

To correct this inconsistency in Hill's (1965) model, we propose to replace the actual overall stress rate $\dot{\sigma}$ applied to the effective medium in Fig. 1 with a different overall rate, denoted as $\dot{\sigma}^{SC}$. To find $\dot{\sigma}^{SC}$, we utilize the fact that the $\mathfrak{B}_r$ given by the transformation field method in (24_1) and (25_1) satisfy both (33_2) and (35), providing of course that the transformation influence functions comply with (10). In particular, we evaluate the $\dot{\sigma}^{SC}$ from the requirement that it provides the same estimate of the local stress rate $\dot{\sigma}_r$ in the Hill's model as does the actual overall rate $\dot{\sigma}$ in the transformation analysis. With reference to (41), this can be recorded as

$$\dot{\sigma}_r = \mathfrak{B}_r\dot{\sigma} = (\mathfrak{M}^* + \mathfrak{M}_r)^{-1}(\mathfrak{M}^* + \mathfrak{M})\dot{\sigma}^{SC}, \tag{42}$$

where the $\mathfrak{B}_r$ are now given by (24_1) or (25_1) rather than (41).

Therefore, application of the overall rate

$$\dot{\sigma}^{SC} = (\mathfrak{M}^* + \mathfrak{M})^{-1}(\mathfrak{M}^* + \mathfrak{M}_r)\mathfrak{B}_r\dot{\sigma} \tag{43}$$

to the self-consistent model of Fig. 1 recovers the local stress and strain rates that coincide with those found by the transformation method. Also, the instantaneous overall compliance of the effective medium subjected to boundary conditions (1) and (43) will coincide with that found from (33_2) and (35). An entirely analogous modification can be easily developed for the variant of the above approach based on the Mori-Tanaka method, where the effective medium of Fig. 1 is replaced by the inelastic matrix, and the prescribed overall stress by the average matrix stress.

Of course, (25_1) with the $\mathfrak{B}_r$ from (26) or (27) already provides the correct estimates of the local fields, but the modification may be useful in finding estimates of the fields in regions surrounding the inhomogeneities. In any event, the comparisons with experiments and the PHA model in §5 below indicate that the K-B-W and Hill models provide a poor resolution of the local fields and are therefore of little value in predicting observed behavior.

5 Bimodal Theory and the PHA Model

The theoretical models that have been useful in interpretation of the experimental results described below are the bimodal plasticity theory (Dvorak and Bahei-El-Din 1987), and the periodic hexagonal array (PHA) model of Dvorak and Teply (1985) and Teply and Dvorak (1988).

The bimodal theory admits two distinct inelastic deformation modes in the fiber system, the fiber-dominated and matrix-dominated modes. Each mode is activated by a different overall stress state and, in conjunction with a yield condition, has a branch of the overall yield surface; the internal envelope of the two branches is the overall yield surface.

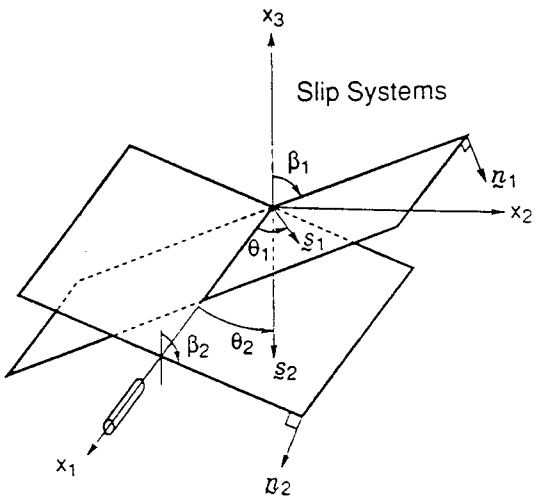


Fig. 2 The slip systems of the matrix-dominated deformation mode of the bimodal plasticity theory of fibrous composites

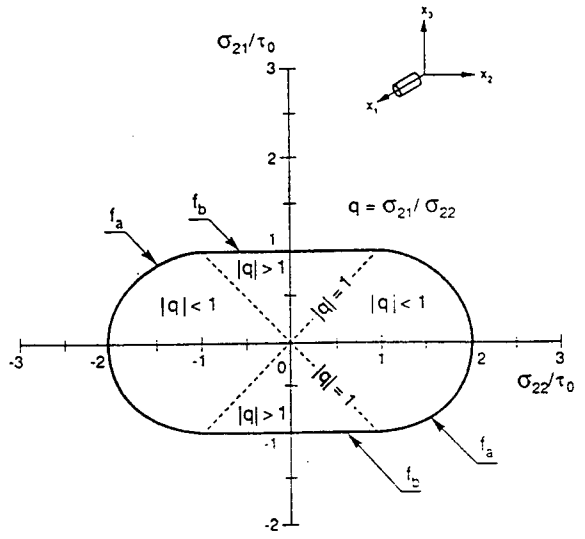


Fig. 3 The initial yield surface of the matrix-dominated deformation mode of the bimodal plasticity theory of fibrous composites

In the fiber-dominated mode (FDM), the composite is regarded as a heterogeneous medium where both the fiber and the matrix participate in carrying the applied load. The local stresses in the phases may be estimated, for example, by the self-consistent or Mori-Tanaka methods. The overall yield surface indicates the magnitudes of the overall stress that cause local stress averages to satisfy the matrix yield condition. In particular, if the fiber remains elastic while the matrix obeys a certain yield condition given in the form $f(\sigma_m) = 0$, then the yield condition of the composite in the overall stress space σ becomes $F(\sigma) = f(\mathbf{B}_m\sigma)$, where $\mathbf{B}_m$ is the elastic stress concentration factor in (5_2). For example, $\mathbf{B}_m$ may be found as a self-consistent estimate with the evaluation suggested by (41_1). More specifically, if $f(\sigma_m)$ is represented by the Mises form, one finds the FDM branch of the overall yield surface as

$$F(\sigma-\alpha)=\frac{1}{2}(\sigma-\alpha)^T(\mathbf{B}_m^T\mathbf{Q}\mathbf{B}_m)(\sigma-\alpha)-\tau_0^2=0, \qquad (44)$$

where α denotes the current position of the center of the yield surface, τ_0 is the matrix yield stress in shear, and $\mathbf{Q}$ is a symmetric 6×6 matrix with $Q_{11} = Q_{22} = Q_{33} = 2/3$, $Q_{12} = Q_{13} = Q_{23} = -1/3$, $Q_{44} = Q_{55} = Q_{66} = 2$, while the remaining coefficients vanish.

In the matrix-dominated mode (MDM) of plastic deformation, all applied load is assumed to be carried by the matrix, while the fiber constrains plastic deformation of the matrix to simple shear straining on planes that are parallel to the fiber axis x_1. The matrix-dominated mode is thus represented by a variant of the continuum slip-model. For the plane state of stress that was applied in the experiments, the slip systems that may operate in the matrix mode are indicated in Fig. 2.

The initial yield condition on any potential slip plane (k) is taken as

$$f(\tau^{(k)}) = (\max \tau_{ns}^{(k)})^2 - \tau_0^2 = 0, \qquad (45)$$

where τ_{ns} denotes the resolved shear stress. The active slip system is defined with reference to Fig. 2 by the normal n_i to the slip plane, and by the slip direction s_j, so that the resolved shear stress in (45) is

$$\tau_{ns}^{(k)} = n_i^{(k)}\sigma_{ij}s_j^{(k)} = (\tau_1^2+\tau_2^2)_{(k)}^{1/2}, \qquad (46)$$

where

$$\tau_1 = \sigma_{21}\cos\beta_1 \quad \tau_2 = \frac{1}{2}\sigma_{22}\sin 2\beta_1. \qquad (47)$$

The max $\tau_{ns}(\beta)$ is evaluated from

$$\tau_{ns}(\partial\tau_{ns}/\partial\beta) = \tau_1(\partial\tau_1/\partial\beta) + \tau_2(\partial\tau_2/\partial\beta) = 0. \qquad (48)$$

For the slip system on the plane $k = 1$ one finds that

$$\beta_1 = \frac{1}{2}\cos^{-1}q^2 \text{ for } |q|\le 1; \quad \beta_1 = 0 \text{ for } |q|\ge 1, \qquad (49)$$

where $q = \sigma_{21}/\sigma_{22}$ if $\sigma_{22} \neq 0$, and the angle θ_1 between the slip direction and x_1 is given by

$$\tan\theta_1 = \frac{1}{q}\sin\beta_1. \qquad (50)$$

The conjugate system on the plane $k = 2$ in Fig. 2 is specified by the angles β_2 and θ_2 that are related to β_1 and θ_1 by

$$\beta_2 = \pi - \beta_1, \quad \theta_2 = \theta_1 \text{ for } |q|\le 1, \quad \beta_2 = 0, \quad \theta_2 = \theta_1 \text{ for } |q|\ge 1, \qquad (51)$$

where $0 \le \beta_1 \le \pi/4$ and $0 \le \theta_1 \le 2\pi$.

Substituting the slip system parameters that assure the maxima of the resolved shear stress under the applied overall plane stress rate, and assuming kinematic hardening for the matrix, one finds the overall yield condition for the MDM mode as

$$f_a(\sigma) = \left(\frac{\sigma_{21}-\alpha_{21}}{\tau_0}\right)^2 + \left(\frac{\sigma_{22}-\alpha_{22}}{\tau_0}\pm 1\right)^2 - 1 = 0 \quad \text{for } |q|\le 1$$

$$f_b(\sigma) = \left(\frac{\sigma_{21}-\alpha_{21}}{\tau_0}\right)^2 - 1 = 0 \quad \text{for } |q|\ge 1. \qquad (52)$$

These relations suggest that the MDM yield surface is an infinite cylinder of oval crossection in the overall plane stress space, with generators parallel to the σ_{11} direction. Its crossection in the $\sigma_{21}\sigma_{22}$-plane for the initial state $\alpha_{21} = \alpha_{22} = 0$, is shown in Fig. 3. Note that this surface is independent of phase moduli and volume fractions.

The internal envelope of the two branches (44) and (52) of the overall surface are plotted in Fig. 4 for the boron aluminum system examined in the experiments. The FDM segment (44) of the overall yield surface resembles an ellipsoid in the overall plane stress space, but since for the B/Al system it contains a part of the MDM oval cylinder, it provides the end caps of the overall surface.

The experimental results that follow confirm the kinematic hardening assumed above, and indicate the evolution of the back stress components of the matrix-dominated mode as

$$d\alpha_{21} = d\sigma_{21}, \quad d\alpha_{22} = d\sigma_{22}, \quad \text{for } |q|\le 1$$

$$d\alpha_{21} = d\sigma_{21}, \quad d\alpha_{22} = 0 \quad \text{for } |q|\ge 1. \qquad (53)$$

For the fiber mode, the derivation of (44) suggests that the

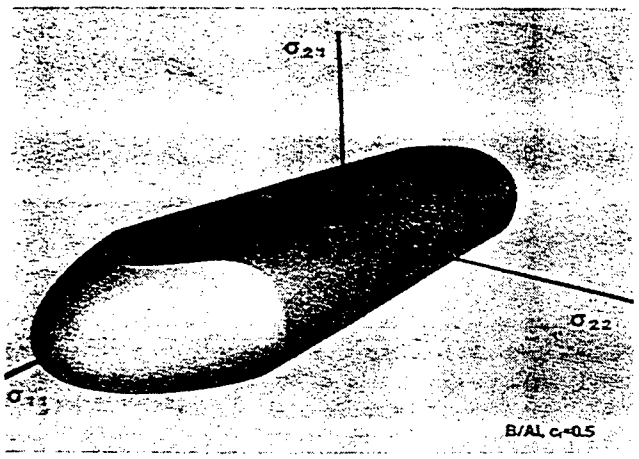


Fig. 4 The branches of the initial yield surface of a boron-aluminum system evaluated from the bimodal plasticity theory of fibrous composites

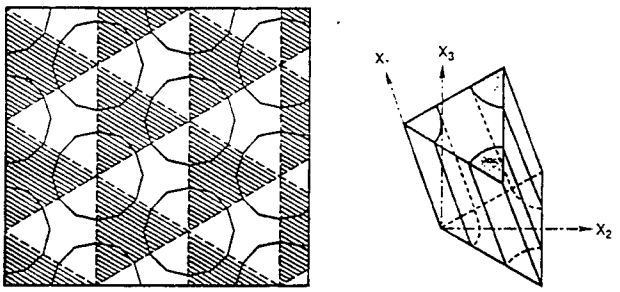


Fig. 5 The periodic hexagonal array (PHA) model of fibrous composites and a unit cell

vectors connecting the local or overall yield surface centers to points within or at the respective yield surfaces are related by

$$(\sigma_m - \alpha_m) = B_m(\sigma - \alpha). \tag{54}$$

As in (53_1), the experiments suggest compliance with the Phillips et al., (1972) hardening rule, $d\alpha_m = d\sigma_m$, hence the differential form of (54) suggests hardening in the fiber-dominated mode as

$$d\alpha = d\sigma. \tag{55}$$

Since both modes operate on the same local volume of the matrix, hardening in either mode affects the entire overall surface, and there is no relative translation of the two branches during deformation. The bimodal theory will be seen to predict the shape and position of the observed yield surfaces, but not the measured plastic strains.

The periodic hexagonal array model assumes that the fibers are represented by regular polygons and distributed as indicated in the transverse plane section shown in Fig. 5. This arrangement permits selection of one of the triangular domains as a unit cell that, when subjected to carefully selected periodic boundary conditions, can represent the deformation field in the entire composite under uniform overall stress or strain. Details of the procedure have been described by Teply and Dvorak (1988). The unit cell is then subdivided into finite elements and the solution can be obtained either by the finite element method, or using the transformation analysis of §3 and 4. Figure 6 shows two meshes used in interpretation of the experiments. If the unit cell is subjected to a series of loads consisting of the six overall stress components of unit magnitude, then the stresses found in the elements $r = 1, 2, \ldots M$, for each such loading represent a column of the stress concentration factor matrix $\mathbf{B}_r$ of the element r. Once these

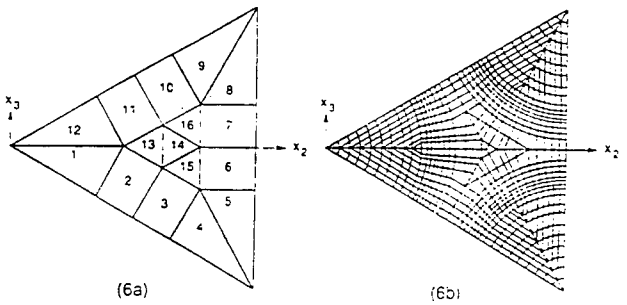


Fig. 6 The subdivision of the PHA unit cell into finite elements

are known, one can prescribe a suitable yield condition for the matrix, and proceed as in the derivation of (44) to find the M branches of the overall yield surface that correspond to the onset of yielding in each element. An incremental elastic-plastic analysis of the PHA model then leads to evaluation of local fields and of the overall response. If the procedure (24) is used, the transformation concentration factors are evaluated from (9); the computational effort can be reduced substantially by taking advantage of the symmetries of the unit cell. The constitutive relations for the elements are of the kind discussed in §4.1. The overall deformation under selected loading can be evaluated, for example, from the element plastic strains found after each increment of the overall stress; these are substituted for the eigenstrains into (6_1), and the resulting overall eigenstrain increment is used in (16), and/or added to the previous increments in (15). A detailed description of the implementation procedure for the PHA model can be found in the recent paper by Dvorak, Bahei-El-Din and Wafa (1993).

6 Interpretation of Experiments

In a departure from much of the current activity in micromechanical modeling, we have supported our work by several experimental studies of actual behavior of inelastic composite materials under incremental loading along a complex path. Most of the completed work was done with the boron-aluminum system at room temperature, similar studies on high-temperature systems are now in progress. The results discussed here were found by Dvorak et al., (1988), Nigam, Dvorak and Bahei-El-Din (1993a, 1993b). Interpretation of the results with theoretical models was discussed by Dvorak et al., (1991).

All the work described was performed on thin-walled tube specimens shown in Fig. 7. The tubes were fabricated by diffusion bonding of monolayer 6061-Al/B sheets by Amercom in Chatsworth, CA. The finished tube had seven layers of fiber in the wall, all aligned in the axial direction, with fairly regular fiber distribution, Fig. 8. The fiber diameter was 142μ, volume fraction $c_f = 0.45$. All specimens were annealed at 400°C for two hours, and C-scanned for damage before testing. Gripping was facilitated by steel fixtures indicated in Fig. 7, which were adhesively bonded at both faces to the ends of the tube. The specimens were instrumented with strain gages and ±45 deg. rosettes for axial, hoop and shear strain measurement. Loading was applied in tension/compression and by internal pressure and torque in a computer-controlled MTS machine. The loading rate was 4.2 MPa/min in any direction. Accuracy of measurements was 0.1 MPa for stress, and 1×10^{-6} for strain.

The specimens were subjected to various loading programs. Here we consider the results found for loading by internal pressure and torque; this produced a transverse normal stress σ_{22} and a longitudinal shear stress σ_{21} in the tube wall. Since no loading compensation was made for the axial tension induced by the internal pressure, an axial normal stress $\sigma_{11} = \sigma_{22}/2$ was induced as well. The measurements were thus made

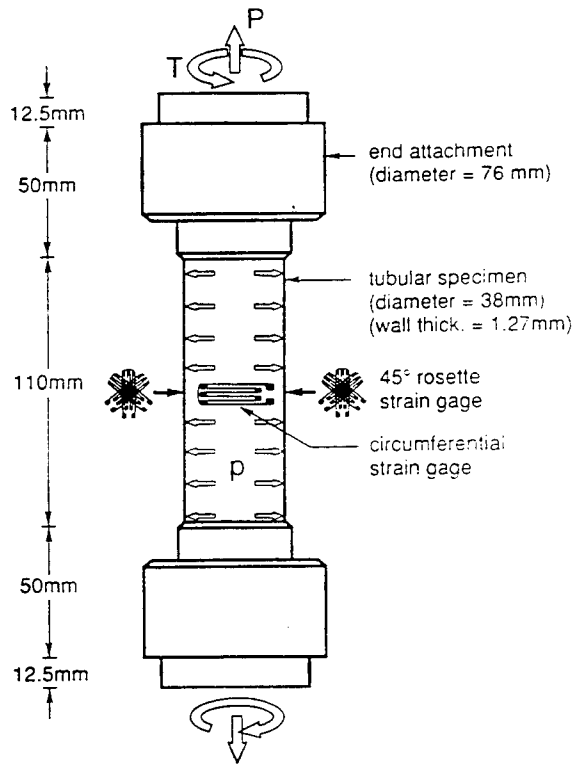
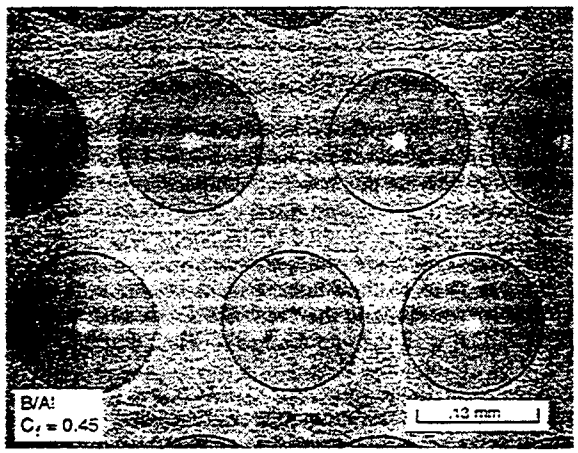


Fig. 7 Dimensions of the boron-aluminum specimen tube used in the experiments



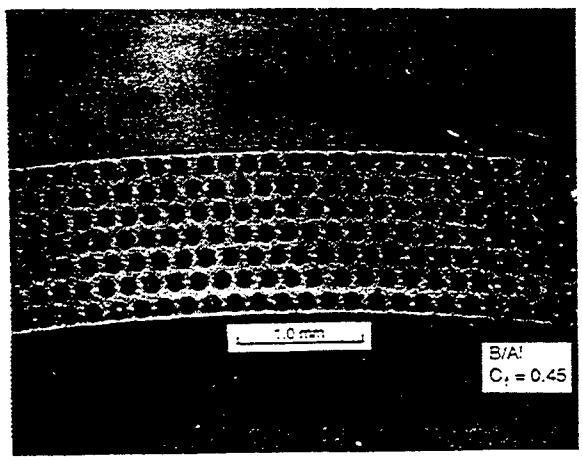


Fig. 8 Micrographs of the crossection of the boron aluminum tube

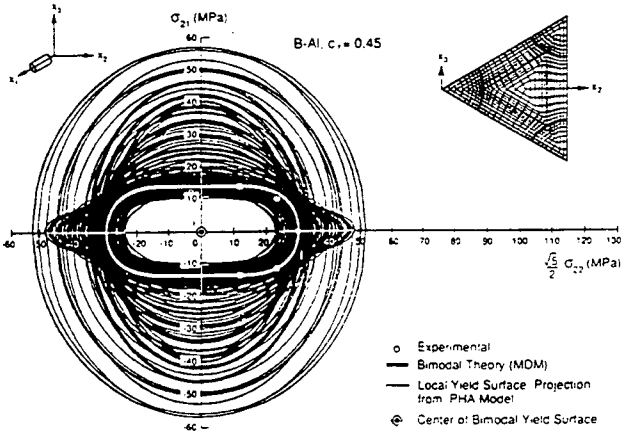


Fig. 9 Cluster of the initial yield surfaces for a fine mesh, with the MDM surface of Fig. 3 and experimentally measured yield points

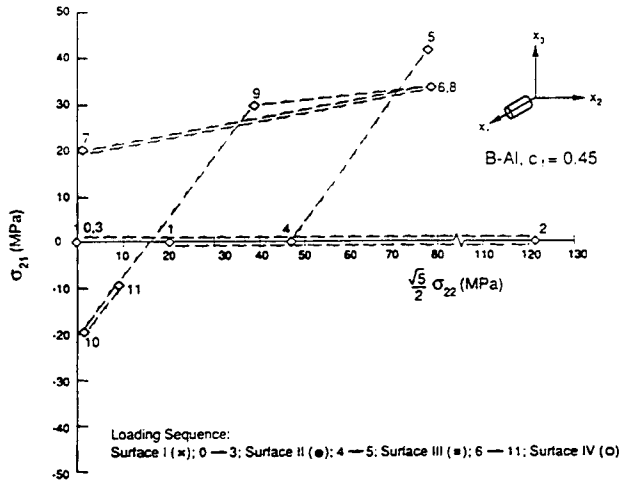


Fig. 10 The loading path applied in the experiments

in a stress plane inclined to the $\sigma_{21}\sigma_{22}$-plane used in Figs. 3 and 4; this was reflected in adjusting the scale on the σ_{22} axis to $(\sqrt{5}/2)$ of the applied stress magnitude. The axial stress was accounted for in modeling.

The work focused on detection of the initial and several subsequent yield surfaces along the loading path, and the plastic strain magnitudes after each load increment. For each yield point, the yield stress was defined by back extrapolation from a small excursion into the plastic region, at zero offset strain. The experimental yield surfaces were constructed by fitting the appropriate sections of the bimodal yield surface of Figs. 3 and 4 to the detected yield points. As indicated by (44) and (52), the matrix yield stress was the only adjustable parameter.

In addition to the bimodal yield surfaces, we constructed initial and subsequent clusters of yield surfaces for the subelements of the unit cell of the PHA model, using the refined mesh of Fig. 9. Figure 9 shows the initial yield surface configuration; the cluster of the subelement yield surfaces, and an adjusted transverse section of the MDM surface from Fig. 3, with the experimentally detected yield points. As expected, the loading excursions to the experimentally detected yield points involved interaction of the load vector with some of the subelement yield surfaces, or micro yielding. The complete loading path applied to the specimen from this initial state is shown in Fig. 10.

Figures 11 and 12 show the rearranged clusters of the subelement surfaces, together with the current bimodal surfaces and the experimental points detected by loading excursions

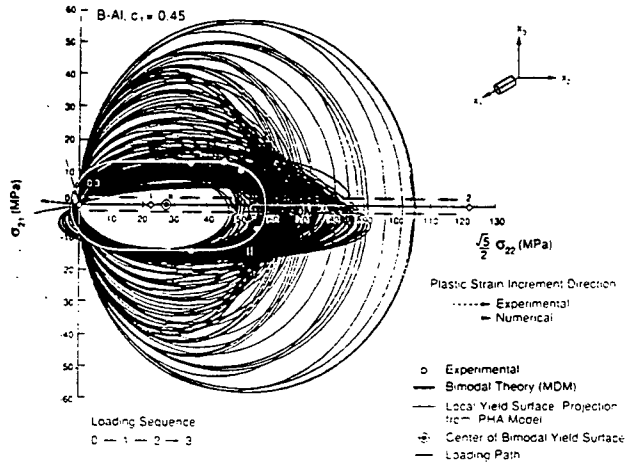


Fig. 11 Rearrangement of the yield surfaces of Fig. 9, after a cycle of internal pressure applied to the tube specimen of Fig. 7

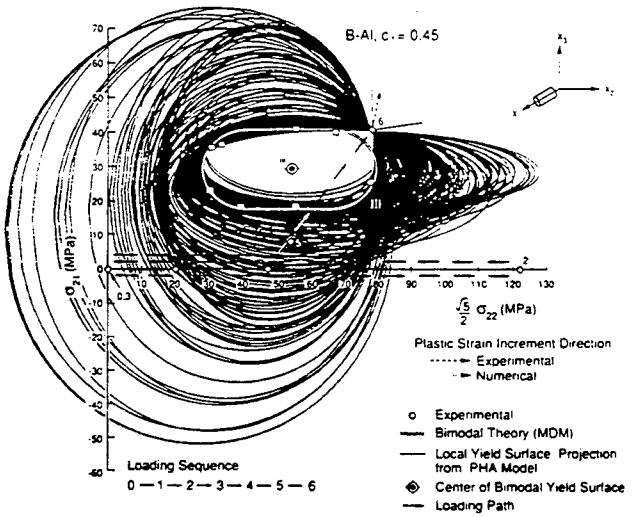


Fig. 12 The yield surfaces of Figs. 9 and 11, after additional loading by pressure and torque

within the bimodal surface from the current end point of the loading path. While the bimodal, experimental and the subelement surfaces follow the Phillips hardening rule (53) and (55), the clusters also undergo internal rearrangement due to the gradual expansion of the plastic region during loading, and the residual stress field (6_2) generated in the subelements by the relaxation stresses or eigenstresses $\lambda_s = \sigma_s^{re} = -\mathbf{L}_s\mu_s$. After sustained loading in a given direction, all the elements yield and the yield surfaces then pass through the loading point. This is particularly evident at point #6 in Fig. 12. Of course, the element yield surfaces become intercepted during excursions from the loading point toward the individual points on the current yield surface. This causes micro yielding and additional rearrangement of the cluster, this is not shown in Fig. 12. However, it is evident that after such rearrangement, the experimentally detected yield surface may not necessarily pass through the loading point such as #6 in Fig. 12. This phenomenon, piercing of the current yield surface, is often observed in experiments of this kind.

At any point of the path, the normals to tangential planes to the surfaces of the currently yielding subelements form a cone of normals that must contain the overall inelastic strain increment vector (Hill, 1967). This is borne out by the experimentally detected increments shown in Figs. 11 and 12. Note that the PHA predictions generally agree with the experimental

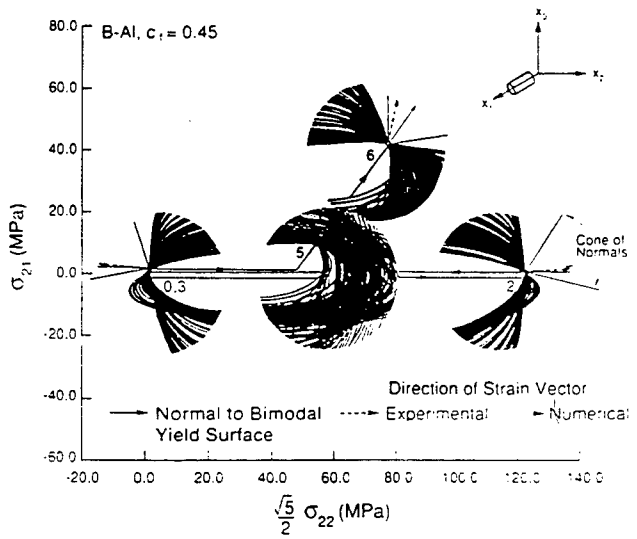


Fig. 13 Details of the yield surface clusters at loading points with experimentally measured and predicted directions of the overall plastic strain rate vectors

observations, while the normals drawn to the bimodal surface approximating the experimentally detected surface tend to deviate substantially from the experimentally measured plastic strains.

This is illustrated further in Fig. 13. The experimentally detected surface should be regarded as an envelope of the instantaneous vertices of the cluster. This explains the lack of normality, without violating the Drucker (1951) postulate. On the other hand, this general property of plastic flow in heterogeneous media disqualifies simple modeling techniques which base the determination of plastic strain increments on normality to a single overall yield surface. This applies in particular to the approaches based on the self-consistent or Mori-Tanaka methods discussed in §4. The bimodal theory would not provide much better estimates and therefore is not intended for this purpose; however, as the experiments show, it is quite useful in predicting the shape and position of the initial and subsequent yield surfaces.

Figures 14 to 16 show comparisons between the predictions of plastic strains along the path of Fig. 10, obtained from the PHA model with the two meshes of Figs. 6 and 9, the matrix mode of the bimodal theory, the Mori-Tanaka version of the uncorrected Hill model discussed in §4 (Gavazzi and Lagoudas, 1991), and from experimental measurements. The inelastic constitutive relation for the matrix in the PHA and bimodal models was derived from the two-surface plasticity theory of Dafalias and Popov (1976); implementation of this theory was described by Dvorak, et al., (1991). The comparisons indicate that, as expected, the Mori-Tanaka and bimodal theories fail to approximate the actual plastic strains. In contrast, the PHA model provides a reasonable approximation, although there is a significant deviation along the path segment 5-6 in Fig. 10. However, the overall agreement is probably better than that one might find in comparisons of the two-surface plasticity theory with similar experiments on unreinforced tubular specimens loaded along an open path.

7 Conclusions

The transformation field analysis is presented here as a general method for solving transformation loading problems for heterogeneous media with many interacting inhomogeneities. The method accommodates any uniform overall loading path and inelastic constitutive equations that conform with the additive decomposition of local strains, as well as any micro-

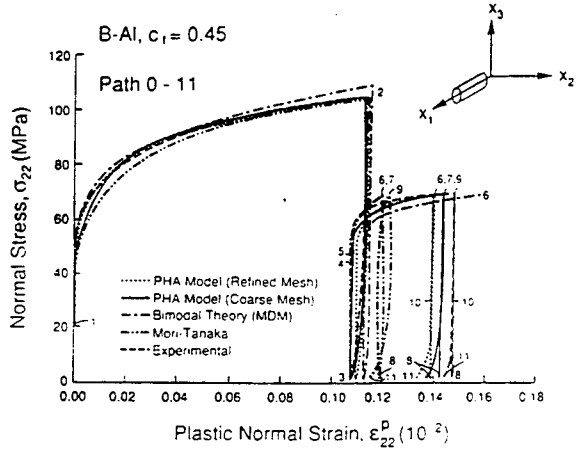


Fig. 14 Observed transverse normal plastic strains for the loading path of Fig. 10, compared with predictions of various models

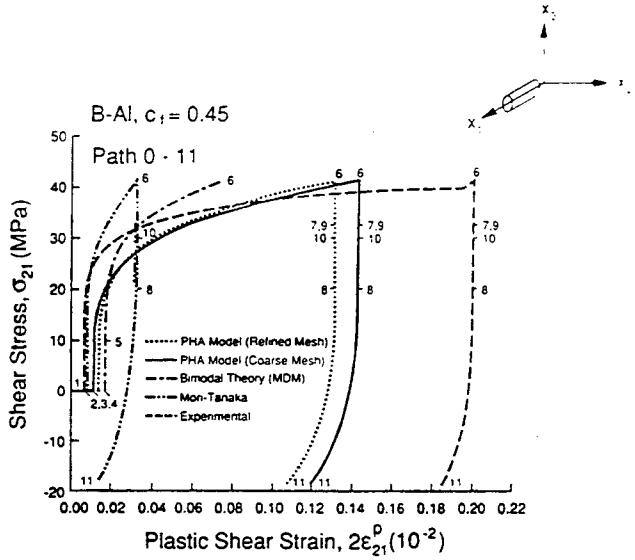


Fig. 15 Observed longitudinal shear plastic strains for the loading path of Fig. 10, compared with predictions of various models

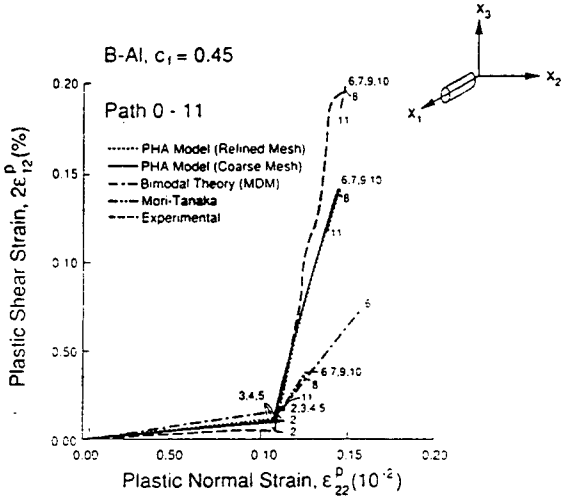


Fig. 16 Observed plastic strains for the loading path of Fig. 10, compared with predictions of various models

mechanical model that offers connections between local and overall fields in representative volumes of elastically deforming heterogeneous aggregate. Indeed, many existing approaches to analysis of inelastic heterogeneous media, such as the unit cell models, and the self-consistent, Mori-Tanaka and other methods based on the Eshelby solution are included as special cases of the TFA procedure. The elastic-plastic, viscoelastic and viscoplastic deformation problems are also treated in a unified manner, by solving a system of governing equations for either total local fields or for their rates. While the nature of the governing equations and the solution methods may vary, their derivation is accomplished in a standard form that incorporates local geometry effects through the transformation influence functions, and local material response through the selected constitutive relations.

The transformation method obviates the need to solve inelastic inclusion problems, indeed, such solutions were shown here in association with models that violate the generalized Levin formula. A correction was proposed for Hill's formulation of one such model.

In comparisons with experimentally measured plastic strains, only the unit cell models appear to provide reasonable approximations to the observed magnitudes. The main reason is the ability of these models to monitor the correct direction of plastic strains. The models that rely on normality to a single overall yield surface are bound to provide misleading predictions, because no such single overall surface actually exists. The experimentally found surfaces are seen as loci of vertices of yield cones formed as inner envelopes of the clusters formed by multiple local branches of the overall yield surface. Normality is thus satisfied only within the cone of normals to the local surfaces. Only those micromechanical models that can reproduce the plastic strain increments within these cones may, in general, provide reliable predictions of the observed behavior.

Acknowledgment

The work surveyed in this paper was supported by grants from the Advanced Research Projects Agency of the Department of Defense, by the Air Force Office of Scientific Research, and by the Mechanics Division of the Office of Naval Research. Professors Yehia Bahei-El-Din and Himanshu Nigam, Dr. Rahul Shah and Mr. Amr Wafa contributed to the various research results described here.

References

Benveniste, Y., Dvorak, G. J., and Chen, T., 1991, "On Diagonal Symmetry of the Approximate Effective Stiffness Tensor of Heterogeneous Media," *J. Mech. Phys. Solids*, Vol. 39, pp. 927–946.

Bruggeman, D. A. G., 1935, "Berechnung Verschiedener Physikalischer Konstanten von Heterogenen Substanzen," *Annalen der Physik*, Vol. 5, p. 636–664.

Budiansky, B., and Wu, T. T., 1962, "Theoretical Prediction of Plastic Strains of Polycrystals," *Proc. 4th U.S. Nat'l Congr. Appl. Mech.*, pp. 1175–1185.

Christensen, R. M., 1971, *Theory of Viscoelasticity, An Introduction*, Academic Press, New York.

Dafalias, Y. F., and Popov, E. P., 1976, "Plastic Internal Variables Formalism of Cyclic Plasticity," *J. Appl. Mech.*, Vol. 43, pp. 645–651.

Drucker, D. C., 1951, "A More Fundamental Approach to Plastic Stress-Strain Relations," *Proc. 1st U.S. Nat'l Congr. Appl. Mech.*, pp. 487–491.

Dvorak, G. J., 1990, "On Uniform Fields in Heterogeneous Media," *Proc. R. Soc. Lond.*, Series A 431, pp. 89–110.

Dvorak, G. J., 1991, "Plasticity Theories for Fibrous Composite Materials," *Metal Matrix Composites, Mechanisms and Properties*, ed., R. K. Everett and R. J. Arsenault, Vol. 2, Academic Press, Boston, pp. 1–77.

Dvorak, G. J., 1992, "Transformation Field Analysis of Inelastic Composite Materials," *Proc. R. Soc. Lond.*, Series A 437, pp. 311–327.

Dvorak, G. J., and Bahei-El-Din, Y. A., 1987, "A Bimodal Plasticity Theory of Fibrous Composite Materials," *Acta Mechanica*, Vol. 69, pp. 219–241.

Dvorak, G. J., Bahei-El-Din, Y. A., Macheret, Y., and Liu, C. H., 1988, "An Experimental Study of Elastic-Plastic Behavior of a Fibrous Boron-Aluminum Composite," *J. Mech. Phys. Solids*, Vol. 36, pp. 665–687.

Dvorak, G. J., Bahei-El-Din, Y. A., Shah, R. S., and Nigam, H., 1991, "Experiments and Modeling in Plasticity of Fibrous Composites," *IUTAM Symposium on Inelastic Deformation of Composite Materials*, George J. Dvorak, ed., Springer-Verlag, New York, pp. 270–293.

Dvorak, G. J., Bahei-El-Din, Y. A., and Wafa, A. M., 1993, "Implementation of the Transformation Field Analysis for Inelastic Composite Materials," *Computational Mechanics*, in print.

Dvorak, G. J., and Benveniste, Y., 1992, "On Transformation Strains and Uniform Fields in Multiphase Elastic Media," *Proc. R. Soc. Lond.*, Series A 437, pp. 291-310.

Dvorak, G. J., and Teply, J. L., 1985, "Periodic Hexagonal Array Models for Plasticity Analysis of Composite Materials," *Plasticity Today: Modeling, Methods and Applications*, W. Olszak Memorial Volume ed., A. Sawczuk and V. Bianchi, Elsevier Science Publishers, Amsterdam, pp. 623-642.

Eshelby, J. D., 1957, "The Determination of the Elastic Field of an Ellipsoidal Inclusion and Related Problems," *Proc. R. Soc. Lond.*, Series A 241, pp. 376-396.

Hershey, A. V., 1954, "The Elasticity of an Isotropic Aggregate of Anisotropic Cubic Crystals," *J. Appl. Mech.*, Vol. 21, pp. 236-240.

Hill, R., 1963, "Elastic Properties of Reinforced Solids: Some Theoretical Principles," *J. Mech. Phys. Solids*, Vol. 11, pp. 357-372.

Hill, R., 1965, "Continuum Micro-Mechanics of Elastoplastic Polycrystals," *J. Mech. Phys. Solids*, Vol. 13, pp. 89-101.

Hill, R., 1967, "The Essential Structure of Constitutive Laws for Metal Composites and Polycrystals," *J. Mech. Phys. Solids*, Vol. 15, pp. 79-95.

Hill, R., 1971, "On Macroscopic Measures of Plastic Work and Deformation in Micro-Heterogeneous Media," *Prikl. Mat. Mekh.* (PMM), Vol. 35, pp. 31-39.

Kröner, E., 1961, "Zur plastischen Verformung des Vielkristalls," *Acta Metal.*, Vol. 9, pp. 155-161.

Lagoudas, D. C., and Gavazzi, A. C., 1991, "Incremental Elastoplastic Behavior of Metal Matrix Composites Based on Averaging Schemes," *IUTAM Symposium on Inelastic Deformation of Composite Materials*, George J. Dvorak, ed., Springer-Verlag, New York, pp. 465-485.

Nigam, H., Dvorak, G. J., and Bahei-El-Din, Y. A., 1993, "An Experimental Investigation of Elastic-Plastic Behavior of a Fibrous Boron-Aluminum Composite: I. Matrix-Dominated Mode," *Int. J. Plasticity*, in print.

Nigam, H., Dvorak, G. J., and Bahei-El-Din, Y. A., 1993, "An Experimental Investigation of Elastic-Plastic Behavior of a Fibrous Boron-Aluminum Composite: II. Fiber-Dominated Mode," *Int. J. Plasticity*, in print.

Levin, V. M., 1967, "Thermal Expansion Coefficients of Heterogeneous Materials," *Mekhanika Tverdogo Tela*, Vol. 2, pp. 88-94, English Translation, *Mech. of Solids*, Vol. 11, pp. 58-61.

Phillips, A., Liu, C. S., and Justusson, J. W., 1972, "An Experimental Investigation of Yield Surfaces at Elevated Temperatures," *Acta Mechanica*, Vol. 21, pp. 119-146.

Rice, J. R., 1970, "On the Structure of Stress-Strain Relations for Time-Dependent Plastic Deformation in Metals," ASME *Journal of Applied Mechanics*, Vol. 37, pp. 728-737.

Teply, J. L., and Dvorak, G. J., 1988, "Bounds on Overall Instantaneous Properties of Elastic-Plastic Composites," *J. Mech. Phys. Solids*, Vol. 36, pp. 29-58.

Modelling Simul. Mater. Sci. Eng. 2 (1994) 571–586. Printed in the UK

The modeling of inelastic composite materials with the transformation field analysis

George J Dvorak†, Yehia A Bahei-El-Din‡ and Amr M Wafa†

† Center for Composite Materials and Structures, Rensselaer Polytechnic Institute, Troy, NY 12180, USA

‡ Structural Engineering Department, Cairo University, Giza, Egypt

Received 4 November 1993, accepted for publication 4 November 1993

Abstract. This paper examines several aspects of numerical implementation of the transformation field analysis (TFA) method in applications to inelastic composite materials. In its general form, the method can accommodate any uniform overall loading path, inelastic constitutive equations, and micromechanical model. The response of a selected model to thermomechanical loads and local inelastic or transformation strains is found through mechanical transformation influence functions, which reflect the chosen microgeometry and the elastic response of the phases. Application of the transformation field analysis to elastic–plastic fibrous composites considers a unit cell model and incremental plasticity constitutive equations. For moderate mesh subdivisions of the unit cell, TFA proved to be more efficient than the finite-element method.

1. Introduction

Transformation field analysis (TFA) is a method for incremental solution of thermomechanical loading problems in inelastic heterogeneous media and composite materials, described in recent papers by Dvorak (1991, 1992). When used with a selected micromechanical model, the analysis provides piecewise uniform approximations of the instantaneous local strain and stress fields in the phases, and estimates of the overall instantaneous thermomechanical properties of a representative volume of the heterogeneous solid. The purpose of the present paper is to examine several different aspects of numerical implementation of the method in solutions of problems for composite materials consisting of elastic–plastic, viscoelastic, and viscoplastic phases. A more detailed description of the implementation procedure for several material types is described by Dvorak and co-workers (1994).

The first three sections of the paper introduce some preliminary concepts: section 2 contains a brief summary of various definitions of local and overall properties; section 3 outlines the concept of eigenstress and eigenstrain influence functions and concentration factors, while section 4 describes the essence of the TFA method. Details of this method for composites with elastic–plastic phases are given in section 5 and this is followed by examples in section 6.

The notation used is fashioned after that introduced by Hill (1963); (6×1) vectors are denoted by boldface lower case Roman or Greek letters, (6×6) matrices by boldface uppercase Roman letters, and $\mathbf{A}\mathbf{A}^{-1} = \mathbf{A}^{-1}\mathbf{A} = \mathbf{I}$, if the inverse exists. Scalars are denoted by italic letters. Bold italic characters are reserved for material properties that change during deformation. Volume averages of fields in V_r, such as $\mathbf{A}_r(\mathbf{x})$ or $\boldsymbol{\epsilon}_r(\mathbf{x})$, or of $\boldsymbol{\sigma}(\mathbf{x})$ in V are denoted by $\mathbf{A}_r$, $\boldsymbol{\epsilon}_r$, or $\boldsymbol{\sigma}$.

0965-0393/94/3A0571+16$19.50 © 1994 IOP Publishing Ltd

2. Local and overall properties

A certain representative volume V of a heterogeneous solid, such as a composite or polycrystal, made of many perfectly bonded phases $r = 1, 2, \ldots, N$, resides in volumes $V_r \in V$. The constitutive relations of the phases may represent inviscid or time-dependent response, and at any time t the total strains and stresses can be additively decomposed as

$$\epsilon_r(\mathbf{x}, t) = \epsilon_r^e(\mathbf{x}, t) + \mu_r(\mathbf{x}, t) \qquad \sigma_r(\mathbf{x}, t) = \sigma_r^e(\mathbf{x}, t) + \lambda_r(\mathbf{x}, t) \tag{1}$$

where $\mathbf{x}$ are material coordinates in a cartesian system in V. The ϵ_r^e and μ_r in (1) denote, respectively, the elastic strain due to certain surface tractions at the boundary of V_r, and an eigenstrain in the phase r. Similarly, the σ_r^e and λ_r in (1) denote the elastic stress and eigenstress in phase r under certain surface displacements applied at the surface V_r.

The eigenstrain and eigenstress fields, henceforth referred to jointly as *transformation fields*, may consist of contributions of distinct physical origin, and may be decomposed further. For example, if only thermal and inelastic effects are considered,

$$\mu_r(\mathbf{x}, t) = \mathbf{m}_r\theta(t) + \epsilon_r^{in}(\mathbf{x}, t) + \cdots \qquad \lambda_r(\mathbf{x}, t) = \mathbf{l}_r\theta(t) + \sigma_r^{re}(\mathbf{x}, t) + \cdots \tag{2}$$

where $\mathbf{m}_r$ and $\mathbf{l}_r$ are the thermal strain and stress tensors. The coefficient of $\mathbf{m}_r$ represent the linear thermal expansion coefficients, ϵ_r^{in} denotes an inelastic strain, and σ_r^{re} a relaxation stress.

With these definitions, (1) become

$$\begin{aligned} \epsilon_r(\mathbf{x}, t) &= \mathbf{M}_r\sigma_r(\mathbf{x}, t) + \mathbf{m}_r\theta(t) + \epsilon_r^{in}(\mathbf{x}, t) \\ \sigma_r(\mathbf{x}, t) &= \mathbf{L}_r\epsilon_r(\mathbf{x}, t) + \mathbf{l}_r\theta(t) + \sigma_r^{re}(\mathbf{x}, t) \end{aligned} \tag{3}$$

together with the interrelations

$$\begin{aligned} \mathbf{m}_r &= -\mathbf{M}_r\mathbf{l}_r \qquad & \epsilon_r^{in}(\mathbf{x}, t) &= -\mathbf{M}_r\sigma_r^{re}(\mathbf{x}, t) \\ \mathbf{l}_r &= -\mathbf{L}_r\mathbf{m}_r \qquad & \sigma_r^{re}(\mathbf{x}, t) &= -\mathbf{L}_r\epsilon_r^{in}(\mathbf{x}, t) \end{aligned}$$

where $\mathbf{L}_r$ and $\mathbf{M}_r = \mathbf{L}_r^{-1}$ are the elastic phase stiffness and compliance tensors, assumed to be diagonally symmetric, positive definite, and constant.

The representative volume V of the heterogeneous medium is defined either as a sufficiently large sample that contains many phases and reflects typical macroscopic properties, or as a suitably selected unit cell of a (usually) periodic model of the actual material geometry. In either case, macroscopically homogeneous response and the implied existence of certain overall or effective properties are assumed under macroscopically uniform overall stress $\sigma(t)$ or uniform overall strain $\epsilon(t)$, prescribed through surface tractions or displacements specified on the surface S of V. When phase eigenstrains are present, we further assume that if V is free of surface tractions, the displacements on S of V are consistent with a macroscopically uniform overall strain $\mu(t)$. Similarly, if the volume V is subjected to zero surface displacements, then $\lambda(\mathbf{x}, t)$ denotes an eigenstress field in V that causes surface tractions on S consistent with a macroscopically uniform overall stress $\lambda(t)$. In analogy with (2), $\mu(t)$ and $\lambda(t)$ will be referred to as the overall transformation fields.

In actual solutions, the continuous fields are usually replaced by piecewise uniform approximations in the phases or in subvolumes Ω_ρ of a discretized unit cell,

$\rho = 1, 2, \ldots, M$, $\Omega_\rho \in V_r$, and $M \geqslant N$. Then, the total overall and local fields are related by

$$\epsilon_\rho(t) = \mathbf{A}_\rho \epsilon(t) \qquad \sigma_\rho(t) = \mathbf{B}_\rho \sigma(t) \tag{4}$$

where $\mathbf{A}_\rho$ and $\mathbf{B}_\rho$ are the mechanical strain and stress concentration factor tensors. Moreover, the total and the transformation fields are related by independent exact relations derived originally by Hill (1963) and Levin (1967)

$$\begin{aligned} \epsilon(t) &= \sum_{\rho=1}^{M} c_\rho \epsilon_\rho(t) \qquad \sigma(t) = \sum_{\rho=1}^{M} c_\rho \sigma_\rho(t) \\ \lambda(t) &= \sum_{\rho=1}^{M} c_\rho \mathbf{A}_\rho^{\mathrm{T}} \lambda_\rho(t) \qquad \mu(t) = \sum_{\rho=1}^{M} c_\rho \mathbf{B}_\rho^{\mathrm{T}} \mu_\rho(t) \end{aligned} \tag{5}$$

where the volume fractions of the subvolumes are given by $c_\rho = \Omega_\rho / V$.

The overall response may now be expressed in terms of the overall elastic stiffness $\mathbf{L}$, or compliance $\mathbf{M}$, and the transformation fields, as

$$\epsilon(t) = \mathbf{M}\sigma(t) + \mu(t) \qquad \sigma(t) = \mathbf{L}\epsilon(t) + \lambda(t) \tag{6}$$

where $\mathbf{M} = \mathbf{L}^{-1}$, $\lambda(t) = -\mathbf{L}\mu(t)$, $\mu(t) = -\mathbf{M}\lambda(t)$. The decomposition (2) applied to the overall quantities suggests that

$$\epsilon(t) = \mathbf{M}\sigma(t) + \mathbf{m}\theta(t) + \epsilon^{\mathrm{in}}(t) \qquad \sigma(t) = \mathbf{L}\epsilon(t) + \mathbf{l}\theta(t) + \sigma^{\mathrm{re}}(t) \tag{7}$$

and the relations (5) provide the well known connections (Hill 1963, Laws 1973)

$$\mathbf{L} = \sum_{\rho=1}^{M} c_\rho \mathbf{L}_\rho \mathbf{A}_\rho \qquad \mathbf{M} = \sum_{\rho=1}^{M} c_\rho \mathbf{M}_\rho \mathbf{B}_\rho \tag{8}$$

$$\mathbf{l} = \sum_{\rho=1}^{M} c_\rho \left(\mathbf{l}_\rho + \mathbf{L}_\rho \mathbf{a}_\rho\right) \qquad \mathbf{m} = \sum_{\rho=1}^{M} c_\rho \left(\mathbf{m}_\rho + \mathbf{M}_\rho \mathbf{b}_\rho\right) \tag{9}$$

where $\mathbf{l}$, $\mathbf{m} = -\mathbf{M}\mathbf{l}$ are the overall thermal stress and strain tensors, and $\mathbf{a}_\rho$, $\mathbf{b}_\rho$ are thermoelastic influence factors of the subvolumes.

3. Local fields

The local elastic and transformation fields are sought in terms of piecewise uniform approximations within phase volumes V_r, or subvolumes Ω_ρ, of discretized phases. Each subelement resides in only one phase r, but each phase may contain one or more subelements. As in (7), the effects of external mechanical loads and the piecewise uniform local transformations are superimposed,

$$\epsilon_\rho(t) = \mathbf{A}_\rho \epsilon(t) + \sum_{\eta=1}^{M} \mathbf{D}_{\rho\eta}\left[\mathbf{m}_\eta \theta(t) + \epsilon_\eta^{\mathrm{in}}(t)\right] \tag{10}$$

$$\sigma_\rho(t) = \mathbf{B}_\rho \sigma(t) + \sum_{\eta=1}^{M} \mathbf{F}_{\rho\eta}\left[\mathbf{l}_\eta \theta(t) + \sigma_\eta^{\mathrm{re}}(t)\right]. \tag{11}$$

$\mathbf{A}_\rho$ and $\mathbf{B}_\rho$ are the usual mechanical concentration factor tensors. Under overall strain $\epsilon(t) = \mathbf{0}$, $\mathbf{D}_{\rho\eta}$ gives the strain caused in Ω_ρ by a unit uniform eigenstrain located in Ω_η. Under overall stress $\sigma(t) = \mathbf{0}$, $\mathbf{F}_{\rho\eta}$ defines the stress in Ω_ρ due to a unit eigenstress in Ω_η. In what follows, $\mathbf{D}_{\rho\eta}$ and $\mathbf{F}_{\rho\eta}$ will be referred to as the transformation concentration factor tensors. If (10) were applied to a transformed ellipsoidal homogeneous inclusion in an infinite solid, the local strain would become $\epsilon_\rho = \mathbf{D}_{\rho\rho}\mu_\rho$, hence $\mathbf{D}_{\rho\rho}$ would be equal to the Eshelby tensor $\mathbf{S}$.

Simple examples of these tensors are found in two-phase media, with phases denoted as $r = \alpha, \beta$ (Dvorak 1990, equations (123)–(125)):

$$\mathbf{D}_{r\alpha} = (\mathbf{I} - \mathbf{A}_r)(\mathbf{L}_\alpha - \mathbf{L}_\beta)^{-1}\mathbf{L}_\alpha \qquad \mathbf{D}_{r\beta} = -(\mathbf{I} - \mathbf{A}_r)(\mathbf{L}_\alpha - \mathbf{L}_\beta)^{-1}\mathbf{L}_\beta \tag{12}$$

$$\mathbf{F}_{r\alpha} = (\mathbf{I} - \mathbf{B}_r)(\mathbf{M}_\alpha - \mathbf{M}_\beta)^{-1}\mathbf{M}_\alpha \qquad \mathbf{F}_{r\beta} = -(\mathbf{I} - \mathbf{B}_r)(\mathbf{M}_\alpha - \mathbf{M}_\beta)^{-1}\mathbf{M}_\beta. \tag{13}$$

In multiphase media, the expressions for the concentration factor tensors were found by Dvorak and Benveniste (1992) in terms of estimates derived with the self-consistent or Mori–Tanaka methods. For either method, the results are

$$\mathbf{D}_{rs} = (\mathbf{I} - \mathbf{A}_r)(\mathbf{L}_r - \mathbf{L})^{-1}(\delta_{rs}\mathbf{I} - c_s\mathbf{A}_s^{\mathrm{T}})\mathbf{L}_s \qquad r, s = 1, 2, \ldots, N \tag{14}$$

$$\mathbf{F}_{rs} = (\mathbf{I} - \mathbf{B}_r)(\mathbf{M}_r - \mathbf{M})^{-1}(\delta_{rs}\mathbf{I} - c_s\mathbf{B}_s^{\mathrm{T}})\mathbf{M}_s \qquad r, s = 1, 2, \ldots, N \tag{15}$$

where $\mathbf{L}$ and $\mathbf{M}$ are the respective estimates of the overall elastic stiffness and compliance tensors, while $\mathbf{A}_r$ and $\mathbf{B}_r$ are the related estimates of the elastic mechanical concentration factor tensors; $\mathbf{L}_r$, $\mathbf{M}_r$ are the phase elastic properties. δ_{rs} is the Kronecker symbol, but no summation is indicated by repeated indices.

It should be noted that applications of the self-consistent and Mori–Tanaka methods are restricted to certain material geometries described at the end of this section.

Evaluation of the mechanical and transformation concentration factor tensors in unit cell models has been discussed by Dvorak *et al* (1994). In particular, the kth column of the $\mathbf{D}_{rs}$ matrix for any two elements V_r and V_s of a unit cell was found to be

$$\mathbf{d}_{\rho\eta}^k = \mathbf{B}_\rho^* \mathbf{P}_\rho \mathbf{K}^{-1}\mathbf{f}_\eta^k \qquad k = 1, 2, \ldots, 6 \tag{16}$$

where the local strains ϵ_ρ are related to the overall displacements $\mathbf{u}$ by $\epsilon_\rho = \mathbf{B}_\rho^* \mathbf{P}_\rho \mathbf{u}$; $\mathbf{K}$ is the overall stiffness matrix; $\mathbf{f}_\eta^k$ is the overall load vector due to the component μ_η^k of μ_η.

To verify the accuracy of the numerical evaluation of the mechanical and transformation influence functions, one may compare the results with the general properties of these functions, derived by Dvorak and Benveniste (1992). There exist two exact relations for the transformation influence functions that evaluate the local fields in Ω_η caused by uniform transformations in Ω_ρ

$$\sum_{\rho=1}^{M} \mathbf{D}_{\eta\rho}(\mathbf{x}) = \mathbf{I} - \mathbf{A}_\eta(\mathbf{x}) \qquad \sum_{\rho=1}^{M} \mathbf{F}_{\eta\rho}(\mathbf{x}) = \mathbf{I} - \mathbf{B}_\eta(\mathbf{x}) \tag{17}$$

$$\sum_{\rho=1}^{M} \mathbf{D}_{\eta\rho}(\mathbf{x})\mathbf{M}_\rho = 0 \qquad \sum_{\rho=1}^{M} \mathbf{F}_{\eta\rho}(\mathbf{x})\mathbf{L}_\rho = \mathbf{0}. \tag{18}$$

In addition, the concentration factor tensors in (10) and (11) must satisfy

$$c_\eta \mathbf{D}_{\eta\rho}\mathbf{M}_\rho = c_\rho \mathbf{M}_\rho \mathbf{D}_{\rho\eta}^{\mathrm{T}} \qquad c_\eta \mathbf{F}_{\eta\rho}\mathbf{L}_\rho = c_\rho \mathbf{L}_\eta \mathbf{F}_{\rho\eta}^{\mathrm{T}} \tag{19}$$

$$\sum_{\rho=1}^{M} c_\rho \mathbf{D}_{\rho\eta} = 0 \qquad \sum_{\rho=1}^{M} c_\rho \mathbf{F}_{\rho\eta} = \mathbf{0} \tag{20}$$

where $\eta, \rho = 1, 2, \ldots, M$, the number of elements, and $c_\eta = \Omega_\eta / V$. These connections are exact but not independent; note that (18) and (19) give (20). Actual solutions then show that only (17) and (18) or (20) are independent. This provides $(2 \times M)$ independent relations for the $(M \times M)$ unknown transformation concentration factor tensors.

It can be verified that the results (12)–(15) satisfy (17)–(20) for two-phase materials of any geometry, and for those multiphase solids that contain or consist of inclusions of similar shape and alignment (Dvorak and Benveniste 1992).

The periodic unit cell models usually have internal symmetries that can facilitate evaluation of the transformation influence factors. While each specific unit cell geometry has to be considered separately, Dvorak *et al* (1994) describe the procedure for the periodic hexagonal array (PHA) model of fibrous composites (Teply and Dvorak 1988).

4. Inelastic response

The transformation concentration factors open the way to evaluation of the inelastic local fields. A specific constitutive relation must be adopted in Ω_η to connect the current values or rates of $\boldsymbol{\epsilon}_\eta^{\mathrm{in}}(t)$ or $\boldsymbol{\sigma}_\eta^{\mathrm{re}}(t)$ to the history of $\boldsymbol{\sigma}_\eta(t-\tau)$ or $\boldsymbol{\epsilon}_\eta(t-\tau)$, and $\theta(t-\tau)$, respectively. For piecewise uniform fields in the local volumes, one can formally write such constitutive relations in the general form

$$\boldsymbol{\sigma}_\eta^{\mathrm{re}}(t) = \mathbf{g}\big(\boldsymbol{\epsilon}_\eta(t-\tau), \theta(t-\tau)\big) \qquad \boldsymbol{\epsilon}_\eta^{\mathrm{in}}(t) = \mathbf{f}\big(\boldsymbol{\sigma}_\eta(t-\tau), \theta(t-\tau)\big). \tag{21}$$

When substituted into (10) and (11), this provides the governing equations for the total local fields

$$\boldsymbol{\epsilon}_\rho(t) + \sum_{\eta=1}^{M} \mathbf{D}_{\rho\eta}\mathbf{M}_\eta \mathbf{g}\big(\boldsymbol{\epsilon}_\eta(t-\tau), \theta(t-\tau)\big) = \mathbf{A}_\rho \boldsymbol{\epsilon}(t) + \mathbf{a}_\rho \theta(t) \tag{22}$$

$$\boldsymbol{\sigma}_\rho(t) + \sum_{\eta=1}^{M} \mathbf{F}_{\rho\eta}\mathbf{L}_\eta \mathbf{f}\big(\boldsymbol{\sigma}_\eta(t-\tau), \theta(t-\tau)\big) = \mathbf{B}_\rho \boldsymbol{\sigma}(t) + \mathbf{b}_\rho \theta(t) \tag{23}$$

where the thermal concentration factor tensors are $\mathbf{a}_\rho = \sum \mathbf{D}_{\rho\eta}\mathbf{m}_\eta$ and $\mathbf{b}_\rho = \sum \mathbf{F}_{\rho\eta}\mathbf{l}_\eta$.

The mechanical and transformation concentration factors depend only on elastic moduli and on local geometry. If these remain constant, the governing equations can be differentiated and used for evaluation of stress and strain increments, or their time rates. In this manner, the inelastic deformation problem for any heterogeneous medium is reduced to evaluation of the various elastic concentration factor tensors or matrices, and to solution of one of the equations (22), (23) along the prescribed overall deformation or stress path.

5. Elastic–plastic systems

In a heterogeneous medium with elastic–plastic phases, let the phase response under the locally uniform fields in V_r or Ω_η be represented by the constitutive relations

$$\begin{aligned} d\boldsymbol{\sigma}_r &= \boldsymbol{L}_r(\boldsymbol{\epsilon}_r - \boldsymbol{\beta}_r)d\boldsymbol{\epsilon}_r + \boldsymbol{l}_r(\boldsymbol{\epsilon}_r - \boldsymbol{\beta}_r)d\theta \\ d\boldsymbol{\epsilon}_r &= \boldsymbol{M}_r(\boldsymbol{\sigma}_r - \boldsymbol{\alpha}_r) + \boldsymbol{m}_r(\boldsymbol{\sigma}_r - \boldsymbol{\alpha}_r)d\theta \end{aligned} \tag{24}$$

where $\boldsymbol{L}_r$ and $\boldsymbol{M}_r$ are the instantaneous stiffness and compliance tensors, and $\boldsymbol{l}_r$, $\boldsymbol{m}_r$ are the thermal stress and strain tensors that typically describe the consequence of a variation of yield stress with temperature. $\boldsymbol{\alpha}_r$ and $\boldsymbol{\beta}_r$ are the back stresses and back strains that define the current centers of the yield and relaxation surfaces. These tensors depend on the past deformation history, hence the instantaneous magnitudes of their coefficients will vary within each local volume V_r or Ω_η. To prevent large errors in local fields, the material model selected should permit refined subdivisions of the representative volume.

Rewritting (21) as

$$\begin{aligned} d\boldsymbol{\sigma}_r^{re} &= \boldsymbol{L}_r^p + \boldsymbol{l}_r^p d\theta & d\boldsymbol{\epsilon}_r^{in} &= \boldsymbol{M}_r^p d\boldsymbol{\sigma}_r + \boldsymbol{m}_r^p d\theta \\ \boldsymbol{L}_r^p &= \boldsymbol{L}_r - \mathbf{L}_r & \boldsymbol{l}_r^p &= \boldsymbol{l}_r - \mathbf{l}_r \\ \boldsymbol{M}_r^p &= \boldsymbol{M}_r - \mathbf{M}_r & \boldsymbol{m}_r^p &= \boldsymbol{m}_r - \mathbf{m}_r \end{aligned} \tag{25}$$

and substituting into (22) and (23), one finds the following two systems of equations for local fields in elastic–plastic heterogeneous media:

$$d\boldsymbol{\epsilon}_\rho + \sum_{\eta=1}^{M} \mathbf{D}_{\rho\eta}\mathbf{M}_\eta \boldsymbol{L}_\eta^p d\boldsymbol{\epsilon}_\eta = \mathbf{A}_\rho d\boldsymbol{\epsilon} + \left(\mathbf{a}_\rho - \sum_{\eta=1}^{M} \mathbf{D}_{\rho\eta}\mathbf{M}_\eta \boldsymbol{l}_\eta^p\right)d\theta \tag{26}$$

$$d\boldsymbol{\sigma}_\rho + \sum_{\eta=1}^{M} \mathbf{F}_{\rho\eta}\mathbf{L}_\eta \boldsymbol{M}_\eta^p d\boldsymbol{\sigma}_\rho = \mathbf{B}_\rho d\boldsymbol{\sigma} + \left(\mathbf{b}_\rho - \sum_{\eta=1}^{M} \mathbf{F}_{\rho\eta}\mathbf{L}_\eta \boldsymbol{m}_\eta^p\right)d\theta. \tag{27}$$

In actual numerical solution, one may reduce these to the matrix forms

$$\{d\boldsymbol{\epsilon}_\rho\} = \left[\mathrm{diag}(\mathbf{I}) + [\mathbf{D}_{\rho\eta}\mathbf{M}_\eta \boldsymbol{L}_\eta^p]\right]^{-1}\left\{[\mathbf{A}_\rho]d\boldsymbol{\epsilon} - [\mathbf{D}_{\rho\eta}\mathbf{M}_\eta]\{\mathbf{l}_\eta + \boldsymbol{l}_\eta^p\}d\theta\right\} \tag{28}$$

$$\{d\boldsymbol{\sigma}_\rho\} = \left[\mathrm{diag}(\mathbf{I}) + [\mathbf{F}_{\rho\eta}\mathbf{L}_\eta \boldsymbol{M}_\eta^p]\right]^{-1}\left\{[\mathbf{B}_\rho]d\boldsymbol{\sigma} - [\mathbf{F}_{\rho\eta}\mathbf{L}_\eta]\{\mathbf{m}_\eta + \boldsymbol{m}_\eta^p\}d\theta\right\}. \tag{29}$$

The solutions are sought in the form

$$\{d\boldsymbol{\epsilon}_\rho\} = [\boldsymbol{A}_\rho]d\boldsymbol{\epsilon} + \{\boldsymbol{a}_\rho\}d\theta \qquad \{d\boldsymbol{\sigma}_\rho\} = [\boldsymbol{B}_\rho]d\boldsymbol{\sigma} + \{\boldsymbol{b}_\rho\}d\theta \tag{30}$$

where the instantaneous strain concentration factors $[\boldsymbol{A}_\rho]$ and the thermal strain concentration factors $\{\boldsymbol{a}_\rho\}$ are found as

$$[\boldsymbol{A}_\rho] = \left[\mathrm{diag}(\mathbf{I}) + [\mathbf{D}_{\rho\eta}\mathbf{M}_\eta \boldsymbol{L}_\eta^p]\right]^{-1}[\mathbf{A}_\rho] \tag{31}$$

$$\{\boldsymbol{a}_\rho\} = -\left[\mathrm{diag}(\mathbf{I}) + [\mathbf{D}_{\rho\eta}\mathbf{M}_\eta \boldsymbol{L}_\eta^p]\right]^{-1}\left\{[\mathbf{D}_{\rho\eta}\mathbf{M}_\eta]\{\boldsymbol{l}_\eta + \boldsymbol{l}_\eta^p\}\right\}. \tag{32}$$

A substitution of (31) into (8), when the latter is written for the instantaneous quantities, then provides the overall instantaneous stiffness matrix for the aggregate as

$$[L] = [c_\rho L_\rho]\Big[\mathrm{diag}(\mathbf{I}) + [\mathbf{D}_{\rho\eta}\mathbf{M}_\eta L_\eta^{\mathrm{p}}]\Big]^{-1}[\mathbf{A}_\rho]. \tag{33}$$

The instantaneous thermal stress vector is found as

$$\{l\} = [c_\rho L_\rho]\Big[\mathrm{diag}(\mathbf{I}) + [\mathbf{D}_{\rho\eta}\mathbf{M}_\eta L_\eta^{\mathrm{p}}]\Big]^{-1}\Big\{\{\mathbf{a}_\rho\} - [\mathbf{D}_{\rho\eta}\mathbf{M}_\eta]\{l_\eta^{\mathrm{p}}\}\Big\} + \Big\{\sum_{\eta=1}^{M} c_\eta l_\eta\Big\}. \tag{34}$$

An analogous procedure yields the overall instantaneous compliance matrix M and the thermal strain vector m. The result is

$$[M] = [c_\rho M_\rho]\Big[\mathrm{diag}(\mathbf{I}) + [\mathbf{F}_{\rho\eta}\mathbf{L}_\eta M_\eta^{\mathrm{p}}]\Big]^{-1}[\mathbf{B}_\rho] \tag{35}$$

$$\{m\} = [c_\rho M_\rho]\Big[\mathrm{diag}(\mathbf{I}) + [\mathbf{F}_{\rho\eta}\mathbf{L}_\eta M_\eta^{\mathrm{p}}]\Big]^{-1}\Big\{\{\mathbf{b}_\rho\} - [\mathbf{F}_{\rho\eta}\mathbf{L}_\eta]\{m_\eta^{\mathrm{p}}\}\Big\} + \Big\{\sum_{\eta=1}^{M} c_\eta m_\eta\Big\}. \tag{36}$$

The solution algorithm for elastic–plastic composites may be constructed as follows.

Step 1. For the given interval $t_1 \leqslant t \leqslant t_{n+1}$ of the prescribed histories $\sigma^0(t)$ and $\theta^0(t)$, select the number of increments n, and compute the time increment $h = (t_{n+1} - t_1)/n$.

Step 2. Set the initial values of the stress field $\sigma_\rho(t_1) = \hat{\sigma}_\rho$, the strain field $\epsilon_\rho(t_1) = \hat{\epsilon}_\rho$, of the center of the yield surface $\alpha_\rho(t_1) = \hat{\alpha}_\rho$ (see the appendix), and of the tensile yield stress $Y_\rho(t_1) = \hat{Y}_\rho$, in the elements $\rho = 1, 2, \ldots, M$.

Step 3. For $k = 1, 2, \ldots, n$, do steps 4–6.

Step 4. Compute the yield function $g_\rho^{(k)}(\sigma_\rho^{(k)} - \alpha_\rho^{(k)}, \theta_k)$ in the appendix.

Step 5. If $g_\rho^{(k)} < 0 \Rightarrow$ volume Ω_ρ is elastic, go to step 6; if $g_\rho^{(k)} = 0$, compute $\{\mathrm{d}\sigma_\rho\}_k$ from (29), with $\mathrm{d}\sigma$ replaced by $\mathrm{d}\sigma^0(t_k)$ and $\mathrm{d}\theta$ replaced by $\mathrm{d}\theta^0(t_k)$: if $(\partial g_\rho/\partial\sigma_\rho)_k \cdot (\mathrm{d}\sigma_\rho)_k \leqslant 0 \Rightarrow$ elastic unloading, go to step 6; if $(\partial g_\rho/\partial\sigma_\rho)_k \cdot (\mathrm{d}\sigma_\rho)_k > 0 \Rightarrow$ plastic loading, compute the instantaneous plastic compliance and thermal strain vectors $M_\rho^{\mathrm{p}}(\sigma_\rho^{(k)} - \alpha_\rho^{(k)}, \theta_k)$, $m_\rho^{\mathrm{p}}(\sigma_\rho^{(k)} - \alpha_\rho^{(k)}, \theta_k)$ in the appendix.

Step 6. Compute the stress field at time t_{k+1}:

$$\{\sigma_\rho\}_{k+1} = \{\sigma_\rho\}_k + (h/2)\{\mathrm{d}\sigma_\rho + \mathrm{d}\sigma_\rho^*\}_k$$
$$\{\mathrm{d}\sigma_\rho^*\}_k = \{\mathrm{d}\sigma_\rho(t_{k+1}, \{\sigma_\rho\}_k + h\{\mathrm{d}\sigma_\rho\}_k)\}$$

where $\mathrm{d}\sigma_\rho(t, \sigma_\rho)$ is given by (29). The corresponding strain, $\epsilon_\rho(t_{k+1})$, $\rho = 1, 2, \ldots, M$, and the center of yield surface $\alpha_\rho(t_{k+1})$, $\rho = 1, 2, \ldots, T$, are found from the constitutive equations given in the appendix; T is the number of elastic–plastic element volumes at time t_k.

The solution depends on the selected magnitude of the time increment h; an error of order h^2 is expected in the Runge–Kutta formula used. Our implementation of the above algorithm included iterations with various magnitudes of the time increment h. Specifically, the solution found at time t_{n+1} for the selected number n of time intervals was compared to

the solution found when the number of time increments was increased to $2n$. The solutions were compared in terms of the magnitude $\|\{\sigma_\rho\}\|$ of the stress vector. If the absolute difference $(\|\{\sigma_\rho\}\|_{n+1} - \|\{\sigma_\rho\}\|_{2n+1})$ was greater than γ, a specified tolerance, the process was repeated with the number of time intervals doubled again. Consequently, a series of solutions corresponding to time intervals n, $2n$, $4n$, $8n$, ... was generated until the selected convergence criterion was satisfied. Other solution strategies may be employed as well, for example, the time increment may be adjusted according to a specified tolerance (Sloan 1987).

6. Examples

To illustrate the numerical results obtained from (29), we apply the above procedure to modeling of the elastic–plastic response of a fibrous boron–aluminium composite. The PHA model described by Dvorak and Teply (1985), and Teply and Dvorak (1988) was used to represent the fibrous material. As shown in figure 1, the fibers are arranged in a hexagonal array and the fiber cross section is approximated by a six- or twelve-sided polygon. The composite volume is then divided into shaded and unshaded triangular prisms. It has been shown in the above work that under overall uniform strain or stress applied to the model composite, one can derive certain periodic boundary conditions for the prisms that guarantee that the local stress and strain fields in the shaded and unshaded prisms are related by a simple coordinate transformation; hence one of the prisms can be selected as the representative unit cell of the fibrous composite. Figure 2 shows the geometry of the unit cell for a hexagonal fiber. Higher-order polygons are used with refined meshes (figure 3). The calculations reported here were performed with the crude mesh of figure 3(a).

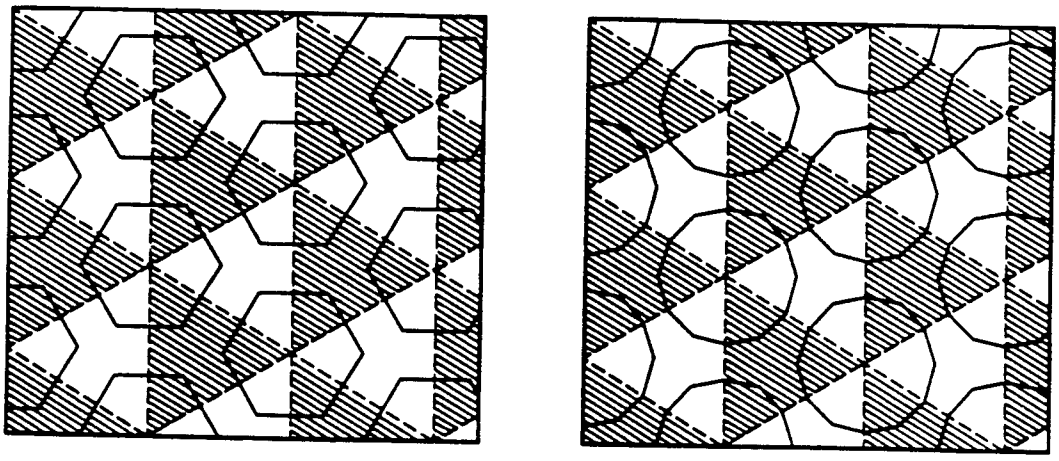


Figure 1. Transverse cross sections of the PHA model microstructures with hexagonal and dodecagonal cylindrical fibers.

In preparation for the TFA solution, the transformation concentration factors $\mathbf{F}_{\rho\eta}$, ρ, $\eta = 1, 2, \ldots, M$, were computed for the M subvolumes of the PHA unit cell with the procedure described briefly in section 3 (see also Dvorak *et al* 1994). The elastic properties of the boron fiber are taken as $E = 379.2$ GPa and $\nu = 0.21$ and those of the aluminium matrix are $E = 68.9$ GPa and $\nu = 0.33$. While the fiber is assumed to remain elastic, the matrix is elastic–plastic with initial tensile yield stress $Y = 24$ MPa. Constitutive equations

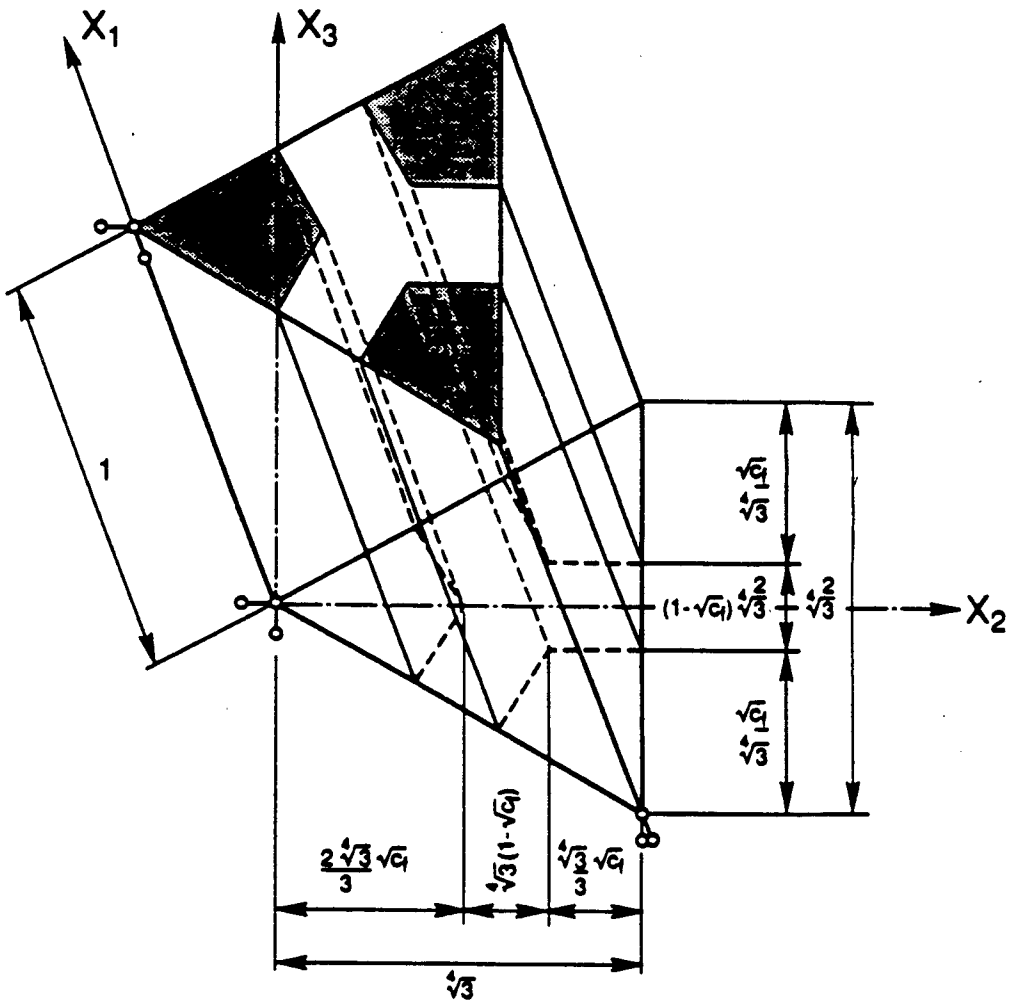


Figure 2. The geometry of the unit cell of the PHA model.

of the matrix assumed the Mises yield condition, the Prager–Ziegler kinematic hardening rule, and a linear stress–plastic strain response with plastic tangent modulus $H = 14$ GPa. Details of the constitutive law implemented in the TFA solution algorithm (section 5) are given in the appendix.

The overall stress–strain response computed under transverse tension σ_{22} and transverse shear σ_{23} using the TFA method is shown in figure 4. The response coincides with the solution found by direct evaluation of the overall strains using the standard elastic–plastic finite-element procedure of the ABAQUS program for the PHA unit cell. In both the TFA and the ABAQUS solutions, the number of load increments was selected as 40. Tables 1 and 2 show the stresses computed in the elements of the coarse mesh, figure 3(a), at the end of the overall normal stress cycle $\sigma_{22} = 0 \rightarrow 100$ MPa $\rightarrow 0$, and at the end of the overall transverse shear stress cycle $\sigma_{23} = 0 \rightarrow 100$ MPa $\rightarrow 0$, respectively. The corresponding plastic strain components ϵ^p_{22} and ϵ^p_{23} in the matrix elements are shown in tables 3 and 4.

The efficiency of the TFA method in comparison with the ABAQUS finite-element (FE) solution was evaluated in terms of the CPU time required in the two load cycles. Under the transverse tension cycle, the ABAQUS solution required 204 s while the TFA solution required 67 s. For the transverse shear loading cycle, the CPU times for the ABAQUS solution and

Table 1. The element stress σ_{22} computed at the end of an overall transverse tension cycle $\sigma_{22} = 0 \rightarrow 100 \rightarrow 0$ MPa.

Element No in figure 3(*a*)	FE solution by ABAQUS (MPa)	TFA solution (MPa)	% difference[a]
Fiber			
1	1.901 832 146 67	1.825 510 336 11	4.01
4	− 3.810 858 370 97	− 3.827 160 550 68	0.43
5	11.855 730 113 30	11.781 861 329 50	0.62
Matrix			
2	−13.643 539 447 0	−13.649 502 348 6	0.04
3	21.200 425 901 3	21.167 538 175 3	0.16
6	−13.726 424 830 9	−13.598 549 014 0	0.93
13	19.070 440 446 1	19.264 129 925 7	1.02
14	−14.550 383 063 1	−14.365 125 551 9	1.27
15	−13.034 267 690 1	−13.005 221 759 8	0.22

[a] ((ABAQUS ma · ude − TFA magnitude)/(ABAQUS magnitude)) × 100.

Table 2. The element stress σ_{23} computed at the end of an overall transverse shear cycle $\sigma_{23} = 0 \rightarrow 100 \rightarrow 0$ MPa.

Element No in figure 3(*a*)	FE solution by ABAQUS (MPa)	TFA solution (MPa)	% difference[a]
Fiber			
1	8.089 626 480 43	8.035 386 999 75	0.67
4	4.387 058 143 16	4.134 745 415 39	0.90
5	0.742 835 469 95	0.741 202 776 04	0.22
Matrix			
2	−1.641 704 393 73	−1.649 721 318 14	0.49
3	−4.375 080 355 53	−4.346 638 830 63	0.65
6	−4.947 529 902 38	−4.917 911 392 98	0.60
13	0.464 416 136 93	0.472 410 022 58	1.72
14	−5.188 596 823 47	−4.943 898 121 39	4.27
15	−4.445 598 537 65	−4.443 584 753 34	0.05

[a] ((ABAQUS magnitude − TFA magnitude)/(ABAQUS magnitude)) × 100.

the TFA method were 263 s and 67 s, respectively. Additional time is required to obtain the transformation concentration factors. This is, however, a once only operation for a given mesh.

Another comparison of the elastic–plastic response computed with the TFA and FE methods was made for the mesh of figure 3(*a*) and a complex loading path in the σ_{22}–σ_{23} stress space (figure 5). Figures 6 and 7 show the overall stress–strain response computed with the TFA method where the numbered symbols correspond to the loading points indicated in figure 5. The local stresses and plastic strains found with the TFA and FE methods at the end of the loading path are compared in tables 5 and 6, respectively, for selected elements. Again the local fields computed by the two methods are essentially identical.

While the TFA method appeared more efficient than the FE method for the unit cell considered in the above example (figure 3(*a*)), the number of operations required in each method depends on the number of elements. The cost of both the TFA and FE solutions depends on many factors, such as the specified tolerance and the number of iterations required to achieve such tolerance. More exact comparisons of the efficiency of the two methods can be made only in specific applications.

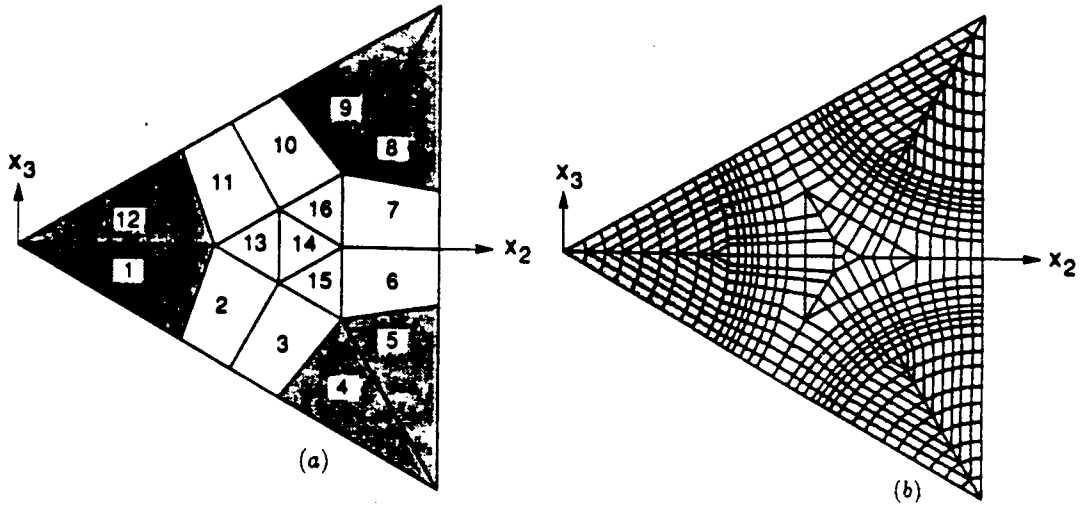


Figure 3. Examples of finite-element meshes in the unit cell of the PHA model.

Table 3. The matrix plastic normal strain ϵ_{22}^{p} computed at the end of an overall transverse tension cycle $\sigma_{22} = 0 \rightarrow 100 \rightarrow 0$ MPa.

Element No in figure 3(*a*)	FE solution by ABAQUS (10^{-6})	TFA solution (10^{-6})	% difference[a]
2	537.233 705 58	533.306 741 20	0.73
3	1153.372 617 18	1154.158 834 61	0.07
6	1151.974 909 64	1152.981 821 29	0.09
13	276.016 801 09	271.873 804 19	1.50
14	− 47.401 785 75	− 50.239 488 19	5.99
15	1158.020 131 50	1158.164 151 96	0.01

[a] ((ABAQUS magnitude − TFA magnitude)/(ABAQUS magnitude)) × 100.

Table 4. The matrix plastic shear strain $2\epsilon_{23}^{p}$ computed at the end of an overall transverse shear cycle $\sigma_{23} = 0 \rightarrow 100 \rightarrow 0$ MPa.

Element No in figure 3(*a*)	FEM solution by ABAQUS (10^{-6})	TFA solution (10^{-6})	% difference[a]
2	2591.297 325 47	2590.428 124 82	0.03
3	1368.390 414 86	1363.588 357 03	0.35
6	1820.690 876 64	1827.880 195 43	0.40
13	3068.747 699 46	3070.460 674 96	0.06
14	− 708.059 347 36	− 724.462 785 67	2.32
15	824.209 068 91	820.199 975 76	0.49

[a] ((ABAQUS magnitude − TFA magnitude)/(ABAQUS magnitude)) × 100.

Note also that the TFA method can readily use any selected constitutive equation for the phases, whereas a separate UMAT routine would be needed for implementation of such equations into the ABAQUS program. Such examples were solved for viscoelastic and viscoplastic systems; these are discussed by Dvorak and co-workers (1994).

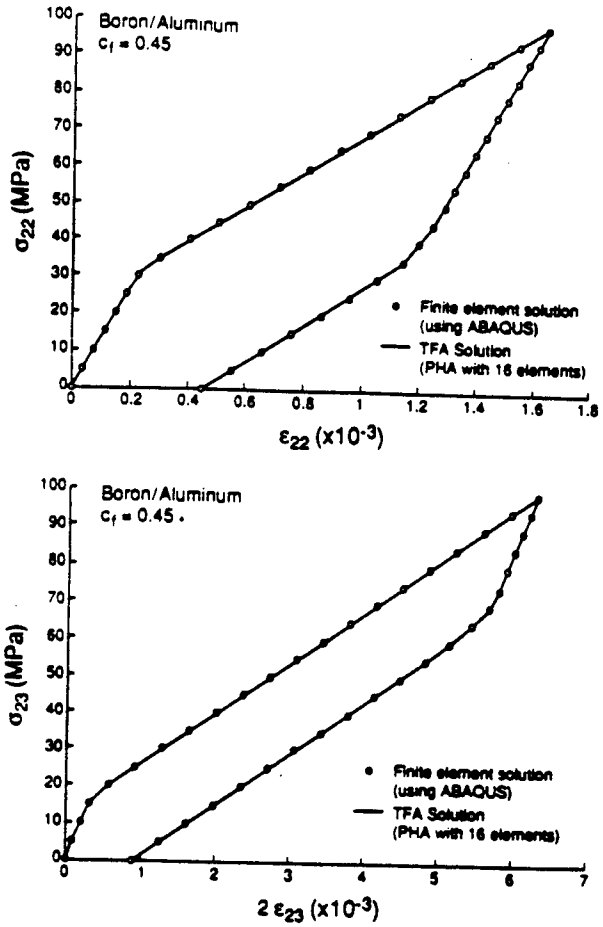


Figure 4. Overall stress–strain predictions found with the finite-element and TFA methods for an elastic–plastic B–Al composite under transverse tension loading and transverse shear loading.

7. Conclusions

The transformation field analysis is a general method for solving inelastic deformation and other incremental problems in heterogeneous media with many interacting inhomogeneities. The various unit cell models, or the corrected inelastic self-consistent or Mori–Tanaka formulations, the so-called Eshelby method, and the Eshelby tensor itself are all seen as special cases of this more general approach. The method easily accommodates any uniform overall loading path, inelastic constitutive equation, and micromechanical model. The model geometries are all incorporated in a similar manner, through the mechanical transformation influence functions or concentration factor tensors derived from elastic solutions for the chosen geometry and the elastic moduli. Thus, there is no need to solve inelastic boundary value or inclusion problems; indeed such solutions are often associated with erroneous procedures that violate (5); this was discussed by Dvorak (1992). In comparison with the finite-element method in unit cell model solutions, the present method is more efficient for cruder meshes. Moreover, there is no need to implement inelastic constitutive equations into a finite-element program. In addition to the examples shown herein, the method can be applied to many other problems, such as those arising in active materials with eigenstrains induced by components made of shape memory alloys or other actuators. Progress has also been made in applications to electroelastic composites, and to problems involving damage

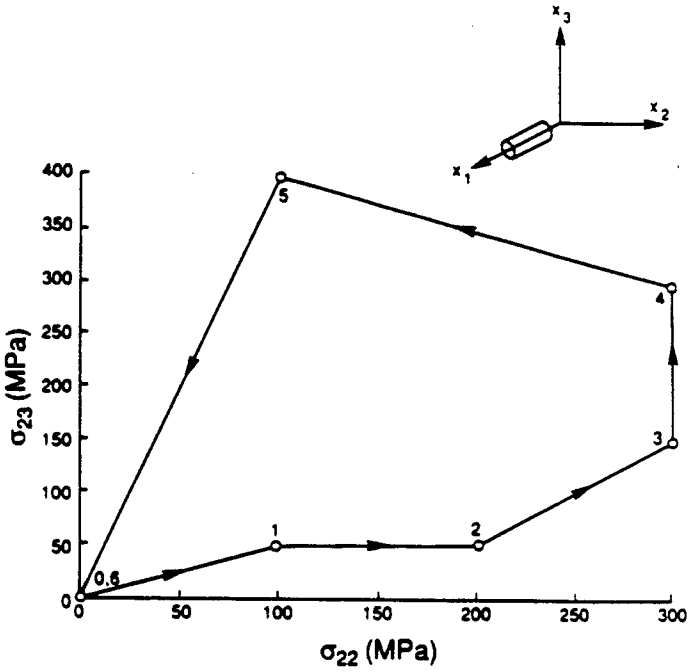


Figure 5. A transverse tension–transverse shear stress path applied to an elastic–plastic B–Al composite.

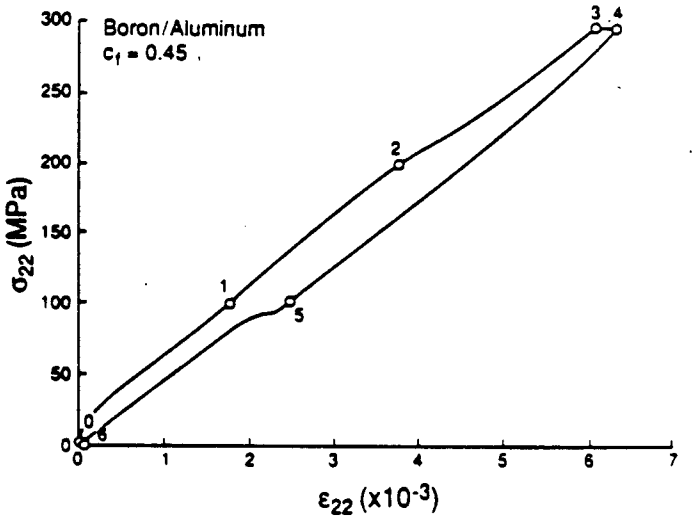


Figure 6. The overall σ_{22}–ϵ_{22} response predicted by the TFA method for the loading path of figure 5.

development in multiphase solids.

Acknowledgments

This work was supported by the Air Force Office of Scientific Research, Office of Naval Research, and by the ONR/ARPA URI program at Rensselaer.

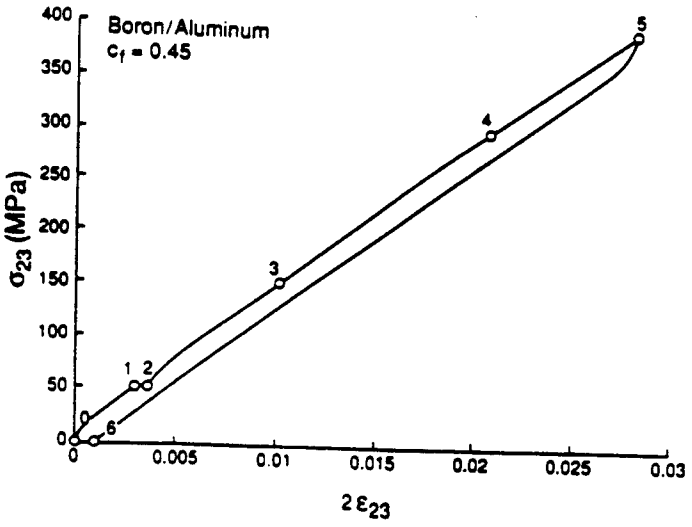


Figure 7. The overall σ_{23}–ϵ_{23} response predicted by the TFA method for the loading path of figure 5.

Table 5. Element stresses σ_{22} and σ_{23} computed at the end of the loading path of figure 5.

Element No[a]	σ_{22} (MPa)			σ_{23} (MPa)		
	ABAQUS	TFA	% difference[b]	ABAQUS	TFA	% difference[b]
Fiber						
1	2.486 314 943	2.484 838 314	0.06	6.199 577 168	6.196 482 812	0.05
4	− 2.496 518 548	− 2.495 716 646	0.03	2.734 338 180	2.732 595 877	0.06
Matrix						
2	−15.199 597 040	−15.195 990 720	0.02	−1.478 601 859	−1.478 106 587	0.03
3	− 0.237 086 563	− 0.233 915 256	1.34	−4.923 139 542	−4.922 870 483	0.01
13	3.611 850 432	3.597 884 176	0.39	0.508 403 072	0.508 454 116	0.01
15	−34.973 727 350	−34.967 938 250	0.02	−5.455 541 995	−5.455 215 211	0.01

[a] See figure 3(*a*).
[b] ((ABAQUS magnitude − TFA magnitude)/(ABAQUS magnitude)) × 100.

Table 6. Matrix plastic strains ϵ_{22}^p and $2\epsilon_{23}^p$ computed at the end of the loading path of figure 5.

Element No[a]	ϵ_{22}^p (10^{-6})			$2\epsilon_{23}^p$ (10^{-6})		
	ABAQUS	TFA	% difference[b]	ABAQUS	TFA	% difference[b]
2	− 14.265 822 5	− 14.267 543 7	0.01	2612.041 23	2612.150 41	0.004
3	− 945.350 097 1	− 945.433 174 0	0.01	1378.968 67	1378.979 82	0.001
13	− 7.695 432 3	− 7.580 595 0	1.49	3077.512 06	3077.522 59	0.000
15	−1014.387 728 0	−1014.377 705 0	0.001	599.298 64	599.438 07	0.020

[a] See figure 3(*a*).
[b] ((ABAQUS magnitude − TFA magnitude)/(ABAQUS magnitude)) × 100.

Appendix

This is a brief summary of constitutive equations for elastic–plastic homogeneous materials subjected to uniform stress or strain and temperature changes. Response under such

thermomechanical loads is determined with the help of a yield surface $g(\sigma, \theta) = 0$, which contains the stress states that cause purely elastic deformations. Assuming kinematic and isotropic hardening, the Mises form of the yield surface is given by

$$g(\sigma, \theta) \equiv \tfrac{3}{2}(\mathbf{s} - \mathbf{a}) : (\mathbf{s} - \mathbf{a}) - Y^2(\theta) = 0 \tag{A1}$$

where $\mathbf{s}$ is the deviatoric stress, $\mathbf{a}$ is the center of the yield surface in the deviatoric stress space, and Y is the yield stress in simple tension. In (A1), we use the notation $(\mathbf{a}:\mathbf{b})$ to denote the inner product of second order tensors a_{ij} and b_{ij}. The elastic behavior is in effect if $g < 0$, or if $g = 0$ and $[(\partial g/\partial\sigma) : d\sigma + (\partial g/\partial\theta)d\theta] \leqslant 0$. On the other hand, elastic–plastic deformation takes place if $g = 0$ and $[(\partial g/\partial\sigma) : d\sigma + (\partial g/\partial\theta)d\theta] > 0$. In this case, the instantaneous plastic compliance M^P, stiffness L^P, and the thermal strain and stress vectors m^P, l^P in (25) are given by (Bahei-El-Din 1990, Shah 1991)

$$M^P = (3/2H)(\mathbf{n} : \mathbf{n}^T) \qquad L^P = -(2G/(1 + H/3G))(\mathbf{n} : \mathbf{n}^T) \tag{A2}$$

$$m^P = -((\sqrt{3}Y'(\theta)/(\sqrt{2}H))\mathbf{n} \tag{A3}$$

$$l^P = (2G/(1 + H/3G))(\mathbf{n}^T\mathbf{m} + (Y'(\theta)/\sqrt{6}G))\mathbf{n} \tag{A4}$$

$$H = (d\bar{\sigma} - Y'(\theta)d\theta)/d\bar{\epsilon}^P \qquad d\bar{\sigma} = \sqrt{(\tfrac{3}{2}d\mathbf{s} : d\mathbf{s})} \qquad d\bar{\epsilon}^P = \sqrt{(\tfrac{2}{3}d\epsilon^P : d\epsilon^P)} \tag{A5}$$

$$\mathbf{n} = (1/\sqrt{(2/3)}Y)[\bar{s}_{11}\bar{s}_{22}\bar{s}_{33}2\bar{s}_{32}2\bar{s}_{31}2\bar{s}_{12}]^T \qquad \bar{\mathbf{s}} = \sigma - \mathbf{a}. \tag{A6}$$

Here, G is the elastic shear modulus, $Y'(\theta) = dY/d\theta$, ϵ^P is the plastic strain vector, and H is the plastic tangent modulus of the stress–plastic strain curve. The product $\mathbf{n}:\mathbf{n}^T$ in (A2) denotes the tensor product $n_{ij}n_{kl}$; $\mathbf{m}$ is the elastic thermal strain tensor.

Evolution of the center of the matrix yield surface $\mathbf{a}$ and the plastic tangent modulus H may be described in several different ways, to fit experimental observations. Specific forms of the Prager–Ziegler and Phillips hardening rules for thermomechanical loads can be found in the articles by Bahei-El-Din (1990), Dvorak (1991) and Shah (1991). The variation of the plastic tangent modulus H can be found with a two-surface plasticity theory such as that given by Dafalias and Popov (1976).

References

Bahei-El-Din Y A 1990 Plasticity analysis of fibrous composite laminates under thermomechanical loads *Thermal and Mechanical Behavior of Metal Matrix and Ceramic Matrix Composites (ASTM STP 1080)* ed J M Kennedy, H H Moeller and W S Johnson (Philadelphia, PA: American Society for Testing and Materials) pp 20–39

Dafalias Y F and Popov E P 1976 Plastic internal variables formalism of cyclic plasticity *J. Appl. Mech.* **43** 645–51

Dvorak G J 1990 On uniform fields in heterogeneous media *Proc. R. Soc.* A **431** 89–110

—— 1991 Plasticity theories for fibrous composite materials *Metal Matrix Composites. Mechanisms and Properties* vol 2, ed R K Everett and R J Arsenault (Boston, MA: Academic) pp 1–77

—— 1992 Transformation field analysis of inelastic composite materials *Proc. R. Soc.* A **437** 311–27

Dvorak G J, Bahei-El-Din Y A and Wafa A M 1994 Implementation of the transformation field analysis for inelastic composite materials *Comput. Mech.* at press

Dvorak G J and Benveniste Y 1992 On transformation strains and uniform fields in multiphase elastic media *Proc. R. Soc.* A **437** 291–310

Dvorak G J and Teply J L 1985 Periodic hexagonal array models for plasticity analysis of composite materials *Plasticity Today: Modeling, Methods and Applications, W Olszak Memorial Volume* ed A Sawczuk and V Bianchi (Amsterdam: Elsevier) pp 623–42

Hill R 1963 Elastic properties of reinforced solids: some theoretical principles *J. Mech. Phys. Solids* **11** 357–72

Laws N 1973 On the thermostatics of composite materials *J. Mech. Phys. Solids* **21** 9–17

Levin V M 1967 Thermal expansion coefficients of heterogeneous materials *Mekh. Tverd. Tela* **2** 88–94 (Engl. Transl. 1967 *Mech. Solids* **11** 58–61)

Shah R S 1991 Modeling and analysis of high temperature inelastic deformation in metal matrix composites *PhD Thesis* Rensselaer Polytechnic Institute, Troy, NY

Sloan S W 1987 Substepping schemes for the numerical integration of elastoplastic stress–strain relations *Int. J. Numer. Methods Eng.* **24** 893–911

Teply J L and Dvorak G J 1988 Bounds on overall instantaneous properties of elastic–plastic composites *J. Mech. Phys. Solids* **36** 29–58

EFFECTIVE LOCAL PROPERTIES FOR MODELLING OF FUNCTIONALLY GRADED COMPOSITE MATERIALS

GEORGE J. DVORAK and JOSEPH R. ZUIKER
Rensselaer Polytechnic Institute, Troy, NY 12180–3590, USA
Wright Laboratory, Wright–Patterson AFB, OH 45433–7817, USA

Abstract

A brief survey is presented of recently developed techniques for estimating overall elastic stiffness of statistically homogeneous multiphase solids subjected to large stress gradients. The stiffness estimates, based on linearly varying fields, provide local properties for a finite element analysis of functionally graded composite materials. Comparisons with selected experiments are encouraging, however, significant differences in local fields and overall response are found in comparisons with predictions obtained from standard homogenization techniques.

1. Introduction

Functionally graded materials are typically manufactured as particulate, layered or fibrous composites with variable concentrations of the phases. In service, they are intended for applications involving large stress and/or temperature gradients, which may produce significantly different local fields in distinct subvolumes of the microstructure. Therefore, both variable local properties and field gradients must be taken into consideration in analysis and design of graded material parts. A finite element analysis is indicated, with element properties derived from a suitable model of the microstructure. However, even if the material property variation is approximated as piecewise uniform, standard homogenization techniques, for statistically homogeneous systems under uniform macroscopic fields, may not provide reliable estimates of effective material response to the gradient stress or deformation fields. Instead, the effect of field gradients must be considered in modelling of the effective element properties.

This paper outlines derivation of overall stiffness estimates for statistically homogeneous composites subjected to linearly varying overall stress or strain fields, in terms of volume fractions, shapes, and elastic moduli of the phases [1,2]. The microstructure is modeled as a collection of ellipsoidal inclusions, and the Asaro–Barnett [3] solution of the non–uniform transformation strain problem, in conjunction with modified dilute approximation and Mori–Tanaka [4] assumptions, is used in finding estimates of mechanical phase concentration factors for linear local fields, and of the overall stiffness. Under given gradient loads, the standard and linear methods predict very different strain energy densities and local and overall strain gradients, in material volumes containing less than about 100 fibres or 1000 particles, which may be comparable in size to finite elements subdividing a graded material part or structure.

D. F. Parker and A. H. England (eds.),
IUTAM Symposium on Anisotropy, Inhomogeneity and Nonlinearity in Solid Mechanics, 103–108.

2. Inclusions and Inhomogeneities in Linearly Varying Fields

For ellipsoidal inclusions in isotropic solids, Eshelby [5], and in anisotropic solids, Asaro and Barnett [3] show that if the applied eigenstrain distribution is linear, then the strain field in the inclusion also varies linearly. In particular, let a large volume V of an elastic material of stiffness $\mathbf{L}_1$ be subjected to the overall strain

$$\epsilon_{ij}^{(0)}(\boldsymbol{x}) = \epsilon_{ij}^{(0)} + \kappa_{ijq}^{(0)}\, x_q\,, \tag{1}$$

imposed by corresponding displacements on its surface S. Let $V_r \in V$ contain a homogeneous ellipsoidal inclusion subjected to the eigenstrain

$$\mu_{kl}^{(r)}(\boldsymbol{x}) = \mu_{kl}^{(r)} + \gamma_{klp}^{(r)}\,(x_p - \bar{x}_p), \tag{2}$$

where $\bar{\boldsymbol{x}}$ is the centroid of V_r. Then, the local strain field in V_r is given by

$$\epsilon_{ij}^{(r)}(\boldsymbol{x}) = \epsilon_{ij}^{(0)}(\boldsymbol{x}) + S_{ijkl}\mu_{kl}^{(r)} + S^*_{ijklqm}\,\gamma_{klq}^{(r)}\,(x_m - \bar{x}_m), \tag{3}$$

where S_{ijkl} is the Eshelby tensor in $\mathbf{L}_1$ and S^*_{ijklqm} is the *linear* Eshelby tensor that relates the linear strain gradient component in the x_m–direction, to the x_q–direction component of the gradient of the applied eigenstrain (2). Using a linear field variant of the equivalent inclusion method, one can show that the strain field in an ellipsoidal inhomogeneity $\mathbf{L}_r$ in V_r, under the overall strain field (1) varies linearly and can be written as,

$$\epsilon_{ij}^{(r)}(\boldsymbol{x}) = \epsilon_{ij}^{(r)} + \kappa_{ijk}^{(r)}\,(x_k - \bar{x}_k^{(r)}), \tag{4}$$

with the evaluation,

$$\hat{\boldsymbol{\epsilon}}_r = [\hat{\mathbf{I}} - \hat{\mathbf{S}}\mathbf{L}_1^{-1}(\hat{\mathbf{L}}_1 - \hat{\mathbf{L}}_r)]^{-1}\hat{\mathbf{K}}_r\hat{\boldsymbol{\epsilon}}_0 \qquad \hat{\boldsymbol{\sigma}}_r = \hat{\mathbf{L}}_r\hat{\boldsymbol{\epsilon}}_r\,, \tag{5}$$

where $\hat{\boldsymbol{\epsilon}}_r$ and $\hat{\boldsymbol{\epsilon}}_0$ are the local and overall linear strain fields, represented by (24x1) and (24x24) matrices, with (6x1) and (6x6) submatrix coefficients,

$$\hat{\boldsymbol{\epsilon}}_r = \{\epsilon_{ij}^{(r)}\ \ \kappa_{ij1}^{(r)}\ \ \kappa_{ij2}^{(r)}\ \ \kappa_{ij3}^{(r)}\}^T \qquad \hat{\boldsymbol{\epsilon}}_0 = \{\epsilon_{ij}^{(0)}\ \ \kappa_{ij1}^{(0)}\ \ \kappa_{ij2}^{(0)}\ \ \kappa_{ij3}^{(0)}\}^T$$

$$\hat{\mathbf{K}}_r = \begin{bmatrix} \mathbf{I} & \bar{\mathbf{x}}_1^{(r)}\mathbf{I} & \bar{\mathbf{x}}_2^{(r)}\mathbf{I} & \bar{\mathbf{x}}_3^{(r)}\mathbf{I} \\ 0 & \mathbf{I} & 0 & 0 \\ 0 & 0 & \mathbf{I} & 0 \\ 0 & 0 & 0 & \mathbf{I} \end{bmatrix} \quad \hat{\mathbf{L}}_r = \begin{bmatrix} \mathbf{L}_r & 0 & 0 & 0 \\ 0 & \mathbf{L}_r & 0 & 0 \\ 0 & 0 & \mathbf{L}_r & 0 \\ 0 & 0 & 0 & \mathbf{L}_r \end{bmatrix} \quad \hat{\mathbf{S}} = \begin{bmatrix} \mathbf{S}_0 & 0 & 0 & 0 \\ 0 & \mathbf{S}_{11} & \mathbf{S}_{12} & \mathbf{S}_{13} \\ 0 & \mathbf{S}_{21} & \mathbf{S}_{22} & \mathbf{S}_{23} \\ 0 & \mathbf{S}_{13} & \mathbf{S}_{23} & \mathbf{S}_{33} \end{bmatrix}$$

The $\mathbf{I}$ and $\hat{\mathbf{I}}$ are (6x6) and (24x24) identity matrices, $\mathbf{L}_1$ is analogous to $\mathbf{L}_r$, $\mathbf{S}_0$ is the (6x6) matrix form of the Eshelby tensor, and $\mathbf{S}_{ij}$ are (6x6) submatrices derived from the linear Eshelby tensor.

3. Statistically Homogeneous Solids under Linear Boundary Conditions

Consider next a representative volume element of a multiphase medium with a microstructure that can be approximated as a collection of inhomogeneities $r = 2, 3, \ldots N$, bonded to a common matrix $r = 1$, with constant phase volume fractions in a representative volume element. Again, the applied overall strain is prescribed as in (1). The local strain fields, which may be nonuniform and possibly discontinuous, are approximated by linear fields (4). Connections between the local and overall fields are obtained from a least square approximation of the local strains and their averages as,

$$\epsilon_{ij}^{(0)} = \frac{1}{V}\int_V \epsilon_{ij}(x)dV,\ \kappa_{ijq}^{(0)}J_{qk} = \frac{1}{V}\int_V (x_k - \bar{x}_k)\epsilon_{ij}(x)dV,\ J_{ij} = \frac{1}{V}(x_i - \bar{x}_i)(x_j - \bar{x}_j)dV \quad (6)$$

$$\epsilon_{ij}^{(r)} = \frac{1}{V_r}\int_{V_r} \epsilon_{ij}(x)dV \qquad \kappa_{ijq}^{(r)}J_{qk}^{(r)} = \frac{1}{V_r}\int_{V_r} (x_k - \bar{x}_k^{(r)})\epsilon_{ij}(x)dV. \quad (7)$$

Substituting (7) into (6), and assuming that V is symmetric with respect to the planes $x_k = \bar{x}_k^{(r)}$, one can find the connection,

$$\hat{C}\,\hat{\epsilon}_0 = \sum_{i=1}^{N} \hat{C}_r\,\hat{\epsilon}_r \quad (8)$$

$$\hat{C} = \begin{bmatrix} I & 0 & 0 & 0 \\ 0 & J_{11}I & 0 & 0 \\ 0 & 0 & J_{22}I & 0 \\ 0 & 0 & 0 & J_{33}I \end{bmatrix} \quad \hat{C}_r = c_r \begin{bmatrix} I & 0 & 0 & 0 \\ \bar{x}_1^{(r)}I & J_{11}^{(r)}I & 0 & 0 \\ \bar{x}_2^{(r)}I & 0 & J_{22}^{(r)}I & 0 \\ \bar{x}_3^{(r)}I & 0 & 0 & J_{33}^{(r)}I \end{bmatrix}.$$

If V is not symmetric, off–diagonal terms appear in the lower (18x18) submatrices.

As in the case of heterogeneous media under uniform boundary conditions, the local strain fields can now be related to the overall strains by certain concentration factors. For the linearly varying local and overall fields, we write

$$\hat{\epsilon}_r = \hat{A}_r\,\hat{\epsilon}_0\,, \quad (9)$$

where $\hat{A}_r$ is the mechanical strain concentration factor matrix that can be evaluated from certain micromechanical models; a similar form can be written for the local stresses. For example, the *dilute approximation* assumes a model composite material reinforced by ellipsoidal inhomogeneities, but neglects their interaction. Each phase is regarded as a solitary inhomogeneity, hence one can utilize (5) to the dilute approximation estimate

$$\hat{\mathbf{A}}_r^{(D)} = [\hat{\mathbf{I}} - \hat{\mathbf{S}}\mathbf{L}_1^{-1}(\hat{\mathbf{L}}_1 - \hat{\mathbf{L}}_r)]^{-1}\hat{\mathbf{K}}_r \,. \tag{10}$$

A modified *Mori–Tanaka* [4] assumption simulates interaction of the phases by embedding each inhomogeneity in a large volume of the matrix ($r = 1$) which is loaded by remotely applied displacements corresponding to the matrix average strain and *strain gradient.* In particular, for a single inhomogeneity in a large volume of matrix of stiffness $\mathbf{L}_1$,

$$\hat{\epsilon}_r = \hat{\mathbf{T}}_r \hat{\epsilon}_1 \qquad \hat{\mathbf{T}}_1 = \hat{\mathbf{I}} \qquad \hat{\mathbf{T}}_r = \hat{\mathbf{A}}_r^{(D)} \text{ for } r > 1. \tag{11}$$

With reference to (8), one can then find the strain concentration factor as

$$\hat{\mathbf{A}}_1^{(M)} = [\hat{\mathbf{C}}_1 + \sum_{s=1}^{N} \hat{\mathbf{C}}_s \hat{\mathbf{T}}_s]^{-1}\hat{\mathbf{C}} \qquad \hat{\mathbf{A}}_r^{(M)} = \hat{\mathbf{T}}_r \hat{\mathbf{A}}_1^{(M)} \text{ for } r > 1. \tag{12}$$

The self–consistent estimate can be formally derived in a similar manner, however, its evaluation is unlikely at present, as the Eshelby tensors (3) would need to be known for an elastic solid with the same gradient stiffness as the effective medium. In contrast to the simple diagonal form shown in (5), this stiffness will have nonzero off–diagonal terms, hence the Asaro–Barnett results will not apply.

The overall or effective gradient stiffness $\hat{\mathbf{L}}$ of the statistically homogeneous medium can be found in terms of the known strain concentration factors. Noting that the local and overall stresses are related, in analogy with (8), as,

$$\hat{\mathbf{C}}\,\hat{\sigma}_0 = \sum_{r=1}^{N} \hat{\mathbf{C}}_r \hat{\sigma}_r \,, \tag{13}$$

we use (5_2) and (9) to find,

$$\hat{\sigma} = \hat{\mathbf{L}}\,\hat{\epsilon}_0 \qquad \hat{\mathbf{L}} = \hat{\mathbf{C}}^{-1} \sum_{r=1}^{N} \hat{\mathbf{C}}_r \hat{\mathbf{L}}_r \hat{\mathbf{A}}_r \,. \tag{14}$$

This effective gradient stiffness can be written in terms of the (6x6) submatrices $\mathbf{L}_{ij}$. To emphasize the differences between (14) and an analogous estimate derived from a standard homogenization method for uniform local and overall fields, we write the expanded forms of the two effective gradient stiffnesses, in terms of the (6x6) submatrices $\mathbf{L}_{ij}$:

$$\hat{\mathbf{L}} = \begin{bmatrix} \mathbf{L}_{00} & 0 & 0 & 0 \\ 0 & \mathbf{L}_{11} & \mathbf{L}_{12} & \mathbf{L}_{13} \\ 0 & \mathbf{L}_{21} & \mathbf{L}_{22} & \mathbf{L}_{23} \\ 0 & \mathbf{L}_{31} & \mathbf{L}_{32} & \mathbf{L}_{33} \end{bmatrix} \qquad \hat{\mathbf{L}}_{std} = \begin{bmatrix} \mathbf{L} & 0 & 0 & 0 \\ 0 & \mathbf{L} & 0 & 0 \\ 0 & 0 & \mathbf{L} & 0 \\ 0 & 0 & 0 & \mathbf{L} \end{bmatrix} . \tag{15}$$

4. Comparisons of Strain Energy Densities

To appreciate the differences between the predictions of local fields and overall properties found from the mean–field or standard Mori–Tanaka method and its gradient form, we evaluate the strain energy density of a specific composite material, with overall gradient stiffness estimated by the two forms (15), under identical boundary conditions. In a given volume V, the strain energy density is

$$W = \frac{1}{2V}\int_V \sigma_{ij}(\mathbf{x})\,\epsilon^{(0)}_{ij}(\mathbf{x})\,dV = \frac{1}{2}\,\hat{\sigma}^T\,\hat{C}\,\hat{L}^{-1}\hat{\sigma}. \tag{16}$$

The composite material has an isotropic carbon (C) matrix (E = 28GPa, $\nu = 0.3$) reinforced by aligned, continuous silicon–carbide (SiC) fibres or spherical particles (E = 320GPa, $\nu = 0.3$); the reinforcement volume fraction is taken as equal to 0.5. However, only a single fibre or particle occupying a 1 mm^3 volume is considered in finding the inertia tensors in (7). We evaluate (16) with the two stiffnesses (15), and show the ratio of W/W_{std} for selected overall loading conditions.

Figure 1 shows the energy ratio as a function of $\eta^0_{113}/\sigma^0_{11}$, the ratio of the applied stress gradient, in the transverse x_3–direction, of the overall normal stress in the fibre direction x_1, to the normal stress itself. When the gradient stress field component is zero, the energy ratio $W/W_{std} = 1$, and there is no difference between the two procedures. This is expected, since the modified method provides the same estimate for the upper left (6x6) sub–matrix as the standard method.

This and other comparisons indicate that, for particle reinforcement with $E_p > E_m$, the energy ratio is larger than one. This suggests that the standard Mori–Tanaka method overestimates the gradient stiffness of the particulate composite. For the fibrous system, the energy ratio may be either higher or lower than one. Thus the standard method will overestimate certain stiffness components while underestimating others. Of course, different conclusions may reached for other than the SiC/C systems.

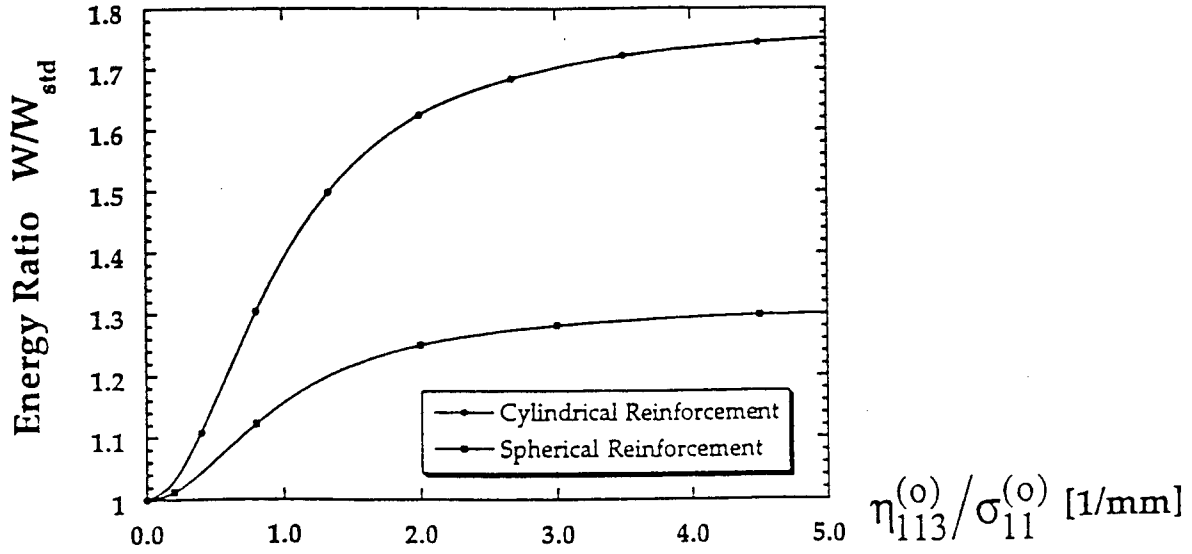


Fig. 1 Comparison of strain energy densities

5. Interpretation of an Experiment

In his 1967 paper, Margolin [6] observed that the bending modulus of thin fibrous glass/epoxy plates was dependent on the thickness of the plate. The plates were formed with 1–10 layers of fibres through the thickness, of constant fibre volume fraction equal to 0.38. In the above gradient stiffness (15_1), for fibres aligned in the x_1–direction, the bending modulus corresponds to $L_{22}[1,1]$, the 1,1 coefficient of the L_{22} submatrix. The extensional modulus is given by $L_{00}[1,1]$. In finding these estimates, the inertia terms in (6) and (7) were computed for a rectangular array of 1 – 10x10 fibres. For the specific phase properties of the tested composite plates, Figure 2 shows a comparison of the measured and computed moduli ratios, using both the gradient and standard stiffness estimates.

This result, and the energy comparison in Fig. 1, imply that the presence of large stress gradients in small heterogeneous volumes may have a significant effect on local response, and therefore, should be accounted for in estimating local properties.

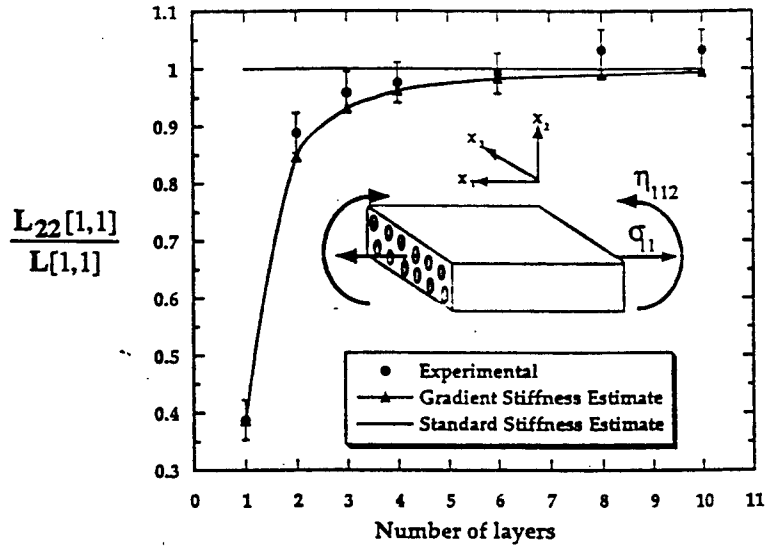


Fig. 2 Comparison of predictions with Margolin's [6] experiments

6. References

1. J.R. Zuiker, *Elastic and inelastic micromechanical analysis of functionally graded materials and laminated structures using transformation fields*, Ph.D. Thesis, Rensselaer Polytechnic Institute, Troy, NY (1993).
2. J.R. Zuiker and G.J. Dvorak, The effective properties of functionally graded composites I. Extension of the Mori–Tanaka method to linearly varying fields, *Composites Engineering* **4** (1994) 19–35.
3. R.J. Asaro and D.M. Barnett, The non–uniform transformation strain problem for an ellipsoidal inclusion, *J. Mech. Phys. Solids* **23** (1975) 77–83.
4. T. Mori and K. Tanaka, Average stress in matrix and average elastic energy of materials with misfitting inclusions, *Acta. Metall.* **21** (1973) 571–574.
5. J.D. Eshelby, Elastic inclusions and inhomogeneities, in I.N. Sneddon and R. Hill (eds), *Progress in Solid Mechanics*, II, North Holland (1961) pp. 89–140.
6. G.G. Margolin, Elasticity modulus in the bending of thin specimens of a unidirectional glass–reinforced plastic, *Polymer Mech.* **3** (1967) 492–493.

journal

J. Am. Ceram. Soc., 78 [1] 205-10 (1995)

Initial Failure Maps for Fibrous CMC Laminates

George J. Dvorak* and Michal Sejnoha

Center for Composite Materials and Structures, Rensselaer Polytechnic Institute, Troy, New York 12180-3590

A simple micromechanics-based procedure is used to evaluate initial failure maps for brittle composite laminates under combined in-plane loads and temperature changes. The maps are derived from local stresses in the fiber, matrix and at their interfaces, and from selected magnitudes of the respective strengths. In a particular loading plane or space, the maps indicate the damage-free load range of the laminate, and the source of likely initial failure by fiber or matrix cracking, or by fiber debonding. An application to $Al_2O_3/MoSi_2$ laminates with unidirectional and $(0/\pm 45)_s$ layups is presented. In this system, the thermal stresses are very small in the 1200°–20°C range; hence laminate failure is dominated by mechanical loads. Propensity to fiber debonding appears to limit the load magnitudes that can be safely applied to the angle-ply laminate.

I. Introduction

Our objective is to find the local stresses in the fibrous plies of a laminated plate of any layup which preserves symmetry about the midplane, as functions of uniform in-plane loads and temperature changes applied to the laminate. The quantities of interest are both the average matrix and fiber stresses, and their distributions at and in the vicinity of the fiber–matrix interface. Extreme values of the stress components are identified, related to certain selected strength magnitudes, and then plotted as branches of the failure maps in the overall or laminate stress plane. Internal envelopes of the various branches represent boundaries on the allowable overall stresses that should not damage the laminate.

The analytical procedure combines the laminated plate theory for evaluation of average ply stresses under the prescribed thermomechanical loads with estimates of the local stresses within the plies, found from a variant of the Mori–Tanaka method, as outlined in Refs. 1 and 2. Systems with coated and cylindrically orthotropic fibers are discussed in Refs. 3 and 4.

II. Local Stresses and Overall Properties

First, we outline evaluation of average stresses in the plies, and in the fiber and matrix phases within the plies, due to uniform thermomechanical loads applied to the laminate. The representative volume element of Fig. 1 is used, with an overall Cartesian coordinate system $\mathbf{X}$ defined such that the X_1X_2 midplane is the plane of symmetry; the plies are numbered in the $\pm X_3$ direction as $i = 1, 2, \ldots, n$, and their total number is $2n$. The volume fraction of the ply (i) is $c_i = t_i/t$, the total thickness of the plate is $2t = 2\Sigma t_i$, and $\Sigma c_i = 1$. Each ply is made of a homogeneous matrix bonded to fibers aligned in a certain direction x_1' that contains the angle ψ_i with the X_1-axis and serves to define a local Cartesian coordinate system $\mathbf{x}^i$ with $x_3^i \equiv X_3$. The elastic symmetry of the plies is at least orthotropic; material symmetry planes coincide with the planes of the $\mathbf{x}^i$ system.

The plate is loaded by self-equilibrated surface tractions, derived from uniform in-plane overall stresses $\boldsymbol{S} = [S_{11}\ S_{22}\ S_{12}]^T$ defined in the $\mathbf{X}$ coordinates, and by a uniform change in temperature $\Delta\theta = \theta - \theta_0$. In the symmetric plate, the resulting deformations are the in-plane overall strains $\boldsymbol{E} = [E_{11}\ E_{22}\ 2E_{12}]^T$. Engineering small strains and the matrix notation are used. The macroscopic response of each ply is identified with that of a homogeneous layer; the layers are assumed to be perfectly bonded; hence the ply strains $\boldsymbol{E}_i = [E_{11}^i\ E_{22}^i\ 2E_{12}^i]^T$ measured in the $\mathbf{X}$ system must satisfy the compatibility condition

$$\boldsymbol{E}_i = \boldsymbol{E} \tag{1}$$

However, the E_{33}^i strains, while uniform, may be different in each ply.

The overall stresses $\boldsymbol{S}$ create a complex stress field within the laminate. Evaluation is simplified by the assumed macroscopic homogeneity of each layer, which provides for uniform average stresses in each ply; these are denoted as $\boldsymbol{S}_i = [S_{11}^i\ S_{22}^i\ S_{12}^i]^T$ in the $\mathbf{X}$ system. The averages may be related to the overall stresses $\boldsymbol{S}$ by

$$\boldsymbol{S}_i = \mathbf{H}_i\boldsymbol{S} + \mathbf{h}_i\Delta\theta \tag{2a}$$

$$\sum_{i=1}^{N} c_i\boldsymbol{S}_i = \boldsymbol{S} \tag{2b}$$

$$\sum_{i=1}^{N} c_i\mathbf{H}_i = \mathbf{I}_3 \tag{2c}$$

$$\sum_{i=1}^{N} c_i\mathbf{h}_i = \mathbf{0} \tag{2d}$$

where the stress distribution factors $\mathbf{H}_i$ and $\mathbf{h}_i$, derived below, are (3×3) and (3×1) matrices, respectively. The remaining relations provide for equilibrium of the membrane forces, and $\mathbf{I}_3$ is a (3×3) identity matrix.

We now proceed to find the stress and strain volume averages in the matrix and fiber phases, in the local coordinate system $\mathbf{x}_i$ in each layer. Thus we first transform the ply averages (1) and (2a) from the overall system $\mathbf{X}$ to the local system $\mathbf{x}_i$, as

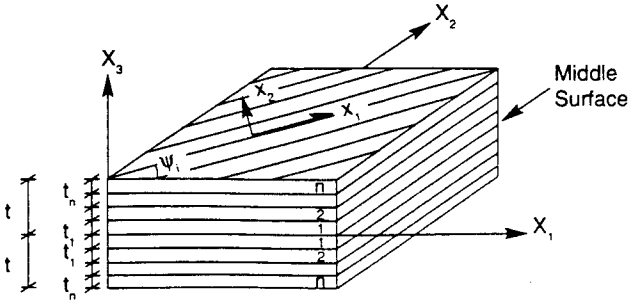


Fig. 1. Representative volume element of a laminated plate.

F. Zok—contributing editor

Manuscript No. 193809. Received February 21, 1994; approved August 19, 1994.
Supported by the ARPA/ONR University Research Initiative Program on "Mechanism-Based Design of High-Temperature Composite Structures" at Rensselaer.
*Member, American Ceramic Society.

$$\boldsymbol{\varepsilon}_i = \mathbf{N}_i \boldsymbol{E}_i \tag{3a}$$

$$\boldsymbol{\sigma}_i = \mathbf{R}_i(\mathbf{H}_i \boldsymbol{S} + \mathbf{h}_i \Delta\theta) \tag{3b}$$

where the matrices $\mathbf{N}_i$ and $\mathbf{R}_i$, in the notation $m = \cos\psi_i$, $n = \sin\psi_i$, are

$$\mathbf{N}_i = \begin{bmatrix} m^2 & n^2 & mn \\ n^2 & m^2 & -mn \\ -2mn & 2mn & (m^2 - n^2) \end{bmatrix} \tag{4a}$$

$$\mathbf{R}_i = \begin{bmatrix} m^2 & n^2 & 2mn \\ n^2 & m^2 & -2mn \\ -mn & mn & (m^2 - n^2) \end{bmatrix} \tag{4b}$$

Then, the phase strain and stress averages in the $\mathbf{x}_i$ system are related to the transformed ply averages (3) and to the local change $\Delta\theta$ by

$$\boldsymbol{\varepsilon}_i^r = \mathbf{A}_i^r \mathbf{N}_i \boldsymbol{E} + \mathbf{a}_i^r \Delta\theta \tag{5a}$$

$$\boldsymbol{\sigma}_i^r = \mathbf{B}_i^r \mathbf{R}_i(\mathbf{H}_i \boldsymbol{S} + \mathbf{h}_i \Delta\theta) + \mathbf{b}_i^r \Delta\theta \tag{5b}$$

where r = f, m; $\mathbf{A}_i^r$, $\mathbf{B}_i^r$, are (6 × 6) mechanical stress concentration factors, and $\mathbf{a}_i^r$, $\mathbf{b}_i^r$ are (6 × 1) thermal stress concentration factors. To find correct phase field averages $\boldsymbol{\varepsilon}^r$ and $\boldsymbol{\sigma}^r$ as (6 × 1) vectors, the products $\mathbf{R}_i\mathbf{H}_i\boldsymbol{S}$ and $\mathbf{R}_i\mathbf{h}_i\Delta\theta$ in Eqs. (5) must be augmented by zeros in rows 3, 4, and 5 into (6 × 1) vectors.

To find the factors $\mathbf{A}_i^r$, $\mathbf{B}_i^r$, $\mathbf{a}_i^r$, $\mathbf{b}_i^r$, $\mathbf{H}_i$, and $\mathbf{h}_i$, we assume that the fiber and matrix are both homogeneous and possibly anisotropic elastic solids, and write the constitutive relations for the elastic phases as

$$\boldsymbol{\sigma}_i^r = \mathbf{L}_i^r \boldsymbol{\varepsilon}_i^r + \mathbf{l}_i^r \Delta\theta \tag{6a}$$

$$\boldsymbol{\varepsilon}_i^r = \mathbf{M}_i^r \boldsymbol{\sigma}_i^r + \mathbf{m}_i^r \Delta\theta \tag{6b}$$

$\mathbf{L}_i^r$ and $\mathbf{M}_i^r = (\mathbf{L}_i^r)^{-1}$ are phase stiffnesses and compliances; $\mathbf{l}_i^r$, $\mathbf{m}_i^r = -\mathbf{M}_i^r\mathbf{l}_i^r$ are phase thermal stress and strain vectors; all are displayed in the Appendix.

Estimates of the mechanical concentration factors $\mathbf{A}_i^r$ and $\mathbf{B}_i^r$ in a fibrous ply can be obtained by several micromechanical methods. Here we use the Mori–Tanaka[5] procedure that also will be useful in finding the stress distribution in the matrix at the interface with the fiber. The assumption is that a representative volume of the fibrous ply is either loaded by an overall uniform stress $\boldsymbol{\sigma}$ or deformed by an overall uniform strain $\boldsymbol{\varepsilon}$, represented by (6 × 1) vectors. The local stresses or strains in phase s = f, m then follow from the expressions $\boldsymbol{\sigma}_s = \mathbf{B}_s\boldsymbol{\sigma}$ or $\boldsymbol{\varepsilon}_s = \mathbf{A}_s\boldsymbol{\varepsilon}$, where[11]

$$\mathbf{A}_s = (\mathbf{L}^* + \mathbf{L}_s)^{-1}(\mathbf{L}^* + \mathbf{L}) \tag{7a}$$

$$\mathbf{B}_s = (\mathbf{M}^* + \mathbf{M}_s)^{-1}(\mathbf{M}^* + \mathbf{M}) \tag{7b}$$

$$\mathbf{L} = \left[\sum c_s(\mathbf{L}^* + \mathbf{L}_s)^{-1}\right]^{-1} - \mathbf{L}^* \tag{7c}$$

$$\mathbf{M} = \left[\sum c_s(\mathbf{M}^* + \mathbf{M}_s)^{-1}\right]^{-1} - \mathbf{M}^* \tag{7d}$$

The $\mathbf{L}$ and $\mathbf{M}$ are estimates of the overall stiffness and compliance of the composite material in the representative volume, $\mathbf{L}_s$ and $\mathbf{M}_s$ are the phase properties, and $\mathbf{L}^*$, $\mathbf{M}^* = (\mathbf{L}^*)^{-1}$ are given in the Appendix. In a two-phase composite, the thermal factors can be derived from the mechanical as[6,7]

$$\mathbf{a}_s = (\mathbf{I} - \mathbf{A}_s)(\mathbf{L}_f - \mathbf{L}_m)^{-1}(\mathbf{l}_m - \mathbf{l}_f) \tag{8a}$$

$$\mathbf{b}_s = (\mathbf{I} - \mathbf{B}_s)(\mathbf{M}_f - \mathbf{M}_m)^{-1}(\mathbf{m}_m - \mathbf{m}_f) \tag{8b}$$

Substituting the moduli of the phases r in layer (i), one obtains the (6 × 6) $\mathbf{A}_i^r$ and $\mathbf{B}_i^r$ matrices needed for evaluation of the local fields (5) in the phases. A similar substitution in Eqs. (8) provides the (6 × 1) $\mathbf{a}_i^r$ and $\mathbf{b}_i^r$ matrices.

To find the stress distribution factors $\mathbf{H}_i$ and $\mathbf{h}_i$ in Eq. (2a) we first reduce the (6 × 6) $\mathbf{L}$ and $\mathbf{M}$ matrices in Eqs. (7c) and (7d) to plane stress forms by deleting the third, fourth, and fifth rows and columns from $\mathbf{M}$. This gives the (3 × 3) ply compliance $\mathbf{M}_i$, and the stiffness $\mathbf{L}_i = \mathbf{M}_i^{-1}$ of the layer (i) in the local ply coordinates $\mathbf{x}_i$. Transformations (3) and (4) from $\mathbf{x}_i$ to the overall system $\mathbf{X}$

$$\bar{\mathbf{L}}_i = \mathbf{N}_i^T \mathbf{L}_i \mathbf{N}_i \tag{9a}$$

$$\bar{\mathbf{M}}_i = \mathbf{R}_i^T \mathbf{M}_i \mathbf{R}_i \tag{9b}$$

$$\bar{\mathbf{l}}_i = \mathbf{N}_i^T \mathbf{l}_i \tag{9c}$$

$$\bar{\mathbf{m}}_i = \mathbf{R}_i^T \mathbf{m}_i \tag{9d}$$

provide the layer properties in the $\mathbf{X}$ coordinates.

Constitutive relations of the plies in the overall system then are

$$\boldsymbol{S}_i = \bar{\mathbf{L}}_i \boldsymbol{E}_i + \bar{\mathbf{l}}_i \Delta\theta \tag{10a}$$

$$\boldsymbol{E}_i = \bar{\mathbf{M}}_i \boldsymbol{S}_i + \bar{\mathbf{m}}_i \Delta\theta \tag{10b}$$

An analogous form is used for the in-plane response of the laminated plate,

$$\boldsymbol{S} = \bar{\mathbf{L}}\boldsymbol{E} + \bar{\mathbf{l}}\Delta\theta \tag{11a}$$

$$\boldsymbol{E} = \bar{\mathbf{M}}\boldsymbol{S} + \bar{\mathbf{m}}\Delta\theta \tag{11b}$$

where the ply and overall stresses and strains are related by Eqs. (1) and (2). Substituting into these equations, we find

$$\mathbf{H}_i = \bar{\mathbf{L}}_i \bar{\mathbf{M}} \tag{12a}$$

$$\mathbf{h}_i = \bar{\mathbf{L}}_i \bar{\mathbf{m}} + \bar{\mathbf{l}}_i \tag{12b}$$

$$\bar{\mathbf{L}} = \sum_{i=1}^{N} c_i \bar{\mathbf{L}}_i \tag{12c}$$

$$\bar{\mathbf{M}} = (\bar{\mathbf{L}})^{-1} \tag{12d}$$

$$\bar{\mathbf{l}} = \sum_{i=1}^{N} c_i \bar{\mathbf{l}}_i \tag{12e}$$

$\mathbf{H}_i$ and $\mathbf{h}_i$ are the distribution factors in Eqs. (2), $\bar{\mathbf{L}}$, $\bar{\mathbf{M}}$ and $\bar{\mathbf{l}}$, $\bar{\mathbf{m}} = -\bar{\mathbf{M}}\bar{\mathbf{l}}$ are the overall in-plane (3 × 3) stiffness and compliance, and (3 × 1) thermal stress and strain matrices of the laminated plate in Eqs. (11).

In addition to the stress averages in the plies and phases, we need to evaluate the local stresses in the matrix, at the interface with the fiber. In doing so, one can use the approach outlined in Refs. 8 and 9 which employs relations between interior (fiber) and exterior (matrix) components of the strain and stress tensors at the interface. Since the distribution of the matrix stresses at some distance from the interface may be of interest, we have used the procedure described in Refs. 1 and 2 where the fiber was embedded in a large volume of the matrix, loaded at a remote boundary by the average matrix stresses $\boldsymbol{\sigma}_i^m$ in Eq. (5b). The local stresses were found from elasticity solutions, for loading by all components of $\boldsymbol{\sigma}_i^m$ and by $\Delta\theta$.

III. Results for the $Al_2O_3/MoSi_2$ System

As an application, we construct initial failure maps of a $(0/\pm 45)_s$ laminate made of the above $MoSi_2$ matrix systems, with $c_f = 0.4$. The phases are taken as isotropic with elastic moduli listed in Table I. These magnitudes were utilized to construct the phase stiffness and compliance matrices, according to Eqs. (A-3) and (A-5). Then, the phase thermal strain vectors $\mathbf{m}_r$ were derived from the CTEs as $\mathbf{m}_r = [\alpha_r, \alpha_r, \alpha_r, 0, 0, 0]^T$, and the thermal stress vector as $\mathbf{l}_r = -\mathbf{L}_r\mathbf{m}_r$. These quantities were substituted into Eqs. (6), and used in Eqs. (A-5), (A-6), (6), and (7) to find the ply properties. Next, certain rows and columns were deleted to arrive at the plane stress forms needed

Table I. Phase Elastic Moduli and Coefficients of Thermal Expansion for the $Al_2O_3/MoSi_2$ System[12]

θ (°C)	E (GPa)		ν		α ($\times 10^{-6}$/°C)	
	Fiber	Matrix	Fiber	Matrix	Fiber	Matrix
1200	290	330	0.24	0.165	8.32	8.7
1000	340	330	0.24	0.165	8.18	8.7
800	352	330	0.24	0.165	7.97	8.7
600	360	330	0.24	0.165	7.69	8.7
400	372	330	0.24	0.165	6.24	8.7
200	376	330	0.24	0.165	6.55	8.7
20	380	330	0.24	0.165	5.60	8.7

in the transformations (9). This was followed by evaluation of overall laminate properties (12). Then, selected loading combinations were applied to the plate element in Fig. 1, and Eqs. (11) with (3) were called upon to provide the average phase stresses. Matrix stress distributions at the interface were then found from the local field equations listed in Refs. 1 and 2.

Figure 2 shows the stress distributions in a unidirectional ply under unit mechanical stresses, plotted as functions of the angle ϕ, measured ccw in the x_2x_3 plane perpendicular to the fiber, from the in-plane x_2 axis of the ply. Thermal stresses were found as well. However, because of the small differences in CTEs, these stresses were of negligible magnitude (10^{-4} MPa/°C). Next, the $0/\pm 45)_s$ laminate was analyzed to evaluate ply and phase local stresses under in-plane loading in the $S_{11}S_{22}$ and $S_{11}S_{12}$ stress planes. The local averages and maximum values evident in Fig. 2 were recorded for each ply, and identified

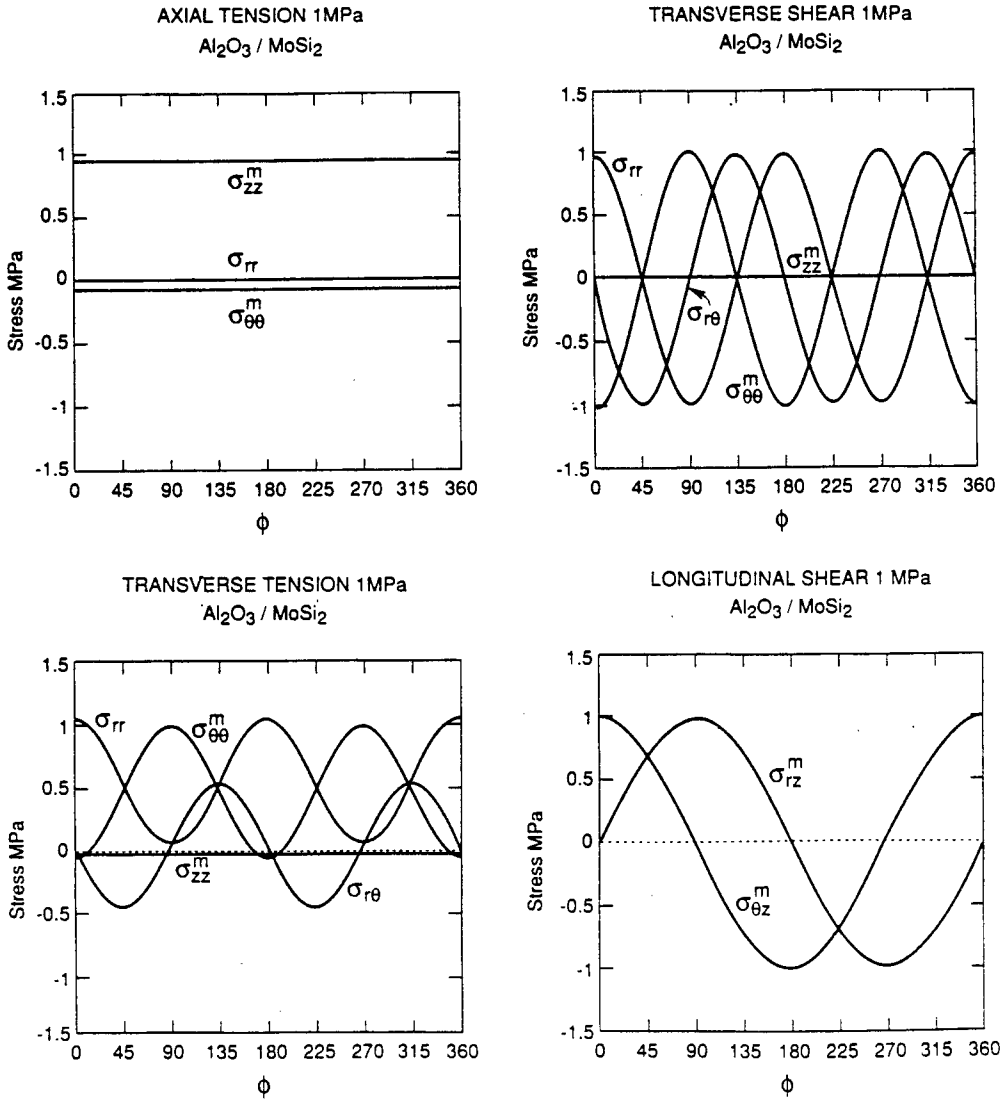


Fig. 2. Local stresses at fiber–matrix interface under unit loads applied to a unidirectional lamina.

with certain selected strengths. The tensile matrix and interface strengths were taken as $\sigma^m_{ult} = 240$ MPa and $(\sigma^{int}_{rr})_{ult} = 50$ MPa, and the compressive matrix strength as $\sigma^m_{ult} = -1000$ MPa. The results are plotted starting with Fig. 3. Each line in the figures corresponds to the selected maximum allowed magnitude of the labeled stress component.

Figures 3 and 4 were constructed for the maximum tensile stresses in the matrix and at the interface of each ply, under overall stresses $S_{11}S_{22}$. The interface hoop stress $\sigma_{\theta\theta}$, which may cause radial cracking, is represented by two branches that correspond to points $a@\phi_i = 0°$ and $b@\phi_i = 90°$ in the cross-sectional $x'_2x'_3$ plane. The internal envelope, represented here by the radial stresses at the interface, indicates the overall stress magnitudes that would cause initial failure in the laminate. Figure 5 shows a compressive failure envelope, for allowable compressive strengths in the matrix. Failure envelopes for the fiber are very similar. Fiber kinking may interfere but is not considered herein. Note that the response is linear. Therefore, while plotted for specific strength magnitudes, Figs. 3–5 and the following figures can be easily adjusted for any other selected strengths by multiplying the scales by the ratio of the new/current strength for each selection. Figures 6–8 show results of the same kind, but for loading in the overall $S_{11}S_{12}$ stress plane. Again, these can be scaled for any selected strength magnitudes.

The allowable tensile load range is small in this system, and may be further reduced by a lower interface strength. Damage should start by fiber debonding. That would change the local stresses and the positions of the failure maps. This case will be discussed elsewhere.

IV. Conclusions

The analysis indicates how significant magnitudes of the local stresses, caused in a fibrous laminate by uniform overall thermomechanical loads, can be found and utilized together with selected local strength magnitudes, in constructing initial failure maps in the overall stress space. The maps identify the components of local stresses which are likely to cause initial cracking of the matrix, fiber, or their interface, in individual plies. The results obtained for the particular $Al_2O_3/MoSi_2$ $(0/\pm 45)_s$ laminate suggest the possibility of interface debonding under relatively low overall in-plane normal stresses applied alone or in biaxial tension. On the other hand, certain overall biaxial normal and/or shear stress states of intermediate magnitude, which include a compressive transverse normal stress, can be applied without risking internal damage. While each failure map may be scaled to reflect the actual local strengths, the positions of individual branches depend on temperature-dependent magnitudes of phase elastic moduli and coefficients of thermal expansion. In most systems, thermal stresses induced during cooling from fabrication temperatures will cause translation of the branches; those may be obtained

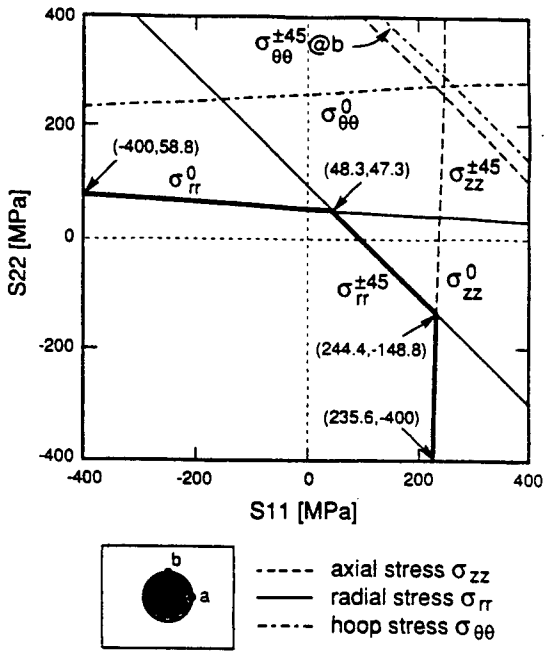


Fig. 4. Magnified failure envelope of Fig. 3.

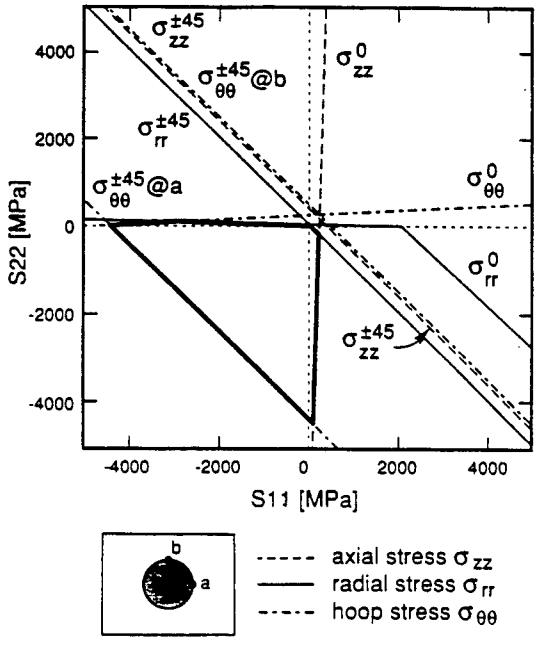


Fig. 3. Tensile failure envelope of an $Al_2O_3/MoSi_2$ $[0/\pm 45]_s$ laminate in the $S_{11}S_{22}$ plane, computed for $\sigma^m_{ult} = 240$ MPa and $(\sigma^{int}_{rr})_{ult} = 50$ MPa.

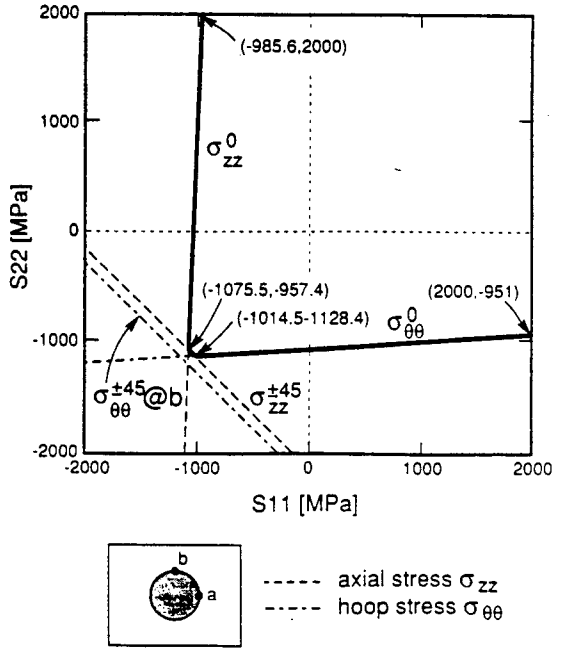


Fig. 5. Compressive failure envelope for the system of Fig. 3, in the $S_{11}S_{22}$ plane, computed for $\sigma^m_{ult} = -1000$ MPa.

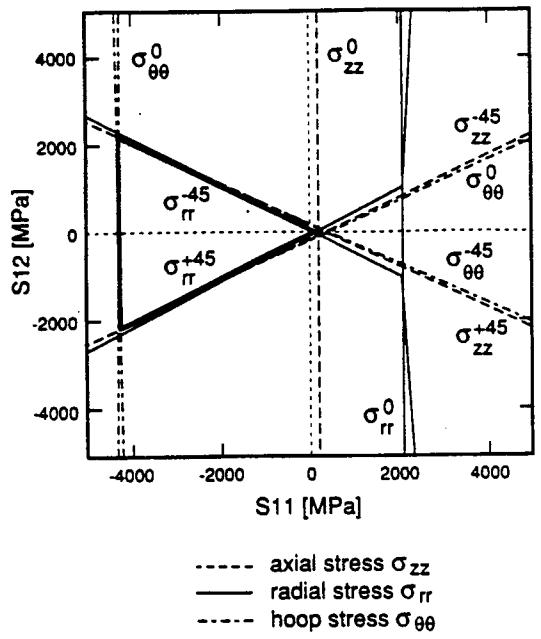


Fig. 6. Tensile failure envelope of an $Al_2O_3/MoSi_2$, $[0/\pm 45]_s$ laminate in the $S_{11}S_{12}$ plane, computed for $\sigma_{ult}^{m} = 240$ MPa and $(\sigma_{rr}^{int})_{ult} = 50$ MPa.

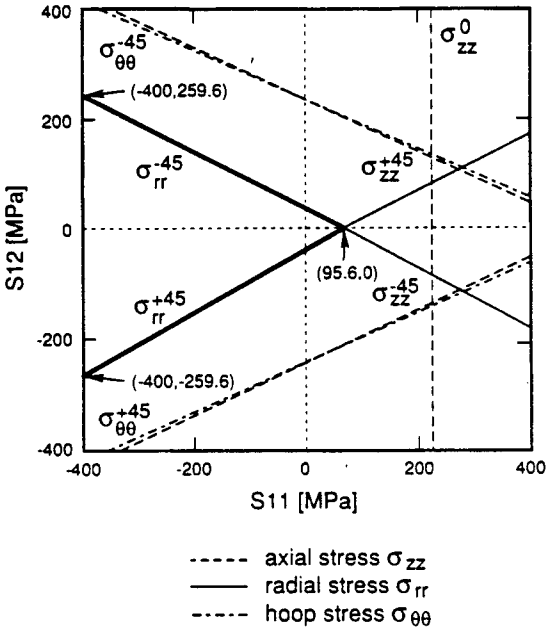


Fig. 7. Magnified failure envelope of Fig. 6.

with the present analysis. However, the effect of evolving damage remains to be resolved.

APPENDIX

Suppose that the fiber and matrix moduli and coefficients of thermal expansion are represented by continuous functions of temperature θ, derived from experimental data. After a uniform change $\Delta\theta$, from a reference θ_0, applied under a uniform stress $\boldsymbol{\sigma}_r$, an unconstrained phase deforms uniformly.

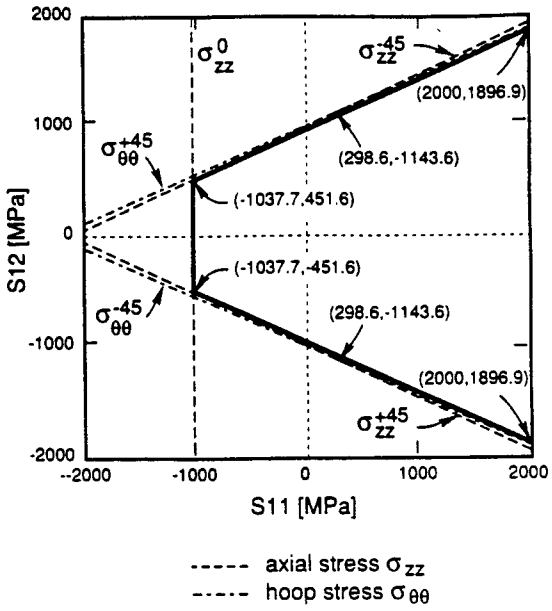


Fig. 8. Compressive failure envelope for the system of Fig. 6, in the $S_{11}S_{12}$ plane, computed for $\sigma_{ult}^{m} = -1000$ MPa.

$$\boldsymbol{\varepsilon}_r = \mathbf{M}_r(\theta)\boldsymbol{\sigma}_r + \int_{\theta_0}^{\theta} \mathbf{m}_r(\theta)\, d\theta \tag{A-1}$$

If the temperature changes under an applied uniform strain, the stress is

$$\boldsymbol{\sigma}_r = \mathbf{L}_r(\theta)\boldsymbol{\varepsilon}_r - \mathbf{L}_r(\theta)\int_{\theta_0}^{\theta} \mathbf{m}_r(\theta)\, d\theta \tag{A-2}$$

where r = f, m denotes the phase, $\mathbf{L}_r(\theta)$ and $\mathbf{M}_r(\theta) = (\mathbf{L}_r(\theta))^{-1}$ are temperature-dependent, (6×6) phase stiffness and compliance matrices, $\mathbf{m}_r(\theta)$ is the (6×1) thermal strain vector of expansion coefficients; their particular forms depend on the elastic symmetry of the phase. A comparison with Eqs. (6) sugests that the term $\mathbf{m}_r^{\prime}\,\Delta\theta$ evaluates as the integral in Eq. (A-1), and the $\mathbf{l}_r^{\prime}\,\Delta\theta$ as the last term in Eq. (A-2): the phase moduli are taken at the current θ.

For a transversely isotropic solid, with x_1 as the axis of rotational symmetry, and compliance matrix $\mathbf{M}$, the constitutive relation $\boldsymbol{\varepsilon} = \mathbf{M}\boldsymbol{\sigma}$ is written using the engineering moduli

$$\begin{bmatrix} \varepsilon_1 \\ \varepsilon_2 \\ \varepsilon_3 \\ \varepsilon_4 \\ \varepsilon_5 \\ \varepsilon_6 \end{bmatrix} = \begin{bmatrix} 1/E_{11} & -\nu_{12}/E_{11} & -\nu_{13}/E_{11} & 0 & 0 & 0 \\ & 1/E_{22} & -\nu_{23}/E_{22} & 0 & 0 & 0 \\ & & 1/E_{22} & 0 & 0 & 0 \\ & & & 1/G_{23} & 0 & 0 \\ & & & & 1/G_{12} & 0 \\ \text{SYM.} & & & & & 1/G_{12} \end{bmatrix} \begin{bmatrix} \sigma_1 \\ \sigma_2 \\ \sigma_3 \\ \sigma_4 \\ \sigma_5 \\ \sigma_6 \end{bmatrix} \tag{A-3}$$

The stiffness $\mathbf{L} = \mathbf{M}^{-1}$ is best written in terms of Hill's moduli.

$$k = -[1/G_{23} - 4/E_{22} + 4\nu_{12}^2/E_{11}]^{-1}$$

$$n = E_{11} + 4k\,\nu_{12}^2 = E_{11} + \ell^2/k$$

$$\ell = 2k\,\nu_{12}$$

$$m = G_{23}$$

$$p = G_{12}$$

The constitutive relation $\boldsymbol{\sigma} = \mathbf{L}\boldsymbol{\varepsilon}$ then is

$$\begin{bmatrix}\sigma_1\\ \sigma_2\\ \sigma_3\\ \sigma_4\\ \sigma_5\\ \sigma_6\end{bmatrix} = \begin{bmatrix} n & \ell & \ell & 0 & 0 & 0\\ & (k+m) & (k-m) & 0 & 0 & 0\\ & & (k+m) & 0 & 0 & 0\\ & & & m & 0 & 0\\ & & & & p & 0\\ \text{SYM.} & & & & & p\end{bmatrix}\begin{bmatrix}\varepsilon_1\\ \varepsilon_2\\ \varepsilon_3\\ \varepsilon_4\\ \varepsilon_5\\ \varepsilon_6\end{bmatrix} \tag{A-4}$$

To estimate the overall moduli $\mathbf{L}$ of heterogeneous solids by the Mori–Tanaka method, one can utilize Eqs. (7) with the constraint tensors $\mathbf{L}^*$ and $\mathbf{M}^*$ derived as stiffnesses and compliances of a cavity in the matrix, having the shape of the reinforcing fiber.[10] Simple expressions[11] can be obtained using the polarization tensor $\mathbf{P}$, represented as a (6 × 6) array with the following nonzero coefficients:

$$P_{22} = P_{33} = \frac{k_m + 4m_m}{8m_m(k_m + m_m)} \tag{A-5a}$$

$$P_{23} = P_{32} = \frac{-k_m}{8m_m(k_m + m_m)} \tag{A-5b}$$

$$P_{44} = \frac{k_m + 2m_m}{2m_m(k_m + m_m)} \tag{A-5c}$$

$$P_{55} = P_{66} = 1/(2p_m) \tag{A-5d}$$

Note that $\mathbf{P}$ is singular, but the Eshelby tensor $\mathbf{S} = \mathbf{PL}_m$, of a transformed homogeneous inclusion in the matrix $\mathbf{L}_m$ is not. The constraint tensors then follow from

$$\mathbf{S} = (\mathbf{L}^* + \mathbf{L}_m)^{-1}\mathbf{L}_m = \mathbf{M}^*(\mathbf{M}^* + \mathbf{M}_m)^{-1} \tag{A-6}$$

Acknowledgments: We thank Drs. W. Coblenz and S. Fishman for serving as monitors for the ARPA/ONR University Research Initiative Program on "Mechanism-Based Design of High-Temperature Composite Structures" at Rensselaer.

References

[1]G. J. Dvorak, T. Chen, and J. Teply, "Thermomechanical Stress Fields in High-Temperature Fibrous Composites. I: Unidirectional Laminates," *Compos. Sci. Technol.*, **43**, 347–58 (1992).

[2]G. J. Dvorak, T. Chen, and J. Teply, "Thermomechanical Stress Fields in High-Temperature Fibrous Composites. II: Laminated Plates," *Compos. Sci. Technol.*, **43**, 359–68 (1992).

[3]Y. Benveniste, G. J. Dvorak, and T. Chen, "Stress Fields in Composites with Coated Inclusions," *Mech. Mater.*, **7**, 305–17 (1989).

[4]T. Chen, G. J. Dvorak, and Y. Benveniste, "Stress Fields in Composites Reinforced by Coated Cylindrically Orthotropic Fibers," *Mech. Mater.*, **9**, 17–32 (1990).

[5]T. Mori and K. Tanaka, "Average Stress in Matrix and Average Elastic Energy of Materials with Misfitting Inclusions," *Acta Metall.*, **21**, 571–94 (1973).

[6]G. J. Dvorak, "Thermal Expansion of Elastic–Plastic Composite Materials," *J. Appl. Mech.*, **53**, 737–43 (1986).

[7]Y. Benveniste and G. J. Dvorak, "On a Correspondence between Mechanical and Thermal Effects in Two-Phase Composites"; pp. 65–81 in *Micromechanics and Inhomogeneity*, in Toshio Mura Anniversary Volume. Edited by G. J. Weng, M. Taya, and H. Abe. Springer-Verlag, New York, 1990.

[8]R. Hill, "An Invariant Treatment of Interfacial Discontinuities in Elastic Composites"; p. 597 in *Continuum Mechanics and Related Problems of Analysis*, N. I. Muskhelishvili 80 Anniversary Volume. Edited by L. I. Sedov. Academy of Sciences SSSR, Moscow, 1972.

[9]N. Laws, "On Interfacial Discontinuities in Elastic Composites," *J. Elasticity*, **5**, 227–35 (1975).

[10]R. Hill, "A Self-Consistent Mechanics of Composite Materials," *J. Mech. Phys. Solids*, **13**, 213–22 (1965).

[11]G. J. Dvorak and Y. Benveniste, "On Transformation Strains and Uniform Fields in Multiphase Elastic Media," *Proc. R. Soc. London*, **A437**, 291–310 (1992).

[12]J. F. Shakelford and W. Alexander (Eds.), *CRC Materials Science and Engineering Handbook*; pp. 360–62, 531–40, 590–92. CRC Press, Boca Raton, FL, 1992. □

Modelling Simul. Mater. Sci. Eng. 4 (1996) 553–580. Printed in the UK

Initial failure maps for ceramic and metal matrix composite laminates

George J Dvorak and Michal Sejnoha

Center for Composite Materials and Structures, Rensselaer Polytechnic Institute, Troy, NY 12180-3590, USA

Received 25 April 1996, accepted for publication 19 September 1996

Abstract. Initial failure maps define damage-free loading regions in the laminate stress space, such that local stresses in the individual phases and interfaces in each ply do not exceed specified strength magnitudes. The maps are constructed here for several symmetric laminates and composite systems loaded by uniform membrane stresses. The $(0/\pm 45)_s$ layup was selected for the $Al_2O_3/MoSi_2$ and SCS-6/Ti_3Al systems, and the $(0/\pm 45/90)_s$ layup for the SCS-6/Timetal-21S composite. Results are presented both in the $S_{11}S_{22}$ and $S_{11}S_{12}$ stress planes, where the x_1-axis coincides with the zero-degree fibre direction. Residual stress effects induced by fabrication and/or thermal changes are included.

1. Introduction

It is well known that fibrous composite laminates may experience progressive damage well before the applied load reaches an ultimate magnitude. While some applications may take advantage of this reserve in load carrying capacity, damage of any kind is undesirable, for example, when it causes excessive stiffness reduction, or exposes the microstructure to corrosive environment. Therefore, it is of interest to identify load levels which guarantee that the local stresses within the individual plies of the laminate do not exceed certain allowable magnitudes.

The problem addressed in the present paper is to determine overall uniform stress levels and temperature changes applied to symmetric laminated plates of any layup that cause local stresses in the matrix, fibre, and at the interface, to reach certain critical magnitudes. These results are summarized in the initial failure maps discussed in section 4. Any specific failure criterion that depends on the local stresses or their combination can be selected by the user. Similar support can be derived for strain-based criteria.

As in our previous work [12, 13, 15], the damage-free load region in a given laminate stress plane is found as an internal envelope of many branches that reflect the local stress maxima at fibre–matrix interfaces and in the phases of individual plies. The underlying mechanical and thermal stress concentration factors are derived through a micromechanical analysis based on the Mori–Tanaka method [4, 21], which is developed here for systems with both coated and uncoated fibres. We also provide for residual stress effects resulting from fabrication and processing, or from phase transformations. In applications to the metal matrix SiC/Ti system, the initial stresses were taken from available analysis of the hot isostatic pressing (HIP) cycle.

Section 2 outlines the transformation field analysis method that provides a theoretical foundation for evaluation of the local stresses within the plies. An analogous transformation

0965-0393/96/060553+28$19.50 © 1996 IOP Publishing Ltd

field analysis of ply stresses in symmetric laminates appears in section 3. Applications to and the resulting initial failure maps for several systems and layups are presented in section 4. Detailed solutions of several inclusion problems are exposed in the appendices.

The symbolic notation used here employs bold-faced capital letters to represent (6 × 6) or, if used with a top bar, (3 × 3) matrices; lower case bold-faced letters denote (6 × 1) or, if with top bar, (3 × 1) vectors. The bold-faced italics E and S denote the (3 × 1) overall laminate strain and stress vectors. Scalars are denoted by light-faced capital and lower-case letters.

2. Local stresses and overall properties of fibrous plies

In preparation for the analysis of the laminate, we first review some of the aspects of micromechanical modelling of unidirectional composite systems. In particular, the evaluation of local fields and overall composite response will be presented in the framework of transformation field analysis (TFA) developed in the last several years by Dvorak and coworkers [8–11, 14]. When used with a selected micromechanical model, the analysis provides approximation of the instantaneous local stress and strain fields in the phases, and estimates of the overall instantaneous thermomechanical properties of a representative volume element (RVE).

2.1. General formulation

We consider an RVE of a matrix-based composite reinforced by aligned coated or uncoated fibres of circular cross section. A Cartesian coordinate system x is defined such that x_1 is parallel to the fibre axis. The geometry of the microstructure in the transverse x_2x_3 plane can be arbitrary, as long as the composite aggregate remains statistically homogeneous. The composite is loaded by certain external tractions, derived from the uniform overall stress σ^0, and by uniform temperature change $\Delta T = T - T_0$. In addition, piecewise uniform eigenstrains μ_ρ can be prescribed in individual phases to account for inelastic strains generated during fabrication and processing, or to simulate the effect of damage by interfacial decohesion. Of course, the thermal strains could be added to these eigenstrains.

To that end, the RVE can be subdivided into certain subvolumes $\rho, \eta = 1, 2, \ldots M$, where the local fields are presumed to be uniform. The local stress fields caused by the above loads in the subvolumes will be evaluated in the form

$$\sigma_\rho(x) = \mathbf{B}_\rho(x)\sigma^0 + \mathbf{b}_\rho(x)\Delta T - \sum_{\eta=1}^{M} \mathbf{F}_{\rho\eta}(x)\mathbf{L}_\eta\mu_\eta \tag{1}$$

where, $x \in$ RVE, $\mathbf{B}_\rho(x)$ is a (6 × 6) mechanical stress concentration factor matrix [17], $\mathbf{b}_\rho(x)$ is the (6 × 1) thermal stress concentration factor [20] and $\mathbf{F}_{\rho\eta}(x)$ is a (6 × 6) transformation concentration matrix [10]. The (6 × 6) elastic stiffness matrix $\mathbf{L}_\eta$ is displayed in detail in appendix A.

It is helpful to recall that for any two-phase composite medium, $\rho, \eta = 1, 2$, the $\mathbf{b}_\rho(x)$ and $\mathbf{F}_{\rho\eta}(x)$ are related to $\mathbf{B}_\rho(x)$ through the exact connections [11]. In particular, for fibrous systems, $\rho, \eta = \mathrm{f}, \mathrm{m}$,

$$\begin{aligned}
\mathbf{b}_\rho(x) &= [\mathbf{I} - \mathbf{B}_\rho(x)](\mathbf{M}_\mathrm{m} - \mathbf{M}_\mathrm{f})^{-1}(\mathbf{m}_\mathrm{f} - \mathbf{m}_\mathrm{m}) \\
\mathbf{F}_{\rho\mathrm{m}}(x) &= [\mathbf{I} - \mathbf{B}_\rho(x)](\mathbf{M}_\mathrm{m} - \mathbf{M}_\mathrm{f})^{-1}\mathbf{M}_\mathrm{m} \\
\mathbf{F}_{\rho\mathrm{f}}(x) &= -[\mathbf{I} - \mathbf{B}_\rho(x)](\mathbf{M}_\mathrm{m} - \mathbf{M}_\mathrm{f})^{-1}\mathbf{M}_\mathrm{f}
\end{aligned} \tag{2}$$

where $\mathbf{I}$ is (6×6) identity matrix, $\mathbf{M}_f$ and $\mathbf{M}_m$ are the phase compliances, while $\mathbf{L}_\rho = \mathbf{M}_\rho^{-1}$; $\mathbf{m}_f$ and $\mathbf{m}_m$ are the thermal strain vectors listing the linear coefficients of thermal expansion of the fibre and matrix, respectively. Substituting (2) into (1) provides the stress fields in the fibre and matrix as

$$\sigma_f(x) = \mathbf{B}_f(x)\sigma^0 + [\mathbf{I} - \mathbf{B}_f(x)](\mathbf{M}_m - \mathbf{M}_f)^{-1}[(\mathbf{m}_f - \mathbf{m}_m)\Delta T + \mu_f - \mu_m]$$
$$\sigma_m(x) = \mathbf{B}_m(x)\sigma^0 + [\mathbf{I} - \mathbf{B}_m(x)](\mathbf{M}_m - \mathbf{M}_f)^{-1}[(\mathbf{m}_f - \mathbf{m}_m)\Delta T + \mu_f - \mu_m]. \tag{3}$$

The corresponding strain fields then follow from the phase constitutive relations

$$\epsilon_\rho(x) = \mathbf{M}_\rho\sigma_\rho(x) + \mathbf{m}_\rho\Delta T + \mu_\rho \qquad \rho = \text{f, m}. \tag{4}$$

Equations (3) imply that the local stress fields can be evaluated in terms of the mechanical stress concentration factors $\mathbf{B}_f(x)$ and $\mathbf{B}_m(x)$ and elastic and thermal properties of the fibre and matrix.

Unfortunately, the pointwise correspondence between mechanical and transformation concentration factor tensors, equations (2), cannot be applied to the systems with coated inclusions. In such cases, the transformation factors are usually evaluated numerically using the finite element method. Moreover, the local fields in coated inclusion are generally not uniform, and hence a special treatment is required to evaluate phase mechanical concentration factors in such systems.

2.2. *Estimates of phase stress averages*

Consider a three-phase composite material reinforced by continuous fibres surrounded by a layer of coating. Here, the relations between the local and overall stress fields are found within the context of a variant of the Mori–Tanaka method [4]. To simplify the formulation we admit only mechanical and thermal loading, see figure 1.

The method approximates the effect of particle interaction on the local stresses by assuming that the stress in each fibre and coating is equal to that of a single coated fibre embedded in an unbounded matrix medium subjected to the as yet unknown average matrix stress $\sigma_m = \mathbf{B}_m\sigma^0 + \mathbf{b}_m\Delta T$, figure 1, where $\mathbf{B}_m$ and $\mathbf{b}_m$ are the volume averages of $\mathbf{B}_m(x)$ and $\mathbf{b}_m(x)$ in (1).

In Benveniste's reformulation of the method [4], the solution of a single inclusion in a large volume of matrix loaded by σ_m assumes the form

$$\sigma_\rho(x) = \mathbf{W}_\rho(x)\sigma_m + \mathbf{w}_\rho(x)\Delta T \qquad \text{with } \rho = \text{f, g, m} \tag{5}$$

where $\mathbf{W}_\rho(x)$ and $\mathbf{w}_\rho(x)$ are the partial mechanical and thermal stress concentration factors referring to single inclusion. To determine σ_m, we recall that the local stress components σ_ρ and the overall uniform applied stress σ^0 satisfy the equilibrium condition

$$\sigma^0 = \sum_\rho c_\rho\sigma_\rho \qquad \text{for } \rho = \text{f, g, m} \tag{6}$$

where $\sum_\rho c_\rho = 1$ represents the volume fraction of individual phases. Substituting (5) into (6) provides

$$\sigma_m = \left[\sum_\rho c_\rho\mathbf{W}_\rho\right]^{-1}\left[\sigma^0 - \Delta T\sum_\rho c_\rho\mathbf{w}_\rho\right] \tag{7}$$

where $\mathbf{W}_\rho$ and $\mathbf{w}_\rho$ are the phase volume averages of $\mathbf{W}_\rho(x)$ and $\mathbf{w}_\rho(x)$ in (5). Since $\mathbf{W}_\rho$ and $\mathbf{w}_\rho$ refer to single inclusion in an infinite matrix, the state of stress in the matrix is affected only in a small volume adjacent to the inclusion. Consequently we obtain

$$\mathbf{W}_m = \mathbf{I} \qquad \mathbf{w}_m = 0. \tag{8}$$

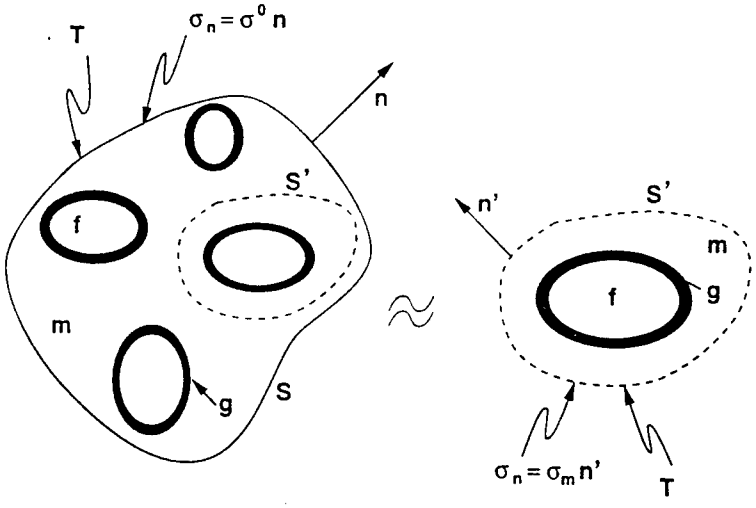


Figure 1. Representation of Mori–Tanaka method for thermoelastic problems.

The fibre and coating volume averages of $\mathbf{W}_\rho(x)$ and $\mathbf{w}_\rho(x)$ are found as

$$\mathbf{W}_\rho = \frac{1}{V_\rho}\int_{V_\rho} \mathbf{W}_\rho(x)\,\mathrm{d}V \qquad \mathbf{w}_\rho = \frac{1}{V_\rho}\int_{V_\rho} \mathbf{w}_\rho(x)\,\mathrm{d}V. \tag{9}$$

Finally, after substituting from (7) back into (5) we arrive at the desired approximation of $\sigma_\rho(x)$.

Evaluation of $\mathbf{W}_\rho$ and $\mathbf{w}_\rho$ for three-phase solids is outlined in appendix B.

In the absence of inelastic effects, the overall and local strain fields are

$$\epsilon = \mathbf{M}\sigma + \mathbf{m}\Delta T \qquad \epsilon_\rho = \mathbf{M}_\rho\sigma_\rho + \mathbf{m}_\rho\Delta T \qquad \rho = \mathrm{f, g, m.} \tag{10}$$

Using results obtained from (8) and (9), one can write the local stress averages in the form

$$\sigma_\rho = \mathbf{W}_\rho\sigma_\mathrm{m} + \mathbf{w}_\rho\Delta T \qquad \text{with } \rho = \mathrm{f, g, m.} \tag{11}$$

The compatibility condition, $c_\mathrm{f}\epsilon_\mathrm{f} + c_\mathrm{m}\epsilon_\mathrm{m} = \epsilon$, together with equations (7), (10) and (11) then yield the desired results

$$\mathbf{M} = \left[\sum_\rho c_\rho \mathbf{M}_\rho\mathbf{W}_\rho\right]\left[\sum_\rho c_\rho\mathbf{W}_\rho\right]^{-1} \tag{12}$$

$$\mathbf{m} = \left[\sum_\rho c_\rho \mathbf{M}_\rho\mathbf{W}_\rho\right]\left[\sum_\rho c_\rho\mathbf{W}_\rho\right]^{-1}\left[-\sum_\rho c_\rho\mathbf{w}_\rho\right] + \sum_\rho c_\rho(\mathbf{M}_\rho\mathbf{w}_\rho + \mathbf{m}_\rho).$$

3. Transformation field analysis in laminated plates

In this section, the transformation field analysis, outlined in section 2.1, is extended to symmetric laminated plates under uniform in-plane loads. The analytical procedure combines the classical laminated plate theory for evaluation of average ply stresses under the prescribed thermomechanical loads with estimates of the local stresses within the plies, found as outlined in the former paragraphs.

The goal is to derive expressions for evaluation of the local stress fields within the plies, in the locations, where damage is likely to be initiated. Those regions are usually found at

or in the vicinity of the fibre–matrix, or coating–matrix interfaces, where the local stresses exceed their corresponding strength magnitudes.

In order to prevent evolution of damage, it is necessary to identify allowable overall stress states that maintain the integrity of the microstructure. In the present study, this is achieved by constructing initial failure maps of laminated plates, as internal envelopes of several branches that identify overall stress combinations which cause components of local stresses to reach the local strength. Internal envelopes of the various branches then represent boundaries on the allowable overall stresses that should not damage the laminate.

3.1. Overall response and ply field averages in laminates

We limit our attention to laminates consisting of $2N$ thin elastic plies ($i = 1, 2, \ldots, N$), arranged in a symmetric layup with respect to the midplane X_1X_2, see figure 2. In-plane membrane forces and the corresponding uniform stresses $S = [S_{11}, S_{22}, S_{12}]^T$, defined in the X coordinates, may be applied together with uniform change in temperature. Moreover, uniform eigenstrains $\mu_i = [\mu^i_{11}, \mu^i_{22}, \mu^i_{12}]^T$ can be introduced in pairs of plies (i), equidistant from the midplane, such that symmetry of the laminate loads about the midplane is preserved. In the symmetric plate, the resulting deformations are the in-plane overall strains $E = [E_{11}, E_{22}, E_{12}]^T$. The overall response of the composite laminate is then given in a form analogous to (4),

$$S = \bar{\mathbf{L}}E + \bar{\mathbf{l}}\Delta T + \bar{\lambda} \qquad E = \bar{\mathbf{M}}S + \bar{\mathbf{m}}\Delta T + \bar{\mu} \tag{13}$$

where the $\bar{\mathbf{m}} = -\bar{\mathbf{L}}\bar{\mathbf{l}}$ is the (3×1) overall thermal strain vector, and $\bar{\lambda} = -\bar{\mathbf{L}}\bar{\mu}$ is the laminate eigenstress; $\bar{\mathbf{L}} = \bar{\mathbf{M}}^{-1}$ denotes the (3×3) overall stiffness of the laminated plate under in-plane loads. In context of the classical laminated plate theory, the overall quantities are derived by integrating the ply constitutive relations over the laminate thickness

$$S = \frac{1}{h}\sum_{i=1}^{N}\int_{-h_i/2}^{h_i/2} S_i \, dx_3 = \frac{1}{h}\sum_{i=1}^{N}\int_{-h_i/2}^{h_i/2} (\bar{\mathbf{L}}_i E_i + \bar{\mathbf{L}}_i \Delta T + \bar{\lambda}_i) \, dx_3. \tag{14}$$

Since the in-plane strains must be equal in all plies and the temperature change is assumed to be uniform, equation (14) provides the plate overall stiffness matrix and the overall thermal stress and eigenstress vectors in the form

$$\bar{\mathbf{L}} = \sum_{i=1}^{N} c_i \bar{\mathbf{L}}_i \qquad \bar{\mathbf{l}} = \sum_{i=1}^{N} c_i \bar{\mathbf{l}}_i \qquad \bar{\lambda} = \sum_{i=1}^{N} c_i \bar{\lambda}_i \tag{15}$$

where $c_i = h_i/h$, $i = 1, \ldots, N$ represents the volume fraction of individual plies. $\bar{\mathbf{L}}_i = \bar{\mathbf{M}}_i^{-1}$ are (3×3) plane stress stiffness and compliance matrices of ith ply written in laminate coordinate system X as

$$\bar{\mathbf{L}}_i = \mathbf{N}_i^T \mathbf{L}_i \mathbf{N}_i \qquad \bar{\mathbf{M}}_i = \mathbf{R}_i^T \mathbf{M}_i \mathbf{R}_i \tag{16}$$

where $\mathbf{N}_i$ and $\mathbf{R}_i$ represent certain transformation matrices such that

$$\mathbf{R}_i^T = (\mathbf{N}_i)^{-1} = \begin{bmatrix} \cos^2\psi_i & \sin^2\psi_i & -\frac{1}{2}\sin 2\psi_i \\ \sin^2\psi_i & \cos^2\psi_i & \frac{1}{2}\sin 2\psi_i \\ \sin 2\psi_i & -\sin 2\psi_i & \cos 2\psi_i \end{bmatrix}. \tag{17}$$

The ply stresses are related to the overall stresses S and the ply eigenstrains by

$$S_i = \mathbf{H}_i S + \mathbf{h}_i \Delta T - \sum_{j=1}^{N} \mathbf{K}_{ij} \bar{\mathbf{L}}_j \bar{\mu}_j \qquad S_i = \mathbf{N}_i^T \sigma_i \tag{18}$$

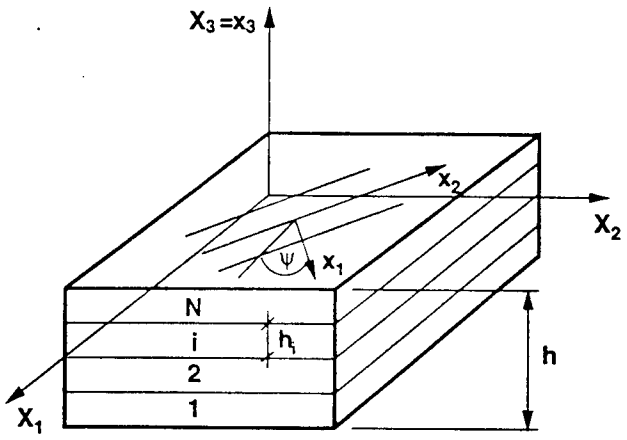


Figure 2. Representative volume element

Table 1. Thermomechanical properties of carbon coating [2].

E_L (GPa)	E_T (GPa)	G_L (GPa)	G_T (GPa)	ν	α_L (10^{-6}/C)	α_T (10^{-6}/C)
172.4	6.9	14.5	3.8	0.3	1.8	28

L and T denote the longitudinal and transverse directions, respectively.

Table 2. Thermomechanical properties of Al_2O_3 fibre [20].

T (C)	E (GPa)	ν	α (10^{-6}/C)
1200	290	0.24	8.32
1000	340	0.24	8.32
800	352	0.24	8.32
600	360	0.24	8.32
400	372	0.24	8.32
200	376	0.24	8.32
20	380	0.24	8.32

where σ_i represents the components of the stress vector in ply (i) now written in the ply coordinate system x. $\mathbf{H}_i$ is the (3×3) ply stress distribution factor, $\mathbf{h}_i$ is the (3×1) ply thermal distribution factor, and $\mathbf{K}_{ij}$ are the ply eigenstress distribution factors. The latter provides the contribution to the stress S_i in ply (i) due to eigenstrain μ_j in ply (j), both for $j = i$ and $j \neq i$. To establish relations between distribution factors and thermoelastic properties of the laminate we first recall the compatibility and equilibrium of the in-plane strain and stress components:

$$E_i = E \qquad \sum_{i=1}^{N} c_i S_i = S. \tag{19}$$

Then, equations (13), (14), (18) and (19) provide

$$\mathbf{H}_i = \bar{\mathbf{L}}_i \bar{\mathbf{M}} \qquad \mathbf{h}_i = \bar{\mathbf{l}}_i - \mathbf{H}_i \bar{\mathbf{l}} \qquad \mathbf{K}_{ij} = \delta_{ij}\mathbf{I} - c_j \mathbf{H}_i \tag{20}$$

Table 3. Thermomechanical properties of SCS6 fibre [12].

T (C)	E (GPa)	υ	α (10^{-6}/C)
900	363	0.25	4.49
760	366	0.25	4.38
700	369	0.25	4.31
640	370	0.25	4.25
580	372	0.25	4.17
490	374	0.25	4.17
430	377	0.25	3.95
310	380	0.25	3.82
140	385	0.25	3.66
22	390	0.25	3.56

Table 4. Thermomechanical properties of $MoSi_2$ matrix [20].

E (GPa)	υ	α (10^{-6}/C)
330	0.165	8.32

Table 5. Thermomechanical properties of Ti_3Al matrix [2].

T (^{circ}C)	E (GPa)	υ	α (10^{-6}/C)
950	32.4	0.3	10.4
760	51.2	0.3	10.4
640	62.0	0.3	10.4
430	63.3	0.3	10.4
260	66.3	0.3	10.4
22	69.0	0.3	10.4

where δ_{ij} is the Kronecker delta symbol and $\mathbf{I}$ is the (3×3) identity matrix. Finally, assuming that each ply has been subdivided into M subelements $\rho, \eta = 1, 2, \ldots, M$, the eigenstrain $\overline{\mu}_j$ is obtained using the modified Levin's formula

$$\overline{\mu}_j = \mathbf{R}_j^{\mathrm{T}} \sum_{\eta=1}^{M} c_\eta^j \mathbf{B}_\eta^{j^{\mathrm{T}}} \mu_\eta^j \tag{21}$$

where $\mathbf{R}_j$ is the transformation matrix given by (17) and $\mathbf{B}_\eta^j$ is the familiar (6×6) stress concentration matrix discussed in section 2.1. Note that the summation in (21) is carried out first and then the result is reduced to a (3×1) vector by deleting rows 3, 4, and 5 to conform with the original formulation of the plate problem based on generalized plane stress assumption.

3.2. Local stress fields in the plies

Now that the ply stresses (18) in the laminate have been determined, we can relate the local stresses within the ply to the overall stress S applied to the laminate, and to the local

Table 6. Thermomechanical properties of Timetal-21S matrix [12].

T (C)	E (GPa)	ν	α (10^{-6}/C)
900	50.0	0.382	12.5
760	51.5	0.378	12.3
700	58.5	0.370	11.9
640	72.0	0.365	11.7
580	83.0	0.365	11.3
490	91.0	0.365	10.7
430	99.5	0.354	10.1
310	104	0.361	9.55
140	110	0.351	8.96
22	116	0.341	8.67

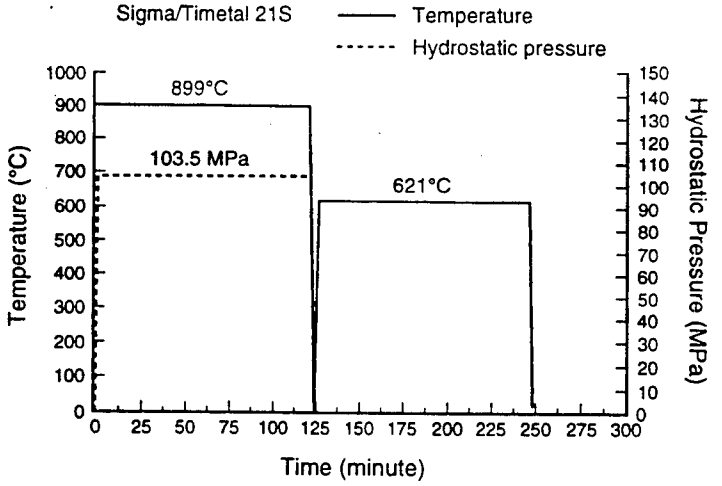


Figure 3. Compressive stress and temperature history applied during fabrication of the SCS6/Timetal-21S composite.

eigenstrains within the plies. First, (1) and (18_2) give

$$\boldsymbol{\sigma}^i_\rho = \mathbf{B}^i_\rho \mathbf{R}_i S_i + \mathbf{b}^i_\rho \Delta T - \sum_{\eta=1}^{M} \mathbf{F}^i_{\rho\eta} \mathbf{L}^i_\eta \boldsymbol{\mu}^i_\eta. \tag{22}$$

Then, using (18) and (21) in (22) we arrive at the final expression

$$\boldsymbol{\sigma}^i_\rho = \mathbf{B}^i_\rho \mathbf{R}_i (\mathbf{H}_i S + \mathbf{h}_i \Delta T) + \mathbf{b}^i_\rho \Delta T - \sum_{\eta=1}^{M} \mathbf{F}^i_{\rho\eta} \mathbf{L}^i_\eta \boldsymbol{\mu}^i_\eta - \mathbf{B}^i_\rho \mathbf{R}_i \sum_{j=1}^{N} \mathbf{K}_{ij} \bar{\mathbf{L}}_j \mathbf{R}_j^{\mathrm{T}} \left[\sum_{\eta=1}^{M} \bar{c}^j_\eta \mathbf{B}^{j^{\mathrm{T}}}_\eta \boldsymbol{\mu}^j_\eta \right] \tag{23}$$

where $\rho, \eta = 1, 2, \ldots, M$ and $j = 1, 2, \ldots, N$. To find correct phase stress averages $\boldsymbol{\sigma}^i_\rho$ as (6×1) vectors, the product $\mathbf{R}_i S_i$ in equation (22) and the products $\mathbf{R}_i(\mathbf{H}_i S + \mathbf{h}_i \Delta T)$ and $\mathbf{R}_i \sum_{j=1}^{N} \mathbf{K}_{ij} \bar{\mathbf{L}}_j \bar{\boldsymbol{\mu}}_j$ in equation (23) have to be augmented by zeros in rows 3, 4, and 5 into (6×1) vectors.

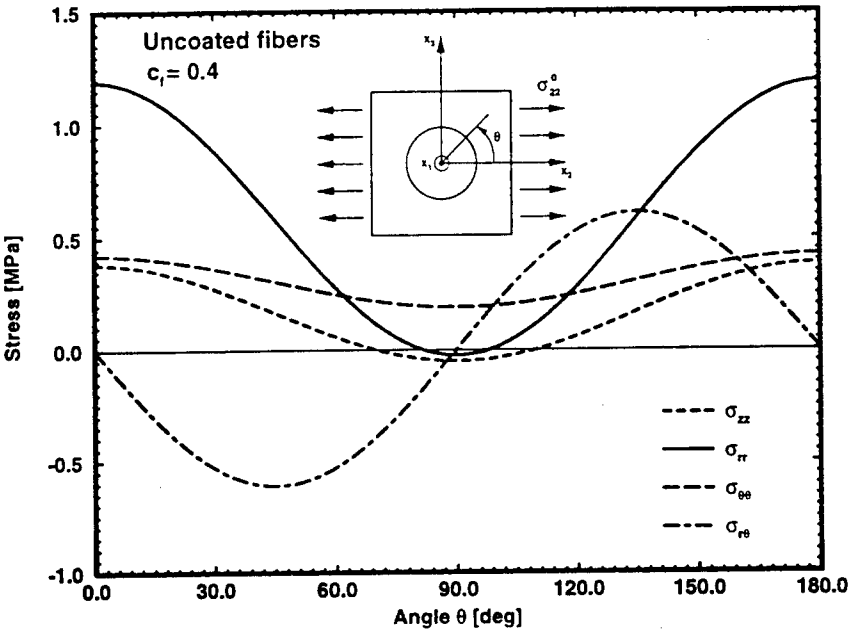


Figure 4. Local stresses in the matrix at the fibre–matrix interface under unit traverse tension applied to a unidirectional lamina of the SCS-6/Ti_3Al system.

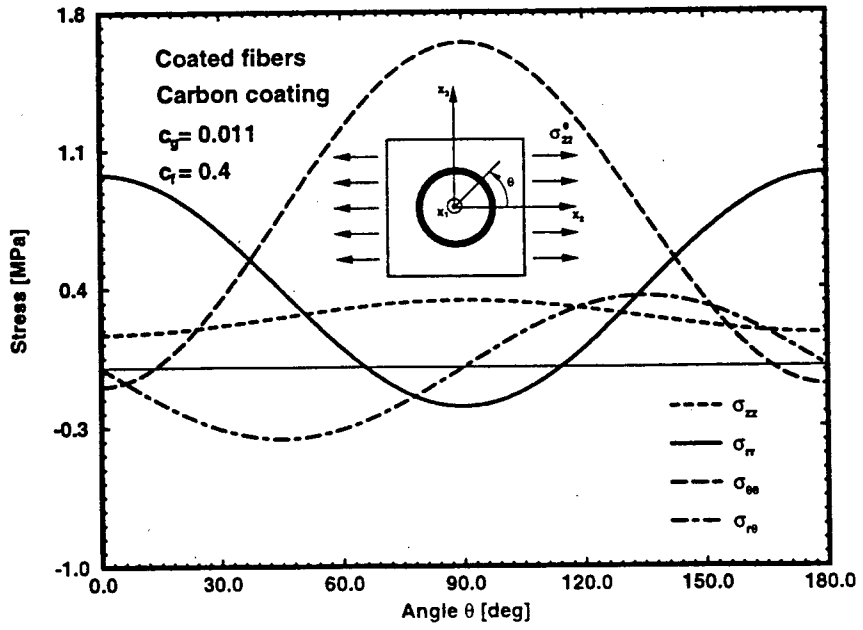


Figure 5. Local stresses in the matrix at the coating–matrix interface under unit traverse tension applied to a unidirectional lamina of the SCS-6/Ti_3Al system with coated fibres.

The first and second terms in (23) represent the local stress caused by the overall stress and uniform change in temperature applied to the laminate, while the third and fourth terms are the contributions of the subvolume eigenstrains in the plies to subvolume p of

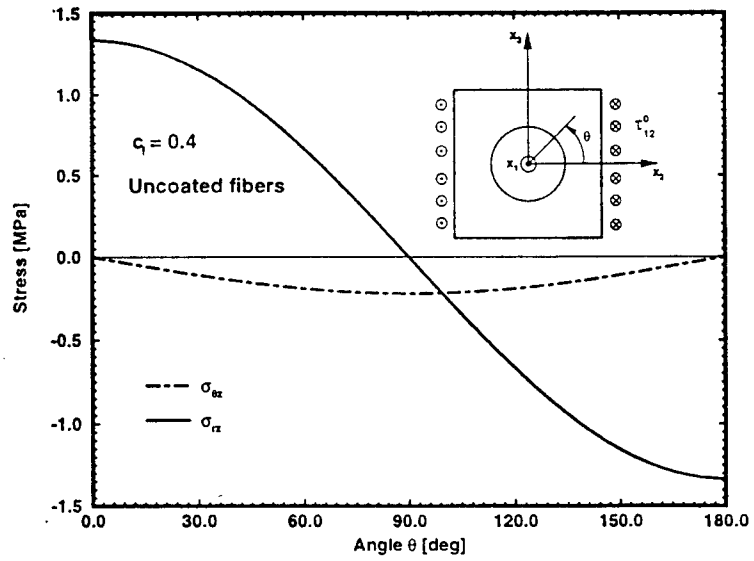


Figure 6. Local stresses in the matrix at the fibre–matrix interface under unit longitudinal shear applied to a unidirectional lamina of the SCS-6/Ti_3Al system.

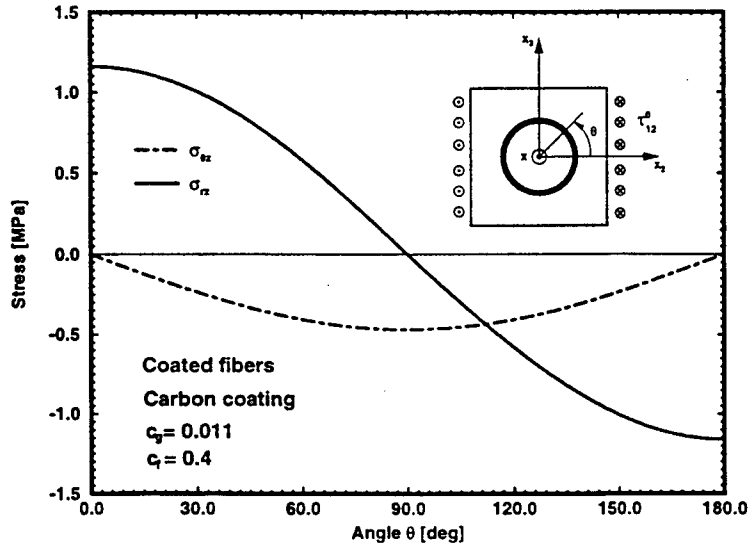


Figure 7. Local stresses in the matrix at the coating–matrix interface under unit longitudinal shear applied to a unidirectional lamina of the SCS-6/Ti_3Al system with coated fibres.

lamina (i). The third term provides the local stresses due to local eigenstrains in lamina (i). The in-plane constraint $\boldsymbol{E} = \boldsymbol{E}_i$ imposed on each lamina causes additional stresses in the subvolumes of the plies when eigenstrains are present in other layers. This effect is given by the fourth term in (23). The usual volume averaging procedure then yields the ply average stresses.

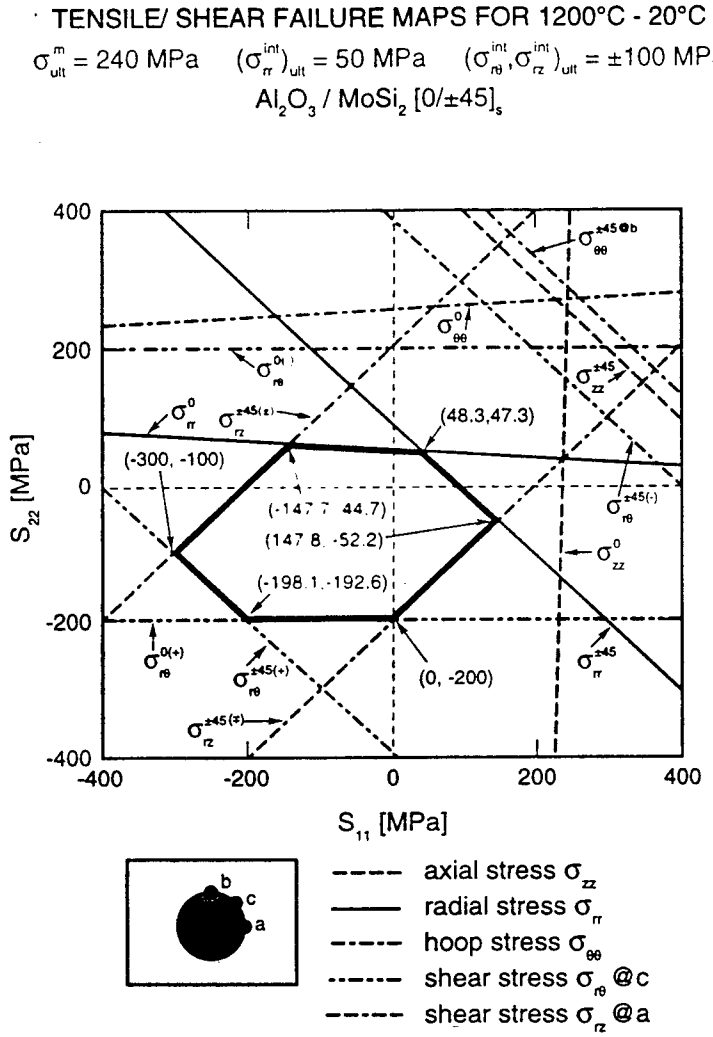


Figure 8. Failure envelopes of $Al_2O_3/MoSi_2$ $(0/\pm45)_s$ laminate in the $S_{11}S_{22}$-plane.

4. Initial failure maps

As an application, we constructed initial failure maps for three laminates. A ceramic/intermetallic $MoSi_2$ matrix reinforced by alumina fibres is chosen to represent an elastic–brittle system, while titanium-based Timetal-21S and Ti_3Al matrices with the silicon carbide SCS6 fibre represent ductile systems with a viscoplastic and elastic–plastic response to thermomechanical loads, respectively. A 10μm thick carbon coating has been added to the fibres in the SCS6/Ti_3Al system. The thermoelastic properties of transversely isotropic carbon coating are listed in table 1. The fibre and matrix phases are assumed to be elastically isotropic in all systems, with thermoelastic properties given in tables 2–6.

Overall properties of the selected systems were found as indicated in appendix A, and the local stresses were evaluated using the detailed analysis outlined in appendix B. Of particular interest were the maxima and minima of stresses at the fibre–matrix interfaces

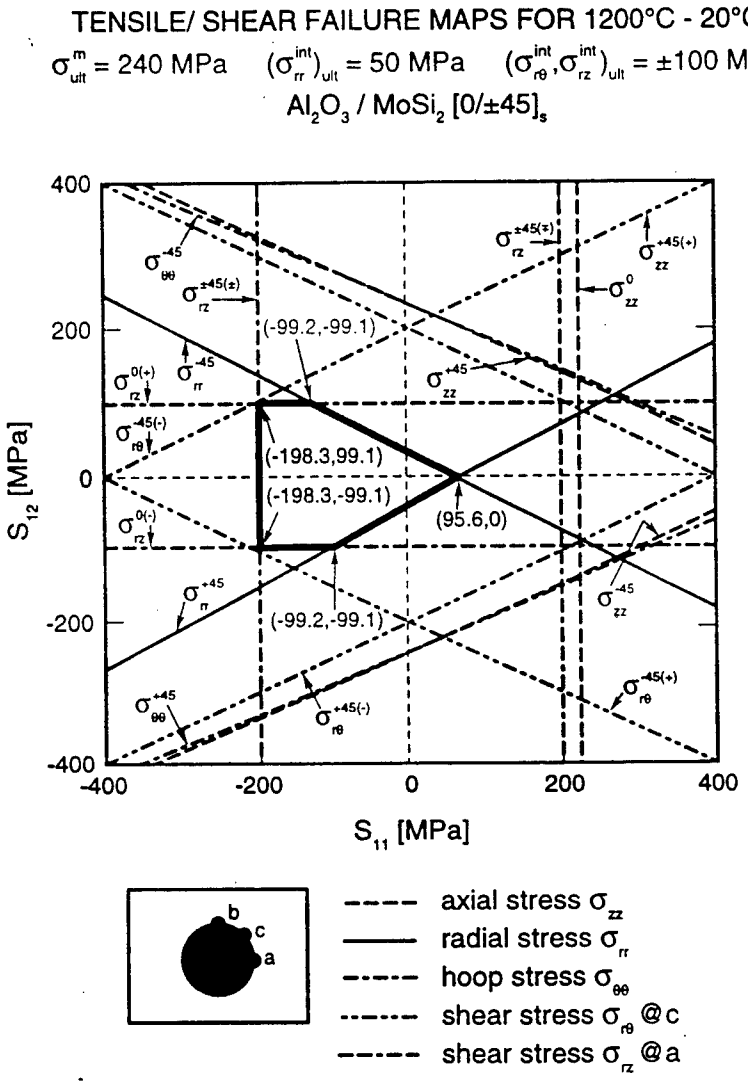


Figure 9. Tensile/shear failure envelopes of $Al_2O_3/MoSi_2$ $(0/\pm45)_s$ laminate in the $S_{11}S_{12}$-plane.

in each ply, the radial normal stress σ_{rr}, and the transverse and longitudinal shear stresses $\sigma_{r\theta}$ and σ_{rz}. The local normal hoop stress $\sigma_{\theta\theta}$ in the matrix at the interface, and the matrix normal stress σ_{zz} were also of interest. These interface and matrix stresses were regarded as most likely to cause damage. Fibre stresses were found to be insignificant relative to fibre strength and are not presented; relevant expressions are available in appendix B.

To illustrate the changes of the interface stress components, we show in figures 4–7 plots of these components in a uniformly loaded and initially stress-free SCS6/Ti_3Al ply, as functions of the angle θ measured in the plane perpendicular to the fibre axis, in the ccw direction from the x_2-axis that is parallel to the midplane of the ply, both for uncoated and coated fibres. The positions and magnitudes the maxima and minima of these components are clearly seen; both are of interest as either of their respective magnitudes may become a

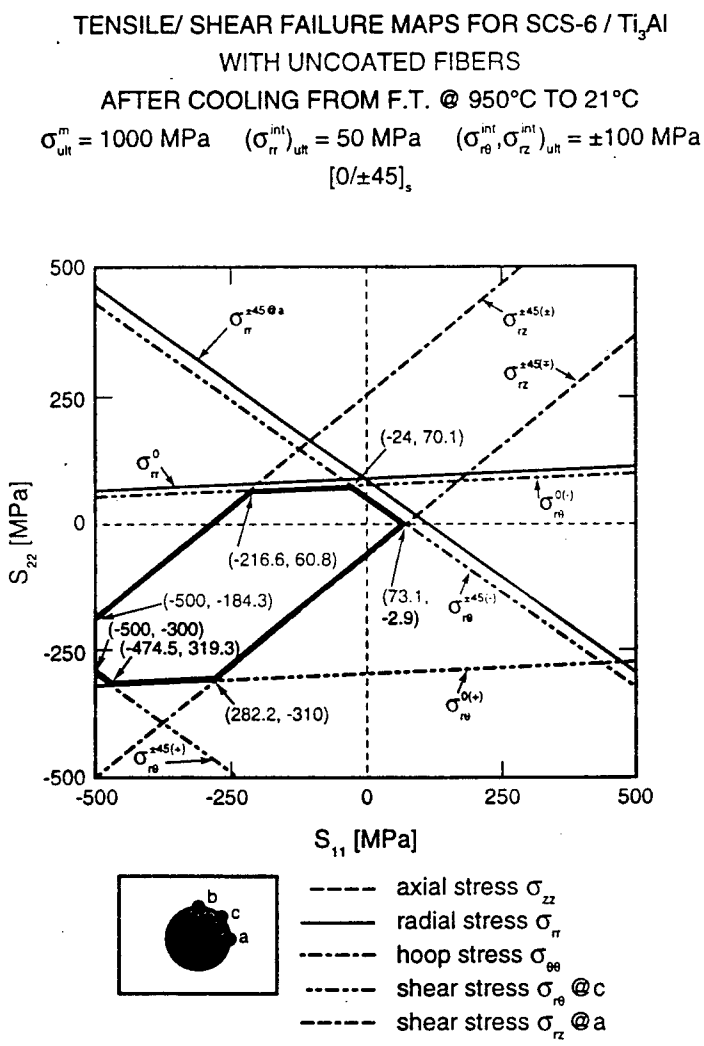


Figure 10. Failure envelopes of SCS-6/Ti_3Al $(0/\pm45)_s$ laminate with uncoated fibres in the $S_{11}S_{22}$-plane.

dominant stress maximum under tensile or compressive overall stresses. In the subsequent laminate analysis, these values and their locations were monitored, scaled, and superimposed with the initial thermal stresses.

The results in figures 4–7 also show that the coating reduces the magnitudes of the radial and shear stress components, but at the expense of higher matrix hoop stresses under transverse tension. However, this apparent disadvantage will be seen not to extend to stress distributions in an undamaged SCS6/Ti_3Al laminate, figures 11 and 13, but may well appear, and needs to be analysed, in other systems and layups. The desirable coating properties, from the standpoint of thermal stress reduction, are evident in table 1; i.e. the high thermal expansion coefficient and low elastic modulus in the transverse plane. A coating with a higher transverse modulus would offer better support for the matrix cavity containing the coated fibre, and thus could reduce the matrix interface stresses in plies under transverse

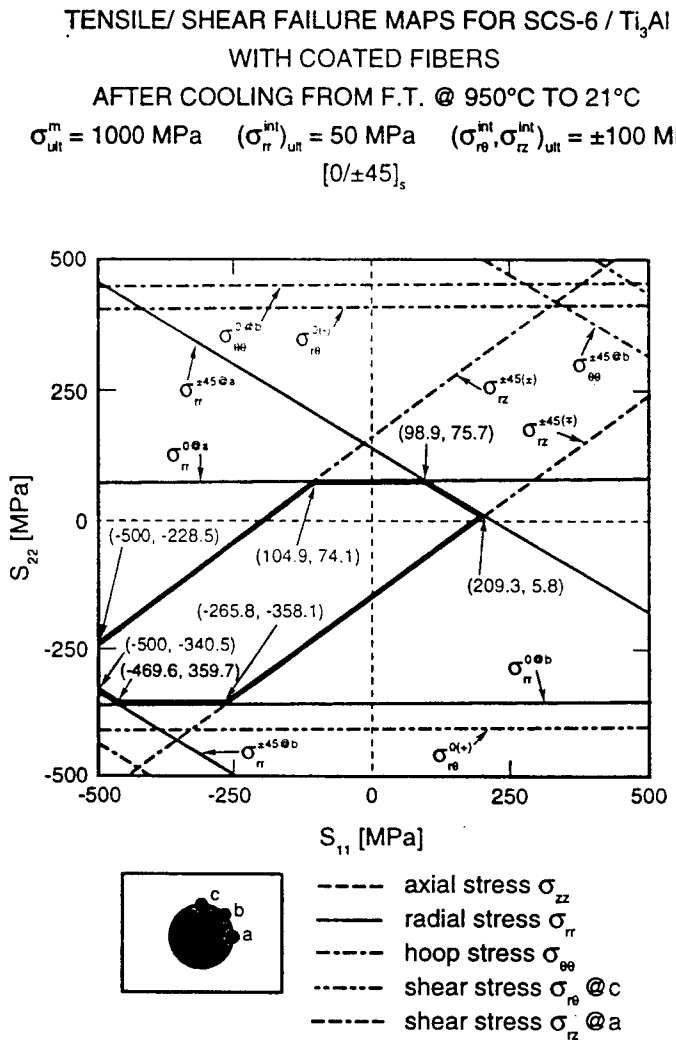


Figure 11. Failure envelopes of SCS-6/Ti_3Al $(0/\pm45)_s$ laminate with coated fibres in the $S_{11}S_{22}$-plane.

tension and longitudinal shear.

In laminate analysis, we first considered the effect of the thermomechanical loading histories applied during fabrication and cooling on the initial stress state in each ply of the selected laminates. In the $Al_2O_3/MoSi_2$ system, the phase thermal expansion coefficients are nearly identical, and thus the thermal stresses are of negligible magnitude. In the SCS6/Ti_3Al system, we considered the effect of cooling to room temperature from the presumably stress-free state at 950 °C. The laminate remained essentially elastic along this path; however, significant thermal residual stresses were generated by the cooling cycle. The SCS6/Timetal 21S system was analysed for the pressure-temperature history supplied by a manufacturer, figure 3. Extensive inelastic deformation had taken place; this was analysed separately in [3]. The resulting residual stresses of interest here are listed in figures 14 and 15.

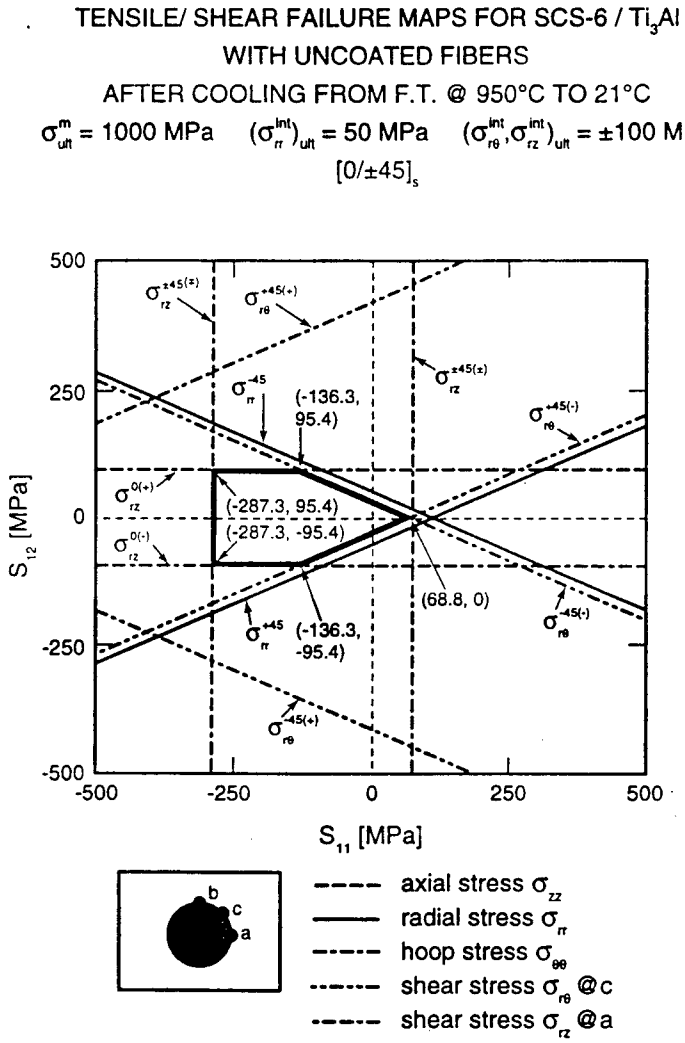


Figure 12. Tensile/shear failure envelopes of SCS-6/Ti_3Al $(0/\pm45)_s$ laminate with uncoated fibres in the $S_{11}S_{12}$-plane.

The failure maps for the above laminates are plotted in figures 8–15. The $Al_2O_3/MoSi_2$ and the SCS6/Ti_3Al laminates were chosen in the $(0/\pm45)_s$ layup, and the SCS6/Timetal 21S system in the $(0/\pm45/90)_s$ layup. All were analysed under uniformly applied overall in-plane biaxial tension/compression $S_{11}S_{22}$, and shear and normal stresses $S_{11}S_{12}$, with the x_1-axis oriented parallel to the zero-layer fibres. The overall stresses were applied within a large magnitude range, as needed to accommodate the entire failure envelope. Average ply stresses caused by the overall stresses were evaluated in each ply and the corresponding local stresses at the interface and in the matrix were found, as they were, for example, in figures 4–7. The initial stresses, if any, within the plies and in the laminate were then superimposed with the respective mechanical stresses. Finally, guided by available experimental data [7], we selected certain critical magnitudes for the radial and shear interface stresses, and for the matrix hoop and axial normal stresses; these are

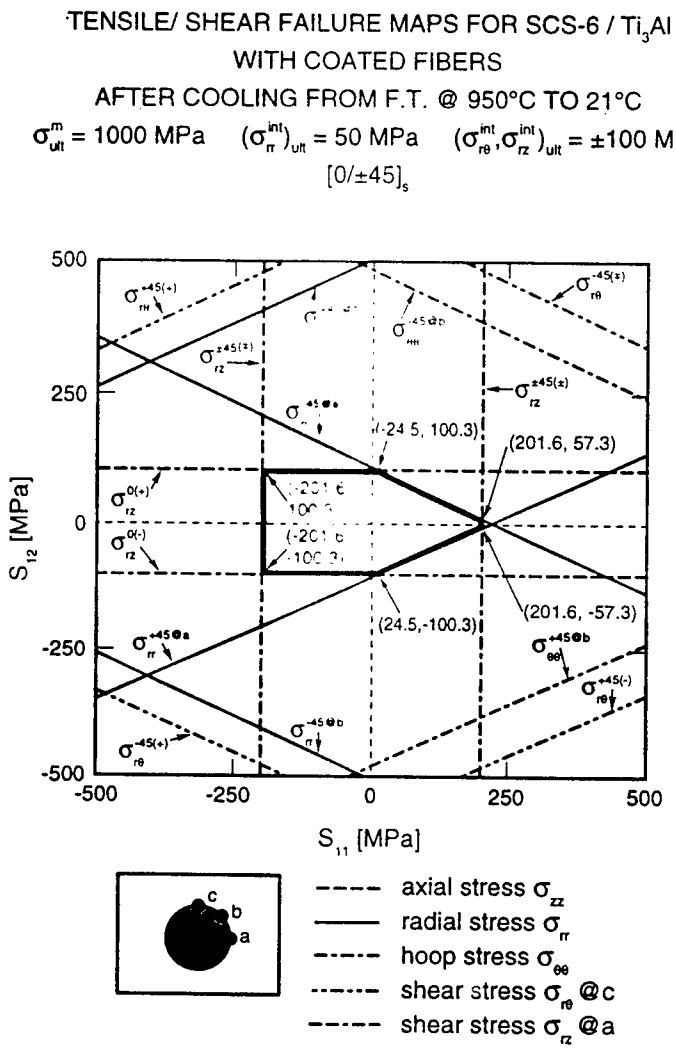


Figure 13. Tensile/shear failure envelopes of SCS-6/Ti_3Al $(0/\pm45)_s$ laminate with coated fibres in the $S_{11}S_{12}$-plane.

listed in figure captions. The overall laminate stresses were then scaled such as to cause, in superposition with the initial stresses, local stresses of the respective selected critical magnitudes at the corresponding locations within each ply. For each local stress component of the critical magnitude, these scaled overall stresses were plotted in the $S_{11}S_{22}$ and $S_{11}S_{12}$ stress planes. These plots are usually straight lines in the overall planes, except when the stress maxima are found at different points of the interface, resulting in piecewise straight lines.

In the said figures, the lines are shown for each component of interest in each ply. They divide the overall stress plane such that for overall stress combinations which are in the part containing the origin, the local stresses are lower than critical, while in the outlying part of the plane, they exceed the selected critical values. Therefore, the branches that are closest to the origin define an internal failure envelope where external loads are not likely to cause

TENSILE FAILURE MAPS FOR SCS-6 / Timetal -21

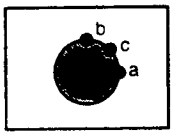
$[0/\pm45/90]_s$

AFTER COOLING FROM F.T. @ 890°C TO 21°C

$\sigma^m_{ult} = \pm 1000$ MPa $\quad (\sigma^{int}_{rr})_{ult} = 50$ MPa $\quad (\sigma^{int}_{r\theta}, \sigma^{int}_{rz})_{ult} = \pm 100$ MPa

Local Residual Stresses @ 21°C

Stress [MPa]	0°/90°-ply	±45°-ply
σ^m_{zz}	475	477
$\sigma^{@a}_{rr}$	-61	-210
$\sigma^{@b}_{rr}$	-233	-239
$\sigma^{@c}_{r\theta}$	-86	-14.6



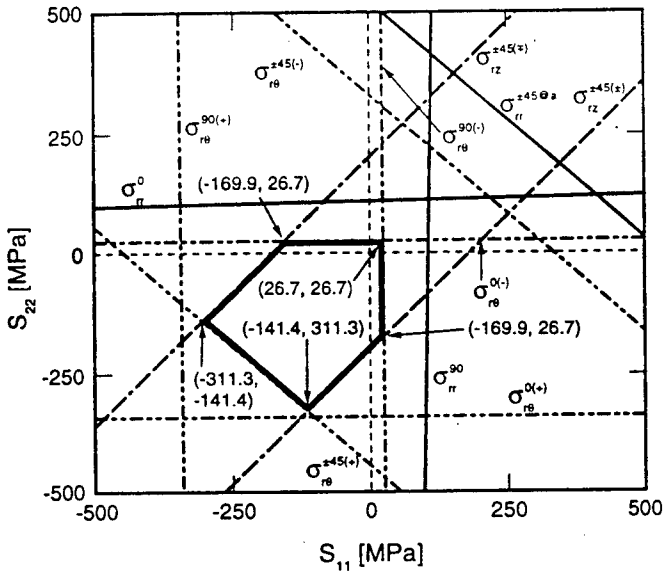


Figure 14. Failure envelopes of a SCS-6/Timetal-21S $(0/\pm45/90)_s$ laminate in the $S_{11}S_{22}$-plane at room temperature.

damage in the laminate. Conversely, if any part of this internal envelope is crossed by the combined overall stresses, a particular damage mode is predicted.

For example, in the $(0/\pm45)_s$, $Al_2O_3/MoSi_2$ laminate, figure 8, failure by radial debonding of the interface in the ±45° plies is predicted under S_{11} tension, and longitudinal shear debonding under S_{11} compression. For S_{22} tension, radial debonding of the interface in the 0° plies is indicated, while transverse shear debonding in the 0° plies and longitudinal shear debonding in the ±45° plies is expected to take place under S_{22} compression. The in-plane overall shear S_{12}, figure 9, promotes radial debonding in the ±45° plies and, in conjunction with the S_{11} compression, longitudinal shear sliding of the fibres in either 0° or in the ±45° plies. The (+) and (−) signs after the stress labels identify the sign of the ±100 MPa shear strength that was activated by the particular branch. The letters a, b or c, in that position identify the interface points where the critical stress was

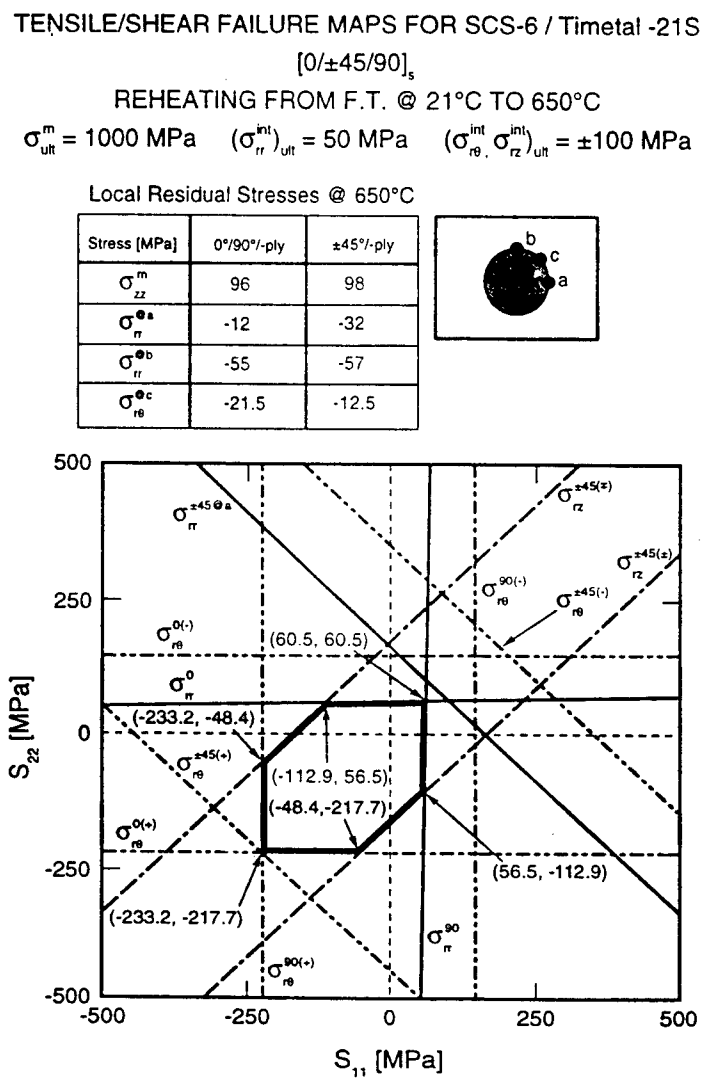


Figure 15. Failure envelopes of a SCS-6/Timetal-21S $(0/\pm45/90)_s$ laminate in the $S_{11}S_{22}$-plane and after reheating to 650 °C.

reached.

In the $(0/\pm45)_s$, SCS6/Ti_3Al laminate, figures 10– 13, the overall shapes of the internal envelopes of the critical stress branches are somewhat similar to those found for the same layup in the $Al_2O_3/MoSi_2$ system. However, there are significant differences in positions of the various branches, due to the different elastic moduli of the phases, and also as a consequence of the initial stresses that are present in this system. For example, under pure S_{11} tension, both longitudinal and transverse shearing of the fibre–matrix interface is predicted, both for the uncoated and coated fibre systems. Note, however, that the coating is responsible for a substantial expansion of the damage-free $S_{11} > 0$ loading range, from about 73 MPa to 209 MPa, figures 10 and 11. However, a large contraction of the damage-free $S_{11} < 0$ loading range is also indicated, as the entire failure envelope appears to translate

toward higher tension stresses. A comparison of figures 12 and 13 suggests expansion of the damage-free S_{12} load range due to the fibre coatings.

The branches for the interface hoop stress in the matrix lie well outside the internal envelope, and are not activated in any of the figures. This suggests that in contrast to the single ply case, figures 4 and 5, use of the fibre coating in the described laminates is not contributing to contraction of the damage-free region. Comparisons of figure 10 with 11 and of figure 12 with 13 also indicate that the coatings cause a substantial expansion of the failure envelope in the tension directions.

Finally, the failure envelopes for the SCS6/Timetal 21S system in the $(0/\pm45/90)_s$ layup appear in figures 14 and 15, and are plotted at 21 °C and after reheating to 650 °C. The residual stresses due to cooling from the fabrication temperature are listed in the figures [3]. Note here the very small safe tension loading range, $S_{11} < 26.7$ MPa, $S_{22} < 26.7$ MPa at RT in figure 14, with transverse shear debonding indicated in the 90° or 0° plies, respectively. At the higher temperature of 650 °C, the tension range expands by a factor of two in both overall stress directions, but the predicted damage mode now changes from transverse shear to radial interface separation.

We emphasize that all the failure envelopes shown were constructed for perfectly bonded systems. Interface debonding or matrix cracking would substantially change the internal stress distribution at the damage location, and thus change the position of the branches. In particular, the matrix hoop stress branches are expected to move much closer to the origin, as radial cracking would be likely to take place at debonded fibres.

Note that the failure maps can be easily adjusted for any other selected strengths by multiplying the scales by the ratio of the new/current strength for each selection, and by replotting the branches in the original stress plane.

Acknowledgments

Financial support was provided by the ARPA/ONR University Research Initiative Program on 'Mechanism-Based Design of High-Temperature Composite Structures' at Rensselaer. Drs W Coblenz and S Fishman served as monitors.

Appendix A. Evaluation of effective mechanical and thermal elastic properties for two-phase composite systems

Suppose that the fibre and matrix moduli and coefficients of thermal expansion are represented by continuous functions of temperature T, derived from experimental data. After a uniform change ΔT, from a reference T_0, applied under a uniform stress σ_ρ, an unconstrained phase deforms uniformly,

$$\epsilon_\rho = \mathbf{M}_\rho(T)\sigma_\rho + \int_{T_0}^{T} \mathbf{m}_\rho(T)\,\mathrm{d}T. \tag{A1}$$

If the temperature changes under an applied uniform strain, the stress is

$$\sigma_\rho = \mathbf{L}_\rho(T)\epsilon_\rho - \mathbf{L}_\rho(T)\int_{T_0}^{T} \mathbf{m}_\rho(T)\,\mathrm{d}T \tag{A2}$$

where $\rho = \mathrm{f}, \mathrm{m}$ denotes the phase, $\mathbf{L}_\rho(T)$ and $\mathbf{M}_\rho(T) = (\mathbf{L}_\rho(T))^{-1}$ are temperature dependent (6×6) phase stiffness and compliance matrices, and $\mathbf{m}_\rho(T)$ is the (6×1) thermal strain vector of expansion coefficients; their particular forms depend on the elastic

symmetry of the phase. A comparison with (4) suggests that the term $\mathbf{m}\Delta T$ evaluates as the integral in (A1); the phase moduli are taken at the current temperature T.

For a transversely isotropic solid, with x_1 as the axis of rotational symmetry, the stress–strain relation

$$\sigma = \mathbf{L}(\epsilon - \mathbf{m}\Delta T - \mu) \tag{A3}$$

is usually written in terms of Hill's moduli

$$\begin{bmatrix} \sigma_1 \\ \sigma_2 \\ \sigma_3 \\ \sigma_4 \\ \sigma_5 \\ \sigma_6 \end{bmatrix} = \begin{bmatrix} n & l & l & 0 & 0 & 0 \\ l & (k+m) & (k-m) & 0 & 0 & 0 \\ l & (k-m) & (k+m) & 0 & 0 & 0 \\ 0 & 0 & 0 & m & 0 & 0 \\ 0 & 0 & 0 & 0 & p & 0 \\ 0 & 0 & 0 & 0 & 0 & p \end{bmatrix} \begin{bmatrix} \epsilon_1 - m_1\Delta T - \mu_1 \\ \epsilon_2 - m_2\Delta T - \mu_2 \\ \epsilon_3 - m_2\Delta T - \mu_3 \\ \epsilon_4 - \mu_4 \\ \epsilon_5 - \mu_5 \\ \epsilon_6 - \mu_6 \end{bmatrix} \tag{A4}$$

where

$$k = -[1/G_{23} - 4/E_{22} + 4\nu_{12}^2/E_{11}]^{-1} \qquad l = 2k\nu_{12}$$
$$n = E_{11} + 4k\nu_{12}^2 = E_{11} + l^2/k \qquad m = G_{23} \qquad p = G_{12}.$$

To estimate the overall moduli $\mathbf{L}$ of heterogeneous medium one can use the Mori–Tanaka procedure outlined in section 2.2. Recall that in the reformulation of the Mori–Tanaka method by Benveniste [4], the local fields in the fibre are approximated by those found when single inclusion is embedded in a large volume of matrix and subjected to remotely applied average stress in the matrix, σ_m. The single fibre problem can be easily solved for fibres with circular or ellipsoidal cross section, in terms of Eshelby's tensor $\mathbf{S}$. If this is the case, the stresses in the fibre are uniform and can be written, in analogy with (5), in the form

$$\sigma_f = \mathbf{W}_f\sigma_m \tag{A5}$$

where the partial concentration factor $\mathbf{W}_\rho$ is given by

$$\mathbf{W}_f = \mathbf{L}_f[\mathbf{I} + \mathbf{S}\mathbf{L}_m^{-1}(\mathbf{L}_f - \mathbf{L}_m)]^{-1}\mathbf{L}_m^{-1}. \tag{A6}$$

The Eshelby tensor $\mathbf{S}$ can be obtained in terms of the polarization tensor $\mathbf{P} = \mathbf{S}\mathbf{L}_m^{-1}$, represented as a (6×6) array with the following non-zero coefficients [25]

$$P_{22} = P_{33} = \frac{k_m + 4m_m}{8m_m(k_m + m_m)} \qquad P_{23} = P_{32} = \frac{-k_m}{8m_m(k_m + m_m)}$$
$$P_{44} = \frac{k_m + 2m_m}{2m_m(k_m + m_m)} \qquad P_{55} = P_{66} = 1/(2p_m). \tag{A7}$$

Note that $\mathbf{P}$ is singular, but the Eshelby tensor $\mathbf{S} = \mathbf{P}\mathbf{L}_m$, of a transformed homogeneous inclusion in the matrix $\mathbf{L}_m$, is not.

The total stress concentration factors $\mathbf{B}_f$ follow from (7)

$$\mathbf{B}_f = \mathbf{W}_f(c_m\mathbf{I} + c_f\mathbf{W}_f)^{-1} \qquad \mathbf{B}_f = (c_m\mathbf{I} + c_f\mathbf{W}_f)^{-1}. \tag{A8}$$

Under purely mechanical loading σ^0, the overall and local mechanical strain averages written as

$$\epsilon = \mathbf{M}\sigma^0 \qquad \epsilon_\rho = \mathbf{M}_\rho\sigma_\rho \qquad \rho = \mathrm{f}, \mathrm{m} \tag{A9}$$

provide, together with connection $c_f\epsilon_f + c_m\epsilon_m = \epsilon$, the estimate of the overall compliance matrix $\mathbf{M}$ [17], see (12_1),

$$\mathbf{M} = c_f\mathbf{M}_f\mathbf{B}_f + c_m\mathbf{M}_m\mathbf{B}_m[c_f\mathbf{M}_f\mathbf{W}_f + c_m\mathbf{M}_m](c_m\mathbf{I} + c_f\mathbf{W}_f)^{-1} \tag{A10}$$

while the stiffness $\mathbf{L} = \mathbf{M}^{-1}$. Finally, in analogy with (4) we can include the thermal and inelastic effects $\mathbf{m}\Delta T + \mu$ into (A9$_1$). These two parts of the overall stain can be found from generalized Levin's formula [11]

$$\mathbf{m}\Delta T + \mu = c_f \mathbf{B}_f^T(\mathbf{m}_f \Delta T + \mu_m) + c_m \mathbf{B}_m^T(\mathbf{m}_f \Delta T + \mu_m). \tag{A11}$$

Appendix B. Evaluation of partial mechanical and thermal stress concentration factors

B.1. Solution procedure 1

First the partial stress influence functions $\mathbf{W}_\rho(x)$ and $\mathbf{w}_\rho(x)$ are evaluated as a superposition of the following loading cases:

1. Axial normal stress
2. Transverse hydrostatic stress
3. Transverse shear stress
4. Transverse tension stress
5. Longitudinal shear stress.

We now proceed to derive stress fields as a solution of three independent auxiliary problems. In what follows, we shall use indices f, g, m referring to the fibre, coating and matrix, respectively. Also, cylindrical coordinate system r, θ, z, figure 16, is adopted in the analysis.

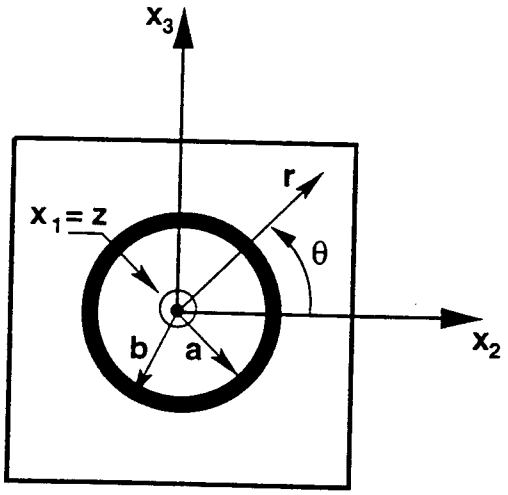


Figure 16. Geometry of coated fibre.

B.1.1. Auxiliary problems. (i) Loading cases 1, 2: axisymmetric stress. The remotely applied stress can be decomposed into uniform normal stress $\sigma_1 = p_0$ in the fibre direction and into an isotropic stress $\sigma_2 = \sigma_3 = \sigma_0$ in the transverse plane, figure 17. The axisymmetric displacement field has the form

$$\begin{aligned} u_r^f &= C_1 r \\ u_r^g &= C_2 r + C_3/r \\ u_r^m &= C_4 r + C_5/r \end{aligned} \tag{B1}$$

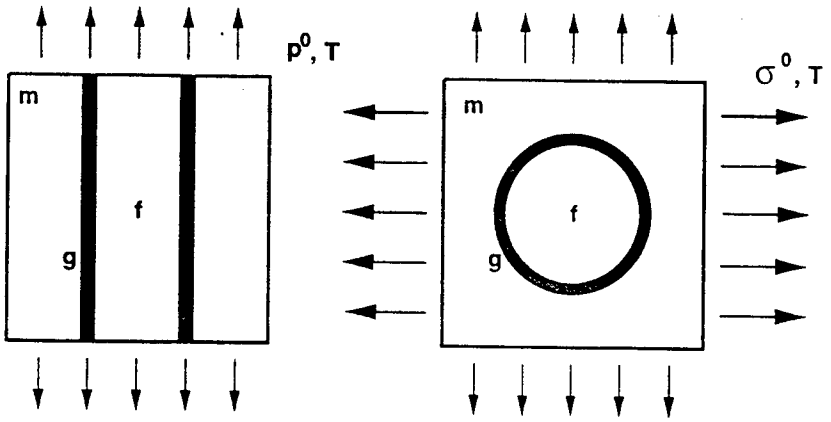


Figure 17. Axisymmetric loading case.

$$u_z^{\mathrm{f}} = u_z^{\mathrm{g}} = u_z^{\mathrm{m}} = \epsilon_z^0 z.$$

The stress field can be then found through the constitutive law as

$$\begin{aligned}
\sigma_z^{\mathrm{f}} &= 2l_{\mathrm{f}}C_1 + n_{\mathrm{f}}\epsilon_z^0 - (n_{\mathrm{f}} + 2l_{\mathrm{f}})\alpha_{\mathrm{f}}^L \Delta T \\
\sigma_r^{\mathrm{f}} &= \sigma_T^{\mathrm{f}} = 2k_{\mathrm{f}}C_1 + l_{\mathrm{f}}\epsilon_z^0 - (l_{\mathrm{f}} + 2k_{\mathrm{f}})\alpha_{\mathrm{f}}^T \Delta T \\
\sigma_z^{\mathrm{g}} &= 2l_{\mathrm{g}}C_2 + n_{\mathrm{g}}\epsilon_z^0 - (n_{\mathrm{g}} + 2l_{\mathrm{g}})\alpha_{\mathrm{g}}^L \Delta T \\
\sigma_r^{\mathrm{g}} &= 2k_{\mathrm{g}}C_2 - 2m_{\mathrm{g}}C_3/r^2 + l_{\mathrm{g}}\epsilon_z^0 - (l_{\mathrm{g}} + 2k_{\mathrm{g}})\alpha_{\mathrm{g}}^T \Delta T \\
\sigma_\theta^{\mathrm{g}} &= 2k_{\mathrm{g}}C_2 + 2m_{\mathrm{g}}C_3/r^2 + l_{\mathrm{g}}\epsilon_z^0 - (l_{\mathrm{g}} + 2k_{\mathrm{g}})\alpha_{\mathrm{g}}^T \Delta T \\
\sigma_z^{\mathrm{m}} &= 2l_{\mathrm{m}}C_4 + n_{\mathrm{m}}\epsilon_z^0 - (n_{\mathrm{m}} + 2l_{\mathrm{m}})\alpha_{\mathrm{m}}^L \Delta T \\
\sigma_r^{\mathrm{m}} &= 2k_{\mathrm{m}}C_4 - 2m_{\mathrm{m}}C_5/r^2 + l_{\mathrm{m}}\epsilon_z^0 - (l_{\mathrm{m}} + 2k_{\mathrm{m}})\alpha_{\mathrm{m}}^T \Delta T \\
\sigma_\theta^{\mathrm{m}} &= 2k_{\mathrm{m}}C_4 + 2m_{\mathrm{m}}C_5/r^2 + l_{\mathrm{m}}\epsilon_z^0 - (l_{\mathrm{m}} + 2k_{\mathrm{m}})\alpha_{\mathrm{m}}^T \Delta T
\end{aligned} \tag{B2}$$

where k_{f}, k_{g}, k_{m}, l_{f}, l_{g}, l_{m}, n_{f}, n_{g}, and n_{m} are Hill's elastic moduli of the phases. The corresponding boundary conditions used to determine unknown integration constants $C_1, \ldots, C_5$ are

$$\begin{aligned}
u_r^{\mathrm{f}} &= u_r^{\mathrm{g}} \qquad \sigma_r^{\mathrm{f}} = \sigma_r^{\mathrm{g}} \qquad \text{at } r = a \\
u_r^{\mathrm{g}} &= u_r^{\mathrm{m}} \qquad \sigma_r^{\mathrm{g}} = \sigma_r^{\mathrm{m}} \qquad \text{at } r = b \\
\sigma_r^{\mathrm{m}} &= \sigma_0 \qquad \text{at } r \longrightarrow \infty.
\end{aligned} \tag{B3}$$

The last condition is obtained as

$$\sigma_z^{\mathrm{m}}(\pm l) = p_0. \tag{B4}$$

(ii) Loading case 3: transverse shear. The remotely applied stress is now defined as, figure 18,

$$\sigma_2 = +\sigma_0 \qquad \sigma_2 = -\sigma_0 \qquad p_0 = 0.$$

Since the pure shear is usually applied in the Cartesian coordinate system according to figure 18, we shall substitute for the rotational angle θ by $\phi = \theta - 45°$ to account for the coordinate transformation. Following Christensen and Lo [6], the displacement field is

found in the form

$$
\begin{aligned}
u_r^{\mathrm{f}} &= \frac{b\sigma_0}{4m_{\mathrm{f}}}\left[C_6(\eta_{\mathrm{f}}-3)\frac{r^3}{b^3}+C_7\frac{r}{b}\right]\cos 2\bar{\phi}\\
u_\theta^{\mathrm{f}} &= \frac{b\sigma_0}{4m_{\mathrm{f}}}\left[C_6(\eta_{\mathrm{f}}+3)\frac{r^3}{b^3}-C_7\frac{r}{b}\right]\sin 2\bar{\phi}\\
u_r^{\mathrm{g}} &= \frac{b\sigma_0}{4m_{\mathrm{g}}}\left[C_8(\eta_{\mathrm{g}}-3)\frac{r^3}{b^3}+C_9\frac{r}{b}+C_{10}(\eta_{\mathrm{g}}+1)\frac{b}{r}+C_{11}\frac{b^3}{r^3}\right]\cos 2\bar{\phi} \qquad \text{(B5)}\\
u_\theta^{\mathrm{g}} &= \frac{b\sigma_0}{4m_{\mathrm{g}}}\left[C_8(\eta_{\mathrm{g}}+3)\frac{r^3}{b^3}-C_9\frac{r}{b}-C_{10}(\eta_{\mathrm{g}}-1)\frac{b}{r}+C_{11}\frac{b^3}{r^3}\right]\sin 2\bar{\phi}\\
u_r^{\mathrm{m}} &= \frac{b\sigma_0}{4m_{\mathrm{m}}}\left[\frac{2r}{b}+C_{12}(\eta_{\mathrm{m}}+1)\frac{b}{r}+C_{13}\frac{b^3}{r^3}\right]\cos 2\bar{\phi}\\
u_\theta^{\mathrm{m}} &= \frac{b\sigma_0}{4m_{\mathrm{m}}}\left[-\frac{2r}{b}-C_{12}(\eta_{\mathrm{m}}-1)\frac{b}{r}+C_{13}\frac{b^3}{r^3}\right]\sin 2\bar{\phi}
\end{aligned}
$$

where

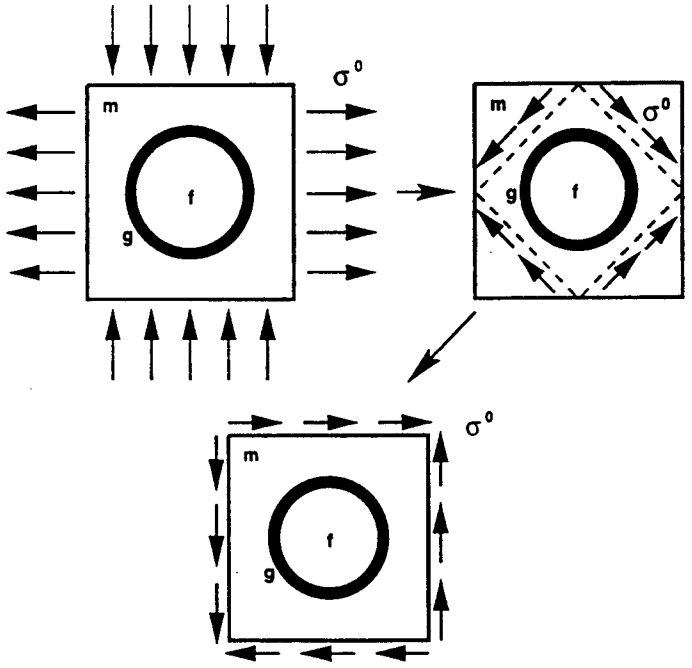


Figure 18. Transverse shear loading case.

$$\eta_i = (k_i + 2m_i)/k_i \qquad i = \mathrm{f}, \mathrm{g}, \mathrm{m} \qquad \text{(B6)}$$

and the stress field is given by

$$\sigma_z^{\mathrm{f}} = \frac{3\sigma_0}{2m_{\mathrm{f}}}C_6 l_{\mathrm{f}}(\eta_{\mathrm{f}}-1)\frac{r^2}{b^2}\cos 2\bar{\phi}$$

$$\sigma_r^{\mathrm{f}} = \frac{\sigma_0}{2m_{\mathrm{f}}}\left\{C_6[3k_{\mathrm{f}}(\eta_{\mathrm{f}}-1)-6m_{\mathrm{f}}]\frac{r^2}{b^2}+C_7 m_{\mathrm{f}}\right\}\cos 2\bar{\phi}$$

$$\sigma_\theta^{\mathrm{f}} = \frac{\sigma_0}{2m_{\mathrm{f}}}\left\{C_6[3k_{\mathrm{f}}(\eta_{\mathrm{f}}-1)+6m_{\mathrm{f}}]\frac{r^2}{b^2} - C_7 m_{\mathrm{f}}\right\}\sin 2\bar{\phi}$$

$$\sigma_{r\theta}^{\mathrm{f}} = \sigma_0\left[3C_6\frac{r^2}{b^2} - \frac{C_7}{2}\right]\sin 2\bar{\phi}$$

$$\sigma_z^{\mathrm{g}} = \frac{\sigma_0}{2m_{\mathrm{g}}}\left\{3C_8 l_{\mathrm{g}}(\eta_{\mathrm{g}}-1)\frac{r^2}{b^2} - C_{10}l_{\mathrm{g}}(\eta_{\mathrm{g}}-1)\frac{b^2}{r^2}\right\}\cos 2\bar{\phi}$$

$$\sigma_r^{\mathrm{g}} = \frac{\sigma_0}{2m_{\mathrm{g}}}\left\{C_8\left[3k_{\mathrm{g}}(\eta_{\mathrm{g}}-1)-6m_{\mathrm{g}}\right]\frac{r^2}{b^2} + C_9 m_{\mathrm{g}}\right.$$
$$\left. -C_{10}[k_{\mathrm{g}}(\eta_{\mathrm{g}}-1)+2m_{\mathrm{g}}]\frac{b^2}{r^2} - 3C_{11}m_{\mathrm{g}}\frac{b^4}{r^4}\right\}\cos 2\bar{\phi}$$

$$\sigma_\theta^{\mathrm{g}} = \frac{\sigma_0}{2m_{\mathrm{g}}}\left\{C_8\left[3k_{\mathrm{g}}(\eta_{\mathrm{g}}-1)+6m_{\mathrm{g}}\right]\frac{r^2}{b^2} - C_9 m_{\mathrm{g}}\right.$$
$$\left. -C_{10}[k_{\mathrm{g}}(\eta_{\mathrm{g}}-1)-2m_{\mathrm{g}}]\frac{b^2}{r^2} + 3C_{11}m_{\mathrm{g}}\frac{b^4}{r^4}\right\}\cos 2\bar{\phi} \qquad \text{(B7)}$$

$$\sigma_{r\theta}^{\mathrm{g}} = \sigma_0\left[3C_8\frac{r^2}{b^2} - \frac{C_9}{2} - C_{10}\frac{b^2}{r^2} - \frac{3}{2}C_{11}\frac{b^4}{r^4}\right]\sin 2\bar{\phi}$$

$$\sigma_z^{\mathrm{m}} = \frac{\sigma_0}{2m_{\mathrm{m}}}C_{12}l_{\mathrm{m}}(1-\eta_{\mathrm{m}})\frac{b^2}{r^2}\cos 2\bar{\phi}$$

$$\sigma_r^{\mathrm{m}} = \frac{\sigma_0}{2m_{\mathrm{m}}}\left\{2m_{\mathrm{m}} - C_{12}[k_{\mathrm{m}}(\eta_{\mathrm{m}}-1)+2m_{\mathrm{m}}]\frac{b^2}{r^2} - 3C_{13}m_{\mathrm{m}}\frac{b^4}{r^4}\right\}\cos 2\bar{\phi}$$

$$\sigma_\theta^{\mathrm{m}} = \frac{\sigma_0}{-2m_{\mathrm{m}}}\left\{2m_{\mathrm{m}} - C_{12}[k_{\mathrm{m}}(\eta_{\mathrm{m}}-1)-2m_{\mathrm{m}}]\frac{b^2}{r^2} + 3C_{13}m_{\mathrm{m}}\frac{b^4}{r^4}\right\}\cos 2\bar{\phi}$$

$$\sigma_{r\theta}^{\mathrm{f}} = -\sigma_0\left[1 + C_{12}\frac{b^2}{r^2} + \frac{3}{2}C_{13}\frac{b^4}{r^4}\right]\sin 2\bar{\phi}.$$

Unknown integration constants $C_6, \ldots, C_{13}$ follow from the interface continuity conditions

$$\begin{aligned} &u_r^{\mathrm{f}} = u_r^{\mathrm{g}} \qquad \sigma_{r\theta}^{\mathrm{f}} = \sigma_{r\theta}^{\mathrm{g}} \qquad \sigma_r^{\mathrm{f}} = \sigma_z^{\mathrm{g}} \qquad \text{at } r = a \\ &u_r^{\mathrm{g}} = u_r^{\mathrm{m}} \qquad \sigma_{r\theta}^{\mathrm{g}} = \sigma_{r\theta}^{\mathrm{m}} \qquad \sigma_r^{\mathrm{g}} = \sigma_r^{\mathrm{m}} \qquad \text{at } r = b \\ &C_{\mathrm{f}}\sigma_z^{\mathrm{f}} + C_{\mathrm{g}}\sigma_z^{\mathrm{g}} + C_{\mathrm{m}}\sigma_z^{\mathrm{m}} = 0. \end{aligned} \qquad \text{(B8)}$$

(iii) Loading case 4: transverse tension stress. The solution of this problem is found as a superposition of transverse hydrostatic stress and the transverse shear stress as shown in figure 19. However, in (B7) the angle $\bar{\phi}$ is now replaced by θ.

(iv) Loading case 5: longitudinal shear. In this problem we have to distinguish two different cases. Particularly, in the first case the remotely applied stress is $\sigma_{yz} = \tau_0$, whereas in the second case the remotely applied stress is $\sigma_{xz} = \tau_0$ as shown in figure 20. We shall first consider the case when $\sigma_{yz} = \tau_0$. The displacement field has the form

$$\begin{aligned} u_z^{\mathrm{f}} &= C_{14} r \sin\theta \\ u_z^{\mathrm{g}} &= (C_{15} r + C_{16}/r)\sin\theta \\ u_z^{\mathrm{m}} &= (C_{17} r + C_{18}/r)\sin\theta \\ u_r^{\mathrm{r}} &= u_\theta^{r} = 0 \qquad \mathrm{r} = \mathrm{f, g, m.} \end{aligned} \qquad \text{(B9)}$$

The stress field can be then written as

$$\sigma_{rz}^{\mathrm{f}} = C_{14} p_{\mathrm{f}} \sin\theta$$

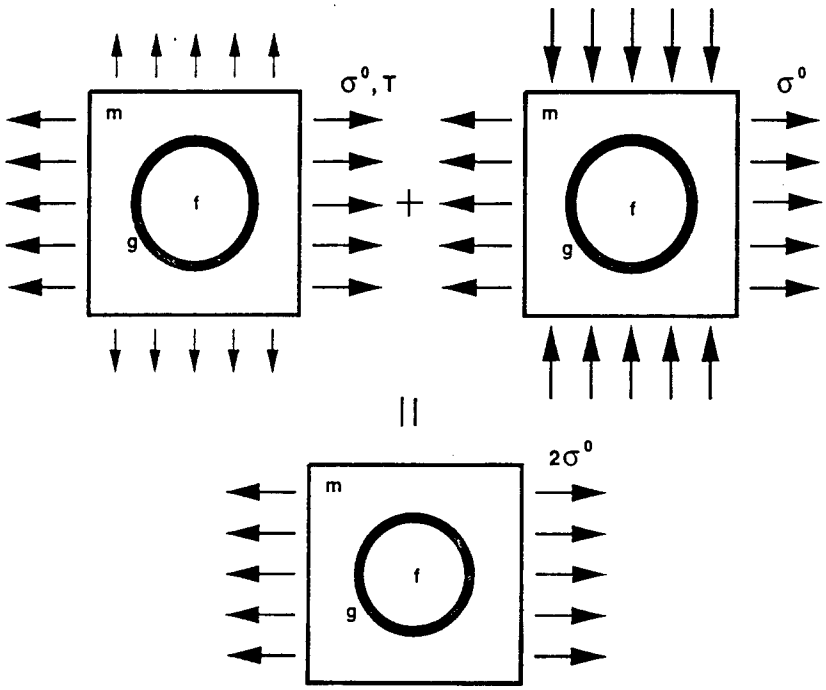


Figure 19. Transverse tension loading case.

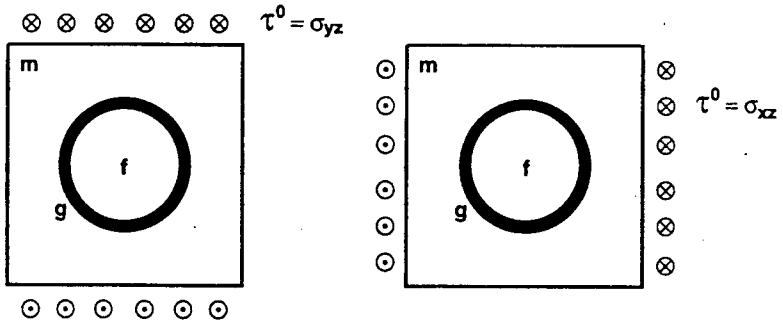


Figure 20. Longitudinal shear loading case.

$$\begin{aligned}
\sigma_{\theta z}^{f} &= C_{14} p_f \cos\theta \\
\sigma_{rz}^{g} &= p_g\,(C_{15} - C_{16}/r^2)\sin\theta \\
\sigma_{\theta z}^{g} &= p_g\,(C_{15} + C_{16}/r^2)\cos\theta \\
\sigma_{rz}^{m} &= p_m\,(C_{17} - C_{18}/r^2)\sin\theta \\
\sigma_{\theta z}^{m} &= p_m\,(C_{17} + C_{18}/r^2)\cos\theta
\end{aligned} \tag{B10}$$

and the corresponding interface continuity conditions together with traction boundary conditions are

$$\begin{aligned}
u_z^f = u_z^g \qquad \sigma_{rz}^f = \sigma_{rz}^g \qquad &\text{at } r = a \\
u_z^g = u_z^m \qquad \sigma_{rz}^g = \sigma_{rz}^g \qquad &\text{at } r = b
\end{aligned} \tag{B11}$$

$$\sigma_{yz}^{m} = \tau_0 \qquad \text{at } r \longrightarrow \infty.$$

For the second case, $\sigma_{xz} = \tau_0$, the displacement field is given by

$$\begin{aligned} u_z^f &= C_{14} r \cos\theta \\ u_z^g &= (C_{15} r + C_{16}/r)\cos\theta \\ u_z^m &= (C_{17} r + C_{18}/r)\cos\theta \\ u_r^r &= u_\theta^r = 0 \qquad r = f, g, m \end{aligned} \tag{B12}$$

and the stress field has the form

$$\begin{aligned} \sigma_{rz}^f &= C_{14} p_f \cos\theta \\ \sigma_{\theta z}^f &= -C_{14} p_f \sin\theta \\ \sigma_{rz}^g &= p_g (C_{15} - C_{16}/r^2)\cos\theta \\ \sigma_{\theta z}^g &= -p_g (C_{15} + C_{16}/r^2)\sin\theta \\ \sigma_{rz}^m &= p_m (C_{17} - C_{18}/r^2)\cos\theta \\ \sigma_{\theta z}^m &= -p_m (C_{17} + C_{18}/r^2)\sin\theta \end{aligned} \tag{B13}$$

subjected to the following boundary conditions:

$$\begin{aligned} &u_z^f = u_z^g \qquad \sigma_{rz}^g = \sigma_{rz}^m \qquad \text{at } r = a \\ &u_z^g = u_z^m \qquad \sigma_{rz}^g = \sigma_{rz}^m \qquad \text{at } r = b \\ &\sigma_{xz}^m = \tau_0 \qquad \text{at } r \longrightarrow \infty. \end{aligned} \tag{B14}$$

The required local stress fields serve to derive the partial stress influence function $\mathbf{W}_\rho(x)$ and $\mathbf{w}_\rho(x)$ by employing the superposition procedure outlined in Dvorak *et al* [12].

B.2. Solution procedure 2

The second step involves evaluation of the partial stress concentration factors $\mathbf{W}_\rho$ and $\mathbf{w}_\rho$. Since $\mathbf{W}_m = \mathbf{I}$ and $\mathbf{w}_m = \mathbf{0}$ the evaluation need to be carried out only for fibre and coating phases, respectively. This can be done by evaluating a fibre and coating volume averages of the components of $\mathbf{W}_\rho(x)$ and $\mathbf{w}_\rho(x)$, where $\rho = f, g$. First the local stresses found above are transformed into the Cartesian coordinate system to conform with the original formulation of $\mathbf{W}_\rho$. The phase volume averages of the local fields are then found as

$$\begin{aligned} \overline{\sigma}_f &= \frac{1}{\pi a^2 z}\int_0^{2\pi}\int_0^a\int_0^z \sigma_f(r,\theta) r \, dz \, dr \, d\theta \\ \overline{\sigma}_g &= \frac{1}{\pi(b^2 - a^2)z}\int_0^{2\pi}\int_a^b\int_0^z \sigma_g(r,\theta) r \, dz \, dr \, d\theta. \end{aligned} \tag{B15}$$

Results for particular loading cases follow.

(i) Loading cases 1,2: axisymmetric stress. Equations (B2) and (B15) provide

$$\begin{aligned} \overline{\sigma}_z^f &= \sigma_z^f \\ \overline{\sigma}_x^f &= \overline{\sigma}_y^f = \sigma_r^f = \sigma_\theta^f \\ \overline{\sigma}_z^g &= \sigma_z^g \\ \overline{\sigma}_x^g &= \overline{\sigma}_y^g = 2k_g C_2 + l_g \epsilon_z^0 - (l_g + 2k_g)\alpha_g^T \Delta T. \end{aligned} \tag{B16}$$

(ii) Loading case 3: transverse shear. Using equations (B7) and (B15) we obtain

$$\begin{aligned}
\overline{\sigma}_x^{\mathrm{f}} &= \sigma_0 \left(\frac{1}{2} C_6 - \frac{3}{2} C_7 \frac{a^2}{b^2} \right) \\
\overline{\sigma}_y^{\mathrm{f}} &= -\overline{\sigma}_x^{\mathrm{f}} \\
\overline{\sigma}_x^{\mathrm{g}} &= \sigma_0 \left(-\frac{3}{2} \frac{a^2 + b^2}{b^2} C_8 + \frac{C_9}{2} \right) \\
\overline{\sigma}_y^{\mathrm{g}} &= -\overline{\sigma}_x^{\mathrm{g}}.
\end{aligned} \tag{B17}$$

(iii) Loading case 5: Longitudinal shear. Providing that $\sigma_{yz} = \tau_0$, equations (B10) and (B15) yield

$$\begin{aligned}
\overline{\sigma}_{xz}^{\mathrm{f}} &= \overline{\sigma}_{xz}^{\mathrm{g}} = 0 \\
\overline{\sigma}_{yz}^{\mathrm{f}} &= p_{\mathrm{f}} C_{14} \\
\overline{\sigma}_{yz}^{\mathrm{g}} &= p_{\mathrm{g}} C_{15}.
\end{aligned} \tag{B18}$$

In the second case, when $\sigma_{xz} = \tau_0$, the average stress components are given by

$$\begin{aligned}
\overline{\sigma}_{yz}^{\mathrm{f}} &= \overline{\sigma}_{yz}^{\mathrm{g}} = 0 \\
\overline{\sigma}_{xz}^{\mathrm{f}} &= p_{\mathrm{f}} C_{14} \\
\overline{\sigma}_{xz}^{\mathrm{g}} &= p_{\mathrm{g}} C_{15}.
\end{aligned} \tag{B19}$$

Note that up to now the remotely applied stresses σ_0, p_0, τ_0 and uniform temperature change ΔT were equal to unity. The partial stress influence functions $\mathbf{W}_p$ and $\mathbf{w}_p$ then follow from the superposition procedure already mentioned in the previous section. Above results together with (5) can now be used to estimate the average stresses in the matrix. Desired stress concentration factors $\mathbf{B}_p(x)$ and $\mathbf{b}_p(x)$ can be finally derived through the solution procedure 1, where the remotely applied stresses are at this time set to be equal to the average stresses in the matrix.

It can also be shown that if we furnish a coating with the matrix material properties, we arrive at the same result as for two-phase medium.

References

[1] Bahei-El-Din Y A, Shah R S and Dvorak G J 1991 Numerical analysis of the rate-dependant behavior of high temperature fibrous composites *Mechanics of Composites at Elevated and Cryogenic Temperatures (ASME AMD 188)* ed S N Singhal (New York, NY: American Society of Mechanical Engineers)

[2] Bahei-El-Din Y A, Dvorak G J and Wu J F 1995 Mechanics of hot isostatic pressing in intermetallic matrix composites *J. Mater. Sci.* **30** 1–23

[3] Bahei-El-Din Y A and Dvorak G J 1996 Isothermal fatigue of Sigma/Timetal 21S laminates, II. Modelling and numerical analysis *Mech. Comp. Mater. Struct.* to appear

[4] Benveniste Y 1987 A new approach to the application of Mori–Tanaka's theory in composite materials *Mech. Mater.* **6** 147–57

[5] Benveniste Y, Dvorak G J and Chen T 1989 Stress fields in composites with coated inclusions *Mech. Mater.* **7** 305–17

[6] Christensen R M and Lo K H 1979 Solution for effective shear properties in three phase sphere and cylinder models *J. Mech. Phys. Solids* **27** 315–30

[7] Clyne T W and Withers P J 1993 *An Introduction to Metal Matrix Composites* (Cambridge: Cambridge University Press)

[8] Dvorak G J 1990 On uniform fields in heterogeneous media *Proc. R. Soc. Lond.* A **431** 89–110

[9] Dvorak G J 1991 Plasticity theories for fibrous composite materials *Metal Matrix Composites, Mechanisms and Properties* vol 2, ed R K Everett and R J Arsenault (Boston: Academic Press) pp 1–77

[10] Dvorak G J 1992 Transformation field analysis of inelastic composite materials *Proc. Roy. Soc. London* A **437** 311–27

[11] Dvorak G J and Benveniste Y 1992 On transformation strains and uniform fields in multiphase elastic media *Proc. Roy. Soc. London.* A **437** 291–310

[12] Dvorak G J, Chen T and Teply J 1992 Thermomechanical stress fields in high-temperature fibrous composites. I: Unidirectional laminates *Comp. Sci. Technol.* **43** 347–58

[13] Dvorak G J, Chen T and Teply J 1992 Thermomechanical stress fields in high-temperature fibrous composites. II: Laminated plates *Comp. Sci. Technol.* **43** 359–68

[14] Dvorak G J, Bahei-El-Din Y A and Wafa A M 1994 Implementation of the transformation field analysis for inelastic composite materials *Model. Simul. Mater. Sci. Eng.* **2** 571–86

[15] Dvorak G J and Sejnoha M 1995 Initial failure maps for fibrous CMC laminates *J. Am. Ceram. Soc.* **78** 205–10

[16] Dvorak G J, Sejnoha M and Srinivas M 1996 Pseudoplasticity of fibrous composite materials *IUTAM Symp. Micromechanics of Plasticity and Damage of Multiphase Materials* ed A Pineau and A Zaoui (Dordrecht: Kluwer) pp 43–50

[17] Hill R 1964 Theory of mechanical properties of fibre-strengthened materials: I. Elastic behaviour *J. Mech. Phys. Solids* **12** 199–212

[18] Hill R A 1965 A self-consistent mechanics of composite materials *J. Mech. Phys. Solids* **13** 213–22

[19] Hill R 1972 An invariant treatment of interfacial discontinuities in elastic composites *Continuum Mechanics and Related Problems of Analysis (N I Muskhelishvili 80 Anniversary Volume)* ed L I Sedov (Moscow: Acad. Sci. SSSR) pp 597

[20] Laws N 1973 On the thermostatics of composite materials *J. Mech. Phys. Solids* **21** 9–17

[21] Mori T and Tanaka K 1973 Average stress in matrix and average elastic energy of materials with misfitting inclusions *Acta Metal* **21** 571

[22] Shakelford J F and Alexander W (eds) 1992 *CRC Materials Science and Engineering Handbook* (Boca Raton, FL: CRC) pp 360–62, 531–40, 560–92

[23] Tanaka K and Mori T 1972 Note on volume integrals of the elastic field around an ellipsoidal inclusion *J. Elasticity* **2** 199

[24] Wafa A M 1994 Application of the transformation field analysis to inelastic composite materials and structures *PhD Thesis* Rensselaer Polytechnic Institute, Troy, NY

[25] Walpole L J 1969 On the overall elastic moduli of composite materials *J. Mech. Phys. Solids* **17** 235

CONVERGENCE OF THE MULTI-GRID METHOD FOR A PERIODIC HETEROGENEOUS MEDIUM. PART 1: 1-D CASE

Jacob Fish and Vladimir Belsky
Department of Civil Engineering and Scientific Computation
Research Center,
Rensselaer Polytechnic Institute, Troy, NY 12180, USA

A multi-grid method for a periodic heterogeneous medium in 1-D is presented. Based on the homogenization theory special intergrid connection operators have been developed to imitate a low frequency response of the differential equations with oscillatory coefficients. The proposed multi-grid method have been proved to have a fast rate of convergence governed by the ratio $q/(4-q)$, where $0 < q \leq 1$ depends on the microstructure. This estimate reveals that the rate of convergence increases as $q \to 0$, which corresponds to the increasing material heterogeneity. Numerical results have been found to be in good agreement with the theoretical estimate.

1. Introduction

The sequence of three papers presents a multi-grid method for a periodic heterogeneous medium. In the first paper we limit ourselves to 1-D problems. We believe that it is essential to demonstrate the fundamental ideas of the proposed methodology, including the mathematical formulation and convergence analysis, in one-dimensional context, first, because the rate of convergence can be only estimated in the closed form for 1-D problems and secondly, because these studies will serve as a vehicle of subsequent derivations in multidimensions. In the two upcoming papers we will extend this formulation to multidimensions (part 2) and will incorporate adaptive features (part 3).

In the first part we consider the boundary value problem for differential equation

$$-\frac{d}{dx}\left(K\left(\frac{x}{\varepsilon}\right)\frac{d}{dx}u\right) = f(x), x \in (0, l), u(0) = 0, u(l) = 0 \tag{1}$$

where $K(y)$ - is 1-periodic function of $y \in (0, 1), y = x/\varepsilon$, such that

$$K(y) \geq K_0 \geq 0$$

Since ε is assumed to be small, we have the differential equation with rapidly oscillatory coefficients.

The traditional approach for solving this problem uses a double scale asymptotic expansion

$$u(x, y) = u^0(x, y) + \varepsilon u^1(x, y) + \varepsilon^2 u^2(x, y) + \ldots \quad (2)$$

where x and y are macroscopic and microscopic co-ordinates, respectively. Under the assumption that the terms $u^k(x, y)$ are 1-periodic functions in the y variable, it is possible to obtain two separate boundary value problems. The former describes the microscopic behavior of the solution; and the latter reflects the macroscopic behavior. The fundamentals of this theory can be found, among others, in [1,2,3].

It is well known [1] that in the limit of $\varepsilon \to 0$ the solution of the source problem (1) approaches weakly in the energy norm the solution of the boundary value problem with homogenized coefficients. Unfortunately, in many practical situations when the value of ε is finite and the solution of the homogenized problem has high gradients, the homogenization theory may err badly in comparison with the exact solution of the source problem (1). The most significant errors are encountered in the portions of the problem domain where the solution has high gradients [4]. Ironically, these are precisely the regions of major interest from the practical standpoint.

One of the alternatives to homogenization is a multiscale computational approach [4]. By this technique a portion of the problem domain where homogenization procedure has been found to be inadequate by means of microscale reduction error indicators [5], is modeled entirely on the microscale, i.e., a finite element size is of the same order of magnitude as that of microconstituents. In the remaining portion of the problem domain, the details of microstructure are ignored and the finite elements are assumed to have effective material properties[4]. The system of linear equations arising from such multiscale computational technique can be solved exactly or approximately by either relaxing traction continuity or by displacement compatibility conditions between the two regions. The latter case is a typical global-local approach [6] which does not guarantee a reliable force transfer to the local region of interest. On the other hand, a solution of the coupled system of equations at several different scales may not be computationally feasible.

In this paper we propose a novel approach which takes advantage of the special nature of differential equations with oscillatory coefficients in order to develop fast iterative solvers for system of linear equations arising from such differential operators. This is accomplished using a multigrid solver with special intergrid connection operator.

The classical multigrid approach with standard linear interpolation operators is not

well suited to approximate the low frequency response, mainly because the low frequency eigenvectors are not smooth in the case of differential equations with oscillatory coefficients. On the other hand, the solution based on the homogenization theory is in good agreement with the lower frequency response of the exact solution of the source problem (1). The basic idea of the proposed methodology is to construct such intergrid connection operator so that the problem on the auxiliary grid would be identical to that with constant effective material coefficients.

It will be shown that the rate of convergence of the proposed two-grid method is mainly governed by a factor $q/(4-q)$, where q ranges from one to zero depending on material heterogeneity. For example, $q = 1$ corresponds to a homogeneous material, while in the case of two phase material with constant coefficients the value of q reduces as the heterogeneity increases, and thus the rate of convergence improves.

The contents of the paper are as follows. Section 2 presents the multi-grid technique based on the homogenization theory. Section 3 describes the solution of the eigenvalue problem for periodic heterogeneous medium in 1-D case. These eigenvalues and eigenvectors are found in close form in order to estimate the rate of convergence of the two-grid process. In section 4 the convergence estimates are presented. In section 5 we conduct several numerical examples to study and validate the present formulation.

2. The fundamentals of multigrid method for a periodic heterogeneous medium

Consider a system of linear equations resulting from the piecewise linear finite element discretization of the source boundary value problem (1)

$$Au = f \qquad u \in R^n \qquad f \in R^n \tag{3}$$

Here A is the $n \times n$ symmetric and positive definite tridiagonal matrix; u and f are n-vector functions corresponding to the initial fine grid where each phase is discretized by at least one finite element. The boundary conditions have been incorporated into this system of equations.

Following the traditional multi-grid technique we introduce the auxiliary coarse grid. We denote the corresponding auxiliary grid functions with subscript 0. For example, u_0 denotes the nodal values of the solution in the auxiliary grid, where $u_0 \in R^m$, $m < n$. We also denote the prolongation operator from the coarse grid to the fine grid by Q:

$$Q \bullet R^m \rightarrow R^n \tag{4}$$

The restriction operator Q^* from the fine-to-coarse grid is conjugated with the prolon-

gation operator, i.e.:

$$Q^* \bullet R^n \to R^m \tag{5}$$

We use superscripts to indicate the iteration count. Let r^i be the residual vector in the i-th iteration defined by

$$r^i = f - Au^i \tag{6}$$

where u^i - is the current approximation of the solution in the i-th iteration.

The problem of the coarse grid correction consists in the minimization of the energy functional on the subspace R^m, i.e.:

$$1/2\,(A\,(u^i + Qu_0^i)\,,\, u^i + Qu_0^i) - (f,\, u^i + Qu_0^i) \to min \qquad u_0^i \in R^m \tag{7}$$

where (.,.) denotes the bilinear form defined by

$$(u, v) = \sum_{j=1}^{n} u_j v_j \qquad u, v \in R^n$$

A direct solution of the equation (7) yields a classical two-grid procedure. Alternatively, one may introduce an additional auxiliary grid for u_0 and so forth, leading to a natural multi-grid sequence. To fix ideas we will consider a two-grid process resulting from the direct minimization of (7)

$$A_0 u_0^i = Q^* (f - Au^i) \tag{8}$$

where $A_0 = Q^* A Q$ -is the restriction of the matrix A. The resulting classical two-grid algorithm can be written in the following manner:

a) coarse grid correction:

$$\begin{aligned} r^i &= f - Au^i \\ u_0^i &= A_0^{-1} Q^* r^i \\ \tilde{u}^i &= u^i + Qu_0^i \end{aligned} \tag{9}$$

where $\tilde{u}^i$ is a partial solution obtained after the coarse grid correction;

b) smoothing:

$$u^{i+1} = \tilde{u}^i + D\,(f - A\tilde{u}^i) \tag{10}$$

If the Jacobi method is employed for smoothing then

$$D = \omega\,(diag\,(A))^{-1} \tag{11}$$

where ω is a weighting factor. Note that in practice it is possible to carry out several smoothing iterations within a single coarse grid correction.

For each iteration we can associate the error vectors e^i, $\tilde{e}^i$ defined by

$$e^i = u - u^i \qquad \tilde{e}^i = u - \tilde{u}^i \tag{12}$$

where u is the exact solution of the source problem. Then the error resulting from the coarse grid correction (9) can be cast into the following form

$$\tilde{e}^i = (I - QA_0^{-1}Q^*A)\,e^i \tag{13}$$

where I is the identity $n \times n$ matrix. Combining equations (10),(12), the influence of smoothing on error reduction is given by:

$$e^{i+1} = (I - DA)\,\tilde{e}^i \tag{14}$$

and from the equations (13), (14) the error vector of the two-grid process with one post-smoothing iteration can be expressed as:

$$e^{i+1} = (I - DA)\,(I - QA_0^{-1}Q^*A)\,e^i \tag{15}$$

For subsequent derivations we will use the following notations:

$$\begin{aligned} G &= I - DA \\ T &= I - QA_0^{-1}Q^*A \end{aligned} \tag{16}$$

Then (15) can be rewritten in the following form

$$e^{i+1} = GTe^i \tag{17}$$

It is essential to note that T and $S = I - T$ are the A-ortogonal projectors [7], namely:

$$(ATv, Sv) = 0 \qquad \forall v \in R^n \tag{18}$$

$$\|v\|_A^2 = \|Tv\|_A^2 + \|Sv\|_A^2 \tag{19}$$

which yields that

$$\|T\|_A \leq 1 \tag{20}$$

Note that the projector T eliminates the effect of the prolongation operator, i.e.:

$$TQ = 0 \tag{21}$$

Now we will turn to the central question of how to construct a prolongation operator Q, for the case of periodic heterogeneous media, so that the auxiliary grid will not contain the details of the microstructure, but on the other hand, will accurately match the low frequency response of the source problem. Prior to answering this question, it is necessary to review some fundamental concepts of the mathematical homogenization theory.

Following the classical homogenization theory, an approximate solution of (1) can be obtained using a two-term asymptotic expansion given by

$$u(x,y) = u^{(0)}(x) + \varepsilon u^{(1)}(x,y) \tag{22}$$

where $u^{(0)}(x)$ is the solution of the homogenized boundary value problem with constant coefficients and

$$u^{(1)}(x,y) = H^{(1)}(y)\frac{d}{dx}u^{(0)}(x) \tag{23}$$

Here $H^{(1)}(y)$ is 1-periodic function in the y variable. Employing the classical perturbation technique [1,2,3], we obtain two uncoupled boundary value problems. The former is the problem in the function $H^{(1)}(y)$, which describes the microscopic behavior of the solution:

$$\begin{gathered} -\frac{d}{dy}\left(K(y)\frac{d}{dy}H^{(1)}(y)\right) = \frac{d}{dy}K(y) \\ 0 \leq y \leq 1 \\ H^{(1)}(0) = 0 \qquad H^{(1)}(1) = 0 \end{gathered} \tag{24}$$

The latter is the boundary value problem for the macroscopic solution

$$-\tilde{K}\frac{d^2}{dx^2}u^{(0)}(x) = f(x),\ u^{(0)}(0) = 0,\ u^{(0)}(l) = 0 \tag{25}$$

where $\tilde{K}$ - is the homogenized effective coefficient given by

$$\tilde{K} = \int_0^1 K(y)\,(\frac{d}{dy}H^{(1)} + 1)\,dy$$

For subsequent derivations we will employ the following well known relations [1-3]:

$$\tilde{K} = \int_0^1 K(y)\,(\frac{d}{dy}H^{(1)} + 1)\,dy = \int_0^1 K(y)\,(\frac{d}{dy}H^{(1)} + 1)^2\,dy$$
$$= \left(\int_0^1 (K(y))^{-1}dy\right)^{-1} \tag{26}$$

$$H^{(1)}(y) = \int_0^y (\frac{\tilde{K}}{K(\xi)} - 1)\,d\xi \tag{27}$$

The basic idea of the proposed multigrid formulation is to construct the prolongation and restriction operators on the basis of the equations (22) and (23). It will be shown that the resulting auxiliary problem would be very effective at eliminating low-frequency components of error and/or residual which are not smooth in the case of heterogeneous medium. Moreover, it will be shown that the matrix A_0 of the auxiliary system (8) corresponds to the finite element approximation of the homogenized boundary value problem with the effective coefficient (25).

Consider a one-dimensional model problem, shown in Fig. 1. The source problem is discretized with $l\,(l > 1)$ finite elements inside each unit cell. For each finite element the material properties are constant, $K = const$. The auxiliary grid nodes coincide with the unit cell boundaries. We denote the length of the unit cell by h and the total number of unit cells by $m - 1$. Then the prolongation operator Q can be expressed in the following manner:

$$[Qu_0]_k = [u_0]_i\,(1 - y_j) + [u_0]_{i+1}\,y_j + H_j^{(1)}\,([u_0]_{i+1} - [u_0]_i)$$
$$k = (i-1)\,l + j \qquad 1 \le i \le m-1 \qquad 1 \le j \le l \tag{28}$$

where $y_j = (x_{(i-1)\,l+j} - x_{(i-1)\,l+1})/h$ for any i; $0 \le y_j \le 1$ are the local co-ordinates

of the grid nodes inside the unit cell; $H_j^{(1)} = H^{(1)}(y_j)$ are calculated from (26), (27).

It is convenient to define the linear interpolation operator by $\tilde{Q}$, which serves as the traditional prolongation operator in the classical multi-grid approach for the second order equations. Then the proposed prolongation operator is given by

$$[Qu_0]_k = [\tilde{Q}u_0]_k + H_j^{(1)}([u_0]_{i+1} - [u_0]_i) \tag{29}$$

The course grid operator, A_0, can be constructed on the basis of (28). We assume that the same piecewise linear finite element shape functions are used for discretization of the initial boundary value problem (1) as well as for the unit cell problem (24). Denoting the shape functions on the fine grid by $N^j(x)$, $1 \le j \le n$, $n = (m-1)l+1$ and using (28) we obtain the following approximation of the solution after the prolongation

$$u(x) = \sum_{j=1}^{n} N^j(x)\,[Qu_0]_j \tag{30}$$

Note that the shape functions of the auxiliary grid, $N_0^i(x)$, can be expressed as a linear combination of $N^j(x)$

$$N_0^i(x) = \sum_{j=1}^{n} N^j(x)\,[\tilde{Q}e_0^i]_j \qquad 1 \le i \le m \tag{31}$$

where $e_0^i \in R^m$ is a unit vector in the auxiliary grid, satisfying the fundamental relation of $[e_0^i]_j = \delta_{ij}$, and δ_{ij} - is the Kronecker delta. Note that $N_0^i(x)$ are the piecewise linear finite element shape functions for the auxiliary grid with a single finite element in each unit cell. Derivative approximation on each element i in the auxiliary grid is given

$$[u'_0] = \left[\sum_{i=1}^{m} (N_0^i)'\,[u_0]_i\right]_k = \frac{([u_0]_{k+1} - [u_0]_k)}{h} \tag{32}$$

$$1 \le k \le m-1$$

Combining (29) - (32) we obtain the following expression for the approximate solution after prolongation

$$u(x) = \sum_{i=1}^{m} (N_0^i)\,[u_0]_i + \sum_{i=1}^{m-1}\sum_{j=1}^{l+1} N^{(i-1)l+j}(x)\, H_j^{(1)}\, h\left[\sum_{k=1}^{m} (N_0^k)'\,[u_0]_k\right]_i \tag{33}$$

Note that periodicity implies that

$$N^{(i-1)l+j}(x) = N^j(hy) = \tilde{N}^j(y)$$
$$1 \le j \le l \qquad y = \frac{x}{h} - (i-1) \qquad 0 \le y \le 1 \qquad \forall i,\ 1 \le i \le m-1 \tag{34}$$

Differentiation of (33) and accounting for periodicity (34), yields

$$u'(x) = \sum_{i=1}^{m} (N_0^i)'\,[u_0]_i \left(1 + \frac{d}{dy}H^{(1)}(y)\right) \tag{35}$$

where $\frac{d}{dy}H^{(1)}(y) = \sum_{j=1}^{l+1} \frac{d}{dy}\tilde{N}^j(y)\,(H_j)^{(1)}$ and $H_j^{(1)}$ is the discrete solution of the microscopic problem (24) at the FE nodes y_j, which is obtained on the basis of the finite element shape functions $\tilde{N}^j(y)$.

Finally, auxiliary grid discrete operator A_0 can be obtained by combining (30), (35) and (26), which yields

$$\begin{aligned}
[A_0]_{ij} &= \sum_{p=1}^{n}\sum_{q=1}^{n}\left(\int_0^l K\left(\frac{x}{\varepsilon}\right) N^p(x)\, N^q(x)\, dx\right)[Qe_0^i]_p\,[Qe_0^j]_q \\
&= \int_0^l \left(\int_0^1 K(y)\left(\frac{d}{dy}H^{(1)} + 1\right)^2 dy\right)(N_0^i(x))'\,(N_0^j(x))'\,dx \\
&= \int_0^l \tilde{K}\,(N_0^i(x))'\,(N_0^j(x))'\,dx \qquad 1 \le i \le m \quad 1 \le j \le m
\end{aligned} \tag{36}$$

It can be seen that the restriction of the source matrix A using the prolongation operator (28) corresponds to the finite element approximation of the boundary value problem (25) with the effective coefficient.

3. The eigenvalue problem for the periodic heterogeneous medium in 1-D case

This section deals with the eigenvalue analysis of the model boundary value problem with the periodic coefficient

$$-\frac{d}{dx}\left(K\left(\frac{x}{\varepsilon}\right)\frac{d}{dx}u\right) = \lambda u,\ x \in (0, l),\ u(0) = 0,\ u(l) = 0 \tag{37}$$

where $K(y)$ is chosen as follows:

$$K(y) = \begin{cases} K_1,\ 0 \le y \le (1-\alpha) \\ K_2,\ (1-\alpha) \le y \le 1 \end{cases} \tag{38}$$

and α represents the volume fraction, $0 \le \alpha \le 1$.

In the following we present a closed form solution of the discretized eigenvalue problem (37), (38), which is required for estimating the rate of convergence of the proposed two-grid method.

The eigenvalue problem defined by (37), (38) is discretized with two elements on each unit cell as shown in Fig. 2. Nodal values corresponding to the boundaries of the unit cells are denoted by u_i, $1 \le i \le m$, while the corresponding nodal values inside the unit cells are defined by $u_{i,i+1}$, $1 \le i \le m-1$. The number of the unit cells is $m-1$.

The effective material properties, $\tilde{K}$, for a model problem defined by (38) follow immediately from (26)

$$\tilde{K} = \frac{K_1 K_2}{K_2(1-\alpha) + K_1\alpha} \tag{39}$$

Proposition 1

Consider a heterogeneous medium formed by a special repetition of the unit cell (38). Each unit cell is discretized with two elements as shown in Fig. 2. Let $(\hat{\varphi}^k, \hat{\lambda}^k)$, $1 \le k \le \tilde{m}-1$, $\tilde{m} = m-1$, be the eigenvectors and the eigenvalues of the discretized eigenvalue problem with the homogenized effective coefficient (39), and let $\hat{\varphi}^k_{i,i+1}$, $1 \le i \le m-1$ be a result of prolongation of the vector $\hat{\varphi}^k$ to the interior node in the unit cell i in accordance with (28) and (27), i.e.:

$$\hat{\varphi}^k_{i,i+1} = \beta\hat{\varphi}^k_i + (1-\beta)\hat{\varphi}^k_{i+1} \tag{40}$$

where

$$\beta = \frac{d_1}{d_1 + d_2}, \; d_1 = K_1 \alpha, \; d_2 = K_2 (1 - \alpha) \tag{41}$$

Furthermore, let (φ^k, λ^k), $1 \le k \le \tilde{n} - 1$, $\tilde{n} = 2\tilde{m}$ be the eigenvectors and the eigenvalues of the discretized problem (37), (38).

Then the Proposition 1 claims that the eigenvectors and the eigenvalues of the one-dimensional problem in the heterogeneous medium (37), (38) are given

$$\lambda^k = \frac{b^k}{b^k + 1} \hat{\lambda}^k$$

$$\varphi_i^k = \hat{\varphi}_i^k, \; 1 \le i \le m \qquad \varphi_{i,i+1}^k = b^k \hat{\varphi}_{i,i+1}^k, \; 1 \le i \le m - 1 \tag{42}$$

$$\lambda^{\tilde{n}-k} = \frac{b^k}{b^k - 1} \hat{\lambda}^k$$

$$\varphi_i^{\tilde{n}-k} = -\hat{\varphi}_i^k, \; 1 \le i \le m \qquad \varphi_{i,i+1}^{\tilde{n}-k} = b^k \hat{\varphi}_{i,i+1}^k, \; 1 \le i \le m - 1$$

$$\lambda^{\tilde{m}} = \frac{d_1 + d_2}{\alpha (1 - \alpha) h}$$

$$\varphi_i^{\tilde{m}} = 0, \; 1 \le i \le m \qquad \varphi_{1,2}^{\tilde{m}} = 1 \qquad \varphi_{i,i+1}^{\tilde{m}} = -\frac{d_2}{d_1} \varphi_{i-1,i}^{\tilde{m}}, \; 2 \le i \le m - 1$$

where

$$b^k = \frac{1}{\left(1 - q \hat{\lambda}^k \frac{h}{4\tilde{K}}\right)^{1/2}} \qquad q = 4\beta (1 - \beta) \tag{43}$$

$$\hat{\lambda}^k = \frac{4\tilde{K}}{h} sin^2 (\frac{k\pi}{2\tilde{m}})$$

$$\hat{\varphi}_i^k = sin (\frac{(i-1)\, k\pi}{\tilde{m}}), \; 1 \le i \le m \tag{44}$$

$$1 \le k \le \tilde{m} - 1$$

Proof of Proposition 1

Consider a discretization of the eigenvalue problem (37), (38) on the basis of the linear finite elements:

$$\begin{cases} -\frac{K_1}{(1-\alpha)\, h} \varphi_i^k + \frac{K_1 \alpha + K_2 (1-\alpha)}{\alpha (1-\alpha)\, h} \varphi_{i,i+1}^k - \frac{K_2}{\alpha h} \varphi_{i+1}^k = \lambda^k \varphi_{i,i+1}^k \\ 1 \le i \le m-1 \\ -\frac{K_2}{\alpha h} \varphi_{i-1,i}^k + \frac{K_1 \alpha + K_2 (1-\alpha)}{\alpha (1-\alpha)\, h} \varphi_i^k - \frac{K_1}{(1-\alpha)\, h} \varphi_{i,i+1}^k = \lambda^k \varphi_i^k \\ 2 \le i \le m-1 \\ \varphi_1^k = 0 \qquad \varphi_m^k = 0 \\ 1 \le k \le \tilde{n} - 1 \end{cases} \tag{45}$$

Inserting (41) into (45) yields

$$\begin{cases} \varphi_{i,i+1}^k - (\beta \varphi_i^k + (1-\beta)\, \varphi_{i+1}^k) = \tilde{\lambda}^k \varphi_{i,i+1}^k & 1 \le i \le m-1 \\ \varphi_i^k - ((1-\beta)\, \varphi_{i-1,i}^k + \beta \varphi_{i,i+1}^k) = \tilde{\lambda}^k \varphi_i^k & 2 \le i \le m-1 \\ \varphi_1^k = 0 \qquad \varphi_m^k = 0 \qquad 1 \le k \le \tilde{n} - 1 \end{cases} \tag{46}$$

where

$$\tilde{\lambda}^k = \frac{\alpha (1-\alpha)\, h}{d_1 + d_2} \lambda^k$$

Taking the following expression from (42)

$$\varphi_i^k = \hat{\varphi}_i^k \qquad 1 \le i \le m$$
$$\varphi_{i,i+1}^k = b\hat{\varphi}_{i,i+1}^k \qquad 1 \le i \le m-1$$
$$1 \le k \le \tilde{m}-1$$

and combining it with (40) and (46) yields

$$\begin{cases} (b-1)\,\hat{\varphi}_{i,i+1}^k = \tilde{\lambda}^k b\hat{\varphi}_{i,i+1}^k & 1 \le i \le m-1 \\ -\hat{\varphi}_{i-1}^k + 2\hat{\varphi}_i^k - \hat{\varphi}_{i+1}^k = \dfrac{\tilde{\lambda}^k + b - 1}{b(1-\beta)\beta}\hat{\varphi}_i^k & 2 \le i \le m-1 \\ \hat{\varphi}_1^k = 0 \qquad \hat{\varphi}_m^k = 0 & 1 \le k \le \tilde{m}-1 \end{cases}$$

The above can be satisfied for any eigenvector, $\hat{\varphi}^k$, of the homogenized problem if, and only if, the following holds

$$\begin{cases} (b-1) = \tilde{\lambda}^k b \\ \dfrac{\hat{\lambda}^k h}{\tilde{K}} = \dfrac{\tilde{\lambda}^k + b - 1}{b(1-\beta)\beta} \end{cases}$$

from where follows

$$b = \pm \frac{1}{\left(1 - \beta(1-\beta)\dfrac{\hat{\lambda}^k h}{\tilde{K}}\right)^{1/2}} \qquad \tilde{\lambda}^k = \frac{b-1}{b}$$

$$\lambda^k = \frac{b-1}{b}\frac{d_1 + d_2}{\alpha(1-\alpha)h} = \frac{b}{b+1}\hat{\lambda}^k$$

The positive values of b lead to the eigenvalues and eigenvectors of the form given in (42) with $b^k = b$, while the negative values of b correspond to $b^k = -b$.

The middle eigenvalue and eigenvector $\tilde{m}$ in (42) follows directly from the eigenvalue problem (45). The eigenvalues and eigenvectors for the homogenized discrete eigenvalue problem can be found, among others, in [8]. □

To this end, we summarize the results of this section in the following compact notation

$$\begin{cases} \lambda^k = \dfrac{4\tilde{K}}{h} \dfrac{\sin^2\left(\frac{k\pi}{2\tilde{m}}\right)}{\left(1+\left(1-q\sin^2\left(\frac{k\pi}{2\tilde{m}}\right)\right)\right)^{1/2}} \\ \lambda^{2\tilde{m}-k} = \dfrac{4\tilde{K}}{h} \dfrac{\sin^2\left(\frac{k\pi}{2\tilde{m}}\right)}{\left(1-\left(1-q\sin^2\left(\frac{k\pi}{2\tilde{m}}\right)\right)\right)^{1/2}} \\ \lambda^{\tilde{m}} = \dfrac{4\tilde{K}}{h}\dfrac{1}{q} \\ b^k = \dfrac{1}{\left(1-q\sin^2\left(\frac{k\pi}{2\tilde{m}}\right)\right)^{1/2}} \\ 1 \le k \le \tilde{m}-1 \end{cases} \tag{47}$$

where

$$q = \frac{4d_1d_2}{(d_1+d_2)^2} \qquad 0 < q \le 1$$

4. Evaluation of the operator T and the estimation of the rate of convergence

In this section we will estimate the rate of convergence of the simple two-grid method applied to the heterogeneous medium (38). In estimating the rate of convergence, the critical step is to find a closed form expression for $T\varphi^k$, where T is the A-orthogonal projector (16) and φ^k are the eigenvectors (42). The result of this product is given in Proposition 2.

Proposition 2

Let T be the A-orthogonal projector (16); $(\varphi^k, \varphi^{\tilde{n}-k})$, $1 \le k \le \tilde{m}-1$ and $\varphi^{\tilde{m}}$ be the

corresponding eigenvectors given in (42); b^k, $1 \le k \le \tilde{m}-1$ be the coefficients defined by (43). Then

$$
\begin{aligned}
T\varphi^k &= \frac{b^k-1}{2b^k}\left(\varphi^k+\varphi^{\tilde{n}-k}\right) \\
T\varphi^{\tilde{n}-k} &= \frac{b^k+1}{2b^k}\left(\varphi^k+\varphi^{\tilde{n}-k}\right) \\
1 &\le k \le \tilde{m}-1 \\
T\varphi^{\tilde{m}} &= \varphi^{\tilde{m}}
\end{aligned}
\tag{48}
$$

where we have used the prolongation and restriction operators defined by (28),(40),(41):

$$
Q = \begin{bmatrix}
1 & & & & \\
\beta & 1-\beta & & & \\
 & 1 & & & \\
 & \beta & 1-\beta & & \\
 & & 1 & & \\
\cdots & \cdots & \cdots & \cdots & \cdots \\
 & & & \beta & 1-\beta \\
 & & & & 1
\end{bmatrix}
\tag{49}
$$

$$
Q^* = \begin{bmatrix}
1 & \beta & & & & & & \\
 & 1-\beta & 1 & \beta & & & & \\
 & & & 1-\beta & 1 & \beta & & \\
\cdots & \cdots & \cdots & \cdots & \cdots & \cdots & \cdots & \cdots \\
 & & & & & & 1-\beta & 1
\end{bmatrix}
\tag{50}
$$

and β is given in (41).

Proof of Proposition 2

Applying the operator (16) to the eigenvectors given in (42) yields

$$T\varphi^k = (I - QA_0^{-1}Q^*A)\,\varphi^k \qquad 1 \le k \le \tilde{n} - 1 \tag{51}$$

where

$$\begin{cases} A\varphi^k = \dfrac{b^k}{b^k + 1}\hat{\lambda}^k\varphi^k \\ A\varphi^{\tilde{n}-k} = \dfrac{b^k}{b^k - 1}\hat{\lambda}^k\varphi^{\tilde{n}-k} \\ 1 \le k \le \tilde{m} - 1 \\ A\varphi^{\tilde{m}} = \lambda^{\tilde{m}}\varphi^{\tilde{m}} \end{cases}$$

Furthermore, inserting (40) - (43) into (50) gives

$$\begin{cases} [Q^*\varphi^k]_i = (-b^k\beta(1-\beta)\hat{\lambda}^k\dfrac{h}{\bar{K}} + b^k + 1)\hat{\varphi}_i^k = \dfrac{b^k+1}{b^k}\hat{\varphi}_i^k \\ [Q^*\varphi^{\tilde{n}-k}]_i = (-b^k\beta(1-\beta)\hat{\lambda}^k\dfrac{h}{\bar{K}} + b^k - 1)\hat{\varphi}_i^k = -\dfrac{b^k-1}{b^k}\hat{\varphi}_i^k \\ 1 \le i \le \tilde{m} \qquad 1 \le k \le \tilde{m} - 1 \end{cases} \tag{52}$$

$$[Q^*\varphi^{\tilde{m}}]_i = (1 - \beta - \frac{d_2}{d_1}\beta)\hat{\varphi}_{i-1,i}^{\tilde{m}} = 0 \qquad 1 \le i \le \tilde{m}$$

Combining (51) and (52) yields

$$\begin{cases} Q^*A\varphi^k = \hat{\lambda}^k\hat{\varphi}^k \\ Q^*A\varphi^{\tilde{n}-k} = -\hat{\lambda}^k\hat{\varphi}^k \end{cases} \qquad 1 \le k \le \tilde{m} - 1$$

$$Q^*A\varphi^{\tilde{m}} = 0$$

and

$$\begin{cases} A_0^{-1}Q^* A\varphi^k = \hat{\varphi}^k & \\ A_0^{-1}Q^* A\varphi^{\tilde{n}-k} = -\hat{\varphi}^k & 1 \le k \le \tilde{m}-1 \end{cases} \qquad (53)$$

$$A_0^{-1}Q^* A\varphi^{\tilde{m}} = 0$$

The prolongation of the eigenvectors for the auxiliary eigenvalue problem on the basis of the prolongation operator (49) can be written as follows:

$$\begin{cases} [Q\hat{\varphi}^k]_{i,i+1} = \beta\hat{\varphi}_i^k + (1-\beta)\hat{\varphi}_{i+1}^k = \hat{\varphi}_{i,i+1}^k = \dfrac{1}{b^k}\varphi_{i,i+1}^k = \dfrac{1}{b^k}\varphi_{i,i+1}^{\tilde{n}-k} & \\ & 1 \le i \le \tilde{m} \\ [Q\hat{\varphi}^k]_i = \hat{\varphi}_i^k = \varphi_i^k = -\varphi_i^{\tilde{n}-k} & 1 \le i \le m \quad 1 \le k \le \tilde{m}-1 \end{cases} \qquad (54)$$

and finally, inserting (54) into (51) yields

$$\begin{cases} [T\varphi^k]_{i,i+1} = \dfrac{b^k-1}{b^k}\varphi_{i,i+1}^k & \\ & 1 \le i \le \tilde{m} \\ [T\varphi^{\tilde{n}-k}]_{i,i+1} = \dfrac{b^k+1}{b^k}\varphi_{i,i+1}^{\tilde{n}-k} & 1 \le k \le \tilde{m}-1 \\ [T\varphi^k]_i = [T\varphi^{\tilde{n}-k}]_i = 0 & 1 \le i \le m \end{cases} \qquad (55)$$

Thus, using the equalities stating that $\varphi_{i,i+1}^k = \varphi_{i,i+1}^{\tilde{n}-k}$ and $p_i^k = -\varphi_i^{\tilde{n}-k}$ in (55) results in (48), which completes the proof of the Proposition 2. □

We now turn to the estimation of the rate of convergence, which is given in the Proposition 3.

Proposition 3

Let the error vector e^i in the i-th iteration of the two-grid process with one post-smoothing Jacobi iteration be represented as the linear combination of the eigenvectors (42):

$$e^i = \sum_{k=1}^{\tilde{m}-1} (a^i{}_k\varphi^k + a^i{}_{\tilde{n}-k}\varphi^{\tilde{n}-k}) + a^i{}_{\tilde{m}}\varphi^{\tilde{m}} \qquad (56)$$

and let's introduce the following notation:

$$S_k^i = a_k^i \frac{b^k - 1}{2b^k} + a_{\tilde{n}-k}^i \frac{b^k + 1}{2b^k} \qquad 1 \le k \le \tilde{m} - 1 \tag{57}$$

Then

$$\begin{cases} a_k^{i+1} = S_k^i \left(1 - \omega q \dfrac{b^k}{b^k + 1} \sin^2\left(\dfrac{k\pi}{2\tilde{m}}\right)\right) \\ a_{\tilde{n}-k}^{i+1} = S_k^i \left(1 - \omega q \dfrac{b^k}{b^k - 1} \sin^2\left(\dfrac{k\pi}{2\tilde{m}}\right)\right) \end{cases} \qquad 1 \le k \le \tilde{m} - 1 \tag{58}$$

$$a_{\tilde{m}}^{i+1} = a_{\tilde{m}}^i (1 - \omega)$$

where

$$S_k^{i+1} = S_k^i \left(1 - \omega \left(2 - q \sin^2\left(\frac{k\pi}{2\tilde{m}}\right)\right)\right) \qquad 1 \le k \le \tilde{m} - 1 \tag{59}$$

and ω - is a weighting factor of the Jacobi method.

Proof of Proposition 3

Inserting (48) into (56) and using the notation (57), yield

$$\begin{aligned} Te^i &= \sum_{k=1}^{\tilde{m}-1} \left(a_k^i \frac{b^k - 1}{2b^k} + a_{\tilde{n}-k}^i \frac{b^k + 1}{2b^k}\right) (\varphi^k + \varphi^{\tilde{n}-k}) + a_{\tilde{m}}^i \varphi^{\tilde{m}} \\ &= \sum_{k=1}^{\tilde{m}-1} S_k^i (\varphi^k + \varphi^{\tilde{n}-k}) + a_{\tilde{m}}^i \varphi^{\tilde{m}} \end{aligned} \tag{60}$$

Applying a single Jacobi iteration (14) to the eigenvectors given in (42) results in the following

$$G\varphi^k = (I - DA)\varphi^k = \left(1 - \omega \frac{\alpha(1-\alpha)h}{d_1 + d_2} \lambda^k\right) \varphi^k \qquad 1 \le k \le \tilde{n} - 1 \tag{61}$$

Inserting the eigenvalues defined in (42) into (61) and using (39), (41), (43) yields

$$\begin{cases} G\varphi^k = \left(1 - \omega q \dfrac{b^k}{b^k + 1} sin^2\left(\dfrac{k\pi}{2\tilde{m}}\right)\right)\varphi^k \\ G\varphi^{\tilde{n}-k} = \left(1 - \omega q \dfrac{b^k}{b^k - 1} sin^2\left(\dfrac{k\pi}{2\tilde{m}}\right)\right)\varphi^{\tilde{n}-k} \end{cases} \qquad 1 \le k \le \tilde{m} - 1 \qquad (62)$$

$$G\varphi^{\tilde{m}} = (1 - \omega)\,\varphi^{\tilde{m}}$$

Combining (60) and (62) yields (58), where the value of S_k^{i+1} is found on the basis of (57)

$$S_k^{i+1} = S_k^i \left(1 - \omega q \frac{(b^k)^2 + 1}{(b^k)^2 - 1} sin^2\left(\frac{k\pi}{2\tilde{m}}\right)\right) \qquad 1 \le k \le \tilde{m} - 1 \qquad (63)$$

Finally, inserting (43) and (44) into (63) results in (59), which completes the proof of the Proposition 3. □

We are now in a position to estimate the rate of convergence on the basis of eigenvalue distribution and the main results given in (47), (56) - (59).

Note that the parameter q (see (41), (43)) can be viewed as a measure of material heterogeneity. For example, the case of $q = 1$ is equivalent to the problem in a homogeneous medium, in the sense that $K_1\alpha = K_2(1 - \alpha)$. Material heterogeneity increases with decreasing the value of parameter q.

Table 1 illustrates the spectrum of eigenvalues for different values of q. It can be seen that eigenvalues are clustered in two regions (except for the middle eigenvalue, which is equal to $(4\tilde{K}/h)\ (1/q)$). The spectral width of the two regions (defined by the difference of the maximum and minimum eigenvalues in the corresponding region) decreases with the decreasing value of q. This clustering of eigenvalues is one of the key reasons for a faster rate of convergence of the two grid process with decreasing the value of q.

We next investigate what is the weighting factor ω^* that maximize the asymptotic rate of convergence in the absence of the error component corresponding to the middle eigenvalue, i.e., $a_{\tilde{m}} = 0$. From (59) follows

$$1-\omega^*(2-q) = -(1-2\omega^*)$$

$$or \qquad \omega^* = \frac{2}{4-q} \qquad 1/2 < \omega^* \le 2/3 \tag{64}$$

Inserting (64) into (59) yields the following estimate of the asymptotic rate of convergence governed by the ratio $\rho = max_k|S_k^{i+1}/S_k^i|$:

$$\rho(\omega) = max_k\left|1-\omega\left(2-q\sin^2\left(\frac{k\pi}{2\tilde{m}}\right)\right)\right|$$

$$\rho^* = \frac{q}{4-q} \qquad 0 < \rho^* \le 1/3 \tag{65}$$

where $\omega^* = 2/3$ and $\rho^* = 1/3$ correspond to the solution of homogeneous problem. It can be seen from (65) that the asymptotic rate of convergence of the two-grid method increases (or ρ^* decreases) with decreasing the value of q (or increasing material heterogeneity).

However, if the error component corresponding to the middle eigenvalue in (58) is taken into account it is necessary to employ $\omega^{**} = 2/3$ resulting in the asymptotic rate of convergence governed by $\rho^{**} = 1/3$. So in the worse scenario we may expect the same rate of convergence as for the homogeneous problem.

The oscillatory nature of the middle eigenvector, $\varphi^{\tilde{m}}$, is described by (42). It can be seen that the eigenvector vanishes on the unit cell boundaries, but oscillates between the unit cell midside nodes in geometric progression with a negative factor depending on material heterogeneity, d_2/d_1. Such oscillatory response is unlikely to be triggered, and thus in practice the rate of convergence is governed by the estimate given in (65).

5. Numerical examples

First, we will analyze the two-grid process for solving the boundary value problem (1),(38) on the basis of uniform finite element grid with two elements on each unit cell as described in section 3 with $\alpha = 0.5$. For the purpose of simulating the singular loading the right hand side function $f(x)$ has been chosen as follows

$$f(x) = \frac{sign(x-l/2)}{|x-l/2|+\delta} \tag{66}$$

where $\delta = 10^{-8}$ and

$$sign(a) = \begin{cases} 1 & if \quad a > 0 \\ -1 & if \quad a < 0 \\ 0 & if \quad a = 0 \end{cases}$$

We carry out the smoothing iterations on the basis of the Gauss-Zeidel method. As a termination criterion we use the following tolerance to bound the ratio of the residual norm versus the norm of the right hand side vector, i.e.,

$$\frac{\|r\|_2}{\|f\|_2} \leq 10^{-8} \tag{67}$$

where $\|v\|_2 = \sum_{i=1}^{n} |v_i| \qquad v \in R^n.$

The results of the numerical experiment are presented in the Table 2, where ρ_{100} and ρ_{1000} characterize the asymptotic rates of convergence for the cases with 100 and 1000 unit cells, respectively. It can be seen that the theoretical rate of convergence (65) ignoring the error component corresponding to the middle eigenvalue agrees well with the numerical result. In both cases the error is rapidly decreasing. On the other hand, the rate of convergence of the multi-grid process with conventional intergrid transfer operators is governed by the value of ρ^{conv}, which is very close to unity ($\rho^{conv} = 0.923 \div 0.992$), indicating very slow rate of convergence. Furthermore, the rate of convergence of the conventional multi-grid process decreases as material heterogeneity increases. This is in contrast to the proposed multi-grid process where the rate of convergence improves with increase in material heterogeneity.

We next consider the same problem with 10 finite elements on each unit cell. The results of this experiment are presented in Table 3. They show that the convergence increases with decreasing the value of the parameter q. Note that the case $K_1/K_2 = 1/1$ corresponds to the standard two-grid method for the boundary value problem with constant coefficient.

The next example deals with the nonuniform fine grid. We use 10 finite elements for the two unit cells, where the solution has a high gradient. In the remaining region we use one element per unit cell, with a homogenized effective coefficient. The ratio of $K_1/K_2 = 1/100$ is considered (Fig. 3). The results of this experiment are shown in Table 4.

The last numerical experiment deals with the three-grid method for the previously defined problem. We use here the additional coarse grid for solving the auxiliary homogenized problem and a standard multi-grid technique for formulating the coarse grid problem. The results of this experiment are shown in Table 5, where ν_1 and ν_2 are the number of pre- and post- smoothing iterations on the fine grid; ν_1^0 and ν_2^0 the corresponding values on the auxiliary grid; N_e the number of finite elements in the finest grid; N_c the number of unit cells; N_0 the number of the elements in the coarsest grid. Results of this experiment are consistent with our previous observations, and confirm our theoretical estimates given in (65).

6. Acknowledgments

The support of the ARPA under grant A10234, the NASA Langley Research Center under grant NAG-1-1356, Sikorsky Aircraft and the National Science Foundation NYI award ECS-9257203 are gratefully acknowledged.

References

1. A. Benssousan, J.L. Lions and G. Papanicoulau, Asymptotic analysis for periodic structures, North Holland, Amsterdam, 1978.

2. E. Sanchez-Palencia and A. Zaoui, Homogenization techniques for composites. Homogenization techniques for composite media, Springer-Verlag, Berlin, 1985.

3. N.S. Bakhvalov and G.P. Panasenko, Homogenization of periodic medium processes, Nauka, Moscow, 1984.

4. J. Fish and A. Wagiman, Multiscale finite element method for a locally nonperiodic heterogeneous medium, Computational Mechanics: The International Journal 21 (1993) 1-17.

5. J. Fish, P. Nayak and M.H. Holmes, Microscale reduction error indicators and estimators for a periodic heterogeneous medium, to appear in International Journal of Numerical Methods in Engineering.

6. S.B. Dong, Global-local finite element methods, in: A.K.Noor and W.D.Pilkey, eds., State-of-the-Art Surveys on Finite Element Technology (ASME, New York, 1983) 451-474.

7. S.F. McCormick, Multigrid methods for variational problems: further results, SIAM J. Numer. Anal. 21 (1984) 255-263.

8. W.L. Briggs, A multigrid tutorial, SIAM, Philadelphia, 1987.

Fig. 1

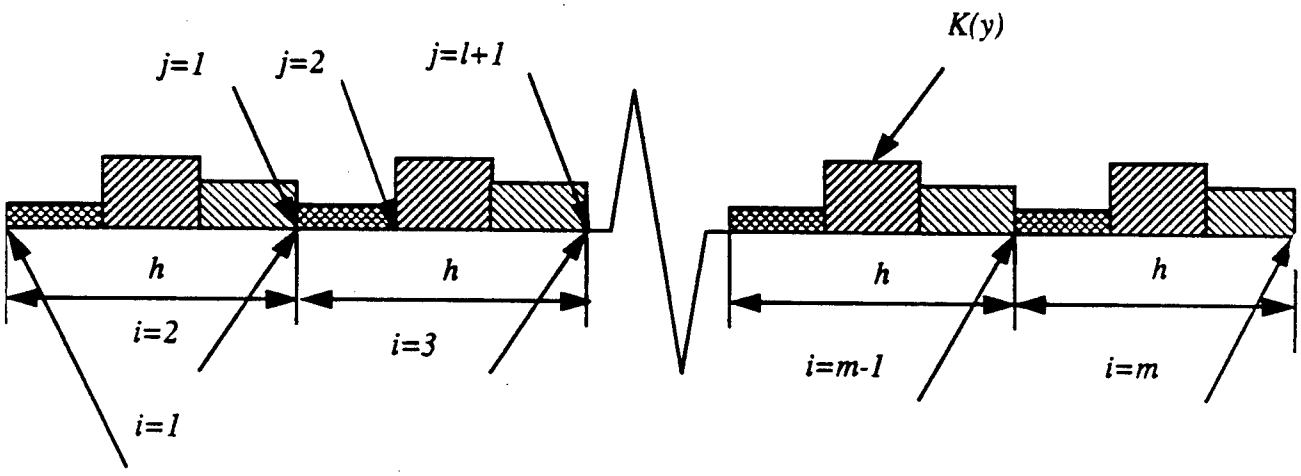


Fig. 2

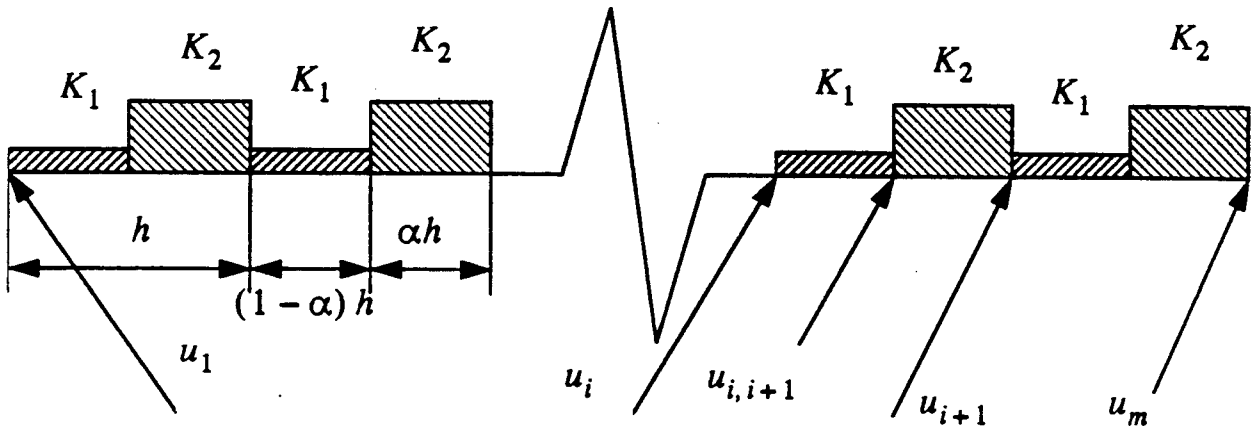


Fig. 3

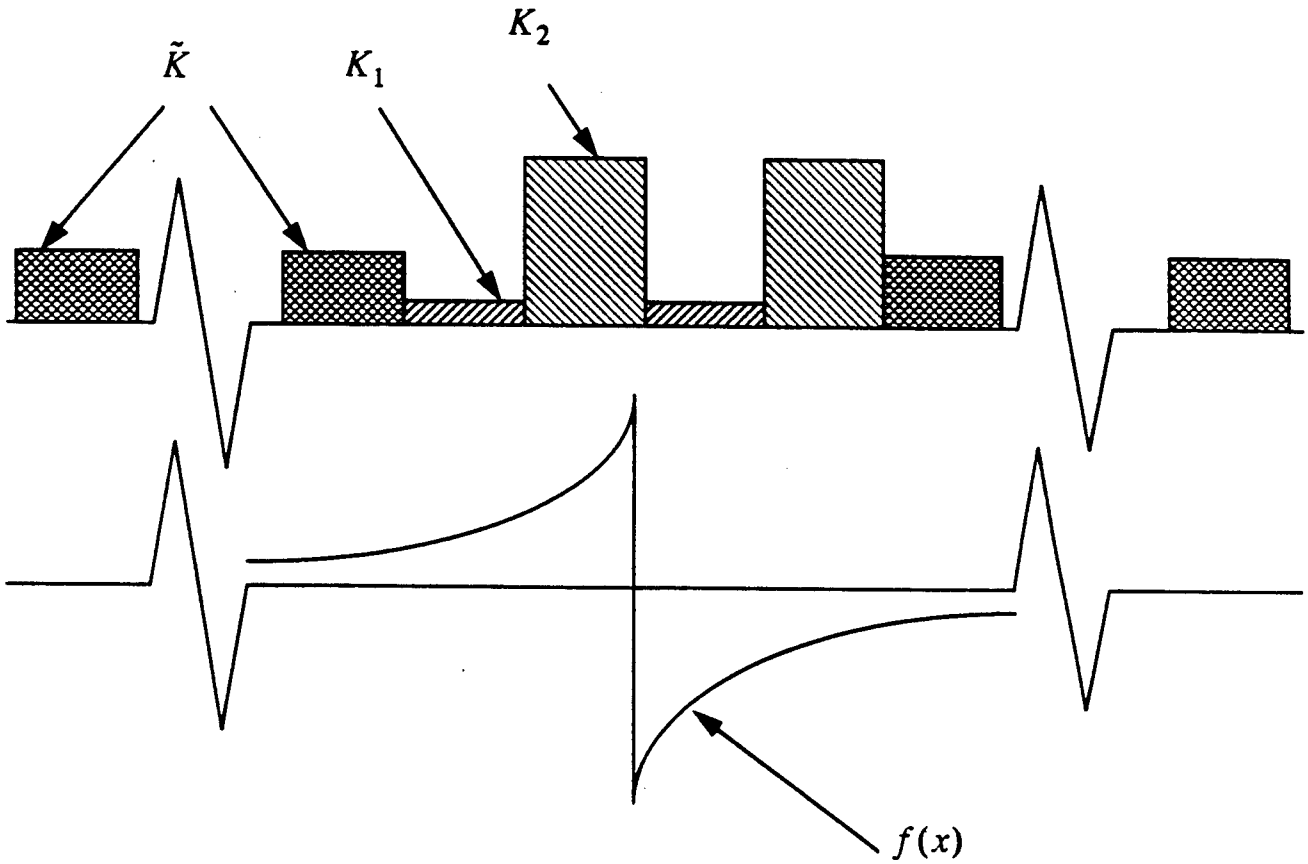


Table 1

$q\backslash k$		1	2	3	4	5
0.1	k	0.0479	0.1743	0.3328	0.4630	10.0000
	$n-k$	19.9521	19.8257	19.6672	19.5370	
0.2	k	0.0480	0.1758	0.3387	0.4748	5.0000
	$n-k$	9.9520	9.8242	9.6613	9.5252	
0.3	k	0.0481	0.1775	0.3451	0.4880	3.3333
	$n-k$	6.6186	6.4892	6.3215	6.1787	
0.4	k	0.0482	0.1792	0.3520	0.5028	2.5000
	$n-k$	4.9518	4.8208	4.6480	4.4972	
0.5	k	0.0483	0.1809	0.3596	0.5198	2.0000
	$n-k$	3.9517	3.8191	3.6404	3.4802	
0.6	k	0.0484	0.1828	0.3678	0.5396	1.6667
	$n-k$	3.2849	3.1506	2.9655	2.7937	
0.7	k	0.0486	0.1847	0.3770	0.5633	1.4286
	$n-k$	2.8086	2.6725	2.4801	2.2938	
0.8	k	0.0487	0.1867	0.3872	0.5928	1.2500
	$n-k$	2.4513	2.3133	2.1128	1.9072	
0.9	k	0.0488	0.1888	0.3988	0.6320	1.1111
	$n-k$	2.1734	2.0334	1.8234	1.5902	
1.0	k	0.0489	0.1910	0.4122	0.6910	1.0000
	$n-k$	1.9511	1.8090	1.5878	1.3090	

Table 2

K_1/K_2	q	ρ^*	ρ_{100}	ρ_{100}^{conv}	ρ_{1000}	ρ_{1000}^{conv}
1/100	0.0392118	0.0099	0.0098	0.92278	0.00982	0.92253
1/1000	0.003992	0.000999	0.000992	0.99192	0.001001	0.99191

Table 3

K_1/K_2	q	number of unit cells	number of smoothing iterations	number of two-grid cycles
1/100	0.03921	100	2	20
			3	13
		1000	2	20
			3	13
1/10	0.3306	100	2	26
			3	20
		1000	2	26
			3	20
1/1	1.0	100	2	69
			3	46
		1000	2	69
			3	46

Table 4

number of unit cells	number of smoothing iterations	number of two-grid cycles
100	2	16
	3	11
1000	2	16
	3	11

Table 5

K_1/K_2	N_e	N_c	N_0	ν_1, ν_2	ν_1^0, ν_2^0	type of the cycle	number of cycles
1/100	1,000	100	50	1	1	V	20
						W	20
				2	2	V	11
						W	11
				2	1	V	12
						W	11
				1	2	V	20
						W	20
1/100	10,000	1,000	500	1	1	V	20
						W	18
				2	2	V	10
						W	10
				2	1	V	10
						W	10
				1	2	V	18
						W	18
1/10	10,000	1,000	500	1	1	V	27
						W	27
				2	2	V	14
						W	14
				2	1	V	14
						W	14
				1	2	V	27
						W	27

ELSEVIER

Comput. Methods Appl. Mech. Engrg. 126 (1995) 17–38

Computer methods in applied mechanics and engineering

Multi-grid method for periodic heterogeneous media Part 2: Multiscale modeling and quality control in multidimensional case

Jacob Fish*, Vladimir Belsky

Department of Civil Engineering and Scientific Computation Research Center, Rensselaer Polytechnic Institute, Troy, NY 12180, USA

Received 1 April 1994; revised 3 January 1995

Abstract

A multi-grid method for a periodic heterogeneous medium in multidimensions is developed. Based on the homogenization theory, special intergrid transfer operators have been developed to simulate a low frequency response of the boundary value problem with oscillatory coefficients. An adaptive strategy is developed to form a nearly optimal two-scale computational model consisting of the finite element mesh entirely constructed on the microscale in the regions identified by the idealization error indicators, while elsewhere, the modeling level is only sufficient to capture the response of homogenized medium. Numerical experiments show the usefulness of the proposed adaptive multi-level procedure for predicting a detailed response of composite specimens.

1. Introduction

The computational complexity of modeling large scale composite structures is enormous primarily due to the multiple scales involved. For example, the typical size of the structure (an airplane or a car) is of the order of magnitude of tens of meters, while the diameter of the fastener hole is of the order of millimeters. Prediction of micro-mechanical failure modes necessitates considerations at even smaller scales. The useful life of a structure depends on the quality of modeling at each scale and the ability of a reliable transfer of the appropriate information between various modeling levels. Thus, the need for reliable analysis techniques at several different scales is crucial.

Mathematical homogenization theory [1–3] or its engineering counterpart [4] have been traditionally used as a primary tool for analyzing heterogeneous medium. Based on the assumptions of micro-structure periodicity and uniformity of macroscopic fields within a unit cell domain, homogenization theory decomposes the boundary value problem in a heterogeneous medium into the unit cell (micro) problem and the global (macro) problem. The computational sequence consists of three steps: (i) solution of the unit cell problem and evaluation of the homogenized material properties, (ii) solution of the macro-problem and (iii) post-processing on the micro-level. Reliability of computations in a heterogeneous medium is strongly linked to the validity of the two basic assumptions (periodicity and uniformity), introduced by the classical homogenization theory. The issue of statistical periodicity has been investigated in [5] and is not addressed here. Instead, we concentrate on the issue of uniformity of macroscopic fields (or absence of it) within the unit cell domain. These studies are motivated by the

* Corresponding author.

0045-7825/95/$09.50 © 1995 Elsevier Science S.A. All rights reserved

well-known fact that in the high gradient regions the macroscopic fields are rapidly varying and their uniformity within the unit cell domain is highly questionable.

This paper proposes an alternative to the classical homogenization that abandons the classical hypothesis of uniformity of the macroscopic fields within the unit cell domain. By this approach, solution obtained from the mathematical homogenization theory is only used to simulate the global response of the discrete heterogeneous medium. The proposed computational scheme can be viewed as a generalization of the multi-grid method for the periodic heterogeneous medium. Within this framework the mathematical homogenization theory serves as a mechanism for capturing the lower frequency response of the discrete heterogeneous medium, while the classical relaxation techniques are employed to capture the oscillatory response.

Previous studies [6] have indicated that for problems in heterogeneous medium eigenvalues corresponding to the lower frequencies are not smooth and thus the classical bi- or tri-linear operators are not suitable for data transfer between the grids. For 1-D problems it has been found [6] that the rate of convergence is governed by the factor $q/(4-q)$, where $0<q\leqslant 1$ depends on the microstructure. This estimate reveals that the rate of convergence increases with the increase in material heterogeneity.

The paper focuses on the issues of adaptive multiscale modeling and fast iterative solution algorithms for problems in heterogeneous media. We will attempt to construct a nearly optimal two-scale computational model consisting of the finite element mesh entirely constructed on the microscale in the regions where there is a necessity to do so, while elsewhere, the modeling level will be only sufficient to capture the response of homogenized medium. The microscale reduction error indicators described in Section 5, are used to assess the quality of homogenized model, and to identify the regions where the homogenized model should be replaced by a model reflecting the details of the microstructure.

Once the two-scale model is constructed, the multigrid-like solvers in the form of MLAT [7] and/or FAC [8, 9] are employed due to their linear asymptotic rate of convergence, as opposed to the roughly quadratic growth in CPU time versus the problem size in the case of the direct coupled global–local solutions (or, to be more precise, NB^2, where N and B are the problem size and the bandwidth, respectively). We show that it is possible to obtain even faster convergence for the case of differential equations with highly oscillatory periodic coefficients if special intergrid transfer operators developed in Section 3 are utilized.

The outline of this paper is as follows. Problem statement and objectives are formulated in Section 2. Special purpose intergrid transfer operators for a periodic heterogeneous medium are derived in Section 3. Section 4 describes an adaptive two-scale computational procedure for periodic heterogeneous medium. Microscale reduction error indicators and estimators aimed at quantifying the quality of homogenization and stearing the adaptive process are given in Section 5. Numerical experiments conclude the manuscript.

2. Problem statement

In modeling heterogeneous media one can adopt two different points of view:

2.1. *Mathematical modeling on the microscale*

In this scenario each phase (fiber and matrix) is assumed to possess homogeneous properties and obey equilibrium and kinematical equations as well as compatibility and traction continuity conditions between the phases. The corresponding strong form of the boundary value problem for a linear elastostatics is given by

$$\sigma_{ij,j} = b_i \quad \text{on } \Omega$$
$$\sigma_{ij} = D_{ijkl}\varepsilon_{kl} \quad \text{on } \Omega$$
$$\varepsilon_{ij} = u_{(i,j)} \quad \text{on } \Omega$$
$$u_i = \bar{u}_i \quad \text{on } \Gamma_u$$

$$\sigma_{ij}n_j = t_i \qquad \text{on } \Gamma_t$$
$$[\sigma_{ij}n_j]_{\Gamma_{\text{int}}} = 0 \qquad [u_i]_{\Gamma_{\text{int}}} = 0 \tag{1}$$

where σ_{ij} and ε_{ij} are the components of the stress and strain tensors, respectively; b_i and t_i represent the body forces and prescribed boundary tractions on the boundary Γ_t, respectively; u_i are the components of the displacement vector; $\bar{u}_i$ are the prescribed displacements on the boundary Γ_u; D_{ijkl} represent the components of the symmetric positive definite fourth-order constitutive tensor; Ω is a problem domain. The last two equations correspond to traction and displacement continuity conditions on the interface, Γ_{int}, between the microconstituents. $[\ldots]_{\Gamma_{\text{int}}}$ denotes the jump operator on Γ_{int}. Symmetric gradient is denoted by $\varphi_{(i,j)} = (\varphi_{i,j} + \varphi_{j,i})/2$. Standard tensorial notation with summation over the repeated indexes is employed.

2.2. Mathematical modeling on the macroscale

Following the classical homogenization theory [1–3], the asymptotic solution of the boundary value problem (1) for the periodic heterogeneous medium can be obtained using two-term double scale asymptotic expansion

$$u_i(x, y) = u_i^0(x) + \varepsilon u_i^1(x, y) \tag{2}$$

where

$$u_i^1(x, y) = h_{ikl}(y)\varepsilon_{kl}^0(x) \qquad \varepsilon_{kl}^0(x) = u_{(k,l)}^0 \tag{3}$$

and x is a macroscopic co-ordinate vector, $y = x/\varepsilon$ is a microscopic position vector. The parameter ε is a representative unit cell size, which is very small in comparison with the dimensions of the problem domain. The periodicity of the microstructure implies that $F(x, y + kY) = F(x, y)$, where vector Y is a basic period of the microscopic co-ordinate system; k is a non-zero integer.

In the representation (3), $h_{ikl}(y)$ is the Y-periodic function, which can be found from the solution of the boundary value problem on the unit cell domain θ subjected to periodic boundary conditions

$$(D_{ijkl}(h_{(k,l)mn} + \delta_{km}\delta_{ln}))_j = 0 \quad \text{on } \theta \tag{4}$$

where δ_{ij} is a Kronecker delta.

The corresponding expansion of the strain tensor is given

$$\varepsilon_{ij} = (\delta_{ik}\delta_{jl} + h_{(i,j)kl})\varepsilon_{kl}^0 + O(\varepsilon) \tag{5}$$

The macroscopic displacement field $u_i^0(x)$ is the solution of the following boundary value problem with homogenized coefficients

$$\begin{aligned} &(\tilde{D}_{ijkl}u_{(k,l)}^0)_j = f_i \quad \text{on } \Omega \\ &u_i^0 = \bar{u}_i \quad \text{on } \Gamma_u \\ &\tilde{D}_{ijkl}u_{(k,l)}^0 n_j = t_i \quad \text{on } \Gamma_t \end{aligned} \tag{6}$$

where

$$\tilde{D}_{mnpq} = \frac{1}{\theta_Y}\int_\theta (\delta_{im}\delta_{jn} + h_{(i,j)mn})D_{ijkl}(\delta_{kp}\delta_{lq} + h_{(k,l)pq})\,\mathrm{d}\theta \tag{7}$$

and θ_Y is the volume of the unit cell.

Each of the two mathematical models is discretized using a finite element method. The corresponding discrete models are termed as micro and macro finite element meshes, each may have various levels of mesh refinement.

It is the primary goal of the paper to find a numerical solution of the micro finite element model. A direct solution of the system of equations resulting from such a discretization is usually computationally

not feasible since it may involve over a million of unknowns. On the other hand, the finite element solution of the macro-model (6)–(7) is generally feasible and can be utilized to capture the lower frequency response of the discrete heterogeneous system, while various smoothing procedures would be very efficient in capturing the oscillatory response of a heterogeneous medium. This suggests that a multi-grid like approach is a natural choice for solving discrete systems constructed on the microscale.

3. The intergrid transfer operators for a periodic heterogeneous medium in multidimensions

In this section we focus on the central issue of constructing the intergrid transfer operators for a periodic heterogeneous medium in multidimensions. The structure of the intergrid transfer operators between the discrete heterogeneous and corresponding homogenized media is defined on the basis of the discrete form of the double scale asymptotic expansion

$$u_i = (N_{ia}(x) + \varepsilon h_{ijk}(y) N_{(j,k)a}(x)) d_a \tag{8}$$

where $N_{ia}(x)$ and $N_{(j,k)a}(x)$ are the displacement and strain interpolants in the macro-mesh, denoted by

$$u_i^0 = N_{ia} d_a \quad \text{and} \quad \varepsilon_{ij}^0 = N_{(i,j)a} d_a \tag{9}$$

and d_a are the corresponding nodal displacements. Hereinafter, capital subscripts A, B, C, ... are reserved for the fine grid (micro mesh) degrees-of-freedom, while lowercase subscripts a, b, c, ... denote auxiliary coarse grid (macro mesh) degrees-of-freedom.

Since the product εh_{ijk} in Eq. (4) is independent of the choice of ε, it is more convenient to analyze the unit cell problem in the co-ordinates of the physical domain; i.e. $\varepsilon h_{ijk}(y) = h_{ijk}(x) = O(\varepsilon)$. Thus, substituting the discrete form of the unit cell solution, $h_{ijk} = N_{iB}(x) d_{jkB}$, into Eq. (8) yields

$$u_i = (N_{ia} + N_{iB} N_{(j,k)a} d_{jkB}) d_a \tag{10}$$

With this introduction the problem of the coarse grid correction is now stated in the following proposition.

PROPOSITION. Let the coarse grid correction problem be formulated on the basis of the interpolation defined in Eq. (10) *and let*

$$A_{ab} d_b = r_a \tag{11}$$

be the coarse grid correction problem, where A_{ab} is the stiffness matrix of the boundary value problem (6) *with homogenized material properties* (7) *in the auxiliary macro-mesh, and r_a is the respective restriction of the micro-mesh residual vector.*

Then, in the limit as $\varepsilon \to 0$ the stiffness matrix A_{ab} coincides with the restriction of the stiffness matrix of the boundary value problem on the micro-mesh (1).

PROOF. Let Q_{Aa} be a standard (for the second-order differential equations) bi-linear or tri-linear coarse-to-fine grid prolongation operator. The nodal degrees of freedom in the two meshes are then related by

$$d_A = Q_{Aa} d_a \tag{12}$$

The hypothesis of $\varepsilon \to 0$ is equivalent to the infinitesimally small mesh size in the micro-mesh, and thus, without loss of generality, the shape functions on the auxiliary grid can be represented as a linear combination of the shape functions on the micro-mesh, i.e.

$$N_{ia}(x) = N_{iA}(x) Q_{Aa} \tag{13}$$

where the coefficients of linear expansion Q_{Aa} follow from the relation $N_{ia} d_a = N_{iA} d_A = N_{iA} Q_{Aa} d_a$.

Inserting (13) into (10) yields

$$u_i(x) = N_{iA}(Q_{Aa} + N_{(j,k)a} d_{jkA}) d_a \tag{14}$$

To construct the homogenization-based prolongation operator $\tilde{Q}_{Aa}$ we evaluate u_i at the micro mesh nodes $x_{\underline{B}}$

$$u_i(x_{\underline{B}}) = d_B = N_{iA}(x_{\underline{B}})(Q_{Aa} + N_{(j,k)a}(x_{\underline{B}})d_{jkA})d_a \tag{15}$$

where underlined subscripts indicate no summation over the repeated indices. Note that the displacement along the spatial co-ordinate i at the node $x_{\underline{B}}$ corresponds to the degree-of-freedom B in the micro grid, i.e. $u_i(x_{\underline{B}}) \equiv d_B$ and $N_{iA}(x_{\underline{B}}) \equiv \delta_{AB}$. Thus

$$d_B = \tilde{Q}_{Ba}d_a \tag{16}$$

where the homogenization-based prolongation operator is defined as follows

$$\tilde{Q}_{Ba} = Q_{Ba} + N_{(j,k)a}(x_{\underline{B}})d_{jkB} \tag{17}$$

It remains to show that $\tilde{Q}_{Aa}$ restricts the stiffness matrix of the micro-mesh, A_{AB}, to the coarse grid in such a way that the resulting stiffness matrix $A_{ab} = \tilde{Q}^*_{aA}A_{AB}\tilde{Q}_{Bb}$ coincides with the stiffness matrix of the macro problem (6) with homogenized material properties (7) in the limit as $\varepsilon \to 0$.

For this purpose we evaluate the strain field by taking the symmetric gradient of the displacement field given in (8)

$$\varepsilon_{ij} = (N_{(i,j)a}(x) + h_{(i,j)kl}(x)N_{(k,l)a}(x))d_a + \mathrm{O}(\varepsilon) \tag{18}$$

In the limit as $\varepsilon \to 0$ the last term can be neglected resulting in the following strain approximation

$$\begin{aligned}\varepsilon_{ij} &= (\delta_{ik}\delta_{jl} + h_{(i,j)kl})N_{(k,l)a}d_a \\ &= N_{(i,j)A}(Q_{Aa} + N_{(k,l)a}d_{klA})d_a\end{aligned} \tag{19}$$

Note that an identical strain approximation can be obtained by direct discretization of the two-term asymptotic strain expansion given in (5).

The macro-mesh stiffness matrix is given by

$$\begin{aligned}A_{ab} &= \int_\Omega N_{(i,j)a}\tilde{D}_{ijkl}N_{(k,l)b}\,\mathrm{d}\Omega \\ &= \sum_{\text{cells}} \frac{1}{\theta_Y}\int_\theta N_{(m,n)a}N_{(p,q)b}\,\mathrm{d}\theta \int_\theta (\delta_{im}\delta_{jn} + h_{(i,j)mn})D_{ijkl}(\delta_{kp}\delta_{lq} + h_{(k,l)pq})\,\mathrm{d}\theta\end{aligned} \tag{20}$$

Further, exploiting the hypothesis of the infinitesimality of the unit cell, as $\varepsilon \to 0$, we note that

$$N_{(i,j)a}(x_{\underline{B}}) = N^I_{(i,j)a} = \text{const} \quad \forall x_{\underline{B}} \in \theta^I \tag{21}$$

where the superscript I denotes the unit cell number.

Finally, inserting (21) into (20) yields

$$A_{ab} = \int_\Omega \tilde{Q}_{Aa}N_{(i,j)A}D_{ijkl}N_{(k,l)B}\tilde{Q}_{Bb}\,\mathrm{d}\Omega = \tilde{Q}^*_{aA}A_{AB}\tilde{Q}_{Bb} \tag{22}$$

which completes the proof of the proposition.

So far the homogenization-based intergrid transfer operators $(\tilde{Q}, \tilde{Q}^*)$ have been derived assuming that $\varepsilon \to 0$. In practice, the value of ε is finite, requiring reformulation of the intergrid transfer operators to maintain C^0 continuity of the prolongated displacement field in the micro mesh. It should be noted that a direct application of the prolongation operator (17) does not uniquely determine the displacement field on the boundaries of the unit cells, since the macroscopic strain field $N_{(j,k)a}(x_{\underline{B}})d_a$ is a C^{-1} continuous function, i.e. it is discontinuous on the boundaries of the macro-elements. Consequently, the prolongated solution is also discontinuous at the interface between the unit cells, overlapping different macro-elements.

To develop a homogenization-based prolongation operator $\tilde{Q}$, that generates C^0 continuous displacements, it is necessary to construct a C^0 continuous strain field in a macro-mesh ε^*_{kl} defined as

$$\varepsilon^*_{kl} = N_a \varepsilon_{kl}(x_a) \tag{23}$$

where $\varepsilon_{kl}(x_a)$ are nodal strain values in the macro-mesh and N_a are the corresponding strain field shape functions. Nodal strain values are typically found by weakly enforcing the equality between the discontinuous finite element strains and their continuous counterpart [10]. By this technique the projection operator C_{ag} is formed to project strain values from a set of sampling points to finite element nodes in the macro-mesh

$$\varepsilon_{kl}(x_a) = C_{ag}\varepsilon_{kl}(x_g) = C_{ag}N_{(k,l)b}(x_g)d_b \tag{24}$$

where the sampling points, x_g, can be either Gauss points, reduced Gauss points or finite element nodes [10].

Substituting (23) and (24) into (17) and evaluating the displacement field at the finite element nodes in the micro-mesh yields the following expression for the *continuous homogenization-based* prolongation operator

$$\tilde{Q}_{Aa} = Q_{Ab}(\delta_{ab} + C_{bg}N_{(k,l)a}(x_g)d_{kl\underline{A}}) \tag{25}$$

In the numerical examples considered in this paper, projection operator C_{ag} was constructed on the patch-by-patch basis as described in [10]. In the case of a 4-node rectangular element it amounts to computing the nodal strain values by averaging the corresponding strain values evaluated at the element centroids, connected to the node.

REMARK. In practice, one has to deal with several different types of unit cells such as in the case of laminated composites where each layer is composed of different unit cells. Even though the macro strain field has been projected to be C continuous, the prolongated displacement field might still be incompatible at the interface between dissimilar unit cells. This requires further modification of the continuous homogenization-based prolongation operator at the interface between the unit cells of different types.

This is accomplished by introducing a transition layer of unit cells at the interface between dissimilar unit cells. The formulation of the unit cell problem in the transition region differs from the interior unit cell in the way the boundary conditions are prescribed.

To clarify this point we consider a transition layer, B^*, in a laminated composite at the interface between two dissimilar layers A and B as shown in Fig. 1. The microstructure in the transition region, B^*, is identical to that in the layer B. The boundary conditions applied to the unit cell in the transition region are of the following categories:

(i) On the faces (edges in 2-D) orthogonal to the interface, the boundary conditions are periodic, i.e. displacements d_{ijA} are equal on the opposite sides of the unit cell.

(ii) On the faces parallel to the interface, the non-homogeneous Dirichlet boundary conditions are assumed instead. The prescribed displacement values are assumed to be equal to those in the neighboring layer. In general, the value of these displacements is not equal to those on the opposite sides of the unit cell.

The unit cell boundary value problems are solved in the following sequence (3-D case). First solve for the interior unit cells (with all periodic boundary conditions). This is followed by the unit cells at the interface between two dissimilar layers (with partially periodic and Dirichlet boundary conditions). Then, the unit cells along the edge connecting four different layers (with partially periodic and Dirichlet boundary conditions), and finally the unit cells connected to eight different unit cells (with Dirichlet boundary conditions only).

4. Multiscale solution algorithm for heterogeneous media

In this section we present the formulation of multiscale solution algorithm for problems in a periodic heterogeneous medium where one or more regions are modeled on the microscale, while elsewhere, the

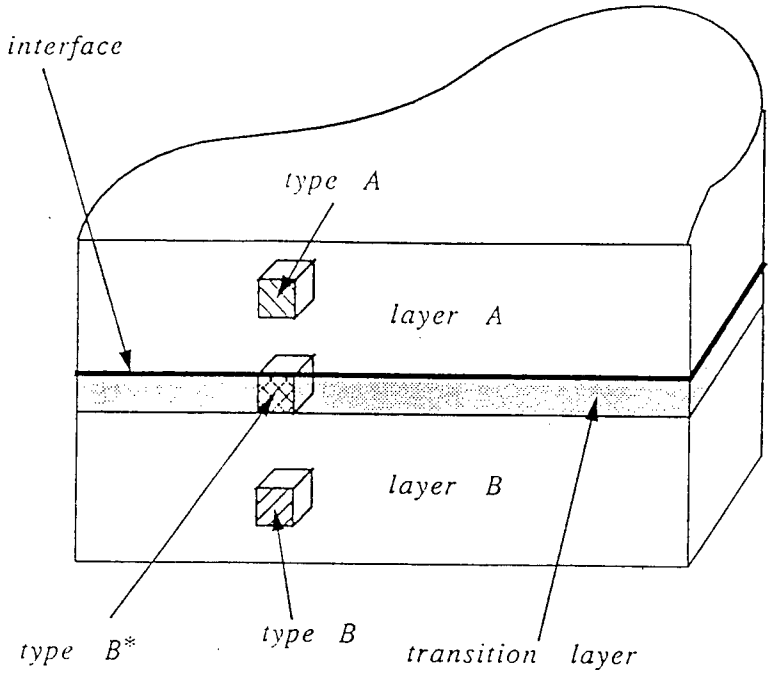


Fig. 1. A transition layer at the interface between two dissimilar layers of unit cells.

medium is treated as homogenized. Our formulation is applicable to general three-dimensional domains with unlimited number of local regions, although for simplicity, illustrations are limited to two-dimensional problems with a single local region. Attention is restricted to a two-level scheme.

4.1. Problem definition and notation

Consider a heterogeneous medium on $\tilde{\Omega}$ which is formed by a special periodicity of a unit cell. Suppose that the Microscale Reduction Error (MRE) indicator to be described in Section 5, indicates that the classical homogenization procedure is not valid on the portion of the problem domain, denoted by $\Omega \subset \tilde{\Omega}$. Therefore, the optimal computational model consists of the finite element grid $\hat{G}$ on $\hat{\Omega} = \tilde{\Omega}/\Omega$, where the elements are assumed to possess homogenized material properties, and a finite element grid G, with much smaller elements constructed on the microscale.

The micro-grid G, is partitioned as follows

$$G = G_I \cup G_L \tag{26}$$

where G_I are the micro-grid nodes at the interface Γ_I between the two regions, and G_L are the interior micro-grid nodes as shown in Fig. 2.

Likewise the macro-grid $\hat{G}$ is partitioned in a similar fashion

$$\hat{G} = \hat{G}_I \cup \hat{G}_G \tag{27}$$

where $\hat{G}_I$ are the macro-grid nodes at the interface Γ_I, which do not have to coincide with the nodes in G_I, and $\hat{G}_G$ are the remaining macro-grid points.

We further define an auxiliary grid $\tilde{G}$ on $\tilde{\Omega}$, where the entire finite element mesh is modeled with homogenized material properties. The grid $\tilde{G}$ is aimed at capturing the lower frequency response of the two-scale grid model $G \cup \hat{G}$. The auxiliary grid is partitioned as follows

$$\tilde{G} = \tilde{G}_I \cup \tilde{G}_L \cup \tilde{G}_G \tag{28}$$

where $\tilde{G}_I = \hat{G}_I$, $\tilde{G}_G = \hat{G}_G$; the grid $\tilde{G}_L$ represents auxiliary grid points on Ω as shown in Fig. 2.

For information transfer between the micro- and macro-grids, we employ continuous homogenization-based prolongation operator $\tilde{Q}$ derived in Section 3, which is partitioned into two blocks for

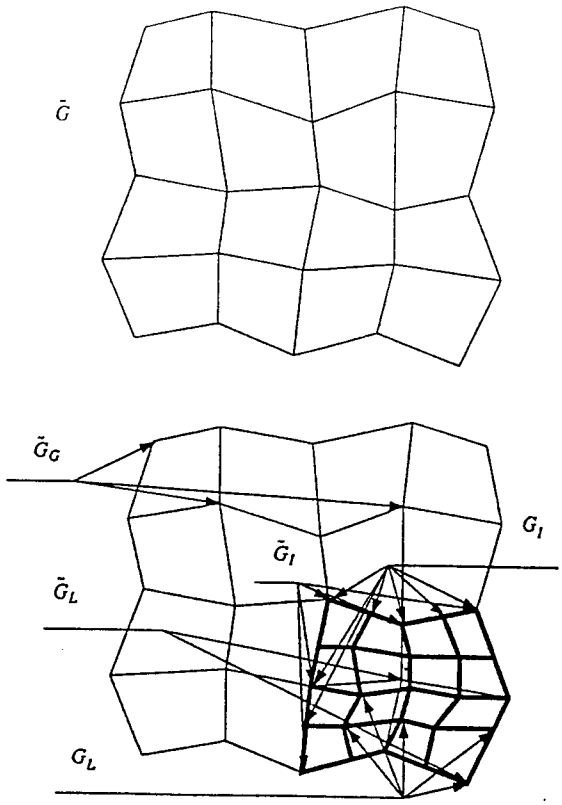


Fig. 2. Partitioning of the auxiliary and micro grids.

convenience. The first denoted by $\hat{Q}$, relates nodal displacements in the macro grid $\hat{G}$ to those in the micro grid G at the interface Γ_I only

$$\hat{Q}: \hat{G} \rightarrow G_I \tag{29}$$

where

$$\hat{Q} = [\tilde{Q}_{II} \quad \tilde{Q}_{IG}] \tag{30}$$

such that

$$\tilde{Q}_{II}: \tilde{G}_I \rightarrow G_I \quad \text{and} \quad \tilde{Q}_{IG}: \tilde{G}_G \rightarrow G_I \tag{31}$$

Note, that as opposed to the standard linear prolongation operator, which relates the information at the interface only, continuous homogenization-based operator $\tilde{Q}_{IG}$ is a function of $\nabla_S N(x_g)$ on $\tilde{\Omega}$ resulting in the information flow from the interior to the boundary and vice versa.

Likewise, we define the second block of the continuous homogenization-based prolongation operator denoted by $\bar{Q}$ which relates the information between the auxiliary coarse grid and the interior micro grid nodes

$$\bar{Q}: \tilde{G} \rightarrow G_L \tag{32}$$

which is partitioned as

$$\bar{Q} = [\tilde{Q}_{LI} \quad \tilde{Q}_{LL}] \tag{33}$$

such that

$$\tilde{Q}_{LI}: \tilde{G}_I \rightarrow G_L \quad \text{and} \quad \tilde{Q}_{LL}: \tilde{G}_L \rightarrow G_L \tag{34}$$

Consequently, the continuous homogenization-based prolongation operator $\tilde{Q}$ can be structured as follows

$$\tilde{Q} = \begin{bmatrix} \tilde{Q}_{II} & 0 & \tilde{Q}_{IG} \\ \tilde{Q}_{LI} & \tilde{Q}_{LL} & 0 \end{bmatrix} \tag{35}$$

The continuous homogenization-based restriction operators $\tilde{Q}^*: G \to \tilde{G}$ and $\hat{Q}^*: G_I \to \hat{G}$ are conjugated to $\tilde{Q}$ and $\hat{Q}$, and are schematically denoted as

$$\tilde{Q}^* = \begin{bmatrix} \tilde{Q}^*_{II} & \tilde{Q}^*_{LI} \\ 0 & \tilde{Q}^*_{LL} \\ \tilde{Q}^*_{IG} & 0 \end{bmatrix} \quad \text{and} \quad \hat{Q}^* = \begin{bmatrix} \tilde{Q}^*_{II} \\ \tilde{Q}^*_{IG} \end{bmatrix} \tag{36}$$

For subsequent derivations we will introduce the following notation:

$\tilde{u} = [\tilde{u}_I; \tilde{u}_L; \tilde{u}_G]^*$ auxiliary grid displacement vector, where $\tilde{u}_I \in \tilde{G}_I$, $\tilde{u}_L \in \tilde{G}_L$, $\tilde{u}_G \in \tilde{G}_G$.

$\hat{u} = [\tilde{u}_I; \tilde{u}_G]^*$ macro-grid displacement vector on $\hat{G}$.

$u = [u_I; u_L]^*$ micro-grid displacement vector, such that $u_I \in G_I$ and $u_L \in G_L$;

$$\tilde{A} = \begin{bmatrix} \tilde{A}_{II} & \tilde{A}_{IL} & \tilde{A}_{IG} \\ \tilde{A}_{LI} & \tilde{A}_{LL} & 0 \\ \tilde{A}_{GI} & 0 & \tilde{A}_{GG} \end{bmatrix}$$ auxiliary grid stiffness matrix on $\tilde{G}$;

$$\hat{A} = \begin{bmatrix} \hat{A}_{II} & \hat{A}_{IG} \\ \hat{A}_{GI} & \hat{A}_{GG} \end{bmatrix}$$ macro-grid stiffness matrix on $\hat{G}$, such that $\hat{A}_{GG} = \tilde{A}_{GG}$ and $\hat{A}_{IG} = \tilde{A}_{IG}$;

$$A = \begin{bmatrix} A_{II} & A_{IL} \\ A_{LI} & A_{LL} \end{bmatrix}$$ micro-grid stiffness matrix on G;

$\tilde{f} = [\tilde{f}_I; \tilde{f}_L; \tilde{f}_G]^*$ auxiliary grid force vector, where $\tilde{f}_I$, $\tilde{f}_L$, $\tilde{f}_G$ are nodal forces acting on grids $\tilde{G}_I$, $\tilde{G}_L$, $\tilde{G}_G$, respectively.

$\hat{f} = [\hat{f}_I; \hat{f}_G]^*$ macro-grid force vector acting on $\hat{G}$, such that $\hat{f}_G = \tilde{f}_G$;

$f = [f_I; f_L]^*$ micro-grid force vector, where f_I and f_L are nodal forces acting on grids G_I and G_L, respectively.

We note that the displacement vectors $\tilde{u}$ and $\hat{u}$ are related via orthogonal assembly operator L given by

$$L = \begin{bmatrix} I & 0 & 0 \\ 0 & 0 & I \end{bmatrix} \tag{37}$$

where I is an identity matrix of an appropriate size, such that

$$\hat{u} = L\tilde{u} \tag{38}$$

We are now in a position to formulate an algebraic system of equations for the two-scale linear elasticity problem in heterogeneous media. It consists of finding a pair of nodal displacement vectors $(\hat{u}, u)$ such that

$$1/2((\hat{A}\hat{u}, \hat{u}) + (Au, u)) - (\hat{f}, \hat{u}) - (f, u) \Rightarrow \min_{(\hat{u}, u)} \tag{39}$$

subjected to the compatibility condition at the interface

$$u_I = \hat{Q}\hat{u} \tag{40}$$

Minimization of (39) with respect to $(\hat{u}, u)$ subjected to the interface condition (40) yields a system of linear equations:

$$\begin{bmatrix} (\hat{A} + \hat{Q}^* A_{II} \hat{Q}) & \hat{Q}^* A_{IL} \\ A_{LI}\hat{Q} & A_{LL} \end{bmatrix} \begin{bmatrix} \hat{u} \\ u_L \end{bmatrix} = \begin{bmatrix} \hat{f} + \hat{Q}^* f_I \\ f_L \end{bmatrix} \tag{41}$$

The system of linear equations (41) can be solved either directly or iteratively. The direct solver is not well suited for an adaptive computational environment, where the region requiring a more detailed interrogation, is not known a priori.

It is our objective to develop an iterative solution procedure, which exploits the solution of the auxiliary problem on $\tilde{G}$ in order: (i) to identify the regions where the homogenized finite element model is inadequate, and (ii) to predict the lower frequency response of the two-scale model.

Section 5 deals with the first item, while in Section 4.2 we focus on developing a two-scale iterative solution scheme.

4.2. *Iterative two-scale solution procedures*

The three-step iterative solution procedure based on minimization of energy functional (39) on various subspaces is given below:

Step 1

Find the correction $\tilde{v}^i$ which minimizes the two-scale energy functional (39) on the subspace of the auxiliary grid functions, i.e.

$$1/2((\hat{A}(\hat{u}^i + L\tilde{v}^i), \hat{u}^i + L\tilde{v}^i) + (A(u^i + \tilde{Q}\tilde{v}^i), u^i + \tilde{Q}\tilde{v}^i)) - (\hat{f}, \hat{u}^i + L\tilde{v}^i) - (f, u^i + \tilde{Q}\tilde{v}^i) \Rightarrow \min_{\tilde{v}^i} \quad (42)$$

where the superscripts refer to the iteration count.

Note that the auxiliary grid correction $\tilde{v}^i$ has a similar partitioning to $\tilde{u}$, i.e.

$$\tilde{v} = [\tilde{v}_I; \tilde{v}_L; \tilde{v}_G]^* \quad \text{and} \quad \hat{v} = [\tilde{v}_I; \tilde{v}_G]^* .$$

A direct minimization of (42) with respect to $\tilde{v}^i$ yields:

$$(L^*\hat{A}L + \tilde{Q}^*A\tilde{Q})\tilde{v}^i = L^*(\hat{f} - \hat{A}\hat{u}^i) + \tilde{Q}^*(f - Au^i) \quad (43)$$

The first term on the left-hand side represents the assembled form of the macro-grid stiffness matrix. In Section 3 we have shown that for an infinitesimally small unit cell the second term represents an assembled form of the stiffness matrix on the auxiliary grid $\tilde{G}_L$, i.e.

$$\lim_{\varepsilon \to 0} (L^*\hat{A}L + \tilde{Q}^*A\tilde{Q}) = \tilde{A} \quad (44)$$

In practice, however, the value of the representative unit cell size ε is finite, and thus (44) is satisfied only approximately. Nevertheless, for the purpose of approximating the auxiliary grid correction $\tilde{v}^i$ we will replace the Jacobian matrix in (43) by $\tilde{A}$. In the adaptive environment this approximation will significantly reduce computational cost, since only a single factorization of the auxiliary stiffness matrix is required, independent of the refinement process.

Step 2

Once the auxiliary grid correction has been carried out it is necessary to update the solution in the auxiliary grid

$$\tilde{u}^{i+1} = \tilde{u}^i + \omega\tilde{v}^i \qquad \hat{u}^{i+1} = \hat{u}^i + \omega L\tilde{v}^i \qquad u^{i+1} = u^i + \omega\tilde{Q}\tilde{v}^i \quad (45)$$

The relaxation parameter is introduced to account for the approximation introduced in (44) as a result of a finite size of the unit cell. The relaxation parameter is found from a 1-D minimization of the energy functional along the direction $\tilde{v}^i$ evaluated in the previous step (43)

$$1/2((\hat{A}(\hat{u}^i + \omega L\tilde{v}^i), \hat{u}^i + \omega L\tilde{v}^i) + (A(u^i + \omega\tilde{Q}\tilde{v}^i), u^i + \omega\tilde{Q}\tilde{v}^i)) - (\hat{f}, \hat{u}^i + \omega L\tilde{v}^i) - (f, u^i + \omega\tilde{Q}\tilde{v}^i) \Rightarrow \min_{\omega} \quad (46)$$

which yields

$$\omega = \frac{(L^*(\hat{f} - \hat{A}\hat{u}^i) + \tilde{Q}^*(f - Au^i), \tilde{v}^i)}{((L^*\hat{A}L + \tilde{Q}^*A\tilde{Q})\tilde{v}^i, \tilde{v}^i)} \tag{47}$$

Step 3

Find the correction v_L^i on the micro-grid, which minimizes the energy functional on the subspace of the functions on the micro-grid G_L, i.e. keeping $\hat{u}^i$ fixed

$$1/2((\hat{A}\hat{u}^i, \hat{u}^i) + (A(u^i + v^i), u^i + v^i)) - (\hat{f}, \hat{u}^i) - (f, u^i + v^i) \Rightarrow \min_{v^i} \tag{48}$$

where $v_l^i = 0$ on Γ_l to maintain compatibility.

The direct minimization of (48) yields

$$A_{LL}v_L^i = f_L - A_{LI}\hat{Q}\hat{u}^i - A_{LL}u_L^i \tag{49}$$

If (49) is directly solved and

$$u_L^{i+1} = u_L^i + v_L^i \tag{50}$$

then the three-steps iterative process described is in the spirit of FAC algorithm [8, 9], subsequently to be referred as FAC-Comp.

It is important to note that since the unit cell is very small, the number of degrees-of-freedom in micro-grid could be larger than in the macro-grid. Secondly, the solution behavior in the micro-grid is highly oscillatory with a lower frequency response similar to that in the auxiliary mesh. These two observations suggest to replace the direct solution of (49) by smoothing of the form given by

$$u_L^{i+1} = u_L^i + \tau^i P_{LL}(f_L - A_{LI}\hat{Q}\hat{u}^i - A_{LL}u_L^i) \tag{51}$$

where P_{LL} is a preconditioner on the micro-grid G_L and τ^i is a relaxation parameter given by

$$\tau^i = \frac{(f_L - A_{LI}\hat{Q}\hat{u}^i - A_{LL}u_L^i, v_L^i)}{(A_{LL}v_L^i, v_L^i)} \tag{52}$$

where $v_L^i = P_{LL}(f_L - A_{LI}\hat{Q}\hat{u}^i - A_{LL}u_L^i)$.

This variant has similar characteristics to the linear version of MLAT [7], and will be termed as MLAT-Comp.

5. The microscale reduction error estimators and indicators

5.1. Formulation

In this section we quantify idealization errors associated with homogenization of periodic heterogeneous medium and present their use in the adaptive procedure. The proposed Microscale Reduction Error (MRE) estimator is based on assessing the uniform validity of the double scale asymptotic expansion [1–3], which is given by a rapidly decreasing asymptotic sequence

$$u_i^\varepsilon = u_i^0(x) + \varepsilon H_{ijk}(y)u_{(j,k)}^0(x) + \varepsilon^2 P_{ijkl}(y)u_{j,kl}^0(x) + O(\varepsilon^3) \tag{53}$$

Following [1–3], the Y-periodic function P_{ijkl} is found from the higher-order equilibrium equation

$$\frac{\partial}{\partial y_p}(D_{ipkl}(P_{(k,l)mnj} + H_{kmn}\delta_{lj})) + D_{ijkl}(H_{(k,l)mn} + \delta_{km}\delta_{ln}) - \tilde{D}_{ijmn} = 0$$
$$\text{on unit cell } \theta_Y \tag{54}$$

Problem (54) is solved using finite element method. The resulting asymptotic expansion of the stress field is given by

$$\sigma_{ij} = A^0_{ijkl}(y)u^0_{(k,l)}(x) + \varepsilon A^1_{ijklq}(y)u^0_{k,lq}(x) + O(\varepsilon^2) \tag{55}$$

where

$$A^0_{ijmn}(y) = D_{ijkl}(H_{(k,l)mn} + \delta_{k,m}\delta_{ln})$$
$$A^1_{ijmnp}(y) = D_{ijkl}(P_{(k,l)mnp} + H_{kmn}\delta_{lp}) \tag{56}$$

In the classical homogenization theory only the first term in (55) is considered, while the second term is neglected. Thus, the quality of the homogenization is assessed on the basis of the relative magnitude of the first term neglected to those taken into account. The resulting Microscale Reduction Error estimator is defined as

$$\eta = \frac{\|\varepsilon A^1 \nabla^2 u^0\|_{0,\Omega}}{\|A^0 \nabla u^0\|_{0,\Omega}} \tag{57}$$

where $\|\cdot\|_{0,\Omega}$ is a L_2-norm defined as

$$\|h(x, y)\|_{0,\Omega} = \frac{1}{Y_A}\left(\sum_{i,j}\int_\Omega \int_Y h^2_{ij}(x, y)\,dY\,d\Omega\right)^{1/2} \tag{58}$$

To steer process of adaptivity we define the MRE indicator, which reflects the relative contribution of individual element in the auxiliary mesh to the total microscale reduction error

$$\eta^e = \beta^e \frac{\|\varepsilon A^1_{klq} u^0_{k,lq}\|_{0,\Omega^e}}{\|A^0_{kl} u^0_{(k,l)}\|_{0,\Omega}} \qquad \beta^e = \frac{\Omega}{\Omega^e} \tag{59}$$

This approach is equivalent to the one employed for discretization error indicator in [11].

3.2. Explicit form of η and η^e in 1D

In this subsection, we derive a closed form MRE indicators and estimators for a 1D model problem in order to study various factors affecting the microscale reduction errors.

Closed form solution of (4), (54) for H and P yields

$$A^0 = \tilde{D} = \left(\frac{1}{h}\int_0^h D^{-1}\,dy\right)^{-1} = \text{const}_1 \tag{60}$$

and

$$A^1 = \frac{\tilde{D}}{h}\int_0^h H\,dy = \text{const}_2 \tag{61}$$

where $\tilde{D}$ are the effective material properties and h is the unit cell size. Inserting (60) and (61) into (57) yields the one-dimensional counterpart of the microscale reduction error estimator given by

$$\eta = \int_0^h \left(\frac{\tilde{D}}{D(y)} - 1\right) dy \frac{\left\|\dfrac{d^2u^0}{dx^2}\right\|_{0,\Omega}}{\left\|\dfrac{du^0}{dx}\right\|_{0,\Omega}} \tag{62}$$

For the unit cell consisting of two phases with compliances $C_1 = 1/D_1$ and $C_2 = 1/D_2$ (the overall compliance $\tilde{C} = C_1 + C_2$, $\tilde{C} = 1/\tilde{D}$), α the volume fraction, the resulting MRE estimators is given by

$$\eta = h \frac{|C_1 - C_2|}{\tilde{C}} \frac{\alpha(1-\alpha)}{2} \frac{\left\| \frac{d^2 u^0}{dx^2} \right\|_{0,\Omega}}{\left\| \frac{du^0}{dx} \right\|_{0,\Omega}} \tag{63}$$

From the above expression we can identify four factors affecting the microscale reduction error:

(1) The size of the unit cell, h.
(2) The normalized difference of compliances, $|C_1 - C_2|/\tilde{C}$.
(3) The fiber volume ratio, $\alpha(1-\alpha)/2$.
(4) The macro strain gradients, $\|d^2u^0/dx^2\|_{0,\Omega}$.

It can be seen that the error estimator is asymptotically exact in the sense that the microscale reduction errors vanish if either the normalized strain gradients are negligible, the unit cell is infinitesimally small, the compliances of the microconstituents are almost identical or the volume ratio is close to either zero or one, which corresponds to a homogeneous material.

6. Numerical results

Our numerical experimentation agenda includes two test problems. The first example deals with a square plate containing a centered crack. Geometry, boundary and symmetry conditions, material properties, loading and unit cell description are shown in Fig. 3. The finest level macro-mechanical grid $\tilde{G}$ with homogenized material properties consists of 64 elements along each co-ordinate where each element coincides with the unique unit cell boundaries.

The distribution of homogenization errors as indicated by MRE indicator is shown in Fig. 4(a). The micro-grid, G, is placed on the portion of the problem domain, which encompasses the contour of $\eta^e > 1$ as shown in Fig. 4(a). For simplicity the grid G on Ω is selected to be of a rectangular shape. Thus, the two-scale model consists of a micro-grid in the region encompassed by 12×20 unit cells in the vicinity of the crack tip, while elsewhere $\tilde{\Omega}/\Omega$, the finite element mesh is constructed on the macro-scale.

The multi-grid process was carried out on three different meshes: two-scale (macro–micro) grid and two auxiliary macro-grids. We used V-cycle with 1 pre- and 1 post-smoothing Gauss–Seidel iterations on the two auxiliary levels and 2 pre- and 2 post-smoothing Jacobi iterations on the finest level. As usual, on the coarsest level we used a direct solver. As a termination criterion we used the following tolerance to bound the ratio of the two-scale grid residual norm versus the norm of the right-hand side vector, i.e.

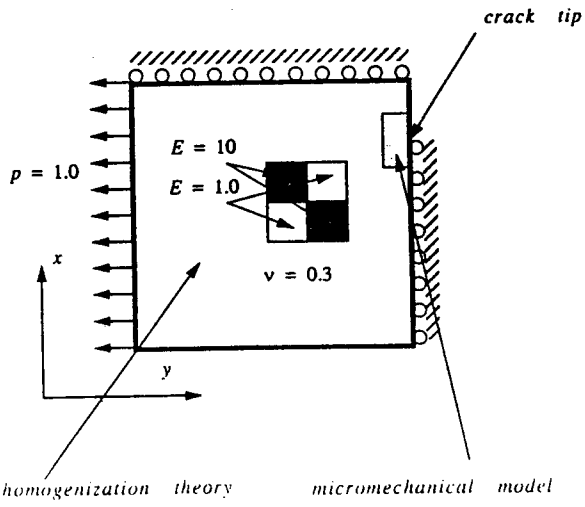
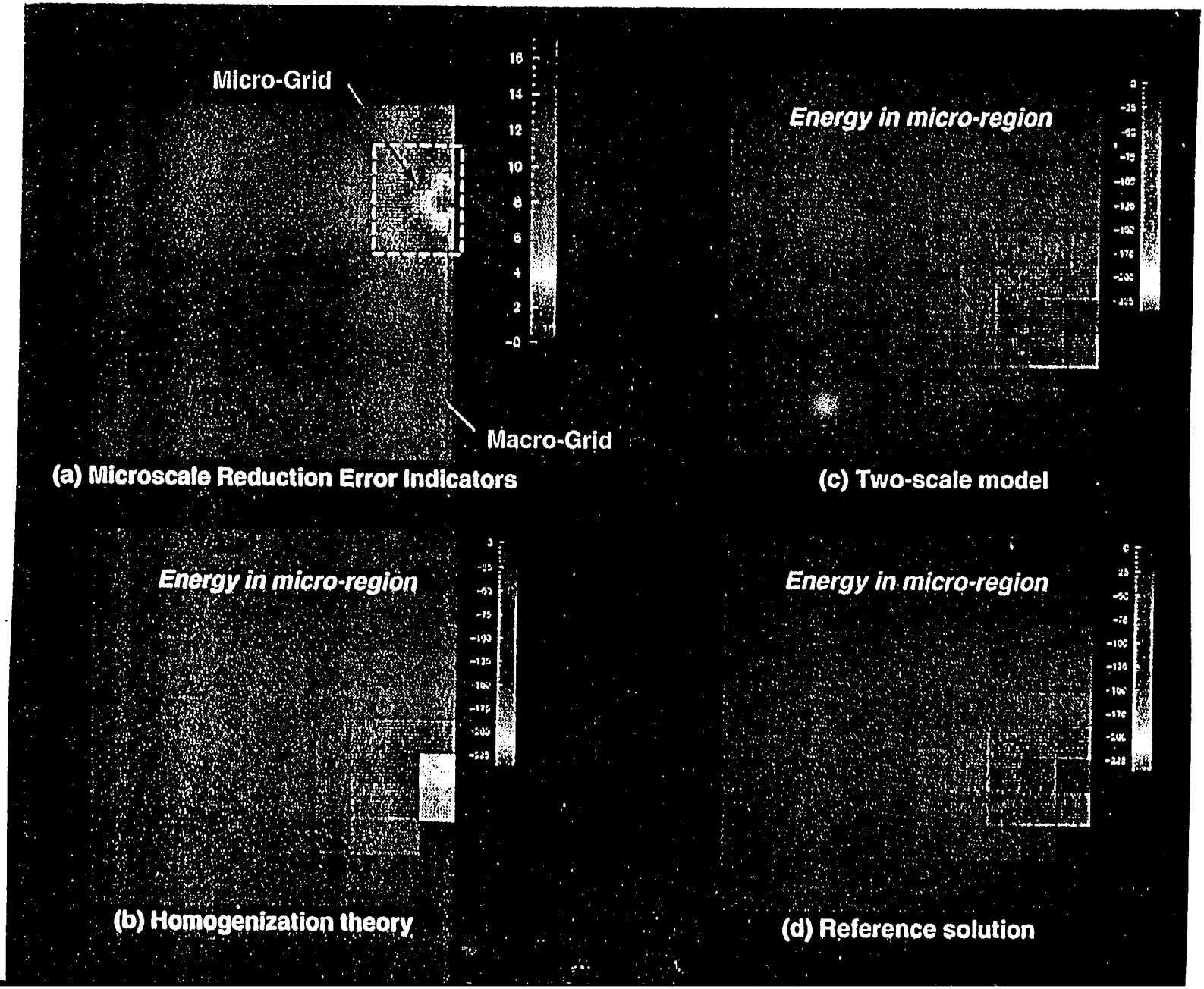


Fig. 3. Plate with the centered crack: geometry, boundary conditions, material properties and loading.



J. Tinsley Oden / Comput. Methods Appl. Mech. Engrg. 126 (1995) 17–38

$$\|r\|_1 / \|f\|_1 \leq \text{eps} \quad \text{where} \quad \|v\|_1 = \sum_{i=1}^{n} |v_i| \quad v \in R^n \tag{64}$$

To obtain convergence with tolerance of $\text{eps} = 10^{-3}$ it was necessary to carry out 14 cycles using MLAT-Comp algorithm and 7 cycles with FAC-Comp method.

The resulting energy distribution absorbed in a unit cell in the micro-grid is shown in Fig. 4(c). For comparison purpose also shown are the results obtained on the basis of the postprocessing from the classical homogenization theory [12] and the reference solution where the entire problem domain $\tilde{\Omega}$ is modeled on the microscale. It can be seen that the postprocessing procedure from the classical homogenization theory significantly underestimates the energy absorbed in the close vicinity to the crack tip. On the other hand in the radius of 2–3 unit cells away from the crack tip, the classical homogenization theory is adequate.

In the second example, we consider a laminated plate $[90_4/0_{16}/90_4]_s$ subjected to uniform axial tension. Geometry, boundary and symmetry conditions and the micro-structure cross section for the different layers are shown in Fig. 5. We considered Glass–Epoxy composite material with the following material properties: $E_1 = 72.3$, $\nu_1 = 0.22$ and $E_2 = 2.92$, $\nu_2 = 0.35$. The uniform tension load was applied normal to the xy plane. The finest level of macro-grid $\tilde{G}$ consists of 24 elements along the co-ordinate x (thickness direction) and 192 along y, each element coinciding with the unique unit cell.

The distribution of the homogenization errors and the region selected for micro-mechanical modeling are shown in Fig. 6(a). The micro-grid consists of 14 400 elements placed in the region encompassed by 24×24 unit cells in the vicinity of the free edge. The two-grid model contains approximately 38 000 degrees-of-freedom. The multi-grid process was carried out on three different meshes: two-scale (macro–micro) grid and two auxiliary macro-grids. We used V-cycle with 1 pre- and 1 post-smoothing Gauss–Seidel iterations on the auxiliary levels; 3 pre- and 3 post-smoothing Jacobi iterations on the finest level and a direct solver on the coarsest level. 1% error of residual (64) was obtained in 8 cycles of MLAT-Comp algorithm and 8 cycles of FAC-Comp method.

Fig. 6(b,c,d) compare the shear stress distribution in the micro-grid as obtained using two-scale model, homogenization theory and the reference solution. Results are consistent with our previous observations, i.e. inadequacy of the postprocessing technique from the classical homogenization theory in the 'hot spots' as opposed to striking accuracy of the two-scale model.

To study boundary layer effect between two dissimilar layers in the axial tension problem we consider a micro-grid of approximately 15 000 degrees-of-freedom on the entire problem domain. The same solution strategy has been employed. It was necessary to perform 5 multi-grid cycles to achieve convergence with tolerance 0.1%. Figs. 7 and 8 compare the distribution of peeling stress σ_x and shear

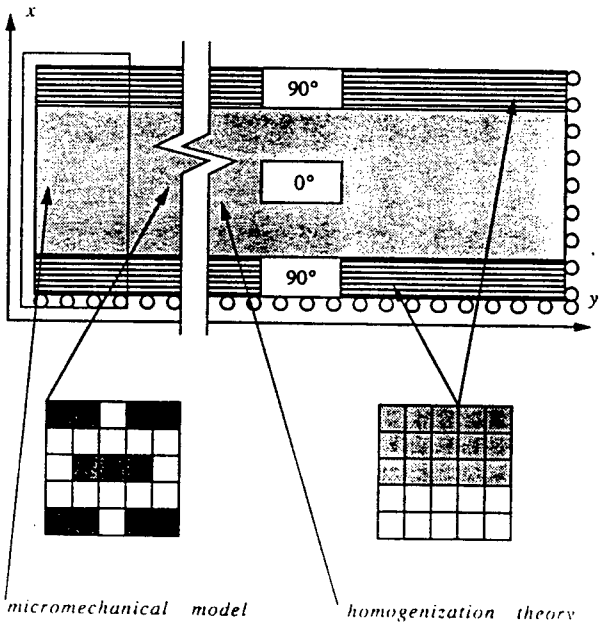
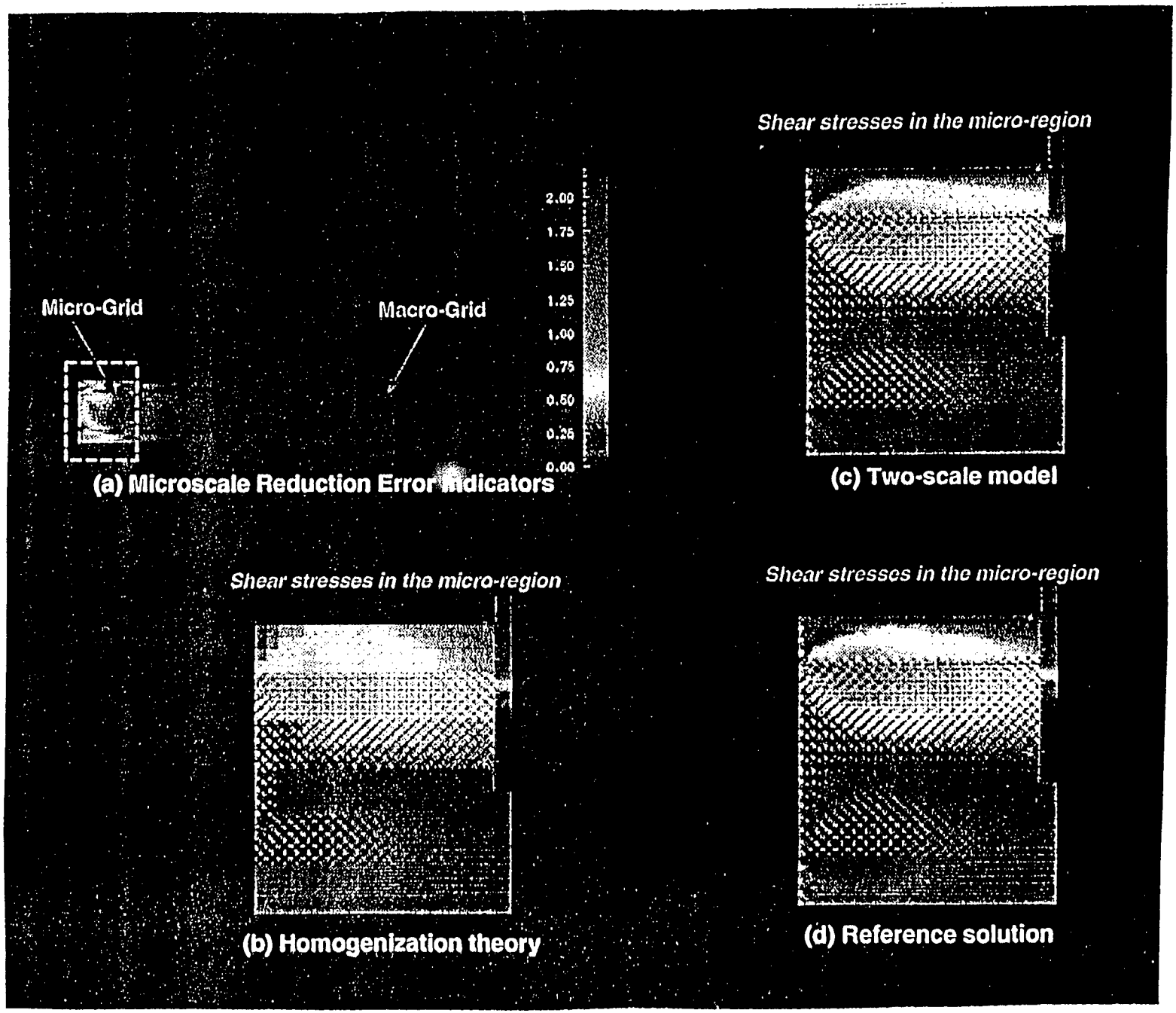


Fig. 5. Plate subjected to the axial tension: geometry, boundary conditions and microstructure.


Micro-Grid
Macro-Grid
2.00
1.75
1.50
1.25
1.00
0.75
0.50
0.25
0.00
(a) Microscale Reduction Error Indicators
Shear stresses in the micro-region
(c) Two-scale model
Shear stresses in the micro-region
(b) Homogenization theory
Shear stresses in the micro-region
(d) Reference solution

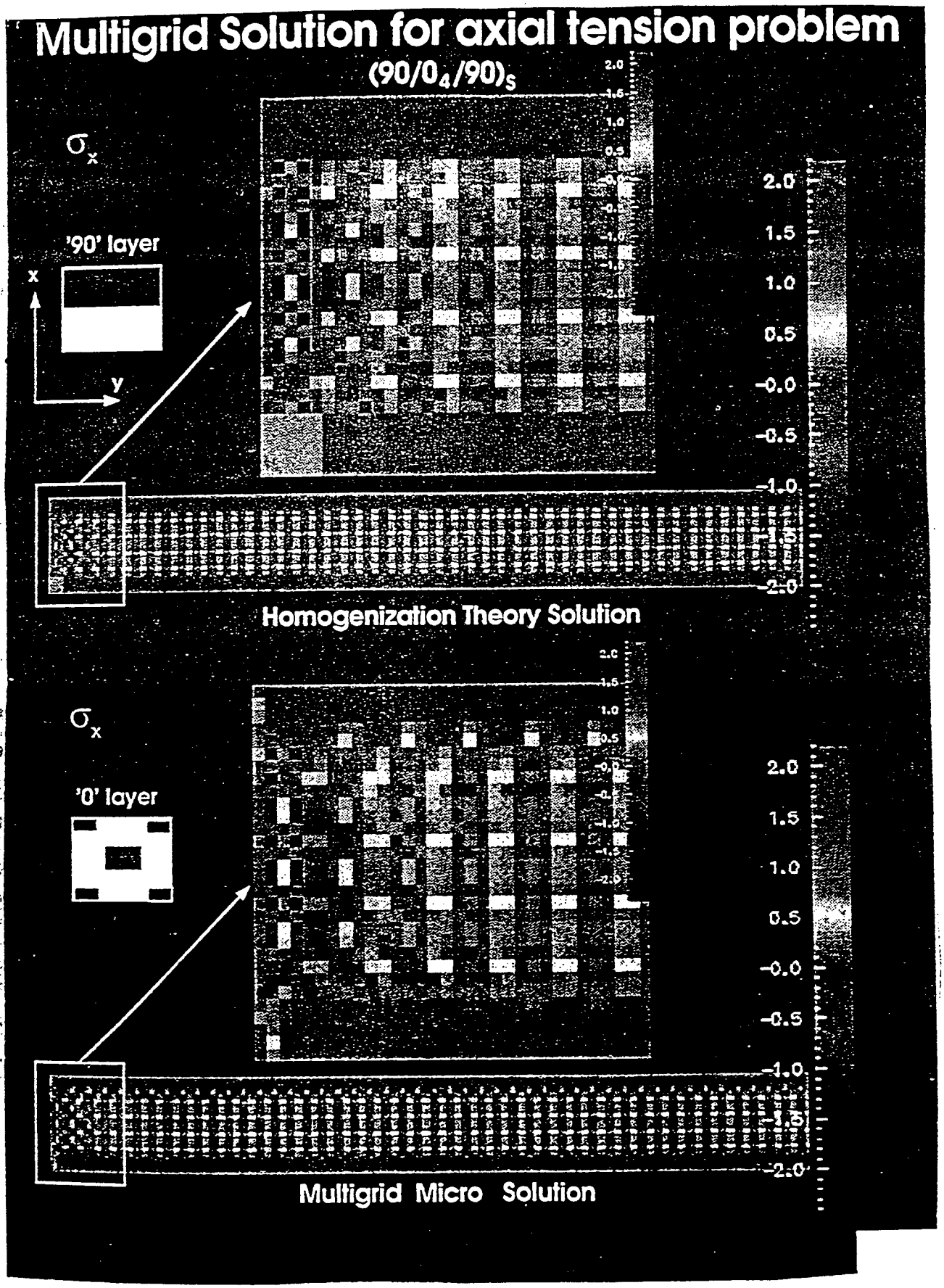


Fig. 7. Plate subjected to the axial tension: the resulting peeling stresses.

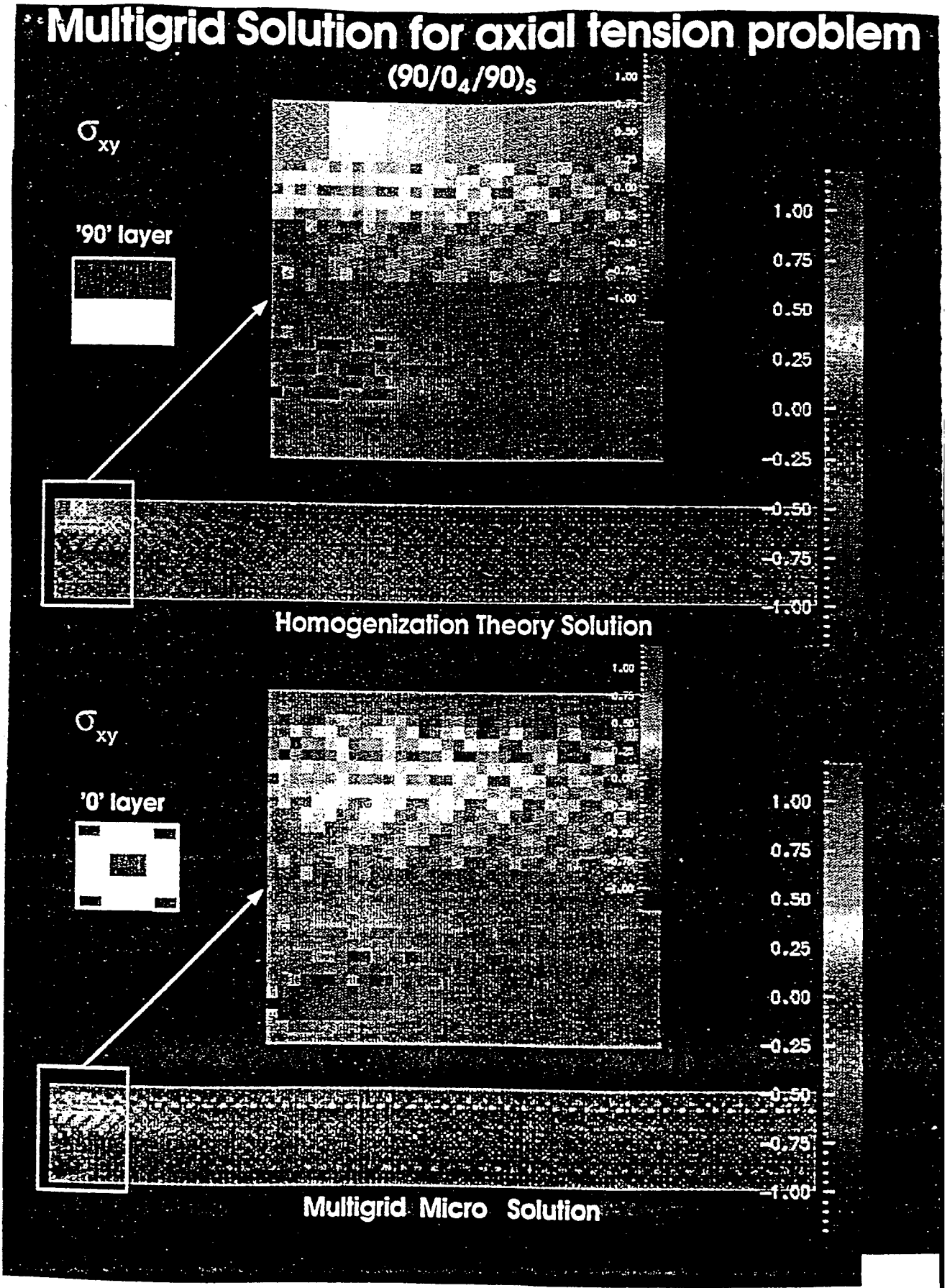


Fig. 8. Plate subjected to the axial tension: the resulting shear stresses.

stress σ_{xy} as obtained using the postprocessing from the classical homogenization theory and the finite element solution of the discrete heterogeneous media. It can be seen that except for the close vicinity to the free edge the values of σ_x as obtained with the two methods are in good agreement. On the other hand, the distribution of shear stress σ_{xy} differs not only in the vicinity of the free edge, but along the entire interface between the two dissimilar layers. The finite element of the discrete heterogeneous model shows oscillatory shear stresses developed along the entire interface, while the solution of homogenized problem shows no such stress concentration. The magnitude of these shear stresses is roughly 1/3 of the shear stresses developed at the interface, but even so, these interface shear stresses may significantly affect the propagation of delamination cracks emanating from the free edge.

The primary reason why the postprocessing technique fails to detect these interface shear stresses is because it permits displacement incompatibility within a unit cell at the interface between dissimilar layers. On the other hand, a finite element solution of the discrete heterogeneous model enforces such compatibility exactly, giving rise to oscillatory shear stresses at the interface.

In the last numerical example we study the effectiveness of MLAT-Comp algorithm for solving very large two-scale models. The problem domain, boundary conditions, loading, and the unit cell model are the same as in the first example. The two-scale model contained a micromechanical finite element mesh in the region of 176×176 unit cells in the vicinity of the crack tip, while elsewhere, the finite elements were treated as homogenized. The macro-mechanical finite element mesh consists of 352 elements along each co-ordinate. Each macro-mechanical finite element coincides with the unique unit cell. Hence, this problem contains 435 074 independent degrees-of-freedom.

The multi-grid processes was carried out on 4 different meshes: two-scale (macro–micro) mesh and three auxiliary macro-mechanical meshes. We used V-cycle with 1 pre- and 1 post-smoothing Guass–Seidel iterations on the two auxiliary levels and 2 pre- and 2 post-smoothing Jacobi iterations on the finest level. As usual, on the coarsest level we used a direct solver. It was necessary to perform 15 multi-grid cycles to provide the convergence with eps = 0.01 in accordance with criteria (64). Only MLAT-Comp algorithm was tested, since the micro-grid contained over 100 000 nodes, and the direct solution on the micro-grid is not practical. This computational process takes about 8.2 hours on the SPARC station LX, which is 17.2 times faster than the use of a skyline direct solver and the storage savings are significant.

Appendix

Two dimensional idealization of $[90_p/0_q]_s$ *laminated plate*

Consider a $[90_p/0_q]_s$ laminated plate as shown in Fig. 9. The uniform axial tension is applied along the co-ordinate Z. In order to reduce the problem dimension to 2-D we assume that the shear stresses σ_{xz}, σ_{yz} and the shear strains ε_{xz}, ε_{yz} are negligible and it is necessary to idealize the microstructure in '90° layer' as a stack of orthotropic layers parallel to the interface.

For the purpose of calculating the equivalent mechanical properties of this layer, we consider the auxiliary problem given in Fig. 10. The elasticity moduli, the Poisson's ratios and the volume fractions are denoted by (E_i, ν_i and k_i), ($i = 1, 2$), respectively.

The homogenized elasticity moduli are found on the basis of the rule of mixtures

$$E_x = E_y = k_1 E_1 + k_2 E_2 \qquad E_z = (k_1 E_1^{-1} + k_2 E_2^{-1})^{-1} \tag{65}$$

The Poisson's ratio in the plane XY is evaluated on the basis of the equilibrium condition along the co-ordinate Y under the uniform tension in X ($\varepsilon_x = 1$)

$$k_1 E_1 (\nu_1 - \nu_{xy}) = k_2 E_2 (\nu_{xy} - \nu_2) \tag{66}$$

which yields

$$\nu_{xy} = \nu_{yx} = (k_1 E_1 \nu_1 + k_2 E_2 \nu_2)/E_x \tag{67}$$

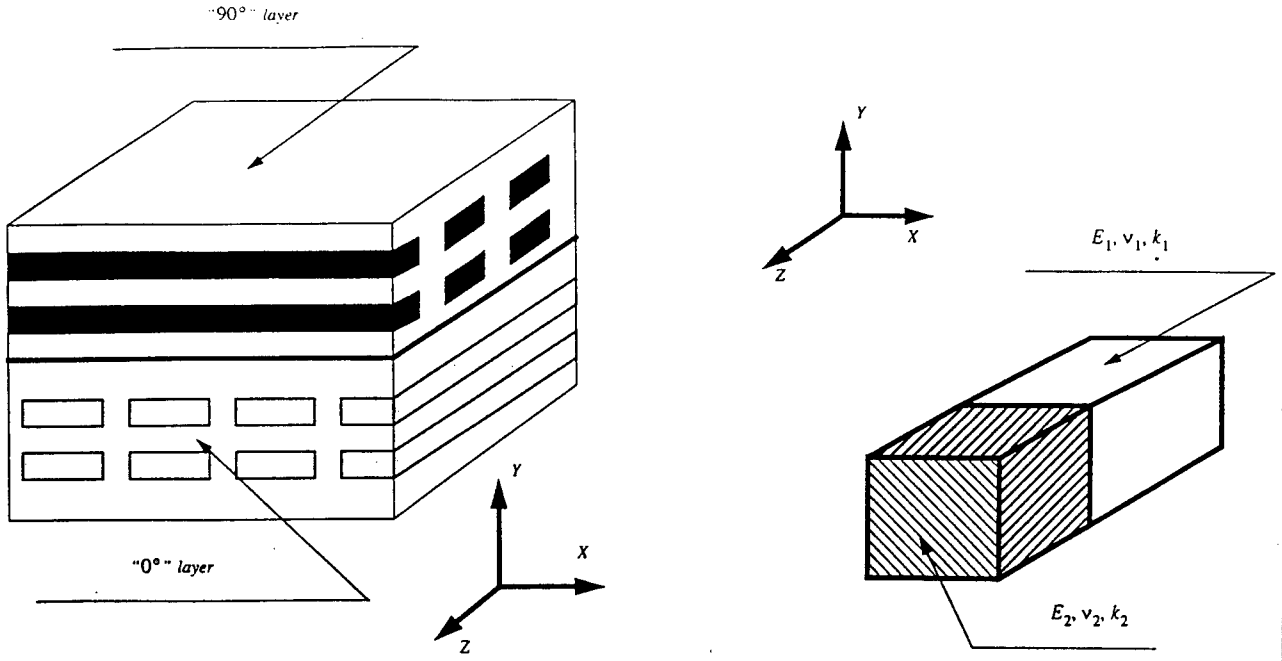


Fig. 9. Two-dimensional idealization of the laminated plate.

Fig. 10. The auxiliary problem for calculation of the equivalent mechanical properties.

Similarly, the equilibrium condition along the co-ordinate X under the uniform tension in Z ($\varepsilon_z =$ yields

$$k_1 E_1(e_1 - \nu_{xz}) = k_2 E_2(\nu_{xz} - e_2)$$
$$e_1 = E_z \nu_1 / E_1 \qquad e_2 = E_z \nu_2 / E_2 \tag{6}$$

Exploiting the relation for orthotropic material, $E_z \nu_{zx} = E_x \nu_{xz}$, and using the symmetry condition in and Y gives

$$\nu_{xz} = \nu_{yz} = E_z(k_1 \nu_1 + k_2 \nu_2)/E_x$$
$$\nu_{zx} = \nu_{zy} = k_1 \nu_1 + k_2 \nu_2 \tag{6}$$

Eqs. (65), (67) and (69) represent the equivalent orthotropic material properties for the two-pha material described in Fig. 10.

In the second part of this appendix we will show that for the axial tension problem in t heterogeneous medium only a two-dimensional discretization is necessary.

Consider the two-scale asymptotic expansion of the strain field for the axial tension problem

$$\varepsilon_{\alpha\beta} = (\delta_{\alpha\gamma}\delta_{\beta\delta} + h_{(\alpha,\beta)\gamma\delta})\varepsilon^0_{\gamma\delta} + h_{(\alpha,\beta)33}\varepsilon^0_{33} + O(\varepsilon)$$
$$= (\delta_{\alpha k}\delta_{\beta l} + h_{(\alpha,\beta)kl})\varepsilon^0_{kl} + O(\varepsilon) \tag{7}$$

and

$$\varepsilon_{33} = \varepsilon^0_{33} = \text{const} \qquad \varepsilon_{\alpha 3} = \varepsilon^0_{\alpha 3} = 0 \tag{7}$$

where Greek subscripts range from one to two. The corresponding strain variation is given by

$$\delta\varepsilon_{\alpha\beta} = (\delta_{\alpha\gamma}\delta_{\beta\delta} + h_{(\alpha,\beta)\gamma\delta})\,\delta\varepsilon^0_{\gamma\delta} + \delta h_{(\alpha,\beta)kl}\varepsilon^0_{kl} \tag{7}$$

while other components of the strain variation vanish.

From the axial tension problem in the uniform tension, $\varepsilon_{33} = \varepsilon^0_{33}$, and the weak form of equilibrium states that

$$\int_\Omega \delta\varepsilon_{\alpha\beta} D_{\alpha\beta mn} \varepsilon_{mn} \, d\Omega = 0 \quad \forall u \in C^0(\Omega) \tag{73}$$

Substituting (70)–(72) into (73) yields

$$\int_\Omega ((\delta_{\alpha\gamma}\sigma_{\beta\delta} + h_{(\alpha,\beta)\gamma\delta}) \, \delta\varepsilon^0_{\gamma\delta} + \delta h_{(\alpha,\beta)kl} \varepsilon^0_{kl}) \times (D_{\alpha\beta\xi\eta}(\delta_{\xi m}\delta_{\eta n} + h_{(\xi,\eta)mn}) + D_{\alpha\beta 33}\delta_{3m}\delta_{3n})\varepsilon^0_{mn} \, d\Omega = 0 \tag{74}$$

Applying the integration rule for highly oscillatory functions on θ [1] results in a macro equilibrium equation

$$\int_{\Omega_x} \delta\varepsilon^0_{\alpha\beta} \tilde{D}_{\alpha\beta\gamma\delta} \varepsilon^0_{\gamma\delta} \, d\Omega_x = -\int_{\Omega_x} \delta\varepsilon^0_{\alpha\beta} \tilde{D}_{\alpha\beta 33} \varepsilon^0_{33} \, d\Omega_x \quad \forall u \in C^0(\Omega) \tag{75}$$

where

$$\begin{aligned} \tilde{D}_{\alpha\beta\gamma\delta} &= \frac{1}{\theta_Y} \int_\theta (\delta_{\alpha\nu}\delta_{\beta\mu} + h_{(\nu,\mu)\alpha\beta}) D_{\nu\mu\eta\xi} (\delta_{\gamma\eta}\delta_{\delta\xi} + h_{(\eta,\xi)\gamma\delta}) \, d\theta \\ \tilde{D}_{\alpha\beta 33} &= \frac{1}{\theta_Y} \int_\theta (\delta_{\alpha\nu}\delta_{\beta\mu} + h_{(\nu,\mu)\alpha\beta})(D_{\nu\mu\eta\xi} h_{(\eta,\xi)33} + D_{\nu\mu 33}) \, d\theta \end{aligned} \tag{76}$$

and micro (unit cell) equilibrium equations

$$\begin{aligned} \int_\theta \delta h_{(\alpha,\beta)kl} D_{\alpha\beta\xi\eta} h_{(\xi,\eta)\nu\mu} \, d\theta &= -\int_\theta \delta h_{(\alpha,\beta)kl} D_{\alpha\beta\nu\mu} \, d\theta \Rightarrow h_{\xi\nu\mu} \\ \int_\theta \delta h_{(\alpha,\beta)kl} D_{\alpha\beta\xi\eta} h_{(\xi,\eta)33} \, d\theta &= -\int_\theta \delta h_{(\alpha,\beta)kl} D_{\alpha\beta 33} \, d\theta \Rightarrow h_{\xi 33} \end{aligned} \tag{77}$$

For details on finite element discretization of macro and micro equations see [13].

Acknowledgments

The authors wish to thank the referee for his comments on the manuscript. The comparison with the conventional multi-grid method as well as the introduction of the appropriate notation were incorporated at his suggestion.

The support of the ARPA under grant A10234 and NYI award ECS-9257203 are gratefully acknowledged.

References

[1] A. Benssousan, J.L. Lions and G. Papanicoulau, Asymptotic Analysis for Periodic Structures (North Holland, Amsterdam, 1978).
[2] E. Sanchez-Palencia and A. Zaoui, Homogenization techniques for composites. Homogenization Techniques for Composite Media (Springer-Verlag, Berlin, 1985).
[3] N.S. Bakhvalov and G.P. Panasenko, Homogenization of Periodic Medium Processes (Nauka, Moscow, 1984).
[4] Z. Hashin, Theory of composite materials, in: F.W. Wend, H. Liebowitz and N. Perrone, eds., Mechanics of Composite Materials (John Wiley, New York, 1991).
[5] E. Kröner, Bounds of effective elastic moduli of disordered materials, J. Mech. Phys. Solids 25 (1977) 137.
[6] J. Fish and V. Belsky, Multigrid method for periodic heterogeneous media. Part 1: Convergence studies for one-dimensional case, Comput. Methods Appl. Mech. Engrg. 126 (1995) 1.

[7] Achi Brandt, Multi-level adaptive solutions to boundary-value problems, Math. Comput. 31 (1977) 333–390.
[8] S.F. McCormick and J.W. Thomas, The fast adaptive composite grid (FAC) method for elliptic equations, Math. Com 46 (1986) 439–456.
[9] Michael A. Heroux and J.W. Thomas, A comparison of FAC and PCG methods for solving composite grid proble Commun. Appl. Numer. Methods 8 (1992) 573–583.
[10] O.C. Zienkiewicz and J.Z. Zhu, Superconvergent derivative recovery techniques and a posteriori error estimation in finite element method. Part 1: A general superconvergent recovery technique, CR/671/91, Institute of Numerical Meth in Engineering, University College of Swansea, UK, 1991.
[11] J. Fish and S. Markolefas, Adaptive s-method for linear elastostatics, Comput. Methods Appl. Mech. Engrg. 104 (1 363–396.
[12] J.M. Guedes and N. Kikuchi, Preprocessing and postprocessing for materials based on the homogenization method adaptive finite element methods, Comput. Methods Appl. Mech. Engrg. 83 (1990) 143–198.
[13] J. Fish and A. Wagiman, Multiscale finite element method for a locally nonperiodic heterogeneous medium, Compu Mech.: Int. J. 21 (1993) 1–17.

THE MULTI-GRID METHOD FOR A PERIODIC HETEROGENEOUS MEDIUM. PART 3: MULTISCALE MODELING AND ADAPTIVITY

Jacob Fish and Vladimir Belsky
Department of Civil Engineering and Scientific Computation
Research Center,
Rensselaer Polytechnic Institute, Troy, NY 12180, USA

An adaptive computational technique for analyzing problems in a periodic heterogeneous medium is developed. The optimal two-scale computational model consists of the finite element mesh constructed entirely on the microscale in the regions identified by the idealization error indicators, while elsewhere, the modeling level is only sufficient to capture the response of homogenized medium. The resulting linear system of equations is solved using two global-local versions of the multi-grid method with homogenization-based intergrid transfer operators. Numerical experiments show the usefulness of the proposed multi-level adaptive technique for predicting the detailed response of composite specimens.

1. Introduction

The computational complexity of modeling large scale composite structures is enormous. For example, the typical size of the structure (an airplane or a car) is of the order of magnitude of tens of meters, while the diameter of the fastener hole is of the order of millimeters. Prediction of micro-mechanical failure modes necessitates considerations at even smaller scales. The useful life of a structure depends on the quality of modeling at each scale and the ability of a reliable transfer of the appropriate information between various modeling levels. Thus, the need for reliable analysis techniques at several different scales is crucial.

In this paper we present an adaptive two-scale computational technique for analyzing problems in periodic heterogeneous medium, which combines the versatility of multi-grid technology [1-3] with inter-scale communication skills of homogenization-based prolongation and restriction operators [4,5], and reliability of microscale reduction error (MRE) estimators and indicators [6]. The primary objectives of this scheme are

two-fold:

(i) The construction of an optimal two-scale computational model

The optimal two-scale computational model consists of the finite element mesh constructed on the microscale in the regions where there is a necessity to do so, while elsewhere, the modeling level is only sufficient to capture the response of homogenized medium. The microscale reduction error indicators described in section 3, are aimed at assessing the quality of homogenized model, and identifying the regions where the homogenized model should be replaced by a more refined computational model reflecting the details of the microstructure.

(ii) An efficient solution of the two-scale computational model

Due to the scaling issue, it is common in practice to obtain a detailed local response by means of post-processing techniques, such as subjecting a local model to the boundary conditions obtained from the global analysis. This approach does not guarantee a reliable force transfer between the global-local regions, but is very efficient in the sense that the total CPU time is the sum of the global and local analyses as opposed to the roughly quadratic growth in CPU time versus the problem size in the case of the direct couple solution (or, to be more precise, NB^2,where N and B are the problem size and the bound width).

The multigrid technology and in particular MLAT [7] and FAC [8,9] are excellent candidates for reliable global-local analyses of well-conditioned problems, mainly because the CPU time is proportional to the problem size. In this paper, we show that it is possible to maintain similar performance for the case of differential equations with highly oscillatory periodic coefficients giving rise to poor-conditioned linear systems [4], if the homogenization-based intergrid transfer operators [5] are employed in the context of MLAT and FAC.

Between the two techniques, MLAT is more sensitive to the formulation of intergrid transfer operators since the communication between the grids is performed through the entire local region domain as opposed to their interface only as in FAC. This has a direct consequence on the performance of the two methods in the case of periodic heterogeneous medium.

In practice, the local regions requiring consideration on the scale of microconstituents may contain tens thousand of degrees-of-freedom. The philosophy of MLAT, which has a natural mechanism for capturing oscillatory response as well as smooth modes of errors, is more suitable in this case. On the other hand, for locally non-periodic micro-

structure or curved boundaries of local regions, that cannot be sufficiently accurate represented by a spatial periodicity of the unit cell, the global-local procedure in the spirit of FAC seems to be a natural choice.

The outline of this paper is as follows. Section 2 describes an adaptive global-local procedure for periodic heterogeneous medium. Microscale reduction error indicators and estimators aimed at quantifying the quality of homogenization and at steering the adaptive process are given in section 3. A numerical experimentation of the proposed adaptive multiscale computational scheme conclude this manuscript.

2. Description of the iterative global-local algorithm for a heterogeneous medium

In this section we present the formulation of an iterative global-local algorithm for solving the problems in a periodic heterogeneous medium where one or more regions are modeled on the microscale, while elsewhere the medium is treated as homogenized. Our formulation is applicable to general three-dimensional domains with unlimited number of local regions, although for simplicity, our illustrations will be limited to two-dimensional problems with a single local region. Attention will be restricted to a two-level scheme.

2.1 Problem definition and notation

Consider a heterogeneous medium on $\tilde{\Omega}$ which is formed by a special periodicity of a unit cell. Suppose, that the Microscale Reduction Error (MRE) indicator to be described in section 3, indicates, that the classical homogenization procedure is not valid on the portion of the problem domain, denoted by $\Omega \subset \tilde{\Omega}$. Therefore, the optimal computational model consists of the finite element grid $\hat{G}$ on $\hat{\Omega} = \tilde{\Omega}/\Omega$, where the elements are assumed to possess homogenized material properties, and a finite element grid G, with much smaller elements constructed on the microscale.

The grid G, subsequently to be referred as a micro-grid, can be partitioned as follows:

$$G = G_I \cup G_L \tag{1}$$

where G_I are the micro-grid nodes at the interface Γ_I between the two regions, and G_L are the interior micro-grid nodes as shown in Fig. 1.

Likewise the grid $\hat{G}$, termed as a macro-grid, is partitioned in a similar fashion:

$$\hat{G} = \hat{G}_I \cup \hat{G}_G \tag{2}$$

where $\hat{G}_I$ are the macro-grid nodes at the interface Γ_I, which do not have to coincide with the nodes in G_I, and $\hat{G}_G$ are the remaining macro-grid points.

We further define an auxiliary grid $\tilde{G}$ on $\tilde{\Omega}$, where the entire finite element mesh is modeled with homogenized material properties. The grid $\tilde{G}$ is aimed at capturing the lower frequency response of the two-scale grid model $G \cup \hat{G}$. The auxiliary grid is partitioned as follows:

$$\tilde{G} = \tilde{G}_I \cup \tilde{G}_L \cup \tilde{G}_G \tag{3}$$

where $\tilde{G}_I = \hat{G}_I, \tilde{G}_G = \hat{G}_G$; the grid $\tilde{G}_L$ represents auxiliary grid points on Ω as shown in Fig. 1.

To transfer the information between the micro- and macro- scales we employ homogenization-based prolongation operator $\tilde{Q}$ developed in [5]:

$$\tilde{Q} = Q + dQC\nabla_s N(x_g) \qquad on \qquad \tilde{\Omega} \tag{4}$$

where Q is the standard linear prolongation operator; d is the unit cell solution; $\nabla_s N(x_g)$ the symmetric gradient of the shape functions in the auxiliary grid evaluated at the Gauss points in the auxiliary mesh; C the projection operator aimed to maintain C^0 continuity of the displacement field on the micro-scale.

It is important to note that in general operator C is of a global nature, i.e., there is an information flow between any Gauss point and grid node in the auxiliary mesh $\tilde{G}$. This leads to the global nature of the homogenization-based prolongation operator (4), i.e., if the grid G is defined on the entire problem domain, there is an information flow between any two points in G and $\tilde{G}$. At the same time, it is possible to employ a projection operator on the patch-by-patch basis [10] which leads to the homogenization-based prolongation operator (4) of a local nature.

In both cases, the homogenization-based prolongation operator $\tilde{Q}$ consists of two parts. The first denoted by $\hat{Q}$, relates the nodal displacements in the macro grid $\hat{G}$ to those in the micro grids G at the interface Γ_I only:

$$\hat{Q} \bullet \hat{G} \rightarrow G_I \tag{5}$$

where

$$\hat{Q} = \left[\tilde{Q}_{II}\, \tilde{Q}_{IG}\right] \tag{6}$$

such that

$$\tilde{Q}_{II} \bullet \tilde{G}_I \rightarrow G_I \qquad and \qquad \tilde{Q}_{IG} \bullet \tilde{G}_G \rightarrow G_I \tag{7}$$

Note, that the standard linear prolongation operator relates the information at the interface only, between $\tilde{G}_I$ and G_I as opposed to operator $\tilde{Q}_{IG}$ which is a function of $\nabla_s N(x_g)$ on $\tilde{\Omega}$ resulting in the information flow between any two points in $\tilde{G}_G$ and G_I.

Likewise we define a second part of the homogenization-based prolongation operator denoted by $\overline{Q}$ which communicates between the auxiliary grid and interior micro grid nodes:

$$\overline{Q} \bullet \tilde{G} \rightarrow G_L \tag{8}$$

where

$$\overline{Q} = \left[\tilde{Q}_{LI}\, \tilde{Q}_{LL}\right] \tag{9}$$

such that

$$\tilde{Q}_{LI} \bullet \tilde{G}_I \rightarrow G_L \qquad and \qquad \tilde{Q}_{LL} \bullet \tilde{G}_L \rightarrow G_L \tag{10}$$

Hence, the final form of homogenization-based prolongation operator $\tilde{Q}$ can be expressed in the following manner

$$\tilde{Q} = \begin{bmatrix} \tilde{Q}_{II} & 0 & \tilde{Q}_{IG} \\ \tilde{Q}_{LI} & \tilde{Q}_{LL} & 0 \end{bmatrix} \tag{11}$$

The homogenization-based restriction operators $\tilde{Q}^* \bullet G \rightarrow \tilde{G}$ and $\hat{Q}^* \bullet G_I \rightarrow \hat{G}$ are conjugated to $\tilde{Q}$ and $\hat{Q}$, and are schematically denoted as

$$\tilde{Q}^* = \begin{bmatrix} \tilde{Q}_{II}^* & \tilde{Q}_{LI}^* \\ 0 & \tilde{Q}_{LL}^* \\ \tilde{Q}_{IG}^* & 0 \end{bmatrix} \qquad and \qquad \hat{Q}^* = \begin{bmatrix} \tilde{Q}_{II}^* \\ \tilde{Q}_{IG}^* \end{bmatrix} \tag{12}$$

For subsequent derivations we will introduce the following notation:

$\tilde{u} = \left[\tilde{u}_I ; \tilde{u}_L ; \tilde{u}_G\right]^*$ - auxiliary grid displacement vector, where $\tilde{u}_I \in \tilde{G}_I$, $\tilde{u}_L \in \tilde{G}_L$, $\tilde{u}_G \in \tilde{G}_G$.

$\hat{u} = \left[\tilde{u}_I ; \tilde{u}_G\right]^*$ - macro-grid displacement vector on $\hat{G}$.

$u = \left[u_I ; u_L\right]^*$ - micro-grid displacement vector, such that $u_I \in G_I$ and $u_L \in G_L$;

$\tilde{A} = \begin{bmatrix} \tilde{A}_{II} & \tilde{A}_{IL} & \tilde{A}_{IG} \\ \tilde{A}_{LI} & \tilde{A}_{LL} & 0 \\ \tilde{A}_{GI} & 0 & \tilde{A}_{GG} \end{bmatrix}$ - auxiliary grid stiffness matrix on $\tilde{G}$;

$\hat{A} = \begin{bmatrix} \hat{A}_{II} & \hat{A}_{IG} \\ \hat{A}_{GI} & \hat{A}_{GG} \end{bmatrix}$ - macro-grid stiffness matrix on $\hat{G}$, such that $\hat{A}_{GG} = \tilde{A}_{GG}$ and $\hat{A}_{IG} = \tilde{A}_{IG}$;

$A = \begin{bmatrix} A_{II} & A_{IL} \\ A_{LI} & A_{LL} \end{bmatrix}$ - micro-grid stiffness matrix on G;

$\tilde{f} = \left[\tilde{f}_I ; \tilde{f}_L ; \tilde{f}_G\right]^*$ - auxiliary grid force vector, where $\tilde{f}_I, \tilde{f}_L, \tilde{f}_G$ are nodal forces acting on grids $\tilde{G}_I$, $\tilde{G}_L$, $\tilde{G}_G$, respectively.

$\hat{f} = \left[\hat{f}_I ; \hat{f}_G\right]^*$ - macro-grid force vector on $\hat{G}$, such that $\hat{f}_G = \tilde{f}_G$;

$f = \left[f_I ; f_L\right]^*$ - micro-grid force vector, where the nodal forces f_I and f_L are applied on the grids G_I and G_L, respectively.

We note that the displacement vectors $\tilde{u}$ and $\hat{u}$ are related via orthogonal assembly operator L given by

$$L = \begin{bmatrix} I & 0 & 0 \\ 0 & 0 & I \end{bmatrix} \tag{13}$$

where I is an identity matrix of an appropriate size, such that

$$\hat{u} = L\tilde{u} \tag{14}$$

We are now in a position to formulate an algebraic system for two-scale linear elasticity problem in heterogeneous media. It consists of finding a pair of nodal displacement vectors $(\hat{u}, u)$ such that

$$1/2\,(\,(\hat{A}\hat{u},\hat{u}) + (Au,u)\,) - (\hat{f},\hat{u}) - (f,u) \rightarrow \min_{(\hat{u},u)} \tag{15}$$

subjected to the compatibility condition at the interface

$$u_I = \hat{Q}\hat{u} \tag{16}$$

Minimization of (15) with respect to $(\hat{u}, u)$ subjected to the interface condition (16) yields a system of linear equations:

$$\begin{bmatrix} (\hat{A} + \hat{Q}^* A_{II}\hat{Q}) & \hat{Q}^* A_{IL} \\ A_{LI}\hat{Q} & A_{LL} \end{bmatrix} \begin{bmatrix} \hat{u} \\ u_L \end{bmatrix} = \begin{bmatrix} \hat{f} + \hat{Q}^* f_I \\ f_L \end{bmatrix} \tag{17}$$

The system of linear equations (17) can be solved either directly or iteratively. The direct solver is not well suited for adaptive computational environment, where the region requiring a more detailed interrogation, is not known a priori.

It is our objective to develop an inheritant iterative solution procedure, which exploits the solution from the auxiliary problem on $\tilde{G}$ in order:

(i) to identify the regions where the homogenized finite element model is inadequate, and

(ii) to predict the lower frequency response of the two-scale model.

Section 3 deals with the first item, while in section 2.2 we focus on developing such an inheritant solution scheme.

2.2. Iterative two-scale solution procedures

The three-step iterative solution procedure, which is based on minimization of energy functional (15) on various subspaces, is summarized below:

Step 1.

Find the correction $\tilde{v}^i$ which minimizes the two-scale energy functional (15) on the subspace of the auxiliary grid functions, i.e.,

$$\begin{aligned} 1/2\,(\,(\hat{A}\,(\hat{u}^i + L\tilde{v}^i)\,,\hat{u}^i + L\tilde{v}^i) + (A\,(u^i + \tilde{Q}\tilde{v}^i)\,,u^i + \tilde{Q}\tilde{v}^i)\,) \\ - (\hat{f},\hat{u}^i + L\tilde{v}^i) - (f,u^i + \tilde{Q}\tilde{v}^i) \rightarrow \min_{\tilde{v}^i} \end{aligned} \tag{18}$$

where the superscripts refer to the iteration count.

The auxiliary grid correction $\tilde{v}^i$ has similar partitioning to $\tilde{u}$, i.e. $\tilde{v} = \left[\tilde{v}_I ; \tilde{v}_L ; \tilde{v}_G\right]^*$ and $\hat{v} = \left[\tilde{v}_I ; \tilde{v}_G\right]^*$.

A direct minimization of (18) with respect to $\tilde{v}^i$ yields:

$$(L^* \hat{A} L + \tilde{Q}^* A \tilde{Q})\, \tilde{v}^i = L^* (\hat{f} - \hat{A}\hat{u}^i) + \tilde{Q}^* (f - A u^i) \tag{19}$$

The first term on the left hand side represents the assembled form of the macro-grid stiffness matrix. It has been shown in [5] that for an infinitesimally small unit cell the second term represents an assembled form of the stiffness matrix on the auxiliary grid $\tilde{G}_L$, i.e.:

$$\lim_{\varepsilon \to 0} (L^* \hat{A} L + \tilde{Q}^* A \tilde{Q}) = \tilde{A} \tag{20}$$

In practice, however, the value of the representative unit cell size ε is finite, and thus (20) is satisfied only approximately. Nevertheless, for the purpose of approximating the auxiliary grid correction v_i we will replace the Jacobian matrix in (19) by $\tilde{A}$. In the adaptive environment this will significantly reduce computational effort. By this technique only a single factorization of the auxiliary stiffness matrix is required, independent of the refinement process, which involves replacement of the homogenized grid by heterogeneous one in the regions identified by Microscale Reduction Error (MRE) indicator.

Step 2.

Once the auxiliary grid correction has been carried out it is necessary to update the solution in the auxiliary grid:

$$\tilde{u}^{i+1} = \tilde{u}^i + \omega \tilde{v}^i \qquad \hat{u}^{i+1} = \hat{u}^i + \omega L \tilde{v}^i \qquad u^{i+1} = u^i + \omega \tilde{Q} \tilde{v}^i \tag{21}$$

The relaxation parameter is introduced to account for the approximation introduced in (20) as a result of a finite size of the unit cell. The relaxation parameter is found from a 1-D minimization of the energy functional along the direction $\tilde{v}^i$ evaluated in the previous step (19):

$$\begin{aligned} 1/2 \,((\hat{A}\,(\hat{u}^i + \omega L \tilde{v}^i)\,,\, \hat{u}^i + \omega L \tilde{v}^i) + (A\,(u^i + \omega \tilde{Q} \tilde{v}^i)\,,\, u^i + \omega \tilde{Q} \tilde{v}^i)\,) \\ - (\hat{f},\, \hat{u}^i + \omega L \tilde{v}^i) - (f,\, u^i + \omega \tilde{Q} \tilde{v}^i) \rightarrow \min_{\omega} \end{aligned} \tag{22}$$

which yields

$$\omega = \frac{(L^*(\hat{f} - \hat{A}\hat{u}^i) + \tilde{Q}^*(f - Au^i), \tilde{v}^i)}{((L^*\hat{A}L + \tilde{Q}^*A\tilde{Q})\tilde{v}^i, \tilde{v}^i)} \tag{23}$$

Step 3.

Find the correction v_L^i on the micro-grid, which minimizes the energy functional on the subspace of the functions on the micro-grid G_L, i.e. keeping $\hat{u}^i$ fixed:

$$1/2((\hat{A}\hat{u}^i, \hat{u}^i) + (A(u^i + v^i), u^i + v^i)) - (\hat{f}, \hat{u}^i) - (f, u^i + v^i) \rightarrow \min_{v^i} \tag{24}$$

where $v_I^i = 0$ on Γ_I to maintain compatibility.

The direct minimization of (24) yields

$$A_{LL}v_L^i = f_L - A_{LI}\hat{Q}\hat{u}^i - A_{LL}u_L^i \tag{25}$$

If (25) is directly solved and

$$u_L^{i+1} = u_L^i + v_L^i \tag{26}$$

then the three-steps iterative process described is in the spirit of FAC algorithm [8,9], subsequently to be referred as FAC-Comp.

Because of the smallness of the unit cell, the number of degrees-of-freedom in micro-grid is of the same order of magnitude or larger than in the macro-grid. Moreover, the solution behavior in the micro-grid is highly oscillatory with a lower frequency response similar to that in the auxiliary mesh. These two observations suggest to replace the direct solution of (25) by smoothing of the form given by

$$u_L^{i+1} = u_L^i + \tau^i P_{LL}(f_L - A_{LI}\hat{Q}\hat{u}^i - A_{LL}u_L^i) \tag{27}$$

where P_{LL} is a preconditioner on the micro-grid G_L and τ^i is a relaxation parameter given by

$$\tau^i = \frac{(f_L - A_{LI}\hat{Q}\hat{u}^i - A_{LL}u_L^i, v_L^i)}{(A_{LL}v_L^i, v_L^i)} \tag{28}$$

where $v_L^i = P_{LL}(f_L - A_{LI}\hat{Q}\hat{u}^i - A_{LL}u_L^i)$.

This variant has similar characteristics to the linear version of MLAT [7], and will be termed as MLAT-Comp.

3. The microscale reduction error estimators and indicators

3.1. Formulation

In this section we quantify idealization errors associated with homogenization of periodic heterogeneous medium and present their use in the adaptive procedure. The proposed Microscale Reduction Error (MRE) estimator is based on assessing the uniform validity of the double scale asymptotic expansion [11-13], which is given by a rapidly decreasing asymptotic sequence:

$$u_i^{\varepsilon} = u_i^0(x) + \varepsilon H_{ijk}(y)\, u^0_{(j,k)}(x) + \varepsilon^2 P_{ijkl}(y)\, u^0_{j,kl}(x) + O(\varepsilon^3) \tag{29}$$

where x is a macroscopic position vector, $y = x/\varepsilon$ is the co-ordinate in the unit cell, and ε is a small parameter of order of the unit cell size.

Following [11-13], functions H, u^0 and P are found by inserting asymptotic expansion into a strong form of equilibrium equation and by identifying equal powers of ε, whic! yields:

$$\frac{\partial}{\partial y_j}\left(D_{ijkl}\left(H_{(k,l)mn} + \delta_{km}\delta_{ln}\right)\right) = 0 \qquad on\ unit\ cell\ \theta_Y \tag{30}$$

$$\frac{\partial}{\partial x_j}\left(\tilde{D}_{ijkl} u^0_{(k,l)}\right) + b_i = 0 \qquad on \qquad \Omega \tag{31}$$

where D_{ijkl} and $\tilde{D}_{ijkl}$ are constitutive tensors of a heterogeneous medium and corresponding effective medium given by

$$\tilde{D}_{pqmn} = \frac{1}{Y_A}\int_Y \left(H_{(i,j)pq} + \delta_{ip}\delta_{jq}\right) D_{ijkl}\left(H_{(k,l)mn} + \delta_{km}\delta_{ln}\right) dY \tag{32}$$

and

$$\frac{\partial}{\partial y_p}\left(D_{ipkl}\left(P_{(k,l)mnj} + H_{kmn}\delta_{lj}\right)\right) + D_{ijkl}\left(H_{(k,l)mn} + \delta_{km}\delta_{ln}\right) - \tilde{D}_{ijmn} = 0 \tag{33}$$

$$on \quad unit \quad cell \qquad \theta_Y$$

Problems (30)-(33) are solved using finite element method [5] starting from the prob

lem (30). The resulting asymptotic expansion of the stress field is given by

$$\sigma_{ij} = A^0_{ijkl}(y)\, u^0_{(k,l)}(x) + \varepsilon A^1_{ijklq}(y)\, u^0_{k,lq}(x) + O(\varepsilon^2) \tag{34}$$

where

$$\begin{aligned} A^0_{ijmn}(y) &= D_{ijkl}(H_{(k,l)mn} + \delta_{k,m}\delta_{ln}) \\ A^1_{ijmnp}(y) &= D_{ijkl}(P_{(k,l)mnp} + H_{kmn}\delta_{lp}) \end{aligned} \tag{35}$$

In the classical homogenization theory only the first term in (34) is considered, while the second term is neglected. Thus, the quality of the homogenization is assessed on the basis of the relative magnitude of the first term neglected to those taken into account. The resulting Microscale Reduction Error estimator is defined as

$$\eta = \frac{\left\| \varepsilon A^1 \nabla^2 u^0 \right\|_{0,\Omega}}{\left\| A^0 \nabla u^0 \right\|_{0,\Omega}} \tag{36}$$

where $\| \bullet \|_{0,\Omega}$ is a L_2 - norm defined as

$$\| h(x,y) \|_{0,\Omega} = \frac{1}{Y_A} \left(\sum_{i,j} \int\int_{\Omega Y} h^2_{ij}(x,y)\, dY d\Omega \right)^{1/2} \tag{37}$$

To steer the adaptive process we define the MRE indicator, which reflects the relative contribution of individual element in the auxiliary mesh to the total microscale reduction error:

$$\eta^e = \beta^e \frac{\left\| \varepsilon A^1_{klq} u^0_{k,lq} \right\|_{0,\Omega^e}}{\left\| A^0_{kl} u^0_{(k,l)} \right\|_{0,\Omega}} \qquad \beta^e = \frac{\Omega}{\Omega^e} \tag{38}$$

This approach is equivalent to the one employed for discretization error indicator [14].

3.2. Explicit form of η and η^e in 1D

In this subsection, we derive a close form of MRE indicators and estimators for a 1D model problem in order to study various factors affecting the microscale reduction errors.

Solution of (30)-(33) for H and P yields:

$$A^0 = \tilde{D} = \left(\frac{1}{h}\int_0^h D^{-1}dy\right)^{-1} = const_1 \tag{39}$$

and

$$A^1 = \frac{\tilde{D}}{h}\int_0^h H dy = const_2 \tag{40}$$

where $\tilde{D}$ are the effective material properties and h is the unit cell size. Inserting (39) and (40) into (36) yields the one-dimensional counterpart of the microscale reduction error estimator

$$\eta = \int_0^h \left(\frac{\tilde{D}}{D(y)} - 1\right) dy \frac{\left\|\frac{d^2u^0}{dx^2}\right\|_{0,\Omega}}{\left\|\frac{du^0}{dx}\right\|_{0,\Omega}} \tag{41}$$

For the unit cell consisting of two phases with compliances $C_1 = 1/D_1$ and $C_2 = 1/D_2$ (the overall compliance $\tilde{C} = C_1 + C_2$, $\tilde{C} = 1/\tilde{D}$), α the volume fraction, the resulting MRE estimator is given by

$$\eta = h\frac{|C_1 - C_2|}{\tilde{C}} \frac{\alpha(1-\alpha)}{2} \frac{\left\|\frac{d^2u^0}{dx^2}\right\|_{0,\Omega}}{\left\|\frac{du^0}{dx}\right\|_{0,\Omega}} \tag{42}$$

From the above expression we can identify four factors affecting the microscale reduction error:

1. The size of the unit cell, h.
2. The normalized difference of compliances, $\frac{|C_1 - C_2|}{\tilde{C}}$.
3. The fiber volume ratio, $\frac{\alpha(1-\alpha)}{2}$.
4. The macro strain gradients, $\left\|\frac{d^2u^0}{dx^2}\right\|_{0,\Omega}$.

It can be seen that the error estimator is asymptotically exact in the sense that the microscale reduction errors vanish if either the normalized strain gradients are negligible, the unit cell is infinitesimally small, the compliances of the microconstituents are almost identical or the volume ratio is close to either zero or one, which corresponds to a homogeneous material.

4. Numerical results

Our numerical experimentation agenda includes two test problems. The first example deals with the square plate with a centered crack subjected to a uniform tension. Geometry, boundary and symmetry conditions, material properties and loading are shown in Fig. 2. The micro-mechanical finite element mesh includes 4 elements per each unit cell corresponding to the material distribution. The finest macro-mechanical grid $\tilde{G}$ with homogenized material properties consists of 64 elements along each co-ordinate where each element coincides with the unique unit cell.

The distribution of homogenization errors as indicated by MRE indicator is shown in Fig. 3a. The micro-grid, G, is placed on the portion of the problem domain, which encompasses the contour of $\eta^e > 1$ as shown in Fig. 3a. For simplicity the grid G on Ω is selected to be of rectangular shape. Thus the two-scale model consists of a micro-grid in the region encompassed by 12x20 unit cells in the vicinity of the crack tip, while elsewhere $\tilde{\Omega}/\Omega$, the finite element mesh is constructed on the macro-scale.

The multi-grid process was carried out on three different meshes: two-scale (macro-micro) grid and two auxiliary macro-grids. We used V-cycle with 1 pre- and 1 post-smoothing Gauss-Zeidel iterations on the two auxiliary levels and 2 pre- and 2 post-smoothing Jacobi iterations on the finest level. As usual, on the coarsest level we used a direct solver. As a termination criterion we used the following tolerance to bound the ratio of the two-scale grid residual norm versus the norm of the right hand side vector, i.e.,

$$\|r\|_2/\|f\|_2 \le eps \qquad where \qquad \|v\|_2 = \sum_{i=1}^{n} |v_i| \qquad v \in R^l \tag{43}$$

To obtain convergence with tolerance of $eps = 10^{-3}$ it was necessary to carry out 14 cycles using MLAT-Comp algorithm and 7 cycles with FAC-Comp method.

The resulting energy distribution absorbed in a unit cell in the micro-grid is shown in

Fig. 3c. For comparison purpose also shown are the results obtained on the basis of the classical homogenization theory and the reference solution where the entire problem domain $\tilde{\Omega}$ is modeled on the microscale. It can be seen that the classical homogenization theory significantly underestimates the energy absorbed in the close vicinity to the crack tip. On the other hand in the radius of 2-3 unit cells away from the crack tip the classical homogenization theory is adequate.

In the second example, we consider a multiscale modeling of laminated plate $[90_4/0_{16}/90_4]_s$ subjected to uniform axial tension. Geometry, boundary and symmetry conditions and the micro-structure cross section for the different layers are shown in Fig. 4. We considered Glass-Epoxy composite material with the following material properties: $E_1 = 72.3$ $\nu_1 = 0.22$ and $E_2 = 2.92$ $\nu_2 = 0.35$. The uniform tension load was applied normal to the xy plane. The finest level of macro-grid $\tilde{G}$ consists of 24 elements along the co-ordinate x (thickness direction) and 192 along y, each element coinciding with the unique unit cell.

The distribution of the homogenization errors and the region selected for micro-mechanical modeling are shown in Fig. 5a. The micro-grid consists of 14,400 elements placed in the region encompassed by 24x24 unit cells in the vicinity of the free edge. The two-grid model contains approximately 38,000 degrees-of-freedom. The multi-grid process was carried out on three different meshes: two-scale (macro-micro) grid and two auxiliary macro-grids. We used V-cycle with 1 pre- and 1 post- smoothing Gauss-Zeidel iterations on the auxiliary levels; 3 pre- and 3 post- smoothing Jacobi iterations on the finest level and direct solver on the coarsest level. 1% error of residual (43) was obtained in 8 cycles of MLAT-Comp algorithm and 8 cycles of FAC-Comp method.

Fig. 5b,c,d compare shear stress distribution in the micro-grid as obtained using two-scale model, homogenization theory and the reference solution. Results are consistent with our previous observations, i.e., inadequacy of the classical homogenization theory in the "hot spots" as opposed to striking accuracy of the two-scale model.

The goal of the last numerical example is to study the effectiveness of MLAT-Comp algorithm for solving large two-scale models. The problem domain, boundary conditions, loading, material properties distribution on the unit cell and the micro-mechanical finite element mesh are the same as in the first example. The computational model contained a micro-mechanical finite element mesh in the region of 176x176 unit cells in the vicinity of the crack tip, while elsewhere, the finite elements were treated as homogenized. The macro-mechanical finite element mesh consists of 352 elements

along each co-ordinate. Each macro-mechanical finite element coincides with the unique unit cell. Hence, this problem contains 435,074 independent degrees-of-freedom.

The multi-grid process was carried out on the 4 different meshes: two-scale (macro-micro) mesh and three auxiliary macro-mechanical meshes. We used V-cycle with 1 pre- and 1 post- smoothing Gauss-Zeidel iterations on the two auxiliary levels and 2 pre- and 2 post- smoothing Jacobi iterations on the finest level. As usual, on the coarsest level we used direct solver. It was necessary to perform 15 multi-grid cycles to provide the convergence with $eps = 0.01$ in accordance with criteria (43). Only MLAT-Comp algorithm was tested, since the micro-grid contained over 100,000 nodes, and the direct solution on the micro-grid is not practical. This computational process takes about 8.2 hours on the SPARC station LX, which is 17.2 times faster than the use of traditional direct solver (even without taking into account the memory difficulties, associated with the direct methods).

Acknowledgments

The support of the ARPA under grant A10234, Sikorsky Aircraft and the National Science Foundation NYI award ECS-9257203 are gratefully acknowledged.

References

1. D. Braess, W. Hackbusch, A new convergence proof for the multigrid method including the V-cycle, SIAM J. Numer. Anal., 20 (1983) 967-975.

2. S.F. McCormick, editor, Multigrid methods, SIAM, Philadelphia, 1987.

3. S.F. McCormick, Multigrid methods for variational problems: further results, SIAM J. Numer. Anal. 21 (1984) 255-263.

4. J.Fish and V. Belsky, Convergence of the multi-grid method for a periodic heterogeneous medium. Part 1: 1-D case, submitted to Computer Methods in Applied Mechanics and Engineering.

5. J.Fish and V. Belsky, The multi-grid method for a periodic heterogeneous medium. Part 2: Multidimensions, submitted to Computer Methods in Applied Mechanics and Engineering.

6. J. Fish, P. Nayak and M.H. Holmes, Microscale reduction error indicators and estimators for a periodic heterogeneous medium, accepted in Computational Mechanic The International Journal, 1994.

7. Achi Brandt, Multi-level adaptive solutions to boundary-value problems, Mathematics of Computations, 31 (1977) 333-390.

8. S.F. McCormick and J.W. Thomas, The fast adaptive composite grid (FAC) method for elliptic equations, Mathematics of Computation 46 (1986) 439-456.

9. Michael A. Heroux and J.W. Thomas, A comparison of FAC and PCG methods for solving composite grid problems, Communications in Applied Numerical Methods, 8 (1992) 573-583.

10. O.C. Zienkiewicz and J.Z. Zhu, Superconvergent derivative recovery techniques and a posteriori error estimation in the finite element method. Part 1: A general superconvergent recovery technique, CR/671/91 Institute of Numerical Methods in Engineering, University College of Swansea, U.K., 1991.

11. A. Benssousan, J.L. Lions and G. Papanicoulau, Asymptotic analysis for periodic structures, North Holland, Amsterdam, 1978.

12. E. Sanchez-Palencia and A. Zaoui, Homogenization techniques for composites. Homogenization techniques for composite media, Springer-Verlag, Berlin, 1985.

13. N.S. Bakhvalov and G.P. Panasenko, Homogenization of periodic medium processes, Nauka, Moscow, 1984.

14. J. Fish and S. Markolefas, Adaptive s-method for linear elastostatics, 104 (1993) 363-396.

Fig. 1 *Partitioning of the auxiliary and micro grids*

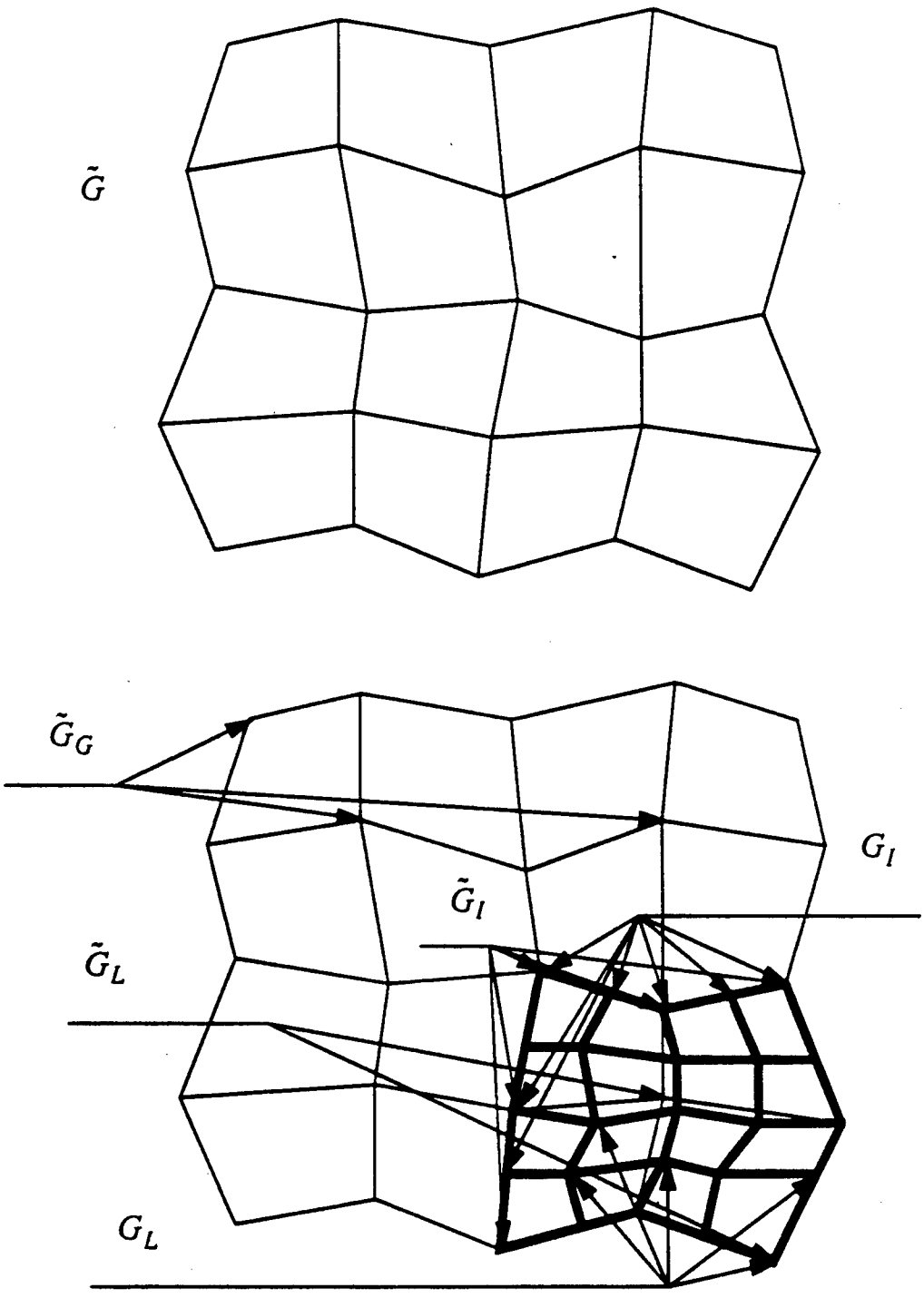


Fig. 2 *Plate with a centered crack: geometry, boundary conditions, material properties and loading*

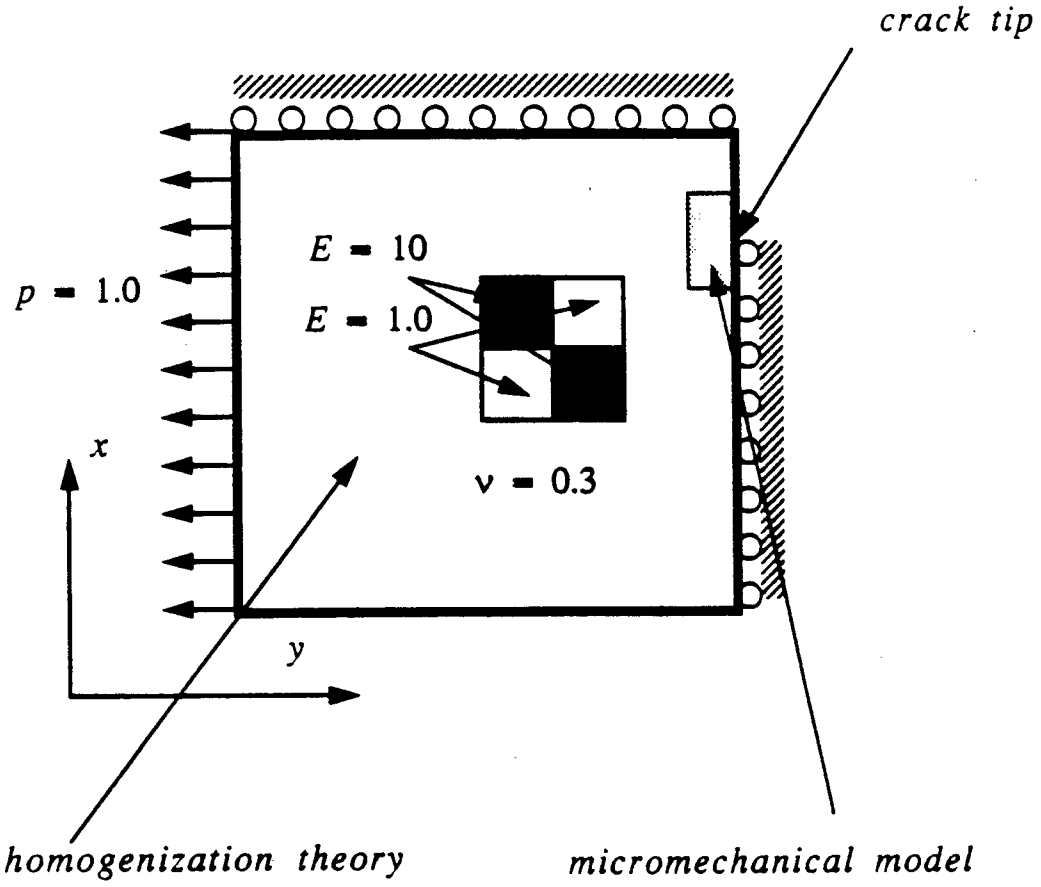


Fig. 3 *Microscale modelling of the plate with a centered crack and comparisons*

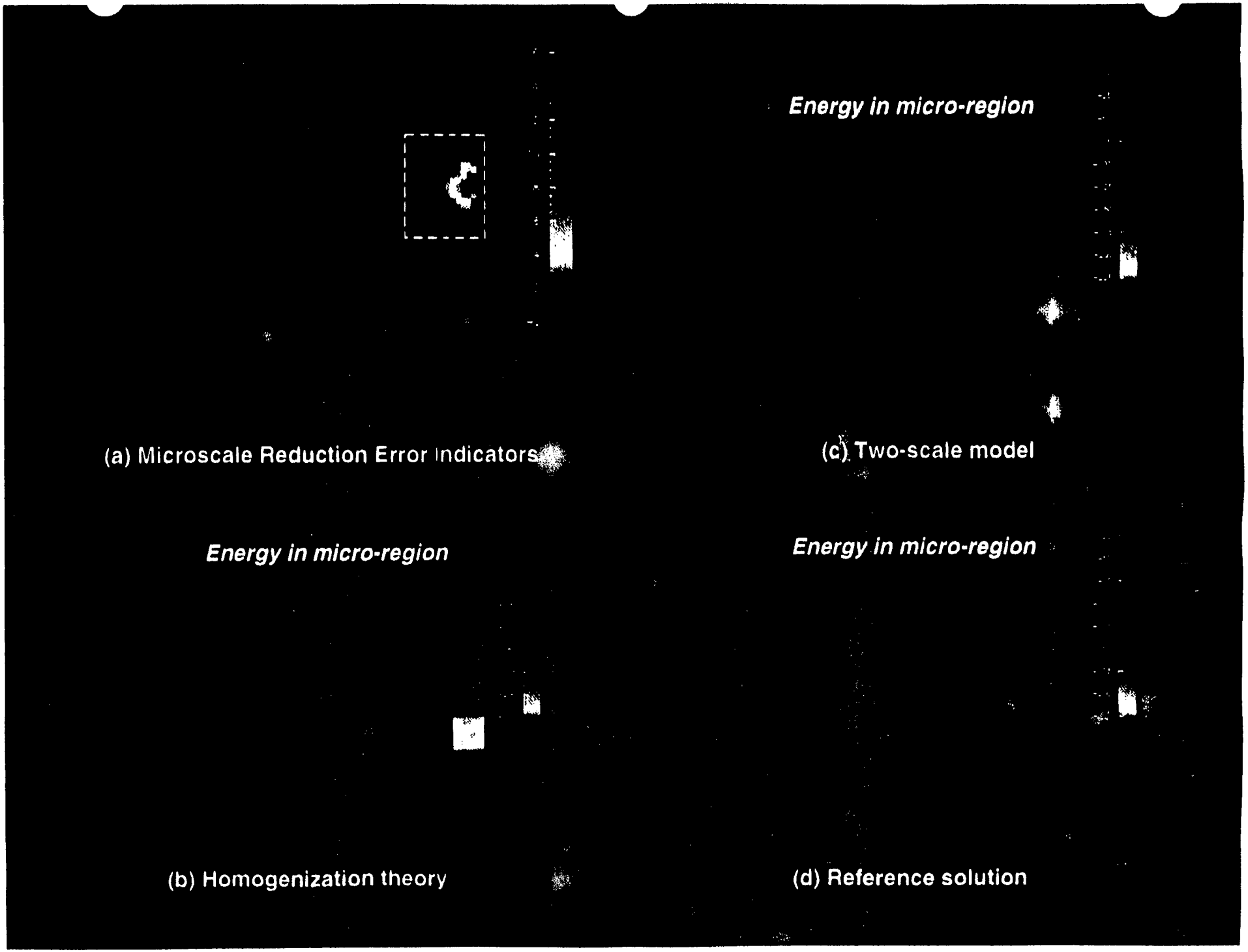

(a) Microscale Reduction Error Indicators
Energy in micro-region
(b) Homogenization theory
Energy in micro-region
(c) Two-scale model
Energy in micro-region
(d) Reference solution

Fig. 4 *Plate subjected to the axial tension: geometry, boundary conditions and micro-structure*

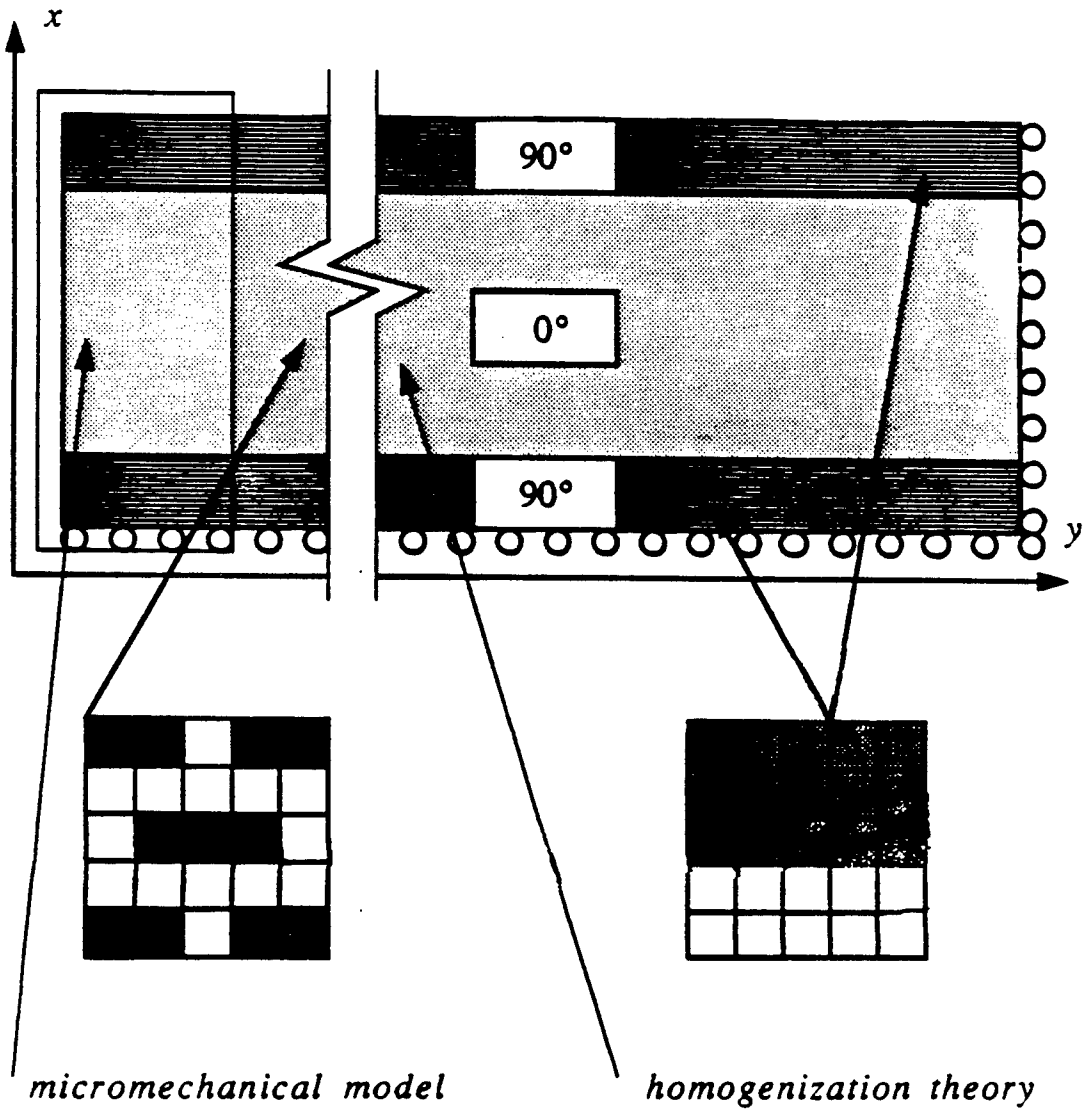
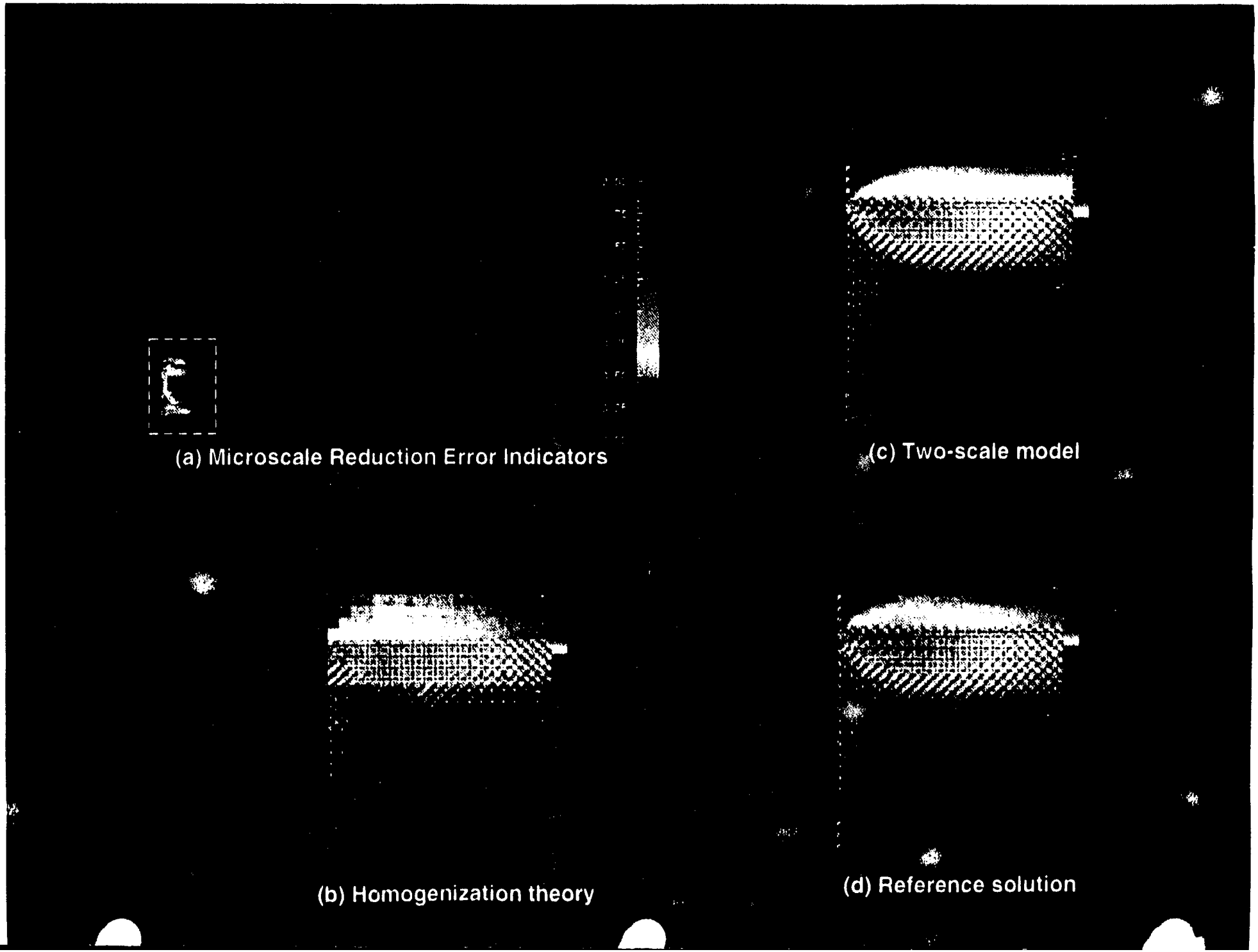


Fig. 5 *Microscale modelling of the plate subjected to the axial tension and comparisons*


(a) Microscale Reduction Error Indicators
(c) Two-scale model
(b) Homogenization theory
(d) Reference solution

Computational Mechanics 16 (1995) 328–340 © Springer-Verlag 1995

The *p*-version of finite element method for shell analysis

J. Fish, R. Guttal

Abstract A new quadrature scheme and a family of hierarchical assumed strain elements have been developed to enhance the performance of the displacement-based hierarchical shell elements. Various linear iterative procedures have been examined for their suitability to solve system of equations resulting from hierarchic shell formulations.

1 Introduction

Since early seventies there has been a disagreement between various sections in the finite element community over the computational efficiency of higher order elements. On one hand there was a clear mathematical evidence of the superior theoretical rate of convergence (measured in terms of the problem size) of the *p*-type methods for properly designed meshes as demonstrated by Babuska, Szabo, and Katz (1981) but on the other hand, it was commonly believed, primarily in the engineering community, that the *h*-method is computationally more efficient due to its superior sparsity. The disagreement has peaked in the early nineties. For example, in the First US Congress on Computational Mechanics, Bathe presented numerical results conducted on Floyd pressure vessel showing the superior performance in terms of CPU time of the *h*-method even for problems for which the exact solution is analytic. At the same conference Carnevali reported IBM research division findings on similar problems suggesting exactly an opposite trend.

In practice, computational efficiency of various finite element versions depends not only on sparsity and theoretical rate of convergence, but is a function of several other factors including adaptivity and quality control, conditioning, distortion sensitivity, locking, model preparation and model improvement, utilization of previous computations and coding simplicity. Ironically, there is no general consensus on the relative merits of some of these factors. For example, it has been argued that for *p*-type methods the finite element mesh is simpler, and thus the time required for data preparation is substantially smaller. Unfortunately in automated computational environment the cost of automatic mesh generation of higher order elements is not necessarily lower than that of the *h*-method (Shephard and Dey 1994).

Communicated by S. N. Atluri, 28 April 1995

J. Fish, R. Guttal
Department of Civil Engineering and Scientific Computation Research Center, Rensselaer Polytechnic Institute, Troy, NY 12180. USA

Correspondence to: J. Fish

The *p*-method has been commended for its versatility in the adaptive process due to its ability to exploit previous computations and the elegance of hierarchical error estimation process (Zeinkiewicz and Craig 1986). However, it is often overlooked that the sequence of lower order finite element meshes generated in the adaptive process can be utilized for both solution and quality control processes by utilizing multigrid technology (Brandt 1977).

Contradicting observations were reported regarding the sensitivity to element distortion. Holzer, Rank, and Werner (1990) present experimental results indicating that higher order elements are less sensitive to mesh distortion, while Ramm, Stander and Matzenmiller (1989) in their review article on assumed strain shell formulation report that 4-node bilinear shell elements are less sensitive to mesh distortion than their quadratic counterparts.

In the realm of opposing views, there is a sound theoretical evidence on superior conditioning of matrices arising from orthogonal basis functions (Zeinkiewicz and Craig 1986), and circumvention of locking with higher order elements as shown by Szabo, Babuska, and Chayapaty (1989). Nevertheless, since the overall computational efficiency is strongly linked to the program architecture, it is not obvious what are the contributing factors of these aspects.

The present work focuses on the computational aspects of the *p*-version for shell analysis. The following aspects are studied:

- How to enhance the performance of shell elements up to the polynomial order of 4–5 using assumed strain formulation.
- How to speed up the computation of element matrices by utilizing previous computations and how to exploit hierarchiality of the *p*-method via special quadrature scheme.
- How to exploit the well conditioning of matrices arising from the *p*-method by utilizing the multigrid like technology with various acceleration schemes for thick and thin shells.

2 Element formulation

2.1 Preliminaries

Consider the geometry of a typical quadrilateral shell element defined by the following relation:

$$\mathbf{X} = \tfrac{1}{2}[(1+\xi_3)\,\mathbf{X}^{top}(\xi_1,\xi_2) + (1-\xi_3)\,\mathbf{X}^{bot}(\xi_1,\xi_2)] \qquad (1)$$

2.2.3
Assumed natural strain field

In order to alleviate membrane and shear locking primarily at lower polynomial we define an assumed natural strain interpolants $\bar{\mathbf{B}}_A^{nat} = \{\bar{b}_{Aij}^{nat}\}$ in the following manner: Let (NG_1, NG_2, NG_3) be the number of quadrature points for the displacement based formulation. To enhance the element performance, we introduce a special set of one-dimensional shape functions $[\phi_I(\xi_1), \phi_K(\xi_2), \phi_M(\xi_3)]$ defined with nodes at reduced quadrature points $(\bar{\xi}_{1I}, \bar{\xi}_{2J}, \bar{\xi}_{3K})$ where $J \in [1, NG_1 - 1]$, $K \in [1, NG_2 - 1]$, $M \in [1, NG_3 - 1]$.

The general form of $\{\bar{b}_{Aij}^{nat}\}$ is given by:

$$\bar{b}_{Aii}^{nat} = \sum_{I=1}^{NG_1-1} b_{Aii}^{nat}(\xi_1 = \bar{\xi}_{1I}, \xi_j, \xi_k)\, \phi_I(\xi_i) \quad \text{no sum on i}$$

$$\bar{b}_{Aij}^{nat} = \sum_{I=1}^{NG_i-1} \sum_{J=1}^{NG_j-1} b_{Aij}^{nat}(\xi_i = \bar{\xi}_{iI}, \xi_j = \bar{\xi}_{jJ}, \xi_k)\, \phi_I(\xi_i)\, \phi_J(\xi_j)$$

$$i \neq j \quad \text{no sum on i, j} \tag{10}$$

2.2.4
Stiffness matrix calculations

Since the constitutive relations are expressed in material coordinate system, the natural strains are transformed to material coordinate system. From Eqs. (4) and (5), the strain components in material coordinate system are defined as:

$$\Xi_{kl} = \frac{\partial \xi_i}{\partial x_k}\frac{\partial \xi_j}{\partial x_l}\varepsilon_{ij} = \left[\frac{\partial x_k}{\partial \xi_i}\right]^{-1}\left[\frac{\partial x_l}{\partial \xi_j}\right]^{-1}\varepsilon_{ij} \equiv T_{klij}\,\varepsilon_{ij} \tag{11}$$

or

$$\boldsymbol{\Xi} = \mathbf{T}\,\boldsymbol{\varepsilon} \tag{12}$$

and the element stiffness matrix can be cast into the classical form:

$$\mathbf{K}^e = \int_\Omega \bar{\mathbf{B}}^{nat^T}\mathbf{D}^e\,\bar{\mathbf{B}}^{nat}\,d\Omega$$

where $\bar{\mathbf{B}}^{nat}$ is defined by Eq. (10) and

$$\mathbf{D}^e = \mathbf{T}^T\mathbf{D}^{\Xi}\mathbf{T} \tag{13}$$

$\mathbf{D}^{\Xi}$ is the constitutive matrix defined in the Material coordinate system.

2.3
H3RANS–Hierarchical (3 – *D*) reduced transverse stiffness, Assumed Natural Strain element

For the purpose of examining the causes of somewhat stiffer behavior of H3-type elements compared to their degenerated counterparts (Stanley, Levitt, Stehlin, and Hurlbut 1992), we consider a beam problem. For elastic isotropic beam the strain energy is given by,

$$U = \frac{1}{2}\int_L (D_B\kappa^2 + D_M\varepsilon^2 + D_S\gamma^2)\,dx \tag{14}$$

where L is the element length; ε, κ, and γ are the membrane strain, curvature and transverse shear strain respectively; D_B, D_M, and D_S are the bending, membrane and shear stiffness constants given by,

$$D_B = \frac{Et^3}{12} \quad D_M = Et \quad D_S = k_s Gt \tag{15}$$

where t is the thickness of the beam of a unit width; E the Youngs modulus; G the shear modulus and k_s the shear correction factor.

In the classical beam formulation the normal strains μ are *a posteriori* calibrated to maintain zero normal stress (plane stress assumption), and thus have no contribution to the strain energy in Eq. (14). It can be seen that as $t \to 0$ the bending energy becomes negligible in comparison to shear and membrane energy giving rise to shear and membrane locking, if the element cannot represent deformed state in which shear and membrane strains vanish through out the element (Belytschko, Stolarski, Liu, Carpenter, and Ong 1985).

In H3-type beam elements normal strains are computed directly from kinematics. These values are not arbitrary and cannot be calibrated to maintain plane stress condition. Thus if two dimensional state of stress is considered, the resulting strain energy takes the following form:

$$U = \frac{1}{2}\int_L (\bar{D}_B\kappa^2 + \bar{D}_M\varepsilon^2 + \varepsilon D_C\mu + D_S\gamma^2 + D_\mu\mu^2)\,dx \tag{16}$$

It can be seen that in H3-type flexural elements spurious coupling between membrane and normal deformation exists giving rise to a parasitic transverse normal strain energy, which is of the same order of magnitude as that of the membrane strain energy if the strains are of equal order. This phenomenon is referred here as the transverse normal locking of H3-type flexural elements.

To ameliorate the locking caused by the transverse normal strains we propose to calibrate the constitutive behavior of H3-type elements to match the strain energy corresponding to H2-type elements without introducing zero energy modes. This is accomplished by modifying coefficients in constitutive tensor in the following way:

$$\bar{D}_M = D_M \quad \bar{D}_B = D_B \quad D_C = 0 \quad D_\mu = \chi D_M \tag{17}$$

where χ is a stabilization parameter aimed at stabilizing the zero transverse normal energy modes of H3-type flexural elements.

2.4
H2ANS–Hierarchic (2 – *D*) Degenerated Assumed Natural Strain element with rotational degrees-of-freedom

In this section we attempt to formulate a degenerated assumed strain shell element, which employs blending functions or Lagrangian basis for geometry mapping and Legendre polynomials for solution interpolation.

As a starting point, the displacement field is expressed in terms of mid-point translations $u_i^f(\xi_1, \xi_2)$ and mid-point rotations $\theta_x(\xi_1, \xi_2)$ which are defined with respect to the fiber coordinate system:

$$\begin{Bmatrix} u_1 \\ u_2 \\ u_3 \end{Bmatrix}_{(\xi_1,\xi_2,\xi_3)} = \begin{Bmatrix} u_1^f \\ u_2^f \\ u_3^f \end{Bmatrix}_{(\xi_1,\xi_2)} + \frac{\xi_3}{2}[-t\,\mathbf{e}_2^f, t\,\mathbf{e}_1^f]_{(\xi_1,\xi_2)}\begin{Bmatrix}\theta_1 \\ \theta_2\end{Bmatrix} \tag{18}$$

Proof. Substituting (20) and (21) into left hand side of (22) yields:

$$\int_\Omega (gh)\,d\Omega = \sum_{i=0}^{n_1}\sum_{j=0}^{n_2}\sum_{k=0}^{n_3}\sum_{s=0}^{m_1}\sum_{t=0}^{m_2}\sum_{r=0}^{m_3} a_{ijk}\,b_{rst}$$

$$\cdot \underbrace{\int_{-1}^{1} \hat{P}_i(\xi_1)\,\hat{P}_r(\xi_1)\,d\xi_1}_{\delta_{ir}} \underbrace{\int_{-1}^{1} \hat{P}_j(\xi_2)\,\hat{P}_s(\xi_2)\,d\xi_2}_{\delta_{js}}$$

$$\cdot \underbrace{\int_{-1}^{1} \hat{P}_k(\xi_3)\,\hat{P}_t(\xi_3)\,d\xi_3}_{\delta_{kt}}$$

$$= \sum_{i=0}^{l_1}\sum_{j=0}^{l_2}\sum_{k=0}^{l_3} a_{ijk}\,b_{ijk} = \sum_{l=1}^{L} a_l\,b_l \qquad (23)$$

Likewise, the right hand side of (22) gives:

$$\sum_{l=1}^{L}\int_\Omega g\phi_l\,d\Omega \int_\Omega h\phi_l\,d\Omega$$

$$= \sum_{i=0}^{l_1}\sum_{j=0}^{l_2}\sum_{k=0}^{l_3}\sum_{s=0}^{n_1}\sum_{t=0}^{n_2}\sum_{r=0}^{n_3}\left(a_{sir}\int_{-1}^{1}\hat{P}_i(\xi_1)\,\hat{P}_s(\xi_1)\,d\xi_1\right.$$

$$\left.\cdot\int_{-1}^{1}\hat{P}_j(\xi_2)\,\hat{P}_t(\xi_2)\,d\xi_2\int_{-1}^{1}\hat{P}_k(\xi_3)\,\hat{P}_r(\xi_3)\,d\xi_3\right)$$

$$\cdot\sum_{p=0}^{m_1}\sum_{q=0}^{m_2}\sum_{v=0}^{m_3}\left(b_{pqv}\int_{-1}^{1}\hat{P}_i(\xi_1)\,\hat{P}_p(\xi_1)\,d\xi_1\int_{-1}^{1}\hat{P}_j(\xi_2)\,\hat{P}_q(\xi_2)\,d\xi_2\right.$$

$$\left.\cdot\int_{-1}^{1}\hat{P}_k(\xi_3)\,\hat{P}_v(\xi_3)\,d\xi_3\right) = \sum_{i=0}^{l_1}\sum_{j=0}^{l_2}\sum_{k=0}^{l_3} a_{ijk}\,b_{ijk} = \sum_{l=1}^{L} a_l\,b_l \qquad (24)$$

The dot product of integral decomposition was originally proposed by Hinnant (1993). The quadrature based on dot product integral decomposition is optimal in terms of number of integrand evaluations for hierarchical systems. To clarify this point we consider a one-dimensional case. Let $\mathbf{g} = \{g_i\}$ and $\mathbf{h} = \{h_j\}$ be vectors whose terms represent the hierarchical sequence with increasing polynomial order, where subscripts on g and h denote the polynomial orders and $i, j \in [0, p]$. In evaluating integrals of the form $G_{ik} = \int g_i \hat{P}_k(\xi)\,d\xi$ and $H_{jl} = \int h_j \hat{P}_l(\xi)\,d\xi$, where $k \in [0, i]$ and $l \in [0, j]$, the number of function evaluations for (g_i, h_j) is $(i+1)$ and $(j+1)$, respectively. Thus the total number of function evaluations for computing all the integrals of the form G_{ik} and H_{jl} is $(p+1)(p+2)$ as opposed to $2(p+1)^2$ for uniform quadrature. It can be shown that this estimate grows exponentially with the increase in the number of space dimensions.

The major drawback of Dot product integral decomposition is the lack of symmetry, which leads to:

1. Non-symmetric stiffness matrix if **g** and **h** are of different polynomial orders (such a situation may arise in the case of material or geometric nonlinearity).
2. Redundancy in evaluating each of the two integrals G_{ik} and H_{jl}, which, except for the term involving constitutive tensor, should be identical.

3.3
Symmetric dot product integral decomposition

In this section we present a variant of Dot product integral decomposition which preserves the symmetry of the stiffness matrix. Consider a typical stiffness term given by

$$k_{AB} = \int_\Omega \underbrace{\mathbf{B}_A^T \mathbf{D}\,\mathbf{B}_B\,J}_{\mathbf{g}_A\,\mathbf{h}_B}\,d\Omega \qquad (25)$$

In an attempt to obtain a symmetric dot product integral decomposition, we decompose the integrand $(\mathbf{g}_A\,\mathbf{h}_B)$ as follows:

$$\mathbf{h}_A^T = \mathbf{g}_A = \mathbf{B}_A^T \mathbf{L}\,J^{1/2} \qquad (26)$$

where L is a lower triangular Cholesky factor of the constitutive matrix D. The resulting stiffness matrix is given by

$$k_{AB} = \sum_{l=1}^{L}\int_\Omega (\mathbf{L}^T\mathbf{B}_A)^T\phi_l J^{1/2}\,d\Omega \int_\Omega \mathbf{L}^T\mathbf{B}_B\,\phi_l J^{1/2}\,d\Omega \qquad (27)$$

Each of the integrals is integrated using Gauss quadrature. The number of quadrature points as well as the maximum polynomial order of the interpolating Legendre polynomials in each direction depends on how well the integrand $\mathbf{L}^T\mathbf{B}_A J^{1/2}$ is approximable by polynomials and what is their polynomial order. We will refer to this integration scheme as Symmetric Dot Product (SDP) Gauss quadrature.

In case when the constitutive tensor D is not positive definite an alternative integrand decomposition is employed. Let

$$\mathbf{g}_A = \mathbf{B}_A^T J^{1/2} \quad \mathbf{h}_B = \mathbf{D}\,J^{1/2}\,\mathbf{B}_B \qquad (28)$$

yielding

$$k_{AB} = \sum_{l=1}^{L}\int_\Omega \mathbf{B}_A^T J^{1/2}\,\phi_l\,d\Omega \int_\Omega \underbrace{\widetilde{\mathbf{D}\,\phi_l}}_{\mathbf{g}_l}\ \underbrace{\mathbf{B}_B J^{1/2}}_{\mathbf{h}_B}\,d\Omega \qquad (29)$$

and further dot product integral decomposition of the second term in (29) yields the following symmetric form:

$$k_{AB} = \sum_{l=1}^{L}\sum_{j=1}^{L}\int_\Omega (\mathbf{B}_A^T J^{1/2})\,\phi_l\,d\Omega \cdot \int_\Omega \underbrace{(\mathbf{D})\,\phi_l\,\phi_j}_{\bar{\mathbf{D}}_{lj}}\,d\Omega \cdot \int_\Omega (\mathbf{B}_B^T J^{1/2})\,\phi_j\,d\Omega \qquad (30)$$

Note that if the constitutive tensor is constant, $\bar{\mathbf{D}}_{lj} = \int_\Omega (\mathbf{D})\,\phi_l\,\phi_j\,d\Omega = \mathbf{D}\,\delta_{lj}$ reducing Eq. (30) to

$$k_{AB} = \sum_{l=1}^{L}\int_\Omega (\mathbf{B}_A^T J^{1/2})\,\phi_l\,d\Omega \cdot \mathbf{D} \cdot \int_\Omega (\mathbf{B}_B^T J^{1/2})\,\phi_l\,d\Omega \qquad (31)$$

In can be easily shown that if D ≠ constant, stiffness matrix evaluations by means of Eq. (30) is more computationally intensive because of the double summation involved. Nevertheless, the triple integral decomposition (30) might be useful in the following two scenarios:

- Thick laminated composite shells with multiple layers and variable jacobian through the thickness.
- Small deformation nonlinear material analysis, where the first term in (30) can be computed only once and then reused in the nonlinear incremental iterative process.

Q_m^{m-1} and Q_{m-1}^m be the restriction and prolongation operators, which transfer the data from level (m) to level $(m-1)$ and vice versa. For the p-method it has a very simple form:

$$Q_m^{m-1} = [I \quad 0] = Q_{m-1}^{m\,T} \tag{39}$$

where I is the order n_{m-1} identity matrix, and 0 is order $(n_m - n_{m-1})$ zero matrix. Note that the restriction of the stiffness matrix is given by:

$$\hat{K}^{m-1} = Q_m^{m-1} K^m Q_{m-1}^m \neq K^{m-1} \tag{40}$$

A single V-cycle has a compact recursive definition given by:

$$z^m := MG^m(r^m, K^m). \tag{41}$$

where r^m is the residual vector. The V-cycle multigrid algorithm is summarized below:

1. Loop $i = 0, 1, 2 \ldots$ until convergence
   if $i = 0 \leftarrow d^m = 0$
2. perform γ_1 pre-smoothing operations

   $${}_{\gamma_1}{}^i d^m := \text{smooth}(\gamma_{1,0}{}^i d^m, K^m, f^m)$$

   where the left superscript and subscript denote the cycle number and smoothing count respectively.
3. Restrict residual from level m to $m-1$

   $$r^{m-1} = Q_m^{m-1}(f^m - K^m {}_{\gamma_1}{}^i d^m)$$

4. Coarse grid correction
   If $(m-1)$ = lowest level, solve directly z^{m-1}
   $= (K^{m-1})^{-1} r^{m-1}$,
   Else $z^{m-1} := MG^{m-1}(r^{m-1}, K^{m-1})$
5. Prolongate from level $m-1$ to m

   $${}_{\gamma_1+1}{}^i d^m = {}_{\gamma_1}{}^i d^m + {}^i\omega Q_{m-1}^m z^{m-1}$$

   where ${}^i\omega$ is a coarse grid relaxation parameter, which minimizes energy functional along the prescribed direction $v^m = Q_{m-1}^m z^{m-1}$. Note that for two grid methods ${}^i\omega = 1$ if $\hat{K}^{m-1} = K^{m-1}$. Otherwise

   $${}^i\omega = \frac{v^{m\,T}(f^m - K^m {}_{\gamma_1+1}{}^i d^m)}{v^{m\,T} K^m v^m} \tag{42}$$

6. Perform γ_2 post-smoothing operations

   $${}^{i+1}{}_0 d^m := \text{smooth}(\gamma_2, {}_{\gamma_1+1}{}^i d^m, K^m, f^m)$$

A variant of the standard V-cycle multigrid method (Brandt 1977) has been proposed by Bank, Dupont and Yserentant (1988). The method termed as hierarchical basis multigrid technique (HBM), is similar to the standard multigrid V-cycle, except that a smaller than the normal subset of unknowns is updated during the smoothing phase at a given level. HBM takes advantage of the fact that smoothing mainly affects highest oscillatory modes of error, and thus relaxation sweeps are performed on the block by block level keeping the rest of the degrees of freedom fixed. It has been shown by Bank, Dupont and Yserentant (1988) that the rate of convergence of HBM method has a logarithmic dependence on the problem size as opposed to multigrid method which has an optimal rate of convergence independent of the mesh size and spectral order. The key question is whether the benefit from reducing the cost of smoothing process over weighs the suboptimal performance of HBM in comparison with the standard multigrid method for thin and thick shells.

4.2
Two parameter acceleration of multigrid method

For ill-conditioned problems, such as thin shells, it is desirable to accelerate the rate of convergence of the multigrid like methods. In this section we present a two parameter acceleration scheme that requires a small fraction of computational effort, but at the same time is efficient in expediting the convergence of the multigrid like methods (MG and HBM).

Let ${}^i r^m$ be the residual vector at the end of i^{th} m-level multigrid cycle. The incremental multigrid solution for the next cycle ${}^i z^m = MG^m({}^i r^m, K^m)$ is used as a predictor in the two parameter acceleration scheme. The solution in the correction phase is then updated as follows:

$${}^{i+1}v = {}^i\alpha\, {}^i z^m + {}^i\beta\, {}^i v \tag{43}$$

$${}^{i+1}d^m = {}^i d^m + {}^{i+1}v \tag{44}$$

where parameters $({}^i\alpha, {}^i\beta)$ are obtained by minimizing the potential energy functional:

$$\frac{1}{2}({}^i d^m + {}^i\alpha {}^i z^m + {}^i\beta {}^i v)^T K^m ({}^i d^m + {}^i\alpha {}^i z^m + {}^i\beta {}^i v)$$

$$- ({}^i d^m + {}^i\alpha {}^i z^m + {}^i\beta {}^i v)^T f^m \rightarrow \min_{{}^i\alpha {}^i\beta} \tag{45}$$

The resulting algorithm is summarized below:

Step 1

$${}^0 d^m = 0, \quad {}^0 r^m = f^m$$

$${}^0 z^m := MG^m({}^0 r^m, K^m)$$

$${}^0 v = {}^0 y = 0$$

$${}^0 x = K^m {}^0 z^m$$

$${}^0\beta = 0; \quad {}^0\alpha = \frac{(f^m, {}^0 z^m)}{({}^0 x^m, {}^0 z^m)} \tag{46}$$

Step 2 Do $i = 0, 1, 2, \ldots$ until convergence

$$\begin{Bmatrix} {}^i\alpha \\ {}^i\beta \end{Bmatrix} = \begin{bmatrix} ({}^i x, {}^i z^m) & ({}^i x, {}^i v) \\ ({}^i x, {}^i v) & ({}^i y, {}^i v) \end{bmatrix}^{-1} \begin{Bmatrix} ({}^i r^m, {}^i z^m) \\ ({}^i r^m, {}^i v) \end{Bmatrix} \quad i > 0 \tag{47}$$

$${}^{i+1}v = {}^i\alpha\, {}^i z^m + {}^i\beta\, {}^i v$$

$${}^{i+1}d^m = {}^i d^m + {}^{i+1}v$$

$${}^{i+1}y = {}^i\alpha\, {}^i x + {}^i\beta\, {}^i y$$

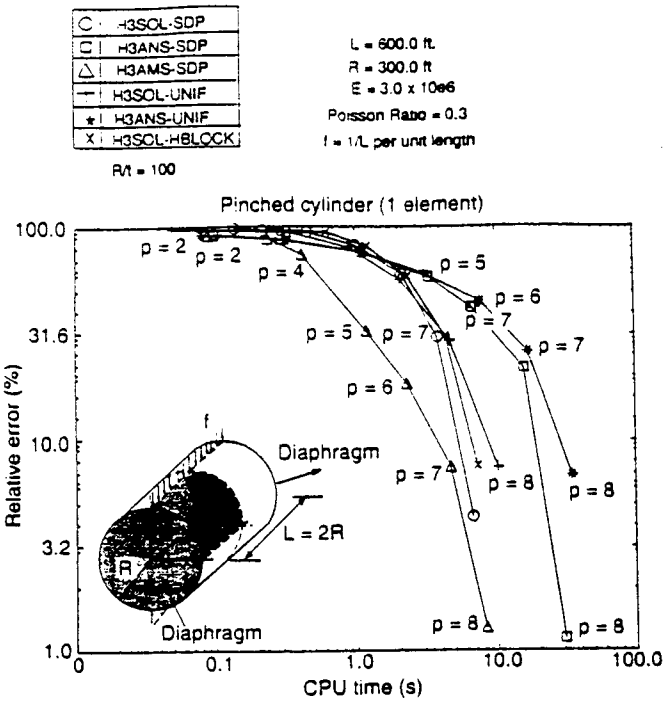


Fig. 3. Comparison of quadrature schemes for H3R-type ($q = 1$) elements for pinched cylinder problem

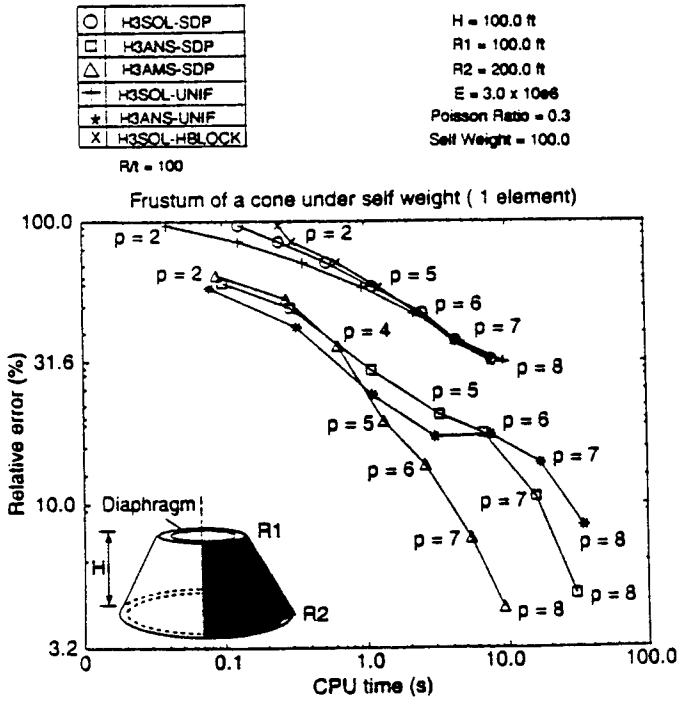


Fig. 4. Comparison of quadrature schemes for H3R-type ($q = 1$) elements for frustum of a cone

Each figure contains six plots:

- (○) HSOL-SDP corresponding to Symmetric Dot Product Gauss quadrature for displacement based element.
- (□) HANS-SDP corresponding to Symmetric Dot Product Gauss quadrature for assumed natural strain element.
- (△) HAMS-SDP corresponding to Symmetric Dot Product Gauss quadrature for assumed material strain element.
- (+) HSOL-UNIF corresponding to Uniform Gauss quadrature scheme for displacement based element.
- (*) HANS-UNIF corresponding to Uniform Gauss quadrature scheme for assumed natural strain element.
- (×) HSOL-HBLOCK corresponding to Hierarchic Block Gauss quadrature scheme for displacement based element.

To preserve hierarchical structure of the stiffness matrix the displacement based shell element has been integrated to accommodate for highly varying metric tensor components $\hat{c}x_i/\hat{c}\xi_i$. For numerical examples considered, the number of integration points for Block Gauss quadrature was selected as $p^{max} - 3$ in inplane direction and $q^{max} + 1$ in transverse direction, where p^{max} and q^{max} are the maximum polynomial orders of the corresponding block in inplane and transverse directions, respectively.

Similarly, for SDP-Gauss quadrature applied to displacement based elements, the order of interpolating Legendre polynomials $\hat{P}_i(\xi_i)$ is selected as $(p_i + l)$ $i \in [1, 2]$ in inplane directions and $(q + m)$ in transverse direction. The corresponding number of integration points are $(p_i + l + 1)$ and $(q + m + 1)$ in inplane and transverse directions, respectively, where (p_1, p_2) are the polynomial orders of the integrand in inplane directions (ξ_1, ξ_2) and q is the polynomial order in transverse direction (ξ_3). Selection of integers l and m is dictated by the variation of the metric tensor $\hat{c}x_i/\hat{c}\xi_i$ in inplane and transverse directions respectively. For example, in case of constant inplane jacobian (the pinched cylinder) we used $l = 1$, $m = 0$ and $l = 2$, $m = 1$ for the case of variable inplane jacobian (frustum of the cone).

In case of HAMS elements the order of interpolating Legendre polynomials is selected such that their polynomial order does not exceed the maximum polynomial order of the basis functions to ensure effectivity of selective polynomial order reduction. On the other hand for lower order blocks the polynomial order for Legendre polynomials is selected the same as for displacement based elements to partially preserve hierarchiality. Thus the order of Legendre polynomials for HAMS element is defined using the following rule:

- For a given integrand with polynomial orders (p_i, q)

  The inplane polynomial order of $\hat{P}_i$

$$= \begin{cases} p_i + l & \text{if } p_i + l < p^{max} \\ p^{max} & \text{otherwise} \end{cases} \tag{48}$$

  The order of Legendre polynomials in transverse direction is selected as $q + m$.
- The number of inplane integration points is selected as $p^{max} + 1$, and $q^{max} + 1$ in transverse direction.

It is evident from Figs. (1–4) that among the displacement (HSOL) based elements, SDP and HBLOCK quadrature schemes are computationally more efficient than the uniform (UNIF) quadrature. The difference between HSOL-SDP and HSOL-HBLOCK is not significant and it can be deduced that for displacement based elements SDP and HBLOCK have a comparable performance. It is apparent from the Figs. (1–4) that HAMS-SDP has higher computational efficiency than

Table 2. Effect of radius to thickness (R/t) ratio on iterative methods. Three cyclinder assembly modeled with 36 (H2AMS) elements

Solver	(R min/t = 100)	(R min/t = 1000)
MG-GS-ACC(4, 6, 8)	300/25	13728/1144
HBM-GS-ACC(4, 6, 8)	271/37	47879/6537
MG-ICC-ACC(4, 6, 8)	235/12	1191/97
HBM-ICC-ACC(4, 6, 8)	250/33	1476/294
PCG-ICC	330/144	1115/660
Direct	536/1	536/1

Table 4. Influence of smoothing procedures of Multigrid-like solvers. Pinched cylinder modeled with 16 (H2AMS) elements, Multigrid-like solvers with (4, 6, 8) levels

Solver	GS-1	JPCG-1	ICC
MG-ACC(R/t = 10)	37/12	57/17	61/6
HBM-ACC(R/t = 10)	23/10	29/11	32/12
MG-ACC(R/t = 100)	115/43	295/97	110/21
HBM-ACC(R/t = 100)	117/72	157/76	110/58
MG-ACC(R/t = 300)	797/315	1359/445	245/59
HBM-ACC(R/t = 300)	632/412	447/221	310/182

performance of the iterative procedures deteriorates, due to increase in the condition number. Assuming that deterioration in conditioning does not affect the accuracy of direct solution due to round off errors, the direct solver has outperformed the iterative procedures for very thin shells (R/t = 1000).

In Table 4 the influence of various popular smoothing procedures (GS - Gauss Seidel; JPCG - Jacobi pre-conditioned conjugate gradient and ICC - Incomplete Cholesky) on the performance multigrid-like solvers (MG-ACC and HBM-ACC) is examined. One smoothing iteration of each procedure is incorporated. The experiments are conducted on the pinched cylinder problem modeled with 16 elements with R/t = 10; R/t = 100 and R/t = 300. For either of the multigrid procedures one Incomplete Cholesky (ICC) smoothing has been found to be optimal in terms of CPU time for both thin (R/t = 100) and very thin (R/t = 300) shells. For relatively thick shells (R/t = 10) the weaker Gauss Seidel smoothing is found to be optimal in terms of CPU time.

In Table 5 we study the performance of multigrid solver (MG-GS-ACC) for the case where the coarse mesh represents the state of plane stress (p = 8, q = 1) while the fine mesh represents 3-D model with (p = 8, q = 3). The coarse grid relaxation parameter defined in Eq. (42) is used for efficient coarse grid correction. Alternatively, one can recompute and factorize the stiffness matrix corresponding to q = 1 with a 3-D constitutive model and then incorporate it for coarse grid correction. For a relatively small problem considered (12 elements, 2208 dofs for q = 1) no significant difference in terms of CPU time has been found between the two methods. Numerical experiments indicate that HBM-ACC is not particularly well suited for transitioning between different mathematical models.

Table 5. Study of Multigrid-like solvers for transitioning from plane stress to 3-D models. pinched cylinder modeled with 12 (H3) elements, Multigrid-like solver MG-GS-ACC with 2 Gauss Seidel smoothing

Element	NDOFS	Direct	2D - 3D	Recomputed
H3RAMS (q = 3)	4416	1203	904/55	877/41
H3SOL (q = 3)	4416	1203	789/48	906/46

Figures 7 and 8 depict the rate of convergence of various elements for the pinched cylinder and the 3 cylinder assembly problems respectively. Percentage relative error in the energy norm is plotted versus the total CPU time required to solve the problem. SDP quadrature scheme for integration of element stiffness matrices and the best solution procedure for a given polynomial order are adopted for all elements. It is evident that H2AMS and H3RAMS have the best performance in degenerated and 3-D categories, respectively.

6
Summary and conclusions

Research efforts have been made to optimize the computational efficiency of the p-method for shell analysis. A new quadrature scheme and a family of hierarachical assumed strain based shell elements have been introduced. Various linear iterative procedures have been examined for their suitability to solve linear system of equations resulting from hierarchic shell formulation.

In Figs. 9 and 10 we compare h and p versions of finite element analysis for the two shell problems, a pinched cylinder

Table 3. Effect of radius to thickness (R/t) ratio on iterative methods. Pinched cylinder modeled with 16 (H2AMS) elements

Solver: R/t =	10	20	30	100	300	1000
MG-GS-ACC(4, 6, 8)	37/12	48/16	57/20	115/43	797/315	5004/1969
HBM-GS-ACC(4, 6, 8)	23/10	33/16	37/19	117/72	632/412	5098/3357
MG-ICC-ACC(4, 6, 8)	61/6	65/7	68/8	110/21	245/59	610/171
HBM-ICC-ACC(4, 6, 8)	32/12	38/15	45/20	110/58	310/182	862/517
PCG(4, 6, 8)	148/24	164/36	187/52	425/232	827/458	1953/1329
PCG-ICC	50/22	60/34	65/42	130/135	258/324	623/860
Direct	242/1	242/1	242/1	242/1	242/1	242/1
MG-ICC-ACC(6, 8)	155/5	158/6	158/6	177/12	235/33	416/98
HBM-ICC-ACC(6,8)	130/7	134/9	139/12	171/30	271/87	541/238
PCG(6, 8)	171/12	184/19	200/30	370/133	532/255	1112/481

References

Babuska, I.; Szabo, B. A.; Katz, I. N. 1981: The *p*-version of the finite element method. SIAM J. Numer. Anal. 18: 512–545

Baker, V. A.; Axelsson, O. 1984: Finite Element Solution of Boundary Value Problem. Academic Press Inc. NY

Bank, R. E.; Dupont, T. F.; Yserentant, H. 1988: The hierarchical basis multigrid method. Numer. Math. 52: 427–458

Belytschko, T.; Stolarski, H.; Liu, W. K.; Carpenter, N.; Ong, J. S.-J. 1985: Stress projection for membrane and shear locking in shell finite elements. Comp. Meth. in Appl. Mech. and Engg. 51: 221–258

Brandt, A. 1977: Multi-level adaptive solutions to boundary-value problems. Mathematics of Computation, 31: 333–390

Carnevali, P.; Morris, R. B.; Tsuji, Y.; Taylor, G. 1992: New Basis Functions and Computational Procedures for *p*-type Finite Element Analysis. RJ 8710 (78272) Engineering Technology. April 3, 1992

Hinnant, H. E. 1993: A Fast method of numerical quadrature for *p*-version finite element matrices. A.I.A.A. 1386.

Holzer, S.; Rank, E.; Werner, H. 1990: An implementation of the *hp*-version of the finite element method for Reissner-Mindlin plate problems. Int. J. Numer. Methods Eng. 30: 459–471

Hughes, T. J. R. 1987: The Finite Element Method. Prentice-Hall.

Park, K. C.; Stanley, G. M. 1986: A curved C^0 Shell element based on Assumed Natural Coordinate Strains. J. of Appl. Mech. 108: 278–290

Ramm, E.; Stander, N.; Matzenmiller, A. 1989: An assessment of Assumed strain methods in finite rotation shell analysis. Eng. Comput. 6

Shephard, M. S.; Dey, S. 1994: Geometric mapping of finite elements on shell geometry. SCOREC report 15

Stanley, G. M.; Levitt, I.; Stehlin, B.; Hurlbut, B. 1992: Adaptive Analysis of Composite Shell Structures via Thickness-tailored 3D Finite Elements. Winter Annual Meeting Anaheim, CA, November 11–13, 1992

Surana, K. S.; Sorem, R. M. 1991: *p*-version hierarchical three dimensional curved shell element for elastostatics. Int. J. Numer. Methods Eng. 31: 649–676

Szabo, B. A.; Sahrmann, G. J. 1988: Hierarchic plate and Shell models based on *p*-extensions. Int. J. Numer. Methods Eng. 26: 1855–1881

Szabo, B. A.; Babuska, I.; Chayapaty, B. K. 1989: Stress computations for nearly incompressible materials by the *p*-version of the Finite Element method. Int. J. Numer. Methods Eng. 28: 2175–2190

Zeinkiewicz, O. C.; Craig, A. 1986: Adaptive Refinement, Error Estimates, Multigrid Solution, and Hierarchic Finite Element Method Concepts. In Babuska, I. Zeinkiewicz, O. C. Gago, J.; Oliveira, E. R. de A. eds. Accuracy Estimates and Adaptive Refinements in Finite Element Computations

Pergamon

0956-0521(95)00018-6

Computing Systems in Engineering, Vol. 6, No. 3, pp. 195–211, 1995
Copyright © 1995 Elsevier Science Ltd
Printed in Great Britain. All rights reserved
0956-0521/95 $9.50 + 0.00

RECENT ADVANCES IN THE *P*-VERSION OF THE FINITE ELEMENT METHOD FOR SHELLS*

JACOB FISH and RAVI GUTTAL

Department of Civil Engineering and Scientific Computation Research Center,
Rensselaer Polytechnic Institute, Troy, NY 12180, U.S.A.

Abstract—Research efforts aimed at optimizing the computational efficiency of the *p*-method are described. These include (i) a novel quadrature scheme for hierarchical shell elements, (ii) a family of assumed strain hierarchical shell elements, (iii) selective polynomial order escalation for assumed strain elements, and (iv) accelerated multigrid-like solution procedures. Numerical experiments indicate that with these enhancements it is possible to speed up the overall computational time of *p*-method for analysis of shells by a factor greater than five for relatively small problems (less than 10 000 dofs), while computational savings for larger problems are even more significant. It has been found that the performance of the enhanced variant of the *p*-method for shells is comparable to that of the *h*-method for low accuracy requirements, and better if higher accuracies are desired.

1. INTRODUCTION

Since the early seventies there has been a disagreement between various sections in the finite element community over the computational efficiency of higher order elements. On one hand there was clear mathematical evidence on the superior theoretical rate of convergence (measured in terms of the problem size) of the *p*-type methods for properly designed meshes,[1] but on the other hand it was commonly believed, primarily in the engineering community, that the *h*-method is computationally more efficient due to its superior sparsity. The disagreement has peaked in the early nineties. For example, in the First US Congress on Computational Mechanics, Bathe presented numerical results conducted on Floyd pressure vessel showing the superior performance in terms of CPU time of the *h*-method even for problems for which the exact solution is analytic. In the same conference Carnevali[2] reported IBM research division findings on similar problems suggesting exactly an opposite trend.

In practice computational efficiency of various finite element versions depends not only on sparsity and theoretical rate of convergence, but is a function of several other factors including adaptivity and quality control, conditioning, distortion sensitivity, locking, model preparation and model improvement, utilization of previous computations and coding simplicity. Ironically, there is no general consensus on the relative merits of some of these factors. For example, it has been argued that for *p*-type methods the finite element mesh is simpler, and thus the time required for data preparation is substantially smaller. Unfortunately, in automated computational environment the cost of automatic mesh generation of higher order elements is not necessarily lower than that of the *h*-method.[3]

The *p*-method has been commended for its versatility in the adaptive process due to its ability to exploit previous computations and the elegance of hierarchical error estimation process.[4] However, it is often overlooked that the sequence of lower order finite element meshes generated in the adaptive process can be utilized for both solution and quality control processes by utilizing multigrid technology.[5]

Contradicting observations were reported regarding the sensitivity to element distortion. Holzer[6] presents experimental results indicating that higher order elements are less sensitive to mesh distortion, while Ramm[7] in his review article on assumed strain shell formulation reports that 4-node bilinear shell elements are less sensitive to mesh distortion than their quadratic counterparts.

In the realm of opposing views, there is sound theoretical evidence on superior conditioning of matrices arising from orthogonal basis functions,[4] and circumvention of locking with higher order elements.[8] Nevertheless, since the overall computational efficiency is strongly linked to the program architecture, it is not obvious what are the contributing factors of these aspects.

The literature on the higher order plate elements is rapidly expanding. For extensive review we refer to the paper by Szabo and Sahrmann[9] and to Refs 6 and 10 for additional references. Application of the

* Paper presented at the 3rd National Symposium on Large-Scale Structural Analysis for High-Performance Computers and Workstations, held 8–11 November 1994, Marriott Waterside, Norfolk, VA, U.S.A.

p-method for general curved shells is quite limited. To our knowledge only two papers[9,11] employ a hierarchical sequence of approximations for curved shell elements.

The present work focuses on the computational aspects of the p-version for shell analysis. Our primary research efforts focus on enhancing element level computations, since the cost of analysis in the p-method is often dominated by the formation of finite element matrices (as opposed to the h-method, where the solution process is generally dominant). The following aspects are studied:

1. How to enhance the performance of shell elements up to the polynomial order of 4–5 using assumed strain formulation.
2. How to speed up the computation of element matrices by utilizing previous computations and how to exploit hierarchiality of the p-method via special quadrature scheme.
3. How to reduce the size of the element matrices by adaptively selecting higher order modes.[12]

On the system of equations level, the applicability of the multigrid technology with various acceleration schemes for thick and thin shells is presented and compared with the direct solver.

2. HIERARCHICAL ASSUMED STRAIN SHELL ELEMENT FORMULATION

2.1. *Assumed strain formulation*

Consider the geometry of a typical quadrilateral shell element defined by the following relation:

$$\mathbf{X} = \tfrac{1}{2}[(1+\xi_3)\mathbf{X}^{\text{top}}(\xi_1,\xi_2) + (1-\xi_3)\mathbf{X}^{\text{bot}}(\xi_1,\xi_2)] \quad (1)$$

where $\mathbf{X}$ denotes position vector of a generic point of the shell in the global Cartesian coordinate system, $\mathbf{X}^{\text{top}}$ and $\mathbf{X}^{\text{bot}}$ are position vectors of the top and bottom surfaces, respectively. The unit vectors in the global Cartesian system are denoted by e_i. Equation (1) represents a smooth mapping of a biunit cube into physical shell domain, with linear interpolation in ξ_3. $\xi_3 = 0$ corresponds to the middle surface of the shell. It is common practice to interpolate the bottom and the top surfaces either using Lagrange polynomials,[11] blending functions[9] or even Legendre polynomials.[2]

The displacement field of a higher order plate/shell theory can be approximated as in[9,13]

$$u_i = \sum_{a=1}^{n_f} f_a(\xi_3) u_{ia}(\xi_1,\xi_2) \quad (2)$$

where $f_a(\xi_3)$ in Eq. (2) represents through-the-thickness variation of the displacement components. Typically, Legendre polynomials are chosen as basis functions for in-plane displacement components $u_{ia}(\xi_1,\xi_2)$ to ensure numerical stability and hierarchiality.

The space spanned by hierarchic shape functions is denoted by $S^{(p,q)}$, where p is in-plane polynomial order of basis functions corresponding to the interpolation order of u_{ia} and q ($q \leqslant p$) is the polynomial order of basis functions in transverse direction identified with the polynomial order of $f_a(\xi_3)$.

Let ξ represent a Natural Element Curvilinear coordinate system. Then the covariant basis vectors $\mathbf{a}_i$ and their contravariants $\mathbf{a}^i$ are defined as follows:

$$\mathbf{a}_i = \frac{\partial X_j}{\partial \xi_i}\mathbf{e}_j \quad \mathbf{a}^i = \frac{\partial \xi_i}{\partial X_j}\mathbf{e}_j \quad \mathbf{a}_i \cdot \mathbf{a}^j = \delta_i^j. \quad (3)$$

We also consider material Cartesian coordinate system denoted by $\mathbf{x}$ where material properties of the element are defined. Plane stress assumption for classical shell theory ($q = 1$) is also exercised in this coordinate system. Unit basis vectors for the Material coordinate system are denoted by $\mathbf{p}_i$. They are defined such that, $\mathbf{p}_3$ is perpendicular to mid-surface and $\mathbf{p}_1$, $\mathbf{p}_2$ are as close as possible to $\mathbf{a}_1$, $\mathbf{a}_2$.[14]

The components of strain tensor in the global (E_{ij}) and material (ϵ_{ij}) coordinate systems respectively, are related by orthogonal transformation

$$\epsilon_{ij} = (\mathbf{e}_i \cdot \mathbf{p}_k)(\mathbf{e}_j \cdot \mathbf{p}_l)E_{kl} \equiv T_{ijkl}E_{kl}. \quad (4)$$

Let $\mathbf{N} \in S^{(p,q)}$ be the shape functions obtained using tensor product of Legendre polynomials,[9] then

$$u_m = \sum_{A=1}^{NMDS} N_{mA}\,\mathrm{d}^A \quad \text{and} \quad E_{mn} = \sum_{A=1}^{NMDS} B_{mnA}\,\mathrm{d}^A \quad (5)$$

where $\mathbf{d}$ is the displacement vector representing the amplitudes of hierarchical modes in global coordinate sytem; $NMDS$ is the number of modes; lower case subscripts denote space dimension, while upper case indices are reserved for mode numbering; B_{mnA} is the symmetric gradient of the shape functions.

Using Eqs (4) and (5) the material strain-displacement relation is denoted by:

$$\epsilon_{ij} = \sum_{A=1}^{NMDS} B_{ijA}^{\text{mat}}\,\mathrm{d}^A = \sum_{A=1}^{NMDS} (T_{ijkl}B_{klA})\,\mathrm{d}^A. \quad (6)$$

To enhance the element performance primarily at lower spectral orders assumed strain formulation is employed. Let (p, q) be the polynomial order of displacement interpolants, then the polynomial order of B_{ijA}^{mat} denoted by $(\gamma_1, \gamma_2, \gamma_3)$ is modified as follows:

$$\begin{aligned} \gamma_\alpha &= p - I_\alpha \quad \alpha \in [1,2] \\ \gamma_3 &= q - I_3 \end{aligned} \quad (7)$$

where I_k is defined as in Ref. 15 to alleviate membrane and shear locking.

$$I_k = \begin{cases} 1 & \text{if } k = i \text{ or } j \quad k \in [1,3] \\ 0 & \text{otherwise.} \end{cases} \quad (8)$$

Following B-bar nomenclature the enhanced material strain field–displacement relation can be conveniently cast into the following form:

$$\bar{\epsilon}_{ij} = \sum_{A=1}^{NMDS} \bar{B}^{mat}_{ijA}\, d^A \tag{9}$$

where $\bar{B}^{mat}_{ijA}$ can be obtained by interpolating B^{mat}_{ijA} between a set of reduced quadrature points.[14] In the present work $\bar{B}^{mat}_{ijA}$ will be obtained by selectively projecting out higher order modes within the quadrature process (as described in Section 3).

Shell element formulation based on Eqs (2–9) will be referred as H3AMS—Hierarchical (3-D) Assumed Material Strain element.

In thin shell limit, retention of 3 degrees-of-freedom at each node on top and bottom surfaces leads to large stiffness coefficients for relative displacements corresponding to shell thickness.[15] This leads to deterioration of rate of convergence for lower polynomial orders. This phenomenon is especially prominent when thickness is small compared to in-plane dimensions. To alleviate this drawback we propose either to reduce stiffness in the transverse direction (such element to be referred as H3RAMS), or to employ hierarchical assumed strain degenerated shell element formulation with rotational degrees-of-freedom denoted by H2AMS. These two elements are described in Sections 2.2 and 2.3.

2.2. *H3RAMS—hierarchical (3-D) with reduced transverse stiffness, assumed material strain element*

For the purpose of examining the causes of somewhat stiffer behavior of solid based elements compared to their degenerated counterparts (with rotational dofs), consider a beam problem. For elastic isotropic beam the strain energy is given by,

$$U = \frac{1}{2}\int_L (D_B\kappa^2 + D_M\epsilon^2 + D_S\gamma^2)\, dx \tag{10}$$

where L is the element length; ϵ, κ, and γ are the membrane strain, curvature and transverse shear strain respectively; D_B, D_M, and D_S are the bending, membrane and shear stiffness constants given by,

$$D_B = \frac{Et^3}{12} \quad D_M = Et \quad D_S = k_s Gt \tag{11}$$

where t is the thickness of the beam of a unit width; E the Young's modulus; G the shear modulus and k_s the shear correction factor.

In 2-D normal strains are computed directly from kinematics. These values are not arbitrary and are not consistent with plane stress condition for thin domains. Thus if two dimensional state of stress is considered, the resulting strain energy takes the following form:

$$U = \frac{1}{2}\int_L (\bar{D}_B\kappa^2 + \bar{D}_M\epsilon^2 + \epsilon D_C\mu + D_S\gamma^2 + D_\mu\mu^2)\, dx \tag{12}$$

where

$$\bar{D}_M = \frac{D_M}{1-\nu^2} \quad \bar{D}_B = \frac{D_B}{1-\nu^2} \quad D_C = 2\nu\bar{D}_M \quad D_\mu = \bar{D}_M \tag{13}$$

In curved continuum based flexural elements spurious coupling between membrane and normal deformation exists giving rise to a parasitic normal strain energy, which is of the same order of magnitude as that of the membrane strain energy if the strains are of equal order. This phenomenon is referred to here as transverse normal locking of solid based flexural elements.

To ameliorate the locking caused by transverse normal strains we propose to calibrate the constitutive behavior of solid based elements to match the strain energy corresponding to degenerated elements without introducing zero energy modes. By this technique the stiffness coefficients in the constitutive tensor are modified in the following way:

$$\bar{D}_M = D_M \quad \bar{D}_B = D_B \quad D_C = 0 \quad D_\mu = \chi D_M \tag{14}$$

where χ is a stabilization parameter aimed at stabilizing the zero transverse normal energy modes of solid based flexural elements.

2.3. *H2AMS—hierarchic (2-D) degenerated assumed material strain element with rotational degrees-of-freedom*

As a starting point, consider the displacement field expressed in terms of mid-point translations $u_i^f(\xi_1, \xi_2)$ and mid-point rotations $\theta_i(\xi_1, \xi_2)$ which are defined with respect to the fiber coordinate system:

$$\begin{Bmatrix} u_1 \\ u_2 \\ u_3 \end{Bmatrix}_{(\xi_1,\xi_2,\xi_3)} = \begin{Bmatrix} u_1^f \\ u_2^f \\ u_3^f \end{Bmatrix}_{(\xi_1,\xi_2)} + \frac{\xi_3}{2}[-t\mathbf{e}_2^f, t\mathbf{e}_1^f]_{(\xi_1,\xi_2)} \begin{Bmatrix} \theta_1 \\ \theta_2 \end{Bmatrix} \tag{15}$$

where the unit vectors $(\mathbf{e}_1^f, \mathbf{e}_2^f, \mathbf{e}_3^f)$ of the fiber coordinate system are defined as follows:

$$\mathbf{e}_3^f = \frac{\mathbf{X}^{top} - \mathbf{X}^{bot}}{t} \quad \mathbf{e}_2^f = \frac{\mathbf{e}_3 \times \mathbf{e}_j}{\|\mathbf{e}_3 \times \mathbf{e}_j\|} \quad \mathbf{e}_1^f = \mathbf{e}_2 \times \mathbf{e}_3, \tag{16}$$

$t(\xi_1, \xi_2)$ is the thickness of the shell defined as,

$$t = \|\mathbf{X}^{top} - \mathbf{X}^{bot}\|. \tag{17}$$

For the purpose of discussion here, the iso-parametric shell element discretization is viewed of consisting of the following two steps:

1. Evaluate the displacement field at the finite element nodes $(\xi_1 = \xi_1^A, \xi_2 = \xi_2^A)$ using Eq. (15): $u_i^A(\xi_3) = u_i(\xi_1 = \xi_1^A, \xi_2 = \xi_2^A, \xi_3)$
2. Interpolate the displacement field using two-dimensional Lagrangian basis functions: $u_i(\xi_1, \xi_2, \xi_3) = N_A^{\text{lag}}(\xi_1, \xi_2) u_i^A(\xi_3)$.

The extension of this approach to the hierarchical formulation where degrees-of-freedom are not associated with the value of the solution at a specific location within the element is as follows: Instead of taking a two-step route, the fields $u_i^I(\xi_1, \xi_2)$ and $\theta_\alpha(\xi_1, \xi_2)$ are directly discretized using the Legendre polynomials. The resulting solution approximation takes the following form:

$$\begin{Bmatrix} u_1 \\ u_2 \\ u_3 \end{Bmatrix} = \sum_{A=1}^{NMDS} N_A(\xi_1, \xi_2) \begin{Bmatrix} u_1^{IA} \\ u_2^{IA} \\ u_3^{IA} \end{Bmatrix} + \sum_{A=1}^{NMDS} N_A(\xi_1, \xi_2) \frac{\xi_3}{2} [-te_2^I, te_1^I]_{(\xi_1, \xi_2)} \begin{Bmatrix} \theta_1^A \\ \theta_2^A \end{Bmatrix} \quad (18)$$

Note that there is a fundamental difference between Eq. (18) and its iso-parametric counterpart. In the classical iso-parametric formulation the variable vector function $e_i^I(\xi_1, \xi_2)$ in Eq. (18) is replaced by a set of constant vectors $e_i^I(\xi_1^A, \xi_2^A)$ representing the fiber coordinate system at a specified node A. Consequently the present formulation gives rise to an additional term Δ_A in the displacement gradient evaluation:

$$\frac{\partial \mathbf{u}}{\partial \xi_\alpha} = \sum_{A=1}^{NMDS} \frac{\partial N_A(\xi_1, \xi_2)}{\partial \xi_\alpha} \begin{Bmatrix} u_1^{IA} \\ u_2^{IA} \\ u_3^{IA} \end{Bmatrix} + \sum_{A=1}^{NMDS} \left[\frac{\partial N_A(\xi_1, \xi_2)}{\partial \xi_\alpha} \frac{\xi_3}{2} [-te_2^I, te_1^I] + \Delta_A \right] \times \begin{Bmatrix} \theta_1^A \\ \theta_2^A \end{Bmatrix} \quad (19)$$

and

$$\Delta_A = N_A(\xi_1, \xi_2) \frac{\xi_3}{2} \left[-\frac{\partial (te_2^I)}{\partial \xi_\alpha}, \frac{\partial (te_1^I)}{\partial \xi_\alpha} \right] \quad (20)$$

where $\alpha \in [1, 2]$. Derivatives of $((te_1^I), (te_2^I))$ are obtained by differentiation of appropriate mapping functions.

3. QUADRATURE SCHEME FOR HIERARCHICAL SHELL ELEMENTS

In this section we present a nearly optimal quadrature scheme for hierarchical systems, which minimizes the number of function evaluations and eliminates the need for explicit strain interpolation between reduced and regular quadrature points.

3.1. *Dot product integral decomposition*

Consider the integral of the form $\int_\Omega g(\xi_1, \xi_2, \xi_3) h(\xi_1, \xi_2, \xi_3)\, d\Omega$ in the natural coordinate system such that $d\Omega = d\xi_1\, d\xi_2\, d\xi_3$ and $-1 < \xi_i < 1$. The integral under consideration may represent a typical stiffness matrix component, where g is a strain-displacement matrix component and h is a strain-displacement matrix term multiplied by a Jacobian and a corresponding component of the constitutive tensor. In the classical Gauss quadrature the integrand (gh) is implicitly curve fit with a polynomial and then integrated in a close form. It will be shown that for hierarchical systems it is more efficient to curve fit separately each term of the integrand (g and h) with orthonormal polynomial:

$$g = \sum_{i=0}^{n_1} \sum_{j=0}^{n_2} \sum_{k=0}^{n_3} \underbrace{a_{ijk}}_{a_I} \overbrace{P_i(\xi_1) P_j(\xi_2) P_k(\xi_3)}^{\phi_I} \equiv \sum_{I=1}^{N} a_I \phi_I(\xi_1, \xi_2, \xi_3) \quad (21)$$

$$h = \sum_{s=0}^{m_1} \sum_{t=0}^{m_2} \sum_{r=0}^{m_3} \underbrace{b_{str}}_{b_J} \overbrace{P_s(\xi_1) P_t(\xi_2) P_r(\xi_3)}^{\sigma_J} \equiv \sum_{J=1}^{M} b_J \phi_J(\xi_1, \xi_2, \xi_3) \quad (22)$$

where $\hat{P}_i$ are normalized Legendre polynomials. For convenience, concise notation is introduced with $a_I \equiv a_{ijk}$, $\phi_I(\xi_1, \xi_2, \xi_3) \equiv \hat{P}_i(\xi_1) \hat{P}_j(\xi_2) \hat{P}_k(\xi_3)$, $N = (n_1 + 1)(n_2 + 1)(n_3 + 1)$ and $M = (m_1 + 1)(m_2 + 1)(m_3 + 1)$.

Using (21) and (22) the integral of $g\ h$ can be decomposed into a dot product of two vectors:

$$\int_\Omega gh\, d\Omega = \sum_{i=0}^{l_1} \sum_{j=0}^{l_2} \sum_{k=0}^{l_3} \int_\Omega g \hat{P}_i(\xi_1) \hat{P}_j(\xi_2) \hat{P}_k(\xi_3)\, d\Omega \cdot \int_\Omega h \hat{P}_i(\xi_1) \hat{P}_j(\xi_2) \hat{P}_k(\xi_3)\, d\Omega = \sum_{I=1}^{L} \int_\Omega g \phi_I\, d\Omega \int_\Omega h \phi_I\, d\Omega \quad (23)$$

where $l_i = \min(n_i, m_i)$ and $L = (l_1 + 1)(l_2 + 1)(l_3 + 1)$.

The proof based on orthogonality of Legendre polynomials was given in Ref. 16 for 1-D problems and in Ref. 17 for multi-dimensions. In Ref. 16 it has been shown that the number of function evaluations required for the dot product integral decomposition can be reduced by approximately a factor of 2^{nsd} compared to the classical Gauss quadrature, where *nsd* is the number of space dimensions.

3.2. *Symmetric dot product integral decomposition for HAMS shell element*

In this section we present a variant of Dot product integral decomposition which preserves the symmetry of the stiffness matrix. Consider a typical stiffness for HAMS element given by

$$k_{AB} = \int_\Omega \underbrace{\bar{\mathbf{B}}_A^{\text{mat}T}\mathbf{D}\bar{\mathbf{B}}_B^{\text{mat}}J}_{\mathbf{g}_A\mathbf{h}_B}\,d\Omega. \tag{24}$$

In an attempt to obtain a symmetric dot product integral decomposition, we decompose the integrand $(\mathbf{g}_A\mathbf{h}_B)$ as follows:

$$\mathbf{h}_A^T = \mathbf{g}_A = \bar{\mathbf{B}}_A^{\text{mat}T}\mathbf{L}J^{1/2} \tag{25}$$

where $\mathbf{L}$ is a lower triangular Cholesky factor of the constitutive matrix $\mathbf{D}$. The resulting stiffness matrix is given by

$$k_{AB} = \sum_{I=1}^{L}\int_\Omega (\mathbf{L}^T\bar{\mathbf{B}}_A^{\text{mat}})^T\phi_I J^{1/2}\,d\Omega \times \int_\Omega \mathbf{L}^T\bar{\mathbf{B}}_B^{\text{mat}}\phi_I J^{1/2}\,d\Omega. \tag{26}$$

Each of the two integrals is integrated using Gauss quadrature. The number of quadrature points as well as the maximum polynomial order of the interpolating Legendre polynomials in each direction depends on how well the integrand $\mathbf{L}^T\bar{\mathbf{B}}_A^{\text{mat}}J^{1/2}$ is approximable by polynomials and what is their polynomial order. We will refer to this integration scheme as Symmetric Dot Product (SDP) Gauss quadrature.

In the case when the constitutive tensor $\mathbf{D}$ is not positive definite an alternative integrand decomposition is employed. Let

$$\mathbf{g}_A = \bar{\mathbf{B}}_A^{\text{mat}T}J^{1/2} \quad \mathbf{h}_B = \mathbf{D}J^{1/2}\bar{\mathbf{B}}_B^{\text{mat}} \tag{27}$$

which yields

$$k_{AB} = \sum_{I=1}^{L}\int_\Omega \bar{\mathbf{B}}_A^{\text{mat}T}J^{1/2}\phi_I\,d\Omega \times \int_\Omega \underbrace{\mathbf{D}\phi_I}_{\mathbf{g}_I}\,\underbrace{\bar{\mathbf{B}}_B^{\text{mat}}J^{1/2}}_{\mathbf{h}_B}\,d\Omega \tag{28}$$

and further dot product integral decomposition of the second term in (28) yields the following symmetric form:

$$k_{AB} = \sum_{I=1}^{L}\sum_{J=1}^{L}\int_\Omega (\bar{\mathbf{B}}_A^{\text{mat}T}J^{1/2})\phi_I\,d\Omega \times \int_\Omega \underbrace{(\mathbf{D})\phi_I\phi_J\,d\Omega}_{\mathbf{D}_{IJ}}\cdot\int_\Omega (\bar{\mathbf{B}}_B^{\text{mat}}J^{1/2})\phi_J\,d\Omega. \tag{29}$$

Note that if the constitutive tensor is constant, $\bar{\mathbf{D}}_{IJ} = \int_\Omega(\mathbf{D})\phi_I\phi_J\,d\Omega = \mathbf{D}\delta_{IJ}$ reducing Eq. (29) to

$$k_{AB} = \sum_{I=1}^{L}\int_\Omega (\bar{\mathbf{B}}_A^{\text{mat}T}J^{1/2})\phi_I \times d\Omega\cdot\mathbf{D}\cdot\int_\Omega (\bar{\mathbf{B}}_B^{\text{mat}}J^{1/2})\phi_I\,d\Omega. \tag{30}$$

It can be easily shown that if $\mathbf{D} \neq$ constant then the stiffness matrix evaluations by means of Eq. (29) is more computationally intensive because of the double summation involved.

The polynomial order of $\phi_I = \hat{P}_i(\xi_1)\hat{P}_j(\xi_2)\hat{P}_k(\xi_3)$ is chosen to selectively project out higher order terms from the strain field. By this technique the typical stiffness matrix term is given by:

$$k_{AB} = \sum_{i=1}^{l_1}\sum_{j=1}^{l_2}\sum_{k=1}^{l_3}\int_\Omega \begin{bmatrix} B_{11A}\hat{\hat{P}}_i(\xi_1)\hat{P}_j(\xi_2)\hat{P}_k(\xi_3) \\ B_{22A}\hat{P}_i(\xi_1)\hat{\hat{P}}_j(\xi_2)\hat{P}_k(\xi_3) \\ B_{33A}\hat{P}_i(\xi_1)\hat{P}_j(\xi_2)\hat{\hat{P}}_k(\xi_3) \\ B_{23A}\hat{P}_i(\xi_1)\hat{\hat{P}}_j(\xi_2)\hat{\hat{P}}_k(\xi_3) \\ B_{12A}\hat{\hat{P}}_i(\xi_1)\hat{\hat{P}}_j(\xi_2)\hat{P}_k(\xi_3) \\ B_{13A}\hat{\hat{P}}_i(\xi_1)\hat{P}_j(\xi_2)\hat{\hat{P}}_k(\xi_3) \end{bmatrix}^T \mathbf{L}J^{1/2}\,d\Omega \int_\Omega \mathbf{L}^T \begin{bmatrix} B_{11B}\hat{\hat{P}}_i(\xi_1)\hat{P}_j(\xi_2)\hat{P}_k(\xi_3) \\ B_{22B}\hat{P}_i(\xi_1)\hat{\hat{P}}_j(\xi_2)\hat{P}_k(\xi_3) \\ B_{33B}\hat{P}_i(\xi_1)\hat{P}_j(\xi_2)\hat{\hat{P}}_k(\xi_3) \\ B_{23B}\hat{P}_i(\xi_1)\hat{\hat{P}}_j(\xi_2)\hat{\hat{P}}_k(\xi_3) \\ B_{12B}\hat{\hat{P}}_i(\xi_1)\hat{\hat{P}}_j(\xi_2)\hat{P}_k(\xi_3) \\ B_{13B}\hat{\hat{P}}_i(\xi_1)\hat{P}_j(\xi_2)\hat{\hat{P}}_k(\xi_3) \end{bmatrix} J^{1/2}\,d\Omega \tag{31}$$

where

$$\hat{\hat{P}}_m(\xi_i) = \begin{cases}\hat{P}_m(\xi_i) & m < l_i \\ 0 & m = l_i\end{cases} \tag{32}$$

which is consistent with Eqs (7) and (8).

4. SOLUTION PROCEDURES FOR HIERARCHICAL SHELL FORMULATION

In this section we present two versions of accelerated multigrid method for solving positive definite systems arising from the p-version discretization of shells:

$$\mathbf{K}^m\mathbf{d}^m = \mathbf{f}^m; \quad m = 1, 2 \ldots, \text{level} \tag{33}$$

where

$$\mathbf{K}^m = \begin{bmatrix}\hat{\mathbf{K}}^{m-1} & \mathbf{K}_{12}^m \\ \mathbf{K}_{21}^m & \mathbf{K}_{11}^m\end{bmatrix} \quad \mathbf{d} = \begin{Bmatrix}\mathbf{d}^{m-1} \\ \mathbf{d}_1^m\end{Bmatrix} \quad \mathbf{f} = \begin{Bmatrix}\mathbf{f}^{m-1} \\ \mathbf{f}_1^m\end{Bmatrix} \tag{34}$$

and m is the level number; $\mathbf{K}^0$ the stiffness matrix on the initial level; $\mathbf{K}^m$ is of order $n_m > n_{m-1}$, where n_{m-1} is the order of the block $\hat{\mathbf{K}}^{m-1}$; $\mathbf{d}^{m-1} \in \Re^{n_{m-1}}$ and $\mathbf{d}_1^m \in \Re^{(n_m - n_{m-1})}$.

The special feature of the Eq. (34) for shell analysis is that lower order block $\hat{\mathbf{K}}^{m-1}$ might be different from the stiffness matrix corresponding to level $(m-1)$, denoted as $\mathbf{K}^{m-1}$ because of either

1. Change in constitutive model from plane stress $(q=1)$ to $3-D$ $(q \geqslant 2)$.
2. Progressive improvement in geometry or
3. Changing quadrature scheme.

Let $\mathbf{Q}_m^{m-1}$ and $\mathbf{Q}_{m-1}^m$ be the restriction and prolongation operators, which transfer the data from level (m) to level $(m-1)$ and vice versa. For the p-method it has a very simple form:

$$\mathbf{Q}_m^{m-1} = [\mathbf{I} \quad \mathbf{0}] = \mathbf{Q}_{m-1}^{m\,T} \tag{35}$$

where $\mathbf{I}$ is the order n_{m-1} identity matrix, and $\mathbf{0}$ is order $(n_m - n_{m-1})$ zero matrix. Note that the restriction of the stiffness matrix is given by:

$$\hat{\mathbf{K}}^{m-1} = \mathbf{Q}_m^{m-1}\mathbf{K}^m\mathbf{Q}_{m-1}^m \neq \mathbf{K}^{m-1}. \tag{36}$$

A single V-cycle has a compact recursive definition given by:

$$\mathbf{z}^m := MG^m(\mathbf{r}^m, \mathbf{K}^m) \tag{37}$$

where $\mathbf{r}^m$ is the residual vector. The V-cycle multigrid algorithm is summarized below:

1. Loop $i = 0, 1, 2 \ldots$ until convergence if $i = 0 \leftarrow \mathbf{d}^m = \mathbf{0}$
2. Perform γ_1 pre-smoothing operations

$$_{\gamma_1}{}^i\mathbf{d}^m := \text{smooth}(\gamma_{1,0}{}^i\mathbf{d}^m, \mathbf{K}^m, \mathbf{f}^m)$$

   where the left superscript and subscript denote the cycle number and smoothing count respectively.
3. Restrict residual from level m to $m-1$

$$\mathbf{r}^{m-1} = \mathbf{Q}_m^{m-1}(\mathbf{f}^m - \mathbf{K}^m{}_{\gamma_1}{}^i\mathbf{d}^m)$$

4. Coarse grid correction
   If $(m-1) =$ lowest level, solve directly $\mathbf{z}^{m-1} = (\mathbf{K}^{m-1})^{-1}\mathbf{r}^{m-1}$,
   Else $\mathbf{z}^{m-1} := MG^{m-1}(\mathbf{r}^{m-1}, \mathbf{K}^{m-1})$
5. Prolongate the solution from level $m-1$ to m

$$_{\gamma_1+1}{}^i\mathbf{d}^m = {}_{\gamma_1}{}^i\mathbf{d}^m + {}^i\omega\,\mathbf{Q}_{m-1}^m\mathbf{z}^{m-1}$$

   where ${}^i\omega$ is a coarse grid relaxation parameter, which minimizes energy functional along the prescribed direction $\mathbf{v}^m = \mathbf{Q}_{m-1}^m\mathbf{z}^{m-1}$. Note that for two grid methods ${}^i\omega = 1$ if $\hat{\mathbf{K}}^{m-1} = \mathbf{K}^{m-1}$.

   Otherwise

$$^i\omega = \frac{\mathbf{v}^{m\,T}(\mathbf{f}^m - \mathbf{K}^m{}_{\gamma_1+1}{}^i\mathbf{d}^m)}{\mathbf{v}^{m\,T}\mathbf{K}^m\mathbf{v}^m} \tag{38}$$

6. Perform γ_2 post-smoothing operations

$$^{i+1}_{0}\mathbf{d}^m := \text{smooth}(\gamma_{2,\gamma_1+1}{}^i\mathbf{d}^m, \mathbf{K}^m, \mathbf{f}^m).$$

A variant of the standard V-cycle multigrid method has been proposed by Bank, Dupont & Yserentan.[18] This method termed as hierarchical basis multigrid technique (HBM), is similar to the standard multigrid V-cycle, except that a smaller than the normal subset of unknowns is updated during the smoothing phase at a given level. Schematically, the smoothing process in HBM takes the following block structure:

$$^{i+1}\mathbf{d}_1^m := \text{smooth}(\gamma_{1,0}{}^i\mathbf{d}_1^m, \mathbf{K}_{11}^m, \mathbf{f}_1^m) \tag{39}$$

HBM takes advantage of the fact that smoothing mainly affects highest oscillatory modes of error, and thus relaxation sweeps are performed on the block by block level keeping the rest of the degrees of freedom fixed. It has been shown that the rate of convergence of HBM method has a logarithmic dependence on the problem size as opposed to multigrid method which has an optimal rate of convergence independent of the mesh size and spectral order.[18] The key question is whether the benefit from reducing the cost of smoothing process over weighs the suboptimal performance of HBM in comparison with the standard multigrid method for thin and thick shells.

For ill-conditioned problems, such as thin shells, it is desirable to accelerate the rate of convergence of the multigrid like methods. In this section we present a two parameter acceleration scheme that requires a small fraction of computational effort, but at the same time is efficient in expediting the convergence of the multigrid like methods (MG and HBM).

Let ${}^i\mathbf{r}^m$ be the residual vector at the end of i^{th} m-level multigrid cycle. The incremental multigrid solution for the next cycle ${}^i\mathbf{z}^m = MG^m({}^i\mathbf{r}^m, \mathbf{K}^m)$ is used as a predictor in the two parameter acceleration scheme. The solution in the correction phase is then updated as follows:

$$^{i+1}\mathbf{v} = {}^i\alpha\,{}^i\mathbf{z}^m + {}^i\beta\,{}^i\mathbf{v} \tag{40}$$

$$^{i+1}\mathbf{d}^m = {}^i\mathbf{d}^m + {}^{i+1}\mathbf{v} \tag{41}$$

where parameters $({}^i\alpha, {}^i\beta)$ are obtained by minimizing the potential energy functional:

$$\tfrac{1}{2}({}^i\mathbf{d}^m + {}^i\alpha\,{}^i\mathbf{z}^m + {}^i\beta\,{}^i\mathbf{v})^T\mathbf{K}^m({}^i\mathbf{d}^m + {}^i\alpha\,{}^i\mathbf{z}^m + {}^i\beta\,{}^i\mathbf{v})$$

$$-({}^i\mathbf{d}^m + {}^i\alpha\,{}^i\mathbf{z}^m + {}^i\beta\,{}^i\mathbf{v})^T\mathbf{f}^m \to \min_{\alpha,\beta} \tag{42}$$

The resulting algorithm is summarized below:

Step 1.

$$^0\mathbf{d}^m = 0, \quad ^0\mathbf{r}^m = \mathbf{f}^m$$

$$^0\mathbf{z}^m := MG^m(^0\mathbf{r}^m, \mathbf{K}^m)$$

$$^0\mathbf{v} = ^0\mathbf{y} = 0$$

$$^0\mathbf{x} = \mathbf{K}^{m0}\mathbf{z}^m$$

$$^0\beta = 0$$

$$^0\alpha = \frac{(\mathbf{f}^m, ^0\mathbf{z}^m)}{(^0\mathbf{x}^m, ^0\mathbf{z}^m)}.$$

Step 2.

Do $i = 0, 1, 2 \ldots$ until convergence

$$\begin{Bmatrix} ^i\alpha \\ ^i\beta \end{Bmatrix} = \begin{bmatrix} (^i\mathbf{x}, ^i\mathbf{z}^m) & (^i\mathbf{x}, ^i\mathbf{v}) \\ (^i\mathbf{x}, ^i\mathbf{v}) & (^i\mathbf{y}, ^i\mathbf{v}) \end{bmatrix}^{-1} \begin{Bmatrix} (^i\mathbf{r}^m, ^i\mathbf{z}^m) \\ (^i\mathbf{r}^m, ^i\mathbf{v}) \end{Bmatrix} \quad i > 0 \tag{43}$$

$$^{i+1}\mathbf{v} = ^i\alpha\,^i\mathbf{z}^m + ^i\beta\,^i\mathbf{v}$$

$$^{i+1}\mathbf{d}^m = ^i\mathbf{d}^m + ^{i+1}\mathbf{v}$$

$$^{i+1}\mathbf{y} = ^i\alpha\,^i\mathbf{x} + ^i\beta\,^i\mathbf{y}$$

$$^{i+1}\mathbf{r}^m = ^i\mathbf{r}^m - ^{i+1}\mathbf{y}$$

$$^{i+1}\mathbf{z}^m := MG^m(^{i+1}\mathbf{r}^m, \mathbf{K}^m)$$

$$^{i+1}\mathbf{x} = \mathbf{K}^{m\,i+1}\mathbf{z}^m.$$

Note that the two parameter acceleration scheme requires no additional matrix–vector multiplication and its benefit clearly overshadows the cost involved in dot product evaluations in Eq. (43) for thin shells. For alternative acceleration schemes, including PCG acceleration see Ref. 17.

5. ADAPTIVITY AND QUALITY CONTROL

Both *a posteriori* error estimation scheme and adaptive strategy are based on hierarchical spectral order enrichment. One of the earliest uses of this approach was by Zienkiewicz and his associates in the early 1980s.[4] By this technique given the finite element solution $u^{p,q}$ corresponding to the finite element space $S^{(p,q)}$ one can hierarchically enrich the space by adding certain hierarchical basis functions to the set already used for $S^{(p,q)}$. If $S^{(p,q,l)}$ is the new space, then we have the hierarchical decomposition

$$S^{(p,q,l)} = S^{(p,q)} \oplus W^l \tag{44}$$

where W^l is the subspace which corresponds to the span of the additional basis functions and l is the list of additional basis functions.

Let the estimated error $\mathbf{E} = \phi\beta \in W^l$ be a linear combination of basis functions ϕ spanning the subspace W^l, then the unknown coefficients β are obtained by minimization of the energy functional on the subspace W^l, that is,

$$\tfrac{1}{2}(\mathbf{K}(\mathbf{u}^{p,q} + \phi\beta), (\mathbf{u}^{p,q} + \phi\beta)) - (\mathbf{f}, \mathbf{u}^{p,q} + \phi\beta) \to \min_{\beta} \tag{45}$$

where $\mathbf{K}$ and $\mathbf{f}$ are the stiffness matrix and the force vector corresponding to the enriched space $S^{(p,q,l)}$ and $(\cdot, \cdot)$ denotes the bilinear form given by

$$(\mathbf{u}, \mathbf{v}) = \sum_{i=1}^{n} u_i v_i. \tag{46}$$

Since the hierarchical basis functions ϕ are typically highly oscillatory functions with compact support, it is common practice to approximate the stiffness matrix corresponding to the subspace W^l by its diagonal form, which further reduces the cost of computing the error estimate. By this technique the error estimate in the energy norm is given by

$$\|\mathbf{E}\| = \left[\sum_{A=1}^{n} \eta_A^2\right]^{1/2} \tag{47}$$

where

$$\eta_A = \tfrac{1}{2}\beta_A^2 K_{AA} \tag{48}$$

and K_{AA} is the stiffness coefficient corresponding to the degree-of-freedom A. η_A is termed as an error indicator which measures the decrease in error of the solution by adding a particular new degree-of-freedom. Adaptive strategy is steered by the magnitude of the error indicators. At each step we add all degrees-of-freedom corresponding to error indicators, such that

$$\eta_A > \gamma\eta_{\max}. \tag{49}$$

Parameter $\gamma \in [0, 1]$ controls the speed of convergence: if γ is zero, then we add all possible degrees-of-freedom; if γ is one, we add none.

Note that this theoretical framework is only valid as long as the finite element matrices are hierarchical, that is lower order matrices are sub-matrices of higher order matrices. Even though solution approximation is hierarchical the resulting finite element matrices will not be in the three cases mentioned in Section 4.

Our experience indicates that the quality of error estimators and indicators as well as the efficiency of adaptive strategy could strongly degrade if the lower order blocks are ot recomputed in the three cases mentioned above.

6. NUMERICAL RESULTS

Our numerical studies include

1. Comparison of SDP with other popular quadrature schemes.
2. Linear solvers for hierarchical systems.
3. Effects of mesh distortion and progressive change of geometry on hierarchic shell elements.
4. Adaptivity and selective polynomial refinement.

A comparison of various quadrature schemes is a difficult task since they provide different results and their performance is implementation dependent. Focusing primarily on the computational efficiency aspects and assuming that each quadrature scheme has been implemented with the optimal efficiency we comprise the following basis for comparison: Solution accuracy (measured in terms of error in the energy norm) vs CPU time required to form a stiffness matrix of the single element. We will conduct numerical examples for two problems quarter of each modeled with a single element: pinched cylinder (constant in-plane Jacobian) and a frustum of a cone (variable in-plane Jacobian). All the experiments are conducted on a Sun Sparc 10 workstation with 128 MB internal memory.

Figures 1–4 show the performance of four types of shell elements: H2-type (degenerated hierarchic shell with 5 dofs per mode[22]) in Fig. 1, H3R-type (hierarchic shell element with $q = 1$ and reduced stiffness in transverse normal direction[22]) in Fig. 2, H3-type $q = 2$ (hierarchic shell element with quadratic through the thickness interpolation) in Fig. 3, and H3-type $q = 4$ (hierarchic shell element with fourth order through thickness interpolation) in Fig. 4.

Each figure contains four plots:

- (○) HSOL-SDP corresponding to Symmetric Dot Product Gauss quadrature for displacement based element.
- (△) HAMS-SDP corresponding to Symmetric Dot Product Gauss quadrature for assumed material strain element.
- (+) HSOL-UNIF corresponding to Uniform Gauss quadrature scheme for displacement based element.
- (×) HSOL-HBLOCK corresponding to Hierarchic Block Gauss quadrature scheme for displacement based element.

In Uniform quadrature entire stiffness matrix is integrated with the same number of quadrature points, which is dictated by the maximum polynomial order of the integrand and does not exploit the hierarchical structure of the stiffness matrix. A variant of the Uniform quadrature scheme, which is partially adapted to take advantage of the hierarchic structure of the stiffness matrix is labeled as *Hierarchic Block*[17] quadrature. By this technique submatrices corresponding to different polynomial orders are integrated with an integration rule corresponding to the maximum polynomial order of the appropriate block.

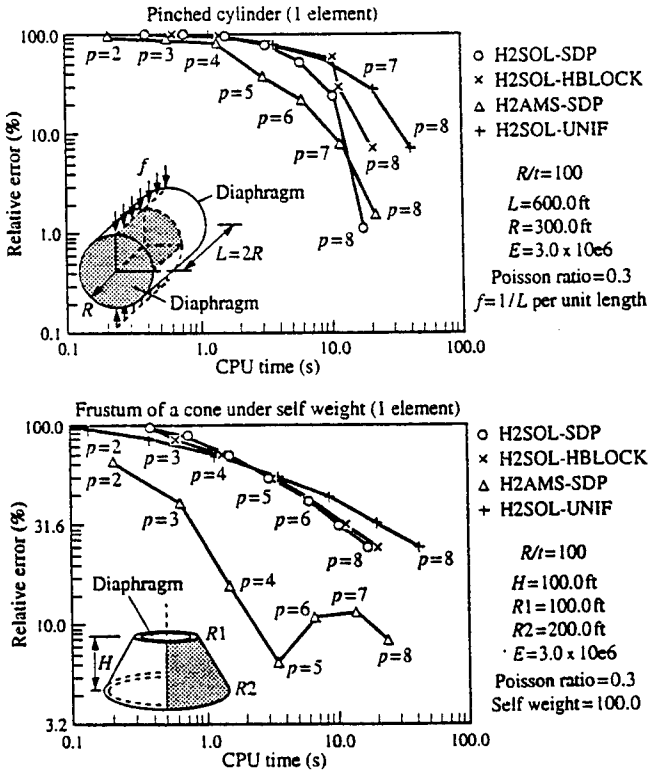


Fig. 1. Comparison of quadrature schemes for H2-type elements.

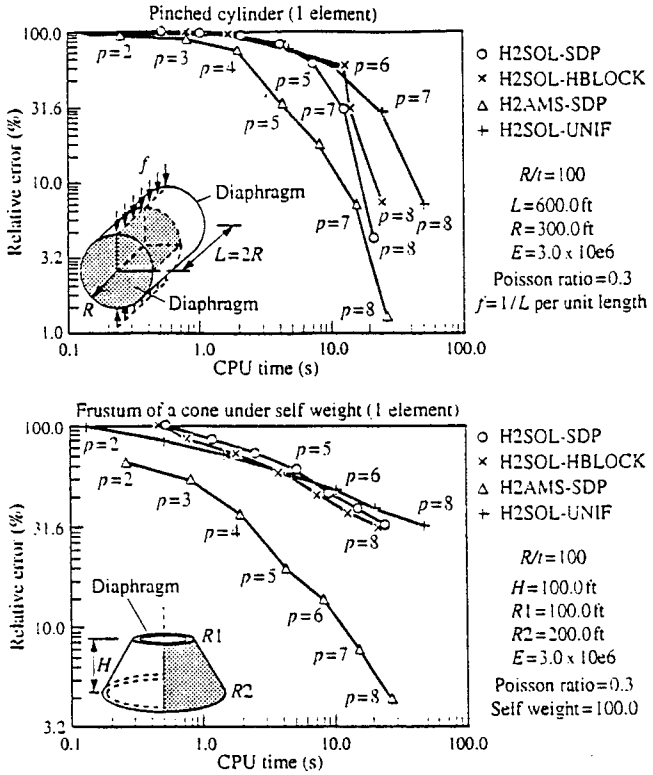


Fig. 2. Comparison of quadrature schemes for H3R-type ($q = 1$) elements.

To preserve hierarchical structure of the stiffness matrix the displacement based shell element has been over integrated to accommodate for highly varying metric tensor components $\partial x_i/\partial \xi_j$. For numerical examples considered, the number of integration points for Block Gauss quadrature was selected as $p^{\max}+3$ in inplane direction and $q^{\max}+1$ in transverse direction, where $p^{\max}$ and $q^{\max}$ are the maximum

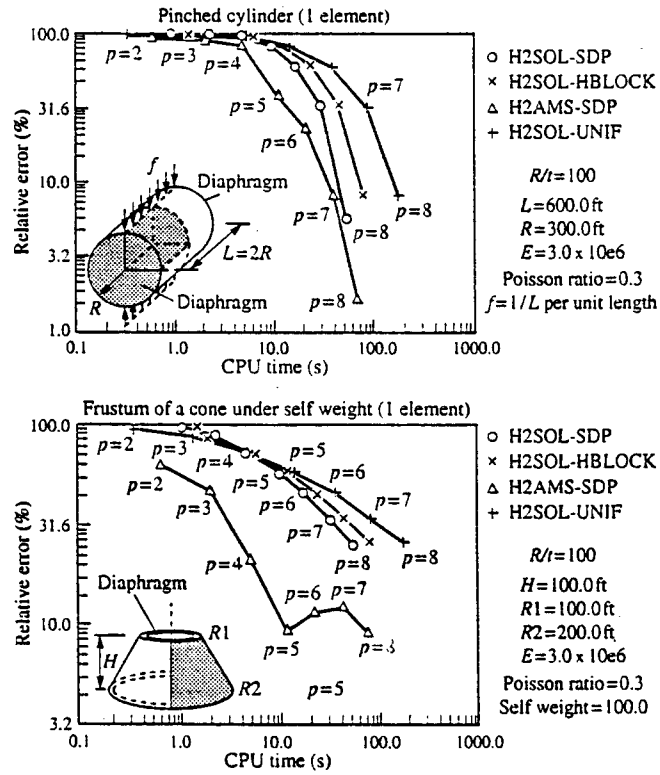


Fig. 3. Comparison of quadrature schemes for H3-type ($q = 2$) elements.

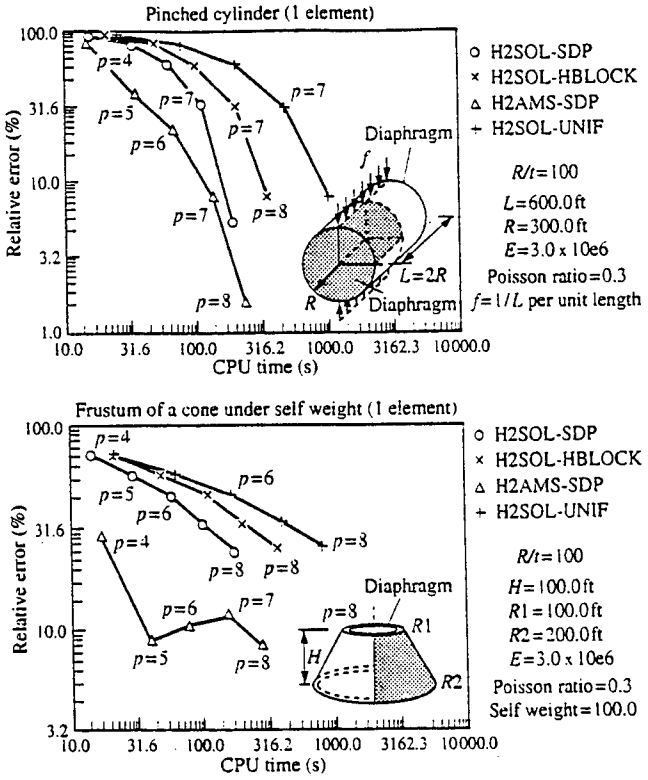


Fig. 4. Comparison of quadrature schemes for H3-type ($q = 4$) elements.

polynomial orders of the corresponding block in inplane and transverse directions, respectively.

Similarly, for SDP-Gauss quadrature applied to displacement based elements, the order of interpolating Legendre polynomials $\hat{P}_i(\xi_i)$ is selected as $(p_i + l)$ $i \in [1, 2]$ in inplane directions and $(q + m)$ in transverse direction. The corresponding number of integration points are $(p_i + l + 1)$ and $(q + m + 1)$ in

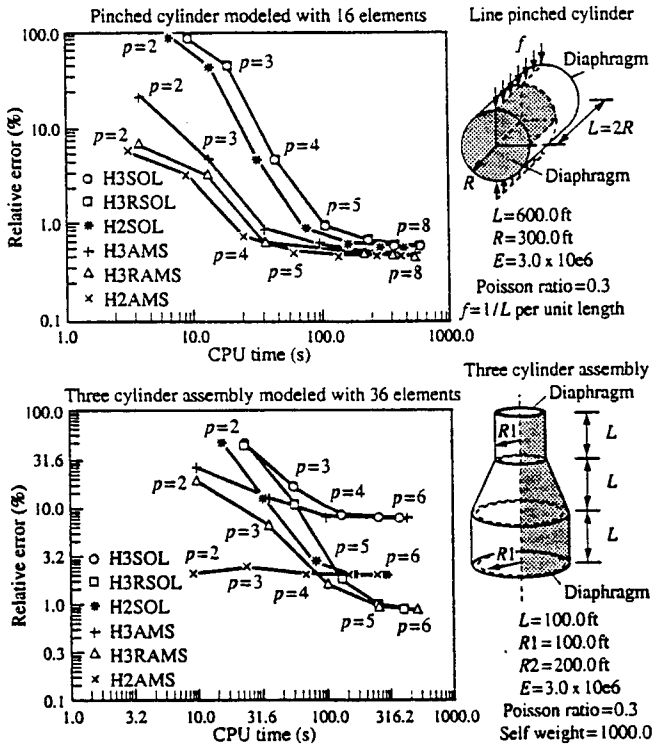


Fig. 5. Rate of convergence in terms CPU time for various elements for the line pinched cylinder problem (16 elements) and the 3 cylinder assembly problem (36 elements).

Table 1. Comparison of iterative schemes for pinched cylinder ($R/t = 100$) modeled with 16 (H2AMS) elements. One Gauss Seidel smoothing for multigrid-like solvers

Solver	(4, 5, 6, 7, 8)	(4, 6, 8)	(6, 8)	(6, 7, 8)
MG-ACC	262.224/22	203.544/28	**147.170/13**	174.360/12
HBM-ACC	219.540/49	188.400/42	189.940/25	193.050/26
MG-PCG	265.140/17	271.710/27	319.490/29	296.710/19
HBM-PCG	288.970/44	276.980/42	410.170/56	442.140/61
MG	693.020/56	626.860/83	424.360/58	381.290/34
HBM	2010.420/435	1464.410/314	1037.970/198	1370.230/266
PCG	519.470/177	670.810/154	380.880/53	316.164/71
Direct	456.308/1	456.308/1	456.308/1	456.308/1

Table 2. Comparison of iterative schemes for three cylinder assembly ($R/t = 100$) modeled with 36 (H2AMS) elements. One Gauss Seidel smoothing for mulitgrid-like solvers

Solver	(4, 5, 6, 7, 8)	(4, 6, 8)
MG-ACC	198.890/8	187.160/12
HBM-ACC	207.180/22	**164.740/17**
MG-PCG	294.940/9	312.150/15
HBM-PCG	397.180/31	414.690/32
MG	284.990/12	296.060/20
HBM	449.710/50	452.550/50
Direct	1231.440/1	1231.440/1

Table 3. Effect of radius of thickness (R/t) ratio on iterative methods. Pinched cylinder modeled with 16 (H2AMS) elements

Solver	($R/t = 10$)	($R/t = 20$)	($R/t = 30$)	($R/t = 100$)	($R/t = 300$)	($R/t = 1000$)
MG-ACC (4, 6, 8)	60.8/10	83.12/11	73.05/12	203.54/28	1023.6/169	8059.7/1292
HBM-ACC (4, 6, 8)	**32.1/8**	**49.39/10**	**53.92/14**	188.40/42	1025.8/275	8718.0/2382
PCG (4, 6, 8)	216.3/27	295.59/40	294.38/56	670.81/154	1398.6/458	3775.2/1329
Direct	456.3/1	456.31/1	456.31/1	456.31/1	456.31/1	**456.31/1**
MG-ACC (6, 8)	89.7/4	95.73/5	95.79/5	**147.17/13**	**373.05/50**	1969.1/309
HBM-ACC (6, 8)	95.5/6	100.38/7	110.17/9	189.94/25	661.88/122	2259.4/449
PCG (6, 8)	228.3/11	241.99/15	255.94/19	380.88/53	722.14/155	1840.0/481

Table 4. Influence of smoothing procedures of multigrid-like solvers. Pinched cylinder modeled with 16 (H2AMS) elements, multigrid-like solvers with (4, 6, 8)

Solver	GS-1	GS-2	JPCG-1	JPCG-2
MG-ACC ($R/t = 100$)	**203.544/28**	211.460/21	754.450/64	705.000/41
HBM-ACC ($R/t = 100$)	**188.400/42**	197.833/35	307.480/55	349.930/52
MG-ACC ($R/t = 300$)	**1023.550/169**	1030.670/100	3311.800/278	2590.820/149
HBM-ACC ($R/t = 300$)	1025.740/275	1300.045/230	**973.970/175**	1009.500/150

Table 5. Study of multigrid-like solvers for transitioning from plane stress to 3-D models. Pinched cylinder modeled with 12 (H2AMS) elements, multigrid-like solver MG-ACC with 2 Gauss Seidel smoothing

Element	NDOFS	Direct	2D–3D	Recomputed
H3RAMS ($q = 3$)	4416	2407.780	1809.54/55	**1753.990/41**
H3SOL ($q = 3$)	4416	2407.780	**1578.69/48**	1811.140/46

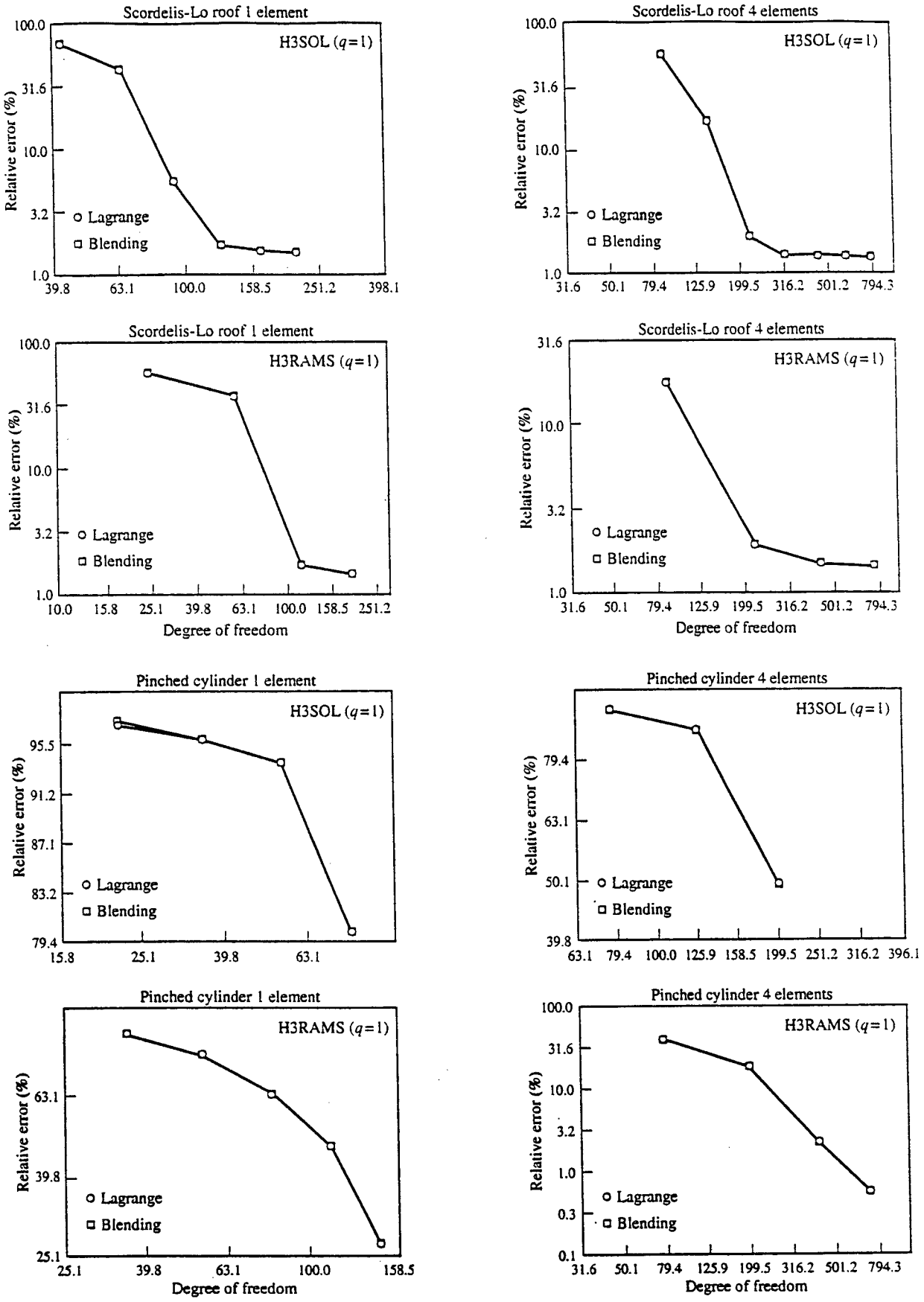


Fig. 6. Experimental rates of convergence for various elements with progressive (Lagrange) and fixed (blending) geometry.

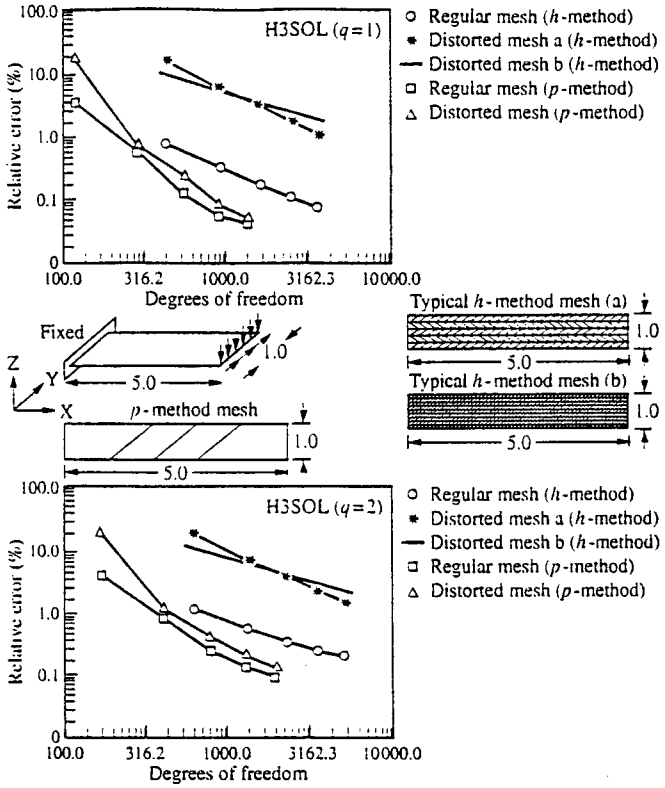


Fig. 7. Effect of mesh distortion on h- and p-versions of finite element method.

inplane and transverse directions, respectively, where (p_1, p_2) are the polynomial orders of the integrand in inplane directions (ξ_1, ξ_2) and q is the polynomial order in transverse direction (ξ_3). Selection of integers l and m is dictated by the variation of the metric tensor $\partial x_i/\partial \xi_j$ in inplane and transverse directions respectively. For example, in case of constant inplane Jacobian (the pinched cylinder) we used $l = 1$, $m = 0$

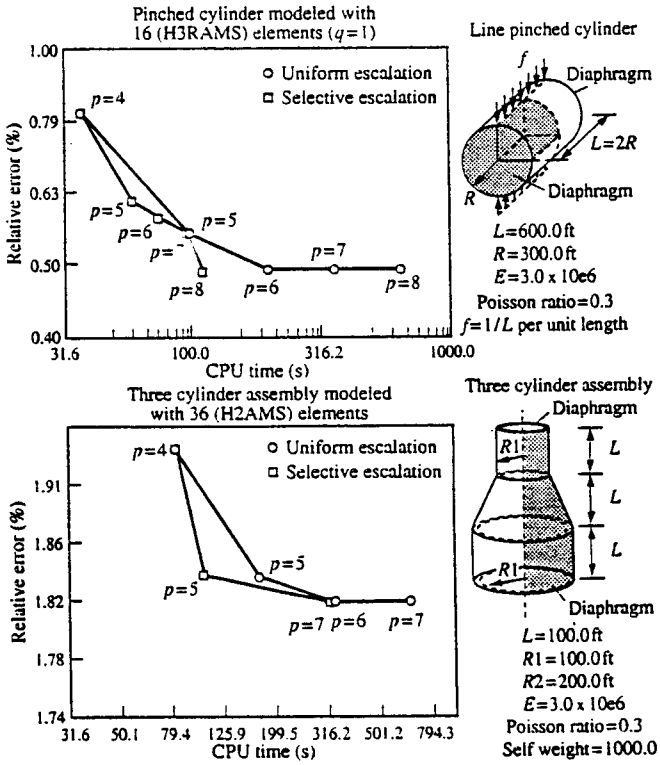


Fig. 8. Effect of selective refinement on rates of convergence.

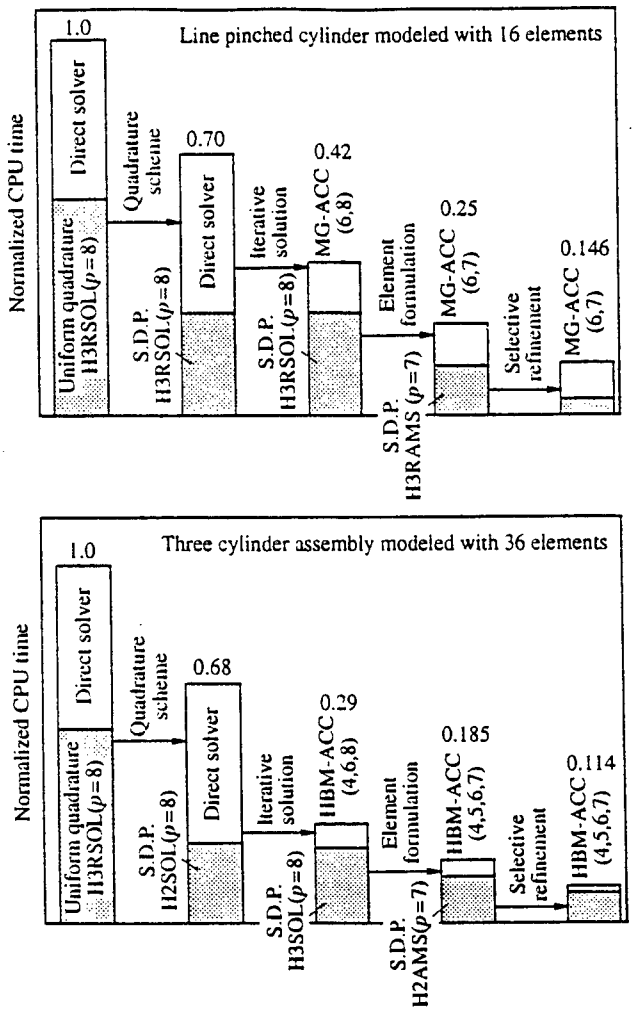


Fig. 9. Factors enhancing computational efficiency of p-method.

and $l = 2$, $m = 1$ for the case of variable inplane Jacobian (frustum of the cone).

In case of HAMS elements the order of interpolating Legendre polynomials is selected such that their polynomial order does not exceed the maximum polynomial order of the basis functions to ensure effectivity of selective polynomial order reduction. On the other hand for lower order blocks the polynomial order of Legendre polynomials is selected the same as for displacement based elements to partially preserve hierarchiality. Thus the order of Legendre polynomials for HAMS element is defined using the following rule:

- For a given integrand with polynomial orders (p_i, q)

  The inplane polynomial order of

$$\hat{p}_i = \begin{cases} p_i + l & \text{if } p_i + l < p^{\max} \\ p^{\max} & \text{otherwise} \end{cases} \tag{50}$$

  The order of Legendre polynomials in transverse direction is selected as $q + m$.

- The number of inplane integration points is selected as $p^{\max} + 1$, and $q^{\max} + 1$ in transverse direction.

It is evident from Figs 1–4 that among the displacement (HSOL) based elements, SDP and HBLOCK quadrature schemes are computationally more efficient than the uniform (UNIF) quadrature. The difference between HSOL-SDP and HSOL-HBLOCK is not significant and it can be deduced that for displacement based elements SDP and HBLOCK have a comparable performance.

Two problems are considered for investigation of linear solution procedures, the line pinched cylinder modeled with 16 elements (2432 dofs) and an assembly of 3 cylinders under dead load modeled with 36 elements (5496 dofs), 12 in each segment as shown in Fig. 5.

In Tables 1 and 2, various linear iterative solvers are compared with the direct (LDU) skyline solver. An attempt to determine the best iterative procedure for the two problems with radius to thickness ratio

100 ($R/t = 100$) has been made. The linear solution methods considered are:

- MG-ACC Multigrid method with two parameter acceleration.
- HBM-ACC Hierarchical Basis Multigrid method with two parameter acceleration.
- MG-PCG Multigrid method with PCG acceleration.
- HBM-PCG Hierarchical Basis Multigrid method with PCG acceleration.
- MG Multigrid method.
- HBM Hierarchical Basis Multigrid method.
- PCG Pre-conditioned Conjugate Gradient method with Block Preconditioner.
- Direct LDU skyline solver.

The columns in Tables 1 and 2 represent different levels employed in the iterative procedure. For example (4, 6, 8) has 3 levels for multigrid-like solvers, the coarse level corresponding to polynomial order 4 and the finest level being polynomial order 8. For the PCG solver, the same notation implies that the preconditioner has 3 blocks corresponding to polynomial orders (1–4), (5, 6) and (7, 8). For the direct solution of the coarse grid stiffness matrix the modes are numbered to minimize the skyline profile. This is accomplished by using the connectivity between topological entities (vertices, edges and faces) as a basis for mode numbering.

It is apparent from Tables 1 and 2 that MG-ACC and HBM-ACC are most efficient iterative solvers among the various iterative solution procedures compared. For the smaller problem with 16 elements (2432 dofs) the most efficient iterative solver has been found to be 3 times faster than the direct solver, and for a moderately larger problem with 36 elements (5496 dofs) this factor has been increased to 7.5. This ratio is likely to increase for larger problems as long as the thickness to span ratio is not decreased.

On the other hand it can be inferred from Table 3 that as the radius to thickness (R/t) ratio becomes larger the performance of the iterative procedures deteriorates, due to increase in the condition number. Assuming that deterioration in conditioning does not affect the accuracy of direct solution due to round off errors, the direct solver has outperformed the iterative procedures for very thin shells ($R/t = 300$) and ($R/t = 1000$).

In Table 4 the influence of various popular smoothing procedures (GS—Gauss Seidel and JPCG—Jacobi pre-conditioned conjugate gradient) on the performance multigrid-like solvers (MG-ACC and HBM-ACC) is examined. The influence of number of smoothing iterations is also studied. The experiments are conducted on the line pinched cylinder problem modeled with 16 elements with $R/t = 100$ and $R/t = 300$. For either of the multigrid procedures one Gauss Seidel (GS-1) smoothing has been found to be optimal in term of CPU time.

Figure 5 depicts the rate of convergence of various elements for the pinched cylinder and the 3 cylinder assembly problems. Percentage relative error in the energy norm is plotted vs the total CPU time required to solve the problem. SDP quadrature scheme for integration of element stiffness matrices and the best solution procedure for a given polynomial order are adopted for all elements. It is evident that H2AMS and H3AMS have the best performance in degenerated and 3-D categories, respectively.

In Table 5 we study the performance of multigrid solver (MG-ACC) for the case where the coarse mesh represents the state of plane stress ($p = 8, q = 1$) while the fine mesh represents 3-D model with ($p = 8, q = 3$). The coarse grid relaxation parameter is used for efficient coarse grid correction. Alternatively, one can recompute and factorize the stiffness matrix corresponding to $q = 1$ with a 3-D constitutive model and then incorporate it for a coarse grid correction. For a relatively small problem considered (12 elements, 2208 dofs for $q = 1$) no significant difference in terms of CPU time has been found between the two methods. Numerical experiments indicate that HBM-ACC is not particularly well studied for transitioning between different mathematical models.

A comparison of rate of convergence for elements with progressive geometry and fixed geometry is depicted in Fig. 6. Progressive geometry mapping is carried out using Lagrange polynomials, the order of the Lagrange polynomials match that of the interpolation functions. Blending mapping functions are used for fixed geometry mapping. It is well known that for lower order elements the super-parametric formulation degrades the element performance, since the rigid body modes are not represented exactly. It can be seen that for higher order elements both approaches possess similar convergence.

The effect of mesh distortion is shown in Fig. 7. It is evident that mesh distortion degrades the performance of both p- and h-versions of finite element method, although the p-version was found to be somewhat less sensitive to mesh distortion.

The influence of selective polynomial escalation is studied in Fig. 8. For all numerical examples considered the value of parameter γ in Eq. (49) was selected between 0.01 and 0.02. In general selective polynomial escalation leads to higher rates of convergence.

7. SUMMARY, CONCLUSIONS AND FUTURE WORK

Research efforts have been made to optimize the computational efficiency of the p-method for shell analysis. A new quadrature scheme and a family of hierarchical assumed strain based shell elements have been introduced. Various linear iterative procedures have been examined for their suitability to solve linear system of equations resulting from hierarchic shell formulation. The key factors enhancing the

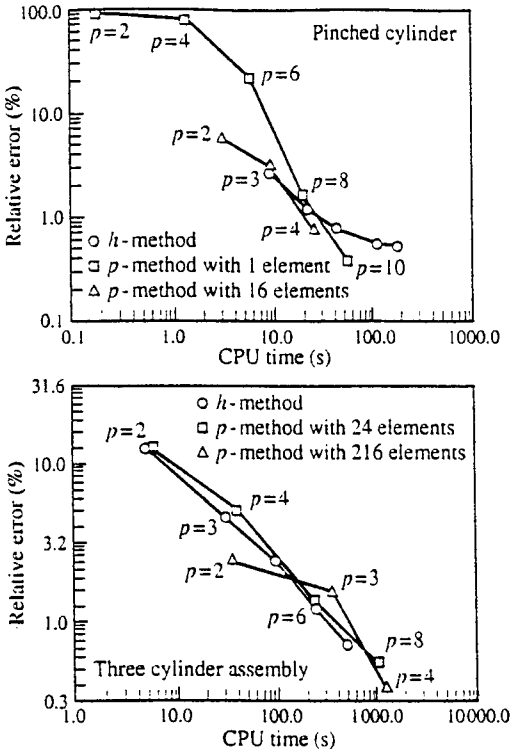


Fig. 10. Experimental comparison of computational efficiency of h and p versions of finite element method.

computational efficiency of the p-method are summarized in Fig. 9 in chronological order for the problems considered. It can be seen that even for a small problem (2944 dofs) a reduction of the total CPU time by a factor of 6.85 has been achieved. For a relatively large problem of 3 cylinder assembly this factor increases to 8.8.

Considerable speed up can be obtained using parallel architectures. All the element level computations including dot product integral decomposition as well as selective polynomial order escalation are completely parallelizable. The multigrid like methods require evaluation of inner products, matrix–vector products and factorization of coarse level stiffness matrix. The latter is bottleneck to parallelism, and thus in a parallel computing environment, it may be more efficient to evaluate approximation to it.[19]

In Fig. 10 we compare h- and p-versions of finite element analysis for the two shell problems, line pinched cylinder and an assembly of 3 cylinders with a square cut out in each cylinder. Assumed strain elements, 9 node ANS for h-method[20] and H2AMS for p-method, have been used. Relative error in energy norm is plotted vs the total CPU time. For the reference solution, 96 and 64 element meshes with $p = 8$ have been considered for the 3 cylinder assembly and pinched cylinder problems respectively. Both h- and p-methods have comparable performance, although the p-method with relatively larger number of elements (16 elements for line pinched cylinder and 216 for 3 cylinder assembly) and lower maximum polynomial order $p^{\max} \leqslant 4$ seems to perform better than a more traditional approach with smaller number of elements but larger maximum polynomial order ($p^{\max} \leqslant 8$). Nevertheless, the differences are insignificant, and thus, superiority claims on the basis of the few problems considered in the paper are premature.

Future research efforts will be concentrated in the following five areas:

1. Develop *a priori* (based on estimated conditioning[21]) and *a posteriori* (based on the performance of iterative process[22]) estimators aimed at predicting optimal solution procedures and their strategy.
2. Reducing the sensitivity of iterative solvers to thickness/span ratio by isolating and solving directly bending dominated lower frequency behavior.
3. Study of h–p assumed strain formulation for shells with selective polynomial order escalation.
4. Extension of hierarchical shell formulation to laminated composites.
5. Developement of pre- and post-processing capabilities for higher order hierarchical shell elements.

REFERENCES

1. I. Babuska, B. A. Szabo and I. N. Katz, "The p-version of the finite element method," *SIAM J. Numer. Anal.* **18**, 512–45 (1981).
2. P. Carnevali, R. B. Morris, Y. Tsuji and G. Taylor, "New basis functions and computational procedures for p-type finite element analysis," RJ 8710 (78272) Engineering Technology, IBM Research Division, San Jose, CA, 1992.
3. M. S. Shephard and S. Dey, "Geometric mapping of finite elements on shell geometry," SCOREC report 15 R. P. I. Troy, NY, 1994.
4. O. C. Zeinkiewicz and A. Craig, "Adaptive refinement, error estimates, multigrid solution, and hierarchic finite element method concepts," I. Babuska, O. C. Zeinkiewicz, J. Gago and E. R. de A. Oliveira. In *Accuracy Estimates and Adaptive Refinements in Finite Element Computations* (1986).
5. A. Brandt, "Multi-level adaptive solutions to boundary-value problems," *Math. Comput.* **31**, 333–90 (1977).
6. S. Holzer, E. Rank and H. Werner, "An implementation of the *hp*-version of the finite element method for Reissner–Mindlin plate problems," *Int. J. numer. Methods Engng*, **30**, 459–71 (1990).
7. E. Ramm, N. Stander and A. Matzenmiller, "An assessment of assumed strain methods in finite rotation shell analysis," *Eng. Comput.* **6** (1989).
8. B. A. Szabo, I. Babuska and B. K. Chayapaty, "Stress computations for nearly incompressible materials by the p-version of the finite element method," *Int. J. numer. Methods Engng*, **28**, 2175–90 (1989).
9. B. A. Szabo and G. J. Sahrmann, "Hierarchic plate and shell models based on p-extensions," *Int. J. numer. Methods Engng*, **26**, 1855–881 (1988).
10. N. U. Ahmed and P. K. Basu, "Higher order modeling of plates by p-version of finite element method," *J. Engng Mech. ASCE*, **119**, 1228–42 (1993).

11. K. S. Surana and R. M. Sorem, "p-Version hierarchical three dimensional curved shell element for elastostatics," *Int. J. numer. Methods Engng*, **31**, 649–76 (1991).
12. A. G. Peano, "Hierarchies and conforming finite elements for plane elasticity and plate bending," *Comp. Maths.* **2**, 211–24 (1976).
13. K. H. Lo, R. M. Christensen and E. M. Wu, "A higher order theory of plate deformation," *J. appl. Mech.*, **44**, 669–76 (1977).
14. T. J. R. Hughes, *The Finite Element Method*, Prentice-Hall, New Jersey, 1987.
15. G. M. Stanley, I. Levitt, B. Stehlin and B. Hurlbut, "Adaptive analysis of composite shell structures via thickness-tailored 3D finite elements," Winter Annual Meeting, Anaheim, CA, 11–13 November 1992.
16. H. E. Hinnant, "A fast method of numerical quadrature for p-version finite element matrices," *A.I.A.A.* **1386**, 1993.
17. J. Fish and R. Guttal, "The p-version of finite element method for shell analysis," *Comput. Mech. Int. J.*, **16**, 1–13 (1995).
18. E. R. Bank, T. F. Dupont and H. Yserentant, "The hierarchical basis multigrid method," *Numer. Math.*, **52**, 427–58 (1988).
19. I. Babuska and H. C. Elman, "Some aspects of parallel implementation of the finite element method on message passing architecture," *J. Comput. appl. Math.*, **27**, 157–87 (1989).
20. K. C. Park and G. M. Stanley, "A curved C^0 shell element based on assumed natural coordinate strains," *J. appl. Mech.*, **108**, 278–90 (1986).
21. J. Mandel, *Adaptive Iterative Solvers in Finite Elements. Solving Large-scale Problems in Mechanics* (Ed. by M. Papadrakakis), John Wiley and Sons, NY, 1993.
22. J. Fish and R. Guttal, "On the assumed strain formulation with selective polynomial order enrichment for p-version shells," *Comput. Struct.* (submitted).
23. R. B. Morris, Y. Tsuji and P. Carnevali, "Adaptive solution strategy for solving large systems of p-type finite element equations," *Int. J. numer. Methods Engng*, **33**, 2059–71 (1992).

An Accelerated Unstructured Multigrid Method for Shells

Jacob Fish, L. Pan, Vladimir
Belsky and S. Gomaa

SCOREC Report #3-1995
Scientific Computation Research Center

Submitted to: *International Journal for Numerical Methods in Engineering*, 1995

Scientific Computation Research Center
Rensselaer Polytechnic Institute
Troy, NY 12180-3590
voice 5182766795
fax 5182764886

An Accelerated Unstructured Multigrid Method for Shells

J. Fish, L. Pan, V. Belsky and S. Gomaa
Department of Civil Engineering and Scientific Computation Research Center
Rensselaer Polytechnic Institute, Troy, NY 12180

ABSTRACT

An accelerated multigrid method, which exploits shell element formulation to speed up the iterative process, is developed for inherently poor conditioned thin domain problems on unstructured grids. Its building blocks are: (i) intergrid transfer operators based on the shell element shape functions, (ii) heavy smoothing procedures in the form of Modified Incomplete Cholesky factor, and (iii) various two- and three-parameter acceleration schemes. Both the flat shell triangular element and the assumed strain degenerated solid shell element are considered. Numerical results show a remarkable robustness for a wide spectrum of span/thickness ratios encountered in practical applications.

1.0 Introduction

This paper focuses on development of efficient iterative solvers for a linear system of equations arising from the finite element discretization of large scale shell structures. On one hand, iterative methods, such as preconditioned conjugate gradient (PCG) and multigrid (MG), offer the promise of substantially reducing operations and storage requirements for large scale systems, but on the other hand, they are not well suited for inherently poor conditioned thin domain problems, such as thin shells.

It is often assumed that for well conditioned three-dimensional problems the number of degrees-of-freedom for which the conjugate gradient method requires the same amount of CPU time as the direct method is in the neighborhood of 500, while a breakeven problem size for the multigrid method is approximately double [1], [2]. There is no doubt that the breakeven problem size for shells will move upwards as the span/thickness ratio increases. This paper attempts to assess the balance between a problem size and a thickness/span ratio that will justify the use of either iterative or direct solvers.

We focus on the accelerated multigrid method for shells, which offers the advantage of possessing an asymptotically optimal rate of convergence with linear complexity, i.e., computational work for achieving a prescribed accuracy is proportional to the number of discrete unknowns. It is important to note that the overhead involved in automatic mesh generation of the hierarchy of auxiliary surface meshes needed for multigrid applications is relatively small in comparison to the total solution time for large thin domain problems,

where a breakeven problem size might be very high.

Since the pioneering work of Fedorenko [3] in 1962, multigrid literature has grown at an astonishing rate. A cumulative review of the technical literature may be found in the Multigrid Bibliography [4], which is periodically updated. Applications of unstructured multigrid method have been typically concentrated in fluid mechanics, with very few attempts in solid mechanics [1], [5], [6], [7], [8], [9]. To our knowledge this is one of the first attempts aimed at investigating the usefulness of the multigrid method for solving a system of discrete equations arising from the finite element discretization of shells. The noteworthy exceptions are the PCG method with incomplete blockwise factorization preconditioner, which can be interpreted as a nested two-grid method[10], and the application of the multigrid method to hierarchical shell systems (p-method) [11], where the multigrid-like solvers are most natural due to the simplicity of intergrid transfer operators, which are simply identity operators.

One of our key goals is to examine the influence of various formulations of the primary multigrid elements, such as coarse grid correction, smoothing or relaxation procedures, intergrid transfer operators, and acceleration schemes, on the overall performance of the iterative process. In section 2, we examine several formulations of intergrid transfer (prolongation and restriction) operators for each of the two shell theories: (i) flat elements, formed by combining a plane membrane element with a plate bending element, and (ii) degenerated solid elements with certain kinematic and mechanical assumptions built in. In the first category we consider the 18 degrees-of-freedom flat shell triangular element [12], [13], which is based on the superposition of the DKT plate element [14] and the membrane element with drilling degrees-of-freedom [15], while the curved 9-node ANS element [16]is used as a representative of the second category.

2.0 The Multigrid Algorithm

As a prelude to subsequent derivations we briefly outline the basic two-grid algorithm for solving a linear systems of equations resulting from the finite element discretization

$$K_{AB}d_B = f_B \tag{1}$$

where capital subscripts are reserved for degrees-of-freedom in the source grid. Tensorial convention is employed with summation over the repeated indices.

The two-grid method summarized below is an iterative process that resolves higher frequency response of the system by means of relaxation methods, while the remaining smooth components of the solution are captured on the auxiliary coarse grid.

- Starting from the source (fine) grid approximation d_B^i, which is obtained at the end of cycle i, perform typically one or two pre-smoothing iterations to smooth out high frequency components of the error and evaluate the fine grid residual r_A
- Restrict the residual from the fine grid to the auxiliary coarse grid

$$r_a = Q_{aA}r_A \tag{2}$$

where lower case subscripts denote the degrees-of-freedom in the auxiliary coarse grid and Q_{aA} is the restriction operator

- Compute the coarse grid correction Δd_b

$$K_{ab}\Delta d_b = r_a \tag{3}$$

where K_{ab} is the coarse grid stiffness matrix obtained either directly on the auxiliary coarse grid or by restricting the fine grid stiffness matrix

$$K_{ab} = Q_{aA}K_{AB}Q_{Bb} \tag{4}$$

The solution of Equation (3) can be carried out by a direct solver, or, if this is still too expensive, by introducing another coarser auxiliary grid and using one or more cycles of the two-grid algorithm.

- Prolongate the displacement correction from the coarse grid to the fine grid and update

$$d_B \Leftarrow d_B + \omega Q_{Bb}\Delta d_b \tag{5}$$

where Q_{Bb} is termed as prolongation operator related to the restriction operator by $\left[Q_{Bb}\right] = \left[Q_{bB}\right]^T$, and ω is a coarse grid relaxation parameter, which minimizes energy functional along the prescribed direction $\Delta d_B = Q_{Bb}\Delta d_b$. Note that $\omega = 1$ for two grid problems, where the coarse grid stiffness matrix is obtained by restriction (4); otherwise,

$$\omega = \frac{\Delta d_B r_B}{\Delta d_C K_{CA}\Delta d_A} \tag{6}$$

- Perform post-smoothing operations starting with the updated solution on the fine grid to obtain a new approximation d_B^{i+1}
- Accelerate the multigrid cycle using two-parameter scheme:

$$d_B^{i+1} \Leftarrow d_B^i + \alpha\left(d_B^{i+1} - d_B^i\right) + \beta\left(d_B^i - d_B^{i-1}\right) \tag{7}$$

where α and β are step sizes (in the corresponding search directions) selected on the basis of minimizing the energy functional. The alternative acceleration scheme in the form of conjugate gradients is briefly described in section 4.

- Check convergence. If necessary, start a new cycle.

The building blocks of the accelarated multigrid algorithm, including (i) the intergrid transfer operators, (ii) smoothing schemes, (iii) coarse grid correction and (iv) acceleration, will be investigated in the subsequent sections.

3.0 The Intergrid Transfer Operators for Shells

3.1 Flat shell triangular element

We consider an 18 degrees-of-freedom flat shell triangular element [12], [13], which is based on the superimposition of the DKT plate element [14] and the membrane plane stress element with drilling degrees-of-freedom [15], subsequently to be referred to as the Discrete Membrane Triangle (DMT).

3.1.1 The DKT Plate Bending Element

The DKT plate bending element is a Discrete Kirchhoff Triangle which satisfies the Kirchhoff hypothesis at some discrete points within the element. For element formulation we refer to [14]. In this section we briefly outline only those element formulation details which are relevant to the construction of intergrid transfer operators.

Let β_1 and β_2 be the rotations of the normal to the midsurface in the local element coordinate system and $\{d_{a'}\}^T = \left[w_1\ \theta_{x_1}\ \theta_{y_1}\ w_2\ \theta_{x_2}\ \theta_{y_2}\ w_3\ \theta_{x_3}\ \theta_{y_3}\right]$ be the nodal degrees-of-freedom of the element corresponding to out-of-plane displacements and midplane rotations, which are related by the set of shape functions $H_{a'}^{\beta_1}$ and $H_{a'}^{\beta_2}$ described in Appendix A.

$$\beta_1 = H_{a'}^{\beta_1} d_{a'} \qquad \beta_2 = H_{a'}^{\beta_2} d_{a'} \qquad \text{.....sum on } a' = [1,9] \tag{8}$$

where the prime on the subscript denotes the quantities with respect to the element local coordinate system.

Let x_A be the coordinates of the node in the source mesh, which lies within one of the auxiliary coarse mesh elements. Then the nodal rotations in the source mesh can be found directly from (8)

$$\theta_1(x_A) = -H_{a'}^{\beta_2}(x_A)\, d_{a'} \qquad \theta_2(x_A) = H_{a'}^{\beta_1}(x_A)\, d_{a'} \quad \text{.....sum on } a' = [1,9] \tag{9}$$

Unfortunately, for the DKT element the transverse displacement w in the interior of the element is not defined [14], since the transverse shear energy is neglected in the element formulation and therefore auxiliary interpolation function for w needs to be constructed. We assume that w is a quadratic field, with shape functions corresponding to three vertex and three midside modes. The midside translations w_4 w_5 and w_6 are found using the cubic variation of w along each side (see Appendix A), which yields

$$w(x_A) = H_{a'}^{w}(x_A)\, d_{a'} \quad \text{.....sum on } a' = [1,9] \tag{10}$$

3.1.2 The DMT Membrane Element

The Discrete Membrane Triangular (DMT) shell element is a 9 degrees-of-freedom plane stress element, which interpolates the in-plane translation field u and v in terms of in-plane translations and drilling rotations at the element vertices

$$u = H^u_{a'} d_{a'} \qquad v = H^v_{a'} d_{a'} \quad \text{.....sum on } a' = [1,9] \tag{11}$$

where $\{d_{a'}\}^T = \left[u_1\ v_1\ \theta_{Z_1}\ u_2\ v_2\ \theta_{Z_2}\ u_3\ v_3\ \theta_{Z_3}\right]$ is the nodal displacement vector, $H^u_{a'}$ and $H^v_{a'}$ are the corresponding shape functions described in Appendix A.

As in the DKT element where the transverse displacement field is not defined, in the DMT a similar situation exists for the rotational(drilling) field with respect to the normal to the element plane. We will construct a linear interpolation for drilling degrees-of-freedom.

3.1.3 The Intergrid Transfer Operators For DKT+DMT Shell Element

Based on (9), (10), (11) and (12), and after proper assembly we obtain

$$\boldsymbol{d}_{A'} = \boldsymbol{Q}_{A'a'} \boldsymbol{d}_{a'} \tag{12}$$

in which $\boldsymbol{d}_{A'}$ and $\boldsymbol{d}_{a'}$ are local nodal vectors in the source and auxiliary meshes, respetively

$$\boldsymbol{d}_{A'} = \left[u_{A'}\ v_{A'}\ w_{A'}\ \theta_{1A'}\ \theta_{2A'}\ \theta_{3A'}\right] \qquad \boldsymbol{d}_{a'} = \left[u_{a'}\ v_{a'}\ w_{a'}\ \theta_{1a'}\ \theta_{2a'}\ \theta_{3a'}\right] \tag{13}$$

A Similar relation can be constructed for nodal vectors given in the global coordinate system

$$\boldsymbol{d}_A = \boldsymbol{Q}_{Aa} \boldsymbol{d}_a \tag{14}$$

where

$$\underline{\boldsymbol{Q}_{Aa}} = \underline{\boldsymbol{T}_{AA'}} \underline{\boldsymbol{Q}_{A'a'}} \underline{\boldsymbol{T}^T_{aa'}} \quad \text{.....no summation over the underlined indices} \tag{15}$$

$\boldsymbol{T}_{AA'}$ and $\boldsymbol{T}_{aa'}$ are local-to-global orthogonal transformation matrices in the source and auxiliary meshes, respectively.

Remark 1: An alternative to the prolongation operator defined on the basis of the element shape functions (8)-(16) one can simply employ a linear interpolation for translational and rotational degrees-of-freedom using classical constant strain triangle shape functions, but as will be shown in section 5, the efficiency will suffer.

Remark 2: In order to construct the intergrid transfer operator given in (15) for general unstructured (unnested) grids it is important to employ an efficient method for collecting and interpolating information from one grid to another. The goal is to find in which coarse grid element each fine grid node lies as well as fine grid local coordinates in the coarse element. This operation can be easily accomplished by looping over all fine grid nodes and coarse grid elements, in which case the search procedure may overshadow the entire

computational cost. A more economical procedure can be obtained by introducing the background grid [17]. For uniformly shaped source grids, the background grid consists of equally-sided brick elements filling the rectangular frame encompassing the entire problem domain. The total number of bricks in the background grid is taken to be equal to the number of elements in the auxiliary coarse grid. The search algorithm consists of two steps: (i) For each point in the source grid, determine in which brick element in the background grid it lies. Store the brick number and count the number of source grid points in each brick. (ii) For each element in the auxiliary coarse grid, determine which bricks in the background grid it covers and check if the corresponding source grid points lie within this element; if they do, calculate the local coordinates; if not, proceed to the next element.

3.2 The ANS Shell Element

The ANS shell is based on a Mindlin/Reissner-like (C^o continuous) degenerated-solid shell formulation with assumed natural strain formulation aimed at circumvent locking and reduce distortion sensitivity [16].

The displacement field of the ANS element is of the classical degenerated solid type

$$\boldsymbol{u}(\xi,\eta,\zeta) = \sum_{a=1}^{n_{en}} N_a(\xi,\eta)\left[\ \bar{\boldsymbol{u}}_a + \frac{1}{2}\zeta h_a\left(\theta_{a2}\boldsymbol{e}^f_{a1} - \theta_{a1}\boldsymbol{e}^f_{a2}\right)\ \right] \tag{16}$$

where $\bar{\boldsymbol{u}}_a$ are nodal translations at the reference surface; $\boldsymbol{e}^f_{a1}, \boldsymbol{e}^f_{a2}, \boldsymbol{e}^f_{a3}$ are orthonormal fiber basis vector at node a, defined so that $\boldsymbol{e}^f_{a3}$ is normal to the plane and $\boldsymbol{e}^f_{a1}, \boldsymbol{e}^f_{a2}$ are as close as possible to the ξ, η coordinate directions; θ_{a1}, θ_{a2} are rotations of the fiber about the basis vectors $\boldsymbol{e}^f_{a1}, \boldsymbol{e}^f_{a2}$, respectively; h_a is the thickness of the shell at node a; $N_a(\xi,\eta)$ are the in-plane n_{en} Lagrangian shape functions.

The prolongation operator for the translational degrees-of-freedom can be directly obtained from the above Lagrangian shape functions

$$\bar{\boldsymbol{u}}_A = N_a(x_A)\,\bar{\boldsymbol{u}}_a \text{.....sum on } a = [1,9] \tag{17}$$

To construct the prolongation operator for the rotational degrees-of-freedom, we first evaluate the relative displacement in the source mesh

$$\Delta\boldsymbol{u}(x_A) = \boldsymbol{u}^{top}(x_A) - \boldsymbol{u}^{bot}(x_A) = \begin{bmatrix}\Delta u_x\\ \Delta u_y\\ \Delta u_z\end{bmatrix}_{x_A} = \sum_{a=1}^{n_{en}} N_a(x_A)\ h_a\left(\theta_{a2}\boldsymbol{e}^f_{a1} - \theta_{a1}\boldsymbol{e}^f_{a2}\right) \tag{18}$$

which is then transformed into a local element coordinate system

$$\begin{bmatrix}\Delta u_1(x_A)\\ \Delta u_2(x_A)\end{bmatrix} = \begin{bmatrix}e_{A1,x} & e_{A1,y} & e_{A1,z}\\ e_{A2,x} & e_{A2,y} & e_{A2,z}\end{bmatrix}\begin{bmatrix}\Delta u_x\\ \Delta u_y\\ \Delta u_z\end{bmatrix}_{x_A} = e_{A\beta,k}\Delta u_k(x_A) \tag{19}$$

where $\beta = 1, 2$ is a free index, and summation over repeated indices over $k = 1, 2, 3$ is exercised. Consequently the rotational field is prolongated as follows:

$$\theta_1(x_A) = -\frac{\Delta u_2(x_A)}{h_A} = N_a^{\theta_{11}}(x_A)\,\theta_{a1} + N_a^{\theta_{12}}(x_A)\,\theta_{a2}$$

$$\theta_2(x_A) = \frac{\Delta u_1(x_A)}{h_A} = N_a^{\theta_{21}}(x_A)\,\theta_{a1} + N_a^{\theta_{22}}(x_A)\,\theta_{a2} \qquad \text{.....sum on } a = [1,9] \qquad (20)$$

where shape functions are summarized in Appendix B. The resulting node-to-node prolongation operator is given by:

$$\left[Q_{Aa}\right] = \begin{bmatrix} N_a(x_A) & 0 & 0 & 0 & 0 \\ 0 & N_a(x_A) & 0 & 0 & 0 \\ 0 & 0 & N_a(x_A) & 0 & 0 \\ 0 & 0 & 0 & N_a^{\theta_{11}}(x_A) & N_a^{\theta_{12}}(x_A) \\ 0 & 0 & 0 & N_a^{\theta_{21}}(x_A) & N_a^{\theta_{22}}(x_A) \end{bmatrix} \qquad (21)$$

Remark 3: An alternative to the prolongation operator for rotational degrees-of-freedom defined on the basis of the element shape functions (18)-(20) is to employ a Lagrangian interpolation identical to the one employed for translation degrees-of-freedom (18).

Remark 4: For higher order ANS meshes, it is convenient to construct an auxiliary mesh from lower order ANS elements. For example, the shape functions of 4-node ANS element $N_a^{4-Node}(X_A)$ can be utilized for prolongating the solution from 9-node ANS elements. Similarly, 9-node elements can serve as an auxiliary mechanism for 16-node elements, and etc.

For higher order elements an alternative, which exploits the fact that membrane dominated modes are of higher frequency than those of bending, will be tested. By this approach only membrane dominated modes of higher order elements are prolongated using lower order element shape functions, whereas bending dominated modes, for which the smoothing process is usually inefficient, are prolongated using an identity operator, and then resolved with a direct solver. Mode separation is carried out in the local fiber coordinate system, which requires transformation of all global quantities, including stiffness, displacement and force vectors from the global to the local fiber coordinate system.

Remark 5: It is important to note that in the case of assumed strain formulation, restriction of the source grid stiffness matrix, $Q_{aA}K_{AB}Q_{Bb}$, does not yield the stiffness matrix of the coarse grid independently recomputed even though the meshes are nested. This is because the assumed strain field is enhanced by projecting certain undesirable modes from the symmetric gradient of the displacement field. Whether it is more computationally efficient to construct the auxiliary coarse mesh stiffness matrix by restriction (eq. (4)) or by recomputation and coarse grid acceleration (6) will be investigated in section 5.

4.0 Acceleration schemes

For ill-conditioned problems various acceleration schemes are essential to speed up the rate of convergence. This is especially true for thin shell problems, where the auxiliary

coarse meshes might be too stiff to accurately capture the lower frequency response of the source problem. However, when both the coarse grid correction and relaxation solutions are appropriately scaled the speedup is often astonishing, by a factor of ten and more, as evident from our numerical examples.

We start by describing the so-called two-parameter acceleration scheme, which uses the incremental multigrid cycle as a search direction, and subsequently scales it to minimize the potential energy functional.

Let r_B^i be the residual at the end of cycle i. The incremental multigrid solution for the next cycle, denoted as $z_B^i = MG\left(r_B^i, K_{AB}\right)$, is used as the predictor in the two parameter acceleration scheme. The solution in the correction phase is then updated as follows:

$$v_B^{i+1} = \alpha^i z_B^i + \beta^i v_B^i \tag{22}$$

$$d_B^{i+1} = d_B^i + v_B^{i+1} \tag{23}$$

where parameters $\left(\alpha^i, \beta^i\right)$ are obtained by minimization of the potential energy functional

$$\frac{1}{2}\left(d_A^i + \alpha^i z_A^i + \beta^i v_A^i\right) K_{AB} \left(d_B^i + \alpha^i z_B^i + \beta^i v_B^i\right) - \left(d_A^i + \alpha^i z_A^i + \beta^i v_A^i\right) f_A \rightarrow \min_{\alpha^i, \beta^i} \tag{24}$$

The resulting algorithm of the two parameter acceleration scheme is summarized below:

Step 1: Initiation

$$d_B^0 = 0 \qquad r_B^0 = f_B \tag{25}$$

$$z_B^0 = MG\left(r_B^0, K_{AB}\right) \tag{26}$$

$$v_B^0 = 0 \qquad y_B^0 = 0 \tag{27}$$

$$x_B^0 = K_{BC} z_C^0 \tag{28}$$

$$\alpha^0 = \frac{z_C^0 f_C}{z_D^0 x_D^0} \qquad \beta^0 = 0 \tag{29}$$

Step 2: Do i = 0, 1, 2, ... until convergence

$$\begin{Bmatrix} \alpha^i \\ \beta^i \end{Bmatrix} = \begin{bmatrix} z_C^i x_C^i & v_A^i x_A^i \\ v_B^i x_B^i & y_D^i x_D^i \end{bmatrix}^{-1} \begin{Bmatrix} z_E^i r_E^i \\ v_F^i r_F^i \end{Bmatrix} \qquad i > 0 \tag{30}$$

$$v_B^{i+1} = \alpha^i z_B^i + \beta^i v_B^i \tag{31}$$

$$d_B^{i+1} = d_B^i + v_B^{i+1} \tag{32}$$

$$y_B^{i+1} = \alpha^i x_B^i + \beta^i y_B^i \tag{33}$$

$$r_B^{i+1} = r_B^i - y_B^{i+1} \tag{34}$$

$$z_B^{i+1} = MG\left(r_B^{i+1}, K_{AB}\right) \tag{35}$$

$$x_B^{i+1} = K_{BC} z_C^{i+1} \tag{36}$$

Note that the two parameter acceleration scheme requires no additional matrix-vector multiplication and for thin shells its benefit clearly overshadows the cost involved in additional vector product evaluations.

An alternative to the acceleration scheme described in equations (26)-(37) is the use of a multigrid cycle as a preconditioner within the conjugate gradient method

$$v_B^{i+1} = MG\left(r_B^i, K_{AB}\right) + \beta^i v_B^i \tag{37}$$

$$d_B^{i+1} = d_B^i + \alpha^i v_B^{i+1} \tag{38}$$

where the parameters α^i, β^i are determined from the line search and K-orthogonality$\left(K_{AB} v_B^i, v_A^{i+1}\right) = 0$, respectively.

5.0 Numerical examples and discussion

Our numerical experimentation agenda includes investigation of various intergrid transfer operators described in section 3 as well as other multigrid elements, such as smoothing, coarse grid correction and acceleration.

Two problems are considered, the line pinched cylinder with end diaphragms, and the assembly of three cylinders with end diaphragms subjected to point load. Geometry, loading, boundary conditions and material properties for the two problems are given in Figures 1(a) and 1(b). Uniform and graded meshes of either ANS or Flat Shell Triangular (FST) elements as shown in Tables 1 and 2, and Figures 2 and 3 have been considered. For uniform meshes, mesh 1 is used as an auxiliary grid for mesh 3, while mesh 2 is auxiliary to mesh 4. The nodes of all auxiliary and source meshes are placed on the exact geometry, which ensures an unnested situation for curved shell structures. All numerical examples were conducted for five different radius/thickness ratios: 50, 100, 200, 500 and 1000. Convergence was measured in terms of the normalized L_2-norm of the residual with tolerance of 10e-6. Computations were carried out on the SPARC 10 workstation.

For flat shell triangular element meshes four different formulations of intergrid transfer operators have been compared.

Bsh-Msh — Bending prolongated using DKT element shape functions (eqs. (8)(10)); Membrane displacements prolongated using DMT element shape functions (eqs. (11)).

Bln-Mln — Bending prolongated using linear field; Membrane prolongated using linear field.

Bsh-Mln — Bending prolongated using DKT element shape functions (eqs. (8)(10)); Membrane prolongated using linear field.

Bln-Msh — Bending prolongated using linear field; Membrane displacements prolongated using DMT element shape functions (eqs. (11)).

Tables 3 and 4 compare computational efficiency (measured in terms of CPU time and number of iterations) of various intergrid transfer operators for the two test problems. From the program architecture standpoint the use of linear basis for prolongating all the fields (Bln-Mln) is very attractive, since no information on element formulation is needed in the solution process. Nevertheless, it is evident from tables 3 and 4, that the computational efficiency of the two-grid method, which exploits the element information and in particular that of the DKT element in the iterative solution process, is by far superior. It can be seen that the optimal computational performance has been obtained with the Bsh-Mln version of the prolongation operator.

In the case of 9-node ANS elements we study the following five different formulations of the intergrid transfer operators defined as:

BiQ9 — 9-node Bi-Quadratic prolongation for midplane displacements and rotations.

BiQ9Mr — 9-node Bi-Quadratic prolongation for midplane displacements (eq. (18)). Midplane rotations are extracted from displacements (eqs.(19)(20)(21)).

BiL4 — 4-node Bi-Linear prolongation for midplane displacements and rotations, i.e. 4-node elements are used as an auxiliary mesh for 9-node elements.

MeBiL4 — Bending prolongated using an identity operator. 4-node Bi-Linear prolongation is used for Membrane only. See Remark 4.

BiQ9Re — 9-node Bi-Quadratic prolongation and restriction operators for all degrees-of-freedom. Coarse mesh stiffness matrix Recomputed and coarse grid solution accelerated using equation (6). See remark 5.

Tables 5 and 6 compare the five intergrid transfer operators for the two test problems. It is evident that the most efficient formulation is the one that recomputes the coarse grid stiffness matrix (BiQ9Re), i.e., the stiffness matrix obtained by any form of restriction fails to effectively capture the lower frequency response of the source mesh. This is not surpris-

ing, because the intergrid transfer operators are formulated on the basis of shape functions only, and do not reflect the enhanced strain field of the assumed strain element. The intergrid transfer operator, which is based on bi-linear prolongation for membrane and identity for bending, MeBiL4, yields fewer cycles, but does not offer savings in terms of the overall performance because the auxiliary mesh is larger and thus CPU time per cycle is longer.

Comparing results in Tables 3 and 4 with those in Tables 4 and 5, it can be seen that a general trend indicates a significantly faster rate of convergence of the flat shell triangular element. Similar observations have been found from the experiments conducted on the two and three level graded meshes as shown in Table 13.

Tables 7 and 8 investigate the influence of acceleration on the rate of convergence in the case of FST and ANS meshes, respectively. It can be seen that acceleration significantly affects the rate of convergence especially as the span thickness ratio increases. The two acceleration schemes, based on the conjugate gradient method and minimization of potential energy functional, described in section 4 have similar performance in terms of number of iterations and CPU time.

In Tables 9 and 10 we investigate two popular smoothing procedures based on Gauss-Seidel and Modified Incomplete Cholesky (MIC) Factorization [18] with 0.05 diagonal scaling for stabilization for both FST and ANS meshes. It is evident that for thick shells, the two smoothers have similar computational performance. For poor conditioned problems (span/thickness ratio over 500) a heavier smoothing procedure, such as MIC, is the most efficient, by far outperforming one or two Gauss-Seidel smoothing iterations.

6.0 Summary and conclusions

Recent years saw a re-emergence of iterative solvers in finite element structural analysis due to increasing demand to analyze very large finite element systems. However, the major obstacle that needs to be overcome before iterative solvers can be routinely used in commercial packages is circumventing their pathological sensitivity to problem conditioning. This paper presents an attempt in this direction in the form of an accelerated multigrid method dedicated for inherently poor conditioned thin domain problems, which exploits the knowledge of the finite element formulation in speeding up the iterative process.

Tables 11-12 compare the performance of the most efficient version of the accelerated multigrid method developed against the conjugate gradient method with Incomplete Cholesky preconditioner and the direct solver with skyline storage for the two problems and the two types of elements considered. In the case of the multigrid solver, the CPU time includes the overhead involved in the auxiliary mesh generation and the data transfer between the grids. Results show remarkable robustness of the accelerated multigrid method for a wide spectrum of span/thickness ratios encountered in practical applications as opposed to the MIC preconditioned conjugate gradient method. Nevertheless, superiority claims with respect to direct methods are premature at this point since (i) no comparisons with some of the state-of-the-art sparse direct solvers [19] have been carried out, and

(ii) no tests were conducted on large scale industry problems. Moreover, we would like to caution that for linear static analysis, any form of the multigrid method requires for each load case a new iterative process (except for the stiffness formation, restriction and factorization on the coarse grid), whereas in a direct solution, factorization is performed only once, and each load case requires only forward reduction and back substitution.

REFERENCES

1 I. D. Parsons and J. F. Hall, 'The Multigrid Method in Solid Mechanics: Part I-Algorithm Description and Behavior,' *Int. J. For Numerical Methods In Engineering*, Vol. 29, 719-737, 1990.

2 T. J. R. Hughes, R. M. Ferencz and J. O. Hallquist, 'Large scale vectorized implicit calculations in solid mechanics on a Cray X-MP/48 utilizing EBE preconditioned conjugate gradients,' *Computer Methods in Applied Mechanics and Engineering*, Vol. 61, pp. 215-248, 1987.

3 R. P. Fedorenko, 'A relaxation method for solving elliptic difference equations,' *USSR Computational Math. and Math. Phys.*, Vol. 1, No. 5, pp.1092-1096, 1962.

4 W. Hackbusch and U. Trottenberg, *Multigrid Methods*, Springer-Verlag, Berlin, 1992.

5 D. Parsons, 'Iterative methods and finite elements: when will convergence occur?,' *USACM Bulletin*, Vol. 7, No. 3, September 1994.

6 J. Fish and V.Belsky, 'Multigrid method for periodic heterogeneous media. Part I: Convergence studies for one-dimensional case,' accepted in *Computer Methods in Applied Mechanics and Engineering*.

7 J.Fish and V.Belsky, 'Multigrid method for periodic heterogeneous media. Part II: Multiscale modeling and quality control in multidimensional case,' accepted in *Computer Methods in Applied Mechanics and Engineering*.

8 J. Fish, M. Pandheeradi and V.Belsky, 'An efficient multilevel solution scheme for large scale nonlinear systems,' accepted in *Int. J. For Numerical Methods In Engineering*.

9 V. Belsky, 'A Multigrid method for variational inequalities in contact problems,' *Computing*, Vol. 51, pp. 293-311, 1993.

10 C. Farhat and N. Sobh, 'A coarse/fine preconditioner for very ill-conditioned finite element problems,' *Int. J. For Numerical Methods In Engineering*, Vol. 28, pp.1715-1723, 1989.

11 J. Fish and R. Guttal, 'The p-version of the finite element method for shell analysis. Part II: hierarchical quadrature and solution procedures,' submitted to *Computational Mechanics: The International Journal*.

12 N. Carpenter, H. Stolarski and T. Belytschko, 'A Flat Triangular Shell Element With Improved Membrane Interpolation,' *Communications In Applied Numerical Methods*,

VOL. 1, 161-168, 1985.

13 J. Fish and T. Belytschko, 'Stabilized Rapidly Convergent 18-Degrees-of-Freedom Flat Shell Triangular Element,' *Int. J. For Numerical Methods In Engineering*, VOL. 33, 149-162, 1992.

14 J. Batoz, 'A Study of Three-Node Triangular Plate Bending Elements,' *Int. J. For Numerical Methods In Engineering*, VOL. 15, 1771-1812, 1980.

15 D.J. Allman, 'A compatible triangular element including vertex rotations for plane elasticity analysis,' *Computers and Structure*, Vol. 19, pp. 1-8, 1984.

16 K.C. Park and G.M. Stanley, 'A curved C^0 shell element based on assumed natural coordinate strains,' *Journal of Applied Mechanics*, Vol. 108, pp. 278-290, 1986.

17 R. Lohner and K. Morgan, 'An Unstructured Multigrid Method for Elliptic Problems,' *Int. J. For Numerical Methods In Engineering*, VOL. 24, 101-115, 1987.

18 O. Axelson and V.A. Barker, *Finite Element Solution of Boundary Value Problems*, Academic Press, NY, 1984.

19 M.A. Badourah, O.O. Storaasli and S.W. Bostic, 'Linear static structural and vibration analysis on high-performance computers,' *Computer Systems in Engineering*, Vol. 4, pp. 363-371, 1993.

APPENDIX

A. Flat Triangular Shell Element Shape Functions

The DKT plate element shape functions corresponding to the rotational degrees-of-freedom $H_{a'}^{\beta_1}$ and $H_{a'}^{\beta_2}$ are given below [14]:

$$
\begin{aligned}
H_1^{\beta_1} &= 1.5\,(a_6 N_6 - a_5 N_5) & H_2^{\beta_1} &= b_5 N_5 + b_6 N_6 \\
H_3^{\beta_1} &= N_1 - c_5 N_5 - c_6 N_6 & H_1^{\beta_2} &= 1.5\,(d_6 N_6 - d_5 N_5) \\
H_2^{\beta_2} &= -N_1 + e_5 N_5 + e_6 N_6 & H_3^{\beta_2} &= -(b_5 N_5 + b_6 N_6)
\end{aligned}
\tag{39}
$$

where N_i are standard 6-node triangular element shape functions, and

$$
\begin{gathered}
a_k = -x_{ij}/l_{ij}^2 \qquad b_k = \frac{3}{4} x_{ij} y_{ij}/l_{ij}^2 \qquad c_k = \left(\frac{1}{4} x_{ij}^2 - \frac{1}{2} y_{ij}^2\right)/l_{ij}^2 \\
d_k = -y_{ij}/l_{ij}^2 \qquad e_k = \left(\frac{1}{4} y_{ij}^2 - \frac{1}{2} x_{ij}^2\right)/l_{ij}^2 \\
l_{ij}^2 = x_{ij}^2 + y_{ij}^2 \qquad x_{ij} = x_i - x_j \qquad y_{ij} = y_i - y_j
\end{gathered}
\tag{40}
$$

where $k = 4, 5, 6$ for the sides $ij = 23, 31, 12$ respectively. The functions $H_4^{\beta_1}$, $H_5^{\beta_1}$, $H_6^{\beta_1}$, $H_4^{\beta_2}$, $H_5^{\beta_2}$, and $H_6^{\beta_2}$ are obtained from the above expressions by replacing N_1 by N_2 and indices 6

and 5 by 4 and 6, respectively. The functions $H_7^{\beta_1}$, $H_8^{\beta_1}$, $H_9^{\beta_1}$, $H_7^{\beta_2}$, $H_8^{\beta_2}$, and $H_9^{\beta_2}$ are obtained by replacing N_1 by N_3 and indices 6 and 5 by 5 and 4, respectively

Following construction given in equation (10) the out-of-plane displacement shape functions $H_{a'}^{w}$ are given by

$$
\begin{aligned}
H_1^w &= 1-\xi-\eta & H_2^w &= \frac{1}{2}(1-\xi-\eta)\,(-y_{12}\xi + y_{31}\eta) \\
H_3^w &= \frac{1}{2}(1-\xi-\eta)\,(x_{12}\xi - x_{31}\eta) & H_4^w &= \xi \\
H_5^w &= \frac{1}{2}\xi\,[-y_{23}\eta + y_{12}(1-\xi-\eta)] & H_6^w &= \frac{1}{2}\xi\,[x_{23}\eta - x_{12}(1-\xi-\eta)] \\
H_7^w &= \eta & H_8^w &= \frac{1}{2}\eta\,[-y_{31}(1-\xi-\eta) + y_{23}\xi] \\
H_9^w &= \frac{1}{2}\eta\,[x_{31}(1-\xi-\eta) - x_{23}\xi]
\end{aligned}
\qquad (41)
$$

where ξ and η are the area coordinates.

The DMT element shape functions $H_{a'}^{u}$ and $H_{a'}^{v}$ are given as in [15]

$$
\begin{aligned}
H_1^u &= 1-\xi-\eta & H_2^u &= 0 & H_3^u &= \frac{1}{2}(1-\xi-\eta)\,(\xi y_{12} - \eta y_{31}) \\
H_4^u &= \xi & H_5^u &= 0 & H_6^u &= \frac{1}{2}\xi\,[-(1-\xi-\eta)\,y_{12} + \eta y_{23}] \\
H_7^u &= \eta & H_8^u &= 0 & H_9^u &= \frac{1}{2}\eta\,[-\xi y_{23} + (1-\xi-\eta)\,y_{31}]
\end{aligned}
\qquad (42)
$$

and

$$
\begin{aligned}
H_1^v &= 0 & H_2^v &= 1-\xi-\eta & H_3^v &= \frac{1}{2}(1-\xi-\eta)\,(-\xi x_{12} + \eta x_{31}) \\
H_4^v &= 0 & H_5^v &= \xi & H_6^v &= \frac{1}{2}\xi\,[(1-\xi-\eta)\,x_{12} - \eta x_{23}] \\
H_7^v &= 0 & H_8^v &= \eta & H_9^v &= \frac{1}{2}\eta\,[\xi x_{23} - (1-\xi-\eta)\,x_{31}]
\end{aligned}
\qquad (43)
$$

The shape functions for the drilling degrees-of-freedom $H_{a'}^{\theta}$ are given by

$$
\begin{aligned}
H_1^\theta &= \frac{3}{2}\left(-N_4 y_{12}/l_{12}^2 + N_6 y_{31}/l_{31}^2\right) & H_2^\theta &= \frac{3}{2}\left(N_4 x_{12}/l_{12}^2 - N_6 x_{31}/l_{31}^2\right) \\
H_3^\theta &= N_1 - \frac{1}{4}(N_4 + N_6) & H_4^\theta &= \frac{3}{2}\left(N_4 y_{12}/l_{12}^2 - N_5 y_{23}/l_{23}^2\right) \\
H_5^\theta &= \frac{3}{2}\left(-N_4 x_{12}/l_{12}^2 + N_5 x_{23}/l_{23}^2\right) & H_6^\theta &= N_2 - \frac{1}{4}(N_4 + N_5) \\
H_7^\theta &= \frac{3}{2}\left(N_5 y_{23}/l_{23}^2 - N_6 y_{31}/l_{31}^2\right) & H_8^\theta &= \frac{3}{2}\left(-N_5 x_{23}/l_{23}^2 + N_6 x_{31}/l_{31}^2\right) \\
H_9^\theta &= N_3 - \frac{1}{4}(N_6 + N_5)
\end{aligned}
\tag{44}
$$

B. Shape Function for ANS Shell Element

Interpolants for the rotational field directly follow from equations (19), (20), (21).

$$
\begin{aligned}
N_a^{\theta_{11}}(x_A) &= \frac{h_a}{h_A} N_a \left(e_{a2}^f(1)\, e_{A2,x} + e_{a2}^f(2)\, e_{A2,y} + e_{a2}^f(3)\, e_{A2,z} \right) \\
N_a^{\theta_{12}}(x_A) &= -\frac{h_a}{h_A} N_a \left(e_{a1}^f(1)\, e_{A2,x} + e_{a1}^f(2)\, e_{A2,y} + e_{a1}^f(3)\, e_{A2,z} \right) \\
N_a^{\theta_{21}}(x_A) &= -\frac{h_a}{h_A} N_a \left(e_{a2}^f(1)\, e_{A1,x} + e_{a2}^f(2)\, e_{A1,y} + e_{a2}^f(3)\, e_{A1,z} \right) \\
N_a^{\theta_{22}}(x_A) &= \frac{h_a}{h_A} N_a \left(e_{a1}^f(1)\, e_{A1,x} + e_{a1}^f(2)\, e_{A1,y} + e_{a1}^f(3)\, e_{A1,z} \right)
\end{aligned}
\tag{45}
$$

TABLE 1. Cylinder Mesh Information

Mesh Type	Num. Nodes R dir	Num. Nodes Y dir
mesh 1	21	21
mesh 2	31	31
mesh 3	41	41
mesh 4	61	61

TABLE 2. Three Cylinder Assembly Mesh Information

Mesh Type	Num. Nodes R dir	Num. Nodes Y dir
mesh 1	25	25
mesh 2	31	31
mesh 3	49	49
mesh 4	61	61

TABLE 3. Comparison of Intergrid Transfer Operators for Flat Shell Triangular element (Pinched cylinder with end diaphragms problem. Incomplete Cholesky Smoothing, 2-parameter Acceleration)

Mesh coarse/fine	Intergrid Transfer	thick/span 1/50	thick/span 1/100	thick/span 1/200	thick/span 1/500	thick/span 1/1000
mesh 1/ 3	Bln-Mln	119.8/ 19	124.7/ 21	139.3/ 28	203.4/ 53	302.5/ 99
	Bsh-Msh	97.1/ 10	99.3/ 11	119.8/ 19	137.1/ 26	181.4/ 43
	Bsh-Mln	93.6/ 8	101.8/ 9	119.0/ 17	139.5/ 26	183.4/ 44
	Bln-Msh	124.8/ 20	128.0/ 21	144.6/ 27	210.2/ 53	326.7/ 99
mesh 2/ 4	Bln-Mln	321.4/ 20	317.4/ 20	331.6/ 22	386.3/ 31	521.7/ 57
	Bsh-Msh	278.2/ 11	281.2/ 11	282.4/ 12	326.6/ 18	391.0/ 30
	Bsh-Mln	257.3/ 8	251.2/ 7	265.7/ 10	320.8/ 18	384.0/ 30
	Bln-Msh	324.6/ 20	325.8/ 20	349.9/ 22	394.9/ 31	564.2/ 57

TABLE 4. Comparison of Intergrid Transfer Operators for Flat Shell Triangular element (Pinched Three Cylinder Assembly with end diaphragms problem. Incomplete Cholesky Smoothing, 2-parameter Acceleration)

Mesh coarse/fine	Intergrid Transfer	thick/span 1/50	thick/span 1/100	thick/span 1/200	thick/span 1/500	thick/span 1/1000
mesh 1/ 3	Bln-Mln	213.8/ 19	205.5/ 20	214.6/ 22	287.5/ 43	559.0/ 123
	Bsh-Msh	181.0/ 10	188.7/ 11	184.9/ 13	231.3/ 23	402.8/ 65
	Bsh-Mln	165.4/ 7	168.8/ 9	170.2/ 10	217.1/ 23	394.9/ 68
	Bln-Msh	229.1/ 19	226.2/ 20	221.3/ 24	309.0/ 43	648.2/ 124
mesh 2/ 4	Bln-Mln	361.1/ 20	369.4/ 20	371.7/ 22	457.2/ 37	752.0/ 88
	Bsh-Msh	320.5/ 11	318.0/ 11	338.9/ 12	395.2/ 21	566.9/ 47
	Bsh-Mln	298.0/ 7	304.5/ 8	344.2/ 10	383.1/ 21	564.5/ 47
	Bln-Msh	393.0/ 19	385.5/ 20	393.0/ 21	480.7/ 34	860.5/ 90

TABLE 5. Comparison of Intergrid Transfer Operators for ANS Shell element (Pinched cylinder with end diaphragms problem. Incomplete Cholesky Smoothing, 2-parameter Acceleration)

Mesh coarse/fine	Intergrid Transfer	thick/span 1/50	thick/span 1/100	thick/span 1/200	thick/span 1/500	thick/span 1/1000
mesh 1/ 3	BiQ9	297.9/ 14	341.1/ 26	423.0/ 51	656.5/ 128	1028.6/ 245
	BiQ9Mr	306.8/ 14	353.9/ 26	450.0/ 51	748.0/ 129	1207.0/ 247
	BiL4	366.0/ 19	430.0/ 36	569.6/ 72	975.6/ 176	1581.0/ 328
	MeBiL4	438.8/ 9	467.1/ 13	645.6/ 21	711.9/ 40	747.4/ 66
	BiQ9Re	270.6/ 10	301.2/ 16	357.3/ 30	536.3/ 79	975.9/ 188
mesh 2/ 4	BiQ9	728.8/ 10	775.0/ 18	905.7/ 34	1283.0/ 83	1895.6/ 167
	BiQ9Mr	753.6/ 11	845.1/ 18	965.7/ 34	1413.6/ 84	2153.8/ 168
	BiL4	929.1/ 13	1056.0/ 24	1260.8/ 48	1993.3/ 121	3160.6/ 242
	MeBiL4	1401.1/ 8	1450.6/ 10	1453.4/ 15	1651.5/ 28	1874.7/ 45
	BiQ9Re	664.9/ 8	672.7/ 12	773.0/ 20	1024.0/ 50	1581.4/ 111

TABLE 6. Comparison of Intergrid Transfer Operators for ANS Shell element (Pinched Three Cylinder Assembly with end diaphragms problem. Incomplete Cholesky Smoothing, 2-parameter Acceleration)

Mesh coarse/fine	Intergrid Transfer	thick/span 1/50	thick/span 1/100	thick/span 1/200	thick/span 1/500	thick/span 1/1000
mesh 1/ 3	BiQ9	449.8/ 12	490.6/ 22	601.5/ 42	867.9/ 103	1340.9/ 200
	BiQ9Mr	467.3/ 12	514.3/ 22	618.1/ 43	981.2/ 103	1564.8/ 203
	BiL4	772.3/ 48	931.1/ 80	1319.0/ 139	2230.8/ 298	> 300
	MeBiL4	966.0/ 38	1126..7/ 59	1350.7/ 86	1856.9/ 153	> 400
	BiQ9Re	413.0/ 11	456.5/ 18	521.7/ 30	835.6/ 77	1365.1/ 164
mesh 2/ 4	BiQ9	729.6/ 11	762.6/ 18	972.8/ 35	1398.1/ 86	1937.1/ 164
	BiQ9Mr	777.3/ 11	819.8/ 19	982.3/ 36	1421.5/ 87	2194.7/ 165
	BiL4	1239.9/ 47	1482.77/ 70	2141.3/ 140	3739.6/ 292	> 300
	MeBiL4	1802.0/ 39	2033.9/ 54	2468.5/ 92	3543.3/ 156	3765.8/ 186
	BiQ9Re	681.2/ 10	733.4/ 14	834.6/ 25	1163.1/ 64	1767.3/ 131

TABLE 7. Comparason of acceleration schemes for Flat Shell Triangular element (Pinched cylinder with end diaphragms problem. Incomplete Cholesky Smoothing)

Mesh coarse/fine	Accel. Type	thick/span 1/50	thick/span 1/100	thick/span 1/200	thick/span 1/500	thick/span 1/1000
mesh 1/ 3	case 1	119.4/ 11	147.8/ 18	232.7/ 37	588.0/ 127	1481.7/ 354
	case 2	93.6/ 8	101.8/ 9	119.0/ 17	139.5/ 26	183.4/ 44
	case 3	92.5/ 8	94.4/ 9	113.8/ 17	138.3/ 26	185.3/ 44
mesh 2/ 4	case 1	336.6/ 14	313.4/ 12	392.2/ 20	779.9/ 61	1760.5/ 166
	case 2	257.3/ 8	251.2/ 7	265.7/ 10	320.8/ 18	384.0/ 30
	case 3	250.1/ 8	247.0/ 7	265.0/ 10	311.2/ 18	384.0/ 30

Note: case 1: without acceleration; case 2: two-parameter acceleration; case 3: CG acceleration.

TABLE 8. Comparason of acceleration schemes for ANS element (Pinched cylinder with end diaphragms problem. Incomplete Cholesky Smoothing)

Mesh coarse/fine	Accel. Type	thick/span 1/50	thick/span 1/100	thick/span 1/200	thick/span 1/500	thick/span 1/1000
mesh 1/ 3	case 1	538.1/ 45	2074.1/ 159	/ >500	/ >1000	/ >1000
	case 2	297.9/ 14	341.1/ 26	423.0/ 51	656.5/ 128	1028.6/ 245
	case 3	300.9/ 14	336.9/ 26	417.7/ 51	674.5/ 128	1054.5/ 245
mesh 2/ 4	case 1	1028.5/ 23	1656.9/ 73	4234/ 273	/ >1000	/ >1000
	case 2	728.8/ 10	775.0/ 18	905.7/ 34	1283.0/ 83	1895.6/ 167
	case 3	716.0/ 10	790.9/ 18	937.6/ 34	1290.8/ 83	1929.5/ 167

Note: case 1: without acceleration; case 2: two-parameter acceleration; case 3: CG acceleration.

TABLE 9. Comparison of smoothing procedures for Flat Shell Triangular element (Pinched cylinder with end diaphragms problem. Two-parameter acceleration)

Mesh coarse/fine	Smoothing Procedure	thick/span 1/50	thick/span 1/100	thick/span 1/200	thick/span 1/500	thick/span 1/1000
mesh 1/ 3	MIC	93.6/ 8	101.8/ 9	119.0/ 17	139.5/ 26	183.4/ 44
	1 GS	109.9/ 14	114.5/ 16	157.3/ 32	340.8/ 101	697.1/ 235
	2 GS	106.4/ 9	113.6/ 11	144.1/ 18	260.8/ 46	544.6/ 114
mesh 2/ 4	MIC	257.3/ 8	251.2/ 7	265.7/ 10	320.8/ 18	384.0/ 30
	1 GS	293.3/ 14	302.4/ 15	344.9/ 21	570.5/ 57	1215.0/ 160
	2 GS	295.5/ 9	294.6/ 9	328.5/ 13	459.6/ 28	829.3/ 63

TABLE 10. Comparison of smoothing procedures for ANS element (Pinched cylinder with end diaphragms problem. Two-parameter acceleration)

Mesh coarse/fine	Smoothing Procedure	thick/span 1/50	thick/span 1/100	thick/span 1/200	thick/span 1/500	thick/span 1/1000
mesh 1/ 3	MIC	297.9/ 14	341.1/ 26	423.0/ 51	656.5/ 128	1028.6/ 245
	1 GS	371.8/ 32	538.7/ 82	1092.8/ 244	/ >300	/ >300
	2 GS	369.1/ 22	521.4/ 47	1060.7/ 140	/ >300	/ >300
mesh 2/ 4	MIC	728.8/ 10	775.0/ 18	905.7/ 34	1283.0/ 83	1895.6/ 167
	1 GS	812.7/ 22	995.4/ 43	1749.7/ 136	/ >300	/ >300
	2 GS	809.4/ 14	1032.5/ 29	1732.4/ 80	/ >300	/ >300

TABLE 11. Comparison of solution methods for flat shell triangular element (Pinched cylinder with end diaphragms problem)

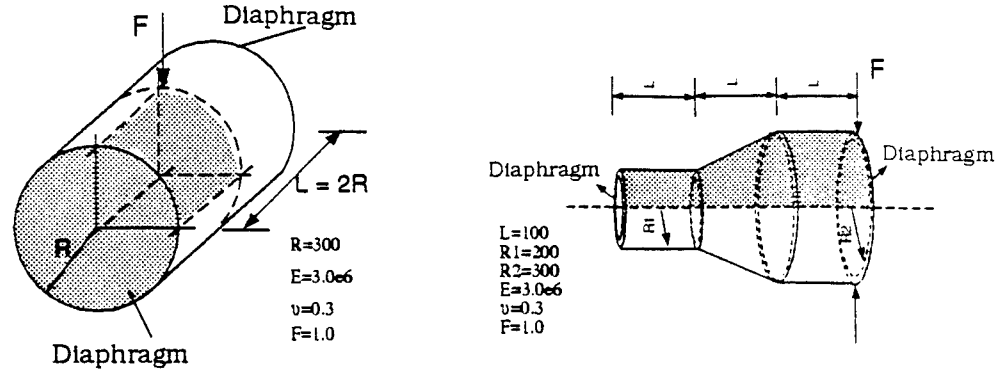
Mesh coarse/fine	Slover Type	thick/span 1/50	thick/span 1/100	thick/span 1/200	thick/span 1/500	thick/span 1/1000
mesh 2/ 4	two-grid	257.3/ 8	251.2/ 7	265.7/ 10	320.8/ 18	384.0/ 30
	PCG	1088.7/ 427	977.8/ 372	1231.1/ 485	> 500	> 500
	direct	864.8				

TABLE 12. Comparison of solution methods for ANS element (Pinched cylinder with end diaphragms problem)

Mesh coarse/fine	Slover Type	thick/span 1/50	thick/span 1/100	thick/span 1/200	thick/span 1/500	thick/span 1/1000
mesh 2/ 4	two-grid	664.9/ 8	672.7/ 12	773.0/ 20	1024.0/ 50	1581.4/ 111
	PCG	1580.7/ 314	2170.8/ 474	> 500	> 500	> 500
	direct	1490.3				

TABLE 13. Comparison of solvers for graded meshes (Pinched cylinder with end diaphragms problem with thick/span 1/100. Two-parameter acceleration)

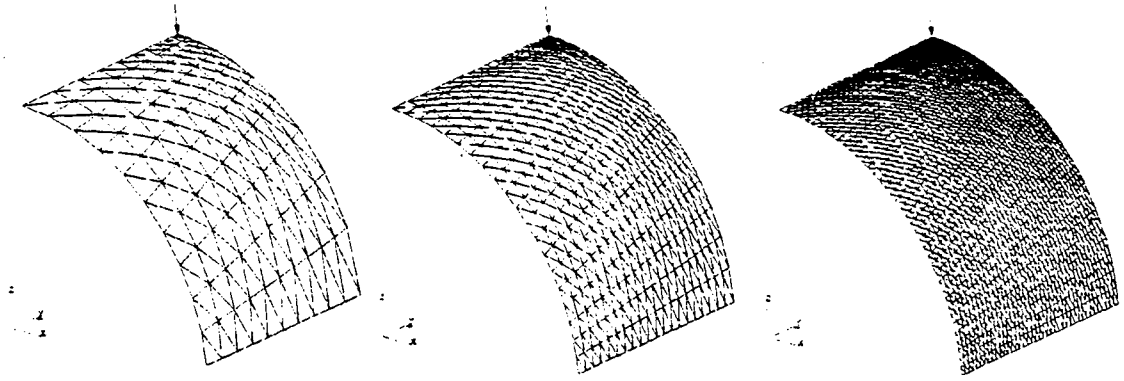
Solver Type	FST	ANS
two grid (2grd/ 3grd)	326.9/ 8	1701.7/ 53
direct	484.4	2278.7
three grid (1grd/2grd/ 3grd)	326.8/ 20	2846.4/ 163
direct	484.4	2278.7



(a). Pinched cylinder with end diaphragms

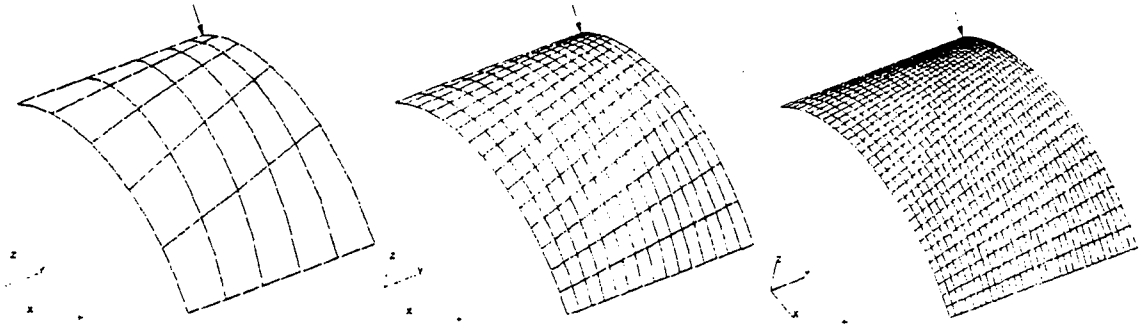
(b). Assembly of three cylinders with end diaphragms

FIGURE 1. Geometry, boundary conditions, material properties



Mesh 1grd Mesh 2grd Mesh 3grd

FIGURE 2. Graded mesh information (Flat shell trangular)



Mesh 1grd Mesh 2grd Mesh 3grd

FIGURE 3. Graded mesh information (Quadrilateral shell element)

Generalized Aggregation Multilevel Solver

Jacob Fish and
Vladimir Belsky

SCOREC Report #11-1996
Scientific Computation Research Center

Submitted to: *International Journal for Numerical Methods in Engineering*

Scientific Computation Research Center
Rensselaer Polytechnic Institute
Troy, NY 12180-3590
voice 5182766795
fax 5182764886

Generalized Aggregation Multilevel Solver

J. Fish and V. Belsky
Department of Civil Engineering and Scientific Computation Research Center
Rensselaer Polytechnic Institute, Troy, NY 12180

ABSTRACT

The paper presents a Generalized Aggregation Multilevel (GAM) solver, which automatically constructs nearly optimal auxiliary coarse models based on the information available in the source grid only. GAM solver is a hybrid solution scheme where approximation space of each aggregate (group of neighboring elements) is adaptively and automatically selected depending on the spectral characteristics of individual aggregates. Adaptive features include automated construction of auxiliary aggregated model by tracing "stiff" and "soft" elements, adaptive selection of intergrid transfer operators, and adaptive smoothing.

An obstacle test consisting of nine industry problems, such as ring-strut-ring structure, casting setup in airfoil, nozzle for turbines, turbine blade and diffuser casing as well as on poor conditioned shell problems, such as High Speed Civil Transport, automobile body and canoe, was designed to test the performance of GAM solver. Comparison to the state of the art direct and iterative (PCG with Incomplete Cholesky preconditioner) is carried out. Numerical experiments indicate that GAM solver possesses an optimal rate of convergence by which the CPU time grows linearly with the problem size, and at the same time, robustness is not compromised, as its performance is almost insensitive to problem conditioning.

1.0 Introduction

The performance of linear solvers in terms of CPU time for symmetric positive definite systems can be approximated as CN^{β}, where N is the number of degrees-of-freedom, and C, β are solution method dependent parameters. The major advantage of direct solvers is their robustness, which is manifested by the fact that parameters C and β are independent of problem conditioning (except for close to singular systems). Direct solvers are ideal for solving small up to medium size problems since the constant C for direct methods is significantly smaller than for iterative solvers, but becomes prohibitively expensive for large scale problems since the value of exponent for direct solvers is higher than for iterative methods. To make direct solvers more efficient various modifications of Gaussian elimina-

tion, which store and compute only the logical nonzeros of the factor matrix [1], have been developed. Nevertheless, fill-inn cannot be avoided but only minimized and serious consideration of iterative methods for large problems is a virtual reality.

Recent years saw a re-emergence of iterative solvers in finite element structural analysis due to increasing demand to analyze very large finite element systems. Conjugate Gradient method with a single level preconditioner, such as SSOR, Modified Incomplete Cholesky (MIC), Element-by-element (EBE), is considered by many commercial finite element code developers (ANSYS, COSMOS, ALGOR) as most suitable for commercial applications. The value of exponent β for CG type methods with a single level preconditioner typically ranges between 1.17 to 1.33 [2] depending on the preconditioner, while the value of constant C increases with degradation in problem conditioning.

Since the pioneering work of Fedorenko [3], multigrid literature has grown at an astonishing rate. This is not surprising since the multigrid-like methods possess an optimal rate of convergence among the iterative techniques β=1, i.e. computational work required to obtain fixed accuracy is proportional to the number of discrete unknowns. The principal idea of multigrid consists of capturing the oscillatory response of the system by means of smoothing, whereas remaining lower frequency response is resolved on the auxiliary coarse grid. Nevertheless, multigrid methods (or multigrid preconditioners within the CG method) thus far had only very little impact in computational structural analysis. There seem to be two basic reasons:

(i) Commercial software packages must be able to automatically produce a full sequence of auxiliary discretizations (finite element or boundary element meshes) that are gradual coarsenings of the source discretization.

(ii) For optimal multigrid convergence smooth solution components relative to a given discretization must be well approximated by subsequent coarser grids. Conventional or geometric multigrid method cannot guarantee that a sequence of auxiliary discretizations will possess this approximation property for general structural mechanics applications. For example, what is a good coarse discretization for frame structure or a wing structure where each panel in the source mesh consists of a single or very few shell element.

These difficulties motivated the development of *Algebraic Multigrid* (AMG) [4] with the intent of providing a black box algebraic solver based on multigrid principles and exhibiting multigrid efficiency. While geometric multigrid approach constructs discretization sequence using auxiliary courser grids, AMG accomplish the same goal on the basis of the information available in the source matrix of equations only. By this technique the coarse level variables selected so as to satisfy certain criteria based on the source grid matrix. The most basic criterion is typically that each fine level degree-of-freedom should be strongly connected to some course level variable. However, the fact that algebraic multigrid uses information available in the source matrix only in constructing auxiliary discretizations, results in suboptimal rate of convergence.

The *aggregation based multilevel solver* is a hybrid scheme where some minor extra information (depending on the type of aggregation scheme) might be used to construct hierarchy of coarser problems, but no sequence of coarser discretization is required. The concept of aggregation has been introduced by Leontief in 1951 [5] in the context input output economics, where commodities in large scale systems where aggregated to produce smaller systems.

The concept of aggregation has been utilized within the context of the multigrid method by Bulgakov [6], [7] and Vanek [8]. In [6] aggregates consisting of non-intersecting groups of neighboring nodes were chosen to have translational degrees of freedom only, and consequently, the auxiliary coarse model could be constructed without knowledge of nodal coordinates or eigenvalue analysis. On the negative side, convergence was only guaranteed for scalar problems such as heat conduction. This algorithm has been improved in [7] by enriching the kinematics of the aggregate with rotational degrees of freedom (three in 3D, one in 2D) and constructing the prolongation operator on the basis of nodal coordinates. In general this approach does not guarantee that the coarse model captures the entire null space of the aggregate, such as in the case of pinned connections in frames or continuum problems where, for example, elements within an aggregate are connected at a single node. Furthermore, the convergence characteristics of this approach have been found to be not satisfactory for poor conditioned problems. These drawbacks motivated development of smoothed aggregation concept [8]. By this technique a tentative piecewise interpolation field consisting of a null space of individual aggregates is first defined and then corrected using Jacobi smoother in attempt to reduce the energy of coarse space basis functions. Our numerical experiments indicate that although smoothed aggregation markedly improves the rate of convergence in well conditioned continuum problems, computational efficiency in poor conditioned problems such as thin shell is not improved and in some cases degrades.

In the earlier aggregation schemes [7], [8] a typical coarsening ratio was about 3^{nsd} for Laplace operator, where nsd is a number of space dimensions. For well conditioned problems this is a nearly optimal ratio resulting in methods with remarkably low computational complexity. Unfortunately, for poor conditioned systems such as thin shells, the coarse problem fails to adequately capture the lower frequency response of the source problem. In attempt to develop a solution procedure possessing an optimal rate of convergence where CPU grows linearly with the problem size without compromising on robustness in the sense that the number of iterations is insensitive to problem conditioning, the present paper presents a generalization of the basic aggregation method by which approximation space of each aggregate is adaptively and automatically selected depending on the spectral characteristics of the aggregate.

The paper is organized as follows. Section 2 reviews the basic multigrid concepts. Mathematical foundation of the Generalized Aggregation Multilevel (GAM) method is given in Section 3. Adaptive features including automated construction of aggregated model by tracing "stiff" and "soft" elements, adaptive selection of intergrid transfer operators, and the Incomplete Cholesky based smoothing procedure with adaptive fill-in are described in Section 4. In Section 5 we conduct numerical studies on 3D industry problems, such as ring-strut-ring structure, casting setup in airfoil, nozzle for turbines, turbine blade and diffuser casing as well as on poor conditioned shell problems, such as High Speed Civil Transport (HSCT), canoe and automobile body. Comparisons to the state of the art direct [1] and iterative (PCG with Incomplete Cholesky preconditioner, Power Solver of ANSYS) are also included in Section 5.

2.0 Multigrid Principles

Consider a linear or linearized system of equations within a Newton-Raphson or related scheme

$$Ku = f \qquad u \in R^n \qquad f \in R^n \tag{1}$$

where K is nxn symmetric positive definite and sparse matrix.

The following notation is adopted. Auxiliary grid functions are denoted with subscript 0. For example, u_0 denotes the nodal values of the solution in the auxiliary grid, where $u_0 \in R^m$, $m < n$. We also denote the prolongation operator from the coarse grid to the fine grid by Q:

$$Q: R^m \rightarrow R^n \tag{2}$$

The restriction operator Q^T from the fine-to-coarse grid is conjugated with the prolongation operator, i.e.:

$$Q^T: R^n \rightarrow R^m \tag{3}$$

In this section superscripts are reserved to indicate the iteration count. Let r^i be the residual vector in the i-th iteration defined by

$$r^i = f - Ku^i \tag{4}$$

where u^i - is the current approximation of the solution in the i-th iteration.

The problem of the coarse grid correction for positive definite systems consists of the minimization of the energy functional on the subspace R^m, i.e.:

$$\frac{1}{2}\left(K\left(u^i + Qu_0^i \right), u^i + Qu_0^i \right) - \left(f, u^i + Qu_0^i \right) \Rightarrow min \quad u_0^i \in R^m \tag{5}$$

where (.,.) denotes the bilinear form defined by

$$(u, v) = \sum_{j=1}^{n} u_j v_j \qquad u, v \in R^n \tag{6}$$

A direct solution of the minimization problem (5) yields a classical two-grid procedure. Alternatively, one may introduce an additional auxiliary grid for u_0 and so forth, leading to a natural multi-grid sequence. To fix ideas we will consider a two-grid process resulting from the direct minimization of (5) which yields

$$K_0 u_0^i = Q^T (f - Ku^i) \tag{7}$$

where $K_0 = Q^T K Q$ -is the restriction of the matrix K. The resulting classical two-grid algorithm can be viewed as a two-step procedure:

a) *Coarse grid correction*

$$r^i = f - Ku^i$$
$$u_0^i = K_0^{-1} Q^T r^i \tag{8}$$
$$\tilde{u}^i = u^i + Q u_0^i$$

where $\tilde{u}^i$ is a partial solution obtained after the coarse grid correction.

b) *Smoothing*

$$u^{i+1} = \tilde{u}^i + D^{-1}(f - K\tilde{u}^i) \tag{9}$$

where D is a preconditioner for smoothing. Any preconditioned iterative procedure which has good smoothing properties and requires little computational work per iteration step, can in principle, be used as a smoother in the multigrid process. In particular, various incomplete factorizations, have been found to possess good smoothing characteristics.

Let u be the exact solution of the source problem, then the error resulting from the coarse grid correction (8) can be cast into the following form

$$\tilde{e}^i = u - \tilde{u}^i = \left(I - QK_0^{-1}Q^T K\right)e^i = \left(I - C^{-1}K\right)e^i \tag{10}$$

where I is the identity $n \times n$ matrix and $C^{-1} = QK_0^{-1}Q^T$ is a course grid preconditioner. Likewise the influence of smoothing on error reduction is given by:

$$e^{i+1} = u - u^{i+1} = \left(I - D^{-1}K\right)\tilde{e}^i \tag{11}$$

and from the equations (9), (10) the error vector of the two-grid process with one post-smoothing iteration can be expressed as:

$$e^{i+1} = \left(I - D^{-1}K\right)\left(I - C^{-1}K\right)e^i \tag{12}$$

Further denoting

$$M = I - D^{-1}K$$
$$T = I - QK_0^{-1}Q^T K \tag{13}$$

equation (12) with ν_1 post-smoothing and one ν_2 pre-smoothing iteration can be cast into in the following concise form

$$e^{i+1} = M^{\nu_1} T M^{\nu_2} e^i \tag{14}$$

Based on equation (13) it can be easily shown that T is a projection operator, i.e. $T = T^2$, and hence $\|T\|_K = 1$.

Equation (14) represents the sufficiency condition for the convergence of multigrid method provided that the iterative procedure employed for smoothing is convergent, i.e.

$\|M\|_K < 1$. For recent advances on convergence analysis for multigrid like methods we refer to [9].

In practice, however, solution increment $u^{k+1} - u^k = P^{-1} r^k$ obtained from the multigrid method is used in the determination of the search direction within the conjugate gradient method. The inverse of the two-grid preconditioner with $\nu_1 = 1 \quad \nu_2 = 0$ can be obtained from equation (12)

$$P^{-1} = D^{-1}\left(I - KC^{-1}\right) + C^{-1} \tag{15}$$

for which the closed form direct expression is given as

$$P = \left[I + (K - D)\, Q\left(Q^T D Q\right)^{-1} Q^T\right] D \quad . \tag{16}$$

3.0 Generalized Aggregation Multilevel (GAM) Solver

In aggregation scheme the coarse model is directly constructed from the source grid by decomposing the whole set of nodes into non-intersecting groups to be referred to as aggregates, and then for each aggregate assigning a reduced number of degrees of freedom. By doing so one reduces dimensionality of the source problem, while maintaining compatibility of the solution. The key issue is how to approximate the solution on each aggregate so that the coarse model, to be referred to as an aggregated model, will effectively capture the lower frequency response of the source system.

We start by relating (*Assertion 1*) the optimal characteristics of the aggregated mesh to the intergrid transfer operator properties of individual aggregates and interface regions between the aggregates.

Assertion 1:

The prolongation operator $Q: R^m \rightarrow R^n$ is considered optimal for fixed $m \leq n$ if $\|Q^T K Q\|_2$ is minimal for all Q satisfying $\|Q\|_2 = 1$ and $rank\, Q = m$. Furthermore, among all the block diagonal prolongation operators, where each block corresponds to the prolongation operator of individual aggregate, the optimal prolongation operator is such that

$$\begin{aligned} &\max_{e,\,a} \left\{ \left\|K_0^a\right\|_2, \left\|K_0^e\right\|_2 \right\} \Rightarrow min\left(Q^a\right) \\ Subjected\ \ to \quad &\left\|Q^a\right\|_2 = 1 \qquad rank\, Q^a = m_a \qquad \forall a \in G \end{aligned} \tag{17}$$

where superscripts a and e denote the aggregates and interface elements between the aggregates, respectively. N_A and N_E is the total number of aggregates and interface ele-

ments, respectively; $Q^a : R^{m_a} \rightarrow R^{n_a}$ and $Q^e : R^{m_e} \rightarrow R^{n_e}$ are the prolongation operators for aggregate a and interface element e; $K_0^a = \left(Q^a\right)^T K^a Q^a$ and $K_0^e = \left(Q^e\right)^T K^e Q^e$ are the corresponding restricted stiffness matrices.

Note that minimization is carried out with respect to the prolongation operator for the aggregates only, that the prolongation operator Q^e for each element in the interface region is uniquely determined from $\{Q^a\}_{a=1}^{N_A}$.

Proof:

Let Φ and Λ be a nxn matrix of unitary eigenvectors and a diagonal nxn matrix of eigenvalues of the stiffness matrix K, respectively, partitioned as $\left[\Phi_0 \; \Phi_1\right]$ and $\begin{bmatrix} \Lambda_0 & 0 \\ 0 & \Lambda_1 \end{bmatrix}$ so that $\|\Lambda_0\|_2 < \tilde{\gamma}$ and $Q = \Phi_0 \alpha$ where Φ_0 consists of m unitary eigenvectors and $\Phi^T \Phi = I$.

The spectral norm of stiffness matrix of the auxiliary model $\|K_0\|_2$ can be bounded utilizing consistency condition [11]

$$\|K_0\|_2 = \|Q^T K Q\|_2 = \|\alpha^T \Lambda_0 \alpha\|_2 \leq \|\alpha\|_2^2 \|\Lambda_0\|_2 \tag{18}$$

Furthermore, since $\|Q\|_2 = \|Q^T Q\|_2^{1/2} = \|\alpha^T \Phi_0^T \Phi_0 \alpha\|_2^{1/2} = \|\alpha\|_2 = 1$ we obtain

$$\|K_0\|_2 \leq \tilde{\gamma} \tag{19}$$

which completes the first part of theorem. For the second part we bound the maximum eigenvalue of the system [10] by the maximum eigenvalue of the subdomain (aggregate or interface element)

$$\|K_0\|_2 \leq \max_{e,a} \{\|K_0^a\|_2, \|K_0^e\|_2\} \tag{20}$$

Assertion 1 states that the quality of aggregated model is governed by the maximum spectral radius of individual subdomains. The next assertion formulates certain minimum requirements for the construction of Q^a aimed at ensuring the lower bound of the minimal eigenvalue of the two-grid preconditioned system $P^{-1}K$. It assumes the worse case scenario where smoothing does not affect lower frequency response errors.

Assertion 2:

Consider the two-level method with $\nu_1 = 1 \quad \nu_2 = 0$ and smoothing affecting only high frequency modes of error. Then the lower frequency response of the two-level system characterized by the lower bound of Rayleigh quotient $\rho(x) = (x^T K x) / (x^T P x)$ is governed by the lowest eigenvalue among all the aggregates provided that the prolongation operator of each aggregate is spanned by the space, which at a minimum contains the null space of that aggregate.

Proof:

Let ϕ^a and λ^a be n_a eigenvectors and eigenvalues of the aggregate a. Nodal solution u^a on each aggregate can be expressed as a linear combination of its eigenvectors

$$\boldsymbol{u}^a = \phi^a \hat{\boldsymbol{u}}^a \tag{21}$$

whereas global solution vector, denoted as $\boldsymbol{u} = \phi \hat{\boldsymbol{u}}$ can be assembled from its aggregates. Let $\begin{bmatrix} \phi_0 & \phi_1 \end{bmatrix}$ and $\begin{bmatrix} \lambda_0 & \boldsymbol{0} \\ \boldsymbol{0} & \lambda_1 \end{bmatrix}$ be the partitions of ϕ and λ, respectively, such that $\|\lambda_0\|_2 < \hat{\gamma}$. Then the system of equations can be transformed into hierarchical form:

$$\begin{bmatrix} \hat{\boldsymbol{K}}_{00} & \hat{\boldsymbol{K}}_{01} \\ \hat{\boldsymbol{K}}_{10} & \hat{\boldsymbol{K}}_{11} \end{bmatrix} \begin{bmatrix} \hat{\boldsymbol{u}}_0 \\ \hat{\boldsymbol{u}}_1 \end{bmatrix} = \begin{bmatrix} \hat{\boldsymbol{f}}_0 \\ \hat{\boldsymbol{f}}_1 \end{bmatrix} \tag{22}$$

where

$$\hat{\boldsymbol{u}}_i = \phi_i^T \boldsymbol{u}_i \qquad \hat{\boldsymbol{f}}_i = \phi_i^T \boldsymbol{f}_i \qquad \hat{\boldsymbol{K}}_{ij} = \phi_i^T \boldsymbol{K} \phi_j \qquad i, j = 0, 1 \tag{23}$$

Similarly, any smoothing preconditioner $\boldsymbol{D}$ can be transformed into hierarchical form $\hat{\boldsymbol{D}}$ as follows

$$\hat{\boldsymbol{D}}_{ij} = \phi_i^T \boldsymbol{D} \phi_j \tag{24}$$

Let $\boldsymbol{Q} = \phi_0$, then the prolongation operator $\hat{Q}$ defined in hierarchical basis is given

$$\hat{\boldsymbol{Q}} = \begin{bmatrix} \phi_0^T \\ \phi_1^T \end{bmatrix} Q = \begin{bmatrix} \boldsymbol{I} \\ \boldsymbol{0} \end{bmatrix} \tag{25}$$

Substituting equations (22)-(25) into (16) yields the two grid preconditioner $\hat{P}$ ($\nu_1 = 1 \quad \nu_2 = 0$) defined in the hierarchical basis

$$\hat{P} = \begin{bmatrix} \hat{K}_{00} & 0 \\ \hat{K}_{10} & \hat{D}_{11} \end{bmatrix} + \begin{bmatrix} 0 & \hat{K}_{00} \\ 0 & \hat{K}_{10} - \hat{D}_{10} \end{bmatrix} \hat{D}_{00}^{-1} \hat{D}_{01} \tag{26}$$

If we further assume that smoothing affects higher frequency response only in the sense that

$$\hat{D}_{00}^{-1} \hat{u}_0 = 0 \qquad \forall \hat{u}_0 \tag{27}$$

then the resulting two-level preconditioner can be cast into the block Gauss-Seidel form:

$$\hat{P} = \begin{bmatrix} \hat{K}_{00} & 0 \\ \hat{K}_{10} & \hat{D}_{11} \end{bmatrix} \tag{28}$$

To estimate the lower bound of Rayleigh quotient of the two-level preconditioned system we utilize again the theorem that bounds the lower eigenvalue of the system (aggregated model) by minimum eigenvalue of any subdomain i consisting of either aggregates a or interface elements e:

$$\min_{i,\,\hat{x}} \{ \rho^i(\hat{x}^i) \} \le \min_{\hat{x}} \{ \rho(\hat{x}) \} \tag{29}$$

It remains to examine under which condition Rayleigh quotient on each aggregate or interface element is bounded from below. For the two-grid preconditioner given in (28) the Rayleigh quotient for each aggregate or interface element is given as

$$\rho^i(\hat{x}^i) = \frac{(\hat{x}_0^i)^T \hat{K}_{00}^i \hat{x}_0^i + 2(\hat{x}_0^i)^T \hat{K}_{01}^i \hat{x}_1^i + (\hat{x}_1^i)^T \hat{K}_{11}^i \hat{x}_1^i}{(\hat{x}_0^i)^T \hat{K}_{00}^i \hat{x}_0^i + (\hat{x}_0^i)^T \hat{K}_{01}^i \hat{x}_1^i + (\hat{x}_1^i)^T \hat{D}_{11}^i \hat{x}_1^i} \tag{30}$$

Let $\mathcal{N}(\hat{K}_{00}^i)$ be the null space of $\hat{K}_{00}^i$ defined as

$$\mathcal{N}(\hat{K}_{00}^i) = \{ (\hat{x}_0^i)^T \hat{K}_{00}^i \hat{x}_0^i = 0 \qquad \forall \hat{x}_0^i \in SPAN(\phi_0^i) \} \tag{31}$$

Then the Rayleigh quotient is bounded from below $\rho^i(\hat{x}^i) > 0$ if $\hat{K}_{00}^i$ contains all the rigid body modes of $\hat{K}^i$, i.e. $\mathcal{N}(\hat{K}_{00}^i) = \mathcal{N}(\hat{K}^i)$. This condition can be easily satisfied if the prolongation operator for each aggregate is spanned by the space containing the rigid body modes of that aggregate. In addition, for all interface elements $\mathcal{N}(\hat{K}_c^e) = \emptyset$,

where $\hat{\boldsymbol{K}}_c^e$ is the interface element stiffness matrix constrained along the boundary between interface elements and aggregates. Loosely speaking, each interface element should be connected to aggregates at a number of degrees of freedom greater or equal then the dimension of the null space of that element $dim\{\mathcal{N}(\hat{\boldsymbol{K}}^e)\}$.

So far we have proposed how to assess the quality of intergrid transfer operators (*Assertion 1*) and what are the properties that it should maintain (*Assertion 2*). In the subsequent proposition we describe a heuristic approach, which on the bases of the two assertions, attempts to construct a nearly optimal aggregated model.

Proposition 1:

For given $\{m_a\}_{a=1}^{N_A}$ a nearly optimal aggregation model can be constructed if (i) prolongation operator $\boldsymbol{Q}^a:\boldsymbol{R}^{m_a} \rightarrow \boldsymbol{R}^{n_a}$ on aggregate a is spanned by $m_a \leq n_a$ eigenvectors corresponding to m_a lowest eigenvalues on aggregate a, where $m_a \geq dim\{\mathcal{N}(\hat{K}^a)\}$, and (ii) in forming the aggregated model soft elements determined by the Gerschgorin upper bound of their maximal eigenvalue $\max_i\left(\sum_j \left|k_{ij}^e\right|\right)$ are placed at the interface, where $\boldsymbol{K}^e = \left[k_{ij}^e\right]$.

Discussion:

We first show that for fixed m_a the prolongation operators $\boldsymbol{Q}^a$ that minimizes $\left\|\boldsymbol{K}_0^a\right\|_2$ is obtained as a linear combination of m_a lowest eigenvectors of $\boldsymbol{K}^a$. This fact directly follows from equation (19) in the context of individual aggregates

$$\left\|\boldsymbol{K}_0^a\right\|_2 \leq \gamma^a \qquad \forall \boldsymbol{Q}^a = \{\left\|\boldsymbol{Q}^a\right\|_2 = 1 \quad rank\,\boldsymbol{Q}^a = m_a\} \tag{32}$$

where γ^a is the maximum eigenvalue of eigenvectors spanning the space of $\boldsymbol{Q}^a$. Furthermore, if we select $\gamma^a \leq \gamma \ \forall a$, then the spectral norm of individual aggregates does not exceed user prescribed tolerance γ.

The spectral radius of the restricted interface element stiffness matrix $\boldsymbol{K}_0^e$ is given as

$$\left\| K_0^e \right\|_2 = \left\| \left(Q^e \right)^T K^e Q^e \right\|_2 \leq \left\| Q^e \right\|_2^2 \left\| K^e \right\|_2 \tag{33}$$

Since Q^e is a diagonal block of Q it can be easily shown that $\left\| Q^e \right\|_2 \leq \left\| Q \right\|_2 = 1$ and thus using Gerschgorin theorem for the maximal eigenvalue of K follows that

$$\left\| K_0^e \right\|_2 \leq \max_i \left(\sum_j \left| k_{ij}^e \right| \right) \tag{34}$$

where $K^e = \left[k_{ij}^e \right]$.

4.0 Adaptive features

This section describes three features of adaptivity built into the Generalized Multilevel Aggregation procedure. Some of the notation in this section differs from that introduced in the previous sections.

First we present the algorithm for automated construction of aggregates on the element-by-element basis as opposed to node-by-node procedure employed in [7,8]. In accordance with this approach it is necessary to determine the rigid-body modes and other low-frequency modes based on the aggregate stiffness matrices. We present two versions of the aggregate formation algorithm: the basic version which utilizes a topological information only, and the adaptive version which in addition to the topological information utilizes elemental stiffness matrices in the process of the aggregated model construction.

The second adaptive feature is related to the selection of parameter γ, which plays a central role in constructing the prolongation operator. This parameter has a direct effect on the restriction of the stiffness matrix, the sparsity pattern of resulting auxiliary stiffness matrix as well as on effectiveness of the auxiliary model to capture the lower frequency response.

Finally, we employ Modified Incomplete Cholesky Factorization for pre- and post-smoothing. The number of fill-ins as well as diagonal-scaling needed to preserve the positive definiteness of the system and to provide the fastest rate of convergence of the iterative process are also determined adaptively.

4.1 Aggregation algorithm

Prior to describing the technical details of the aggregation algorithm we introduce the concept of "stiff" and "soft" elements which is utilized in the process of aggregate formation.

The element is considered "stiff" if the spectral radius of its stiffness matrix is relatively large compared to other elements and vice versa. Following Proposition 1, we will attempt wherever possible to place "soft" elements at the interface between the aggregates, and "stiff" elements within the aggregates. This approach is a counterpart of the idea of "weak" and "strong" nodal connectivity employed in [8] in the context of node-by-node aggregation.

The approximation for the maximum eigenvalue can be easily estimated using Gerschgorin theorem in the context of the element stiffness matrices:

$$\max_a \lambda_e^a \le \beta^e \quad \beta^e = \max_i \left(\sum_j \left| k_{ij}^e \right| \right) \tag{35}$$

In the remaining of this subsection we focus on the aggregation algorithm.

Consider the finite element mesh containing N_E elements and N_N nodes. Let $C(i)$ be the set of nodes belonging to the element E^i:

$$C(i) = \{N^j : N^j \in E^i\} \tag{36}$$

The goal of the aggregation algorithm described below is to construct a set of N_A aggregates denoted as

$$A = \{A^i, i \in [1, N_A]\} \tag{37}$$

satisfying the following conditions:

(i). *Element-by-element aggregation*:

$$A^i = \{E^j, j \in M_E^i\} \tag{38}$$

$M_E^i \subset [1, N_E]$ - set the of element numbers corresponding to the aggregate i

(ii). *Disjoint covering*: elements belonging to different aggregates can not be neighbors. Two elements E^i and E^j are considered to be neighbors if

$$C(i) \cap C(j) \neq \emptyset \tag{39}$$

(iii). *Full nodal covering*: each node belongs to some aggregate:

$$\bigcup_{\{i:E^i \in A\}} C(i) = \{N^j, j \in [1, N_N]\} \tag{40}$$

(iv). *Marking the 'slave' nodes and nodes with essential boundary conditions as separate aggregates*: each node containing either essential boundary condition and/or 'slave' degree(s)-of-freedom, which depends on so called 'master' degree(s)-of-freedom, is considered as an aggregate. Denote the set of such nodes as N_{NB}.

Step 1. Setup.

1.1. For each node $N^j, j = [1, N_n]$ select the elements containing this node:

$$B(j) = \{E^i:N^j \in E^i\} \tag{41}$$

1.2. For each element $E^i, i = [1, N_e]$ select the set of neighboring elements $NE(i)$, that are the elements containing common nodes:

$$NE(i) = \{E^k:E^k \in B(j), j \in C(i)\} \backslash E^i \tag{42}$$

Step 2. Start-up aggregation.

2.1. Define the set of elements NA available for aggregation. These are all the elements which do NOT contain nodes with essential boundary conditions or the 'slave' nodes:

$$NA = [1, N_e] \backslash \{B(j), N^j \in N_{NB}\} \tag{43}$$

2.2. Find the "peripheral" element E^s, that is the element with minimal number of neighbors:

$$s = \underset{i \in NA}{\arg min} |NE(i)| \tag{44}$$

where $|X|$ is a number of elements in the set X. Element E^s is a starting element for the aggregation algorithm.

2.3. Setup:

-the current aggregate counter $i = 1$;

- the set of interface elements $NI = [1, N_e] \backslash NA$, i.e. the elements between different aggregates.

Step 3. Formation of the current aggregate.

Basic aggregation version:

aggregate A^i contains the element E^s and **all** it's available neighbors:

$$A^i = E^s \cup (NE(s) \cap NA) \tag{45}$$

Adaptive aggregation version:

aggregate A^i contains the element E^s and **those** of it's available neighbors which satisfy the relative stiffness condition:

$$A^i = E^s \cup \{E^j \in NE(s) \cap NA, \beta^j \geq \mu\beta^s\} \tag{46}$$

where β^j is a Gerschgorin upper bound on the stiffness matrix maximal eigenvalue of the element E^j, and μ is a coarsening parameter.

Step 4. Update the sets of the interface and available elements.

4.1. Update the set of the interface elements:

$$NI = NI \cup \{\left(E^k \in NE(j), E^j \in A^i\right) \cap \left(E^k \notin A^i\right)\} \tag{47}$$

4.2. Update the set of the available elements:

$$NA = NA \backslash \{\left(E^k \in NE(j), E^j \in A^i\right) \cup A^i\} \tag{48}$$

Step 5. Find the new starting element.

5.1. Form the set of "frontal" elements FR, that are available elements neighboring to the interface elements:

$$FR = \{\left(E^k \in NE(j), E^j \in NI\right) \cap NA\} \tag{49}$$

5.2. Basic version: select **arbitrary** new starting element belonging to FR:

$$E^s \in FR \tag{50}$$

Adaptive version: select the **stiffest** new starting element from FR:

$$s = \underset{j:E^j \in FR}{\arg max}\left(\beta^j\right) \tag{51}$$

Step 6. Stopping criteria.

If $FR = \emptyset$ then stop; else $i = i + 1$ and repeat *steps 3-6*.

Remark 1. For simplicity we only presented the aggregation algorithm for lower order elements. In the case of higher order elements the "full nodal covering" requirement may not be satisfied at the completion of the algorithm described above. There will be a significant number of nodes belonging to the elements in the interface region giving rise to very large auxiliary coarse model. To further reduce the size of the auxiliary model the same aggregation algorithm is recursively applied for the interface elements only until all the nodes would be covered by some aggregate. This procedure also provides a "cleaning" phase to ensure that all nodes in the source grid are included within one of the aggregates.

Remark 2. A similar scheme can be applied for the p-type discretization with only exception that the aggregates may contain only a single element in order to reduce the aggregate size. Higher order modes in the interface region are treated as indicated in the Remark 1.

Remark 3. The aggregation algorithm described in this section deals with multi-point constrains in the conventional way since the elements containing the "slave" nodes form a separate aggregate. Each multi-point constrain can be represented as follows:

$$x_s = Tx_m \tag{52}$$

where x_s, x_m are the 'slave' and 'master' degrees-of-freedom, respectively; T is a transformation matrix representing the multi-point constrain (MPC) data. In accordance with (52) the vector $x = (x_s, x_m)^T$ can be expressed as:

$$x = \begin{bmatrix} T \\ I \end{bmatrix} x_m \tag{53}$$

Given the decomposition of the element stiffness matrix K_e for elements containing the 'slave' degrees-of-freedom

$$K_e = \begin{bmatrix} K_e^{ss} & K_e^{sm} \\ K_e^{ms} & K_e^{mm} \end{bmatrix} \quad (54$$

the modified element stiffness matrix $\tilde{K}_e$ corresponding to master degrees-of-freedom only is given by:

$$\tilde{K}_e = T^T K_e^{ss} T + K_e^{ms} T + T^T K_e^{sm} + K_e^{mm} \quad (55$$

4.2 Adaptive construction of prolongation operator

One of the key issue in the proposed aggregation procedure is a selection of parameter γ. All the eigenvectors of the eigenvalue problem on each aggregate corresponding to the eigenvalues $\lambda^a \leq \gamma$ are included within the diagonal block of the global prolongation operator. In order to make this parameter dimensionless the eigenvalue problem on each aggregate is formulated in the following manner:

$$\boldsymbol{K}^a \phi^a = \lambda^a \boldsymbol{D}^a \phi^a \quad (56$$

where $\boldsymbol{D}^a$ is a diagonal of $\boldsymbol{K}^a$. Typically 6-50 modes are needed to satisfy $\lambda^a \leq \gamma$ requirement. Lanczos algorithm with partial orthogonalization [13] was adopted.

The value of the parameter γ determines effectiveness of coarse grid correction. In the limit as $\gamma \rightarrow \max_a \lambda^a$ auxiliary problem captures the response of the source system for all frequencies and therefore the two-level procedure converges in a single iteration even without smoothing. On the negative side, for large values of γ, eigenvalue analysis on each aggregate becomes prohibitively expensive and the auxiliary matrix becomes both large and dense. At the other extreme in the limit as $\gamma \rightarrow 0$ the prolongation operator contains the rigid body modes of all the aggregates only, and thus auxiliary problem becomes inefficient for ill-posed problems.

4.3 Adaptive smoothing

Selection of smoothing procedure is another important issue as the cost of smoothing is a major expense in multi-level procedures. Comprehensive studies conducted in [12

revealed that one of the most efficient smoothing schemes is based on Modified Incomplete Cholesky factorization (MIC). We employed two versions of MIC, with and without additional fill-ins using "by value" as the fill-in strategy. By this technique one compares the values of the terms in the incomplete factor and chooses the largest ones to be included [14]. One of the most important parameters in both versions is the diagonal-scaling parameter α which insures positive definiteness of the incomplete factor. The value of α is determined adaptively. Its optimal value depends on the number of fill-ins. For larger number of fill-ins the optimal value of the diagonal-scaling decreases. The optimal number of fill-ins is determined experimentally, whereas the value of the diagonal-scaling parameter is determined adaptively by incrementally increasing it until all positive pivots are obtained.

5.0 Numerical examples

An obstacle test as shown in Figures 1 and 2 comprised of the following industry and model problems was designed to (i) determine the optimal values of computational parameters and to (ii) compare GAM solver with existing state-of-the-art solvers:

Diffuser Casing with Gates for Casting: 10 node tetrahedral elements; 131,529 d.o.f.s.

Turbine Blade with Platform: 10 node tetrahedral elements; 207,840 d.o.f.s.

Nozzle for Turbines: 10 node tetrahedral elements; 131,565 d.o.f.s.

Casting Setup for Casting in Airfoil: 10 node tetrahedral elements; 158,166 d.o.f.s.

Concentric Ring-Strut-Ring Structure: 4 node tetrahedral elements; 102,642 d.o.f.s.

High Speed Civil Transport (HSCT): MIN3 [15] shell elements; 88,422 d.o.f.s.

Automobile Body: 3 node DKT+DMT shell [16], 2 node beam elements; 265,128 d.o.f.s.

Automobile Body: MIN3 [15] shell and 2 node beam elements; 265,128 d.o.f.s.

Concrete canoe: 8 node ANS [17] shell elements; 132,486 d.o.f.s.

5.1 Parametric study

In this section we present the results of numerical investigation of the following computation parameters: limiting eigenvalue parameter γ for selection of the modes to be included in the prolongation operator; number of fill-ins and diagonal scaling parameter α for Modified Incomplete Cholesky factorization; and coarsening computation parameter μ.

5.1.1 Prolongation parameters

In order to determine optimal value of γ in terms of the CPU time we have carried out extensive computational experiments for wide range of industrial problems, including well-posed and ill-posed cases. Surprisingly, it has been found that the optimal value of γ is independent of the problem condition and slightly differs for different problems. For example, it can be seen that for poorly conditioned HSCT problem (Figure 3) significant reduction of the number of iterations was observed as γ increased from 0.0020 to 0.0040. Optimal value of γ, which minimizes the CPU time for this problem was equal to 0.0035 independently of quality of MIC smoother (number of fill-ins and diagonal scaling parameter). On the other hand, for the Diffuser Casing (Figure 4), Automobile Body (Figure 6), Concentric Ring-Strut-Ring Structure and Joint of Two Cylinders problems the CPU time was practically independent of γ. However, for the Nozzle for Turbine problem (Figure 5) significant reduction of the number of iterations was observed for relatively large values of γ ranging from 0.0075 to 0.0100 and the optimal value of γ, which minimizes the CPU time for this problem, was equal to 0.0100. Based on these results we have built in $\gamma = 0.0050$ for further numerical studies and comparisons, which provides a reasonably good performance for all problems considered.

5.1.2 Smoothing parameters

The efficiency of MIC based smoothing procedure highly depends on the two computational parameters: the number of fill-ins and the diagonal-scaling. Typically, increasing the number of fill-ins allows to decrease the value of the diagonal-scaling parameter. It can be seen (Figure 3 and Figure 7) that for the HSCT, Diffuser Casing, Concentric Ring-Strut-Ring Structure problems the optimal value of fill-ins is equal to $5 - 6$, with minimal value of diagonal-scaling parameter α which ensures positive pivots. For the HSCT problem the effect of number of fill-ins and the value α presented in Figure 3 indicated that the optimal computational performance is obtained with 4-6 fill-ins. For the Nozzle for Turbines (Figure 5) and Joint of Two Cylinders problems it was observed that the number of fill-ins has no effect on the effectiveness of the iterative process. We did not consider number of fill-ins greater then 8 due to increased in-core memory requirements.

Based on the computational experiment the following strategy has been developed for determination of nearly optimal values of α and number of fill-ins:

- MIC with number of fill-ins is equal to 6
- Initial diagonal-scaling parameter $\alpha = 0.01$
- Increasing α by the increment of $\Delta\alpha = 0.0025$ if non-positive pivot is encountered in the process of incomplete factorization, or if the two-level iteration procedure diverges.

5.1.3 Aggregation parameters

Numerical experiments in obstacle test indicated that the value of the coarsening parameter μ had very little effect on the convergence of the iteration procedures. The only problem where considerable improvement was observed was a 2-D problem for randomly distributed short fibers in matrix material, where fiber/matrix stiffness ratio was equal to 100. The problem was modeled using quadrilateral finite elements. For this problem converge solution was achieved in 23 iterations using basic aggregation algorithm, while using adaptive version of aggregation procedure with optimal value $\mu = 1.68$ the convergence was achieved in 18 iterations. In subsequent studies we employed the basic version of aggregation procedure.

5.2 Comparison with other solvers and discussion

First we present the comparison of GAM solver with traditional Skyline Direct solver. Figure 9 shows the rate of convergence in term of CPU time versus problem size for the Diffuser Casing with Gates for Casting problem. It can be seen that in contrast to other solvers considered the CPU time grows linearly with problem size for GAM solver. Even for relatively small problem with 35,000 d.o.f.s. GAM outperforms traditional Skyline solver by factor of 27. For the problem with 70,000 d.o.f.s. GAM solver outperforms Sparse Direct solver by factor of 9 and PCG with Modified Incomplete Cholesky preconditioner by factor of 12.

In the second set of problems GAM is compared with "smoothed aggregation" technic introduced in [8]. We have observed that for a 2-D model elasticity problem on a square domain this approach gives an improvement in terms of number of iterations (16 instead of 23). However for ill-posed shell problem (HSCT) the number of iteration becomes almost twice larger (154) in comparison with the basic GAM version. Furthermore, smoothing of the approximation field on each aggregate creates denser prolongation operator, which in turn increases CPU time of restriction and yields denser auxiliary matrix.

Table 1 contains split up CPU times including aggregation, restriction of stiffness matrix, factorization of auxiliary matrix, incomplete factorization of source matrix, and iterative procedure of GAM solver for all obstacle test problems. Finally, Table 2 and Table 3 compare GAM Solver in terms of the CPU and memory requirements with the Sparse Direct Solver [1] and PCG Solver with Modified Incomplete Cholesky preconditioner. Computations were carried out on SUN SPARC 10/51 Workstation.

So far only in-core solution methods have been considered. Clearly an ultimate solution engine should have an out-of-core capabilities, since it is not usually possible to keep the entire stiffness matrix in RAM. An out-of-core version of GAM is currently being investigated.

REFERENCES

1 A.George and J.W.H. Liu, 'The evolution of the minimum degree ordering algo-

rithm,' *Report CS-87-06*, North York, Otario York University, 1987.

2 O.Axelsson and V.A.Barker, '*Finite Element Solution of Boundary Value Problems*,' Academic Press, 1984.

3 R. P. Fedorenko, 'A relaxation method for solving elliptic difference equations,' *USSR Computational Math. and Math. Phys.*, Vol. 1, No. 5, pp.1092-1096, 1962.

4 A.Brandt, S.F.McCormick, and J.W.Ruge, 'Algebraic multigrid (AMG) for sparse matrix equations' in *Sparsity and Its Applications*, D.J. Evans, ed., Cambridge Univ. Press, Cambridge, 1984.

5 W. Leontief, '*The Structure of the American Economy 1919-1939*, Oxford U.P., NY, 1951.

6 V.E.Bulgakov, 'Multi-level iterative technique and aggregation concept with semi-analytical preconditioning for solving boundary-value problems', *Communications in Numerical Methods in Engineering*, Vol. 9, 649-657, (1993).

7 V.E.Bulgakov and G.Kuhn, 'High-performance multilevel iterative aggregation solver for large finite-element structural analysis problems', *Int. J. For Numerical Methods In Engineering*, Vol. 38, 3529-3544, (1995).

8 P. Vanek, 'Acceleration of convergence of a two-level algorithm by smoothing transfer operator,' *Applications of Mathematics*, Vol. 37, pp. 265-274, (1992).

9 W. Hackbusch and U. Trottenberg, *Multigrid Methods*, Springer-Verlag, Berlin, 1992.

10 I. Fried, 'Discretization and round-off Errors in the Finite Element Analysis of elliptic Boundary Value Problems and Eigenvalue Problems, *Ph.D. Thesis, MIT*, 1971.

11 G.W. Stewart, '*Introduction to matrix computations*,' Academic Press, NY, 1973.

12 O. Axelsson, 'Analysis of Incomplete Matrix Factorizations as Multigrid Smoothers for Vector and Parallel Computers,' *Applied Mathematics and Computation*, Vol. 19, 3-22, (1986).

13 H.D.Simon, 'The Lanczos algorithm with partial reorthogonalization,' *Math. Comp.* 42, pp. 115-142, (1984).

14 M.A. Ajiz and A.Jennings, 'A robust incomplete Cholesky conjugate gradient algorithm,' *Int. J. For Numerical Methods In Engineering*, Vol. 20, pp. 949-966, (1984)

15 A. Tessler, 'A C^0 Anisotropic three-node shallow shell element,' *Comp. Meth. Appl. Mech. Eng.*, Vol. 78, pp. 89-103, (1990).

16 J. Fish and T.Belytschko, 'Stabilized rapidly convergent 18-degrees-of-freedom flat shell triangular element,' *Int. J. For Numerical Methods In Engineering*, Vol. 33, pp. 149-162, (1992)

17 K.C.Parks and G,Stanley, 'A curved C^0 shell element based on assumed natural coordinate strains,' *Journal of Applied Mechanics*, Vol. 108, 1986, pp.278-290.

Figures and Tables Captions

Figure 1: Obstacle test 3D problems.

Figure 2: Obstacle test shell problems.

Figure 3: GAM solver performance in terms of (a) iteration count, and (b) CPU seconds as a function of limiting eigenvalue parameter γ and number of fill-ins for HSCT problem with MIN3 elements.

Figure 4: GAM solver performance in terms of (a) iteration count, and (b) CPU seconds as a function of limiting eigenvalue parameter γ and number of fill-ins for Diffuser Casing problem with 10-node Tets.

Figure 5: GAM solver performance in terms of (a) iteration count, and (b) CPU seconds as a function of limiting eigenvalue parameter γ and number of fill-ins for Nozzle for Turbines problem.

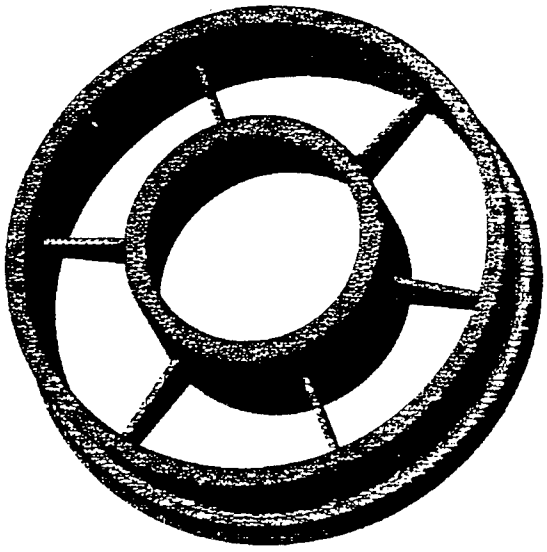
Figure 6: GAM solver performance in terms of (a) iteration count, and (b) CPU seconds as a function of limiting eigenvalue parameter γ and number of fill-ins for Automobile Body problem with DKT+DMT elements.

Figure 7: GAM solver performance in terms of iteration count and CPU seconds as a function of number of fill-ins (limiting eigenvalue parameter $\gamma = 0.00625$) for (a) Diffuser Casing problem with 10-node Tets, and (b) Ring-Strut-Ring problem with 4-node Tets.

Table 1: GAM solver breakdown times in seconds.

Table 2: Comparisons of GAM, PCG(MIC) and Sparse [1] solvers in terms of CPU seconds and iteration count.

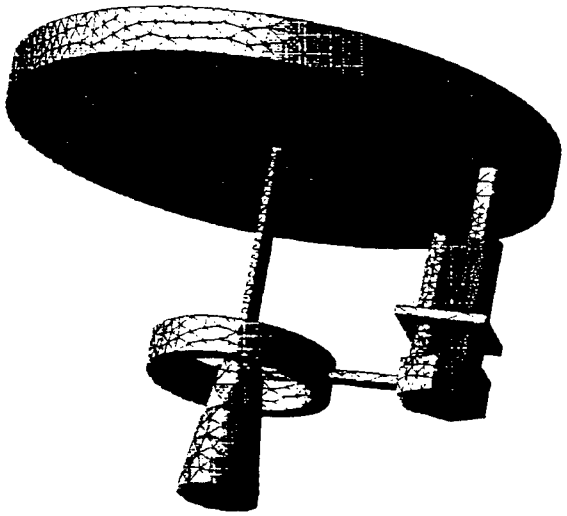
Table 3: Comparisons of GAM, PCG(MIC) and Sparse [1] solvers in terms of memory (MB).



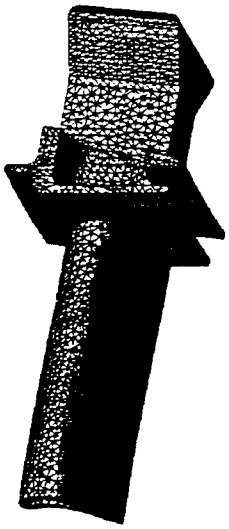
Concentric Ring-Strut-Ring Structure
DOFS: 102,642
EL_TYPE: 4 NODE TET



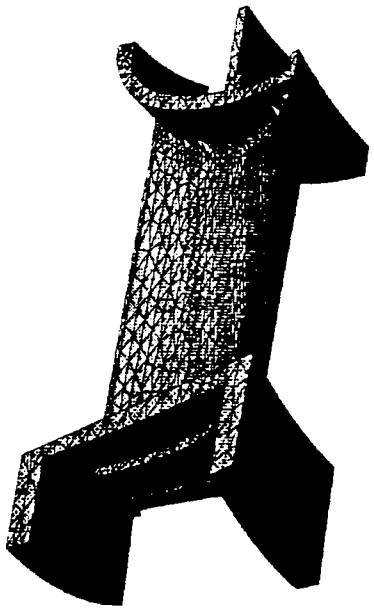
Casting Setup for Casting in Airfoil
DOFS: 158,166
EL_TYPE: 10 NODE TET



Diffuser Casing with Gates for Casting
DOFS: 131,529
EL_TYPE: 10 NODE TET

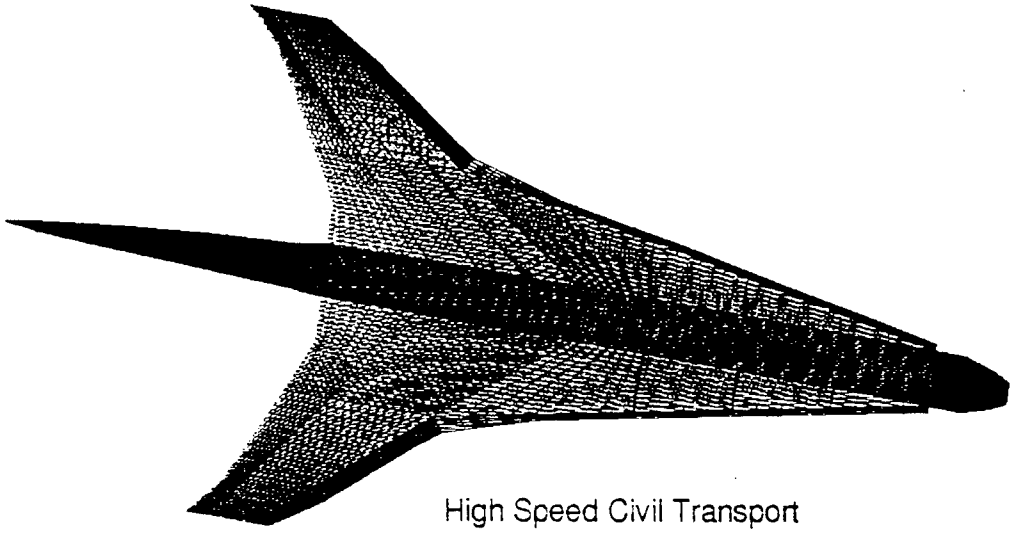


Turbine Blade with Platform
DOFS: 207,840
EL_TYPE: 10 NODE TET

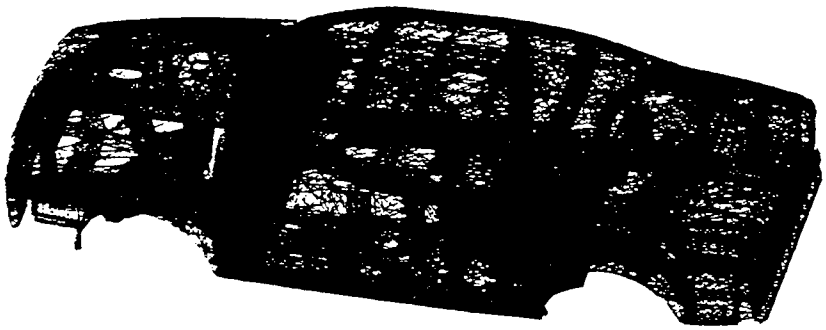


Nozzle for Turbines
DOFS: 131,565
EL_TYPE: 10 NODE TET

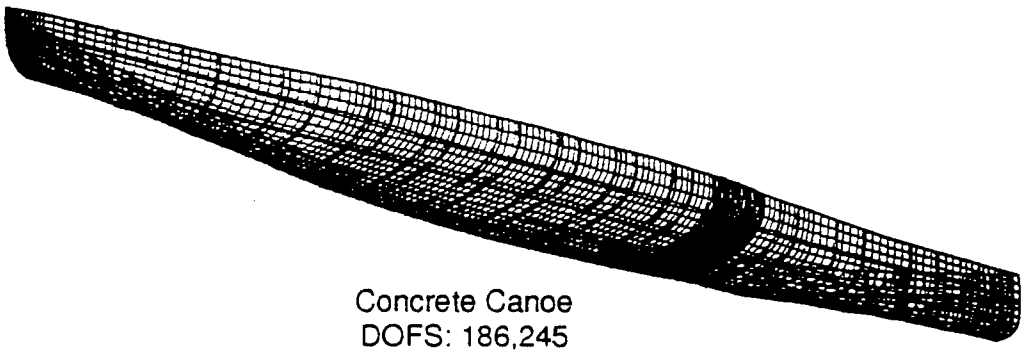
Figure 1



High Speed Civil Transport
DOFS: 88,422
EL_TYPE: MIN3S, DKT-DMT



Automobile Body
DOFS: 265,128
EL_TYPES: MIN3S, BEAM



Concrete Canoe
DOFS: 186,245
EL_TYPE: 8-node ANS

Figure 2

Finite Deformation Plasticity for Composite Structures: Computational Models and Adaptive Strategies

Jacob Fish and Kamlun Shek
Departments of Civil, Mechanical and Aerospace Engineering
Rensselaer Polytechnic Institute
Troy, NY 12180

Abstract

We develop computational models and adaptive modeling strategies for obtaining an approximate solution to a boundary value problem describing the finite deformation plasticity of heterogeneous structures. A nearly optimal mathematical model consists of an averaging scheme based on approximating eigenstrains and elastic concentration factors in each micro phase by a constant in the macro problem subdomains where modeling errors are small, whereas elsewhere, a more detailed mathematical model based on piecewise constant approximation of eigenstrains and elastic concentration factors is utilized. The methodology is developed within the framework of "statistically homogeneous" composite material and local periodicity assumptions.

1.0 Introduction

In this manuscript, we develop a theory and methodology for obtaining an approximate solution to a boundary value problem describing the finite deformation plasticity of heterogeneous structures. The theory is developed within the framework of "statistically homogeneous" composite material and local periodicity assumptions. For readers interested in theoretical and computational issues dealing with various aspects of nonperiodic heterogeneous media we refer to [7][9][28][37].

The challenge of solving structural problems with accurate resolution of microstructural fields undergoing inelastic deformation is enormous. This subject has been an active area of research in the computational mechanics community for more than two decades. Numerous studies have dealt with the utilization of the finite element method [12][13] [18][21][22][24][30][34], the boundary element method [11], the Voronoi cell method [10], the spectral method [1], the transformation field analysis [5], and the Fourier series expansion technique [26] for solving PDEs arising from the homogenization of nonlinear composites. The primary goals of these studies were twofold: (i) develop macroscopic constitutive equations that would enable solution of an auxiliary problem with nonlinear homogenized (smooth) coefficients, and (ii) establish bounds for overall nonlinear properties [2][29][32][33][34][35].

Attempts at solving large scale nonlinear structural systems with accurate resolution of microstructural fields are very rare [10][12][26] and successes were reported for small problems and/or special cases. This is because for linear problems a unit cell or a representative volume problem has to be solved only once, whereas for nonlinear history dependent systems, it has to be solved at every increment and for each macroscopic (Gauss) point. Furthermore, history data has to be updated at a number of integration points equal to the product of the number of Gauss points in the macro and micro (unit cell) domains.

To illustrate the computational complexity involved we consider an elasto-plastic analysis of the composite flap problem [8] with fibrous microstructure as shown in Figures 1 and 2. The structural problem is discretized with 788 tetrahedral elements (993 degrees of freedom), whereas fibrous microstructure is discretized with 98 elements in the fiber domain and 253 elements in the matrix domain, totaling 330 degrees of freedom. The CPU time on SPARC 10/51 workstation for this problem was over 7 hours, as opposed to 10 seconds if von Mises metal plasticity was used instead, which means that 99.9% of CPU time is spent on stress updates.

With the exception of [6][12][19] most of the research activities focused on small deformation inelastic response of microconstituents and their interfaces. This is partially justified due to high stiffness and relatively low ductility of fibrous composite materials. However, when hardening is low and the stress measures are comparable to the inelastic tangent modulus, or in the case of thin structures undergoing large rotations, large deformation formulation is required.

One of the objectives of the present manuscript is to extend the recent formulation of the mathematical homogenization theory with eigenstrains developed by the authors in [8] to account for finite deformation and thermal effects. In addition, adaptive strategies are devised to ensure reliability and efficiency of computations. In Section 2 we derive a closed form expression relating arbitrary transformation fields to mechanical fields in the phases. In Sections 3 and 4 we employ an additive decomposition of rate of deformation into elastic rate of deformation governed by hypoelasticty and inelastic rate of deformation. Section 3 focuses on the *2*-point approximation scheme (for two phase materials), where each point represents an average response within a phase. The local response within each phase is then recovered by means of post-processing. In Section 4 we describe the *n*-point scheme model, where *n* denotes the number of elements in the microstructure. Section 5 is devoted to modeling error estimation and adaptive strategy. We devise an adaptive *2/n*-point model, where the *2*-point scheme is used in regions where modeling errors are small, whereas elsewhere the *n*-point scheme is employed. Numerical experiments conducted in Section 6 investigate the *2*-point, the *n*-point, and the adaptive *2/n*-point schemes in the context of finite deformation plasticity.

2.0 Mathematical Homogenization with Eigenstrain for Small Deformations

In this section we generalize the classical mathematical homogenization theory [3][4] for heterogeneous media to account for eigenstrains. We regard all inelastic strains, phase transformation and temperature effects as eigenstrains in an otherwise elastic body. We will derive closed form expressions relating arbitrary eigenstrains to mechanical fields in a multi-phase composite medium. In this section attention is restricted to small deformations.

The microstructure of a composite material is assumed to be locally periodic (Y-periodic) with a period represented by a unit cell domain or a Representative Volume Element (RVE), denoted by Θ, as shown in Figure 3. Y-periodicity implies that all response functions, such as displacements, stresses and strains, are periodic with periods proportional to the ratio of the representative micro and macro structures, denoted by ς. Let $\boldsymbol{x}$ be a macroscopic coordinate vector in macro domain Ω and $\boldsymbol{y} \equiv \boldsymbol{x}/\varsigma$ be a microscopic position vector in Θ. For any periodic function f, we have $f(\boldsymbol{x}, \boldsymbol{y}) = f(\boldsymbol{x}, \boldsymbol{y} + \boldsymbol{k}\hat{\boldsymbol{y}})$ in which vector $\hat{\boldsymbol{y}}$ is the basic period of the microstructure and $\boldsymbol{k}$ is a 3 by 3 diagonal matrix with integer components. Adopting the classical nomenclature, any Y-periodic function f can be represented as

$$f^{\varsigma}(\boldsymbol{x}) \equiv f(\boldsymbol{x}, \boldsymbol{y}(\boldsymbol{x})), \tag{1}$$

where superscript ς denotes a Y-periodic function f. The indirect macroscopic spatial derivatives of f^{ς} can be calculated by the chain rule as

$$f^{\varsigma}_{,x_i}(\boldsymbol{x}) \equiv f_{;x_i}(\boldsymbol{x}, \boldsymbol{y}) = f_{,x_i}(\boldsymbol{x}, \boldsymbol{y}) + \frac{1}{\varsigma} f_{,y_i}(\boldsymbol{x}, \boldsymbol{y}) \tag{2}$$

$$f_{;y_i}(\boldsymbol{x}, \boldsymbol{y}) = f_{,y_i}(\boldsymbol{x}, \boldsymbol{y}) + \varsigma f_{,x_i}(\boldsymbol{x}, \boldsymbol{y}) = \varsigma f_{;x_i}(\boldsymbol{x}, \boldsymbol{y}) \tag{3}$$

where the comma followed by a subscript variable x_i or y_i denotes a partial derivative with respect to the subscript variable (i.e. $f_{,x_i} \equiv \partial f/\partial x_i$ and $f_{,y_i} \equiv \partial f/\partial y_i$). A semi-colon followed by a subscript variable x_i denotes a partial derivative with respect to the remaining x components (2), but a full derivative with respect to y_i, and vice versa when a semi-colon is followed by subscript variable y_i (3). Summation convention for repeated right hand side subscripts is employed, except for subscripts x and y.

We assume that micro-constituents possess homogeneous properties and satisfy equilibrium, constitutive, kinematics and compatibility equations as well as jump conditions at the interface between the micro-phases. The corresponding boundary value problem is governed by the following equations:

$$\sigma^{\varsigma}_{ij;x_j} + b_i = 0 \quad \text{in} \quad \Omega \tag{4}$$

$$\sigma^{\varsigma}_{ij} = L_{ijkl}(\varepsilon^{\varsigma}_{kl} - \mu^{\varsigma}_{kl}) \quad \text{in} \quad \Omega \tag{5}$$

$$\varepsilon^{\varsigma}_{ij} = u^{\varsigma}_{(i;x_j)} \quad \text{in} \quad \Omega \tag{6}$$

$$\omega^{\varsigma}_{ij} = u^{\varsigma}_{[i;x_j]} \quad \text{in} \quad \Omega \tag{7}$$

$$u^{\varsigma}_i = \bar{u}_i \quad \text{on} \quad \Gamma_u \tag{8}$$

$$\sigma^{\varsigma}_{ij} n_j = \bar{t}_i \quad \text{on} \quad \Gamma_t \tag{9}$$

where σ^{ς}_{ij}, $\varepsilon^{\varsigma}_{ij}$ and ω^{ς}_{ij} are components of stress, strain and rotation tensors; L_{ijkl} and μ^{ς}_{ij} are components of elastic stiffness and eigenstrain tensors, respectively; b_i is a body force assumed to be independent of $\boldsymbol{y}$; u^{ς}_i denotes the components of the displacement vector; the subscript pairs with regular and square parenthesizes denote the symmetric and anti-symmetric gradients defined as

$$u^{\varsigma}_{(i;x_j)} \equiv \frac{1}{2}(u^{\varsigma}_{i;x_j} + u^{\varsigma}_{j;x_i}), \qquad u^{\varsigma}_{[i;x_j]} \equiv \frac{1}{2}(u^{\varsigma}_{i;x_j} - u^{\varsigma}_{j;x_i}) \tag{10}$$

Ω denotes the macroscopic domain of interest with boundary Γ; Γ_u and Γ_t are boundary portions where displacements $\bar{u}_i$ and tractions $\bar{t}_i$ are prescribed, respectively, such that $\Gamma_u \cap \Gamma_t = \varnothing$ and $\Gamma = \Gamma_u \cup \Gamma_t$; n_i denotes the normal vector on Γ. We assume that the interface between the phases is perfectly bonded, i.e. $[\sigma^{\varsigma}_{ij}\hat{n}_j] = 0$ and $[u^{\varsigma}_i] = 0$ at the interface, Γ_{int}, where $\hat{n}_i$ is the normal vector to Γ_{int} and $[\bullet]$ is a jump operator.

In the following, displacements $u^{\varsigma}_i(\boldsymbol{x}) = u_i(\boldsymbol{x}, \boldsymbol{y})$ and eigenstrains $\mu^{\varsigma}_{ij}(\boldsymbol{x}) = \mu_{ij}(\boldsymbol{x}, \boldsymbol{y})$ are approximated in terms of double scale asymptotic expansions on $\Omega \times \Theta$:

$$u_i(\boldsymbol{x}, \boldsymbol{y}) \approx u^0_i(\boldsymbol{x}, \boldsymbol{y}) + \varsigma u^1_i(\boldsymbol{x}, \boldsymbol{y}) + \ldots \tag{11}$$

$$\mu_{ij}(\boldsymbol{x}, \boldsymbol{y}) \approx \mu^0_{ij}(\boldsymbol{x}, \boldsymbol{y}) + \varsigma \mu^1_{ij}(\boldsymbol{x}, \boldsymbol{y}) + \ldots \tag{12}$$

Strain and rotation expansions on $\Omega \times \Theta$ can be obtained by substituting (11) into (6) and (7) with consideration of the indirect differentiation rule (2)

$$\varepsilon_{ij}(\boldsymbol{x}, \boldsymbol{y}) \approx \frac{1}{\varsigma}\varepsilon^{-1}_{ij}(\boldsymbol{x}, \boldsymbol{y}) + \varepsilon^0_{ij}(\boldsymbol{x}, \boldsymbol{y}) + \varsigma \varepsilon^1_{ij}(\boldsymbol{x}, \boldsymbol{y}) + \ldots \tag{13}$$

$$\omega_{ij}(x, y) \approx \frac{1}{\varsigma}\omega_{ij}^{-1}(x, y) + \omega_{ij}^{0}(x, y) + \varsigma\omega_{ij}^{1}(x, y) + \ldots \tag{14}$$

where strain and rotation components for various orders of ς are given as

$$\varepsilon_{ij}^{-1} = \varepsilon_{yij}(u^0), \qquad \varepsilon_{ij}^{s} = \varepsilon_{xij}(u^s) + \varepsilon_{yij}(u^{s+1}), \quad s = 0, 1, \ldots \tag{15}$$

$$\omega_{ij}^{-1} = \omega_{yij}(u^0), \qquad \omega_{ij}^{s} = \omega_{xij}(u^s) + \omega_{yij}(u^{s+1}), \quad s = 0, 1, \ldots \tag{16}$$

and

$$\varepsilon_{xij}(u^s) = u^s_{(i,x_j)}, \qquad \varepsilon_{yij}(u^s) = u^s_{(i,y_j)} \tag{17}$$

$$\omega_{xij}(u^s) = u^s_{[i,x_j]}, \qquad \omega_{yij}(u^s) = u^s_{[i,y_j]} \tag{18}$$

Stresses and strains for different orders of ς are related by the constitutive equation (5)

$$\sigma_{ij}^{-1} = L_{ijkl}\varepsilon_{kl}^{-1}, \qquad \sigma_{ij}^{s} = L_{ijkl}(\varepsilon_{kl}^{s} - \mu_{kl}^{s}), \quad s = 0, 1, \ldots \tag{19}$$

The resulting asymptotic expansion of stress is given as

$$\sigma_{ij}(x, y) \approx \frac{1}{\varsigma}\sigma_{ij}^{-1}(x, y) + \sigma_{ij}^{0}(x, y) + \varsigma\sigma_{ij}^{1}(x, y) + \ldots \tag{20}$$

Inserting the stress expansion (20) into equilibrium equation (4) and making the use of (2) yields the following equilibrium equations for various orders:

$$O(\varsigma^{-2}): \quad \sigma_{ij,y_j}^{-1} = 0 \tag{21}$$

$$O(\varsigma^{-1}): \quad \sigma_{ij,x_j}^{-1} + \sigma_{ij,y_j}^{0} = 0 \tag{22}$$

$$O(\varsigma^{0}): \quad \sigma_{ij,x_j}^{0} + \sigma_{ij,y_j}^{1} + b_i = 0 \tag{23}$$

$$O(\varsigma^{s}): \quad \sigma_{ij,x_j}^{s} + \sigma_{ij,y_j}^{s+1} = 0, \quad s = 1, 2, \ldots \tag{24}$$

Consider the $O(\varsigma^{-2})$ equilibrium equation (21) first. Pre-multiplying it by u_i^0 and integrating over a unit cell domain Θ yields

$$\int_{\Theta} u_i^0 \sigma_{ij,y_j}^{-1}\, d\Theta = 0 \tag{25}$$

and subsequently integrating by parts gives

$$\int_{\Gamma_\Theta} u_i^0 \sigma_{ij}^{-1} n_j\, d\Gamma_\Theta - \int_{\Theta} u^0_{(i,y_j)} L_{ijkl} u^0_{(k,y_l)}\, d\Theta = 0 \tag{26}$$

where Γ_Θ denotes the boundary of Θ. The boundary integral term in (26) vanishes due to the periodicity of boundary conditions on Γ_Θ. Furthermore, since the elastic stiffness L_{ijkl} is positive definite, we have

$$u^0_{(i,y_j)} = 0 \qquad \Rightarrow \qquad u^0_i = u^0_i(\boldsymbol{x}) \tag{27}$$

and

$$\sigma^{-1}_{ij}(\boldsymbol{x}, \boldsymbol{y}) = \varepsilon^{-1}_{ij}(\boldsymbol{x}, \boldsymbol{y}) = \omega^{-1}_{ij}(\boldsymbol{x}, \boldsymbol{y}) = 0 \tag{28}$$

We proceed to the $O(\varsigma^{-1})$ equilibrium equation (22) next. From equations (15) and (19) follows

$$\{L_{ijkl}(\varepsilon_{xkl}(\boldsymbol{u}^0) + \varepsilon_{ykl}(\boldsymbol{u}^1) - \mu^0_{kl})\}_{,y_j} = 0 \quad \text{on} \quad \Theta \tag{29}$$

To solve for (29) up to a constant we introduce the following separation of variables

$$u^1_i(\boldsymbol{x}, \boldsymbol{y}) = H_{ikl}(\boldsymbol{y})\{\varepsilon_{xkl}(\boldsymbol{u}^0) + d^\mu_{kl}(\boldsymbol{x})\} \tag{30}$$

where H_{ikl} is a Y-periodic function, d^μ_{kl} is a macroscopic portion of the solution resulting from eigenstrains, i.e. if $\mu^0_{kl}(\boldsymbol{x}, \boldsymbol{y}) = 0$ then $d^\mu_{kl}(\boldsymbol{x}) = 0$. It should be noted that both H_{ikl} and d^μ_{kl} are symmetric with respect to indices k and l. Based on (30) $O(\varsigma^{-1})$ equilibrium equation takes the following form:

$$\{L_{ijkl}((I_{klmn} + G_{klmn})\varepsilon_{xmn}(\boldsymbol{u}^0) + G_{klmn}d^\mu_{mn}(\boldsymbol{x}) - \mu^0_{kl})\}_{,y_j} = 0 \quad \text{on} \quad \Theta \tag{31}$$

where

$$I_{klmn} = \frac{1}{2}(\delta_{mk}\delta_{nl} + \delta_{nk}\delta_{ml}), \qquad G_{klmn}(\boldsymbol{y}) = H_{(k,y_l)mn}(\boldsymbol{y}) \tag{32}$$

and δ_{mk} is the Kronecker delta. Since equation (31) should be valid for arbitrary combination of macroscopic strain field $\varepsilon_{xmn}(\boldsymbol{u}^0)$ and eigenstrain field μ^0_{kl}, we first consider $\mu^0_{kl} \equiv 0$, $\varepsilon_{xmn}(\boldsymbol{u}^0) \neq 0$ and then $\varepsilon_{xmn}(\boldsymbol{u}^0) \equiv 0$, $\mu^0_{kl} \neq 0$ which yields the following two governing equations on Θ:

$$\{L_{ijkl}(I_{klmn} + H_{(k,y_l)mn})\}_{,y_j} = 0 \tag{33}$$

$$\{L_{ijkl}(H_{(k,y_l)mn}d^\mu_{mn} - \mu^0_{kl})\}_{,y_j} = 0 \tag{34}$$

Equation (33) together with the periodic boundary conditions comprise a standard linear boundary value problem on Θ. For complex microstructures finite element method is often used to solve for $H_{ikl}(\boldsymbol{y})$, which yields a set of linear algebraic system with six right hand side vectors [7]. In absence of eigenstrains, the asymptotic fields can be written in terms of the macroscopic strain $\bar{\varepsilon}_{ij} \equiv \varepsilon_{xij}(\boldsymbol{u}^0)$ and the macroscopic rotation $\bar{\omega}_{ij} \equiv \omega_{xij}(\boldsymbol{u}^0)$:

$$\varepsilon_{ij} = \bar{\varepsilon}_{ij} + G_{ijkl}\bar{\varepsilon}_{kl} + O(\varsigma), \qquad \omega_{ij} = \bar{\omega}_{ij} + \hat{G}_{ijkl}\bar{\varepsilon}_{kl} + O(\varsigma) \tag{35}$$

where

$$\hat{G}_{ijkl}(\boldsymbol{y}) = H_{[i,y_j]kl}(\boldsymbol{y}) \tag{36}$$

The terms G_{ijkl} and $\hat{G}_{ijkl}$ are known as polarization functions. It can be shown that the integrals of the polarization functions on Θ vanish due to periodicity conditions.

The elastic homogenized stiffness $\bar{L}_{ijkl}$ follows from $O(\varsigma^0)$ equilibrium equation [7]:

$$\bar{L}_{ijkl} \equiv \frac{1}{|\Theta|}\int_\Theta L_{ijmn}A_{mnkl}\, d\Theta = \frac{1}{|\Theta|}\int_\Theta A_{mnij}L_{mnst}A_{stkl}\, d\Theta \tag{37}$$

where

$$A_{klmn} = I_{klmn} + G_{klmn} \tag{38}$$

A_{klmn} is often referred to as an elastic strain concentration function and $|\Theta|$ is the volume of a unit cell.

After solving (33) for H_{imn}, we proceed to (34) for finding d^{μ}_{kl} subjected to periodic boundary conditions. Pre-multiplying (34) by H_{ist} and then integrating the resulting equation by parts with consideration of the periodic boundary conditions yields

$$\int_\Theta G_{ijst}L_{ijkl}(G_{klmn}d^{\mu}_{mn}(\boldsymbol{x}) - \mu^0_{kl})\, d\Theta = 0 \tag{39}$$

Rewriting this equation in terms of strain concentration function A_{ijkl} and manipulating it with (37) yields

$$d^{\mu}_{ij} = \frac{1}{|\Theta|}(\tilde{L}_{ijkl} - \bar{L}_{ijkl})^{-1}\int_\Theta G_{mnkl}L_{mnst}\mu^0_{st}\, d\Theta \tag{40}$$

where

$$\tilde{L}_{ijkl} = \frac{1}{|\Theta|}\int_{\Theta} L_{ijkl}\, d\Theta \tag{41}$$

The superscript -1 denotes the reciprocal tensor. The $O(\varsigma^0)$ approximation to the asymptotic strain (13) and rotation fields (14) reduces to:

$$\varepsilon_{ij} = \bar{\varepsilon}_{ij} + G_{ijkl}(\bar{\varepsilon}_{kl} + d^{\mu}_{kl}) + O(\varsigma) \tag{42}$$

$$\omega_{ij} = \bar{\omega}_{ij} + \hat{G}_{ijkl}(\bar{\varepsilon}_{kl} + d^{\mu}_{kl}) + O(\varsigma) \tag{43}$$

Let $\Psi \equiv \{\psi^{(\eta)}(y)\}_1^n$ be a set of C^{-1} continuous functions, then the separation of variables for the $O(\varsigma^0)$ eigenstrains is assumed to have the following decomposition:

$$\mu^0_{ij}(x, y) = \sum_{\eta=1}^{n} \psi^{(\eta)}(y)\, \mu^{(\eta)}_{ij}(x) \tag{44}$$

The resulting asymptotic expansion of the strain and rotation fields (13), (14) can be expressed as follows:

$$\varepsilon_{ij}(x, y) = \bar{\varepsilon}_{ij}(x) + G_{ijkl}(y)\bar{\varepsilon}_{kl}(x) + \sum_{\eta=1}^{n} D^{(\eta)}_{ijkl}(y)\, \mu^{(\eta)}_{kl}(x) + O(\varsigma) \tag{45}$$

$$\omega_{ij}(x, y) = \bar{\omega}_{ij}(x) + \hat{G}_{ijkl}(y)\bar{\varepsilon}_{kl}(x) + \sum_{\eta=1}^{n} \hat{D}^{(\eta)}_{ijkl}(y)\, \mu^{(\eta)}_{kl}(x) + O(\varsigma) \tag{46}$$

where $D^{(\eta)}_{ijkl}(y)$ and $\hat{D}^{(\eta)}_{ijkl}(y)$ are the eigenstrain influence functions, which can be expressed in terms of polarization functions $G_{ijkl}(y)$ and $\hat{G}_{ijkl}(y)$ as follows

$$D^{(\eta)}_{ijkl}(y) = \frac{1}{|\Theta|} G_{ijmn}(\tilde{L}_{mnpq} - \bar{L}_{mnpq})^{-1} \int_{\Theta} G_{rspq} L_{rskl} \psi^{(\eta)}\, d\Theta \tag{47}$$

$$\hat{D}^{(\eta)}_{ijkl}(y) = \frac{1}{|\Theta|} \hat{G}_{ijmn}(\tilde{L}_{mnpq} - \bar{L}_{mnpq})^{-1} \int_{\Theta} G_{rspq} L_{rskl} \psi^{(\eta)}\, d\Theta \tag{48}$$

In particular, if Ψ is a set of piecewise constant functions such that

$$\psi^{(\eta)}(y_\rho) = \begin{cases} 1 & \text{if } y_\rho \in \Theta^{(\eta)} \\ 0 & \text{otherwise} \end{cases} \tag{49}$$

and $\Theta^{(\eta)}$ is the subdomain η within a unit cell, $c^{(\eta)}$ the subdomain volume fraction given by $c^{(\eta)} \equiv |\Theta^{(\eta)}|/|\Theta|$ and satisfying $\sum_{\eta=1}^{n} c^{(\eta)} = 1$, then (45) and (46) reduce to:

$$\begin{aligned} \varepsilon_{ij}^{(\rho)} &= \frac{1}{|\Theta^{(\rho)}|}\int_{\Theta^{(\rho)}} \varepsilon_{ij}\, d\Theta = \bar{\varepsilon}_{ij} + G_{ijkl}^{(\rho)}\bar{\varepsilon}_{kl} + \sum_{\eta=1}^{n} D_{ijkl}^{(\rho\eta)}\mu_{kl}^{(\eta)} + O(\varsigma) \\ \omega_{ij}^{(\rho)} &= \frac{1}{|\Theta^{(\rho)}|}\int_{\Theta^{(\rho)}} \omega_{ij}\, d\Theta = \bar{\omega}_{ij} + \hat{G}_{ijkl}^{(\rho)}\bar{\varepsilon}_{kl} + \sum_{\eta=1}^{n} \hat{D}_{ijkl}^{(\rho\eta)}\mu_{kl}^{(\eta)} + O(\varsigma) \end{aligned} \tag{50}$$

where

$$D_{ijkl}^{(\rho\eta)} = c^{(\eta)} G_{ijmn}^{(\rho)} (\tilde{L}_{mnpq} - \bar{L}_{mnpq})^{-1} G_{rspq}^{(\eta)} L_{rskl}^{(\eta)} \tag{51}$$

$$\hat{D}_{ijkl}^{(\rho\eta)} = c^{(\eta)} \hat{G}_{ijmn}^{(\rho)} (\tilde{L}_{mnpq} - \bar{L}_{mnpq})^{-1} G_{rspq}^{(\eta)} L_{rskl}^{(\eta)} \tag{52}$$

and

$$(G_{ijkl}^{(\eta)}, \hat{G}_{ijkl}^{(\eta)}) = \frac{1}{|\Theta^{(\eta)}|}\int_{\Theta^{(\eta)}} (G_{ijkl}, \hat{G}_{ijkl})\, d\Theta \tag{53}$$

We will refer to the piecewise constant model defined by (50) as the n-point scheme model. Equation (50)a has been originally derived by Dvorak [5] on the basis of transformation field analysis. Finally, we integrate the $O(\varsigma^0)$ equilibrium equation (23) over Θ. The $\int_{\Theta} \sigma_{ij,y_j}^{1} d\Theta$ term vanishes due to periodicity and we obtain:

$$\left(\frac{1}{|\Theta|}\int_{\Theta} \sigma_{ij}^{0}\, d\Theta\right)_{,x_j} + b_i = 0 \qquad \text{on} \qquad \Omega \tag{54}$$

Substituting the constitutive relation (19) and the asymptotic expansion of strain tensor (42) into the above equation yields the macroscopic equilibrium equation

$$\left(\frac{1}{|\Theta|}\int_{\Theta} L_{ijkl}(A_{klmn}\bar{\varepsilon}_{mn} + G_{klmn}d_{mn}^{\mu} - \mu_{kl}^{0})\, d\Theta\right)_{,x_j} + b_i = 0 \tag{55}$$

Finally, if we define the macroscopic stress $\bar{\sigma}_{ij}$ as

$$\bar{\sigma}_{ij} \equiv \frac{1}{|\Theta|}\int_{\Theta} \sigma_{ij}^{0}\, d\Theta \tag{56}$$

then the equilibrium equations (54) and (55) can be further simplified as follows:

$$\bar{\sigma}_{ij,x_j} + b_i = 0, \qquad \{\bar{L}_{ijkl}(\bar{\varepsilon}_{kl} - \bar{\mu}_{kl})\}_{,x_j} + b_i = 0 \tag{57}$$

where $\bar{\mu}_{ij}$ is the overall eigenstrain given by

$$\bar{\mu}_{ij} = -\frac{1}{|\Theta|}\bar{L}^{-1}_{ijkl}\int_{\Theta} L_{klmn}(G_{mnpq}d^{\mu}_{pq} - \mu^{0}_{mn})\, d\Theta \tag{58}$$

Replacing G_{mnpq} by $A_{mnpq} - I_{mnpq}$ and manipulating (58) with (37) and (40), the overall eigenstrain field can be expressed as

$$\bar{\mu}_{ij} = \frac{1}{|\Theta|}\int_{\Theta} B_{klij}\mu^{0}_{kl}\, d\Theta, \qquad B_{ijkl} = L_{ijmn}(\mathbf{y})A_{mnpq}(\mathbf{y})\bar{L}^{-1}_{pqkl} \tag{59}$$

Equation (59) represents the well-known Levin's formula [23] relating the local and overall eigenstrains, and B_{ijkl} is often referred to as the elastic stress concentration function.

Remark 1: As a special case we consider a composite medium consisting of two phases, matrix and reinforcement, with respective volume fractions $c^{(m)}$ and $c^{(f)}$ such that $c^{(m)} + c^{(f)} = 1$. Superscripts m and f represent matrix and reinforcement phases, respectively. $\Theta^{(m)}$ and $\Theta^{(f)}$ denote the matrix and reinforcement domains such that $\Theta = \Theta^{(m)} \cup \Theta^{(f)}$. We assume that eigenstrains and elastic strain concentration factors are constant within each phase. This yields the simplest variant of (50) where n=2. The corresponding approximation scheme is termed as the 2-point model. The overall elastic properties are given by [5]

$$\bar{L}_{ijkl} = \sum_{r=m}^{f} c^{(r)}L^{(r)}_{ijmn}(I_{mnkl} + G^{(r)}_{mnkl}) \tag{60}$$

and the overall stress reduces to:

$$\bar{\sigma}_{ij} = c^{(m)}\sigma^{(m)}_{ij} + c^{(f)}\sigma^{(f)}_{ij} \tag{61}$$

3.0 *2*-Point Scheme for Finite Deformation Plasticity

For finite deformation analysis the left superscript denotes the configuration: ${}^{t+\Delta t}\square$ is the current configuration at time $t + \Delta t$, whereas ${}^{t}\square$ is the configuration at time t. For simplicity, we will often omit the left superscript for the current configuration, i.e., $\square \equiv {}^{t+\Delta t}\square$. To extend the small deformation formulation to account for finite deformation effects the following assumptions are made:

A1: Phase stress objectivity

We will assume that the principle of objectivity is satisfied for each phase. Then the Cauchy stress rate for phase r is given as:

$$\dot{\sigma}_{ij}^{(r)} = \mathring{\sigma}_{ij}^{(r)} + \hat{\dot{\sigma}}_{ij}^{(r)} \qquad \text{where} \qquad \hat{\dot{\sigma}}_{ij}^{(r)} = \Lambda_{ik}^{(r)}\sigma_{kj}^{(r)} - \sigma_{ik}^{(r)}\Lambda_{kj}^{(r)} \tag{62}$$

where the superposed dot represents the material time derivative. The rate of deformation and spin tensor components, denoted as $\dot{\varepsilon}_{ij}^{\varsigma(r)}$ and $\dot{\omega}_{ij}^{\varsigma(r)}$, respectively, are defined as

$$\dot{\varepsilon}_{ij}^{\varsigma(r)}(\boldsymbol{x}) \equiv v_{(i;x_j)}^{\varsigma(r)} \qquad \text{and} \qquad \dot{\omega}_{ij}^{\varsigma(r)}(\boldsymbol{x}) \equiv v_{[i;x_j]}^{\varsigma(r)} \tag{63}$$

where $v_{i;x_j}^{\varsigma(r)}$ is the phase velocity gradient. The asymptotic expansion of the phase velocity is given as

$$v_i^{\varsigma(r)}(\boldsymbol{x}) \equiv v_i^{(r)}(\boldsymbol{x}, \boldsymbol{y}) \approx v_i^{0(r)}(\boldsymbol{x}, \boldsymbol{y}) + \varsigma v_i^{1(r)}(\boldsymbol{x}, \boldsymbol{y}) + \ldots \tag{64}$$

$\mathring{\sigma}_{ij}^{(r)}$ is the objective rate of the Cauchy stress in phase r, which represents the material response due to deformation, whereas $\Lambda_{ij}^{(r)} = \dot{\mathfrak{R}}_{ik}^{(r)}\{\mathfrak{R}_{kj}^{(r)}\}^{-1}$ represents the rate of rotation.

Remark 2: The choice of rotation $\mathfrak{R}_{ij}^{(r)}$ depends on the microstructure. For fibrous composites it is natural to assume that $\mathfrak{R}_{ij}^{(r)}$, represents the fiber rotation from the configuration aligned along the unit vector ${}^{t}m_i$ to the current configuration aligned along the vector m_i. Thus

$$m_i = \mathfrak{R}_{ij}^{(r)}\,{}^{t}m_j \qquad \text{and} \qquad \dot{m}_i = \dot{\mathfrak{R}}_{ip}^{(r)}\{\mathfrak{R}_{pj}^{(r)}\}^{-1}m_j \equiv \bar{\Lambda}_{ij}^{(r)}m_j \tag{65}$$

Following Lee [20] it can be shown that $\bar{\Lambda}_{ij}^{(r)}$ is related to the spin and rate of deformation tensors by:

$$\bar{\Lambda}_{ij}^{(r)} = \dot{\omega}_{ij}^{(r)} + \dot{\varepsilon}_{ik}^{(r)}m_k m_j - \dot{\varepsilon}_{jk}^{(r)}m_k m_i \tag{66}$$

The choice of rotations in textile and particle composites is less obvious. We refer to [16] for the discussion on various choices.

A2: Additive decomposition of hypoelastic and inelastic rate of deformation

The theoretical and practical reasons favoring additive decomposition over multiplicative decomposition for fibrous composites were discussed in [27]. In the present work we adopt the additive decomposition of rate of deformation into elastic ${}_{e}\dot{\varepsilon}_{ij}^{(r)}$ and inelastic rate of deformation $\dot{\mu}_{ij}^{(r)}$, which gives

$$\dot{\varepsilon}_{ij}^{(r)} = {}_e\dot{\varepsilon}_{ij}^{(r)} + \dot{\mu}_{ij}^{(r)} \tag{67}$$

Furthermore, we will assume the hypoelastic constitutive equation relating the objective Cauchy stress rate with rate of elastic deformation:

$$\mathring{\sigma}_{ij}^{(r)} = L_{ijkl}^{(r)}(\dot{\varepsilon}_{kl}^{(r)} - \dot{\mu}_{kl}^{(r)}) \tag{68}$$

A3: Midpoint integration scheme for micro- and macro-coordinates

In a typical time step $t + \Delta t$, the configuration of the macro- and micro-structure may be expressed as a sum of the configuration at the previous step t and the displacement increment:

$${}^{t+\Delta t}x_i = {}^{t}x_i + \Delta u_i^0 \tag{69}$$

$${}^{t+\Delta t}y_i = {}^{t}y_i + \Delta \hat{u}_i \tag{70}$$

The macroscopic displacement increment Δu_i^0 is found from the incremental solution of the macro-problem, whereas displacement increment in the RVE is given by:

$$\Delta \hat{u}_i(\boldsymbol{x}, \boldsymbol{y}) = \{\Delta \bar{\varepsilon}_{ij}(\boldsymbol{x}) + \Delta \bar{\omega}_{ij}(\boldsymbol{x})\} y_j + \Delta u_i^1(\boldsymbol{x}, \boldsymbol{y}) \tag{71}$$

The first term in (71) represents the contribution of macroscopic solution, whereas the second term $\Delta u_i^1(\boldsymbol{x}, \boldsymbol{y})$ accounts for oscillatory Y-periodic field. Figure 4 schematically illustrates the decomposition of the deformation field in the RVE.

Strain and rotation increments are integrated using the midpoint rule to obtain a second order accuracy:

$$\Delta \bar{\varepsilon}_{ij} = \frac{1}{2}\left(\frac{\partial \Delta u_i^0}{\partial^{t+\Delta t/2}x_j} + \frac{\partial \Delta u_j^0}{\partial^{t+\Delta t/2}x_i}\right) \qquad \Delta \bar{\omega}_{ij} = \frac{1}{2}\left(\frac{\partial \Delta u_i^0}{\partial^{t+\Delta t/2}x_j} - \frac{\partial \Delta u_j^0}{\partial^{t+\Delta t/2}x_i}\right) \tag{72}$$

where the midpoint coordinates are defined as

$${}^{t+\Delta t/2}x_i \equiv \frac{1}{2}({}^{t}x_i + {}^{t+\Delta t}x_i), \qquad {}^{t+\Delta t/2}y_i \equiv \frac{1}{2}({}^{t}y_i + {}^{t+\Delta t}y_i) \tag{73}$$

Similarly, the periodic portion of the solution increment Δu_i^1 is obtained by integrating (30) using the midpoint rule:

$$\Delta u_i^1 = H_{imn}({}^{t+\Delta t/2}y)(\Delta \bar{\varepsilon}_{mn}(\boldsymbol{x}) + \Delta d_{mn}^{\mu}(\boldsymbol{x})) \tag{74}$$

where the increment of inelastic strain is defined in Section 4.

A4: Additive decomposition of material and rotational response

There are several formulations aimed at extending the small deformation formulation to account for large deformation effects. One of the most popular approaches is known as the co-rotational method where all the fields of interest are transformed into the rotated $\mathfrak{R}$-system [16]. In the $\mathfrak{R}$-system, the form of constitutive equations is analogous to small deformation theory. A simpler approach, proposed by Hallquist [14] and improved by Hughes and Winget [17] to preserve incremental objectivity, is based on the additive incremental decomposition of material and rotational response. The latter procedure is adopted in the present manuscript.

For two phase material, the integration scheme [17] decomposes stresses and back stresses as follows:

$$ {}^{t+\Delta t}\sigma_{ij}^{(r)} = {}^{t}\hat{\sigma}_{ij}^{(r)} + \Delta\sigma_{ij}^{(r)}, \qquad {}^{t}\hat{\sigma}_{ij}^{(r)} = \mathfrak{R}_{ki}^{(r)}\, {}^{t}\sigma_{kl}^{(r)}\, \mathfrak{R}_{lj}^{(r)} \tag{75} $$

$$ {}^{t+\Delta t}\alpha_{ij}^{(r)} = {}^{t}\hat{\alpha}_{ij}^{(r)} + \Delta\alpha_{ij}^{(r)}, \qquad {}^{t}\hat{\alpha}_{ij}^{(r)} = \mathfrak{R}_{ki}^{(r)}\, {}^{t}\alpha_{kl}^{(r)}\, \mathfrak{R}_{lj}^{(r)} \tag{76} $$

where $\alpha_{ij}^{(r)}$ is the back stress. The midpoint rule is utilized to compute the phase rotations [17]

$$ \mathfrak{R}_{ij}^{(r)} = \delta_{ij} + \left(\delta_{ik} - \frac{1}{2}\Delta\omega_{ik}^{(r)}\right)^{-1} \Delta\omega_{kj}^{(r)} \tag{77} $$

Remark 3: For homogeneous materials the integration scheme [17] uncouples the material and rotational responses. In the present formulation phase rotations in each phase, $\mathfrak{R}_{ij}^{(r)}$, depend on phase eigenstrains, which are unknown prior to stress integration, and thus material and rotational responses are fully coupled and have to be updated simultaneously.

A5: Constant phase volume fractions

For the *2*-point scheme derived in Section 3 we will assume that phase volume fractions remain constant throughout the analysis. This is apparently true in the case of elastic fibers undergoing small strains and incompressible matrix material. In addition, we assume that the elastic properties of the phases are independent of temperature. Based on the first-order approximation methods, such as the Mori-Tanaka method [25] and Self Consistent method [15], the strain concentration factors and eigenstrain influence functions can be assumed to be constants throughout the entire analysis. These assumptions will allow us to carry out the entire analysis without updating the configuration of the unit cells. For the *n*-point scheme model, described in Section 4, these restrictions will be removed.

3.1 Implicit Integration of Constitutive Equation

For the elastically deforming reinforcement the only source of eigenstrain rate is due to temperature effects, i.e., $\dot{\mu}_{ij}^{(f)} = {}_{\theta}\dot{\varepsilon}_{ij}^{(f)}$ where ${}_{\theta}\dot{\varepsilon}_{ij}^{(f)}$ is the thermal rate of deformation in reinforcement domain. The eigenstrain rate in the matrix phase is comprised of both the thermal, ${}_{\theta}\dot{\varepsilon}_{ij}^{(m)}$, and the plastic, ${}_{p}\dot{\varepsilon}_{ij}^{(m)}$, rate of deformation effects, such that $\dot{\mu}_{ij}^{(m)} = {}_{\theta}\dot{\varepsilon}_{ij}^{(m)} + {}_{p}\dot{\varepsilon}_{ij}^{(m)}$. The phase thermal rate of deformation can be expressed as

$$ {}_{\theta}\dot{\varepsilon}_{ij}^{(r)} = \xi_{ij}^{(r)}\dot{\theta} \tag{78} $$

where θ denotes the temperature and $\xi_{ij}^{(r)}$ are components of the phase thermal expansion tensor.

Combining the rate form of (50), (68), (69), (75) and Assumptions 3 and 4 it can be shown that the following relations for the phase stresses hold:

$$ {}^{t+\Delta t}\sigma_{ij}^{(r)} = {}^{t}\hat{\sigma}_{ij}^{(r)} + R_{ijkl}^{(r)}\Delta\bar{\varepsilon}_{kl} - \sum_{s=m}^{f} Q_{ijkl}^{(rs)}\Delta\mu_{kl}^{(s)}, \quad r = m, f \tag{79} $$

where $\Delta\mu_{kl}^{(s)}$ is the overall phase eigenstrain increment to be defined later in this section and

$$ \left.\begin{aligned} R_{ijkl}^{(r)} &= L_{ijpq}^{(r)}(I_{pqkl} + G_{pqkl}^{(r)}) \\ Q_{ijkl}^{(rs)} &= L_{ijpq}^{(r)}(\delta_{rs}I_{pqkl} - D_{pqkl}^{(rs)}) \end{aligned}\right\} \quad r, s = m, f \tag{80} $$

Consider the yield function of the following form:

$$ \Phi^{(m)}(\sigma_{ij}^{(m)} - \alpha_{ij}^{(m)}, Y^{(m)}) = \frac{1}{2}(\sigma_{ij}^{(m)} - \alpha_{ij}^{(m)})P_{ijkl}(\sigma_{kl}^{(m)} - \alpha_{kl}^{(m)}) - \frac{1}{3}\{Y^{(m)}\}^2 \tag{81} $$

where $Y^{(m)}$ is the yield stress of the matrix phase in a uniaxial test, which evolves according to the hardening laws assumed; $\alpha_{ij}^{(m)}$ corresponds to the center of the yield surface in the deviatoric stress space, or simply the back stress. Evolution of the back stress is assumed to follow the kinematic hardening rule. For von Mises plasticity, P_{ijkl} is a projection operator which transforms an arbitrary second order tensor to the deviatoric space:

$$ P_{ijkl} = I_{ijkl} - \frac{1}{3}\delta_{ij}\delta_{kl} \tag{82} $$

For simplicity we assume that the plastic rate of deformation in the matrix phase follows the associative flow rule:

$$ {}_p\dot{\varepsilon}_{ij}^{(m)} = \frac{\partial \Phi}{\partial \sigma_{ij}^{(m)}} \dot{\lambda}^{(m)} = \aleph_{ij}^{(m)} \dot{\lambda}^{(m)}, \qquad \aleph_{ij}^{(m)} = P_{ijkl}(\sigma_{kl}^{(m)} - \alpha_{kl}^{(m)}) \tag{83} $$

We adopt a modified version of the hardening evolution law [16] in the context of isotropic, homogeneous, elasto-plastic matrix phase. A scalar material dependent parameter β $(0 \le \beta \le 1)$ is used as a measure of the proportion of isotropic and kinematic hardening and $\lambda^{(m)}$ is a plastic parameter to be determined by the consistency condition (81). Accordingly, the evolution of the yield stress $Y^{(m)}$ and the back stress $\alpha_{ij}^{(m)}$ can be expressed as follows:

$$ \dot{Y}^{(m)} = \frac{2\beta h}{3} Y^{(m)} \dot{\lambda}^{(m)} \tag{84} $$

$$ \mathring{\alpha}_{ij}^{(m)} = \frac{2(1-\beta)h}{3} P_{ijkl}(\sigma_{kl}^{(m)} - \alpha_{kl}^{(m)}) \dot{\lambda}^{(m)} \tag{85} $$

where $\beta = 0$ corresponds to a pure isotropic hardening; $\beta = 1$ is the widely used Ziegler-Prager kinematic hardening rule [36] for metals; h is a hardening parameter defined as the ratio between effective stress rate and the effective plastic strain rate.

Integration of (83), (84) and (85) is carried out using the backward Euler scheme:

$$ {}^{t+\Delta t}_{p}\varepsilon_{ij}^{(m)} = {}^{t}_{p}\varepsilon_{ij}^{(m)} + {}^{t+\Delta t}\aleph_{ij}^{(m)} \Delta\lambda^{(m)} \tag{86} $$

$$ {}^{t+\Delta t}Y^{(m)} = {}^{t}Y^{(m)} + \frac{2\beta h}{3} {}^{t+\Delta t}Y^{(m)} \Delta\lambda^{(m)} \tag{87} $$

$$ {}^{t+\Delta t}\alpha_{ij}^{(m)} = {}^{t}\hat{\alpha}_{ij}^{(m)} + \frac{2(1-\beta)h}{3} P_{ijkl}({}^{t+\Delta t}\sigma_{kl}^{(m)} - {}^{t+\Delta t}\alpha_{kl}^{(m)}) \Delta\lambda^{(m)} \tag{88} $$

where $\Delta\lambda^{(m)} \equiv {}^{t+\Delta t}\lambda^{(m)} - {}^{t}\lambda^{(m)}$, and ${}^{t}\hat{\alpha}_{ij}^{(m)}$ is the rotated back stress defined in (76). The phase rotation increment follows from (50), (78) and (83):

$$ \Delta\omega_{ij}^{(r)} = \Delta\bar{\omega}_{ij} + \hat{G}_{ijkl}^{(r)} \Delta\bar{\varepsilon}_{kl} + \hat{D}_{ijkl}^{(rm)} P_{klmn}(\sigma_{mn}^{(m)} - \alpha_{mn}^{(m)}) \Delta\lambda^{(m)} + \sum_{s=m}^{f} \hat{D}_{ijkl}^{(rs)} \xi_{kl}^{(s)} \Delta\theta \tag{89} $$

In the following we omit the left superscript for the current step $t + \Delta t$. Using the backward Euler scheme for the rate form of $\sigma_{ij}^{(m)}$ in (79) and (86) yields the following relation for the Cauchy stress in the matrix domain:

$$ \sigma_{ij}^{(m)} = {}_{tr}\sigma_{ij}^{(m)} - Q_{ijkl}^{(mm)} \aleph_{kl}^{(m)} \Delta\lambda^{(m)} \tag{90} $$

where ${}_{tr}\sigma_{ij}^{(m)}$ is a trial Cauchy stress in the matrix phase defined as

$$ {}_{tr}\sigma_{ij}^{(m)} \equiv {}^{t}\hat{\sigma}_{ij}^{(m)} + R_{ijkl}^{(m)}\Delta\bar{\varepsilon}_{kl} - \sum_{s=m}^{f} Q_{ijkl}^{(ms)}\xi_{kl}^{(s)}\Delta\theta \tag{91} $$

The process is termed elastic if:

$$ ({}_{tr}\sigma_{ij}^{(m)} - \alpha_{ij}^{(m)})P_{ijkl}({}_{tr}\sigma_{kl}^{(m)} - \alpha_{kl}^{(m)}) - \frac{2}{3}\{Y^{(m)}\}^2\Big|_{\Delta\lambda^{(m)}=0} < 0 \tag{92} $$

Otherwise the process is plastic, which is the focus of our subsequent derivation.

Subtracting (88) from (90) we arrive at the following result:

$$ \sigma_{ij}^{(m)} - \alpha_{ij}^{(m)} = (I_{ijkl} + \Delta\lambda^{(m)}\wp_{ijkl})^{-1}({}_{tr}\sigma_{kl}^{(m)} - {}^{t}\hat{\alpha}_{kl}^{(m)}) \tag{93} $$

where

$$ \wp_{ijkl} = Q_{ijst}^{(mm)}P_{stkl} + \frac{2}{3}(1-\beta)hP_{ijkl} \tag{94} $$

The value of $\Delta\lambda^{(m)}$ is obtained by satisfying the consistency condition which assures that the stress state in the plastic process lies on the yield surface at the end of the current load step. To this end, equations (87) and (93) are substituted into the yield condition (81), $\Phi^{(m)}(\sigma_{ij}^{(m)} - \alpha_{ij}^{(m)}, Y^{(m)}) = 0$, which produces a nonlinear equation for $\Delta\lambda^{(m)}$. A standard Newton's method is applied to solve for $\Delta\lambda^{(m)}$:

$$ \Delta\lambda_{k+1}^{(m)} = \Delta\lambda_{k}^{(m)} - \left\{\frac{\partial\Phi^{(m)}}{\partial\Delta\lambda^{(m)}}\right\}^{-1}\Phi^{(m)}\Big|_{\Delta\lambda_k^{(m)}} \tag{95} $$

where k is the iteration count. It can be shown that the derivative $\partial\Phi^{(m)}/\partial\Delta\lambda^{(m)}$ required in (95) has the following form:

$$ \frac{\partial\Phi^{(m)}}{\partial\Delta\lambda^{(m)}} = \aleph_{ij}^{(m)}C_{ijkl}^{(m)}(\sigma_{kl}^{(m)} - \alpha_{kl}^{(m)}) - \frac{4\beta h\{Y^{(m)}\}^2}{9 - 6\beta h\Delta\lambda^{(m)}} \tag{96} $$

The expression for $C_{ijkl}^{(m)}$ is derived in Appendix A. The converged value of $\Delta\lambda^{(m)}$ is then used to compute the phase stresses. The overall stress is computed from (61).

3.2 Consistent Linearization

While integration of the constitutive equations affects the accuracy of the solution, the formation of a tangent stiffness matrix consistent with the integration procedure is essential to maintain the quadratic rate of convergence if one is to adopt the Newton method for the solution of nonlinear system of equations on the macro level [31].

The starting point is the incremental form of the constitutive equations (79):

$$\sigma_{ij}^{(r)} = {}^{t}\hat{\sigma}_{ij}^{(r)} + R_{ijkl}^{(r)}\Delta\bar{\varepsilon}_{kl} - Q_{ijkl}^{(rm)}\aleph_{kl}^{(m)}\Delta\lambda^{(m)} - \sum_{s=m}^{f} Q_{ijkl}^{(rs)}\xi_{kl}^{(s)}\Delta\theta \tag{97}$$

Taking material time derivative of (88), (89) and (97) yields:

$$\dot{\alpha}_{ij}^{(m)} = \dot{\hat{\alpha}}_{ij}^{(m)} + \frac{2(1-\beta)h}{3}\{\aleph_{ij}^{(m)}\dot{\lambda}^{(m)} + P_{ijpq}(\dot{\sigma}_{pq}^{(m)} - \dot{\alpha}_{pq}^{(m)})\Delta\lambda^{(m)}\} \tag{98}$$

$$\begin{aligned}\Delta\dot{\omega}_{ij}^{(r)} = {} & \Delta\dot{\bar{\omega}}_{ij} + \hat{G}_{ijkl}^{(r)}\Delta\dot{\bar{\varepsilon}}_{kl} + \hat{D}_{ijkl}^{(rm)}\{\aleph_{kl}^{(m)}\dot{\lambda}^{(m)} + P_{klpq}(\dot{\sigma}_{pq}^{(m)} - \dot{\alpha}_{pq}^{(m)})\Delta\lambda^{(m)}\} \\ & + \sum_{s=m}^{f}\hat{D}_{ijkl}^{(rs)}\xi_{kl}^{(s)}\dot{\theta}\end{aligned} \tag{99}$$

$$\begin{aligned}\dot{\sigma}_{ij}^{(r)} = {} & {}^{t}\dot{\hat{\sigma}}_{ij}^{(r)} + R_{ijkl}^{(r)}\Delta\dot{\bar{\varepsilon}}_{kl} - Q_{ijkl}^{(rm)}\{\aleph_{kl}^{(m)}\dot{\lambda}^{(m)} + P_{klpq}(\dot{\sigma}_{pq}^{(m)} - \dot{\alpha}_{pq}^{(m)})\Delta\lambda^{(m)}\} \\ & - \sum_{s=m}^{f} Q_{ijkl}^{(rs)}\xi_{kl}^{(s)}\dot{\theta}\end{aligned} \tag{100}$$

Subtracting (98) from (100) for $r = m$ yields:

$$\begin{aligned}\dot{\sigma}_{ij}^{(m)} - \dot{\alpha}_{ij}^{(m)} = {} & {}^{t}\dot{\hat{\sigma}}_{ij}^{(m)} - {}^{t}\dot{\hat{\alpha}}_{ij}^{(m)} + R_{ijkl}^{(m)}\Delta\dot{\bar{\varepsilon}}_{kl} - \sum_{s=m}^{f} Q_{ijkl}^{(ms)}\xi_{kl}^{(s)}\dot{\theta} \\ & - \wp_{ijkl}\{(\sigma_{kl}^{(m)} - \alpha_{kl}^{(m)})\dot{\lambda}^{(m)} + (\dot{\sigma}_{kl}^{(m)} - \dot{\alpha}_{kl}^{(m)})\Delta\lambda^{(m)}\}\end{aligned} \tag{101}$$

where

$${}^{t}\dot{\hat{\sigma}}_{ij}^{(m)} - {}^{t}\dot{\hat{\alpha}}_{ij}^{(m)} = \frac{\partial(\hat{\sigma}_{ij}^{(m)} - \hat{\alpha}_{ij}^{(m)})}{\partial\Delta\omega_{kl}^{(m)}}\Delta\dot{\omega}_{kl}^{(m)} \tag{102}$$

Combining (99), (101), (102), (210), (211) with the consistent linearizations of $\Delta\dot{\bar{\varepsilon}}_{kl}$ and $\Delta\dot{\bar{\omega}}_{kl}$ (given in Appendix B) yields:

$$\dot{\sigma}_{ij}^{(m)} - \dot{\alpha}_{ij}^{(m)} = (I_{ijkl} + \Delta\lambda^{(m)}W_{ijkl}^{(m)})^{-1}({}_{\nu}S_{klst}v_{s,x_t}^{0} + {}_{\theta}S_{kl}\dot{\theta} + {}_{\lambda}S_{kl}\dot{\lambda}^{(m)}) \tag{103}$$

where

$${}_{\nu}S_{klst} = ({}_{\sigma}U_{klmn}^{(m)} - {}_{\alpha}U_{klmn}^{(m)})(M_{[mn]st} + \hat{G}_{mnuv}M_{(uv)st}) + R_{klmn}M_{(mn)st} \tag{104}$$

$${}_{\theta}S_{kl} = \sum_{s=m}^{f}\{({}_{\sigma}U_{klpq}^{(m)} - {}_{\alpha}U_{klpq}^{(m)})\hat{D}_{pqst}^{(ms)} - Q_{klst}^{(ms)}\}\xi_{st}^{(s)} \tag{105}$$

$$ {}_{\lambda}S_{kl} = -W^{(m)}_{klst}(\sigma^{(m)}_{st}-\alpha^{(m)}_{st}) \tag{106} $$

and $W^{(m)}_{ijkl}$, ${}_{\sigma}U^{(m)}_{klmn}$ and ${}_{\alpha}U^{(m)}_{klmn}$ are defined in (215), (210) and (211), respectively. It remains to eliminate $\dot{\lambda}^{(m)}$ from (103), by utilizing the linearized form of the consistency condition (81) and equation (87) which gives

$$ \aleph^{(m)}_{ij}(\dot{\sigma}^{(m)}_{ij} - \dot{\alpha}^{(m)}_{ij}) - \frac{4\beta h\{Y^{(m)}\}^2\dot{\lambda}^{(m)}}{9-6\beta h\Delta\lambda^{(m)}} = 0 \tag{107} $$

Substituting (103) into (107) results in

$$ \dot{\lambda}^{(m)} = \Gamma^{(m)}_{kl}({}_{v}S_{klst}v^0_{s,\,x_t} + {}_{\theta}S_{kl}\dot{\theta}) \tag{108} $$

where

$$ \Gamma^{(m)}_{kl} = \frac{(9-6\beta h\Delta\lambda^{(m)})\,\aleph^{(m)}_{ij}(I_{ijkl}+\Delta\lambda^{(m)}W^{(m)}_{ijkl})^{-1}}{4\beta h\{Y^{(m)}\}^2-(9-6\beta h\Delta\lambda^{(m)})\,\aleph^{(m)}_{mn}(I_{mnst}+\Delta\lambda^{(m)}W^{(m)}_{mnst})^{-1}{}_{\lambda}S_{st}} \tag{109} $$

and thus (103) can be simplified as

$$ \dot{\sigma}^{(m)}_{ij} - \dot{\alpha}^{(m)}_{ij} = {}_{v}\underset{\sim}{S}_{ijkl}v^0_{k,\,x_l} + {}_{\theta}\underset{\sim}{S}_{ij}\dot{\theta} \tag{110} $$

where

$$ {}_{v}\underset{\sim}{S}_{ijkl} = (I_{ijmn}+\Delta\lambda^{(m)}W_{ijmn})^{-1}({}_{v}S_{mnkl} + {}_{\lambda}S_{mn}\Gamma^{(m)}_{pq}\,{}_{v}S_{pqkl}) \tag{111} $$

$$ {}_{\theta}\underset{\sim}{S}_{ij} = (I_{ijmn}+\Delta\lambda^{(m)}W_{ijmn})^{-1}({}_{\theta}S_{mn} + {}_{\lambda}S_{mn}\Gamma^{(m)}_{pq}\,{}_{\theta}S_{pq}) \tag{112} $$

Finally, by substituting (108), (110), (210) and (226) into (100), we get a closed form expression relating the phase Cauchy stress rate $\dot{\sigma}^{(r)}_{ij}$ with the macroscopic velocity gradient $v^0_{k,\,x_l}$ and the temperature rate $\dot{\theta}$

$$ \dot{\sigma}^{(r)}_{ij} = D^{(r)}_{ijkl}v^0_{k,\,x_l} + d^{(r)}_{ij}\dot{\theta} \tag{113} $$

where

$$ \begin{aligned} D^{(r)}_{ijkl} &= R^{(r)}_{ijmn}M_{(mn)kl} + {}_{\sigma}U^{(r)}_{ijpq}(M_{[pq]kl} + \hat{G}^{(r)}_{pqmn}M_{(mn)kl}) \\ &\quad + ({}_{\sigma}U^{(r)}_{ijpq}\hat{D}_{pqmn} - Q^{(rm)}_{ijmn})(\aleph^{(m)}_{mn}\Gamma^{(m)}_{uv}\,{}_{v}S_{uvkl} + \Delta\lambda^{(m)}P_{mnpq}\,{}_{v}\underset{\sim}{S}_{pqkl}) \end{aligned} \tag{114} $$

and

$$d_{ij}^{(r)} = \sum_{s=m}^{f} ({}_{\sigma}U_{ijpq}^{(r)}\hat{D}_{pqkl}^{(rs)} - Q_{ijkl}^{(rs)})\xi_{kl}^{(s)}$$
$$+ ({}_{\sigma}U_{ijpq}^{(r)}\hat{D}_{pqmn} - Q_{ijmn}^{(rm)})(\aleph_{mn}^{(m)}\Gamma_{pq}^{(m)}{}_{\theta}S_{pq} + \Delta\lambda^{(m)}P_{mnpq\ \theta}S_{pq}) \tag{115}$$

The overall consistent instantaneous stiffness D_{ijkl} is obtained from the rate form of (61) and Assumption A5:

$$\dot{\bar{\sigma}}_{ij} = D_{ijkl}v_{k,x_l}^{0} + d_{ij}\dot{\theta} \tag{116}$$

where

$$D_{ijkl} = c^{(m)}D_{ijkl}^{(m)} + c^{(f)}D_{ijkl}^{(f)}, \qquad d_{ij} = c^{(m)}d_{ij}^{(m)} + c^{(f)}d_{ij}^{(f)} \tag{117}$$

The overall consistent tangent operator is derived from the consistent linearization of the weak form of the macroscopic equilibrium equation (57). Consider the internal force vector expressed in terms of the quantities defined in the deformed configuration

$$f_A^{int} = \int_{\Omega} N_{iA,x_j}\bar{\sigma}_{ij}\, d\Omega \tag{118}$$

where N_{iA} is a set of shape functions in the macroscale.

Prior to linearization, the internal force vector is defined in the reference configuration ${}^{t}\Omega$ as

$$f_A^{int} = \int_{{}^{t}\Omega} N_{iA,{}^{t}x_m}F_{mj}^{-1}\bar{\sigma}_{ij}J_x\, d^{t}\Omega \tag{119}$$

where J_x is the jacobian between the macro-configurations at times t and $t+\Delta t$; F_{jm} is the macroscopic deformation gradient defined as

$$F_{jm} = x_{j,{}^{t}x_m} \equiv {}^{t+\Delta t}x_{j,{}^{t}x_m} \qquad \text{and} \qquad F_{mj}^{-1} = {}^{t}x_{m,x_j} \equiv {}^{t}x_{m,{}^{t+\Delta t}x_j} \tag{120}$$

Linearization of (119) yields

$$\frac{d}{dt}f_A^{int} = \int_{{}^{t}\Omega} N_{iA,{}^{t}x_m}\{\dot{F}_{mj}^{-1}\bar{\sigma}_{ij}J_x + F_{mj}^{-1}\dot{\bar{\sigma}}_{ij}J_x + F_{mj}^{-1}\bar{\sigma}_{ij}\dot{J}_x\}d^{t}\Omega \tag{121}$$

Substituting (116) into (121) and exploiting the kinematical relations $\dot{J}_x = J_x v_{k,x_k}^{0}$, $\dot{F}_{mj}^{-1} = -F_{ml}^{-1}v_{l,x_j}^{0}$ and the finite element discretization $v_{k,x_l}^{0} = N_{kB,x_l}\dot{q}_B$ yields:

$$\frac{d}{dt}f_A^{int} = \int_\Omega N_{iA,x_j}\bar{D}_{ijkl}N_{kB,x_l}\,d\Omega\,\dot{q}_B + \int_\Omega N_{iA,x_j}d_{ij}\,d\Omega\,\dot{\theta} \tag{122}$$

$$\bar{D}_{ijkl} = D_{ijkl} + \delta_{kl}\bar{\sigma}_{ij} - \delta_{kj}\bar{\sigma}_{il} \tag{123}$$

where D_{ijkl} and d_{ij} are defined in (117); $\dot{q}_B$ denotes the velocity degree of freedoms associated with the finite element mesh. The first integral in (122) represents the consistent tangent stiffness matrix for the macro-problem.

Remark 4: For the purpose of linearization it is convenient to approximate phase rotations within a unit cell by a constant field such that $\dot{\omega}_{ij}^{(r)} \approx \dot{\bar{\omega}}_{ij}$. The resulting rotated stress and back stress rates are given as

$$\dot{\hat{\sigma}}_{ij}^{(r)} = \Delta\dot{\bar{\omega}}_{ik}\sigma_{kj}^{(r)} - \sigma_{ik}^{(r)}\Delta\dot{\bar{\omega}}_{kj}, \qquad \dot{\hat{\alpha}}_{ij}^{(m)} = \Delta\dot{\bar{\omega}}_{ik}\alpha_{kj}^{(m)} - \alpha_{ik}^{(m)}\Delta\dot{\bar{\omega}}_{kj} \tag{124}$$

Therefore, (104) to (106) can be simplified as

$${}_vS_{ijkl} = R_{ijmn}M_{(mn)kl} - \{\delta_{in}(\sigma_{mj}^{(m)} - \alpha_{mj}^{(m)}) + \delta_{jn}(\sigma_{im}^{(m)} - \alpha_{im}^{(m)})\}M_{[mn]kl} \tag{125}$$

$${}_\theta S_{ij} = -\sum_{s=m}^{f} Q_{ijkl}^{(ms)}\xi_{kl}^{(s)}, \qquad {}_\lambda S_{ij} = -\wp_{ijkl}(\sigma_{kl}^{(m)} - \alpha_{kl}^{(m)}) \tag{126}$$

and $W_{ijkl}^{(m)} = \wp_{ijkl}$ in (103), (109), (111) and (112). $D_{ijkl}^{(r)}$ and $d_{ij}^{(r)}$ in (114) and (115) are written as

$$\begin{aligned} D_{ijkl}^{(r)} = {} & R_{ijmn}^{(r)}M_{(mn)kl} - (\delta_{in}\sigma_{mj}^{(r)} + \delta_{jn}\sigma_{im}^{(r)})M_{[mn]kl} \\ & - Q_{ijmn}^{(rm)}(\aleph_{mn}^{(m)}\Gamma_{uv}^{(m)}{}_vS_{uvkl} + \Delta\lambda^{(m)}P_{mnpq}\,{}_v\underset{\sim}{S}_{pqkl}) \end{aligned} \tag{127}$$

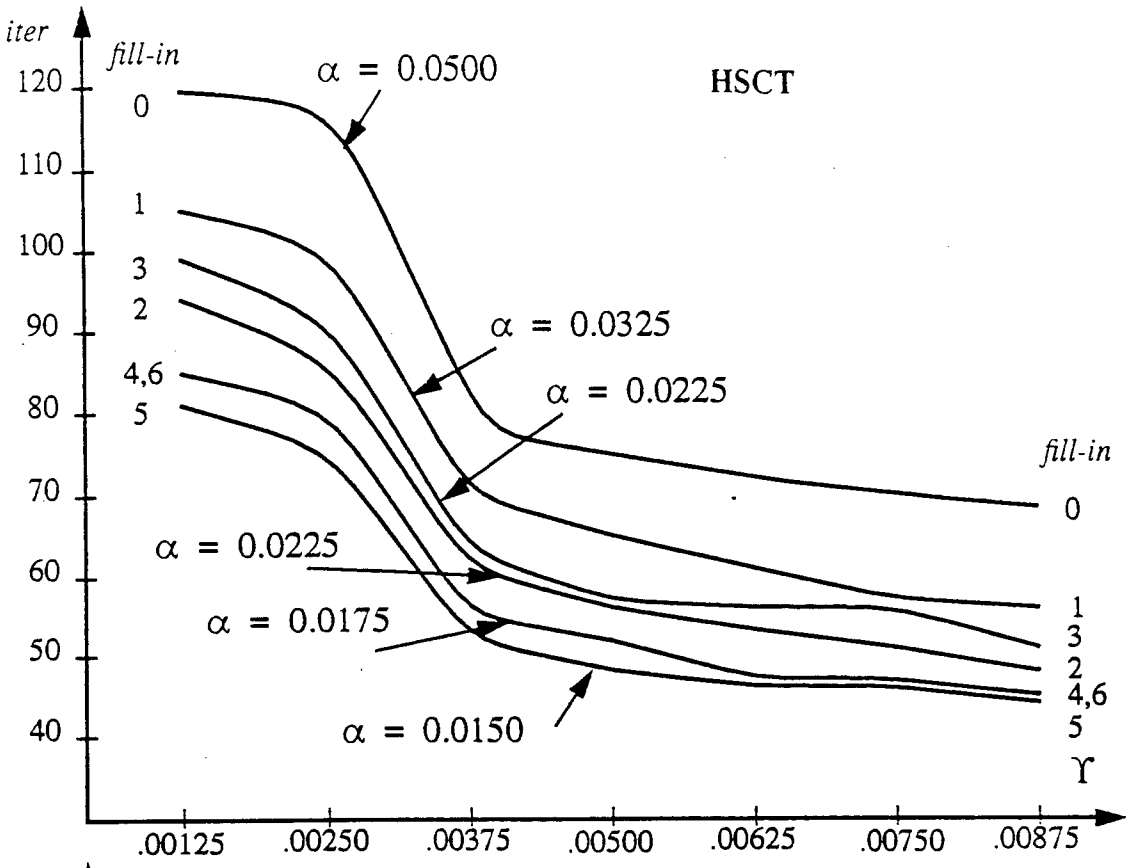
and

$$d_{ij}^{(r)} = -Q_{ijmn}^{(rm)}(\aleph_{mn}^{(m)}\Gamma_{pq}^{(m)}{}_\theta S_{pq} + \Delta\lambda^{(m)}P_{mnpq}\,{}_\theta\underset{\sim}{S}_{pq}) - \sum_{s=m}^{f} Q_{ijkl}^{(rs)}\xi_{kl}^{(s)} \tag{128}$$

4.0 *n*-Point Scheme for Finite Deformation Plasticity

In this section we consider a unit cell model discretized with n elements. The n-point scheme model assumes that eigenstrains are piecewise constant, i.e., they are constant within each element, but may vary from element to element. Our starting point (Section 4.1) is a rate form of the governing equations representing the finite deformation plasticity of periodic heterogeneous media. Implicit integration of constitutive equations followed by consistent linearization are presented in Sections 4.2 and 4.3.

FIGURE 3


iter
fill-in
120
110
100
90
80
70
60
50
40
0
1
3
2
4,6
5
α = 0.0500
α = 0.0325
α = 0.0225
α = 0.0225
α = 0.0175
α = 0.0150
HSCT
fill-in
0
1
3
2
4,6
5
ϒ
.00125
.00250
.00375
.00500
.00625
.00750
.00875

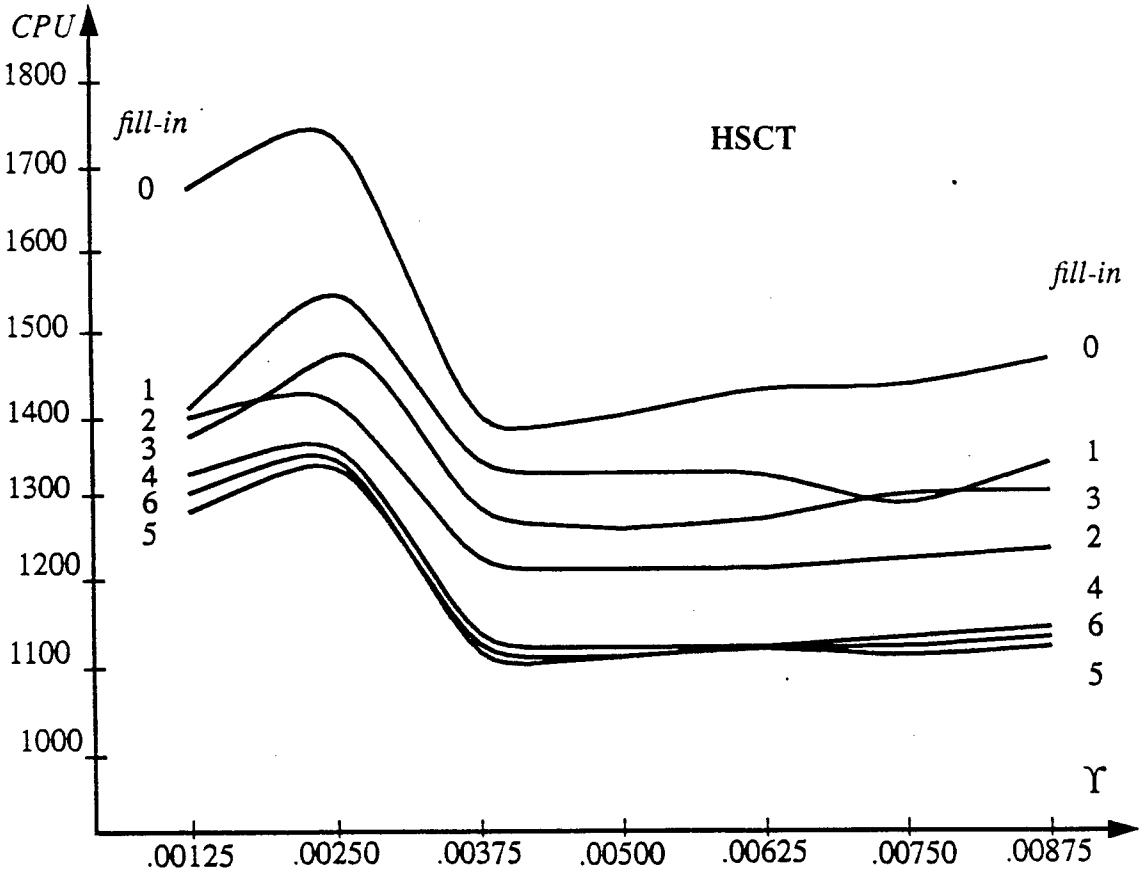
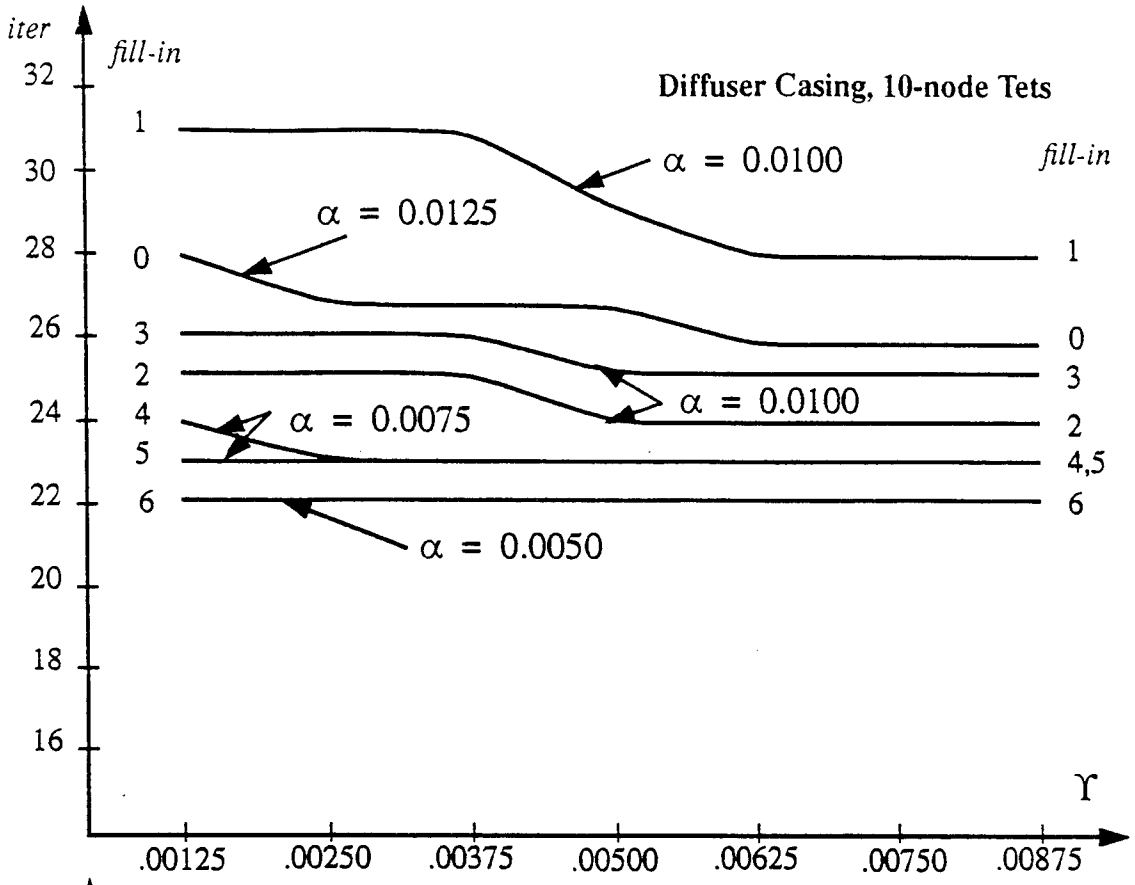

CPU
1800
1700
1600
1500
1400
1300
1200
1100
1000
fill-in
0
1
2
3
4
6
5
HSCT
fill-in
0
1
3
2
4
6
5
ϒ
.00125
.00250
.00375
.00500
.00625
.00750
.00875

FIGURE 4


iter
fill-in
Diffuser Casing, 10-node Tets
32
30
28
26
24
22
20
18
16
1
0
3
2
4
5
6
α = 0.0100
α = 0.0125
α = 0.0100
α = 0.0075
α = 0.0050
fill-in
1
0
3
2
4,5
6
Υ
.00125
.00250
.00375
.00500
.00625
.00750
.00875

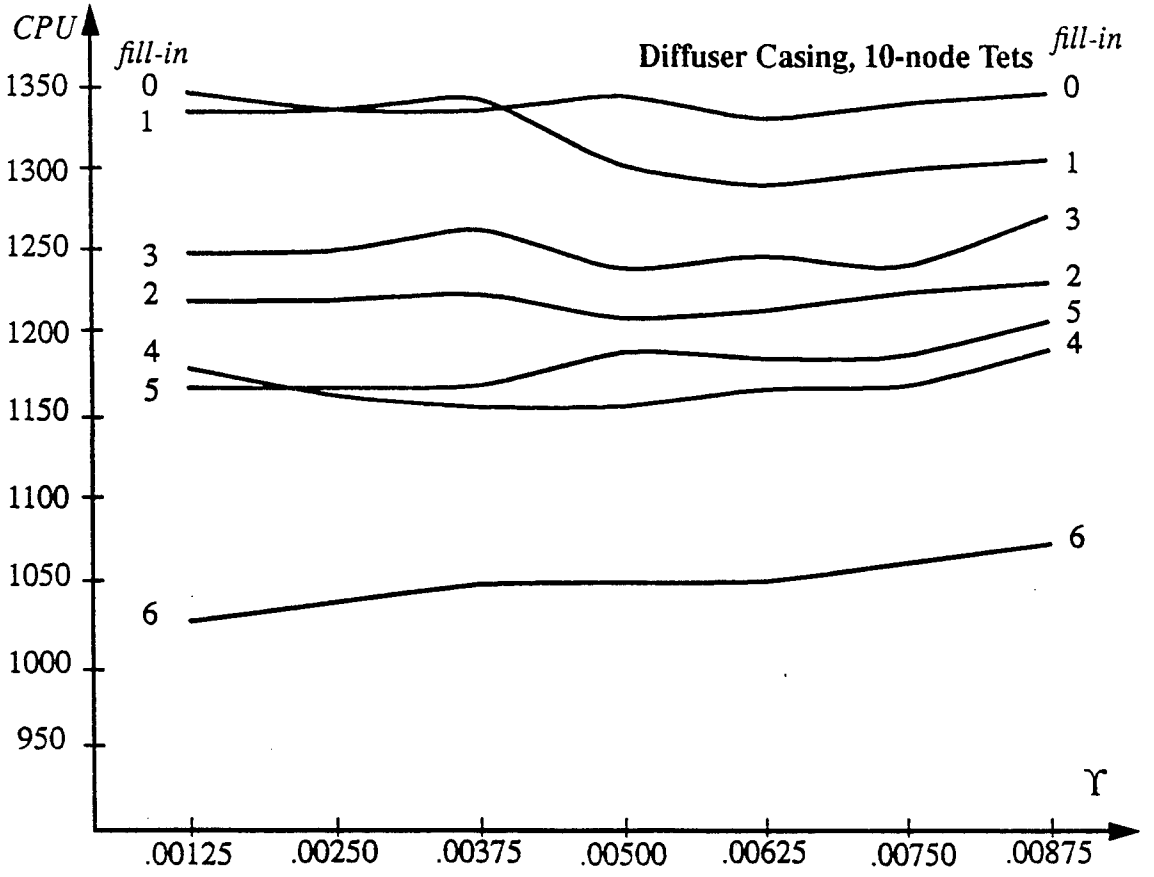
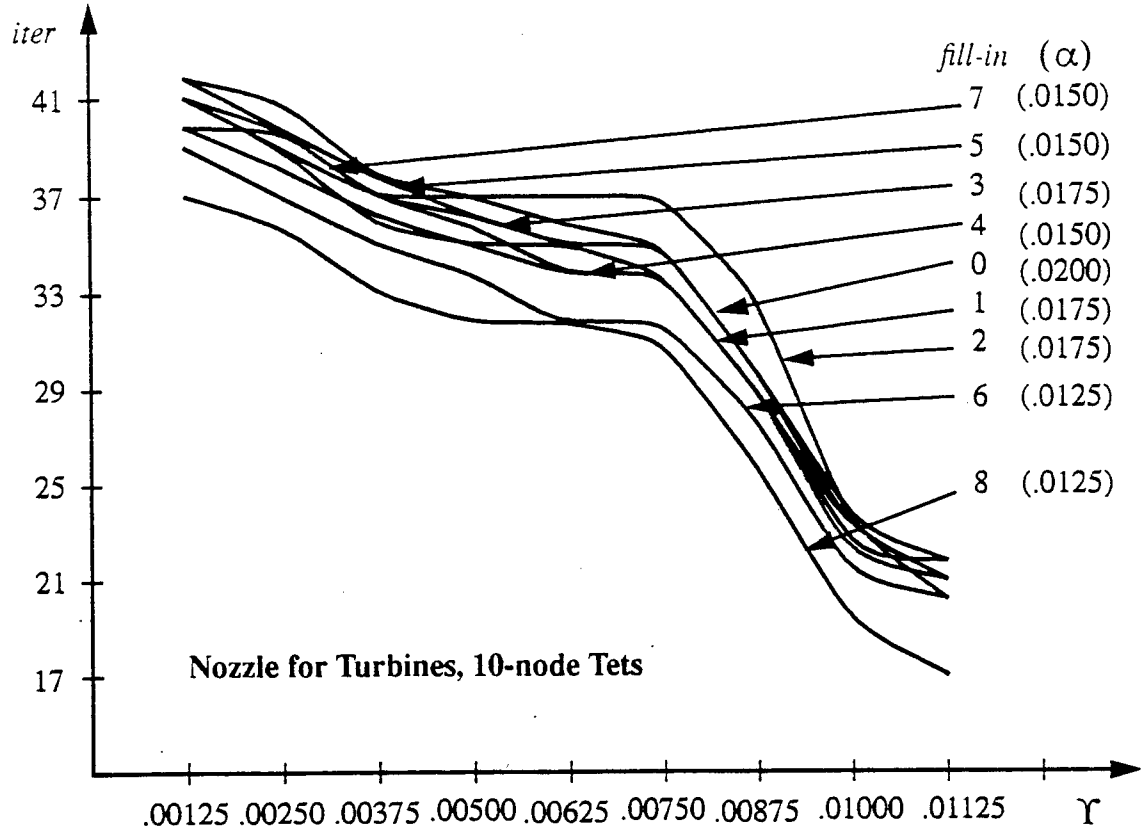

CPU
fill-in
Diffuser Casing, 10-node Tets
fill-in
1350
1300
1250
1200
1150
1100
1050
1000
950
0
1
3
2
4
5
6
0
1
3
2
5
4
6
Υ
.00125
.00250
.00375
.00500
.00625
.00750
.00875

FIGURE 5


iter
41
37
33
29
25
21
17
fill-in (α)
7 (.0150)
5 (.0150)
3 (.0175)
4 (.0150)
0 (.0200)
1 (.0175)
2 (.0175)
6 (.0125)
8 (.0125)
Nozzle for Turbines, 10-node Tets
.00125 .00250 .00375 .00500 .00625 .00750 .00875 .01000 .01125 ϒ

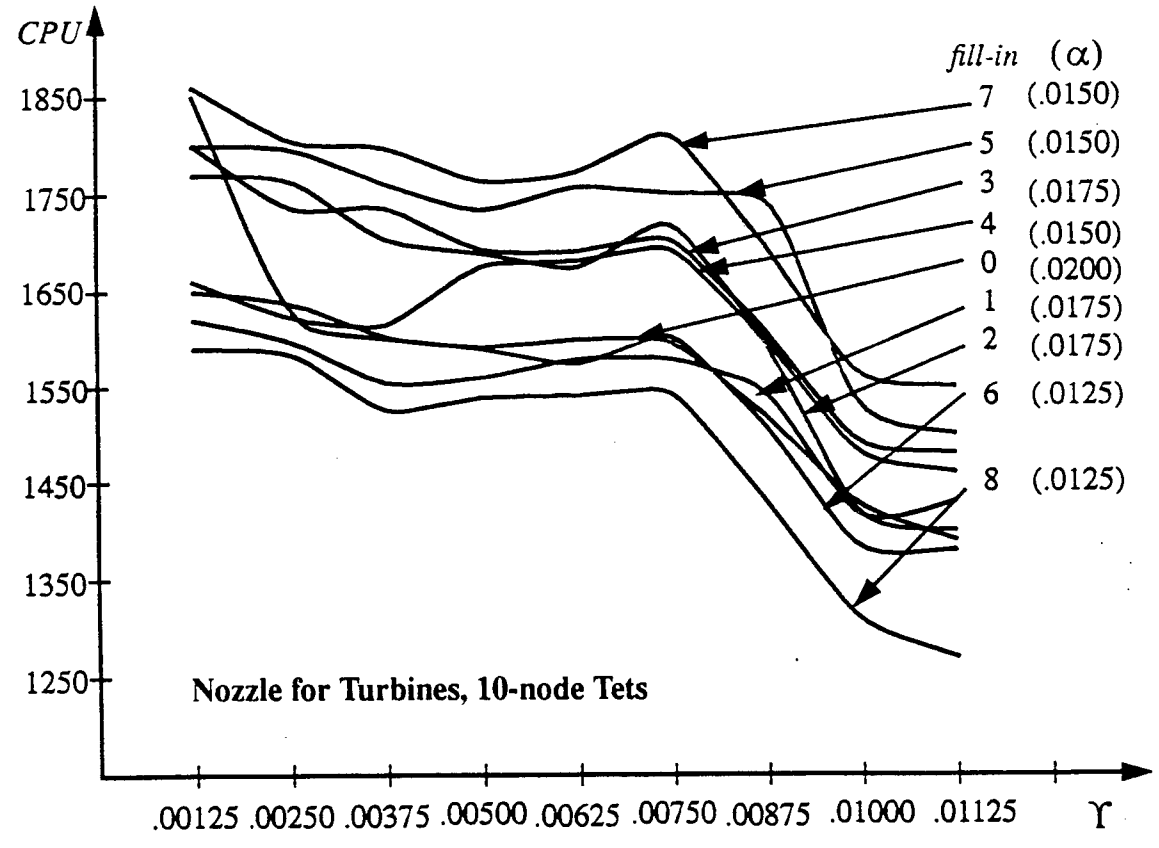
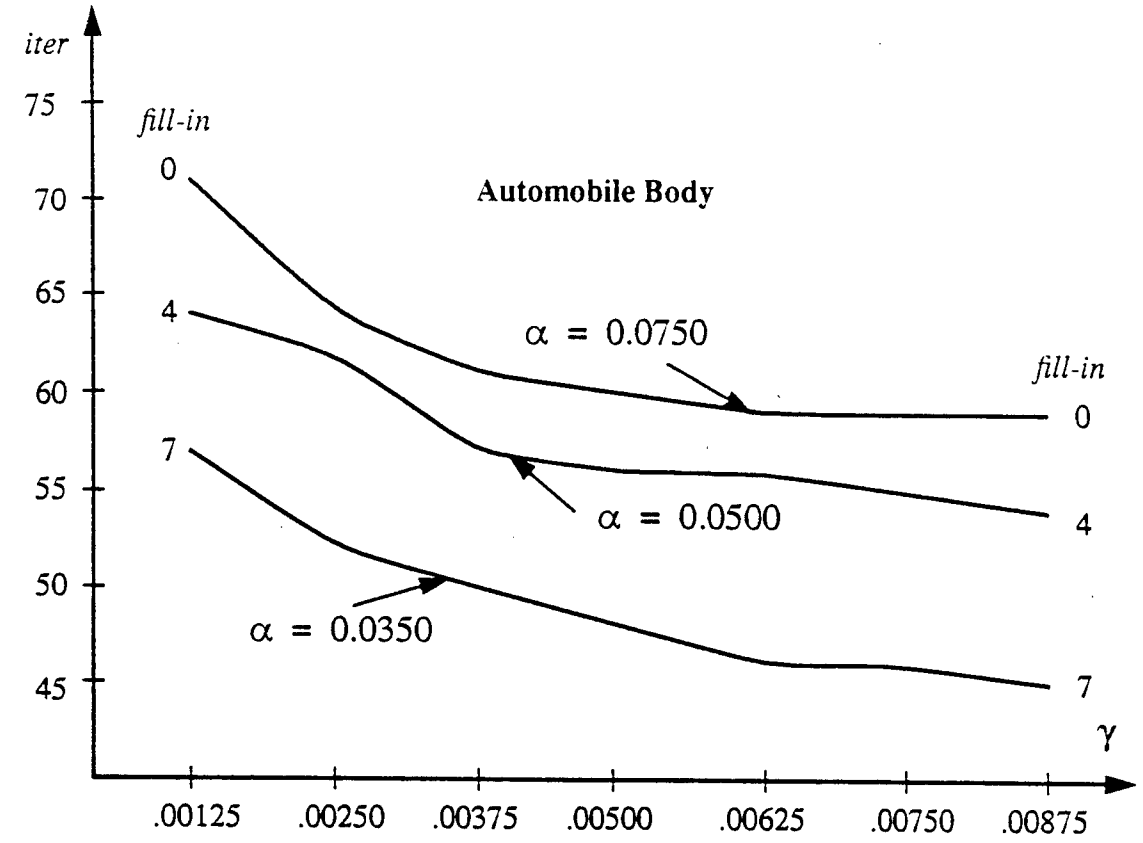
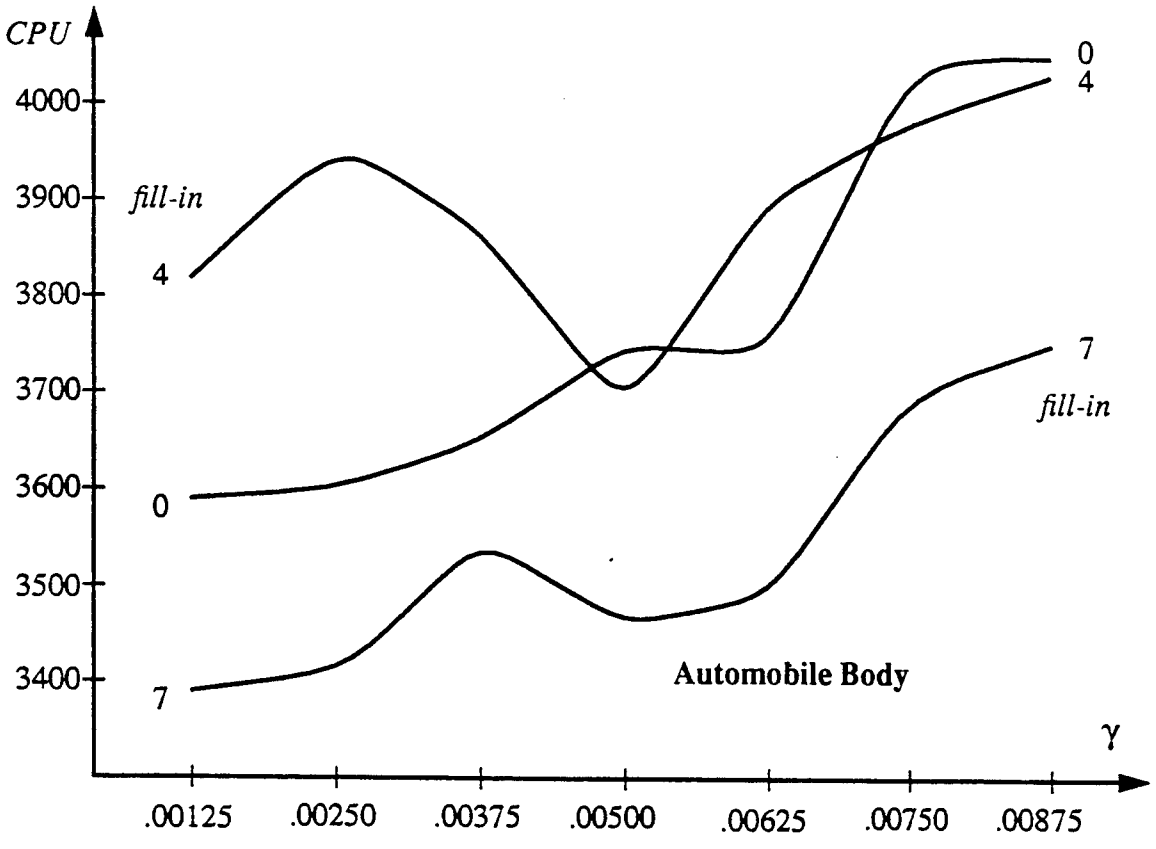

CPU
1850
1750
1650
1550
1450
1350
1250
fill-in (α)
7 (.0150)
5 (.0150)
3 (.0175)
4 (.0150)
0 (.0200)
1 (.0175)
2 (.0175)
6 (.0125)
8 (.0125)
Nozzle for Turbines, 10-node Tets
.00125 .00250 .00375 .00500 .00625 .00750 .00875 .01000 .01125 ϒ

FIGURE 6


iter
75
70
65
60
55
50
45
fill-in
0
4
7
Automobile Body
α = 0.0750
α = 0.0500
α = 0.0350
fill-in
0
4
7
γ
.00125
.00250
.00375
.00500
.00625
.00750
.00875


CPU
4000
3900
3800
3700
3600
3500
3400
fill-in
4
0
7
0
4
7
fill-in
Automobile Body
γ
.00125
.00250
.00375
.00500
.00625
.00750
.00875

INTERNATIONAL JOURNAL FOR NUMERICAL METHODS IN ENGINEERING, VOL. 39, 3641–3662 (1996)

THE *s*-VERSION OF FINITE ELEMENT METHOD FOR LAMINATED COMPOSITES

JACOB FISH AND RAVI GUTTAL

Department of Civil Engineering and Scientific Computation Research Center, Rensselaer Polytechnic Institute, Troy, NY 12180, U.S.A.

SUMMARY

The *s*-version of the finite element method is developed for laminated plates and shells. By this technique the global domain is idealized using 2-D Equivalent Single Layer model. The regions where ESL model errs badly in capturing localized phenomena are superimposed by a stack of 3-D elements. Assumed strain formulation and selective polynomial order escalation in the two models, as well as fast iterative procedures, are employed to maintain a high level of computational efficiency.

KEY WORDS: mesh superposition; laminated composites; shell finite elements

1. INTRODUCTION

Laminated composites present to the analyst a hard nut to crack due to inadequacy of Equivalent Single Layer (ESL) theories in resolving 3-D phenomena on one hand and computational complexity of layer-wise or 3-D models on the other hand. A natural remedy is a global-local approach in which different regions of the problem domain are described with different types of models. We refer to Reference 1 for a comprehensive review of global-local techniques for composite laminates and to References 2 and 3 for various aspects of reliability, convergence and accuracy of global-local techniques.

Here we focus only on the class of global-local techniques that advocates hierarchical solution strategy in the sense that information from the analysis of an ESL model is exploited in resolution of local effects using Discrete Layer (DL) mesh. Among the most popular hierarchical global-local strategies are various forms of multigrid and composite grid methods,[4–9] as well as methods based on hierarchical decomposition of approximation space.[1,10–16] Recently the composite grid method originated for displacement-based linear systems has been extended to hybrid systems.[17] Engineering global-local approaches which approximate a detailed response by means of post processing techniques, such as subjecting a refined discrete layer model to the boundary conditions extracted from the global ESL model, can be viewed as a single iteration within the composite grid procedure. For various improvements of this simple 'zoom' technique we refer to References 18–20.

The present paper is an extension of our previous work on the *s*-version of the finite element method in 2-D[10–13] to laminated plates and shells. In this paper we emphasize the utility of the mesh superposition technique to:

(a) Identify the location of the critical regions where DL model is needed using Dimensional Reduction Error (DRE) indicators.

CCC 0029–5981/96/213641–22
© 1996 by John Wiley & Sons, Ltd.
Received 19 September 1995
Revised 2 April 1996

(b) Accurately and efficiently predict both local and global effects using assumed strain formulation, selective polynomial order escalation and dedicated iterative solution procedures for hierarchical systems.

The outline of the paper is as follows: In Section 2 the *s*-method is introduced in the context of laminated plates and shells. Assumed strain formulation and a novel quadrature scheme are briefly discussed in Section 3. Dimensional Reduction Error indicators and quality control techniques are described in Section 4. A brief discussion on the feasibility of iterative and direct solvers for the *s*-method is presented in Section 5. Numerical examples conclude the manuscript.

2. MESH SUPERPOSITION FOR LAMINATED COMPOSITES

Consider a heterogeneous medium on domain Ω with boundary Γ as shown in Figure 1. The boundary Γ is decomposed as $\Gamma = \Gamma_u \cup \Gamma_t$, where Γ_u is the boundary with prescribed displacements and Γ_t with prescribed traction. The critical region to be superimposed by a local mesh is denoted by Ω^L, $\Omega^L \subset \Omega$. Domains Ω and Ω^L are subdivided independently into element domains such that $\bigcup \Omega_e^G = \Omega$ and $\bigcup \Omega_e^L = \Omega^L$. Let Γ^{GL} be the boundary between the two meshes such that $\Gamma \cap \Gamma^{GL} = \emptyset$. Let $\mathbf{u}^G$ be the global displacement field defined on Ω and $\mathbf{u}^L$ be the local displacement field defined on the local region Ω^L. The total displacement field is constructed by superposition:

$$\mathbf{u} = \mathbf{u}^G + \mathbf{u}^L \tag{1}$$

In the case of laminated plates and shells, the global displacement field $\mathbf{u}^G$ is represented by the Equivalent Single Layer (ESL) model. The ESL model on Ω^G is discretized using a hierarchic degenerated plate/shell finite elements.[14]

In the notation employed in this manuscript, indices (1, 2) correspond to inplane co-ordinates and index 3 corresponds to the transverse direction as shown in Figure 1. The Greek subscripts represent the inplane spatial components (1, 2) only. The lower case Latin subscripts indicate spatial components (1, 2, 3) except for subscripts a, b and e which are reserved for element numbers. Uppercase subscripts indicate degrees of freedom. Summation convention is employed for repeated indices unless otherwise specified.

The displacement field $\mathbf{u}^G$ is expressed in terms of mid-point translations $u_i^t(\xi_1, \xi_2)$ and mid-point rotations $\theta_\alpha(\xi_1, \xi_2)$ which are defined with respect to the fiber co-ordinate system as:

$$\begin{Bmatrix} u_1^G \\ u_2^G \\ u_3^G \end{Bmatrix} = \sum_{A=1}^{\text{NMDS}} N_A^G(\xi_1, \xi_2) \begin{Bmatrix} u_{1A}^t \\ u_{2A}^t \\ u_{3A}^t \end{Bmatrix} + \sum_{A=1}^{\text{NMDS}} N_A^G(\xi_1, \xi_2) \frac{\xi_3}{2} [-t\mathbf{e}_2^f, t\mathbf{e}_1^f](\xi_1, \xi_2) \begin{Bmatrix} \theta_{1A} \\ \theta_{2A} \end{Bmatrix} \tag{2}$$

Where $\{N_A^G\}$ are the hierarchic basis of the interpolation space $S^G(\Omega^G, p^G, q)$ (defined as in Reference 14), p^G is the maximum inplane polynomial order, q the polynomial order in transverse direction and $\Omega^G = \Omega$. NMDS are the number of hierarchic modes in the superimposed mesh. Note that there is a fundamental difference between equation (2) and its iso-parametric counterpart. In the classical iso-parametric formulation the variable vector functions $\mathbf{e}_i^f(\xi_1, \xi_2)$ in equation (2) are replaced by a set of constant vectors $\mathbf{e}_i^f(\xi_1^A, \xi_2^A)$ representing the fibre co-ordinate system at the node A. The present formulation gives rise to an additional term in the displacement gradient evaluation, resulting from the derivatives of $\mathbf{e}_i^f$. For a detailed formulation of hierarchic degenerated plate/shell element see Reference 14.

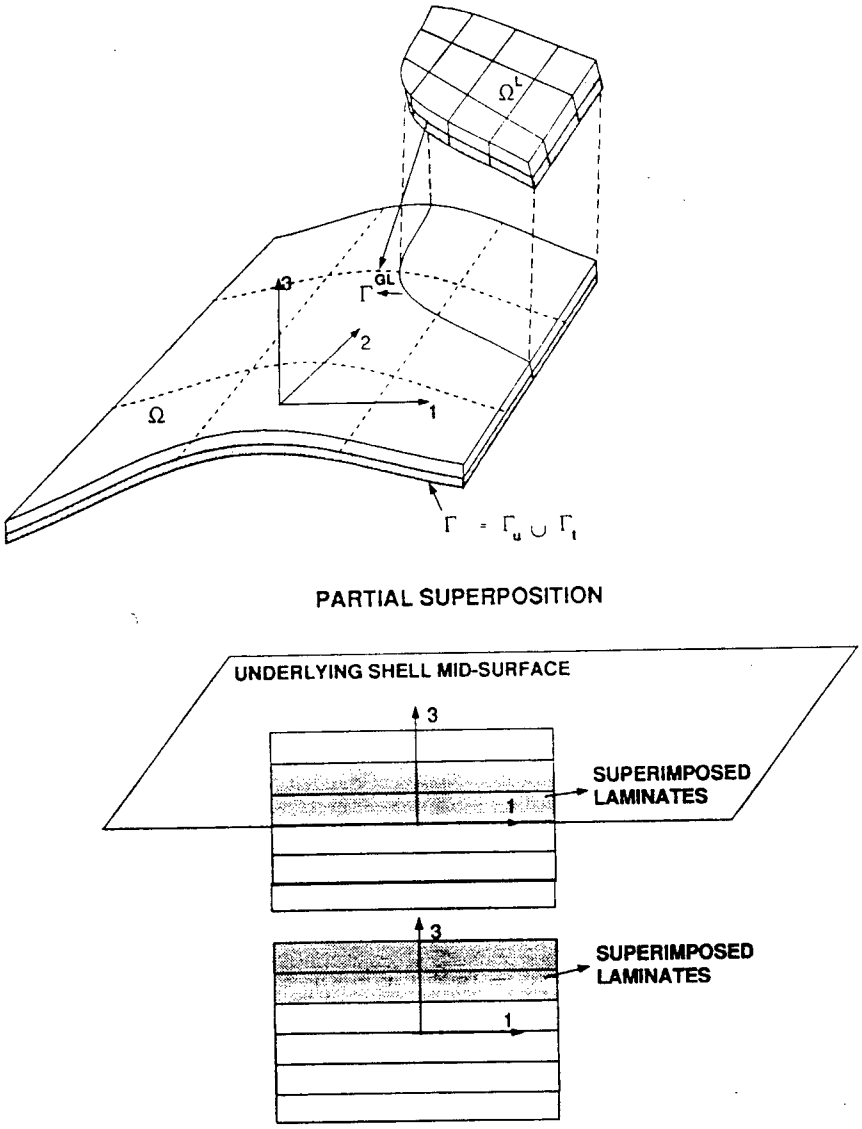


Figure 1. Mesh superposition on laminated shell

To resolve the localized phenomena a Discrete Layer model is superimposed in the critical region Ω^L. The DL model is discretized in terms of 3-D hierarchical C^0 continuous shape functions $\{N_i^L\}$, spanning the interpolation space $S^L(\Omega^L, p^L)$ (defined in Reference 21), where p^L is the maximum polynomial order. Thus the local displacement field is expressed as:

$$u_m^L = \sum_{A=1}^{NMDS} N_{mA}^L a_A \tag{3}$$

where **a** is the displacement vector representing the amplitudes of the hierarchic modes in the superimposed mesh.

To satisfy the C^0 displacement compatibility between the global (ESL) and local (DL) meshes, the following homogeneous boundary conditions are imposed on the local mesh at the boundary between the two meshes (Γ^{GL}):

$$u_\alpha^L = 0 \quad \text{on } \Gamma^{GL} \alpha \in [1, 2] \tag{4}$$

where α corresponds to the inplane co-ordinates of the shell. Note that the local displacement field is not constrained in the transverse (X_3) direction on Γ^{GL} as the underlying shell model has no extension mode in this direction. These constraints are equivalent to the so called telescopic constraints in finite element jargon.

The inhomogeneous displacement boundary conditions $\mathbf{u}^P$ on Γ_u can be approximated with the global mesh, although better resolution of prescribed fields can be obtained by prolonging the remainder of the field

$$\mathbf{u}^L = I^L(\mathbf{u}^P - \mathbf{u}^{PG}) \quad \text{on } \Gamma_u \tag{5}$$

to the local mesh.[2,10-14] In (5) I^L is the prolongation operator from the local to global mesh and $\mathbf{u}^{PG} = \mathbf{u}^G$ on Γ_u.

To demonstrate the basic structure of the discrete equations, a linear elastostatics problem is considered. The discrete equations are obtained using Galerkin approximation of the weak form which states: Given the spaces,

$$\begin{aligned}
U^G &= \{\mathbf{u}^G | \mathbf{u}^G \in S^G(\Omega^G, p^G, q, l^G);\ \mathbf{u}^G \in C^0(\Omega^G);\ \mathbf{u}^G = \mathbf{u}^{PG} \text{ on } \Gamma_u\} \\
W^G &= \{\mathbf{w}^G | \mathbf{w}^G \in S^G(\Omega^G, p^G, q, l^G);\ \mathbf{w}^G \in C^0(\Omega^G);\ \mathbf{w}^G = 0 \text{ on } \Gamma_u\} \\
U^L &= \{\mathbf{u}^L | \mathbf{u}^L \in S^L(\Omega^L, p^L, l^L);\ \mathbf{u}^L \in C^0(\Omega^L);\ \mathbf{u}^L = I^L(\mathbf{u}^P - \mathbf{u}^{PG}) \text{ on } \Gamma_u;\ u_\alpha^L = 0 \text{ on } \Gamma^{GL}\} \\
W^L &= \{\mathbf{w}^L | \mathbf{w}^L \in S^L(\Omega^L, p^L, l^L);\ \mathbf{w}^L \in C^0(\Omega^L);\ \mathbf{w}^L = 0 \text{ on } \Gamma_u;\ w_\alpha^L = 0 \text{ on } \Gamma^{GL}\}
\end{aligned} \tag{6}$$

where $\alpha \in [1, 2]$ and $i \in [1, 3]$.
Find

$$\mathbf{u}^G \in U^G, \quad \mathbf{u}^L \in U^L, \quad \mathbf{u} = \mathbf{u}^G + \mathbf{u}^L \tag{7}$$

such that for all $\mathbf{w}^G \in W^G$, $\mathbf{w}^L \in W^L$, $\mathbf{w} = \mathbf{w}^G + \mathbf{w}^L$

$$a(\mathbf{w}^G + \mathbf{w}^L, \mathbf{u}^G + \mathbf{u}^L)_\Omega = (\mathbf{w}^G + \mathbf{w}^L, b_i)_\Omega + (\mathbf{w}^G + \mathbf{w}^L, t_i)_\Gamma \tag{8}$$

where S^G is the aforementioned interpolation space for the global domain Ω^G, and l^G is the list of active degrees of freedom to be determined in the adaptive process on the basis of the contribution of the corresponding basis functions towards reduction of discretization errors (Section 4). Similarly S^L is the interpolation space for the local domain Ω^L and l^L is the corresponding list of active degrees of freedom determined adaptively. b_i and t_i are prescribed body and traction forces respectively. $a(\cdot, \cdot)$ and $(\cdot, \cdot)$ are bilinear symmetric forms defined by

$$a(\mathbf{P}, \mathbf{Q}) = \int_\Omega P_{(i,j)} D_{ijkl} Q_{(i,j)} \, d\Omega \tag{9}$$

$$(\mathbf{P}, \mathbf{Q})_\Gamma = \int_\Gamma P_i Q_i \, d\Gamma \tag{10}$$

$$(\mathbf{P}, \mathbf{Q})_\Omega = \int_\Omega P_i Q_i \, d\Omega \tag{11}$$

D_{ijkl} is the constitutive tensor. The parenthesis about lower case subscripts designate the symmetric part of a second-order tensor.

Discrete equations are obtained by substituting interpolants (2, 3) for both the trial and test functions into the weak form (8) and requiring arbitrariness of the local and global variations. The

structure of the resulting equation is given as:

$$\mathbf{K}\mathbf{d} = \mathbf{f} \tag{12}$$

where

$$\mathbf{K} = \begin{bmatrix} K^{G}_{AD} & K^{C}_{AE} \\ K^{C}_{BD} & K^{L}_{BE} \end{bmatrix} \quad \mathbf{d} = \begin{Bmatrix} d_D \\ a_E \end{Bmatrix} \quad \mathbf{f} = \begin{Bmatrix} f^{ext}_A \\ h^{ext}_B \end{Bmatrix} \tag{13}$$

and.

$$K^{G}_{AD} = a(\mathbf{N}^{G}_{A}, \mathbf{N}^{G}_{D}) = \int_{\Omega} B^{G}_{ijA} \hat{D}_{ijkl} B^{G}_{klD} \, d\Omega \tag{14}$$

$$K^{L}_{BE} = a(\mathbf{N}^{L}_{B}, \mathbf{N}^{L}_{E}) = \int_{\Omega^{L}} B^{L}_{ijB} D_{ijkl} B^{L}_{klE} \, d\Omega \tag{15}$$

$$K^{C}_{AE} = a(\mathbf{N}^{G}_{A}, \mathbf{N}^{L}_{E}) = \int_{\Omega^{L}} B^{G}_{ijA} D_{ijkl} B^{L}_{klE} \, d\Omega \tag{16}$$

$$f^{ext}_{A} = (N^{G}_{A}, \mathbf{b})_{\Omega} + (N^{G}_{A}, \mathbf{t})_{\Gamma_t} = \int_{\Omega} N^{G}_{iA} b_i \, d\Omega + \int_{\Gamma} N^{G}_{iA} t_i \, d\Gamma \tag{17}$$

$$h^{ext}_{B} = (N^{L}_{B}, \mathbf{b})_{\Omega^{L}} + (N^{L}_{B}, \mathbf{t})_{\Gamma_t} = \int_{\Omega^{L}} N^{L}_{iB} b_i \, d\Omega + \int_{\Gamma} N^{L}_{iB} t_i \, d\Gamma \tag{18}$$

$\mathbf{B}^{G}$ and $\mathbf{B}^{L}$ are the strain-displacement matrices corresponding to the ESL and DL models, respectively. The **B**-matrix is modified using the assumed strain method[22] to enhance the element performance as described in the next section. Effective (or smeared) laminate material properties $\hat{D}_{ijkl}$ are used for calculation of global stiffness matrix and plane stress assumption is incorporated in $\Omega \backslash \Omega^{L}$. 3-D material properties are used for the matrices in the local region.

To maintain rank sufficiency of the stiffness matrix **K** the global and local interpolation spaces must be mutually exclusive. For structured mesh superposition (S_s-version of FEM[10]) exclusively considered here, this can be accomplished explicitly as demonstrated below:

From the definition of spaces $S^{G}(\Omega^{L}, p^{G}, q)$ and $S^{L}(\Omega^{L}, p^{L})$ it is evident that

$$S^{L}(\Omega^{L}, p^{L}) \cap S^{G}(\Omega^{L}, p^{G}, q) \neq \emptyset \tag{19}$$

Hence redundant modes are encountered in the system (12), since a linear combination of underlying mesh basis functions can replicate a superimposed mesh basis function or vice versa.

Define an auxiliary space

$$\hat{S}(\Omega^{L}) = S^{L}(\Omega^{L}, p^{L}) \cap S^{G}(\Omega^{L}, p^{G}, q) \tag{20}$$

so that the rank sufficiency of the stiffness matrix **K** can be maintained using the following interpolation space:

$$S(\Omega) \equiv S^{G}(\Omega^{G}, p^{G}, q) \cup (S^{L}(\Omega^{L}, p^{L}) \backslash \hat{S}(\Omega^{L})) \tag{21}$$

or

$$S(\Omega) \equiv S^{L}(\Omega^{L}, p^{L}) \cup (S^{G}(\Omega^{G}, p^{G}, q) \backslash \hat{S}(\Omega^{L})) \tag{22}$$

The two decompositions of the space $S(\Omega)$ (21) and (22) in the local region denoted by, $S(\Omega^{L})$, represent a complete space of polynomial order p^{L}. The decomposition given in (21) is more

convenient from the computational efficiency stand point because it allows to exploit previous computations in certain cases discussed in Section 5.

In order to construct the space $S(\Omega^L)$ we decompose it as a tensor product of two spaces:

$$S(\Omega^L) = S_{2D}(A^L, p_A^L) \otimes S_{1D}(T, t, p_t^L) \tag{23}$$

where S_{2D} is spanned by 2-D hierarchical basis of order p_A^L [21]define over the mid-surface of the shell over the local region A^L and S_{1D}^L is spanned by 1-D hierarchical basis functions of order p_t^L defined within each layer $t_i \subset T$, such that $\bigcup t_i = T$.

Each of the two spaces is constructed from a set of basis functions in the global and local meshes:

$$S_{2D}(A^L, p_A^L) = S_{2D}^G(A^L, p_A^G) \cup [S_{2D}^L(A^L, p_A^L) \setminus \hat{S}_{2D}^L(A^L)] \tag{24}$$

$$S_{1D}(T, t, p_t^L) = S_{1D}^G(t = T, q) \cup [S_{1D}^L(T, t, p_{1t}^L) \setminus \hat{S}_D^L(T, t)] \tag{25}$$

For the lower order plate/shell theories based on either Kirchhoff or Reissner hypothesis the through the thickness variation of inplane displacements u_x are linear, that is, $q = 1$ and $\dim[S_{1D}^G(t = T, q)] = 2$, while the transverse displacement u_3 variation is constant, that is, $q = 0$ and $\dim[S_{1D}^G(t = T, q)] = 1$.

To define the subspace in the local mesh which is to be constrained, $\hat{S}^L$ we limit ourselves to the case where the global space defined on the local region is a subspace of the local superimposed space, that is, $S^G(\Omega^L, p^G, q) \subset S^L(\Omega^L, p^L)$. In this scenario it is sufficient to constrain dofs of the local mesh corresponding to the following subspace:

$$\hat{S}^L = S_{1D}^G \otimes S_{2D}^G \tag{26}$$

This implies that it is necessary to constrain a number of shell surfaces or layer interfaces in the superimposed (DL) mesh equal to $\dim[S_{1D}^G]$. In numerical examples we have constrained the top and bottom surfaces for inplane displacement and a bottom (or top) surface for the transverse displacement.

The second case of practical interest is that of partial superposition in the transverse direction as shown in Figure 1. This is especially important for multilayer composite with hundreds of layers, where it is desirable to superimpose only in the vicinity of most critical layers. In this scenario it is necessary to enlarge the constraint set $\hat{S}^L$ to maintain displacement compatibility between global and local meshes by constraining the dofs in the superimposed mesh at the global-local interface Γ^{GL}.

For the case of unstructured superposition (S_u-version) the redundant modes are eliminated during the solution phase as elucidated in Reference 11. In the current work only the structured mesh superposition methodology has been considered.

Remark. The *s*-method can be utilized to hierarchically model discontinuous fields.[12] By this technique a mathematical model free of discontinuities is superimposed by an additional field able to represent the discontinuity. The mathematical validation of this technique was given in Reference 12. In the present study the global ESL mesh free of delamination is superimposed by a local 3-D mesh with delamination (discontinuity) modelled by double nodes along the delamination surface. Numerical investigation is presented in Section 5.

3. ASSUMED STRAIN FORMULATION

To enhance the performance of the degenerated plate/shell elements primarily at lower spectral orders ($p \leqslant 4$) an assumed strain formulation is employed. The formulation of the enhanced

strain–displacement matrix $\bar{\mathbf{B}}$ can be obtained by interpolating B_{ijA} between a set of reduced quadrature points[23] or by selectively projecting out higher-order modes in the quadrature process as described in this section.

The formulation of assumed strain displacement matrix based on interpolating certain information between a set of reduced quadrature points is computationally taxing for higher-order elements ($p > 4$), making the stiffness calculations cumbersome. To speed up this process Symmetric Dot Product (SDP) quadrature scheme (presented in Reference 14) which exploits the hierarchical structure of the stiffness matrix and eliminates the need for explicit strain interpolation between reduced and regular quadrature points has been developed in the context of the s-method. We briefly outline the SDP quadrature scheme in the context of laminated composites.

Consider the integral of the form $\int_\Omega g(\xi_1, \xi_2, \xi_3)\, h(\xi_1, \xi_2, \xi_3)\, \mathrm{d}\Omega$ in the natural co-ordinate system such that $\mathrm{d}\Omega = \mathrm{d}\xi_1\, \mathrm{d}\xi_2\, \mathrm{d}\xi_3$ and $-1 \leqslant \xi_i \leqslant 1$. The integral under consideration may represent a typical stiffness matrix component, where g is a strain–displacement matrix component and h is a strain–displacement matrix term multiplied by a jacobian and a corresponding component of the constitutive tensor. In the classical Gauss quadrature the integrand (gh) is implicitly curve fit with a polynomial and then integrated in a closed form. It has been shown in Reference 24 that for hierarchical systems it is more efficient to curve fit separately each term of the integrand (g and h) with orthonormal polynomials (ϕ) which allows one to decompose the integral into a dot product of two vectors

$$\int_\Omega gh\, \mathrm{d}\Omega = \sum_{I=1}^{L} \int_\Omega g\, \phi_I\, \mathrm{d}\Omega \int_\Omega h\, \phi_I\, \mathrm{d}\Omega \tag{27}$$

where the following concise notation is being used $\phi_I(\xi_1, \xi_2, \xi_3) \equiv \hat{P}_i(\xi_1)\, \hat{P}_j(\xi_2)\, \hat{P}_k(\xi_3)$ where $\hat{P}_i$ are normalized Legendre polynomials. $L = (l_1 + 1)(l_2 + 1)(l_3 + 1)$; where l_i, $i \in [1, 3]$ are polynomial orders of ϕ_I in ξ_1, ξ_2, ξ_3 directions, defined as in Reference 14. The proof is based on the orthogonality of Legendre polynomials and is given in References 14 and 24. Now consider a typical stiffness term

$$k_{AB} = \int_\Omega \underbrace{\mathbf{B}_A^{\mathrm{T}} \mathbf{D} \mathbf{B}_B\, J}_{\mathbf{g}_A \mathbf{h}_B}\, \mathrm{d}\Omega \tag{28}$$

Let

$$\mathbf{g}_A = \mathbf{B}_A^{\mathrm{T}}\, J^{1/2} \quad \mathbf{h}_B = \mathbf{D}\, J^{1/2}\, \mathbf{B}_B \tag{29}$$

yielding

$$k_{AB} = \sum_{I=1}^{L} \int_\Omega \mathbf{B}_A^{\mathrm{T}}\, J^{1/2}\, \phi_I\, \mathrm{d}\Omega \int_\Omega \overbrace{\mathbf{D}\, \phi_I}^{\mathbf{g}_I} \underbrace{\mathbf{B}_B\, J^{1/2}}_{\mathbf{h}_B}\, \mathrm{d}\Omega \tag{30}$$

and further dot product integral decomposition of the second term in (30) yields the following symmetric form:

$$k_{AB} = \sum_{I=1}^{L} \sum_{J=1}^{L} \int_\Omega (\mathbf{B}_A^{\mathrm{T}} J^{1/2})\, \phi_I\, \mathrm{d}\Omega \cdot \underbrace{\int_\Omega (\mathbf{D})\, \phi_I \phi_J\, \mathrm{d}\Omega}_{\mathbf{D}_{IJ}} \cdot \int_\Omega (\mathbf{B}_B^{\mathrm{T}} J^{1/2})\, \phi_J\, \mathrm{d}\Omega \tag{31}$$

where the strain–displacement matrix $\mathbf{B}$ and the constitutive tensor are expressed in the element material co-ordinate system. For the exact integration of the term $\mathbf{B}_A^{\mathrm{T}} J^{1/2}$ the maximum polynomial order of Legendre polynomial ϕ_I has to be equal to the maximum polynomial order of the integrand $\mathbf{B}_A^{\mathrm{T}} J^{1/2}$. In practice the maximum polynomial order of ϕ_I is matched with the maximum polynomial order of $\mathbf{B}_A^{\mathrm{T}}$ assuming a constant jacobian. Locking is alleviated by selectively projecting out the $\mathbf{B}$ matrix terms on to a reduced space spanned by Legendre polynomials resulting in

$$\int_\Omega \bar{\mathbf{B}}_A J^{1/2} \phi_I \, \mathrm{d}\Omega = \int_\Omega \begin{bmatrix} b_{A11} \hat{\bar{P}}_i(\xi_1) \hat{P}_j(\xi_2) \hat{P}_k(\xi_3) \\ b_{A22} \hat{P}_i(\xi_1) \hat{\bar{P}}_j(\xi_2) \hat{P}_k(\xi_3) \\ b_{A33} \hat{P}_i(\xi_1) \hat{P}_j(\xi_2) \hat{\bar{P}}_k(\xi_3) \\ b_{A23} \hat{P}_i(\xi_1) \hat{\bar{P}}_j(\xi_2) \hat{\bar{P}}_k(\xi_3) \\ b_{A12} \hat{\bar{P}}_i(\xi_1) \hat{\bar{P}}_j(\xi_2) \hat{P}_k(\xi_3) \\ b_{A13} \hat{\bar{P}}_i(\xi_1) \hat{P}_j(\xi_2) \hat{\bar{P}}_k(\xi_3) \end{bmatrix} J^{1/2} \, \mathrm{d}\Omega \tag{32}$$

where

$$\hat{\bar{P}}_m(\xi_t) = \begin{cases} \hat{P}_m(\xi_t), & m < l_t \\ 0, & m = l_t \end{cases} \tag{33}$$

Equation (33) is consistent with selective interpolation between reduced quadrature points.[22,23]

Note that if the constitutive tensor is constant, $\mathbf{D}_{IJ} = \int_\Omega \mathbf{D} \phi_I \phi_J \, \mathrm{d}\Omega = \mathbf{D} \delta_{IJ}$. In case of Laminated Plates and Shells, $\mathbf{D}_{IJ}$ is pre-integrated.

4. ADAPTIVE STRATEGY

Based on the information from *a posteriori* error estimators and indicators the adaptive procedure aims to achieve the following objectives:

(a) Demarcation of critical regions where DL model should be superimposed.
(b) Polynomial refinement in both global (ESL) and local (DL) meshes until the desired level of accuracy is obtained.

The error indicators presented in this section are based on the earlier work by the authors.[10] The estimated error in the ESL model, referred as Dimensional Reduction Error (DRE), $\mathbf{E}$, is approximated by a linear combination of some basis functions ϕ.

$$\mathbf{E} = \phi \beta \in E(\Omega^\star) \tag{34}$$

where β are determined by solving the minimization auxiliary problem:

$$\frac{\partial}{\partial \beta} \left\{ \frac{1}{2} a(\mathbf{u}^{\mathrm{FE}} + \mathbf{E}, \mathbf{u}^{\mathrm{FE}} + \mathbf{E})_\Omega - (\mathbf{u}^{\mathrm{FE}} + \mathbf{E}, \mathbf{b})_\Omega - (\mathbf{u}^{\mathrm{FE}} + \mathbf{E}, \mathbf{t})_\Gamma \right\} = 0 \tag{35}$$

and the functional space E is defined to maintain C^0 continuity of the augmented field $\mathbf{u}^{\mathrm{FE}} + \mathbf{E}$ and to satisfy essential boundary conditions, that is

$$E = \{\mathbf{E} | \mathbf{E} = \phi \beta \in C^0(\Omega^\star); \mathbf{E} \in S^E(\Omega^\star, p^E); \mathbf{E} = 0 \text{ on } \Omega \backslash \Omega^\star\} \tag{36}$$

We now define the subspace S^E. For the process of identification of critical regions in the ESL plate/shell model the $\mathbf{u}^{\mathrm{FE}}$ corresponds to a given ESL finite element solution and ϕ represents

layer-wise 3-D finite element interpolants. To estimate the dimensional reduction error indicators, the space S^E is chosen as a 3-D discrete layer interpolation space defined on the entire domain $\Omega^\star = \Omega$, with maximum polynomial order $p^E = 1$. It is desirable that the computational effort of the error estimation process be only a fraction of the finite element solution, hence in practice only an approximation for β is calculated. We will be seeking for an approximation of β by replacing the Hessian matrix $a(\phi, \phi)$ resulting from (35) by its diagonal. The resulting energy norm of the estimated error for each element is obtained by

$$\eta_e = \sum_{A}^{\text{NDOFS}} \left\{ \frac{1}{2} \beta_A^2 a(\phi_A, \phi_A)_{\Omega^e} \right\}^{1/2} \tag{37}$$

where NDOFS are the total number of degrees of freedom in the element 'e'. The critical elements which need to be superimposed are selected such that

$$\eta_e \geqslant \gamma_e \max_e (\eta_e) \tag{38}$$

where parameter $\gamma_e \in [0, 1]$ controls the number of elements to be superimposed with $\gamma = 0$ corresponding to uniform superposition over the entire domain.

We now consider adaptive strategy based on selective polynomial escalation in the two meshes. Consider a given finite element space consisting of underlying and superimposed meshes

$$S^{\text{FE}} = S^{\text{G}}((\Omega^{\text{G}} \setminus \Omega^{\text{L}}), p^{\text{G}}, q, l^{\text{G}}) \cup [S^{\text{L}}(\Omega^{\text{L}}, p^{\text{L}}, l^{\text{L}}) \setminus \hat{S}^{\text{L}}(\Omega^{\text{L}})] \tag{39}$$

and let us define a higher order space S^{E} obtained by increasing the polynomial order of both global and local interpolants.

$$S^{\text{E}} = [S^{\text{G}}((\Omega^{\text{G}} \setminus \Omega^{\text{L}}), p^{\text{G}} + 1, q) \cup S^{\text{L}}(\Omega^{\text{L}}, p^{\text{L}} + 1) \setminus \hat{S}^{\text{L}}(\Omega^{\text{L}})] \setminus S^{\text{FE}} = \text{SPAN}\{\phi_A\} \tag{40}$$

As before, the approximations for β are found by replacing the Hessian matrix $a(\phi, \phi)$ by its diagonal. Error indicators corresponding to each higher-order degree of freedom are calculated as:

$$\eta_A = \{ \tfrac{1}{2} \beta_A^2 a(\phi_A, \phi_A) \}^{1/2} \quad \text{no sum on } A \tag{41}$$

in both meshes. The degree-wise indicators η_A is used in selection of critical basis functions which reduce the error similar to the element-wise error indicators (38). The list of active degrees of freedom l^{G} and l^{L} is appended with those degrees of freedom which correspond to the error indicators η_A (41) such that

$$\eta_A \geqslant \gamma \max_A (\eta_A) \tag{42}$$

where parameter $\gamma \in [0, 1]$ controls the speed of convergence with $\gamma = 0$ corresponding to uniform polynomial escalation.

5. MULTIGRID METHOD FOR HIERARCHICAL SYSTEMS

The structure of the stiffness matrix resulting from the s-method is quite dense unlike the banded structure of the lower-order elements. This is due to use of higher-order elements and explicit coupling between global and local meshes. The deterioration of the sparsity significantly affects the total solution time in the case of conventional sky-line or sparse matrix equation solvers. On the other hand, the hierarchical structure of s-method has a positive effect on the system conditioning. This suggests that iterative equation solvers are ideal to expedite the solution process. In our previous work[14] we have developed efficient Multigrid-like iterative solvers for

p-method. These solvers are generalized to deal with positive-definite systems arising from the superposition of ESL and DL meshes. We consider a hierarchical system:

$$\mathbf{K}^m \mathbf{d}^m = \mathbf{f}^m; \quad m = \underbrace{0, 1, 2, \ldots m^G}_{\text{global levels}}, \overbrace{m^G + 1, \ldots, m^G + m^L}^{\text{local levels}} \tag{43}$$

where

$$\mathbf{K}^m = \begin{bmatrix} \hat{\mathbf{K}}^{m-1} & \mathbf{K}^m_{12} \\ \mathbf{K}^m_{21} & \mathbf{K}^m_{11} \end{bmatrix}, \quad \mathbf{d}^m = \begin{Bmatrix} \mathbf{d}^{m-1} \\ \mathbf{d}^m_1 \end{Bmatrix}, \quad \mathbf{f}^m = \begin{Bmatrix} \mathbf{f}^{m-1} \\ \mathbf{f}^m_1 \end{Bmatrix} \tag{44}$$

and m is the level number; $\mathbf{K}^0$ the stiffness matrix on the initial level; $\mathbf{K}^m$ is of order $n_m > n_{m-1}$, where n_{m-1} is the order of the block $\hat{\mathbf{K}}^{m-1}$; $\mathbf{d}^m_1 \in \Re^{(n_m - n_{m-1})}$ and $\mathbf{d}^{m-1} \in \Re^{n_{m-1}}$.

The special feature of equation (44) for superposition analysis is that lower order block $\hat{\mathbf{K}}^{m-1}$ might be different from the stiffness matrix corresponding to level $(m-1)$, $\mathbf{K}^{m-1}$, because of either

1. change in constitutive model from plane stress ($q = 1$) to 3-D ($q \geqslant 2$),
2. progressive improvement in geometry or
3. changing quadrature scheme.

The global plate/shell model may exhibit somewhat stiffer behaviour at lower polynomial orders which may not well represent a lower frequency response of the total superimposed system. This is related to the well known problem of 'locking' which is characteristic of lower order plates and shells.

We now present a variant of the multigrid method for solving positive-definite systems defined by equation (44). Let $\mathbf{Q}^{m-1}_m$ and $\mathbf{Q}^m_{m-1}$ be the restriction and prolongation operators, which transfer the data from level (m) to level $(m-1)$ and vice versa. Due to the hierarchiality of the s-method it has a very simple form:

$$\mathbf{Q}^{m-1}_m = [\mathbf{I} \quad \mathbf{0}] = \mathbf{Q}^{m^T}_{m-1} \tag{45}$$

where $\mathbf{I}$ is the order n_{m-1} identity matrix, and $\mathbf{0}$ is order $(n_m - n_{m-1})$ zero matrix. A single V-cycle has a compact recursive definition given by

$$\mathbf{z}^m := MG^m(\mathbf{r}^m, \mathbf{K}^m) \tag{46}$$

where $\mathbf{r}^m$ is the residual vector. The V-cycle multigrid algorithm is summarized below:

1. Loop $i = 0, 1, 2, \ldots$ until convergence
   if $i = 0 \leftarrow \mathbf{d}^m = 0$
2. perform γ_1 pre-smoothing operations

$$^{i}_{\gamma_1}\mathbf{d}^m := \text{smooth}(\gamma_{1,0}\, {}^{i}\mathbf{d}^m, \mathbf{K}^m, \mathbf{f}^m)$$

   where the left superscript and subscript denote the cycle number of smoothing count respectively.
3. Restrict residual from level m to $m-1$

$$\mathbf{r}^{m-1} = \mathbf{Q}^{m-1}_m (\mathbf{f}^m - \mathbf{K}^m\, {}^{i}_{\gamma_1}\mathbf{d}^m)$$

4. Coarse grid correction

   If $(m-1)$ = lowest level, solve directly $\mathbf{z}^{m-1} = (\mathbf{K}^{m-1})^{-1}\mathbf{r}^{m-1}$,

   Else $\mathbf{z}^{m-1} := MG^{m-1}(\mathbf{r}^{m-1}, \mathbf{K}^{m-1})$

5. Prolongate from level $m-1$ to m

$$_{\gamma_1+1}{}^{i}\mathbf{d}^{m} = {}_{\gamma_1}{}^{i}\mathbf{d}^{m} + {}^{i}\omega\,\mathbf{Q}_{m-1}^{m}\mathbf{z}^{m-1}$$

   where ${}^{i}\omega$ is a coarse grid relaxation parameter, which minimizes energy functional along the prescribed direction $\mathbf{v}^{m} = \mathbf{Q}_{m-1}^{m}\mathbf{z}^{m-1}$ and is given as

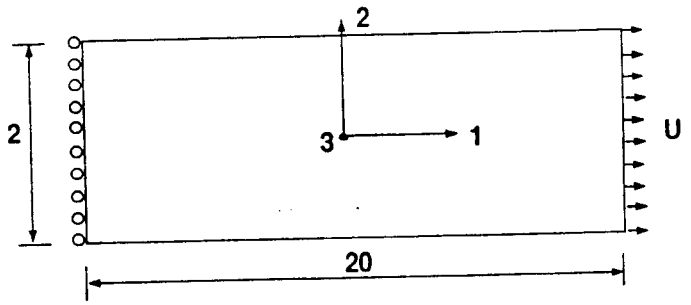
$$ {}^{i}\omega = \frac{\mathbf{v}^{m\mathrm{T}}(\mathbf{f}^{m} - \mathbf{K}^{m}\,{}_{\gamma_1+1}{}^{i}\mathbf{d}^{m})}{\mathbf{v}^{m\mathrm{T}}\mathbf{K}^{m}\mathbf{v}^{m}} \tag{47}$$

   Note that for two grid methods ${}^{i}\omega = 1$ if $\hat{\mathbf{K}}^{m-1} = \mathbf{K}^{m-1}$.

6. Perform γ_2 post-smoothing operations

$$ {}^{i+1}_{0}\mathbf{d}^{m} := \text{smooth}\,(\gamma_{2,\gamma_1+1}\,{}^{i}\mathbf{d}^{m}, \mathbf{K}^{m}, \mathbf{f}^{m})$$

Another variant of the standard V-cycle multigrid method[9] has been proposed by Bank *et al.*[25] The method termed as hierarchical basis multigrid technique (HBM), is similar to the standard



Thickness of each lamina = 0.125
E_1 = 20.0 x 10^6 psi,
$E_2 = E_3$ = 2.10 x 10^6 psi
$G_{12} = G_{23} = G_{13}$ = 0.85 x 10^6 psi,
$\nu_{12} = \nu_{23} = \nu_{13}$ = 0.21.

D.R.E. INDICATOR CONTOURS AT 45/-45 INTERFACE

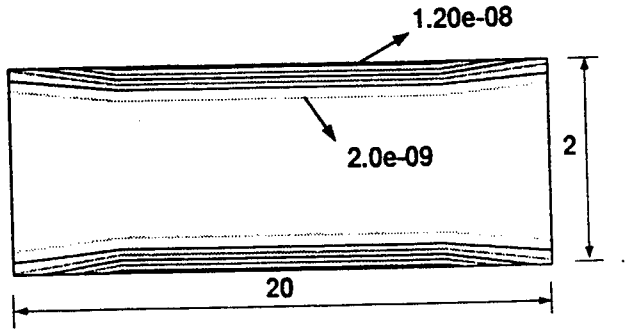


Figure 2. Axial tension (45/ − 45), problem

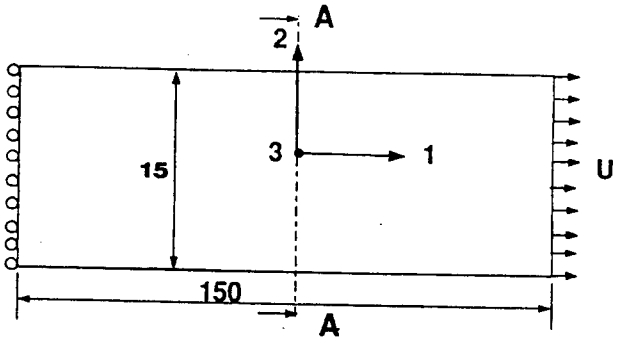
multigrid V-cycle, except that a smaller than the normal subset of unknowns is updated during the smoothing phase at a given level. HBM takes advantage of the fact that smoothing mainly affects highest oscillatory modes of error, and thus relaxation sweeps are performed on the block by block level keeping the rest of the degrees of freedom fixed. It has been shown by Bank *et al.*[25] that the rate of convergence of HBM method has a logarithmic dependence on the problem size as opposed to multigrid method which has an optimal rate of convergence independent of the mesh size and spectral order.

For ill-conditioned problems, such as thin laminated plates and shells, it is desirable to accelerate the rate of convergence of the multigrid like methods. The acceleration schemes (two parameter and conjugate gradients) require a small fraction of computational effort, but at the same time have been found to be very efficient in expediting the convergence of the multigrid like methods.[14]

6. NUMERICAL EXPERIMENTS

Numerical experiments are conducted to investigate the performance of *s*-method for modeling laminated composites in terms of accuracy and computational efficiency. The following classical test problems are considered:

(a) $(45/-45)_s$ laminate in axial tension,[26-28]
(b) $(45/0/-45/90)_s$ laminate in axial tension,[26]



Thickness of each lamina = 0.125
$E_1 = 19.5 \times 10^6$ psi,
$E_2 = E_3 = 1.48 \times 10^6$ psi
$G_{12} = G_{23} = G_{13} = 0.8 \times 10^6$ psi,
$\nu_{12} = \nu_{23} = \nu_{13} = 0.30.$

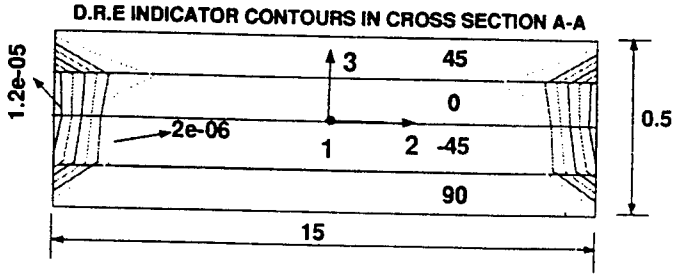


Figure 3. Axial tension problem $(90/-45/0/45)_s$ composite laminate

(c) edge delamination test for $(0/35/-35/90)_s$ laminate,[26]
(d) composite laminate Scordelis-lo roof.

Geometry, boundary conditions and material properties for the axial tension problems are illustrated in Figures 2 and 3.

Our numerical experimentation agenda involves investigation of the following aspects:

(a) ability of Dimensional Reduction Errors to capture critical regions,
(b) the influence of mesh gradation, selective polynomial escalation and assumed strain formulation on the rate of convergence,
(c) comparative study of iterative and direct solution techniques for laminated composites.

Contour lines of the estimated error $(45/-45)_s$ and $(45/0/-45/90)_s$ laminates subjected to axial tension are given in Figures 2 and 3, respectively. The contour lines were obtained by interpolating estimated elemental errors. The estimated error distribution substantiates the well known fact that edge effects are prominent near the free edges of the laminates. A layer-wise finite element mesh is superimposed over the critical elements.

In our current study identical inplane mesh subdivision for underlying and overlying meshes has been employed. Numerical comparison of meshes with different gradation in resolving 3-D stress fields in $(45/-45)_s$ laminate is illustrated in Figure 5. The uniform superimposed mesh shown in Figure 4 is obtained by layer-wise subdivision in the transverse direction. The two

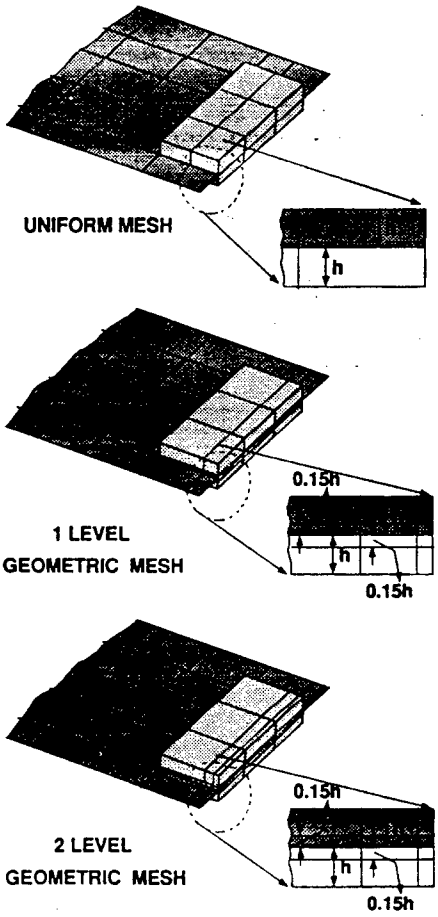


Figure 4. Different meshes used for free edge stress estimation

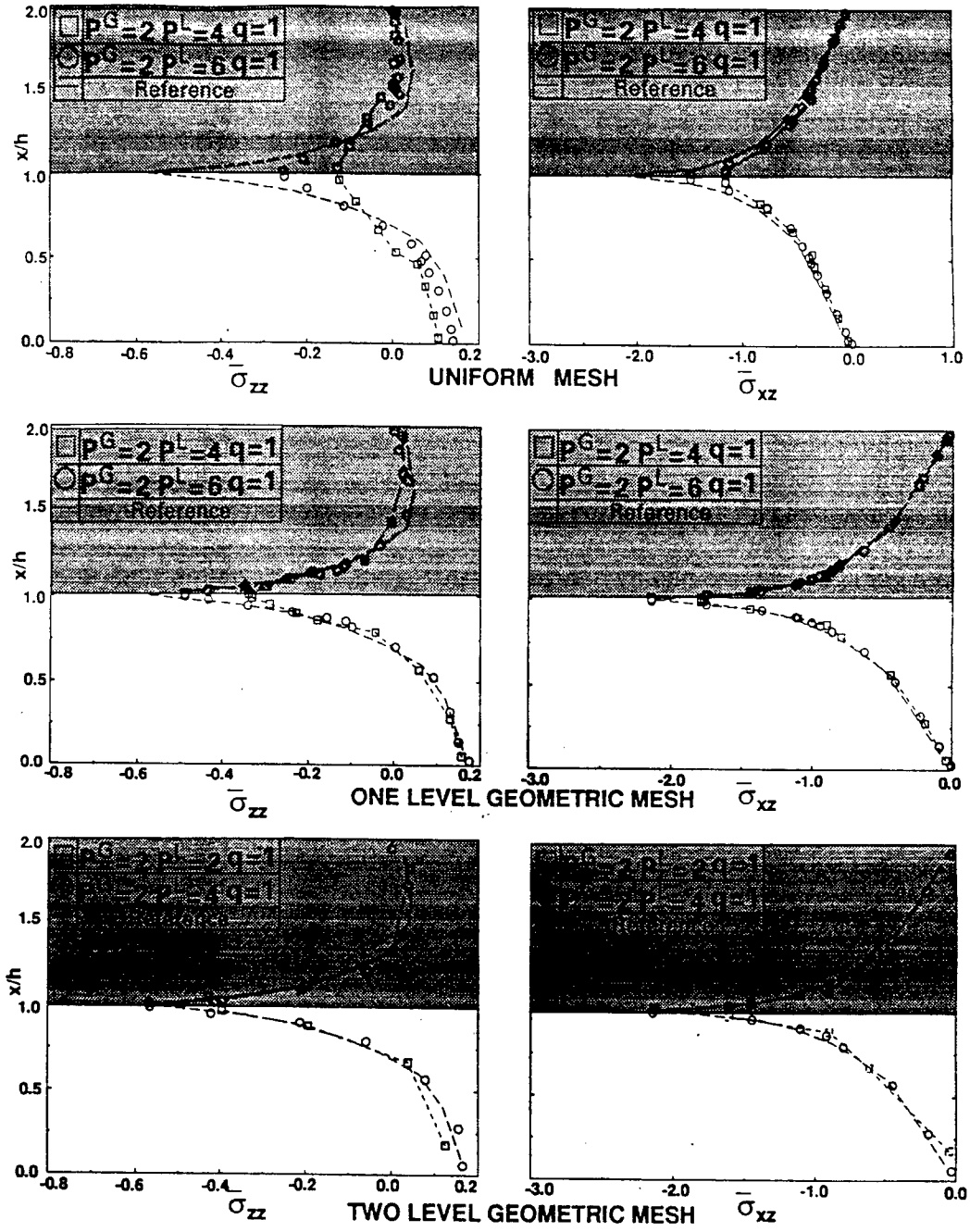


Figure 5. Comparison of meshes for $(45/-45)_s$ laminate

geometric meshes in Figure 4 have layers of elements graded towards the free edge and the ply interface with a common factor of 0·15. Normalized stress distribution ($\bar{\sigma}_{i3} = \sigma_{i3}/\varepsilon_0$ where ε_0 = axial strain) near the free edges for each type of mesh is shown in Figure 5. The reference stress distributions at the free edges are depicted from.[26–28] It is evident from the plots in Figure 5 that geometric meshes are vital to accurately estimate the stress field near free edges and polynomial order escalation alone in uniform meshes is not sufficient.

Assumed strain and displacement based elements (for both underlying the superimposed models) as well as the quadrature schemes are compared in Figure 6. The CPU times required for the calculation of total (global and local) stiffness employing SDP and uniform quadrature schemes are compared for the $(45/-45)_s$ problem modelled with two level geometric mesh (Figure 4). Plots of absolute maximum stress and error in energy norm versus the total CPU time for stiffness calculation are shown in Figure 6. Both formulations are quite competent in estimating maximum stresses, although the assumed strain formulation has faster convergence.

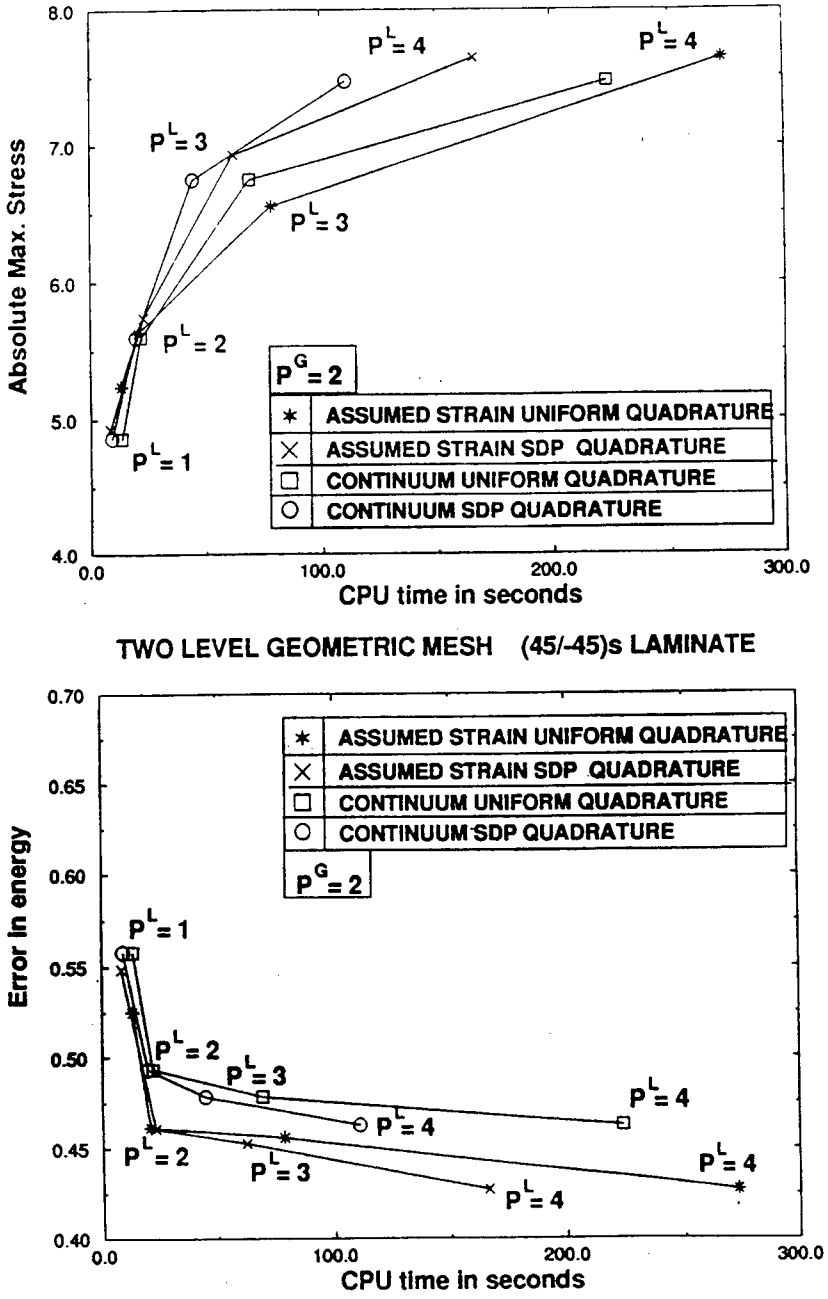


Figure 6. Comparison of quadrature schemes

Moreover it is evident that SDP quadrature is computationally more efficient than the uniform quadrature scheme for both assumed strain and displacement based elements.

To study the effect of selective polynomial order escalation on the resolution of free edge stresses, the $(45/-45)_s$ and $(45/0/-45/90)_s$ laminates modelled with meshes as shown in Figures 7 and 8 respectively, are considered. In Figures 7 and 8 plots of maximum stresses with and without selective polynomial order escalation for the local mesh are presented for $(45/-45)_s$ and $(45/0/-45/90)_s$ laminates. It is evident that selective polynomial order escalation speeds up the rate of convergence. In the problems considered the parameter γ (42) was set equal to 0·01 and selective polynomial order escalation was performed only on the local mesh.

In Figure 9 the composite laminate Scordelis-lo roof problem is investigated. The elemental error densities in a 4×4 uniform mesh are illustrated. The two elements with maximum errors are superimposed with discrete layer mesh. The parameter γ_e was chosen as 0·75. The convergence in energy norm and in the maximum normal stress with uniform and selective polynomial escalation are depicted in the plots. Selective polynomial escalation is carried out in both local and global meshes. It is evident from the plots that selective polynomial escalation in the local mesh alone is not sufficient unless the global mesh is sufficiently refined.

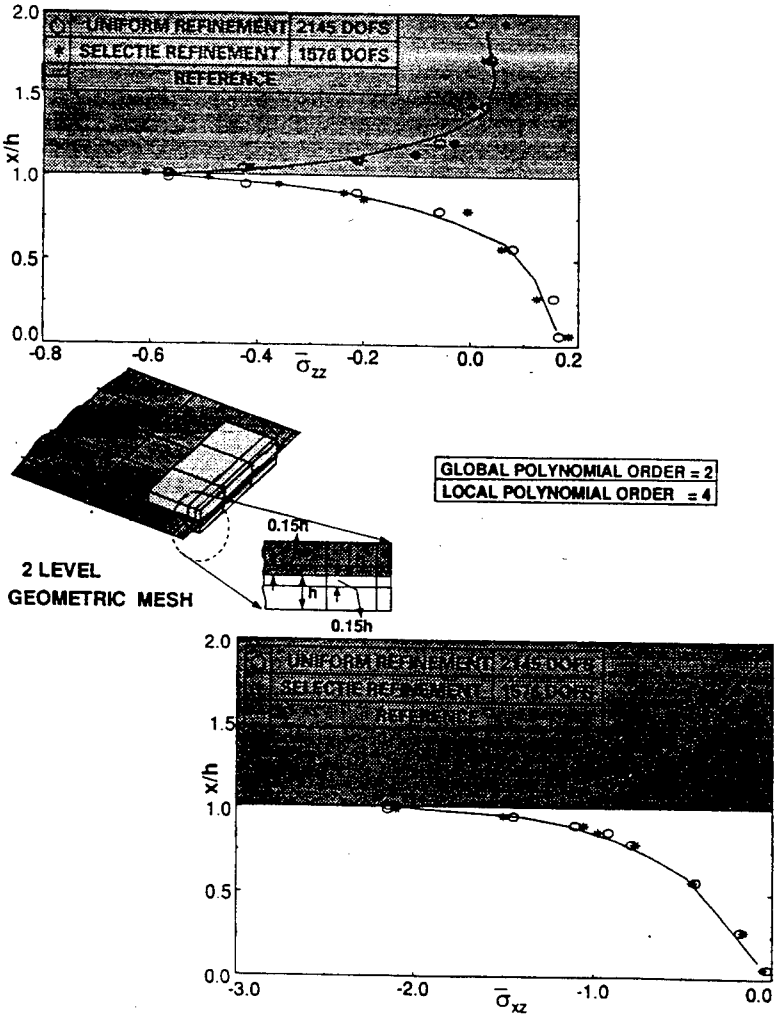


Figure 7. Effect of selective refinement $(45/-45)_s$ laminate

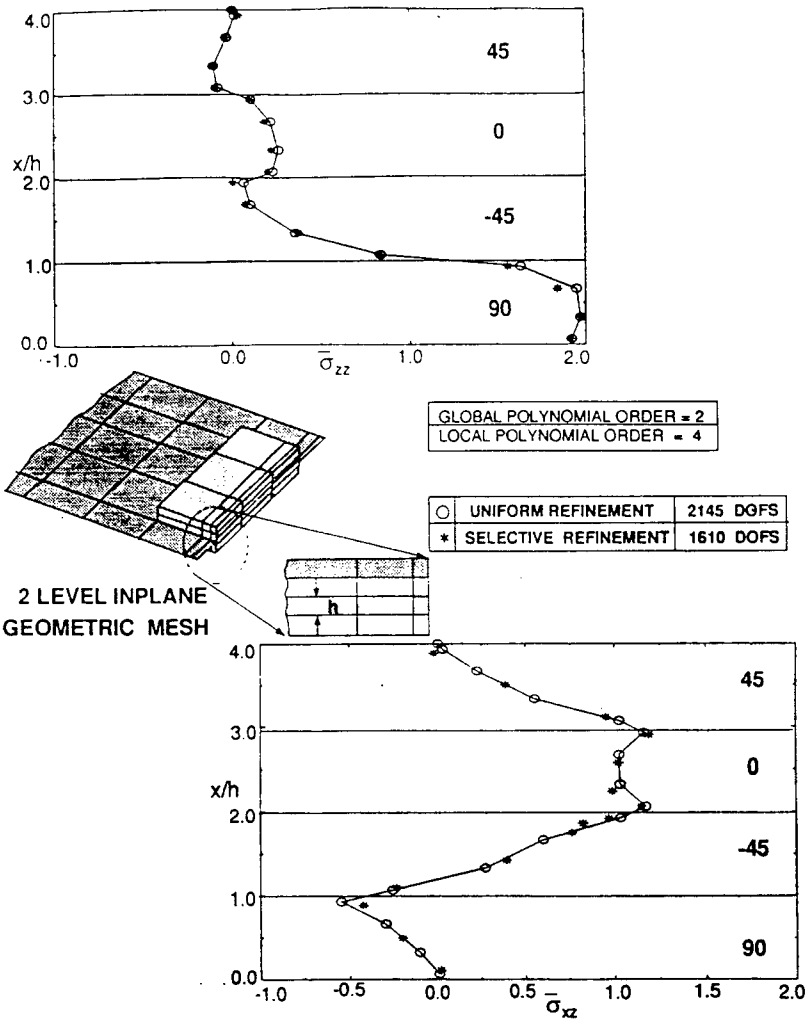


Figure 8. Effect of selective refinement $(45/0/-45/90)_s$ laminate

Partial through-the-thickness mesh superposition where only two $(0, -45)$ lamina are superimposed in the $(45/0/-45/90)_s$ laminate, is presented in Figure 10. It can be seen that the accuracy of stresses at the $(0/-45)$ interface is not significantly compromised due to the partial superposition.

The edge delamination (EDT) problem is used to test the ability of the model to predict energy release rates. The particular laminate chosen for this experiment is $(0/35/-35/90)_s$, since this problem has been analysed using layer-wise theory in Reference 28 and using quasi-3-D finite element model in Reference 29. The geometry, boundary conditions, symmetry and material properties are illustrated in Figure 11. The specimen has four delaminations two along each free edge at the $-35/90$ and $90/-35$ interfaces. The delamination surface interpenetration has been ignored in the current study. Three-dimensional Virtual crack closure method[30] is used to calculate the total energy release rate and its components. In Figure 11 normalized energy release rates are plotted versus the specimen length. The energy release rates are normalized as follows:

$$(\bar{G}, \bar{G}_I, \bar{G}_{II}) = \frac{(G, G_I, G_{II})}{\varepsilon_0^2 0{\cdot}5t\, L} \tag{48}$$

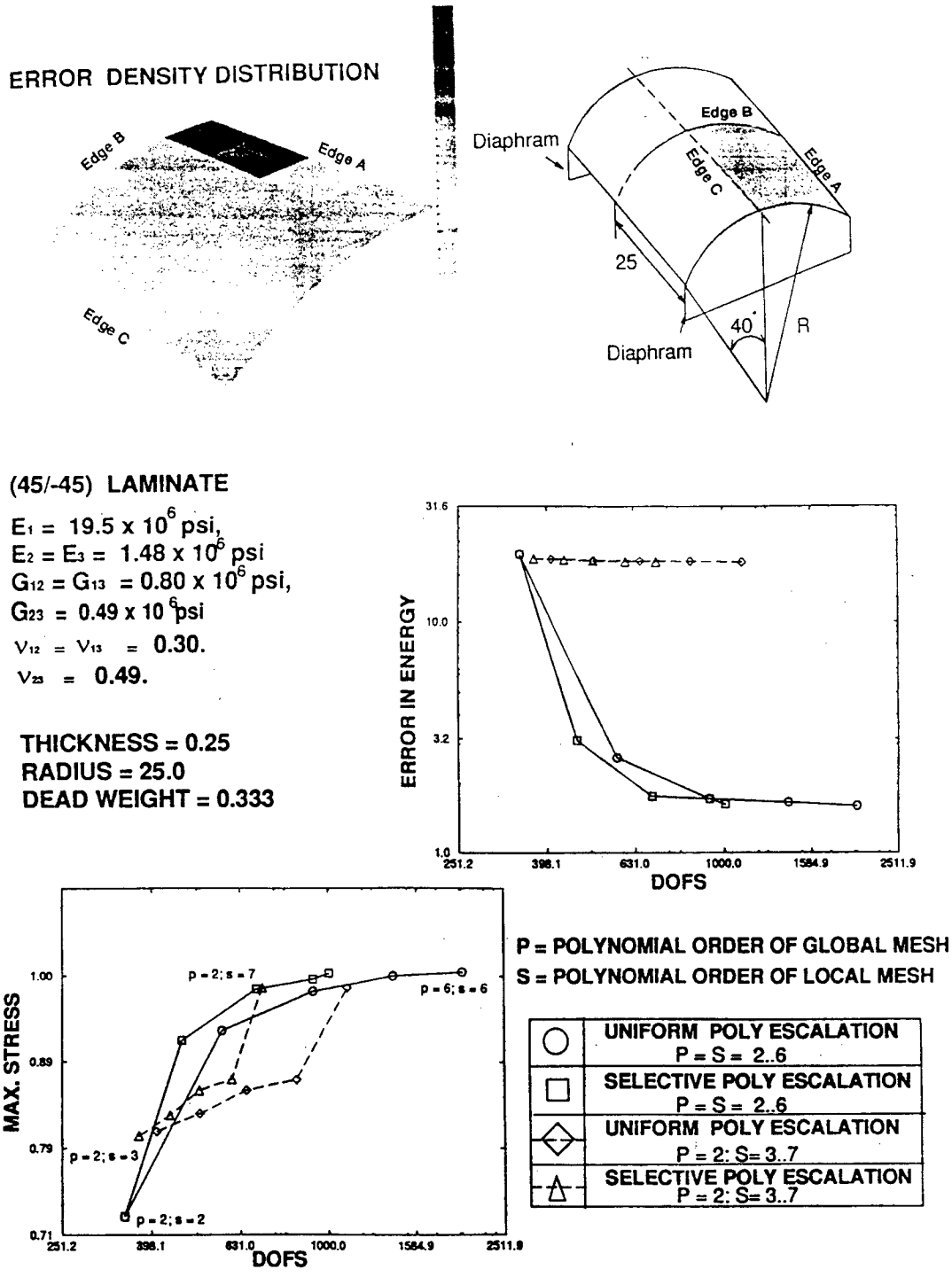


Figure 9. Scordelis-lo roof problem

where L is the length of the specimen, t the total thickness and ε_0 the uniform axial strain. It was observed that the contribution of mode III towards the total energy release rate was negligible and mode II was the prominent contributor. The energy release rates are fairly constant along the central portion of the specimen and show a decrease near the ends, where the delamination

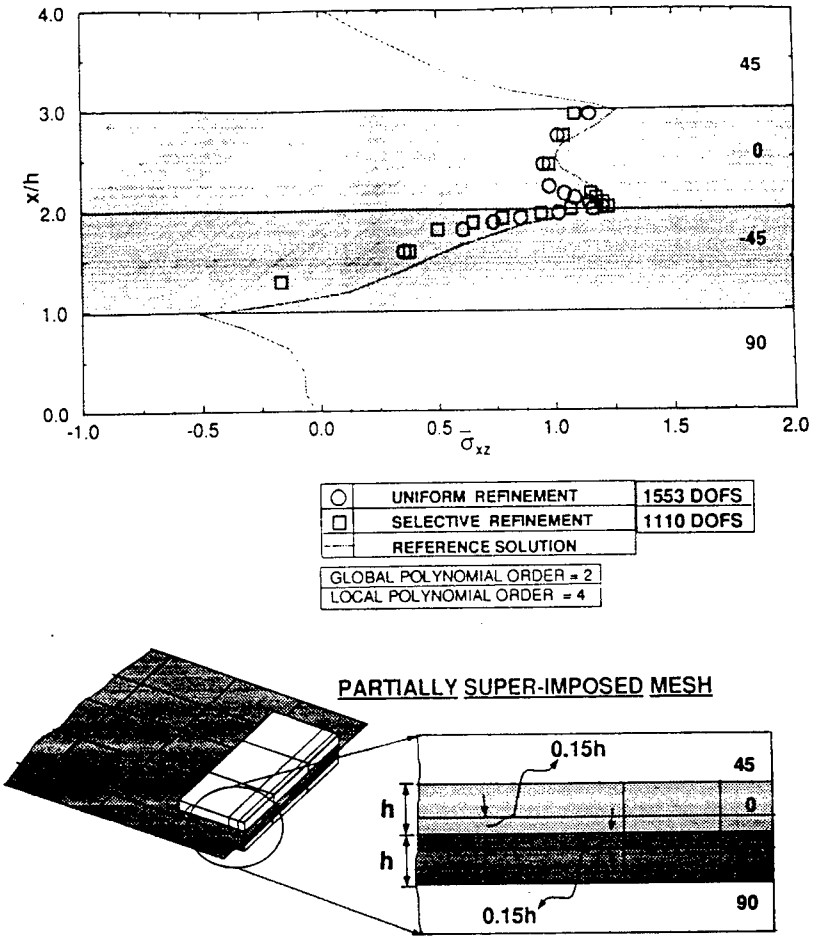


Figure 10. Interlaminar stresses at free edge partial superposition on (− 45/0) plys

surfaces are constrained against relative motion to simulate friction grips. The results presented match closely with the results presented in Reference 28 in the central portion of the specimen.

Finally we study the performance of various solution techniques for solving a positive definite linear system of equations resulting from *s*-version of finite element formulation. The $(45/0/-45/90)_s$ laminate problem (Figure 8) and the Scordelis-lo roof problem have been considered. The solution procedures considered are:

(a) MG-ICC-ACC: Multigrid method with In-Complete Cholesky smoothing and two parameter acceleration,
(b) HBM-ICC-ACC: Hierarchical Basis Multigrid method with In-Complete Cholesky smoothing and two parameter acceleration,
(c) PCG-ICC: Pre-conditioned Congujate Gradient Method with In-Complete Cholesky Preconditioner,
(d) Direct: LDU skyline solver,
(e) Sparse Direct: The space direct solver developed by NASA.[31]

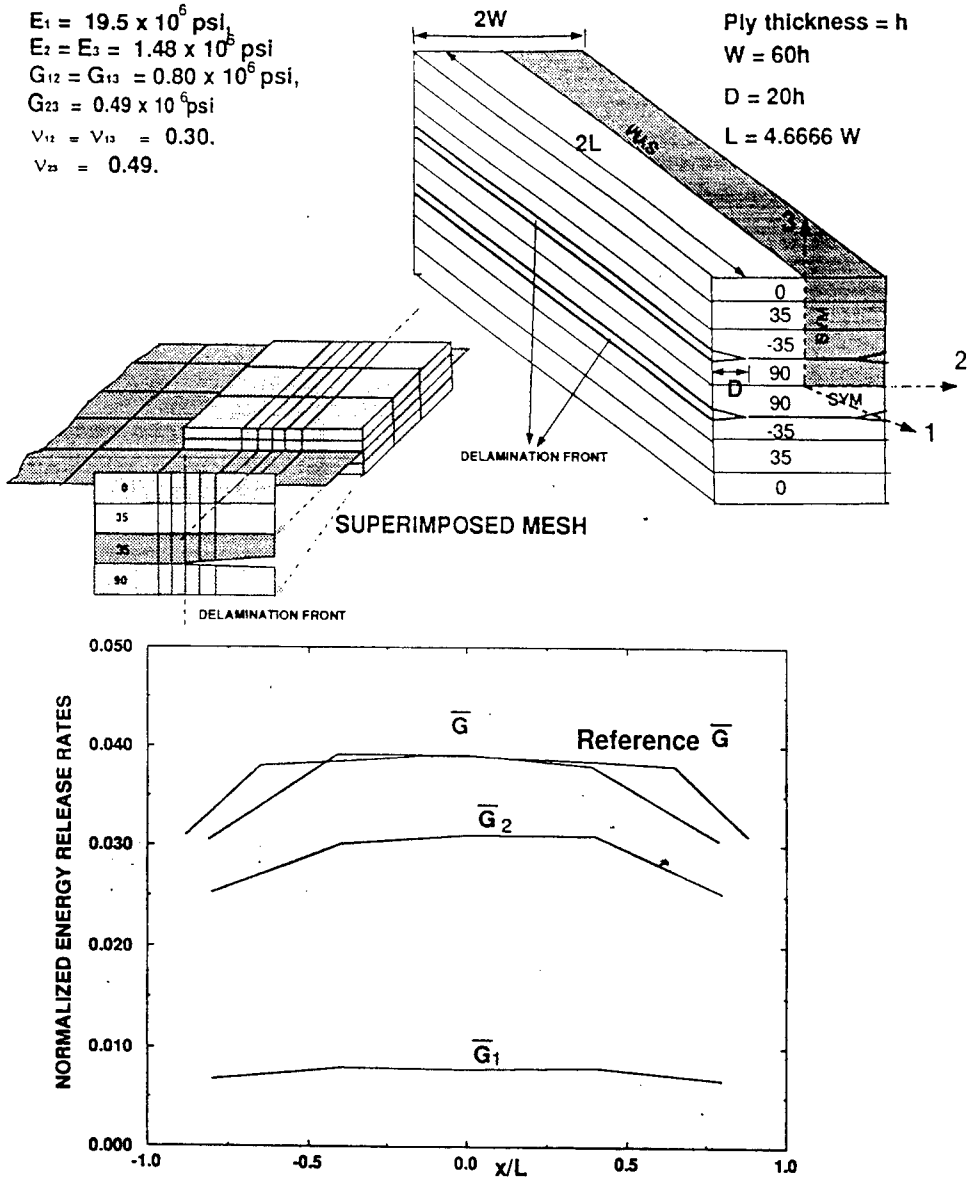


Figure 11. Edge delamination tension test

It is evident from the plot of number of degrees of freedom versus CPU time required for solution in Figure 12 that the Multigrid-like solvers have better performance for larger well conditioned systems (number of dofs > 2000) than the sparse direct solver. Amongst the MG-like solvers HBM is computationally more efficient because Incomplete Cholesky factorization of the block diagonal matrix (used for HBM-ICC smoothing) is relatively inexpensive compared to that of the entire dense matrix used for MG-ICC smoothing. For the Scordelis-lo roof problem the breakeven problem size between iterative and direct solvers moves upwards, because of poor conditioning of the stiffness matrix. The Incomplete Cholesky smoothing has been found to be superior that the Gauss Seidel smoothing in particular for poor conditioned thin domain problems. All the experiments were conducted on a Sun Sparc 10 workstation.

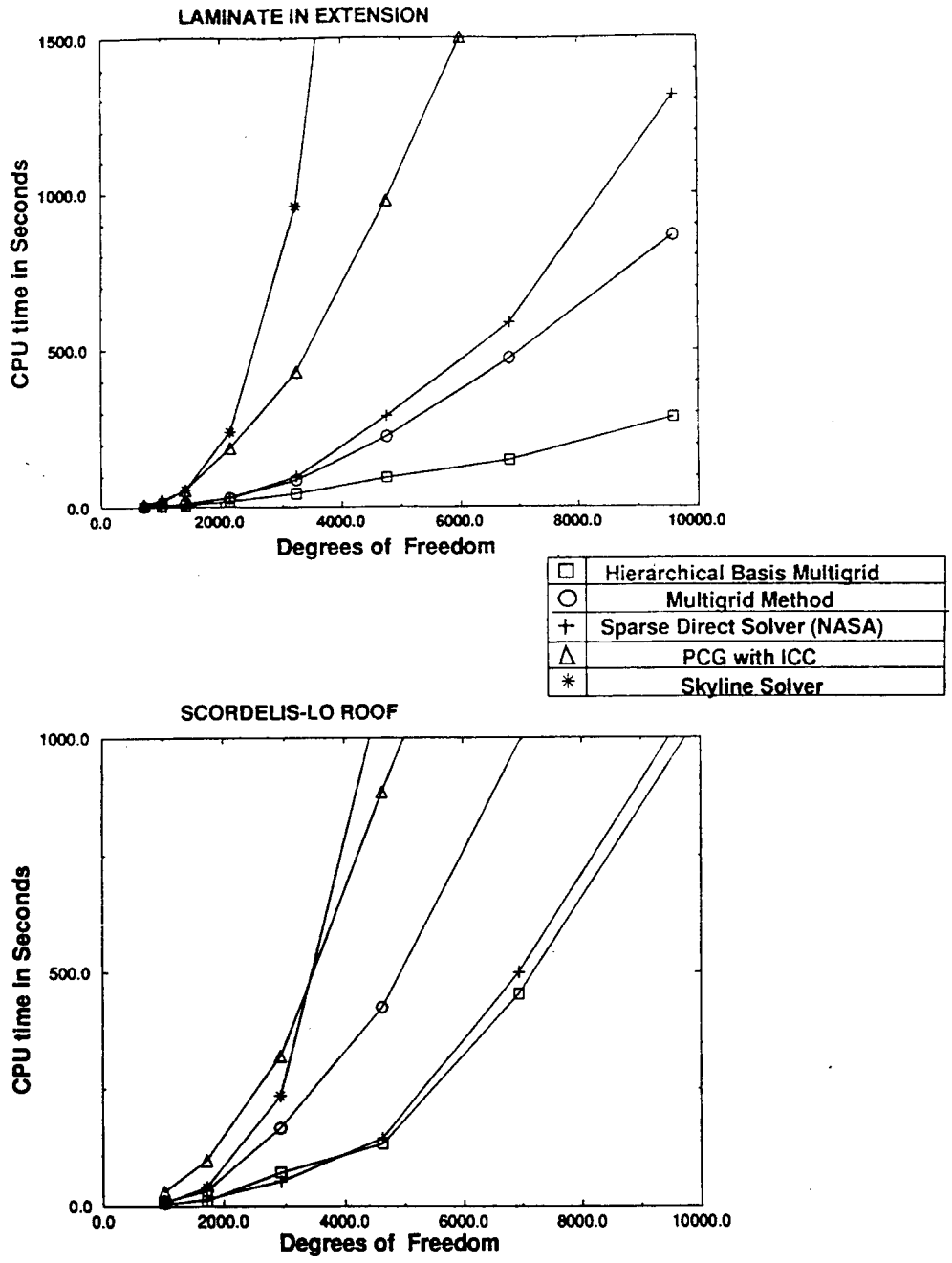


Figure 12. Comparison of solution methods for *s*-method

REFERENCES

1. J. N. Reddy and D. H. Robbins, 'Theories and computational models for composite laminates', *Appl. Mech. Rev.*, **47**, 147–169 (1994).
2. J. Fish and S. Markolefas, 'Adaptive global-local refinement strategy based on interior error estimates of the *h*-method', *Int. j. numer. methods eng.*, **37**, 828–838 (1994).
3. I. Babuska, S. Stroubulis, C. S. Upadhyay and S. K. Gangaraj, 'A posterior estimation and adaptive control of the polluting error in the *h*-version of the finite element method', *Technical note BN-1175*, Institute for Physical Science and Technology, Univ. of Maryland, College Park, MD.

4. S. F. McCormick and J. W. Thomas, 'The fast adaptive composite grid (FAC) method for elliptic equations', *Math. Comp.*, **46**, 439–456 (1986).
5. J. Bramble, R. E. Ewing, J. E. Pasciak and A. H. Schatz, 'A preconditioning technique for the efficient solution of problems with local grid refinement', *Comp. Meth. Appl. Mech. Eng.*, **67**, 149–159 (1988).
6. J. E. Flaherty, P. K. Moore and C. Ozturan, 'Adaptive overlapping methods for parabolic systems', in J. E. Flaherty, P. J. Paslow, M. S. Shephard and J. D. Vasilakis (eds.), *Adaptive Methods for Partial Differential Equations*, SIAM, Philadelphia, PA, 1989.
7. J. D. Whitcomb, 'Iterative global-local finite element analysis', *Comput. Struct.*, **40**, 1027–1031 (1991).
8. J. Fish and V. Belsky, 'Multigrid method for periodic heterogeneous media. Part 2: Multiscale modeling and quality control in multidimensional case', *Comp. Methods Appl. Mech. Eng.*, **126**, 17–38 (1995).
9. A. Brandt, 'Multi-level adaptive solutions to boundary-value problems', *Math. Comp.*, **31**, 333–390 (1977).
10. J. Fish, S. Markolefas, R. Guttal and P. Nayak, 'On adaptive multilevel superposition of finite element meshes for linear elastostatics', *Appl. Numer. Math.*, **14**, 135-164 (1994).
11. J. Fish, 'The *s*-version of the finite element method', *SCOREC report #18-1990*, Rensselaer Polytechnic Institute Troy, NY 12180; and *Comput. Struct.*, **43**, 539–547 (1990).
12. J. Fish, 'Hierarchical modeling of discontinuous fields', *Commun. appl. numer. methods*, **8**, 443–453 (1992).
13. J. Fish and S. Markolefas, 'The *s*-version of the finite element method for multi-layer laminates', *Int. j. numer. methods eng.*, **33**, 1081–1105 (1992).
14. J. Fish and R. Guttal, 'The *p*-version of finite element method for shell analysis', *Comp. Mech. Int. J.*, **16**, 1–13 (1995).
15. T. Belytschko, J. Fish and A. Bayliss, 'The spectral overlay on finite elements for problems with high gradients', *Comp. Methods Appl. Mech. Eng.*, **81**, 71–89 (1990).
16. H. Yserentant, 'On multilevel splitting of finite element spaces', *Numer. Math.*, **49**, 379–412 (1986).
17. J. Fish, V. Belsky and M. Pandheeradi, 'Composite grid method for hybrid systems', *Comp. Methods Appl. Mech. Eng.*, (1996) (accepted).
18. A. K. Noor, W. S. Burton and J. M. Peters, 'Predictor-corrector procedures for stress and free vibration analyses of multilayered composite plates and shells', *Comp. Methods Appl. Mech. Eng.*, **82**, 341–363 (1990).
19. N. F. Knight, J. B. Ransom, O. H. Griffin and D. M. Thompson, 'Global/local methods research using a common structural analysis framework', *Finite Elements Anal. Des.*, **9**, 91–112 (1991).
20. K. M. Mao and C. T. Sun, 'A refined global-local finite element analysis method', *Int. j. numer. methods eng.*, **32**, 29–43 (1991).
21. B A. Szabo and I. Babuska, *Finite element Analysis*, Wiley, New York, 1991.
22. K. C. Park and G. M. Stanley, 'A curved C^0 shell element based on assumed natural coordinate strains', *J. Appl. Mech.*, **108**, 278–290 (1986).
23. T. J. R. Hughes, *The Finite Element Method*, Prentice-Hall, Englewood Cliffs, N.J., 1987.
24. H. Hinnant, 'A fast method of numerical quadrature for *p*-version finite element matrices', *A.I.A.A.*, 1386 (1993).
25. R. E. Bank, T. F. Dupont and H. Yserentant, 'The hierarchical basis multigrid method', *Numer. Math.*, **52**, 427–458 (1988).
26. J. D. Whitcomb, I. S. Raju and J. G. Goree 'Reliability of the finite element method for calculating free edge stresses in composite laminates', *Comput. Struct.*, **15**, 23–27 (1982).
27. S. S. Wang and I. Choi, 'Boundary-layer effects in composite laminates: part 2-free-edge stress solutions and basic characteristics', *J. Appl. Mech.*, **49**, 549–560 (1982).
28. D. H. Robbins, Y. S. N. Reddy and J. N. Reddy, 'Analysis of inter-laminar stresses and failures using a layer-wise laminate theory', in J. N. Reddy and K. L. Reifsnider (eds.), *Local Mechanics Concepts for Composite Material Systems*, 1991, pp. 309–340.
29. I. S. Raju, J. H. Crews Jr. and M. A. Aminpour, 'Convergence of strain energy release rate components for edge-delaminated composite laminates, *NASA Technical Memorandum* 86135, 1987.
30. K. N. Shivakumar, P. W. Tan and J. C. Newman, 'A virtual crack closure technique for calculating stress-intensity factors for cracked three-dimensional bodies', *Int. J. Fracture*, **36**, R43–R50 (1988).
31. Olaf. Storaasli, NASA. LaRC. Hampton VA, 23681.

Computational Plasticity for Composite Structures Based on Mathematical Homogenization: Theory and Practice

Jacob Fish, Kam-Lun Shek,
Muralidharan Pandheeradi and
Mark S. Shephard

SCOREC Report #7-1996
Scientific Computation Research Center

Submitted to: *Computer Methods in Applied Mechanics and Engineering*

Scientific Computation Research Center
Rensselaer Polytechnic Institute
Troy, NY 12180-3590
voice 5182766795
fax 5182764886

Computational Plasticity for Composite Structures Based on Mathematical Homogenization: Theory and Practice

Jacob Fish, Kamlun Shek, Muralidharan Pandheeradi, Mark S. Shephard
Departments of Civil and Mechanical Engineering and
Scientific Computational Research Center
Rensselaer Polytechnic Institute
Troy, NY 12180, U.S.A.

Abstract

The paper generalizes the classical mathematical homogenization theory for heterogeneous medium to account for eigenstrains. Starting from the double scale asymptotic expansion for the displacement and eigenstrain fields we derive a close form expression relating arbitrary eigenstrains to the mechanical fields in the phases. The overall structural response is computed using an averaging scheme by which phase concentration factors are computed in the average sense for each micro-constituent, and history data is updated at two points (reinforcement and matrix) in the microstructure, one for each phase. Macroscopic history data is stored in the database and then subjected in the post-processing stage onto the unit cell in the critical locations.

For numerical examples considered, the CPU time obtained by means of the two-point averaging scheme with variational micro-history recovery was 30 seconds on SPARC 10/51 as opposed to 7 hours using classical mathematical homogenization theory. At the same time the maximum error in the microstress field in the critical unit cell was only 3.5% in comparison with the classical mathematical homogenization theory.

1 Introduction

Metal matrix composites reinforced by aligned continuous fibers may exhibit a significant amount of elastic-plastic deformation caused by plastic flow of the matrix. Although the fibers strengthen the matrix substantially, the local stress concentration caused by the presence of fibers may trigger plastic flow of the matrix at a lower overall stress level than the yield stress of the unreinforced matrix. The total strains seen in fibrous system are up to 0.01–0.02, seldom exceeding the failure strain of the fiber. Consequently, the utilization of high strength of the metal matrix composites requires a consideration of the elasto-plastic deformation primarily in the small strain regime [14].

In modeling heterogeneous media it is tempting to adopt a macroscopic point of view, which considers the composite as a homogeneous medium with anisotropic properties that have to be determined. Several authors [28] applied anisotropic yield criterion developed by Hill [22] for elasto-plastic analysis of fibrous composites. On the other hand Dvorak and Rao [14] and Lin et al. [26] have shown that Hill's anisotropic yield criterion (originally designed for metals) assuming that hydrostatic stress does not influence yielding and that there is no Bauschinger effect is not valid for fibrous composites.

Under these circumstances micromechanical analysis of composite materials, which provides the overall composite behavior from the properties of individual constituents (reinforcement and matrix) and their interaction, seems to be the only viable alternative. Most of the current micromechanical methods approximate the local fields within each phase either as uniform [1, 11, 12], or as piecewise constant [2, 3, 33]. Micromechanical approaches can be also classified into the following two categories: (i) those that require evaluation of instantaneous concentration function by solving the rate form of an inclusion or unit cell problem [1, 2, 3, 11, 12, 33], and (ii) those that require evaluation of elastic concentration function only. The latter is based on the transformation field analysis recently developed by Dvorak [9, 10]. An excellent survey of these micromechanical approaches for plasticity of fibrous composites is given in [9, 11] and references therein provide good insight into this approach.

Methods based on a multiple scale asymptotic expansion, which are parallel to micromechanical approaches for linear systems appeared in the mid 70's by the name of mathematical homogenization. The mathematical homogenization method is advantageous in the sense that it provides convergence characteristics of certain norms of interest in addition to only bounds of equivalent material properties. The fundamentals of mathematical homogenization theory can be found, among others, in [5, 21, 29]. Various higher order mathematical homogenization theories and their finite element application were described in [17, 19]. A variant of the classical mathematical homogenization that abandons the classical hypothesis of uniformity of the macroscopic fields within the unit cell domain has been developed in [15, 16]. By this approach the solutions obtained from the mathematical homogenization theory are only used to simulate the global response of the discrete heterogeneous medium, whereas the classical relaxation techniques are employed to capture the oscillatory response.

For small deformation plasticity a mathematical homogenization theory has been established by Suquet [31, 32]. Finite element application issues were addressed in [20]. In these attempts the uncoupling of scales was carried out for a linearized system in a similar fashion to that of the linear problem. References [2, 3, 33] represent the micromechanical approaches parallel to the mathematical homogenization for plasticity [20, 31, 32] in terms of the formulation and computational complexity involved.

One of the objectives of the present work is to develop a mathematical homogenization theory with eigenstrains — a counterpart to the micromechanical approach based on the transformation field analysis recently developed by Dvorak [9, 10]. In Section 2.1 we derive a closed form expression relating arbitrary transformation fields to mechanical fields in the

phases, which for the case of piecewise constant transformation fields reduce to the form derived by Dvorak [8] on the basis of the uniform fields concept. This is followed by the derivation of return mapping stress update procedures in Section 2.3 and consistent tangent operators for heterogeneous systems in Section 2.4.

From the practical stand point, solution of large scale nonlinear structural systems with accurate resolution of microstructural fields is not yet feasible. For linear problems a unit cell or a representative volume problem has to be solved only once, whereas for nonlinear history dependent systems it has to be solved at every increment and for each macroscopic (Gauss) point. Furthermore, history data has to be updated at a number of integration points equal to the number of Gauss points in the macro problem multiplied by the number of Gauss points in the unit cell. To illustrate the computational complexity involved we consider elasto-plastic analysis of the composite (titanium matrix) flap problem shown in Figure 1a. The macrostructure is discretized with 788 tetrahedral elements (993 degrees of freedom), whereas microstructure, as shown in Figure 1b, is discretized with 98 elements in the reinforcement domain and 253 in the matrix domain, totaling 330 degrees of freedom. The CPU time on SPARC 10/51 for this problem was 7 hours, as opposed to 10 seconds if metal plasticity was used instead, which means that 99.96% of CPU time is spent on stress updates. Under these circumstances it seems that the statement made by Hill [23] that " ... for non-linear systems, the computations needed to establish any constitutive law are formidable indeed ... " is still valid almost 30 years later.

The second objective of the present work is to device an efficient computational scheme that will enable to solve large scale structural systems in heterogeneous media at a cost comparable to problems in homogeneous media without significantly compromising on solution accuracy. The proposed computational procedure consists of the following three steps:

- Compute the overall structural response using two-point mathematical homogenization scheme with eigenstrains (Section 2) by which the concentration factors are computed in the average sense for each phase, i.e. history data is updated only at two points (reinforcement and matrix) in the microstructure, one for each phase.
- Store the history of macroscopic fields in the database.
- Post-process the microscopic solution (Section 3) by subjecting the unit cell to the macroscopic solution history in the critical locations.

Numerical experiments conducted in Section 6 indicate that when the proposed computational scheme is combined with the state of the art solution technique for large scale nonlinear system [18] one can solve large scale nonlinear structural systems in range of 60,000–90,000 unknowns in less than 3 hours of CPU time on SUN SPARC station 10/51.

Throughout this paper, we will use boldface letters to represent vectors and matrices and lightface letters to scalar quantities or tensor components. Besides, Einstein's summation convention for repeated indexes is assumed unless indicated explicitly. In the contracted

notation the indexes confirm with the definition $11 \equiv 1$, $22 \equiv 2$, $33 \equiv 3$, $12 \equiv 4$, $13 \equiv 5$ and $23 \equiv 6$. Strain and eigenstrain vectors are with engineering components; stress and back stress vectors are with tensor components. $\mathbf{A}^T$ and $\mathbf{A}^{-1}$ denote the transpose and inverse of matrix $\mathbf{A}$, respectively.

2 Mathematical Homogenization with Eigenstrain

In this section, we generalize the classical mathematical homogenization theory [4, 5] for heterogeneous medium to account for eigenstrains. We will regard all inelastic strains as eigenstrains in an otherwise elastic body. Attention will be limited to small deformations.

The microstructure of a composite is assumed to be periodic (Y-periodic) so that the homogenization process can be performed in a unit cell domain, denoted by Θ. This implies that all the response functions, such as displacement and stress, are also periodic with periods proportional to the ratio of the characteristic lengths, ε, between the micro representative volume element and the macroscopic structure. Let $\boldsymbol{x}$ be a macroscopic co-ordinate vector and $\boldsymbol{y} \equiv \boldsymbol{x}/\varepsilon$ be a microscopic position vector. For any periodic response function f, we have $f(\boldsymbol{x}, \boldsymbol{y}) = f(\boldsymbol{x}, \boldsymbol{y} + \boldsymbol{k}\boldsymbol{Y})$ in which vector $\boldsymbol{Y}$ is the basic period of the microstructure and $\boldsymbol{k}$ is a 3 by 3 diagonal matrix with components of any finite integers. Adopting classical nomenclature any Y-periodic function f can be represented as

$$f^{\varepsilon}(\boldsymbol{x}) \equiv f(\boldsymbol{x}, \boldsymbol{y}(\boldsymbol{x}))$$

where superscript ε denotes that the corresponding function f is Y-periodic and is a function of macroscopic spatial variables. The indirect macroscopic spatial derivatives of f^{ε} can be calculated by the chain rule as

$$f^{\varepsilon}_{,x_i}(\boldsymbol{x}) = f_{,x_i}(\boldsymbol{x}, \boldsymbol{y}) + \frac{1}{\varepsilon} f_{,y_i}(\boldsymbol{x}, \boldsymbol{y}) \tag{1}$$

where subscripts followed by a comma denote partial derivatives with respect to the subscript variables (i.e. $f_{,x_i} = \partial f / \partial x_i$).

In Section 2.1 we will derive closed form expressions relating arbitrary eigenstrains to mechanical fields as well as to the overall eigenstrain in a multi-phase composite medium.

2.1 Formulation for Multi-Phase Composite Medium

In modeling a heterogeneous medium, micro-constituents are assumed to possess homogeneous properties and satisfy equilibrium, constitutive, kinematics and compatibility equations as well as jump conditions on the interface boundary between the micro-phases. The

corresponding boundary value problem is governed by the following equations.

$$\sigma^\varepsilon_{ij,x_j} + b_i = 0 \quad \text{in} \quad \Omega \quad \text{(equilibrium equations)} \tag{2}$$
$$\sigma^\varepsilon_{ij} = \mathrm{L}_{ijkl}(\epsilon^\varepsilon_{kl} - \mu^\varepsilon_{kl}) \quad \text{in} \quad \Omega \quad \text{(constitutive equations)} \tag{3}$$
$$\epsilon^\varepsilon_{ij} = u^\varepsilon_{(i,x_j)} \quad \text{in} \quad \Omega \quad \text{(kinematic equations)} \tag{4}$$
$$u^\varepsilon_i = \bar{u}_i \quad \text{on} \quad \Gamma_u \quad \text{(displacement boundary conditions)} \tag{5}$$
$$\sigma^\varepsilon_{ij} n_j = \bar{t}_i \quad \text{on} \quad \Gamma_t \quad \text{(traction boundary conditions)} \tag{6}$$

in which σ^ε_{ij}, $\epsilon^\varepsilon_{ij}$ are stress and strain tensors; L_{ijkl} and μ^ε_{ij} are elastic stiffness and eigenstrain tensors, respectively: b_i is a body force; u_i denotes a displacement vector; the subscript pair with parenthesis denotes the symmetric gradient defined as $u^\varepsilon_{(i,x_j)} = (u^\varepsilon_{i,x_j} + u^\varepsilon_{j,x_i})/2$; Ω is the macroscopic domain of interest with boundary Γ; Γ_u and Γ_t are prescribed displacement and traction non-intersected boundary portions such that $\Gamma_u \cup \Gamma_t = \Gamma$; $\bar{u}_i$ and $\bar{t}_i$ are prescribed displacements on Γ_u and traction on Γ_t; n_i denotes the normal vector on Γ. Here we assume that the interface between the phases is perfectly bonded, i.e. $\lfloor \sigma^\varepsilon_{ij} \hat{n}_j \rfloor = 0$ and $\lfloor u^\varepsilon_i \rfloor = 0$ on the interface boundary Γ_{int} where $\hat{n}_j$ is the normal vector on Γ_{int} and $\lfloor \bullet \rfloor$ is a jump operator.

The displacement $u^\varepsilon_i(\boldsymbol{x})$ and eigenstrain $\mu^\varepsilon_{ij}(\boldsymbol{x})$ are then replaced by $u_i(\boldsymbol{x}, \boldsymbol{y})$ and $\mu_{ij}(\boldsymbol{x}, \boldsymbol{y})$ and approximated by the corresponding double scale asymptotic expansions:

$$u_i(\boldsymbol{x}, \boldsymbol{y}) \approx u^0_i(\boldsymbol{x}, \boldsymbol{y}) + \varepsilon u^1_i(\boldsymbol{x}, \boldsymbol{y}) + \cdots \tag{7}$$
$$\mu_{ij}(\boldsymbol{x}, \boldsymbol{y}) \approx \mu^0_{ij}(\boldsymbol{x}, \boldsymbol{y}) + \varepsilon \mu^1_{ij}(\boldsymbol{x}, \boldsymbol{y}) + \cdots \tag{8}$$

Expansion for strain tensor can be obtained by substituting (7) into (4) with consideration of the indirect differentiation rule (1)

$$\epsilon_{ij}(\boldsymbol{x}, \boldsymbol{y}) \approx \frac{1}{\varepsilon} \epsilon^{-1}_{ij}(\boldsymbol{x}, \boldsymbol{y}) + \epsilon^0_{ij}(\boldsymbol{x}, \boldsymbol{y}) + \varepsilon \epsilon^1_{ij}(\boldsymbol{x}, \boldsymbol{y}) + \cdots \tag{9}$$

in which the strain tensor for various orders of ε is given as

$$\begin{aligned} \epsilon^{-1}_{ij} &= \epsilon_{ijy}(\boldsymbol{u}^0) \\ \epsilon^s_{ij} &= \epsilon_{ijx}(\boldsymbol{u}^s) + \epsilon_{ijy}(\boldsymbol{u}^{s+1}), \quad s = 0, 1, \cdots \end{aligned} \tag{10}$$

where

$$\epsilon_{ijx}(\boldsymbol{u}^s) = u^s_{(i,x_j)}, \qquad \epsilon_{ijy}(\boldsymbol{u}^s) = u^s_{(i,y_j)}$$

The stress and strain tensors for different $O(\varepsilon^s)$ are related by the constitutive rules (3)

$$\begin{aligned} \sigma^{-1}_{ij} &= \mathrm{L}_{ijkl} \epsilon^{-1}_{kl} \\ \sigma^s_{ij} &= \mathrm{L}_{ijkl}(\epsilon^s_{kl} - \mu^s_{kl}), \qquad s = 0, 1, \cdots \end{aligned} \tag{11}$$

and thus the stress tensor can be written as

$$\sigma_{ij}(\boldsymbol{x}, \boldsymbol{y}) \approx \frac{1}{\varepsilon} \sigma^{-1}_{ij}(\boldsymbol{x}, \boldsymbol{y}) + \sigma^0_{ij}(\boldsymbol{x}, \boldsymbol{y}) + \varepsilon \sigma^0_{ij}(\boldsymbol{x}, \boldsymbol{y}) + \cdots \tag{12}$$

Inserting the stress tensor asymptotic expansion (12) into equilibrium equations (2) and making the use of (1) yields the following equilibrium equations for various orders

$$O(\varepsilon^{-2}) \quad : \quad \sigma^{-1}_{ij,y_j} = 0 \tag{13}$$

$$O(\varepsilon^{-1}) \quad : \quad \sigma^{-1}_{ij,x_j} + \sigma^{0}_{ij,y_j} = 0 \tag{14}$$

$$O(\varepsilon^{0}) \quad : \quad \sigma^{0}_{ij,x_j} + \sigma^{1}_{ij,y_j} + b_i = 0 \tag{15}$$

$$O(\varepsilon^{s}) \quad : \quad \sigma^{s}_{ij,x_j} + \sigma^{s+1}_{ij,y_j} = 0, \qquad s = 1, 2, \cdots \tag{16}$$

Consider the $O(\varepsilon^{-2})$ equilibrium equations (13) first. Pre-multiplying it by u^0_i and integrating over a unit cell domain Θ yields

$$\int_{\Theta} u^0_i \sigma^{-1}_{ij,y_j} d\Theta = 0$$

and subsequent integration by parts results in

$$\int_{\Gamma_\Theta} u^0_i \sigma^{-1}_{ij} n_j \, d\Gamma_\Theta - \int_{\Theta} u^0_{(i,y_j)} \mathrm{L}_{ijkl} u^0_{(k,y_l)} \, d\Theta = 0$$

in which Γ_Θ denotes the boundary of Θ. The boundary integral term in the above equation vanishes due to the periodicity of boundary conditions on Γ_Θ. Since the elastic stiffness tensor L_{ijkl} is positive definite, we have

$$u^0_{(i,y_j)} = 0 \quad \Longrightarrow \quad u^0_i = u^0_i(\boldsymbol{x})$$

Next, we proceed to the $O(\varepsilon^{-1})$ equilibrium equations (14). From equations (11,10) follows

$$\Big(\mathrm{L}_{ijkl} \Big(\epsilon_{klx}(\boldsymbol{u}^0) + \epsilon_{kly}(\boldsymbol{u}^1) - \mu^0_{kl} \Big) \Big)_{,y_j} = 0 \quad \text{on} \quad \Theta \tag{17}$$

To solve for equation (17) up to a constant we introduce the following separation of variables

$$u^1_i(\boldsymbol{x}, \boldsymbol{y}) = \mathrm{H}_{imn}(\boldsymbol{y}) \left(\epsilon_{mnx}(\boldsymbol{u}^0) + d^{\mu}_{mn}(\boldsymbol{x}) \right)$$

in which H_{imn} is a Y-periodic function with symmetry on indexes m and n, d^{μ}_{mn} is a macroscopic portion of the solution resulting from eigenstrains, i.e. if $\mu^0_{ij}(\boldsymbol{x}, \boldsymbol{y}) = 0$ then $d^{\mu}_{mn}(\boldsymbol{x}) = 0$. With this form of u^1_i we rewrite $O(\varepsilon^{-1})$ equilibrium equation (17) as

$$\Big(\mathrm{L}_{ijkl} \left(\left(\delta_{km}\delta_{ln} + \Psi_{klmn} \right) \epsilon_{mnx}(\boldsymbol{u}^0) + \Psi_{klmn} d^{\mu}_{mn} - \mu^0_{kl} \right) \Big)_{,y_j} = 0 \tag{18}$$

where

$$\Psi_{klmn}(\boldsymbol{y}) = \mathrm{H}_{(k,y_l)mn}(\boldsymbol{y})$$

and δ_{km} is the Kronecker delta. Since equation (18) is satisfied for arbitrary macroscopic strain field $\epsilon_{mnx}(\boldsymbol{u}^0)$, and eigenstrain field μ^0_{ij}, one may first consider $\mu^0_{kl} \equiv 0$, $\epsilon_{mnx}(\boldsymbol{u}^0) \neq 0$

and then $\epsilon_{mnx}(\boldsymbol{u}^0) \equiv 0$. $\mu^0_{kl} \neq 0$ which yields the following two governing equations in a unit cell domain

$$\left(\mathrm{L}_{ijkl}(\delta_{km}\delta_{ln} + \Psi_{klmn})\right)_{,y_j} = 0 \tag{19}$$

$$(\mathrm{L}_{ijkl}\Psi_{klmn})_{,y_j} d^{\mu}_{mn} - (\mathrm{L}_{ijkl}\mu^0_{kl})_{,y_j} = 0 \tag{20}$$

Equation (19) is the standard linear unit cell equation [5] subjected to periodic boundary conditions that can be solved in Θ. Finite element method can be used for solving this problem [19, 21]. In absence of eigenstrains, $\epsilon_{klx}(\boldsymbol{u}^0)$ is related to the total strain by

$$\epsilon_{kl} = \mathrm{A}_{klmn}\epsilon_{mnx}(\boldsymbol{u}^0) + O(\varepsilon)$$

where

$$\mathrm{A}_{klmn} = \frac{1}{2}(\delta_{km}\delta_{ln} + \delta_{kn}\delta_{lm}) + \Psi_{klmn}$$

A_{klmn} is often referred to as elastic strain concentration function. It should be noted that A_{klmn} and Ψ_{klmn} possess minor symmetry such that $\mathrm{A}_{klmn} = \mathrm{A}_{lkmn} = \mathrm{A}_{klnm}$ and $\Psi_{klmn} = \Psi_{lkmn} = \Psi_{klnm}$, but not the major symmetry in general. The elastic homogenized stiffness tensor $\bar{\mathrm{L}}_{ijkl}$ follows from $O(\varepsilon^0)$ equilibrium equation [17]

$$\bar{\mathrm{L}}_{ijkl} \equiv \frac{1}{|\Theta|}\int_{\Theta} \mathrm{L}_{ijmn}\mathrm{A}_{mnkl}\, d\Theta = \frac{1}{|\Theta|}\int_{\Theta} \mathrm{A}_{mnij}\mathrm{L}_{mnst}\mathrm{A}_{stkl}\, d\Theta \tag{21}$$

in which $|\Theta|$ is the volume of a unit cell.

In the following derivations, we will adopt matrix notation. The matrix representation of Ψ_{klmn} is given as

$$\boldsymbol{\Psi} = \begin{pmatrix} \Psi_{1111} & \Psi_{1122} & \Psi_{1133} & \Psi_{1112} & \Psi_{1113} & \Psi_{1123} \\ \Psi_{2211} & \Psi_{2222} & \Psi_{2233} & \Psi_{2212} & \Psi_{2213} & \Psi_{2223} \\ \Psi_{3311} & \Psi_{3322} & \Psi_{3333} & \Psi_{3312} & \Psi_{3313} & \Psi_{3323} \\ 2\Psi_{1211} & 2\Psi_{1222} & 2\Psi_{1233} & 2\Psi_{1212} & 2\Psi_{1213} & 2\Psi_{1223} \\ 2\Psi_{1311} & 2\Psi_{1322} & 2\Psi_{1333} & 2\Psi_{1312} & 2\Psi_{1313} & 2\Psi_{1323} \\ 2\Psi_{2311} & 2\Psi_{2322} & 2\Psi_{2333} & 2\Psi_{2312} & 2\Psi_{2313} & 2\Psi_{2323} \end{pmatrix}$$

The stiffness matrix $\mathbf{L}$ is arranged similarly although it does not have the multiplier two in the last three rows. The strain concentration function can be written in matrix notation as follows

$$\mathbf{A} = \mathbf{I} + \boldsymbol{\Psi}$$

where $\mathbf{I}$ is a 6 by 6 identity matrix.

After solving equation (19) for $\boldsymbol{\Psi}$, we now proceed to equation (20) for finding $\boldsymbol{d}^{\mu}$ subjected to periodic boundary conditions. Pre-multiplying (20) by H_{ist} and then integrating the resulting equation by parts with consideration to the periodic boundary conditions yields

$$\int_{\Theta} \boldsymbol{\Psi}^T\mathbf{L}\left(\boldsymbol{\Psi}\boldsymbol{d}^{\mu} - \boldsymbol{\mu}^0\right) d\Theta = 0$$

Rewriting this equation in terms of strain concentration function $\mathbf{A}$ and manipulating it with equation (21) yields

$$\boldsymbol{d}^{\mu} = \frac{1}{|\Theta|}(\tilde{\mathbf{L}} - \bar{\mathbf{L}})^{-1} \int_{\Theta} \boldsymbol{\Psi}^T \mathbf{L} \boldsymbol{\mu}^0 \, d\Theta \tag{22}$$

where

$$\tilde{\mathbf{L}} = \frac{1}{|\Theta|} \int_{\Theta} \mathbf{L} \, d\Theta$$

and thus the $O(\varepsilon^0)$ approximation to asymptotic strain field (9) reduces to

$$\boldsymbol{\epsilon} = \mathbf{A} \boldsymbol{\epsilon}_x(\boldsymbol{u}^0) + \boldsymbol{\Psi} \boldsymbol{d}^{\mu} + O(\varepsilon) \tag{23}$$

Let $\boldsymbol{\psi} \equiv \{\psi_\eta(\boldsymbol{y})\}_1^{N_e}$ be a set of C^{-1} continuous functions, then the separation of variables for eigenstrains is assumed to have the following decomposition:

$$\boldsymbol{\mu}^0(\boldsymbol{x}, \boldsymbol{y}) = \sum_{\eta=1}^{N_e} \psi_\eta(\boldsymbol{y}) \, \boldsymbol{\mu}_\eta^0(\boldsymbol{x})$$

The resulting asymptotic expansion of the strain field (9) can be expressed as follows

$$\boldsymbol{\epsilon}(\boldsymbol{x}, \boldsymbol{y}) = \mathbf{A}(\boldsymbol{y}) \, \boldsymbol{\epsilon}_x(\boldsymbol{u}^0) + \sum_{\eta=1}^{N_e} \mathbf{D}_\eta(\boldsymbol{y}) \, \boldsymbol{\mu}_\eta^0(\boldsymbol{x}) + O(\varepsilon) \tag{24}$$

in which $\mathbf{D}_\eta(\boldsymbol{y})$ are the eigenstrain influence functions given in terms of strain concentration function $\boldsymbol{\Psi}(\boldsymbol{y})$ as follows

$$\mathbf{D}_\eta(\boldsymbol{y}) = \frac{1}{|\Theta|} \boldsymbol{\Psi} \, (\tilde{\mathbf{L}} - \bar{\mathbf{L}})^{-1} \int_{\Theta} \boldsymbol{\Psi}^T \, \mathbf{L} \, \psi_\eta \, d\Theta \tag{25}$$

In particular, if $\boldsymbol{\psi}$ is a set of piecewise constant functions such that

$$\psi_\eta(\boldsymbol{y}_\rho) = \begin{cases} 1 & \text{if } \boldsymbol{y}_\rho \in \Theta_\eta \\ 0 & \text{otherwise} \end{cases} \tag{26}$$

and Θ_η is the domain of element η within the unit cell, c_η the element volume fraction given by $c_\eta \equiv |\Theta_\eta|/|\Theta|$ and satisfying $\sum_\eta c_\eta = 1$, then equation (25) reduces to the expression given in [8]

$$\mathbf{D}_{\rho\eta} = c_\eta \boldsymbol{\Psi}_\rho (\tilde{\mathbf{L}} - \bar{\mathbf{L}})^{-1} \boldsymbol{\Psi}_\eta^T \mathbf{L}_\eta \tag{27}$$

in which

$$\mathbf{D}_{\rho\eta} = \frac{1}{|\Theta_\rho|} \int_{\Theta_\rho} \mathbf{D}_\eta \, d\Theta, \qquad \boldsymbol{\Psi}_\rho = \frac{1}{|\Theta_\rho|} \int_{\Theta_\rho} \boldsymbol{\Psi} \, d\Theta$$

Finally we consider $O(\varepsilon^0)$ equilibrium equation (15) and integrate it over Θ. The $\int_\Theta \sigma^1_{ij,y_j} d\Theta$ term vanishes due to periodicity and we obtain

$$\left(\frac{1}{|\Theta|}\int_\Theta \sigma^0_{ij}\, d\Theta\right)_{,x_j} + b_i = 0 \quad \text{on} \quad \Omega$$

Substituting the constitutive relation (11) and the asymptotic expansion of strain tensor (23) into the above equation yields

$$\left(\frac{1}{|\Theta|}\int_\theta \mathrm{L}_{ijkl}\left(\mathrm{A}_{klmn}\epsilon_{mnx}(u^0) + \Psi_{klmn}d^\mu_{mn} - \mu^0_{kl}\right) d\Theta\right)_{,x_j} + b_i = 0 \tag{28}$$

If we define the macroscopic stress tensor $\bar{\sigma}_{ij}$ and corresponding macroscopic strain tensor $\bar{\epsilon}_{ij}$ as

$$\bar{\sigma}_{ij} = \frac{1}{|\Theta|}\int_\Theta \sigma^0_{ij}\, d\Theta, \qquad \bar{\epsilon}_{ij} = \epsilon_{ijx}(\boldsymbol{u}^0) \tag{29}$$

then the equilibrium equation (28) can be simplified as follows

$$\bar{\sigma}_{ij,x_j} + b_i = 0 \qquad \text{or} \qquad \bar{\mathrm{L}}_{ijkl}\left(\bar{\epsilon}_{kl} - \bar{\mu}_{kl}\right)_{,x_j} + b_i = 0$$

where $\bar{\boldsymbol{\mu}}$ is the overall eigenstrain tensor given by

$$\bar{\boldsymbol{\mu}} = -\frac{1}{|\Theta|}\bar{\mathbf{L}}^{-1}\int_\Theta \mathbf{L}(\boldsymbol{\Psi}\boldsymbol{d}^\mu - \boldsymbol{\mu}^0)\, d\Theta$$

Replacing $\boldsymbol{\Psi}$ by $\mathbf{A} - \mathbf{I}$ and manipulating the above equation with equations (21) and (22), the expression for overall eigenstrain field can be simplified as

$$\bar{\boldsymbol{\mu}} = \frac{1}{|\Theta|}\int_\Theta \mathbf{B}^T\boldsymbol{\mu}^0\, d\Theta, \qquad \mathbf{B}(\boldsymbol{y}) = \mathbf{L}(\boldsymbol{y})\mathbf{A}(\boldsymbol{y})\bar{\mathbf{L}}^{-1} \tag{30}$$

Equation (30) represents the well-known Levin's formula [25] relating the local and overall eigenstrains in which $\mathbf{B}(\boldsymbol{y})$ is often referred to as elastic stress concentration function.

2.2 Two-Point Averaging Scheme for Two-Phase Composite Medium

Consider a composite medium consisting of two phases, matrix and reinforcement, with respective volume fractions c_m and c_f such that $c_m + c_f = 1$, where subscripts m and f represent matrix and reinforcement phases, respectively. In this section, we develop a fast computational scheme by which only the overall structural response is sought, whereas local fields are computed by post-processing which will be presented in Section 4. For this purpose, we will define average phase concentration factors as

$$\mathbf{A}_m = \frac{1}{|\Theta_m|}\int_{\Theta_m} \mathbf{A}\, d\Theta, \qquad \mathbf{A}_f = \frac{1}{|\Theta_f|}\int_{\Theta_f} \mathbf{A}\, d\Theta \tag{31}$$

where Θ_m and Θ_f denote the matrix and reinforcement domains such that $\Theta_m \cup \Theta_f = \Theta$. Since the elastic stiffness of each phase is constant, the overall elastic material properties are given by

$$\bar{\mathbf{L}} = c_m \mathbf{L}_m \mathbf{A}_m + c_f \mathbf{L}_f \mathbf{A}_f$$

Furthermore, in a two-phase composite with uniform phase eigenstrains, i.e. $\boldsymbol{\psi} = \lfloor \psi_m, \psi_f \rfloor^T$ and ψ_m, ψ_f defined as in (26), under assumption of $\varepsilon \to 0$ the average phase strains can be written, in analogue to (24), as

$$\boldsymbol{\epsilon}_r = \mathbf{A}_r \bar{\boldsymbol{\epsilon}} + \mathbf{D}_{rm} \boldsymbol{\mu}_m + \mathbf{D}_{rf} \boldsymbol{\mu}_f, \qquad r = m, f \tag{32}$$

The resulting eigenstrain influence factors reduce to

$$\begin{aligned} \mathbf{D}_{rm} &= (\mathbf{I} - \mathbf{A}_r)(\mathbf{L}_m - \mathbf{L}_f)^{-1} \mathbf{L}_m \\ \mathbf{D}_{rf} &= (\mathbf{I} - \mathbf{A}_r)(\mathbf{L}_f - \mathbf{L}_m)^{-1} \mathbf{L}_f, \qquad r = m, f \end{aligned} \tag{33}$$

where the following relations have been used

$$\lim_{\varepsilon \to 0} (c_m \mathbf{A}_m + c_f \mathbf{A}_f) = \mathbf{I}, \qquad \tilde{\mathbf{L}} = \bar{\mathbf{L}}^T, \qquad \bar{\mathbf{L}} = \bar{\mathbf{L}}^T$$

These results are identical to those obtained by Dvorak in [8] based on a uniform fields concept. Finally, for the two-phase composite, equation (29a) reduces to

$$\bar{\boldsymbol{\sigma}} = c_m \boldsymbol{\sigma}_m + c_f \boldsymbol{\sigma}_f \tag{34}$$

2.3 Implicit Integration of the Constitutive Equations

Since the plastic strains (or, equivalently the relaxation stresses) are nonlinear function of stresses (or strains), it is necessary to integrate the constitutive equations along the prescribed loading path in order to obtain the current stress state. It is possible to advance the solution through the plastic deformation process by adopting a simple explicit integration scheme that uses instantaneous compliance/stiffness of the phases and instantaneous stress concentration factors. This approach has been used in [9] for certain assumed yield function, flow rule and hardening laws for multi-phase systems.

Explicit schemes usually require small time or load steps. In this section we present simple, computationally efficient implicit procedures for the elasto-plastic stress updates for two-phase composite media. We assume general anisotropic reinforcement material which remains elastic throughout the loading history, and elasto-plastic matrix phase with isotropic elastic properties and following von Mises yield function with a linear combination of isotropic and kinematic hardening.

We assume an elastic reinforcement, i.e. $\boldsymbol{\mu}_f = 0$, and a single source of eigenstrain due to matrix plasticity, denoted by $\boldsymbol{\mu}_m$. Combining (3) and (32) one obtains the following relations for matrix and reinforcement stresses:

$$\boldsymbol{\sigma}_r = \mathbf{R}_r \bar{\boldsymbol{\epsilon}} - \mathbf{Q}_{rm} \boldsymbol{\mu}_m, \qquad r = m, f \tag{35}$$

where

$$\mathbf{R}_r = \mathbf{L}_r \mathbf{A}_r, \qquad \mathbf{Q}_{rm} = \mathbf{L}_r (\delta_{rm} \mathbf{I} - \mathbf{D}_{rm}), \qquad r = m, f \tag{36}$$

Consider the yield function of the following form:

$$\Phi_m(\boldsymbol{\sigma}_m, \boldsymbol{\alpha}_m, \hat{\sigma}_m) \equiv \frac{1}{2}(\boldsymbol{\sigma}_m - \boldsymbol{\alpha}_m)^T \mathbf{P} (\boldsymbol{\sigma}_m - \boldsymbol{\alpha}_m) - \frac{1}{3}\hat{\sigma}_m^2 = 0 \tag{37}$$

where $\hat{\sigma}_m$ is the yield stress of the matrix material in uniaxial test, which evolves according to the hardening laws assumed. $\boldsymbol{\alpha}_m$ corresponds to the center of the yield surface in the deviatoric stress space, also called "back stress". Evolution of $\boldsymbol{\alpha}_m$ is assumed to follow the kinematic hardening rule. For von Mises plasticity $\mathbf{P}$ is defined as follows:

$$\mathbf{P} = \hat{\mathbf{P}}^T \mathbf{T} \hat{\mathbf{P}}, \qquad \hat{\mathbf{P}} = \frac{1}{3} \begin{pmatrix} 2 & -1 & -1 & 0 & 0 & 0 \\ -1 & 2 & -1 & 0 & 0 & 0 \\ -1 & -1 & 2 & 0 & 0 & 0 \\ 0 & 0 & 0 & 3 & 0 & 0 \\ 0 & 0 & 0 & 0 & 3 & 0 \\ 0 & 0 & 0 & 0 & 0 & 3 \end{pmatrix}$$

in which $\mathbf{T}$ is a 6 by 6 diagonal matrix with 1 in the first three locations and 2 in the remaining three locations; $\hat{\mathbf{P}}$ is a projection operator satisfying $\hat{\mathbf{P}} = \hat{\mathbf{P}}\hat{\mathbf{P}}$ and $\mathbf{P} = \mathbf{P}\hat{\mathbf{P}} = \hat{\mathbf{P}}\mathbf{P}$, which transforms a vector from non-deviatoric space to deviatoric space.

For simplicity we assume that matrix plastic strain rate follows the associative flow rule:

$$\dot{\boldsymbol{\mu}}_m = \dot{\lambda}_m \frac{\partial \Phi_m}{\partial \boldsymbol{\sigma}_m} = \dot{\lambda}_m \boldsymbol{\mathcal{N}}_m, \qquad \boldsymbol{\mathcal{N}}_m = \mathbf{P}(\boldsymbol{\sigma}_m - \boldsymbol{\alpha}_m) \tag{38}$$

We adopt a modified version of the hardening evolution law [24] in the context of isotropic, homogeneous, elasto-plastic matrix phase. A scalar, material dependent parameter β ($0 \leq \beta \leq 1$) is used as a measure of the proportion of isotropic and kinematic hardening and λ_m is a plastic parameter determined by the consistency condition. Accordingly, the evolution of the yield stress $\hat{\sigma}_m$ and the back stresses $\boldsymbol{\alpha}_m$ can be expressed in the following rate forms:

$$\dot{\hat{\sigma}}_m = \frac{2}{3}\dot{\lambda}_m \beta H \hat{\sigma}_m, \qquad \dot{\boldsymbol{\alpha}}_m = \frac{2}{3}\dot{\lambda}_m (1-\beta) H \hat{\mathbf{P}}(\boldsymbol{\sigma}_m - \boldsymbol{\alpha}_m) \tag{39}$$

While $\beta = 0$ refers to pure isotropic hardening, $\beta = 1$ is merely the widely used Ziegler-Prager kinematic hardening rule [34] for metals without isotropic hardening. H is a hardening parameter defined as the ratio between effective stress rate to effective plastic strain rate.

Other laws for kinematic hardening have also been proposed in the literature, for instance [6, 27].

Integration of (38.39) is carried out by the backward Euler scheme:

$$
\begin{aligned}
{}^{i}\boldsymbol{\mu}_m &= {}^{i-1}\boldsymbol{\mu}_m + {}^{i}\Delta\lambda_m \mathbf{P}({}^{i}\boldsymbol{\sigma}_m - {}^{i}\boldsymbol{\alpha}_m) && (40)\\
{}^{i}\hat{\sigma}_m &= {}^{i-1}\hat{\sigma}_m + \frac{2}{3}{}^{i}\Delta\lambda_m \beta H {}^{i}\hat{\sigma}_m && (41)\\
{}^{i}\boldsymbol{\alpha}_m &= {}^{i-1}\boldsymbol{\alpha}_m + \frac{2}{3}{}^{i}\Delta\lambda_m (1-\beta) H \hat{\mathbf{P}}({}^{i}\boldsymbol{\sigma}_m - {}^{i}\boldsymbol{\alpha}_m) && (42)
\end{aligned}
$$

where the left superscript refers to the load step count, i being the current step. The proposed implicit procedure for the evaluation of ${}^{i}\boldsymbol{\sigma}_m$ and ${}^{i}\boldsymbol{\sigma}_f$ is described in what follows. Here we omit the left superscript for the current step i, such that all variables without left superscripts refer to the current load step.

Using the backward Euler scheme for the rate form of $\boldsymbol{\sigma}_m$ in (35), and (40) one obtains the following relation for matrix stresses:

$$
\boldsymbol{\sigma}_m = \boldsymbol{\sigma}_m^{tr} - \Delta\lambda_m \mathbf{Q}_{mm}\mathbf{P}(\boldsymbol{\sigma}_m - \boldsymbol{\alpha}_m) \tag{43}
$$

where $\boldsymbol{\sigma}_m^{tr}$ is a trial stress defined as

$$
\boldsymbol{\sigma}_m^{tr} \equiv {}^{i-1}\boldsymbol{\sigma}_m + \mathbf{R}_m \Delta\bar{\boldsymbol{\epsilon}}
$$

Subtracting (42) from (43) we arrive at the following result

$$
\boldsymbol{\sigma}_m - \boldsymbol{\alpha}_m = \left\{\mathbf{I} + \Delta\lambda_m \left(\mathbf{Q}_{mm}\mathbf{P} + \frac{2}{3}(1-\beta)H\hat{\mathbf{P}}\right)\right\}^{-1} (\boldsymbol{\sigma}_m^{tr} - {}^{i-1}\boldsymbol{\alpha}_m) \tag{44}
$$

The value of $\Delta\lambda_m$ must be obtained by satisfying the consistency condition which assures that the stress state lies on the yield surface at the end of the current load step. To this end, (44) and (41) are substituted into the yield condition (37) so that $\Phi_m(\boldsymbol{\sigma}_m, \boldsymbol{\alpha}_m, \hat{\sigma}_m) = 0$, which produces a nonlinear equation for $\Delta\lambda_m$. A standard Newton's method is applied to solve for $\Delta\lambda_m$:

$$
\Delta\lambda_m^k = \Delta\lambda_m^{k-1} - \left(\frac{\partial\Phi_m}{\partial(\Delta\lambda_m)}\right)^{-1} \Phi_m \Big|_{\Delta\lambda_m^{k-1}} \tag{45}
$$

It can be easily shown that the derivative $\partial\Phi_m/\partial(\Delta\lambda_m)$ required in (45) has the following form

$$
\begin{aligned}
\frac{\partial\Phi_m}{\partial(\Delta\lambda_m)} = &-(\boldsymbol{\sigma}_m - \boldsymbol{\alpha}_m)^T \mathbf{P}\left\{\left(\mathbf{Q}_{mm}\mathbf{P} + \frac{2}{3}(1-\beta)H\hat{\mathbf{P}}\right)^{-1} + \Delta\lambda_m \mathbf{I}\right\}^{-1} (\boldsymbol{\sigma}_m - \boldsymbol{\alpha}_m)\\
&- \frac{4}{9}\beta H \hat{\sigma}_m^2
\end{aligned}
$$

The converged value of $\Delta\lambda_m$ is then used in combination with (44). (42) and (43) to compute the back stresses and matrix stresses. whereas (40) and (35) provide the stresses in the reinforcement. The relation (34) is used to obtain the overall stresses. In addition. the overall plastic strain $\bar{\boldsymbol{\mu}}$ can be calculated from the Levin's formula (30) as

$$\bar{\boldsymbol{\mu}} = c_m \mathbf{B}_m^T \boldsymbol{\mu}_m, \qquad \mathbf{B}_m = \mathbf{L}_m \mathbf{A}_m \bar{\mathbf{L}}^{-1} \tag{46}$$

2.3.1 Initial Estimate of $\Delta\lambda_m$

The iterative scheme (45) for the solution of $\Delta\lambda_m$ might be slow or even diverge if the initial value chosen is far from the actual value. For this reason it is necessary to come up with a better starting estimate than the obvious choice of zero for the evaluation of $\Delta\lambda_m$. We propose an initial guess computed based on an approximation that makes the integration procedure equivalent to that used for the isotropic homogeneous case where $\Delta\lambda_m$ may be obtained in closed form for linear hardening. The procedure is explained below:

Pre-multiplication of the equation (44) by $\hat{\mathbf{P}}$ yields:

$$\hat{\mathbf{P}}\left(\boldsymbol{\sigma}_m^{tr} - {}^{i-1}\boldsymbol{\alpha}_m\right) = \left\{\hat{\mathbf{P}} + \Delta\lambda_m\left(\hat{\mathbf{P}}\mathbf{Q}_{mm}\mathbf{P} + \frac{2}{3}(1-\beta)H\hat{\mathbf{P}}\hat{\mathbf{P}}\right)\right\}(\boldsymbol{\sigma}_m - \boldsymbol{\alpha}_m) \tag{47}$$

Next, we introduce the approximation that $\hat{\mathbf{P}}\mathbf{Q}_{mm}\mathbf{P} \approx \hat{\mathbf{P}}\mathbf{L}_m\mathbf{P} = 2G_m\hat{\mathbf{P}}$ (where G_m being the shear modulus of the matrix material), which is analogous to the exact relation in isotropic homogeneous case where $\mathbf{Q}_{mm}$ is simply the linear elastic stiffness tensor, see (35). With this approximation, and the identity $\hat{\mathbf{P}}\hat{\mathbf{P}} = \hat{\mathbf{P}}$, (47) becomes:

$$\left\{1 + \Delta\lambda_m\left(2G_m + \frac{2}{3}(1-\beta)H\right)\right\}\hat{\mathbf{P}}(\boldsymbol{\sigma}_m - \boldsymbol{\alpha}_m) = \hat{\mathbf{P}}(\boldsymbol{\sigma}_m^{tr} - {}^{i-1}\boldsymbol{\alpha}_m) \tag{48}$$

Let $\|\boldsymbol{v}\|_{\mathbf{A}} = (\boldsymbol{v}^T\mathbf{A}\boldsymbol{v})^{1/2}$ be the $\mathbf{A}$-norm of an arbitrary vector $\boldsymbol{v}$ in $\mathbb{R}^n$, then taking the $\mathbf{T}$-norm on both sides of (48) yields

$$\left\{1 + \Delta\lambda_m\left(2G_m + \frac{2}{3}(1-\beta)H\right)\right\}\sqrt{\frac{2}{3}}\,\hat{\sigma}_m = \left\|\boldsymbol{\sigma}_m^{tr} - {}^{i-1}\boldsymbol{\alpha}_m\right\|_{\mathbf{P}}$$

where (37) has been used. This expression, together with the relation (41) gives the initial approximation for $\Delta\lambda_m$ as

$$\Delta\lambda_m = \frac{\sqrt{\frac{3}{2}}\left\|\boldsymbol{\sigma}_m^{tr} - {}^{i-1}\boldsymbol{\alpha}_m\right\|_{\mathbf{P}} - {}^{i-1}\hat{\sigma}_m}{{}^{i-1}\hat{\sigma}_m\left(2G_m + \frac{2}{3}(1-\beta)H\right) + \beta H\sqrt{\frac{2}{3}}\left\|\boldsymbol{\sigma}_m^{tr} - {}^{i-1}\boldsymbol{\alpha}_m\right\|_{\mathbf{P}}} \tag{49}$$

2.4 Consistent Tangent Operator

While an accurate integration of the constitutive equations is necessary to update the stresses given the kinematics and the initial state, and thereby to compute the residual or gradient

vector on the finite element mesh. the formation of a tangent stiffness matrix that is consistent with the integration procedures followed is essential to maintain quadratic rate of convergence if one is to adopt a standard Newton's method for the solution of the global nonlinear system [30].

We start by expressing the incremental form of the relations (35) in terms of total quantities:

$$\boldsymbol{\sigma}_r - {}^{i-1}\boldsymbol{\sigma}_r = \mathbf{R}_r(\bar{\boldsymbol{\epsilon}} - {}^{i-1}\bar{\boldsymbol{\epsilon}}) - \mathbf{Q}_{rm}\mathbf{P}(\boldsymbol{\sigma}_m - \boldsymbol{\alpha}_m)(\lambda_m - {}^{i-1}\lambda_m), \qquad r = m, f \tag{50}$$

where (40) has been used. Taking the material time derivative of (50) for the matrix phase and keeping in mind that all quantities are known at the previous load step $i-1$ one obtains:

$$\dot{\boldsymbol{\sigma}}_m = \mathbf{R}_m\dot{\bar{\boldsymbol{\epsilon}}} - \mathbf{Q}_{mm}\left(\boldsymbol{\mathcal{N}}_m\dot{\lambda}_m + \mathbf{P}(\dot{\boldsymbol{\sigma}}_m - \dot{\boldsymbol{\alpha}}_m)\Delta\lambda_m\right) \tag{51}$$

In order to compute $\dot{\lambda}$, we take material time derivative of the yield surface (37), i.e. $\dot{\Phi}_m = 0$, and make use of the relations in (39), which yields

$$\dot{\lambda}_m = \frac{9}{4H\hat{\sigma}_m^2}\boldsymbol{\mathcal{N}}_m^T\dot{\boldsymbol{\sigma}}_m \tag{52}$$

Consequently, equation (39b) can be expressed as follows

$$\dot{\boldsymbol{\alpha}}_m = \frac{3(1-\beta)}{2\hat{\sigma}_m^2}\hat{\mathbf{P}}(\boldsymbol{\sigma}_m - \boldsymbol{\alpha}_m)\boldsymbol{\mathcal{N}}_m^T\dot{\boldsymbol{\sigma}}_m \tag{53}$$

Once again substituting (52) and (53) into (51) we get the following expression relating $\dot{\bar{\boldsymbol{\epsilon}}}$ and $\dot{\boldsymbol{\sigma}}_m$

$$\dot{\boldsymbol{\sigma}}_m = \mathfrak{D}_m\dot{\bar{\boldsymbol{\epsilon}}} \tag{54}$$

where

$$\mathfrak{D}_m = \left(\mathbf{I} + \Delta\lambda_m\mathbf{Q}_{mm}\mathbf{P} + \frac{9 - 6(1-\beta)H\Delta\lambda_m}{4H\hat{\sigma}_m^2}\mathbf{Q}_{mm}\boldsymbol{\mathcal{N}}_m\boldsymbol{\mathcal{N}}_m^T\right)^{-1}\mathbf{R}_m \tag{55}$$

A similar result can be obtained which relates the rate of the reinforcement stress and the overall strain rate, starting from (50) and proceeding in an analogous manner. The final expression can be shown to be

$$\dot{\boldsymbol{\sigma}}_f = \mathfrak{D}_f\dot{\bar{\boldsymbol{\epsilon}}} \tag{56}$$

where

$$\mathfrak{D}_f = \mathbf{R}_f - \left(\Delta\lambda_m\mathbf{Q}_{fm}\mathbf{P} + \frac{9 - 6(1-\beta)H\Delta\lambda_m}{4H\hat{\sigma}_m^2}\mathbf{Q}_{fm}\boldsymbol{\mathcal{N}}_m\boldsymbol{\mathcal{N}}_m^T\right)\mathfrak{D}_m \tag{57}$$

Finally, the overall consistent tangent stiffness matrix $\mathfrak{D}$ is obtained from the rate form of (34), (54) and (56):

$$\dot{\bar{\boldsymbol{\sigma}}} = \mathfrak{D}\dot{\bar{\boldsymbol{\epsilon}}}, \qquad \mathfrak{D} = c_f\mathfrak{D}_f + c_m\mathfrak{D}_m \tag{58}$$

3 Incremental Mathematical Homogenization

This section deals with the incremental form of the mathematical homogenization theory. The solution found by this approach will serve as a reference solution to the two-point averaging approach discussed in the previous section. The derivation is similar to that in Section 2, but the phase constitutive relation is now in rate form and the elastic stiffness as well as the elastic strain concentration function become instantaneous quantities represented by script letters corresponding to the Roman letters of their elastic counterparts. Moreover, the incremental approach will provide a systematic way to post-process the solution obtained from two-point averaging scheme to a general unit cell domain and consequently the critical stress level in the unit cell can be assessed. An algorithm combining the two-point averaging approach presented in the previous section and the micro-history recovery procedure developed in this section is given in Section 4.

3.1 Formulation for Multi-Phase Medium

The rate form of governing equations is identical to that given in Section 2.1 except that the constitutive relation relates instantaneous quantities as

$$\dot{\boldsymbol{\sigma}}^s = \mathfrak{L}\,\dot{\boldsymbol{\epsilon}}^s, \qquad s = -1, 0, \cdots$$

where $\mathfrak{L}$ denotes the instantaneous stiffness matrix.

Following the procedure outlined in Section 2.1 and considering the rate form of the $O(\varepsilon^{-2})$ equilibrium equation (13), pre-multiplying it by $\dot{u}_i^0$ and integrating over Θ and then taking integration by parts one obtains

$$\int_{\Gamma_\Theta} \dot{u}_i^0 \dot{\sigma}_{ij}^{-1} n_j \, d\Gamma_\Theta - \int_\Theta \dot{u}^0_{(i,y_j)} \mathfrak{L}_{ijkl} \dot{u}^0_{(k,y_l)} \, d\Theta = 0 \tag{59}$$

where the first term vanishes due to periodic boundary conditions. Since the phase material may exhibit softening, the instantaneous stiffness tensor $\mathfrak{L}_{ijkl}$ may not be positive definite and thus

$$\dot{u}^0_{(i,y_j)} = 0 \quad \Longrightarrow \quad \dot{u}_i^0 = \dot{u}_i^0(\boldsymbol{x})$$

may not be the only possible solution, but nevertheless will be considered here. Introducing separation of variables

$$\dot{u}_i^1(\boldsymbol{x}, \boldsymbol{y}) = \mathfrak{H}_{imn}(\boldsymbol{y})\, \dot{\epsilon}_{mnx}\left(\dot{\boldsymbol{u}}^0\right)$$

to the rate form of the $O(\varepsilon^{-1})$ equilibrium equation (14), we obtain an equation analogous to (18)

$$\left(\mathfrak{L}_{ijkl}(\delta_{km}\delta_{ln} + \Psi^{in}_{klmn})\right)_{,y_j} = 0 \quad \text{on} \quad \Theta \tag{60}$$

where

$$\Psi^{in}_{klmn} = \mathfrak{H}_{(k,y_l)mn}$$

Equation (60) resembles its linear elastic counterpart (19), with the only exception that $\mathfrak{L}_{ijkl}$ is history dependent. A weak form of (60) can be obtained by pre-multiplying (60) by $\delta\mathfrak{H}_{ist}$ and integrating it over a unit cell domain, and subsequently integrating it by parts which yields

$$\int_\Theta \delta\Psi^{in}_{ijst}\mathfrak{L}_{ijkl}\Psi^{in}_{klmn}\, d\Gamma_\Theta = -\int_\Theta \delta\Psi^{in}_{ijst}\mathfrak{L}_{ijmn}\, d\Theta \tag{61}$$

for arbitrary $\delta\Psi^{in}_{ijst} \in C^{-1}$. The corresponding discrete system of equations is given by

$$\mathrm{K}_{AB}h_{mnB} = f_{mnA} \tag{62}$$

where

$$\mathrm{K}_{AB} = \int_\Theta \mathrm{N}^{\Theta}_{(i,j)A}\mathfrak{L}_{ijkl}\mathrm{N}^{\Theta}_{(k,l)B}\, d\Theta, \qquad f_{mnA} = -\int_\Theta \mathrm{N}^{\Theta}_{(i,j)A}\mathfrak{L}_{ijmn}\, d\Theta$$

$$\mathfrak{H}_{kmn} = \mathrm{N}^{\Theta}_{kA}h_{mnA}, \qquad \Psi^{in}_{mnkl} = \mathrm{N}^{\Theta}_{(k,l)A}h_{mnA}$$

and $\mathbf{N}^{\Theta}$ is the matrix containing appropriate shape functions for the unit cell problem.

The instantaneous strain concentration function $\mathfrak{A}(\boldsymbol{y})$ and the local strain rate are given by

$$\mathfrak{A}(\boldsymbol{y}) = \mathbf{I} + \boldsymbol{\Psi}^{in}(\boldsymbol{y}), \qquad \dot{\epsilon}(\boldsymbol{x},\boldsymbol{y}) = \mathfrak{A}(\boldsymbol{y})\,\dot{\bar{\epsilon}}(\boldsymbol{x}) \tag{63}$$

3.2 Implicit Stress Update Procedure for Incremental Homogenization

The implicit stress update procedure derived in this section can be used within a macroscopic iterative scheme to obtain a reference solution for comparison to the two-point averaging procedure. Alternatively, if the strain increment is given for certain Gaussian points in the macroscopic domain, the current stress update scheme can be used as a stand-alone post-processing module to recover local fields in a unit cell domain.

We start from the constitutive relation for a typical Gaussian point $y_\rho \in \Theta_m$

$$\dot{\boldsymbol{\sigma}}_\rho = \mathbf{L}_\rho(\dot{\boldsymbol{\epsilon}}_\rho - \dot{\boldsymbol{\mu}}_\rho)$$

Substituting for the local strain rate (63b) and local plastic strain rate (38) yields

$$\dot{\boldsymbol{\sigma}}_\rho = \mathbf{L}_\rho\left(\mathfrak{A}_\rho\dot{\bar{\boldsymbol{\epsilon}}} - \dot{\lambda}_\rho\mathbf{P}(\boldsymbol{\sigma}_\rho - \boldsymbol{\alpha}_\rho)\right)$$

Applying the backward Euler integration scheme to the above equation gives

$$\boldsymbol{\sigma}_\rho = {}^{i-1}\boldsymbol{\sigma}_\rho + \mathbf{L}_\rho \mathfrak{A}_\rho \Delta\bar{\boldsymbol{\epsilon}} - \Delta\lambda_\rho \mathbf{L}_\rho \mathbf{P}(\boldsymbol{\sigma}_\rho - \boldsymbol{\alpha}_\rho) \tag{64}$$

and together with (42) yields

$$\boldsymbol{\sigma}_\rho - \boldsymbol{\alpha}_\rho = \left\{\mathbf{I} + \Delta\lambda_\rho \left(\mathbf{L}_\rho \mathbf{P} + \frac{2}{3}(1-\beta)H\hat{\mathbf{P}}\right)\right\}^{-1} \left({}^{i-1}\boldsymbol{\sigma}_\rho + \mathbf{L}_\rho \mathfrak{A}_\rho \Delta\bar{\boldsymbol{\epsilon}} - {}^{i-1}\boldsymbol{\alpha}_\rho\right) \tag{65}$$

Note that the instantaneous strain concentration factors $\mathfrak{A}_\rho$ are obtained from the solution of equation (62) which depends on the instantaneous stiffness at each microscopic Gaussian point. Therefore, $\mathfrak{A}_\rho$ is a function of $\Delta\boldsymbol{\lambda}$ which is a vector containing all the plastic parameters in Θ_m, $\Delta\boldsymbol{\lambda} \equiv \lfloor \Delta\lambda_1, \Delta\lambda_2, \cdots, \Delta\lambda_{n_y} \rfloor^T$. Substituting (65) into yield function (37) for each Gaussian point in Θ_m yields a set of n_y nonlinear equations $\boldsymbol{\Phi} \equiv \lfloor \Phi_1, \Phi_2, \cdots, \Phi_{n_y} \rfloor^T$ with n_y unknown plastic parameters which can be solved by using Newton's method

$$\Delta\boldsymbol{\lambda}^k = \Delta\boldsymbol{\lambda}^{k-1} - \left(\frac{\partial\boldsymbol{\Phi}}{\partial(\Delta\boldsymbol{\lambda})}\right)^{-1} \boldsymbol{\Phi}\Big|_{\Delta\boldsymbol{\lambda}^{k-1}} \tag{66}$$

A typical term in the Jacobian matrix is given as

$$\begin{aligned}\frac{\partial\Phi_\rho}{\partial\Delta\lambda_\eta} = &-(\boldsymbol{\sigma}_\rho - \boldsymbol{\alpha}_\rho)^T \mathbf{P} \left\{\mathbf{I} + \Delta\lambda_\rho \left(\mathbf{L}_\rho \mathbf{P} + \frac{2}{3}(1-\beta)H\hat{\mathbf{P}}\right)\right\}^{-1} \\ &\left\{\delta_{\rho\eta}\left(\mathbf{L}_\rho \mathbf{P} + \frac{2}{3}(1-\beta)H\hat{\mathbf{P}}\right)(\boldsymbol{\sigma}_\rho - \boldsymbol{\alpha}_\rho) - \mathbf{L}_\rho \frac{\partial\mathfrak{A}_\rho}{\partial(\Delta\lambda_\eta)}\Delta\bar{\boldsymbol{\epsilon}}\right\} \\ &- \delta_{\rho\eta}\frac{4}{9}\beta H\hat{\sigma}_\rho^2\end{aligned} \tag{67}$$

In the above expression, the evaluation of $\partial\mathfrak{A}_\rho/\partial(\Delta\lambda_\eta)$ is not trivial, and hence we introduce the following approximation

$$\mathfrak{A}_\rho \approx {}^{i-1}\mathfrak{A}_\rho$$

such that the above Jacobian matrix (67) is approximated by the following diagonal matrix

$$\begin{aligned}\frac{\partial\Phi_\rho}{\partial\Delta\lambda_\eta} \approx &-\delta_{\rho\eta}(\boldsymbol{\sigma}_\rho - \boldsymbol{\alpha}_\rho)^T \mathbf{P} \left\{\left(\mathbf{L}_\rho \mathbf{P} + \frac{2}{3}(1-\beta)H\hat{\mathbf{P}}\right)^{-1} + \Delta\lambda_\rho \mathbf{I}\right\}^{-1} (\boldsymbol{\sigma}_\rho - \boldsymbol{\alpha}_\rho) \\ &- \delta_{\rho\eta}\frac{4}{9}\beta H\hat{\sigma}_\rho^2\end{aligned} \tag{68}$$

At each modified Newton iteration of (66), we need to evaluate the residue vector $\boldsymbol{\Phi}$ which in turn requires a solution of (62). The iterative process continues until the residual norm $\|\boldsymbol{\Phi}\|_2$ vanish up to a certain tolerance. The updated stress at each Gaussian point in Θ_m can then be calculated with (64). For the Gaussian point in the reinforcement domain Θ_f, the updated stress can also be obtained using (64) with $\Delta\lambda_\rho \equiv 0$. The macroscopic stress then follows from equation (29).

4 Two-Point Averaging Scheme with Variational Micro-History Recovery

As discussed in the previous sections, the computation of nonlinear composite systems using multi-phase incremental homogenization scheme is computationally expensive since the number of nonlinear equations to be solved at each macroscopic Gaussian point is equal to the number of plastic Gaussian points in a unit cell. Furthermore, for every microscopic iteration (66) a solution of the linear unit cell problem (62) is required. Nevertheless, multi-phase incremental homogenization scheme can be used as a stand-alone post-processing tool to recover the micro-history for selected number of points. In Section 6 we will show that the computational complexity of the two-point averaging approach is comparable to that of homogeneous case, but the resulting average phase strains are sufficiently accurate to predict critical microscopic fields of interest.

In this section, we merge the two approaches discussed in Sections 2 and 3. In the combined scheme the overall structural response is computed using the two-point averaging scheme and the micro-history in the unit cell domain corresponding to the critical regions in the macroscopic domain is recovered by means of the incremental homogenization method. The critical regions may be defined as those where the macroscopic effective stress (maximum stress criterion) or the effective overall plastic strains (maximum plastic strain criterion) exceed certain criteria such that

$$\sqrt{\frac{3}{2}}\,\|\bar{\boldsymbol{\sigma}}\|_{\mathbf{P}} > \sigma_{cr} \qquad \text{or} \qquad \sqrt{\frac{2}{3}}\,\|\bar{\boldsymbol{\mu}}\|_{\mathbf{P}} > \mu_{cr} \tag{69}$$

in which σ_{cr} and μ_{cr} are prescribed critical threshold values, and $\bar{\boldsymbol{\sigma}}$ and $\bar{\boldsymbol{\mu}}$ are computed from (34) and the Levin's formula (46), respectively.

The overall analysis procedure is divided into two stages. In the first, denoted as *macroscopic finite element analysis*, a nonlinear composite structural problem is solved using finite element method based on the two-point averaging approach developed in Section 2. The macroscopic analysis of the composite structure is carried out and the macroscopic strain histories are stored in a history database at Gaussian points in the critical regions. In the second stage, referred to as *micro-history recovery*, the microstress distribution in the unit cell is sought. The strain history at macroscopic Gaussian points for critical regions are extracted from the database. Then, the macroscopic strain history is applied to the unit cell through the incremental homogenization procedure discussed in Section 3.2. Since the micro-history recovery is performed only at a select number of Gaussian points of interest without affecting macroscopic analysis, the computational cost is low.

The finite element formulation of a composite problem that incorporates the nonlinear constitutive model presented in Section 4 yields a discrete system of equilibrium equations schematically denoted as:

$$\boldsymbol{r} \equiv \boldsymbol{f}_{ext} - \boldsymbol{f}_{int} = 0 \tag{70}$$

where $\boldsymbol{r}$ is a macroscopic residual vector, $\boldsymbol{f}_{ext}$ is the external force vector, and $\boldsymbol{f}_{int}(\bar{\boldsymbol{\sigma}})$ is the vector of internal forces. A macroscopic iterative solution procedure is employed for this set of nonlinear equations.

Note that for small to medium size problems, it is possible to apply a classical Newton's method for the solution of (70). The consistent tangent operator developed in Sections 2.4 ensures that the resulting iterative scheme retains the quadratic rate of convergence provided that the standard requirements for the Jacobian and the initial approximation are maintained [7]. However, Newton's method becomes expensive because it requires the computation and factorization of the tangent stiffness matrix at every iteration for large-scale problems. An efficient solution algorithm for large scale problems based on multigrid technology is briefly discussed in Section 5. The overall analysis procedure is summarized as below:

Macroscopic Finite Element Analysis

1. Solve for the elastic strain concentration factors in a specified unit cell domain using (62) with elastic stiffnesses replacing the instantaneous quantities
2. Calculate the 2-point average elastic strain concentration factors $\mathbf{A}_r$ from (31)
3. Construct eigenstrain influence factors $\mathbf{D}_{rs}$ from (33) and then $\mathbf{R}_r$ and $\mathbf{Q}_{rs}$ as shown in (36)
4. Initialize macroscopic displacements; microscopic stresses and state variables
5. Define the macroscopic load increment

   if end-of-load-step *then*
   stop
   else
   continue
   endif

6. Evaluate consistent tangent operators $\mathfrak{D}$ from (58) if Newton's method is adopted
7. Solve for macroscopic displacement increments and then compute macroscopic strain increments
8. Carry out implicit stress update at each macroscopic Gaussian point
   - Compute initial estimate of $\Delta\lambda_m$ by equation (49)
   - Solve $\Delta\lambda_m$ by Newton's iteration with (45)
   - Update matrix stress and state variables using (44) and (40–43)
   - Calculate macroscopic stress with (34)
9. Update displacements, stresses and state variables
10. Calculate the L_2 norm of macroscopic residue vector $\|\boldsymbol{r}\|_2$ in (70) and check convergence

if $\|\boldsymbol{r}\|_2 <$ Tolerance *then*
update equilibrium history
write macroscopic strain history to database
return to step 5
else
return to step 6
endif

Micro-History Recovery

1. Identify critical regions using maximum stress criterion or maximum plastic strain criterion (69)
2. Extract macroscopic strain increment for Gaussian points in critical regions from history database
3. Carry out implicit macroscopic stress update for critical unit cells
   - Compute modified tangent operator (68)
   - Calculate instantaneous stiffness tensor for each phase
   - Solve unit cell problem for $\mathfrak{A}(\boldsymbol{y})$
   - Evaluate L_2 norm of residue vector $\|\boldsymbol{\Phi}\|_2$ in the unit cell
   - Perform iteration for $\Delta\boldsymbol{\lambda}$ until $\|\boldsymbol{\Phi}\|_2 <$ Tolerance
4. Recover microstress distribution in Θ using the converged plastic parameter $\Delta\boldsymbol{\lambda}$ (64)
5. *return* to step 2

5 Solution Procedures for Large Scale Systems

As discussed in the previous section, Newton's method is not an optimal choice for large-scale problems. The popular alternatives to the Newton's method include the BFGS quasi-Newton method and multigrid methods. Even though the BFGS method is known to be robust and stable for general nonlinear systems, its convergence is greatly affected by the choice of the initial approximation to the tangent stiffness matrix. Usually it is necessary to start the procedure from the *exact* linear stiffness matrix, which again becomes expensive for large-scale problems. On the other hand, the Newton-multigrid method, where a standard linear multigrid method is used to solve the linearized system within the Newton's method, suffers from its sensitivity to the conditioning of the linearized system. This limitation becomes pronounced for problems with significant amount of plastic flow and small hardening slope.

A novel nonlinear hybrid solver was introduced in [18], which builds on the advantages of multigrid- and BFGS- like methods and at the same time eliminates the undesirable characteristics of each to the maximum extent possible. It combines the Full Approximation Storage (FAS) version of the multigrid method and the BFGS quasi-Newton method to form

a fast, efficient solution method for nonlinear systems. Here we only summarize the fundamental features of the new FAS-BFGS solution procedure, and refer to [18] for a complete description of the method as well as the detailed algorithms. The basic characteristics of the new solution approach include:

- **Full approximation storage**
  Solve the nonlinear system directly, instead of solving a sequence of linearized problems within Newton method, using the FAS philosophy.

- **Continuous inter- and intra- cycle BFGS updates**
  The conventional nonlinear relaxation procedure on the finest and all the intermediate grids is replaced by a continuous BFGS procedure which exploits the information from previous cycles. This is schematically illustrated in Figure 2. The continuous BFGS smoothing procedures on the finest and all the intermediate grids are started from the diagonal of the Jacobian matrix for the particular grid. A restart of the BFGS procedures is done periodically after a fixed number of cycles. The handling of the solution in the coarsest grid is also different in the sense that continuous BFGS updates are performed on the coarsest grid as well. This eliminates the need for the computation and factorization of the coarsest grid Jacobian matrix at every multigrid cycle.

- **Consistency of history data**
  Update the history variables on each grid level directly using their values from the previous load (time) step and the displacements from the current step by performing the integration of the appropriate constitutive relations. As noted in [18], such independent history updates on all the grids are essential for the successful application of FAS method for history-dependent problems such as plasticity.

6 Numerical Examples and Discussion

In the following, we present numerical examples to test the accuracy and efficiency of the proposed numerical procedures. Although the numerical procedures are general enough to handle complicated microstructures, such as weave fabric or particulate composite, the microstructure of the composite chosen for the following model problems, is the most widely used continuous fibrous system. The phase properties are given as follows:

SiC Fiber: Young's modulus = 379.2 GPa, Poisson's ratio = 0.21, fiber volume fraction c_f=0.27
Titanium Matrix: Young's modulus = 68.9 GPa, Poisson's ratio = 0.33, yield stress $\hat{\sigma}_m$ = 24 MPa, isotropic hardening modulus H = 14 GPa, β = 1.

6.1 The Nozzle Flap Problem

The nozzle flap problem is solved using the two-point averaging scheme with micro-history recovery and multi-point incremental homogenization procedures for the reference solution. The objective of this numerical study is to investigate the two-point averaging scheme with variational micro-history recovery in terms of accuracy (in both macro- and micro-scales), computational efficiency and memory consumption. The finite element mesh for one-half of the flap (due to symmetry) is shown in Figure 1a. The flap is subjected to an aerodynamic force (simulated by a uniform pressure) on the back of the flap and a symmetric boundary condition is applied on the symmetric face. Furthermore, we assume that the pin-eyes are rigid and a rotation is not allowed so that all the degrees of freedom on the pin-eye surfaces are fixed. There is about 15 percent of plastic zone in the model due to the loading.

For this problem, we adopt the classical Newton's method for both procedures. The CPU time is 30 seconds for the macroscopic analysis using two-point averaging scheme, plus approximately 160 seconds for each Gaussian point where a micro-history recovery procedure is applied. On the other hand, the CPU time for the incremental homogenization approach takes about 7 hours. Moreover, memory requirement ratio for these two approaches is roughly 1:250.

Solutions obtained by both approaches are compared using the relative error measure defined as

$$\text{Relative Error of } U = \frac{U^{mp} - U^{tp}}{U^{mp}}$$

where U^{mp} is a solution obtained using the multi-point incremental homogenization procedure and U^{tp} denotes the corresponding solution computed using the two-point averaging scheme. The vertical displacement for points 1, 2 and 3 shown in Figure 1a, as obtained by both approaches are depicted in Figure 3. The maximum displacement appears at point 1 where relative error is less than 1 percent. The maximum effective stress appears at the pin-eye of the middle flap (Gaussian point A). Micro-histories are recovered for the unit cells corresponding to the macroscopic Gaussian points A, B, and C. The maximum relative error at Gaussian points A, B and C are 2.8, 3.5 and 2.8 percent, respectively, as shown in Figure 4.

6.2 Large Scale Problems

Two 3-dimensional example problems are chosen for numerical experimentation on large scale systems, both modeled using 4-node tetrahedral elements. Two auxiliary grids are used for both the problems for solution through FAS-BFGS and Newton-multigrid methods.

The first example is a two-cylinder problem [18] as shown in Figure 5. All the degrees of freedom on one end are fixed and uniform loadings are applied along all the three directions

on the remaining three place faces. The finest grid for this problem carried a total of 63,918 degrees of freedom. The loading takes the solution well beyond elastic limit.

The second model problem is a machine part with 94,953 degrees of freedom at the finest mesh shown in Figure 6. We apply uniform loading along all three directions at the end-face and fix the cylindrical hole at the other end. Again, a large portion of the part is in the plastic region.

Tables 1 and 2 summarize the performance of the various solution schemes on the two composite model problems. A comparison of the CPU times presented reveals that while the FAS-BFGS method appears to be clearly superior to the other methods. The efficiency of the FAS-BFGS algorithm even in the case of composite problems with computationally complex stress update procedures should be encouraging considering the fact that this method requires many more gradient vector evaluations than say, the classical Newton's method and by extension the Newton-multigrid method. In general, this behavior of FAS-BFGS can be expected for large-scale problems modelled in such a way that the computational effort is dominated by the formation and factorization of the tangent stiffness matrix. For unit cell models with hundreds of elements in the cell, for e.g., the major part of the computation will be to update the stresses and evaluate the gradient or residual force vector, in which case the FAS-BFGS procedure may not be the optimal choice.

method	no. of iterations	cpu hours	remarks
Newton	8	32	Projected time
BFGS	23	4.5	Projected time
Newton-multigrid	8	2.67	
FAS-BFGS	23	1.37	

Table 1: Comparison of Solution Schemes for the Two-cylinder Problem

method	no. of iterations	cpu hours	remarks
Newton	8	46	Projected time
BFGS	28	9.3	Projected time
Newton-multigrid	8	6.70	
FAS-BFGS	27	2.75	

Table 2: Comparison of Solution Schemes for the Machine Part Problem

Acknowledgment

The authors express their sincere appreciation to Prof. George J. Dvorak for his constructive suggestions. The support by the ARPA/ONR, under grant N00014-92-J-1779, Mechanism-Based Design for Composite Structures program in Rensselaer Polytechnic Institute is gratefully acknowledged.

References

[1] J. Aboudi. Continuum theory for fiber-reinforced elastic-viscoplastic composites. *International Journal of Engineering Science*, 20, 1982.

[2] J. Aboudi. Elastoplasticity theory for composite materials. *Solid Mechanics Archives*, 11, 1986.

[3] M. L. Accorsi and S. Nemat-Nasser. Bounds on the overall elastic and instantaneous elasto-plastic moduli of periodic composites. *Mechanics of Materials*, 5, 1986.

[4] N. S. Bakhvalov and G. P. Panasenko. *Homogenisation: Averaging Processes in Periodic Media*. Kluwer Academic Publishers, 1989.

[5] A. Benssousan, J. L. Lions, and G. Papanicoulau. *Asymptotic Analysis for Periodic Structure*. North-Holland, 1978.

[6] J. L Chaboche. Time independent constitutive theories for cyclic plasticity. *International Journal of Plasticity*, 2, 1986.

[7] J. E. Dennis and R. B. Schnabel. *Numerical Methods for Unconstrained Optimization and Nonlinear Equations*. Prentice-Hall, 1983.

[8] G. J. Dvorak. On uniform fields in heterogeneous media. *Proceedings of Royal Society of London*, A431, 1990.

[9] G. J. Dvorak. Plasticity theories for fibrous composite materials. In R. K. Everett and R. J. Arsenault, editors, *Metal Matrix Composites: Mechanisms and Properties*. Academic Press, 1991.

[10] G. J. Dvorak. Transformation field analysis of inelastic composite materials. *Proceedings of Royal Society of London*, A437, 1992.

[11] G. J. Dvorak and Y. A. Bahei-El-Din. Plasticity analysis of fibrous composites. *Journal of Applied Mechanics*, 49, 1982.

[12] G. J. Dvorak and Y. A. Bahei-El-Din. A bimodal plasticity theory of fibrous composite materials. *Acta Mechanica*, 69, 1987.

[13] G. J. Dvorak and Y. Benveniste. On transformation strains and uniform fields in multiphase elastic media. *Proceedings of Royal Society of London*, A437, 1992.

[14] G. J. Dvorak and M. S. M. Rao. Axisymmetric plasticity theory of fibrous composites. *International Journal of Engineering Science*, 14, 1976.

[15] J. Fish and V. Belsky. Multigrid method for periodic heterogeneous media: I. convergence studies for one dimensional case. *Computer Methods in Applied Mechanics and Engineering*, 126, 1995.

[16] J. Fish and V. Belsky. Multigrid method for periodic heterogeneous media: II. multiscale modeling and quality control in multidimensional case. *Computer Methods in Applied Mechanics and Engineering*, 126, 1995.

[17] J. Fish, P. Nayak, and M. H. Holmes. Microscale reduction error indicators and estimators for a periodic heterogeneous medium. *Computational Mechanics*, 14, 1994.

[18] J. Fish, M. Pandheeradi, and V. Belsky. An efficient multi-level solution scheme for large scale nonlinear systems. *International Journal of Numerical Methods in Engineering*, 38, 1995.

[19] J. Fish and A. Wagiman. Multiscale finite element method for a locally nonperiodic heterogeneous medium. *Computational Mechanics*, 12, 1992.

[20] J. M. Guedes. *Nonlinear Computational Models for Composite Materials Using Homogenization*. PhD thesis, University of Michigan, 1990.

[21] J. M. Guedes and N. Kikuchi. Preprocessing and postprocessing for materials based on the homogenization method with adaptive finite element methods. *Computer Methods in Applied Mechanics and Engineering*, 83, 1990.

[22] R. Hill. A theory of the yielding and plastic flow of anisotropic metals. *Proceedings of Royal Society of London*, A193, 1948.

[23] R. Hill. The essential structure of constitutive laws for metal composites and polycrystals. *Journal of the Mechanics and Physics of Solids*, 15, 1967.

[24] T. J. R. Hughes. Numerical implementation of constitutive models: Rate-independent deviatoric plasticity. In S. Nemat-Nasser, R. J. Asaro, and G. A. Hegemier, editors. *Theoretical Foundation for Large Scale Computations for Nonlinear Material Behavior*. Martinus Nijhoff Publishers, 1983.

[25] V. M. Levin. Thermal expansion coefficients of heterogeneous materials. *Mekhanika Tverdogo Tela*, 2, 1967.

[26] T. H. Lin, D. Salinas, and Y. M. Ito. Effects of hydrostatic stress on the yielding of cold rolled metals and fiber-reinforced composites. *Journal of Composite Materials*, 26, 1972.

[27] A. Phillips and H. Moon. An experimental investigation concerning yield surfaces and loading surfaces. *Acta Mechanica*, 27, 1977.

[28] S. A. Rizzi, A. R. Leewood, J. F. Doyle, and C. T. Sun. Elastic-plastic analysis of Boron/Aluminium composite under constrained plasticity conditions. *Journal of Composite Materials*, 21, 1987.

[29] E. Sanchez-Palencia and A. Zaoui. *Homogenization Techniques for Composite Media*. Springer-Verlag, 1985.

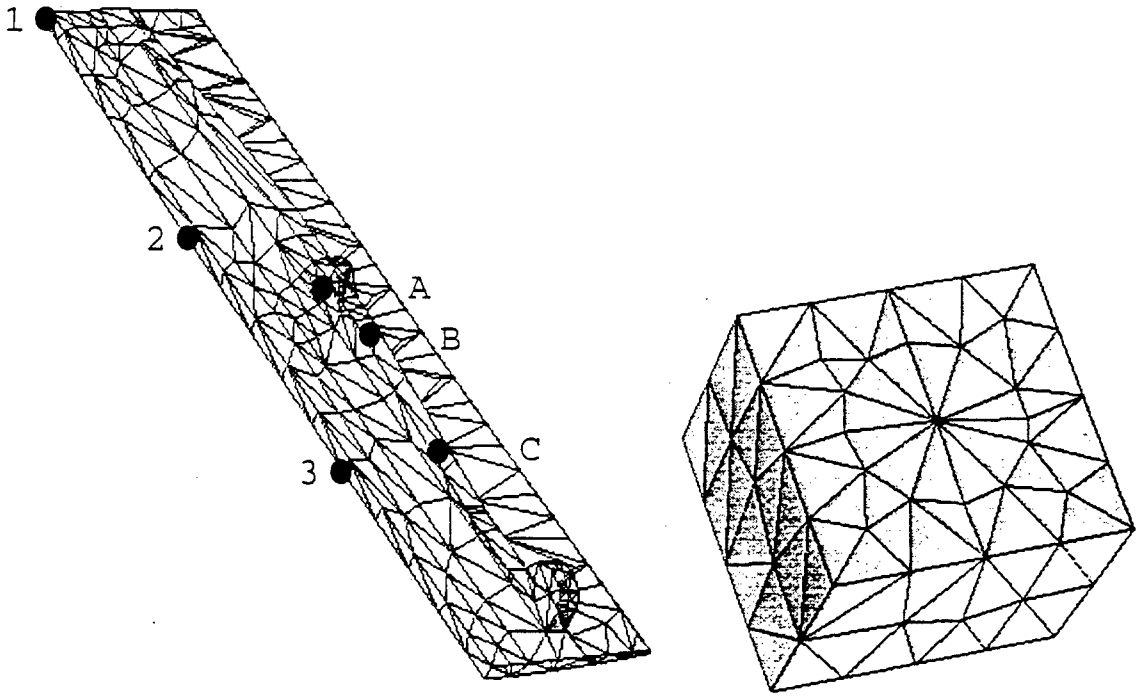
[30] J. C. Simo and R. L. Taylor. Consistent tangent operators for rate-independent elastoplasticity. *Computer Methods in Applied Mechanics and Engineering*, 48, 1985.

[31] P. M. Suquet. *Plasticité et Homogeneisation.* PhD thesis, Université Pierre et Marie Curie, Paris 6, 1982.

[32] P. M. Suquet. Elements of homogenization for inelastic solid mechanics. In E. Sanchez-Palencia and A. Zaoui, editors, *Homogenization Techniques for Composite Media.* Springer-Verlag, 1987.

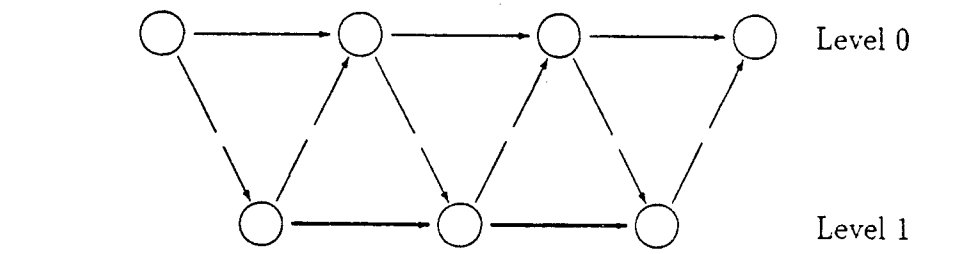
[33] J. L. Teply and G. J. Dvorak. Bounds on overall instantaneous properties of elastic-plastic composites. *Journal of the Mechanics and Physics of Solids*, 36, 1988.

[34] H. Zielger. A modification of Prager's hardening rule. *Quarterly of Applied Mathematics*, 17, 1959.



(a) FE Mesh for the Nozzle Flap Problem (b) FE Mesh for the Unit Cell Model

Figure 1: FE meshes for the Nozzle Flap Problem and the Unit Cell Model



——→ Continuous BFGS smoothing starting from diagonal stiffness
— —→ Multigrid-like prolongation and restriction operations
——→ Continuous BFGS coarse grid correction

Figure 2: Schematic Illustration of Continuous BFGS Updates

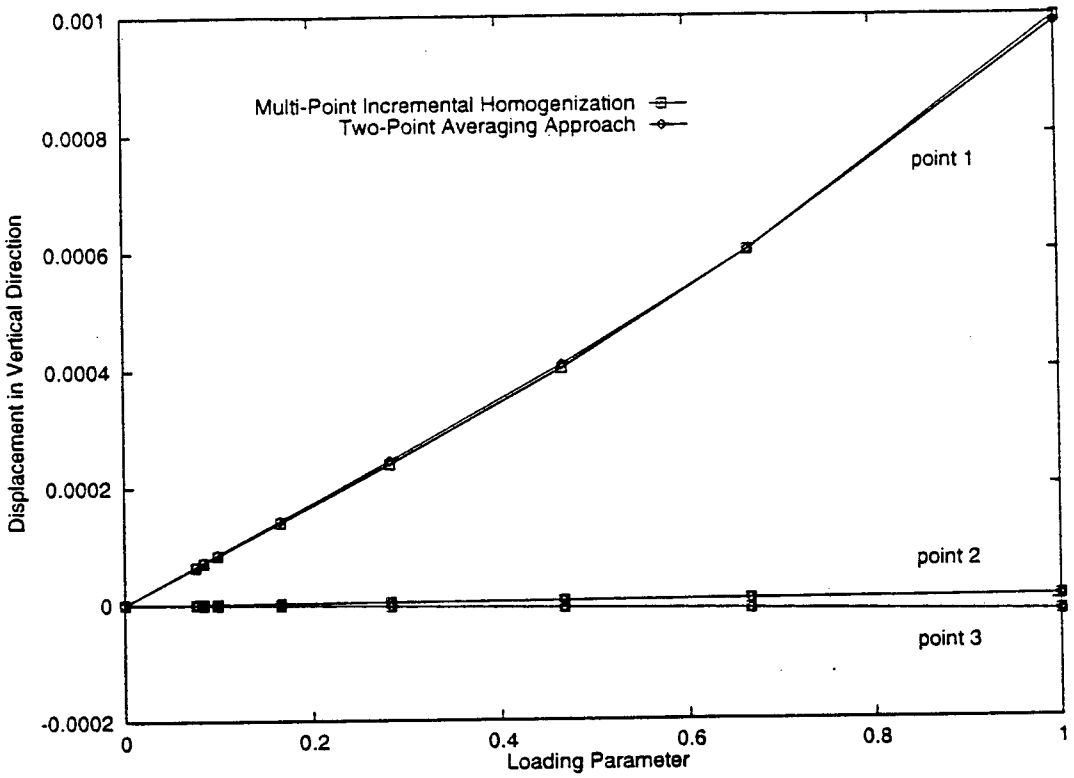
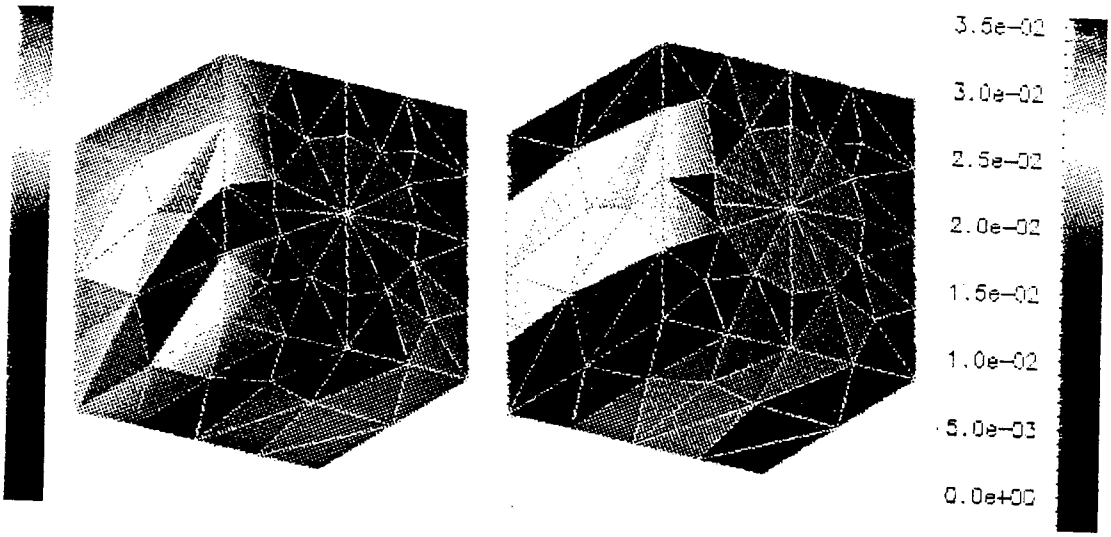


Figure 3: Displacement Comparison

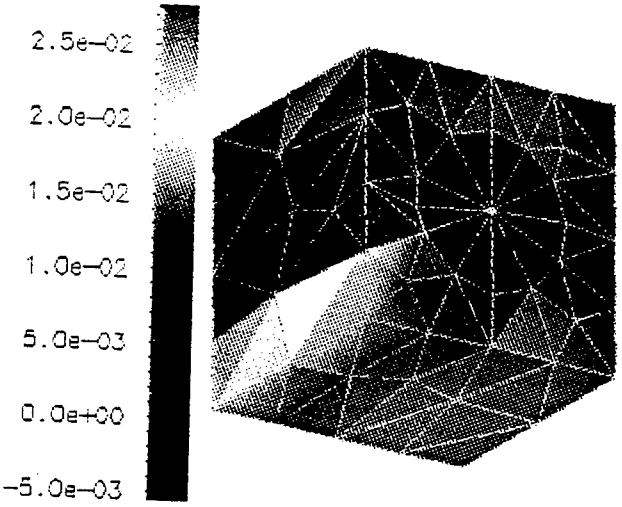


(a) Gaussian Point A

Max. Effective Stress = 551.6 MPa
Min. Effective Stress = 38.7 MPa
Max. Relative Error = 2.8 %

(b) Gaussian Point B

Max. Effective Stress = 427.7 MPa
Min. Effective Stress = 35.0 MPa
Max. Relative Error = 3.5 %



(c) Gaussian Point C

Max. Effective Stress = 286.4 MPa
Min. Effective Stress = 30.1 MPa
Max. Relative Error = 2.8 %

Figure 4: Unit Cell Relative Error for Effective Stress

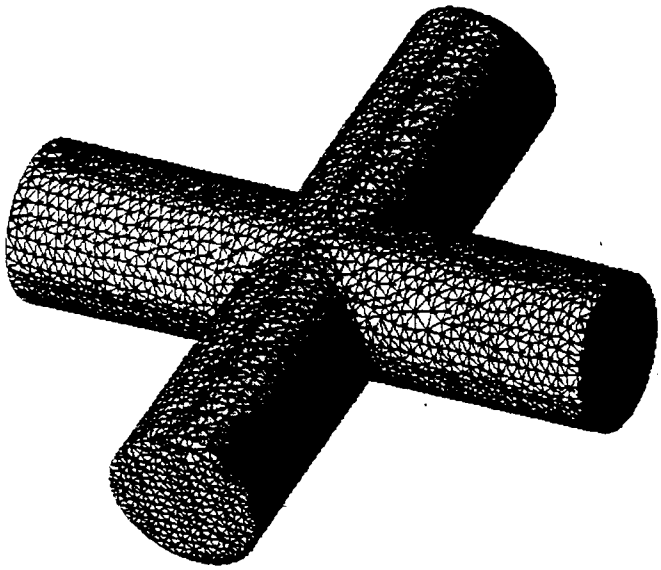


Figure 5: FE Mesh for the Two-Cylinder Problem

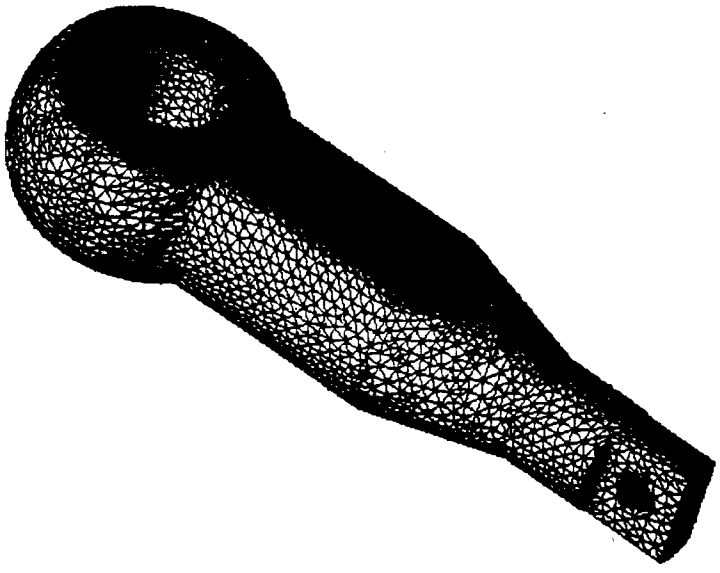


Figure 6: FE Mesh for the Machine Part Problem

ELSEVIER

Applied Numerical Mathematics 23 (1997) 241–258

APPLIED NUMERICAL MATHEMATICS

Hierarchical composite grid method for global–local analysis of laminated composite shells

J. Fish *, A. Suvorov, V. Belsky

Department of Civil Engineering and Scientific Computation Research Center, Rensselaer Polytechnic Institute, Troy, NY 12180, USA

Abstract

A hierarchical version of the composite grid method (denoted as HFAC), which exploits the solution of the shell model in studying local effects via a 3D solid model, is developed. Convergence studies on a beam/2D model problem indicate that the spectral radius of the point iteration matrix for the HFAC method is $O(1)$ and $O((L/H)^2)$ with exact and approximate auxiliary coarse grid solutions, respectively, where L and H are the span and the thickness of the beam, respectively. Numerical experiments in multidimensions confirm these findings.
© 1997 Elsevier Science B.V.

Keywords: Composite grid; Multigrid; Global–local; Hierarchical; Laminated composites; Shells

1. Introduction

Global–local techniques for laminated composite shells, which merge the Equivalent Single Layer (ESL) model aimed at predicting overall response with the Discrete Layer (DL) model intended for capturing local effects, are recently receiving an increasing attention. We refer to [26] for a comprehensive review of global–local techniques for composite laminates and to [2,14] for various aspects of reliability, convergence and accuracy of global–local techniques.

In this paper, we are focusing only on the class of global–local techniques that advocates a hierarchical solution strategy in the sense that information from the analysis of an ESL model is exploited in the resolution of local effects using a DL model. Among the most popular hierarchical global–local strategies are the various forms of multigrid and composite grid methods [5,6,9,16,22,23,28] as well as the methods based on hierarchical decomposition of approximation space [4,7,8,11–13,15,26,29]. Recently, the composite grid method, originated for displacement-based linear systems, has been extended to hybrid systems [10]. Engineering global–local approaches, which approximate a detailed response by means of postprocessing techniques, such as subjecting a refined discrete layer model to

* Corresponding author. E-mail: fish@rpi.edu.

0168-9274/97/$17.00 © 1997 Elsevier Science B.V. All rights reserved.
PII S0168-9274(96)00068-2

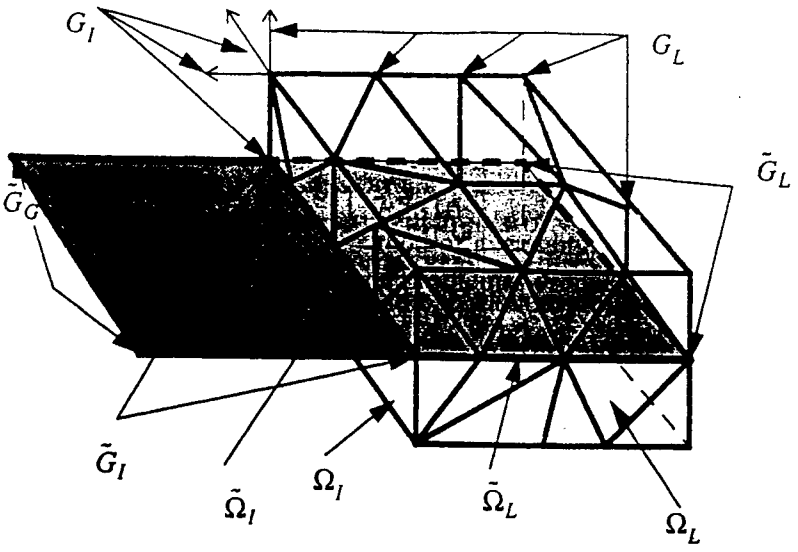


Fig. 1. Partitioning of the shell-3D global–local model.

the boundary conditions extracted from the global ESL model, can be viewed as a single iteration within the composite grid procedure. For various improvements of this simple "zoom" technique, we refer to [19,20,24].

The present paper presents a hierarchical version [9] of the composite grid method (denoted as HFAC) [23], which exploits the solution of the shell model in the process of solving a coupled global–local problem. The outline of the paper is as follows: In Section 2 the principles of the composite grid method are outlined in the context of laminated plates and shells. A convergence analysis on a model beam/2D problem is carried out in Section 3. These studies show that the spectral radius of the point iteration matrix for the HFAC method is $O(1)$ and $O((L/H)^2)$ with exact and approximate auxiliary coarse grid solutions, respectively, where L and H are the span and the thickness of the beam, respectively. Numerical studies in multidimensions conclude the paper.

2. Hierarchical composite grid method

In this section, we present the formulation of a global–local solution algorithm for problems where one or more regions, requiring a detailed local resolution, are modeled as a 3D solid model, whereas elsewhere the shell model is used.

2.1. Problem definition and notation

We adopt the notation introduced in [9,10]. Consider a finite element mesh $\widetilde{G}$ consisting of shell elements on $\widetilde{\Omega}$, which is a dimensionally reduced domain of Ω as shown in Fig. 1. Let G be a 3D solid finite element mesh placed on the subregion $\Omega_L \in \Omega$. The composite grid consists of the shell model in the complement of $\widetilde{\Omega}_L$ in $\widetilde{\Omega}$, and the 3D solid mesh on Ω_L.

We partition the 3D solid mesh G (subsequently referred to as the fine or local grid) as

$$G = G_I \cup G_L \tag{1}$$

where G_I represents the interface degrees of freedom in Ω_I, and G_L the internal degrees of freedom. The mesh consisting of shell elements (coarse or auxiliary grid) is partitioned as follows:

$$\widetilde{G} = \widetilde{G}_I \cup \widetilde{G}_L \cup \widetilde{G}_G \tag{2}$$

where $\widetilde{G}_I$ represents the degrees of freedom associated with the coarse finite element nodes at the interface $\widetilde{\Omega}_I$, $\widetilde{G}_L$ the degrees of freedom associated with the interior coarse grid points in $\widetilde{\Omega}_L$, and $\widetilde{G}_G$ the degrees of freedom associated with the remaining coarse grid nodes as shown in Fig. 1. For convenience, we define the shell grid outside the local region as $\widehat{G} = \widetilde{G}_I \cup \widetilde{G}_G$ so that $\widetilde{G} = \widehat{G} \cup \widetilde{G}_L$. Finally, the composite grid, denoted as G^{C} is defined as follows:

$$G^{\mathrm{C}} = \widehat{G} \cup G_L. \tag{3}$$

For information transfer between the two levels, we employ the prolongation operator $\widetilde{Q}$, which is partitioned into two blocks for convenience. The first block, denoted by $\widehat{Q}$, relates the degrees-of-freedom in $\widehat{G}$ to those corresponding to the interface degrees of freedom of G, i.e., G_I:

$$\widehat{Q} : \widehat{G} \to G_I \tag{4}$$

where

$$\widehat{Q} = [\widetilde{Q}_I \quad 0] \tag{5}$$

such that

$$\widetilde{Q}_I : \widetilde{G}_I \to G_I. \tag{6}$$

Likewise, we define the second block of the prolongation operator, denoted by $\overline{Q}$, which correlates the information between $\widetilde{G}_I \cup \widetilde{G}_L$ and the internal degrees of freedom of G, i.e., G_L:

$$\overline{Q} : \widetilde{G}_I \cup \widetilde{G}_L \to G_L \tag{7}$$

which is partitioned as

$$\overline{Q} = [\widetilde{Q}_{LI} \quad \widetilde{Q}_{LL}] \tag{8}$$

such that

$$\widetilde{Q}_{LI} : \widetilde{G}_I \to G_L \quad \text{and} \quad \widetilde{Q}_{LL} : \widetilde{G}_L \to G_L. \tag{9}$$

Consequently, the operator $\widetilde{Q}$ can be structured as follows:

$$\widetilde{Q} = \begin{bmatrix} \widetilde{Q}_I & 0 & 0 \\ \widetilde{Q}_{LI} & \widetilde{Q}_{LL} & 0 \end{bmatrix}. \tag{10}$$

The restrictions operators $\widetilde{Q}^{\mathrm{T}} : G \to \widetilde{G}$ and $\widehat{Q}^{\mathrm{T}} : G_I \to \widehat{G}$ are transposed of $\widetilde{Q}$ and $\widehat{Q}$, respectively. For subsequent derivations we will introduce the following notation:

$$\widetilde{u} = [\widetilde{u}_I \ \widetilde{u}_L \ \widetilde{u}_G]^{\mathrm{T}} \quad \text{where } \widetilde{u}_I \in \widetilde{G}_I,\ \widetilde{u}_L \in \widetilde{G}_L,\ \widetilde{u}_G \in \widetilde{G}_G.$$

$$\widehat{u} = [\widetilde{u}_I \ \widetilde{u}_G]^{\mathrm{T}} \quad \text{where } \widehat{u} \in \widehat{G}.$$

$$u = [\widehat{Q}\widehat{u} \ u_L]^{\mathrm{T}} \quad \text{where } u_L \in G_L.$$

$$\tilde{A} = \begin{bmatrix} \tilde{A}_{II} & \tilde{A}_{IL} & \tilde{A}_{IG} \\ \tilde{A}_{LI} & \tilde{A}_{LL} & 0 \\ \tilde{A}_{GI} & 0 & \tilde{A}_{GG} \end{bmatrix} \quad \text{stiffness matrix on } \tilde{G}.$$

$$\hat{A} = \begin{bmatrix} \tilde{A}_{II} & \tilde{A}_{IG} \\ \tilde{A}_{GI} & \tilde{A}_{GG} \end{bmatrix} \quad \text{stiffness matrix on } \hat{G}.$$

$$A = \begin{bmatrix} A_{II} & A_{IL} \\ A_{LI} & A_{LL} \end{bmatrix} \quad \text{stiffness matrix on } G.$$

$\tilde{f} = [\tilde{f}_I \ \tilde{f}_L \ \tilde{f}_G]$ force vector, where $\tilde{f}_I$, $\tilde{f}_L$, $\tilde{f}_G$ are nodal forces acting on grids $\tilde{G}_I$, $\tilde{G}_L$, $\tilde{G}_G$, respectively.

$\hat{f} = [\tilde{f}_I \ \tilde{f}_G]^{\mathrm{T}}$ force vector acting on $\hat{G}$.

$f = [f_I \ f_L]$ where f_I and f_L are nodal forces acting on grids G_I and G_L, respectively.

We note that the displacement vectors $\tilde{u}$ and $\hat{u}$ are related via orthogonal operator L given by

$$T = \begin{bmatrix} I & 0 & 0 \\ 0 & 0 & I \end{bmatrix} \tag{11}$$

where I is an identity matrix of an appropriate size, such that

$$\hat{u} = T\tilde{u}. \tag{12}$$

We now may formulate an algebraic system of equations for the two-level linear problem. It consists of finding a pair of nodal displacements vectors $(\hat{u}, u)$ such that

$$\tfrac{1}{2}\big((\hat{A}\hat{u}, \hat{u}) + (Au, u)\big) - \big(\hat{f}, \hat{u}\big) - (f, u) \Rightarrow \min_{(\hat{u},u)} \tag{13}$$

where $(\cdot,\cdot)$ denotes the bilinear form defined by

$$(u, v) = \sum_{j=1}^{n} u_j v_j, \quad u, v \in \mathbb{R}^n. \tag{14}$$

Minimization of (13) with respect to $(\hat{u}, u)$ subjected to the interface condition (13) yields a system of linear equations on the composite grid:

$$\begin{bmatrix} \hat{A} + \hat{Q}^{\mathrm{T}} A_{II} \hat{Q} & \hat{Q}^{\mathrm{T}} A_{IL} \\ A_{LI}\hat{Q} & A_{LL} \end{bmatrix} \begin{bmatrix} \hat{u} \\ u_L \end{bmatrix} = \begin{bmatrix} \hat{f} + \hat{Q}^{\mathrm{T}} f_I \\ f_L \end{bmatrix}. \tag{15}$$

The system of linear equations (15) can be solved either directly or iteratively. It is our objective to develop a hierarchical global–local procedure, which exploits the solution of the auxiliary shell model on the entire problem domain.

2.2. Two-level solution procedures

In this section, we describe a four-step procedure for solving the system of linear equations (15). The iterative solution procedure based on the minimization of energy functional (13) is given below.

Step 1. Find the correction $\delta\widetilde{u}^i$ which minimizes the two-level energy functional (13) on the subspace of the coarse grid functions:

$$\tfrac{1}{2}\big((\widehat{A}(\widehat{u}^i + T\delta\widetilde{u}^i), \widehat{u}^i + T\delta\widetilde{u}^i\big) + \big(A(u^i + \widetilde{Q}\delta\widetilde{u}^i), u^i + \widetilde{Q}\delta\widetilde{u}^i\big)\big) - \big(\hat{f}, \widehat{u}^i + T\delta\widetilde{u}^i\big) - \big(f, u^i + \widetilde{Q}\delta\widetilde{u}^i\big) \Rightarrow \min_{\delta\widetilde{u}^i} \tag{16}$$

where the superscripts refer to the iteration count. Note that the coarse grid correction $\delta\widetilde{u}$ has a similar partitioning to $\widetilde{u}$, i.e.,

$$\delta\widetilde{u} = \big[\delta\widetilde{u}_I \delta\widetilde{u}_L \delta\widetilde{u}_G\big]^{\mathrm{T}} \quad \text{and} \quad \delta\widehat{u} = \big[\delta\widetilde{u}_I \delta\widetilde{u}_G\big]^{\mathrm{T}}.$$

The direct minimization of (16) with respect to $\delta\widetilde{u}$ yields:

$$\big(T^{\mathrm{T}}\widehat{A}T + \widetilde{Q}^{\mathrm{T}}A\widetilde{Q}\big)\delta\widetilde{u}^i = T^{\mathrm{T}}\big(\hat{f} - \widehat{A}\widehat{u}^i\big) + \widetilde{Q}^{\mathrm{T}}\big(f - Au^i\big). \tag{17}$$

The first term $T^{\mathrm{T}}\widehat{A}T$ on the left-hand side represents the assembled form of the coarse grid stiffness matrix, whereas the second term $\widetilde{Q}^{\mathrm{T}}A\widetilde{Q}$ represents the restricted stiffness matrix of the 3D elasticity model in the local region. For the purpose of approximating the coarse grid correction $\delta\widetilde{u}$ we will replace the two terms by the stiffness matrix of the shell model on the entire problem domain, i.e.,

$$\widetilde{A} \Leftarrow T^{\mathrm{T}}\widehat{A}T + \widetilde{Q}^{\mathrm{T}}A\widetilde{Q}. \tag{18}$$

Substitution (18) represents a major departure from the classical FAC method. In fact, this approximation may not be necessarily good because there might be a significant difference between the two mathematical models for thin domain elasticity problems (see, for example, [18]). Nevertheless, this approximation is absolutely must if the composite grid method is to be considered as a viable alternative to engineering global–local approaches in aerospace industries. A typical all-shell grid $\widetilde{G}$ often consists of over a million degrees of freedom, whereas local grids G constructed in the vicinity of cutouts, fasteners, holes and other interconnects are orders of magnitude smaller. In a large scale computational environment this approximation will significantly reduce computational cost, since only a single factorization of $\widetilde{A}$ is required for numerous redesigns of local features.

Step 2. Once the coarse grid correction has been carried out, it is necessary to update the solution:

$$\widetilde{u}^{i+1} = \widetilde{u}^i + \delta\widetilde{u}^i, \qquad \widehat{u}^{i+1} = \widehat{u}^{i+1} + T\delta\widetilde{u}^i, \qquad u^{i+1} = u^i + \widetilde{Q}\delta\widetilde{u}^i. \tag{19}$$

Step 3. Find the correction Δu_L on the fine mesh, which minimizes the energy functional on the subspace of the functions on G_L, i.e., keeping $\widehat{u}^i$ fixed

$$\tfrac{1}{2}\big((\widehat{A}\widehat{u}^i, \widehat{u}^i) + \big(A(u^i + \Delta u^i), u^i + \Delta u^i\big)\big) - \big(\hat{f}, \widehat{u}^i\big) - \big(f, u^i + \Delta u^i\big) \Rightarrow \min_{\Delta u^i} \tag{20}$$

where $\Delta u_I = 0$ to maintain compatibility.

The direct minimization of (20) yields

$$A_{LL}\Delta u_L^i = f_L - A_{LI}\widehat{Q}\widehat{u}^i - A_{LL}u_L^i. \tag{21}$$

If (21) is solved exactly, i.e.,

$$\Delta u_L^i = A_{LL}^{-1}\left(f_L - A_{LI}\widehat{Q}\widehat{u}^i - A_{LL}u_L^i\right) \tag{22}$$

then the corresponding iterative process will be referred as HFAC-ex. Alternatively, A_{LL} can be replaced by preconditioner P_{LL}, which yields

$$\Delta u_L^i = \tau_i P_{LL}^{-1}\left(f_L - A_{LI}\widehat{Q}\widehat{u}^i - A_{LL}u_L^i\right) \tag{23}$$

where τ_i is a relaxation parameter given by

$$\tau_i = \frac{(f_L - A_{LI}\widehat{Q}\widehat{u}^i - A_{LL}u_L^i, \nu_L^i)}{(A_{LL}\nu_L^i, \nu_L^i)} \tag{24}$$

and $\nu_L^i = P_{LL}^{-1}(f_L - A_{LI}\widehat{Q}\widehat{u}^i - A_{LL}u_L^i)$. The latter will be referred as HFAC-ap.

Step 4. Since the approximation introduced in (18) is not necessarily good, we view Steps 1–3 as a nonsymmetric preconditioner, and thus displacements $\widetilde{u}^i$, $\widehat{u}^i$, u^i computed in Step 2 are updated using a two-parameter acceleration scheme. For convenience, the total correction on the fine grid, i.e., $\widetilde{Q}\delta\widetilde{u}^i + \Delta u^i$, is denoted here by $\mathrm{d}u^i$. Then, we ultimately update the solution according to

$$\begin{aligned}
\widetilde{u}^{i+1} &= \widetilde{u}^i + \alpha\delta\widetilde{u}^i + \beta\delta\widetilde{u}^{i-1},\\
\widehat{u}^{i+1} &= \widehat{u}^i + \alpha T\delta\widetilde{u}^i + \beta T\delta\widetilde{u}^{i-1},\\
u^{i+1} &= u^i + \alpha\,\mathrm{d}u^i + \beta\,\mathrm{d}u^{i-1},
\end{aligned} \tag{25}$$

where the parameters α, β are found from the minimization of the energy functional on the subspace spanned by the vectors $[(T\delta\widetilde{u}^i)_G\,\mathrm{d}u^i]^{\mathrm{T}}$ and $[(T\delta\widetilde{u}^{i-1})_G\,\mathrm{d}u^{i-1}]^{\mathrm{T}}$:

$$\begin{aligned}
&\tfrac{1}{2}\Big(\big(\widehat{A}\big(\widehat{u}^i + \alpha T\delta\widetilde{u}^i + \beta T\delta\widetilde{u}^{i-1}\big), \widehat{u}^i + \alpha T\delta\widetilde{u}^i + \beta T\delta\widetilde{u}^{i-1}\big)\\
&\quad + \big(A\big(u^i + \alpha\,\mathrm{d}u^i + \beta\,\mathrm{d}u^{i-1}\big), u^i + \alpha\,\mathrm{d}u^i + \beta\,\mathrm{d}u^{i-1}\big)\Big)\\
&\quad - \big(\hat{f}, \widehat{u}^i + \alpha T\delta\widetilde{u}^i + \beta T\delta\widetilde{u}^{i-1}\big) - \big(f, u^i + \alpha\,\mathrm{d}u^i + \beta\,\mathrm{d}u^{i-1}\big) \Rightarrow \min_{\alpha,\beta}.
\end{aligned} \tag{26}$$

A direct minimization of (26) with respect to α and β yields:

$$\begin{bmatrix} c_{11} & c_{12} \\ c_{12} & c_{22} \end{bmatrix} \begin{bmatrix} \alpha \\ \beta \end{bmatrix} = \begin{bmatrix} r_1 \\ r_2 \end{bmatrix} \tag{27}$$

where

$$\begin{aligned}
c_{11} &= \big(T^{\mathrm{T}}\widehat{A}T\delta\widetilde{u}^i, \delta\widetilde{u}^i\big) + \big(A\,\mathrm{d}u^i, \mathrm{d}u^i\big),\\
c_{22} &= \big(T^{\mathrm{T}}\widehat{A}T\delta\widetilde{u}^{i-1}, \delta\widetilde{u}^{i-1}\big) + \big(A\,\mathrm{d}u^{i-1}, \mathrm{d}u^{i-1}\big),\\
c_{12} &= \big(T^{\mathrm{T}}\widehat{A}T\delta\widetilde{u}^i, \delta\widetilde{u}^{i-1}\big) + \big(A\,\mathrm{d}u^i, \mathrm{d}u^{i-1}\big),\\
r_1 &= \big(T^{\mathrm{T}}\big(\hat{f} - \widehat{A}\widehat{u}^i\big), \delta\widetilde{u}^i\big) + \big(f - Au^i, \mathrm{d}u^i\big),\\
r_2 &= \big(T^{\mathrm{T}}\big(\hat{f} - \widehat{A}\widehat{u}^i\big), \delta\widetilde{u}^{i-1}\big) + \big(f - Au^i, \mathrm{d}u^{i-1}\big).
\end{aligned} \tag{28}$$

2.3. Intergrid transfer operators

Let P_A be the finite element node in the 3D solid mesh at the interface Ω_I and let P_{A_i} represent its degrees of freedom with $P_{A_\alpha} = [P_{A_1}\ P_{A_2}]$ corresponding to in-plane degrees of freedom and P_{A_3} to the transverse normal degrees of freedom. Likewise $\widetilde{P}_a$ denotes the nodes in the shell model at the interface $\widetilde{\Omega}_I$ having either 5 or 6 degrees of freedom per node.

We will construct the interface prolongation operator $\widetilde{Q}_I : \widetilde{G}_I \to G_I$ (needed for both HFAC-ex and HFAC-ap procedures) assuming the so-called "telescopic" constraints at the shell/3D interface, where the in-plane degrees of freedom $P_{A_\alpha} \in \Omega_I$ and transverse degrees of freedom at the midplane $\{P_{A_3}(\zeta = 0)\} \in \Omega_I$ are considered as the slave nodes, i.e., belong to the set G_I, whereas the transverse degrees of freedom outside the midplane $\{P_{A_3}(\zeta) \neq 0\} \in \Omega_I$ belong to the set G_L rather than G_I. Here, for simplicity, we assume that there exists a layer of nodes in the 3D solid mesh at the midplane, as shown in Fig. 1.

The interface prolongation operator $\widetilde{Q}_I$ consists of nodal blocks Q_I^{Aa} corresponding to mapping the solution from the coarse mesh node $\widetilde{P}_a$ to P_A, where the projection of the fine grid node P_A onto the shell surface is within the shell element connected to node $\widetilde{P}_a$. Using the shell element formulation based on the degenerated solid model, the nodal interface prolongation operator Q_I^{Aa} in the local fiber coordinate system is given by

$$Q_I^{Aa} = \begin{bmatrix} \widetilde{N}_a(\xi_A,\eta_A) & 0 & 0 & 0 & \frac{1}{2}h_A\zeta_A\widetilde{N}_a(\xi_A,\eta_A) \\ 0 & \widetilde{N}_a(\xi_A,\eta_A) & 0 & -\frac{1}{2}h_A\zeta_A\widetilde{N}_a(\xi_A,\eta_A) & 0 \\ 0 & 0 & \widetilde{N}_a(\xi_A,\eta_A) & 0 & 0 \end{bmatrix}. \tag{29}$$

Note that the first three columns correspond to translational degrees of freedom, whereas columns 4 and 5 correspond to rotational degrees of freedom in the fiber coordinate system. The first two rows correspond to the prolongation of the in-plane degrees of freedom, whereas row three designates prolongation at the midplane in the transverse direction. $\widetilde{N}_a(\xi_A,\eta_A)$ denotes the in-plane shape function corresponding to the shell element node $\widetilde{P}_a$ computed at the fine grid node P_A; ξ_A, η_A, ζ_A are the natural coordinates in the shell computed at fine grid node P_A.

If the HFAC-ap scheme is employed, then, in addition to $\widetilde{Q}_I$ it is necessary to construct the prolongation operator $\overline{Q} : \widetilde{G}_I \cup \widetilde{G}_L \to G_L$. Let $\widehat{\overline{Q}}^{Aa}$ be the initial value of nodal blocks $\overline{Q}^{Aa}$ in the fiber coordinate system obtained from the degenerated solid model in a similar fashion to that in Eq. (29). Since the lower order shell theories [12] do not take into account the fiber elongation in the transverse normal direction, it is necessary to correct the transverse normal displacements by the integral over transverse normal strains. The resulting nodal prolongation operator in the fiber coordinate system is given as

$$\overline{Q}^{Aa} = \widehat{\overline{Q}}^{Aa} - \begin{bmatrix} 0 \\ 0 \\ \sum_{i=1}^{5} \int_0^{\zeta_A} \dfrac{D_{6i}\widetilde{B}_{ai}(\xi_A,\eta_A)}{D_{66}}\,\mathrm{d}\zeta \end{bmatrix} \tag{30}$$

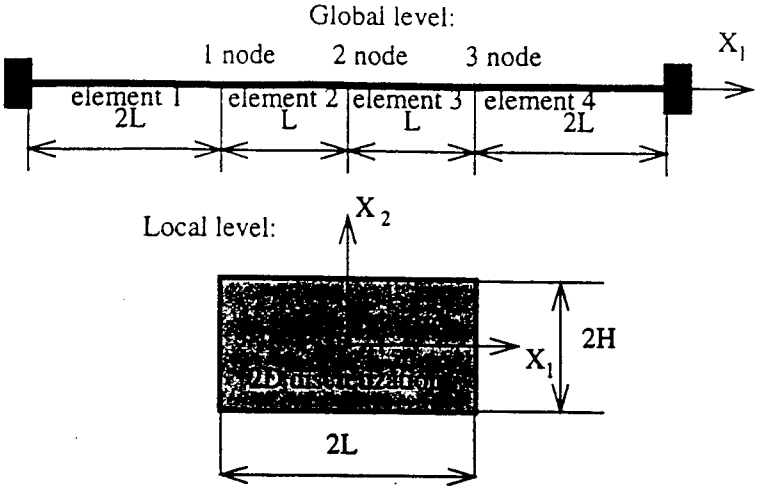


Fig. 2. Discretization of the model problem.

where $\boldsymbol{D}$ is the three-dimensional constitutive matrix corresponding to the transverse normal stress, and $\widetilde{\boldsymbol{B}}_{ai}$ is the block of the strain-displacement matrix of the shell element corresponding to the shell node $\widetilde{P}_a$.

3. Model problem

In this section the rate of convergence of the iterative procedure described in the previous section is estimated in the closed form for beam/2D model problem shown in Fig. 2.

For the 2D domain on $-L \leqslant x_1 \leqslant L$, $-H \leqslant x_2 \leqslant H$ the governing elasticity equations in the tensorial notation are given as:

$$\sigma_{ij,j} + b_i = 0, \quad \sigma_{ij} = \lambda u_{k,k}\delta_{ij} + 2\mu u_{(i,j)}, \qquad i,j = 1,2, \tag{31}$$

where λ, μ are material constants; σ_{ij} the symmetric stress tensor; δ_{ij} the Kronecker delta; comma denotes the spatial derivative; parentheses around the subscripts represent the symmetric gradient.

For the beam domain on $L < x_1 \leqslant 2L$, $-2L \leqslant x_1 < -L$ the governing elasticity equations are the same, but in addition, the following Timoshenko beam constrains are imposed to restrict the kinematics of the beam:

$$\sigma_{i2} = 0, \qquad u_1(x_1, x_2) = -\theta(x_1)x_2, \qquad \int_{-H}^{H} x_2 \, \mathrm{d}x_2 = 0, \tag{32}$$

where θ is the beam rotation. The essential boundary conditions are applied at the two ends of the beam, i.e., $u_1(x_1 = \mp 2L) = -\theta(x_1 = \mp 2L) = 0$. Compatibility is enforced at the beam/2D interface:

$$\begin{aligned} &u_1(x_1 = \mp L) = -\theta(x_1 = \mp L)x_2, \\ &u_2\big(x_1 = \mp(L+\varepsilon)\big) = u_2\big(x_1 = \mp(L-\varepsilon), x_2 = 0\big), \quad 0 < \varepsilon \ll 1. \end{aligned} \tag{33}$$

3.1. Model description

We consider the finite element discretization depicted in Fig. 2. On the global level we use Timoshenko's beam elements with quadratic shape functions for the transverse displacements and linear shape functions for the rotations. Timoshenko's beam element has been chosen since it represents one-dimensional counterpart of the Mindlin–Reissner shell/plate element. For the local model, a single p-type 2D element is employed with nonuniform polynomial order of displacement interpolation functions in x and y denoted as p and q, respectively.

We first focus on the construction of the discrete system of equations for the model problem. The displacement field of the 2D element can be cast into the following form:

$$u_i = \sum_{J=1}^{4} U_{iJ} a_J \tag{34}$$

where $\boldsymbol{a} = [\nu_1\ \theta_1\ \nu_2\ \theta_2]^{\mathrm{T}}$ is the vector of nodal displacements (two translations and two rotations), and U_{iJ}, $i = 1,2$, $J = 1,4$, is the solution of the two-dimensional problem corresponding to the prescribed Jth unit nodal displacement while keeping the other nodal displacements constrained. Note that the constraints between the beam and the 2D element are of telescopic type, i.e., at the interface u_1 is prescribed for all y, while u_2 is prescribed only at $y = 0$. It is not the objective of this paper to study the influence of various global–local interface conditions on the solution accuracy. Instead, we are only focusing on the convergence characteristics of the iterative process given the interface conditions employed in practical applications [1].

The functions U_{iJ} are discretized as follows:

$$U_{iJ} = \sum_{l} \sum_{m} d_{iJlm} \Phi_l(\xi) \Psi_m(\eta) \tag{35}$$

where $\xi = 1/L$ and $\eta = 1/H$, $\Phi_l(\xi)$ and $\Psi_m(\eta)$ are the basis functions given as

$$\Phi_1 = -\frac{\xi - 1}{2}, \qquad \Phi_2 = -\frac{\xi + 1}{2}, \qquad \Phi_{k+1} = \sqrt{\frac{2k-1}{2}} \int_{-1}^{\xi} P_{k-1}(t)\,\mathrm{d}t, \quad k = 2,3,\ldots, \tag{36}$$

and

$$\Psi_n = \eta^{n-1}, \quad n = 1,2,\ldots, \tag{37}$$

where $P_k(\xi)$ are Legendre polynomials of order k.

Let $\boldsymbol{K}\boldsymbol{d}_{iJ} = 0$ be the discrete system of equations arising from the discretization given in (35) subjected to Jth unit displacement on the boundary, where $\boldsymbol{d}_{iJ} = \{d_{iJlm}\}$ and $\boldsymbol{K}$ is the corresponding stiffness matrix. The coefficients d_{iJlm} may be found exactly or approximately. The former is denoted as HFAC-ex, while the latter is termed HFAC-ap.

Once the coefficients d_{iJlm} are found, one may find the coefficients of the stiffness matrix for 2D element with the interface nodal degrees of freedom $\boldsymbol{a} = [\nu_1\ \theta_1\ \nu_2\ \theta_2]^{\mathrm{T}}$:

$$A_{JK} = \int_{\Omega_e} U_{(aJ,b)} D_{abfg} U_{(fK,g)}\,\mathrm{d}\Omega_e \quad \text{(sum over repeated indices)} \tag{38}$$

where $J = 1,\ldots,4$, $K = 1,\ldots,4$, D_{abfg} are the components of the 2D plain-strain elastic constitutive tensor, $u_{(ij)}$ are the components of the symmetric part of the tensor $\nabla \boldsymbol{u}$.

3.2. Convergence properties of the algorithm

The point iteration matrix $S: e_I^i \mapsto e_I^{i+1}$ derived in Appendix A is given as

$$S = I - \tilde{Q}\tilde{A}^{-1}\tilde{Q}^{\mathrm{T}}A \tag{39}$$

where e_I^i is the solution error at the interface in iteration i and $\tilde{Q}$ is the prolongation operator $\tilde{Q}$ equal to

$$\tilde{Q} = \begin{bmatrix} 1 & 0 & 0 & 0 & 0 & 0 \\ 0 & 1 & 0 & 0 & 0 & 0 \\ 0 & 0 & 1 & 0 & 0 & 0 \\ 0 & 0 & 0 & 1 & 0 & 0 \end{bmatrix}. \tag{40}$$

More details on Eqs. (39) and (40) are given in Appendix A.

In this section, we present closed form expressions for the spectral radius of the iteration matrices for different values of p and q, denoted by $\rho(S^{p,q})$, where p is the in-plane polynomial order (x_1 direction) and q is the polynomial order through the thickness of the beam (x_2 direction). These expressions have been obtained using the symbolic math package Maple [21]. In what follows we give a Taylor series expansions about the point $H/L = 0$, where $\nu < 0.5$ is Poisson's ratio.

3.2.1. HFAC-ex algorithm

$$\rho(S^{2,1}) = \begin{cases} \dfrac{2}{33}(1-\nu)\left(\dfrac{H}{L}\right)^{-2} + \dfrac{2}{5445}\dfrac{1375\nu^2 + 1504\nu - 752}{1-2\nu} + \mathrm{O}\left(\left(\dfrac{H}{L}\right)^2\right), & \text{for } \nu \leqslant 0.497, \\ \dfrac{2}{3}\left(\dfrac{\nu^2}{1-2\nu}\right), & \text{otherwise,} \end{cases}$$

$$\rho(S^{3,1}) = \begin{cases} \dfrac{8}{33}\dfrac{(1+\nu)(1-3\nu)}{(1-2\nu)} + \mathrm{O}\left(\left(\dfrac{H}{L}\right)^2\right), & \text{for } \nu \leqslant 0.277, \\ \dfrac{2}{3}\left(\dfrac{\nu^2}{1-2\nu}\right), & \text{otherwise,} \end{cases}$$

$$\rho(S^{2,2}) = \frac{2}{33}(1-\nu)\left(\frac{H}{L}\right)^{-2} - \left(\frac{1343}{4840} + \frac{19}{396}\nu\right) + \mathrm{O}\left(\left(\frac{H}{L}\right)^2\right),$$

$$\rho(S^{2,3}) = \frac{2}{33}(1-\nu)\left(\frac{H}{L}\right)^{-2} - \left(\frac{1343}{4840} + \frac{19}{396}\nu\right) + \mathrm{O}\left(\left(\frac{H}{L}\right)^2\right),$$

$$\rho(S^{3,2}) = \frac{8}{33} - \frac{4}{1815}\frac{(33\nu^2 - 330\nu + 406)}{1-\nu}\left(\frac{H}{L}\right)^2 + \mathrm{O}\left(\left(\frac{H}{L}\right)^4\right).$$

It can be seen that the HFAC-ex method for the model problem converges ($\rho(S) < 1$) independently of material parameters, provided $p \geqslant 3$ and $q \geqslant 2$. In the case of linear through-the-thickness

discretization, the iterative process diverges independently of in-plane discretization as the material approaches the incompressible limit, i.e., $\nu \to 0.5$.

Similarly, in the case of insufficient in-plane discretization ($p < 3$), HFAC-ex diverges for thin shells ($H/L \to 0$).

3.2.2. HFAC-ap algorithm

We first consider a Gauss–Seidel preconditioner of the form $(l+d)^{-1}$, where l is the lower triangular part of A_{LL} in (21), and d is the main diagonal of A_{LL}.

$$\rho(S^{2,1}) = \begin{cases} \dfrac{2}{33}(1-\nu)\left(\dfrac{H}{L}\right)^{-2} + \dfrac{2}{5445}\dfrac{1375\nu^2+1504\nu-752}{1-2\nu} + \mathrm{O}\left(\left(\dfrac{H}{L}\right)^2\right), & \text{for } \nu \leqslant 0.497, \\ \dfrac{2}{3}\left(\dfrac{\nu^2}{1-2\nu}\right), & \text{otherwise,} \end{cases}$$

$$\rho(S^{3,1}) = \frac{7}{100}(1-\nu)\left(\frac{H}{L}\right)^{-2} + \frac{99\nu^2-98\nu+49}{1-2\nu} + \mathrm{O}\left(\left(\frac{H}{L}\right)^2\right).$$

$$\rho(S^{2,2}) = \frac{2}{33}(1-\nu)\left(\frac{H}{L}\right)^{-2} + \frac{1}{557568}\frac{87362\nu^2+286437\nu-154609}{1-2\nu} + \mathrm{O}\left(\left(\frac{H}{L}\right)^2\right),$$

$$\rho(S^{2,3}) = \frac{2}{33}(1-\nu)\left(\frac{H}{L}\right)^{-2} + \frac{1}{557568}\frac{87362\nu^2+286437\nu-154609}{1-2\nu} + \mathrm{O}\left(\left(\frac{H}{L}\right)^2\right),$$

$$\rho(S^{3,2}) = \frac{7}{100}(1-\nu)\left(\frac{H}{L}\right)^{-2} + \frac{1}{600}\frac{177\nu^2-784\nu+392}{1-2\nu} + \mathrm{O}\left(\left(\frac{H}{L}\right)^2\right).$$

For large values of Poisson's ratio $\nu \to 0.5$, higher order terms in H/L cannot be truncated since they contain terms of the form $1/(1-2\nu)^n$ $(n > 0)$ that grow unboundedly for incompressible materials, thereby affecting the spectral radius considerably even for small values of H/L.

For all cases considered the spectral radius was $\mathrm{O}((H/L)^{-2})$, indicating that HFAC-ap scheme with fixed number of smoothing iterations is inappropriate for thin shells. Next, we investigate whether stronger smoothing, in the form of two symmetric Gauss–Seidel sweeps, which correspond to the preconditioner $(l+d)^{-1}d(l+d)^{-T}$, can eliminate the lower order term.

$$\rho(S^{2,1}) = \begin{cases} \dfrac{2}{33}(1-\nu)\left(\dfrac{H}{L}\right)^{-2} + \dfrac{2}{5445}\dfrac{1375\nu^2+1504\nu-752}{1-2\nu} + \mathrm{O}\left(\left(\dfrac{H}{L}\right)^2\right), & \text{for } \nu \geqslant 0.497, \\ \dfrac{2}{3}\left(\dfrac{\nu^2}{1-2\nu}\right), & \text{otherwise,} \end{cases}$$

$$\rho(S^{3,1}) = \frac{1}{99}(1-\nu)\left(\frac{H}{L}\right)^{-2} + \frac{1}{16335}\frac{11000\nu^2+8654\nu-4327}{1-2\nu} + \mathrm{O}\left(\left(\frac{H}{L}\right)^2\right).$$

For the case of $p = 3$, $q = 1$ we also consider the SSOR preconditioner of the form $\omega(2-\omega)(l+d)^{-1}d(l+d)^{-T}$, which yields

$$\rho(S^{3,1}_{\omega}) = \frac{1-\nu}{99}(5\omega^6 - 30\omega^5 + 90\omega^4 - 160\omega^3 + 180\omega^2 - 120\omega + 36)\left(\frac{H}{L}\right)^{-2} + \mathrm{O}(1)$$

with $\omega = 1$ giving the optimal choice.

$$\rho(S^{2,2}) = \frac{2(1-\nu)}{33}\left(\frac{H}{L}\right)^{-2} + \frac{1}{1393920}\frac{284240\nu^2 + 681608\nu - 385739}{1-2\nu} + O\left(\left(\frac{H}{L}\right)^2\right),$$

$$\rho(S^{2,3}) = \frac{2(1-\nu)}{33}\left(\frac{H}{L}\right)^{-2} + O(1),$$

$$\rho(S^{3,2}) = \frac{1}{99}(1-\nu)\left(\frac{H}{L}\right)^{-2} + O(1).$$

For all the polynomial orders p, q considered, the SSOR preconditioner reduced considerably the coefficient of the term $O((H/L)^{-2})$ as compared to GS preconditioner even though, this term was not completely removed.

In our last experiment conducted on the model problem, we have perturbed the stiffness matrix of the local grid (2D element) with a small fraction ($\eta \to 0$) of its diagonal, i.e.,

$$A^{\text{new}} = A + \eta\,\text{diag}(A), \tag{41}$$

and then have solved the local problem exactly. The resulting spectral radius has been symbolically computed using Maple:

$$\rho(S_\eta^{3,1}) = \left[\frac{10}{9}(1-\nu)\eta^2 + O(\eta^3)\right]\left(\frac{H}{L}\right)^{-2} + O(1). \tag{42}$$

It can be seen that a small perturbation of the exact local factor has a devastating influence as $H/L \to 0$, since a typical L/H ratio is over 1000 in aerospace and mechanical engineering applications and over 100 in civil engineering applications. This phenomenon is a direct consequence of the approximation introduced in (18).

4. Numerical examples

Two problems are considered for numerical investigation of computational efficiency of HFAC-ex and HFAC-ap procedures in the context of shell/3D global–local problems. The first test problem is a thick laminated shell subjected to axial tension. The second is a thin cylindrical shell. In both cases, local effects developed at the free edge are of interest.

As a termination criterion, we use the ratio of the residual norm versus the norm of the right-hand side vector, i.e.,

$$\frac{\|r\|_2}{\|f\|_2} \leqslant \text{eps} \quad \text{and} \quad \|v\|_2 = \left(\sum_{i=1}^{n} v_i^2\right)^{0.5} \tag{43}$$

where the tolerance is chosen to be eps $= 10^{-6}$. All computations have been carried out on a SUN SPARC 10/41 workstation.

4.1. $(45/-45)_s$ *laminate in extension*

We consider a thick four-layer $(45/-45)_s$ laminate subjected to axial tension. Geometry, boundary conditions and material properties are shown in Fig. 3. The plies in the laminate are of equal thickness

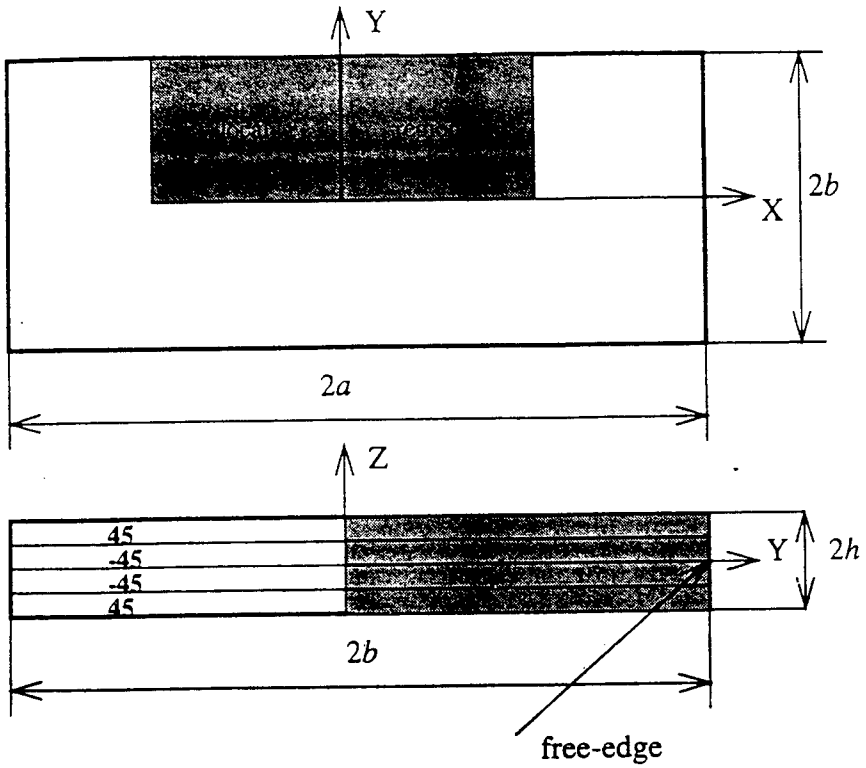


Fig. 3. Axial tension problem definition. $a/b = 10$, $b/h = 4$, $h = 2h_k$, $b/h_k = 8$, $E_1 = 20\times10^6$ psi, $E_2 = E_3 = 2.1\times10^6$ psi, $G_{12} = G_{23} = G_{13} = 0.85 \times 10^6$ psi, $\nu_{12} = \nu_{23} = \nu_{13} = 0.21$. Displacement boundary conditions: $u_1(a, y, z) = u_0$, $u_1(-a, y, z) = 0$, $u_2(-a, 0, z) = u_2(a, 0, z) = 0$, $u_3(-a, 0, z) = 0$.

Table 1
Convergence studies for laminated plate problem

Method type	Number of relaxation sweeps (HFAC-ap)	Number of cycles	CPU (sec) factorization	CPU (sec) iterative solution	CPU (sec) total
HFAC-ap	1	57	30	274	800
HFAC-ap	2	38	30	250	776
HFAC-ap	3	31	30	247	774
HFAC-ap	4	28	30	265	800
HFAC-ap	5	24	30	264	788
HFAC-ex	–	10	595	85	1050

idealized as a homogeneous, orthotropic material. Subscript "1" denotes the direction parallel to the fibers, subscript "2" for in-plane direction perpendicular to the fibers, and subscript "3" for the out-of-plane direction.

ANS shell elements [25] are used in the global region and 10-node tetrahedrals in the local region. The local mesh is graded towards the free edge of the laminate. On the coarse mesh, the number of nodes is 171 and the number of shell finite elements is 36. On the fine mesh, the number of nodes is 11,530 and the number of tetrahedral elements is 7,233. For HFAC-ap we employ an Incomplete Cholesky Factorization preconditioner by value with zero fill-ins. Table 1 compares convergence of the HFAC-ap and HFAC-ex algorithms. It can be seen that although the number of cycles required for HFAC-ap is significantly higher than for HFAC-ex, the CPU time for HFAC-ap is lower. This example suggest that for thick domain problems, where $(L/H)^2$ term is not dominant, HFAC-ap with a relatively weak coarse grid preconditioner is an optimal choice.

4.2. *Isotropic cylindrical shell problem*

In this subsection, we study a thin isotropic cylindrical shell problem. Geometry, displacement boundary conditions, material properties are depicted in Fig. 4.

As in the previous example, ANS shell elements are placed in the global region, whereas a 10-node tetrahedral unstructured mesh is used in the local region. The coarse model consists of 171 nodes and 36 shell elements. For the fine model three meshes were considered: (i) 226 10-node tetrahedral finite elements (467 nodes), (ii) 980 10-node tetrahedral finite elements (1,820 nodes), 3,318 10-node tetrahedral finite elements (5,840 nodes). All fine level meshes have the same number of 3D elements through the thickness direction (approximately 2 elements), whereas the number of elements is approximately varied by a factor of 2 in the in-plane direction for the 3D meshes considered. The coarsest mesh of 3D elements has the size of a 3D element in the in-plane direction roughly the same as that

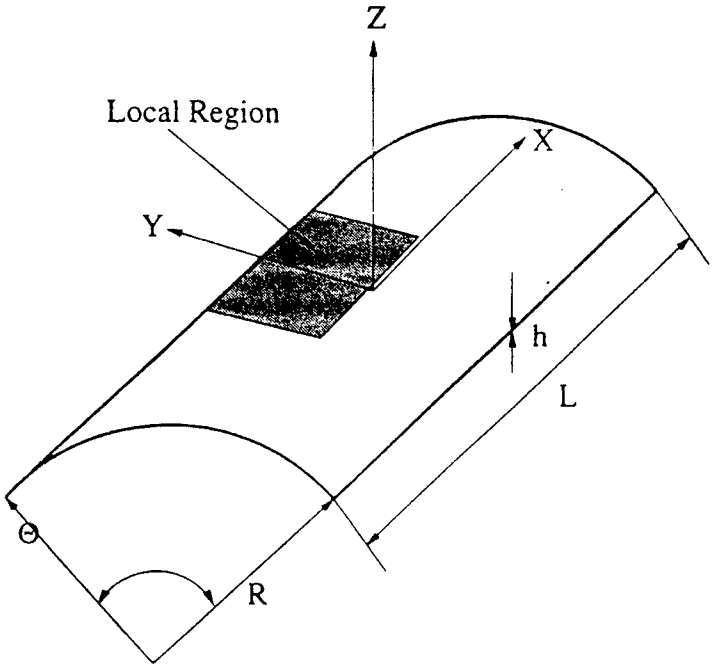


Fig. 4. Cylindrical shell problem definition. $L = 675$ mm, $R = 300$ mm, $h = 3$ mm, $\Theta = \pi/2$, $E = 26$ GPa, $\nu = 0.3$. Displacement boundary conditions: $u_1(-L/2, y, z) = 0$, $u_1(-L/2, y, z) = 1$ mm, $u_2(-L/2, 0, z) = u_2(L/2, 0, z) = 0$, $u_3(-L/2, 0, z) = 0$.

Table 2
Convergence studies for cylindrical shell problem (226 elements in the fine grid)

Method type	Number of relaxation sweeps (HFAC-ap)	Number of cycles	CPU (sec) factorization	CPU (sec) iterative solution	CPU (sec) total
HFAC-ap	5	1615	0.8	726	760
HFAC-ex	–	25	1.3	5	33

Table 3
Convergence studies for cylindrical shell problem (980 elements in the fine grid)

Method type	Number of relaxation sweeps (HFAC-ap)	Number of cycles	CPU (sec) factorization	CPU (sec) iterative solution	CPU (sec) total
HFAC-ap	5	580	3	1143	1240
HFAC-ex	–	14	16	12	100

Table 4
Convergence studies for cylindrical shell problem (3318 elements in the fine grid)

Method type	Number of relaxation sweeps (HFAC-ap)	Number of cycles	CPU (sec) factorization	CPU (sec) iterative solution	CPU (sec) total
HFAC-ap	5	377	14	2690	2980
HFAC-ex	–	11	179	24	364

of the shell element. Tables 2–4 provide the information on convergence characteristics for the three fine meshes considered. It can be seen that, by increasing the number of the elements in the in-plane directions, both HFAC-ex and HFAC-ap converge faster. This phenomenon is in good agreement with our analytical convergence estimates in Section 3. Moreover, numerical experiments reveal that the convergence of HFAC-ap with a weak course grid preconditioner is very poor. This finding confirms our analytical studies in Section 3 indicating that for thin beams or shells the $(L/H)^2$ term completely dominates the convergence characteristics of the HFAC-ap scheme, unless the coarse grid problem is solved up to a very tight tolerance.

5. Conclusions

A hierarchical version of the composite grid method (denoted as HFAC-ex and HFAC-ap), which exploits the solution of the shell model in studying local effects via a 3D solid model, is developed. Convergence studies on a beam/2D model problem indicate that the spectral radius of the point iteration matrix for HFAC-ex method is O(1), whereas for HFAC-ap it is $O((L/H)^2)$, where L and H are the

span and the thickness of the beam, respectively. Numerical experiments in multidimensions confirm these findings.

The major departure between the present paper and the work pioneered by McCormick [22,23] is in the approximation introduced in Eq. (18). This approximation may not be necessarily good because there might be a significant difference between the shell and the 3D models for thin domain elasticity problems. A typical all-shell grid $\widetilde{G}$ often consists of over a million degrees of freedom, whereas local grids G constructed in the local regions requiring better resolution are orders of magnitude smaller. Thus the approximation (18) will significantly reduce the computational cost, since only a single factorization of $\widetilde{A}$ is required for numerous redesigns of local features.

As a by-product of the approximation introduced in (18), two factors have been found to be absolutely critical to maintain reasonable rates of convergence of the iterative process for thin domain problems:

(i) *The local problem has to be solved exactly or up to a very tight tolerance.* For our numerical model, the thin cylindrical shell problem, it took 377–1615 cycles for the MIC smoother by value, with up to 20 fill-ins and 5 smoothings to converge as opposed to 11–25 cycles with a direct solver. In our analytical model we have found that a small perturbation to the exact local factor has a devastating influence on the convergence as $H/L \to 0$.

(ii) *The two-parameter acceleration in the two-step scheme.* It is necessary to consider a single cycle of the HFAC method as a nonsymmetric preconditioner and to accelerate the iterative process with a two-parameter acceleration scheme rather than with a more popular conjugate gradient method. None of the numerical examples considered converges without acceleration. In fact they rapidly diverge, as opposed to better than 0.5 rate of convergence with the two-parameter acceleration scheme. This is because the 3D model is typically much stiffer than a shell model resulting in a poor preconditioning.

Appendix A. Derivation of the point iteration matrix

In this section, we derive the point iteration matrix $S: e_I^i \to e_I^{i+1}$ for the model problem given in Section 3.1, where the subscript i denotes the iteration count. For the model problem described in Section 3.1, we condensed out the internal degrees of freedom of the local grid yielding $e_I = \widehat{e}_I$. Also $\widetilde{G}_G$ can be excluded from the consideration due to the boundary conditions prescribed at the end points of the beam. Under these circumstances, the prolongation operator $\widetilde{Q}$ in (10) can be simplified if we define it as the operator relating the nodal displacements in $\widetilde{G}_I \cup \widetilde{G}_L$ to those in G_I, i.e., $\widetilde{Q}: \widetilde{G}_I \cup \widetilde{G}_L \to G_I$, where $\widetilde{Q}$ is given in Eq. (40).

The errors in the two subsequent iterations are related as follows:

$$e_I^{i+1} = e_I^i - \widetilde{Q}\delta\widetilde{u}^i. \tag{A.1}$$

Combining (39) with (16) with exact Jacobians replaced by $\widetilde{A}$ yields

$$e_I^{i+1} = e_I^i - \widetilde{Q}\widetilde{A}^{-1}\left(T^{\mathrm{T}}\left(\hat{f}_I - \widehat{A}_{II}\widehat{u}_I^i\right) + \widetilde{Q}^{\mathrm{T}}\left(f_I - Au_I^i\right)\right) \tag{A.2}$$

where T is defined as $T = [I\ 0]$ and I is identity matrix of an appropriate size. Since $T = \widetilde{Q}$ and $\widehat{u}_I = u_I$, Eq. (A.1) may be written as

$$e_I^{i+1} = e_I^i - \widetilde{Q}\widetilde{A}^{-1}\widetilde{Q}^{\mathrm{T}}\left(\widehat{A}_{II} + A\right)c_I^i. \tag{A.3}$$

Defining

$$\mathcal{A} = \widehat{A}_{II} + A \tag{A.4}$$

where A, once again, is determined according to (38), one can write

$$e_I^{i+1} = Se_I^i \tag{A.5}$$

where the iteration matrix S is equal to

$$S = I - \widetilde{Q}\widetilde{A}^{-1}\widetilde{Q}^{\mathrm{T}}\mathcal{A}. \tag{A.6}$$

References

[1] *ABAQUS Theory Manual, Version 5.4* (Hibbitt, Karlsson & Sorensen, 1994).

[2] I. Babuška, S. Stroubulis, C.S. Upadhyay and S.K. Gangaraj, A posteriori estimation and adaptive control of the polluting error in the h-version of the finite element method, Technical Note BN-1175, Institute for Physical Science and Technology, University of Maryland, College Park, MD.

[3] R.E. Bank, T.F. Dupont and H. Yserentant, The hierarchical basis multigrid method, *Numer. Math.* 52 (1988) 427–458.

[4] T. Belytschko, J. Fish and A. Bayliss, The spectral overlay on finite elements for problems with high gradients, *Comput. Methods Appl. Mech. Engrg.* 81 (1990) 71–89.

[5] J. Bramble, R.E. Ewing, J.E. Pasciak and A.H. Schatz, A preconditioning technique for the efficient solution of problems with local grid refinement, *Comput. Methods Appl. Mech. Engrg.* 67 (1988) 149–159.

[6] A. Brandt, Multi-level adaptive solutions to boundary-value problems, *Math. Comp.* 31 (1977) 333–390.

[7] J. Fish, The s-version of the finite element method, SCOREC Report #18-1990, Rensselaer Polytechnic Institute Troy, NY; also: *Comput. & Structures* 43 (1990) 539–547.

[8] J. Fish, Hierarchical modeling of discontinuous fields, *Comm. Appl. Numer. Methods* 8 (1992) 443–453.

[9] J. Fish and V. Belsky, Multigrid method for periodic heterogeneous media. Part 2: Multiscale modeling and quality control in multidimensional case, *Comput. Methods Appl. Mech. Engrg.* 126 (1995) 17–38.

[10] J. Fish, V. Belsky and M. Pandheeradi, Composite grid method for hybrid systems, *Comput. Methods Appl. Mech. Engrg.*, to appear.

[11] J. Fish and R. Guttal, The p-version of finite element method for shell analysis, *Comput. Mech. Internat. J.* 16 (1995) 1–13.

[12] J. Fish and R. Guttal, The s-version of finite element method for laminated composite shells, *Internat. J. Numer. Methods Engrg.*, to appear.

[13] J. Fish and S. Markolefas, The s-version of the finite element method for multilayer laminates, *Internat. J. Numer. Methods Engrg.* 33 (1992) 1081–1105.

[14] J. Fish and S. Markolefas, Adaptive global–local refinement strategy based on interior error estimates of the h-method, *Internat. J. Numer. Methods Engrg.* 37 (1994) 828–838.

[15] J. Fish, S. Markolefas, R. Guttal and P. Nayak, On adaptive multilevel superposition of finite element meshes for linear elastostatics, *Appl. Numer. Math.* 14 (1994) 135–164.

[16] J.E. Flaherty, P.K. Moore and C. Ozturan, Adaptive overlapping methods for parabolic systems, in: J.E. Flaherty, P.J. Paslow, M.S. Shephard and J.D. Vasilakis, eds., *Adaptive Methods for Partial Differential Equations* (SIAM, Philadelphia, PA, 1989).

[17] H. Hinnant, A fast method of numerical quadrature for p-version finite element matrices, *AIAA J.* (1993) 1386.
[18] T.J.R. Hughes, *The Finite Element Method* (Prentice-Hall, Englewood Cliffs, NJ, 1987).
[19] N.F. Knight, J.B. Ransom, O.H. Griffin and D.M. Thompson, Global/local methods research using a common structural analysis framework, *Finite Elem. Anal. Design* 9 (1991) 91–112.
[20] K.M. Mao and C.T. Sun, A refined global–local finite element analysis method, *Internat. J. Numer. Methods Engrg.* 32 (1991) 29–43.
[21] *Maple V, Release 3* (Waterloo Maple Software, 1994).
[22] S.F. McCormick, *Multilevel Adaptive Methods for Partial Differential Equations* (SIAM Frontiers, III, 1987).
[23] S.F. McCormick and J.W. Thomas, The fast adaptive composite grid (FAC) method for elliptic equations, *Math. Comp.* 46 (1986) 439–456.
[24] A.K. Noor, W.S. Burton and J.M. Peters, Predictor-corrector procedures for stress and free vibration analyses of multilayered composite plates and shells, *Comput. Methods Appl. Mech. Engrg.* 82 (1990) 341–363.
[25] K.C. Park and G.M. Stanley, A curved C^0 shell element based on assumed natural coordinate strains, *J. Appl. Mech.* 108 (1986) 278–290.
[26] J.N. Reddy and D.H. Robbins, Theories and computational models for composite laminates, *Appl. Mech. Rev.* 47 (1994) 147–169.
[27] B.A. Szabo and I. Babuška, *Finite Element Analysis* (Wiley, 1991).
[28] J.D. Whitcomb, Iterative global–local finite element analysis, *Comput. & Structures* 40 (1991) 1027–1031.
[29] H. Yserentant, On multilevel splitting of finite element spaces, *Numer. Math.* (1986) 379–412.

4.1 Governing Equations

The governing equations consist of: equilibrium (4), kinematics in the rate form (63), boundary conditions (8), (9), and the constitutive equation in the rate form

$$\dot{\sigma}_{ij}^{\varsigma} = \overset{\circ}{\sigma}_{ij}^{\varsigma} + \Lambda_{ik}^{\varsigma}\sigma_{kj}^{\varsigma} - \sigma_{ik}^{\varsigma}\Lambda_{kj}^{\varsigma} \tag{129}$$

where

$$\overset{\circ}{\sigma}_{ij}^{\varsigma} = \mathcal{L}_{ijkl}(\dot{\varepsilon}_{kl}^{\varsigma} - \xi_{kl}\dot{\theta}) \tag{130}$$

$\mathcal{L}_{ijkl}$ denotes the instantaneous stiffness properties. In the following, we adopt Jaumann rate, i.e., $\Lambda_{kj}^{\varsigma} = \dot{\omega}_{kj}^{\varsigma}$.

Double scale asymptotic expansion of the velocity field (64) provides the starting point for the asymptotic analysis. Substituting the asymptotic expansions (20), (64) into constitutive equation (130) based on the Jaumann rate yields:

$$\dot{\sigma}_{ij}^{s} = \overset{\circ}{\sigma}_{ij}^{s} + \frac{1}{2}\sum_{r=-1}^{s}(\sigma_{il}^{r}\delta_{jk} + \sigma_{jl}^{r}\delta_{ik} - \sigma_{ik}^{r}\delta_{jl} - \sigma_{jk}^{r}\delta_{il})l_{kl}^{s-r+1}, \qquad s = -1, 0, \ldots \tag{131}$$

where l_{kl}^{s} is the velocity gradient given as

$$l_{kl}^{-1} = v_{k,x_l}^{0} \qquad \text{and} \qquad l_{kl}^{s} = v_{k,x_l}^{s+1} + v_{k,y_l}^{s}, \quad s = 0, 1, \ldots \tag{132}$$

Further assuming that $O(\varsigma^{-1})$ Cauchy stress vanishes, $\dot{\sigma}_{ij}^{-1} = \mathcal{L}_{ijkl}v_{k,y_j}^{0} = 0$, yields $v_i^0 = v_i^0(\boldsymbol{x})$ provided that $\mathcal{L}_{ijkl}$ is not singular. We proceed to the $O(\varsigma^{-1})$ equilibrium equation (22):

$$\sigma_{ij,y_j}^{0}(\boldsymbol{x}, \boldsymbol{y}) = 0 \tag{133}$$

To solve for (133) up to a constant we introduce the following separation of variables:

$$v_i^1(\boldsymbol{x}, \boldsymbol{y}) = \mathcal{H}_{ikl}(\boldsymbol{y})\{v_{k,x_l}^{0}(\boldsymbol{x}) + d_{kl}^{\theta}(\boldsymbol{x})\} \tag{134}$$

Note that plastic effects are now hidden in the Y-periodic function $\mathcal{H}_{ikl}(\boldsymbol{y})$, whereas d_{kl}^{θ} accounts for temperature effects only.

Premultiplying (133) by the Y-periodic function $\mathcal{H}_{ikl}(\boldsymbol{y})$, then integrating over the deformed unit cell domain Θ and carrying out integration by parts yields

$$\phi(\boldsymbol{x}, \boldsymbol{y}) = \int_{\Theta}\mathcal{H}_{ikl,y_j}\sigma_{ij}^{0}\,d\Theta = 0 \tag{135}$$

Linearization of (135) is carried out by taking the material time derivative, $\dot{\phi} = 0$. For this purpose we express the integrand of (135) in the reference configuration, say at time t, $\mathcal{H}_{ikl,\,y_j}\sigma^0_{ij}\,d\Theta = \mathcal{H}_{ikl,\,{}^t y_m}\,\mathcal{F}^{-1}_{mj}\,\sigma^0_{ij}\,J_y\,d^t\Theta$ where $\mathcal{F}_{jm} = y_{j;{}^t y_m}$ denotes the deformation gradient in the unit cell and J_y is the corresponding jacobian. By utilizing equations (2) and (3) it can be shown that $y_{j;{}^t y_m} = x_{j;{}^t x_m}$.

Consequently, linearization of (135) yields:

$$\int_{{}^t\Theta} \mathcal{H}_{ikl,\,{}^t y_m}(\dot{\mathcal{F}}^{-1}_{mj}\sigma^0_{ij}J_y + \mathcal{F}^{-1}_{mj}\dot{\sigma}^0_{ij}J_y + \mathcal{F}^{-1}_{mj}\sigma^0_{ij}\dot{J}_y)d^t\Theta = 0 \tag{136}$$

Substituting (130), (131), (132) and (134) into (136) and exploiting kinematical relations $\dot{J}_y = J_y l^0_{kk}$ and $\dot{\mathcal{F}}^{-1}_{mj} = -\mathcal{F}^{-1}_{ml}l^0_{lj}$ gives:

$$\int_\Theta \mathcal{H}_{ikl,\,y_j}\{(\mathcal{L}_{ijmn} + \mathcal{T}_{ijmn})l^0_{mn} - \mathcal{L}_{ijmn}\xi_{mn}\dot{\theta}\}d\Theta = 0 \tag{137}$$

where

$$l^0_{mn} = (\delta_{ms}\delta_{nt} + \mathcal{H}_{mst,\,y_n}(\boldsymbol{y}))v^0_{s,\,x_t}(\boldsymbol{x}) + \mathcal{H}_{mst,\,y_n}(\boldsymbol{y})\dot{d}^\theta_{st}(\boldsymbol{x}) \tag{138}$$

$$\mathcal{T}_{ijmn} = \delta_{mn}\sigma^0_{ij} + \frac{1}{2}(\delta_{im}\sigma^0_{jn} - \delta_{jm}\sigma^0_{in} - \delta_{in}\sigma^0_{jm} - \delta_{jn}\sigma^0_{im}) \tag{139}$$

Since (137) is satisfied for arbitrary macro-fields $v^0_{s,\,x_t}(\boldsymbol{x})$ and $\dot{d}^\theta_{st}(\boldsymbol{x})$ we can obtain two integral equations in Θ:

$$\int_\Theta \mathcal{H}_{ikl,\,y_j}(\mathcal{L}_{ijmn} + \mathcal{T}_{ijmn})(\delta_{ms}\delta_{nt} + \mathcal{H}_{mst,\,y_n})d\Theta = 0 \tag{140}$$

$$\int_\Theta \mathcal{H}_{ikl,\,y_j}\{(\mathcal{L}_{ijmn} + \mathcal{T}_{ijmn})\mathcal{H}_{mst,\,y_n}\dot{d}^\theta_{st} - \mathcal{L}_{ijmn}\xi_{mn}\dot{\theta}\}d\Theta = 0 \tag{141}$$

Equation (140) is solved using the finite element method for $\mathcal{H}_{ikl}$. Note that equation (140) is solved for nine right hand side vectors corresponding to nine uniform velocity gradient fields as opposed to six constant strain modes in the case of small deformations.

After solving (140) for $\mathcal{H}_{ikl}$, $\dot{d}^\theta_{ij}$ can be obtained from (141) as

$$\dot{d}^\theta_{ij} = \frac{1}{|\Theta|}(\tilde{\mathcal{L}}_{ijkl} - \bar{\mathcal{L}}_{ijkl})^{-1}\int_\Theta \mathcal{H}_{rkl,\,y_s}\mathcal{L}_{rsuv}\xi_{uv}\dot{\theta}d\Theta \tag{142}$$

where

$$\tilde{\mathcal{L}}_{ijkl} = \frac{1}{|\Theta|}\int_{\Theta}(\mathcal{L}_{ijkl} + \mathcal{T}_{ijkl})d\Theta \tag{143}$$

$$\overline{\mathcal{L}}_{ijkl} = \frac{1}{|\Theta|}\int_{\Theta}(\mathcal{L}_{ijmn} + \mathcal{T}_{ijmn})\mathcal{H}_{mkl,\,y_n}d\Theta \tag{144}$$

Once $\mathcal{H}_{ikl}$ and d_{ij}^{θ} are computed, the $O(\varsigma^0)$ approximation of $\dot{\varepsilon}_{ij}^{\varsigma}$ and $\dot{\omega}_{ij}^{\varsigma}$, denoted as $\dot{\varepsilon}_{ij}$ and $\dot{\omega}_{ij}$, are given as

$$\dot{\varepsilon}_{ij} = \mathcal{A}_{ijkl}v^0_{k,\,x_l} + a_{ij}\dot{\theta} \tag{145}$$

$$\dot{\omega}_{ij} = \hat{\mathcal{A}}_{ijkl}\,v^0_{k,\,x_l} + \hat{a}_{ij}\dot{\theta} \tag{146}$$

where

$$\mathcal{A}_{ijkl}(\boldsymbol{y}) = \frac{1}{2}(\delta_{ik}\delta_{jl} + \delta_{jk}\delta_{il}) + \mathcal{H}_{(i,\,y_j)kl}(\boldsymbol{y}) \tag{147}$$

$$\hat{\mathcal{A}}_{ijkl}(\boldsymbol{y}) = \frac{1}{2}(\delta_{ik}\delta_{jl} - \delta_{jk}\delta_{il}) + \mathcal{H}_{[i,\,y_j]kl}(\boldsymbol{y}) \tag{148}$$

$$a_{ij} = \mathcal{H}_{(i,\,y_j)kl}(\tilde{\mathcal{L}}_{klpq} - \overline{\mathcal{L}}_{klpq})^{-1}\int_{\Theta}\mathcal{H}_{prs,\,y_q}\mathcal{L}_{rsuv}\xi_{uv}\dot{\theta}d\Theta \tag{149}$$

$$\hat{a}_{ij} = \mathcal{H}_{[i,\,y_j]kl}(\tilde{\mathcal{L}}_{klpq} - \overline{\mathcal{L}}_{klpq})^{-1}\int_{\Theta}\mathcal{H}_{prs,\,y_q}\mathcal{L}_{rsuv}\xi_{uv}\dot{\theta}d\Theta \tag{150}$$

4.2 Implicit Integration of Constitutive Equations

We start from the constitutive relation for a typical element ρ in Θ:

$$\mathring{\sigma}_{ij}^{(\rho)} = \begin{cases} L_{ijkl}^{(\rho)}(\dot{\varepsilon}_{kl}^{(\rho)} - \xi_{kl}^{(\rho)}\dot{\theta}) & \text{if } \rho \in \Theta^{(f)} \\ L_{ijkl}^{(\rho)}(\dot{\varepsilon}_{kl}^{(\rho)} - \xi_{kl}^{(\rho)}\dot{\theta} - {}_p\dot{\varepsilon}_{kl}^{(\rho)}) & \text{if } \rho \in \Theta^{(m)} \end{cases} \tag{151}$$

For elements in the matrix phase (151) can be written as

$$\mathring{\sigma}_{ij}^{(\rho)} = L_{ijkl}^{(\rho)}\{\mathcal{A}_{klmn}^{(\rho)}\,v^0_{m,\,x_n} + (a_{kl}^{(\rho)} - \xi_{kl}^{(\rho)})\dot{\theta} - \aleph_{kl}^{(\rho)}\dot{\lambda}^{(\rho)}\} \tag{152}$$

Applying the backward Euler integration scheme to (152) gives

$$\sigma_{ij}^{(\rho)} = {}^{t}\mathring{\sigma}_{ij}^{(\rho)} + L_{ijkl}^{(\rho)}\{\mathcal{A}_{klmn}^{(\rho)}\,(\Delta\bar{\varepsilon}_{mn} + \Delta\bar{\omega}_{mn}) + (a_{kl}^{(\rho)} - \xi_{kl}^{(\rho)})\Delta\theta - \aleph_{kl}^{(\rho)}\Delta\lambda^{(\rho)}\} \tag{153}$$

and exploiting the equation for the back stress in element ρ (88) yields

$$\sigma_{ij}^{(\rho)} - \alpha_{ij}^{(\rho)} = (I_{ijmn} + \Delta\lambda^{(\rho)} \underset{\sim}{\wp}_{ijmn}^{(\rho)})^{-1} \underset{\sim}{\Im}_{mn}^{(\rho)} \tag{154}$$

and

$$\underset{\sim}{\wp}_{ijmn}^{(\rho)} = L_{ijuv}^{(\rho)} P_{uvmn} + \frac{2}{3}(1-\beta)hP_{ijmn} \tag{155}$$

$$\underset{\sim}{\Im}_{mn}^{(\rho)} = {}^{t}\hat{\sigma}_{mn}^{(\rho)} - {}^{t}\hat{\alpha}_{mn}^{(\rho)} - L_{mnpq}^{(\rho)}\{\mathcal{A}_{pqst}^{(\rho)}(\Delta\bar{\varepsilon}_{st} + \Delta\bar{\omega}_{st}) + (a_{pq}^{(\rho)} - \xi_{pq}^{(\rho)})\Delta\theta\} \tag{156}$$

in which ${}^{t}\hat{\sigma}_{mn}^{(\rho)}$ and ${}^{t}\hat{\alpha}_{mn}^{(\rho)}$ are the rotated stress and back stress defined in (75) and (76) where the $\Delta\omega_{ij}^{(\rho)}$ is given as

$$\Delta\omega_{ij}^{(\rho)} = \hat{\mathcal{A}}_{ijkl}^{(\rho)}(\Delta\bar{\varepsilon}_{kl} + \Delta\bar{\omega}_{kl}) + \hat{a}_{ij}^{(\rho)}\Delta\theta \tag{157}$$

Note that the instantaneous concentration factors $\mathcal{A}_{ijkl}^{(\rho)}$, $\hat{\mathcal{A}}_{ijkl}^{(\rho)}$, $a_{ij}^{(\rho)}$ and $\hat{a}_{ij}^{(\rho)}$ computed from (147) to (150) depend on the instantaneous material properties (see (140)), which in turn depend on vector of plastic parameters $\Delta\underset{\sim}{\lambda}$ in $\Theta^{(m)}$, $\Delta\underset{\sim}{\lambda} \equiv [\Delta\lambda^{(1)}, \Delta\lambda^{(2)}, \ldots, \Delta\lambda^{(n_y)}]^T$. Substituting (154) and (87) into the yield function (81) for each element in $\Theta^{(m)}$ yields a set of n nonlinear equations $\underset{\sim}{\Phi} \equiv [\Phi^{(1)}, \Phi^{(2)}, \ldots, \Phi^{(n_y)}]^T$ with n_y unknown plastic parameters. The system of nonlinear equations is solved by the Newton method:

$$\Delta\lambda_{k+1}^{(\rho)} = \Delta\lambda_{k}^{(\rho)} - \left\{\frac{\partial\Phi^{(\rho)}}{\partial\Delta\lambda^{(\eta)}}\right\}^{-1} \Phi^{(\eta)}\Big|_{\Delta\lambda_k^{(\rho)}} \tag{158}$$

A typical term in the Jacobian matrix is given as

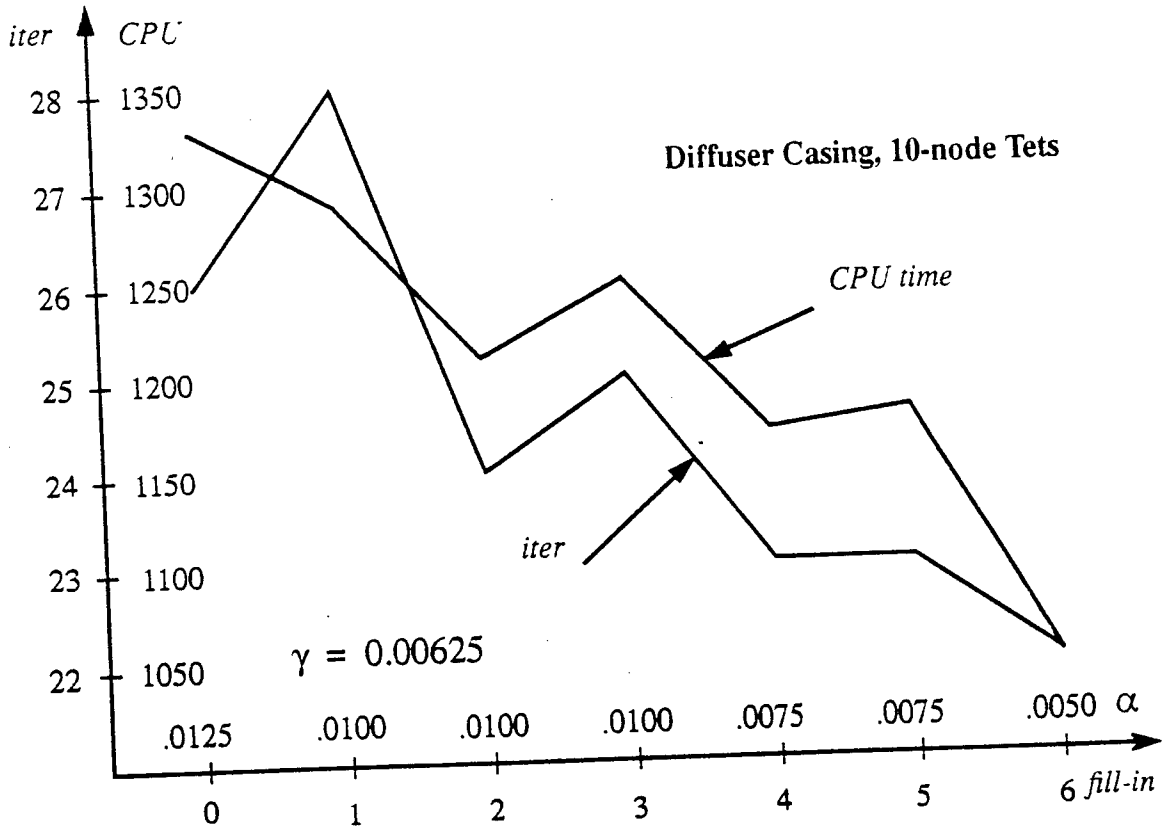
$$\frac{\partial\Phi^{(\rho)}}{\partial\Delta\lambda^{(\eta)}} = \aleph_{ij}^{(\rho)}\{I_{ijmn} + \Delta\lambda^{(\rho)} \underset{\sim}{\wp}_{ijmn}^{(\rho)}\}^{-1}\chi_{mn}^{(\rho\eta)} - \frac{4\delta_{\rho\eta}\beta h\{Y^{(\rho)}\}^2}{9 - 6\beta h\Delta\lambda^{(\rho)}} \tag{159}$$

where

$$\chi_{mn}^{(\rho\eta)} = \frac{\partial\underset{\sim}{\Im}_{mn}^{(\rho)}}{\partial\Delta\lambda^{(\eta)}} - \delta_{\rho\eta}\underset{\sim}{\wp}_{mnpq}(\sigma_{pq}^{(\rho)} - \alpha_{pq}^{(\rho)}) \tag{160}$$

$$\frac{\partial\underset{\sim}{\Im}_{mn}^{(\rho)}}{\partial\Delta\lambda^{(\eta)}} = \frac{\partial({}^{t}\hat{\sigma}_{mn}^{(\rho)} - {}^{t}\hat{\alpha}_{mn}^{(\rho)})}{\partial\Delta\lambda^{(\eta)}} - L_{mnpq}^{(\rho)}\left(\frac{\partial\mathcal{A}_{pqst}^{(\rho)}}{\partial\Delta\lambda^{(\eta)}}(\Delta\bar{\varepsilon}_{st} + \Delta\bar{\omega}_{st}) + \frac{\partial a_{pq}^{(\rho)}}{\partial\Delta\lambda^{(\eta)}}\Delta\theta\right) \tag{161}$$

FIGURE 7


iter
CPU
28
27
26
25
24
23
22
1350
1300
1250
1200
1150
1100
1050
Diffuser Casing, 10-node Tets
CPU time
iter
γ = 0.00625
.0125
.0100
.0100
.0100
.0075
.0075
.0050
α
0
1
2
3
4
5
6 fill-in

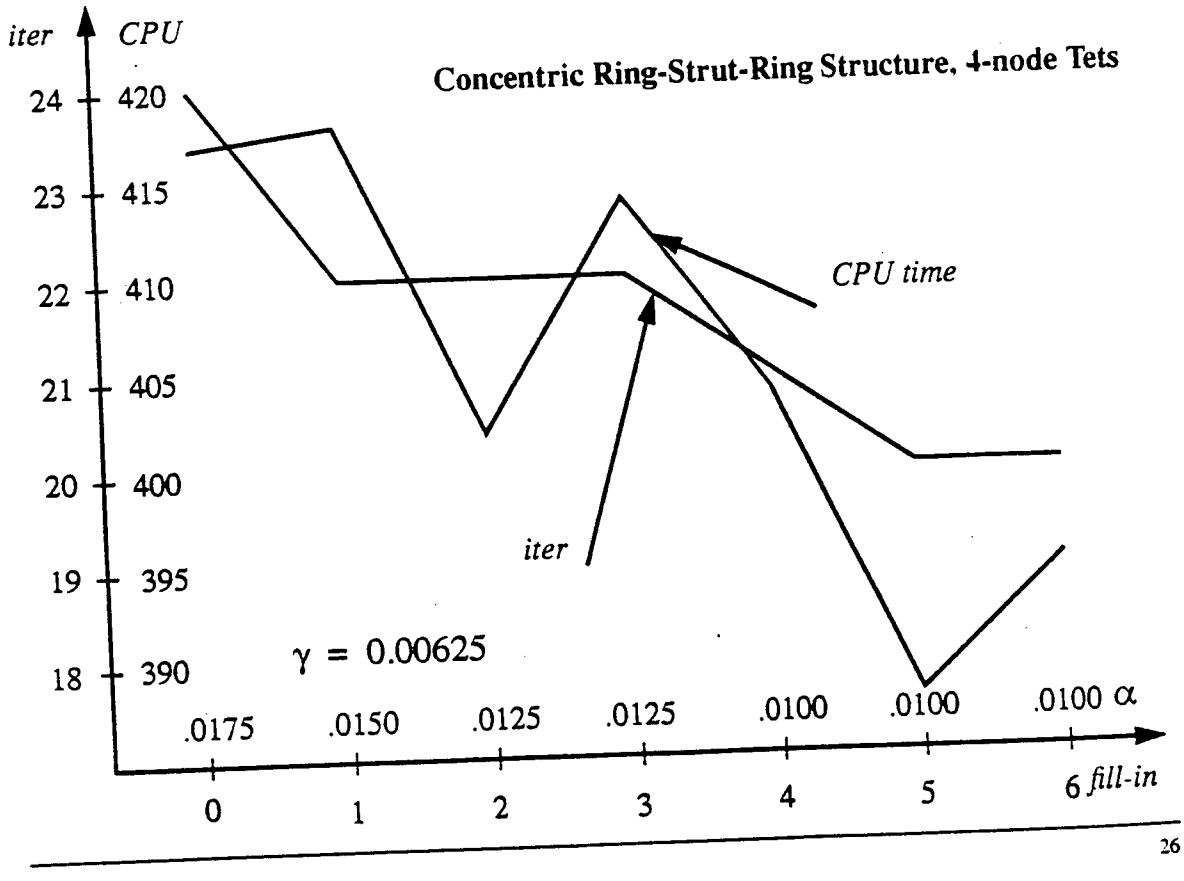

iter
CPU
24
23
22
21
20
19
18
420
415
410
405
400
395
390
Concentric Ring-Strut-Ring Structure, 4-node Tets
CPU time
iter
γ = 0.00625
.0175
.0150
.0125
.0125
.0100
.0100
.0100
α
0
1
2
3
4
5
6 fill-in

TABLE 1

Problem title	Solver (total)	Aggregation	Restriction	Factorization	Incomplete factorization	Iteration process	Number of iterations
Diffuser Casing	1021	162	110	126	93	530	22
Turbine Blade	2378	294	280	861	190	753	19
Concentric Structure	346	97	19	17	29	184	18
Nozzle for Turbine	1288	165	166	137	103	717	34
Casting Setup	1493	197	150	169	114	863	30
HSCT (MIN3)	1255	85	117	341	34	678	56
Automobile(DKT +DMT)	2778	266	209	258	217	1828	48
Automobile (MIN3)	3146	324	390	622	230	1580	42
Canoe	1126	110	110	48	98	760	32

TABLE 2

Problem title	Sparse	PCG (MIC)		GAM	
	CPU(s)	CPU(s)	# of iterations	CPU(s)	# of iterations
Diffuser Casing	8692	12276	1531	1021	22
Turbine Blade	out of memory	9862	757	2378	19
Concentric Structure	687	3881	1083	346	18
Nozzle for Turbine	7271	8290	1056	1288	34
Casting Setup	3150	33879	3755	1493	30
HSCT (MIN3)	994	24685	7278	1255	56
Automobile (DKT+DMT)	2678	76003	5939	2788	48
Automobile (MIN3)	2678	83877	6594	3146	42
Canoe	1351	8106	1254	1126	32

TABLE 3

Problem title	Sparse	PCG (MIC)	GAM
Diffuser Casing	995	141	172
Turbine Blade	>1500	255	311
Concentric Structure	337	51	79
Nozzle for Turbine	996	138	169
Casting Setup	1012	149	199
HSCT (MIN3)	207	71	99
Automobile (DKT+DMT)	512	205	255
Automobile (MIN3)	512	205	265
Canoe	395	61	88

In equation (161) $\partial({}^t\hat{\sigma}^{(\rho)}_{mn} - {}^t\hat{\alpha}^{(\rho)}_{mn})/\partial\Delta\lambda^{(\eta)}$ depends on the derivatives of $\mathcal{A}^{(\rho)}_{pqst}$ and $a^{(\rho)}_{pq}$ with respect to $\Delta\lambda^{(\eta)}$. Evaluation of these derivatives is not trivial and hence the following approximation is employed:

$$\mathcal{A}^{(\rho)}_{pqst} \approx {}^t\mathcal{A}^{(\rho)}_{pqst}, \qquad a^{(\rho)}_{pq} \approx {}^t a^{(\rho)}_{pq} \tag{162}$$

resulting in the block diagonal approximation of the jacobian matrix

$$\frac{\partial\Phi^{(\rho)}}{\partial\Delta\lambda^{(\eta)}} \approx -\delta_{\rho\eta}\left(\aleph^{(\rho)}_{ij}\hat{\chi}^{(\rho)}_{ij} + \frac{4\beta h\{Y^{(\rho)}\}^2}{9 - 6\beta h\Delta\lambda^{(\rho)}}\right) \tag{163}$$

where

$$\hat{\chi}^{(\rho)}_{ij} = (I_{ijmn} + \Delta\lambda^{(\rho)}\underset{\sim}{\wp}^{(\rho)}_{ijmn})^{-1}\underset{\sim}{\wp}^{(\rho)}_{mnpq}(\sigma^{(\rho)}_{pq} - \alpha^{(\rho)}_{pq}) \tag{164}$$

At each modified Newton iteration step the residual vector $\underset{\sim}{\Phi}$ is evaluated and the instantaneous concentration factors are recomputed from (140). The iterative process proceeds until the residual norm $\|\underset{\sim}{\Phi}\|_2$ vanishes up to a certain tolerance. The updated stress, yield stress and back stress for elements in $\Theta^{(m)}$ are calculated from (153), (87) and (88), respectively. For elements in $\Theta^{(f)}$, stresses can be obtained using (153) with $\Delta\lambda^{(\rho)} \equiv 0$. Finally, the macroscopic stress follows from (56).

4.3 Consistent Linearization for Incremental Homogenization Scheme

The instantaneous consistent stiffness properties are derived from consistent linearization of the constitutive equations. For elements in $\Theta^{(m)}$, taking the material time derivative of (153) and (88), and making the use of (226) yields:

$$\begin{aligned}\dot{\sigma}^{(\rho)}_{ij} = {}^t\dot{\hat{\sigma}}^{(\rho)}_{ij} &+ L^{(\rho)}_{ijmn}\{\dot{\mathcal{A}}^{(\rho)}_{mnkl}(\Delta\bar{\varepsilon}_{kl} + \Delta\bar{\omega}_{kl}) + \mathcal{A}^{(\rho)}_{mnpq}M_{pqkl}v^0_{k,x_l}\} \\ &+ L^{(\rho)}_{ijmn}\{\dot{a}^{(\rho)}_{mn}\Delta\theta + (a^{(\rho)}_{mn} - \xi^{(\rho)}_{mn})\dot{\theta} - \aleph^{(\rho)}_{mn}\dot{\lambda}^{(\rho)} - P_{mnpq}(\dot{\sigma}^{(\rho)}_{pq} - \dot{\alpha}^{(\rho)}_{pq})\Delta\lambda^{(\rho)}\}\end{aligned} \tag{165}$$

and

$$\dot{\alpha}^{(\rho)}_{ij} = {}^t\dot{\hat{\alpha}}^{(\rho)}_{ij} + \frac{2(1-\beta)h}{3}\{\aleph^{(\rho)}_{ij}\dot{\lambda}^{(\rho)} + P_{ijpq}(\dot{\sigma}^{(\rho)}_{pq} - \dot{\alpha}^{(\rho)}_{pq})\Delta\lambda^{(\rho)}\} \tag{166}$$

Substituting (226) into (165), then subtracting (166) from the resulting equation yields

$$\begin{aligned}\dot{\sigma}^{(\rho)}_{ij} - \dot{\alpha}^{(\rho)}_{ij} = {}^t\dot{\hat{\sigma}}^{(\rho)}_{ij} - {}^t\dot{\hat{\alpha}}^{(\rho)}_{ij} &+ L^{(\rho)}_{ijmn}\{\mathcal{A}^{(\rho)}_{mnpq}M_{pqkl}v^0_{k,x_l} + (a^{(\rho)}_{mn} - \xi^{(\rho)}_{mn})\dot{\theta}\} \\ &- \underset{\sim}{\wp}^{(\rho)}_{ijmn}\{(\sigma^{(\rho)}_{mn} - \alpha^{(\rho)}_{mn})\dot{\lambda}^{(\rho)} + (\dot{\sigma}^{(\rho)}_{mn} - \dot{\alpha}^{(\rho)}_{mn})\Delta\lambda^{(\rho)}\}\end{aligned} \tag{167}$$

where in analogy to (162), we approximate $\mathcal{A}^{(\rho)}_{mnkl} = 0$ and $\dot{a}^{(\rho)}_{mn} = 0$.

From equations (210), (211), (220) follows that

$$ {}^{t}\dot{\hat{\sigma}}^{(\rho)}_{ij} = {}_{\sigma}U^{(\rho)}_{ijmn}(\hat{\mathcal{A}}^{(\rho)}_{mnst} M_{stkl} v^{0}_{k,x_l} + \hat{a}^{(\rho)}_{mn}\dot{\theta}) \tag{168} $$

$$ {}^{t}\dot{\hat{\alpha}}^{(\rho)}_{ij} = {}_{\alpha}U^{(\rho)}_{ijmn}(\hat{\mathcal{A}}^{(\rho)}_{mnst} M_{stkl} v^{0}_{k,x_l} + \hat{a}^{(\rho)}_{mn}\dot{\theta}) \tag{169} $$

Substituting (168) and (169) into (167) and collecting terms of $\dot{\sigma}^{(\rho)}_{ij} - \dot{\alpha}^{(\rho)}_{ij}$ gives

$$ \dot{\sigma}^{(\rho)}_{ij} - \dot{\alpha}^{(\rho)}_{ij} = (I_{ijkl} + \Delta\lambda^{(\rho)} \underset{\sim}{\wp}^{(\rho)}_{ijkl})^{-1}({}_{v}\Xi_{klst} v^{0}_{s,x_t} + {}_{\theta}\Xi_{kl}\dot{\theta} + {}_{\lambda}\Xi_{kl}\dot{\lambda}^{(m)}) \tag{170} $$

where

$$ {}_{v}\Xi_{klst} = \{({}_{\sigma}U^{(\rho)}_{klmn} - {}_{\alpha}U^{(\rho)}_{klmn})\hat{\mathcal{A}}^{(\rho)}_{mnuv} + L^{(\rho)}_{klmn}\mathcal{A}^{(\rho)}_{mnuv}\} M_{uvst} \tag{171} $$

$$ {}_{\theta}\Xi_{kl} = ({}_{\sigma}U^{(\rho)}_{klmn} - {}_{\alpha}U^{(\rho)}_{klmn})\hat{a}^{(\rho)}_{mn} + L^{(\rho)}_{klmn}(a^{(\rho)}_{mn} - \xi^{(\rho)}_{mn}) \tag{172} $$

$$ {}_{\lambda}\Xi_{kl} = -\underset{\sim}{\wp}^{(\rho)}_{klmn}(\sigma^{(m)}_{mn} - \alpha^{(m)}_{mn}) \tag{173} $$

The value $\dot{\lambda}^{(\rho)}$ can be computed from the linearization of consistency conditions (see also Section 3.2) which yields

$$ \dot{\lambda}^{(\rho)} = \Upsilon^{(\rho)}_{kl}({}_{v}\Xi_{klst} v^{0}_{s,x_t} + {}_{\theta}\Xi_{kl}\dot{\theta}) \tag{174} $$

where

$$ \Upsilon^{(\rho)}_{kl} = \frac{(9 - 6\beta h\Delta\lambda^{(\rho)})\,\aleph^{(\rho)}_{ij}(I_{ijkl} + \Delta\lambda^{(\rho)}\underset{\sim}{\wp}^{(\rho)}_{ijkl})^{-1}}{4\beta h\{Y^{(\rho)}\}^2 - (9 - 6\beta h\Delta\lambda^{(\rho)})\,\aleph^{(\rho)}_{mn}(I_{mnst} + \Delta\lambda^{(\rho)}\underset{\sim}{\wp}^{(\rho)}_{mnst})^{-1}\,{}_{\lambda}\Xi_{st}} \tag{175} $$

and then substituting (174) into (170) yields

$$ \dot{\sigma}^{(\rho)}_{ij} - \dot{\alpha}^{(\rho)}_{ij} = {}_{v}\underset{\sim}{\Xi}_{ijkl} v^{0}_{k,x_l} + {}_{\theta}\underset{\sim}{\Xi}_{ij}\dot{\theta} \tag{176} $$

where ${}_{v}\underset{\sim}{\Xi}_{ijkl}$ and ${}_{\theta}\underset{\sim}{\Xi}_{ij}$ have identical structure to ${}_{v}\underset{\sim}{S}_{ijkl}$ and ${}_{\theta}\underset{\sim}{S}_{ij}$ in (111) and (112) except that the symbols S are replaced by Ξ, and $\Gamma^{(m)}$ by $\Upsilon^{(\rho)}$.

Substituting (174), (176) into (165) yields

$$ \dot{\sigma}^{(\rho)}_{ij} = \mathcal{D}^{(\rho)}_{ijkl} v^{0}_{k,x_l} + \mathcal{A}^{(\rho)}_{ij}\dot{\theta} \qquad \text{for} \qquad \rho \in \Theta^{(m)} \tag{177} $$

where

$$\mathcal{D}^{(\rho)}_{ijkl} = {}_{\sigma}U^{(\rho)}_{ijmn}\hat{\mathcal{A}}^{(\rho)}_{mnst}M_{stkl} + L^{(\rho)}_{ijmn}\mathcal{A}^{(\rho)}_{mnpq}M_{pqkl}$$
$$-L^{(\rho)}_{ijmn}(\aleph^{(\rho)}_{mn}\Upsilon^{(\rho)}_{pq\,\nu}\underline{\Xi}_{pqkl} + \Delta\lambda^{(\rho)}P_{mnpq\,\nu}\underline{\Xi}_{pqkl}) \tag{178}$$

and

$$\mathcal{d}^{(\rho)}_{ij} = {}_{\sigma}U^{(\rho)}_{ijmn}\hat{a}^{(\rho)}_{mn} + L^{(\rho)}_{ijmn}\{(a^{(\rho)}_{mn} - \xi^{(\rho)}_{mn}) - \aleph^{(\rho)}_{mn}\Upsilon^{(\rho)}_{pq\,\theta}\underline{\Xi}_{pq} - \Delta\lambda^{(\rho)}P_{mnpq\,\theta}\underline{\Xi}_{pq}\} \tag{179}$$

Similarly, the stress rate for elements in $\Theta^{(f)}$ is given by

$$\dot{\sigma}^{(\eta)}_{ij} = \mathcal{D}^{(\eta)}_{ijkl}v^{0}_{k,\,x_l} + \mathcal{d}^{(\eta)}_{ij}\dot{\theta} \qquad \text{for} \qquad \eta \in \Theta^{(f)} \tag{180}$$

where

$$\mathcal{D}^{(\eta)}_{ijkl} = {}_{\sigma}U^{(\eta)}_{ijmn}\hat{\mathcal{A}}^{(\eta)}_{mnst}M_{stkl} + L^{(\eta)}_{ijmn}\mathcal{A}^{(\eta)}_{mnpq}M_{pqkl} \tag{181}$$

$$\mathcal{d}^{(\eta)}_{ij} = {}_{\sigma}U^{(\eta)}_{ijmn}\hat{a}^{(\eta)}_{mn} + L^{(\eta)}_{ijmn}(a^{(\eta)}_{mn} - \xi^{(\eta)}_{mn}) \tag{182}$$

The overall instantaneous stiffness $\mathcal{D}_{ijkl}$ is obtained from the rate form of (61), equations (178), (179), (181) and (182):

$$\dot{\bar{\sigma}}_{ij} = \mathcal{D}_{ijkl}v^{0}_{k,\,x_l} + \mathcal{d}_{ij}\dot{\theta} \tag{183}$$

where

$$\mathcal{D}_{ijkl} = \sum_{\eta=1}^{n} c^{(\eta)}\mathcal{D}^{(\eta)}_{ijkl}, \qquad \mathcal{d}_{ij} = \sum_{\eta=1}^{n} c^{(\eta)}\mathcal{d}^{(\eta)}_{ij} \tag{184}$$

$c^{(\eta)}$ denotes the ratio between the volume of element η and the volume of the unit cell at time $t + \Delta t$.

Finally, linearization of internal force vector yields:

$$\frac{d}{dt}f^{int}_{A} = \int_{\Omega} N_{iA,\,x_j}\overline{\mathcal{D}}_{ijkl}N_{kB,\,x_l}\,d\Omega\,\dot{q}_B + \int_{\Omega} N_{iA,\,x_j}\mathcal{d}_{ij}\dot{\theta}\,d\Omega \tag{185}$$

$$\overline{\mathcal{D}}_{ijkl} = \mathcal{D}_{ijkl} + \delta_{kl}\bar{\sigma}_{ij} - \delta_{kj}\bar{\sigma}_{il} \tag{186}$$

where the first integral in (185) represents the consistent macroscopic tangent stiffness matrix for the *n*-point scheme model.

Remark 5: Approximating the piecewise constant phase rotations by a constant field in the entire unit cell domain as in Remark 4, (171) and (172) can be simplified as

$$ {}_{v}\Xi_{klst} = L^{(\rho)}_{klmn} \mathcal{A}^{(\rho)}_{mnuv} M_{uvst} - \{\delta_{kn}(\sigma^{(\rho)}_{ml} - \alpha^{(\rho)}_{ml}) + \delta_{ln}(\sigma^{(\rho)}_{km} - \alpha^{(\rho)}_{km})\} M_{[mn]st} \tag{187} $$

$$ {}_{\theta}\Xi_{kl} = L^{(\rho)}_{klmn}(a^{(\rho)}_{mn} - \xi^{(\rho)}_{mn}) \tag{188} $$

where (124) has been used. For elements in $\Theta^{(m)}$ (178) and (179) can be written as

$$ \begin{aligned} \mathcal{D}^{(\rho)}_{ijkl} &= L^{(\rho)}_{ijmn} \mathcal{A}^{(\rho)}_{mnpq} M_{pqkl} - \{\delta_{kn}(\sigma^{(\rho)}_{ml} - \alpha^{(\rho)}_{ml}) + \delta_{ln}(\sigma^{(\rho)}_{km} - \alpha^{(\rho)}_{km})\} M_{[mn]st} \\ &\quad - L^{(\rho)}_{ijmn}(\aleph^{(\rho)}_{mn} \Upsilon^{(\rho)}_{pq} {}_{v}\Xi_{pqkl} + \Delta\lambda^{(\rho)} P_{mnpq} {}_{v}\Xi_{pqkl}) \end{aligned} \tag{189} $$

and

$$ d^{(\rho)}_{ij} = L^{(\rho)}_{ijmn}\{(a^{(\rho)}_{mn} - \xi^{(\rho)}_{mn}) - \aleph^{(\rho)}_{mn} \Upsilon^{(\rho)}_{pq} {}_{\theta}\Xi_{pq} - \Delta\lambda^{(\rho)} P_{mnpq} {}_{\theta}\Xi_{pq}\} \tag{190} $$

On the other hand, for elements in $\Theta^{(f)}$ (181) and (182) are given by

$$ \mathcal{D}^{(\eta)}_{ijkl} = L^{(\eta)}_{ijmn} \mathcal{A}^{(\eta)}_{mnpq} M_{pqkl} - (\delta_{in}\sigma^{(\eta)}_{mj} + \delta_{jn}\sigma^{(\eta)}_{im}) M_{[mn]kl} \tag{191} $$

and

$$ d^{(\eta)}_{ij} = L^{(\eta)}_{ijmn}(a^{(\eta)}_{mn} - \xi^{(\eta)}_{mn}) \tag{192} $$

5.0 Adaptive Model Construction

In Sections 3 and 4 we presented two schemes for modeling inelastic behavior of composite structures: the *2*-point scheme and the *n*-point scheme. In the *n*-point scheme we employed a piecewise constant approximation of the eigenstrain field, whereas in the *2*-point scheme the eigenstrain field and the elastic concentration factors in each phase are approximated by a constant. For the Nozzle Flap problem considered in [8] (see also Figure 1) the *2*-point scheme is over three orders of magnitude faster than the *n*-point scheme. For linear problems the *2*-point scheme with post-processing [5][8][9][13] is identical to the *n*-point scheme, whereas for nonlinear problems there is no such guarantee.

If we assume that the *n*-point and the *2*-point schemes are optimal in terms of accuracy and speed, respectively, then it is natural to attempt to merge the two in a single model. In such a hybrid model, the *2*-point scheme should be only used in regions where the modeling errors are small, whereas elsewhere the *n*-point scheme should be employed. We will refer to such a hybrid modeling strategy as the adaptive *2/n*-point scheme.

The modeling error $e^{2\text{-}pt}$ associated with the *2*-point scheme can be defined as follows

$$ e^{2\text{-}pt} = \left\| v^{ex} - v^{2\text{-}pt} \right\|_{\square} \tag{193} $$

where $\square = \Omega \times \Theta$ and

$$\|f\|_{\square}^2 = \frac{1}{\Theta}\int_{\Theta}\int_{\Omega} f^2 d\Theta d\Omega \tag{194}$$

v is an appropriate solution measure; the superscript *ex* refers to the exact solution within the framework of the mathematical homogenization theory, i.e., assuming solution periodicity. For estimation of errors resulting from lack of periodicity we refer to [9][28].

The key questions are: (i) how to estimate v^{ex}, (ii) what is a suitable measure for v, (iii) how to make the process of error estimation efficient, and (iv) how to utilize the model error estimation for adaptive construction of the *2/n*-point model.

It is appropriate to recall that as the number elements in the unit cell is increased the solution obtained from the *n*-point scheme, denoted as $v^{n\text{-}pt}$, approaches the exact solution, i.e., $\lim_{n\to\infty} v^{n\text{-}pt} \to v^{ex}$. Even though the rate of convergence may not be monotonic, it is reasonable to assume that for sufficiently large n the modeling error associated with the *2*-point scheme can be approximated as

$$e^{2\text{-}pt} \approx E^{2\text{-}pt} = \left\| v^{n\text{-}pt} - v^{2\text{-}pt} \right\|_{\square} \tag{195}$$

We now turn to the second issue: the choice of v. In this context it is essential to interpret the *2*-point scheme approach as consisting of two steps: analysis on the macroscale and post-processing on the microscale. In the first step, a nonlinear macro-analysis is carried out using the finite element method which utilizes the *2*-point scheme. Consequently, the macroscopic deformation history is stored in a database at macro-Gauss points. In the post-processing step, the deformation field in a unit cell corresponding to critical macro-points is extracted from the database, and then subjected onto the unit cell as an external loading. Finally, the *n*-point scheme is employed to solve for selected unit cell problems.

Based on the above interpretation of the *2*-point scheme, it follows that if the macroscopic deformation field obtained with the *2*-point scheme is identical to one obtained with the *n*-point scheme, then the model error estimator, $E^{2\text{-}pt}$, should indicate zero error. In other words, v should be a measure of the macroscopic deformation field, whereas $\square = \Omega$. Possible deformation measures are: the macroscopic deformation gradient tensor, $\boldsymbol{F}$ (the component form is defined in (120)), and/or incremental deformation measures represented by a pair $\Delta\bar{\varepsilon}$, $\Delta\bar{\omega}$. The former accounts for accumulation of errors

$$E_F^{2\text{-}pt} = \left\| \boldsymbol{F}^{n\text{-}pt} - \boldsymbol{F}^{2\text{-}pt} \right\|_{\Omega} \tag{196}$$

whereas the latter controls the incremental errors

$$E_{\Delta}^{2\text{-}pt} = \sqrt{\left\| \Delta\bar{\varepsilon}^{n\text{-}pt} - \Delta\bar{\varepsilon}^{2\text{-}pt} \right\|_{\Omega}^2 + \left\| \Delta\bar{\omega}^{n\text{-}pt} - \Delta\bar{\omega}^{2\text{-}pt} \right\|_{\Omega}^2} \tag{197}$$

In Section 6 we will show that in a confined deformation pattern, where small plastic zones are encompassed by elastically deforming solid, the modeling errors, $E^{2\text{-}pt}$, are very small, whereas in large plastic zones dominated by matrix deformation, the modeling errors, $E^{2\text{-}pt}$, might be significant. For simplicity, we adopt the incremental estimator (197).

We now turn to the computational efficiency issue. Estimation of modeling error based on equations (196) and (197) necessitates solution of the *n*-point scheme model. As indicated earlier the computational cost of the *n*-point scheme model is enormous, and hence, only an estimate of $E^{2\text{-}pt}$, denoted $\underset{\sim}{E}^{2\text{-}pt}$, will be evaluated. The philosophy behind our modeling error estimator is somewhat similar to that employed for estimation of discretization errors, namely, if the mathematical model (or discretization) is locally altered, then in absence of the pollution errors the solution outside the local region is not significantly affected, and thus the bulk of the error can be computed on the local level. This process avoids the need for solving an auxiliary global problem and replaces it by solving a sequence of problems on small local domains.

When the aforementioned procedure is applied for estimation of discretization errors, the computational cost of solving the local problem is relatively low, reducing the cost of discretization error estimation to one of a manageable size. Unfortunately, this is not the case for estimation of modeling error $\underset{\sim}{E}^{2\text{-}pt}$. Even though the aforementioned process involves multiple solutions of small local problems (for example, on the macro-element domains), the cost of applying the *n*-point scheme on each macro-element is formidable in a large scale computational environment. Therefore, the costly *n*-point scheme should be utilized only for those macro-elements which have been identified as "having potential to be critical" by some simple cost-effective engineering-based criteria. One possible engineering criterion is the magnitude of the deformation, measured by a norm of one of the macroscopic strain measures. When this norm exceeds some critical value, the corresponding macro element is tagged for *a-posteriori* model error estimation.

We now focus on the adaptive *2/n*-point model construction. Consider the *2/n*-point model at time *t*, consisting of the *2*-point scheme model in the portion of the macro-domain ${}^{t}\Omega^{2\text{-}pt} \subset {}^{t}\Omega$ and the *n*-point scheme model in the remainder ${}^{t}\Omega^{n\text{-}pt}$ such that ${}^{t}\Omega^{2\text{-}pt} \cup {}^{t}\Omega^{n\text{-}pt} = {}^{t}\Omega$. The goal is to adaptively construct the *2/n*-point model at time $t + \Delta t$, consisting of subdomains ${}^{t+\Delta t}\Omega^{2\text{-}pt}$ and ${}^{t+\Delta t}\Omega^{n\text{-}pt}$. Let ${}_{cr}{}^{t}\Omega^{2\text{-}pt} = \bigcup_{e}^{{}_{cr}n} {}_{cr}{}^{t}\Omega_{e}^{2\text{-}pt}$ be a subdomain in ${}^{t}\Omega^{2\text{-}pt}$ consisting of ${}_{cr}n$ macro-element subdomains ${}_{cr}{}^{t}\Omega_{e}^{2\text{-}pt}$ which have been tagged as critical by the aforementioned engineering criterion, as shown in Figure 5.

Let ${}_{cr}{}^{\tau}\Delta\bar{\varepsilon}_{e}^{2\text{-}pt}$ and ${}_{cr}{}^{\tau}\Delta\bar{\omega}_{e}^{2\text{-}pt}$ be the macro- strain and rotation increments on ${}_{cr}{}^{\tau}\Omega_{e}^{2\text{-}pt}$ at $\tau \le t$. The first step in the adaptive process is to post-process the unit cell solution at time

t for all macro-elements on ${}^{t}_{cr}\Omega_e^{2\text{-}pt}$ by utilizing the n-point scheme model outlined in Section 4.

Let ${}_{cr}\boldsymbol{r}_e^{2\text{-}pt}$ be the residual for all the elements on ${}^{t}_{cr}\Omega_e^{2\text{-}pt}$ defined as

$$ {}_{cr}\boldsymbol{r}_e^{2\text{-}pt} = {}^{t+\Delta t}_{cr}\boldsymbol{f}_e^{2\text{-}pt} - {}^{t}_{cr}\boldsymbol{f}_e^{2\text{-}pt} \tag{198} $$

where ${}^{t}_{cr}\boldsymbol{f}_e^{2\text{-}pt}$ is the corresponding internal force vector. In the second step, for all elements in ${}^{t}_{cr}\Omega_e^{2\text{-}pt}$ the incremental nonlinear problem defined as

$$ {}_{cr}\boldsymbol{r}_e^{2\text{-}pt} = \mathbf{0} \tag{199} $$

is solved twice: first, by using the 2-point scheme model, and second, by utilizing the n-point scheme model with initial conditions obtained via post-processing. The estimated error on ${}^{t}_{cr}\Omega_e^{2\text{-}pt}$ is computed by utilizing equation (197)

$$ E_{\Delta^e}^{2\text{-}pt} = \sqrt{\left\| {}_{cr}\Delta\bar{\varepsilon}_e^{n\text{-}pt} - {}_{cr}\Delta\bar{\varepsilon}_e^{2\text{-}pt} \right\|^2_{{}^{t}_{cr}\Omega_e^{2\text{-}pt}} + \left\| {}_{cr}\Delta\bar{\omega}_e^{n\text{-}pt} - {}_{cr}\Delta\bar{\omega}_e^{2\text{-}pt} \right\|^2_{{}^{t}_{cr}\Omega_e^{2\text{-}pt}}} \tag{200} $$

where the strain and rotation increments are evaluated by solving equation (199).

The total modeling error is then estimated as

$$ E_{\Delta}^{2\text{-}pt} \approx \sqrt{\sum_{e \in {}^{t}_{cr}\Omega_e^{2\text{-}pt}} \left(E_{\Delta^e}^{2\text{-}pt}\right)^2} \tag{201} $$

To steer the process of adaptivity we define the modeling error indicator η_e on ${}^{t}_{cr}\Omega_e^{2\text{-}pt}$ as

$$ \eta_e = \frac{E_{\Delta^e}^{2\text{-}pt}}{\max\limits_{e}\left(E_{\Delta^e}^{2\text{-}pt}\right)} \tag{202} $$

and we replace the 2-point scheme model by the n-point scheme model for all the elements on ${}^{t}_{cr}\Omega_e^{2\text{-}pt}$ for which $\eta_e \geq tol$.

6.0 Numerical Experiments and Discussion

Our numerical experimentation agenda consists of three examples. The first is used to validate our finite deformation plasticity formulation. The second and the third examples test

the proposed adaptive $2/n$-point scheme in a deformation pattern with large plastic zones dominated by matrix deformation as well as in a typical confined deformation pattern, where a small plastic zone is encompassed by an elastically deforming solid.

6.1 Uniform Macro-Strain Loading

The objective of the first example is to carry out a qualitative assessment of the large deformation formulation. The primary "suspect" is equation (71) which decomposes displacement field in the microstructure into two parts: the macroscopic part which comes from the integration of the nonperiodic macroscopic strain and rotation increments (the first term in (71)) and the periodic microscopic part (the second term in (71)). Note that solution update in the unit cell domain directly from the asymptotic expansion of the displacement field (11) is not feasible, because in the limit as $\varsigma \to 0$, only the macroscopic part has contribution. On the other hand, if $\boldsymbol{u}^1$ is considered only, then the nonperiodic finite deformation patterns are not accounted for.

As a test problem we select a macro problem subjected to the state of uniform strain field (or linear displacement field). A unit cell consists of a stiff elastic cylindrical fiber embedded in a compliant plastically deforming matrix. The phase properties are given as below:

Fiber: Young's modulus = 68.9 GPa, Poisson's ratio = 0.21
Matrix: Young's modulus = 6.89 GPa, Poisson's ratio = 0.33, yield stress = 24 MPa, isotropic hardening modulus = 0.689 GPa, $\beta = 1$.

We consider a uniform transverse tension, transverse shear and longitudinal shear loading conditions. The overall principal Green strain does not exceed 25% in all three cases. Figures 6 to 8 show the contribution of macroscopic and microscopic fields to the total deformation field in the unit cell. It can be seen that each of the two contributing parts alone significantly distort the circular fiber cross section, but their sum recovers the original fiber shape, as expected in a matrix dominated loading condition.

6.2 The 3D Beam Problem

To validate the computational models and adaptive strategies proposed we comprise a test case, where a significant portion of the structure is subjected to the matrix dominated deformation in a load or stress control mode (as opposed to displacement control). This is the worse possible scenario in terms of accuracy for the 2-point scheme. The problem configuration is shown in Figure 9. The macro problem is discretized with 5635 tetrahedral finite elements. The microstructure is the same one used in the previous example. The fiber direction coincides with the beam's longitudinal direction. In the region of length l_1 from the fixed end the beam is subjected to the shear deformation (which is the matrix dominated mode) whereas in the remainder of the problem domain, l_2 length, the beam is in pure bending, which is a fiber dominated mode of loading. The phase properties are summarized below:

Fiber: Young's modulus = 37.92 GPa, Poisson's ratio = 0.21
Matrix: Young's modulus = 6.89 GPa, Poisson's ratio = 0.33, yield stress = 24 MPa, isotropic hardening modulus = 0.689 GPa, $\beta = 1$.

The loading is applied in 15 load steps. The maximal vertical displacement at the free end is over one third of the length of the beam and the stresses exceed the elastic limit in all macro-elements.

The problem is solved using the 2-point scheme with micro-history recovery, the adaptive *2/n*-point scheme, and the *n*-point scheme for a comparison purpose. Figure 10 shows the evolution of the normalized estimated local error in the vicinity of the fixed end as obtained with the 2-point scheme (equation (202)). It can be seen that the maximal normalized local error in the region dominated by matrix deformation is 40%. In a region dominated by the fiber deformation the error does not exceed 3%. The distribution of the local principal stress error in the critical unit cell (denoted by point A in Figure 10) as obtained with the 2-point scheme and micro-history postprocessing is shown in Figure 11. It can be seen that the normalized error in the unit cell is of the same magnitude as the normalized local error in the macrostructure. Figure 12 illustrates the evolution of the normalized local error in the macrostructure obtained using the adaptive *2/n*-point scheme model. The maximal normalized local error is less than 1% and the normalized error in the unit cell follows the same trend as shown in Figure 13.

We conclude that the adaptive *2/n*-point scheme model outperforms the 2-point scheme model in terms of accuracy (0.8% maximal error as compared to 40%), and the *n*-point scheme model in terms of CPU time as it is 14 times faster than the *n*-point scheme.

6.3 The Nozzle Flap Problem

For the final numerical example, we consider a typical aerospace component where only a small region experiences inelastic deformation. The finite element mesh describing the macrostructure of the Nozzle Flap is shown in Figure 1. We consider two types of microstructures: (i) the fibrous unit cell (as in the previous example) and the plain weave fabric microstructure shown in Figure 14. The fibrous unit cell contains 98 elements in the fiber domain and 253 elements in the matrix domain. The fiber volume fraction is 0.27. The plain weave microstructure has 370 elements in the fiber bundle and 1196 in the matrix domain. The bundle volume fraction is 0.25. The phase properties are:

Fiber, fiber bundle: Young's modulus = 379.2 GPa, Poisson's ratio = 0.21
Matrix: Young's modulus = 68.9 GPa, Poisson's ratio = 0.33, yield stress = 24 MPa, isotropic hardening = 14 GPa, $\beta = 1$.

The Nozzle Flap is subjected to an aerodynamic force (simulated by a uniform pressure) on the back of the flap. We assume that the pin-eyes are rigid and a rotation is not allowed so that all the degrees of freedom on the pin-eye surfaces are fixed. The loading takes the solution well into the inelastic region in the vicinity of the pins: 15% of elements experience inelastic deformation in the case of fibrous microstructure, and 29% in the case of plain weave.

The problem is analyzed using the adaptive *2/n*-point scheme model. Figure 15 shows that the 2-point scheme model yields the maximum normalized local error in the macrostructure below 1% (for the plain weave microstructure). Hence, if the tolerance for switching from the *2*-point scheme to the *n*-point scheme is higher than 1%, adaptive strategy selects the *2*-point scheme model in the entire macro problem domain. The normalized local error in the unit cell located at Point C of Figure 15 is 2.5% for fibrous microstructure and 6.5% for the plain weave, as shown in Figures 16 and 17.

For the problem with the fibrous unit cell, the CPU time on a SPARC 10/51 is 30 seconds for the macroscopic analysis and 120 seconds for postprocessing a single point. For the plain weave microstructure, the macroscopic analysis consumes 30 seconds, whereas postprocessing takes 510 seconds per point. On the other hand, the *n*-point scheme consumes 7 hours of CPU time for fibrous composite and over 55 hours of CPU time for plain weave. Memory requirement ratios are approximately 1:250 for the fibrous unit cell and 1:1200 for the plain weave in favor of the *2/n*-point scheme (or *2*-point scheme).

Acknowledgment

The authors gratefully acknowledge the support for this work by Air Force Office of Scientific Research under grant F49620-97-1-0090 and ARPA/ONR under grant N00014-92-J-1779.

References

1 J. Aboudi, "A Continuum Theory for Fiber-Reinforced Elastic-Viscoplastic Composites," *International Journal of Engineering Science*, 20, 1982.

2 M. L. Accorsi and S. Nemat-Nasser, "Bounds on the Overall Elastic and Instantaneous Elastoplastic Moduli of Periodic Composites," *Mechanics of Materials*, 5, 1986.

3 A. Benssousan, J. L. Lions and G. Papanicoulau, *Asymptotic Analysis for Periodic Structure*, North-Holland, 1978.

4 N. S. Bakhvalov and G. P. Panasenko, *Homogenisation: Averaging Processes in Periodic Media*, Kluwer Academic Publishers, 1989.

5 G.J. Dvorak, "Transformation Field Analysis of Inelastic Composite Materials," *Proceedings Royal Society of London*, A437, 1992.

6 N. Fares and G. J. Dvorak, "Large Elastic-Plastic Deformations of Fibrous Metal Matrix Composites," *Journal of the Mechanics and Physics of Solids*, 39, 1991.

7 J. Fish, P. Nayak and M. H. Holmes, "Microscale Reduction Error Indicators and Estimators for a Periodic Heterogeneous Medium," *Computational Mechanics*, 14, 1994.

8 J. Fish, K. Shek, M. Pandheeradi and M. S. Shephard, "Computational Plasticity for Composite Structures Based on Mathematical Homogenization: Theory and Practice," *Computer Methods in Applied Mechanics and Engineering*, accepted for publication.

9 J. Fish and A. Wagiman, "Multiscale Finite Element Method for Locally Nonperiodic

Heterogeneous Medium," *Computational Mechanics,* 12, 1993.

10 S. Ghosh and S. Moorthy, "Elastic-Plastic Analysis of Arbitrary Heterogeneous Materials with the Voronoi Cell Finite Element Method," *Computer Methods in Applied Mechanics and Engineering*, 121, 1995.

11 M. Gosz, B. Moran and J. D. Achenbach, "Matrix Cracking in Transversely Loaded Fiber Composites with Compliant Interphases," AMD-Vol. 150/AD-Vol. 32, *Damage Mechanics in Composites*, ASME, 1992.

12 J. M. Guedes, *Nonlinear Computational Models for Composite Materials Using Homogenization*, PhD thesis, University of Michigan, 1990.

13 J. M. Guedes and N. Kikuch, "Preprocessing and Postprocessing for Materials Based on the Homogenization Method with Adaptive Finite Element Methods," *Computer Methods in Applied Mechanics and Engineering*, 83, 1990.

14 J. O. Hallquist, *NIKE2D: An Implicit, Finite Deformation, Finite Element Code for Analyzing the Static and Dynamic Response of Two Dimensional Solids*, University of California, Lawrence Livermore National Laboratory, Report UCID-19156, 1979.

15 R. Hill, "A Self Consistent Mechanics of Composite Materials," *Journal of the Mechanics and Physics of Solids*, 13, 1965.

16 T. J. R. Hughes, "Numerical Implementation of Constitutive Models: Rate-Independent Deviatoric Plasticity," in S. Nemat-Nasser, R. J. Asaro and G. A. Hegemier, editors, *Theoretical Foundation for Large Scale Computations for Nonlinear Material Behavior*, Martinus Nijhoff Publishers, 1983.

17 T. J. R. Hughes and J. Winget, "Finite Rotation Effects in Numerical Integration of Rate Constitutive Equations Arising in Large Deformation Analysis," *International Journal of Numerical Methods in Engineering*, 15, 1980.

18 S. Jansson, "Homogenized Nonlinear Constitutive Properties and Local Stress Concentrations for Composites with Periodic Internal Structure," *International Journal of Solids and Structures*, 29, 1992.

19 A. L. Kalamkarov, *Composite and Reinforced Elements of Construction*, John Wiley and Sons, 1992.

20 E. H. Lee, R. L. Mallett and T. B. Wertheimer, "Stress Analysis for Kinematic Hardening in Finite Deformation Plasticity," *Journal of Applied Mechanics*, 105, 1983.

21 F. Lene and D. Leguillon, "Homogenized Constitutive Law for a Partially Cohesive Composite Material," *International Journal of Solids and Structures*, 18, 1982.

22 F. Lene, "Damage Constitutive Relations for Composite Materials," *Engineering Fracture Mechanics*, 25, 1986.

23 V. M. Levin, "Thermal Expansion Coefficients of Heterogeneous Materials," *Mekhan ika Tverdogo Tela*, 2, 1967.

24 C. J. Lissenden and C. T. Herakovich, "Numerical Modeling of Damage Development

and Viscoplasticity in Metal Matrix Composites," *Computer Methods in Applied Mechanics and Engineering*, 126, 1995.

25 T. Mori and K. Tanaka, "Average Stress in Matrix and Average Elastic Energy of Materials with Misfitting Inclusions," *Acta Metallurgica*, 21, 1973.

26 H. Moulinec and P. Suquet, "A Fast Numerical Method for Computing the Linear and Nonlinear Properties of Composites," *C. R. Acad. Sc. Paris II*, 318, 1994.

27 S. Nemat-Nasser, "On Finite Plastic Flow of Crystalline and Geomaterials," *Journal of Applied Mechanics*, 105, 1983.

28 J. T. Oden and T. I. Zohdi, *Analysis and Adaptive Modeling of Highly Heterogeneous Elastic Structures,* TICAM Report 56, University of Texas at Austin, 1996.

29 P. Ponte Castaneda, "New Variational Principles in Plasticity and Their Applications to Composite Materials," *Journal of the Mechanics and Physics of Solids*, 40, 1992.

30 E. Sanchez-Palencia and A. Zaoui, *Homogenization Techniques for Composite Media*, Springer-Verlag, 1987.

31 J. C. Simo and R. L. Taylor, "Consistent Tangent Operators for Rate-Independent Elastoplasticity," *Computer Methods in Applied Mechanics and Engineering*, 48, 1985.

32 P. M. Suquet, *Plasticite et Homogeneisation*, These de Doctorat d' Etat, Universite Pierre et Marie Curie, Paris 6, 1982.

33 P. M. Suquet, "Elements of Homogenization for Inelastic Solid Mechanics," in E. Sanchez-Palencia and A. Zaoui, editors, *Homogenization Techniques for Composite Media,* Springer-Verlag, 1987.

34 J. L. Teply and G. J. Dvorak, "Bounds on Overall Instantaneous Properties of Elastic-Plastic Composites," *Journal of the Mechanics and Physics of Solids*, 36, 1988.

35 J. R. Willis, "On Methods for Bounding the Overall Properties of Nonlinear Composites," *Journal of the Mechanics and Physics of Solids*, 39, 1991.

36 H. Zielger, "A Modification of Prager's Hardening Rule," *Quarterly of Applied Mathematics*, 17, 1959.

37 T. I. Zohdi, J. T. Oden and G. J. Rodin, *Hierarchical Modeling of Heterogeneous Bodies,* TICAM Report 21, University of Texas at Austin, 1996.

7.0 Appendixes

A.0 Derivation of $\partial(\sigma_{ij}^{(m)} - \alpha_{ij}^{(m)})/\partial\Delta\lambda^{(m)}$ in (96)

Consider equation (93):

$$\sigma_{ij}^{(m)} - \alpha_{ij}^{(m)} = (I_{ijkl} + \Delta\lambda^{(m)} \wp_{ijkl})^{-1} ({}_{tr}\sigma_{kl}^{(m)} - {}^{t}\hat{\alpha}_{kl}^{(m)}) \tag{203}$$

Taking the derivative of (203) with respect to $\Delta\lambda^{(m)}$ yields:

$$\frac{\partial}{\partial\Delta\lambda^{(m)}}(\sigma_{ij}^{(m)} - \alpha_{ij}^{(m)}) = (I_{ijkl} + \Delta\lambda^{(m)} \wp_{ijkl})^{-1} \left(- \wp_{klmn}(\sigma_{mn}^{(m)} - \alpha_{mn}^{(m)}) + \frac{\partial}{\partial\Delta\lambda^{(m)}}({}_{tr}\sigma_{kl}^{(m)} - {}^{t}\hat{\alpha}_{kl}^{(m)}) \right) \tag{204}$$

where the last term can be written as

$$\frac{\partial({}_{tr}\sigma_{kl}^{(m)} - {}^{t}\hat{\alpha}_{kl}^{(m)})}{\partial\Delta\lambda^{(m)}} = \frac{\partial({}^{t}\hat{\sigma}_{kl}^{(m)} - {}^{t}\hat{\alpha}_{kl}^{(m)})}{\partial\Delta\lambda^{(m)}} = \frac{\partial({}^{t}\hat{\sigma}_{kl}^{(m)} - {}^{t}\hat{\alpha}_{kl}^{(m)})}{\partial\Delta\omega_{pq}^{(m)}} \frac{\partial\Delta\omega_{pq}^{(m)}}{\partial\Delta\lambda^{(m)}} \tag{205}$$

and

$$\begin{aligned} \frac{\partial {}^{t}\hat{\sigma}_{kl}^{(r)}}{\partial\Delta\omega_{pq}^{(r)}} &= \left(\frac{\partial\Re_{sk}^{(r)}}{\partial\Delta\omega_{pq}^{(r)}} \Re_{tl}^{(r)} + \Re_{sk}^{(r)} \frac{\partial\Re_{tl}^{(r)}}{\partial\Delta\omega_{pq}^{(r)}} \right) {}^{t}\sigma_{st}^{(r)} \\ &= (\delta_{ms}\delta_{nk}\Re_{tl}^{(r)} + \delta_{mt}\delta_{nl}\Re_{sk}^{(r)}) \, {}^{t}\sigma_{st}^{(r)} \frac{\partial\Re_{mn}^{(r)}}{\partial\Delta\omega_{pq}^{(r)}} \end{aligned} \tag{206}$$

The rotation $\Re_{mn}^{(r)}$ of phase r is defined in (77) as

$$\Re_{mn}^{(r)} = \delta_{mn} + \left(\delta_{mr} - \frac{1}{2}\Delta\omega_{mr}^{(r)} \right)^{-1} \Delta\omega_{rn}^{(r)} \tag{207}$$

The derivative of $\Re_{mn}^{(r)}$ is calculated using the chain rule:

$$\frac{\partial\Re_{mn}^{(r)}}{\partial\Delta\lambda^{(m)}} = \frac{\partial\Re_{mn}^{(r)}}{\partial\Delta\omega_{pq}^{(r)}} \frac{\partial\Delta\omega_{pq}^{(r)}}{\partial\Delta\lambda^{(m)}} \tag{208}$$

in which

$$\frac{\partial\Re_{mn}^{(r)}}{\partial\Delta\omega_{pq}^{(r)}} = (2\delta_{mp} - \Delta\omega_{mp}^{(r)})^{-1}(\delta_{qn} + \Re_{qn}^{(r)}) \tag{209}$$

Consequently, equation (206) can be expressed as

$${}_{\sigma}U_{klpq}^{(r)} \equiv \frac{\partial {}^{t}\hat{\sigma}_{kl}^{(r)}}{\partial\Delta\omega_{pq}^{(r)}} = (\delta_{nk}\Re_{tl}^{(r)} \, {}^{t}\sigma_{mt}^{(r)} + \delta_{nl}\Re_{sk}^{(r)} \, {}^{t}\sigma_{sm}^{(r)})(2\delta_{mp} - \Delta\omega_{mp}^{(r)})^{-1}(\delta_{qn} + \Re_{qn}^{(r)}) \tag{210}$$

Similarly, we have

$$ {}_{\alpha}U^{(m)}_{klpq} \equiv \frac{\partial^t \hat{\alpha}^{(m)}_{kl}}{\partial \Delta\omega^{(m)}_{pq}} = (\delta_{nk}\Re^{(m)}_{tl}\,{}^t\alpha^{(m)}_{mt} + \delta_{nl}\Re^{(m)}_{sk}\,{}^t\alpha^{(m)}_{sm})(2\delta_{mp} - \Delta\omega^{(m)}_{mp})^{-1}(\delta_{qn} + \Re^{(m)}_{qn}) \tag{211} $$

Taking derivative of (89) with respect to $\Delta\lambda^{(m)}$ yields:

$$ \frac{\partial \Delta\omega^{(m)}_{pq}}{\partial \Delta\lambda^{(m)}} = \hat{D}^{(mm)}_{pqmn} P_{mnkl}\left((\sigma^{(m)}_{kl} - \alpha^{(m)}_{kl}) + \Delta\lambda^{(m)} \frac{\partial}{\partial \Delta\lambda_m}(\sigma^{(m)}_{kl} - \alpha^{(m)}_{kl})\right) \tag{212} $$

Substituting equations (210), (211) and (212) into (205), and then inserting the result into (204), gives

$$ \frac{\partial}{\partial \Delta\lambda^{(m)}}(\sigma^{(m)}_{ij} - \alpha^{(m)}_{ij}) = C^{(m)}_{ijkl}(\sigma^{(m)}_{kl} - \alpha^{(m)}_{kl}) \tag{213} $$

where

$$ C^{(m)}_{ijkl} = -(I_{ijmn} + \Delta\lambda^{(m)} W^{(m)}_{ijmn})^{-1} W^{(m)}_{mnkl} \tag{214} $$

$$ W^{(m)}_{mnkl} = \wp_{mnkl} - ({}_{\sigma}U^{(m)}_{mnst} - {}_{\alpha}U^{(m)}_{mnst})\hat{D}^{(mm)}_{stpq} P_{pqkl} \tag{215} $$

B.0 Consistent Linearization of $\Delta\bar{\varepsilon}_{ij}$ and $\Delta\bar{\omega}_{ij}$

We derive the equations for $\Delta\dot{\bar{\varepsilon}}_{ij}$ and $\Delta\dot{\bar{\omega}}_{ij}$ consistent with the midpoint integration of rate of deformation and rotation. The left superscript $t + \Delta t$ is omitted.

Taking the material time derivative of (72) yields:

$$ \frac{d}{dt}\Delta\bar{\varepsilon}_{ij} = \frac{1}{2}\frac{d}{dt}\left(\frac{\partial \Delta u^0_i}{\partial^{t+\Delta t/2} x_j} + \frac{\partial \Delta u^0_j}{\partial^{t+\Delta t/2} x_i}\right) \tag{216} $$

The material time derivative of the first term in the parenthesis of (216) can be written as

$$ \frac{d}{dt}\left(\frac{\partial \Delta u^0_i}{\partial^{t+\Delta t/2} x_j}\right) = \frac{\partial v^0_i}{\partial^t x_k}\frac{\partial^t x_k}{\partial^{t+\Delta t/2} x_j} + \frac{\partial \Delta u^0_i}{\partial^t x_k}\frac{d}{dt}\left(\frac{\partial^t x_k}{\partial^{t+\Delta t/2} x_j}\right) \tag{217} $$

where

$$ \frac{d}{dt}\left(\frac{\partial^t x_k}{\partial^{t+\Delta t/2} x_j}\right) = -\frac{\partial^t x_k}{\partial^{t+\Delta t/2} x_m}\frac{d}{dt}\left(\frac{\partial^{t+\Delta t/2} x_m}{\partial^t x_n}\right)\frac{\partial^t x_n}{\partial^{t+\Delta t/2} x_j} \tag{218} $$

Consequently, (217) can be expressed as

$$\frac{d}{dt}\left(\frac{\partial \Delta u_i^0}{\partial^{t+\Delta t/2} x_j}\right) = \frac{\partial v_i^0}{\partial^{t+\Delta t/2} x_j} - \frac{\partial \Delta u_i^0}{\partial^{t+\Delta t/2} x_m} \frac{d}{dt}\left(\frac{\partial^{t+\Delta t/2} x_m}{\partial^t x_n}\right) \frac{\partial^t x_n}{\partial^{t+\Delta t/2} x_j} \tag{219}$$

where

$$\frac{d}{dt}\left(\frac{\partial^{t+\Delta t/2} x_m}{\partial^t x_n}\right) = \frac{\partial}{\partial^t x_n}\left(\frac{d}{dt}{}^{t+\Delta t/2} x_m\right) = \frac{\partial}{\partial^t x_n}\left\{\frac{d}{dt}\left(\frac{x_m + {}^t x_m}{2}\right)\right\} = \frac{1}{2}\frac{\partial v_m^0}{\partial^t x_n} \tag{220}$$

Substituting (220) into (219) gives

$$\frac{d}{dt}\left(\frac{\partial \Delta u_i^0}{\partial^{t+\Delta t/2} x_j}\right) = \left(\delta_{im} - \frac{1}{2}\frac{\partial \Delta u_i^0}{\partial^{t+\Delta t/2} x_m}\right) \frac{\partial v_m^0}{\partial^{t+\Delta t/2} x_j} \tag{221}$$

Equation (221) can be further simplified as

$$\frac{d}{dt}\left(\frac{\partial \Delta u_i^0}{\partial^{t+\Delta t/2} x_j}\right) = \frac{\partial^t x_i}{\partial^{t+\Delta t/2} x_m} \frac{\partial v_m^0}{\partial^{t+\Delta t/2} x_j} \tag{222}$$

where the following equality has been utilized.

$$\delta_{im} - \frac{1}{2}\frac{\partial \Delta u_i^0}{\partial^{t+\Delta t/2} x_m} = \frac{\partial}{\partial^{t+\Delta t/2} x_m}\left({}^{t+\Delta t/2} x_i - \frac{1}{2}\Delta u_i^0\right) = \frac{\partial^t x_i}{\partial^{t+\Delta t/2} x_m} \tag{223}$$

Defining M_{ijkl} as

$$M_{ijkl} \equiv \frac{\partial^t x_i}{\partial^{t+\Delta t/2} x_k} \frac{\partial x_l}{\partial^{t+\Delta t/2} x_j} \tag{224}$$

We have

$$\frac{d}{dt}\left(\frac{\partial \Delta u_i^0}{\partial^{t+\Delta t/2} x_j}\right) = M_{ijkl}\, v^0_{k,\,x_l} \tag{225}$$

Substituting (225) into (216) and preforming the same procedure for $\Delta\dot{\bar{\omega}}_{ij}$, we obtain the final expressions for $\Delta\dot{\bar{\varepsilon}}_{ij}$ and $\Delta\dot{\bar{\omega}}_{ij}$ as

$$\Delta\dot{\bar{\varepsilon}}_{ij} = M_{(ij)kl}\, v^0_{k,\,x_l}, \qquad \Delta\dot{\bar{\omega}}_{ij} = M_{[ij]kl}\, v^0_{k,\,x_l} \tag{226}$$

Note that in the case of backward Euler integration $M_{ijkl} = \delta_{ik}\delta_{jl}$.

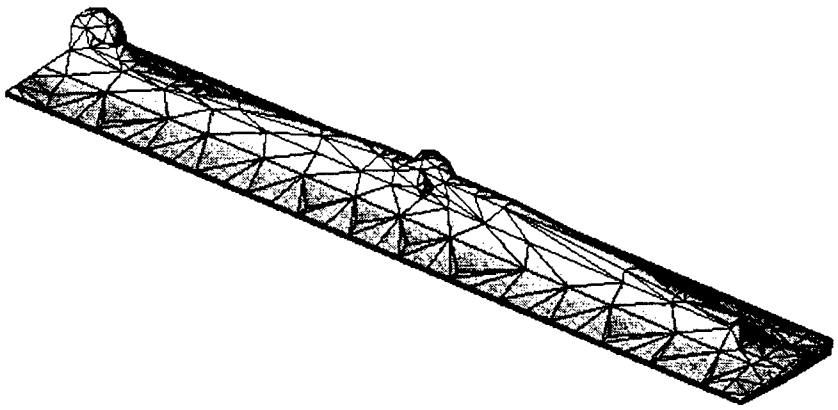


Figure 1: Finite element mesh for the nozzle flap problem

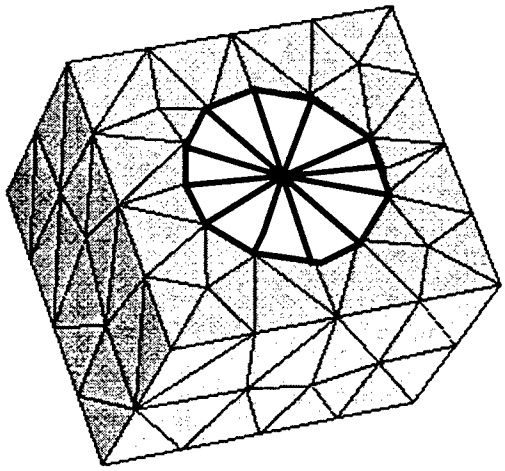


Figure 2: Finite element mesh for the fibrous unit cell

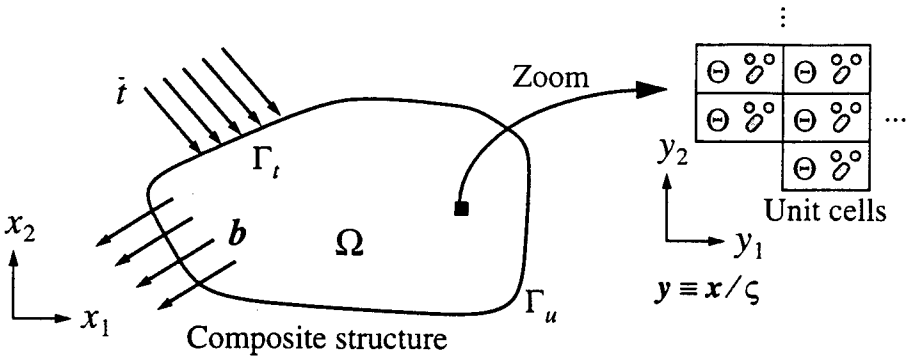


Figure 3: Macroscopic and microscopic structures

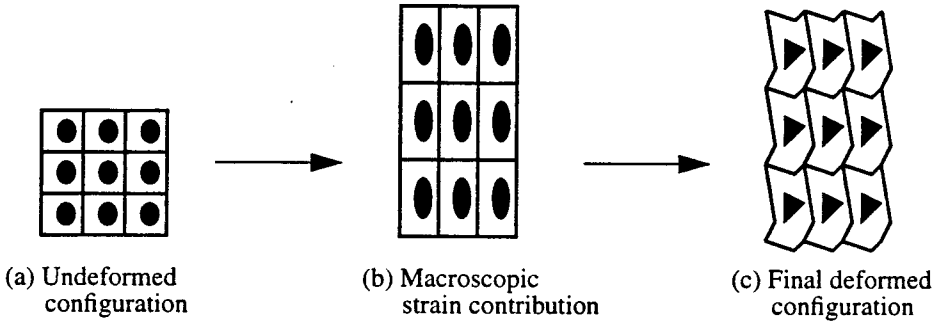


Figure 4: Decomposition of deformation in the microstructure

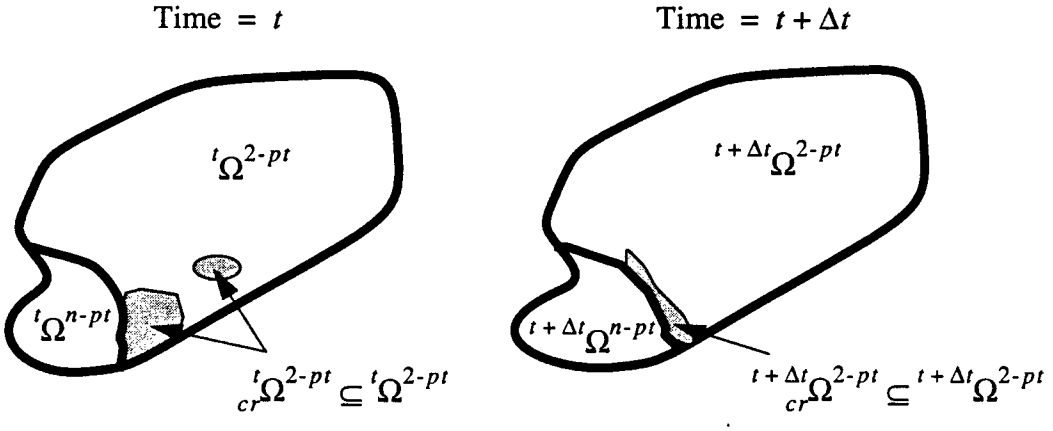


Figure 5: Adaptive model construction

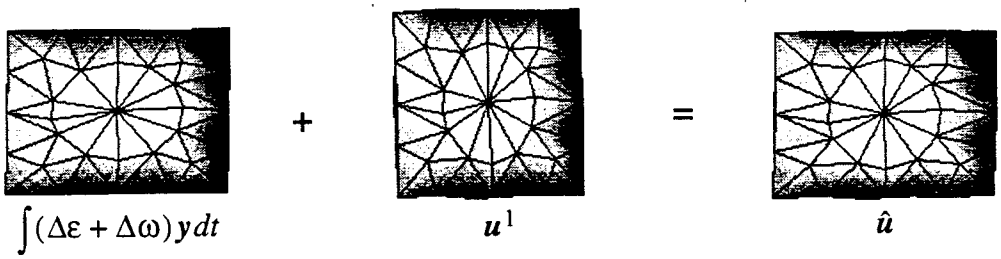


Figure 6: Deformation of unit cell under transverse tension

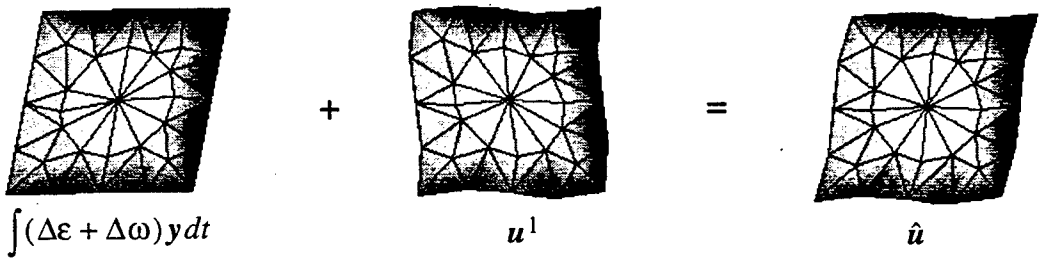


Figure 7: Deformation of unit cell under transverse shear

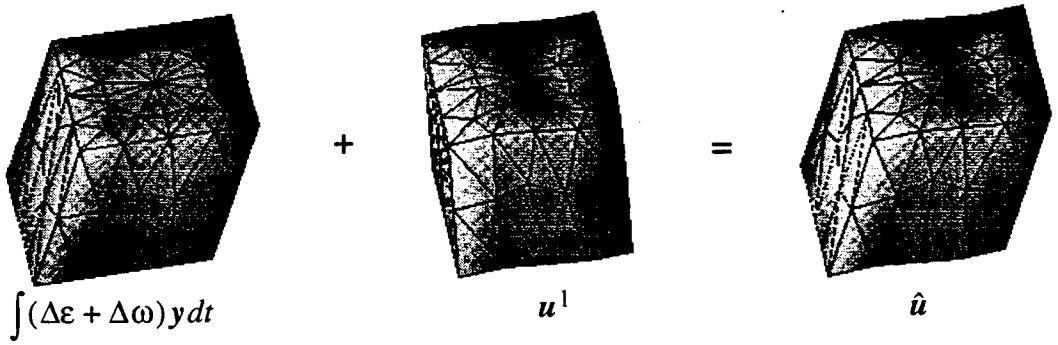


Figure 8: Deformation of unit cell under longitudinal shear

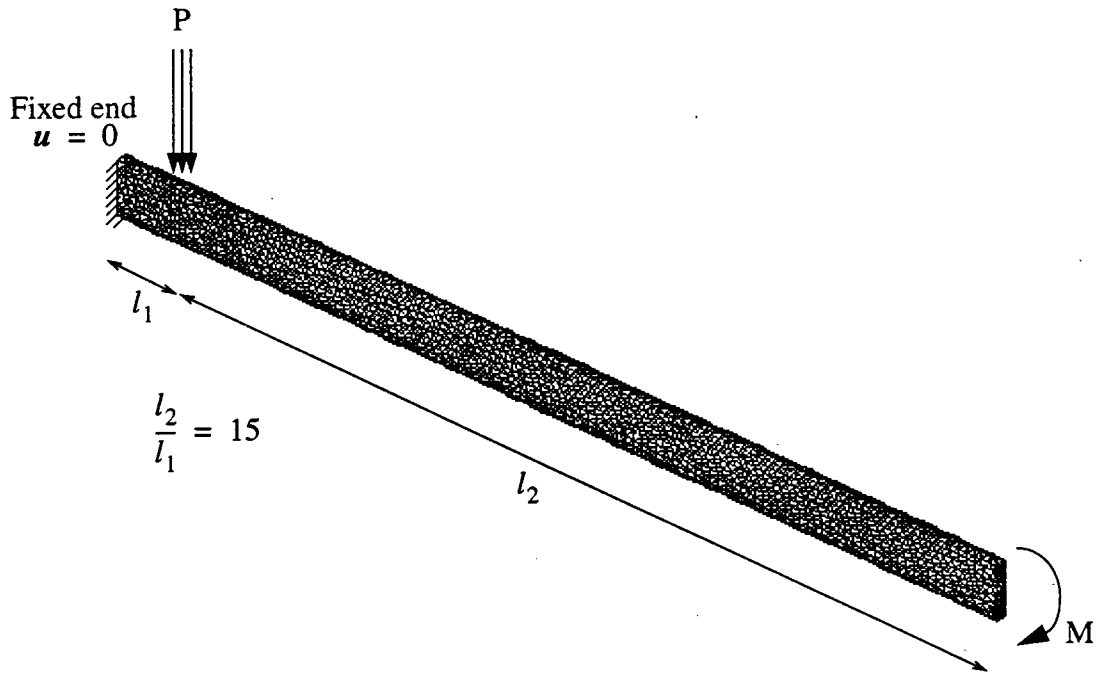


Figure 9: Finite element mesh for the 3D beam problem

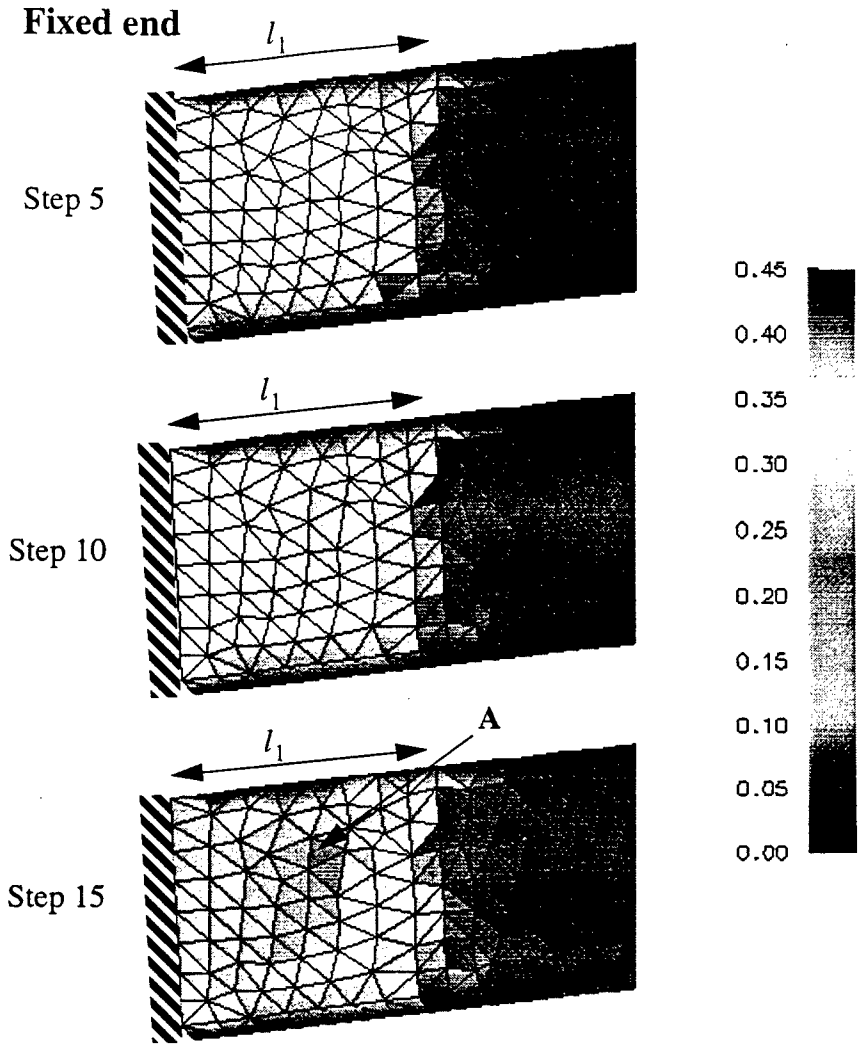
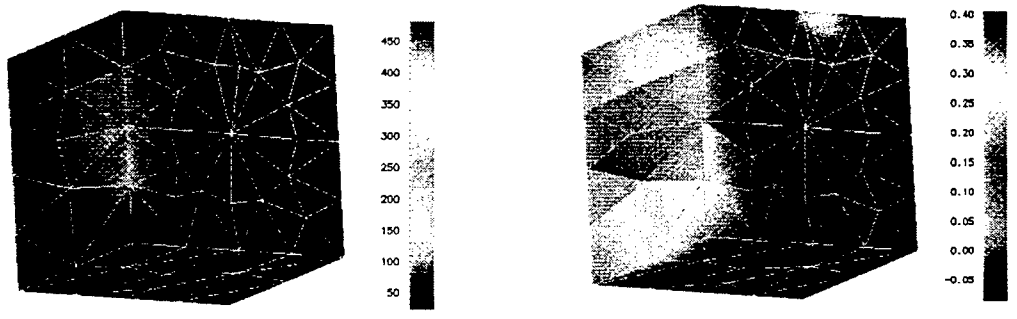


Figure 10: Distribution of the normalized local error with the 2-point model



Effective stress

Normalized error of effective stress

Figure 11: Effective stress and normalized error at point A with the 2-point model

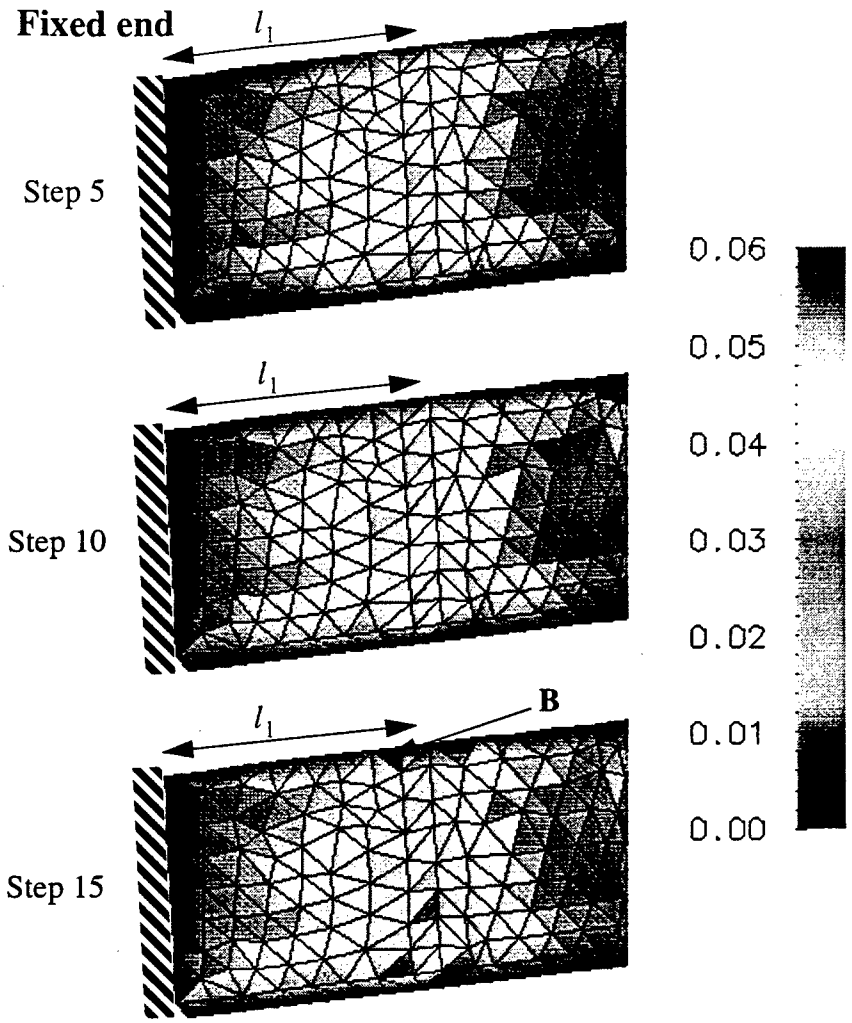
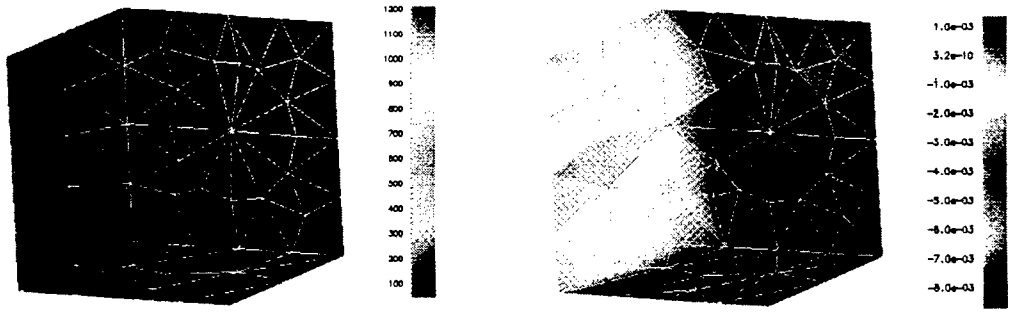


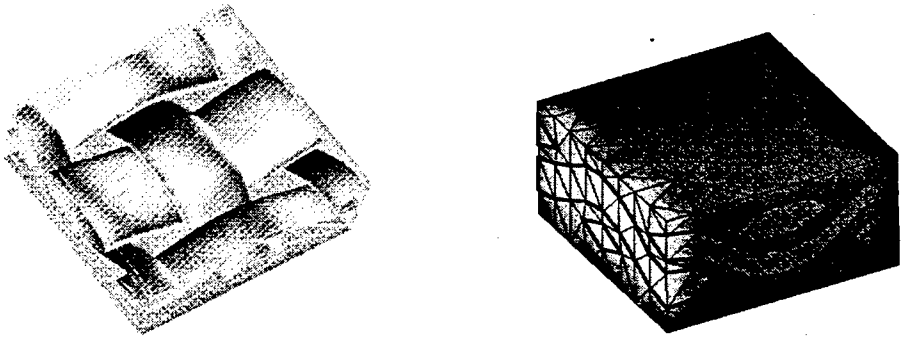
Figure 12: Distribution of the normalized local error with the *2/n*-point model



Effective stress

Normalized error of effective stress

Figure 13: Effective stress and normalized error at point B with the *2/n*-point model



(a) Geometric model (b) Finite element mesh

Figure 14: Geometric model and FE mesh of the plain weave unit cell

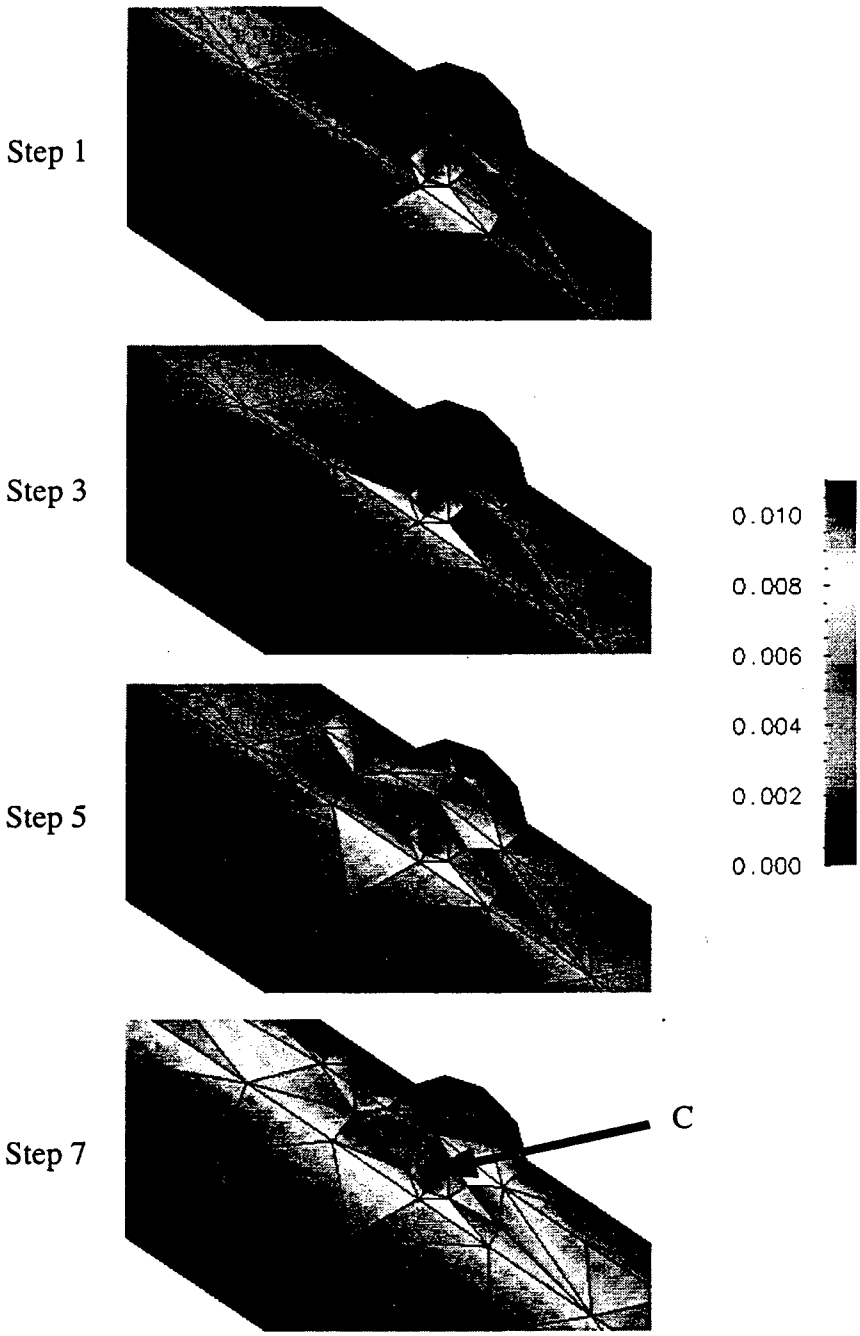
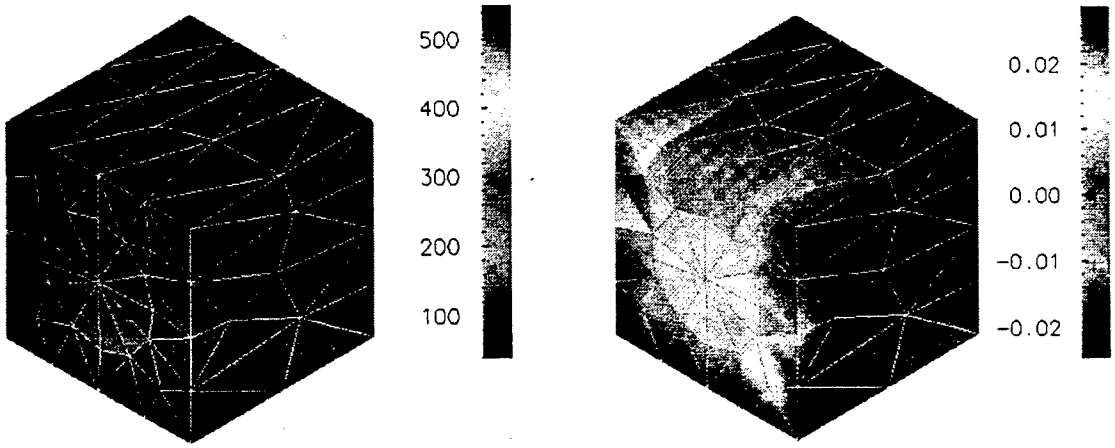
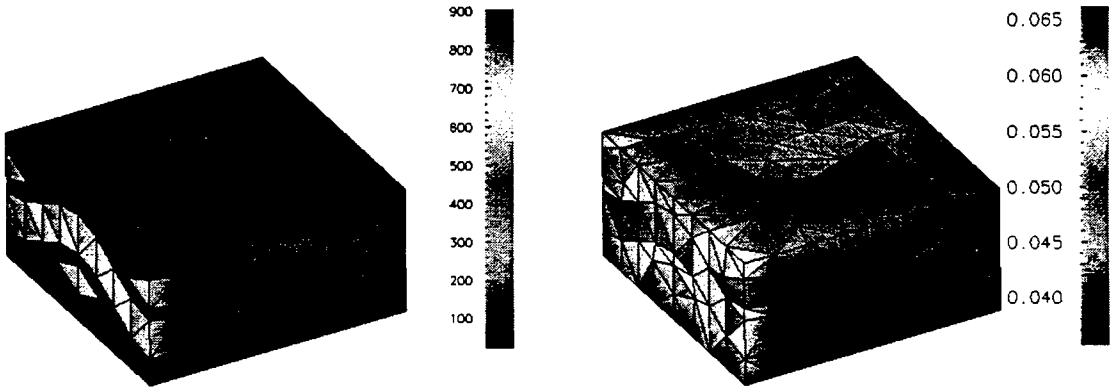


Figure 15: Distribution of the normalized local error in the nozzle flap with plain weave unit cell



Effective stress Normalized error of effective stress

Figure 16: Effective stress and normalized error for fibrous unit cell



Effective stress Normalized error of effective stress

Figure 17: Effective stress and normalized error for plain weave unit cell

ELSEVIER

Finite Elements in Analysis and Design 19 (1995) 325–348

FINITE ELEMENTS IN ANALYSIS AND DESIGN

Analysis model visualization and graphical analysis attribute specification system

Robert M. O'Bara, Mark W. Beall, Mark S. Shephard*

Scientific Computation Research Center, Rensselaer Polytechnic Institute, Troy, NY 12180, USA

Abstract

A visual environment for defining and manipulating engineering analysis information has been developed. This environment: (i) allows queries and modifications of the topology and geometry that defines a geometric model obtained from various geometric modeling systems, (ii) abstracts the modeler's functionality needed to associate analysis information, (iii) provides a hierarchical attribute association model, and (iv) gives a graphical user interface to both the geometric modeler abstraction and attribute management system. Finally graphical issues relating to performance, portability and flexibility of different workstation environments are discussed.

1. Introduction

Today there exist many commercial modelers that are used to define the geometric domains of engineered products. These packages can be classified into the following two groups:

1. A set of library routines which allow a programmer to construct a model and make inquires. Examples of such libraries are SHAPES [1], Parasolid [2], and ACIS [3].
2. A modeling environment that provides an interactive graphical interface for model construction and an underlying set of geometric modeling routines. Examples of such environments are Unigraphics [4] and CATIA [5]

The programming, user interfaces, and functionality of these modelers can vary greatly from system to system. This variation in the interfaces makes it difficult for both users and programmers to be able to switch between different modeling systems as needed. There has been work done to construct PDES/STEP [6], which is a standard common data description that is modeler

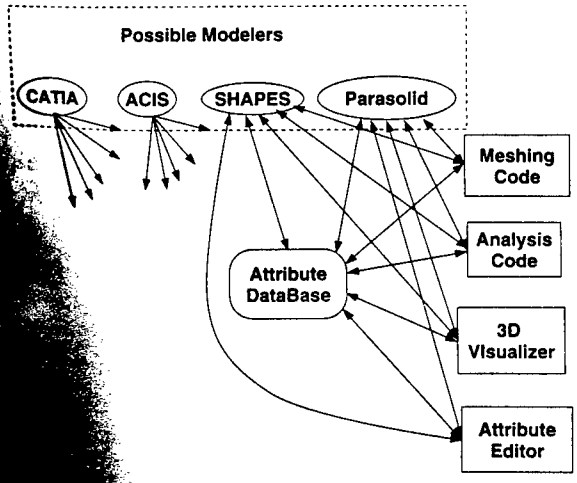
* Corresponding author.

Elsevier Science B.V.
SSDI 0168-874X(94)00068-9

independent. However, access to the geometric data is not sufficient for more advanced analysis frameworks which need to modify the geometry of the model for analysis, append analysis attribute information, and generate numerical analysis discretizations. An abstraction of a geometric model allows the interrogation, analysis specification, and modification of the model and would provide an analyst or programmer a tool which is independent of any particular modeler, thus making the transition from one modeler to the other relatively simple. A modeler independent graphical user interface is also desirable to allow users to perform the operations required for model modification and attribute specification. Without such an abstraction the interface between modelers and analysis packages that use them can end up looking like Fig. 1, where each package has its own interface and much work must be done to port the system to a different modeler. The abstraction, presented in this paper, simplifies the interface to the model and the analysis atrributes as shown in Fig. 2.

The definition of an engineering analysis problem consists of the geometric domain and the "analysis attributes", consisting of loads, boundary conditions, material properties, and initial conditions. The analysis attributes are best related to the model by associating them with the topological entities in the model [7]. This can be done outside of the modeling package with the information being stored in a database system [8, 9]. However, in some cases, proper specification of the analysis attributes may require additions and/or modifications of the geometric model. Since many of the models are three dimensional, these modifications will also need to be viewed in 3D along with the visualization of the attribute information itself. In addition, the attributes typically have relations among themselves which need to be viewed and maintained.

This paper describes a modeler independent interface being implemented to address these issues. In designing the interface to the modeler, an object-oriented approach is used that allows the tight integration of both data, that represents the topological entities, and functionality, such as inquiries and modification operations. The resulting abstraction is then mapped to specific modelers.



binatorics problem resulting from using odelers and separate attribute databases. Each its own interface to each modeler.

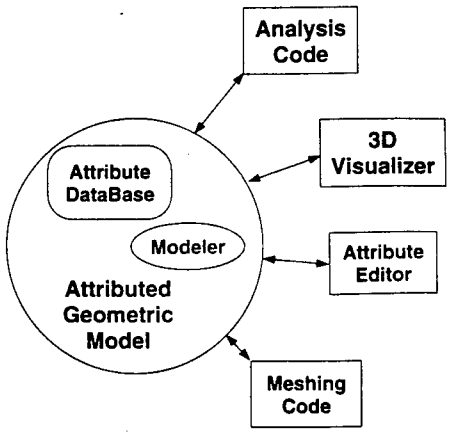


Fig. 2. Unified object-oriented approach that provides a common interface to both geometric and anlaysis information and eliminates the combinatorics problem.

The abstraction is also used in associating analysis attributes as well as designing graphical interfaces.

By using an object-oriented approach, a unified system that represents the various levels of geometric models as well as the attribute information has been developed. This abstraction, called the Attributed Geometric Model, is used by the analysis process, as well as by visual interfaces (see Fig. 2).

A unified object oriented approach provides a common interface to both geometric and analysis information and eliminates the combinatorics problem. Two user interfaces that work with the Attributed Geometric Model are discussed. The first is the Model Graphical Interface which is a modeler-independent user interface that allows interaction with a geometric model. The interface provides basic 3D displaying controls such as lighting, color selection, and filtering out unwanted geometry.

The second is the Attribute Graphical Interface which allows attribute specification/modification through an intuitive graphical interface in which the user enters attributes via a set of visual widgets. These widgets provide initial syntax checking and can be specialized to provide semantic checking. The current implementation uses 2D widgets for attribute specification. With the integration of the 3D model visualizer, attributes can be visualized relative to the geometric model. This includes visualizing the auxiliary geometry that may be associated with the attribute as well as the attribute itself.

The hierarchical relationship between attributes also needs to be visualized in order to allow a user to modify associations between collections of attributes. The current design is to view the representation as a graph which represents the relations between attributes. Modifications to the attribute relations can be made by directly modifying this graph-based representation.

The remainder of the paper describes the design of the complete system, which includes the abstractions of both the geometric model and analysis attributes, as well as their graphical user interfaces. Issues regarding hardware and software environments are also presented.

2. System design

The overall system is broken down into four parts: the geometric model abstraction, the attribute abstraction, the model graphical interface, and the attribute graphical interface. The first two parts are abstractions used to hide the implementation details of a particular modeler and attributing system, and to provide a consistent programming interface. The second two parts are user interfaces, that build on the abstractions, to allow users to interactively view and modify model and attribute information.

2.1. Object-oriented model abstraction

The object-oriented abstraction presents a unified view of an attributed geometric model which allows a programmer to modify geometry/topology, and attribute information. In addition the implementation of the abstraction for a given modeler may also increase the functionality of the modeler. An example of this is enhancing a 2-manifold modeler to be able to represent non-manifold models.

In order to abstract the Attributed Geometric Model, both the geometric model, which is maintained by the modelling environment, and the attribute database, which may be integrated with the modeler or implemented by a set of external routines, must be abstracted as well as their association with each other. The abstraction used for the modeler must be very general to be able to encompass the functionality of any modeler that it is implemented for. For this reason an abstraction based on the Radial-Edge Data Structure [10, 11] is used. This representation has been shown to be complete and sufficient for the representation of general non-manifold models.

For a complete description of the Radial-Edge Data Structure see references [10, 11]. In brief terms it is best described as a topological hierarchy consisting of regions (three-dimensional entities that are bounded by shells), shells (sets of faces that define a closed surface), faces (two dimensional entities that are bounded by loops, loops (sets of edges that form closed curves), edges (one dimensional entities that are bounded by vertices) and vertices (zero dimensional entities). For the remainder of this paper the term "topent" will be used to refer to any one of these topological entities.

The actual abstraction is done in terms of the topents that make up the model. There are objects that represent the regions, shells, faces, loops, edges and vertices. There is also an object that represents the model which acts as a container for the topent objects. The objects for the topents and the model are the entire public interface for the model abstraction and completely hide the modeler for which the interface has been implemented, as shown in Fig. 3.

The interface for the model and the topents is given below. These operators, especially the geometric query operators, reflect a bias to the operators needed for automatic mesh generation, as this is one of the first areas that the modeler abstraction is being used. The list of operators is expanded as needed to fit other application areas.

1. *Model operators*
   a. Query
      - Get_top_level( ) – returns a list of topents that represents the top level topology (topents that are not connected to a higher dimension topent).

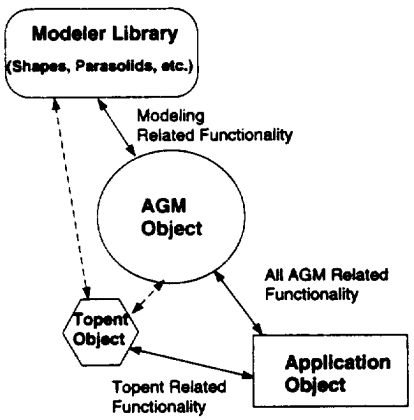


Fig. 3. Approach to the Attributed Geometric Model/modeler relationship problem.

- Get_all_{topent_type} – returns a list of all topents in the model of that type. For example, Get_all_vertices( ).
- Get(topent_name) – returns the topent(s) that have the name "topent_name".
- Get_number_of_{topent_type} – returns the number of topents in the model of a given type.

b. Modification
- Add( ) – add a topent to the model.
- Remove( ) – remove a topent from the model.

2. *Topent topological operators*

a. Query
- Sub( ) – returns a list of topents that are used in the definition of that particular topent. For example, shell1.sub( ) returns a list of faces that form shell1.
- Sup( ) – creates a list of all topents that the given topent is used in the definition of. For example, vertex1.sup( ) returns a list of edges that use vertex1.
- Get_type( ) – returns the type of the topent.
- Adjacent( ) – checks if one topent is adjacent to another, i.e. face1.adjacent(edge1) checks if edge1 is being used by face1.

b. Modification
- Attach( ) – attach one topent to another. For example shell1.attach(face1) adds face1 to the list of faces that defines shell1.
- Detach( ) – detach one topent from another.

3. *Topent geometric operators*

a. Query
- Point evaluation function – Since all topents are associated with parameterized geometry, there must be some way of calculating point evaluations. For example, edge1(t0) would return a point that corresponds to edge1's parametric function evaluated at t0.
- Closest_point( ) – Given a point in space, find the closest point on the given topent.
- Normal( ) – Returns the normal space of a topent at a given point.
- Tangent( ) – Returns the tangent space of a topent at a given point.
- Tolerance( ) – Returns the modeler tolerance associated with a particular topent.
- Range( ) – Returns the range of the topents parametric space.
- Find_intersection( ) – Finds the points of intersections on a topent of the topent and a geometric construct such as a line or plane. Only finds the location of the intersections, does not modify the model.
- Geomerty( ) – returns a geometric representation of the topent suitable for visualization purposes

b. Modification – This is only a partial list.
- Create( ) – create topents.
- Delete( ) – delete topent.
- Intersect( ) – return the intersection of two topents.
- Union( ) – return the union of two topents.
- Split( ) – split topent with another topent (intersect the two topents and separate the target topent at the intersection).

- Imprint( ) – imprint topent on another topent (project one topent onto another of eq higher order and split at the boundary of the projection).
- Merge ( ) – merge two topents into a single topent.

2.1.1. Implementation

The amount of work that needs to be done to implement the interface for any given m depends greatly on the capabilities of the modeler and on whether is it necessary to expand capabilities. For a modeler that is capable of representing nonmanifold models, the job is more straightforward than for one that is not capable of such a representation assuming one goals is to be able to represent nonmanifold models using that modeler. Our initial implemen uses Shapes from XOX Corp. [1] as the modeler since it matches up well to the abstraction th been selected for the modeler. In this case it is often just a matter of matching up appli programming interface calls in Shapes to the corresponding Attributed Geometric Model rou

The next modeler that has been interfaced to the Attributed Geometric Model is Parasolid Shape Data [2]. The current version of Parasolid is not capable of representing nonma models. However, Parasolid has been used as a nonmanifold modeler by utilizing an interfa top of Parasolid that keeps a Radial Edge representation of the topology of the model t independent of the representation stored by Parasolid itself.

2.2. Analysis attribute model abstraction

An analysis attribute is any information in addition to the geometric model that is neec specify a particular problem for analysis [8]. Many attributes, such as loads and ma properties, are tensorial in nature. Other attributes may be best described using a character s Every model entity may have one or more attributes associated with it. Using this associat the attributes with the geometric model and information which gives the classification of the element mesh with respect to the geometric model (what entity of the model a mesh en associated with), it is possible to determine which attributes apply to what entities in the element mesh. This methodology has been found to be very powerful when dealing wi adaptive finite element environment.

In addition to the association of the attributes to model entities, attribute information i grouped into a "part of" hierarchy consisting of the following classifications:

1. Case – a collection of one or more Groups, Sets or Attributes.
2. Group – a collection of one or more Sets or Attributes.
3. Set – a collection of Attributes of the same type.
4. Attribute.

Attribute groupings form acyclic directed graphs with cases at the root and individual attri at the leaves of the graph. In addition, the arcs in the graph may contain a multiplier that is ap to all descendent nodes connected by that arc (Fig. 4).

The information stored in an attribute consists of a tensor, where each component may arbitrary function, a list of associated topents, and a unique identifier. The tensor may also symmetry properties that reduce the number of independent components.

The proper evaluation of an attribute may require access to the definition of the geometry topent that it is associated with. An example of this would be a load that is defined to be norn

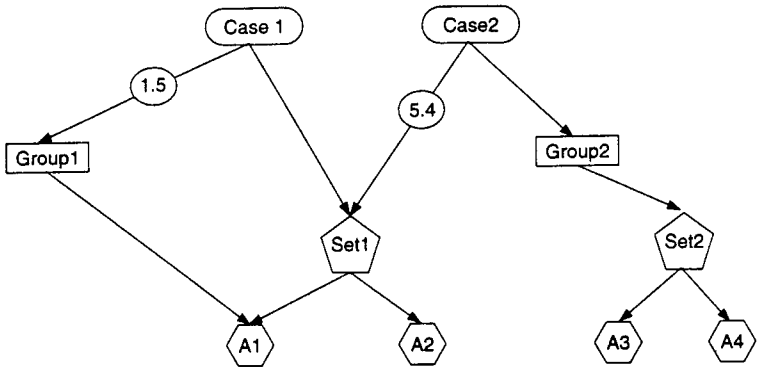


Fig. 4. Sample Attribute directed acyclic graph.

the surfaces on which it is applied. To evaluate the vector that represents this load requires finding the normal to the surface at each point it is to be evaluated at.

In some cases it may be necessary to modify the topology of the geometric model to properly reflect the application of an attribute. An example of this situation is when an essential boundary condition is applied over a portion of a topent. In this case, to properly analyze the situation it is necessary that the boundaries of the elements that discretize the topent properly reflect the boundary of the essential boundary condition. The only way to ensure this is to split the topent along the boundary where the attribute is applied.

Both of the cases above require access to the modelers functionality to properly deal with analysis attributes. It is easy to see how a generic interface to the modelers functionality reduces the effort of implementing such a functionality with multiple modelers.

The abstraction of the attribute database is relatively straightforward. Attribute entities (or atents), such as cases, groups, sets, and attributes, have interface calls which include:

1. Add(atent, multiplier) – adds an atent and zero or more multipliers to a grouping. For example case1.add(attribute1, mult1).
2. Remove(atent) – removes an atent from a grouping.
3. Get_children( ) – get the children atents along with their multipliers.
4. Get_parents( ) – get the parent atents along with their multipliers.
5. Add(topent) – adds a topent to an attribute.
6. Remove(topent) – removes a topent from an attribute.
7. Evaluate( ) –returns the evaluated tensor which describes that attribute at a particular location.

2.3. *Model Graphical Interface*

Some modelers are only accessible via a routine library and do not provide direct visual feedback to the user. Other environments provide graphical interfaces; however, they tend not to provide a uniform "look & feel" across different modelers. By providing a "modeler independent" 3D graphical user interface, users are able to view and interact with models without the need to learn multiple systems. In addition, when the system is "integrated" with the Attribute Graphical

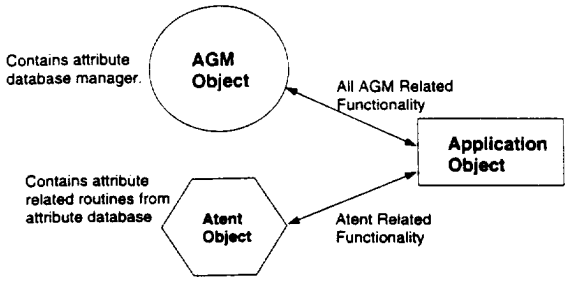


Fig. 5. Approach to the Attributed Geometric Model/attribute relationship problem.

Interface, discussed in the next section, users are able to select topological entities in 3D and inspect the associated attributes as well as select attributes and examine the associated topological elements.

The Model Graphical Interface provides a means of spatially viewing the geometric representation of the model. Based on the degree of 3D graphics acceleration available on the workstation, the types of renderings produced by the Model Graphical Interface include the following:

1. Wireframe.
2. Gouraud shaded surfaces [12].
3. Texture-mapped surfaces [13].

Texture mapping is a rendering technique that visualizes additional information associated with surface geometry and is useful when visualizing attribute information. For example, a pressure distribution can be used to texture a surface.

In addition to producing smooth shaded, hidden surface/hidden line images, the Model Graphical Interface also provides a more realistic visualization of the model in terms of depth perception by providing stereo viewing. Stereoscopic viewing involves rendering two different images which correspond to the different views seen by the right and left eye of the viewer [14]. These images are presented to the viewer using a device that allows each eye to see the image created for it. The device currently being used is a liquid shutter system that alternately "black-out" one of the eyes, and is sychronized with the display's refresh rate. The speed at which this is done is fast enough to produce images with no perceived flicker. The two images are then fused by the viewer's cognitive system into a spatially perceived 3D scene. When used in conjunction with a head tracking system, the viewer has the illusion of a solid 3D object suspended in space.

The Model Graphical Interface can render surfaces, curves, and points. The mechanism used to extract a topent's geometry to be visualized is via the Geometry( ) member function. Traditionally in the case of curve and surface geometry, the modeler would generate a discretized first order approximation (polylines and polygons). Current graphics libraries often contain higher order primitives such as non-uniform rational B-Spline (NURBS) curves and surfaces [15], as well as quadrilateral and triangular meshes [16–19]. The Model Graphical Interface has been designed to make use of these higher-order primitives by passing them directly to the graphics engine when appropriate. These primitives allow the application to exactly specify (or at least better approximate) the geometry. In addition, the use of these higher-level primitives can dramatically improve the time required to visualize the geometry. For example, to transform a bi-cubic surface requires the transformation of only 16 control points instead of 100 triangles typically used to approximate it

for display by polygons. In addition, some of these primitives are accelerated in hardware. For example, almost all 3D accelerators are very efficient at processing triangle strips, and some of the latest accelerators such as SUN Microsystems' ZX can process NURBS curves and surfaces in hardware.

In terms of the user interface, the Model Graphical Interface provides the following:

1. The ability to interactively change a viewer's position and orientation in space as well as allowing multiple views. The mechanisms of specifying the view include:
   a. A virtual trackball to specify the orientation of the viewer [21].
   b. Use of a 6D tracking system that can determine the position and orientation of the user's head [22].
   c. Selecting specific topents and tell the system to "look at them" [23].
2. Control over several light sources to provide better spatial perception as well as obtaining a better feel for the shape of the geometry.
3. The ability to specify color/optical (such as shininess) attributes to different topents, including back-facing attributes.
4. The ability to control transparency of topents. This could be useful when dealing with models that have internal structure such as regions.
5. The ability to hide different topents in order to view internal geometric structure.
6. In addition to the original model geometry, the Model Graphical Interface is able to display the following representations:
   a. Augmented geometry that results from the application of different cases of analysis attributes.
   b. Simplified or idealized geometry.
7. Control topent selection based on the following criteria:
   a. Spatially.
   b. Name of the topent.
   c. Type of the topent.
   d. Association with another topent.
8. An interface to model modification functions such as solid modeling intersection and union operators.
9. A graph-based representation of the model's topology and allow selection/modification operations by interacting with the graph.
10. A textual representation of the model using 2D window-based widgets.

The Model Graphical Interface provides the user with backface functionality in order to better distinguish the orientation of faces and shells. In terms of a polygon, the backface refers to the side of the polygon in which the surface normal points away from the viewer. By allowing the backface to have different properties from the frontface (the side whose surface normal points towards the viewer), the user can determine relative orientation. It can also be used to determine inconsistencies in the specification of the geometry. In addition, the user can remove all pieces of geometry that are currently backfacing. This functionality is referred to as backface culling and in the case of viewing closed surface objects, this can increase system performance dramatically.

Backface culling is one way of reducing the load placed on the graphics subsystem and can be very important when dealing with lower-end systems. In order to further reduce graphics complexity the Model Graphical Interface provides alternative representations of the geometric model such

as a graph-based representation of the model's topology as well as a textual representation. In addition to being less graphics intensive, the textual form can be more intuitive in terms of modifying model information. For example, it may be much easier to type in a vertex's coordinates than it is to try to precisely pick it with the mouse.

Besides efficiency, another important issue is how topents can be selected by the user. The most intuitive method is spatially by either selecting a particular topent or by defining a region in space and thereby selecting all topents that lie within that region. Since topents are spatially connected, it may be very difficult to select a particular topent without accidently choosing its spatially neighbor. For example, how does a user select a vertex without choosing the edge or face that is connected to it. The solution used in the Model Graphical Interface is to provide filtering in the selection process. Topents can be filtered out based on their name, type, or association with another topent. For example, a user can specify that all topents associated with the named "Region1" are not selectable. In addition to spatial selection, topents can be selected based on their name. This mechanism has been extended so that users can specify text patterns which can include "wildcards" in order to select several topents at the same time. A user can also select topents based on topological associativity. For example, a user can select all vertices that are associated with a particular face. Finally, a user can select topents via their association with attribute information by using the Attribute Graphical Interface.

2.3.1. Examples of model visualization

The first commercial modeler that has been integrated into the Attributed Geometric Model Abstraction has been the SHAPES modeler from XOX Corporation [1]. Fig. 6 shows a surface

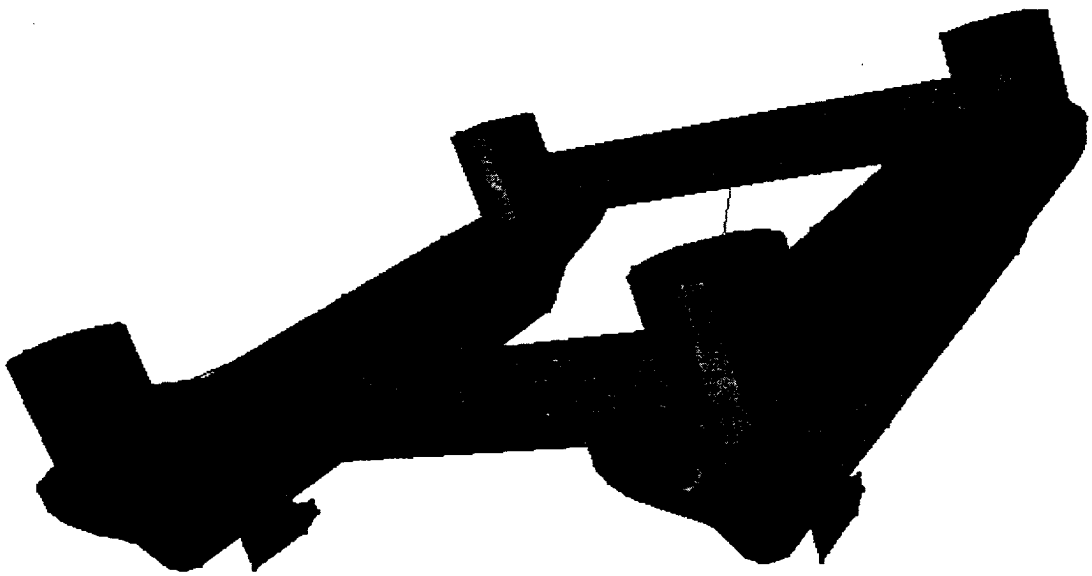


Fig. 6. Model Graphical Interface display of a model of an oil platform using the SHAPES geometric modeler. Note the nonmanifold edges that represent the guy wires and the non-manifold faces that represent the rudders. Model courtesy of XOX Corp.

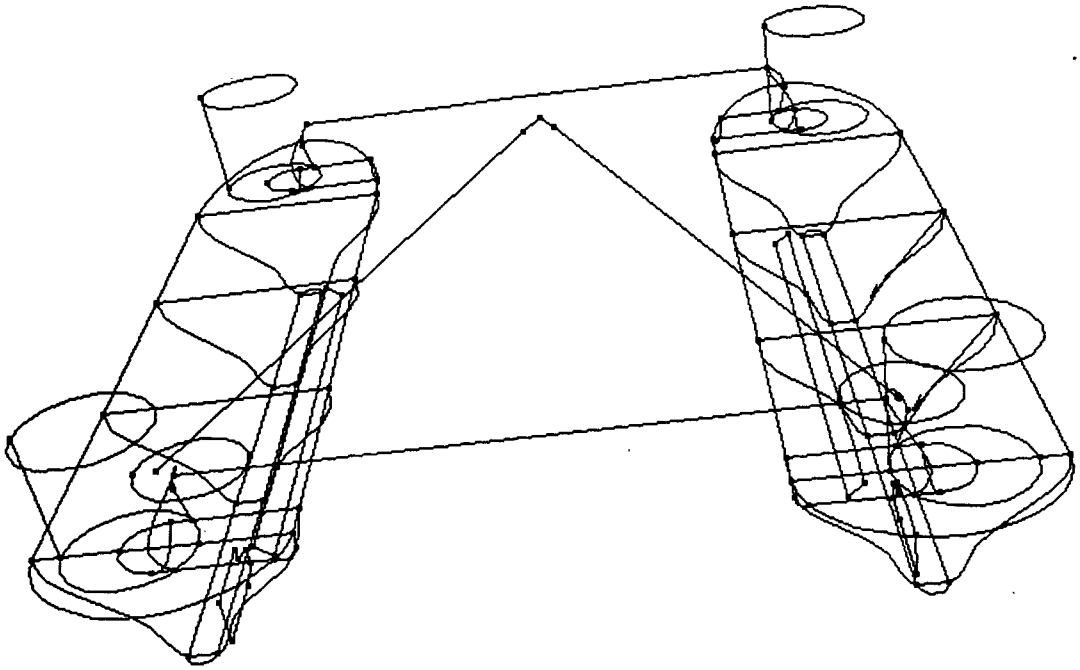


Fig. 7. Model Graphical Interface display of only the edges and vertices of the oil platform model.

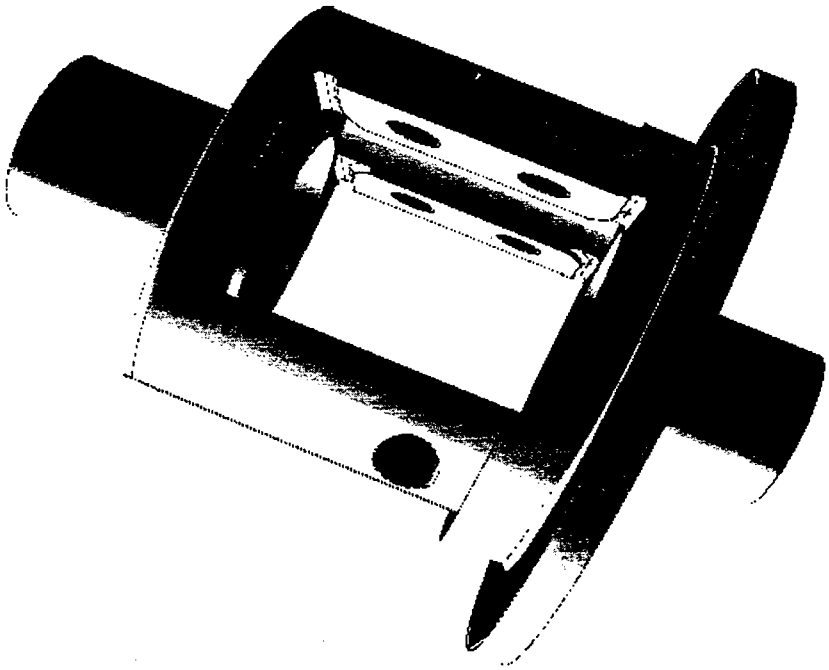


Fig. 8. Model Graphical Interface display of an electrical part using the Parasolid geometric modeler. Model supplied by PDA.

rendering of a SHAPES model of an oil platform that was being viewed via the Model Graphical Interface. Fig. 7 was the result of hiding all of the faces of the model. This figure shows all of the edge contours of the model as well as the model vertices. Fig. 8 shows a surface rendering of a Parasolid model of an electrical part from PDA.

To show the flexibility of both the model abstraction and the graphical interface, a finite element modeler, which was developed by the Scientific Computation Research Center at RPI, was also abstracted and visualized by the interface. Figs. 9 and 10 show two different views of a mechanical part. The first figure shows all of the faces and vertices in the model, while the second figure shows the edges of the model. Fig. 11 shows a zoomed in view of the part's faces and edges.

One of the important features of the interface is the ease with which it can be customized. In the case of the finite element modeler, functionality was added to view the octree representation in addition to the model itself, as shown in Fig. 12. As in the case of viewing topents, the display of the octree can be controlled interactively. In Fig. 13 only the octree structure is being viewed . As previously mentioned, the ability to control the display of the model is an important feature of the interface, as shown in Fig. 14. This figure shows the same view as Fig. 11, but also displays the octree model.

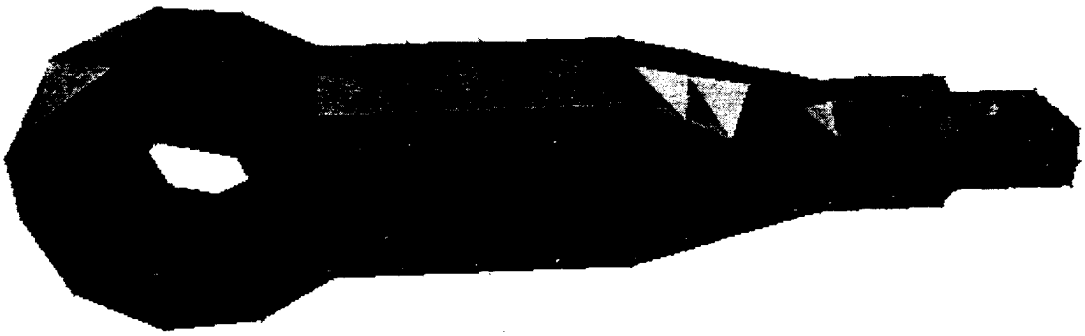


Fig. 9. Finite element mesh showing faces.

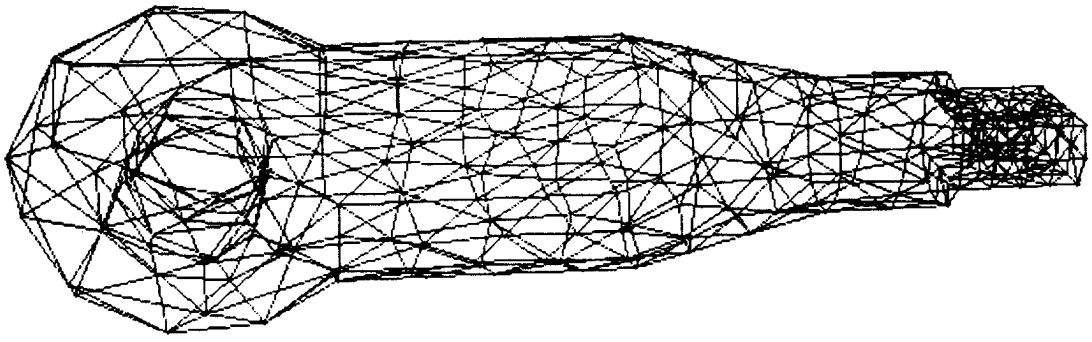


Fig. 10. Finite element mesh showing edges.

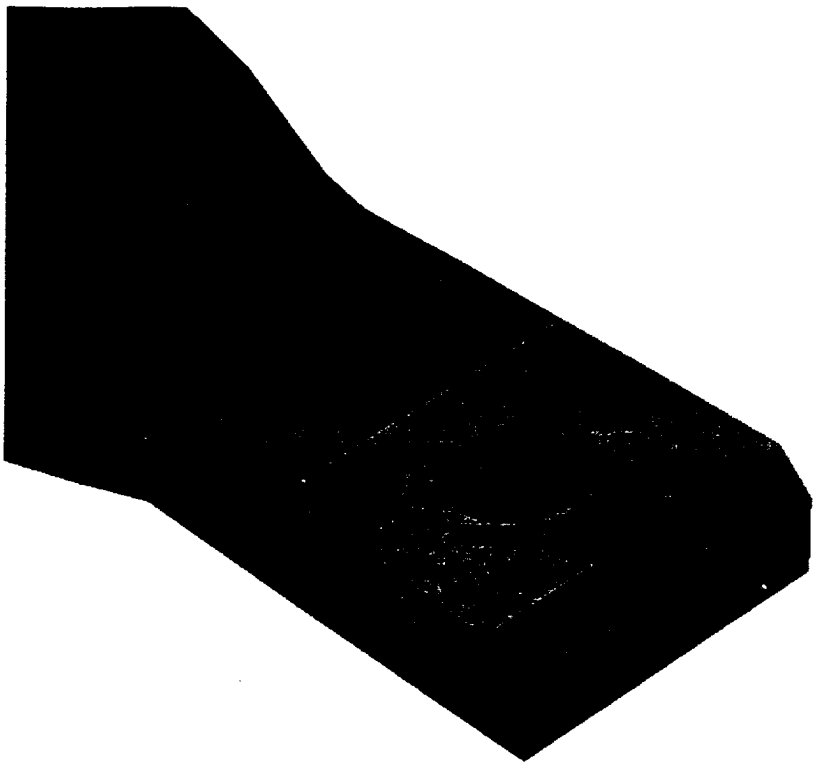


Fig. 11. A magnified view of the part.

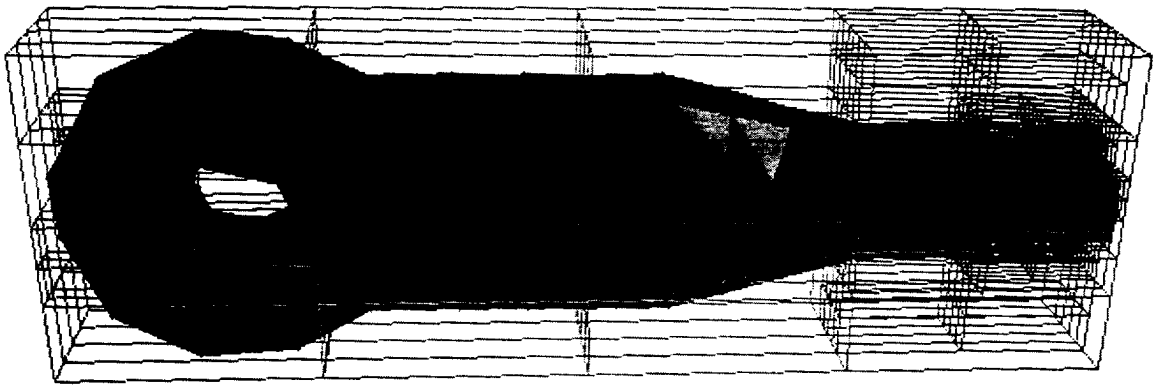


Fig. 12. Finite element mesh showing faces, edges, and its associated octree.

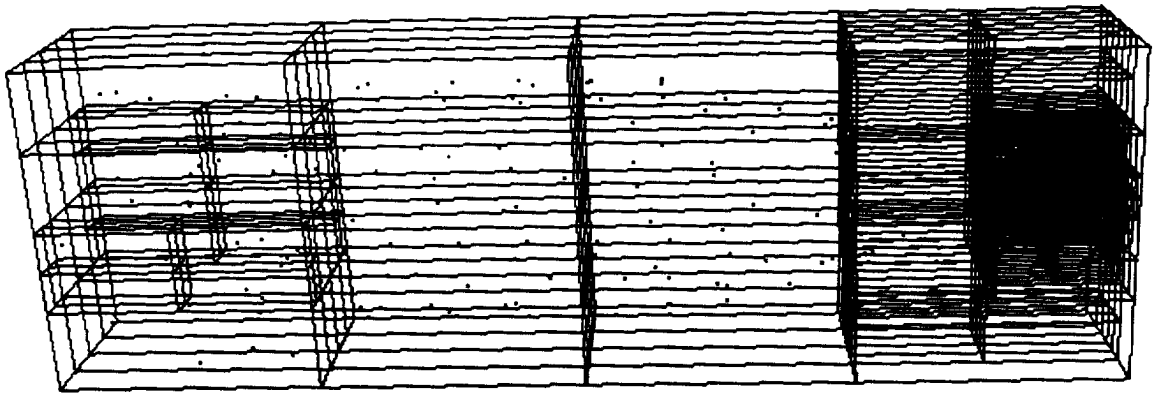


Fig. 13. Display of octree used in creation of previous finite element meshes.

Another important feature that was added in the finite element version of the interface was the ability to the execute the interface from a program in order to use it as a debugging tool for automatic mesh generation code. Fig. 15 shows the control panel to the debugger version. The continue button, located in the upper right of the panel, allows the developer to transfer control back to the program while still viewing the model.

2.4. *Analysis Attribute Graphical Interface*

The Attribute Graphical Interface serves as a graphical interface used to define, view, and modify analysis attributes and their association with topents in the geometric model. The Attribute Graphical Interface also addresses the clustering of attributes into the hierarchical structure. Unlike the Model Graphical Interface, the Attribute Graphical Interface involves more use of 2D visualization techniques such as icons and text since the information tends to be more mathematical or relation oriented. However, the attribute/topent relationship as well as physical ramifications of the attribute do have spatial components that need to be visualized in 3D. In those cases, there is less distinction between the Model Graphical Interface and Attribute Graphical Interface.

As with the Model Graphical Interface, one of the most important issues is controlling the selection process. In the case of attributes, one approach to doing this is via a list, see Fig. 16. Since the number of choices may be very large, filtering mechanisms had been added to help structure the information. For example, the choice list can be filtered based on the type of attribute entity (atent) or the specific type of an attribute. While building attribute hierarchies, atents will not always be "properly associated", which refers to atents which do not have a case as an ancestor and/or an attribute that is associated with a topent as a descendant. The Attribute Graphical Interface can provide a list of such entities as well as what association is missing. An atent can also be selected by entering its name or a pattern which then selects all atents that match. Another way in which atents can be selected is via a graph representation of the hierarchy with the nodes representing the atent and arcs showing the associativity (see Fig. 17). This form is very useful in changing atent

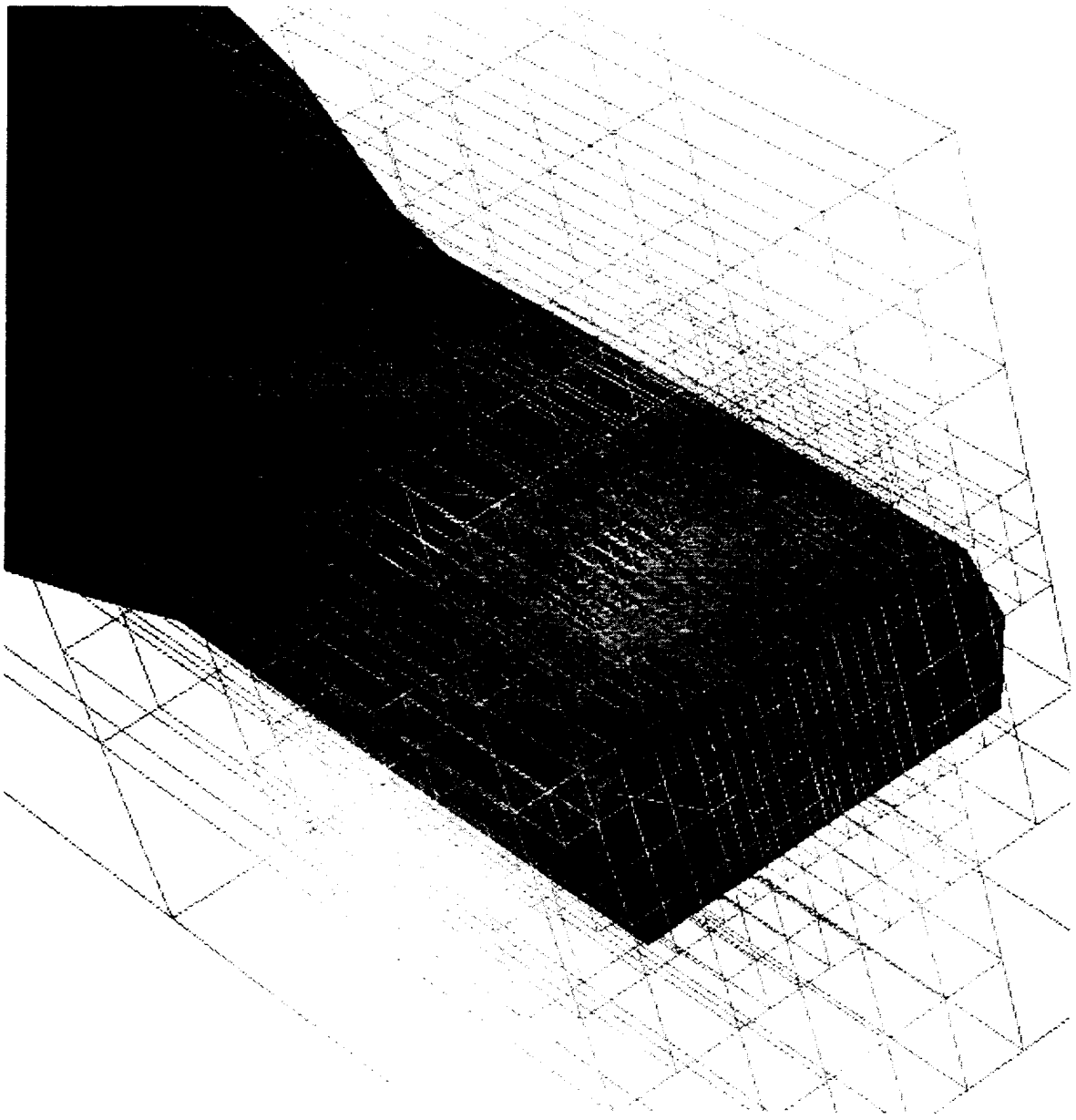


Fig. 14. A magnified view of the part and it's associated octree.

associations. An atent can also be selected via its relationship with another atent (see Fig. 18). Finally, an attribute can be selected by its association with a topent that has been selected via the Model Graphical Interface.

In addition to modifying an atent's association via a graph representation, a user can change the hierarchy via a selection panel as shown in Figs. 19 and 20. In this method, a user is presented with

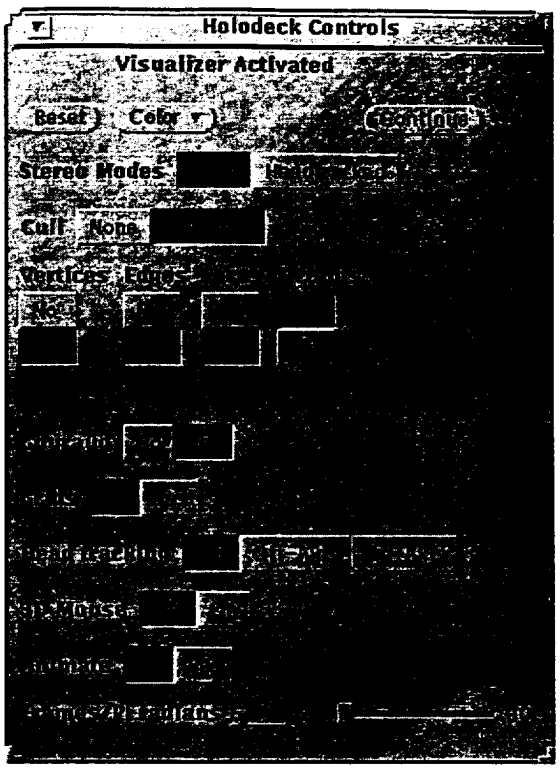


Fig. 15. Mesh Debugger Version of the Model Graphical Interface's main control panel (for high performance 3D platforms).

a list of possible children for a specific atent, as well as its current children list. The user can then modify the multiplier values between the associations.

Figs. 21 and 22 show similar panels for the creation and modification of attributes. Since most of the analysis information is tensorial in nature, the user is presented with a spreadsheet like interface for entering the distribution function for each element in the tensor. This method can be very tedious when dealing with tensors whose order is greater than 2. For example, a compliance tensor is 4th order which results in 81 entries (assuming that the space is 3 dimensional). Fortunately many tensors can be completely defined by a reduced set of parameters due to symmetry. For example, liner isotropic material, which is a 4th order tensor, can be completely defined by specifying the Young's Modulus and Poisson's Ratio. The Attribute Graphical Interface allows designers to add these specialized types of attributes that can result in simplified attribute specification as well as providing semantic checking such as specifying bounds on an entry's value.

In addition to textual and 2D iconic representations of attribute information, the Attribute Graphical Interface, in conjunction with the Model Graphical Interface, can visualize the information in the same space as the geometric model. For example, 3D first order tensors, such as forces, can be visualized using 3D arrow glyphs, while scalar fields such as temperature can be texture mapped onto the surface of the model.

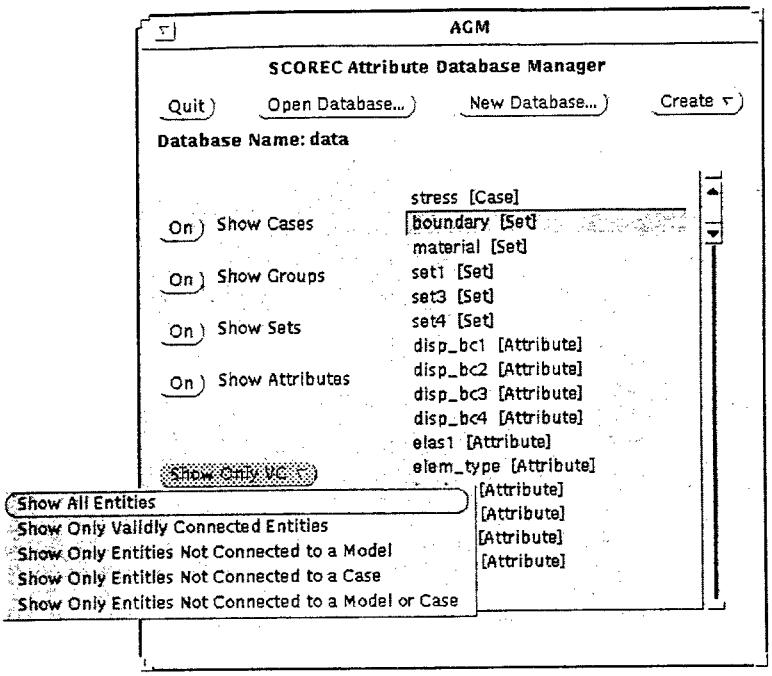


Fig. 16. Attribute Graphical Interface's main attribute manager panel. The buttons on the left side control filtering based on type as well as association.

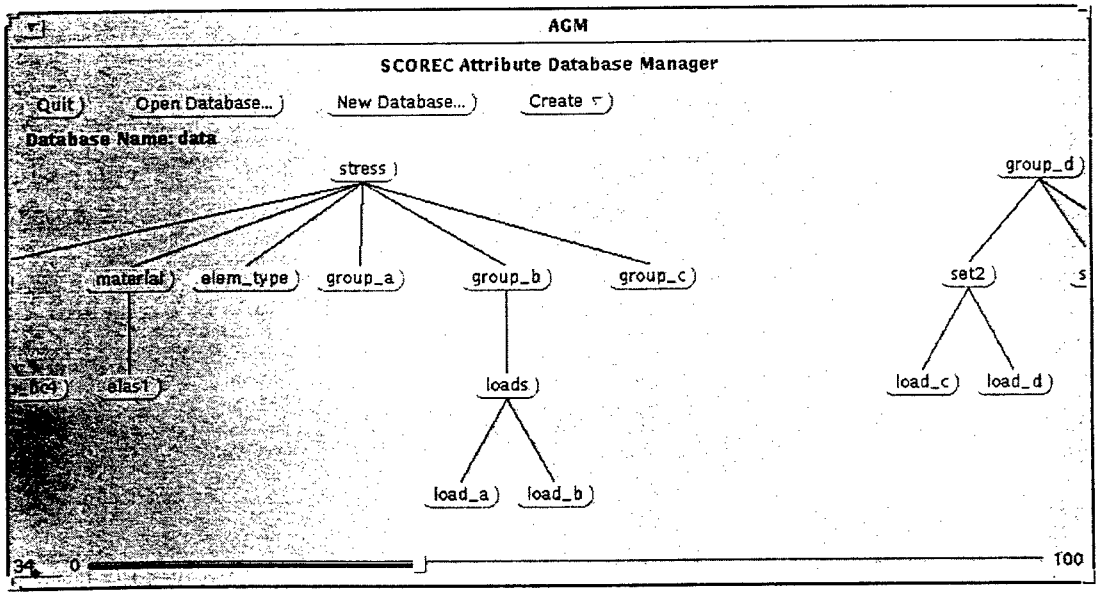


Fig. 17. A graphical representation of an attribute hierarchy showing all of the associations between attributes. A user can modify associations by changing the arcs between attributes.

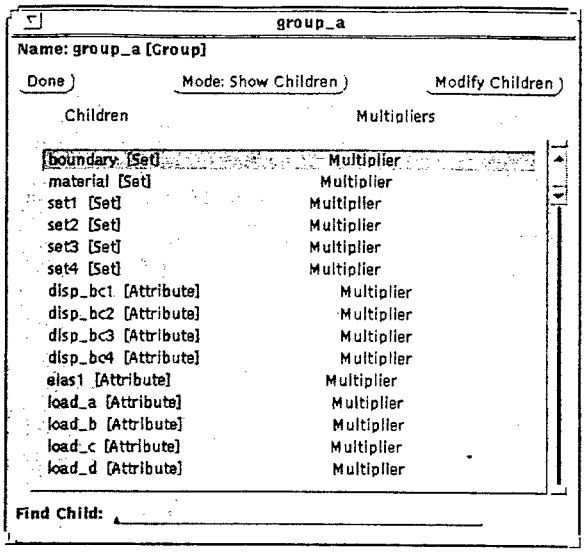


Fig. 18. Attribute Graphical Interface's attribute collector panel (in this example, the collector is a Attr Group).

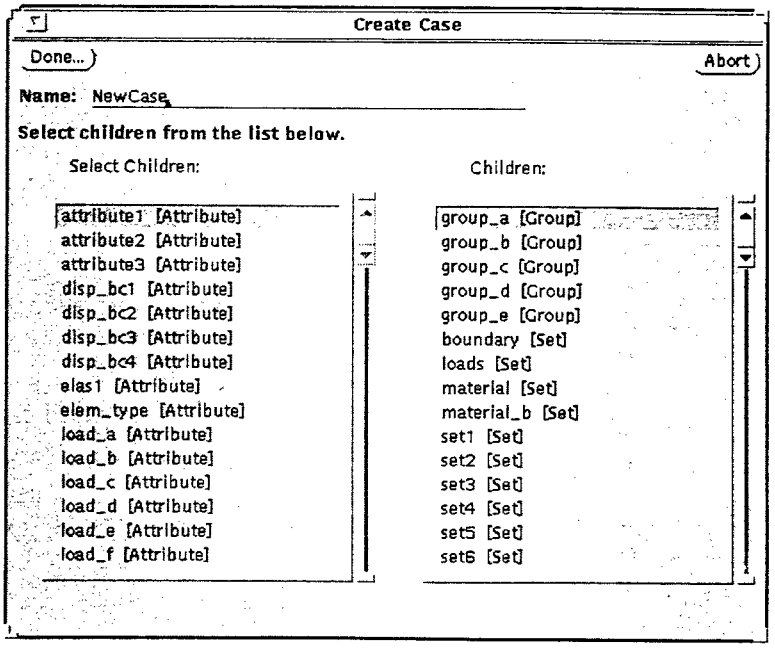


Fig. 19. Attribute Graphical interface's attribute collector panel for editing children.

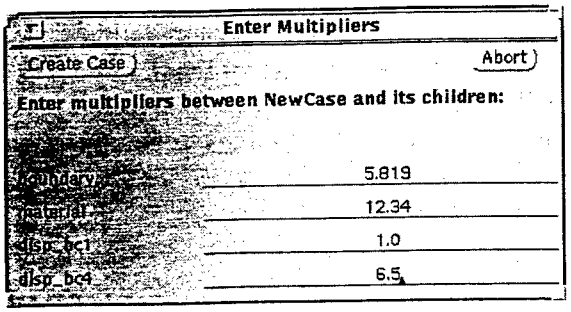


Fig. 20. Attribute Graphical Interface's multiplier editing panel.

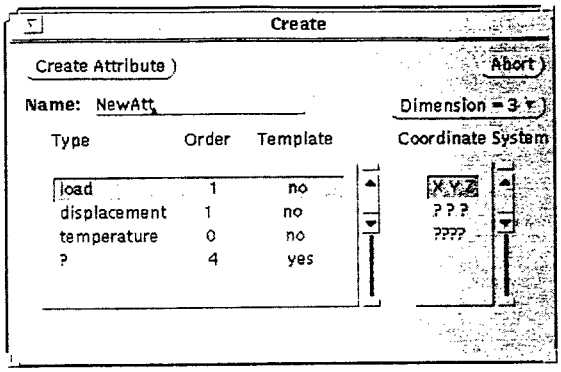


Fig. 21. Attribute Graphical Interface's new attribute panel.

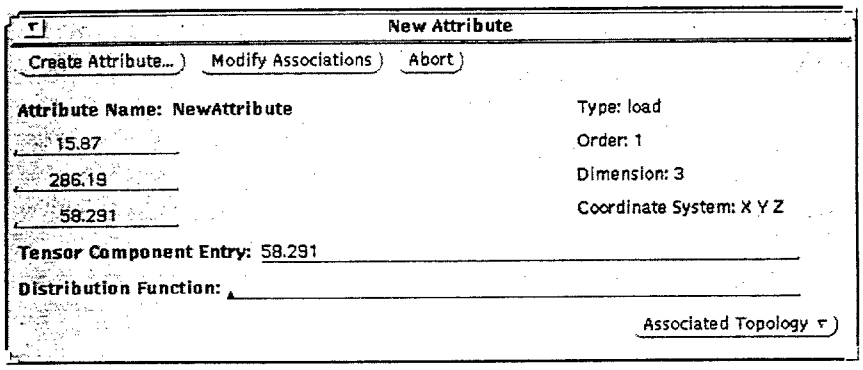


Fig. 22. Attribute Graphical Interface's attribute editing panel.

2.5. *Integrating the analysis process*

By having the modeler and attribute abstraction provided by the Attributed Geometric Model available it is more straight forward to provide adaptive procedures access to the geometry based problem definition information required for properly updating the discrete models as they are adaptively enriched. Specifying attributes on a model in the manner described here, as opposed to specifying them on a finite element mesh, allows everything after the specification of the problem to be solved, to obtaining the solution to a prespecified accuracy to be automated. Steps such as creation of an analysis model, where the geometry may be an idealization of the actual geometry, generation of a finite element mesh, running an analysis, and refinement of both the mesh and the model idealizations based on error estimates, can all be integrated together and be done automatically.

3. Hardware/software environments

The previous sections have discussed the design and functionality of the abstraction of the Attributed Geometric Model, as well as the graphical interfaces that allow users to visually interact with it. Since the graphical interfaces are designed to be interactive, the graphics capabilities of the workstation are extremely important and may force the deactivation of certain functionality. For example, not all workstations are capable of stereoscopic displays. This section discusses the types of hardware platforms that the graphical interfaces are designed to run on as well as trade-offs in terms of functionality. In addition, the types of graphics environments that were available for implementing the graphical interfaces are addressed.

3.1. Hardware environments

The Model Graphical Interface and Attribute Graphical Interface are designed to run on a variety of UNIX platforms independent of their 3D graphics capabilities, which include rendering speed, and special graphics functionalities such as transparency and texture mapping. Although 3D graphics acceleration is preferable it is not a requirement. As a result of using a "2D" system, some of the more advance visual capabilities (such as interactively viewing smooth shaded geometry) may not be available. The reason for supporting the 2D platforms is due to the number of these types of workstations that exist in the engineering environment. As the cost of 3D accelerators continues to drop and PEX-stations (graphics terminals that have hardware to support PEX , a 3D extension to the X windowing system) become more available, it is expected that within the next couple of years, the typical workstation will have basic 3D support such as built in hidden line/hidden surface support in hardware. The major issue that results from supporting a range of graphics workstations is maintaining a level of system response time that will not frustrate the user. In order to do this, the interfaces need to determine the type of 3D acceleration that is available and customize themselves in the following manner:

1. Remove functionality that is not supported on that specific platform. For example, stereo viewing requires a head tracking system, stereo glasses, etc. If they do not exist on the workstation, then all of the controls pertaining to it are removed or deactivated.
2. Changing the default behavior. For example, on systems that do not have any 3D accelerator, the geometry is displayed using a wireframe model without hidden line/hidden surfacing enabled. The behavior can also change based on the model complexity. For example, on a 3D system rendering at 30 000 triangles/s, the default behavior may be smooth shaded geometry for models that have <1000 planar faces (assuming an update rate of 30 frames/s) and wireframed geometry for more complicated models.

The breakdown of features on various platforms is as follows:

1. "2D" systems – no 3D accelerator (such as SPARC/GX).
   a. Ability to enter/view attribute information via Attribute Graphical Interface.
   b. Ability to view interactively wireframe representation of geometry and select topents spatially from the wireframe and text labels.
   c. Allow the user to view static smooth surface representation.
   d. Ability to "overlay" analysis information onto surface geometry.

2. Basic 3D systems – graphics accelerators which support hidden line/hidden surface and have performance <80 000 triangles/s (such as SPARC/GS). The interfaces on these system support all functionality supported in "2D" systems; however, the default is to view smooth shaded geometry. The main restrictions on these systems are:
   a. The lack of special features such as hardware supported transparency.
   b. The limit to the model complexity that can be viewed as smooth shaded geometry (<4000 faces).
3. High performance 3D systems – graphics accelerators which support advance functionality such as transparency and anti-aliasing [16, 13] with a performance ⩽ 600 000 triangles/s (such as SPARC/ZX and Indigo2 Extreme).
   a. All functionality supported in basic 3D systems.
   b. Ability to view smooth surface representations of complex geometry (⩽ 30 000 triangles).
   c. Advanced viewing operations such as making topents transparent in order to see internal detail.
4. Advanced 3D systems – graphics accelerators which support texture mapping and have performance > 600 000 triangles/s (such as Onyx Reality Engine2 [24]).
   a. All functionality supported in High Performance 3D Systems
   b. Ability to deal with models which are represented by more than 30 000 triangles.
   c. Ability to use more advanced visualization techniques for overlaying analysis information onto the geometry.

3.2. *Software environments*

The Model Graphical Interface and Attribute Graphical Interface were designed to be platform independent in terms of the brand of workstation that can be used with the interfaces. This is primarily a software environment issue concerning the graphics libraries that the interfaces use.

3.2.1. *2D software environments*

The Attribute Graphical Interface is implemented using X11 in order that it will run both distributively and on the most number of platforms; however, a decision had to be made regarding which library to use. The following is a list of libraries that are generally available:

1. XLIB [25] – A set of C routines that directly manage the X11 protocol.
2. MOTIF 1.2 Toolkit [26] – A C-based library that implements the MOTIF look & feel via a set of X widgets.
3. TCL/TK [27] – a language developed by the University of California that can be integrated into an application by source code modification.
4. Interviews [28] – a C++ toolkit developed by Stanford.
5. Fresco [29] – A C++ interface that is included with the current release of X11 (X11R6).
6. NextStep (or OpenStep) [16] – a C++ interface designed by Next Corporation.

In addition to the above, the MOTIF 2.0 Toolkit which will include a C++ interface will be available in the fourth quarter of 1994.

The major problem with using XLIB, MOTIF 1.2, or TCL is that these are C or C-like systems that are designed to work well with structure-based designs but not necessarily with designs using

object-oriented languages such as C++. Interviews is a relatively old interface that is being used in the design of Fresco and will be probably replaced by the new interface. Interviews also has its own look and feel in terms of user interaction. The problem with Fresco is that it currently lacks certain critical functionality such as menus. Next step is currently only available on a small number of platforms but will soon be available on several platforms including SUNs (aka OpenStep).

In the long term the software will support the MOTIF look & feel in order to be compliant to the de facto standard as well as using a true C++ library in order to facilitate code development. Therefore, the Attribute Graphical Interface will be eventually implemented in either MOTIF 2.0, Fresco, or possibly OpenStep; however, in order to have a working prototype, the initial Attribute Graphical Interface is implemented in an interface library that was developed at RPI called the Modular Interface Library Kit (MILK). MILK is a C++ interface toolkit built on top of XView, which currently supports the OPENLOOK look and feel, and currently runs on SUN, IBM, and SGI platforms.

3.2.2. 3D software environments

In terms of available 3D graphics libraries that are currently available, the list includes:

1. PHIGS [17] – ANSI/ISO Standard that includes a C interface.
2. PEXLIB[19] – a set of C routines that directly manage the PEX protocol (3D extensions to X).
3. GL[18] – a proprietary C library developed by SGI.
4. Inventor[31] – a proprietary C++ library developed by SGI.
5. XGL[32] – a proprietary C library developed by SUN.

The problem with using C-based routines for the 3D development are the same as those for the 2D. One of the major requirements for the library is that it be dynamically extensible and allow a designer to be able to add new primitives and new functionality. For example, the Model Graphical Interface requires graphical primitives that can be associated with a topent's geometry that is produced via the Geometry member function call. The only commercial C++ library that is currently available is Inventor which currently only runs on SGI.

The researchers at RPI have developed a C++ library called BAGEL which is written on top of GL and XGL and runs on SUN, SGI, and IBM platforms. The current prototype of the Model Graphical Interface is implemented using the BAGEL library. It should be possible to port the library's device driver to the PEXlib platform and thus be able to develop on any PEX-based machine such as the HP. In addition, the library should be ported to the new OPENGL library developed by SGI.

4. Closing remarks

A modeler-independent abstraction that encompasses the necessary functionality for querying and manipulating a geometric model has been developed. Using this abstraction, and an abstraction for the specification of analysis attributes, a system has been developed that allows programmers to access model and attribute information in a consistent and intuitive manner. The initial implementation of the system has been done with the commercial modeler Shapes from the XOX Corporation. In addition, graphical user interfaces have been implemented to allow visualization of

model and specification of analysis attribute information. The same system was used to develop an interactive visual tool to view finite element meshes for the purpose of debugging automatic mesh generators. The graphical interfaces were designed to be platform independent and to be usable on workstations with a large range of graphics performance.

Further work is being done to integrate other modelers into the system. This process is very straightforward due to the object-oriented abstraction selected for the model.

Acknowledgments

The authors gratefully acknowledge the support of ARPA/ONR under grant N00014-92-J-1779, "Mechanism-Based Design of Composite Materials", and the National Science Foundation under grant ASC-93-18184, "Understanding Human Joint Mechanics through Advanced Computational Model".

References

[1] XOX Corporation, Two Appletree Square, Suite 334, Minneapolis, Minnesota 55425, *SHAPES Reference Manual, Release* 2.0.5., July 20, 1993.

[2] Shape Data Limited, Parker's House, 46 Regent Stree, Cambridge CB2 1DB, England, *PARASOLID v4.0 Programming Reference Manual*, August 1991.

[3] Spatial Technology, Inc., 2425th St., Building A, Boulder, Colorado, *ACIS Interface Guide and ACIS API Guide*, December 1992.

[4] Electronic Data Systems Corp., Unigraphics Division,13736 Riverport Drive, Maryland Heights, MO 63043, *Unigraphics User Manual, Version 10.2*, December 1993.

[5] Dassault Systemes, IBM Corporation, 11601 Wilshire Boulevard, LA, CA, *CATIA Solids Geometry – Geometry Interface Reference Manual*; *CATIA Solids Geometry – Geometry Interface Reference Manual*; *CATIA Solids Geometry – Mathematical Subroutine Package Reference Manual*; *CATIA Base – Mathematical Subroutine Package Reference Manual*, 1988. Pub. Nums. SH50-0059-0; SH50-0058-0; SH50-0089-0.

[6] International Standards Organization, "Industrial automation systems and integration – Product data representation and exchange – Part 1: Overview and fundamental principles", Technical Report ISO/DIS 10303-1, U.S. Product Data Association, 1993.

[7] M.S. Shephard and P.M. Finnigan, "Toward automatic model generation", in: A.K. Noor and J.T. Oden (eds.), *State-of-the-Art Surveys on Computational Mechanics*, ASME, New York, pp. 335–366, 1989.

[8] M.S. Shephard, "The specification of physical attribute information for engineering analysis", *Eng. Comput* **4**, pp. 145–155, 1988.

[9] V. Wong, "Qualification and management of analysis attriubtes with application to multi-procedural analyses for multichip modules", Masters thesis, Scientific Computation Research Center, Report 23–1994, Rensselaer Polytechnic Institute, Troy, New York, June 1994.

[10] K.J. Weiler, "The radial-edge structure: A topological representation for non-manifold geometric boundary representations", in: M.J. Wozny, H.W. McLaughlin and J.L. Encarnacao (eds.), *Geometric Modelling for CAD Applications*, North Holland, Amsterdam, pp. 3–36, 1988.

[11] K.J. Weiler, "Topological structures for geometric modeling", Ph.D. Thesis, Rensselaer Design Research Center, Rensselaer Polytechnic Institute, Troy, NY, May 1986.

[12] H. Gouraud, "Continuous shading of curved surfaces", *IEEE Trans. Comput.* **6**, pp. 623–629, 1971.

[13] A. Watt and M. Watt, *Advanced Animation and Rendering Techniques, Theory and Practice*, Addison Wesley, Reading, MA, 1992.

[14] L.F. Hodges, "Tutorial: Time-multiplexed stereoscopic computer graphics", *IEEE Comput. Graphics Appl.* **12**(2), pp. 20–30, 1992.
[15] G. Farin, *Curves and Surfaces for Computer Aided Geometric Design, A Practical Guide*, Academic Press, New York, 3rd edn., 1993.
[16] J.D. Foley, A. Van Dam, S.K. Feiner and J.F. Hughes, *Computer Graphics – Principles and Practices*, The Systems Programming Series, Addison-Wesley, Reading, MA, 2nd edn., 1990.
[17] PHIGS + Committee, "PHIGS + Functional Description, Revision 3.0", *Comput. Graphics* **22**(3), pp. 125–218, 1988.
[18] Silicon Graphics Computer Systems, *Graphics Library Programming Guide.*
[19] T. Gaskins, *PEXlib Programming Manual*, O'Reilly and Associates Inc., 1992.
[20] M.F. Deering and S.R. Nelson, "Leo: A system for cost effective 3d shaded graphics", in: *Proceedings of SIGGRAPH 93,* Addison-Wesley, Reading, MA, p. 101–108, 1993.
[21] J. Hultquist, A virtual trackball, in: A.S. Glassner (ed.), *Computer Graphics Gems*, pp. 462–463, 1993.
[22] Logitech Inc., *2D/6D Mouse Technical Manual.*
[23] M. Gleicher and A. Witkin, "Through-the-lens camera control", in: *Proceedings. of SIGGRAPH 92,* Addison-Wesley, Reading, MA, p. 331–340, 1992.
[24] K. Akeley, "Reality engine graphics", in: *proceedings of SIGGRAPH 93,* Addison-Wesley, Reading, MA, p.109–142, 1993.
[25] A. Nye, *Xlib Programming Manual*, Vol. 1. O'Reilly & Associates, 2nd edn. 1990.
[26] D. Young, *X Window Systems Programming and Applications With Xt OSF/MOTIF Edition.* Prentice Hall, Englewood cliffs, NJ, 1990.
[27] J.K. Ousterhout, *Tcl and the Tk Toolkit*, Addison-Wesley, Reading, MA, 1994.
[28] *InterViews Reference Manual*, Leland Stanford Junior University, 1991.
[29] X Consortium Working Group Draft, *Fresco Sample Implementation Reference Manual*, 0.7 edition.
[30] Sun Microsystems, Inc., *OPEN LOOK – Graphical User Interface Application Style Guidelines*, Addison-Wesley, Reading, MA 1990.
[31] J. Wernecke, *The Inventor Mentor*, Addison-Wesley, Reading, MA, 1994.
[32] Sun Microsystems, Inc. XGL Graphics Library – Technical White Paper, 1990.

Pergamon

J. Mech. Phys. Solids, Vol. 45, No. 8, pp. 1281–1302, 1997
© 1997 Elsevier Science Ltd
Printed in Great Britain. All rights reserved
0022-5096/97 $17.00+0.00

PII: S0022-5096(97)00007-0

MICROMECHANICAL MODELS FOR GRADED COMPOSITE MATERIALS†

THOMAS REITER‡, GEORGE J. DVORAK

Center for Composite Materials and Structure, Rensselaer Polytechnic Institute, Troy, NY 12180-3590, U.S.A.

and

VIGGO TVERGAARD

Department of Solid Mechanics, Technical University of Denmark, DK 2800 Lyngby, Denmark

(*Received* 9 *May* 1996; *in revised form* 11 *December* 1996)

ABSTRACT

Elastic response of selected plane-array models of graded composite microstructures is examined under both uniform and linearly varying boundary tractions and displacements, by means of detailed finite element studies of large domains containing up to several thousand inclusions. Models consisting of piecewise homogeneous layers with equivalent elastic properties estimated by Mori–Tanaka and self-consistent methods are also analysed under similar boundary conditions. Comparisons of the overall and local fields predicted by the discrete and homogenized models are made using a C/SiC composite system with very different Young's moduli of the phases, and relatively steep composition gradients.

The conclusions reached from these comparisons suggest that in those parts of the graded microstructure which have a well-defined continuous matrix and discontinuous second phase, the overall properties and local fields are predicted by Mori–Tanaka estimates. On the other hand, the response of graded materials with a skeletal microstructure in a wide transition zone between clearly defined matrix phases is better approximated by the self-consistent estimates. Certain exceptions are noted for loading by overall transverse shear stress. The results suggest that the averaging methods originally developed for statistically homogeneous aggregates may be selectively applied, with a reasonable degree of confidence, to aggregates with composition gradients, subjected to both uniform and nonuniform overall loads. © 1997 Elsevier Science Ltd

Keywords: A. microstructure, A. voids and inclusions, B. layered material, B. particulate reinforced material.

1. INTRODUCTION

We are concerned with graded composite materials, consisting of one or more dispersed phases of spatially variable volume fractions embedded in a matrix of another phase, that are subdivided by internal percolation thresholds or wider transition zones between the different matrix phases.

A detailed description of the geometry of actual graded composite microstructures is usually not available, except perhaps for information on volume fraction dis-

† Dedicated to Professor Franz Ziegler on his 60th birthday.

‡ On leave from Institute of Lightweight Structures, Technical University of Vienna, Austria.

tribution and approximate shape of the dispersed phase or phases. Therefore, evaluation of thermomechanical response and local stresses in graded materials must rely on analysis of micromechanical models with idealized geometries. While such idealizations may have much in common with those that have been developed for analysis of macroscopically homogeneous composites, there are significant differences between the analytical models for the two classes of materials. It is well known that the response of macroscopically homogeneous systems can be described in terms of certain thermoelastic moduli that are evaluated for a selected representative volume element, subjected to uniform overall thermomechanical fields. However, such representative volumes are not easily defined for systems with variable phase volume fractions, subjected to nonuniform overall fields.

Regardless of such concerns, a variety of methods originally developed to describe the behavior of macroscopically homogeneous composites have been applied in thermoelastic analyses of FGM components. At the most elementary level, rule-of-mixture approaches have been employed, for example, by Fukui *et al.* (1994), Lee and Erdogan (1994/1995), and Markworth and Saunders (1995) in elastic systems. Giannakopoulos *et al.* (1995) and Finot and Suresh (1996) used this approach in elastic–plastic systems. Miller and Lannutti (1993) estimated elastic moduli and averages of the Hashin–Shtrikman bounds for statistically homogeneous systems, while Hirano *et al.* (1990) introduced a fuzzy-set estimate based on the Mori–Tanaka (1973) method, with an assumed transition function to account for the effect of changes of the matrix and inclusion phases. The method was also used in investigations of thermoelastic behavior of FGM structures (Tanaka *et al.*, 1993a,b; Hirano and Wakashima, 1995). Additional references appear in the review by Markworth *et al.* (1995) and in Williamson *et al.* (1993).

The purpose of the present study is to test the proposition that for two-phase graded materials with a single volume fraction gradient, the overall elastic response can be obtained from homogeneous layer models, with the layer moduli estimated in terms of the local volume fractions, and matrix and inclusion moduli, by certain existing micromechanical methods. Section 2 introduces the graded material models and describes the traction and mixed boundary conditions employed in the present study. Both uniform and linearly varying overall stress and strain fields are considered. Section 3 explains the replacement of the discrete material models with piecewise homogeneous layered materials with equivalent elastic constants. The Mori–Tanaka and self-consistent estimates of the effective overall moduli in two-phase particulate aggregates, and the related local field averages, are also summarized here. The results of the many comparative studies are illustrated by examples in Section 4. Finally, Section 5 provides a summary of conclusions that should be useful in applications of the approximate averaging methods to various graded material configurations.

2. THE TWO-PHASE GRADED MATERIAL MODEL

2.1. *Model geometry*

The graded material models selected for the proposed comparative studies are based on a planar hexagonal array of inclusions in continuous matrices. Figure 1

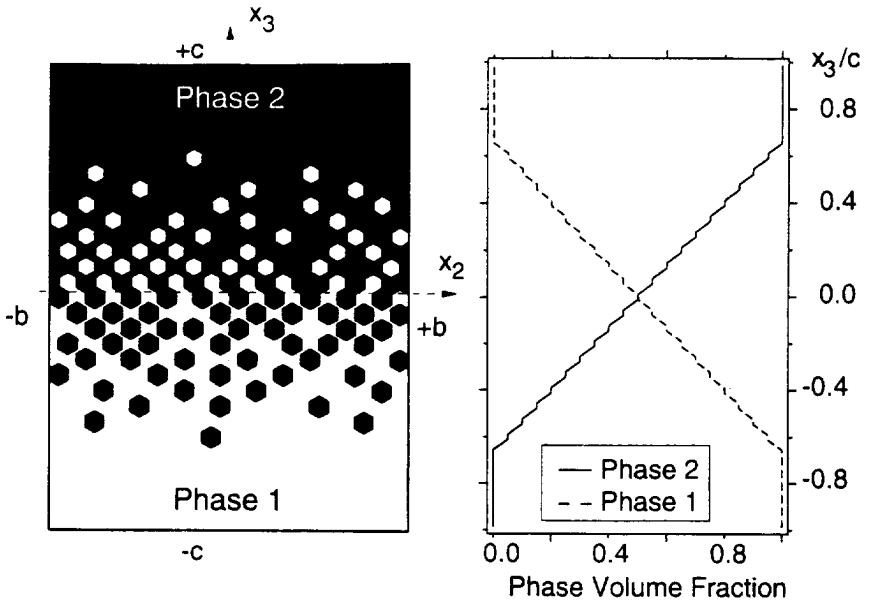


Fig. 1. A two-phase graded material Model 1 with a linear volume fraction gradient in the x_3-direction and a distinct percolation threshold.

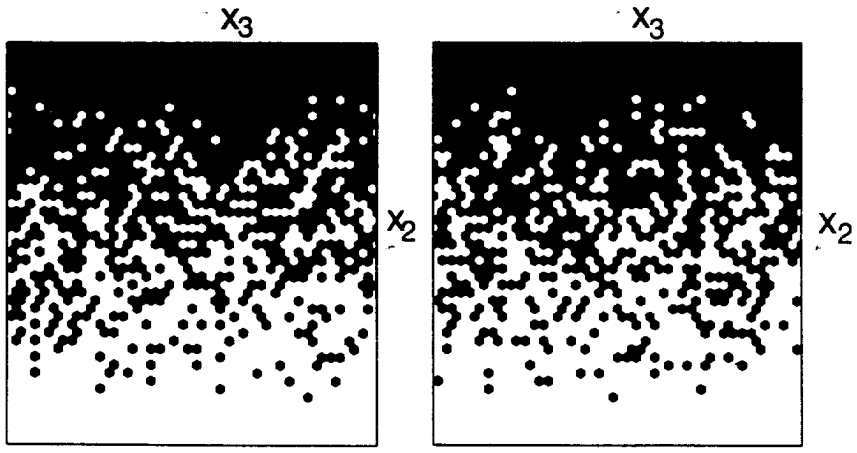


Fig. 2. Two examples of Models 2, the five graded material models used, with a linear volume fraction gradient in the x_3-direction and a wide transition zone.

shows a microstructure with a distinct threshold between the two matrix phases; this microstructure will be referred to as Model 1. Figure 2 illustrates two of the five microstructures of Model 2, with a wide transition zone of a skeletal microstructure, which were used in the comparisons. Figure 3 presents an arrangement incorporating both the skeletal transition zone (Model 3) and a threshold (Model 1.2); such a

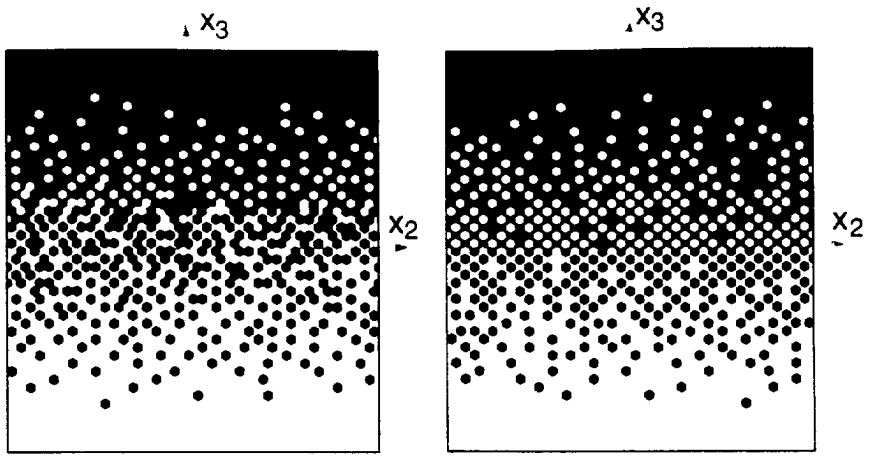


Fig. 3. Two-phase graded materials with a linear volume fraction gradient: Model 3 (left) with a transition zone, and Model 1.2 (right) with a percolation threshold.

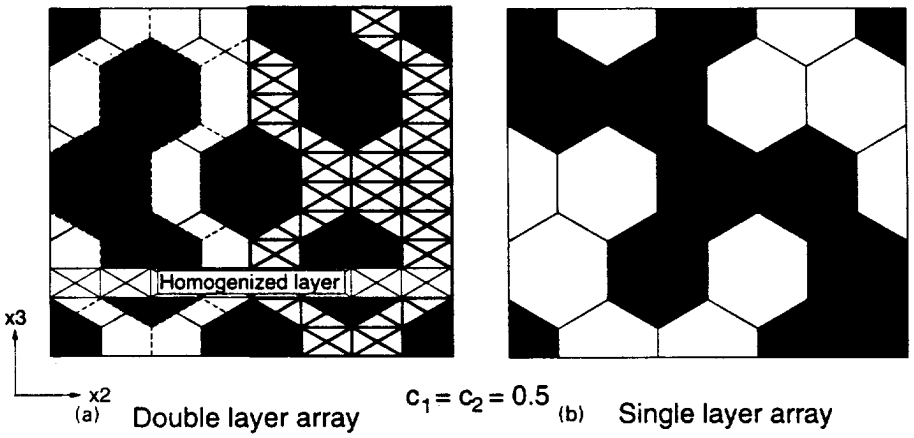


Fig. 4. (a) A double-layer array of hexagonal cells, and finite element discretization with 24 triangles per cell; (b) the two-phase model in a single layer array. The phase volume fractions are $c_r = 0.5$, $r = 1, 2$, in both arrays.

microstructure may result by mixing two phases of different grain size. Figure 4(a) shows in detail the two overlapping arrays used in generating the graded material models, with a relative displacement in the x_2-direction equal to one half width of one hexagonal cell. In contrast to the early ($c_f \simeq 0.3$) clustering observed in the single-layer array [Fig. 4(b)], the double-layer array preserves separation of the inclusions to higher volume concentrations ($c_f \simeq 0.6$), while also offering an optional selection of certain other inclusion shapes. Both arrangements provide for rows of hexagonal cells parallel to the x_2-axis, and the number of inclusions in each row defines the row volume fraction. Volume fraction gradients in the x_3-direction are simulated by

changing the number of inclusions in subsequent rows; many different gradient magnitudes can be generated in this manner.

The array of Fig. 1 has 20 hexagonal cells in each row, and 30 rows in the x_3-direction. The first five top and bottom rows consist of pure phase 2 and phase 1, respectively. A constant volume fraction gradient was generated by adding a single inclusion in each successive row. This provides for a rather steep gradient and thus for a more stringent test of the model comparisons; published micrographs of actual systems suggest rates equal to 1/5 to 1/10 of the present magnitude. The arrays of Figs 2 and 3 have 50 rows and 40 hexagonal cells per row. Again, the five end rows are homogeneous, then one inclusion is added in each next row. The resulting composition gradients are thus half as steep as that of Fig. 1. Placement of inclusions in the five Models 2 illustrated by Fig. 2 was made automatically, using a random number generator. The Models 1, 1.2 and 3 of Figs 1 and 3 were generated manually.

As implied by the use of planar arrays, the typically particulate microstructure of a graded material is replaced here by a graded fibrous system. The latter appears to be more suitable for the intended comparisons, since realizations of fiber systems are much better understood than those of three-dimensional composites with randomly dispersed particles. The finite element mesh of Fig. 4(a) subdivides each fiber into 24 three-noded triangular elements. The element properties are described in Section 2.4. Convergence of the model with respect to the coarseness of the finite element discretization was established by comparisons of selected results of the present model with a 96-element per fiber model, which showed no significant deviations in overall stiffness. Note in Fig. 4(a) the 'homogenized layer' of elements aligned with the x_2-direction; such layers were used in finding volume averages of local fields computed in finite element analysis of the discrete two-phase graded material models; they are also employed in the homogenized models discussed in Section 3.

Other meshing schemes may be implemented with automatic mesh generators. These may offer better approximations of the local fields, but should yield similar field averages and overall response for a given phase density. The scheme selected here is more advantageous since it can also be used to generate certain graded microstructures.

2.2. *Traction boundary conditions*

Both traction and displacement, as well as mixed boundary conditions involving uniform and linearly varying distributions were applied to the material models. The surface tractions can be converted into equivalent overall stresses which, in the case of linear distributions, are subject to certain equilibrium conditions. These can be established by considering a volume V of an elastic homogeneous medium with any physically admissible material symmetry, such that with the possible exception of a thin layer at the surface S, the stress field within V is a linear function of Cartesian coordinates,

$$\sigma_{ij}(\mathbf{x}) = \sigma_{ij} + \eta_{ijk}x_k = \sigma_{ji} + \eta_{jik}x_k, \quad \mathbf{x} \in V. \tag{1}$$

To be admissible, this field must satisfy the equations of equilibrium in the absence of body forces

$$\partial\sigma_{ij}(\mathbf{x})/\partial x_j = 0 \Rightarrow \eta_{ijj} = 0, \quad i,j = 1,2,3. \tag{2}$$

Inside a homogeneous medium, the strains caused by (1) are also linear functions of coordinates and, therefore, identically satisfy the equations of compatibility. Of course, the linear strain distribution may not be preserved in graded and/or heterogeneous systems, hence the stresses in V may not vary linearly.

To find the overall stress field that supports (1), it is convenient to define the volume V as a cuboid,

$$-a \leqslant x_1 \leqslant a, \quad -b \leqslant x_2 \leqslant b, \quad -c \leqslant x_3 \leqslant c, \tag{3}$$

with surfaces S parallel to the principal coordinate planes. Traction continuity at the interfaces (3) requires that the exterior components of the stress tensor (1) on (3) be equal to the respective overall components. In particular, on any plane $x_2 = \beta$ in (3), the overall stresses are

$$\sigma^0_{2i}(x_1, x_3) = \sigma^0_{2i} + \eta^0_{2ij} x_j, \quad i = 1,2,,3, \quad j = 1,3, \tag{4}$$

with the uniform components

$$\sigma^0_{21} = \bar{\sigma}_{21} + \eta_{212}\beta, \quad \sigma^0_{22} = \bar{\sigma}_{22} + \eta_{222}\beta, \quad \sigma^0_{23} = \bar{\sigma}_{23} + \eta_{232}\beta. \tag{5}$$

The top bar denotes a constant part of the uniform overall stress that can be prescribed at will. Note that the components (5) are dissimilar at $x_2 = \beta = \pm b$ in (3). Traction continuity at these surfaces planes provides

$$\eta^0_{2i1} = \eta_{2i1}, \quad \eta^0_{2i3} = \eta_{2i3}, \quad i = 1,2,3. \tag{6}$$

Similarly, on any plane $x_3 = \gamma$ in (3), the overall stresses are

$$\sigma^0_{3i}(x_1, x_2) = \sigma^0_{3i} + \eta^0_{3ij} x_j, \quad i = 1,2,3, \quad j = 1,2, \tag{7}$$

with the uniform components

$$\sigma^0_{31} = \bar{\sigma}_{31} + \eta_{313}\gamma, \quad \sigma^0_{32} = \bar{\sigma}_{32} + \eta_{323}\gamma, \quad \sigma^0_{33} = \bar{\sigma}_{33} + \eta_{333}\gamma, \tag{8}$$

and the overall stress gradients equal to the interior components,

$$\eta^0_{3i1} = \eta_{3i1}, \quad \eta^0_{3i2} = \eta_{3i2}, \quad i = 1,2,3. \tag{9}$$

Analogous overall stress expressions can be written for the planes $x_1 = \alpha$, in analogy to (6) and (9), i.e.

$$\eta^0_{1i2} = \eta_{1i2}, \quad \eta^0_{1i3} = \eta_{1i3}, \quad i = 1,2,3. \tag{10}$$

Equations (6), (9), and (10) suggest that 18 overall stress gradients may be prescribed and are continuous on (3). However, symmetry (1_2) of the stress tensor requires that

$$\eta_{QRR} = \eta^0_{RQR}, \quad R = 1,2,3, \quad \text{no sum on } R, \quad Q \neq R, \tag{11}$$

which implies that only 15 of the overall gradients can be prescribed independently. Six of the corresponding internal gradients appear directly in the equilibrium equations (2). Together with traction continuity on (3), (2) then provide the remaining three internal gradients that cannot be determined from the overall stresses:

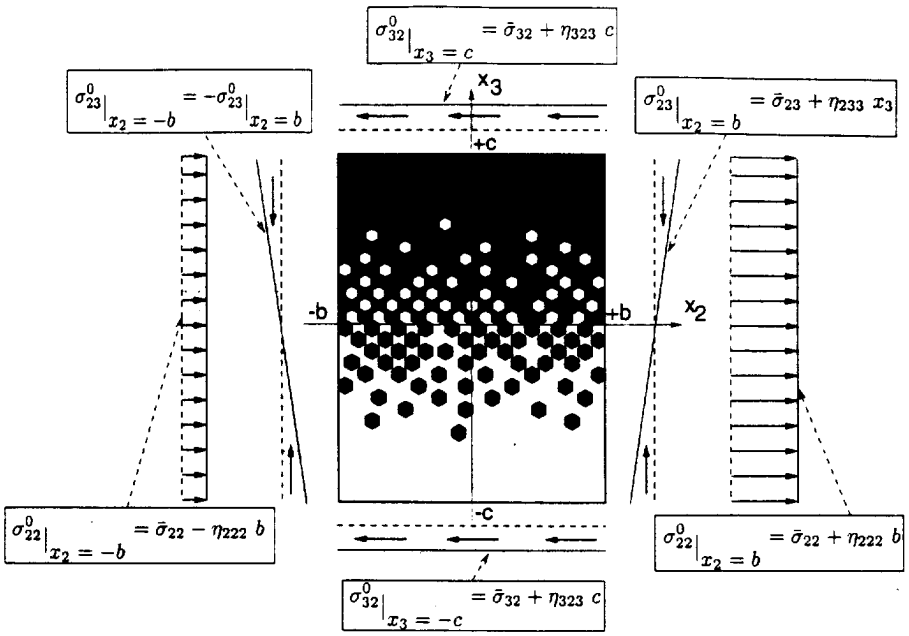


Fig. 5. The overall stresses supporting a plane stress state involving the single applied shear stress gradient $\eta^0_{233} = \eta^0_{323}$.

$$-\eta_{111} = \eta^0_{122} + \eta^0_{133}, \quad -\eta_{222} = \eta^0_{211} + \eta^0_{233}, \quad -\eta_{333} = \eta^0_{311} + \eta^0_{322}. \tag{12}$$

Conservation of momentum and of the moment of momentum of the overall tractions on the surface S of V returns the expected symmetries $\bar{\sigma}_{ij} = \bar{\sigma}_{ji}$, $\eta^0_{ijk} = \eta^0_{jik}$, with $\eta^0_{ikk} = 0$.

As an example, we consider the overall linearly varying stress field involving a single applied shear stress gradient $\eta^0_{233} = \eta^0_{323}$. According to (12), the normal stress gradient $-\eta_{222} = \eta^0_{233}$ is induced by this application. The resulting equilibrium field of linearly varying tractions is applied as boundary conditions on a unit thickness layer with inhomogeneous properties in the x_2x_3-plane (Fig. 5). The model of Fig. 1 is used in this illustration. In applying the in-plane stresses of Fig. 5 to the models of a graded fibrous composite, the stress and moment resultants on the planes $x_1 = \text{const.}$ were required to vanish, and the said planes remained plane during deformation. These boundary conditions are discussed in Section 2.4 below.

Note that the right-hand side of (12) includes only shear stress gradients. Therefore, applied normal stress gradients, such as η^0_{223} or η^0_{332}, do not activate any additional components, but cause only simple fields $\sigma^0_{22} = \bar{\sigma}_{22} + \eta^0_{223}x_3$ or $\sigma^0_{33} = \bar{\sigma}_{33} + \eta^0_{332}x_2$, respectively, continuous across planar boundaries; these can be easily added to those in Fig. 5.

It is probably obvious that the overall stresses (4) and (7), and those on planes $x_1 = \alpha$, are in equilibrium and remain independent both of the properties of the material in V and of the size of V. Hence, overall stress fields defined by selected stress gradients that satisfy (12) may be applied to arbitrary volumes of both homogeneous

and graded solids. Of course, in the latter, the internal stresses may not be linear functions of coordinates except, for example, in layered materials under shear, as discussed below.

2.3. *Displacement and mixed boundary conditions*

In analogy to (1), consider a volume V of a homogeneous solid with linearly varying overall and local strains,

$$\varepsilon_{ij}^{(0)}(\mathbf{x}) = \varepsilon_{ij}^{(0)} + \kappa_{ijm}^{(0)} x_m, \quad \varepsilon_{ij}(\mathbf{x}) = \varepsilon_{ij} + \kappa_{ijm} x_m. \tag{13}$$

The corresponding overall displacement field is (Zuiker, 1993)

$$u_i^0 = \varepsilon_{ij}^{(0)} x_j + (1/2)[\kappa_{ijk}^{(0)} + \kappa_{ikj}^{(0)} - \kappa_{jki}^{(0)}] x_j x_k. \tag{14}$$

Taking the strain (13_2) into the elastic constitutive relation with a constant stiffness, one finds the local stress,

$$\sigma_{ij}(\mathbf{x}) = L_{ijkl}\varepsilon_{kl}(\mathbf{x}), \tag{15}$$

which must satisfy the equilibrium equations

$$\partial\sigma_{ij}(\mathbf{x})/\partial x_j + X_i = 0, \tag{16}$$

so that the strain gradients (13_2) are constrained by the Navier relations,

$$L_{ijkl}\kappa_{klj} + X_i = 0. \tag{17}$$

Consider again the cuboid volume (3) of a homogeneous solid subjected to the displacements (14). The internal strains are linear functions of coordinates. The interior or in-plane components of the strain tensor in V must be continuous on S. The exterior or out-of-plane components may be discontinuous. Surface tractions must be continuous. For example, on any plane $x_1 = \alpha$ one can verify that the interior strain gradient components are κ_{222}, κ_{223}, κ_{232}, κ_{233}, κ_{332}, and κ_{333}; they are equal there to their overall counterparts in (13_1). The exterior components are κ_{112}, κ_{113}, κ_{122}, κ_{123}, κ_{132}, and κ_{133}. Among the latter, the κ_{113} and κ_{133} are the interior components on $x_2 = \beta$, while the κ_{112} and κ_{122} are interior components on the plane $x_3 = \gamma$. On the respective planes, these components are again equal to those in (13); of the 18 components, 15 are independent. The κ_{123}, κ_{132}, and κ_{231}, do not appear as interior components on any plane. However, if the 15 interior strain gradients are prescribed on the surface planes, then these three internal gradients may be evaluated, if the solution exists, from the three relations (17).

In conclusion, if the volume V that is subjected to (14) contains a homogeneous (or homogenized) elastic material with constant stiffness coefficients L_{ijkl}, there are 15 constant internal strain gradients equal to the corresponding overall gradients prescribed by (14). The remaining internal gradients κ_{123}, κ_{132}, κ_{231} can be found from (17), if the solution exists. However, if the volume V subject to boundary conditions that agree with (14) contains a material of variable stiffness, the internal strain gradients may no longer be constant, and since (17) by itself is not sufficient for their evaluation within V, they cannot be found from (14) alone, except for the values of the continuous interior components on S.

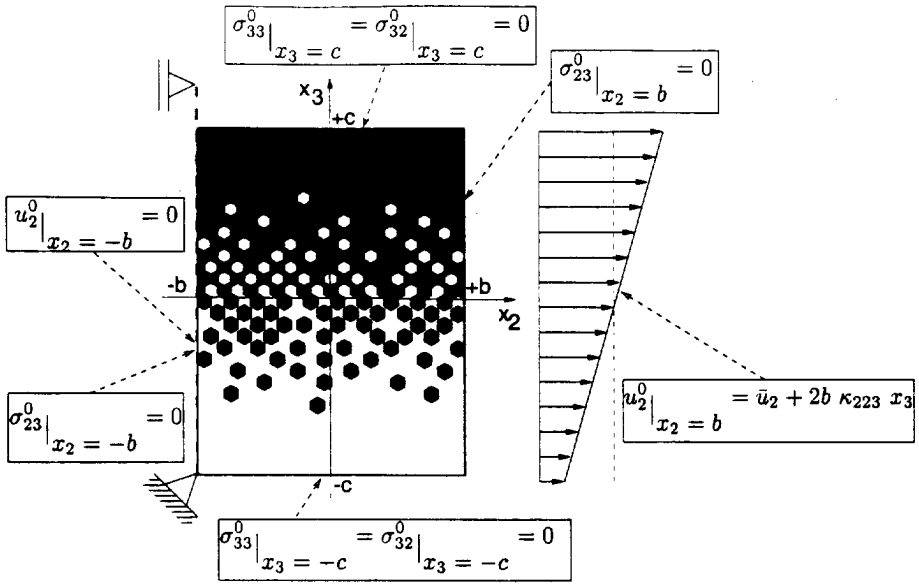


Fig. 6. Overall stresses and displacements applied to cause linearly varying transverse normal strain.

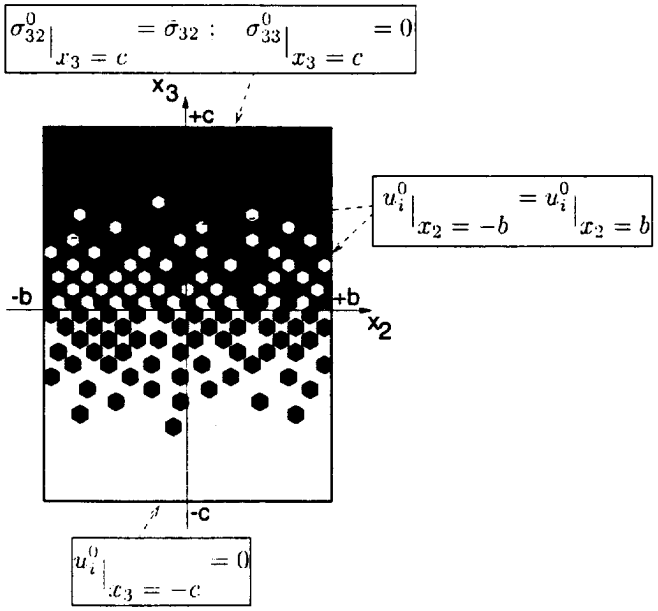


Fig. 7. Overall stresses and displacements applied with a transverse shear stress at $x_3 = c$.

In what follows, we select both pure linear tractions boundary conditions and mixed conditions that simulate such deformation states as uniform normal strain, pure bending, and shear. These are displayed in Figs 5–7. Again, in each case, all

stress resultants with components in the x_1-direction are required to vanish, and the planes $x_1 = \text{const.}$ are required to remain planes during deformation (see Section 2.4.).

2.4. *Generalized plane strain conditions*

In actual solutions, the selected models of the graded fibrous material were implemented as two-dimensional finite element models of constant unit thickness in the x_1-direction, chosen as the diameter of a circle containing one hexagonal cell shown in Fig. 2, using the ABAQUS generalized plane strain elements. The underlying theory allows for a finite thickness solution domain, bounded in the thickness direction by two planes that are parallel before deformation. During deformation, the planes can move as rigid bodies relative to each other. However, it is assumed that the deformation is uniform in the thickness direction, so that the relative motion of the two planes causes only normal strain in that direction. The relative motion of the planes is completely described by the displacement $\Delta u_1(x_2^0, x_3^0)$ of a selected point on one of the planes from its image on the other plane, and by the relative rotations $\Delta\phi_2$, $\Delta\phi_3$ about x_2, x_3, respectively, defined here as positive according to the right-hand rule. In general, this adds at most three degrees of freedom to the system of equations; implementation is accomplished with Lagrangian multipliers. The relative displacement of any point on one plane from its image on the other plane is then given by

$$\Delta u_1(x_2, x_3) = \Delta u_1(x_2^0, x_3^0) - (x_2 - x_2^0)\,\Delta\phi_3 + (x_3 - x_3^0)\,\Delta\phi_2. \tag{18}$$

In the context of the above strains and strain gradients, this implies that

$$\varepsilon_{11} \neq 0, \quad \varepsilon_{12} = \varepsilon_{13} = 0, \quad \kappa_{112} \neq 0, \quad \kappa_{113} \neq 0, \quad \kappa_{12i} = \kappa_{13i} = 0, \tag{19}$$

where $i = 1, 2, 3$. Similar relations hold for the overall components.

In the absence of constraints on the Δu_1 displacement of the bounding planes, the boundary conditions (18) enforce a superposition of axial and pure bending deformations; the resultants of the axial normal force and moments about the x_2 and x_3 axes being zero.

3. THE HOMOGENIZED GRADED MATERIAL MODEL

3.1. *The replacement scheme*

Since detailed finite element analysis of a discrete two-phase or multi-phase graded material model may not be feasible in all applications, it is useful also to employ a homogenized model of the graded material, consisting of parallel homogeneous layers with certain effective elastic moduli. The layer properties are estimated with a suitable averaging method, while the layer thicknesses and the phase volume fractions within the layer are selected to approximate the actual phase volume fraction variation in the graded composite. The finite element mesh of Fig. 4(a) was retained in the homogenized model and one homogeneous layer was located in each row of elements

parallel to the x_2-axis, even though such mesh refinement would not be needed in ordinary applications. Note that three rows of elements separate the center lines of the hexagonal fibers, hence a total of 90 layers were used to represent the 30 rows of hexagons in the x_3-direction in Fig. 1, while 150 layers were needed for the arrays of Figs 2 and 3. The volume fractions of the phases in each layer were determined in terms of the number of fiber and matrix elements present. Also, both phase and overall stress and strain field averages in each layer were found in terms of the respective element fields. Of course, the same boundary conditions were applied to the models in each comparison.

3.2. *The Mori–Tanaka and self-consistent methods*

Since these averaging methods have been extensively described in the literature, we present here only the results needed for their application to particulate composites. More extensive expositions of the Mori–Tanaka (1973) method can be found in Benveniste (1987) and Chen *et al.* (1992), and of the self-consistent method in Hill (1965) and Walpole (1969). Conditions limiting the use of these two methods in multi-phase systems have been identified by Benveniste *et al.* (1991), and their extensive similarities noted by Dvorak and Benveniste (1992).

Both methods provide estimates of the average local stress and strain fields in the phases of a composite material occupying a certain representative volume that is subjected to a uniform overall stress or strain. The local field averages are then used to evaluate the overall elastic moduli of the composite aggregate. The results are first-order estimates, found in terms of phase elastic moduli and volume fractions, while actual phase shapes are approximated by similar ellipsoidal shapes.

Although the size of the representative volume used by the two methods is not exactly specified, the expectation is that it should be much larger than the diameter of a typical inclusion. In the above replacement scheme, the methods are used to estimate the moduli of each of the 90 (or 150) layers representing the 30 (or 50) rows of hexagonal cells. These are long layers of 20 (or 40) hexagonal cells, but their thickness is equal to about 1/3 of the inclusion spacing. However, recall that in the discrete two-phase models, the composition gradient was generated by adding one inclusion in each next row of hexagonal cells. The volume fraction thus remains nominally constant in each three contiguous element layers, and then changes by 0.05 (or 0.025) in the next three layers. Moreover, in the discrete two-phase models, the inclusions are added at distant locations, causing isolated local disturbances in composition perceived by only a few adjacent inclusions. Therefore, with few exceptions, the inclusions in the present microstructure (with a rather steep gradient) reside in what appear to be sufficiently large volumes of constant composition.

Another concern pertains to the assumption of uniform overall fields applied to the representative volume. As will be seen below, the stress and deformation fields in the homogenized model are far from uniform. The role of field gradients in the response of heterogeneous solids was recently studied by Zuiker (1993) and Zuiker and Dvorak (1994a, b, c). The gradient effects were found to be important in fields of low average magnitude. However, when the field averages are high, their contribution to the energy of the inclusion far outweighs that of the gradients (Dvorak and Zuiker, 1995).

In conclusion, while the replacement scheme does not exactly comply with the usual assumptions of the homogenization methods, the departures do not appear to seriously compromise its validity. This is borne out in the comparisons described below.

3.3. *Estimates of overall moduli and local fields*

A simple implementation of the methods in two-phase systems starts with evaluation of the overall moduli. In most functionally graded materials, the local effective moduli should be approximated by those of a matrix-based composite reinforced by spherical particles. Useful in applications are the following results for a random distribution of isotropic particles in an isotropic matrix. Let K_1, G_1 denote the bulk and shear moduli, respectively, and c_1 the volume fraction of the matrix phase. The K_2, G_2, c_2 denote the elastic constants and volume fraction of the particle phase; $c_1+c_2=1$.

The Mori–Tanaka estimate of the overall bulk and shear moduli K and G of such a particle-reinforced composite was derived by Benveniste (1987) as

$$(K-K_1)/(K_2-K_1) = c_2\alpha'/[(1-\nu_2)+c_2\alpha'],$$
$$(G-G_1)/(G_2-G_1) = c_2\beta'/[(1-\nu_2)+c_2\beta'], \tag{20}$$

where (Berryman, 1980) $\alpha' = (K_1+4G_1/3)/(K_2+4G_1/3)$, $\beta' = (G_1+F_1)/(G_2+F_1)$, and $F_1 = (G_1/6)[(9K_1+8G_1)/(K_1+2G_1)]$.

The self-consistent estimate of the bulk and shear moduli of the above composite system was obtained by Hill (1965) as

$$\alpha''/K = c_1/(K-K_2)+c_2/(K-K_1),$$
$$\beta''/G = c_1/(G-G_2)+c_2/(G-G_1), \tag{21}$$

where $\alpha'' = 3-5\beta'' = K/(K+4G/3)$. Note that in contrast to (20), these are implicit expressions for the unknown K and G, and that they are invariant with respect to phase exchange. It turns out that for $K \geqslant 0$, $G \geqslant 0$, β'' has the range $2/5 \leqslant \beta'' < 3/5$. After substituting for α'', (21_1) can be solved for K in terms of G:

$$1/(K+4G/3) = c_1/(K_1+4G/3)+c_2/(K_2+4G/3), \tag{22}$$

while G can be obtained by solving (numerically) the quartic equation

$$[c_1K_1/(K_1+4G/3)+c_2K_2/(K_2+4G/3)]+5[c_1G_2/(G-G_2)+c_2G_1/(G-G_1)]+2=0. \tag{23}$$

Analogous expressions for composites reinforced by aligned or randomly oriented "needle" (=short-fiber) and disc-shaped (=platelets or flakes) isotropic inhomogeneities were derived with the self-consistent method of Walpole (1969). The Mori–Tanaka estimates of the moduli for such systems are given by (20), with appropriate α' and β' taken from Berryman (1980), and for anisotropic reinforcement see Chen *et al.* (1992).

The overall moduli of fiber composites are estimated in a similar manner. In the present work, the replacement of the two-phase model by the homogenized model

utilized the Mori–Tanaka estimates by Chen *et al.* [1992, equations (8)–(12)], and the self-consistent estimates of Hill [1965, equations (1.6)–(1.9)].

Evaluation of the local stress estimates in the phases can be easily accomplished once the overall moduli of a composite system are known (Hill, 1965). Suppose that a representative volume of the composite material is subjected to certain uniform overall stress or strain fields, written as (6×1) vectors in the form

$$\boldsymbol{\sigma}^0 = \{\sigma_{11}^0 \ \sigma_{22}^0 \ \sigma_{33}^0 \ \sigma_{23}^0 \ \sigma_{13}^0 \ \sigma_{12}^0\}^T, \ \boldsymbol{\varepsilon}^0 = \{\varepsilon_{11}^0 \ \varepsilon_{22}^0 \ \varepsilon_{33}^0 \ 2\varepsilon_{23}^0 \ 2\varepsilon_{13}^0 \ 2\varepsilon_{12}^0\}^T, \quad (24)$$

and that the estimated phase ($r = 1, 2$) volume averages of the local fields are

$$\boldsymbol{\sigma}_r = \{\sigma_{11} \ \sigma_{22} \ \sigma_{33} \ \sigma_{23} \ \sigma_{13} \ \sigma_{12}\}_r^T, \ \boldsymbol{\varepsilon}_r = \{\varepsilon_{11} \ \varepsilon_{22} \ \varepsilon_{33} \ 2\varepsilon_{23} \ 2\varepsilon_{13} \ 2\varepsilon_{12}\}_r^T. \quad (25)$$

The local averages and overall fields are connected as

$$\boldsymbol{\sigma}^0 = c_1\boldsymbol{\sigma}_1 + c_2\boldsymbol{\sigma}_2, \quad \boldsymbol{\varepsilon}^0 = c_1\boldsymbol{\varepsilon}_1 + c_2\boldsymbol{\varepsilon}_2, \quad (26)$$

and the overall and local constitutive relations are then written in the form

$$\boldsymbol{\sigma}^0 = \mathbf{L}\boldsymbol{\varepsilon}^0, \quad \boldsymbol{\varepsilon}^0 = \mathbf{M}\boldsymbol{\sigma}^0, \quad \boldsymbol{\sigma}_r = \mathbf{L}_r\boldsymbol{\varepsilon}_r, \quad \boldsymbol{\varepsilon}_r = \mathbf{M}_r\boldsymbol{\sigma}_r, \quad (27)$$

where the $\mathbf{L}$, $\mathbf{L}_r$, and $\mathbf{M} = \mathbf{L}^{-1}$, $\mathbf{M}_r = \mathbf{L}_r^{-1}$ are the (6×6) overall and local stiffness and compliance matrices. The overall and average local fields can be related by (6×6) mechanical concentration factor matrices

$$\boldsymbol{\varepsilon}_r = \mathbf{A}_r\boldsymbol{\varepsilon}^0, \quad \boldsymbol{\sigma}_r = \mathbf{B}_r\boldsymbol{\sigma}^0, \quad (28)$$

where, for a two-phase system, the concentration factors are evaluated as

$$c_1\mathbf{A}_1 = (\mathbf{L}_1 - \mathbf{L}_2)^{-1}(\mathbf{L} - \mathbf{L}_2), \quad c_1\mathbf{B}_1 = (\mathbf{M}_1 - \mathbf{M}_2)^{-1}(\mathbf{M} - \mathbf{M}_2),$$
$$c_2\mathbf{A}_2 = -(\mathbf{L}_1 - \mathbf{L}_2)^{-1}(\mathbf{L} - \mathbf{L}_1), \quad c_2\mathbf{B}_2 = -(\mathbf{M}_1 - \mathbf{M}_2)^{-1}(\mathbf{M} - \mathbf{M}_1), \quad (29)$$

and, according to (26), must satisfy,

$$c_1\mathbf{A}_1 + c_2\mathbf{A}_2 = \mathbf{I}, \quad c_1\mathbf{B}_1 + c_2\mathbf{B}_2 = \mathbf{I}, \quad (30)$$

where $\mathbf{I}$ is a (6×6) identity matrix. Note that the validity of (28) and (29) does not depend on the method used to obtain the overall $\mathbf{L}$ or $\mathbf{M}$; several different approaches are available, including experimental measurements.

4. COMPARISONS OF MODEL PREDICTIONS

4.1. *Material system*

The discrete two-phase models of a graded material shown in Figs 1–3, and the homogenized model described in Section 3, were compared in their predictions of local stresses or strains and overall response, under the boundary conditions discussed in Sections 2.2–2.4. The material selected was the C/SiC system (Sasaki and Hirai,

Table 1. *Phase properties of the C/SiC system*

Material	E (GPa)	ν	α (10^{-6}/°C)
Phase 1: carbon	28	0.3	9.3
Phase 2: silicon carbide	320	0.3	4.2

1991), with the elastic moduli E and ν, and the coefficients of thermal expansion α, given in Table 1. This system was chosen because of the relatively large difference in phase elastic moduli. Moreover, as discussed in Section 2.1, the composition gradient in the model material was made about five time steeper than that in the actual systems described in the literature. Both these features should elevate the heterogeneity of the model material, thus making it more difficult to achieve satisfactory comparisons of the discrete and homogenized models, and reinforcing the validity of conclusions based on observed agreement between the model predictions. Also, due to the large phase moduli differences, the Mori–Tanaka estimates coincide with the Hashin–Shtrikman upper or lower bounds on elastic moduli, when the stiffer phase serves as a matrix or reinforcement, respectively.

The notation used in displaying the results employs the following shorthand:

Phase 0 refers to the graded composite material itself. The stress or strain in this "phase" is the volume average (26) in the layer of elements shown in Fig. 4(a).

FEM indicates that the quantity in question was determined from local fields found in element layers of the discrete two-phase model [Fig. 4(a)]. To minimize artificial oscillations, this is a three-point moving average of the values computed in the layers.

MTM1 denotes results that were found by finite element analysis of the homogenized model, with overall moduli and/or other properties estimated by the Mori–Tanaka method, such that the (carbon) phase 1 in Table 1 was regarded as the continuous matrix.

MTM2 denotes results found as in MTM1, but with the (SiC) phase 2 serving as matrix and phase 1 as the reinforcement.

SCS denotes results found by finite element analysis of the homogenized model, where the overall properties were estimated by the self-consistent method.

4.2. *Linear overall shear stress*

The first comparative results were obtained for loading by the linearly changing overall shear stress (Fig. 5). This is a relatively simple loading case, since the composite (phase 0) stress average is a linear function of coordinates in the model volume. Figure 8 shows the $\sigma_{23}^{(s)}(x_3)$, $s = 0, 1, 2$, phase stress averages in the element layers obtained from the local fields computed with the finite element analysis of the discrete model of Fig. 1. The averages are taken over the volumes of the respective phase 1 and 2 elements residing in layers aligned with the x_2-axis, as indicated in Fig. 4; the average shear stress in the composite itself (phase 0) is found from phase 1 and 2 averages and volume fractions in (26). Note that, as expected, the average shear stress in the composite changes linearly in the x_3-direction. This result is also recovered

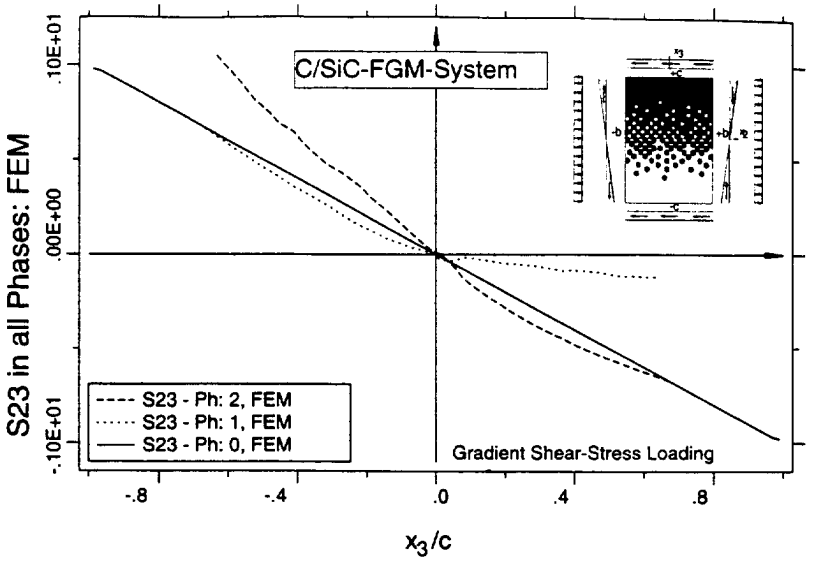


Fig. 8. Average stresses σ_{23} in the phases of the two-phase model of Fig. 1, under the linear overall shear stress state of Fig. 5. The averages were obtained from the computed fields in element layers illustrated in Fig. 4. The applied stress $\sigma^0_{23}(x_3) = 1(x_3/c)$ MPa.

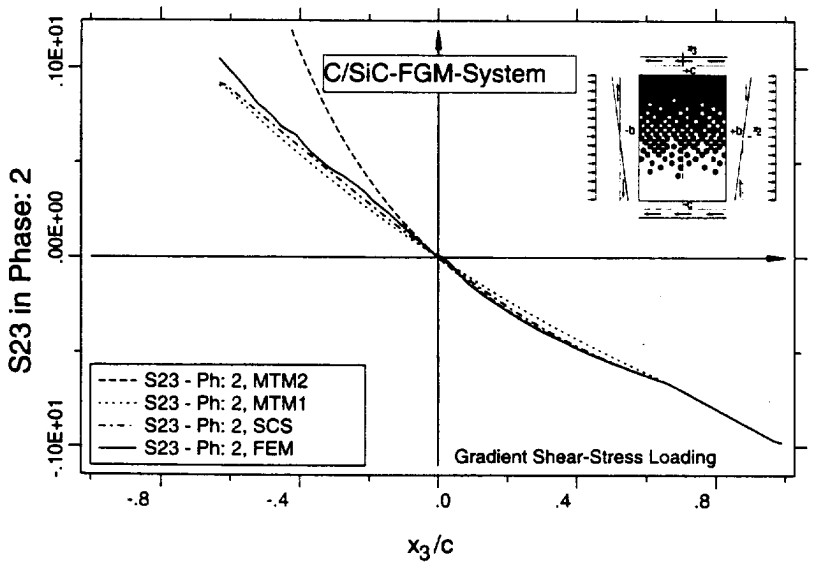


Fig. 9. Comparison of average stresses σ_{23} computed by several different methods in phase 2 (SiC) of the graded composite material model of Fig. 1. MTM1 is applicable at $x_3 < 0$, and MTM2 at $x_3 > 0$. The averages were obtained from the computed fields in element layers illustrated in Fig. 4. The applied stress $\sigma^0_{23}(x_3) = 1(x_3/c)$ MPa.

when the phase volume average stresses are estimated with the Mori–Tanaka method, with either phase serving as matrix in $-c \leqslant x_3 \leqslant c$, and also when the phase stress averages are estimated with the self-consistent scheme. Figure 9 provides comparisons

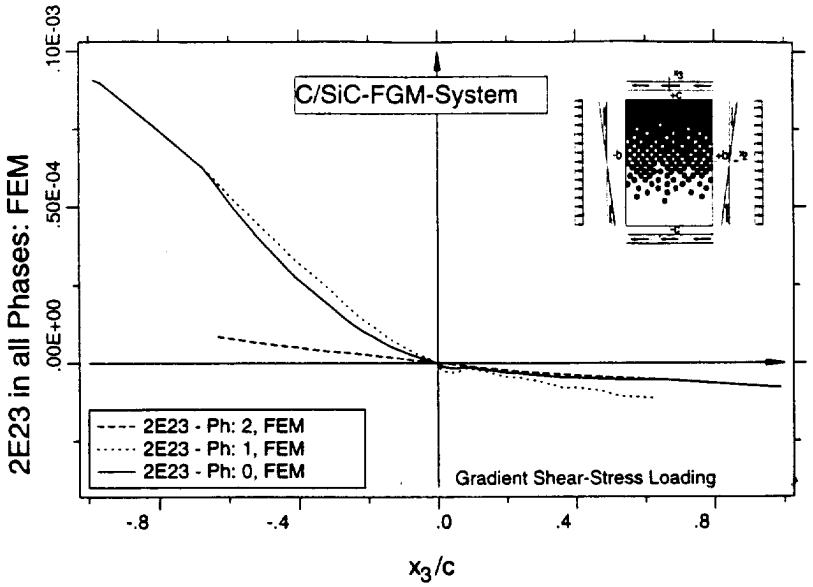


Fig. 10. Average strains $2\varepsilon_{23}$ computed in the phases of the two-phase model of Fig. 1, under the linear overall shear stress state of Fig. 5. The averages were obtained from the computed fields in element layers illustrated in Fig. 4. The applied stress $\sigma^0_{23}(x_3) = 1(x_3/c)$ MPa.

of several estimates of the $\sigma^{(2)}_{23}(x_3)$ stress average in phase 2 (SiC) with the FEM result found from the finite element analysis of the discrete graded material model. Both the self-consistent (SCS) estimate, and the MTM1 and MTM2 estimates in the respective parts of the model volume, are in good agreement with the FEM result. Note that MTM1 is applicable at $x_3 < 0$, and MTM2 at $x_3 > 0$.

Figure 10 presents the distribution of the element layer-averaged $2\varepsilon^{(0)}_{23}(x_3)$ strain component in the composite (phase 0) and phases 1 and 2, where the underlying strain field was obtained by finite element analysis of the discrete model of Fig. 1. As expected, the 0-phase average converges to that in the respective matrix phase and the two curves coincide in the homogeneous end layers. A comparison of the layer-averaged $2\varepsilon^{(1)}_{23}(x_3)$ strains in phase 1 was also made with the different estimates; in their respective regions, the MTM1 and MTM2 results followed the FEM results rather closely, somewhat better than those of the self-consistent scheme.

4.3. *Overall transverse strain*

This loading configuration, shown schematically in Fig. 6, was first applied as a uniform overall strain, to the two-phase models of Figs 1–3. Five models of the type shown in Fig. 2 were analysed; the results presented below are averages of the stresses computed in the five models. The purpose here was to study the effect of graded phase distributions on the overall and local stresses. Of course, the estimates depend only on the phase volume fractions in each element layer, which are determined by the composition gradient. Therefore these estimates are not sensitive to the actual dis-

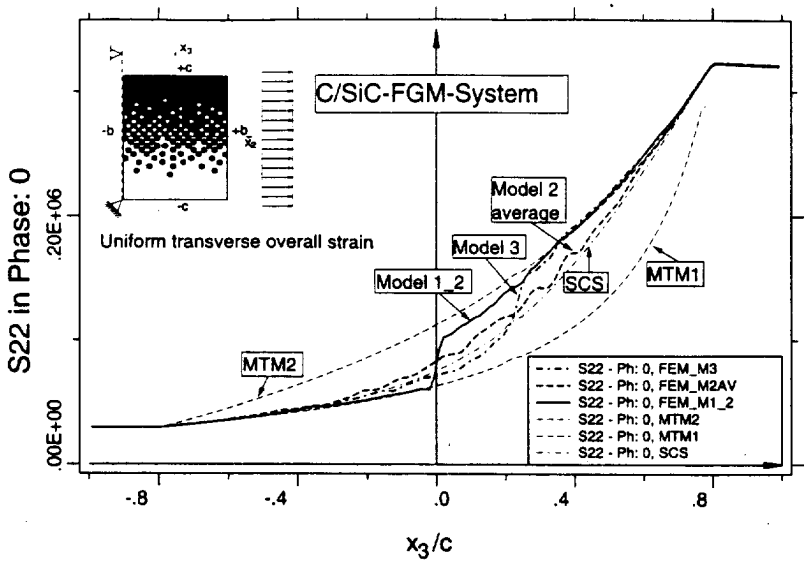


Fig. 11. Comparison of the normal stress averages $\sigma_{22}^{(0)}(x_3)$ in the composite (phase 0) obtained under uniform transverse overall strain $\varepsilon_{22}^{(0)}(x_3) = 1.0$, for the Models 2, 1.2 and 3 of Figs 2 and 3, with several different methods.

tribution. However, as the following comparisons show, the predictions of the discrete models with different microstructural arrangements are best approximated by different estimates.

In Fig. 11, we compare the composite-averaged stresses $\sigma_{22}^{(0)}(x_3)$ evaluated by the finite element method in the five different two-phase models of the type shown in Fig. 2 (Models 2), and in the model of Fig. 3 (Model 3), with the Mori–Tanaka and self-consistent estimates. In Fig. 12, a similar comparison is presented of the $\sigma_{22}^{(2)}(x_3)$ stresses found in Phase 2 (SiC). The results suggest that if the particle distribution provides for a rather wide skeletal zone between the respective matrix phases, then the self-consistent estimate of the stress distribution approximates rather well the results obtained by averaging the transverse composite stresses computed in the discrete two-phase models. This is illustrated in Fig. 12, both for the models of Fig. 2 and also in the transition from phase 1 toward the threshold at $x_3/c \simeq 0.2$ in the models of Fig. 3.

Additional comparisons of the discrete and homogenized models were made under the linearly varying transverse overall strains of Fig. 6, applied to the model of Fig. 1. The applied displacement boundary conditions produced two distinct overall strain states, one with the distribution $\varepsilon_{22}^0(x_3) = 0.5(1 + x_3/c)$, and another with $\varepsilon_{22}^0(x_3) = 0.5x_3/c$, where $-c \leqslant x_3 \leqslant c$. For these overall strains, Figs 13 and 14 show the resulting distributions of the average stress $\sigma_{22}^{(2)}(x_3)$ in the (SiC) phase 2. In both cases, the FEM local stress average follows closely the MTM1 and MTM2 estimates in the regions where they are valid. Of course, the same is true for the composite (phase 0) and phase 1 (C) stress averages.

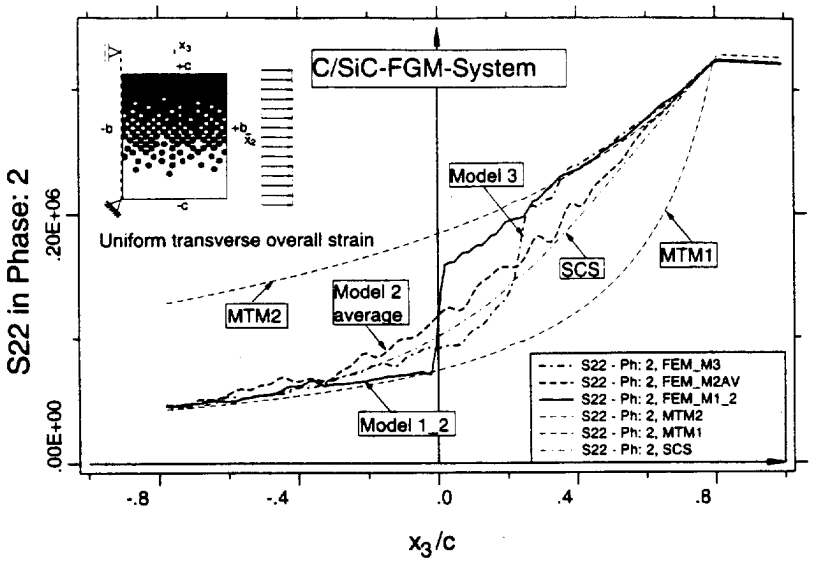


Fig. 12. Comparison of the normal stress averages $\sigma_{22}^{(2)}(x_3)$ in phase 2 (SiC) obtained under uniform transverse overall strain $\varepsilon_{22}^{(0)}(x_3) = 1.0$, for the Models, 2, 1.2 and 3 of Figs 2 and 3, with several different methods.

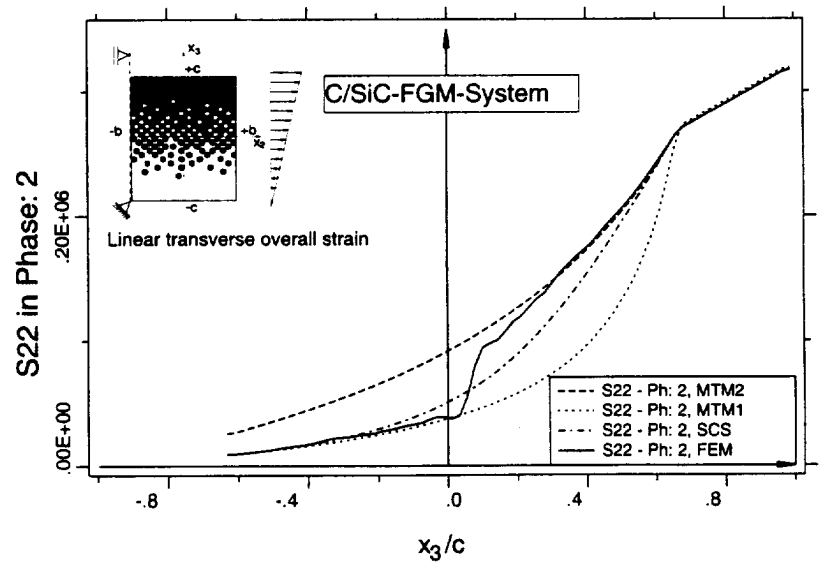


Fig. 13. Comparison of the normal stress averages $\sigma_{22}^{(2)}(x_3)$ in phase 2 (SiC) obtained under linear transverse overall strain $\varepsilon_{22}^{(0)}(x_3) = 0.5(1 + x_3/c)$, for the model of Fig. 1, with several different methods.

4.4. *Uniform transverse shear stress*

The boundary conditions that create this loading state are shown in Fig. 6. The graded layer is loaded by a uniform surface shear stress, while being supported on a

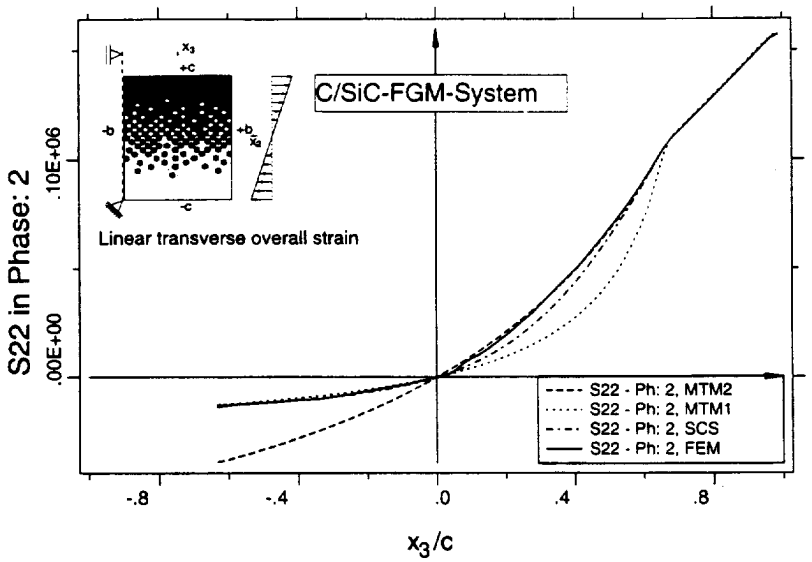


Fig. 14. Comparison of the normal stress averages $\sigma_{22}^{(2)}(x_3)$ in phase 2 (SiC) obtained under linear transverse overall strain $\varepsilon_{22}^{(0)}(x_3) = 1(x_3/c)$, for the model of Fig. 1, with several different methods.

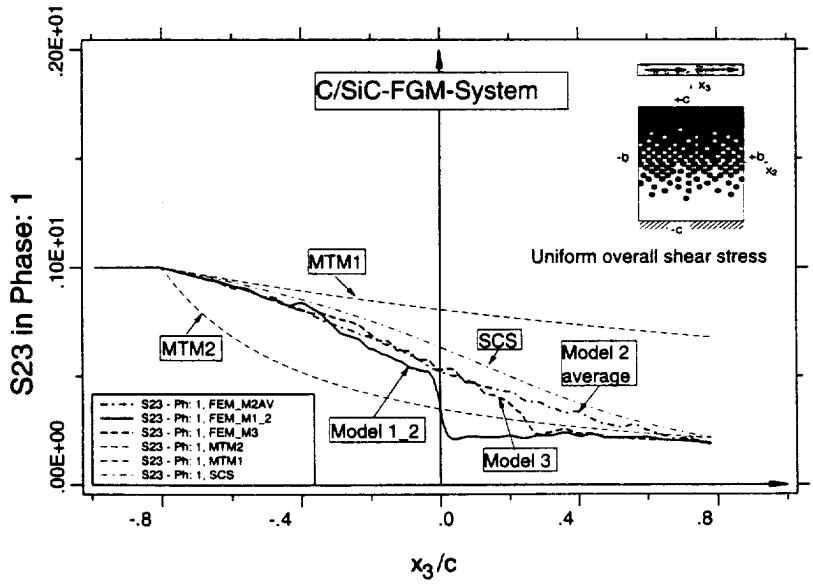


Fig. 15. Comparison of the shear stress averages $\sigma_{32}^{(1)}(x_3)$ in phase 1 (C) obtained under the constant transverse shear stress $\bar{\sigma}_{32} = 1.0$ MPa (Fig. 7), using several models and approximate methods.

rigid substrate. The average stress in the composite (phase 0) is uniform and equal to the applied stress in $-c \leqslant x_3 \leqslant c$. The two-phase model of Fig. 1 was used here, together with its homogenized counterpart. Figure 15 provides a comparison between

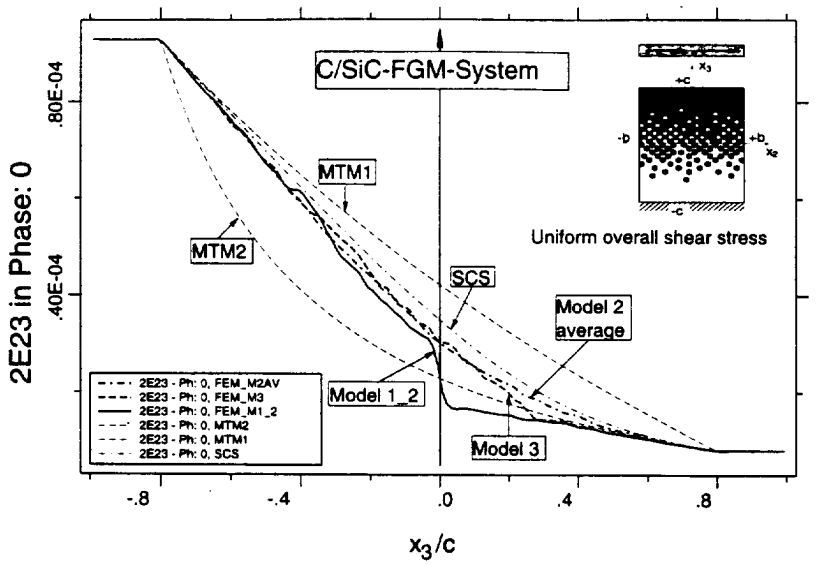


Fig. 16. Comparison of the shear strain averages $2\varepsilon_{32}^{(0)}(x_3)$ in the composite (phase 0) obtained under the constant transverse shear stress $\bar{\sigma}_{32} = 1.0$ MPa (Fig. 7), using several different models and methods.

the phase 1 (C) stresses $\sigma_{32}^{(1)}(x_3)$ found from the different models. Figure 16 shows the composite (phase 0) strains $2\varepsilon_{32}^{(0)}(x_3)$. As before, the self-consistent method approximates quite closely the computed average response of the five Model 2 microstructures. The discrete Models 1.2 and 3 also appear to be well represented by this method in the part of the microstructure with the carbon matrix. However, both models predict higher stresses in the SiC phase and higher stiffness than the self-consistent and MTM2 estimates in the other part of the microstructure with the SiC matrix.

5. CLOSURE

The elastic response of several plane-array models of graded composite microstructures, under different traction and mixed boundary conditions, has been examined by detailed finite element studies, and the results compared with those provided by equivalent piecewise homogeneous models. In the case of the one-directional gradient of the phase volume fractions used here, the actual microstructure was replaced by a material consisting of thin layers, and the effective elastic constants of the layers were estimated by the Mori–Tanaka and self-consistent methods, in terms of phase volume fractions and approximated ellipsoidal inclusion shape. To make the results of the comparisons more convincing, a C/SiC composite system with the phases assumed to be isotropic was chosen because of the large difference in the Young's moduli of the phases. Also, relatively steep composition gradients were selected. The expectation is that the conclusions derived will remain valid in systems with less dissimilar phase moduli, and both smaller and moderately variable gradients. The overall applied loads (Figs 5–7) involved linearly varying as well as constant

shear stresses, and uniform and linearly changing overall strains, transverse to the direction of the composition gradient.

The conclusions reached from these studies indicate that in those parts of the graded microstructure that have a well-defined continuous matrix and discontinuous reinforcement, the overall properties and local fields are closely predicted by Mori–Tanaka estimates. For example, in the model of Fig. 2 with a definite threshold separating the respective matrix phases, the two Mori–Tanaka estimates gave a very close approximation of the response of the discrete two-phase model under identical boundary conditions. On the other hand, the response of the model graded materials with a skeletal microstructure that does not have a well-defined matrix, was better approximated by the self-consistent estimates. For example, both the overall and local field averages evaluated by finite element analysis of the discrete two-phase Models 2 and 3 of Figs 2 and 3, showed distinct transitions toward the respective estimates, in response to the changing configurations of the graded microstructure.

Although limited to the particular cases studied, the results suggest that the micromechanical methods originally developed for statistically homogeneous aggregates can be applied with a reasonable degree of confidence to composites with relatively steep composition gradients and very dissimilar phase moduli. However, certain exceptions should be noted, as observed under transverse shear loading in Figs 15 and 16.

ACKNOWLEDGEMENTS

The work of TR was supported by a grant from the Max Kade Foundation, and that of GJD by the DARPA/ONR University Research Initiative project on the mechanism-based design of composite structures at Rensselaer. This effort was initiated under partial funding from the Direktor Ib Henriksen's Fulbright Grant to GJD at the Department of Solid Mechanics, Technical University of Denmark.

REFERENCES

Benveniste, Y. (1987) A new approach to the application of Mori–Tanaka's theory in composite materials. *Mech. Mater.* **6,** 147–157.

Benveniste, Y., Dvorak, G. J. and Chen, T. (1991) On diagonal and elastic symmetry of the approximate effective stiffness tensor of heterogeneous media. *J. Mech. Phys. Solids* **39,** 927–946.

Berryman, J. G. (1980) Long-wavelength propagation in composite elastic media, II. Ellipsoidal inclusions. *J. Acoust. Soc. Am.* **68,** 1820–1831.

Chen, T., Dvorak, G. J. and Benveniste, Y. (1992) Mori–Tanaka estimates of the overall elastic moduli of certain composite materials. *J. Appl. Mech.* **59,** 539–546.

Dvorak, G. J. and Benveniste, Y. (1992) On transformation strains and uniform fields in multiphase elastic media. *Proc. R. Soc. Lond.* **A437,** 291–310.

Dvorak, G. J. and Zuiker, J. (1995) Effective local properties for modelling of functionally graded composite materials. IUTAM Symposium on *Anisotropy, Inhomogeneity and Nonlinearity in Solid Mechanics*, ed D. F. Parker and A. H. England, pp. 103–108. Kluwer Academic Publishers, Netherlands.

Finot, M. and Suresh, S. (1996) Small and large deformation of thick and thin-film multi-

layers: effects of layer geometry, plasticity and compositional gradients. *J. Mech. Phys. Solids*, in press.

Fukui, Y., Takashima, K. and Ponton, C. B. (1994) Measurement of Young's modulus and internal friction of an *in situ* Al–Al_3Ni functionally gradient material. *J. Mater. Sci.* **29,** 2281–2288.

Giannakopoulos, A. E., Suresh, S., Finot, M. and Olsson, M. (1995) Elastoplastic analysis of thermal cycling: layered materials with compositional gradients. *Act Metall. Mater.* **43**(4), 1335–1354.

Hashin, Z. and Shtrikman, S. (1963) A variational approach to the theory of the elastic behavior of multiphase materials. *J. Mech. Phys. Solids* **11,** 127–140.

Hill, R. (1965) A self-consistent mechanics of composite materials. *J. Mech. Phys. Solids* **13,** 213–222.

Hirano, T. and Wakashima, K. (1995) Mathematical modelling and design. *MRS Bull.* **Jan.,** 40–42.

Hirano, T., Teraki, J. and Yamada, T. (1990) On the design of functionally gradient materials. *Proc. 1st Int. Symp. on Functionally Gradient Materials*, ed. M. Yamanouchi, M. Koizumi, T. Hirai and I. Shiota, pp. 5–10.

Lee, Y.-D. and Erdogan, F. (1994/1995) Residual/thermal stresses in FGM and Laminated thermal barrier coatings. *Int. J. Fract.* **69,** 145–165.

Levin, V. M. (1967) Thermal expansion coefficients of heterogeneous materials. *Mekhanika Tverdogo Tela* **2,** 88–94.

Markworth, A. J. and Saunders, J. H. (1995) A model of structure optimization for a functionally graded material. *Mater. Lett.* **22,** 103–107.

Markworth, A. J., Ramesh, K. S. and Parks, W. P. (1995) Review: modelling studies applied to functionally graded materials. *J. Mater. Sci.* **30,** 2183–2193.

Miller, D. P., Lannutti, J. J. (1993) Fabrication and properties of functionally graded $NiAl/Al_2O_3$ composites. *J. Mater. Res.* **8**(8), 2004–2013.

Mori, T. and Tanaka, K. (1973) Average stress in matrix and average elastic energy of materials with misfitting inclusions. *Acta Metall.* **21,** 571–574.

Sasaki, M. and Hirai, T. (1991) Fabrication and properties of functionally gradient materials. *J. Ceram. Soc. Jap.* **99,** 1002–1013.

Tanaka, K., Tanaka, Y., Enomoto, K., Poterasu, V. F. and Sugano, Y. (1993a) Design of thermoelastic materials using direct sensitivity and optimization methods. Reduction of thermal stresses in functionally gradient materials. *Comp. Meth. Appl. Mech. Engng* **106,** 271–284.

Tanaka, K., Tanaka, Y., Watanabe, H., Poterasu, V. F. and Sugano, Y. (1993b) An improved solution to thermoelastic material design in functionally gradient materials: scheme to reduce thermal stresses. *Comp. Meth. Appl. Mech. Engng* **109,** 377–389.

Walpole, L. J. (1969) On the overall elastic moduli of composite materials. *J. Mech. Phys. Solids* **17,** 235–251.

Williamson, R. L., Rabin, B. H. and Drake, J. T. (1993) Finite element analysis of thermal residual stresses at graded ceramic–metal interfaces. Part I. Model description and geometrical effects. *J. Appl. Phys.* **74**(2), 1311–1320.

Zuiker, J. (1993) Elastic and inelastic micromechanical analysis of functionally graded materials and laminated structures using transformation fields. Ph.D. thesis, Rensselaer Polytechnic Institute, Troy, NY.

Zuiker, J. and Dvorak, G. (1994a) The effective properties of functionally graded composites—I. Extension of the Mori–Tanaka method to linearly varying fields. *Comp. Engng* **4**(1), 19–35.

Zuiker, J. and Dvorak, G. (1994b) Coupling in the mechanical response of functionally graded composite materials. *ASME-AMD* **193,** 73–80.

Zuiker, J. and Dvorak, G. (1994c) The effective properties of composite materials with constant reinforcement density by the linear Mori–Tanaka method. *Trans. ASME J. Engng Mater. Techn.* **116,** 428–437.

PRINTER'S COPY

MICROMECHANICAL MODELS FOR GRADED COMPOSITE MATERIALS: II. THERMOMECHANICAL LOADING

Thomas Reiter* and George J. Dvorak

Center for Composite Materials and Structures
Rensselaer Polytechnic Institute
Troy, NY 12180–3590, U.S.A.

ABSTRACT

Thermoelastic response of several discrete and homogenized models of unconstrained graded composite layers is examined for both uniform changes in temperature and steady–state heat conduction in the gradient direction. Detailed finite element studies of the overall response and local fields in the discrete models are conducted, using large plane–array domains containing simulated skeletal and particulate microstructures. Homogenized layered models, with the same composition gradient and effective properties derived from the Mori–Tanaka and/or self–consistent methods, are analyzed under identical boundary conditions. Comparisons of temperature distributions, and of overall and local stress and strain fields predicted by the discrete and homogenized models are made in the C/SiC composite system, with very different phase properties and relatively steep composition gradient, that was used in the first part of this study (T. Reiter, G. J. Dvorak and V. Tvergaard, *J. Mech. Phys. Solids*, Vol. **45**, pp. XXX–XXX, 1997)

Homogenized models of combined microstructures which employ only a single averaging method do not provide reliable agreements with the discrete model predictions. However, close agreement with the discrete models is shown by homogenized models which derive effective properties estimates from several averaging methods: In those parts of the graded microstructure which have a well–defined continuous matrix and discontinuous reinforcement, the effective moduli, expansion coefficients and heat conductivities are approximated by the appropriate Mori–Tanaka estimates. In skeletal microstructures that often form a transition zones between clearly defined matrix and reinforcement phases, the effective properties are approximated by the self–consistent estimates. The results do not support the proposition that nonlocal or new micromechanical theories are required for modeling of graded microstructures.

Key words: Thermomechanical processes, fiber–reinforced composite, particulate reinforced material, finite elements, averaging methods.

* On leave from the Institute of Lightweight Structures, Technical University of Vienna, Austria.

1. INTRODUCTION

This is a second part of an investigation of validity of micromechanical averaging methods in applications to graded elastic composite materials with particulate and skeletal microstructures. As in Part (I) (Reiter, Dvorak and Tvergaard 1997), several discrete models of such microstructures with a single composition gradient are selected together with certain replacement schemes for construction of corresponding homogenized models with layered mesostructures. While Part (I) was concerned with comparisons of overall and local stress and strain fields in the discrete and homogenized graded layers under mechanical loading and deformation constraints, the present work compares these fields in unconstrained layers subjected to a uniform thermal change or to different temperatures applied at the layer surfaces.

Section 2 describes the discrete model geometries, the finite element discretization, and the thermomechanical boundary conditions applied to the models. Section 3 presents the replacement schemes and a summary of the property estimation procedures for elastic moduli, coefficient of thermal expansion and heat conductivity. Comparisons of discrete and homogenized model predictions are made Section 4, for the same C/SiC composite system that was used in Part (I); again, the large differences in phase property magnitudes and steep composition gradients are adopted, in order to make good agreement more difficult to achieve. In addition to the thermal stress and strain fields, we also compare the model predictions of temperature distributions during steady–state heat conduction through the thickness of the graded layers. Section 5 concludes with the observation that replacement schemes that combine self–consistent property estimates in skeletal parts of the microstructure with Mori–Tanaka estimates in regions with a well–defined matrix, provide homogenized models that closely approximate the response of discrete models to the same thermomechanical loads.

References to paragraphs or equations in Part (I) are denoted as (I, §3) or (I–(20–23)). As in (I), we use the following shorthand notation to describe the results: *Phase 0* refers to the graded composite material itself. *Phases 1 and 2* denote the carbon and SiC constituent materials. *FEM* indicates that the quantity in question was found from one of the discrete two–phase models. *MTM1* denotes results that were found by finite element analysis of the homogenized model, with overall moduli and/or other properties estimated by the Mori–Tanaka method, such that the carbon material (Phase 1) was regarded as the continuous matrix r = 1. *MTM2* denotes results found as in MTM1, but with the SiC phase (2) serving as matrix and the carbon phase (1) as reinforcement. *SCS* denotes results found by finite element analysis of the homogenized model, where the overall properties were estimated by the self–consistent method which makes no distinction between matrix and reinforcement phases.

2. DISCRETE GRADED MATERIAL MODELS

The graded material models selected for the detailed examinations of the local fields were derived from a double–layer planar hexagonal array of inclusions in continuous matrices, described in §2.1 of (I). Of the models employed in (I), we utilize here the Model 1.2 shown in Fig. 1a, the five randomly generated microstructures of Model 2, illustrated here by the example in Fig. 1b, and the discrete Model 3 in Fig. 2, shown here with two different replacement schemes discussed in §3 below. Each of the discrete models consist of 50 rows of hexagonal cells, with 40 cells per row. The five end rows are homogeneous, then one inclusion is added in each next row. The resulting composition gradient is uniform, equal to 0.025/row, of the same magnitude in all three models. The composition gradients observed in actually fabricated microstructures are usually much smaller, equal to about 1/5 to 1/10 of the above magnitude.

As implied by the selection of the planar arrays, the typically particulate microstructure of a graded material is replaced here by a fibrous system. The mechanical and thermal fields in the models of Figs. 1 and 2 were obtained from two–dimensional finite element solutions, using the ABAQUS generalized plane strain elements. The underlying theory allows for a domain bounded in the thickness direction by two planes that are parallel before deformation. The thickness was taken as equal to the larger diameter of one hexagonal cell. During deformation, the planes can move as rigid bodies relative to each other, and the deformation in the thickness direction is assumed to be limited to a uniform normal strain. The resultants of the axial normal force and of the moments about the x_2 and x_3 axes on each of the bounding planes are equal to zero (I, §2.4).

Figure 3 shows the details of the geometry of the double layer array of hexagonal cells, and layers of elements aligned with the x_2–direction; the homogenized layer properties are discussed in §3. Each matrix or fiber cell is subdivided into 24 three–noded triangular elements. Three rows of elements separate the center lines of the rows of hexagonal fiber cells, hence a total of 150 layers represent the 50 hexagon rows that can be counted in the x_3–direction. With eight elements in each intersection of the averaging layer with one of the 40 hexagonal cell, a total of 320 elements were used within each layer, for a total of 48,000 elements in each of the models shown in Figs. 1&2. Convergence with respect to the coarseness of the finite element discretization was established by comparisons of overall stiffnesses and also of selected mechanical loading results found with the present and a 96–element per fiber models; no significant deviations were found.

The thermomechanical boundary conditions applied to the models are shown in Fig. 4 for loading by a temperature gradient, the same mechanical boundary conditions were applied in comparisons involving a uniform thermal change in the entire volume. Each model serves as a unit cell representing a section of a long, unconstrained layer of the graded material, extending in the x_2–direction, and subjected to either identical or dissimilar surface temperatures.

As in (I, §2.1), volume averages of local fields computed in finite element analysis of the discrete graded material models were found from the actual values obtained in the elements within each layer. A three–point moving average of the layer averages was employed to reduce oscillations caused by local stress and strain concentrations within the layers.

3. HOMOGENIZED GRADED MATERIAL MODELS

3.1 *Replacement schemes*

In most applications, the discrete graded material models may be replaced by homogenized models. A medium made of many parallel homogeneous layers with certain effective properties can be used for this purpose in systems with a single composition gradient. Solutions of boundary value problems for the homogenized model may again be found by the finite element method, but with much coarser meshes. However, the mesh and the boundary conditions used in analyzing the discrete models were retained in the present solutions of the thermomechanical boundary value problems for the layered systems. Closed–form solutions may be available for certain loading conditions, e.g., in two–dimensional simple tension/compression, shear, or bending problems.

The layer thicknesses were chosen as equal to those of the element layers, Fig. 3. The constituent volume fractions in the layers are specified by the single composition gradient selected for the discrete models in Figs. 1 and 2. The overall effective properties of the homogeneous layers were estimated by a suitable averaging method. The self–consistent and Mori–Tanaka estimates were used to evaluate the effective elastic moduli, thermal expansion coefficients, and heat conductivities of the composite materials within each layer, in terms of phase volume fractions and the respective phase properties. These methods do not consider the details of the geometry of the graded microstructure; however, the self–consistent method, which does not distinguish between matrix and reinforcement, appears appropriate for skeletal microstructures, and the Mori–Tanaka scheme for microstructures with a well–defined matrix phase.

To test this proposition, different replacement schemes were used. The discrete Models 1.2 and the five variants of Model 2 in Fig. 1 are compared with homogenized models constructed using the MTM1, MTM2 and SCM estimates of thermomechanical properties for the entire thickness of the graded layer. This is similar to the replacement schemes used in (I), for model comparisons in graded layers constrained by prescribed surface displacements and/or tractions.

In contrast, Model 3 in Fig. 2 is homogenized in two different ways. The COMB3.1 variant applies the MTM1 or MTM2 effective property estimates in the surface regions where there is, respectively, a well–defined C Phase 1 or SiC Phase 2 matrix. Between these two regions, in the skeletal part of the microstructure, the SCM property estimates are applied, together with certain transition layers described in §3.3 below. The COMB3.2 Model uses a similar replacement scheme, without the SCM estimates in the skeletal part.

3.2 *The Mori–Tanaka and self–consistent estimates of layer properties*

Only the results actually needed in the model comparisons are summarized here, more extensive descriptions of the general connections and of self–consistent method can be found in Hill (1963, 1965) and Walpole (1969), and applications to thermomechanical problems in Laws (1973). The Mori–Tanaka (1973) method formulation used here was proposed by Benveniste (1987). A unified form of the two methods was derived by Dvorak and Benveniste (1992), and conditions limiting their validity by Benveniste, Dvorak and Chen (1991). The correspondence between mechanical and thermal local fields was found by Benveniste and Dvorak (1990).

Each layer is considered as a representative volume of composite material subjected to certain uniform overall stress $\overset{0}{\boldsymbol{\sigma}}$ or strain $\overset{0}{\boldsymbol{\epsilon}}$, and to a uniform change in temperature θ from some reference magnitude. The volume averages of the local fields in the constituent phases (r = 1, 2) are denoted as $\boldsymbol{\sigma}_r$ and $\boldsymbol{\epsilon}_r$. In either case, the respective field vectors have the generic form,

$$\sigma = \{\sigma_{11}\ \sigma_{22}\ \sigma_{33}\ \sigma_{23}\ \sigma_{13}\ \sigma_{12}\}^{T} \qquad \epsilon = \{\epsilon_{11}\ \epsilon_{22}\ \epsilon_{33}\ 2\epsilon_{23}\ 2\epsilon_{13}\ 2\epsilon_{12}\}^{T}. \tag{1}$$

The thermoelastic response of the composite and phases is written as,

$$\overset{0}{\sigma} = \mathbf{L}\,\overset{0}{\epsilon} + \boldsymbol{\ell}\,\theta \qquad \overset{0}{\epsilon} = \mathbf{M}\,\overset{0}{\sigma} + \mathbf{m}\,\theta \tag{2}$$

$$\sigma_r = \mathbf{L}_r\,\epsilon_r + \boldsymbol{\ell}_r\,\theta \qquad \epsilon_r = \mathbf{M}_r\,\sigma_r + \mathbf{m}_r\,\theta \tag{3}$$

where the $\mathbf{L}$, $\mathbf{L}_r$ and $\mathbf{M} = \mathbf{L}^{-1}$, $\mathbf{M}_r = \mathbf{L}_r^{-1}$ are the (6x6) overall and local stiffness and compliance matrices, and $\boldsymbol{\ell} = -\mathbf{L}\,\mathbf{m}$, $\mathbf{m} = -\mathbf{M}\,\boldsymbol{\ell}$ are the thermal stress and strain vectors; for example, the $\mathbf{m}$ vector lists the linear coefficients of thermal expansion. The magnitudes of the overall elastic moduli used in finding the overall stiffness $\mathbf{L}$ of the homogenized layers can be evaluated using either Mori–Tanaka or self–consistent estimates, both for particulate (I–(20–23)) and fibrous systems (Chen, Dvorak and Benveniste 1992).

The overall and average local fields can be related by the (6x6) mechanical and (6x1) thermal concentration factor matrices,

$$\epsilon_r = \mathbf{A}_r\,\overset{0}{\epsilon} + \mathbf{a}_r\,\theta \qquad \sigma_r = \mathbf{B}_r\,\overset{0}{\sigma} + \mathbf{b}_r\,\theta \tag{4}$$

For a two–phase system, the concentration factors are,

$$\begin{aligned} c_1\mathbf{A}_1 &= (\mathbf{L}_1 - \mathbf{L}_2)^{-1}(\mathbf{L} - \mathbf{L}_2) & c_1\,\mathbf{B}_1 &= (\mathbf{M}_1 - \mathbf{M}_2)^{-1}(\mathbf{M} - \mathbf{M}_2) \\ c_2\mathbf{A}_2 &= -(\mathbf{L}_1 - \mathbf{L}_2)^{-1}(\mathbf{L} - \mathbf{L}_1) & c_2\,\mathbf{B}_2 &= -(\mathbf{M}_1 - \mathbf{M}_2)^{-1}(\mathbf{M} - \mathbf{M}_1) \end{aligned} \tag{5}$$

$$\begin{aligned} \mathbf{a}_r &= -(\mathbf{I} - \mathbf{B}_r)(\mathbf{M}_1 - \mathbf{M}_2)^{-1}(\mathbf{m}_1 - \mathbf{m}_2) \\ \mathbf{b}_r &= (\mathbf{I} - \mathbf{A}_r)(\mathbf{L}_1 - \mathbf{L}_2)^{-1}(\boldsymbol{\ell}_1 - \boldsymbol{\ell}_2). \end{aligned} \tag{6}$$

The local averages and overall fields are connected by,

$$\overset{0}{\sigma} = \Sigma\, c_r\,\sigma_r \qquad \overset{0}{\epsilon} = \Sigma\, c_r\,\epsilon_r \tag{7}$$

hence the concentration factors must satisfy,

$$\Sigma\, c_r\,\mathbf{A}_r = \mathbf{I} \qquad \Sigma\, c_r\,\mathbf{B}_r = \mathbf{I} \qquad \Sigma\, c_r\,\mathbf{a}_r = 0 \qquad \Sigma\, c_r\,\mathbf{b}_r = 0. \tag{8}$$

where **I** is a (6x6) identity matrix and 0 is a (6x1) null vector.

The overall thermal stress and strain vectors can then be found in the form (Levin 1967, Laws 1973),

$$\begin{aligned} \boldsymbol{\ell} &= \boldsymbol{\ell}_1 + (\mathbf{L}-\mathbf{L}_1)(\mathbf{L}_1-\mathbf{L}_2)^{-1}(\boldsymbol{\ell}_1-\boldsymbol{\ell}_2) \;=\; \Sigma\, c_r\,(\boldsymbol{\ell}_r + \mathbf{L}_r\,\mathbf{a}_r) \\ \mathbf{m} &= \mathbf{m}_1 + (\mathbf{M}-\mathbf{M}_1)(\mathbf{M}_1-\mathbf{M}_2)^{-1}(\mathbf{m}_1-\mathbf{m}_2) \;=\; \Sigma\, c_r\,(\mathbf{m}_r + \mathbf{M}_r\,\mathbf{b}_r) \end{aligned} \tag{9}$$

Note that the validity of (3) to (9) does not depend on the method used in obtaining **L** or **M**; several different approaches are admissible, including experimental measurements.

The effective thermal conductivity κ of the layers was found with the same method used in approximating the elastic moduli, under the assumption of zero thermal resistance at interface boundaries. The Mori–Tanaka estimates for particulate and fibrous composites with isotropic phases were found by Hatta and Taya (1986), in terms of phase conductivities κ_r and volume fractions c_r. For an isotropic two–phase composite with reinforcement (r = 2) by spherical particles in a matrix (r = 1), the results is,

$$\kappa \;=\; \kappa_1 - [3c_2(\kappa_1-\kappa_2)\kappa_1]/[c_1(\kappa_1-\kappa_2) + 3\kappa_1] \tag{10}$$

For the two–dimensional fiber array models of Figs. 1 and 2, the effective conductivities in the axial and transverse directions were found from,

$$\kappa_A \;=\; c_1\kappa_1 + c_2\kappa_2 \qquad\qquad \kappa_T \;=\; \kappa_1 - [2c_1(\kappa_1-\kappa_2)\kappa_1]/[c_2(\kappa_1-\kappa_2) + 2\kappa_1] \tag{11}$$

The self–consistent counterpart to (10) was derived by Hashin (1968), in the implicit form,

$$c_1(\kappa_1-\kappa)/(\kappa_1+2\kappa) + c_2(\kappa_2-\kappa)/(\kappa_2+2\kappa) \;=\; 0 \tag{12}$$

For the fiber systems, we have used Davies' results (Hale 1976, eqns.25, 27),

$$\kappa_A \;=\; c_1\kappa_1 + c_2\kappa_2 \qquad\qquad \kappa_T \;=\; \kappa_1 - 2c_2\kappa_T(\kappa_1-\kappa_2)/(\kappa_T+\kappa_2) \tag{13}$$

3.3 *Transition functions*

To accommodate the discontinuities in the homogenized material properties predicted at the boundaries between the different regions of the COMB3.1 and COMB3.2 models in Fig. 2, the following transition functions were defined. Let $\phi_\alpha \neq \phi_\beta$ denote the magnitudes of a certain effective material parameter predicted by two different averaging methods (α) and (β) at a given volume fraction $c_2 = c_{2b}$ of reinforcement (r = 2) in a matrix (r = 1) at a such region boundary. Moreover, let

$$\phi = \mu(c_2)\,\phi_\alpha + (1 - \mu(c_2))\,\phi_\beta \tag{14}$$

define the value of the material parameter within a small interval $c_{2b} \pm \delta/2$, such that,

$$\begin{aligned} \mu(c_2) &= 1 && \text{for } c_2 < c_{2b} - \delta/2 \\ \mu(c_2) &= F(c_2) && \text{for } c_{2b} - \delta/2 < c_2 < c_{2b} + \delta/2 \\ \mu(c_2) &= 0 && \text{for } c_2 > c_{2b} + \delta/2 \end{aligned} \tag{15}$$

A linear transfer function $F(c_2)$ would assume the form,

$$F(c_2) = 1/2 - (c_2 - c_{2b})/\delta \tag{16}$$

while the third–order transfer function actually used herein was taken as,

$$F(c_2) = 2[(c_2 - c_{2b})/\delta]^3 - 3(c_2 - c_{2b})/(2\delta) + 1/2 \tag{17}$$

4. COMPARISONS OF MODEL PREDICTIONS

4.1 Phase and overall properties

The composite material selected for the comparative studies was the C/SiC system (Sasaki, et al., 1991). Both phases were regarded as isotropic, with the following phase elastic moduli E_r and ν_r, coefficients of thermal expansion α_r, and heat conductivity κ_r:

Table 1 Phase properties of the C/SiC system

Material	E_r (GPa)	ν_r	α_r ($10^{-6}/^0C$)	κ_r ($Wm^{-1}/^0C$)
(Phase 1) Carbon	28	0.3	9.3	9.5
(Phase 2) Silicon carbide	320	0.3	4.2	135

This system appears to be particularly suitable for comparisons of different micromechanical models because of the large differences in the Young's modulus, thermal conductivities and expansion coefficients. Together with the relatively steep composition gradients used in the models, the choice of dissimilar phase properties serves to enhance the heterogeneity of the model materials, and thus makes satisfactory comparisons between the discrete and homogenized model predictions more difficult to achieve.

The phase properties were used to estimate effective properties of homogenized layers of constant composition, this effective medium is referred to as Phase 0. The stress or strain in a layer is the volume average (7) in one layer of elements, as shown in Fig. 3. We recall from §1 that *MTM1* denotes results that were found with overall moduli and/or other properties estimated by the Mori–Tanaka method, such that the carbon material (Phase 1) in Table 1 was regarded as the continuous matrix that was labeled as r = 1 in §3. *MTM2* denotes results found as in MTM1, but with the SiC phase (2) serving as matrix (r = 1 in §3) and the carbon phase (1) as reinforcement (r = 2 §3). *SCS* denotes results found by finite element analysis of the homogenized model, where the overall properties were estimated by the self–consistent method which makes no distinction between matrix and reinforcement phases.

Estimates of the overall in–plane Young's modulus E_{22}, linear CTE α, and thermal conductivity κ are plotted in Figs. 5 to 7 as functions of the SiC volume fraction in the graded C/SiC system, represented by the several homogenized counterparts of the discrete models shown in Figs. 1 and 2. The plotted magnitudes were evaluated using the

expressions in §3.2. The COMB3.1 and COMB3.2 plots for the model of Fig. 2 utilized also the transition function (15), (16) and (17).

4.2 Uniform change in temperature

Here we compare selected results obtained with the discrete and homogenized models under the mechanical boundary conditions shown in Fig. 4 combined with a uniform thermal change. Figure 8 shows the overall strain $2\epsilon_{22}^{(0)}(x_3)$ computed for a uniform change in temperature with the discrete Models 1.2, 2, and 3, and the homogenized Mori–Tanaka (MTM1, MTM2) and self–consistent (SCS) models. Note that the linear variation of the overall normal strain is required by the mechanical boundary conditions in Fig. 4. The predictions of the three discrete models are quite similar, however, as expected, the three homogenized models provide rather different predictions of the overall response; the self–consistent model shows best agreement with response of the discrete models, particularly with Model 2, while the Mori–Tanaka estimates, with a single phase 1 or phase 2 representing the matrix everywhere, deviate significantly.

Figures 9 and 10 present the average local strains $2\epsilon_{22}^{(p)}(x_3)$ in the C and SiC Phases 1 and 2, computed from the three discrete and three homogenized models. The MTM1 and MTM2 estimates are not useful, however, the self–consistent model approximates closely the strain averages found from the five computer–generated Models 2, which have predominantly skeletal microstructures. Figure 11 extracts from Figs. 8 to 10 the discrete Model 3 overall and local strain averages $2\epsilon_{22}^{(p)}(x_3)$ in Phases p = 0, 1, 2, and compares them with those predicted by the homogenized model COMB3.1 of Fig. 2a. Figure 12 compares the same Model 3 strain averages with those predicted by the homogenized model COMB3.2 of Fig. 2b. Both homogenized models provide a dramatic improvement in the predictions of the said local strain averages; COMB3.1 appears to be a better choice. It will be appreciated that the improvement is made possible by the close approximation of

the variable overall properties of the homogeneous layers that the COMB3–type models provide through the thickness $-c < x_3 < c$. These comparisons suggest that under the uniform temperature change, the self–consistent model provides good predictions of both the overall and local strain averages for the discrete Model 2, while the COMB3 models offer close predictions of such strains for the discrete Model 3.

Figure 13 refers again to the uniformly heated graded layer, and illustrates very good agreement between discrete and homogenized model predictions of the overall and local average stresses $\sigma_{22}^{(r)}(x_3)$ in phase 0 (composite), and in Phases 1 (C) and 2 (SiC). A similar comparison was obtained with the COMB3.2 model. The results were extracted from a broader set, much like that shown in Figs. 8–10, which also included a satisfactory comparison of the Model 2 results with self–consistent estimates of the local averaged fields. The MTM1 and MTM2 models, when applied alone, were again not useful.

In conclusion, the COMB–type models predictions of the overall and local fields in the uniformly heated layer compare very favorably with those of the discrete Model 3. Similar agreement should be expected between Model 1.2 and a corresponding COMB–type model. In the the five Models 2, the self–consistent scheme provides satisfactory predictions.

In comparing the strain distributions in Figs. 11 and 12 with the stresses in Figs. 13, one may consult Table 1 for the magnitudes of the linear expansion coefficient α_r of the two phases. The large expansion in the carbon–rich layer accounts for the positive total strain in this layer, Figs. 11 and 12. However, the constraint by very stiff SiC–rich layer causes compressive stress and elastic strain in the carbon (Phase 1), Fig. 13. Note the expected stress changes in the bent SiC (Phase 2) layer, the sharp increases at the percolation threshold, and the drop into negative territory models as $x_3/c \rightarrow 1$.

4.3 Different surface temperatures

When the graded composite layer is subjected to the thermomechanical boundary conditions of Fig. 4, solution of a steady–state heat conduction problem for the

temperature field in the crossection $-c < x_3 < c$ precedes evaluation of the local and overall stresses and strains thermomechanical fields. In the discrete models, the actual phase heat conductivity κ_r (Table 1) was prescribed in the elements. In the homogenized models, the respective model estimates of the heat conductivities of the homogenized layers (Fig. 7) were specified for the finite element solution. Also, adjoint solutions of the multilayer homogenized models were constructed for comparison (Ozisik 1968, §6.2). The stress and strain fields were then evaluated in each homogenized model for the temperature distribution predicted by that model.

Figure 14 compares the discrete Model 3 results with the homogenized model solutions of the steady–state heat conduction problem. Since the conductivity of the graded material depends on the composition gradient, Fig. 7, the temperature distribution in the layer thickness is not linear. The discrete Model 1.2 and Model 2 solutions of the heat conduction problem are similar to that of Model 3, indicating that the composition gradient rather than details of phase geometry influence the temperature distribution. Among the homogenized models, the Model 3.1 and SCS estimates of the heat conductivity yield temperature distributions that are in close agreement with those of the discrete models. The Mori–Tanaka estimates deviate significantly from the discrete model predictions.

Evaluations and comparisons of the transverse strain average caused by the temperature gradient in all phases was made as in Phase 1 are shown in Figs. 8–10. The self–consistent prediction was again in good agreement with the transverse strain average of the five Model 2 microstructures. A similar agreement holds for the two discrete Models 1.2 and 3, but only in the region with Phase 1 matrix. In the Phase 2 matrix region, the Models 1,2 and 3 show agreement with the MTM2 strain estimate.

Figure 15 presents the comparisons of the overall and phase averages of the transverse normal strains $2\epsilon_{22}^{(r)}(x_3)$, which were found between the discrete Model 3 and the homogenized model COMB3.1. Note that the overall strain average, denoted here as that

in Phase 0, is nearly uniform through the thickness, indicating that the selected composition gradient cancels the effect of temperature variation through the thickness, so that in the x_3–direction, the graded layer responds as a homogeneous layer subjected to a uniform change in temperature. This behavior is often desired in graded materials. Somewhat different, but also approximately linear overall strain predictions were found with the MTM1, MTM2 and SCS models.

Figure 16 shows the distribution of transverse normal stress averages $\sigma_{22}^{(r)}(x_3)$ in the composite (Phase 0) and in the two constituent phases according to Model 3 and COMB3.1 The agreement is very good. A good agreement was also found between the Model 2 predictions and self–consistent estimates of the transverse normal stress.

5. CLOSURE

The average local and overall thermomechanical elastic fields generated in the graded microstructures of the discrete models by a uniform change in temperature are well predicted by homogenized models which combine several averaging methods in estimating graded material behavior. In systems with a single composition gradient, the discrete microstructure can be replaced by a layered material with certain effective properties. In those parts of the graded material which have a well–defined matrix, the effective properties can be estimated by the respective Mori–Tanaka models. In parts with a skeletal structure, self–consistent estimates appear to be appropriate. Suitable transition functions can be used to assure continuity of the effective properties at interfaces between different model territories.

The temperature distribution corresponding to unidirectional heat conduction through the thickness a graded layer appears to depend primarily on the phase volume fractions rather than microstructural geometry. It was well predicted by a homogenized layered model, where the effective heat conductivities of the layers were estimated by either

Model 3.1 or the self–consistent method. In modeling the overall and phase stress and strain averages, good agreement between discrete and homogenized models was again found with the combined models, particularly with COMB3.1 model, but often also with the COMB3.2 model.

The results suggest that the standard averaging methods, when applied to the respective parts of the graded microstructure, should provide accurate estimates of overall and local stress and strains fields, as well as temperature distributions in thermomechanically loaded graded materials. They do not support the proposition that either nonlocal or higher–order micromechanical theories are required. A higher–order theory appears appropriate only in those locations where the field averages are very low and the gradients very high (Dvorak and Zuiker 1995).

Acknowledgement: The work of TR was supported by a grant from the Max Kade Foundation, and that of GJD by the DARPA/ONR University Research Initiative project on Mechanism–based design of composite structures at Rensselaer. This effort was initiated under partial funding from the Direktor Ib Henriksen's Fulbright Grant to GJD at the Department of Solid Mechanics, Technical University of Denmark.

REFERENCES

Benveniste, Y.,1987, "A new approach to the application of Mori–Tanaka's theory in composite materials," *Mechanics Mater.*, Vol.**6**, pp. 147–157.

Benveniste, Y., G. J. Dvorak, 1990, "On a correspondence between mechanical and thermal effects in two–phase composites," in *Micromechanics and Inhomogeneity*, ed. by G. J. Weng, M. Taya and H. Abe, Springer Verlag, New York, pp. 65–81.

Benveniste, Y., G. J. Dvorak and T. Chen, 1991, "On diagonal and elastic symmetry of the approximate stiffness tensor of heterogeneous media," *J. Mech. Phys. Solids*, Vol. **39**, pp. 927–946.

Chen, T., G. J. Dvorak and Y. Benveniste, 1992, "Mori–Tanaka estimates of the overall moduli of certain composite materials," *J. Appl. Mech.*, Vol. **59**, pp. 539–546.

Dvorak, G. J. and Y. Benveniste, 1992, "On transformation strains and uniform fields in multiphase elastic media," *Proc. Royal Soc. London,* Vol. **A437**, pp. 291–310.

Dvorak, G. J. and J. R. Zuiker, 1995, "Effective local properties for modeling of functionally graded composite materials," *IUTAM Symposium on Anisotropy, Inhomogeneity and Nonlinearity in Solid Mechanics*, ed. by D. F. Parker and A. H. England, Kluver Acad. Publishers, Dordrecht, pp.103–108.

Hale, D. K., 1976, "Review: the physical properties of composite materials," J. Mat. Sci., Vol. **11**, 2105–214

Hashin, Z., 1968, "Assessment of the self consistent scheme approximation: conductivity of particulate composites," J. Compos. Mat., Vol. **2**, 284–300.

Hatta, H., and Taya, M, 1986, Equivalent inclusion method for steady state heat conduction in composites. Intl. J. Engng. Sci., Vol. **24**, 1159–1172.

Hill, R., 1963, "Elastic properties of reinforced solids: Some theoretical principles," *J. Mech. Phys. Solids*, Vol. **11**, pp. 357–372.

Hill, R., 1965, "A self–consistent mechanics of composite materials," *J. Mech. Phys. Solids*, Vol. **13**, pp. 213–222.

Mori, T. and Tanaka, K., 1973, "Average stress in matrix and average energy of materials with misfitting inclusions," *Acta Metall.*, Vol **21**, pp. 571–574.

Ozisik, M. N., 1968, *Boundary Value Problems of Heat Conduction*, Intl. Textbook Co., Scranton, Pa, 503 pp.

Reiter, T, Dvorak, G. J. and Tvergaard, V., 1997, Micromechanical models for graded composite materials, *J. Mech. Phys. Solids*, Vol. **45**, pp. XXX–XXX.

Walpole, L. J., 1969, "On the overall elastic moduli of composite materials," *J. Mech. Phys. Solids*, Vol. **17**, pp. 235–251.

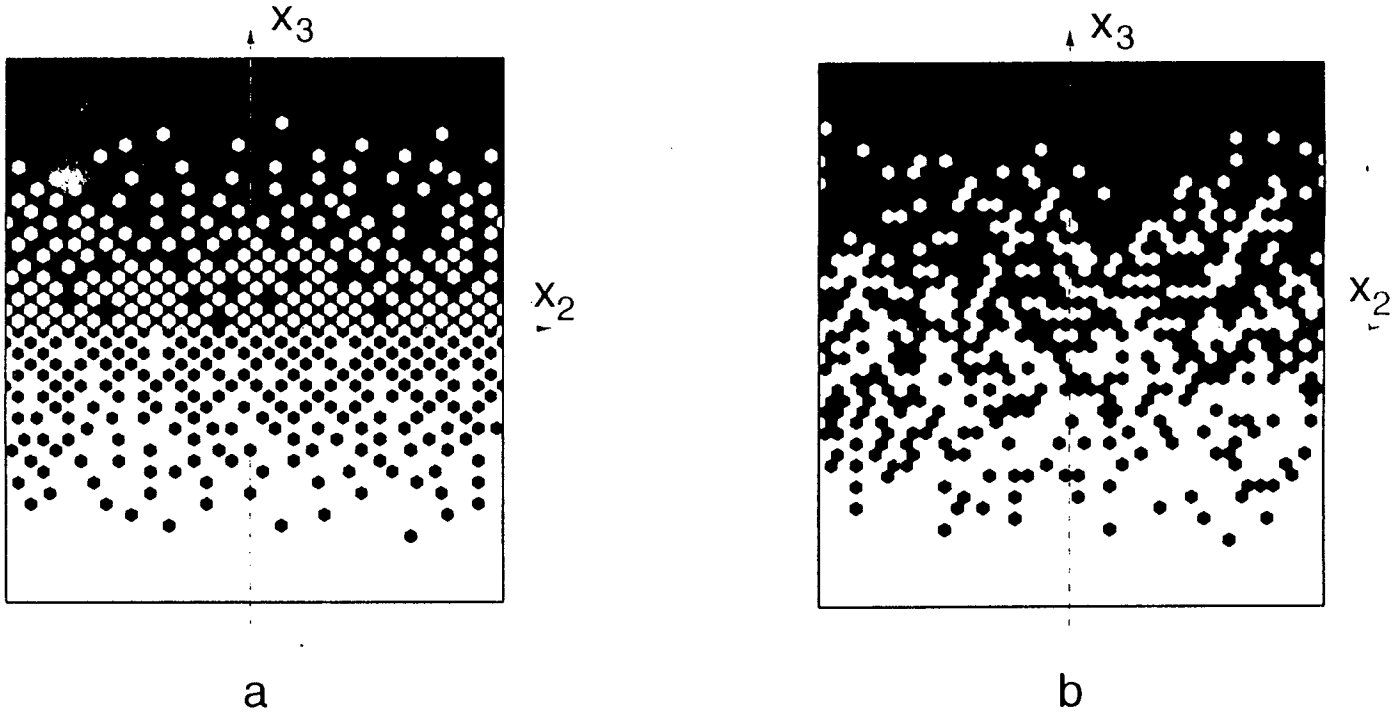


Fig. 1 (a) The two–phase graded material Model 1.2. (b) One of the five computer–generated random microstructures of Model 2. Both models have the same linear volume fraction gradient in the x_3–direction.

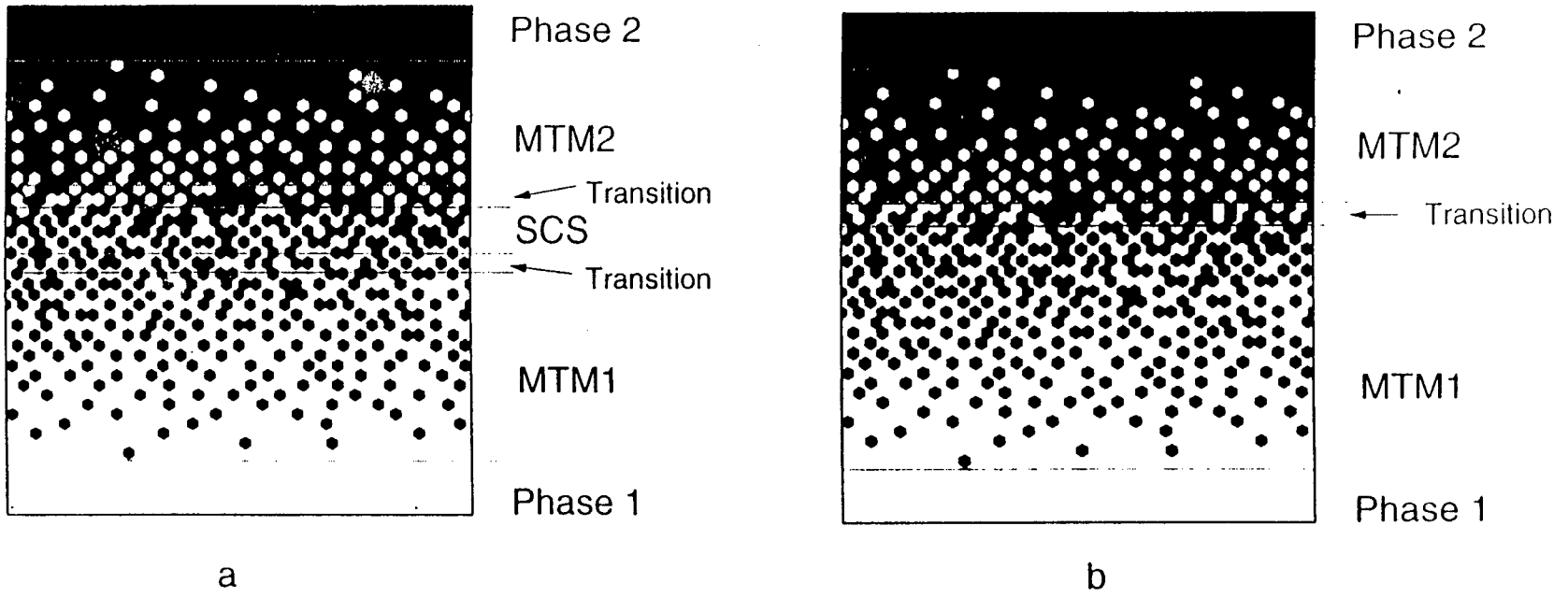


Fig. 2 The two–phase graded material Model 3, with homogenization subdivisions (a) COMB3.1 and (b) COMB3.2. MTM1 denotes a Mori– Tanaka model with Phase 1 (C) as matrix. SCS is the self–consistent scheme, and MTM2 stands for a Mori–Tanaka model with Phase 2 (SiC) serving as matrix.

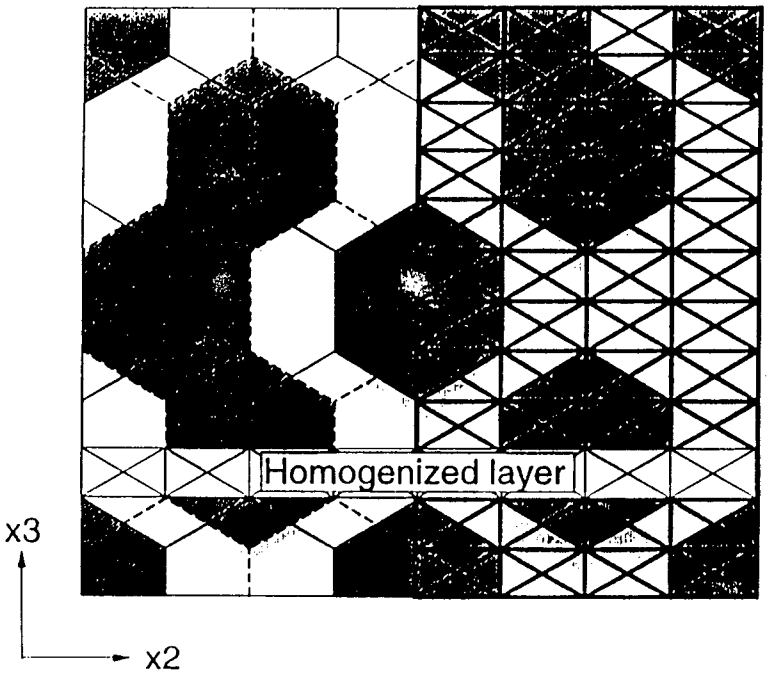


Fig. 3 A double–layer array of hexagonal cells, and finite element discretization with 24 triangles per cell. A single layer of elements is used in replacements by homogenized models and in evaluations of volume averages of local fields.

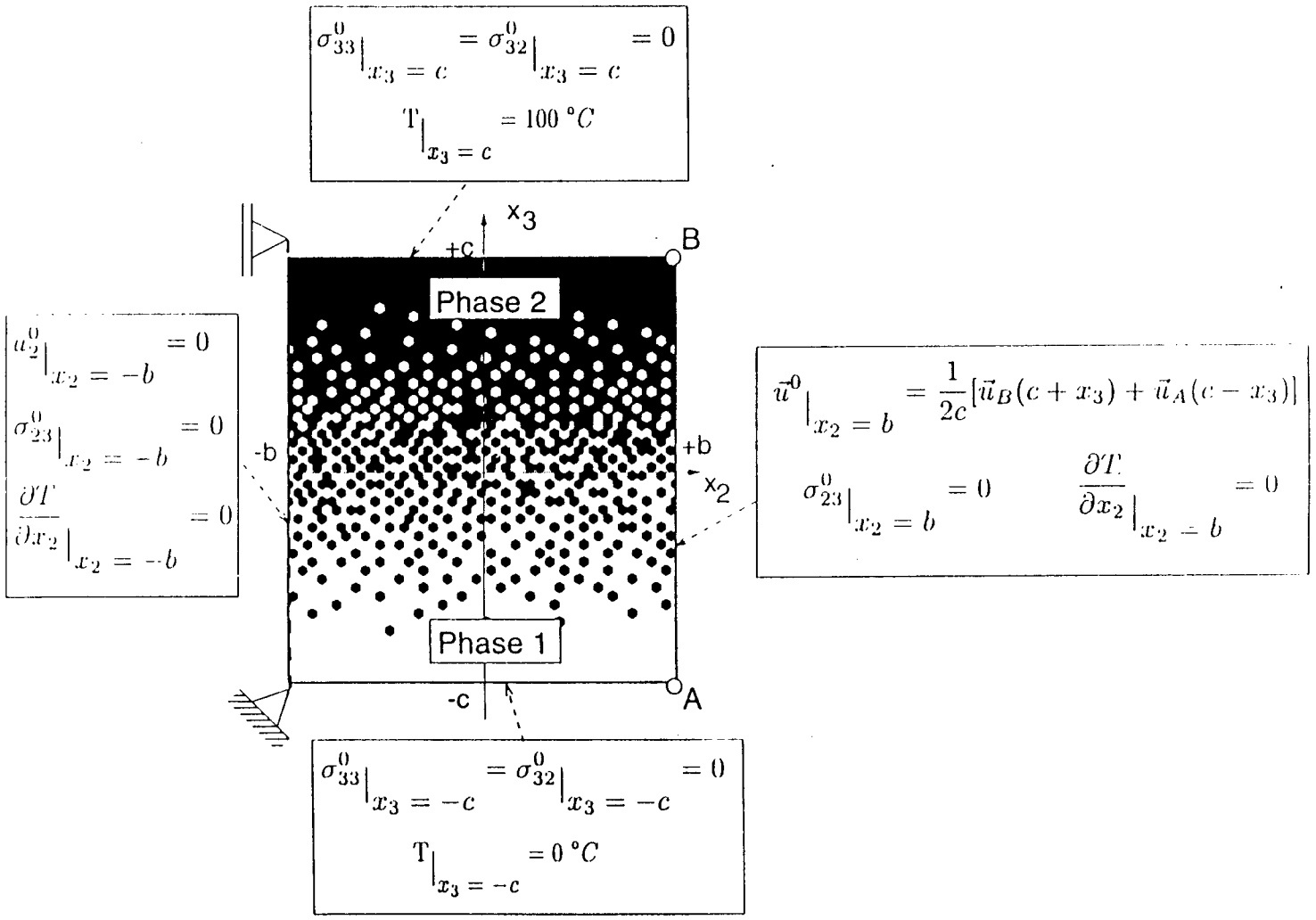


Fig. 4 Boundary conditions applied to the graded material models subjected to a temperature gradient. The same mechanical boundary conditions were applied for the uniform change in temperature by 100°C.

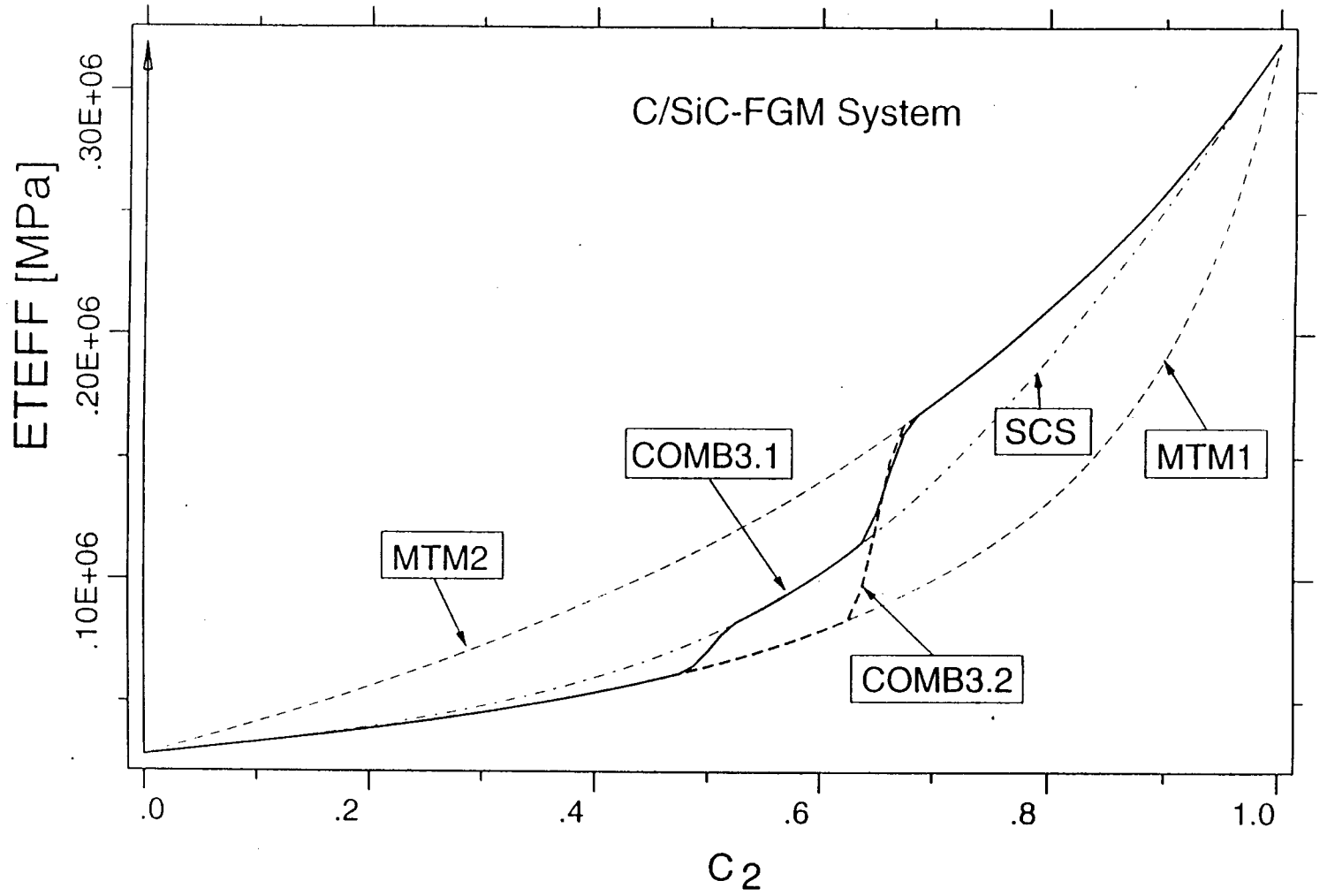


Fig. 5 Estimates of the overall Young's modulus $E_{22}(x_3)$ by various methods. The COMB3.1 and COMB3.2 correspond to the subdivisions shown in Fig. 2. The transitions in COMB3.1 are centered at $c_2 = 0.5$ and $c_2 = 0.66$, and in COMB3.2 at $c_2 = 0.65$. The width of the transition layers is equal to 0.05 on the c_2 scale; c_2 is volume fraction of SiC.

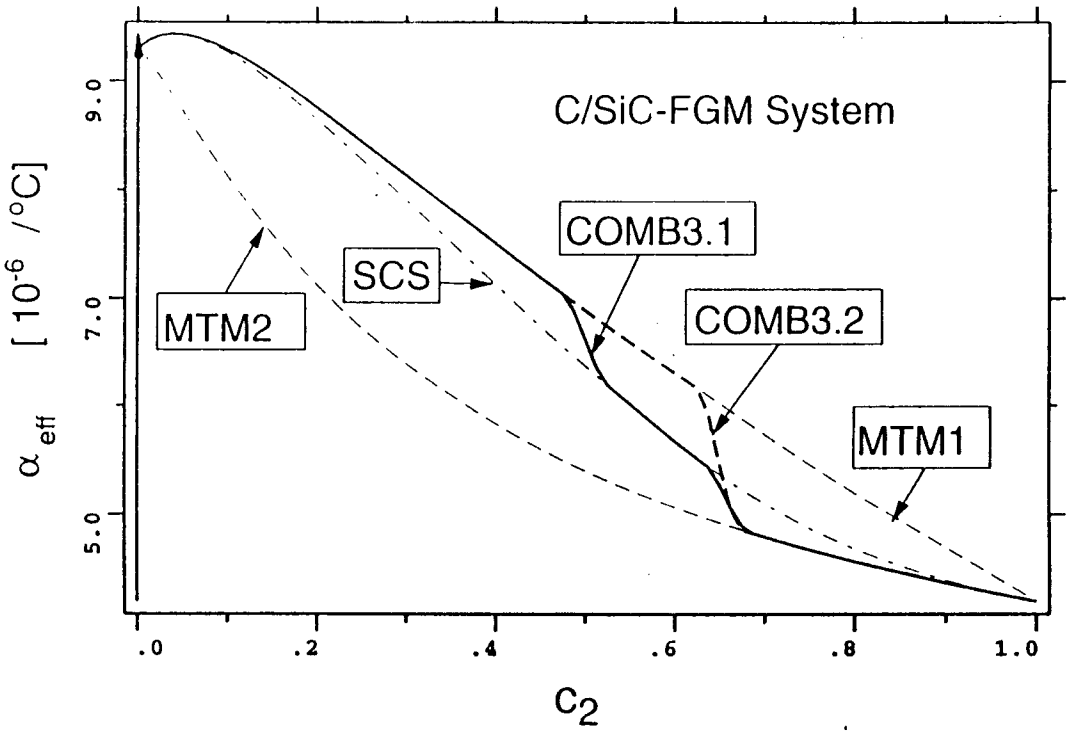


Fig. 6 Estimates of the overall coefficient of thermal expansion $\alpha(x_3)$ by various methods, as functions of the volume fraction c_2 of SiC. The subdivision dimensions are described in Fig. 5.

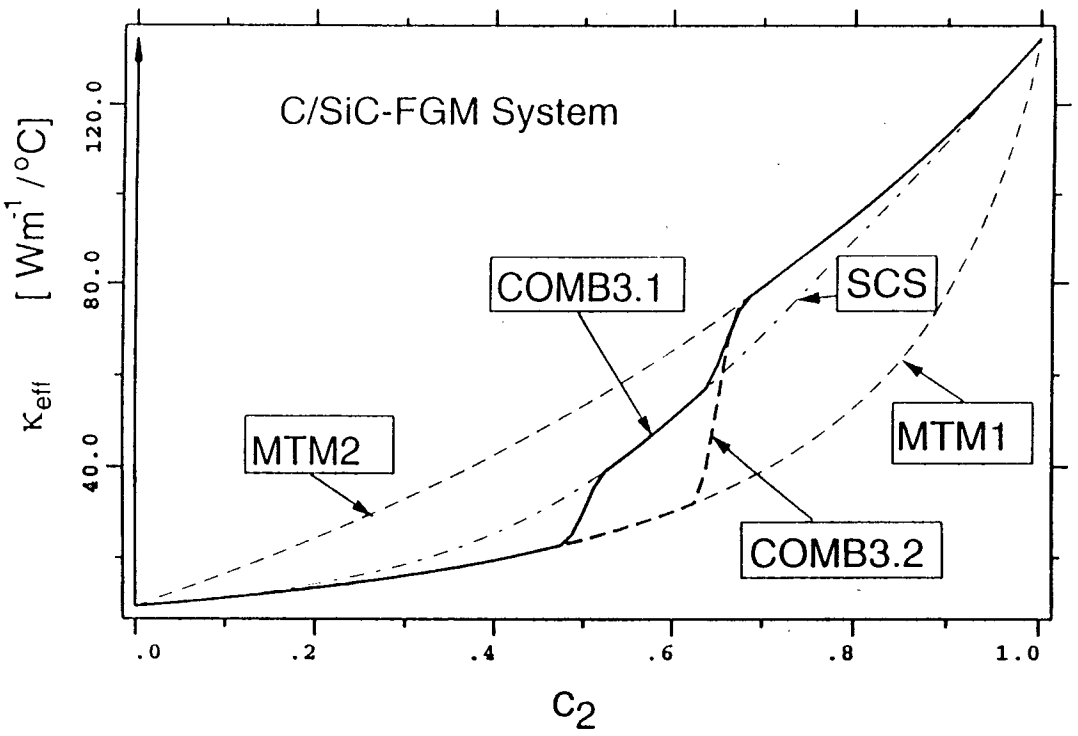


Fig. 7 Estimates of the overall heat conductivity $\kappa(x_3)$ by various methods, as functions of the volume fraction c_2 of SiC. The subdivision dimensions are described in Fig. 5.

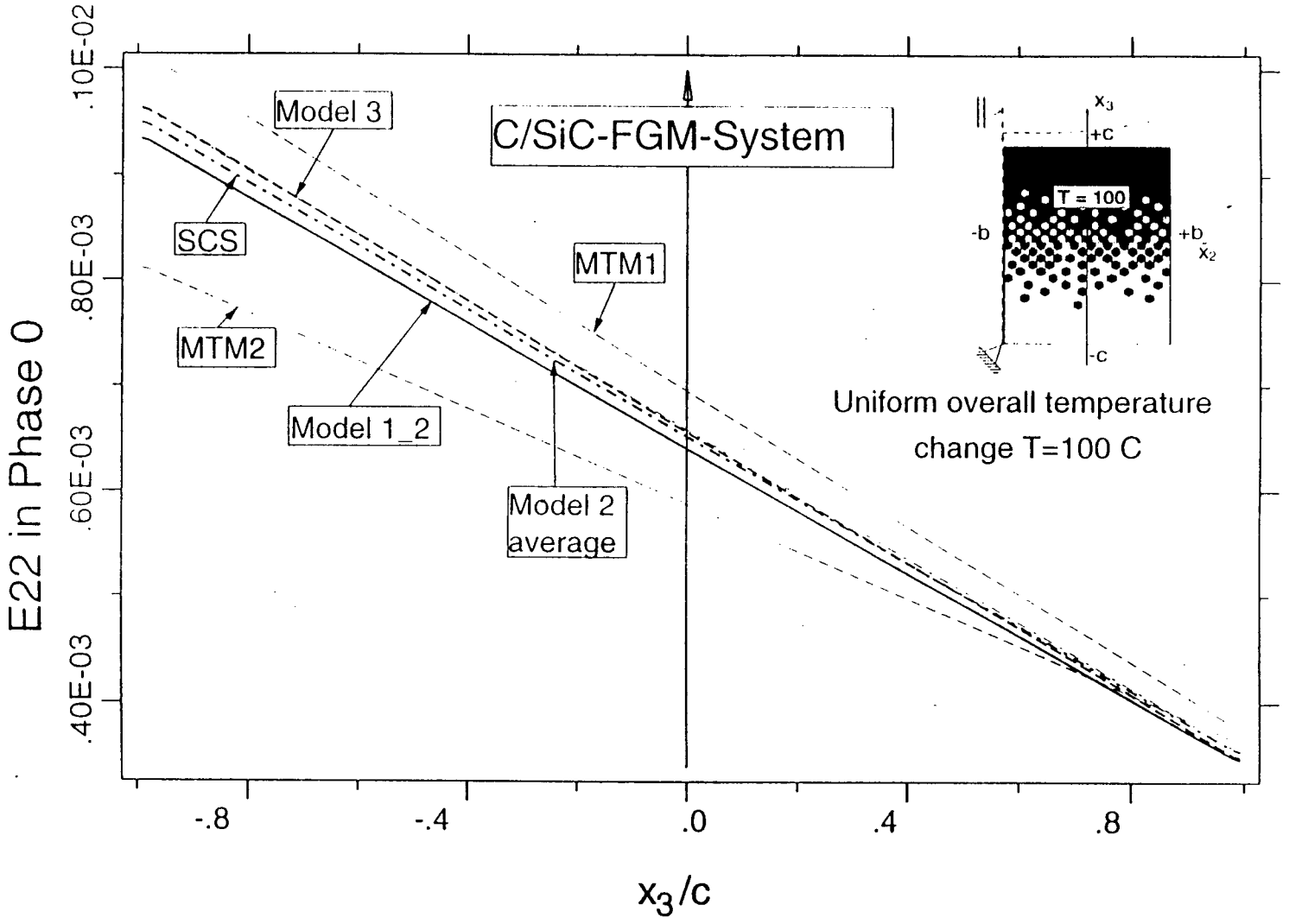


Fig. 8 Overall transverse strain $2\epsilon_{22}^{(0)}(x_3)$ computed for a uniform change in temperature with the discrete Models 1.2, 2, and 3, and homogenized models MTM1, MTM2 and SCS.

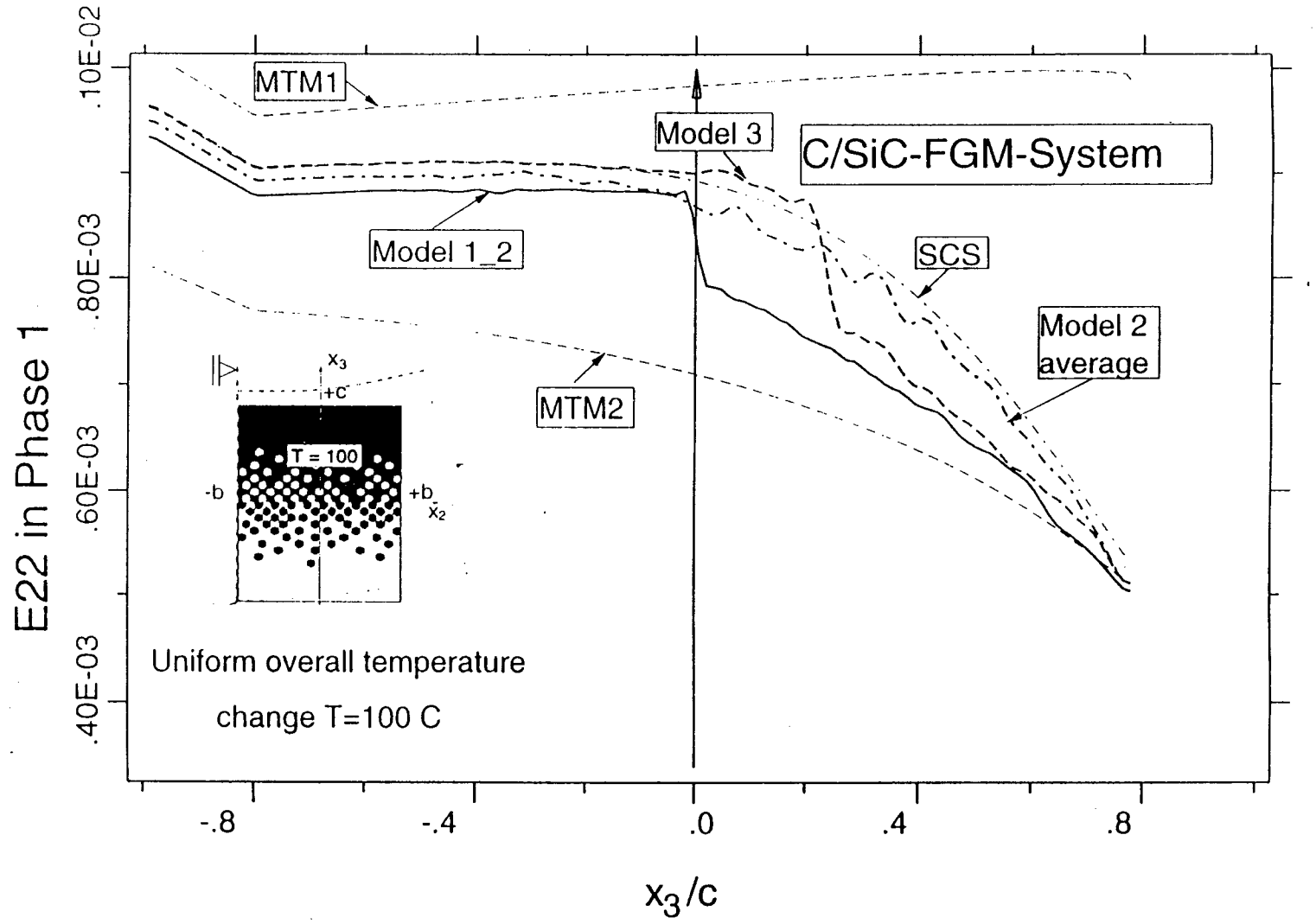


Fig. 9 Average transverse strain $2\epsilon_{22}^{(1)}(x_3)$ in Phase 1 (C), computed with the discrete and homogenized models.

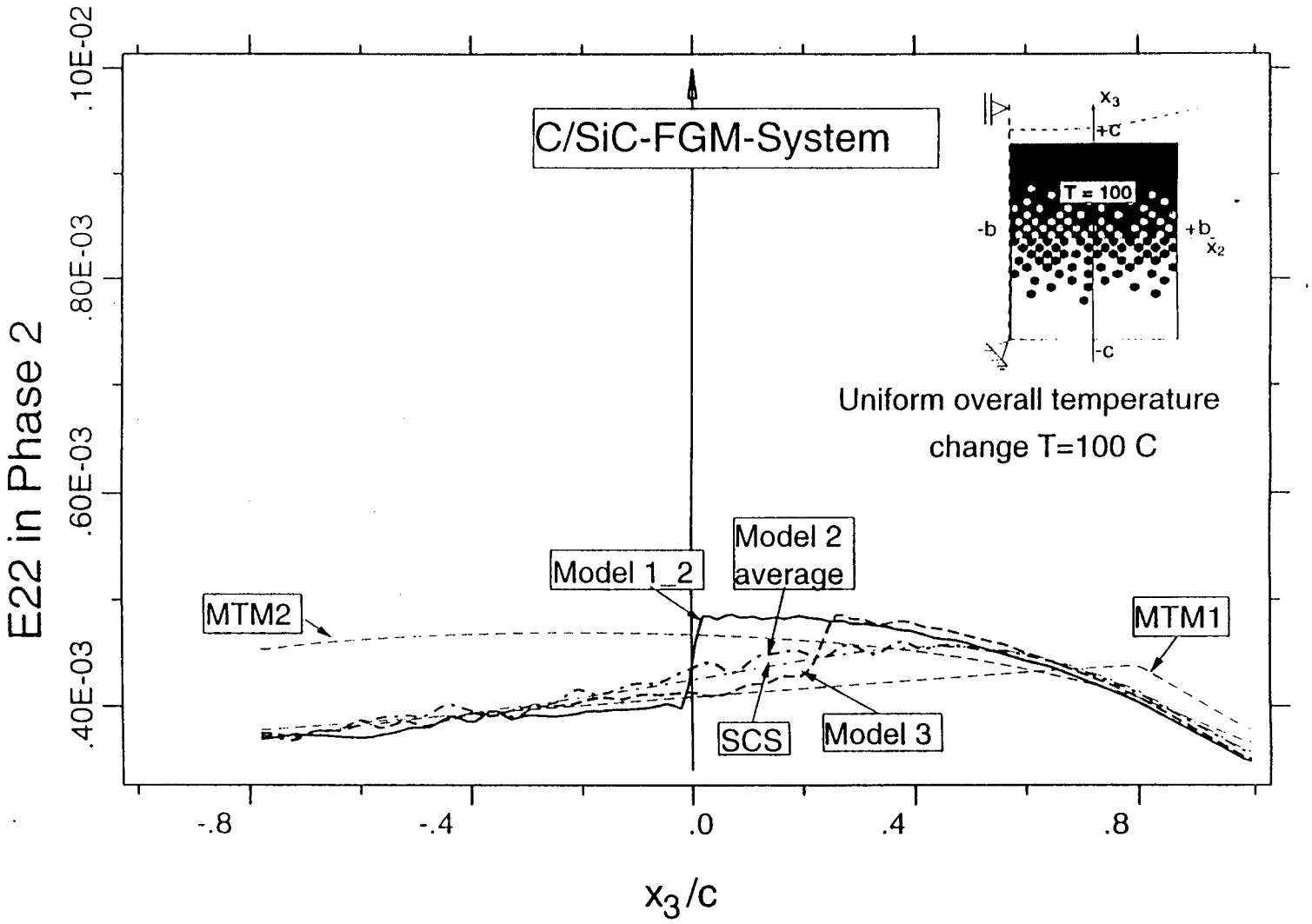


Fig. 10 Average transverse strain $2\epsilon_{22}^{(2)}(x_3)$ in Phase 2 (SiC), computed with the discrete and homogenized models.

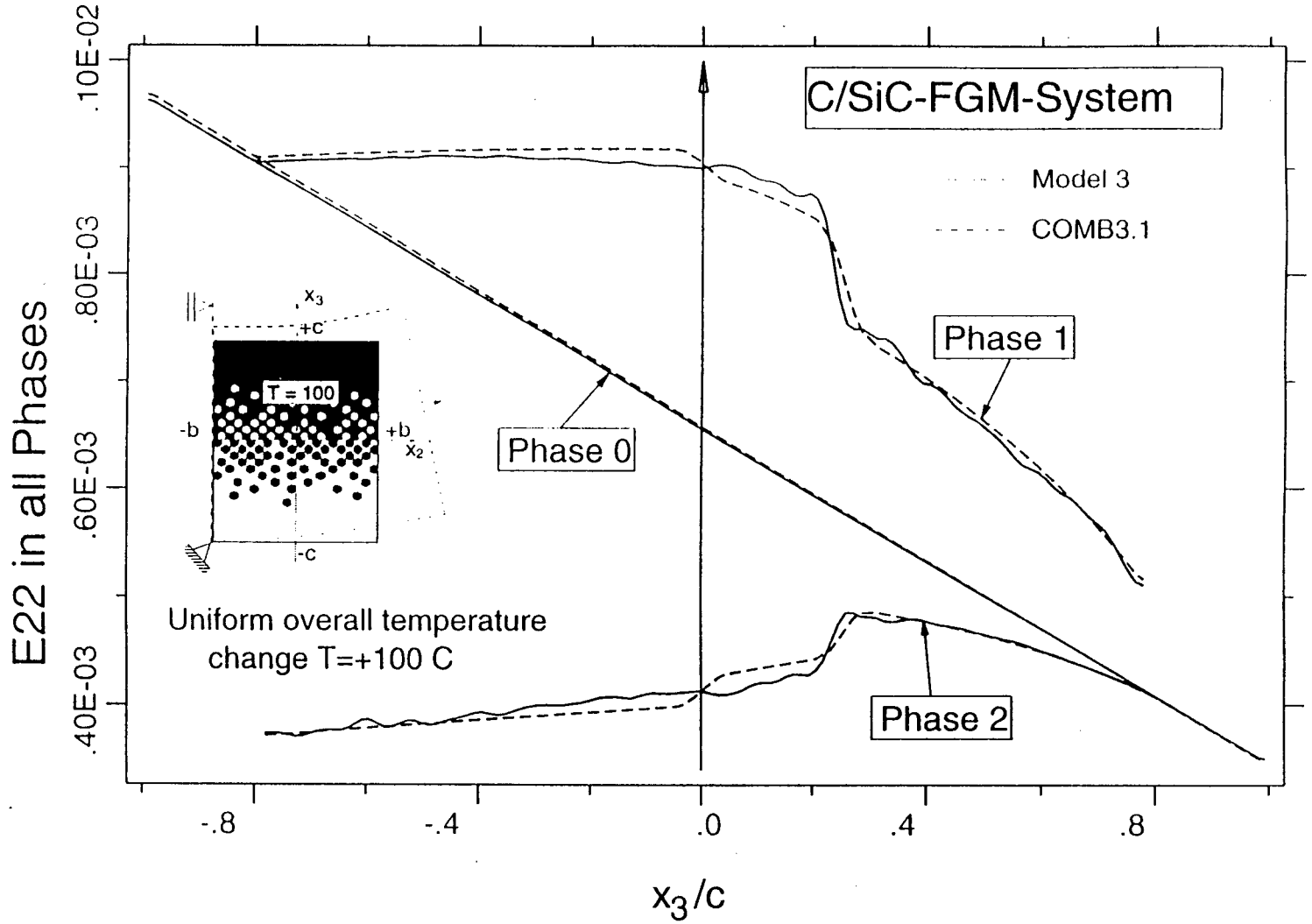


Fig. 11 Comparison of the average transverse strains $2\epsilon_{22}^{(r)}(x_3)$ caused by a uniform change in temperature, computed in the composite (Phase 0) and in Phase 1 (C) and Phase 2 (SiC) using the discrete Model 3 (solid lines), and the homogenized model COMB3.1 (dashed lines).

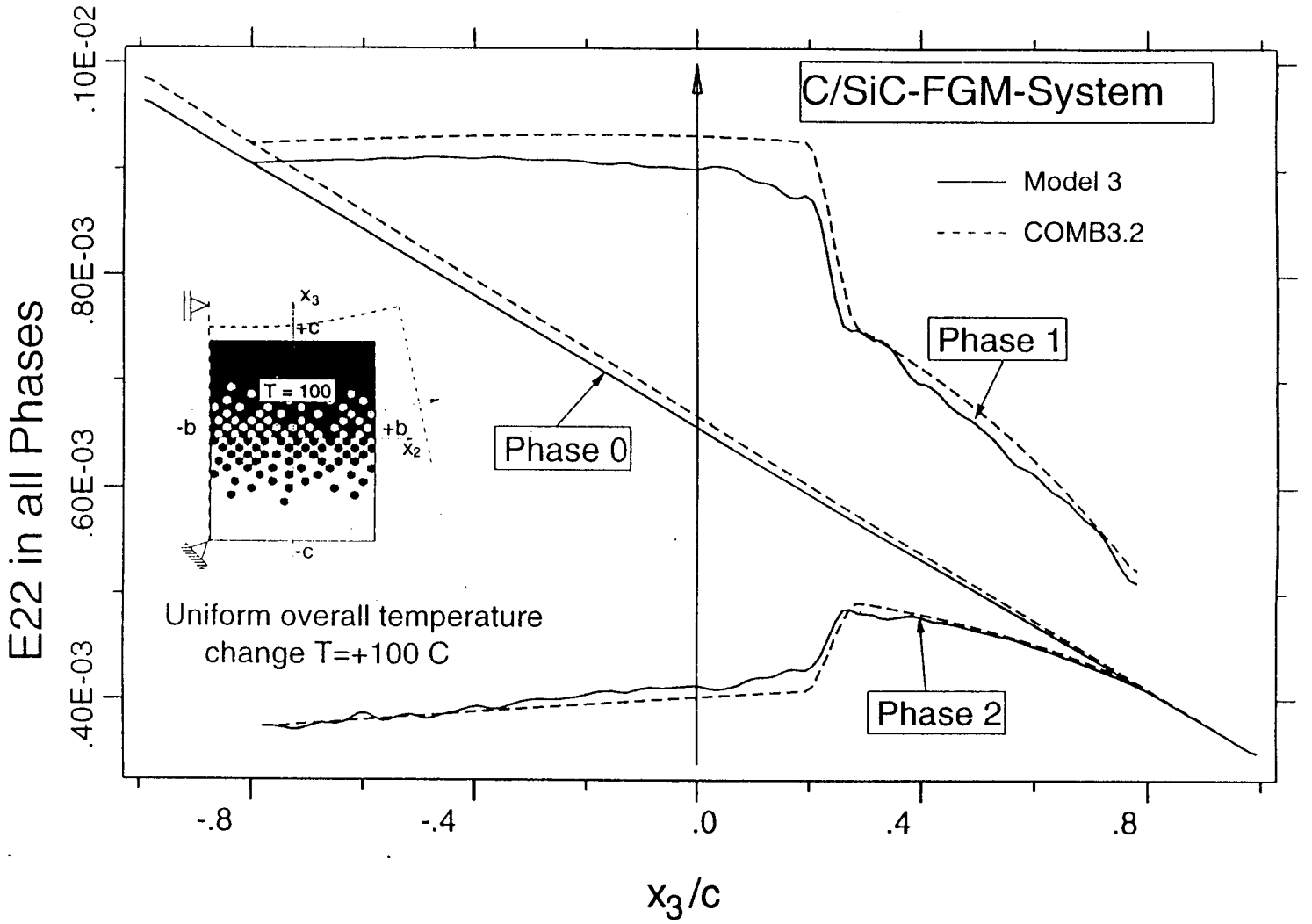


Fig. 12 Comparison of the average transverse strains $2\epsilon_{22}^{(r)}(x_3)$ caused by a uniform change in temperature, computed in the composite (Phase 0) and in Phases 1 (C) and 2 (SiC) with the discrete Model 3 (solid lines), and the homogenized model COMB3.2 (dashed lines).

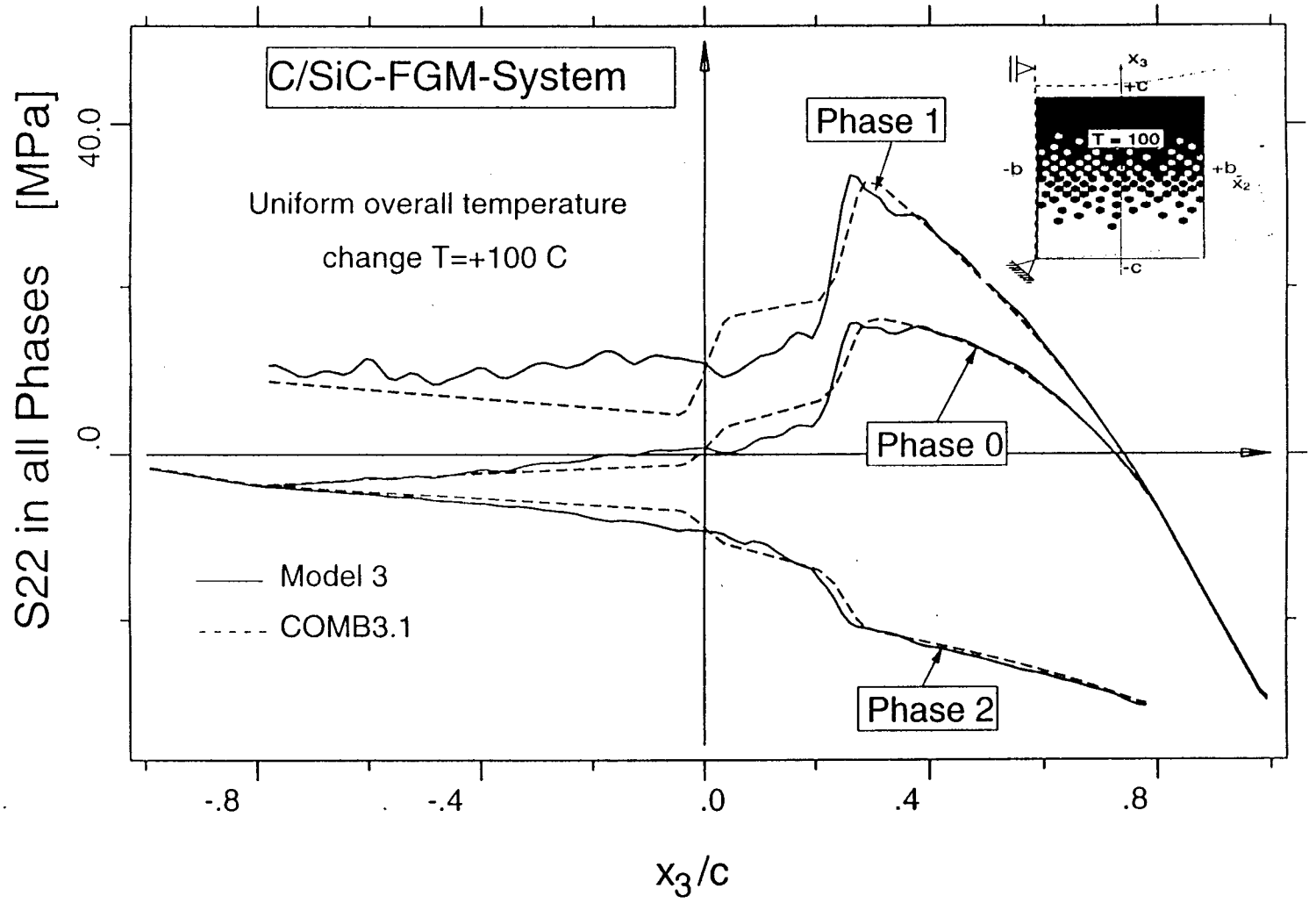


Fig. 13 Comparison of the average transverse stresses $\sigma_{22}^{(r)}(x_3)$ caused by a uniform change in temperature, computed in the composite (Phase 0) and in Phases 1 (C) and 2 (SiC), using the discrete Model 3 (solid lines), and the homogenized model COMB3.1 (dashed lines).

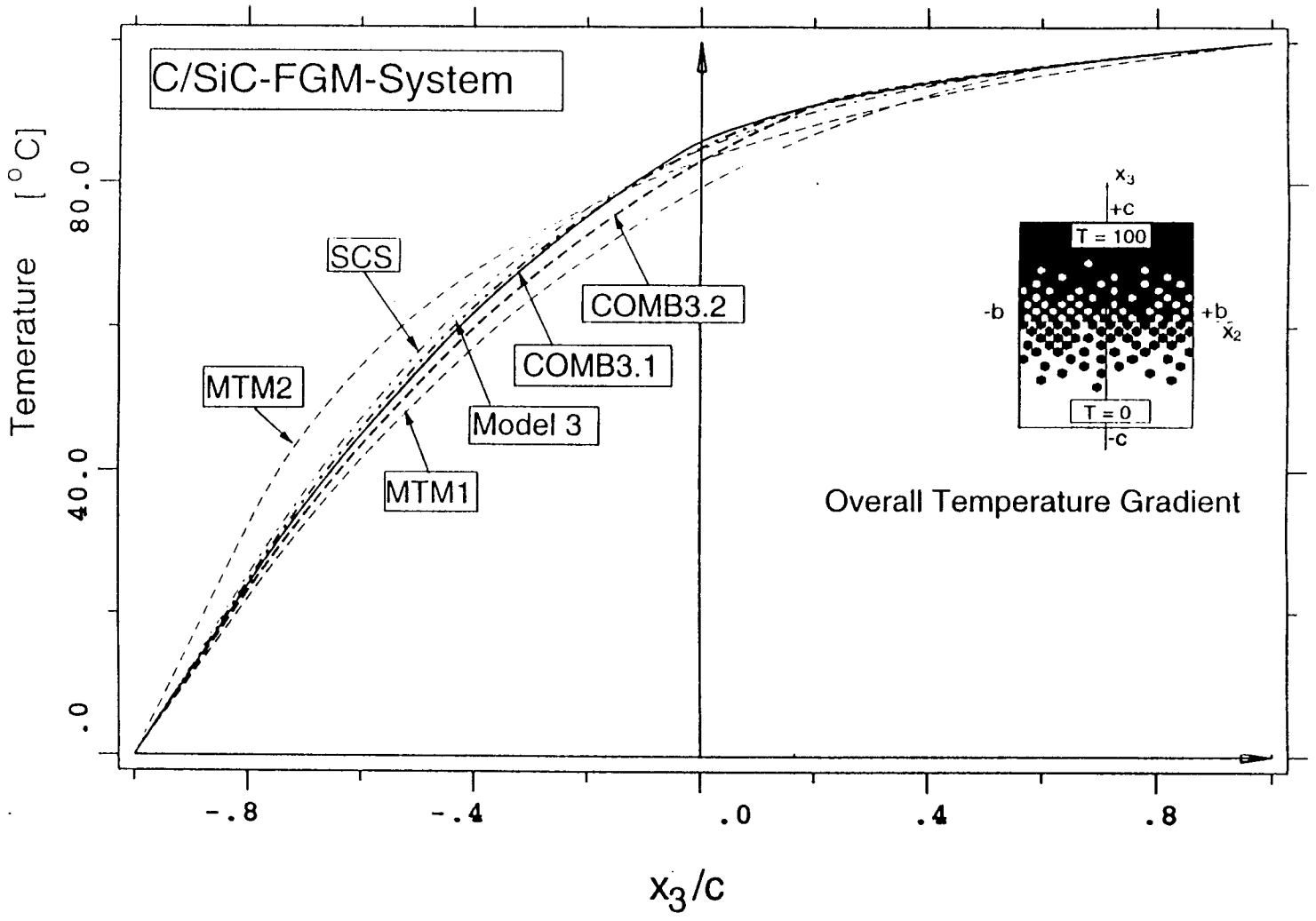


Fig. 14 Temperature distributions in the graded layer subjected to different surface temperatures, evaluated from discrete and homogenized models.

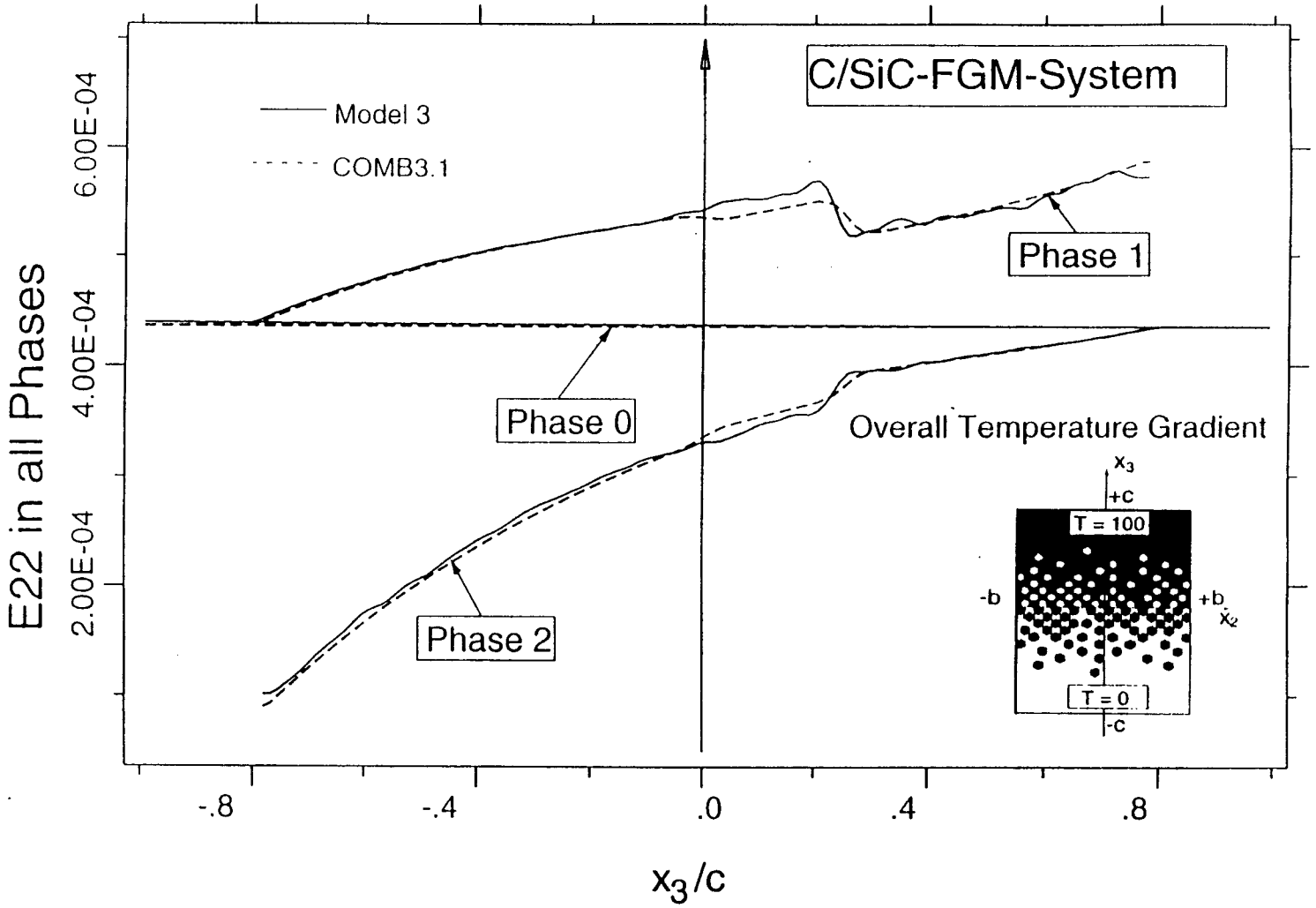


Fig. 15 Comparison of the average transverse strains $2\epsilon_{22}^{(r)}(x_3)$ caused by different surface temperatures, computed in the composite (Phase 0) and in Phases 1 (C) and 2 (SiC) with the discrete Model 3 (solid lines) and homogenized model COMB3.1 (dashed lines).

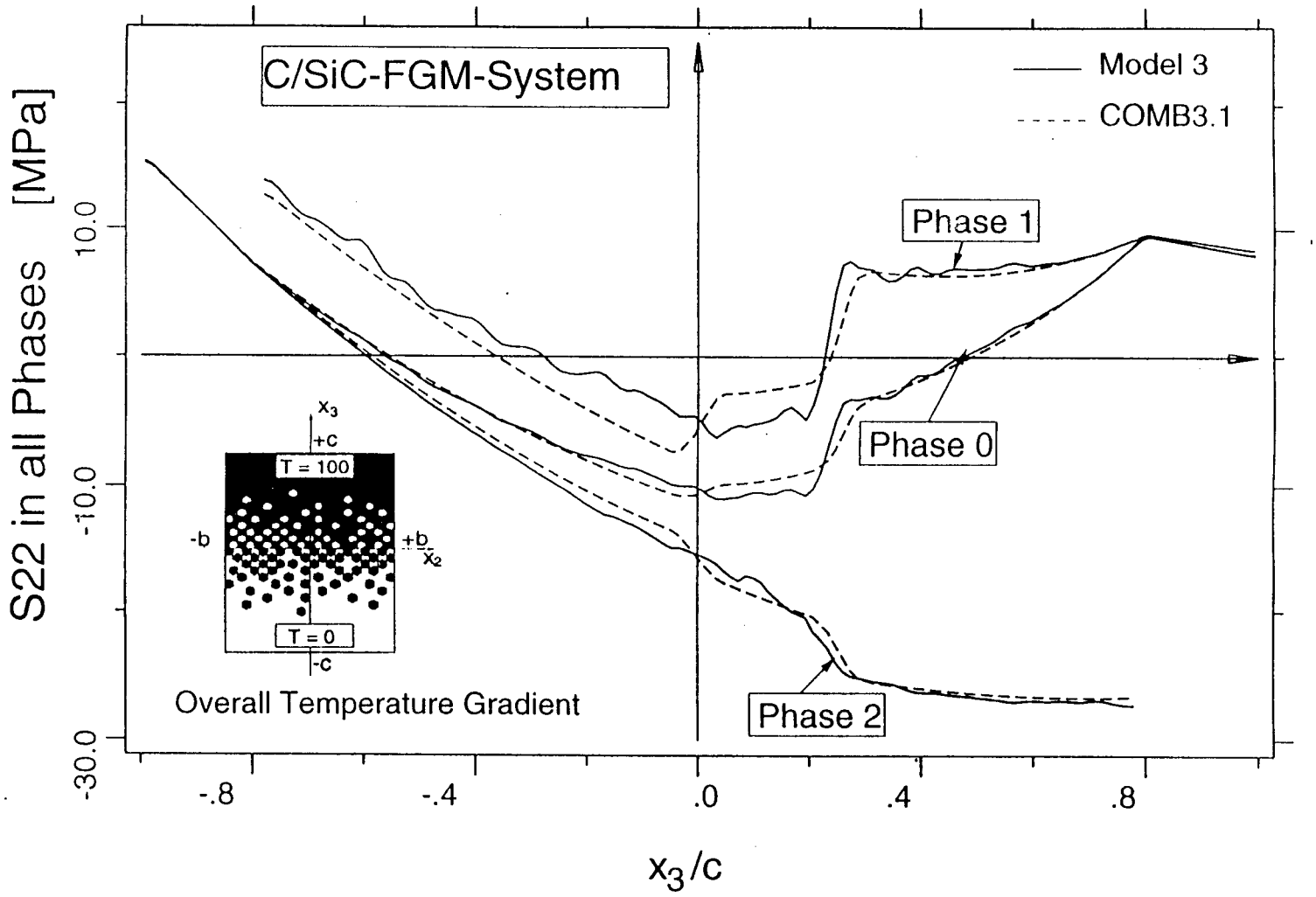


Fig. 16 Average transverse stress $\sigma_{22}^{(2)}(x_3)$ caused by caused by different surface temperatures, computed in the composite (Phase 0) and in Phases 1 (C) and 2 (SiC) using the discrete Model 3 (solid lines) and the homogenized model COMB3.1 (dashed lines).

Bimodal Plasticity Evaluation Tool

Kam-Lun Shek,† Mark W. Beall,† George J. Dvorak‡ and Mark S. Shephard†
†Scientific Computation Research Center
‡Department of Civil and Environment Engineering
Rensselaer Polytechnic Institute
Troy, NY 12180, USA

Abstract

For conceptual design and improving the process of metal matrix fibrous composite laminates, qualitative understanding of the evolution and interaction of the yield surfaces under thermo-mechanical loadings is essential. For this sake, a visualization tool is developed by using IBM Visualization Data Explorer. It is based on bimodal plasticity theory of Dvorak and Bahei-El-Din in which two distinct deformation modes are considered. The overall yield surface is the inner envelope of the two yield surfaces corresponding to two deformation modes among all laminae. By this evaluation tool, the two yield surfaces for two modes and their combined surface for each ply as well as the overall yield surface among all layers can be visualized freely in any 2D or 3D subspace of the 6-dimensional overall stress space, for individual layer or all layers. Also, some interesting features of the bimodal theory, that have not been reported, are found with this tool. In this paper, the theories behind are reviewed, the technical aspects of the program are discussed and some examples are given.

1 Introduction

It has been reported that inelastic deformations are not unusual in many actual metal matrix composite systems in the course of fabrication and processing [6]; moreover temperature changes in service may lead to yielding and raise the dimensional stability problem, it has been shown that some composite systems can be dimensional unstable under certain thermo-mechanical loadings [19]. However, the yield strains are usually small relative to the failure strain because of the high strength of fibers and the good ductility of the metal matrix phase. Therefore, it is critical to understand and design the metal matrix composite systems considering inelastic behavior.

For the sake of a better understanding of the behavior of the mathematical model and to more fully utilize the strength of materials, a visualization tool that gives qualitative insight to the thermo-mechanical behavior of metal matrix fibrous composite laminates is

developed. In the conceptual design stage, with the help of the visualization tool, designers can examine different design strategies, simulate different thermo-mechanical loading paths for the process and fabrication, and gain an understanding of the evolution and interaction of the yield surfaces. As a result, a better design of the laminates and improvement of the fabrication and processing are expected.

It is assumed here that the composite systems consist of transversely isotropic elastic fibers with circular cross section and an isotropic elastic-plastic matrix. The laminates are symmetric but the thickness of the layers can be varied. The visualization tool based on the bimodal plasticity theory is developed by using IBM Visualization Data Explorer [15, 16]. The bimodal plasticity theory, due to Dvorak and Bahei-El-Din [7, 2], provides a good estimation to the yield surface of metal matrix fibrous composites [8]. Furthermore, the computational effectiveness of the bimodal theory has been shown in reference [19].

In the bimodal plasticity theory, the plastic deformation of a composite lamina can be described in terms of two deformation modes, namely matrix dominated mode and fiber dominated mode. The two deformation modes give different branches of the overall yield surface which identify the state of stress that activates a particular mode, and indicate the conditions for mode transition in a given composite system. The overall yield surface for the laminated composite is, therefore, the inner envelope of the combined yield surface among all layers. The thermal shift of the yield surface is determined by using Dvorak's decomposition procedure [4, 5] which converts a uniform thermal loading to a mechanical one. Application of the bimodal theory to symmetric laminated plates can be found in [1] which, basically, distributes the external loading into individual layers in layers' local coordinates and then bimodal plasticity applies.

In the present visualization tool, the yield functions are calculated over a uniform grid within a bounding box. Afterwards the isosurfaces at which the yield functions equal to zero are established by the IBM Visualization Data Explorer [15, 16], Data Explorer for short. The two yield surfaces for two deformation modes and their combined surface for each layer, as well as the overall yield surface among all layers, can be visualized freely in any 2-dimensional or 3-dimensional subspace of the 6-dimensional overall stress space, for individual layer or all layers. Also, the branches from different layers in the overall yield surface are represented by different colors. It is accomplished by mapping different values to the yield surfaces of the layers, and the colors of the overall yield surface for different branches depend on their own values of colors.

The user interface, composed of four control panels and an image manipulation panel, is constructed with a set of visual program modules supplied by the Data Explorer. With the control panels, users interactively input the description of the laminates, degree of temperature changes and the visualization options. Also, a small material database is used so that the constituent properties are not explicitly needed in the user interface. The fundamental view options of Data Explorer, such as zooming, changing the view points, rotation of the images etc., are controlled through the image manipulation panel.

Section 2 describes the theory of bimodal plasticity and the decomposition procedure. Also,

some interesting features of the bimodal theory that have not been reported are discussed. In section 3, the application of the bimodal theory and the decomposition procedure to symmetric laminated plates are summarized. A general description of the visualization tool and the technical aspects are discussed in section 4. Finally, examples for different composite systems are given, in section 5, to show the capabilities of the tool and indicates how the information given by the program can be used to help making design decisions.

2 Bimodal Plasticity

The bimodal plasticity theory is a semi-phenomenological model [7, 2] which describes the plastic deformation of the metal matrix fibrous composite systems consisting of elastic fibers and elastic-plastic matrix. This theory has been shown in good agreement with the experiments performed by Dvorak and associates [8] for boron/aluminum at room temperature. Also, it has been implemented into ABAQUS — a commercial finite element package and its computational effectiveness has been shown by Wu [19]. Moreover, this theory applies to thermo-viscoplasticity [13] and damage analysis of laminates [10].

Two deformation modes exist in such composite systems, namely, the matrix dominated mode (MDM) and the fiber dominated mode (FDM). The shape of the MDM yield surface is material independent but its size depends on the magnitude of the yield stress of the matrix. In this mode, the plastic deformation is caused by slipping on matrix planes which are parallel to the fiber axis, in a way analogous to the deformation of single crystals. This mode can only be activated in those composite systems where the axial shear moduli of the fibers are substantially larger than that of the matrix. In the FDM, both phases deform together in the elastic and plastic ranges. It is treated as a general case of plastic deformation of a heterogeneous medium. In contrast to the MDM, the FDM is always activated except for a particular loading direction that generates a hydrostatic state of stress in the matrix. The stresses in both phases are calculated with the help of stress concentration factors. They are, as well as the overall stiffness of the composite, approximated by the Mori-Tanaka averaging method [17].

The yield surface predicted by this theory is somewhat different from that by micromechanical models. It has open ends in the overall stress space if von Mises criterion is adopted. This feature, as well as the material independency of MDM yield surface mentioned above, have not been reported in previous work and the physical interpretation of such features are discussed in this section. The overall yield surface, at this point, is the envelope combined by the MDM and FDM yield surfaces.

Since the actual yielding happens when one of the yielding modes be activated, the combined yield function can be calculated by comparing the function values of the MDM and FDM and adopting the one with larger numerical value which implies the stress state for that deformation mode is closer to the actual yield stress.

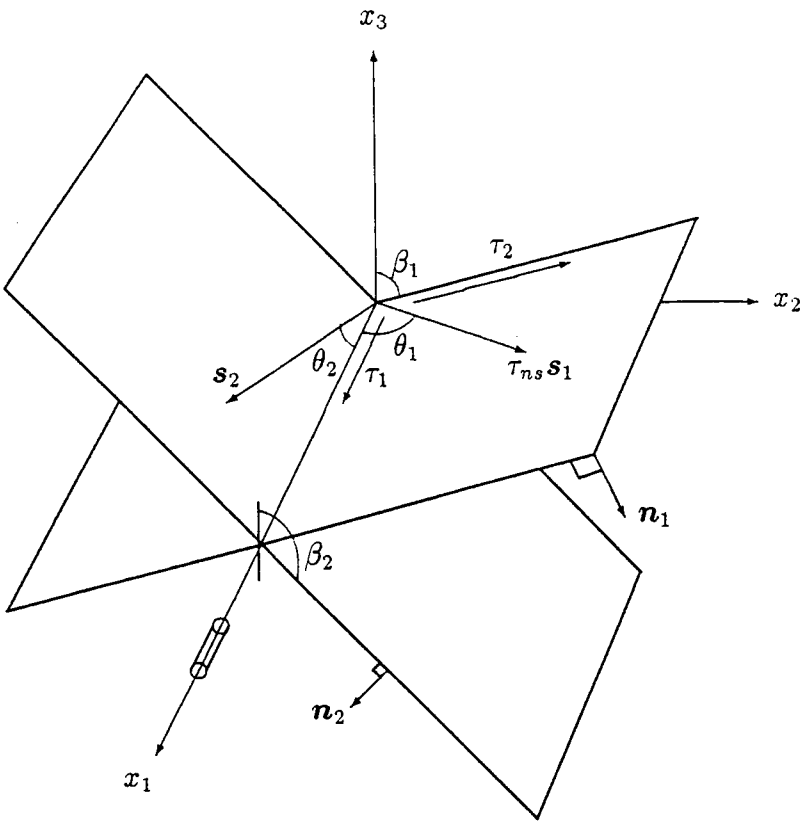


Figure 1: Geometry of Slip Systems

2.1 Matrix Dominated Mode

The mechanism of the MDM is characterized by the plastic shear deformation in the matrix on slip planes which are parallel to the fiber orientation, and in certain slip direction on these planes. The shape of the MDM yield surface is material independent but its size depends on the magnitude of the yield stress of the matrix phase; i.e. the shape of the yield surface corresponding to this mode does not change with the material moduli and the volume fractions of both phases. This mode can only be activated in those composite systems where the axial shear moduli of the fibers are substantially larger than that of the matrix, such as boron/aluminum (B/Al) and silicon-carbide/titanium-aluminum (SiC/Ti_3Al).

Consider a thin layer of a fibrous composite under macroscopically uniform state of plane stress. The fibers are aligned in the direction of the Cartesian coordinate x_1, the x_1x_2 plane coincides with the midplane of the layer. Figure 1 shows the geometry of the two slip systems $k = 1, 2$, that may become active under a macroscopic state of plane stress. The $\boldsymbol{n}_k$ denotes the unit vector normal to the slip plane k, $\boldsymbol{s}_k$ is the slip direction, β_k is the angle between the slip plane k and the x_1x_3 plane and θ_k is the angle between $\boldsymbol{s}_k$ and x_1 axis. Notice that the symbols now do not with subscript k for simplicity, so

$$\begin{aligned} \boldsymbol{n} &= [0,\ \cos\beta,\ -\sin\beta]^T \\ \boldsymbol{s} &= [\cos\theta,\ \sin\beta\sin\theta,\ \cos\beta\sin\theta]^T \end{aligned}$$

For a specific overall stress state $\boldsymbol{\sigma} = [\sigma_{11}, \sigma_{22}, \sigma_{33}, \sigma_{23}, \sigma_{13}, \sigma_{12}]^T$ with the center of yield surface $\boldsymbol{\alpha} = [\alpha_{11}, \alpha_{22}, \alpha_{33}, \alpha_{23}, \alpha_{13}, \alpha_{12}]^T$, the resolved shear stress τ_{ns} on a slip plane of normal $\boldsymbol{n}$ in slip direction of $\boldsymbol{s}$ is

$$\tau_{ns} = n_i\ (\sigma_{ij} - \alpha_{ij})\ s_j$$

The resolved shear stress τ_{ns} can further be resolved on the slip plane with components τ_1 and τ_2 by setting $\theta = 0$ and $\pi/2$ respectively, in the above equation,

$$\begin{aligned} \tau_1 &= \cos\beta\ (\sigma_{12} - \alpha_{12}) - \sin\beta\ (\sigma_{31} - \alpha_{31}) \\ \tau_2 &= \frac{1}{2}\sin 2\beta\ [(\sigma_{22} - \alpha_{22}) - (\sigma_{33} - \alpha_{33})] + \cos 2\beta\ (\sigma_{32} - \alpha_{32}) \end{aligned}$$

hence

$$\tau_{ns}^2 = \tau_1^2 + \tau_2^2$$

Among all the possible slip systems, the active slip planes are those have maximum resolved shear stress τ_{ns}, in words, the derivative of τ_{ns} with respect to the angle β is equal to zero

$$[\tau_{ns}(\beta)]_{max} \quad \Longrightarrow \quad \frac{\partial \tau_{ns}}{\partial \beta} = 0$$

and

$$\frac{\partial \tau_{ns}}{\partial \beta} = A\sin 4\beta + B\cos 4\beta - C\sin 2\beta - D\cos 2\beta \tag{1}$$

where

$$\begin{aligned} A &= \frac{1}{4}\left[(\sigma_{22} - \alpha_{22}) - (\sigma_{33} - \alpha_{33})\right]^2 - (\sigma_{23} - \alpha_{23})^2 \\ B &= (\sigma_{23} - \alpha_{23})\ [(\sigma_{22} - \alpha_{22}) - (\sigma_{33} - \alpha_{33})]\ . \\ C &= \frac{1}{2}\left[(\sigma_{12} - \alpha_{12})^2 - (\sigma_{13} - \alpha_{13})^2\right] \\ D &= (\sigma_{12} - \alpha_{12})(\sigma_{13} - \alpha_{13}) \end{aligned}$$

This equation can be arranged as the following form,

$$2B\cos^2 2\beta - D\cos 2\beta - B = (C - 2A\cos 2\beta)\ \sin 2\beta$$

By squaring the both sides of this trigonometric equation, it can be converted to a quartic equation, which can be solved analytically,

$$a_0 + a_1\, y + a_2\, y^2 + a_3\, y^3 + a_4\, y^4 = 0 \tag{2}$$

where

$$y = \cos 2\beta$$

and

$$\begin{aligned} a_0 &= B^2 - C^2 \\ a_1 &= 4AC + 2BD \\ a_2 &= -4\,(A^2 + B^2) + C^2 + D^2 \\ a_3 &= -4\,(AC + BD) \\ a_4 &= 4\,(A^2 + B^2) \end{aligned}$$

Details of solving this quartic equation can be found in standard mathematics handbooks or in [19]. Since this quartic equation is obtained by squaring the trigonometric equation 1, it can be easily shown that not all the roots of equation 2 are roots of the original trigonometric equation. A verification by back substitution of the roots into equation 1 is needed. Then the slip planes are defined as

$$\beta = \pm\,\frac{1}{2}\,\cos^{-1} y$$

Thus, the yield function of the matrix dominated mode is defined, for the case of kinematic hardening, as the following

$$[\tau_{ns}^2(\beta)]_{max} - \tau_0^2 = 0 \tag{3}$$

where

$[\tau_{ns}(\beta)]_{max}$ is the maximum resolved shear stress
τ_0 is the matrix yield stress in simple shear test

2.2 Fiber Dominated Mode

In the FDM, both phases deform together in the elastic and plastic ranges. It is treated as a general case of plastic deformation of a heterogeneous medium. In contrast to the matrix dominated mode, the fiber dominated mode is always activated except for a particular loading direction that generates a hydrostatic state of stress in the matrix phase (see section 2.4) which does not initiate plastic deformation in von Mises sense. Accurate micromechanical models for such deformation process are too complicated and computational inefficient for interactive visualization. It is useful to assume that the overall yield condition for onset of macroscopic plastic deformation is defined in terms of local stress averages [7]; therefore, averaging models, for instance, self consistent model and Mori-Tanaka method [17], can be adopted to find the local stress in the phases. In this evaluation tool, we use the Mori-Tanaka averaging scheme to estimate the overall stiffness as well as the stress concentration factors. Recalling that the fiber is assumed to be elastic and the matrix is elastic-plastic, the yield function of this mode in the overall stress space can be defined by making use of the matrix stress concentration factor. The Mori-Tanaka scheme is discussed in next section.

The fiber dominated yield function can be written in the following functional form

$$g_m(\boldsymbol{\sigma}_m - \boldsymbol{\alpha}_m) = 0$$

where g_m is a generic function that satisfies the well known Drucker's postulate and the subscript m stands for the matrix. This equation can be transformed into the overall stress space by the connection of matrix stress concentration factor $\boldsymbol{B}_m$

$$(\boldsymbol{\sigma} - \boldsymbol{\alpha}) = \boldsymbol{B}_m^{-1}(\boldsymbol{\sigma}_m - \boldsymbol{\alpha}_m)$$

in which $\boldsymbol{\sigma}$ and $\boldsymbol{\alpha}$ are the stress and the center of yield surface in the overall stress space. Then the fiber dominated yield function can be written as

$$g(\boldsymbol{\sigma} - \boldsymbol{\alpha}) = 0$$

In this effort, we select g_m in the von Mises form of yield criterion for the isotropic matrix, so the yield function is written as

$$g_m = \frac{1}{2}\,\boldsymbol{\sigma}_m^T \boldsymbol{Q} \boldsymbol{\sigma}_m - \tau_0^2 = 0$$

where

$$\boldsymbol{Q} = \begin{pmatrix} \frac{2}{3} & -\frac{1}{3} & -\frac{1}{3} & 0 & 0 & 0 \\ -\frac{1}{3} & \frac{2}{3} & -\frac{1}{3} & 0 & 0 & 0 \\ -\frac{2}{3} & -\frac{1}{3} & \frac{2}{3} & 0 & 0 & 0 \\ 0 & 0 & 0 & 2 & 0 & 0 \\ 0 & 0 & 0 & 0 & 2 & 0 \\ 0 & 0 & 0 & 0 & 0 & 2 \end{pmatrix}$$

and τ_0 is the matrix yield stress in simple shear test as in MDM. The yield function in overall stress space is

$$g = \frac{1}{2}(\boldsymbol{\sigma} - \boldsymbol{\alpha})^T \boldsymbol{B}_m^T \boldsymbol{Q} \boldsymbol{B}_m (\boldsymbol{\sigma} - \boldsymbol{\alpha}) - \tau_0^2 = 0 \tag{4}$$

with $\boldsymbol{\alpha} = \boldsymbol{0}$ for an initial yield surface of a stress free composite.

Note that, since the constant matrix $\boldsymbol{Q}$ in the above equations is singular, the matrix $\boldsymbol{B}_m^T \boldsymbol{Q} \boldsymbol{B}_m$ is also singular. This implies that the yield surface of the FDM is an open surface in the six dimensional overall stress space. This is discussed in detail in section 2.4 and an example is given in section 5. Particularly, the rank of $\boldsymbol{Q}$ in $\sigma_{11}\sigma_{22}\sigma_{33}$ subspace is two, therefore, the yield surface in this subspace is an open elliptical cylinder.

2.3 Mori-Tanaka Method

The Mori-Tanaka method [17] is one of the most popular methods for estimation of overall elastic moduli and phase concentration factors of composite materials. For the case considered here, a binary, matrix based composite system, the method assumes that the stress or strain in the fiber can be evaluated from a solution of the Eshelby's inclusion problem [11].

This suggests four partial concentration factors $\boldsymbol{T}$, $\boldsymbol{t}$, $\boldsymbol{W}$ and $\boldsymbol{w}$, they connect the local strain and stress fields as follows,

$$\boldsymbol{\epsilon}_f = \boldsymbol{T}\,\boldsymbol{\epsilon}_m + \boldsymbol{t}\,\theta, \qquad \boldsymbol{\sigma}_f = \boldsymbol{W}\,\boldsymbol{\sigma}_m + \boldsymbol{w}\,\theta$$

where $\boldsymbol{T}$ and $\boldsymbol{t}$ are stress concentration factors and $\boldsymbol{W}$ and $\boldsymbol{w}$ are strain concentration factors relate to single fibers (or particles) in an infinite matrix, the Eshelby's problem, and θ is the temperature increment with respect to the reference temperature. Also, they relate to materials moduli as

$$\boldsymbol{W} = \boldsymbol{L}_f\,\boldsymbol{T}\,\boldsymbol{M}_m$$

$$
\begin{aligned}
\boldsymbol{w} &= \boldsymbol{L}_f\,\boldsymbol{T}\,\boldsymbol{m}_m + \boldsymbol{L}_f\,\boldsymbol{t} + \boldsymbol{l}_f \\
\boldsymbol{T} &= [\boldsymbol{I} + \boldsymbol{P}(\boldsymbol{L}_f - \boldsymbol{L}_m)]^{-1} \\
\boldsymbol{t} &= (\boldsymbol{I} - \boldsymbol{T})(\boldsymbol{L}_m - \boldsymbol{L}_f)^{-1}(\boldsymbol{l}_f - \boldsymbol{l}_m)
\end{aligned}
$$

where $\boldsymbol{L}_r$ and $\boldsymbol{M}_r = \boldsymbol{L}_r^{-1}$ are the stiffness and compliance tensor; $\boldsymbol{l}_r$ is the thermal stress tensor and $\boldsymbol{m}_r$ is the thermal strain tensor of the expansion coefficients, such that $\boldsymbol{l}_r = -\boldsymbol{L}_r\boldsymbol{m}_r$ and $\boldsymbol{I}$ is a 6 by 6 identity matrix. Throughout the paper, the subscript or superscript $r = m, f$ stands for the matrix and the fiber phases, respectively.

The matrix $\boldsymbol{P}$ is a constant matrix which depends only on the matrix elastic moduli and the shape of the inclusion. In our case, unidirectional composite with cylindrical fibers aligned parallel to x_1,

$$
\boldsymbol{P} = \begin{pmatrix}
0 & 0 & 0 & 0 & 0 & 0 \\
0 & \frac{k_m+4m_m}{8m_m(k_m+m_m)} & -\frac{k_m}{8m_m(k_m+m_m)} & 0 & 0 & 0 \\
0 & -\frac{k_m}{8m_m(k_m+m_m)} & \frac{k_m+4m_m}{8m_m(k_m+m_m)} & 0 & 0 & 0 \\
0 & 0 & 0 & \frac{k_m+2m_m}{2m_m(k_m+m_m)} & 0 & 0 \\
0 & 0 & 0 & 0 & \frac{1}{2p_m} & 0 \\
0 & 0 & 0 & 0 & 0 & \frac{1}{2p_m}
\end{pmatrix}
$$

in which k_m, m_m, p_m are Hill's elastic moduli of matrix.

Therefore stress concentration factors can be obtained as

$$
\begin{aligned}
\boldsymbol{B}_f &= \boldsymbol{W}\,[c_m\boldsymbol{I} + c_f\boldsymbol{W}]^{-1} \\
\boldsymbol{B}_m &= \frac{1}{c_m}\,(\boldsymbol{I} - c_f\boldsymbol{B}_f)
\end{aligned}
$$

where c_m, c_f are volume fractions of matrix and fiber, respectively. Once $\boldsymbol{B}_m$ is found, the yield surface governed by fiber dominated mode is well defined in equation 4.

The explicit expressions of the overall elastic Hill's moduli by Mori-Tanaka method as defined by Chen and Dvorak [3] are

$$
\begin{aligned}
p &= \frac{2c_f p_m p_f + c_m(p_m p_f + p_m^2)}{2c_f p_m + c_m(p_f + p_m)} \\
m &= \frac{m_m m_f(k_m + 2m_m) + k_m m_m(c_f m_f + c_m m_m)}{k_m m_m + (k_m + 2m_m)(c_f m_m + c_m m_f)} \\
k &= \frac{c_f k_f(k_m + m_m) + c_m k_m(k_f + m_m)}{c_f(k_m + m_m) + c_m(k_f + m_m)}
\end{aligned}
$$

$$
\begin{aligned}
l &= \frac{c_f l_f (k_m + m_m) + c_m l_m (k_f + m_m)}{c_f (k_m + m_m) + c_m (k_f + m_m)} \\
n &= c_m n_m + c_f n_f + (l - c_f l_f - c_m l_m) \frac{l_f - l_m}{k_f - k_m}
\end{aligned}
$$

where p, m, k, l and n are elastic Hill's moduli. Then the overall elastic stiffness matrix is

$$
\bar{\boldsymbol{L}} = \begin{pmatrix}
n & l & l & 0 & 0 & 0 \\
l & k+m & k-m & 0 & 0 & 0 \\
l & k-m & k+m & 0 & 0 & 0 \\
0 & 0 & 0 & m & 0 & 0 \\
0 & 0 & 0 & 0 & p & 0 \\
0 & 0 & 0 & 0 & 0 & p
\end{pmatrix} \tag{5}
$$

This matrix is needed to construct the distribution factor in section 3. In this matrix, k, l and n are not independent, they are related by a universal connection [14],

$$
\frac{l - c_m l_m - c_f l_f}{n - c_m n_m - c_f n_f} = \frac{k - k_m}{l - l_m} = \frac{k_m - k_f}{l_m - l_f}
$$

between overall and phase moduli as well as volume fractions. Therefore, only three of the five overall Hill's moduli are independent.

2.4 Open Ends of the Yield Surface

For certain micromechanical models of composites, such as the periodic hexagonal array model [18], the predicted overall yield surface is always closed in stress space. This is not the case for the bimodal theory since it uses the average stresses for the phases instead of the actual local stresses. The overall yield surface predicted by the bimodal theory is open along a particular loading direction that depends on the stress concentration factor of the matrix phase $\boldsymbol{B}_m$ if von Mises criterion is used.

It is easy to show that the rank of the constant matrix $\boldsymbol{Q}$ in section 2.2 is five and the matrix $\boldsymbol{B}_m$ is of full rank. By the theory of linear algebra, the rank of the matrix $\boldsymbol{B}_m^T \boldsymbol{Q} \boldsymbol{B}_m$ is also five, that is, one of the eigenvalues of the matrix $\boldsymbol{B}_m^T \boldsymbol{Q} \boldsymbol{B}_m$ is zero. Following the principal axis theorem [12], one can conclude that the length of one of the semi-axes of the hyper-elliptical surface in the six dimensional overall stress space is infinity along the direction of the eigenvector corresponding to the zero eigenvalue. Such the eigenvector represents the loading direction that produces a hydrostatic stress in the matrix phase, that stress state will not generate any plastic deformation in the von Mises sense. The same conclusion can be drawn by a more engineering approach as following. The general form of $\boldsymbol{B}_m$ for transversely isotropic fibers embedded in isotropic matrix is

$$B_m = \begin{pmatrix} b_1 & b_2 & b_2 & 0 & 0 & 0 \\ b_3 & b_4 & b_5 & 0 & 0 & 0 \\ b_3 & b_5 & b_4 & 0 & 0 & 0 \\ 0 & 0 & 0 & b_6 & 0 & 0 \\ 0 & 0 & 0 & 0 & b_7 & 0 \\ 0 & 0 & 0 & 0 & 0 & b_7 \end{pmatrix}$$

where b_1 to b_7 are functions of material moduli of both phases and their volume fractions. If the assumption that initial yielding of the composite is governed by the average matrix stress is accepted, then it follows from the above formulation that there exist certain stress ratio for which yielding does not take place. To seek an external overall stress that induces hydrostatic stress in matrix, implying no yielding in case of von Mises yield criterion, one can make use the following equation

$$\begin{Bmatrix} q \\ q \\ q \\ 0 \\ 0 \\ 0 \end{Bmatrix} \sigma_0 = \begin{pmatrix} b_1 & b_2 & b_2 & 0 & 0 & 0 \\ b_3 & b_4 & b_5 & 0 & 0 & 0 \\ b_3 & b_5 & b_4 & 0 & 0 & 0 \\ 0 & 0 & 0 & b_6 & 0 & 0 \\ 0 & 0 & 0 & 0 & b_7 & 0 \\ 0 & 0 & 0 & 0 & 0 & b_7 \end{pmatrix} \begin{Bmatrix} 1 \\ \lambda \\ \lambda \\ 0 \\ 0 \\ 0 \end{Bmatrix} \sigma_0$$

The left hand side of the equation represents a hydrostatic stress in matrix phase and the right hand side is the overall stress that generates the hydrostatic matrix stress. It is easy to find that when

$$\lambda = \frac{b_3 - b_1}{2b_2 - b_4 - b_5} \tag{6}$$

the above equation holds. So, loading by this ratio of overall stress, the resulting average stress in the matrix phase is hydrostatic and yielding does not occur. In other words, the yield surface is open along the direction of such ratio of overall stress. An example for SiC/Ti_3Al in $\sigma_{11}\sigma_{22}\sigma_{33}$ overall stress space is given to show this case in section 5.

2.5 Decomposition Procedure

By using Dvorak's decomposition procedure [4, 5], one can convert a uniform temperature change on a two-phase composite medium to an equivalent mechanical loading and a uniform stress field which is hydrostatic in the matrix phase and transversely isotropic in the fiber phase. Since the uniform stress field generated by the temperature change is hydrostatic in the matrix phase, it has no effect to the yield surfaces. Therefore, the rigid body translation (thermal shift) of the yield surfaces of the composite that depends solely on the

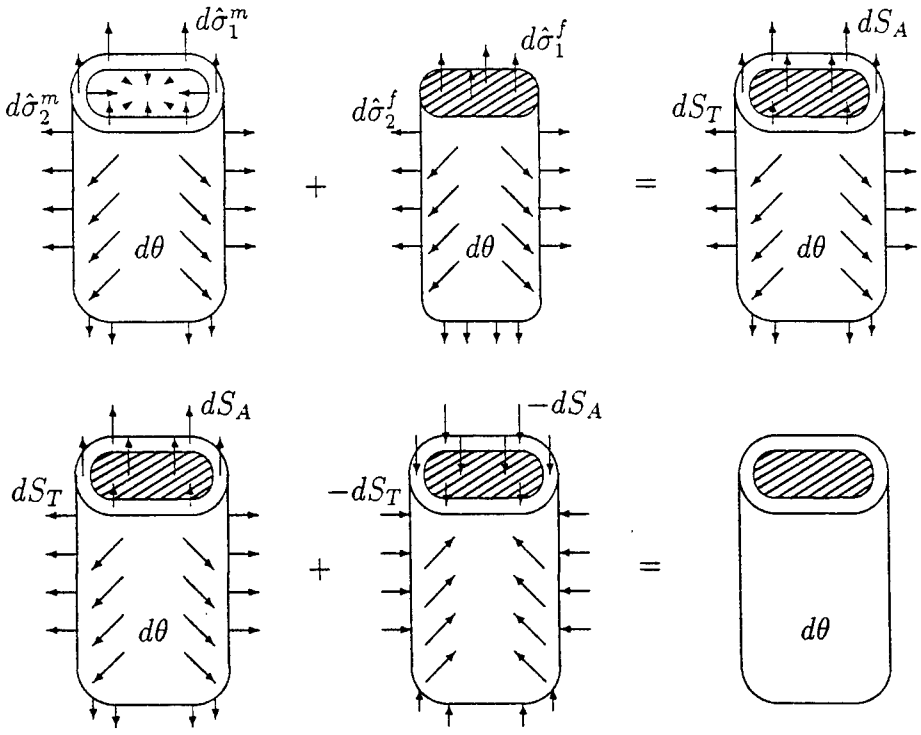


Figure 2: Decomposition Procedure

equivalent mechanical loading can then be found. Figure 2 shows schematically the steps in this procedure. It is summarized as follows:

1. The composite is separated into fiber and matrix phases which are subjected to surface tractions to maintain local phase stresses and strains.

2. A uniform temperature change $d\theta$ is applied to both phases which causes different local thermal strains and makes the phases incompatible if they are reassembled. To assure compatibility of phases, uniform tractions, $d\hat{\sigma}_1^r$ in axial direction and $d\hat{\sigma}_2^r$ in transverse direction, are applied to the phases simultaneously with temperature change.

3. $d\hat{\sigma}_1^r$ and $d\hat{\sigma}_2^r$ are found from the compatibility of phases and equilibrium of tractions at phase interfaces and on the surface of the composite.

4. The dS_A and dS_T are auxiliary uniform surface stresses which are added on the surface of the composite to preserve overall equilibrium while $d\hat{\sigma}_1^r$ and $d\hat{\sigma}_2^r$ are applied to the phases.

5. The phases are reassembled and the surface stresses are removed.

Readers can refer to the original work of Dvorak [4, 5] for detail derivations, only the relevant results are given here. The stress increments, $d\boldsymbol{\sigma}_f$ and $d\boldsymbol{\sigma}_m$, caused by simultaneous application of a overall stress increment $d\boldsymbol{\sigma}$ and a uniform temperature change $d\theta$ are:

$$d\boldsymbol{\sigma}_f = s_T \boldsymbol{\gamma} d\theta + \boldsymbol{B}_f(d\boldsymbol{\sigma} - \boldsymbol{s}_a d\theta), \qquad d\boldsymbol{\sigma}_m = s_T \tilde{\boldsymbol{I}} d\theta + \boldsymbol{B}_m(d\boldsymbol{\sigma} - \boldsymbol{s}_a d\theta) \tag{7}$$

where

$$\begin{aligned} \boldsymbol{s}_a &= [s_A, s_T, s_T, 0, 0, 0]^T \\ \boldsymbol{\gamma} &= [1, 1, \gamma, 0, 0, 0]^T \\ \tilde{\boldsymbol{I}} &= [1, 1, 1, 0, 0, 0]^T \\ \gamma &= \frac{s_A - c_m s_T}{c_f s_T} \end{aligned}$$

and

$$s_A = \frac{a_3 b_1 - a_1 b_3}{a_1 b_2 - a_2 b_1}, \qquad s_T = \frac{a_2 b_3 - a_3 b_2}{a_1 b_2 - a_2 b_1}$$

$$a_1 = \frac{n_f + \frac{c_m}{c_f} l_f}{k_f E_{lf}} - \frac{2}{3K_M}, \qquad a_2 = -\frac{l_f}{c_f k_f E_{lf}}, \qquad a_3 = 2\,(\alpha_{tf} - \alpha_m)$$

$$b_1 = \frac{l_f}{k_f E_{lf}} + \frac{1}{3K_m} + \frac{c_m}{c_f E_{lf}}, \qquad b_2 = -\frac{1}{c_f E_{lf}}, \qquad b_3 = \alpha_m - \alpha_{lf}$$

in which

K_m	is the matrix bulk modulus
α_m	is the matrix thermal expansion coefficient
E_{lf}	is the fiber axial Young's modulus
α_{lf}	is the fiber axial thermal expansion coefficient
α_{tf}	is the fiber transverse thermal expansion coefficient

In the above equations, the term $s_T \tilde{\boldsymbol{I}} d\theta$ is hydrostatic in the matrix, in words, the yield surfaces are not affected by this term. So, from the second term of the above equations, the equivalent overall stress for a temperature change, $d\theta$, is $-\boldsymbol{s}_a d\theta$. Therefore, it can be regarded as a rigid body movement of the center of the yield surfaces in overall stress space with the magnitude of $\boldsymbol{s}_a d\theta$ with respect to their original location.

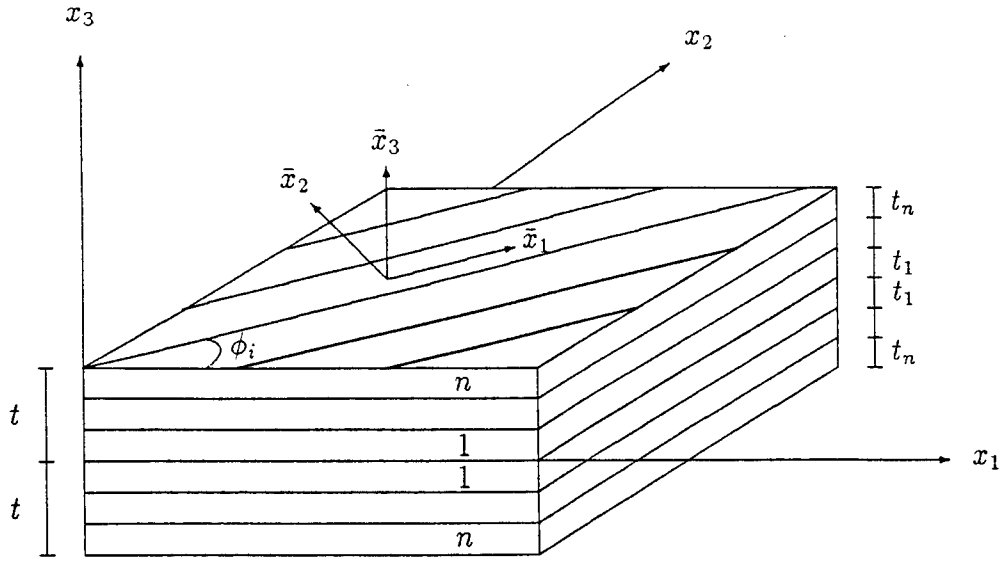


Figure 3: Geometry of a Fibrous Laminate

3 Bimodal Theory and Decomposition Procedure for Laminates

The bimodal plasticity theory and the decomposition procedure have been extended and applied to symmetric composite laminates by Bahei-El-Din [1]. Consider a symmetric laminated plate consisting of $2n$, perfectly bonded, identical fibrous laminae in which the matrix is isotropic and the fiber is transversely isotropic, and their thermo-mechanical properties do not vary with temperature and time. The fiber volume fraction is assumed equal in all layers but layer thickness can be different. The ply volume fractions are defined as $c_i = t_i/t$, where t_i are the ply thicknesses and $2t$ is the laminate thickness.

This arrangement can be regarded as macroscopically orthotropic, with three mutually perpendicular planes of symmetry such that one of these, the x_1x_2 plane, is the midplane of the plate and is parallel to the $\bar{x}_1\bar{x}_2$ planes associated with the laminae. The x_1 direction is referred to as the 0° direction. Fiber orientation of lamina i is specified with the angle ϕ_i between the $\bar{x}_1$ axis and the x_1, as shown in figure 3.

The laminated plate is assumed to be subjected to the general in-plane mechanical loadings and uniform changes in temperature. Both the plate and each of the plies are under the state of plane stress. The procedure of solving this problem is summarized as follows:

1. Distribute the overall loadings to the individual layers by using the distribution factors in global coordinate system.

2. Convert the ply loadings to their ply-coordinate systems, $\bar{x}_j$, then the bimodal theory for unidirectional lamina can be applied.

3. Apply a modified decomposition procedure to find the thermal shift of the layers.

3.1 Distribution Factors

Denoting the stress and strain for ply i in the global coordinate system, $x_j, j = 1,2,3$ by $\boldsymbol{\sigma}_i = [\sigma^i_{11}, \sigma^i_{22}, \sigma^i_{33}, \sigma^i_{23}, \sigma^i_{13}, \sigma^i_{12}]^T$ and $\boldsymbol{\varepsilon}_i = [\varepsilon^i_{11}, \varepsilon^i_{22}, \varepsilon^i_{33}, 2\varepsilon^i_{23}, 2\varepsilon^i_{13}, 2\varepsilon^i_{12}]^T$; ply stiffness and compliance by $\boldsymbol{L}_i$ and $\boldsymbol{M}_i$; and the symbols with an overbar are their counterparts in local coordinate systems, in which $\bar{\boldsymbol{L}}_i$ is found by using Mori-Tanaka method with equation 5. Therefore, the constitutive equations for ply i are

$$\boldsymbol{\sigma}_i = \boldsymbol{L}_i\boldsymbol{\varepsilon}_i, \qquad \boldsymbol{\varepsilon}_i = \boldsymbol{M}_i\boldsymbol{\sigma}_i$$

where

$$\boldsymbol{L}_i = \boldsymbol{T}_i^{-1}\bar{\boldsymbol{L}}_i\boldsymbol{R}\boldsymbol{T}_i\boldsymbol{R}^{-1}, \qquad \boldsymbol{M}_i = \boldsymbol{L}_i^{-1}$$

and

$$\boldsymbol{T}_i = \begin{pmatrix} \cos^2\phi_i & \sin^2\phi_i & 0 & 0 & 0 & 2\cos\phi_i\sin\phi_i \\ \sin^2\phi_i & \cos^2\phi_i & 0 & 0 & 0 & -2\cos\phi_i\sin\phi_i \\ 0 & 0 & 1 & 0 & 0 & 0 \\ 0 & 0 & 0 & \cos\phi_i & -\sin\phi_i & 0 \\ 0 & 0 & 0 & \sin\phi_i & \cos\phi_i & 0 \\ -\cos\phi_i\sin\phi_i & \cos\phi_i\sin\phi_i & 0 & 0 & 0 & \cos^2\phi_i - \sin^2\phi_i \end{pmatrix} \tag{8}$$

$$\boldsymbol{R} = \begin{pmatrix} 1 & 0 & 0 & 0 & 0 & 0 \\ 0 & 1 & 0 & 0 & 0 & 0 \\ 0 & 0 & 1 & 0 & 0 & 0 \\ 0 & 0 & 0 & 2 & 0 & 0 \\ 0 & 0 & 0 & 0 & 2 & 0 \\ 0 & 0 & 0 & 0 & 0 & 2 \end{pmatrix}$$

The inverse of matrix $\boldsymbol{T}$ can be found by replacing ϕ_i by $-\phi_i$. The overall constitutive equations of the laminated plate are

$$\boldsymbol{\sigma} = \boldsymbol{L}\boldsymbol{\varepsilon}, \qquad \boldsymbol{\varepsilon} = \boldsymbol{M}\boldsymbol{\sigma}$$

where $\boldsymbol{\sigma}$ and $\boldsymbol{\varepsilon}$ are the overall stress and strain; $\boldsymbol{L}$ and $\boldsymbol{M}$ denote the overall stiffness and compliance. Since all the layers are perfectly bonded and subjected to in-plane loadings and uniform thermal loadings (the thermal loadings are converted to the equivalent mechanical loadings as explained in next section), the strains must be equal in all plies:

$$\boldsymbol{\varepsilon} = \boldsymbol{\varepsilon}_1 = \boldsymbol{\varepsilon}_2 = \cdots = \boldsymbol{\varepsilon}_n$$

and the stresses in individual layers must be in equilibrium with the overall stress:

$$\boldsymbol{\sigma} = c_1\boldsymbol{\sigma}_1 + c_2\boldsymbol{\sigma}_2 + \cdots + c_n\boldsymbol{\sigma}_n$$

From these equations, one can obtain the overall stiffness as follow:

$$\boldsymbol{L} = c_1\boldsymbol{L}_1 + c_2\boldsymbol{L}_2 + \cdots + c_n\boldsymbol{L}_n$$

Defining the stress distribution factors, $\boldsymbol{H}_i$, which relate the ply stresses to the overall stress as

$$\boldsymbol{\sigma}_i = \boldsymbol{H}_i\boldsymbol{\sigma}$$

with the following property:

$$c_1\boldsymbol{H}_1 + c_2\boldsymbol{H}_2 + \cdots + c_n\boldsymbol{H}_n = \boldsymbol{I}$$

Then the distribution factors are found as

$$\boldsymbol{H}_i = \boldsymbol{L}_i\boldsymbol{M}$$

These results make it possible to find the phase stresses for individual layers in the local coordinate systems [9], for instance, the matrix stress of layer i, $\boldsymbol{\sigma}_{m(i)}$, is

$$\boldsymbol{\sigma}_{m(i)} = \boldsymbol{B}_{m(i)}\boldsymbol{T}_i\boldsymbol{H}_i\boldsymbol{\sigma} \tag{9}$$

in which $\boldsymbol{B}_{m(i)}$ are the stress concentration factor of the matrix phase for layer i.

3.2 Equivalent Thermal Loadings

The decomposition procedure discussed in section 2.5 was extended and applied to symmetric laminates by Bahei-El-Din [1]. The extension consists of treating the individual layer of the laminate as the phases of the unidirectional lamina. The layers are separated and the procedure in section 2.5 applies. The auxiliary uniform tractions (thermal shift of the MDM and FDM yield surfaces) for layer i in local coordinates are transformed to global coordinates by the transformation matrices T_i defined in equation 8. By considering the compatibility of the plies and the equilibrium of the auxiliary tractions, one can get the equivalent stress increment $d\boldsymbol{\sigma}^{eq}$ corresponding to a uniform change of temperature for the laminate in global coordinates as

$$d\boldsymbol{\sigma}^{eq} = -[s_1, s_2, s_T, 0, 0, s_3]^T d\theta \tag{10}$$

where

$$s_1 = s_A C_1 + s_T C_2, \qquad s_2 = s_A C_2 + s_T C_1, \qquad s_3 = \frac{1}{2}\left(s_A - s_T\right) C_3$$

$$C_1 = \sum_{i=1}^{n} c_i \cos^2 \phi_i, \qquad C_2 = \sum_{i=1}^{n} c_i \sin^2 \phi_i, \qquad C_3 = \sum_{i=1}^{n} c_i \sin 2\phi_i$$

and s_A, s_T are found in section 2.5.

Once $d\boldsymbol{\sigma}^{eq}$ is obtained, one can combine it with the mechanical loading, and transform the combined loading for individual plies in local coordinate systems by equation 9. Thus, the MDM and FDM yield surfaces for each ply can be found from the equations mentioned in section 2. The overall yield surface for the laminated plate is the most inner portion of the MDM and FDM surfaces among all layers.

4 Visualization Tool

The present visualization tool is designed for users to gain qualitative insight to the thermo-mechanical behavior of metal matrix fibrous composite laminates and therefore fully utilize the strength of materials. It is especially useful in the conceptual design stage where designers can examine different design strategies, simulating different thermo-mechanical loading paths for the process and fabrication. Based on the understanding of the evolution and interaction of the yield surfaces, a better design of the laminates and improvement of the fabrication and processing are expected.

As a qualitative evaluation tool, the visualization tool is designed to be flexible so that users can easily isolate the behavior of interest, for instance, one can isolate a particular layer

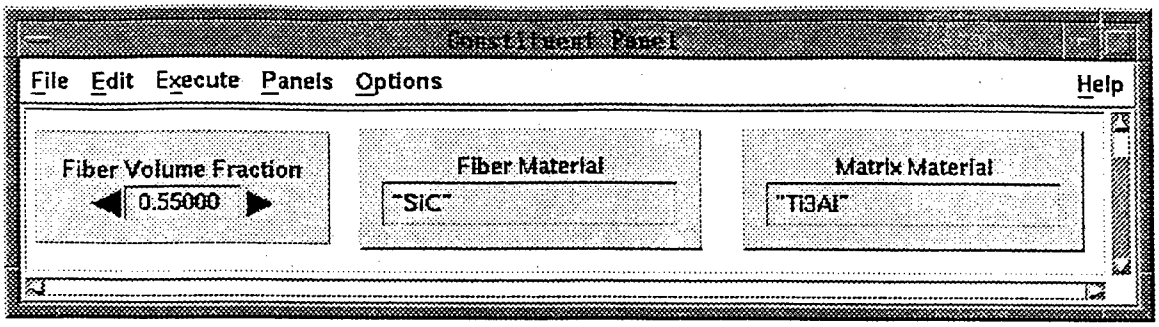


Figure 4: Constituent Panel

in a laminated plate and inspect the yield surfaces of the two deformation modes. On the other hand, one can turn off the deformation modes and display their combined surface of all layers, and see the yield surface interactions between the layers. At the same time, one can increase the temperature and see the evolution as well as the interaction among the surfaces. The visualization tool is written in C on a IBM RISC System/6000 workstation under the AIX operating system using the X Window System and Motif window manager.

This tool has two main modules, the bimodal module and the user interface module. The latter module is based on the IBM Visualization Data Explorer [15, 16] which provides a standard set of functional and visualization modules, such as selector, interactor, isosurface, streamline and autocolor etc. With such modules, one can select particular data objects from the whole data set and visualize them in variety ways. The interactor module is a data acquisition module that interacts with the user and therefore is used to define the material system and loading states. The operation of the program is interactively controlled by four control panels and a image manipulation panel.

The bimodal module consists of a set of routines that calculate the yield functions over a uniform grid based on the theories discussed in the sections 2 and 3. It is driven by the user interface module from where it obtains the needed information, such as the name of constituent materials, volume fractions, stack sequence of layers, display options etc. Two typical control panels that interact with the user are shown in figures 4 and 5. They make use of the interactor module that is basically standard widgets of Motif window manager, such as stepper, dial and slider widgets. The material properties of the constituents are stored in a small materials database that new materials can be added easily. Once the calculation of the yield functions are performed, they are passed back to the user interface module and then the isosurfaces, where the yield functions are equal to zero, are constructed by the appropriate visualization modules.

The colormap of branches from different layers of the overall yield surface is set in such a way that the branch from the first layer is red and the branch from the last layer is blue. A color bar is accompanied with the image of the yield surfaces that indicates what color stands for which layer.

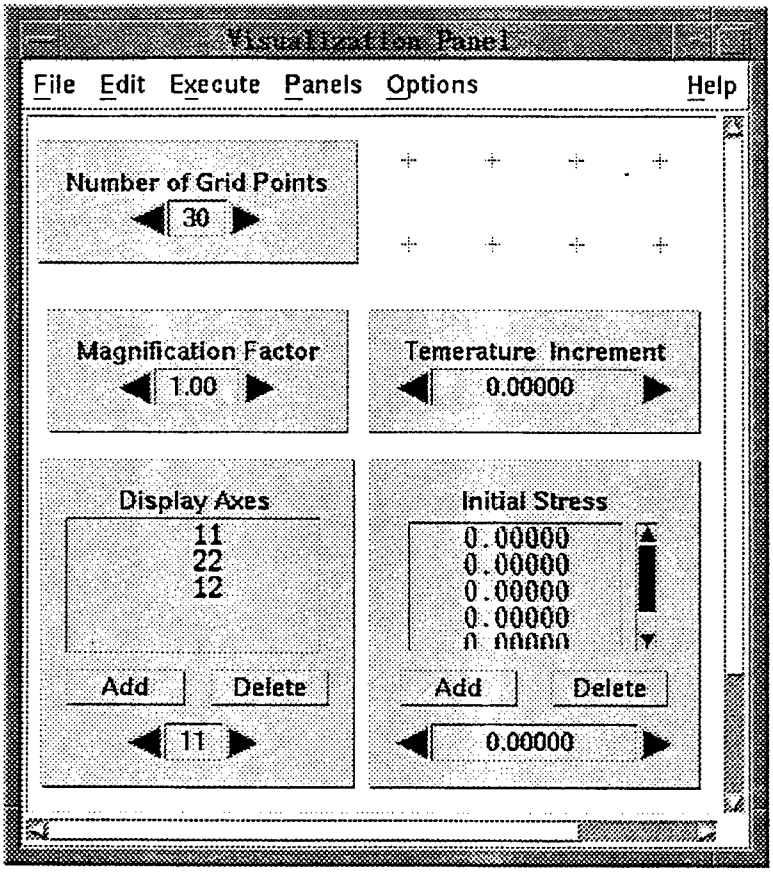


Figure 5: Visualization Panel

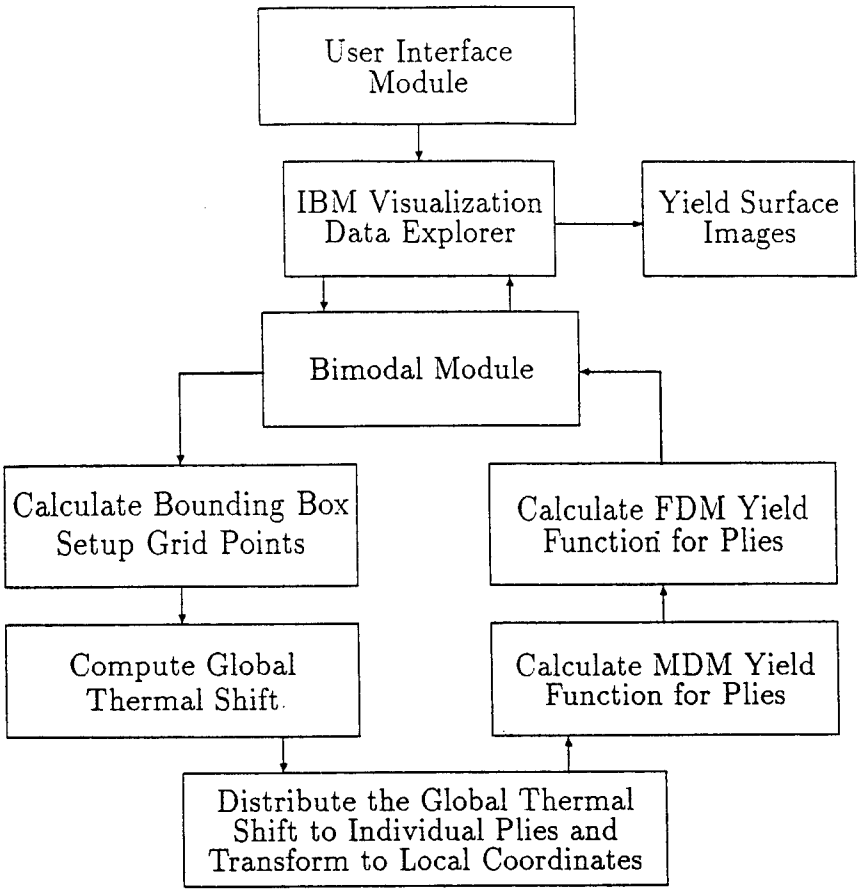


Figure 6: Program Flow Chart

4.1 Program Flow

The flow chart of the visualization tool is shown in figure 6. It starts from the user interface module that obtains the laminate descriptions and display options from the user; then the bimodal module calculates the MDM and the FDM yield functions for each ply over the uniform grid in a bounding box. Both the these two modules are built on top of Data Explorer, making use of its functional modules and data flow capabilities. The size of the bounding box depends on the size of the largest FDM surface. Afterwards, the values of the yield functions are passed back to Data Explorer to generate the yield surface images.

4.2 User Interface Module

The user interface module is composed of four control panels and a image manipulation panel where they are linked with a visualization control module, as shown in figure 7. Users input

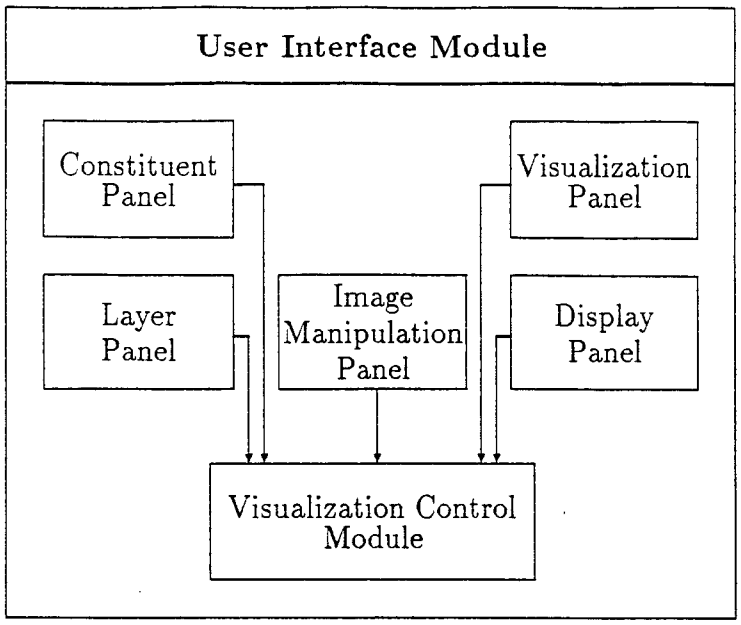


Figure 7: Structure of User Interface

the design parameters and display options with the control panels. A materials database is used to minimized the input. Such information is passed to the bimodal module through the data flow channels of Data Explorer, in which the data set of the yield functions are computed. Then the visualization control module selects information from the data set and generates the yield surface images which is chosen by the users through the control panels. Users can manipulate the yield surface images by the manipulation panel.

4.2.1 Control Panels

The four control panels, namely constituent, layer, visualization and display, respectively, is constructed by a set of interactor modules supplied by Data Explorer. The constituent panel and the visualization panel are shown in figures 4 and 5, the other panels are similar. The interactor module is basically a standard widget of Motif window manager in X window system, therefore, users familiar with basic X window system will not have difficulty using this tool. The functionality of the panels are:

Constituent Panel: The names of the constituents and the fiber volume fraction are inputed in this panel, as in figure 4. The elastic moduli and thermal expansion coefficients of the constituents are stored in the database, this minimizes the input needed from the user.

Layer Panel: In this panel, the number of layer, the thickness t_i and the orientation ϕ_i of each ply are given. Since it is assumed that the laminate is symmetric, information for only one half of the layers is needed.

Visualization Panel: This panel, shown in figure 5, allows users to input visualization parameters and thermo-mechanical situations of the laminate:

1. Density of the grid points in which the yield functions are evaluated.
2. Magnification factor for the bounding box.
3. Chose of any 2-D or 3-D subspace in the 6-D stress space to display.
4. Temperature increment with respect to the original state.
5. Initial stress components that are not in the displayed subspace.

Display Panel: There are four switches in this panel. This switches control which yield surface of which layer is displayed. Users can pick a particular layer of interest and display the yield surface for the individual deformation mode or display all of them at the same time; or show the combined surface with different colors represent different branches of two modes. Also, users can display all the yield surfaces from all layers and change the temperature at the same time to evaluate the evolution of the surfaces and their interaction between the layers.

Image Manipulation Panel: Fundamental view options, such as zooming, changing the view points, rotation of the images etc., can be controlled through this panel.

4.2.2 Visualization Control Module

The visualization control module is basically a module that contains a data object selector and a set of primitive visualization modules, such as isosurface, autoaxis and autocolor etc. The primitive visualization modules and the data object selector are supplied by the Data Explorer.

This control module controls the flow of the information obtained from the control panels and directs the selected data objects from the bimodal module to a particular set of visualization modules to generate the yield surface images on which are isosurfaces of zero value. Also, it identifies the branches of the yield surface that come from different layers and gives ordinal color indexes to the branches. The autocolor module (a primitive visualization module) assigns the appropriate colors for them. The color is set in such a way that the branch from the first layer is red and that from the last layer is blue.

4.3 Bimodal Module

The procedure of the bimodal module is shown in figure 6. The bimodal module solves a set of eigenvalue problems that give the size of the FDM surface for each layer as discussed in

Properties	SiC (982°C)	Ti_3Al (950°C)	B	Al
Young's modulus (MPa)	413000	46000	400000	72500
Poisson's ratio	0.25	0.3	0.2	0.33
Coefficient of thermal expansion (10^{-6}/°C)	6.3	18	4.7	0.234
Initial yield stress in simple shear test (MPa)		115.47		13.65

Table 1: Material Properties

section 2.4. According to the largest size of the FDM surface, the size of the bounding box is defined and the uniform grid is constructed. Equation 10 is used to calculate the global thermal shift. Then combining with the initial stress components of the non-displayed stress subspace, it distributes the overall stress to the plies and transforms the ply stresses to their local coordinates with equation 9. Afterwards, the MDM and FDM yield functions for each layer are found by equation 3 and 4.

5 Examples

In this section, two examples are given to show the yield surfaces of which different design parameters are specified for two composite systems. The interaction of the deformation modes between layers and the evolution under temperature change are shown. Also, a figure is shown the open ends of the yield surface that is different from those obtained from micromechanical models. The constituents properties are listed in table 1, the fiber orientation is along $x1$. In the following figures, the green surfaces represent the MDM surfaces while the FDM's are in yellow.

The first example shows the yield surfaces of a SiC/Ti_3Al composite laminated plate consisting of six layers and the stack sequence is $(0°/\pm 45°)_s$ and contains a fiber volume fraction 0.55. All layers have the same thickness. Since the plate is symmetric, only three set of yield surfaces are distinct. The MDM and FDM yield surfaces of all layers is displayed in $\sigma_{11}\sigma_{22}\sigma_{12}$ overall stress space, as shown in figure 8. For this composite system, the MDM is activated due to the large difference between the shear moduli of the phases. The set of surfaces oriented along σ_{11} direction represent the 0° layer and it interacts with the other two set of surfaces orient to different directions. The overall yield surface for the laminated plate is shown in figure 9. In this figure, the blue branch comes from the 0° layer; green from the $-45°$ layer and red represents the 45° layer. Figure 10 shows the laminate subjected to a temperature change of 500°C. It is clear that the overall yield surface shifts in σ_{11} and σ_{22} direction and the $-45°$ layer becomes more critical since the green area becomes larger than the former one.

The second example shows the difference of the yield surfaces of a B/Al unidirectional

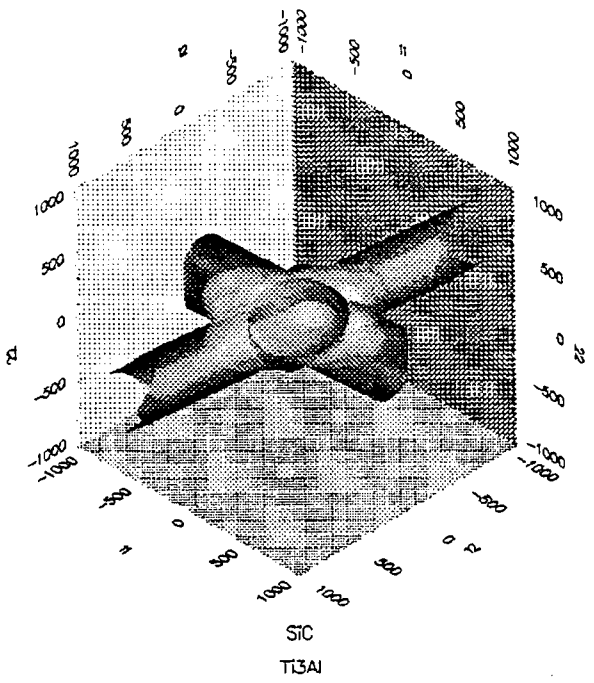


Figure 8: Yield Surfaces of a SiC/Ti_3Al Laminate

lamina between different fiber volume fractions. Figure 11 shows the composite of fiber volume fraction of 0.7 and figure 12 shows that of 0.4. The MDM surface for both cases are exactly the same because the MDM surfaces are independent of material moduli and volume fractions as discussed in section 2. The FDM surface of the one of $c_f = 0.7$ is substantially larger than the other one in σ_{11} direction but close in the other directions. Finally, figure 13 shows the open ends of the yield surfaces in $\sigma_{11}\sigma_{22}\sigma_{33}$ space.

6 Closure

In this paper, a visualization tool for the evaluation of the interaction and evolution of the yield surfaces for metal matrix fibrous composite system is developed. With the help of the tool, users can obtain qualitative insight to the thermo-mechanical behavior of the composite system; furthermore, interesting features of the bimodal theory that have not been reported are found. Detail computation procedures and technical aspects of the program are discussed.

References

[1] Y. A. Bahei-El-Din. Uniform fields, yielding and thermal hardening in fibrous composite

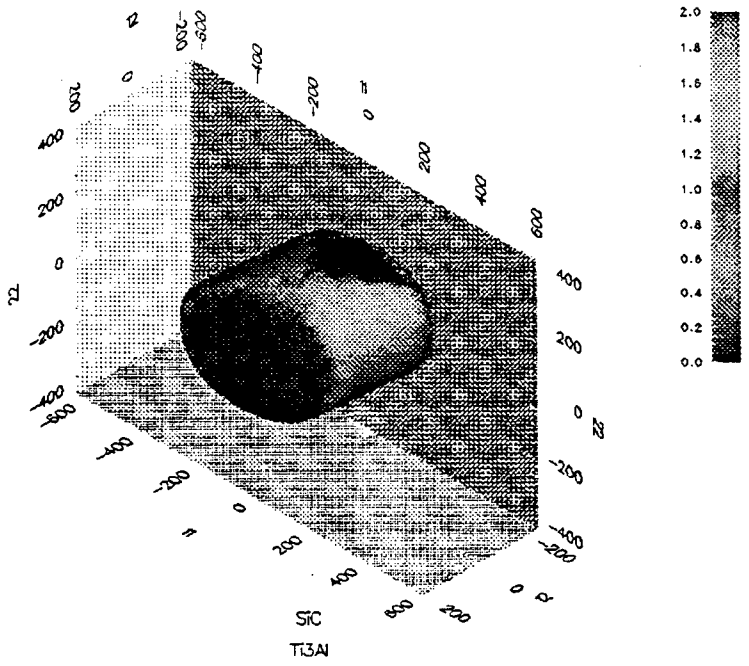


Figure 9: Overall Yield Surface of a SiC/Ti_3Al Laminate

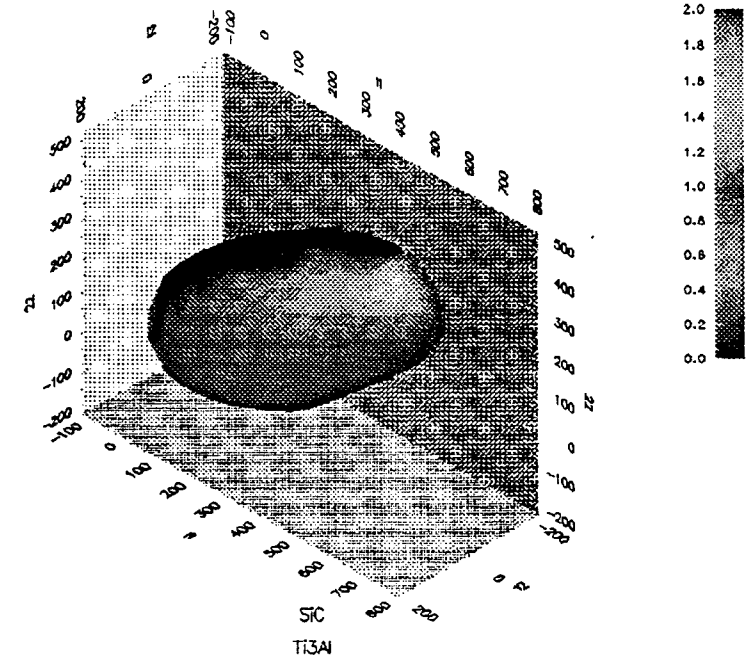


Figure 10: Overall Yield Surface of a SiC/Ti_3Al Laminate with Temperature Change

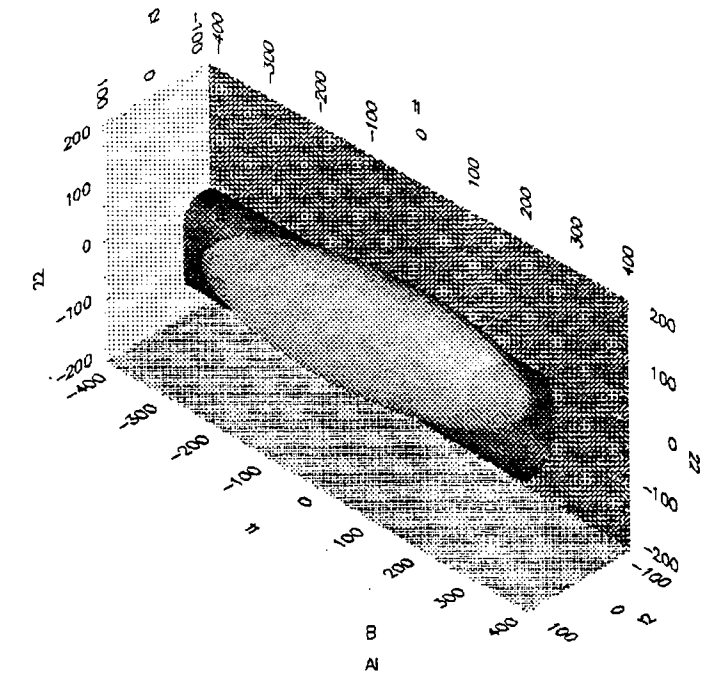


Figure 11: Yield Surfaces of a B/Al Lamina, $c_f = 0.7$

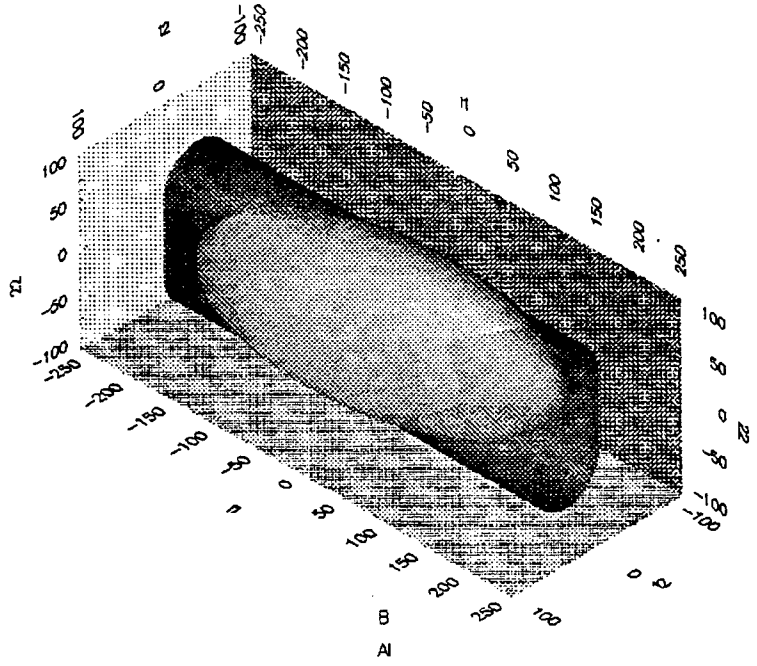


Figure 12: Yield Surfaces of a B/Al Lamina, $c_f = 0.4$

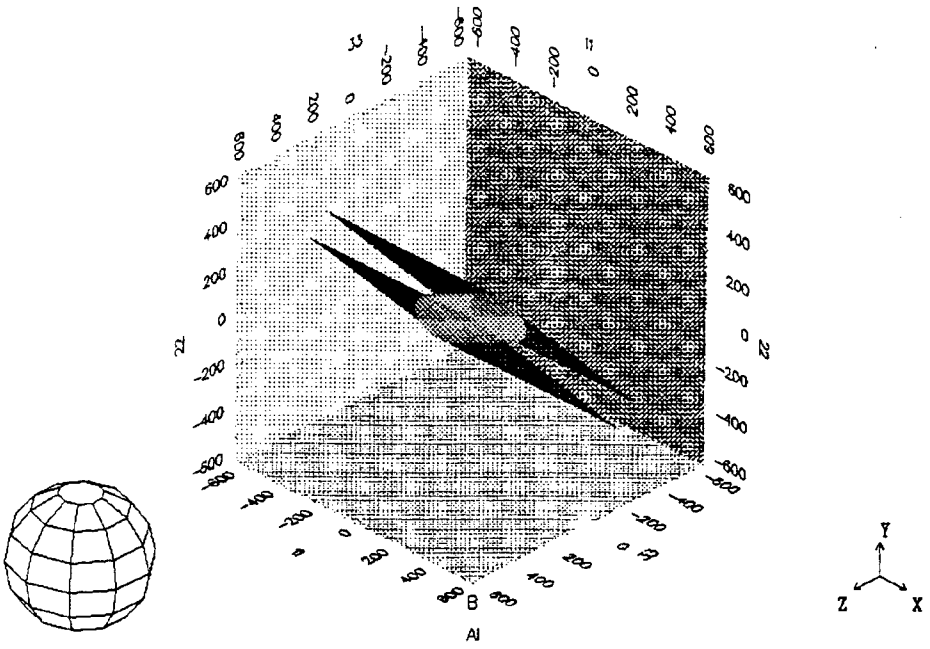


Figure 13: Yield Surfaces of a B/Al Lamina with Open Ends

laminates. *International Journal of Plasticity*, 8, 1992.

[2] Y. A. Bahei-El-Din and G. J. Dvorak. New results in bimodal plasticity of fibrous composite materials. In A. S. Khan and M. Tokuda, editors, *Advances in Plasticity 1989*. Pergamon Press, 1989.

[3] T. Chen and G. J. Dvorak. Mori-tanaka estimates of the overall elastic moduli of certain composite materials. *Journal of Applied Mechanics*, 59, 1992.

[4] G. J. Dvorak. Thermal expansion of elastic-plastic composite materials. *Journal of Applied Mechanics*, 108, 1986.

[5] G. J. Dvorak. Thermomechanical deformation and coupling in elastic-plastic composite materials. In H. D. Bui and Q. S. Nguyen, editors, *Thermomechanical Couplings in Solids*. Elsevier Science Publishers B. V., 1987.

[6] G. J. Dvorak. Plasticity theories for fibrous composite materials. In R. K. Everett and R. J. Arsenault, editors, *Metal Matrix Composites: Mechanisms and Properties*. Academic Press, 1991.

[7] G. J. Dvorak and Y. A. Bahei-El-Din. A bimodal plasticity theory of fibrous composite materials. *Acta Mechanica*, 69, 1987.

[8] G. J. Dvorak, Y. A. Bahei-El-Din, Y. Macheret, and C. H. Liu. An experimental study of elastic-plastic behavior of a fibrous boron-aluminum composite. *Journal of the Mechanics and Physics of Solids*, 36, 1988.

[9] G. J. Dvorak, T. Chen, and J. Teply. Thermomechanical stress fields in high temperature fibrous composites. ii: Laminated plates. *Composites Science and Technology*, 43, 1992.

[10] G. J. Dvorak, D. C. Lagoudas, and C. M. Huang. Fatigue damage of metal matrix composite laminates: Bimodal theory and damage optimization. In G. J. Dvorak and D. C. Lagoudas, editors, *Microcracking Induced Damage in Composites.* The American Society of Mechanical Engineers, 1990.

[11] J. D. Eshelby. The determination of the elastic field of an ellipsoidal inclusion, and related problems. *Proceedings of Royal Society of London*, A241, 1957.

[12] S. H. Friedberg, A. J. Insel, and L. E. Spence. *Linear Algebra.* Prentice-Hall, 1979.

[13] R. B. Hall. *Matrix-Dominated Thermoviscoplasticity in Fibrous Metal Matrix Composite Materials.* PhD thesis, Rensselaer Polytechnic Institute, 1990.

[14] R. Hill. Theory of mechanical properties of fiber-strengthened materials — i. elastic behaviour. *Journal of the Mechanics and Physics of Solids*, 12, 1964.

[15] IBM. *IBM Visualization Data Explorer, Programmer's Reference*, 1992.

[16] IBM. *IBM Visualization Data Explorer, User's Guide*, 1992.

[17] T. Mori and K. Tanaka. Average stress in matrix and average elastic energy of materials with misfitting inclusions. *Acta Metallurgica*, 21, 1973.

[18] J. L. Teply. *Periodic Hexagonal Array Model for Plasticity Analysis of Composites Materials.* PhD thesis, University of Utah, 1984.

[19] J. F. Wu. *Numerical Techniques for Elastic-Plastic Analysis of Fibrous Metal Matrix Composites.* PhD thesis, Rensselaer Polytechnic Institute, 1991.

Reliable Automated Engineering Analysis in an Integrated Design Environment

Mark S. Shephard, Vincent S. Wong,
Raymond R. Collar and Rolf Wentorf

SCOREC Report #6-1993
Scientific Computation Research Center

To appear: Conference Proceedings of NAFEMS 1993 International Conference, Brighton, England, May 26-29, 1993

Scientific Computation Research Center
Rensselaer Polytechnic Institute
Troy, NY 12180-3590
voice 5182766795
fax 5182764886

RELIABLE AUTOMATED ENGINEERING ANALYSIS IN AN INTEGRATED DESIGN ENVIRONMENT

M.S. Shephard[1], V.S. Wong[2], R.R. Collar[3], and R. Wentorf[4]

SUMMARY

This paper considers recent developments in specific areas needed to support reliable automated engineering modeling tools. The areas discussed are the integration of finite element modeling and geometric modeling using functional operators, the management of analysis attribute information, and the framework of an engineering analysis idealization control system.

1 INTRODUCTION

The availability of inexpensive computational power, generalized numerical analysis procedures and geometric modeling systems have prompted a number of researchers and developers to consider the additional capabilities needed to effectively combine and extend these tools to provide a powerful computational environment supporting engineering design. The efforts carried out in this area range from developing data models to transfer geometry to finite element applications, to a posteriori error estimation techniques to predict the mesh discretization errors. This paper discusses a selected set of developments which are a part of providing engineers with reliable tools to support the application of finite element analysis during design.

A key focus in the development of finite element tools must be ensuring their ability to reliably determine the requested performance parameters given a computerized definition of the artifact. Technologies that contribute to reliable finite element analysis in a design environment include:

1. Links between the geometric definition of an artifact and the discretization procedures which generate the finite element model.
2. Procedures for specifying the analysis attribute information needed to define a physical problem and linking it to the geometric representation of the domain.
3. Analysis idealization procedures to transform the computerized representation of the artifact into an idealized model appropriate for finite element analysis. These procedures must also be able to operate within the feedback loop of an adaptive analysis process.
4. Automatic finite element mesh generation procedures which can interact with the geometric model to generate the mesh, and interact with the adaptive analysis procedures to update the mesh as needed.
5. A posteriori error estimation procedures to measure the approximation errors introduced by the idealization steps.
6. Idealization update procedures for automatically improving the analysis idealizations.

---

1 Professor of Civil and Mechanical Engng., and Director of Scientific Computation Research Center, Rensselaer Polytechnic Institute, Troy, NY 12180-3590 USA

2 Graduate Research Assistant

3 Graduate Research Assistant

4 Research Engineer

Many of the papers in these proceedings address recent advances in one or more of these areas. Adaptive techniques to control mesh discretization errors for a variety of application areas are discussed. Recent developments in, and application of, automatic 3-D mesh generation are considered. Data transfer based on the STEP standard is also considered.

The links from the geometric definition and analysis attributes may be supported using standard data transfer methods. Alternatively a functional approach may be used. In this approach the analysis application interacts directly with the geometric modeling and attribute management systems to obtain the required information. Section 2 briefly reviews an operator driven approach to support the interaction of analysis applications with the geometric representation of the artifact. Section 3 considers the design and implementation of a generalized manager to house and control the analysis attribute information.

In addition to reliably controlling the mesh discretization errors, techniques are needed to perform and control all the idealization steps required to transform the computerized representation of the artifact to a numerical analysis model which will provide the requested level of accuracy. As with the idealization step of mesh discretization, these techniques must automatically perform the idealization steps within an adaptive feedback loop. Section 4 describes the framework of an idealization control system.

2 FUNCTIONAL INTEGRATION OF FINITE ELEMENT ANALYSIS WITH COMPUTER-AIDED GEOMETRIC MODELING SYSTEMS

The automatic generation of analysis idealizations and numerical discretizations of a physical problem requires a complete and unique representation of the physical domain. A substantial amount of research and development has been devoted to the creation of complete and unique geometric representations. Initially these efforts focused on the two-manifold representations referred to as solid models [9, 10]. More recently, the domain coverage of complete and unique representations has been extended to more general combinations of solids, surfaces and curves, referred to as non-manifold representations [6, 20].

One approach for providing the information needed for idealized model generation and discretization is a data file of the geometric model and data files of the information created by each idealization step. This approach has a number of deficiencies, as exemplified by considering the interactions of the analysis idealization steps with the domain definition. Analysis idealization processes must at least interrogate the geometric representation to obtain information not inherently in the model's data file. In addition, a number of the idealization processes require the modification of the geometric representation to define the idealized geometric form appropriate for the analysis. One approach supporting both of these needs employs operators that directly use the functionality of the geometric modeling system during the idealization steps. Such an approach is consistent with the dynamic interface methods of the CAM-I Application Interface Specification [3]. The application of such approaches for general finite element applications has been considered in reference [15], and has been shown to be the only method which ensures the reliability of interactions of applications with a geometric representation [17].

An example of an idealization procedure using such an approach is the Finite Octree automatic mesh generator [16]. The Finite Octree mesh generator interacts with the geometric modeling system through a set of 19 geometric operators [5]. All the operators are keyed via the topological entities of vertex, edge and face. Approximately one half of the operators

request basic topological associativities. The geometric interrogations used are limited to determining pointwise quantities such as the intersection points and surface normals. Most geometric modeling systems provide basic sets of interrogation operators in terms of callable routines. More recent geometric modeling systems are built using a tool kit of such routines making it easy for applications such as finite element mesh generators to access the needed functionality. The Finite Octree operators have been successfully developed for multiple geometric modeling systems including Parasolid (Fig. 1).

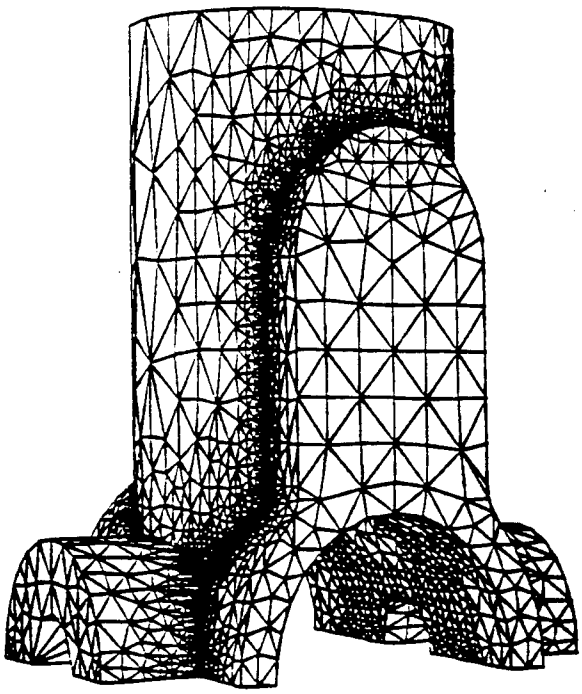


Figure 1. Finite Octree meshes of Parasolid models.

2.1 Example of Operator Driven Approach to Construct and Discretize Geometric Models for Multi-Chip Modules

An example application of the use of an operator driven approach to both define and discretize models, is the thermomechanical analysis of local regions of multi-chip modules using automated adaptive finite element techniques [1, 14].

A multi-chip module (MCM) is a complex three-dimensional object constructed of a number of substrate layers with embedded wires, which are connected between layers to make the appropriate electrical connections [19]. The most commonly used description of an MCM is a CIF file [7, 8]. The CIF file is not a complete geometric representation, but it provides a convenient structure for the specification of microelectronic components and is easy to interpret.

The automated adaptive finite element procedures used to analyze the MCM require a 3-D, multi-material solid model. Assuming the information in the CIF files corresponds to a valid geometry, a viable approach to construct the solid model is to use a specific knowledge-base to parse and translate the information into commands to automatically drive a solid modeling system through available modeling operators.

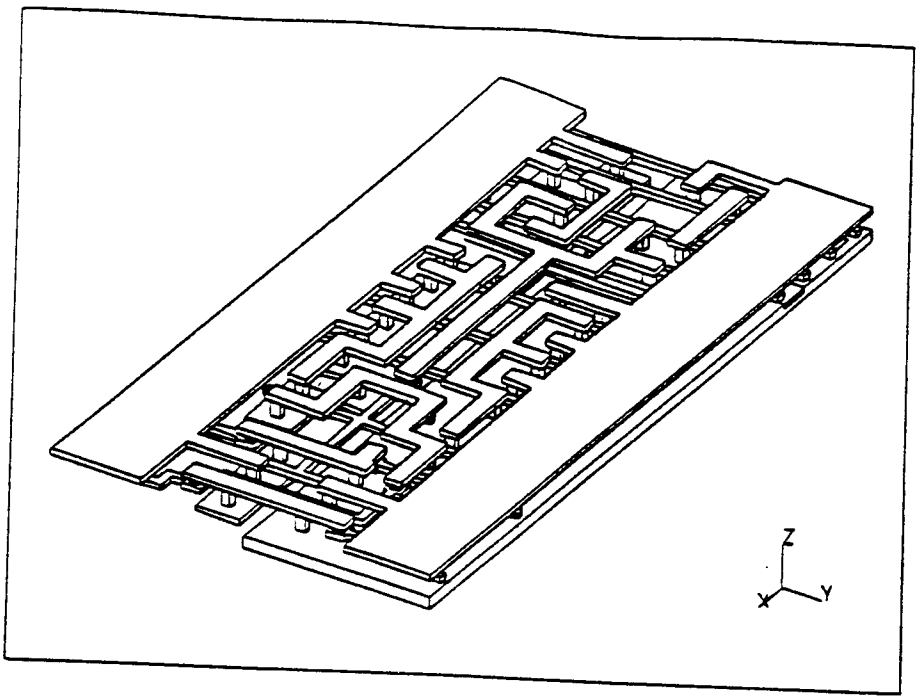


Figure 2. Parasolid model of a chip component from CIF.

A CIF file contains a 2-D layer description of the MCM in terms of rectangles, polygons, circles, and paths. When attributed with a thickness parameter, the CIF entity can be formed into an appropriate primitive in the solid modeling system. The primitives of a single material type can then be unioned to form a continuous solid. The network of wires, vias, contacts and interconnects in the MCM can be created in this manner. Figure 2 shows an example of a chip component created by a procedure which drives Parasolid [12] from CIF files.

The complete geometric representation must also include the insulating material around the wires, the solder bumps and the substrate, with a proper representation of the interfaces between them. Current solid modeling systems can not provide such non-manifold representations as needed by the automatic mesh generation procedures.

An examination of the functionalities of Parasolid indicated the existence of all the basic geometric operators, referred to here as *partial Booleans*, which allow for selective creation and retention of the desired geometries and topologies of all the entities needed for this class of non-manifold model. However, it does not currently provide all the non-manifold adjacency information required to maintain an understanding of the interactions of the various material regions. Typically the partial Booleans create two sets of coincident faces, edges, and vertices at the contact faces. Such redundant topology represents inconsistencies which will cause the automatic mesh generator to fail. However, by maintaining an understanding of the redundant relationships, it is possible to postprocess the model to eliminate the redundant entities and construct the correct topological uses needed by a proper non-manifold representation. In the current efforts, the radial-edge topological structure [20] is constructed.

With the non-manifold structure automatically constructed using the solid modeler operators, the initial finite element model can be automatically generated by Finite Octree using its operator interface (Fig. 3).

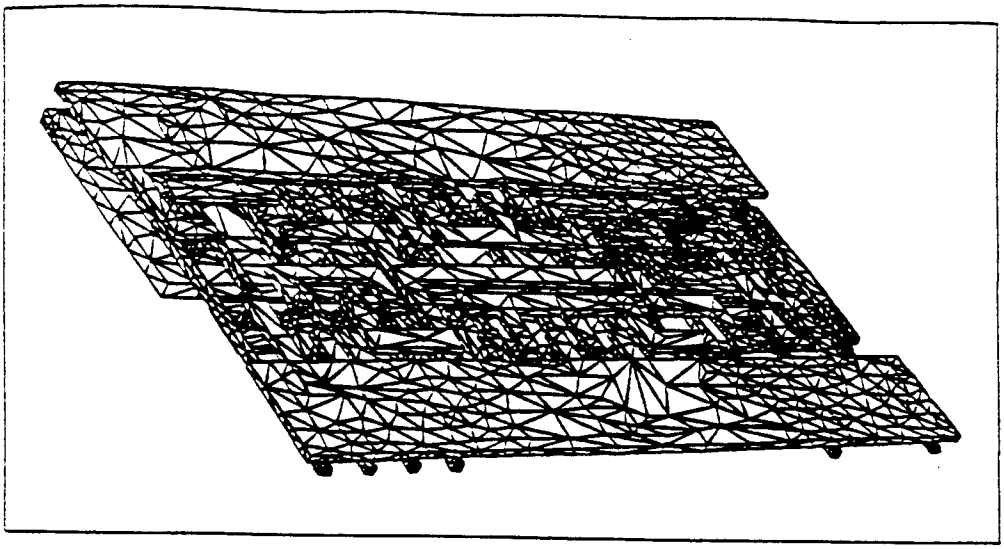


Figure 3. An example mesh of a Parasolid model of a chip component.

3 ANALYSIS ATTRIBUTE SPECIFICATION STRUCTURE

A general structure to support the specification of analysis attributes must i) allow for the specification of any attribute information, ii) house the organization of attributes to support a particular analysis process, and iii) maintain the associativity of the attributes with the geometric domain. Therefore, the structure to support attributes consists of three major groups of information: physical information, organizational information, and relational information. In general, attributes are tensorial in nature and possess spatial distributions [13].

The physical information used to prescribe an attribute is i) tensor order, ii) coordinate system, iii) tensor symmetry, and iv) distribution information of each tensor component (Fig. 4). A structure with considerable flexibility for the specification of attribute information has been developed based on these generalities. For example, distributions can be in terms of other distributions, or they can be results of a previous analysis. A key to this flexibility is the equation parser which reads in an equation, parses it, and stores it in a binary tree array in reverse Polish form. All the information needed for the evaluation of the tree is also stored. Depending on the components of the equation, the information can be values of the predefined constants, pointers to built-in or user functions, pointers to the predefined distributions, or pointers to the predefined attributes. An evaluation routine then evaluates the binary tree array, taking values from the appropriate places. To handle the complexity of general distributions and the manipulation of data and attributes from one analysis to another, **yacc**, a program that generates a parser based on a set of grammatical rules of the desired language, is used to generate the parser.

The organizational part of the attribute structure defines the groupings of the sets of attributes in relation to all working analysis cases. To support the various levels of groupings of attributes required in a design environment, a multi-level grouping structure complete with multipliers has been defined. Figure 5 gives a general indication of the type of groupings the organizational structure supports. In actual implementation this hierarchy is generalized into an efficient link structure.

The relational information ties the attribute information to the domain description through links to the appropriate topological entities. For example,

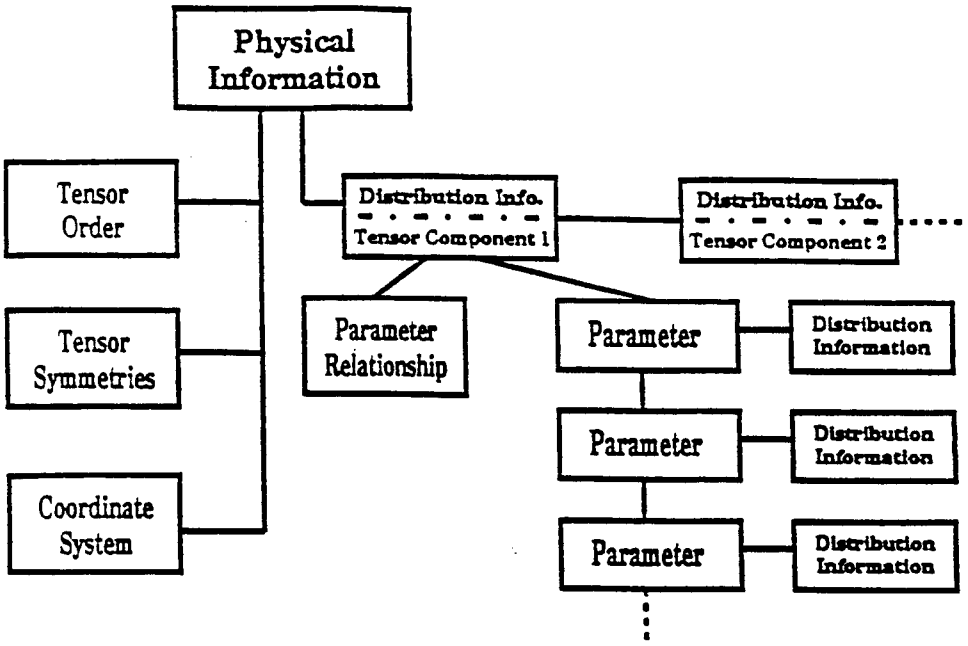


Figure 4. Basic structure to support the physical information defining an attribute.

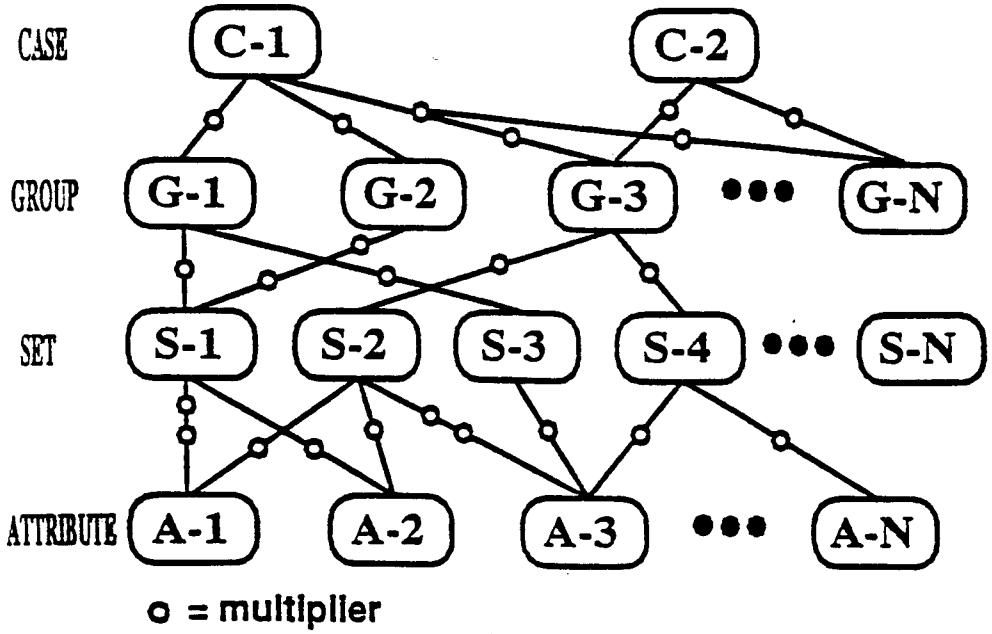


Figure 5. Organizational groupings supported by the attribute structure.

a surface load will be linked to the model face corresponding to that surface. If an attribute is defined to act over the complete topological entity the relational information is straightforward. However, attributes may act on portions of topological entities, or they may be defined in terms of auxiliary geometric entities defined solely for the specification of the attribute. In these cases the original geometric representation of the domain must be augmented by the auxiliary geometric entities and the appropriate relational information must be stored to produce the representation appropriate for the analysis discretization

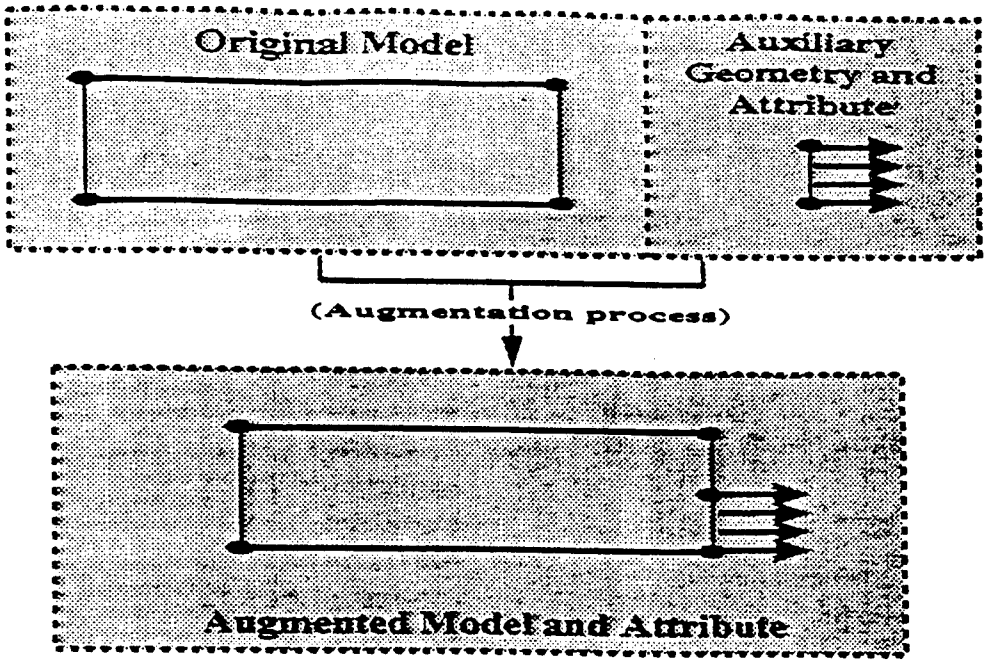


Figure 6. Relationship between the original model, the auxiliary geometry and edge load, and augmented model.

procedure. This process is depicted in Figure 6 for the simple case of an edge load over a portion of an edge.

A set of 64 operators have been defined to support the required augmentation processes. These operators are separated into categories of (i) definition of geometric and topological entities, (ii) interrogation of existing geometric and topological data bases, (iii) manipulation of geometric and topological entities, (iv) definition of attributes, (v) interrogation of attribute information, and (vi) manipulation of attributes.

4 ENGINEERING ANALYSIS IDEALIZATION CONTROL SYSTEM

The ability to apply idealization control during engineering design requires a framework which can house various levels of analysis idealization control with intelligent design methodologies and engineering analysis tools. The framework of a system that is specifically structured to support the idealizations used in engineering modeling and analysis is described in references [18, 21]. The system architecture is consistent with the architectures being considered to support design modeling systems in reference [4].

The heart of the system is the representation of the object being designed and the modelers that support that representation. To support the functions necessary in the design evolution of an object, its representation is housed in linked functional and geometric model structures, each of which are controlled by the appropriate modelers. The other operational components of the modeling system are the applications. The applications include analysis procedures to answer performance questions, algorithms to alter the design based on analysis results, and procedures to plan the manufacturing processes, etc. Applications are separated into two groups based on the technology underlying their implementation, not on the functions addressed. The first group is analytically-based applications. The majority of the applications in this group are numerical analysis and optimization procedures. The second group

is knowledge-based applications. Knowledge-based applications operate from codified heuristics placed in rule sets.

The task of analysis idealization control falls to the process navigator which guides the operation of the system. The process navigator interacts with the models, applications, and databases to track the various activities that have been performed and guides the application of those that are requested. The first task of the process navigator is to accept a request to perform an analysis, and determine if the basic information and capabilities required to perform the task exist. It is then responsible for formulating and controlling the idealization steps required to perform the requested analysis. It is also responsible for maintaining information about the status of the design and the tasks that have been performed previously.

4.1 Analysis Goals and Strategies

The execution of an analysis begins with the user specifying the goal to be performed. Within the system, a graph of all analysis goals is maintained to support the process of selecting valid analysis goals. The coordination of this process is accomplished by both rule-based and algorithmic procedures. The analysis goals vary in their level of detail, depending on the number of other analysis goals required for their completion. To accommodate this difference in level of detail, the analysis goals are placed in a hierarchy with the most detailed goals at the bottom level. The hierarchy is reflected in an analysis goal menu, which presents the analysis goals available at a given time in the design process.

Once a valid analysis goal is specified, the appropriate analysis strategy is initiated and applied in an automated manner. In general, there are a number of *a priori* and *a posteriori* idealization evaluation procedures associated with each idealization step. Evaluation procedures within the adaptive feedback loop of a strategy range from complex analytically based procedures to simple rules.

To support the addition and modification of goals and strategies by analysis experts, a set of generalized editing tools are provided for definition and manipulation of the goal graphs and analysis strategies. The ability to define feedback loops through the idealization steps to support *a posteriori* idealization improvement is a critical aspect of this process since the reliability of an analysis requires both the evaluation and improvement of idealizations. When the system is used in the context of engineering design, some goals may originate (automatically) from both the desired functional relationships between components in the functional model of the design, or from the criterion used to decide among design alternatives. In the reverse sense, an analysis goal and its results are a source of constraints for the functional, attribute and geometric models as they are refined to the next level of detail. The system is designed to track such situations.

4.2 Example Application of Engineering Idealization Modeling System

The example application considered is the design of planar brackets. The feature-based functional model representation indicates the functional relationships of various manufacturing features. The functional and geometric information is used in conjunction with a stress analysis to determine which features have a negligible effect on the stress solution. The example presented demonstrates a procedure for geometric simplification of lightening holes in low stress areas. Figure 7 shows the functional and geometric model for a bracket example.

The tools needed for cost effective, reliable, automatic stress analysis are available in the form of automated adaptive finite element analysis programs

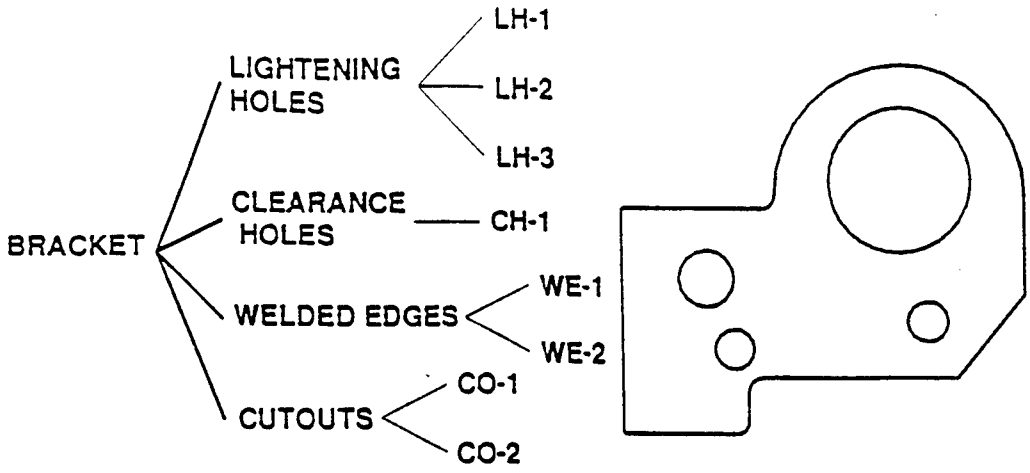


Figure 7. Functional and geometric model for an example bracket.

[2]. However, their effective application in design requires the development of procedures to control the idealization errors associated with geometric and boundary condition simplifications present during the design process. Techniques to control these idealizations are particularly important during the design process since it is often desirable to perform analyses at times when geometry and boundary conditions are not yet fully known. It is typically the purpose of the analysis to aid in the determination of the values or acceptable limits of those quantities.

Rule-based idealization procedures to control geometric simplifications consider the analysis goal and the state of the design in making the preliminary idealizations for the initial analysis step. The functional model uses its links to the geometric model, and information on the state of the design, to communicate the feasibility of the idealization procedures under consideration, and to indicate if the analysis goal can be addressed at the current point in the design process. The functional modeler also interrogates the geometric representation to determine needed geometric parameters, or to perform required geometric reasoning.

The procedure for determining when circular holes can be neglected uses the results from an analysis in combination with analytic solutions. The first step is to geometrically determine candidate holes. A candidate hole is one that is assumed to be small enough to cause only local variations in the load paths through the structure. A candidate hole must be far enough from a boundary that known analytic expressions may be used as meaningful indicators. For the sample bracket (Fig. 8), the three small holes (LH-1, LH-2, LH-3) are selected as candidate holes, creating an idealized functional representation (Fig. 8).

The second step is to perform a stress analysis with all candidate holes neglected. This is accomplished by the automated adaptive analysis procedures. The topological model entities associated with the loops defining the candidate holes are flagged to be neglected. The mesh generation process then simply does not use these (Fig. 9).

The third step is to use the stresses from the finite element analysis to estimate the peak stress around each neglected hole and update the idealization if necessary. The peak stresses are found by multiplying the stresses determined in the area of the hole by a stress concentration factor derived from analytic solutions [11].

If the peak stress around a neglected hole is below a threshold, that idealization is accepted, if it is above, the idealization must be improved. The next mesh is generated using the updated model idealization. Subsequent

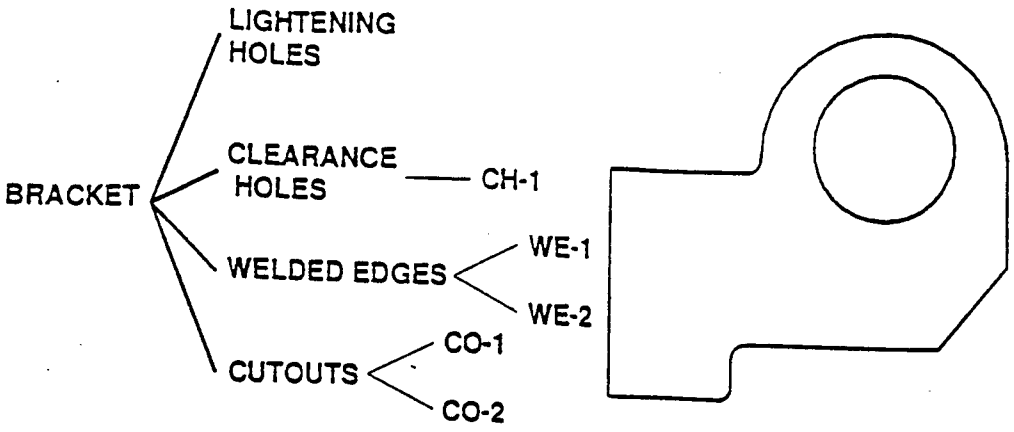


Figure 8. Idealized geometry and functional model including geometric simplifications.

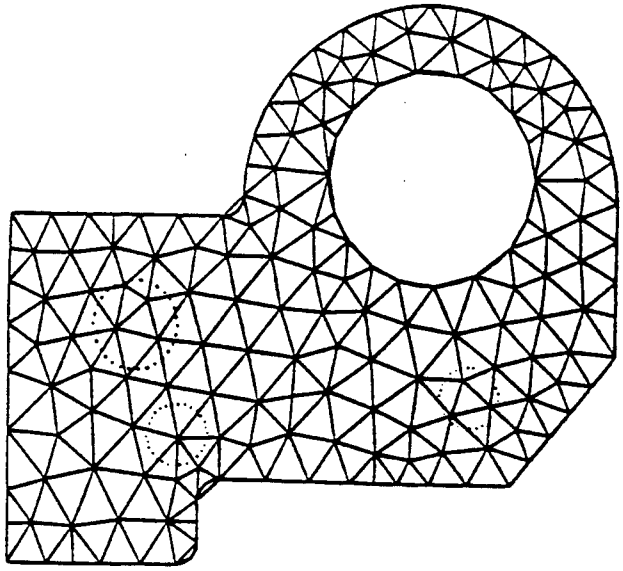


Figure 9. Discretization of idealized bracket.

analyses also examine the solution error and adaptively update the discretized model accordingly. For the sample bracket, the stresses in the area of two of the candidate holes (LH-1, LH-2) are found to exceed the threshold of interest. This change is reflected in both the idealized functional representation (Fig. 10) and the discretized model (Fig. 11).

A similar procedure can be used in the reverse case of a designer wishing to perform a stress analysis of a plate where lightening holes, which were not previously defined, are to be added. In this case the results of a preliminary analysis considering no lightening holes, combined with the stress concentration estimation procedures can be used to identify those areas where lightening holes could safely be added. Once a preliminary set of lightening holes have been designed the above procedure can be repeated. Since a preliminary set of lightening holes are now defined, the second analysis differs from the first in that an appropriate thickness or modulus reduction procedure accounting for the number, size and overall location of the lightening holes can be used.

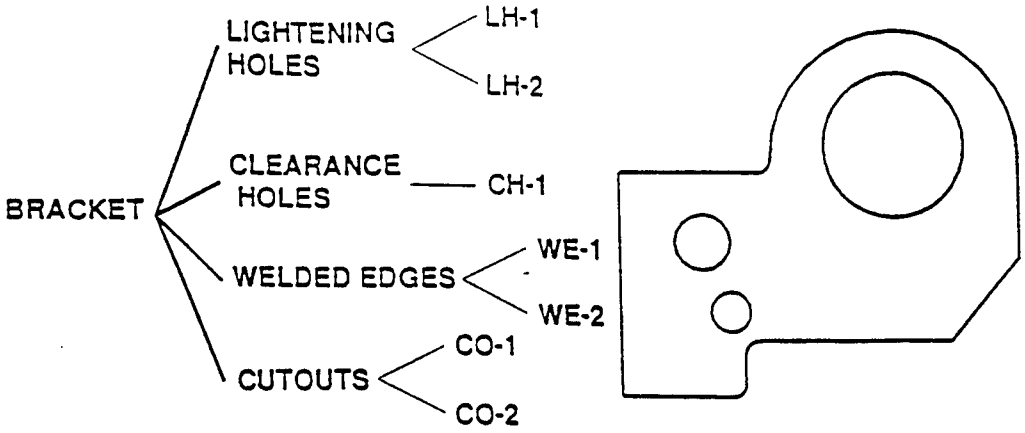


Figure 10. Idealized geometry and functional model with final idealizations.

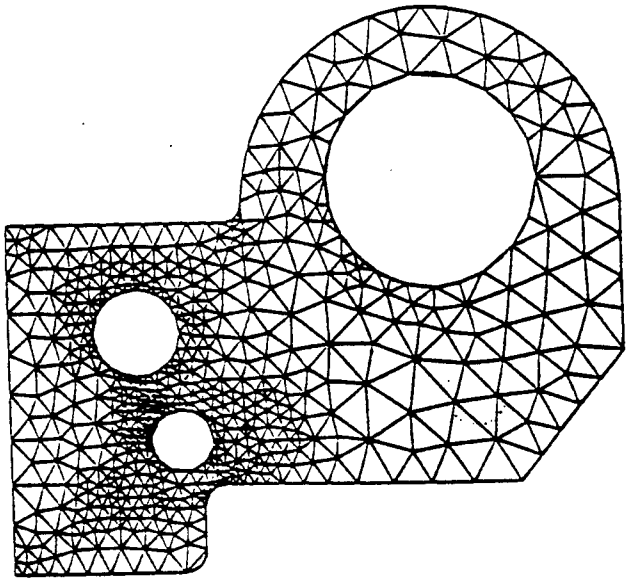


Figure 11. Discretization of the improved idealized bracket.

5 REFERENCES

[1] Peggy. L. Baehmann, T. -L. Sham, L. -Y. Song, and Mark. S. Shephard. Thermal and thermo-mechanical analysis of multichip modules using adaptive finite element techniques. In D. Agonafer and R. L. Fulton, editors, *Computer Aided Design in Electronic Packaging*, volume EEP-3, pages 57–63, New York, NY, 1992. ASME.

[2] Peggy L. Baehmann and Mark S. Shephard. Adaptive multiple level h-refinement in automated finite element analyses. *Eng. with Computers*, 5(3/4):235–247, 1989.

[3] CAM-I. Applications interface specification (restructured version). Technical report, CAM-I Report R-86-GM-01, Arlington, TX, Jan. 1986.

[4] J. R. Dixon, E. C. Libardi, and E. H. Nielsen. Unresolved research issues in development of design-with-features. In *Geometric Modeling for Product Engineering*, pages 183–196. North-Holland, Amsterdam, 1990.

[5] M. K. Georges. Geometric operators for the Finite Octree mesh generator. Technical Report SCOREC Report # 13-1991, Scientific Computation

Research Center, Rensselaer Polytechnic Institute, Troy, NY 12180-3590, 1990.

[6] E. L. Gursoz, Y. Choi, and F. B. Priz. Vertex-based representation of non-manifold boundaries. In M. J. Wozny, J. U. Turner, and K. Priess, editors, *Geometric Modeling Product Engineering*, pages 107–130. North Holland, 1990.

[7] R. W. Hon and C. H. Sequin. A guide to lsi implementation, 2nd edition. Technical Report SSL-79-7, XEROX, Palo Alto, CA, 1980.

[8] C. Mead and L. Conway. *Introduction to VLSI Systems*. Addison-Wesley Publ. Co., Reading, MA, 1980.

[9] A. A. G. Requicha and H. B. Voelcker. Solid modeling: A historic summary and contemporary assessment. *IEEE Computer Graphics and Applications*, 2(3):9–24, 1982.

[10] A. A. G. Requicha and H. B. Voelcker. Solid modeling: Current status and research directions. *IEEE Computer Graphics and Applications*, 3(7):25–37, 1983.

[11] R. J. Roark and W. C. Young. *Formulas for Stress and Strain*. McGraw-Hill, New York, NY, fifth edition, 1975.

[12] Shape Data Limited, Parker's House, 46 Regent Street Cambridge CB2 1DB England. *PARASOLID v4.0 Programming Reference Manual*, August 1991.

[13] M. S. Shephard. The specification of physical attribute information for engineering analysis. *Engineering with Computers*, 4:145–155, 1988.

[14] M. S. Shephard, P. L. Baehmann, Y. L. Le Coz, and T. -L. Sham. Methodology for the integration of global/local thermal and thermo-mechanical analysis of multichip modules. In D. Agonafer and R. L. Fulton, editors, *Computer Aided Design in Electronic Packaging*, volume EEP-3, pages 65–72, New York, NY, 1992. ASME.

[15] M. S. Shephard and P. M. Finnigan. Toward automatic model generation. In A. K. Noor and J. T. Oden, editors, *State-of-the-Art Surveys on Computational Mechanics*, pages 335–366. ASME, 1989.

[16] M. S. Shephard and M. K. Georges. Automatic three-dimensional mesh generation by the Finite Octree technique. *Int. J. Numer. Meth. Engng.*, 32(4):709–749, 1991.

[17] M. S. Shephard and M. K. Georges. Reliability of automatic 3-D mesh generation. *Comp. Meth. Appl. Mech. Engng.*, 101:443–462, 1992.

[18] M. S. Shephard, E. V. Korngold, and R. Wentorf. Design systems supporting engineering idealizations. In *Geometric Modeling for Product Engineering*, pages 279–300. North-Holland, Amsterdam, 1990.

[19] R. R. Tummala and E. J. Rymaszewski, editors. *Microelectronics Packaging Handbook*. Van Nostrand Reinhold, Chichester, 1986.

[20] K. J. Weiler. The radial-edge structure: A topological representation for non-manifold geometric boundary representations. In M. J. Wozny, H. W. McLaughlin, and J. L. Encarnacao, editors, *Geometric Modeling for CAD Applications*, pages 3–36. North Holland, 1988.

[21] R. Wentorf, A. Budhiraja, R. R. Collar, M. S. Shephard, and P. L. Baehmann. Two prototypes testing the use of an expert system in the control of structural analysis idealizations. In E. N. Houstis, J. R. Rice, and R. Vichnevetsky, editors, *Intelligent Scientific Software*, pages 283–326. North Holland, Amsterdam, 1992.

Computational Mechanics 17 (1995) 196–207 © Springer-Verlag 1995

Automatic construction of 3-D models in multiple scale analysis

M. S. Shephard, M. W. Beall, R. Garimella, R. Wentorf

Abstract This paper discusses techniques for the automatic construction of numerical analysis models for multiple scale analyses which employ interacting models at two, or more, physical scales. Consideration is given to the methods to define the geometric representations and generate the discretizations needed by the numerical analysis procedures. The application of the techniques to multichip modules and composite structures, with interacting macromechanical and micromechanical level analyses, is demonstrated. In the multichip module analyses both heat conduction and thermomechanical analysis are performed using different numerical analysis techniques, and the two interaction of the analyses at the through levels is through a basic global/local methodology. The composite structure analysis considers crack propagation at the micromechanical level interacting with the macromechanical analysis through finite element based adaptive multiscale analysis. In both example applications the focus of the discussion is on the automatic construction of the required geometric models and their automatic discretization.

1 Introduction

The need for more accurate determination of quantities of interest has led to an increased use of interrelated analyses in which the discretization processes are perfomed at multiple physical scales. For example, in the two applications considered in this paper, the thermomechanical analysis of multichip modules and the fracture analysis of composite structures, analyses performed at a macromechanical level are coupled to analyses performed at the micromechanical level over critical portions of the domain of interest. In addition to the development of the analysis procedures required, it is necessary to provide the appropriate modeling and discretization environment. The focus of this paper is on the development of automated techniques to support these modeling and discretization procedures.

Communicated by S. N. Atluri, 19 June 1995

M. S. Shephard, M. W. Beall, R. Garimella, R. Wentorf
Scientific Computation Research Center, Rensselaer Polytechnic Institute, Troy, NY, 12180-3590, USA

Correspondence to: M. S. Shephard

The authors wish to acknowledge the support of the Wright-Patterson AFB, under Contract No. F333615-91-K-1717 and ARPA/ONR under grant N00012-92J-1779

In today's engineering environment, the amount of time and effort involved in performing an analysis using numerical analysis techniques is often dominated by the construction of the discrete representation, the mesh, of the domain of interest as needed for the analysis at hand. Since it is becoming more common for a computerized representation of the problem domain (a geometric model) to be available to the analyst, procedures to efficiently discretize these domains are being developed. The use of such geometric models provides a common basis to support multiple related analyses where different discretization methodologies can be used. Performing an engineering analysis also requires information on materials, loads, boundary conditions and initial conditions. The support of automated analysis procedures requires that this information, referred to as analysis attributes, be defined in terms of the geometric model.

The generation of a discrete representation of a given domain and its numerical analysis constitute only two of the steps in performing an engineering analysis. A critical step performed before these steps is the process of determining an idealization of the physical problem appropriate for the analysis. For example, in the case of a composite structure it is common to assume that the information of interest can be determined by replacing the microstructural detail by a homogeneous macrostructure. In the applications considered in this paper, at least two levels of idealization are used in a complete analysis process. Since the goal is to provide automated procedures to control all steps in these analyses, the procedures must include a general idealization control framework. The inclusion of such a framework has the immediate benefit of providing a feedback loop which can support adaptive idealization control processes. Section 2 discusses the techniques used to support the general definition of the problem which is used in the automatic construction of the analysis models. Section 3 discusses the idealization control framework used by the model construction processes for multiple scale analyses.

To demonstrate the application of this methodology, two multiscale analysis applications are described. Section 4 discusses a set of procedures developed to support global/local heat conduction and the thermomechanical analysis of multichip modules where the local level analysis employs the detailed microstructure in that area. Section 5 overviews the application of the methods to the multiscale adaptive analysis of the fracture of composite structures.

2 Problem definition to support automated model construction

Automation of a set of engineering analyses requires that all analysis models, and their discretizations, be derived from

a single problem definition. The two key components of this definition are the domain description (the geometric model), and the analysis and idealization attributes defined in terms of it. This single problem definition is used to support the construction of all the models employed in performing the analysis. For sake of discussion this single problem definition, from which all other models are derived, is referred to as the primary problem definition.

2.1 Geometric model

The geometric models constructed from the primary problem definition, in support of multiscale analyses, vary from a representation of the middle surface of a composite structure, to one containing multiple volumes representing the micromechanical structure of a composite material. The representations used must also be able to support the requirements of automated discretization construction procedures, such as automatic 3-D mesh generators which perform a large number of interrogations on a geometric representation. The primary model must be structured such that the various idealized engineering analysis models can be constructed, and the interactions between those interactions controlled. For example, at the highest level, a composite structure may be idealized geometrically as a surface, while at a second level a portion is represented as a multi-layer volume or surface, while on a third level a local region of the microstructural components are represented as volume elements.

Over the years, geometric model representations and associated software systems have been developed which can support these various forms of geometric representations. Of the various forms, only the general non-manifold geometric representations (Weiler 1988) are capable of representing the general combinations of volumes, surfaces and curves required by the various forms of analyses. Geometric modeling systems that can support the full range of geometric operations required to support engineering analysis idealization and discretization processes are highly complex, requiring a massive development effort. Since a number of commercial software packages have been developed that provide at least the base geometric modeling capabilities, the analysis idealization and discretization procedures developed in this work directly employ those functionalities. The obvious advantage of this approach is that those development efforts are not repeated. There are, in addition, important technical advantages to this approach since the geometric calculations can directly employ the tolerances employed in the geometric modeler (Shephard and Georges, 1992).

The specific requirements placed on the primary geometric model representation depend on the analysis model idealization and discretization procedures used. One approach is to assume a detailed geometric representation at the lowest physical scale is available. This is not an advantageous approach since the model sizes would be unacceptably large, the construction of the higher level models can be more complicated than the automatic construction of low level models, and the user construction of detailed lower level models can be burdensome to the design process. The approach taken here is that the representation stored has enough information so that all the required idealized geometric models can be automatically built. As demonstrated in the two applications considered, the actual forms used can vary, however, in both cases there is sufficient information to automatically construct the complete non-manifold geometric models required for the automatic discretization generation procedures.

The most geometrically demanding processes typically involve the construction of the idealized geometric models for specific analyses from the primary geometric model. One class of such operations are dimensional reductions where, for example, the middle surface of a complex three-dimensional solid, which is thin in some, through the thickness direction is needed for a macromechanical level analysis. Another example is the construction of a multi-material solid model of a representative unit cell from basic composite construction specifications. Such models are required when micromechanical models are included in the analysis process. The approach used to address these needs is to employ the geometric construction functionalities of commercial solid modelers, driven by appropriate knowledge housed in the primary model and the analysis strategy being executed. Figure 1a shows the unit cell for a composite weave automatically constructed in the Parasolid non-manifold solid modeling procedure using basic manufacturing parameters that define the weave.

Automatic discretization procedures, such as automatic finite element mesh generators, must also interact with the geometric model, interrogating it to determine information not

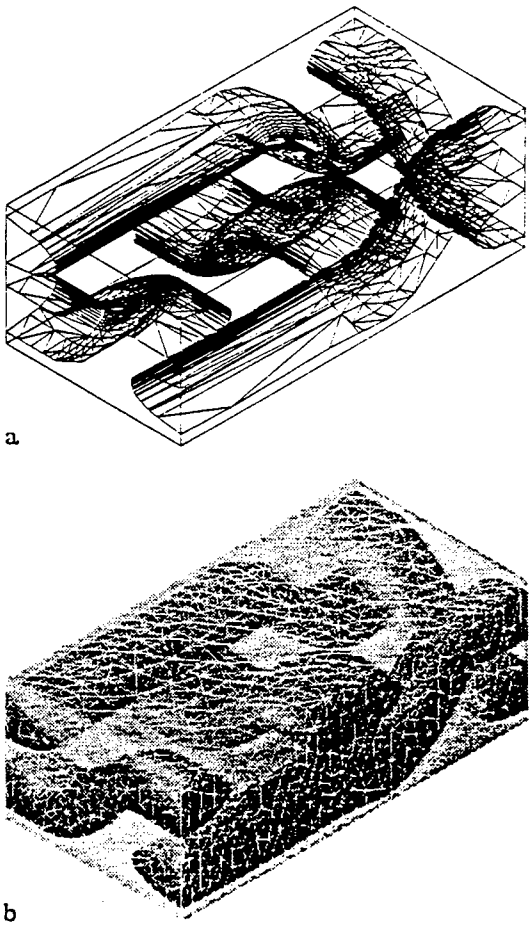


Fig. 1a, b. Automatically constructed and meshed unit cell model

directly stored in the data structures of the geometric model. Since most commercial geometric modelers provide libraries of basic geometric interrogations, it is possible to develop the automatic discretization generation procedures employing operators built on those libraries. An example of one such mesh generator is Finite Octree (Shephard and Georges, 1991) which interacts with the geometric modeling system through a specific set of 21 geometric operators. The integration of Finite Octree with a new geometric modeling system only requires the creation of those geometric operators with respect to that modeler. This requires no knowledge of the operation of the mesh generator, or the data structures internal to the geometric modeling system. What is required is a knowledge of the basic interrogation operators available from the geometric modeling system which can be used to build the specific Finite Octree geometric operators. Using this approach Finite Octree has been integrated with four geometric modeling systems including Parasolid, ACIS, SHAPES and an in-house modeler. Figure 1b shows an automatically generated Finite Octree mesh of the unit cell in Fig. 1a.

One complexity in the use of commercial solid systems modeling to support multiple scale analysis is that they have historically been limited to 2-manifold geometric models, which, put simply, limited the objects represented to faces which have solid material on one side, and edges with only two faces coming into them. However, a careful examination of the detailed functionalities of commercial 2-manifold geometric modelers indicates that although they cannot properly represent non-manifold geometric models, they can often perform the basic geometric operations required to define the entities needed for specific classes of non-manifold models. For example, there are operators to support modified union operations needed to combine individual material assemblies. These operations create sets of coincident faces, edges, and vertices at each of the contact faces. Such redundant topology represents inconsistencies which will cause the automatic mesh generator to fail. By maintaining an understanding of the redundant relationships, the model's topological representation is postprocessed to eliminate the redundant entities and construct the correct topological use needed by a proper non-manifold representation. One method to store this information is the radial-edge, non-manifold, topological structure (Weiler 1988). Seeing the need for non-manifold representations, commercial solid modeling systems are altering their internal data representations so they can properly represent non-manifold objects.

2.2
Analysis and idealization attributes

Analysis attributes are the information past the geometric model needed to specify an analysis model. Analysis attributes include material, boundary condition, load, and initial condition information. Idealization attributes define the information needed to convert a primary model to the idealized model used in an analysis process. Examples of idealization information are specification of the use of the middle surface for an overall deformation analysis, and the information defining the microstructure of a unit cell.

The specification of attributes is typically done employing ad-hoc processes specific to the analysis procedure. Such approaches do not properly support an automated environment when a number of different analysis techniques may be applied. To support an automated environment, the analysis and idealization attributes must be defined directly in terms of the physical parameters and associated directly with the geometric representation of the primary geometric model. When defined in this manner they can be properly transferred to the idealized analysis models and their discretizations. An attribute manager, following the basic approach outlined in Shephard (1988), has been developed to support these requirements (Wong 1994).

Since the physical description of all analysis attributes are in terms of tensorial quantities, their effective specification must be in terms of various order tensors and their distribution. The most convenient means to score a tensor is in terms of its components defined in a particular coordinate system. Since many of the tensors used to define physical quantities possess various forms of symmetry, it is advantageous to account for these symmetries to minimize the amount of information required to specify an attribute. Based on this, the components of the structure used to define the attributes' physical information are (i) the order of the tensor, (ii) an indication of the coordinate system the attribute is defined in, (iii) the symmetries possessed by the attribute, and (iv) the distribution information defining each component of the tensor in the given coordinate system.

The specification of a particular analysis requires the proper grouping of a number of individual attributes. Since a number of basic attributes, such as material parameters, are likely to be used in multiple analyses, it is advantageous to allow the single specification of an attribute and to collect the attributes appropriate for an analysis into the specific analysis case desired. A hierarchical organization structure that allows the convenient collection of attributes, including the application of multipliers, has been put into place.

The third major component of the attribute manager is the association of the attributes with the geometric description of the domain. At the primary model level, this is the association of the attributes with entities in the primary geometric model. When the primary model is defined in a solid modeling system, a scheme of associating the attributes with the correct topological entities in the geometric model, including basic augmentation functions to support when an attribute is defined over a portion of an entity, is sufficient (Shephard and Finnigan, 1989). Additional complications are introduced in the case of multiple scale analyses because it is necessary to properly transfer the appropriate attribute information from the primary attribute definition to the idealized modes used in the analysis process. The transfer of the attributes must correctly deal with such processes as dimensional reductions and replacement of a set of heterogeneous constituents with a homogeneous continuum. The case of dimensional reduction is complicated by the geometric operations required. Determining average material properties is complicated by the fact that it is, in itself, an analysis process and consideration of the range of procedures available to determine them with their relative cost versus accuracy trade-offs. In a properly controlled multiple scale analysis structure, this process must be adaptively controlled in the same manner as all the analysis steps.

A specific set of procedures within the attribute manager have been developed to support the definition of attributes, their

grouping into analysis cases and their association with both the primary geometric model and the various idealized geometric models (Wong 1994). These procedures are used in conjuction with the analysis idealization control procedures described in the next section to support the multiple scale analysis applications described in this paper.

3
Control of analysis idealizations processes

Given a primary problem definition and the modeling tools required to convert the information into the input required for the various analysis processes, an overall structure is needed to control the execution of each of the idealization and discretization steps performed. Since the range of analysis idealization and discretization processes vary widely, this overall structure must be quite general.

By combining specific methodologies developed for controlling engineering decision processes, with the feedback loop structure of adaptive procedures, an analysis idealization control mechanism, called an analysis strategist, has been developed (Shephard, et al. 1990; Wentorf and Shephard, 1993). The analysis strategist considers an engineering analysis as a stepwise process of reducing the physical description and behaviors of the system into a set of solvable algebraic equations representing one or more of the behaviors of interest of a design, object or process. At each step decisions must be made as to what specific idealizations to employ. The selection of a specific idealization must consider the goal of the analysis and the interaction of this idealization step with others. The analysis goal specifies the domain of interest, the type of result desired, the limiting time (cost) and the desired reliability of the results. The reliability and accuracy of an analysis is a function of the approximation errors created by each idealization step. Since it is often possible to obtain better estimates of the error introduced by a particular idealization based on a posteriori evaluation, the analysis strategist employs a feedback loop where the influence of idealization steps can be examined and the idealization improved in a re-analysis loop until the desired level of accuracy is obtained.

The strategy is an abstract plan or template which is selected from a library and then refined into a detailed sequence of software operations. The strategy is represented by a network of frames (Minsky 1981), where each frame represents a computational component which performs a function. A frame groups information about the entity which it represents using slots, where each slot has a label, one or more values, and data which characterizes the type of the value and its source called "facets". The values may also be linked with other frames, called "relationships". The relationships connecting the computational components represent the characteristics of the information which is input and output by the component. Naturally, the characteristics of the output of one component must match with the input characteristics of the next. Each component of the strategy can be refined, in a recursive manner, into a sub-network of more specific components, where the total inputs and outputs of the refined network are inherited from the less refined "parent" component. The refinement stops when the plan is sufficiently detailed to be implemented by a modeling operation, database query, execution of an analysis package, etc. As a last resort, if no source for information critical to the analysis can be found, the user is queried. In essence, the refined strategy is a functional model of an analysis "machine" which takes the given domain as input and creates the desired results of the analysis goal. Reasoning based solely on this information flow net is only one aspect of refining and implementing an analysis strategy.

The physics of the design must also be used to create suitable models for achieving the desired analyzed results. This is done by using a functional model of the artifact being analyzed, which specifies the required physical phenomenon, the geometry and attributes used to implement each functional component and the physical relationship between functional components (Wentorf, Shephard and Korngold, 1989). For example, if the purpose or function is to transfer load as part of a load path, and the refinement of that function is specified in terms of flanges, holes, bolts, pre-tensioning torques, etc. (functional components, geometric forms and attributes), then the basic modeling ingredients for idealizing the connection between domains in the analysis model are available. The functional model is represented using frames and has additional relationship slots which link the corresponding geometric and attribute entities with each component. The network is processed with rules, some of which traverse the physical relationship slots of the network, performing graph based operations, while other rules match with specific component slot values. An example of the former rules are that which establish "load paths" in a functional network by using "structurally connected" type relationships. The rules produce a network of idealized components, also with additional relationships pointing to the corresponding idealized geometric and attribute entities. The processes used to create the idealized model are complex and involve interactions between the three modelers. For example, the proximity or extent of a geometric feature may need to be evaluated in order to determine whether it should be included in the idealized model. If a component has a slot value used for idealization and it is modeled explicitly in the primary model, e.g. geometric proximity, then the value is filled by an external procedure call to the geometric modeler automatically when the component is created.

As a minimum, the idealization control process must consider the physics envisioned for the design. Extra intelligence is added if the system can automatically deduce physical phenomenon beyond the original design intent. For example, a structural connection can also imply a thermal connection relevant to heat transfer analysis.

A third category of knowledge used to refine and implement an idealization control strategy is analysis expertise. They may be based upon knowledge of the theory used to formulate the computational component (e.g. a linear elastic model) or may be based upon experience matching modeling technique with empirical results. This knowledge is used to estimate and evaluate the time (cost) and reliability of the results, and can determine the next best computational component or idealized model constituent to use for feedback strategies. Mathematical modeling and applicability description slots in each computational component, combined with access to cost/error estimation procedures provides the representations needed for reasoning.

The mechanism for control of idealization processes must be able to reason about what must be recomputed if the problem

definition parameters change. For example, when examining ceramic composite material failure by cracking, using a linear elastic theory, a change in material processing temperature does not require reanalysis for determining the applied stresses. This can be deduced from the detailed strategy network and increases the apparent performance of the strategy in this case.

4
Application to global/local analysis of multichip modules

4.1
Global/local analysis procedures

A multichip module (MCM) is characterized by having a number of layers containing wires and vias in various configurations, in conjunction with a general chip and cooling structure layout. The prediction of a mechnical failure, such as a wire fracture due to thermomechanical loading, is critical to ensuring the ability of a multichip interconnect to perform its intended electrical functions. The accurate prediction of these failures must involve the local microstructural details of the MCM at a potential failure site, in an analysis accounting for nonlinear behavior. However, analyzing a finite element discretization of the entire MCM microstructure would produce a set of equations with orders of magnitude and more unknowns than can be realistically solved on today's computers.

An alternative methodology to analyze MCMs is to employ global/local procedures, in which cost effective global analyses are performed to provide the boundary condition information needed for an accurate local analysis of the critical regions where the wires, vias, etc. are fully represented. Both the global and local analyses employ continuum models to provide a mathematical description of the heat conduction and thermomechanical behavior. In addition, it is assumed that the heat conduction and thermomechanical problems are uncoupled.

To be computationally efficient, the global analyses procedures employ a more extensive set of idealizations on both the physical scale of the analysis and the behavior of the governing continuum equations. To limit the size of the systems required, the detailed geometry of the interconnect is eliminated by employing averaging techniques to convert each layer in the MCM into an equivalent homogeneous medium. In the global analysis problems it is sufficient to employ linear constitutive relationships.

The global analysis procedures are based on a variational technique in which the differential equations and certain interface and boundary conditions are satisfied exactly. Therefore, the numerical solution process must only perform area integrals, as opposed to full volume integrals and the number of unknowns in the procedure does not increase as the number of interconnect layers increases. See Sham, et al. (1993) and Tiersten, et al. (1993) for a description of the specific procedures developed for the global heat conduction and thermomechanical analysis of MCMs.

Because the interconnect is idealized in a layerwise fashion for the global analyses, the based domain information needed includes the "in-plane" dimensions, the thickness and volume fractions for each layer. In addition, knowledge of the chip arrangements on the upper surface is required. Because it does not need any information from other analyses, the global heat conduction analysis is the first analysis performed. It provides the global thermomechanical analysis with the global temperature field.

The local heat conduction analysis is performed using a stochastic for solving Laplace's equation based on the floating random-walk method, (Le Coz and Iverson, 1992).The local heat conduction analysis employs the temperature defined by the global heat conduction analysis on the boundary of the local window.

Since the details of the local stress fields are critical to the prediction of failure quantities, the local thermomechanical analysis procedure must accurately represent the local geometric detail in an analysis, including nonlinear material behavior. The most effective means to meet these goals is to employ an automated adaptive finite element methodology (Shephard, et al. 1993). The local thermomechanical analysis obtains displacement boundary conditions from the global thermomechanical analysis and a temperature field from the local heat conduction analysis.

4.2
Construction of idealized geometric models and their discretization

The four analysis procedures employ three different idealized geometric and discrete representations which must be generated from the available primary definition. The most appropriate unique geometric representation, from which to generate the numerical analysis discretizations, is a non-manifold solid model. However, consideration of the design and manufacturing representations employed for MCMs indicates a more commonly used domain description is a CIF file (Mead and Conway, 1980). Although convenient, a CIF file is not a complete and unique geometric representation of the non-manifold geometry of an MCM. Therefore, the approach taken in this work is to use the CIF file, attributed with a limited amount of additional needed information, as the basis of the MCMs primary definition, and to develop the procedures required to interpret the CIF files to construct the idealized geometric model needed by the automated discretization generation procedures.

The current assumptions and associated limitations on the CIF file are: (i) entities are defined on a layer-by-layer basis with all layers being explicitly represented, (ii) entities within a layer are rectangular parallelepipeds with edges aligned with the edges of the interconnect, (iii) all entities defined in the CIF file are associated with a specific layer, and (iv) neighboring material regions must share one or more faces. These assumptions and limitations can be altered by the application of new CIF file interpretation rules, combined with the appropriate construction procedures.

The global heat connection and thermoelastic analyses employ a layerwise discrete representation of the overall interconnect configuration, where each layer is assigned the appropriate averaged material properties. The procedure to determine this information employs the attributed CIF file to construct models of each layer from which the calculation of layerwise volume fractions can be determined for use in the material property averaging procedure. The size and position of the chips on the top surface of the MCM is also obtained from the information in the CIF file.

The idealized geometric representation for the local thermal analysis must represent the microstructure in the local window as a set of materially homogeneous rectangular parallelepipeds with all edges in one of the three perpendicular directions. The current restrictions on the primary model match this requirement. Given the set of parallelepipeds, the discretization for the local heat conduction analysis is simply the diagonal endpoints and thermal conductivity of the parallelepipeds. Geometric and material data for the local heat conduction analysis are directly extracted from the CIF format, and extended to three-dimensions. Layer thciknesses, wire thicknesses, and corresponding thermal conductivities are extracted from the analaysis attribute information.

The goal of local thermomechanical analysis is to be able to predict the initiation of local failures such as a wire fracture. Since failure phenomena are strongly influenced by the local geometric details of the numerical analysis, model generation and discretization generation procedures must be able to deal with these details. Although current CIF file restrictions limit the amount of geometric detail in the primary geometric model, the procedures developed for the local thermal mechanical analyses do not suffer from such limitations. Simple methods to avoid these restrictions are demonstrated below.

The finite element discretizations for the local thermomechanical analyses are automatically constructed using the Finite Octree mesh generator (Shephard and Georges, 1991) which is capable of creating graded meshes of general 3-D non-manifold domains (Weiler 1988). However, to operate Finite Octree requires the domain to be meshed to be defined within a solid modeling system which supports the required geometric interrogations. Since the CIF file maintains only basic geometric parameters, it is incapable of supporting the required geometric interrogations. Therefore, it was necessary to develop a procedure to build, from the information in the CIF file, the non-manifold solid model in a geometric modeling system that can support the mesh generator's geometric interrogations. In the current efforts both Parasolid and ACIS solid modeling systems, with the proper non-manifold extensions for multiple material domains, have been developed.

The procedure used to generate the multiple material solid model in an extended solid modeling system starts with a CIF file containing a 2-D description of the MCM layers in terms of rectangles, polygons, circles, and paths. When attributed with a thickness parameter, each such CIF entity can be formed into an appropriate solid primitive in the solid modeling system. The primitives of a single material type are intersected against a box defining the local window of the analysis and then unioned to form the collection of solid bodies of that material type referred to as a material assembly. To make this process computationally efficient, CIF file entities which do not interact with the selected parallelepiped are not included in the Boolean operation processes. For example, layers with z-values that do not overlap the parallelepiped need not be considered, while entities in layers of interest which do not overlap the xy-rectangle of the parallelepiped need not be considered. Pairs of material assemblies are examined and their interactions defined by performing appropriate modified Boolean operations. If there is no interaction, proceed to the next pair of material assemblies. If their interaction is only at common boundaries, it is resolved by the elimination of the appropriate pairs of duplicate entities. If their interactions include domain overlap, rules as to how to handle the overlay region are invoked and the new common boundary interactions are recorded.

Figure 2 shows non-manifold solid models built using three different local windows defined in the vicinity of a specific chip in a seven layer MCM. The largest window shows the entire area under the chip, while the other two windows show close-ups of a specific critical junction area.

Figure 3 shows a simple three-dimensional test example, the automatically generated initial mesh, and the adaptively refined mesh of a highly local region. As expected the elemental error estimators predicted refinement at the juncture of the via and wire.

An examination of the results of the adaptive analysis indicate a overly high stress concentration at the intersections of the vertical and horizontal components of the wires caused by using a shape corner to represent this region. To obtain more realistic stress values, a geometry closer to that which is actually manufactured is required in the local thermomechanical analysis. Figure 4 shows the original CIF level idealization and a more realistic geometry for the intersection of two wires and the area under a solder connection. This more realistic geometry is automatically constructed using the same basic process as above, except additional

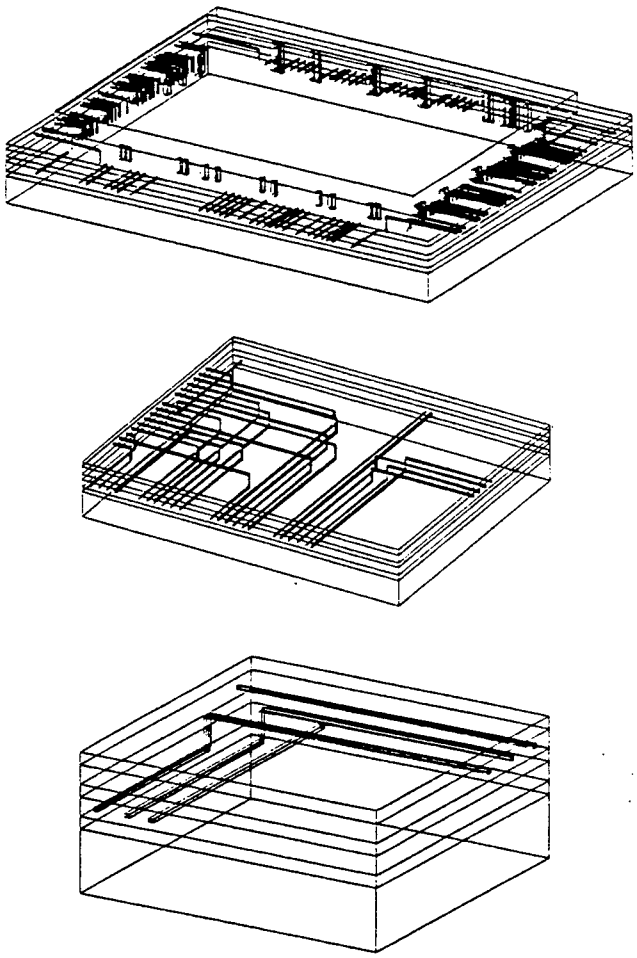


Fig. 2. Views of a Parasolid model of a simple one chip interconnect created from a CIF file

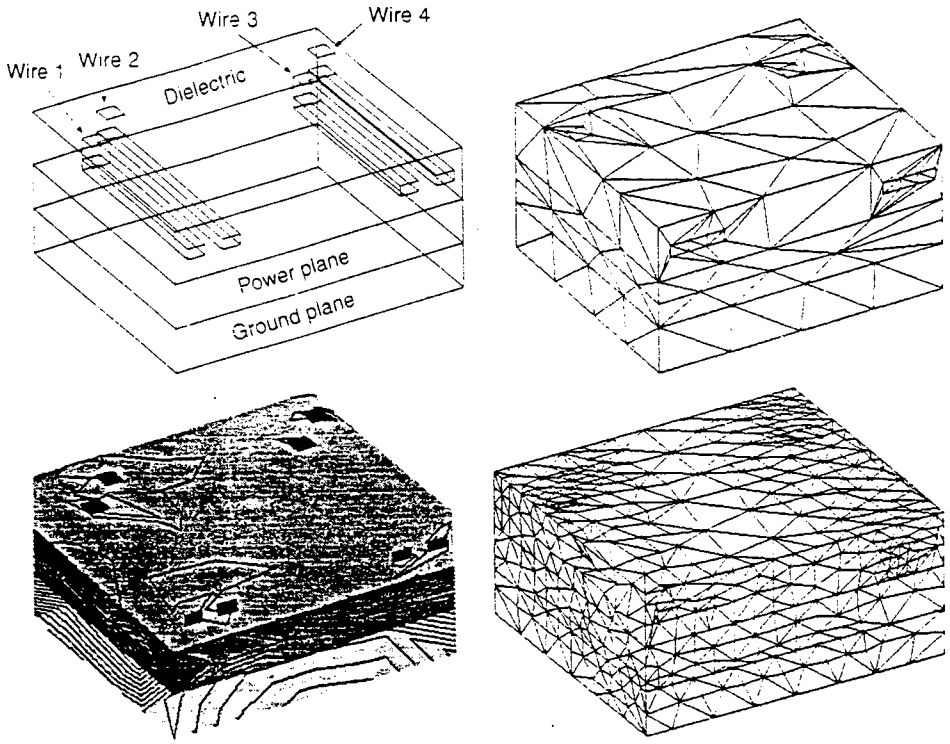


Fig. 3. Three-dimensional test example with initial and adaptively refined finite element mesh. Meshes show only the element faces on material boundaries

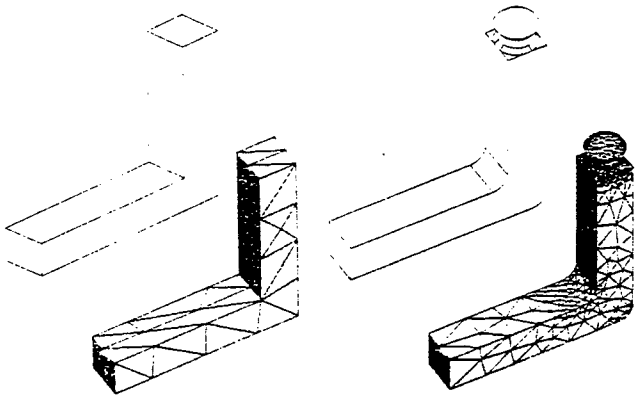


Fig. 4. Models and meshes of wires, vias and solders in local window with sharp corners blended

attribute information on how the component geometries would actually blend during manufacture has been added and the solid model construction procedures extended to account for that information.

5
Application to adaptive multiscale analysis of composite structures

Composite structures are a natural area for multiscale modeling. Good estimates of overall behavior can be obtained by analyses using homogenized microstructures. However, the failure processes that must be taken into account typically initiate at the scale of the microstructural constituents. Modeling an entire component at the scale of the microstructural constituents is not a practical approach due to the extreme size of the resulting problem. However in areas where failure is likely to initiate, it is necessary to perform analyses on the microstructural scale to model the initiation of the failure and its effects on the rest of the structure.

As the microscale damage evolves, it affects the behavior of the composite at the macroscale. Therefore, it is necessary to perform the analysis in such a manner that this coupling between the scales is represented. One technique that shows much promise for this type of analysis is the multiscale analysis of Fish and Belsky (1995a, b).

5.1
Multiscale composite analysis

The multiscale analysis being used for composites is a three level analysis . The top level is the component (macro) level, where all the material properties are considered to be homogenized. The bottom level is the microstructural level where all the details of the microstructure and damage that is occurring is represented. The middle level serves as a transition between these two levels and incorporates any macro level damage. During an analysis the top level remains unchanged while the second and third level are automatically created and updated throughout the analysis.

The analysis uses an iterative multigrid procedure to solve the problem. A homogenization based prolongation operator (Fish and Belsky, 1995a, b) is used to couple the solution between the transition mesh (with homogeneous material properties) and the micro-mesh (with heterogeneous material properties). Further information regarding the details of the analysis can be found in the references.

5.2
Example–Crack propagation

The example used to demonstrate the model building procedures necessary for multiscale composite analysis is the propagation of a crack through the microstructure of a composite plate. To predict the growth of the crack it is necessary to have a detailed representation of the microstructure near the crack front. However in other areas of the model, such as far ahead of the crack or sufficiently behind it, such detail is unnecessary and a homogenezied representation of the microstructure can be used. Thus for this analysis the micro-model will be needed only in a small area around the crack tip.

The primary problem definition consists of a solid geometric model of the physical structure being analyzed (the macro-model) with appropriate analysis attributes and idealization attributes that describe the layup and microstructure of the composite. These attributes include the type of microstructure, the parameters needed to build a unit cell as described below, the material properties of the constituents and the orientation of the unit cell with respect to the macro-model.

In addition, the primary problem definition also includes the initial geometry of the crack. It is assumed at this point, for the sake of simplicity, that the initial crack geometry is a convex, planar polygon. As the crack grows it is allowed to become non-convex and non-planar. The crack is assumed to remain a single face throughout the analysis, although it may develop interior holes. The crack front is the set of edges that bound this face including any edges bounding interior holes.

5.2.1
Unit cell construction

Before any analysis can be done, a model of the microstructure of the composite must be created. Currently the microstructure geometry is assumed to be periodic and, thus, can be represented by the repetition of a single unit cell. This unit cell is used for the calculation of homogenized material properties using standard homogenization procedures (Bakhvalov and Panasenko, 1989; Guedes and Kikuchi, 1991) and for construction of the microscale model of the composite. Both the model and the mesh of the unit cell must be periodic.

Common composite unit cells are: aligned fibers, random chopped fibers, random particles, and woven fibers. Samples of unit cells of each of these types are shown in Fig. 5. The unit cells fall into two categories: those with prescribed structure and those with random structure. The unit cells with prescribed structure, such as the aligned fiber and the woven fiber cells in Fig. 5, are created from a parametric model of the unit cell. The parameters in the model include fiber size, volume fraction, and other geometric properties of the unit cell. The unit cell is constructed by first creating a cuboid of the correct size of its boundary and then creating each reinforcement as specified by the parameter values (e.g. for the aligned fiber unit cell, the diameter of the fibers is calculated from the fiber volume fraction), then the reinforcements are unioned with the boundary to create the finished model.

The unit cells with random structure, such as the chopped fibers and particles in Fig. 5, are generated using a stochastic procedure as follows. For each piece of microstructure in the

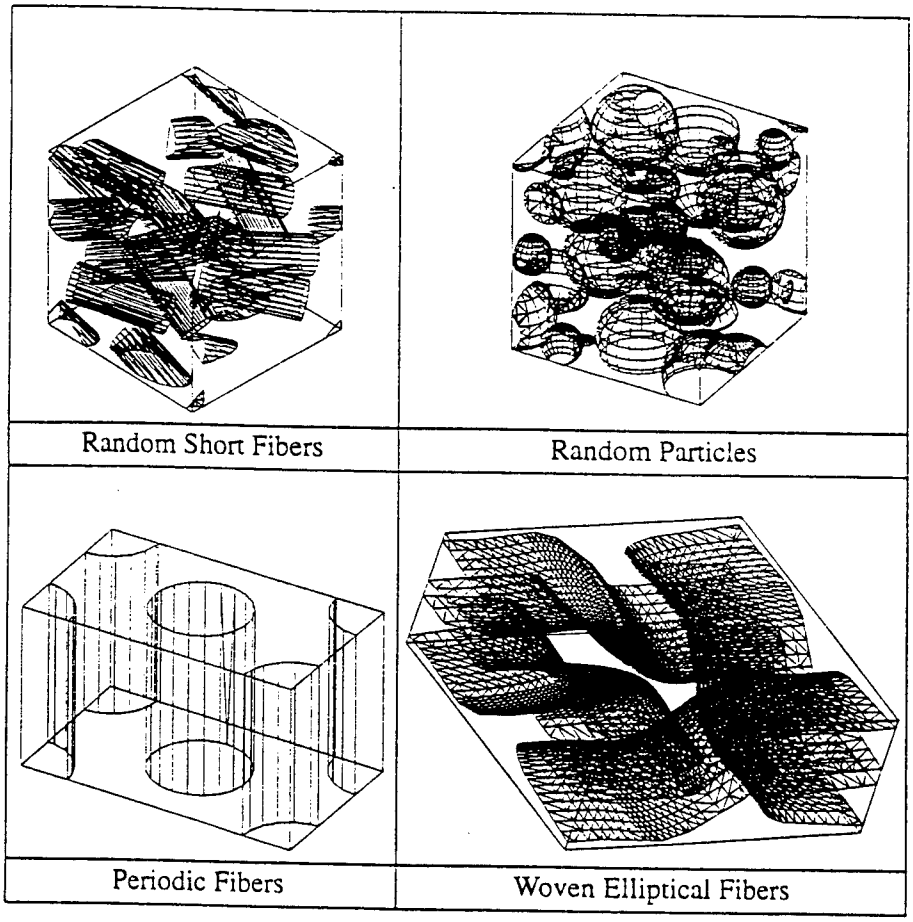


Fig. 5. A sample of the various types of unit cells that can be created

unit cell a random location, and orientation, if needed, is selected. A check is then made to determine if the "periodic extension", described below, of this piece of microstructure will interfere with any already in the unit cell. If it does not then it is inserted into the unit cell and the process is repeated until the correct volume fraction is reached.

Before each piece of microstructure can be checked for interference with others it must be determined if it intersects any of the boundaries of the unit cell. If it does intersect any boundary of the unit cell then, to enforce periodicity of the model, that piece of microstructure must be duplicated so that it enters the unit cell from the opposite side. This duplication must be done for each boundary of the unit cell that the piece of microstructure intersects. The union of the original piece of microstructure and all of its periodic duplicates is called its "periodic extension". It is this periodic extension that must be checked for interference with existing microstructure and, if there is no interference, unioned with the model. This procedure works well as long as the volume fraction of the reinforcement is not too high. When the volume fraction of the reinforcement is too high (the volume of which depends on the shape of reinforcement, but is typically 30–40%) it becomes difficult to insert the needed amount of reinforcement into the model due to interference with previous inserted reinforcements.

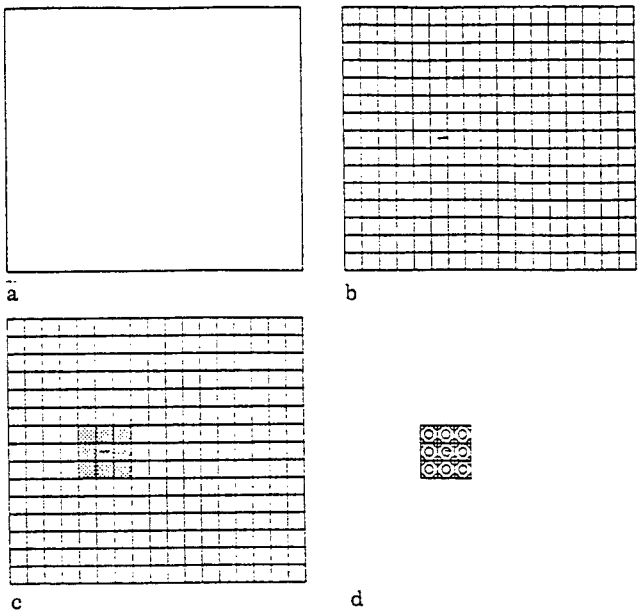


Fig. 6a–d. Defining the domain of the micro model

5.2.2
Microscale model

The microscale model fully represents the geometry of the microstructure of the composite. It is only created for regions of the macro-model that are a small distance (on the order of several unit cells) from the crack front. The first step in creating the microscale model is to determine its domain. The basic idea to determine this is to follow the crack front through a three dimensional regular grid where each cell in the grid represents the boundary of a unit cell. Each grid cell that the front intersects must be included in the microscale model. In addition several layers of unit cells around those that the front passes through need to be modeled to ensure the accuracy of the analysis process. This procedure is described in more detail below and is illustrated for a simple 2-D problem in Fig. 6:

1. Define a regular grid over the macroscale model where each cell in the grid is one unit cell in size (Fig. 6b). This grid must be defined so that when the unit cells are inserted in the grid locations the correct microstructure is created. Thus, it is necessary for the grid to be aligned with the fiber direction for composites with continuous aligned fibers. The grid is only defined not actually created in the geometric modeler.
2. Determine which grid cells the curve that defines the crack front passes through, this is the minimal domain for the micro-model. This is illustrated by the grey filled cell in Fig. 6c. In the 2-D example shown, the crack front is simply the two ends of the crack, however for a 3-D problem the front is a closed curve.

   For the 3-D problem determining the grid cells that the crack passes through is done as follows: Pick a point on the curve and determine which cell the point is in, add this cell to the list of cells that the crack front passes through. Find which cell face, edge or vertex the curve passes through as it exits the cell by intersecting the curve with the planes defined by each cell face. Add the cell on the opposite side of the face to the list of cells that the crack front passes through, if the crack front passes through an edge or vertex then add all the cells touching that edge or vertex. Continue this procedure, tracking the curve as it passes from one cell to another until the entire curve have been traversed.
3. Extend this minimal model by adding n layers of cells surrounding the minimal cells to the model (Fig. 6c shows one layer of these cells added, shaded dark grey). This defines the domain of the micro-model.

Once the domain of the micro-model has been determined the actual model can be constructed. The construction is done by duplicating the model for a single unit cell and translating and rotating it so that it aligns with the grid. This is done for each cell in the grid that has been determined to be needed in the micro model. The boundaries of adjacent unit cells are then sewn together to make a single model. This model, when unioned with the portion of the crack model that is interior to the unit cells, makes up the microscale model.

The results of this process in 3-D are shown in Figs. 7 and 8. The 3-D problem being modeled is a flat plate with a delamination as shown in Fig. 7a. Also shown near the middle of the plate is the delamination crack. The simple unit cell for an aligned fiber microstructure, as shown in Fig. 7b, is being used. The microscale model of the area around the delamination is shown in Fig. 8. This model includes the explicit representation of both the microstructure and the crack.

The mesh that is created for the micro-model has the restriction that, for the exterior faces of the model, the mesh must be identical to that which is on the boundary of the unit cell that was used to calculate the homogenized material properties. This requirement on the boundary mesh is imposed by the analysis. The mesh on the interior of the model has no restrictions. To create the mesh for this model the faces on

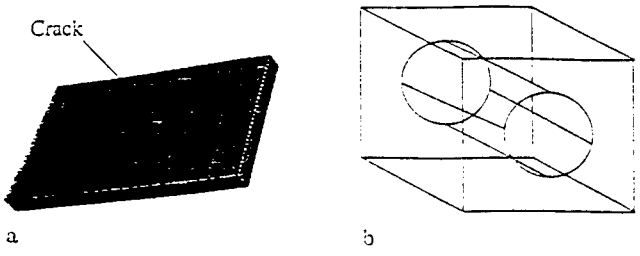


Fig. 7a, b. Macro-model and unit cell

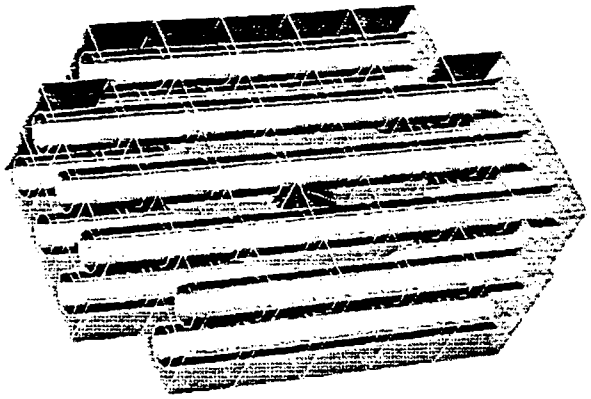


Fig. 8. Microscale model of delamination crack

the boundary of the model are first meshed using the mesh from the boundary of the unit cell. Then the other (interior) faces of the model are meshed using the Finite Octree mesh generator (Shephard and Georges). Finally the interior of the model is meshed using an element removal procedure that works from the given boundary mesh.

5.2.3
Transition model

The transition model is defined to tie the microscale model to the mesh of the macroscale model. To create the transition model, the outer boundary of the unit cells in the micro-model must be found. This is done in the same manner as the creation of the micro-model, except a cuboid of the size of the boundary of the unit cell is used instead of the model of the unit cell. The result of this procedure on the 3-D model is shown in Fig. 9a, note that all of the internal structure of the model, as compared to Fig. 8, has been eliminated, except for the crack.

The outer boundary of the transition model is the boundary of the union of all elements in the mesh of the macro-model that the micro-model is interior or close to. The procedure for finding these elements is as follows (illustrated for the 2-D case in Fig. 10.)

Given the domain of the micro-model as found above and the macro-mesh as illustrated in Figs. 10a, b, first find the elements which have a non-null intersection with the micro-model domain. In addition any elements which are considered very close to the micro-model domain is added to those that intersect it. The definition of 'close" in this case depends on the relative size of the elements in the macro-mesh

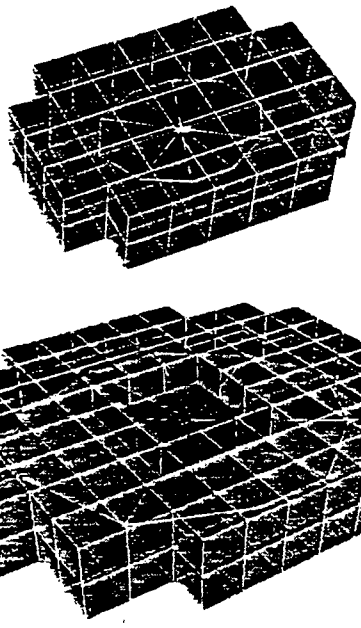


Fig. 9a, b. Boundary of micro-model

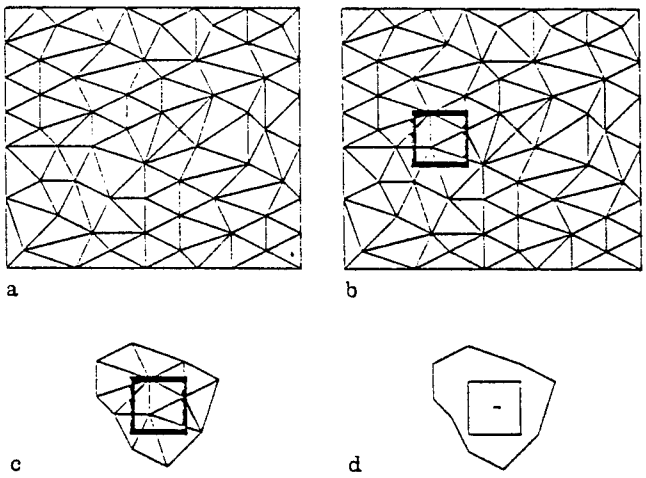


Fig. 10a–d. Construction of the transition model

to the size of the unit cells. The goal is to ensure that the transition mesh is a smooth change in element sizes from those in the macro-mesh to those in the micro-mesh. Once the elements of interest have been found, a model is constructed that is the boundary of the union of all of these elements and the inner structure of the transition model (the outer boundary of the micro-model) is inserted.

This same process carried out on the 3-D models shown previously results in the geometry shown in Fig. 11.

The mesh for the transition model does not need to be compatible with the mesh of the macro-model, however there should be no elements on the boundary of the transition mesh that are in more than one macro-mesh element face. This is ensured by constructing the transition model so that the edges of the macro-mesh are retained on the boundary (i.e. co-planar faces on the boundary are not unioned to make

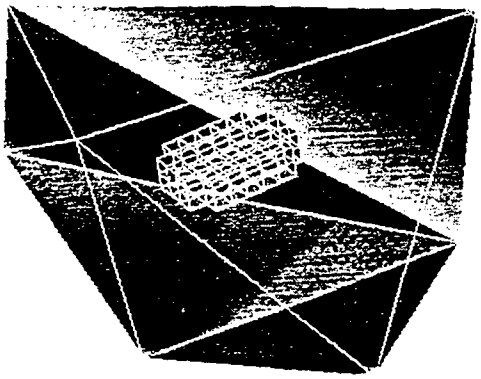


Fig. 11. Transition model

a single face, the edges that define the original faces are retained).

5.3 Model updates

One of the results of the analysis is the direction and distance that the crack front moves at each step. For the next analysis step to take place the models and meshes must be updated to reflect this growth of the crack. The steps in the model update are as follows:

1. Update crack representation in micro model to reflect the growth of the crack (Fig. 12a)
2. If the crack front exits a unit cell, the micro and transition models are updated as follows:
   a. Update the micro model domain (add unit cells ahead of crack and remove them behind (Fig. 12b)) to ensure that the micromodel exists for the desired distance ahead of the crack front.
   b. Update the transition model, including adding the domain of more elements from the macro mesh if micro model grows into them as shown in Figs. 12c, d.

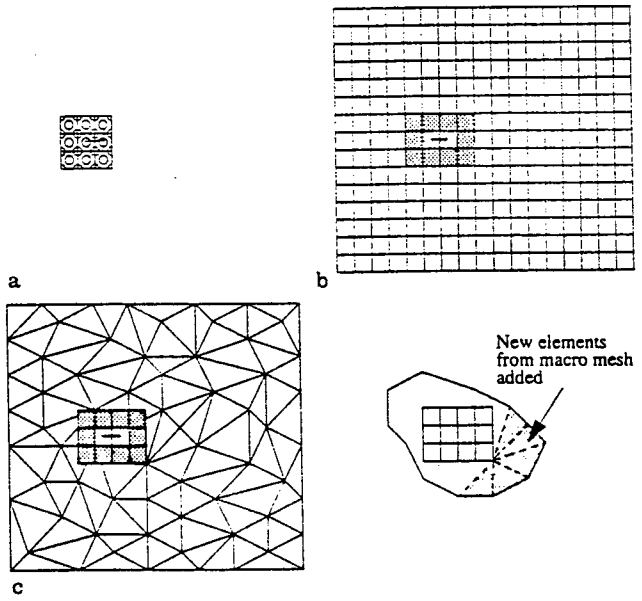


Fig. 12a–d. Micro and transition model updates

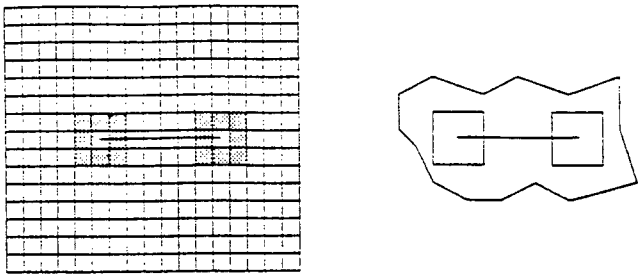


Fig. 13. Further update of micro and transition models

One goal is to keep the updates as local as possible to minimize the amount of geometric manipulation that must be done and to minimize the amount of the model that must be remeshed at each step. This step in the 3-D example is shown in Fig. 9 which shows the inner boundary of the transition model after the update.

As the crack grows there will be a portion of the crack that is far enough away from the front to not need to be modeled at the micro-scale as shown in Fig. 13. In this case all of the geometry of the crack must still be contained interior to the transition model. For these analyses this is done by only adding macro-mesh elements to the transition model and never removing them as the crack grows. Thus, although the micro-model domain only surrounds the area immediately around the crack tip, the transition model encompasses the entire crack.

In 3-D the elimination of the unnecessary areas behind the crack front from the micro-model keeps the problem size reasonable as the crack front grows. Without this the problem size would quickly grow to be much too large to solve. Figure 9b shows the 3-D example after the crack has grown.

Meshing the update models needs to be done as locally as possible. If the only change is that the crack has grown a small amount (i.e. no new unit cells have been added to the micro-model) the mesh is only updated locally around the crack front. When new unit cells are added to the micro-model, they can be meshed using the mesh that was created on the unit cell when the homogenization procedure was done. This is a simple procedure since the mesh on the boundary of the micro-mesh is identical to the mesh on the boundary of the unit cell.

6 Closing remarks

The successful application of advanced multiple scale procedures requires the ability to effectively develop the required analysis models. This paper has presented a framework and associated procedures for the automatic construction of models and meshes as required for multiple scale analyses. Specific sets of model construction procedures have been demonstrated for two multiple scale analysis procedures which employ different modeling and analysis procedures. Key ingredients in these example applications include the geometric modeler, automatic mesh generator, attribute manager, and the model building and discretization strategies used to ensure the correct idealized analysis models are constructed and discretized.

References

Bakhvalov, N. S.; Panasenko, G. P. 1989: Homogenization: averaging processes in periodic media, Mathematical Problems in the Mechanics of Composite Materials, Kluwer Academic Publishers

Fish, J.; Belsky, V. 1995a: Multigrid method for periodic heterogeneous media. Part 1: Convergence studies for one-dimensional case, Comp. Meth. Appl. Mech. Engng., to appear

Fish, J.; Belsky, V. 1995b: Multigrid method for periodic heterogeneous media. Part 2: Multiscale modeling and quality control in multidimensional case, Comp. Meth. Appl. Mech. Engng., to appear

Guedes, J. M.; Kikuchi, N. 1991: Premat/postmat. A Computer Software for Computational Mechanics of Composite Materials, Proceedings of the International Conference and Exhibition on Computer Applications to Materials Science and Engineering, Elsevier Science Publishers

Le Coz, Y. L.; Iverson, R. B. 1992: A stochastic algorithm for high speed capacitance extraction in integrated circuits. Solid State Electronics. 35: 1005–1012

Mead, C.; Conway, L. 1980: Introduction to VLSI Systems, Reading MA, Addison-Wesley

Minsky, M. 1981: A Framework for Representing Knowledge, in Winston (1975b) 211–280. Reprinted in Haugeland (1981) 95–128

Sham, T.-L.; Tiersten, H. F.; Baehmann, P. L.; Song, L.-Y.; Zhou, Y. S.; Lwo, B. J.; Le Coz, Y. L.; Shephard, M. S. 1993: A global-local procedure for the heat conduction analysis of multichip modules. Advances in Electronic Packaging 1993, 2: 551–562, NY, ASME

Shephard, M. S. 1988: The specification of physical attribute information for engineering analysis, Engineering with Computers, 4: 145–155

Shephard, M. S.; Finnigan, P. M. 1989: Toward automatic model generation. State-of-the-Art Surveys on Computational Mechanics, A. K. Noor and J. T. Oden, editors, 355–366, NY, ASME

Shephard, M. S.; Baehmann, P. L.; Georges, M. K.; Korngold, E. V. 1990: Framework for the reliable generation and control of analysis idealizations, Comp. Meth. Appl. Mech. Engng., 82: 257–280

Shephard, M. S.; Georges, M. K. 1991: Automatic three-dimensional mesh generation by the Finite Octree technique. Int. J. Numer. Meth. Engng. 32(4): 709–749

Shephard, M. S.; Georges, M. K. 1992: Reliability of automatic 3-D mesh generation. Comp. Meth. Applied Mechanics and Engng. 101: 443–462

Shephard, M. S.; Sham, T.-L.; Song, L.-Y.; Wong, V. S.; Garimella, R.; Tiersten, H. F.; Lwo, B. J.; Le Coz, Y. L.; Iverson, R. B. 1993: Global/local analyses of multichip modules: Automated 3-D model construction and adaptive finite element analysis. Advances in Electronic Packaging 1993, 1: 39–49, NY, ASME

Tiersten, H. F.; Sham, T.-L.; Lwo, B. J.; Zhou, Y. S.; Song, L.-Y.; Baehmann, P. L.; Le Coz, Y. L.; Shephard, M. S. 1993: A global-local procedure for the thermoelastic analysis of multichip modules. Advances in Electronic Packaging 1993, 1: 103–118, NY, ASME

Weiler, K. J. 1988: The radial-edge structure: A topological representation for non-manifold geometric boundary representations. Geometric Modeling for CAD Applications, M. J. Wozny, H. W. McLaughlin and J. Encarnacao, editors., 3–36, North Holland

Wentorf, R.; Shephard, M. S.; Korngold, E. V. 1989: The Use of Functional Models to Control Engineering Idealizations, Proceedings of the 1989 ASME International Computers in Engineering Conference and Exposition, Anaheim, California, July, 63–70

Wentorf, R.; Shephard, M. S. 1993: Automated Analysis Idealization Control, CONCURRENT ENGINEERING: Automation, Tools, and Techniques, Andrew Kusiak Ed., 41–73, John Wiley, New York

Wong, V. S. 1994: Qualification and management of analysis attributes with application to multi-procedural analysis of multi-chip modules, TR23-1994, Scientific Computation Research Center, Troy, NY

CHAPTER 3

Analysis Data for Visualization

MARK S. SHEPHARD AND
WILLIAM J. SCHROEDER

MODERN ANALYSIS AND design is based upon complex numerical modeling techniques. These techniques typically decompose a problem into many smaller pieces, and then solve the simpler but much larger problem on a computer. The results of such analysis, however, generate such large data size as to be nearly incomprehensible. To address this problem, engineers and scientists have turned to visualization. In this chapter we present an overview of engineering analysis techniques, and describe the forms of data that might be expected from such analysis.

3.1 INTRODUCTION

The goal of visualizing engineering analysis is an improved understanding of the results of the information generated in that analysis process. It is not difficult to imagine the potential advantages of using advanced visualization methodologies to convert masses of discrete numbers, often measured in gigabits, produced by a numerical analysis procedure into physically meaningful images. What is more difficult is the actual construction of the visualization techniques, which can provide a faithful depiction of those results in a manner appropriate for the engineer or scientist who performed the analysis. The development of successful visualization techniques for engineering analysis results requires a knowledge of, (i) the basic analysis procedures used, (ii) the information input and output from the analysis procedure, and (iii) the goals of the analyst applying the visualization procedures.

0-8493-9050-8/95/$0.00+$.50
© 1995 by CRC Press Inc.

This chapter provides a very brief introduction into the ways commonly used numerical analysis techniques operate, as well as the forms and methods used to construct the discrete models they require. Consideration is then given to the form of the output information produced by these procedures. This analysis input and output information provides the raw data to be used for producing meaningful visualizations. The chapter concludes with an examination of how that information can be visualized.

3.2 NUMERICAL ANALYSIS TECHNIQUES

Engineering analysis is the process of taking given "input" information defining the physical situation at hand and, through an appropriate set of manipulations, converting that input into a different form of information, the "output," which provides the answer to some questions of interest. The goal of visualization techniques, when used in conjunction with engineering analysis, is to provide the most meaningful means for engineers to view both the "input" and "output."

Although there are several classes of analysis problems, this chapter focuses on one class which typically provides the greatest challenges to the visualization of the output. In this class of problem the input consists of some physical domains for which there are known boundary conditions, initial conditions and loads. The goal of the analysis is to determine one or more response variables over that domain. The common method to develop and perform an analysis is to select, or derive, a mathematical model appropriate for the physical problem that can accept as input the material properties, initial conditions, boundary conditions and loads, and produce as output the desired response variables. The mathematical models produced by this process are typically sets of partial differential equations. In some simple cases, the exact continuous solution to these equations can be determined. However, in most cases such exact continuous solutions are not available.

For these classes of problems, where exact solutions are not available, the introduction of the digital computer has had a profound impact on the way in which engineering analysis is performed, and on its role in the engineering design process. Today, most engineering analyses associated with the solution of partial differential equations over general domains are performed using generalized numerical analysis procedures which approximate the continuous problem in terms of a discrete system. This yields large sets of algebraic equations which can be quickly solved by the computer. Software to perform these analyses is readily available in the engineering community. Therefore, these numerical analyses are now performed on a routine basis during engineering design.

A major problem confronted by users of these techniques is that the volume and form of the discrete information produced does not lend itself to simple interpretation, particularly when an understanding of the behavior of the parameters of interest over the domain of the analysis is desired. Properly constructed visualization techniques represent the key technology needed to extract the desired information from the volumes of discrete data produced by the analysis procedure.

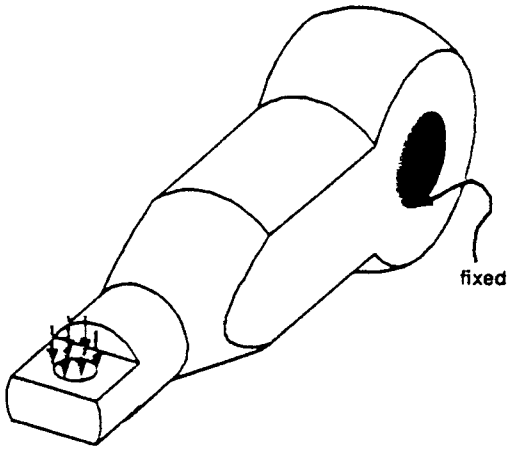


Figure 3.1. Solid model of a mechanical part showing loads and boundary conditions

As a simple example of the power of the numerical analysis techniques available today, consider the geometric model of a mechanical part shown in Figure 3.1 defined in a commercial solid modeling system. We wish to determine the deflections and stresses for this model subjected to the loads and boundary conditions also shown in Figure 3.1. For this example an automated adaptive analysis was performed in which the engineer simply specified the level of accuracy desired. Given the desired accuracy, the geometric model and analysis attributes of loads, material properties and boundary conditions, finite element procedures automatically generated the mesh, analyzed it, and adaptively improved it until the specified accuracy was obtained. The final mesh for this example is shown in Figure 3.2. At that point the engineer is faced with the problem of interpreting the results of the analysis which for even this simple example constitute many megabytes of data. The visualization techniques discussed in this book are key to supporting that results interpretation process.

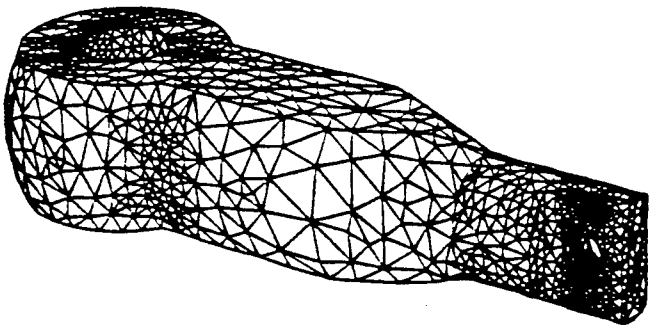


Figure 3.2. Automatically generated and adaptively refined finite element model of a mechanical part

3.3 BRIEF OVERVIEW OF ELEMENT BASED DISCRETIZATION TECHNIQUES

The majority of current numerical analysis procedures for solving partial differential equations employ cell-based discretizations of the domain of interest. The commonly applied cell-based discretization techniques are finite element, finite difference, boundary element and finite volume.

In finite difference methods the continuous differential operators are replaced by difference equations, using the value of the dependent variables at discrete locations. With all differential operators replaced by difference equations, the solution by finite differences consists of covering the domain with a set of evaluation points to be used in the difference equations. The values of the dependent variables at these locations are only known at specific locations dictated by the boundary and initial conditions. In a properly formulated problem, the substitution of these known values and the differenced load yields a solvable system algebraic equation in terms of the values of the dependent variables at the difference locations.

A different set of steps is employed in the application of finite element, boundary element, and finite volume techniques. In these techniques a two-step process is performed. The first step is to convert the governing partial differential equations, the strong form, into an equivalent integral form, the weak form. The weak form is then discretized by approximating the appropriate terms in the weak form by given distributions written in terms of unknown multipliers. The mathematical manipulations performed in the construction of the weak form differentiate the basic methods and dictate the requirements placed on the distributions which can be validly used. The details of the specific method are further dictated by the methods used to construct the distributions. The commonly applied methods employ piecewise distributions which are non-zero only over individual cells, typically called elements, written in terms of values on their boundary. By the proper matching of the boundary values on neighboring elements, the valid distribution over the entire domain is constructed. Appendix 3.9 outlines the basic mathematical steps in the finite element method. Interested readers should consult basic finite element references for additional information [13, 26, 30].

3.3.1 Commonly Used Element Geometry and Shape Functions

As indicated in the Appendix to this chapter, a key ingredient in the construction of the finite element equations is the selection of element shape functions and the integration of the operators, equations (3.13–3.15) over the domain of the elements. The selection of the element shape functions must satisfy specific requirements so that the elemental integrations and their summation are meaningful. Considering the generic second order partial differential equation (Equation 3.9) which can represent many of the physical problem types of interest, the minimum requirement is that the dependent variable and first partial derivatives are continuous within the element, C^1, and the dependent variable be

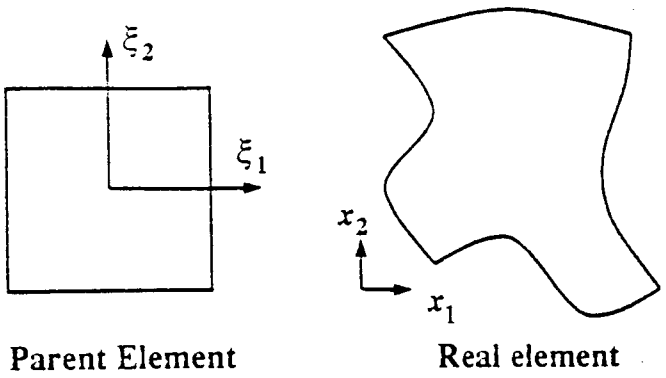


Figure 3.3. Parametric coordinate system for element description

continuous between elements C^0. Considering the use of topologically simple finite elements, for example three- and four-sided in 2-D, these requirements are easily met by selecting the value of the dependent variable at locations on the boundary of the element and using polynomial shape functions. For example, it is easily shown that the C^1 intra-element and C^0 inter-element continuity requirements are easily met by selecting linear element shape functions written in terms of the values at the triangle's vertices. Considering a simple scalar field, the element shape functions for the linear triangular element can be written as

$$u^h = \sum_{a=1}^{3} N_a d_a^e \qquad [3.1]$$

where d_a^e are the values of u^h evaluated at the node a of element e, and N_a are linear shape functions having a value one at node a and zero at the other nodes.

If all finite elements were constructed using linear shape functions acting over simplex[1] elements, the process of visualizing finite element results would be simplified. This is not, however, the case. It is common in finite element analysis to employ higher order functions to represent both the variation of the dependent variable over the element as well as its shape. To support the process of forming the elemental integrals needed these higher order elements typically employ a parametric coordinate system. Figure 3.3 depicts a parent element in the parametric coordinate system and the real element in a global coordinate system for a 2-D quadrilateral. The 3-D parametric coordinate system for a brick adds a ξ_3 coordinate to that shown in 2-D. Area and volume coordinates are typically used for triangular and tetrahedral elements [8].

Using parametric coordinate systems the variation of the dependent variables and element shape are written as

$$u^h = \sum_{a=1}^{n_{en}} N_a(\xi) d_a \qquad [3.2]$$

1. Triangles in 2-D and tetrahedra in 3-D

and

$$\underline{x} = \sum_{a=1}^{n_{sh}} N_a^s(\xi)\underline{\tilde{x}}_a \qquad [3.3]$$

where $\underline{x}$ represents the shape of the element, $N_a(\xi)$ are the dependent variable shape functions written in terms of the parametric coordinate system, $N_a^s(\xi)$ are element geometry shape functions written in terms of the parametric coordinate system, and $\underline{\tilde{x}}_a$ represents the discrete shape parameters, such as the global coordinates of points on the boundary of the element.

The most commonly used finite element shape functions are defined in terms of linear, quadratic or cubic Lagrange polynomials interpolated through nodes on the closure of the element [8, 13, 30]. In 2- and 3-D the individual shape functions are combinations of products of 1-D Lagrange polynomials. The use of nodal interpolation and parametric coordinates make it easy to construct these shape functions to satisfy the C^0 inter-element continuity requirements, since the values along a boundary are uniquely defined in terms of nodal values on that boundary, and nodal values are common to neighboring elements sharing boundaries. It is also common in the use of these shape functions to employ the same shape functions for the dependent variables and element geometry. Such elements are referred to as isoparametric elements. Figure 3.4 shows the common forms of these elements, from linear to cubic shape functions over four sided 2-D elements.

Over the past several years finite element developers have expanded the classes of geometric functions used in the construction of finite elements. One of the main drivers of these developments is the desire to employ *p-version* finite element techniques. Unlike fixed polynomial order finite element methods where the solution accuracy is increased by increasing the number of finite elements (the so called *h-version*), the *p-version* maintains a fixed mesh and increases the solution accuracy

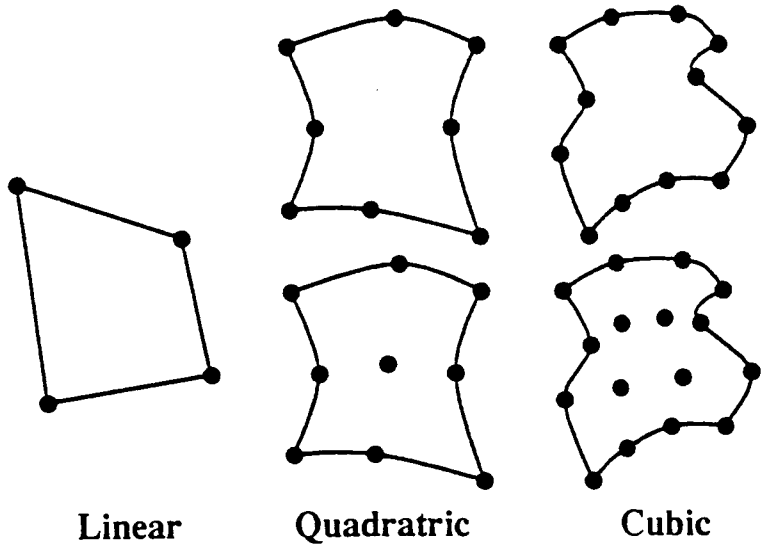


Figure 3.4. Common isoparametric element forms

by increasing the polynomial order of the finite elements. It is also possible to combine the two technologies yielding the *hp-version* of the finite element method which has been shown to provide the greatest increases in solution accuracy for a fixed computational effort [26].

In the *p-version* the polynomial order of elements in the mesh can become quite high in which case the Lagrangian type shape functions commonly used in the *h-version* are not acceptable. Therefore, Lagendre polynomials are commonly used for the dependent variable shape functions in *p-version* elements because they are numerically well conditioned, allow the hierarchic construction of element matrices, and can be easily used to construct meshes where the polynomial order varies over the mesh. One minor drawback is that the individual degrees of freedom (dof) terms are no longer just the value of the dependent variable at a node point. Instead, they are often various higher order derivatives evaluated at element mid-edges, mid-faces and at the centroid of the element. These dof are selected and shared between elements such that maintaining the required C^0 inter-element continuity is not difficult.

The finite elements employed in p-version meshes are typically quite large, and cover sizeable portions of the boundary of the domain being analyzed. Therefore, it is critical that the geometry shape functions used for these elements introduce very little approximation error. For example, it is common to have only four element edges around a circular hole. Clearly, a piecewise linear geometry approximation which would yield a square would introduce substantial errors into the analysis results. One approach that has been applied to construct geometric shape functions is to employ transfinite mapping techniques using implicit geometric functions for the geometric boundary of the elements of a high order geometric approximation [10, 11].

3.3.2 Element Integration

With the shape functions selected for the dependent variables and geometry of the elements the next task is to perform integrals over the elements to form the element stiffness matrices and load vectors. Consider a term in the stiffness matrix

$$k^e_{pq} = a\left(N_a, N_b\right) = \int_{\Omega_e} \mathcal{H}^1(N_a)\left(\mathcal{G}^1(N_b)\right)d\Omega \qquad [3.4]$$

where, for sake of discussion, we examine a 2-D element and a particular typical integral as

$$k^e_{pq} = \int_{\Omega_e} \lambda N_{a,x_1} N_{b,x_2} dx_1 dx_2 \qquad [3.5]$$

where N_{a,x_i} in the x_i first partial derivative of N_a. Since the element shape functions are written in the parametric coordinate system ξ, the relationship between the coordinate systems must be established. Consideration of Equation 3.3 shows it is easy to form N_{a,ξ_i}, therefore the N_{a,x_i} are found by first applying the chain rule of differentiation for N_{a,ξ_i} which in 2-D can be written

$$\begin{Bmatrix} \frac{\partial}{\partial \xi_1} \\ \frac{\partial}{\partial \xi_2} \end{Bmatrix} \qquad [3.6]$$

and then inverting that expression to yield

$$\begin{Bmatrix} \frac{\partial}{\partial x_1} \\ \frac{\partial}{\partial x_2} \end{Bmatrix} = \frac{1}{|J|} \begin{bmatrix} \frac{\partial x_2}{\partial \xi_2} & -\frac{\partial x_2}{\partial \xi_1} \\ -\frac{\partial x_1}{\partial \xi_2} & \frac{\partial x_1}{\partial \xi_1} \end{bmatrix} \begin{Bmatrix} \frac{\partial}{\partial \xi_1} \\ \frac{\partial}{\partial \xi_2} \end{Bmatrix} \qquad [3.7]$$

where $[J]$ is referred to as the Jacobian matrix and $|J|$ is its determinate. Note that the terms in Equation 3.7 are easily constructed by the use of Equation 3.3 and the element geometry shape functions. The final substitution required in Equation 3.5 is the proper coordinate change to integrate in the local coordinates. This is accomplished by the use of $dx_1 dx_2 = |J|\, d\xi_1 \xi_2$. Substituting these into the specific case of Equation 3.5 yields

$$k_{pq}^e = \int_{\Omega_e} \left(\lambda(\xi)\right)\left(N_{a,x_1}(\xi)\right)\left(N_{b,x_2}(\xi)\right)|J| d\xi_1 d\xi_2 \qquad [3.8]$$

$$= \int_{\Omega_e} \lambda \left\{ \frac{1}{|J|} \left(\frac{\partial x_2}{\partial \xi_2} \frac{\partial N_a}{\partial \xi_1} - \frac{\partial x_2}{\partial \xi_1} \frac{\partial N_a}{\partial \xi_2} \right) \right\} \left\{ \frac{1}{|J|} \left(-\frac{\partial x_1}{\partial \xi_2} \frac{\partial N_b}{\partial \xi_1} + \frac{\partial x_1}{\partial \xi_1} \frac{\partial N_b}{\partial \xi_2} \right) \right\} |J| d\xi_1 d\xi_2$$

Since the final form of the element stiffness integrals are in terms of rational polynomials, they are not easily integrated in closed form. Therefore, numerical integration techniques are employed [13, 26, 30]. Since the integrals are over fixed domains in the parametric coordinate system, optimal techniques such as Gauss quadrature are typically applied.

3.4 METHODS TO CONSTRUCT AND CONTROL ELEMENT MESHES

A key aspect of the finite element method is the construction of the finite element mesh used to represent the domain over which the analysis technique will be applied. Consideration of the type and distribution of finite elements in the mesh is key because:

- The accuracy and computational efficiency of the finite element method is dictated by type and distribution of finite elements.

- The generation of the finite element mode dominates the cost of application of the finite element method. Its construction typically represents 70–80% of the total cost.
- The finite element mesh is the approximate representation of the domain to which solution results will be tied. It represents a basic component of the information used for visualization processes.

The next subsection indicates the methods used to generate finite element meshes. The following subsection mentions the area of adaptive techniques to control the mesh to provide the desired level of accuracy.

3.4.1 Mesh Generation

In the early application of the finite element method there was no computerized representation of the domain, and few tools were available to generate the finite element mesh. Therefore, the finite element meshes were manually drawn and converted into the computer by creating input "decks" defining each and every finite element entity. As computing hardware began to mature, and interactive graphics techniques became cost effective, interactive finite element preprocessors became available. These programs provided users with tools to interactively define the boundaries of mesh patches, which could then be filled with finite elements using appropriate mapping procedures. These programs had a major impact on the finite element model generation process. However, they still represented a bottom-up approach to the generation of the domain to be analyzed in terms of finite element mesh entities.

Over the years these finite element preprocessors have been extended to allow simple links with computer-aided geometric modeling systems. These links allow users to import basic boundary entities from the geometric modeling system, which can then be manipulated and used in the construction of the finite element entities which bound mesh patches. Today the majority of finite element meshes are generated using these interactive graphics tools based on these techniques.

Recently, fully automatic mesh generators, capable of operating directly with the CAD representation to produce meshes of domains without user interaction, have been introduced [9, 22]. An automatic mesh generator can be defined as an algorithmic procedure which can create a mesh, under program control and without user input or intervention. All automatic mesh generation approaches must address the same basic issues of

- Determining a distribution of mesh vertices to provide the form of mesh gradation requested.
- Constructing the higher order finite element entities of mesh edges, faces and regions using the node points, and
- Ensuring the resulting triangulation represents a valid finite element mesh.

The primary differences in the approaches developed are the manner in which they perform the steps above. At one end of the spectrum are techniques which

(i) place all the mesh vertices throughout the domain to be meshed, (ii) apply a criterion to connect the points to create a set of elements, and (iii) apply an assurance algorithm to convert the initial triangulation into a geometric triangulation. At the other end of the spectrum is a technique that works directly off the geometric model, carefully removing elements one at a time, creating individual mesh vertices on an as needed basis, and ensuring that at each step in the process the requirements of a geometric triangulation are satisfied.

Currently four algorithmic approaches receiving considerable attention are Delaunay [2, 5, 20], advancing front [3, 15], medial axis [12, 27], and octree techniques [4, 14, 20, 24].

An example of an automatic mesh generator is the Finite Octree procedure in which the mesh is generated as a two-step meshing process [24]. In the first step the geometric domain is discretized into a set of discrete cells that are stored in a regular tree structure, referred to as the Finite Octree. In the second step the individual cells within the Finite Octree are discretized into finite elements, with specific care to ensure the proper matching to the elements in the neighboring cells. All of the individual operations performed during the mesh generation process are performed in such a manner to ensure the result is a geometric triangulation of the original domain [21, 25].

The construction of the Finite Octree can be easily visualized by first placing the domain to be meshed into a parallelopiped cell, typically a cube, which encloses it. This original cell, which represents the root of the Finite Octree, is subdivided into its eight octants, which represent the eight cells at the first level of the tree. Each of these cells can be recursively subdivided into its eight octants producing the next level in the tree for that cell. Since the finite elements to be generated in the second step are of the size of the individual cells, element size and gradation are controlled by those cells that are subdivided, and how many times they are subdivided. The regular tree structure of the Finite Octree supports efficient procedures to generate the resulting mesh.

An important difference between the Finite Octree representation, and a basic octree decomposition of a domain, is that during the generation of the Finite Octree a cell level discrete representation of the portion of the domain within the cell is constructed. This construction is simple for the cells entirely inside or outside the object being meshed. It is those cells that contain portions of the boundary of the domain for which carefully structured geometric interrogation processes are required to ensure that the discrete cell level representation is topologically equivalent and geometrically similar to the portion of the geometric domain in that cell. The discrete geometric information generated during this process is stored in a non-manifold topological data structure, a compact form of which is also used to store the final mesh [29]. Figure 3.5 shows a Finite Octree decomposition of the model shown in Figure 3.2.

The finite element mesh is generated on a cell-by-cell basis using a set of element removal operators. The cell level element removal procedures employ the pointwise geometric interrogations to ensure that the resulting mesh is topologically compatible and geometrically similar to the geometric domain. When a cell is meshed, the information in the Finite Octree, and a non-manifold topological

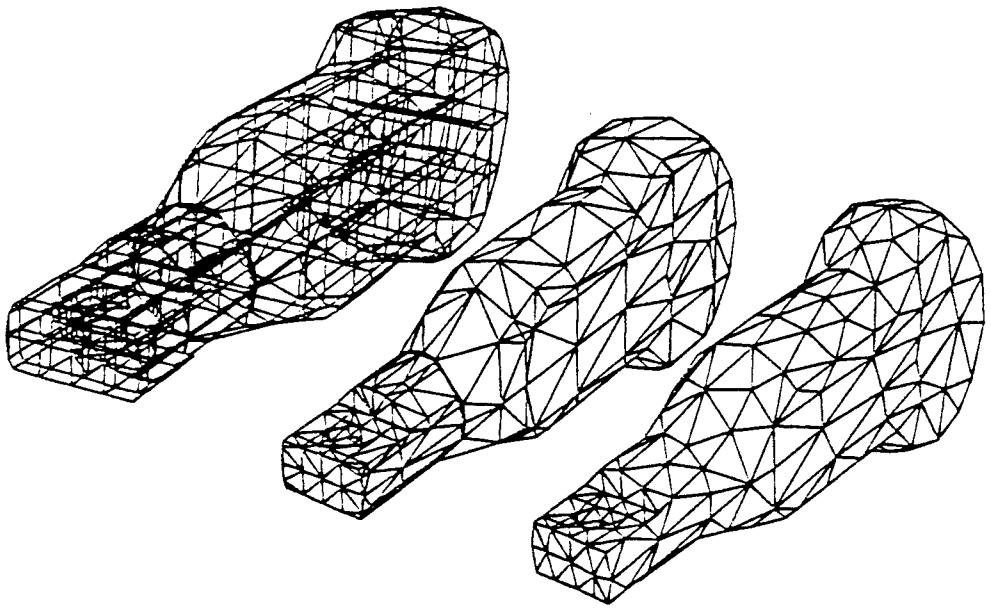


Figure 3.5 Finite Octree decomposition of domain (left), element mesh after element removal (center), and after mesh finalization (right) for the example problem.

data structure, is used to ensure that it will properly match the mesh in any neighboring cells that have already been meshed. After the mesh has been generated a specific set of finalization procedures are applied to eliminate poorly shaped elements and to reposition the node points to improve the shapes of those that are maintained. Figure 3.5 shows the mesh for the example problem after the application of the element removal procedures and after the finalization procedures are applied.

For a more complete technical explanation of the Finite Octree mesh generation procedure the interested reader is referred to Reference [24].

3.4.2 Adaptive Finite Element Mesh Control

Since the accuracy of the solution obtained is a function of the finite element mesh, it is critical that the type and distribution of finite elements within the domain be controlled. Broadly speaking the methods to control the finite element discretization can be grouped as *a priori* and *a posteriori*. In *a priori* methods, the individual generating the mesh exercises explicit control on the type and distribution of finite elements, based on their knowledge of the physical problem being solved. Since the individual analyzing the problem does not have perfect knowledge of the problem (if they had that knowledge, they would not need a finite element analysis), the *a priori* methods can provide a computationally efficient mesh, but the actual accuracy of the analysis is not known. The goal of *a posteriori* mesh control is to employ the results of the previous analysis to estimate the mesh discretization errors and then improve, in an optimal manner, the mesh until the desired degree of accuracy is obtained. Such *a posteriori* mesh control

capabilities, referred to as *adaptive methods,* are capable of generating efficient meshes for a wide variety of problems as well as providing explicit error values [1, 7, 16, 17, 18].

The combination of an automatic mesh generator and adaptive analysis techniques allows the reliable automation of finite element analysis. The main components of such an automated adaptive finite element procedure are:

- An automatic mesh generator that can create valid graded meshes in arbitrarily complex domains
- A finite element analysis procedure capable of solving the given physical problem
- An *a posteriori* error estimation procedure to predict the mesh discretization errors, and to indicate where it must be improved
- A mesh enrichment procedure to update the mesh discretization

Clearly, the *a posteriori* error estimation procedures are central to the ability of an adaptive procedure to reliably control the mesh discretization errors. The approaches that have been developed to estimate the errors range from simple indicators that indicate where the solution variables are changing rapidly, to procedures that convert the residuals of the approximate solution to bounded estimates of the errors in norms, e.g., measures, of interest.

There are also a number of possible methods to enrich the finite element discretization based on the results of the error estimation and correction process. They include (i) moving nodes in a fixed mesh topology (r-refinement), (ii) subdividing selected elements in the mesh into smaller elements (h-refinement), (iii) increasing the order of polynomials (p-refinement), and (iv) superimposing selective enriched mesh overlays (s-refinement). Each of these methods has relative advantages and disadvantages. Often, a combination of methods provides the most effective strategy. For example, the optimal combination of h- and p-refinement has been shown, both theoretically and numerically, to provide greatly improved computational efficiency over the application of a single method.

Figure 3.6 shows a comparison of *a priori* and adaptive *a posteriori* mesh control. The mesh on the left was defined using *a priori* mesh control, where the user specified a finer mesh at the common areas of stress concentration around the holes. This mesh was then used as an initial mesh in an adaptive analysis procedure, aiming for less than the 5% error, that produces the mesh on the right. A comparison of the two meshes indicates that the initial mesh was not fine enough around two holes and at specific reentrant corners, while it was finer than required around the third hole.

3.5 VISUALIZATION GOALS

Since the fundamental goal of visualization is effective communication, it is imperative to understand both the audience of the communication as well as the information that needs to be communicated. In the following section we describe

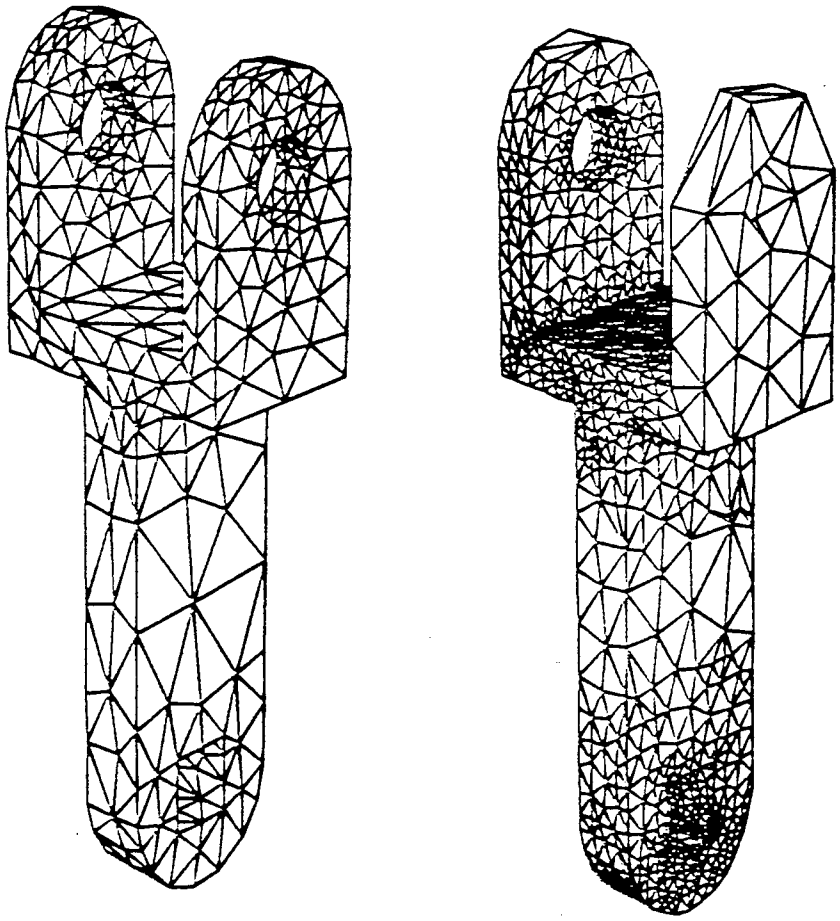


Figure 3.6 Initial mesh (left) and adaptively refined mesh (right) for the second automated adaptive example.

both the potential users of visualization in engineering analysis, as well as the results data that must be communicated to these users.

From the most general perspective the information available to the visualization process consists of the geometric description of the domain, the analysis attributes of loads material properties and boundary conditions defined in terms of that domain, and the distribution of the solution results of interest over that domain. What is actually available to the visualization process are two descriptions: the problem specification and attributes in terms of the original geometric model (e.g., CAD model), and the analysis results tied in a discrete manner to the computational mesh (e.g., finite element mesh).

The discussion given here focuses on the computational mesh description of the domain and attributes, and the results defined in terms of the mesh. An alternative approach is to visualize results data in terms of the original geometric description of the domain. Although we do not discuss this approach here, the basic idea is to perform an inverse mapping from the results data of the mesh to the original geometry. In either case the computational mesh, analysis attributes, and results data necessarily serve as the starting point for visualization.

3.5.1 Goals of Visualizing Results

The goal of the visualization process is to effectively communicate the potentially large data available from the engineering analysis process. Typical users of engineering analysis tools often fall into one of two categories: the *design* or *product* engineer, and the *methods* engineer or analyst.

The design engineer is generally interested in synthesis of function. Engineering analysis and visualization is used to perform overall evaluation of the product. The design engineer is typically looking for an understanding of a design or product in order to improve it. A typical example is designing a compressor blade in a jet engine. The design engineer looks carefully for stress concentrations and vibration response, and may adjust the structure to avoid resonance conditions or material fatigue problems. Numerical values are often required to characterize a particular design point, such as determining the peak magnitude of the stress, or to compare the natural frequencies of the compressor blade to upstream stimulus. The actual solution process of the engineering analysis is of little concern to the design engineer, as long as the solution is accurate enough for his needs.

In comparison, the analyst is generally interested in the details of the engineering analysis. Often the analyst is responsible for creating analysis tools for the design engineer to use, or performs analysis of particularly challenging analytical problems. Hence the primary concern of the analyst is the accuracy of results, and the sensitivity of results to variations in input parameters. This requires detailed understanding of the solution process. The analyst may also require information to guide the solution process, that is adjusting model and simulation inputs to provide proper convergence to solution. As a typical example, an analyst might evaluate the location of shock fronts in a supersonic flow analysis around a compressor blade in a jet engine. Effective visualization provides enough insight into the solution process to adjust parameters controlling numerical stability and modify analytical models as necessary.

3.5.2 Types of Analysis Variables to Be Visualized

The data available for visualization from engineering analysis can be roughly categorized into *mesh geometry* and the *solution data* associated with the mesh geometry. Although this classification is obvious in light of the previous discussion of engineering analysis techniques, this distinction between geometry and data is blurred in many visualization applications. In volume visualization the geometry is completely implicit, and the data available for visualization is assumed to be a series of values implicitly associated with a regular array of points. In finite difference analysis, the topology is implicitly assumed; (i.e., a regular array of points in conjunction with i-j-k dimensions), and the geometry is specified as an (implicitly) ordered sequence of coordinate locations.

Mesh geometry is the computational mesh including intermediate mesh geometry and topology hierarchy. For example, in three dimensions tetrahedral or hexahedral elements are often used to discretize the domain. Many visualization techniques require the triangle and quadrilateral faces of these elements for viewing results, or may require the ability to move across element boundaries (as

in streamline generation). Mesh geometry also includes intermediate meshes from any enriched mesh overlays (s-refinement), or may be *time* dependent due to adaptive solution techniques or a truly transient analysis. Mesh geometry is generally used to form the viewing context for visualization techniques such as mapping color corresponding to stress level on the surface, or deforming the geometry according to the displacement field.

Solution data consists of both primary and secondary solution variables. The primary variables result directly from the solution process of the system of global equations (e.g., displacements in structural analysis), while secondary solution variables are typically related to derivatives of the primary variables (e.g., stresses or strains). In some cases, results data includes surface fluxes that may be associated with a particular face or edge of the element.

Visualization techniques are often characterized according to the form of solution data. Typical classifications include scalar data, vector data, and tensor data. Scalar data is an array of scalar (i.e., single-values, each value uniquely associated with a point in space. Examples include temperature or pressure data. Vector data is an array of n-dimensional vectors, where n is the dimension of the computational domain. Example vector data includes velocity, displacement, or momentum fields. Tensors are generalized specifications of data in the form of matrices. Common tensors include the second-order stress tensor (a 3×3 matrix in 3-D) and the fourth-order elastic stress-strain tensor (a 9×9 matrix in 3-D). Scalar and vector data are zero-order and first-order instances of tensors, respectively.

3.6 REPRESENTATION OF MESH AND RESULTS DATA

A major issue facing implementors of 3-D visualization systems is the representation of data. On the one hand, visualization systems must be as general as possible, since they must interface to a broad range of data sources. Visualization systems are also constrained by limitations on computer performance. Computer hardware vendors offer efficient paths for 3-D graphics by providing hardware-accelerated graphics primitives such as points, lines, and polygons. Using these primitives as compared to generating visualizations in software produces order of magnitude differences in speed. On the other hand, modern analysis systems depend upon sophisticated mathematical techniques for modelling complex physics. The result is that most visualization systems make significant compromises in both the representation and mapping of results data into visual representations in order to facilitate the interactive exploration of data.

This section describes a data structure that explicitly represents computational meshes and results data. This structure is not typical of most visualization systems. Some use structures quite similar to the hierarchical structures described here, and require limited mapping from one form to the next. Other visualization methods (e.g., volume visualization) represent data in terms of structures completely independent of the computational mesh. These methods may be properly referred to as sampling techniques, and the representation of this data is not treated here.

3.6.1 Mesh Geometry

Representations of mesh geometry are dependent upon the particular analysis techniques employed. For example, finite difference techniques use a topologically regular grid in conjunction with an ordered list of point coordinates to specify geometry. In the discussion that follows, mesh geometry is assumed to be of a finite element type. This type is the most general form, and other geometry types can be mapped into it.

Historically, the representations of a finite element mesh consisted of a *list of element connectivities and node point coordinates* (Figure 3.7 (a)). In particular, a type flag is used to represent the topology of the element, and an ordered list of nodes in combination with a list of nodal point coordinates is used to specify the geometry of the mesh. This information, combined with the knowledge of how to employ the element type flag, can be used to construct any information regarding the shape of an element. Although it is a compact structure, it lacks the generality needed for some of the more advanced finite elements and their combination with adaptive analysis procedures. A more general approach is to consider the hierarchy of topological entities and describe the finite elements in terms of these entities and their adjacencies.

Topological hierarchies provide a general framework for engineering analysis [23, 28, 29]. This means that topology is an explicit abstraction, which serves as an organizing structure for data. In engineering analysis, topology serves as the link between geometrically specified computational models (Figure 3.1) and the numerical methods (e.g., the mesh) necessary to solve these problems (Figure 3.2). Organizing data according to topology shields the user from the details of the geometric representation (splines, implicit surfaces, etc.) and computational mesh, while providing a mechanism to map information from one representation to the other.

A simple hierarchical structure for mesh geometry is shown in Figure 3.7(b). The topology of each n-dimensional element is defined in terms of its $(n-1)$-dimensional boundaries. Each n-dimensional topological entity may also have a geometric specification (i.e., shape and location) associated with it. For example, a vertex is associated with a position in space, an edge with a parametric space, and a face with a spline surface.

Advanced modeling of composite structures, evolving and or non-manifold geometry, and adaptive analysis techniques benefit greatly from the addition of additional *classification, adjacency,* and *use* information. Classification is a necessary step for rigorous generation of finite element meshes, and is simply an association of each entity in the mesh topological hierarchy with a corresponding topological entity in the original geometric model [19, 21]. Classification information is the hook that allows mapping problem specifications in terms of geometry to a discretized computational model, and then back again to visualize results. Adjaceny information is the relationship in terms of physical proximity and order of one topological entity to another. An example of one adjacency relationship is the group of faces in cyclic order around an edge. Use information is a modeling convenience that specifies the way one topological entity is used in the

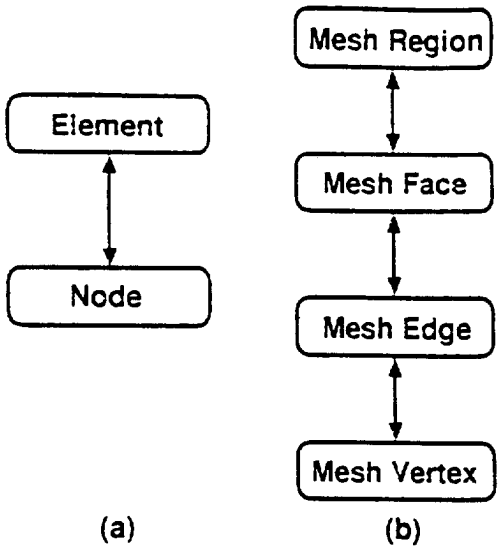


Figure 3.7 Traditional mesh structure (a) and hierarchical structure(b).

definition of another; (e.g., the direction or orientation of the defining topology). Both adjacency and use information are useful in complex analytical problems such as evolving geometry, where boundary contact occurs and modification to the underlying geometric representation is required.

3.6.2 Data Representation

As described previously the results data from a finite element analysis may consist of scalar (zero order tensor), vector (1st order tensors), or tensor information. The location of this information may be on element nodes, within the element at interior points, or possibly on the element boundary.

The hierarchical mesh geometry representation is a convenient structure in which to house this information. Scalar, vector, or tensor data located at element nodes is associated with the mesh vertices. Surface or edge fluxes are associated with the faces or edges. Interior element data are associated with the region. In some cases the interior element data may be extrapolated to, and stored with, the mesh vertices.

A particularly important issue is the native representational form of the analysis results. That is, if the analysis system generates results in double precision form, the visualization system should represent data in native form as well. This is particularly important when the results are of small size (byte or short), since representing a small type with a large type can unnecessarily consume enormous memory resources. Related to this issue is computational form: visualization algorithms should use enough accuracy to produce correct visualizations.

Probably the overriding issue in representing analysis results is choosing a compact representational form. Since the expressed purpose of visualization is to effectively communicate information, visualization systems are most effective when they can treat large data.

3.7 MAPPING ANALYSIS RESULTS TO VISUALIZATIONS

Producing visualizations requires mapping results data into visual representations. Typical procedures involve either sampling the results data on a regular grid (i.e., volume visualization), or conversion of analytical forms (nodes and elements) into graphical forms (points, lines, polygons). Once this mapping is accomplished, the techniques described in later chapters of this book are applied to generate the visual images. The remainder of this chapter provides an overview of the mapping from results data into forms necessary for visualization. Particular emphasis is placed on the approximations and potential errors involved in the mapping process.

3.7.1 Extrapolation and Interpolation

Because of the nature of engineering analysis, solution data is available at a finite set of points within the computational mesh. Primary solution variables are typically available at node points of the mesh, while secondary variables are often calculated at points interior to the element where they are known to be more accurate. The discrete nature of solution data is of major concern in the visualization process, because information is frequently required at locations other than that directly available from the solution. Hence this information must be derived by performing both interpolation or extrapolation, depending upon the location of the solution data. Generally this mapping process requires an intimate knowledge of the analysis technique, and should be carried out using the same element approximation functions used for formulation of the system equations.

Extrapolation is used when results data is available interior to mesh elements, and a data value is desired in outer regions such as element node locations. Results data is frequently available only at select interior points, because solution accuracy is known to be greatest there. Extrapolating stresses from integration points to element nodes is a typical example.

A simple extrapolation scheme is based on normalizing the element shape functions so that the integration points are located at the corners (i.e., at $\xi = (\pm 1)$), and then evaluating the data at the element node points. Another common extrapolation scheme is based on the least squares process. Typically, interior values are known interior to an element on a small array of points (e.g., $2 \times 2 \times 2$ or $3 \times 3 \times 3$) located in the parametric space of the element. Stresses are assumed to vary as a product of low order polynomials (usually linear or quadratic), and the least squares coefficients are generated from the integration point values and evaluated at the element nodes.

There are two major difficulties with extrapolation. When extrapolating from the element interior to the node points, different values for each node will be generated from each of the elements that use that node. The usual approach in this situation is to average the contributions from each element to generate a single value. Extrapolation may also produce errors as a result of the difference between the order of the approximation function in the element and the actual physics of

the problem. In elliptic partial differential equations the maximum value will always occur at the domain boundary and extrapolation techniques produce results that underestimate peak values. Analytic solutions of stress concentrations around geometric features clearly show polynomial rates of stress increase much higher than the extrapolation equations above.

Interpolation is used when results data is available throughout a region of the element, and a data value is desired within that region. The most common case arises when results data is available at the element nodes, and an interior element data value is required. Interpolation is based on the element shape functions of Equation 3.1, where in this case U represents results data available at the element nodes.

A common problem with both extrapolation and interpolation techniques is that they require specifying locations (where a data value is desired) in terms of the element coordinate system. Unfortunately many visualization algorithms specify point location in global coordinates. Hence the use of interpolation and extrapolation techniques frequently requires transforming a global coordinate into an element coordinate. This process involves identifying the particular element the point is in, as well as solving Equation 3.25 for the element coordinates ξ. Because the element geometry functions are typically products of polynomials, closed-form solutions are generally not available. Instead, numerical techniques such as Newton's method can be used to solve the systems of equations for the element coordinates [6].

3.7.2 Mapping to Visualization Forms

There are two common approaches to mapping engineering analysis data into visualizations. These are 1) data sampling and 2) conversion of mesh geometry and results data directly into graphical primitives.

Data sampling is a conceptually simple process (Figure 3.8(a)). Results data are sampled on a structured array of points using interpolation and/or extrapolation. The user need only specify the resolution and position of the sampling array, taking care to sample at a high enough frequency to capture the details of the solution. Standard volume visualization techniques (Chapter 6) are then used to generate the visual images.

Data sampling is particularly useful for visualizing analysis results based on higher-order shape functions, or for selected regions within the domain. A significant problem with this method is that the data size of the sampled data grows with the cube of the sampling density, since current techniques are not adaptive. Hence, the danger is that limitations on computer resource may result in errors due to undersampling the results data.

Conversion of results data to graphics primitives is another common mapping technique. This process involves matching element types to available graphics primitives (Figure 3.8(b)). For a small set of linear element types (i.e., points, lines, triangles, and quadrilaterals) this mapping is direct, as long as results data is available at the element nodes, otherwise extrapolation needs to be employed. Other linear 3-D elements such as hexahedra and tetrahedra can be decomposed by

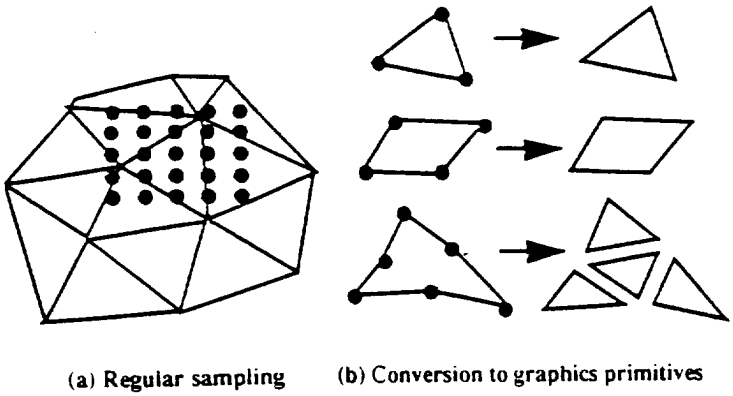


Figure 3.8 Sampling data (a) and primitive conversion (b).

mapping the element faces to triangles and quadrilaterals. Higher order elements are often broken into many primitives depending upon the topology of the elements and possibly the nature of the solution within the element.

Mapping to graphics primitives is the most common technique today, since it provides information that graphics hardware can efficiently process. This results in highly interactive visualization systems. The basic problem with this approach is that decomposing non-linear elements into linear graphics primitives results in significant loss of accuracy. Decomposition of higher order elements is particulary difficult because of the complex topology of the element. The decomposition should also be driven by the particulars of the analytical solution, which is rarely performed in practice.

Another important effect during the mapping of results data to visualizations is due to the linear interpolation schemes employed during the rendering process. This effect is common to both data sampling and primitive conversion techniques (Figure 3.9). Data sampling techniques depend upon volume rendering to gener-

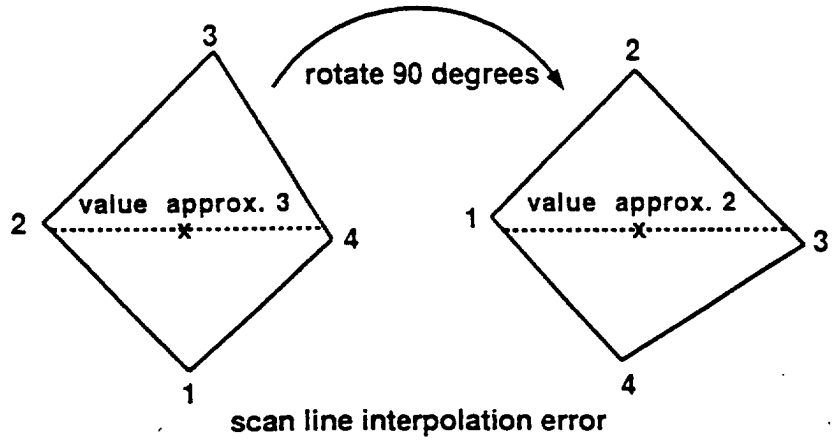


Figure 3.9 The application of basic linear interpolation

ate the image. Volume rendering in turn uses nearest neighbor or tri-linear interpolation methods to generate data values. These methods generate interpolated values different from that obtained by using element shape functions, especially for higher order elements such as those employed in the adaptive *p-refinement* finite element method. The primitive conversion technique suffers a similar problem, since a linear interpolation scheme is employed during the rendering (i.e., scan conversion) process. Also, because the relative orientation of the graphics primitives may vary with respect to the direction of the scan conversion, the interpolation process will generate different visualizations depending upon the orientation of the primitives.

3.8 SUMMARY

Typical modern engineering and analysis techniques are based upon discretizing a problem domain into small pieces, or elements. Over each element an approximation function is used to represent the behavior of the element in terms of unknown solution variables. These variables are gathered into large systems of equations and then solved on a computer. The results of this computation can be further processed to yield derivatives and other related solution variables. The forms of these data are usually scalar, vector, or arbitrary tensor. Visualization techniques are then used to map the solution information back into the original problem domain.

Visualization is a relatively young field, and significant improvements are needed to better support engineering analysis. A major problem is that analysis and visualization are often viewed as disconnected activities. Visualization techniques must be tightly coupled with engineering analysis to accurately convey the full form and range of results data. Computer graphics vendors also must be encouraged to directly support advanced visualization functionality such as higher-order graphics primitives and/or programmable interpolation functions. New visualization techniques must be developed to extend current scalar and vector techniques, and to provide effective tensor visualization.

3.9 APPENDIX: CONSTRUCTION AND DISCRETIZATION OF WEAK FORM OF THE GOVERNING EQUATIONS

Weak forms representing the mathematical description of a physical problem can either be directly stated in terms of some integral principal, or can be constructed from the governing differential equations. Assume the mathematical description of a boundary value problem of interest is given as a second order partial differential equation form as[2]:

2. Consideration of higher order partial differential equations, and initial value problems where time is also an independent variable, adds to the terms considered here. However, the primary issues discussed are the same. Specific comments on accounting for time are given in later sections.

Given $\underline{f}: \Omega \rightarrow \Re, \underline{g}: \Gamma_g \rightarrow \Re$, and $\underline{h}: \Gamma_h \rightarrow \Re$, find $\underline{u}$ such that [3.9]

$$\mathcal{D}^2(\underline{u}) - \underline{f} = 0 \text{ on } \Omega$$

$$\underline{u} = \underline{g} \text{ on } \Gamma_g \qquad [3.10]$$

$$\mathcal{B}^1(\underline{u}) = \mathcal{F}(\underline{\sigma}) = \underline{h} \text{ on } \Gamma_h$$

where $\underline{u}$ is the primary dependent variable, $\underline{f}$ is the forcing function, $\underline{g}$ are prescribed boundary conditions, $\underline{h}$ are prescribed flux conditions, $\mathcal{D}^2$ is a second order differential operator, $\mathcal{B}^1$ is a first order differential operator, $\mathcal{F}(\underline{\sigma})$ is an algebraic operator acting on the fluxes $\underline{\sigma}$, Ω is the domain of the analysis, Γ_g is the portion of the boundary on which the prescribed boundary conditions are prescribed, and Γ_h is the portion of the boundary on which the prescribed flux conditions are prescribed.

Solid mechanics is one such problem area where the dependent variables, $\underline{u}$, are the displacements, the forcing functions, $\underline{f}$, are body loads, the prescribed boundary conditions are displacements, $\underline{g}$, and tractions, $\underline{h}$, and the secondary variables of interest are the stresses, $\underline{\sigma}$. As discussed later, the users of the finite element analysis procedures are interested in visualization of both the primary and secondary variables of interest.

A common method to construct a weak form of the partial differential equations (see Equation 3.9), begins by multiplying the domain equation by a weighting function, integrating over the domain, and setting that to zero.

$$\int_{\Omega} \underline{w}\left(\mathcal{D}^2(\underline{u}) - \underline{f}\right) d\Omega = 0 \qquad [3.11]$$

If Equation 3.11 is satisfied for all admissible weighting functions $\underline{w}$, and the boundary conditions of Equation 3.10 are satisfied, the exact solution to the problem is obtained. Obtaining this solution is as difficult as solving the original system Equations 3.9 and 3.10. The advantage of the weak form comes when finite dimensional spaces are used for the weighting and trial functions, $\underline{w}$ and $\underline{u}$, respectively. In this case the solution to Equation 3.11 provides only a weighted integral solution to Equation 3.9, since Equation 3.11, which is only an approximate solution, will not in general be satisfied at all points.

Although it is possible to directly construct approximate numerical solutions to the basic weighted integral form of Equation 3.11, it is not a convenient form for two major reasons. It requires trial and weight functions that must satisfy all boundary conditions as does Equation 3.10 in their full and homogeneous form, respectively. Commonly applied weighted residual methods perform mathematical manipulations which yield more convenient integral forms. For example, by the proper application of integration by parts and the divergence theorem, Equation 3.11 can be manipulated to produce an equivalent, but more useful, weak form:

Given $\underline{f}:\Omega\rightarrow\Re$ and $\underline{g_i}:\Gamma_i\rightarrow\Re$, $\underline{u}=\underline{g}$ on Γ_g, [3.12]

and $\underline{w}=0$ on Γ_g, find $\underline{u}$ such that

$$\int_\Omega \mathcal{H}^1(\underline{w})\left(\mathcal{G}^1(\underline{u})\right)d\Omega=\int_\Omega \underline{w}\underline{f}d\Omega+\int_{\Gamma_h}\underline{w}\underline{h}d\Gamma$$

for all admissible weight functions $\underline{w}$, where $\mathcal{H}^1$ and $\mathcal{G}^1$ are first order differential operators which depend on $\mathcal{D}^2$ and the mathematical manipulations. In Equation 3.12 it was assumed that the mathematical manipulations were performed such that the last integral did recover the natural boundary condition term, $\underline{h}$.

It is convenient at this point to introduce the commonly used abstract operators, with specific properties, for the individual terms in Equation 3.12. This allows the direct application of the discretization procedure outlined below to any class of problem which satisfies the operators' properties [13, 26]. For the current example define

$$a(\underline{w},\underline{u})=\int_\Omega \mathcal{H}^1(\underline{w})\left(\mathcal{G}^1(\underline{u})\right)d\Omega \qquad [3.13]$$

$$\left(\underline{w},\underline{f}\right)=\int_\Omega \underline{w}\underline{f}d\Omega \qquad [3.14]$$

$$\left(\underline{w},\underline{h}\right)_\Gamma=\int_{\Gamma_h}\underline{w}\underline{h}d\Gamma \qquad [3.15]$$

With this notation Equation 3.12 becomes

$$a\left(\underline{w},\underline{u}\right)=\left(\underline{w},\underline{f}\right)+\left(\underline{w},\underline{h}\right)_\Gamma \qquad [3.16]$$

Following Reference [13], the discretization of Equation 3.16 to yield the form used by numerical methods begins by approximating the infinite dimensional spaces for $\underline{u}$ and $\underline{w}$ with finite dimensional spaces $\underline{u^h}$ and $\underline{w^h}$. To satisfy non-zero essential boundary conditions while selecting functions from spaces satisfying the appropriate boundary conditions, it is convenient to write

$$\underline{u^h}=\underline{v^h}+\underline{g^h} \qquad [3.17]$$

The terms $\underline{v^h}$ and $\underline{w^h}$ must satisfy homogeneous essential boundary conditions, $\underline{w^h}=\underline{v^h}=0$ on Γ_g, and $\underline{g^h}$ must satisfy, at least approximately, the essential boundary conditions, $\underline{g^h}=\underline{g}$ on Γ_g. Substitution of these functions into Equation 3.16 yields

$$a\left(\underline{w^h},\underline{v^h}\right)=\left(\underline{w^h},\underline{f}\right)+\left(\underline{w^h},\underline{h}\right)_\Gamma-a\left(\underline{w^h},\underline{g^h}\right) \qquad [3.18]$$

which must hold for any admissible weighting functions $\underline{w^h}$.

In the finite element method the domain being analyzed is discretized into a set of finite elements over which the functions $\underline{v^h}$ and $\underline{w^h}$ are written in terms of degrees of freedom (dof) times piecewise functions that are nonzero over only a small subset of the finite elements, typically those that share the dof. In equation form these functions can be written as[3]

$$\underline{w^h} = \sum_{A \in n - n_g} N_A c_A \qquad [3.19]$$

and

$$\underline{v^h} = \sum_{A \in n - n_g} N_A d_A \qquad [3.20]$$

where N_A are shape functions, typically piecewise polynomials, c_A are constants and d_A are the dof that are to be determined. The use of capital subscripts indicates a function or multiplier associated with the global system.

Since $\underline{v^h}$ and $\underline{w^h}$ satisfy only the homogeneous version of the essential boundary conditions, and the trial functions, $\underline{u^h}$, must satisfy the essential boundary conditions, it is convenient to expand the function $\underline{g^h}$ as

$$\underline{g^h} = \sum_{A \in n_q} N_A g_A \qquad [3.21]$$

where N_A and g_A are constructed to satisfy the essential boundary exactly, in a pointwise sense, or in an integrated sense.

Substitution of Equations 3.19, 3.20 and 3.21 into Equation 3.18 yields

$$a\left(\sum_{A \in n - n_g} N_A c_A, \sum_{B \in n - n_g} N_B d_B\right) = \left(\sum_{A \in n - n_g} N_A c_A, \underline{f}\right) + \left(\sum_{A \in n - n_g} N_A c_A, \underline{h}\right)_\Gamma \qquad [3.22]$$

$$-a\left(\sum_{A \in n - n_g} N_A c_A, \sum_{B \in n_g} N_B g_B\right)$$

Based on the properties of the operators used Equation 3.22 can be rewritten as

$$\sum_{A \in n - n_g} c_A \qquad [3.23]$$

$$\left[\sum_{B \in n - n_g} a\left(N_A, N_B\right) d_B - \left(N_A, \underline{f}\right) - \left(N_A, \underline{h}\right)_\Gamma + \sum_{B \in n_g} a\left(N_A, N_B\right) g_B\right]$$

$$= 0$$

Since the weighting functions are arbitrary, the individual multipliers c_A in

3. In the simplified expressions given here the vector expressions are directly expressed in terms of the element shape functions. In a more detailed explanation of the finite element method it is common to write the expansions in terms of the individual vector components.

Equation 3.23 can take on any value. This means the term in the square brackets must be equal to zero for all values of A. That is:

$$\sum_{B \in n-n_g} a\left(N_A, N_B\right) d_B = \left(N_A, \underline{f}\right) + \left(N_A, \underline{h}\right)_\Gamma - \sum_{B \in n_g} a\left(N_A, N_B\right) g_B, A \in n - n_g \quad [3.24]$$

which represents a set of algebraic equations which can be written in matrix form

$$\mathbf{K}\mathbf{d} = \mathbf{F} \quad [3.25]$$

where the terms in the vector d are the unknown degrees of freedom, and the terms in the stiffness matrix, K, and load vector, F, are given by

$$K_{PQ} = a\left(N_A, N_B\right) \quad [3.26]$$

and

$$F_p = \left(N_A, \underline{f}\right) + \left(N_A, \underline{h}\right)_\Gamma - \sum_{B \in n_g} a\left(N_A, N_B\right) g_B \quad [3.27]$$

The subscripts P and Q range over the number of dof in the problem and are related to the subscripts A and B through a mapping process that tracks the fact that some of the possible dof are associated with dof in the final problem and other potential dof, A, $B \in n - n_g$ are used to account for the essential boundary conditions, $B \in n_g$.

A key to the effective application of finite element methods is the ability to calculate the terms in the stiffness matrix of Equation 3.25 with element contributions. To give an indication of the key aspects of that process, consider the case where the individual dof, d_P corresponds to the nodal values of the unknown field, the finite element mesh consists of three-noded triangles, and the global shape function, N_A is a piecewise linear function which has a value of one at the node of interest and zero at the edges opposite the vertex (left side of Figure 3.10). In

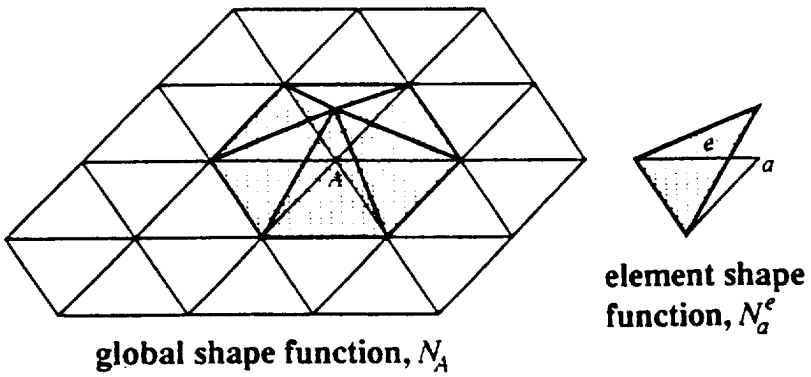


Figure 3.10 Global shape function and one of its elemental contributions

finite element methods the global shape function is constructed as the appropriate sum of elemental shape functions, N_a^e, (right side of Figure 3.10) where the superscript identifies an element and the lowercase subscript identifies the degrees of freedom on the elemental level.

The integral operators, Equations 3.10–3.15, can be written one element at a time to yield the elemental stiffness matrix, $\mathbf{k}^e$ and load vector $\mathbf{f}^e$, where the individual terms are given in terms of the elemental dof as

$$k_{pq}^e = a\left(N_a, N_b\right) \qquad [3.28]$$

and

$$f_p^e = \left(N_a, \underline{f}\right) + \left(N_a, \underline{h}\right)_\Gamma - \sum_{b \in n_q} a\left(N_a, N_b\right) g_b \qquad [3.29]$$

here the integrations are over the domain of the element and its appropriate boundary segments. Since the local dof have an equivalence to the global dof, and the properties of the integral operators and shape functions are such that the integral of a sum of element contributions is equal to the sum of the integrals of the element contributions, the global equations can be constructed by the appropriate summation of element contributions represented by

$$\mathbf{K} = \overline{\sum_{e=1}^{n_{el}} \mathbf{k}^e}, \quad \mathbf{F} = \overline{\sum_{e=1}^{n_{el}} \mathbf{f}^e} \qquad [3.30]$$

where the summation process adds the terms for the element matrices into the correct locations of the global matrices based on the mapping of local to global dof labeling.

3.10 REFERENCES

[1] I. Babuska, O. C. Zienkiewicz, J. Gago, and d. A. Oliveria, editors. *Accuracy Estimates and Adaptive Refinements in Finite Element Computations.* John Wiley, Chichester, 1986.

[2] T. J. Baker. Automatic mesh generation for complex three-dimensional regions using a constrained Delaunay triangulation. *Engineering with Computers,* 5: pages 161–175, 1989.

[3] T. D. Blacker and M. B. Stephenson. Paving: "A new approach to automated quadrilateral mesh generation." *Int. J. Numer. Meth. Engng.,* 32(4): pages 811–847, 1991.

[4] E. K. Buratynski. "A fully automatic three-dimensional mesh generator for complex geometries." *Int. J. Numer. Meth. Engng.,* 30: pages 931–952, 1990.

[5] J. C. Cavendish, D. A. Field, and W. H. Frey. "An approach to automatic three-dimensional mesh generation." *Int. J. Numer. Meth. Engng.,* 21: pages 329–347, 1985.

[6] S. D. Conte and C. de Boor. *Elementary Numerical Analysis.* McGraw Hill Book Co., New York, NY, 1972.

[7] J. E. Flaherty, P. J. Paslow, M. S. Shephard, and J. D. Vasilakis, editors. *Adaptive Methods for partial Differential Equations.* SIAM, Philadelphia, PA, 1989.

[8] R. H. Gallagher. *Finite Element Analysis: Fundamentals.* Prentice Hall, Englewood Cliffs, NJ, 1975.

[9] P. L. George. *Automatic Mesh Generation.* John Wiley and Sons, Ltd, Chichester, 1991.

[10] W. J. Gordon and C. A. Hall. "Transfinite element methods: Blending function interpolation over arbitrary curved element domain." *Int. J. Numer. Meth. Engng.,* 21: pages 109–129, 1973.

[12] H. N. Gursoy and N. M. Patrikalakis. "Automatic interrogation and adaptive subdivision of shape using medial axis transform." *Advances in Engineering Software,* 13: pages 287–302, 1991.

[13] T. J. R. Hughes. *The Finite Element Method: Linear Static and Dynamic Finite Element Analysis.* Prentice Hall, Englewood Cliffs, NJ, 1987.

[14] A. Kela. "Hierarchical octree approximations for boundary representation-based geometric models." *Computer Aided Design*, 21: pages 355–362, 1989.

[15] R. Löhner and P. Parikh. "Three-dimensional grid generation by the advancing front method." *Int. J. Num. Meths. Fluids*, 8: pages 1135–1149, 1988.

[16] A. K. Noor, editor. *Adaptive, Multilevel and Hierarchical Computational Strategies.* ASME, 345 East 47th Street, NY, NY, 1992.

[17] J. T. Oden, editor. *Computer Methods in Applied Mechanics and Engineering*, volume 82. North Holland, 1990. Special issue devoted to the reliability of finite element computations.

[18] J. T. Oden and L. Demkowicz, editors. *Computer Methods in Applied Mechanics and Engineering*, volume 101. North Holland, 1992. Second special issue devoted to the reliability of finite element computations.

[19] W. J. Schroeder. *Geometric Triangulations: with Application to Fully Automatic 3D Mesh Generation.* PhD thesis, Rensselaer Polytechnic Institute, Scientific Computation Research Center, RPI, Troy, NY 12180-3590, May 1991.

[20] W. J. Schroeder and M. S. Shephard. "A combined octree/Delaunay method for fully automatic 3-D mesh generation." *Int. J. Numer. Meth. Engng.*, 29: pages 37–55, 1990.

[21] W. J. Schroeder and M. S. Shephard. "On rigorous conditions for automatically generated finite element meshes." In J. turner, J. Pegna, and M. Wozny, editors, *Product Modeling for Computer-Aided Design and manufacturing*, pages 267–281. North Holland, 1991.

[22] M. S. Shephard. "Approaches to the automatic generation and control of finite element meshes." *Applied Mechanics Review*, 41(4): pages 169–185, 1988.

[23] M. S. Shephard and P. M. Finnigan. "Toward automatic model generation." In A. K. Noor and J. T. Oden, editors, *State-of-the-Art Surveys on Computational Mechanics*, pages 335–366. ASME, 1989.

[24] M. S. Shephard and M. K. Georges. "Automatic three-dimensional mesh generation of the Finite Octree technique." *Int. J. Numer. Meth. Engng.*, 32(4): pages 709–749, 1991.

[25] M. S. Shephard and M. K. Georges. "Reliability of automatic 3-D mesh generation." *Comp. Meth. Appl. Mech. Engng.*, 101: pages 443–462, 1992.

[26] B. A. Szabo and I. Babuska. *Finite Element Analysis.* Wiley Interscience, New York, 1991.

[27] T. K. H. Tam and C. G. Armstrong. "2-D finite element mesh generation by medial axis subdivision." *Advances in Engng. Software*, 13(5/6): pages 313–324, 1991.

[28] K. J. Weiler. *Topological Structures for Geometric Modeling.* PhD thesis, Rensselaer Design Research Center, Rensselaer Polytechnic Institute, Troy, NY, May 1986.

[29] K. J. Weiler. "The radial-edge structure: A topological representation for non-manifold geometric boundary representations." In M. J. Wozny, H. W. McLaughlin, and J. L. Encarnacao, editors, *Geometric Modeling for CAD Applications*, pages 3–36. North Holland, 1988.

[30] O. C. Zienkiewicz and R. L. Taylor. *The Finite Element Method—Volume 1.* McGraw Hill Book Co., New York, 4th edition, 1987.

The American Society of Mechanical Engineers

Reprinted From
AMD– Vol. 193, Mechanics and Materials for Electronic Packaging
Editors: M. L. Dunn, M. Taya, and M. Saka
Book No. G00937 – 1994

COUPLING IN THE MECHANICAL RESPONSE OF FUNCTIONALLY GRADED COMPOSITE MATERIALS

Joseph R. Zuiker
Metals and Ceramics Division, Materials Directorate
USAF Wright Laboratory
Wright-Patterson AFB, Ohio

George J. Dvorak
Department of Civil and Environmental Engineering
Center for Composite Materials and Structures
Rensselaer Polytechnic Institute
Troy, New York

ABSTRACT

Many micromechanical methods estimate effective mechanical properties that relate average stress and strain in a heterogeneous body. It is usually assumed that the same properties relate higher order variations (linear, for example) in stress and strain and that these higher order variations are uncoupled from the average response. Here, we present a modified Mori-Tanaka method that provides estimates of effective properties relating linear variation of the stress and strain fields in a heterogeneous body. In general, the modified Mori-Tanaka stiffness estimates that relate linear variation in the stress and strain are not equal to those relating average stress and strain. Further, when the reinforcing phase volume fraction varies with position, the average and linearly varying response of the representative volume are coupled. Results are presented for the simple case of a particulate-reinforced, functionally graded microstructure.

1. INTRODUCTION

Most techniques for estimating effective properties of heterogeneous media are based on boundary conditions derived from uniform stress or strain fields. The properties thus obtained relate average stress and average strain in the body and are usually assumed to relate higher order variations in the stress and strain accordingly. (i.e., linearly varying stress and linearly varying strain are related by the same effective stiffness as average stress and strain.) It is a well-established fact (Margolin, 1967; Pagano 1974) that these higher order relationships may differ significantly from the average field relations in certain structures such as fiber reinforced plates. In general, though, the average and higher order responses of the material are uncoupled (with the notable exception of unsymmetric laminated plates) such that if a higher order applied field is judged to be small, it can safely be assumed that the higher order response is equally small. Functionally graded materials (FGMs) with continuous variation in microstructure do not possess a statistically homogeneous microstructure. This leads to coupling between the average and higher order responses of the material, which may lead to significant errors in analysis if not accurately accounted for.

As a first step towards understanding this interaction, the standard Mori-Tanaka method (Mori and Tanaka, 1973; Benveniste, 1987) or MTM has been extended (Zuiker and Dvorak, 1994a, 1995) to define effective mechanical properties relating the linear variation in stress and strain across a representative volume element or RVE. The standard Mori-Tanaka method leads to accurate predictions over a wide range of constituent material properties and reinforcement volume fractions (Christensen et al., 1992) and possesses the attractive feature of producing closed-form estimates. However, the effective stiffness matrix estimates are generally not diagonally symmetric (Qiu and Weng, 1990; Ferrari, 1991). Diagonally symmetric estimates are obtained for two phase systems, multiphase systems in which the dispersed inhomogeneities have a similar shape and alignment (Benveniste et al., 1991), and multiphase systems in which the alignment is random (Chen et al., 1992).

Here, we employ the modified MTM to consider non-statistically homogeneous microstructures and examine first order estimates of the coupling that occurs between the average and linearly varying stress and strain fields. In section 2 we derive suitable boundary conditions and introduce symbolic (24x24) matrix notation. The equivalent inclusion method (Eshelby, 1957, 1961) is then reviewed for linearly varying applied fields followed by introduction of a least squares approximation to the discontinuous, linearly varying stress and strain fields in a heterogeneous RVE. Finally, mechanical strain concentration factors and effective stiffness are estimated by the modified Mori-Tanaka method. In section 3, problems particular to the micromechanical analysis of FGMs are discussed and stiffness estimates are presented for statistically homogeneous and functionally graded microstructures of similar materials.

Both tensor and matrix notation are used herein. Tensor quantities are denoted by plain face upper case or lower case Greek or Roman characters with the number of subscripts denoting the order of the tensor, and standard summation notation is used. For example, stress is denoted as σ_{ij}. A tensor or matrix followed by (x) indicates a function of position. Vectors and matrices are denoted by boldface lower case and upper case Greek or Roman letters, respectively. Vectors and matrices with a ^ are (24x1) and (24x24) respectively; those without are (6x1) or (6x6), respectively; and those of other sizes are denoted by boldface letters followed by subscripts indicating matrix dimensions. A superscript T indicates the transpose of the matrix, and a superscript -1 indicates the inverse. For example, $\mathbf{A}$ is a (6x6) matrix, $\hat{\boldsymbol{\sigma}}$ is a (24x1) vector, $\mathbf{Z}_{(6x18)}$ is a (6x18) matrix, and $\hat{\mathbf{L}}$ is a (24x24) matrix. We shall refer to this as symbolic matrix notation.

2. MECHANICAL RESPONSE BY THE MODIFIED MORI-TANAKA METHOD

2. 1 First Order Boundary Value Problems

A homogeneous elastic medium of volume V, defined in Cartesian coordinates x_k, is loaded on the surface S of V by tractions derived from a linearly varying stress field,

$$T_i^{(o)}(\mathbf{x}) = \sigma_{ij}^{(o)}(\mathbf{x})n_j(\mathbf{x}), \tag{1}$$

where $\mathbf{x} \in S$ and $n_j(\mathbf{x})$ is the outward unit normal to S. The linearly varying stress field,

$$\sigma_{ij}^{(o)}(\mathbf{x}) = \sigma_{ij}^{(o)} + \eta_{ijk}^{(o)}x_k, \tag{2}$$

consists of the second order tensor $\sigma_{ij}^{(o)}$ of uniform components and the third order tensor $\eta_{ijk}^{(o)}$, which defines the stress gradient in the x_k coordinate direction. Also, $\sigma_{ij}^{(o)}(\mathbf{x})$ satisfies equilibrium such that in the absence of body forces,

$$\eta_{iij}^{(o)} = 0. \tag{3}$$

Symmetry of the stress tensor implies that $\sigma_{ij}^{(o)} = \sigma_{ji}^{(o)}$ and $\eta_{ijk}^{(o)} = \eta_{jik}^{(o)}$; accordingly, $\sigma_{ij}^{(o)}$ has 6 independent components, and $\eta_{ijk}^{(o)}$ has at most 18; however, the constraints (3) reduce the latter number to 15.

Alternatively, the same body may be subjected to surface displacements $u_i(\mathbf{x})$, $\mathbf{x} \in S$, derived from the linearly varying strain field,

$$\varepsilon_{ij}^{(o)}(\mathbf{x}) = \varepsilon_{ij}^{(o)} + \kappa_{ijq}^{(o)}x_q, \tag{4}$$

consisting of average strains $\varepsilon_{ij}^{(o)}$ and strain gradients $\kappa_{ijq}^{(o)}$ in the x_q direction. It can be verified that the underlying displacement field is (Muskhelishvili, 1953, page 44)

$$u_i^{(o)} = \varepsilon_{ij}^{(o)}x_j + \frac{1}{2}\left(\kappa_{ijk}^{(o)} + \kappa_{ikj}^{(o)} - \kappa_{jki}^{(o)}\right)x_jx_k, \tag{5}$$

and that this creates an equilibrated stress field if, in the absence of body forces,

$$L_{ijkl}\kappa_{klj}^{(o)} = 0, \tag{6}$$

where $L_{ijkl} = M_{ijkl}^{-1}$ is the stiffness tensor. Both the stress field (2) satisfying (3), and the strain field (4) satisfying (6) create linearly varying strain fields, which always satisfy compatibility.

The linear stress and strain fields are related as

$$\begin{aligned}\sigma_{ij}^{(o)} + \eta_{ijm}^{(o)}x_m &= L_{ijkl}\left(\varepsilon_{kl}^{(o)} + \kappa_{klq}^{(o)}x_q\right),\\ \varepsilon_{ij}^{(o)} + \kappa_{ijm}^{(o)}x_m &= M_{ijkl}\left(\sigma_{kl}^{(o)} + \eta_{klq}^{(o)}x_q\right).\end{aligned} \tag{7}$$

These constitutive relations can be written using the symbolic matrix notation of section 1. Inasmuch as the result should not depend on the choice of x_q, we define

$$\begin{aligned}\hat{\boldsymbol{\varepsilon}} &= \left\{\varepsilon_{ij} \quad \kappa_{ij1} \quad \kappa_{ij2} \quad \kappa_{ij3}\right\}^T,\\ \hat{\boldsymbol{\sigma}} &= \left\{\sigma_{ij} \quad \eta_{ij1} \quad \eta_{ij2} \quad \eta_{ij3}\right\}^T,\end{aligned} \tag{8}$$

and rewrite (7) in the form that relates the respective field averages and gradients,

$$\hat{\boldsymbol{\sigma}} = \hat{\mathbf{L}}\hat{\boldsymbol{\varepsilon}}, \qquad \hat{\boldsymbol{\varepsilon}} = \hat{\mathbf{M}}\hat{\boldsymbol{\sigma}}, \tag{9}$$

where

$$\hat{\mathbf{L}} = \begin{bmatrix}\mathbf{L} & \mathbf{0} & \mathbf{0} & \mathbf{0}\\ \mathbf{0} & \mathbf{L} & \mathbf{0} & \mathbf{0}\\ \mathbf{0} & \mathbf{0} & \mathbf{L} & \mathbf{0}\\ \mathbf{0} & \mathbf{0} & \mathbf{0} & \mathbf{L}\end{bmatrix}, \quad \hat{\mathbf{M}} = \begin{bmatrix}\mathbf{M} & \mathbf{0} & \mathbf{0} & \mathbf{0}\\ \mathbf{0} & \mathbf{M} & \mathbf{0} & \mathbf{0}\\ \mathbf{0} & \mathbf{0} & \mathbf{M} & \mathbf{0}\\ \mathbf{0} & \mathbf{0} & \mathbf{0} & \mathbf{M}\end{bmatrix}. \tag{10}$$

Here $\mathbf{L} = \mathbf{M}^{-1}$ is the (6x6) matrix form of the stiffness tensor and $\mathbf{0}$ is the (6x6) null matrix. This relationship is exact and holds everywhere in a homogeneous body of any shape and size provided that boundary conditions (1) or (5) are derived from stress or strain fields satisfying (3) or (6), respectively.

2.2 The Equivalent Inclusion Method

An inclusion is defined as a region in a homogeneous body subjected to a prescribed eigenstrain distribution. For ellipsoidal inclusions in isotropic solids (Eshelby, 1961) and

anisotropic solids, (Asaro and Barnett, 1975) it has been shown that if the applied eigenstrain distribution varies linearly, then the strain field in the inclusion also varies linearly. In particular, for an inclusion r, occupying volume V_r with the centroid $\bar{x}_p^{(r)}$, subjected to the eigenstrain

$$\mu_{kl}^{(r)}(\mathbf{x}) = \mu_{kl}^{(r)} + \gamma_{klp}^{(r)}\left(x_p - \bar{x}_p^{(r)}\right), \tag{11}$$

and embedded in a large volume V of an elastic material, if the eigenstrain is written in symbolic matrix notation as

$$\hat{\mu}_r = \left\{\mu_{ij}^{(r)} \quad \gamma_{ij1}^{(r)} \quad \gamma_{ij2}^{(r)} \quad \gamma_{ij3}^{(r)}\right\}^T, \tag{12}$$

then the resulting strain field in V_r may be written as

$$\hat{\varepsilon}_r = \hat{S}\hat{\mu}_r, \tag{13}$$

where

$$\hat{S} = \begin{bmatrix} S_o & 0 & 0 & 0 \\ 0 & S_{11} & S_{12} & S_{13} \\ 0 & S_{21} & S_{22} & S_{23} \\ 0 & S_{31} & S_{32} & S_{33} \end{bmatrix}. \tag{14}$$

Here, S_o is the (6x6) matrix form of the Eshelby tensor, and S_{ij} represent components of the linear Eshelby tensor (Zuiker, 1993; Zuiker and Dvorak, 1995).

An inhomogeneity is defined in an otherwise homogeneous body as a region with different elastic properties. Using the equivalent inclusion method of Eshelby (1957, 1961) and the work of Sendeckyj (1967), it can be shown that the strain field in an ellipsoidal inhomogeneity varies linearly when the inhomogeneity is embedded in a large volume V of homogeneous material subjected to boundary conditions derived from a linearly varying strain field as in (4). The resulting relation between the strain in V_r and that applied to V is (Zuiker and Dvorak, 1994b)

$$\hat{\varepsilon}_r = \left[\hat{I} - \hat{S}\hat{L}_1^{-1}\left(\hat{L}_1 - \hat{L}_r\right)\right]^{-1}\hat{K}_r\hat{\varepsilon}_o, \tag{15}$$

where $\hat{I}$ is the (24x24) identity matrix, $\hat{L}_1$ and $\hat{L}_r$ are the matrix and inhomogeneity stiffness matrices written in a form similar to (10_1),

$$\begin{aligned} \hat{\varepsilon}_r &= \left\{\varepsilon_{ij}^{(r)} \quad \kappa_{ij1}^{(r)} \quad \kappa_{ij2}^{(r)} \quad \kappa_{ij3}^{(r)}\right\}^T, \\ \hat{\varepsilon}_o &= \left\{\varepsilon_{ij}^{(o)} \quad \kappa_{ij1}^{(o)} \quad \kappa_{ij2}^{(o)} \quad \kappa_{ij3}^{(o)}\right\}^T, \\ \hat{K}_r &= \begin{bmatrix} I & \bar{x}_1^{(r)}I & \bar{x}_2^{(r)}I & \bar{x}_3^{(r)}I \\ 0 & I & 0 & 0 \\ 0 & 0 & I & 0 \\ 0 & 0 & 0 & I \end{bmatrix}, \end{aligned} \tag{16}$$

and it is assumed that the origin lies at the centroid of V.

2.3 Overall and Local Field Averages in Heterogeneous Media

We consider a volume of an elastic solid loaded on the surface S either by the displacements of (5) or the tractions of (1) and now admit a heterogeneous microstructure that can be approximated by a collection of inhomogeneities. Our goal is to establish connections between the local and overall stress and strain fields that will be useful later, in derivation of overall elastic properties.

Let V be subjected to surface displacements (5) that create a linearly varying overall strain field (4) in V. With the required symmetries and equations (6) satisfied, (4) would represent the actual strain field in a homogeneous body. However, in a heterogeneous solid, the actual field may be very different and possibly discontinuous. Therefore, we define average strains and average strain gradients by a first order polynomial approximation to the actual field,

$$\varepsilon_{ij}(\mathbf{x}) = \bar{\varepsilon}_{ij} + \bar{\kappa}_{ijk}x_k + \xi_{ij}(\mathbf{x}), \tag{17}$$

where $\varepsilon_{ij}(\mathbf{x})$ is the actual field, $\bar{\varepsilon}_{ij}$ and $\bar{\kappa}_{ijk}$ define a linearly varying approximation of $\varepsilon_{ij}(\mathbf{x})$, $\xi_{ij}(\mathbf{x})$ is the strain field error tensor, and the origin is at the centroid of V. We define $\bar{\varepsilon}_{ij}$ and $\bar{\kappa}_{ijk}$ by minimizing $\xi_{ij}(\mathbf{x})$ in a least squares sense over V by defining

$$e = \frac{1}{V}\int_V \xi_{ij}(\mathbf{x})\xi_{ij}(\mathbf{x})dV, \tag{18}$$

and evaluating $\partial e/\partial\bar{\varepsilon}_{ij} = 0$ and $\partial e/\partial\bar{\kappa}_{ijk} = 0$, to obtain

$$\begin{aligned} \bar{\varepsilon}_{ij} &= \frac{1}{V}\int_V \varepsilon_{ij}(\mathbf{x})dV, \\ \bar{\kappa}_{ijm}J_{mk} &= \frac{1}{V}\int_V x_k\varepsilon_{ij}(\mathbf{x})dV, \\ J_{mk} &= \frac{1}{V}\int_V x_m x_k dV. \end{aligned} \tag{19}$$

Although other approximations are possible, the selected one reduces to that used with uniform overall fields (Hill, 1963) when the gradients vanish.

To assure that the linear approximation of the actual overall field satisfies the prescribed boundary conditions (5) and (6), we require that $\bar{\varepsilon}_{ij} = \varepsilon_{ij}^{(o)}$, and $\bar{\kappa}_{ijk} = \kappa_{ijk}^{(o)}$. These relations hold for statistically homogeneous volumes and approximately for non-statistically homogeneous volumes provided that the centroid of V is positioned at the origin (Zuiker, 1993).

Next, let the representative volume V be subdivided into subvolumes V_r that contain the individual phases or their subdivisions. The local strain in V_r is written as

$$\varepsilon_{ij}^{(r)}(\mathbf{x}) = \varepsilon_{ij}^{(r)} + \kappa_{ijm}^{(r)}\left(x_m - \bar{x}_m^{(r)}\right), \tag{20}$$

where $\bar{x}_m^{(r)}$ is the centroid of V_r. This is also evaluated by a least squares approximation and provides

$$\varepsilon_{ij}^{(r)} = \frac{1}{V_r}\int_{V_r}\varepsilon_{ij}(x)dV,$$
$$\kappa_{ijq}^{(r)} J_{qk}^{(r)} = \frac{1}{V_r}\int_{V_r}(x_k - \bar{x}_k^{(r)})\varepsilon_{ij}(x)dV, \tag{21}$$

where

$$\bar{x}_i^{(r)} = \frac{1}{V_r}\int_{V_r} x_i dV,$$
$$J_{ij}^{(r)} = \frac{1}{V_r}\int_{V_r}(x_i - \bar{x}_i^{(r)})(x_j - \bar{x}_j^{(r)})dV. \tag{22}$$

Using (19), (21), and (22), we may relate the local and overall strain approximations as

$$\hat{C}\hat{\varepsilon} = \sum_{r=1}^{N}\hat{C}_r\hat{\varepsilon}_r, \tag{23}$$

where

$$\hat{C} = \begin{bmatrix} I & 0 & 0 & 0 \\ 0 & J_{11}I & J_{12}I & J_{13}I \\ 0 & J_{12}I & J_{22}I & J_{23}I \\ 0 & J_{13}I & J_{23}I & J_{33}I \end{bmatrix},$$
$$\hat{C}_r = c^{(r)}\begin{bmatrix} I & 0 & 0 & 0 \\ \bar{x}_1^{(r)}I & J_{11}^{(r)}I & J_{12}^{(r)}I & J_{13}^{(r)}I \\ \bar{x}_2^{(r)}I & J_{12}^{(r)}I & J_{22}^{(r)}I & J_{23}^{(r)}I \\ \bar{x}_3^{(r)}I & J_{13}^{(r)}I & J_{23}^{(r)}I & J_{33}^{(r)}I \end{bmatrix}, \tag{24}$$

and $c^{(r)} = V_r/V$.

Similar operations in terms of stresses lead to the subvolume stress field approximations

$$\sigma_{ij}^{(r)} = \frac{1}{V_r}\int_{V_r}\sigma_{ij}(x)dV,$$
$$\eta_{ijm}^{(r)} J_{mk}^{(r)} = \frac{1}{V_r}\int_{V_r}(x_k - \bar{x}_k^{(r)})\sigma_{ij}(x)dV, \tag{25}$$

and the overall RVE stress approximations

$$\bar{\sigma}_{ij} = \frac{1}{V}\int_V \sigma_{ij}(x)dV,$$
$$\bar{\eta}_{ijm}J_{mk} = \frac{1}{V}\int_V \sigma_{ij}(x)x_k dV, \tag{26}$$

which are related as

$$\hat{C}\hat{\sigma} = \sum_{r=1}^{N}\hat{C}_r\hat{\sigma}_r. \tag{27}$$

As in the analysis of heterogeneous media under uniform boundary conditions, the local strain and stress fields at a point, $\varepsilon(x)$ and $\sigma(x)$, respectively, can be related to their overall counterparts by certain concentration factors. For the linearly varying overall fields, we write

$$\varepsilon(x) = A^*_{(6x24)}(x)\hat{\varepsilon}, \quad \sigma(x) = B^*_{(6x24)}(x)\hat{\sigma}, \tag{28}$$

where $A^*_{(6x24)}(x)$ and $B^*_{(6x24)}(x)$ are (6x24) matrices representing the mechanical influence functions for evaluation of the local fields. We may substitute (28_1) and (28_2) into (21) and (25), respectively, and write the resulting linear field approximations as

$$\hat{\varepsilon}_r = \hat{A}_r\hat{\varepsilon}, \quad \hat{\sigma}_r = \hat{B}_r\hat{\sigma}, \tag{29}$$

where $\hat{A}_r$ and $\hat{B}_r$ are mechanical concentration factor matrices. From (23), (27), and (29) we find that

$$\hat{C} = \sum_{r=1}^{N}\hat{C}_r\hat{A}_r, \quad \hat{C} = \sum_{r=1}^{N}\hat{C}_r\hat{B}_r. \tag{30}$$

Evaluation of the concentration factors follows from analysis of certain micromechanical models. Here, these concentration factors are approximated by modifying the Mori-Tanaka method, originally developed for composites subjected uniform overall fields. Consider a particular inhomogeneity embedded in a continuous matrix that contains many inhomogeneities and is subjected to boundary conditions (5), as shown in Figure 1a. We assume that the strain in this inhomogeneity is equal to that of single inhomogeneity embedded in an otherwise homogeneous matrix subjected to boundary conditions derived from the average strain and strain gradient in the matrix that contains many inhomogeneities, as shown in Figure 1b.

The strain field in V_r is

$$\hat{\varepsilon}_r = \hat{T}_r\hat{\varepsilon}_1, \tag{31}$$

where $\hat{T}_r$ is a partial concentration factor matrix for V_r and, from (15),

$$\hat{T}_r = \hat{I}, \quad r = 1,$$
$$\hat{T}_r = \left[\hat{I} - \hat{S}\hat{L}_1^{-1}\left(\hat{L}_1 - \hat{L}_r\right)\right]^{-1}\hat{K}_r, \quad r > 1, \tag{32}$$

where the Eshelby tensors in (32_2) are evaluated for the matrix phase. To relate matrix phase strains to remote strains substitute (31) into (23), solve for $\hat{\varepsilon}_1$, substitute the result into (31), and compare with (29_1) to obtain

$$\hat{A}_1 = \left[\hat{C}_1 + \sum_{s=2}^{N} \hat{C}_s \hat{T}_s\right]^{-1} \hat{C}, \quad \hat{A}_r = \hat{T}_r \hat{A}_1, \quad r>1. \quad (33)$$

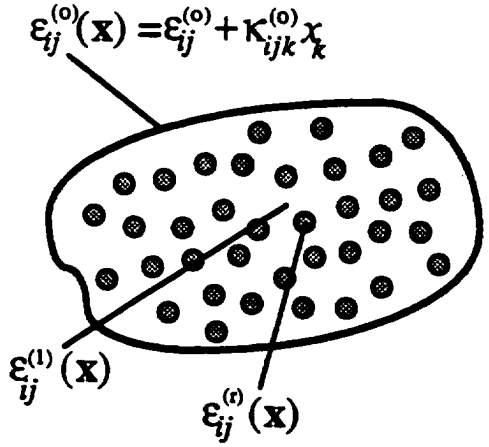


FIGURE 1A
RVE SUBJECTED TO BOUNDARY CONDITIONS
DERIVED FROM A LINEARLY VARYING STRAIN FIELD

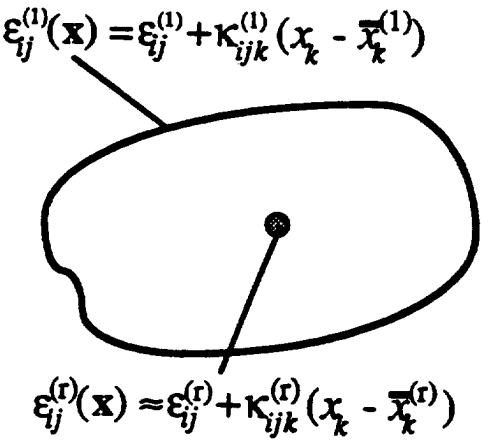


FIGURE 1B
APPROXIMATE PROBLEM SOLVED BY THE
MODIFIED MORI-TANAKA METHOD.

2.4 Effective Stiffness and Compliance

Now that the local fields have been related to the overall averages and to the prescribed boundary conditions, we proceed with evaluation of the effective stiffness and compliance of the composite medium.

In a homogeneous phase, the linearly varying fields can be written in symbolic matrix notation, in analogy with (9), as

$$\hat{\sigma}_r = \hat{L}_r \hat{\varepsilon}_r, \qquad \hat{\varepsilon}_r = \hat{M}_r \hat{\sigma}_r, \quad (34)$$

where $\hat{L}_r$ and $\hat{M}_r$ are similar to $\hat{L}$ and $\hat{M}$ in (9) with $L^{(r)}$ and $M^{(r)}$ replacing L and M, respectively, and $M^{(r)} = L^{(r)-1}$ is the (6x6) compliance matrix in V_r.

To derive an effective stiffness $\hat{L}$ which relates overall stress and strain, $\hat{\sigma}$ and $\hat{\varepsilon}$, for a heterogeneous RVE, we begin with (27), substitute for $\hat{\sigma}_r$ via (34_1), for $\hat{\varepsilon}_r$ via (29_1), and compare with (9_1) to obtain

$$\hat{L} = \hat{C}^{-1} \sum_{r=1}^{N} \hat{C}_r \hat{L}_r \hat{A}_r. \quad (35)$$

A similar form of the overall compliance follows from (23), (34_2) and (29_2) as

$$\hat{M} = \hat{C}^{-1} \sum_{r=1}^{N} \hat{C}_r \hat{M}_r \hat{B}_r. \quad (36)$$

We can now evaluate the stiffness and compliance matrices, (35) and (36), using the general relations in §2.3. The estimate of $\hat{A}_r$ found from the modified Mori-Tanaka method in (33) provides

$$\hat{L} = \hat{C}^{-1}\left[\hat{C}_1 \hat{L}_1 + \sum_{r=2}^{N} \hat{C}_r \hat{L}_r \hat{T}_r\right] \hat{A}_1. \quad (37)$$

3. FUNCTIONALLY GRADED COMPOSITE MATERIALS

3.1 Formulation of the problem

Functionally graded materials are often manufactured by methods that mix two or more particulate phases in varying concentrations within a given volume. All phases may be present in some parts of the volume, while only one phase may be found in other parts, e.g., at a surface. Each phase occupies a certain distribution of subvolumes, and the elastic properties of each phase at a point are unaffected by the surrounding material. Depending on the local phase volume fractions, one of the phases may be regarded as a "matrix" containing "inhomogeneities" of the other phases. However, such roles cease to hold if the volume concentration of the particulate phase exceeds the percolation threshold and both phases form interpenetrating networked microstructures.

Of course, under any definition, overall properties of graded materials change with position, hence a representative volume element (RVE) that is typical of the material on average (Hill 1963) does not exist. For any finite size RVE, the internal variation in reinforcement volume fraction will induce coupling between the average and gradient response of the material. Let us therefore consider some *local volume element* (LVE) of specified dimension with known average and rate of change in reinforcement volume fraction. If such an LVE is accepted in lieu of a representative volume, the results of section 2 can be applied to approximately analyze the effect of reinforcement gradients on $\hat{L}$. This stiffness

may then be used, for example, to describe element response in a finite element procedure for analysis of any graded-material structural shape under arbitrary loads.

3.2 Stiffness Estimates

Detailed analysis of (10), (14), (24), (32), (33), and (37) (Zuiker, 1993; Zuiker and Dvorak, 1995) shows that if the distribution of reinforcements within a heterogeneous volume V is symmetric about the origin, or if it is statistically homogeneous and V contains enough reinforcements, then certain terms in $\hat{\mathbf{L}}$ become insignificant or reduce to zero. We can examine the forms of these matrices in terms of (6x6) submatrices relating the average response and gradients in each of the material directions. Doing so, we see that for statistically homogeneous (or symmetric) RVEs and for functionally graded LVEs, respectively, we have the general forms of the overall stiffness

$$\hat{\mathbf{L}}_{SH} = \begin{bmatrix} \mathbf{L}_{00} & \mathbf{0} & \mathbf{0} & \mathbf{0} \\ \mathbf{0} & \mathbf{L}_{11} & \mathbf{L}_{12} & \mathbf{L}_{13} \\ \mathbf{0} & \mathbf{L}_{21} & \mathbf{L}_{22} & \mathbf{L}_{23} \\ \mathbf{0} & \mathbf{L}_{31} & \mathbf{L}_{32} & \mathbf{L}_{33} \end{bmatrix},$$

$$\hat{\mathbf{L}}_{FGM} = \begin{bmatrix} \mathbf{L}_{00} & \mathbf{L}_{01} & \mathbf{L}_{02} & \mathbf{L}_{03} \\ \mathbf{L}_{10} & \mathbf{L}_{11} & \mathbf{L}_{12} & \mathbf{L}_{13} \\ \mathbf{L}_{20} & \mathbf{L}_{21} & \mathbf{L}_{22} & \mathbf{L}_{23} \\ \mathbf{L}_{30} & \mathbf{L}_{31} & \mathbf{L}_{32} & \mathbf{L}_{33} \end{bmatrix}. \tag{38}$$

Note that the (6x6) null matrices in (38_1) represent the coupling terms between average and gradient response. Thus, in a statistically homogeneous RVE, there is no coupling. In addition, it has been shown for spherical reinforcements (Zuiker and Dvorak, 1994b) and fibrous reinforcements (Zuiker and Dvorak, 1995) that for many RVEs, the effective properties of $\hat{\mathbf{L}}_{SH}$ relating the gradient response approach those of the average response. That is, $\mathbf{L}_{12}$, $\mathbf{L}_{13}$, $\mathbf{L}_{23}$, $\mathbf{L}_{21}$, $\mathbf{L}_{31}$, and $\mathbf{L}_{32}$ approach **0**, and $\mathbf{L}_{11}$, $\mathbf{L}_{22}$, and $\mathbf{L}_{33}$ approach $\mathbf{L}_{00}$.

In (38_2), the coupling terms are non-zero. Thus average loads applied to the RVE produce a gradient response, which is unaccounted for by the standard Mori-Tanaka method and most existing micromechanics formulations. To examine the magnitude and behavior of these terms, consider the case of spherical SiC reinforcements (E_{SiC} = 320 GPa, ν_{SiC} = 0.25) embedded in a continuous carbon matrix (E_C = 28 GPa, ν_C = 0.3). The reinforcing spheres are distributed at points that comprise a simple cubic lattice, and variable particle size is incorporated to produce the desired volume fraction gradient. The particle size is varied only in the x_1 direction such that the reinforcement volume fraction varies linearly as

$$c(\mathbf{x}) = c_0 + g x_1. \tag{39}$$

Figure 2 shows components of the (6x6) submatrices of both (38_1) and (38_2), $\mathbf{L}_{00}[3,3]$ and $\mathbf{L}_{11}[3,3]$, as a function of N, the number of particles along an edge of V. V is taken as a cube centered at the origin with edges aligned parallel to the coordinate directions. Thus, V contains N^3 particles. An RVE with N=2 is inset in Figure 2. N has little affect on the magnitude of $\mathbf{L}_{00}[3,3]$ for both graded and statistically homogeneous microstructures, but has significant effect on $\mathbf{L}_{11}[3,3]$. This sensitivity of $\mathbf{L}_{11}$ to N is more pronounced in fibrous composites and has been shown to compare well with experimental measurements (Zuiker and Dvorak, 1994a).

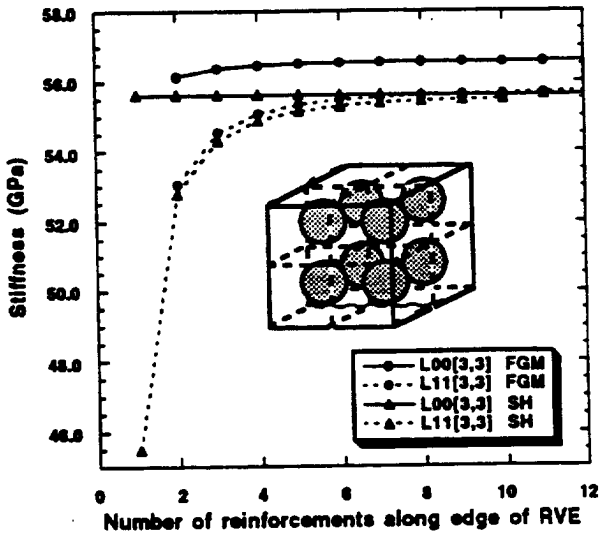


FIGURE 2
EFFECT OF NUMBER OF PARTICLES ON EFFECTIVE RESPONSE OF STATISTICALLY HOMOGENEOUS AND FUNCTIONALLY GRADED MATERIALS

Figure 3 shows components of $\mathbf{L}_{00}[3,3]$, $\mathbf{L}_{11}[3,3]$, $\mathbf{L}_{01}[3,3]$ and $\mathbf{L}_{10}[3,3]$ for an LVE that contains three particles along each 1 mm side and has a total SiC volume fraction of 0.25. These four stiffness terms give the average and x_1 variation of σ_{33} due to the average and x_1 variation in ε_{33}. It should not be surprising that $\mathbf{L}_{00}[3,3]$ and $\mathbf{L}_{11}[3,3]$ grow with increasing g. Starting at a fixed reinforcement volume fraction c_0, increasing c_0 by a specified amount will increase the average stiffness by an amount that is greater than the corresponding decrease in effective stiffness produced when c_0 is reduced by the same specified amount. Thus, as g increases, the LVE contains material of higher and lower effective stiffness, but the contribution of the increased stiffness region outweighs that of the reduced stiffness region.

An important observation from Figure 3b is that $\hat{\mathbf{L}}_{FGM}$ is *not* symmetric whereas $\hat{\mathbf{L}}_{SH}$ is symmetric (Zuiker and Dvorak, 1994b). Figure 3b also shows that a gradient in the applied strain field produces relatively little change in the resultant average stress field as evidenced by the low value of

$L_{01}[3,3]$ in comparison with $L_{00}[3,3]$ and $L_{11}[3,3]$. However, the average strain field produces a significant stress gradient for large g. This is evidenced by the fact that $L_{10}[3,3]$ is on the order of $L_{00}[3,3]$ and $L_{11}[3,3]$ for large g.

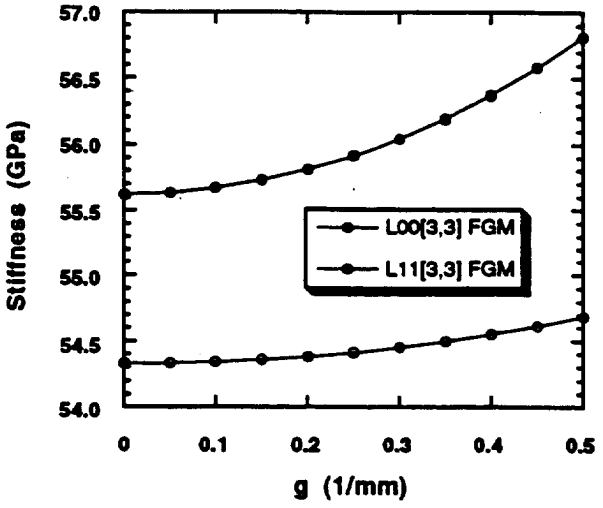


FIGURE 3A
EFFECT OF REINFORCEMENT GRADIENT ON EFFECTIVE STIFFNESS OF PARTICULATE SiC REINFORCED CARBON.

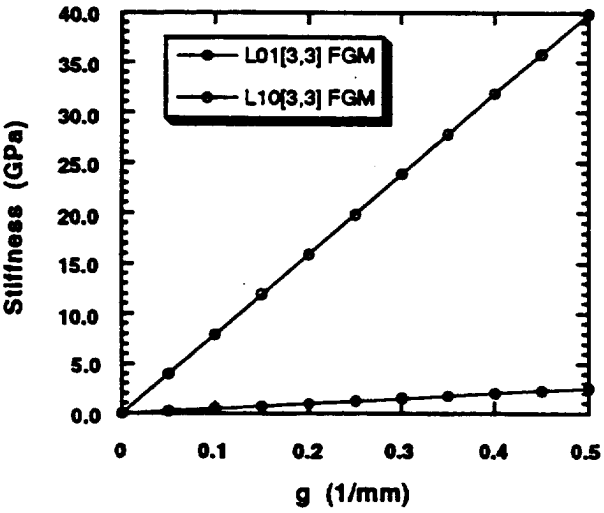


FIGURE 3B
EFFECT OF REINFORCEMENT GRADIENT ON COUPLING TERMS IN EFFECTIVE STIFFNESS OF PARTICULATE SiC REINFORCED CARBON..

4. CLOSURE

The modified Mori-Tanaka method has been shown to be useful in estimating coupling in the mechanical response of functionally graded composite materials. Simple examples show that these coupling effects can be significant. However, the magnitude of these effects in a given structure can only be determined by using these methods within a structural analysis, such as finite element methods, to determine the actual loads. Lack of such tools has raised the question of accuracy in previous structural analyses of FGMs that have not considered this coupling phenomena (McManus, 1993). These methods will require unique stiffness estimates in each element due to the variable reinforcement volume fraction. The method presented here is attractive in that estimates of $\hat{L}_{FGM}$ can be produced in a matter of seconds on a personal computer given material properties and microstructural information. Aboudi et al. (1994) have also investigated the coupling of the average and higher order response of FGMs by extending the Method of Cells (Aboudi, 1987). However, this method appears to require significantly more computational effort than the modified MTM.

Finally, the modified Mori-Tanaka method, as presented here, is suitable only for particulate microstructures wherein one phase may be taken as the continuous matrix phase and all others may be approximated as discrete ellipsoidal inhomogeneities suspended within the continuous matrix. In a typical functionally graded structure, one encounters a smooth transition from a suspension of phase A in a matrix of phase B, to an interpenetrating network of continuous phases A and B, to a suspension of phase B in a matrix of phase A. Work has been presented on estimating the properties of networked microstructures (Herano et al., 1991; Nan et al., 1993), but only within the standard micromechanics context in which coupling between average and higher order responses is neglected.

REFERENCES

Aboudi, J., 1987, "Closed Form Constitutive Equations for Metal Matrix Composites", International Journal of Engineering and Science, Vol. 25, pp. 1229-1240.

Aboudi, J., Pindera, M.-J., and Arnold, S.M., 1994, "Elastic response of metal matrix composites with tailored microstructures to thermal gradients", International journal of Solids and Structures, Vol. 31, pp. 1393-1428.

Asaro, R.J. and Barnett, D.M., 1975, "The Non-Uniform Transformation Strain Problem for an Anisotropic Ellipsoidal Inclusion", Journal of the Mechanics and Physics of Solids, Vol. 23, pp. 77-83.

Benveniste, Y., 1987, "A New Approach to the Application of Mori-Tanaka's Theory in Composite Materials", Mechanics of Materials, Vol. 6, pp. 147-157.

Benveniste, Y., Dvorak, G.J. and Chen, T., 1991, "On Diagonal and Elastic Symmetry of the Approximate Stiffness Tensor of Heterogeneous Media", Journal of the Mechanics and Physics of Solids, Vol. 39, pp. 927-946.

Chen, T., Dvorak, G.J. and Benveniste, Y., 1992, "Mori-Tanaka Estimates of the Overall Elastic Moduli of Certain Composite Materials", ASME Journal of Applied Mechanics, Vol. 59, pp. 539-546.

Christensen, R., Schantz, H. and Shapiro, J., 1992, "On the Range of Validity of the Mori-Tanaka Method", Journal of the Mechanics and Physics of Solids, Vol. 40, pp. 69-73.

Eshelby, J.D., 1957, "The Determination of the Elastic Field of an Ellipsoidal inclusion and Related Problems", Proceedings of the Royal Society of London A., Vol. 241, pp. 376-396.

Eshelby, J.D., 1961, "Elastic Inclusions and Inhomogeneities", Progress in Solid Mechanics, Vol. II, I.N. Sneddon and R. Hill, ed., North Holland, Amsterdam, pp. 89-140.

Ferrari, M., 199[illegible], "Asymmetry and the high concentration limit of the Mori-Tanaka effective medium theory", Mechanics of Materials, Vol. 11, pp. 251-256.

Herano, T., Teraki, J. and Yamada, T., 1991, "Applications of Fuzzy Theory to the Design of Functionally Gradient Materials", SMiRT 11 Transactions, Vol. SD1, pp. 49-54.

Hill, R., 1963, "Elastic Properties of Reinforced Solids: Some Theoretical Principles", Journal of the Mechanics and Physics of Solids, Vol. 11, pp. 357-372.

Margolin, G.G., 1967) "Elasticity Modulus in the Bending of Thin Specimens of a Unidirectional Glass-Reinforced Plastic", Polymer Mechanics, Vol. 3, pp. 492-493.

McManus, H.L., 1993, "Analysis Needs for Functionally Gradient Materials", TELAC Report 93-15, Massachusetts Institute of Technology, Cambridge.

Mori, T. and Tanaka, K., 1973, "Average Stress in Matrix and Average Elastic Energy of Materials with Misfitting inclusions", Acta Metallurgica, Vol. 21, pp. 571-574.

Muskhelishvili, N.I., 1953, Some Basic Problems of the Mathematical Theory of Elasticity, Noordhoff Ltd., Groningen.

Nan, C.-W., Yuan, R.-Z. and Zhang, L.-M., 1993, "The Physics of Metal/Ceramic FGMs", Functionally Gradient Materials, J.B. Holt et al., ed., The American Ceramic Society, Westerville, OH.

Pagano, N.J., 1974, "The Role of Effective Moduli in the Elastic Analysis of Composite Laminates", Composite Materials, G.P. Sendeckyj, ed., Academic Press, Inc.

Qiu, Y.P. and Weng, G.J., 1990, "On the application of Mori-Tanaka's theory involving transversely isotropic inclusions", International Journal of Engineering and Science, Vol. 28, pp. 1121-1137.

Sendeckyj, G.P., 1967, "Ellipsoidal Inhomogeneity Problem", Ph.D. Thesis, Northwestern University, Evanston, IL.

Zuiker, J.R., 1993, "Elastic and Inelastic Micromechanical Analysis of Functionally Graded Materials and Laminated Structures using Transformation Fields", Ph.D. Thesis, Rensselaer Polytechnic Institute, Troy, NY.

Zuiker, J.R. and Dvorak, G.J., 1994a, "On the Effective Properties of Functionally Graded Composites-I. Extension of the Mori-Tanaka Method to Linearly Varying Fields", Composites Engineering, Vol. 4, pp. 19-35.

Zuiker, J.R. and Dvorak, G.J., 1994b, "On the Effective Properties of Composite Materials by the Linear Field Mori-Tanaka Method", ASME Journal of Engineering Materials and Technology, in press

Zuiker, J.R. and Dvorak, G.J., 1995, "On the Elastic Response of Functionally Graded Materials with Large Gradients in Reinforcement Density", in preparation

SECURITY CLASSIFICATION OF THIS PAGE

REPORT DOCUMENTATION PAGE

Form Approved
OMB No. 0704-0188

1a. REPORT SECURITY CLASSIFICATION Unclassified	1b. RESTRICTIVE MARKINGS
2a. SECURITY CLASSIFICATION AUTHORITY	3. DISTRIBUTION / AVAILABILITY OF REPORT Unrestricted
2b. DECLASSIFICATION / DOWNGRADING SCHEDULE	
4. PERFORMING ORGANIZATION REPORT NUMBER(S)	5. MONITORING ORGANIZATION REPORT NUMBER(S)
6a. NAME OF PERFORMING ORGANIZATION CENTER FOR COMPOSITE MATERIALS AND STRUCTURES - RENSSELAER POLYTECHNIC INSTITUTE 6b. OFFICE SYMBOL (If applicable)	7a. NAME OF MONITORING ORGANIZATION OFFICE OF NAVAL RESEARCH
6c. ADDRESS (City, State, and ZIP Code) RENSSELAER POLYTECHNIC INSTITUTE TROY, NEW YORK 12180-3590	7b. ADDRESS (City, State, and ZIP Code) 800 NORTH QUINCY STREET ARLINGTON, VA 22217-5000
8a. NAME OF FUNDING / SPONSORING ORGANIZATION DEFENSE ADVANCED RESEARCH PROJECTS AGENCY 8b. OFFICE SYMBOL (If applicable)	9. PROCUREMENT INSTRUMENT IDENTIFICATION NUMBER #N00014-92J-1779
8c. ADDRESS (City, State, and ZIP Code) 1400 WILSON BLVD. ARLINGTON, VA 22209	10. SOURCE OF FUNDING NUMBERS PROGRAM ELEMENT NO. / PROJECT NO. / TASK NO. / WORK UNIT ACCESSION NO.

11. TITLE (Include Security Classification)
MECHANISM-BASED DESIGN OF COMPOSITE STRUCTURES

12. PERSONAL AUTHOR(S)
George J. Dvorak

13a. TYPE OF REPORT	13b. TIME COVERED	14. DATE OF REPORT (Year, Month, Day)	15. PAGE COUNT
FINAL	FROM 920501 TO 970830	970930	698

16. SUPPLEMENTARY NOTATION

17. COSATI CODES			18. SUBJECT TERMS (Continue on reverse if necessary and identify by block number)
FIELD	GROUP	SUB-GROUP	HIGH TEMPERATURE COMPOSITES, COMPUTER-AIDED DESIGN, PROCESSING, PERFORMANCE

19. ABSTRACT (Continue on reverse if necessary and identify by block number)

Final results obtained on the Mechanism-Based Design of Composite Structures Program at Rensselaer Polytechnic Institute, are described in three volumes. Volume one contains the Executive Summary and reprints of papers on Micromechanics and Computer-Aided Design Tools. Volume two is a continuation of reprints of papers on Micromechanics and Computer-Aided Design Tools. The third Volume contains reprints of papers on Processing and Performance.

20. DISTRIBUTION / AVAILABILITY OF ABSTRACT ☒ UNCLASSIFIED/UNLIMITED ☐ SAME AS RPT. ☐ DTIC USERS	21. ABSTRACT SECURITY CLASSIFICATION Unclassified
22a. NAME OF RESPONSIBLE INDIVIDUAL	22b. TELEPHONE (Include Area Code) / 22c. OFFICE SYMBOL